

REPORT DOCUMENTATION PAGE				Form Approved OMB No. 0704-0188	
Public reporting burden for this collection of information is estimated to average 1 hour per response, including the time for reviewing instructions, searching existing data sources, gathering and maintaining the data needed, and completing and reviewing the collection of information. Send comments regarding this burden estimate or any other aspect of this collection of information, including suggestions for reducing the burden, to Department of Defense, Washington Headquarters Services, Directorate for Information Operations and Reports (0704-0188), 1215 Jefferson Davis Highway, Suite 1204, Arlington, VA 22202-4302. Respondents should be aware that notwithstanding any other provision of law, no person shall be subject to any penalty for failing to comply with a collection of information if it does not display a currently valid OMB control number. PLEASE DO NOT RETURN YOUR FORM TO THE ABOVE ADDRESS.					
1. REPORT DATE (DD-MM-YYYY) 06-01-2004		2. REPORT TYPE Conference Proceedings		3. DATES COVERED (From - To) 9 September 2003 - 12 September 2003	
4. TITLE AND SUBTITLE 2003 International Conference on Antenna Theory and Techniques (ICATT)			5a. CONTRACT NUMBER FA8655-03-1-5060		
			5b. GRANT NUMBER		
			5c. PROGRAM ELEMENT NUMBER		
6. AUTHOR(S) Conference Committee			5d. PROJECT NUMBER <div style="font-size: 2em; font-weight: bold; text-align: center;">20040204 271</div>		
7. PERFORMING ORGANIZATION NAME(S) AND ADDRESS(ES) Kharkov National University of Radio Electronics Lenin Prospekt, 14 Kharkov 61166 Ukraine				REPORT NUMBER N/A	
9. SPONSORING/MONITORING AGENCY NAME(S) AND ADDRESS(ES) EOARD PSC 802 BOX 14 FPO 09499-0014				10. SPONSOR/MONITOR'S ACRONYM(S)	
				11. SPONSOR/MONITOR'S REPORT NUMBER(S) CSP 03-5060	
12. DISTRIBUTION/AVAILABILITY STATEMENT Approved for public release; distribution is unlimited.					
13. SUPPLEMENTARY NOTES Copyright 2003, IEEE. Available from: IEEE Operations Center, 445 Hoes Lane, P.O. Box 1331, Piscataway, NJ 08855-1331. The Department of Defense has permission to use for government purposes only. All other rights are reserved by the copyright holder.					
14. ABSTRACT The Final Proceedings for 2003 International Conference on Antenna Theory and Techniques (ICATT), 9 September 2003 - 12 September 2003 This is an interdisciplinary conference. Topics include: 1. General antenna theory; 2. Reflector, lens and hybrid antennas; 3. Antenna arrays; 4. Adaptive antennas, signal processing; 5. Broadband and multi-frequency antennas; 6. Low-gain, printed antennas 7. Antennas for mobile communication; 8. Antennas for remote sensing; 9. Antenna measurements; 10. Analytical and numerical methods; 11. Microwave components and circuits fiber-optics links; 12. Industrial and medical applications of microwave technologies 13. Electromagnetic compatibility; 14. Antenna radomes and absorbers; 15. Electromagnetism at the high school					
15. SUBJECT TERMS EOARD, Electromagnetics, Antennas					
16. SECURITY CLASSIFICATION OF:			17. LIMITATION OF ABSTRACT UL	18. NUMBER OF PAGES 2 Volumes	19a. NAME OF RESPONSIBLE PERSON MICHAEL KJ MILLIGAN, Lt Col, USAF
a. REPORT UNCLAS	b. ABSTRACT UNCLAS	c. THIS PAGE UNCLAS			19b. TELEPHONE NUMBER (Include area code) +44 (0)20 7514 4955

IVth International Conference on

Antenna Theory and Techniques

Volume 1

Organizers

National Antenna Association (NAA) of Ukraine
Kharkiv National University of Radio Electronics
Karazin Kharkiv National University
Sevastopol National Technical University
National Technical University of Ukraine "Kyiv Polytechnic
Institute"
Academy of Sciences of Applied Radio Electronics
IEEE AP/C/EMC/SP Kharkiv Joint Chapter of the Ukraine Section
Ministry of Education and Science of Ukraine

9 – 12 September 2003

Sevastopol, Ukraine

Best Available Copy

Co-organizers

Kharkiv Military University
National Academy of Sciences of Ukraine
Radio Astronomy Institute NASU

We wish to thank the following for their contribution to the success of this Conference:

Sponsorship

European Office of Aerospace Research and Development of the USAF
IEEE Region 8 Office

Scientific-Production Company "TERA Ltd" (Kyiv, Ukraine)

Scientific-Production Company "ROMSAT Ltd" (Kyiv, Ukraine)

Ternopil State Scientific-Production Enterprise "Promin" (Ukraine)

"UkrAviaZakaz Ltd" (Kyiv, Ukraine)

Scientific-Production Enterprise "Sovremennyye Volokonnye Materialy" ("Modern Fiber Materials") of the Ukrainian Academy of Sciences

Technical Support

IEEE AP-S

Publishing House IPRZhR (Moscow, Russia)

Publishing House "Izvestiya Vuzov" (Kyiv, Ukraine)

Moscow Chapter IEEE

This material is based upon work supported by the European Office of Aerospace Research and development under grant FA8655-03-15060

2003 International Conference on Antenna Theory and Techniques

IEEE Catalog Number:	03EX699
ISBN:	0-7803-7881-4
Library of Congress:	2003103227

Copyright and Reprint Permission: Abstracting is permitted with credit to the source. Libraries are permitted to photocopy beyond the limit of U.S. copyright law for private use of patrons those articles in this volume that carry a code at the bottom of the first page, provided the per-copy fee indicated in the code is paid through Copyright Clearance Center, 222 Rosewood Drive, Danvers, MA 01923. For other copying, reprint or republication permission, write to IEEE Copyrights Manager, IEEE Operations Center, 445 Hoes Lane, P.O. Box 1331, Piscataway, NJ 08855-1331. All rights reserved. Copyright ©2003 by the Institute of Electrical and Electronics Engineers, Inc.

ICATT'03 CHAIRMAN Yakov S. Shifrin, Ukraine

ICATT'03 TECHNICAL PROGRAM COMMITTEE

Co-Chairmen

Nicolay N. Kolchigin (Ukraine)

Fedor F. Dubrovka (Ukraine)

Members

Adrian Alden (Canada)

Lev D. Bakhrakh (Russia)

Alex B. Gershman (Canada)

Nicolay N. Gorobets (Ukraine)

David Jackson (USA)

Peter Edenhofer (Germany)

Elya Joffe (Israel)

Victor Kravchenko (Russia)

Kees van't Klooster (the Netherlands)

Aleksander A. Konovalenko (Ukraine)

David I. Lekhvitskiy (Ukraine)

Anatoly S. Ilinskiy (Russia)

Leo Ligthart (the Netherlands)

Lyubov M. Lobkova (Ukraine)

Konstantin A. Lukin (Ukraine)

Sergey A. Masalov (Ukraine)

Josef Modelski (Poland)

Gennadiy A. Morozov (Russia)

Dimitry M. Sazonov (Russia)

Hiroshi Shigesawa (Japan)

Tadashi Takano (Japan)

Dimitry I. Voskresensky (Russia)

Felix Yanovski (Ukraine)

Yuriy Yukhanov (Russia)

Vadim I. Zamyatin (Ukraine)

Wen Xun Zhang (China)

ICATT'03 ORGANIZING COMMITTEE

Co-Chairmen

Mukhailo F. Bondarenko (Ukraine)

Victor A. Karpenko (Ukraine)

Members

Aleksander G. Luk'yanchuk

Vladimir M. Shokalo (Ukraine)

Victor A. Katrich (Ukraine)

Vladimir I. Karpenko (Ukraine)

Aleksander I. Dokhov (Ukraine)

Gennadiy I. Churyumov (Ukraine)

Mikhail B. Egorov (Ukraine)

Marianna V. Ivashina (the Netherlands)

Vyacheslav V. Khardikov (Ukraine)

Nina G. Maksimova (Ukraine)

Vladimir I. Pravda (Ukraine)

Yaroslav O. Rospopa (Ukraine)

Anna V. Shishkova (Ukraine)

Vladimir G. Syrotyuk (Ukraine)

Peter L. Tokarsky (Ukraine)



Welcome to ICATT'2003 !

During four days (9-12 September, 2003) Sevastopol will be a host of the International Conference on Antenna Theory and Techniques (ICATT'03). Since 1995 it is the fourth meeting of such a kind in Ukraine. To a certain degree, ICATT is a successor of the regularly held earlier in the USSR antenna conferences organized and unchangeably chaired by Aleksander A. Pistol'kors - the widely recognized head of the Soviet antenna school.

It should be noted that notwithstanding hard times that Ukraine and Russia go through now, the antenna science keeps actively advancing. The evidence of this is the present conference, whose scale remarkably exceeds that of previous ICATTs in the number of presented papers, the number of participants and the number of guests from "far and near abroad". Over 220 papers have been submitted to the ICATT'03 Program Committee from

Ukraine, Russia, Mexico, the Netherlands, Japan, Italy, USA, Canada, Belarus, Azerbaijan, Ireland, Denmark, France, Austria, Poland, China, Korea. These papers are to be presented at three morning plenary sessions and at afternoon meetings of 14 sessions.

Special attention was paid to selection of invited speakers among the recognized antenna scientists from different countries. Undoubtedly, their review presentations in a number of the modern applied electromagnetics directions will be met by the ICATT'03 participants with a great interest and will be especially useful for young scientists. I am also sure that with a great interest the conference participants will attend on the 12th of September the Ukraine National Centre of Space Vehicles Control and Tests in Eupatoria, where they can become acquainted with a number of unique large antennas.

All this gives me a confidence that ICATT'03 will be fruitful and stimulative for a further progress of antenna science and engineering.

ICATT03 is being held in Sevastopol rich with many monuments reflecting ancient and heroic history of this wonderful maritime city. The ICATT'03 attendees will take also a chance to seeing sights of the Southern Coast of the Crimea. There are planned also other exciting social events. All this will additionally adorn your stay in Sevastopol.

I would like to thank all organizers, many my colleagues who performed a bulky work on the conference preparation and publishing its Proceedings, and of course all the participants who have made ICATT'03 possible.

I would like also to thank our sponsors (especially European Office of Aerospace Research and Development of the USAF) for their financial contribution to the ICATT'03 organization and support of young scientists.

I wish all the ICATT'03 participants a successful work at the conference meetings, pleasant contacts with colleagues and nice time in the sunny Crimea on the shore of the warm Black Sea.

Yakov S. Shifrin

Chairman of ICATT'2003

TABLE OF CONTENTS

VOLUME I

INVITED PAPERS

01. GPR ANTENNA SIMULATIONS AND OPTIMIZATIONS IN TIME DOMAIN <i>L. P. Ligthart, A. G. Yarovoy, A. Y. Kirana</i>	21
02. APERTURE ANTENNA RADIATION <i>D. J. Kozakoff and V. Tripp</i>	25
03. ROBUST ADAPTIVE BEAMFORMING: AN OVERVIEW OF RECENT TRENDS AND ADVANCES IN THE FIELD <i>A. B. Gershman</i>	30
04. ON LOSSES OF COHERENT SIGNAL IN THE ADAPTIVE DETECTOR WITH NON- COHERENT INTEGRATION <i>D. I. Lekhovitskiy, P. M. Flekser, S. V. Polishko</i>	36
05. FOCUSING OF THE SPATIALLY SEPARATED ADAPTIVE ANTENNA ARRAYS ON MULTIPLE RADIATION SOURCES BY METHOD OF CORRELATION IDENTIFICATION OF THE BEARINGS <i>Yu. N. Sedyshev, P. Yu. Sedyshev, S. N. Rodenko</i>	42
06. EXPERIENCE OF ANTENNA COMPLEXES CREATION FOR THE RADARS OF DISTANT DETECTING AND SPACE AREA MONITORING <i>G. A. Evstropov, V. A. Rogulyev, S. D. Saprykin, V. P. Sosulnikov, E. A. Starostenkov</i>	47
07. HIGH-PERFORMANCE HORNS WITH OPTIMIZED WAVING TAPER <i>H. Deguchi, M. Tsuji, H. Shigesawa</i>	52
08. RADIO TELESCOPE RT-70 IN EVPATORIA AND SPACE INVESTIGATIONS <i>A. A. Konovalenko, L. N. Lytvynenko, C. G. M. van't Klooster</i>	57
09. NEEDS FOR GIGANTIC ANTENNAS FOR SPACE USE AND THEIR TECHNICAL PROBLEMS <i>T. Takano</i>	63
10. TRACKING AND COMMUNICATION MEANS DEVELOPED AT THE SPECIAL MECHANICAL ENGINEERING DESIGN OFFICE <i>V. G. Himmelman, G. S. Kuchinsky</i>	68
11. REMOTE SENSING OF TROPOSPHERE FOR AVIATION SAFETY: ANTENNA ASPECT <i>F. J. Yanovsky</i>	71
12. BROADBAND PHASED ARRAY WITH WIDE-ANGLE SCANNING <i>D. I. Voskresensky, E. V. Ovchinnikova</i>	77
13. MICROWAVE DEVICES WITH THE DISTRIBUTED NONLINEARITY <i>Ya. S. Shifrin, A. I. Luchaninov</i>	81
14. MULTI-FACED AND MULTIBEAM DBF ANTENNA FOR HIGH ALTITUDE PLATFORM STATION STAGES OF ANTENNA DEVELOPMENT <i>B.-J. Ku, Y.-S. Kim, B.-S. Kang, D.-S. Ahn, A. S. Belyaev, Ye. N. Egorov, N. V. Vladimirov, S. A. Ganin, A. C. Reutov, Yu. A. Suserov, A. M. Shitikov, A. V. Shishlov, A. G. Shubov</i>	87
15. WIDEBAND DUAL POLARIZED PLANAR ANTENNA ARRAYS <i>F. F. Dubrovka, S. Y. Martynyuk</i>	91

16. MODELING AND SIMULATION OF THE FUSED BAYESIAN-REGULARIZATION METHOD FOR REMOTE SENSING IMAGERY WITH SYNTHETIC APERTURE ARRAYS <i>Y. V. Shkvarko, J. L. Leyva-Montiel, J. Acosta-Salas</i>	97
17. DEVELOPMENT OF MICROWAVE TECHNOLOGIES FOR THE OIL AND GAS EXTRACTION COMPLEX <i>G. A. Morozov, O. G. Morozov, M. R. Galimov</i>	101

GENERAL ANTENNA THEORY

01. THE DIFFER-INTEGRAL THEORY OF FRACTAL ANTENNAS <i>V. M. Onufriyenko</i>	107
02. EXACT ABSORBING CONDITIONS IN INITIAL BOUNDARY-VALUE PROBLEMS OF THE THEORY OF PULSE WAVE RADIATION <i>Yu. K. Sirenko, V. L. Pazynin, A. I. Vyazmitinova, K. Yu. Sirenko</i>	110
03. ANALYSIS OF SCATTERING BY INHOMOGENEOUS DIELECTRIC OBJECTS WITH HIGHER-ORDER HIERARCHICAL MOM <i>O. S. Kim, E. Jørgensen, P. Meincke, O. Breinbjerg</i>	113
04. DECOUPLING OF APERTURE ANTENNAS WITH IMPEDANCE STRUCTURES <i>D. J.-F. Essiben, Y. V. Yukhanov</i>	117
05. SYNTHESIS OF ANISOTROPIC IMPEDANCE PLANE <i>Yu. V. Yukhanov</i>	121
06. ANALYSIS OF WAVEGUIDE-SLOT RADIATORS IN THE PRESENCE OF DISSIPATIVE MEDIUM <i>L. P. Yatsuk, A. A. Komyachko, Yu. V. Zhironkin, T. G. Nazarenko</i>	125
07. THE SYNTHETIC APERTURE METHOD IN THE ENVIRONMENT MICROWAVE INTERFEROMETER RADIOMETRY <i>B. G. Kutuza, G. K. Zagorin</i>	130
08. CALCULATION OF MUTUAL COUPLING COEFFICIENTS IN PRESENCE CYLINDER <i>M. Yu. Zvezdina</i>	134
09. ACCOUNT OF CYLINDRICAL BODIES PECULIARITIES IN THE ANALYSIS OF DIPOLE CHARACTERISTICS <i>M. Yu. Zvezdina</i>	138
10. FIELD OF A SURFACE ANTENNA BASED ON AN IMPEDANCE CYLINDER <i>D. D. Gabriel'yan, M. Yu. Zvezdina, O. S. Labunko</i>	141
11. SCATTERING OF ELECTROMAGNETIC FIELDS ON COMPLEX SPATIAL LATTICES OF MAGNETODIELECTRIC SPHERES <i>A. I. Kozar</i>	145
12. METHOD OF GENERALIZED EIKONAL AND NEW 2-D SCATTERING ANALYTICAL SOLUTIONS <i>M. V. Vesnik</i>	149
13. THE VIDEOPULSE SCATTERING IN INHOMOGENEOUS MEDIA CONTAINING CONDUCTIVE CYLINDER OBJECTS <i>L. A. Varyanitz-Roshchupkina</i>	152
14. THE LINEAR WIRE IN ANISOTROPIC MEDIUM <i>E. O. Yatsenko, N. M. Yatsenko</i>	156
15. THE KONTOROVICH-LEBEDEV TRANSFORMS AND THE SEMI-INVERSION METHOD IN MODEL EXCITATION PROBLEMS FOR A SLOTTED CONICAL ANTENNAS <i>V. A. Doroshenko</i>	158
16. MUTUAL RESISTANCES BETWEEN HORIZONTAL WIRE ANTENNAS NEAR AN INTERFACE <i>P. L. Tokarsky</i>	161
17. EFFECT OF MUTUAL COUPLING IN CRUCIFORM DIPOLE ON SCATTERING PERFORMANCES <i>T. V. Peretyatko</i>	165

18. THE STATISTICAL TESTS METHOD APPLICATION FOR CALCULATING OF THE AXISYMMETRIC ANTENNAS CHARACTERISTICS <i>G. A. Levagin, I. N. Bondarenko, V. N. Chepiga</i>	168
19. THE USE OF THE RELATIVISTIC EFFECT FOR OBTAINING NEGATIVE PERMITTIVITY <i>K. N. Klimov, B. V. Sestroretsky, V. A. Ruchenkov, T. V. Kamishev, S. M. Godin, V. V. Roshchin</i>	171
20. THE MODEL OF CREATION OF ROTATING STATIONARY ELECTROMAGNETIC FORMATIONS IN VACUUM <i>B. V. Sestroretsky, K. N. Klimov, S. M. Godin, V. V. Roshchin, T. V. Kamishev, V. A. Ruchenkov</i>	173
21. MODELING OF PLANE ELECTROMAGNETIC WAVE DIFFRACTION ON A CONICAL ANTENNA <i>E. K. Semenova, V. A. Doroshenko</i>	178

ANTENNA SYNTHESIS

01. THE THEORY OF FRACTAL ANTENNA ARRAYS <i>V. F. Kravchenko</i>	183
02. R-FUNCTION THEORY IN PROBLEMS OF ELECTROMAGNETIC WAVE RADIATION FROM ARBITRARILY SHAPED WAVEGUIDES <i>V. F. Kravchenko, M. A. Basarab</i>	190
03. SOLVING AN ARBITRARILY SHAPED FLAT RADIATOR SYNTHESIS PROBLEM BY THE R-FUNCTION METHOD <i>M. A. Basarab</i>	196
04. SYNTHESIS OF RESONANT ANTENNAS WITH SEMITRANSSPARENT EXTERNAL BOUNDARIES <i>M. I. Andriychuk, O. F. Zamorska</i>	199
05. THE USE OF ATOMIC FUNCTION FOR INNER PROBLEM SOLUTION FOR WIRE ANTENNAS <i>Y. Y. Bobkov</i>	203
06. AN OVERVIEW OF APPLICATIONS OF THE APERTURE ORTHOGONAL POLYNOMIALS METHOD IN THE DEVELOPMENT OF ANTENNA SYSTEMS <i>V. I. Gusevsky</i>	206
07. EMPLOYING THE APERTURE ORTHOGONAL POLYNOMIALS METHOD IN THE DESIGN OF SPARSE UNEQUALLY SPACED PHASED ARRAYS <i>V. I. Gusevsky, M. V. Lavrentiev</i>	209
08. ABOUT ONE GRADIENT PROCEDURE OF DETERMINATION OF THE BRANCHING POINTS OF NONLINEAR INTEGRAL EQUATION ARISING IN THE THEORY OF ANTENNA SYNTHESIS <i>B. M. Podlevskiy</i>	213
09. APPLICATION OF THE KRAVCHENKO-DARBOUX AND KRAVCHENKO- BESICOVITCH TWO-DIMENSIONAL FRACTAL FUNCTIONS IN ANTENNA THEORY <i>V. M. Masyuk</i>	216
10. METHODS FOR MATHEMATICAL MODELING OF FRACTAL ANTENNA ARRAYS <i>V. M. Masyuk</i>	220
11. THE METHOD FOR APPROXIMATION OF A TWO-DIMENSIONAL FIELD DISTRIBUTION BY ATOMIC FUNCTIONS <i>M. V. Golubin</i>	224

REFLECTOR AND LENS ANTENNAS

01. ANALYSIS OF PARTIALLY DIELECTRIC-LOADED COAXIAL HORN ANTENNAS <i>F. F. Dubrovka, O. O. Krupnov, V. O. Rospopa</i>	229
02. SYNTHESIS OF OFFSET-FED GREGORIAN VSAT ANTENNAS <i>F. F. Dubrovka, R. F. Dubrovka, O. S. Kim, V. H. Syrotyuk, H. P. Khymych</i>	233
03. SIMULATIONS OF THE ESA PLANCK HFI BEAMS OF POLARIZED AND MULTI-MODE HORNS <i>V. B. Yurchenko, J. A. Murphy, J.-M. Lamarre</i>	237
04. DIRECTIVITY OF RECTANGULAR APERTURE ELECTROMAGNETIC RADIATION <i>S. V. Butakova</i>	241
05. THE INVESTIGATION OF RADIATION CHARACTERISTICS OF FRESNEL ANTENNA FOR Q-BAND <i>V. I. Magro, V. M. Morozov</i>	245
06. CALCULATION OF NON-AXISYMMETRICAL PARABOLIC REFLECTOR ANTENNAS <i>A. V. Alpatova, A. M. Gorin, I. N. Kad'kalo</i>	248
07. COMBINED REFLECTOR - LENS MONOPULSE ANTENNA <i>M. P. Natarov, V. V. Glamazdin, V. N. Skresanov, A. I. Shubny</i>	251
08. AN ULTRA-WIDEBAND FEED FOR AXISSYMMETRICAL REFLECTOR ANTENNA <i>M. M. Bilanovskij, V. M. Glushenko, G. O. Ena, M. M. Litvin, S. M. Litvin, O. E. Shrenk</i>	255
09. COMPARISON OF THE EFFICIENCY OF VARIOUS OPTIMIZATION METHODS IN THE PROBLEMS OF THE FOCUSED APERTURE <i>O. V. Potapova</i>	258
10. ON A PROBLEM OF IMPLEMENTATION OF MONOPULSE SELF-STEERING ON AN INFORMATION SIGNAL <i>A. V. Usichenko, A. S. Soroka, Y. A. Umzar, A. G. Rudnik</i>	261
11. HYBRID ANTENNAS WITH SHAPED REFLECTORS FOR LIMITED BEAM STEERING <i>A. S. Reutov, A. V. Shishlov</i>	264
12. REFLECTIVITY OF ROUGH METAL SURFACES OVER MILLIMETER WAVE RANGE <i>R. V. Vorobjov</i>	268

ANTENNA ARRAYS

01. CLOSELY SPACED TRANSVERSE SLOTS IN RECTANGULAR WAVEGUIDE <i>S. L. Berdnik, V. A. Katrich, V. A. Lyaschenko</i>	273
02. LEAKY-WAVE ANTENNA WITH INCLINED SLOTS IN A WAVEGUIDE <i>V.A. Katrich, S. A. Martynenko, S. V. Pshenichnaya</i>	276
03. ASYMPTOTIC SOLUTION OF INTEGRAL EQUATION INTO A PROBLEM OF COUPLING BETWEEN WAVEGUIDES THROUGH NARROW SLOTS <i>M. V. Nesterenko V. A. Katrich</i>	280
04. FORMING A PARTIALLY POLARIZED WAVE BY NON-COHERENT SOURCES OF THE NOISE FIELD <i>L. G. Kornienko, V. A. Kovalchuk</i>	285
05. A NOVEL APPROACH TO SCANNING ANTENNAS DESIGN <i>K. A. Lukin</i>	288

06. SYNTHETIC APERTURE ANTENNA FOR NEAR FIELD APPLICATIONS	<i>K. A. Lukin, M. P. Natarov, V. N. Skresanov</i>	290
07. LASER SEISMO-ACOUSTIC ANTENNA ARRAY	<i>M. N. Dubrov, R. F. Matveev</i>	294
08. PHASED ARRAY ANTENNA ON A RADIAL WAVEGUIDE	<i>E. N. Voronin, F. I. Emel'chenkov, Yu. V. Kotov, A. S. Luk'yanov</i>	296
09. AN ANTENNA SYSTEM OF A CONTINUOUS WAVE RADAR	<i>S. D. Andrenko, I. A. Vyazmitinov and Y. B. Sidorenko</i>	300
10. IN-PHASE EXCITATION OF INFINITE PHASED ANTENNA ARRAY	<i>S. V. Chumachenko</i>	304
11. THE SCANNING ANTENNA FOR A 3-MM MULTICHANNEL RADIOMETER	<i>A. P. Yevdokymov and V. V. Kryzhanovskiy</i>	307
12. METHOD OF ELIMINATING INTERFERENCE NOUGHTS OF RADIATION PATTERN OF BASE STATION ANTENNA ARRAY	<i>V. Yatskevich, Ye. Bulikov</i>	310
13. INVESTIGATION OF PERIODICAL SEQUENCES OF CIRCUMFERENTIAL SLOTS IN CIRCULAR WAVEGUIDES	<i>S. A. Pogarsky and V. A. Chumachenko</i>	312
14. SWITCHING HEMISPHERICAL ANTENNA ARRAY	<i>E. V. Lukashuk, Y. V. Kolosova</i>	315
15. A LINEAR DOLPH - CHEBYSHEV ANTENNA GRID FOR SPEAKING-TRUMPET RADIATORS	<i>V. N. Bakhvalov, V. F. Kulishenko, E. V. Lukashuk</i>	318
16. LINEAR PHASED ANTENNA ARRAY WITH LOW LEVEL OF SIDE RADIATION	<i>V. N. Bakhvalov, V. A. Burmasov, Yu. V. Klonova, Yu. V. Kolosova</i>	320
17. SUPPRESSION OF MUTUAL INFLUENCE OF ANTENNA CHANNELS, WHICH ACCOMPLISH SELF-POINTING GUIDED BY INFORMATION SIGNAL THROUGH GEOMETRIC RATIOS OPTIMIZATION OF IRRADIATORS CONSTRUCTION	<i>Y. V. Kolosova, V. N. Rudenko, V. A. Burmasov</i>	323
18. PERISCOPE ANTENNA RERADIATOR BASED ON TWO COUPLED ARRAYS	<i>V. I. Zamiatin, V. N. Perekaty, Y. V. Yefimova</i>	327

ADAPTIVE ANTENNA ARRAYS AND SIGNAL PROCESSING

01. WEIGHT ERROR LOSS IN MIMO SYSTEMS WITH ADAPTIVE TRANSMIT AND RECEIVE BEAMFORMERS	<i>V. T. Ermolayev, A. G. Flaksman, I.P. Kovalyov, I. M. Averin</i>	333
02. ORTHOGONALIZED ALGORITHMS FOR FIR ANC ADAPTIVE SYSTEMS	<i>D. Tapia-Sanchez, R. Bustamente Bello, H. Perez-Meana and M. Nakano-Miyatake</i>	337
03. DECISION FEEDBACK EQUALIZERS FOR HIGH SPEED DATA COMMUNICATIONS	<i>E. G. Lee, J. A. Bastián, M. Nakano-Miyatake, H. Pérez-Meana</i>	341
04. EXPERIMENTAL INVESTIGATIONS OF AN INTERFERENCE CANCELLER WITH THE MODULATION ALGORITHM OF THE WEIGHING COEFFICIENTS GENERATION	<i>S. V. Artuyinov, A. V. Kobzev, V. R. Khachaturov</i>	345
05. OPTIMAL ARRAY MULTIMODE SIGNAL PROCESSING IN THE PRESENCE OF MODAL MISMATCH	<i>E. Yu. Gorodetskaya, D. M. Kharlamova, A. I. Malekhanov</i>	348

06. THE OPTIMIZATION OF A SIGNAL PROCESSING IN RADAR WITH SCANNING ANTENNA ARRAY <i>A. D. Pluzhnikov, E. N. Pribludova</i>	352
07. SPACE-TIME PROCESSING IN THREE-DIMENSIONAL FORWARD SCATTERING RADAR <i>A. V. Myakinkov, A. G. Ryndyk</i>	355
08. THE ROBUST SPATIOTEMPORAL FILTERING OF SIGNALS IN CORRELATED NOISE <i>O. V. Sytnik</i>	359
09. HYBRID OPTOELECTRONIC PROCESSOR FOR DETECTION, DIRECTION FINDING AND RECEPTION OF COMPLEX SIGNALS <i>A. Yu. Grinev, D. V. Bagno, V. V. Rozdobudko, V. S. Temchenko</i>	362
10. ANTENNA ARRAY SIGNAL PROCESSING WITH SUPERRESOLUTION BY 2-D UNITARY TLS-ESPRIT WITH STRUCTURE WEIGHTING <i>V. I. Vasylyshyn</i>	366
11. QUALITATIVE INDICES OF THE METHOD OF DETERMINING THE NUMBER OF SIMULTANEOUSLY ACTING SIGNALS <i>N. M. Nikitin, L. G. Shatsman</i>	370
12. CORRECTION OF SMART ANTENNAS RECEIVING CHANNELS CHARACTERISTICS FOR 4G MOBILE COMMUNICATIONS <i>V. I. Slyusar, I. V. Titov</i>	374
13. THE VARIANT OF EQUATION OF DIRECTION FINDING CHARACTERISTIC OF THE AMPLITUDE SUM-DIFFERENCE DIRECTION FINDER <i>V. A. Kryachko</i>	376
14. THE PERSPECTIVE DIRECTIONS OF THE TECHNICAL MODERNIZATION OF INTER-PERIOD SIGNAL PROCESSING SYSTEMS OF PULSE ATC RADARS <i>D. I. Lekhovitsky, V. I. Zaritsky, I. G. Kirillov, S. I. Burkovsky</i>	378
15. MEASUREMENTS OF RECEPTION DIRECTION OF DETERMINISTIC SIGNAL AGAINST SPATIALLY-CORRELATED INTERFERENCES WITH THE USE OF THE ADAPTIVE ANTENNA ARRAY <i>S. T. Bagdasaryan, V. A. Tarshin, V. A. Vasilyev</i>	381
16. ALGORITHM OF SPATIAL SELECTION OF UNCORRELATED SIGNALS <i>O. Z. Sultanov</i> ..	384
17. THE METHOD OF DETERMINATION OF THE AMPLITUDE AND PHASE DISTRIBUTION IN ANTENNA APERTURE PLANE <i>I. B. Shirokov</i>	387
18. COMPUTER SIMULATION OF TARGET BACKSCATTERING AS ELEMENT OF PERSPECTIVE RADAR DESIGN <i>S. P. Leshchenko, V. M. Orlenko, Y. D. Shirman</i>	389
19. COMBINED DIRECTION FINDERS OF NOISE RADIATION SOURCES BASED ON ADAPTIVE LATTICE FILTERS <i>D. I. Lekhovitsky, D. V. Atamansky, V. V. Djus, N. A. Staheev</i>	394
20. PERFECTION OF THE ALGORITHM FOR UNCORRELATED SIGNALS ANGULAR DISCRIMINATION BY MEANS OF WAVELET TRANSFORMATION <i>L. A. Titarenko, B. Yu. Bordjugov</i>	398
21. EFFECTIVE PARAMETER ESTIMATION OF EXPONENTIAL SIGNALS IN ADAPTIVE ARRAYS <i>M. V. Andreev, O. O. Drobakhin</i>	401
22. MULTI-BASE INSAR WITH ENHANCED SIGNAL PROCESSING <i>A. V. Ksendzuk, V. K. Volosyuk</i>	405
23. PHASED ANTENNA ARRAY WITH EXCITATION ADAPTIVE TO CONSTRUCTION DISTORTIONS <i>U. R. Liepin, D. V. Karlov, G. A. Golovin, N. N. Petrushenko</i>	409
24. AN ADAPTIVE PARAMETER ESTIMATION OF GAUSSIAN SIGNAL IN THE PRESENCE OF AN UNKNOWN GAUSSIAN NOISE <i>V. I. Turchin</i>	411

25. AN ADAPTIVE PARAMETRIC ESTIMATION OF SPACE-TIME DETERMINISTIC SIGNAL AGAINST UNKNOWN GAUSSIAN NOISE BACKGROUND <i>A. A. Rodionov, V. I. Turchin</i>	414
26. ADAPTIVE ALGORITHM OF FILTRATION OF TARGET TRAJECTORY PARAMETERS <i>V. D. Karlov, U. I. Rafalskii, S. V. Yarovoy, N. N. Petrushenko, A. V. Chelpanov</i>	417
27. SIGNAL PROCESSING USING METHODS OF DIMENSIONALITY REDUCTION OF REPRESENTATION SPACE <i>V. V. Popovskiy</i>	419
28. ADAPTIVE ANTENNA ARRAYS IN THE AUXILIARY RECEIVING CHANNEL OF THE INTERFERENCE COMPENSATOR FOR USER RADIOACCESS SYSTEMS <i>Yu. Yu. Kolyadenko</i>	421
29. INTELLECTUAL ANTENNAS AND ELECTROMAGNETIC COMPATIBILITY IN THE FUTURE SYSTEMS OF MOBILE COMMUNICATION <i>V. S. Blinov</i>	424

VOLUME IV

LOW-GAIN ANTENNAS, PRINTED ANTENNAS, ANTENNAS FOR MOBILE COMMUNICATIONS

01. ELEMENT SHAPE OPTIMIZATION OF PLANAR PERIODIC STRUCTURES <i>M. Bozzi and L. Perregini</i>	453
02. TOTAL ANALYSIS OF RADIATION CHARACTERISTICS OF ELECTRIC DIPOLE WITH RECTANGULAR SCREEN <i>N. N. Gorobets, N. P. Yeliseyeva</i>	459
03. POLARIZATION CHARACTERISTICS OF AN OPEN-ENDED CIRCULAR WAVEGUIDE <i>A. V. Shishkova, S. N. Pivnenko, N. N. Gorobets</i>	465
04. COMPUTATIONAL METHOD FOR LINEAR ANTENNAS WITH IMPEDANCE ELEMENTS <i>N. N. Gorobets and V. V. Ovsyanikov</i>	468
05. RADIATION FIELD OF A CYLINDRICAL SPIRAL NEAR TO A SMALL REFLECTOR OF CASSEGRAIN ANTENNA <i>L. M. Lobkova</i>	472
06. ONE-REFLECTING HYBRID ANTENNA <i>L. M. Lobkova, V. V. Golovin, M. A. Boromekova, U. N. Tyschuk</i>	474
07. ON IMPROVEMENT OF THE RADIATION PERFORMANCE OF THE OPEN-ENDED CIRCULAR WAVEGUIDE <i>S. P. Skobelev</i>	477
08. MICROWAVE METAL DISK ANTENNA WITH AXIS-SYMMETRIC EXCITATION <i>I. Ivanchenko, A. Korolev, S. Karelin, E. Laz'ko, N. Lukyanova (Bliznyuk), N. Popenko</i>	481
09. THE ANTENNA SYSTEM FOR THE BASE STATION OF MOBILE COMMUNICATION <i>A. V. Antonov and Yu. M. Gerasimov</i>	485
10. THE METHOD TO NOISE RESISTANT RISING FOR BIORTHOGONAL ANTENNA SYSTEM <i>A. E. Mishchenko</i>	488
11. MODELLING OF THE MULTIPLE-ARM CONICAL SPIRAL ANTENNAS FOR VARIOUS APPLICATIONS <i>M. B. Protsenko, A. V. Lukyanchikov, A. V. Troitskiy, P. A. Komarov</i>	491

INVITED PAPERS

GPR ANTENNA SIMULATIONS AND OPTIMIZATIONS IN TIME DOMAIN

L. P. Ligthart, A. G. Yarovoy, A. Y. Kirana

International Research Centre for Telecommunications-Transmission and Radar
Faculty of Information Technology and Systems Delft University of Technology
Mekelweg 4, 2628 CD Delft, The Netherlands
<l.p.ligthart@irctr.tudelft.nl>, <a.yarovoy@irctr.tudelft.nl>

Abstract

The development and optimization of transient antennas for Ground Penetrating Radar would be difficult without numerical simulations of their performance. To this end the FDTD algorithm should be considered as a useful and powerful tool for transient antenna analysis. As an example of such analysis we describe simulations of the dielectric wedge antenna. Good agreement between theoretical predictions and experimental results was observed. Some of the antenna characteristics (like the radial component of the electric field in the near zone, the radiated waveform and the antenna footprint in different grounds) cannot be measured easily, so the correct theoretical (numerical) model is essential for their determination. The numerical model of the antenna can also be used for optimization of the antenna. As an example of such optimization we present a design of the shield for the dielectrically embedded dipole antenna.

Keywords: transient antennas, finite-difference time-domain algorithm, Ground Penetrating Radar.

1. INTRODUCTION

There are only a few types of antennas widely used in Ground Penetrating Radar (GPR) systems: resistively loaded bow ties, TEM horns and their modifications and spiral antennas (Daniels, 1996). Every antenna type has its advantages and disadvantages, and not any of these types fully satisfy the demands of the GPR designers. That is why it is believed that a main breakthrough in GPR hardware can be achieved in optimizing the antenna system. GPR antennas possess two principal features: they are (ultra) wideband and they couple EM energy into the ground. Additionally, antennas used in video impulse GPR should handle transient signals properly (they should physically transmit and receive short pulses of EM energy). The improvement of existing transient antennas and the development of new ones can be accelerated considerably by performing accurate numerical simulations and numerical optimizations of different antenna prototypes. To this end fast forward solvers, preferably in time domain, are required. The mathematical background for such solvers can be either the integral equation method (Rao and Wilton, 1991) or finite difference (finite element) time domain (Taflove, 1995) algorithms.

The integral equation method is widely used for simulations of metal transient antennas (f.e. Lestari, Yarovoy and Ligthart, 2001; Leat, Shuley and Stick-

ley, 1998). However, this method suffers from two serious disadvantages. First, simulations should be performed in frequency domain (in time domain the method leads to numerically unstable algorithms) and thus it is very difficult to visualize the transient processes in the antenna (which is very helpful for the antenna designer). Second, the method does not allow simulation of antennas that consists of both metal and dielectric parts (in widely-used realizations of the method dielectric parts should be separated by at least one cell of the mesh from the metal, however from experiments it is known that such separation drastically changes the antenna properties).

Finite-Difference (and Finite-Element) Time-Domain algorithms are free from both above-mentioned disadvantages. These algorithms allow the simulation of fields in complicated structures, which can include both dielectrics and metals (Taflove, 1995). The simulations are performed directly in time domain, so the visualization of transient processes in antennas can be done straightforwardly. Also the ground can be incorporated easily into the model without increasing the complexity of the model (in the integral equation method the ground can be incorporated via the Green's functions. It increases the complexity of the algorithm, requires the air-ground interface to be flat and is computational time intensive. Despite of its simplicity and general applicability the FDTD algorithm has not been widely used for GPR antenna analysis. The reasons for this are not

only the demand for high computational power required for simulations but also the difficulties in the correct implementation of the FDTD algorithm for complex structures.

In this paper we present results of the FDTD model development for the Dielectric Wedge Antenna or DWA (Yarovoy, Schukin and Ligthart, 2000; Yarovoy et al., 2002). A photo of the antenna is shown in Fig. 1. This antenna consists of a dielectric-metal structure, with a complex geometry, that cannot be easily described in the rectangular mesh. For the simulations we used in house developed FDTD software (Mur, 1999). Comparison between simulated and measured antenna characteristics (antenna input impedance, antenna transfer function, antenna footprint) shows good agreement.

We also present an example of optimization of another GPR antenna, i.e. the Dielectric Embedded Dipole or DEDA (de Jongh et al., 1998), using its FDTD model by profiling the "conventional" rectangular brick-shaped metal case and its absorber layer. The original antenna is shown in Fig. 2.

2. FDTD MODEL

In order to use an FDTD model for antenna optimisation, the model must meet two major demands: a high accuracy and a short computation time. The demand of minimal computation time is qualitatively different from the minimal computer storage demanded in a number of previous papers on FDTD simulations of transient antennas (Schlager, Smith and Maloney, 1994).

To reduce the domain size of the computation and therefore to decrease the computation time, we used the geometrical symmetries of the antenna. In this way, only one quarter of the real antenna had to be simulated. On the planes of symmetry zero-valued boundary conditions for the relevant tangential components of electric (or magnetic) field were used depending on the type of field symmetry. The domain of computation is further terminated by second-order Mur absorbing boundary conditions (Mur, 1998). During simulation of the antenna above the ground the domain outside the antenna is filled with two homogeneous media, which represent air and the ground. At places where the air-ground interface reaches the absorbing boundaries, simple first-order Mur absorbing boundary conditions were used.

The FDTD model employs a uniform mesh, the domain of computation being divided into rectangular parallelepipeds of equal size. Despite of the larger number of cells (in comparison with non-uniform meshes, e.g. the "ballooned" mesh in (Schlager, Smith and Maloney, 1994)), such a mesh leads to a computationally simpler, and therefore faster algorithm. The cell size was chosen such that the maximum distance between adjacent corners of the staircase is much smaller than one wavelength (in the dielectric material) at the highest frequency of interest for the incident pulse. Such an approach makes it possible to

avoid resonance phenomena due to the staircase approximation (Schlager, Smith and Maloney, 1994). By varying the parameters of the FDTD model (cell size, position of absorbing boundaries, etc.) we achieved a computational error which is substantially below -40 dB within the observation time window.

The antenna metal flairs are essentially 3D structures and they do not coincide with any coordinate plane. That is why the staircase approximation of the metal flairs was a laborious part of the model development. By shaping the flairs in a rectangular grid we took special care to avoid any air gap between the dielectric wedge and metal and to give some overlap of the "metal" cells by an increase of the wedge width. Such overlapping is essential for preventing of EM field leakage through the metal flair (Foster, 2000).

Another crucial part of the model is the feed point. During simulations, the antenna is fed by a current source placed in the feed point of the antenna between the metal flair and the electrical wall at the plane of symmetry. The magnitude of the current is constant along the source and varies in time as a time-differentiated Gaussian pulse. The current is described by

$$I(t) = -2I_0(t - 4\tau) \frac{\exp\left[-\left((t - 4\tau)/\tau\right)^2\right]}{\tau^2}, \quad (1)$$

where I_0 is the magnitude of the feeding pulse (in the equation it is assumed that the I_0 is equal to 1 A and τ is the pulse duration. The pulse centre was delayed by four pulse widths to avoid the usage of negative times. The transient excitation (1) does not have a DC component, so it cannot "charge" the FDTD grid, which has a property of a distributed capacitor (Wagner and Schneider, 1998). Only for visualization purposes the antenna was excited by a Gaussian pulse,

$$I_{monopulse}(t) = I_0 \exp\left[-\left((t - 4\tau)/\tau\right)^2\right], \quad (2)$$

which provides a better resolution in space. The influence of the feeding line was modelled by a lumped 50 Ω resistor and an 0.001 pF capacitor (the capacitance of the grid (Wagner and Schneider, 1998) is also taken into account) placed in parallel with the feeding current. The influence of the feed model on antenna radiation is demonstrated in Fig. 3. In this figure theoretical responses are normalized with respect to the maximal value of the experimental one. It can be seen that proper feed point loading allows to achieve excellent agreement in the late time antenna response.

3. NUMERICAL ANALYSIS OF THE DIELECTRIC WEDGE ANTENNA

One of the key characteristics of the antenna is its input impedance. For transient antennas it is possible to distinguish between input impedance (which is determined in the assumption of an infinitely long antenna) and the antenna impedance in its classical sense (this impedance takes into account the reflec-

tions from the antenna terminations). Both impedances are shown in Fig. 4. From this Figure it can be seen that the antenna is almost perfectly matched to the feeding line in the frequency band from about 200 MHz until 4.2 GHz (the antenna input resistance is close to the 50 Ω impedance of the feeding line and the antenna input reactance is close to zero). Reflections from the antenna aperture cause oscillations of the antenna impedance around the value of the input impedance. The amplitude of these oscillations depends on the ground type because reflection from the antenna aperture varies for different ground types. Generally, the ground plays the role of a resistive loading of the antenna, reducing the reflection from the aperture and the late time ringing caused by this reflection.

4. NUMERICAL OPTIMIZATION OF THE DIELECTRIC EMBEDDED DIPOLE ANTENNA

From FDTD simulations of the complete antenna we have found that the topside wall of the metal case affects the antenna signal response considerably (despite of adding some absorbing material beneath the wall). We can take advantage from this phenomenon to strengthen the signal response. To achieve that goal, we reduce the amount of absorber on the topside wall and seek out some alternative profiles to the topside wall that can focus the signal to a certain direction (i.e. boresight direction). A few stair-case profiles, which produce larger peak to peak amplitudes and can lower the unwanted antenna ringing level, have been suggested as the result of this study. Examples of stair-case profiles and continuous profiles are shown in Fig. 5. The antenna has been further improved through optimization of the absorber layer thickness and absorber layer profiles, which is attached to the side walls of the metal case. The results of this optimization are shown in Fig. 6. According to simulations the optimized version of the antenna has more than 1.5 times larger peak-to-peak amplitude of the radiated signal, shorter pulse duration and up to 11% lower ringing level than the first DEDA antenna. Theoretical findings will be verified by experimental work in the nearest future.

6. CONCLUSION

We have shown the principal possibility to use FDTD algorithm for analysis and optimization of transient antennas.

ACKNOWLEDGEMENTS

The authors would like to thank Dr. A.D. Schukin and Dr. I.V. Kaploun for manufacturing and valuable discussions on the dielectric wedge antenna and the dielectric embedded dipole antenna.

This research is supported by the Technology Foundation STW, applied science division of NWO

and the technology program of the Ministry of Economic Affairs of the Netherlands.

REFERENCES

1. Daniels D. J., 1996. Surface-Penetrating Radar, London: The Inst. Electrical Eng.
2. Foster P. R., 2000. CAD for Antenna System, Electronics and Communication Engineering J., No. 2, pp.3-14.
3. Jongh R. V. de, Yarovoy A. G., Ligthart L. P., Kaploun I. V., and Schukin A. D., 1998, "Design and analysis of new GPR antenna concepts", Proc. Seventh International Conference on Ground Penetrating Radar, vol. 1, pp.81-86.
4. Leat C. J., Shuley N. V., and Stickley G. F., 1998. Complex Image Model for Ground-Penetrating Radar Antennas, IEEE Trans. Antennas Propagation, Vol. AP-46, No. 10, pp. 1483-1488.
5. Lestari A. A., Yarovoy A. G., and Ligthart L. P., 2001. Numerical Analysis of Transient Antennas, Proc. Int. Conf. On Electromagnetics in Advance Applications (ICEAA'01), Torino, Italy, Sept. 10-14, 2001, pp. 435- 438.
6. Mur G., 1998. Total-Field Absorbing Boundary Conditions for the Time-Domain Electromagnetic Field Equations, IEEE Trans. Electromagnetic Compatibility, Vol. EMC-40, No. 2, pp. 100-102.
7. Mur G., 1999. FDTD3D: the Time-Domain Finite-Difference Code in C++, IRCTR Technical Report, Delft University of Technology, 71p.
8. Rao S. M., and Wilton D. R., 1991. Transient Scattering by Conducting Surfaces of Arbitrary Shape, IEEE Trans. Antennas Propagation, Vol. AP-39, No. 1, pp. 39-56.
9. Schlager K. L., Smith G. S., and Maloney J. G., 1994. Optimization of Bow-Tie antenna for Pulse Radiation, IEEE Trans. Antennas Propagat., Vol. AP-42, No. 7, pp.975-982.
10. Taflov A., 1995. Computational Electrodynamics: the finite-difference time-domain method. Artech House.
11. Wagner C. L., and Schneider J. B., 1998. Divergent Fields, Charge, and Capacitance in FDTD Simulations, IEEE Trans. Microwave Theory and Techniques, Vol. MTT-46, No. 12, Parti, pp. 2131-2136.
12. Yarovoy A. G., Schukin A. D. and Ligthart L. P., 2000. Development of Dielectric Filled TEM-Horn. Proceedings on Millennium Conference on Antennas & Propagation, Davos, Switzerland, 9-14 April 2000.
13. Yarovoy A. G., Schukin A. D., Kaploun I. V., and Ligthart L. P., 2002. The Dielectric Wedge Antenna, IEEE Trans. Antennas Propagation, Vol. AP-50, pp. 1460-1472.

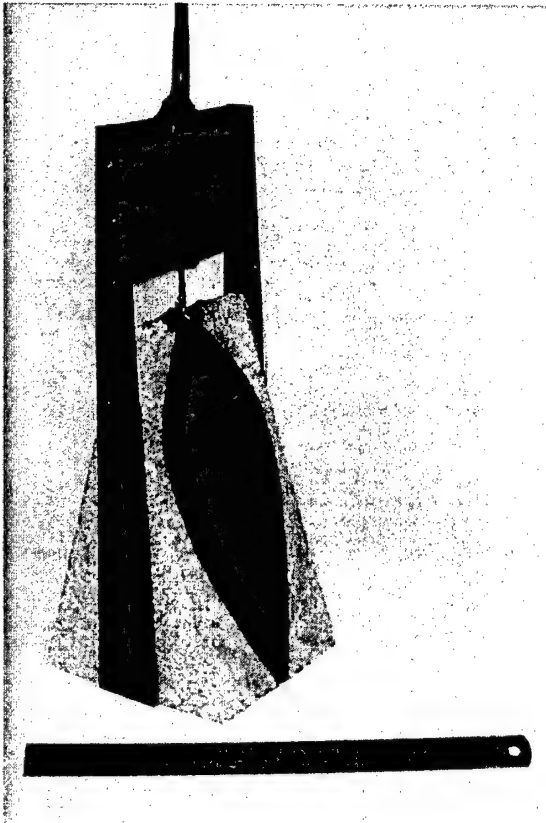


Fig. 1. Photo of the dielectric wedge antenna with a 30 cm ruler.

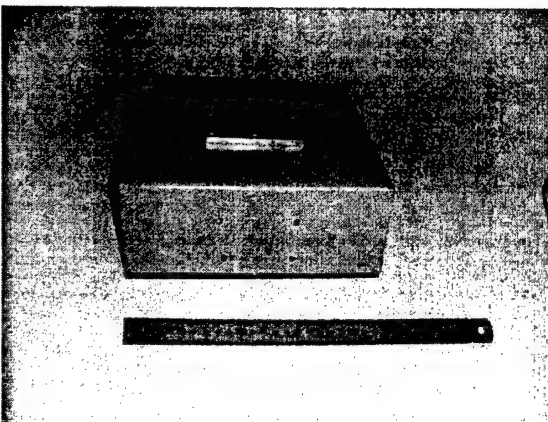


Fig. 2. Photo of the dielectric embedded dipole antenna with a 30 cm ruler.

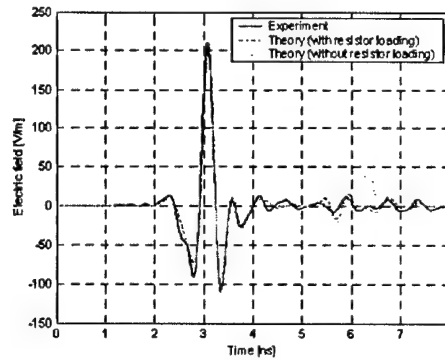


Fig. 3. Comparison of radiated DWA waveforms in the far-field.

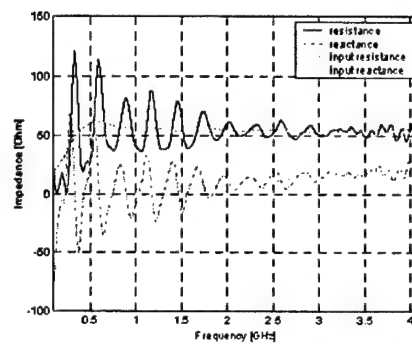


Fig. 4. Dielectric wedge antenna impedance.

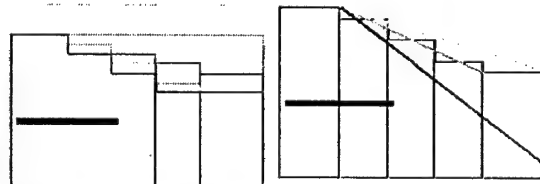


Fig. 5. Various DEDA topside wall staircase profiles (left) and continuous profiles (right).

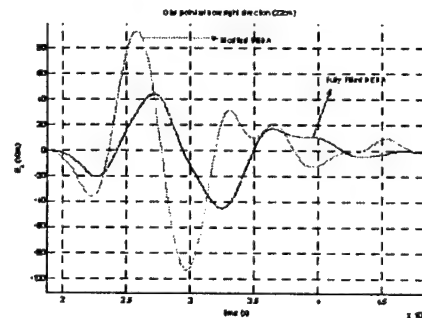


Fig. 6. Simulation results for a modified DEDA and original antenna. The metal case has a flat topside wall.

APERTURE ANTENNA RADIATION

D. J. Kozakoff¹ and V. Tripp²

¹ DeVry University, Alpharetta, GA, USA
<dr.kozakoff@usdigicomm.com>

² USDigiComm Corporation, Alpharetta, GA, USA
<corporate@usdigicomm.com>

Abstract

The technique that can be applied to the calculation of aperture antenna radiation patterns is the equivalence principle followed by physical optics. The equivalence principle is based on replacing the physical antenna aperture with a virtual antenna aperture consisting of an ensemble of Huygen's sources, each of which is a source of spherical wavelets. The total pattern is taken as a construction of these Huygen's secondary waves. A Fourier transform relation exists between the amplitude distribution of these sources, and the radiation pattern in angle space.

For most aperture antenna problems, these classical techniques are adequate and give reasonably accurate results. However, more modern analysis techniques such as method of moments (MOM), finite element method (FEM), and the finite difference time domain (FDTD) method are also discussed. These are more robust and accurate, but the complexity and large amount of computer resources required must be traded off with the accuracy desired.

1. INTRODUCTION

Aperture antennas are used at microwave and the millimeter wave frequencies. There are a large number of categories for which the radiated electromagnetic fields can be considered to emanate from a plane aperture. This includes reflector antennas, lenses and horn antennas. The geometry of the aperture may be any shape. Aperture antennas are very popular for aircraft applications because they can be flush mounted onto the surface and the aperture opening can be covered with a radome to protect the antenna from the environmental conditions [1]. This is implemented to maintain the aerodynamic profile of high-speed aircraft.

In order to evaluate the far-field radiation patterns, it is necessary to know the surface currents on the radiating surfaces of the antenna. Field equivalence [2] is a principle by which the actual sources on an antenna aperture can be replaced by equivalent sources on an external closed surface outside of the antenna aperture. The fictitious sources are equivalent within a region if they produce the same fields within that region. Huygen's principle [3] states that the equivalent source at each point on the external surface is a source of spherical waves and that a secondary wavefront can be constructed as the envelope of these spherical waves [4, 5].

Using these concepts, the electrical and magnetic fields in the equivalent aperture region is determined, and the fields elsewhere are assumed to be zero. In most applications the closed surface is selected so that

most of it coincides with the conducting parts of the physical antenna aperture structure. This is preferred because the vanishing of the tangential electrical field components over the conducting parts of the surface reduces the limits of integration.

Equivalence techniques are useful for electrically large parabolic reflector antennas, when the aperture plane is defined immediately in front of the reflector. This method can also be applied to small aperture waveguide horn antennas. However, for very small horn antennas with an aperture dimension of less than one wavelength, the assumption of zero fields outside the aperture fails unless the horn is completely surrounded by a planar conducting flange [6].

2. LINE SOURCE RADIATION

Consider a line source of length L_w using the coordinate system illustrated in Fig. 1. A line source is treated with a one-dimensional Fourier transform [7]. Assume that the source is positioned in a ground plane of infinite extent. The applicable transform is [8, 10]:

$$E(\theta) = \int_{-\infty}^{\infty} E(x) e^{jkx \sin \theta} dx, \quad (1)$$

$$E(x) = \int_{-\infty}^{\infty} E(\theta) e^{-jkx \sin \theta} d\theta, \quad (2)$$

where $k = 2\pi/\lambda$. For real values of θ , the distribution represents radiated power, while outside this re-

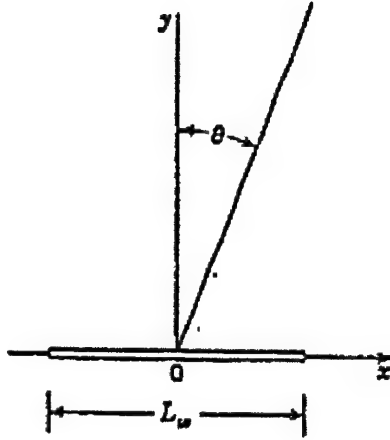


Fig. 1. Coordinate system used to analyze linear aperture of length L_w .

gion it represents reactive or stored power [11]. For a finite aperture, the Fourier integral representation equation (1) may be re-written as [9]:

$$E(\theta) = \int_{-L_w/2}^{L_w/2} E(x) e^{jk \sin \theta x} dx. \quad (3)$$

For a uniform distribution in which the amplitude is constant over the aperture region $-L_w/2 \leq x \leq L_w/2$, the radiation pattern has the narrowest radiation pattern beam width of any other distribution, but on the other hand has the highest first sidelobe level of -13.2 dB. To make a relative comparison of this and other line source distributions, we must first normalize the distributions in order that the total radiated power is the same relative to the uniform case.

We have applied a computer code to compute the secondary radiation patterns produced a line source with a uniform, cosine raised to power n , and cosine on a pedestal P aperture distributions. The results shown in Table 1 compare the gain, main lobe beam width, and the first side-lobe levels for each. All gain levels are compared with the uniform illumination case and total radiated power is assumed in each case. The important radiation values can be found from the three parameters (K_1 , K_2 and K_3) in this Table by applying the following formulas:

$$\theta_o = \frac{K_1}{L_w/\lambda}, \quad (4)$$

$$\theta_n = \frac{K_2}{L_w/\lambda}, \quad (5)$$

$$\theta_{sl} = \frac{K_3}{L_w/\lambda}, \quad (6)$$

where, θ_o = Half power beamwidth (degrees)

θ_n = Null to null beamwidth (degrees)

θ_{sl} = Position of first sidelobe from the main lobe (degrees)

L_w/λ = Aperture dimension in wavelengths.

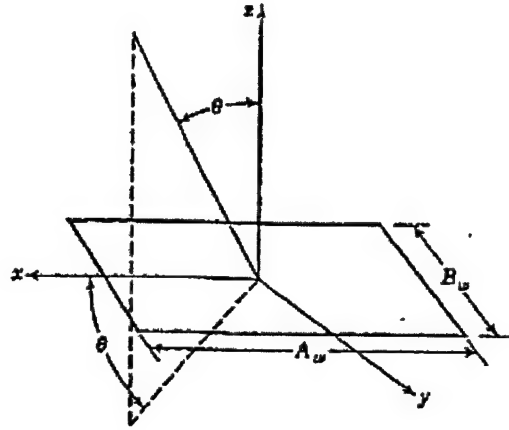


Fig. 2. Coordinate system used to analyze rectangular aperture of dimensions A_w , B_w .

3. RECTANGULAR APERTURES

The rectangular aperture shown in Fig. 2 is a common microwave antenna shape. Because of its configuration, the rectangular coordinate system is the most convenient system in which to express the electromagnetic fields at the aperture. Rectangular horns, in particular, can be analyzed as aperture antennas. Incident fields are replaced by equivalent electrical and magnetic currents. With use of vector potentials, the far fields are found as a superposition of each source. Generally, one can assume that the incident field is a propagating free-space wave, the electrical and magnetic fields of which are proportional to each other. This will give the Huygens source approximation and allow us to use integrals of the electric field in the aperture plane. Each point in the aperture is considered as a source of radiation.

Assuming a rectangular aperture of dimension A_w in the x -plane and B_w in the y -plane, the radiation pattern may then be obtained from the integral [12]:

$$E(\theta, \phi) = \int_{-B_w/2}^{B_w/2} \int_{-A_w/2}^{A_w/2} E(x, y) e^{j(k_x x + k_y y)} dx dy, \quad (7)$$

in which $E(x, y)$ is the aperture distribution and the directional wave numbers are given by: $k_x = k \sin \theta \cos \phi$ and $k_y = k \sin \theta \sin \phi$. These are also known as the x and y components of the propagation vector k [13].

For many kinds of rectangular aperture antennas such as horns, the aperture distributions in the two principal plane dimensions are independent. These types of distributions are said to be separable. The total radiation pattern is obtained for separable distributions as the product of the pattern functions obtained from the one-dimensional Fourier transforms corresponding to the two principal plane distributions:

$$E(x, y) = E(x)E(y). \quad (8)$$

Table 1. Radiation characteristics of various linear aperture distributions

Type of distribution	Comments	Parameter K_1	Parameter K_2	Parameter K_3	1 st Sidelobe Level, dB.	Peak Gain Relative to Uniform
Uniform		50.67	114.67	82.00	-13.26	0.0
Cosine raised to power " n "	$n = 1$	68.67	172.00	108.33	-23.00	-0.91
	$n = 2$	82.67	229.22	135.50	-31.46	-1.76
	$n = 3$	95.33	286.67	163.00	-39.29	-2.40
	$n = 4$	106.00	344.00	191.00	-46.74	-2.89
	$n = 5$	116.67	402.00	219.00	-53.93	-3.30
Cosine on pedestal " P "	$P = 0.0$	68.67	172.00	108.33	-23.01	-0.91
	$P = 0.1$	64.67	162.00	98.00	-23.00	-0.68
	$P = 0.2$	62.00	152.67	97.00	-21.66	-0.50
	$P = 0.3$	59.33	144.67	93.67	-20.29	-0.35
	$P = 0.4$	58.00	138.00	90.67	-18.92	-0.24
	$P = 0.5$	56.00	132.67	88.33	-17.65	-0.15

If the rectangular aperture distribution is not able to be separated, the directivity pattern is found in a similar manner to the line-source distribution except that the aperture field is integrated over two-dimensions rather than one dimension [8]. This double Fourier transform can also be applied to circular apertures and can be easily evaluated on a PC computer.

4. CIRCULAR APERTURES

Circular aperture antennas shown in Fig. 3 form the largest single class of aperture antennas. The most convenient coordinate system used to analyze the radiation from a circular aperture of diameter D_w is the spherical coordinate system where the aperture lies in the x - y plane. The radiation can be described in terms of the spherical coordinate components θ and φ . The radiation pattern from a circular aperture can be calculated by applying Huygen's principle in a similar way that we did for rectangular apertures. The simplest form of a circular aperture distribution is one in which the field does not vary with φ and is rotationally symmetric. This is not always true.

As was the case with rectangular apertures, a Fourier-transform relationship exists between the antenna

distribution $E(p)$ and the far-field radiation pattern $E(u)$. For a circular symmetric aperture distribution, the radiation pattern can be written in normalized form [7]:

$$E(u) = \frac{1}{\pi^3} \int_0^{2\pi} \int_0^\pi E(p) e^{jpu \cos(\phi - \phi')} p dp d\phi', \quad (9)$$

where,

$$u = \frac{D_w \sin \theta}{\lambda}.$$

And the normalized radius is,

$$p = \frac{2\pi r}{D_w}.$$

A computer code was applied to compute the secondary pattern characteristic produced by a uniform, cosine raised to a power n , cosine on a pedestal P , and parabolic raised to power n distributions. The results shown in Table 2. The important radiation values of half power beamwidth, null to null beamwidth and position of the first sidelobes relative to the main lobe are found from the three parameters (K_1 , K_2 and K_3) in this Table by formulas similar to (4) through (6), but replacing the linear aperture dimension in wavelengths with the circular aperture diameter in wavelengths. That is:

$$\theta_o = \frac{K_1}{D_w / \lambda}, \quad (10)$$

$$\theta_n = \frac{K_2}{D_w / \lambda}, \quad (11)$$

$$\theta_{sl} = \frac{K_3}{D_w / \lambda}, \quad (12)$$

$D_w / \lambda =$ Aperture diameter in wavelengths.

5. MODERN FULL-WAVE METHODS

There are aperture antennas that can be advantageously addressed with analysis approaches known as full-wave methods. The application of such methods

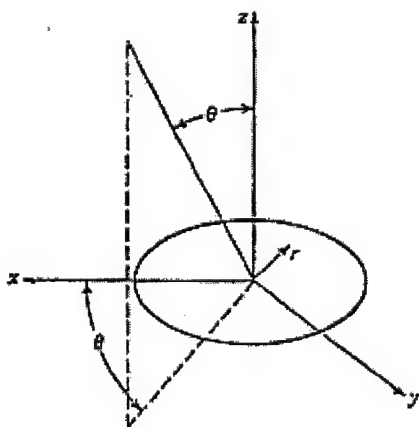


Fig. 3. Coordinate system used to analyze circular aperture of diameter D_w

Table 2. Radiation characteristics of various circular aperture distributions

Type of distribution	Comments	Parameter K_1	Parameter K_2	Parameter K_3	1 st Sidelobe Level, dB.	Peak Gain Relative to Uniform
Uniform		59.33	140.00	93.67	-17.66	0.0
Cosine raised to power " n "	$n = 1$	74.67	194.67	119.33	-26.07	-1.42
	$n = 2$	88.00	250.00	145.50	-33.90	-2.89
	$n = 3$	99.33	306.67	173.00	-41.34	-4.04
	$n = 4$	110.00	362.67	200.30	-48.51	-4.96
	$n = 5$	120.00	420.00	228.17	-55.50	-5.73
Cosine on pedestal " P "	$P = 0.0$	74.67	194.67	119.33	-26.07	-1.42
	$P = 0.1$	70.67	183.33	112.67	-25.61	-0.98
	$P = 0.2$	68.67	174.00	107.83	-24.44	-0.66
	$P = 0.3$	66.00	166.00	104.17	-23.12	-0.43
	$P = 0.4$	64.67	159.60	99.47	-21.91	-0.27
	$P = 0.5$	63.33	154.67	97.83	-20.85	-0.17
Parabolic raised to power " n "	$n = 0$	59.33	140.00	93.67	-17.66	0.0
	$n = 1$	72.67	187.33	116.33	-24.67	-1.24
	$n = 2$	84.67	232.67	138.67	-30.61	-2.55
	$n = 3$	94.67	277.20	160.17	-35.96	-3.58
	$n = 4$	104.00	320.33	181.33	-40.91	-4.43

has rapidly expanded with the explosion of high power PC computers in recent decades. Analysis methods are called full-wave when they start with the fundamental equations of electromagnetics and discretize them such that they can be reduced to linear matrix equations suitable for solving by a computer. The advantage is that there are no approximations in principle, only the size of the discrete interval, which is usually between 10 and 20 intervals per wavelength. There are three primary full-wave methods used in electromagnetics; the finite element method (FEM) [15-18], the method of moments (MOM) [19-21], and the finite difference time domain (FDTD) method [22, 23]. The MOM discretizes Maxwell's wave equations in their integral form, the FDM discretizes the equations in the differential form, and the FEM method discretizes the equations after casting them in a variational form. All three techniques have been applied to aperture antenna analysis [24-26].

The MOM method finds natural application to antennas because it is based on surfaces and currents, whereas the other two methods are based on volumes and fields. This means that for MOM, only the antenna aperture surface structure must be discretized and solved, whereas for FEM and FDTD, all volumes of interest must be discretized. For antenna radiation, the far field would require an inordinate amount of space were it not for the recent development of absorbing boundary conditions. These boundary conditions approximate the radiation conditions of infinite distance in the space very near the radiating structure.

The MOM works by solving for currents on all surfaces in the presence of a source current or field. The radiated field is then obtained by integration of these currents, much like it was obtained in the physical optics approaches. Thus, the MOM can be applied to any aperture antenna that the PO technique can be applied to, unless the problem is too large for the

available computer resources. Ensemble [27] is commercially available software package that is a 2.5-dimensional MOM program used primarily for patch antennas or antennas that can be modeled as layers of dielectrics and conductors. If the top layer is a conductor with radiating holes, the holes are aperture antennas, which this program is designed to analyze.

There is another full-wave commercial software packages that are widely used for aperture antenna problems, the High Frequency Structure Simulator (HFSS) [28]. This is a 3-dimensional FEM software package with extensive modeling and automatic meshing capability. It is best for horn antennas or other kinds of antennas formed by apertures in various non-layered structures. The latest version uses the "perfectly matched layer" type of absorbing boundary conditions.

In practice, full-wave methods cannot be directly applied to high-gain aperture antennas like reflectors or lenses without difficulties because these structures are usually many wavelengths in size which requires large amount of computational resources. Often, however, if there is symmetry in the problem that can be exploited, the number of unknowns for which to solve can be greatly reduced. For instance, a high gain reflector antenna that has circular symmetry allows for body-of-revolution (BOR) symmetry [29, 30] simplifications in the modeling. Similarly, a large lens requires a computer program with dielectric capability [31] in addition to BOR symmetry modeling.

REFERENCES

1. D. J. Kozakoff, Analysis of Radome Enclosed Antennas, Artech House Publishers, Norwood, MA, 1997.
2. S. A. Schelkunoff, Some equivalence theorems of electromagnetics and their application to radiation

- problems, Bell System Technical Journal, 15: 92-112, 1936.
3. C. Huygens, *Traite de La Lumiere*, Leyden, 1690. Translated into English by S. P. Thompson, Chicago, IL, University of Chicago Press, 1912.
4. J. D. Kraus and K. R. Carter, *Electromagnetics*, 2nd edition, New York, McGraw-Hill Book Company, pp.464-467.
5. A. Sommerfeld, *Theorie der Beugung*, in P. Frank and R. von Mises (Editors), *Die Differential und Integralgleichungen der Mechanik und Physik*, Braunschweig, Germany: Vieweg, 1935.
6. C. A. Balanis, *Antenna Theory Analysis and Design*, New York: Harper and Row Publishers, 1982.
7. A. D. Oliver, Basic Properties of Antennas, in A. W. Rudge, et al, (Editors), *The Handbook of Antenna Design*, IEE Electromagnetic Wave Series UK, London: UK, Peter Peregrinus Publishers, 1986, Chapter 1.
8. H. Jasik, Fundamentals of Antennas, in R. C. Johnson (Editor), *Antenna Engineering Handbook*, 3rd Edition, New York: McGraw Hill Book Company, 1993.
9. J. D. Kraus, *Antennas*, 2nd Edition, New York: McGraw Hill Book Company, 1988.
10. H. G. Booker and P. C. Clemmow, The Concept of an Angular Spectrum of Plane Waves and its Relation to That of Polar Diagram and Aperture Distribution, *Proceedings of the IEEE*, London, UK, Ser. 3, 97: 11-17, 1950.
11. D. R. Rhodes, The Optimum Line Source for the Best Mean Square Approximation to a Given Radiation Pattern, *IEEE Transactions on Antennas and Propagation*, AP-11, 440-446, 1963.
12. R. S. Elliot, *Antenna Theory and Design*, Englewood Cliffs, NJ: Prentice Hall Book Company, 1987.
13. I. S. Sokolnikoff and R. M. Redheffer, *Mathematics of Physics and Modern Engineering*, New York: McGraw Hill Book Company, 1958.
14. S. Silver, *Microwave Antenna Theory and Design*, New York: McGraw Hill Book Company, 1949.
15. J. L. Volakis, A. Chatterjee and L. C. Kempel, *Finite Element Methods for Electromagnetics*, IEEE Press, New York (ISBN 0-7803-3424-6) and Oxford University Press, London (0-10-850479-9) 1998.
16. P. P. Sylvester and G. Pelosi, Editors, *Finite Elements for Wave Electromagnetics: Methods and Techniques*, IEEE Press, New York, 1994.
17. P. P. Sylvester and R. L. Ferrari, *Finite Elements for Electrical Engineers*, Cambridge University press, New York, 1992.
18. J. Jin, *The Finite Element Method in Electromagnetics*, John Wiley InterScience, New York, 1993.
19. R. F. Harrington, *Field Computation by Moment Methods*, Macmillan Company, New York, 1968.
20. E. K. Miller, L. Medgyesi-Mitschang, E. H. Newman, Editors, *Computational Electromagnetics, Frequency Domain Method of Moments*, IEEE Press, New York, 1992.
21. R. C. Hansen, Editor, *Moment Methods in Antennas and Scattering*, Artech House, Norwood, MA (ISGN 0890064660), 1990.
22. A. Taflov, *Computational Electromagnetics: The Finite Difference Time Domain Method*, Artech House, Norwood, MA, 1995.
23. K. S. Kunz, R. J. Luebbers, *The Finite Difference Time Domain Method for Electromagnetics*, CRC Press, Cleveland, OH (ISBN 0949386578), 1993.
24. D. Chun, R. N. Simons and L.P. B. Kotehi, Modeling and Characterization of Cavity Backed Circular Aperture Antenna with Suspended Stripline Probe Feed, *IEEE Antennas and Propagation Society International Symposium*, 2000 Digest, Salt Lake City, UT, 2000.
25. J. Y. Lee, T. S. Horng, N. G. Alexopoulos, Analysis of Cavity Backed Aperture Antennas with a Dielectric Overlay, *IEEE Transactions on Antennas and Propagation*, Vol. 42, No.11, November 1994, pp. 1556-1562.
26. D. Sullivan and J. L. Young, Far-Field Time-Domain Calculation from Aperture Radiators Using the FDTD Method, *IEEE Transactions Antennas and Propagation*, Vol.49, No.3, March 2001, pp.464-469.
27. Ensemble Software, Version 6.1, Ansoft Corporation, Four Station Square, Suite 200, Pittsburgh, PA 15219, Tel. 412-261-3200.
28. HFSS, Ansoft Corporation, Four Station Square, Suite 200, Pittsburgh, PA 15219, Tel. 412-261-3200.
29. Z. Altman and R. Mittra, Combining an Extrapolation Technique with the method of Moments for Solving Large Scattering Problems Involving Bodies of Revolution, *IEEE Transactions on Antennas and Propagation*, Volume 44, No. 4, April 1996, pp. 548-553.
30. A. D. Greenwood and J. M. Jin, Finite Element Analysis of Complex Axisymmetric Radiating Structures, *IEEE Transactions on Antennas and Propagation*, Vol.47, No.8, August 1999, p.1260.
31. J. M. Putnam and L. N. Medgyesi-Mitschang, Combined Field Integral Equation for Inhomogeneous Two- and Three-Dimensional Bodies: The Junction Problem, *IEEE Transactions on Antennas and Propagation*, Vol.39, No.5, May 1991, pp.667-672.

ROBUST ADAPTIVE BEAMFORMING: AN OVERVIEW OF RECENT TRENDS AND ADVANCES IN THE FIELD

A. B. Gershman

Smart Antenna Research Team (SmART)
Department of Communication Systems
Gerhard-Mercator University, Duisburg, Germany
(on leave from the Communication Research Laboratory
Department of Electrical and Computer Engineering
McMaster University, Hamilton, Ontario, Canada)

ABSTRACT

In recent decades, adaptive arrays have been widely used in sonar, radar, wireless communications, microphone array speech processing, medical imaging and other fields. In practical array systems, traditional adaptive beamforming algorithms are known to degrade if some of exploited assumptions on the environment, sources, or antenna array become wrong or imprecise. Therefore, the robustness of adaptive beamforming techniques against environmental and array imperfections and uncertainties is one of the key issues.

In this paper, we present an overview of recent trends and advances in the field of robust adaptive beamforming.

Keywords: Robust adaptive beamforming, worst-case performance optimization, diagonal loading, array response mismatch, uncertainty set.

1. INTRODUCTION

The traditional approach to the design of adaptive beamformers assumes that no components of the desired signal are present in the beamformer training data [1], [2]. In such a case, adaptive beamforming is known to be sufficiently robust against errors in the array response to the desired signal and limited training sample size and a variety of rapidly converging techniques have been developed for this case [1]. Although the assumption of signal-free training snapshots may be relevant in certain specific cases (e.g., in some radar and active sonar problems), there are many applications where the interference and noise observations are always "contaminated" by the signal component.

Typical examples of such applications include wireless communications, passive sonar, microphone array speech processing, and medical imaging. It is well known that even in the ideal case where the signal steering vector (array response) is precisely known at the receiving sensor array, the presence of the desired signal in the training data snapshots can lead to

essentially reduced convergence rates of adaptive beam-forming algorithms relative to the signal-free training data case [3], [4]. This may cause a severe performance degradation of adaptive beamforming techniques in scenarios with a small training sample size.

In practical situations, the performance degradation of adaptive beamforming techniques may become even more substantial because of a possible violation of underlying assumptions on the environment, sources, or sensor array. One of typical causes of such a performance degradation is a mismatch between the nominal (presumed) and actual array responses to the desired signal. Adaptive array techniques are known to be very sensitive even to slight errors of this type because in the presence of such errors adaptive beamformers tend to misinterpret the desired signal components in array observations as an interference and to suppress these components by means of adaptive nulling instead of maintaining distortionless response towards them [3], [4]. This phenomenon is often referred to as signal self-nulling.

Errors in the array response to the desired signal frequently occur in practice because of look direction errors, imperfect array calibration (distorted array shape), as well as unknown environmental wavefront distortions, local scattering, and sensor mutual coupling. Another typical cause of array response errors in wireless communications is a restricted amount of

Supported in parts by the Wolfgang Paul Award Program of the Alexander von Humboldt Foundation (Germany) and German Ministry of Education and Research, the Premier Research Excellence Award Program of the Ministry of Energy, Science, and Technology (MEST) of Ontario, and the Natural Sciences and Engineering Research Council (NSERC) of Canada.

pilot symbols/intervals. In such cases, robust approaches to adaptive beamforming are required [3, 5-7].

Besides array response errors, performance degradation of adaptive beamforming can be additionally caused by a nonstationary character of the beamformer training data [8-10]. This phenomenon can be caused by a nonstationary behavior of the propagation channel, by interferer and antenna motion, as well as antenna vibration. There are several implications of such a nonstationarity. First of all, it naturally restricts the training sample size and leads to a degraded performance of adaptive beamforming algorithms even in the case of signal-free training snapshots. Furthermore, if the desired signal is present in the beamformer training snapshots, this type of degradation becomes much stronger than in the signal-free training data case [3, 4]. Finally, in the case of rapidly moving interferers the performance can break down because the array weights are not able to adapt fast enough to compensate for the interferer motion. Therefore, interference cancellation may be insufficient in such cases where robust approaches to adaptive beamforming are required [3, 5-7]. The same situation occurs in the case of moving antenna arrays, e.g., towed arrays of hydrophones in sonar [11] or moving antenna platforms in airborne applications [10].

2. TRADITIONAL APPROACHES

The beamformer output is given by

$$y(k) = \mathbf{w}^H \mathbf{x}(k), \quad (1)$$

where k is the time index, $\mathbf{x}(k)$ is the $M \times 1$ complex vector of array observations, \mathbf{w} is the $M \times 1$ complex vector of beamformer weights, M is the number of array sensors, and $(\cdot)^H$ is the Hermitian transpose. The training snapshot vector is given by

$$\mathbf{x}(t) = \mathbf{s}_s(t) + \mathbf{i}(t) + \mathbf{n}(t), \quad (2)$$

where $\mathbf{s}_s(t)$, $\mathbf{i}(t)$, and $\mathbf{n}(t)$ are the statistically independent components of the desired signal, interference, and sensor noise, respectively. In the particular case when the desired signal is a point source and has a time-invariant wavefront, we have $\mathbf{s}_s(t) = s(t)\mathbf{a}_s$, as where $s(t)$ is the complex signal waveform and as is the $M \times 1$ signal steering vector.

The optimal weight vector can be obtained through maximizing the Signal-to-Interference-plus-Noise Ratio (SINR) [1]

$$\text{SINR} = \frac{\mathbf{w}^H \mathbf{R}_s \mathbf{w}}{\mathbf{w}^H \mathbf{R}_{i+n} \mathbf{w}}, \quad (3)$$

where

$$\mathbf{R}_s \triangleq \mathbf{E}\{\mathbf{s}_s(t)\mathbf{s}_s^H(t)\} \quad (4)$$

and

$$\mathbf{R}_{i+n} \triangleq \mathbf{E}\{[\mathbf{i}(t) + \mathbf{n}(t)][\mathbf{i}(t) + \mathbf{n}(t)]^H\} \quad (5)$$

are the $M \times M$ signal and interference-plus-noise co-variance matrices, respectively, and $\mathbf{E}\{\cdot\}$ denotes the statistical expectation. Generally, the matrix \mathbf{R}_s can have an arbitrary rank, i.e.,

$$1 \leq \text{rank}\{\mathbf{R}_s\} \leq M. \quad (6)$$

However, in the special case of a point signal source we have

$$\mathbf{R}_s = \sigma_s^2 \mathbf{a}_s \mathbf{a}_s^H \quad (7)$$

and, hence, $\text{rank}\{\mathbf{R}_s\} = 1$, where $\sigma_s^2 = \mathbf{E}\{|s(t)|^2\}$. It is well known that the SINR in (3) can be maximized via maintaining distortionless response to the desired signal while minimizing the output interference-plus-noise power:

$$\min_{\mathbf{w}} \mathbf{w}^H \mathbf{R}_{i+n} \mathbf{w} \text{ s. t. } \mathbf{w}^H \mathbf{R}_s \mathbf{w} = 1. \quad (8)$$

In the rank-one signal case, the constraint in (8) can be rewritten in a more familiar form $\mathbf{w}^H \mathbf{a}_s = 1$. This approach is usually referred to as the Minimum Variance Distortionless Response (MVD) beamforming. The solution to (8) is given by

$$\mathbf{w}_{\text{opt}} = \rho\{\mathbf{R}_{i+n}^{-1} \mathbf{R}_s\}, \quad (9)$$

where $\rho\{\cdot\}$ is the operator which returns the principal eigenvector of a matrix. In the rank-one signal case, the solution (9) can be rewritten in a more familiar form [1]

$$\mathbf{w}_{\text{opt}} = \alpha \mathbf{R}_{i+n}^{-1} \mathbf{a}_s, \quad (10)$$

where $\alpha = (\mathbf{a}_s^H \mathbf{R}_{i+n}^{-1} \mathbf{a}_s)^{-1}$. In practical applications, the matrix \mathbf{R}_{i+n} is unavailable and is replaced in (9) and (10) by the sample covariance matrix [1]

$$\hat{\mathbf{R}} = \frac{1}{N} \sum_{n=1}^N \mathbf{x}(n) \mathbf{x}^H(n) = \frac{1}{N} \mathbf{X} \mathbf{X}^H, \quad (11)$$

where $\mathbf{X} = [\mathbf{x}(1), \mathbf{x}(2), \dots, \mathbf{x}(N)]$ is the $M \times N$ matrix of the beamformer training data and N is the number of snapshots available (training sample size).

One of the most popular approaches to robust adaptive beamforming in the cases of arbitrary signal array response errors and small training sample size is the diagonal loading method [5], [12], [13], [14]. Its key idea is to regularize the solution for the weight vector [13] by adding a quadratic penalty term to the objective function in (8) as

$$\min_{\mathbf{w}} \mathbf{w}^H \hat{\mathbf{R}} \mathbf{w} + \gamma \mathbf{w}^H \mathbf{w} \text{ s. t. } \mathbf{w}^H \mathbf{R}_s \mathbf{w} = 1, \quad (12)$$

where γ is the loading factor. The solution to (12) is given by

$$\mathbf{w}_{\text{DL}} = \rho\{(\hat{\mathbf{R}} + \gamma \mathbf{I})^{-1} \mathbf{R}_s\}, \quad (13)$$

where \mathbf{I} is the identity matrix. In the rank-one signal case, this solution can be written in a more familiar form [5], [13], [14]

$$\mathbf{w}_{DL} = (\hat{\mathbf{R}} + \gamma \mathbf{I})^{-1} \mathbf{a}_s. \quad (14)$$

It is well-known that diagonal loading can improve the adaptive beamforming performance in scenarios with an arbitrary signal array response mismatch [3], [5], [13]. However, the main shortcoming of this method is that there is no easy and reliable way of choosing the parameter γ .

Another popular approach to robust adaptive beamforming is the eigenspace-based beamformer [4], [15]. This approach is only applicable to the point signal source case. The key idea of this method is to use, instead of the presumed steering vector \mathbf{a}_s , the projection of \mathbf{a}_s onto the sample signal-plus-interference subspace. Write the eigendecomposition of (11) as

$$\hat{\mathbf{R}} = \hat{\mathbf{E}} \hat{\mathbf{\Lambda}} \hat{\mathbf{E}}^H + \hat{\mathbf{G}} \hat{\mathbf{\Gamma}} \hat{\mathbf{G}}^H, \quad (15)$$

where the $M \times (L+1)$ matrix $\hat{\mathbf{E}}$ contains the $L+1$ signal-plus-interference subspace eigenvectors of $\hat{\mathbf{R}}$, and the $(L+1) \times (L+1)$ diagonal matrix $\hat{\mathbf{\Lambda}}$ contains the corresponding eigenvalues of this matrix. Similarly, the $M \times (M-L-1)$ matrix $\hat{\mathbf{G}}$ contains the $(M-L-1)$ noise-subspace eigenvectors of $\hat{\mathbf{R}}$, while the $(M-L-1) \times (M-L-1)$ diagonal matrix $\hat{\mathbf{\Gamma}}$ is built from the corresponding eigenvalues. The number of interfering sources L is assumed to be known. The weight vector of the eigenspace-based beamformer is given by

$$\mathbf{w}_{eig} = \hat{\mathbf{R}}^{-1} \mathbf{v}, \quad (16)$$

where $\mathbf{v} = \mathbf{P}_{\hat{\mathbf{E}}} \mathbf{a}_s$ and $\mathbf{P}_{\hat{\mathbf{E}}} = \hat{\mathbf{E}}(\hat{\mathbf{E}}^H \hat{\mathbf{E}})^{-1} \hat{\mathbf{E}}^H = \hat{\mathbf{E}} \hat{\mathbf{E}}^H$ is the orthogonal projection matrix onto the estimated signal-plus-interference subspace.

When used in adequate situations, the eigenspace-based beamformer is known to be one of the most powerful techniques applicable to arbitrary steering vector mismatch case [15]. However, very serious shortcomings of this approach are that it is entirely based on the low-rank stationary model of the training data and requires exact knowledge of L . Furthermore, this approach is limited to high Signal-to-Noise-Ratio (SNR) cases because at low SNRs the estimation of the projection matrix onto the signal-plus-interference subspace breaks down due to a high probability of subspace swaps [16].

In situations with nonstationary training data, several advanced methods have been developed to mitigate performance degradation of adaptive beamformers. In [10], a power series expansion based approach is used to obtain a class of robust solutions for nonstationary array weights. However, the algorithms obtained are restricted by scenarios with slowly moving jammers only. To preserve the adaptive array performance in situations with a higher mobility of in-

terferers, several authors exploited the idea of artificial broadening the adaptive beam pattern nulls in unknown interferer directions using either point [8], [9], [11] or derivative [17]-[20] null constraints. The first approach is usually referred to as the Data-Driven Constraints (DDC) method, while the second one is called the Matrix Taper (MT) method. Relationships between the DDC and MT approaches have been studied in [21] where it has been shown that the DDC method can be interpreted and implemented as a specific form of matrix taper.

3. RECENT ADVANCES

As follows from the previous section, all traditional approaches to robust adaptive beamforming are ad hoc techniques. Only recently have some theoretically rigorous robust adaptive beamforming approaches been proposed in this field [16, 22-28]. A common idea used in these algorithms is to define the so-called uncertainty sets and optimize worst-case performance.

First of all, let us consider the non-point signal source case and discuss the robust beamformer derived in [24-25]. Following this work, we assume that both the signal and interference-plus-noise covariance matrices are known with some errors. That is, there is always a certain mismatch between the actual and presumed values of these matrices. This yields

$$\tilde{\mathbf{R}}_s = \mathbf{R}_s + \Delta_1, \quad (17)$$

$$\tilde{\mathbf{R}}_{i+n} = \mathbf{R}_{i+n} + \Delta_2, \quad (18)$$

where \mathbf{R}_s and \mathbf{R}_{i+n} are the presumed signal and interference-plus-noise covariance matrices, respectively, whereas $\tilde{\mathbf{R}}_s$ and $\tilde{\mathbf{R}}_{i+n}$ are their actual values. Here, Δ_1 and Δ_2 are the unknown matrix mismatches.

In the presence of the mismatches Δ_1 and Δ_2 , equation (3) for the output SINR of an adaptive array has to be rewritten as

$$\text{SINR} = \frac{\mathbf{w}^H \tilde{\mathbf{R}}_s \mathbf{w}}{\mathbf{w}^H \tilde{\mathbf{R}}_{i+n} \mathbf{w}}. \quad (19)$$

Let Δ_1 and Δ_2 be norm-bounded by some known constants [24]

$$\|\Delta_1\| \leq \epsilon, \quad \|\Delta_2\| \leq \gamma, \quad (20)$$

where $\|\cdot\|$ denotes the Frobenius norm. Note that (20) defines the uncertainty sets for the signal and interference-plus-noise covariance matrices, respectively. To provide robustness against possible norm-bounded mismatches as in (20), it has been proposed in [24] and [25] to obtain the beamformer weight vector by means of maximizing the worst-case output SINR:

$$\max_w \min_{\Delta_1, \Delta_2} \frac{w^H (\mathbf{R}_s + \Delta_1) w}{w^H (\mathbf{R}_{i+n} + \Delta_1) w}, \quad (21)$$

$$\forall \|\Delta_1\| \leq \varepsilon, \|\Delta_2\| \leq \gamma$$

where Δ_1 and Δ_2 are Hermitian matrices.

The problem (21) can be rewritten as

$$\max_w \frac{\min_{\|\Delta_1\| \leq \varepsilon} w^H (\mathbf{R}_s + \Delta_1) w}{\min_{\|\Delta_2\| \leq \gamma} w^H (\mathbf{R}_{i+n} + \Delta_2) w}. \quad (22)$$

$$\forall \|\Delta_1\| \leq \varepsilon, \|\Delta_2\| \leq \gamma$$

Using the Lagrange multiplier method, it has been proved in [24] that, if ε is smaller than the maximal eigenvalue of \mathbf{R}_s , the problem (22) is equivalent to

$$\min_w w^H (\mathbf{R}_{i+n} + \gamma \mathbf{I}) w \text{ s.t. } w^H (\mathbf{R}_s + \varepsilon \mathbf{I}) w = 1. \quad (23)$$

Similar to (8), the solution to the robust MVDR beam-forming problem (23) can be expressed in a closed-form. After replacing \mathbf{R}_{i+n} by $\hat{\mathbf{R}}$, it can be written as [24-25]

$$w_{\text{rob}} = \rho \{ (\hat{\mathbf{R}} + \gamma \mathbf{I})^{-1} (\mathbf{R}_s + \varepsilon \mathbf{I}) \}. \quad (24)$$

From (24), it is clear that the worst-case performance optimization approach leads to a new diagonal loading based beamformer where both the negative and positive types of diagonal loading are used.

Unfortunately, the beamformer (24) does not take into account that $\hat{\mathbf{R}}$ must be non-negative definite. Although ignoring this non-negative definiteness constraint we simply "strengthen" the worst case and this does not affect the performance of the robust beamformer in most of scenarios [24], it is interesting to consider a more adequate formulation of the robust beamforming problem that can take into account this constraint. For the point source case, this problem has been recently addressed in [16] and [26]. Following this approach, let us consider the signal steering vector mismatch

$$\delta = \tilde{\mathbf{a}}_s - \mathbf{a}_s, \quad (25)$$

instead of the signal covariance matrix mismatch \mathbf{A} of (17). Here, $\tilde{\mathbf{a}}_s$ and \mathbf{a}_s are the actual and presumed steering vectors, respectively. Similar to (20), we assume that the norm of the mismatch vector is bounded as [16]

$$\|\delta\| \leq \epsilon, \quad (26)$$

where the constant ϵ is known. The idea is to incorporate robustness into the MVDR beamforming problem by means of imposing the distortionless response constraint which, for all mismatched steering vectors, guarantees that the array response is not smaller than one. Using such a constraint, the robust formulation of the MVDR adaptive beamformer can be written as the following constrained minimization problem [16]

$$\min_w w^H \hat{\mathbf{R}} w \text{ s.t. } |w^H (\mathbf{a}_s + \delta)| \geq 1 \quad \forall \|\delta\| \leq \epsilon. \quad (27)$$

Note that the main modification with respect to the original rank-one MVDR problem is that instead of requiring fixed distortionless response towards the single steering vector \mathbf{a}_s , such distortionless response is now maintained in (27) by means of inequality constraints for a continuum of all possible steering vectors given by the uncertainty set

$$\{c | c = \mathbf{a}_s + \delta, \|\delta\| \leq \epsilon\}. \quad (28)$$

The constraints in (27) guarantee that the distortionless response will be maintained in the worst case, i.e., for the particular vector δ ($\|\delta\| \leq \epsilon$) which corresponds to the smallest value of $|w^H (\mathbf{a}_s + \delta)|$

It has been proven in [16] that if $|w^H \mathbf{a}_s| > \epsilon \|w\|$ then the problem (27) is equivalent to

$$\min_w w^H \hat{\mathbf{R}} w \text{ s.t. } w^H \mathbf{a}_s \geq \epsilon \|w\| + 1. \quad (29)$$

Note that the original problem (27) appears to be computationally intractable, whereas (29) represents the so-called Second-Order Cone (SOC) programming problem which can be easily solved using standard and highly efficient interior point method software [29].

Interestingly, the inequality constraint in (29) can be proven to be equivalent to the equality constraint $w^H \mathbf{a}_s \geq \epsilon \|w\| + 1$ [16], [26]. Taking this into account, we can rewrite (29) as

$$\min_w w^H \hat{\mathbf{R}} w \text{ s.t. } |w^H \mathbf{a}_s - 1| \geq \epsilon^2 w^H w. \quad (30)$$

The solution to (30) can be found by means of Lagrange multiplier method and can be expressed in the following form:

$$w = \frac{\lambda}{\lambda \mathbf{a}_s^H (\hat{\mathbf{R}} + \lambda \epsilon^2 \mathbf{I})^{-1} \mathbf{a}_s - 1} (\hat{\mathbf{R}} + \lambda \epsilon^2 \mathbf{I})^{-1} \mathbf{a}_s. \quad (31)$$

Equation (31) shows that the robust beamformer in (29) belongs to the class of diagonal loading techniques. Note, however, that it is not possible to use (31) directly for computing the optimal weight vector because it is not clear how to obtain the Lagrange multiplier λ in a closed form.

Several extensions of this approach have been considered. In [26], the robust formulation (27) has been extended to the case where the uncertainty is anisotropic [26]. Furthermore, the authors of [26] and [27] derived several alternative algorithms based on Newton's method rather than SOC programming.

In [22], the approach of [16] has been extended to the case in which, besides the steering vector mismatch, there is a nonstationarity of the training data (which may be caused by nonstationary interferers and propagation channel, as well as antenna motion or vibration). The approach of [22] suggests, instead of modelling uncertainty in the covariance matrix (as in

(18)), to model such an uncertainty by means of adding it directly to the data matrix \mathbf{X} . To take into account nonstationarity of the training data, let us introduce the mismatch matrix

$$\Delta = \tilde{\mathbf{X}} - \mathbf{X}, \quad (32)$$

where $\tilde{\mathbf{X}}$ and \mathbf{X} are, respectively, the actual and presumed data matrices at the beamforming sample (which is often referred to as the test cell). The presumed data matrix \mathbf{X} corresponds to the actually received data. However, in on-line problems, this data corresponds to the measurements that are made prior to the test cell. Therefore, because of nonstationarity effects, such past data samples may inadequately model the test cell, where the actual data matrix is unknown and equal to $\tilde{\mathbf{X}}$. Hence, in the nonstationary case, the actual sample covariance matrix can be written as

$$\hat{\mathbf{R}} = \frac{1}{N} \tilde{\mathbf{X}} \tilde{\mathbf{X}}^H = \frac{1}{N} (\mathbf{X} + \Delta)(\mathbf{X} + \Delta)^H \quad (33)$$

It is important to stress that, according to (33), the matrix $\hat{\mathbf{R}}$ is guaranteed to be Hermitian and non-negative definite. However, this matrix is unknown because the type of nonstationarity (and, therefore, the mismatch Δ) are unknown.

To combine the robustness against interference nonstationarity and steering vector errors, the authors of [22] use ideas similar to that proposed in [16] and [26]. That is, they assume that the norms of both the steering vector mismatch δ and the data matrix mismatch Δ are bounded by known constants:

$$\|\delta\| \leq \epsilon, \quad \|\Delta\| \leq \eta, \quad (34)$$

Then, the robust formulation of the MVDR beamforming problem can be written in the following form [22]:

$$\begin{aligned} \min_w \max_{\|\Delta\| \leq \eta} & \|(\mathbf{X} + \Delta)^H \mathbf{w}\| \\ \text{s.t. } & |\mathbf{w}^H (\mathbf{a}_s + \delta)| \geq 1, \forall \|\delta\| \leq \epsilon \end{aligned} \quad (35)$$

This problem further extends (27) by means of incorporating an additional robustness against nonstationary training data. The essence of (35) is that the output power of adaptive beamformer is minimized for the scenario with the worst-case nonstationarity of the training data subject to the additional constraint which maintains distortionless response for the worst-case steering vector mismatch.

To simplify the problem (35), the authors of [22] have proved that

$$\max_{\|\Delta\| \leq \eta} \|(\mathbf{X} + \Delta)^H \mathbf{w}\| = \|\mathbf{X}^H \mathbf{w}\| + \eta \|\mathbf{w}\|. \quad (36)$$

Using (36) and further transforming the constraint (see (29)), the problem (35) has been converted to

$$\min_w \|\mathbf{X}^H \mathbf{w}\| + \eta \|\mathbf{w}\| \quad \text{s.t. } \mathbf{w}^H \mathbf{a}_s \geq \epsilon \|\mathbf{w}\| + 1, \quad (37)$$

which can be viewed as an extended version of (29). Note that (37) also belongs to the class of SOC

programming problems and can be efficiently solved using standard interior point method software [29]. The combination of the approach (37) and the matrix taper method of [17-20] has been considered in [23].

4. CONCLUSIONS

In this paper, robustness issues that emerge in adaptive beamforming have been considered. The term "robustness" can be understood as a certain number of formal constraints or ad-hoc modifications that are incorporated into adaptive beamforming algorithms to preserve them from degradation under a certain model mismatch.

In summary, the area of robust adaptive beamforming remains a field of intensive study over many years. Current and future research trends in this field include the design of robust beamformers based on the idea of worst-case performance optimization, the development of techniques which combine different types of robustness into a single scheme, their performance study in application to a variety of practical problems, as well as investigation of theoretical relationships between new algorithms emerging in this field.

5. REFERENCES

1. R. A. Monzingo and T. W. Miller, *Introduction to Adaptive Arrays*, Wiley, NY, 1980.
2. H. L. Van Trees, *Optimum Array Processing*, Wiley, NY, 2002.
3. A. B. Gershman, "Robust adaptive beamforming in sensor arrays," *Int. Journ. Electronics and Communications*, invited paper, vol. 53, pp. 305-314, Dec. 1999.
4. D. D. Feldman and L. J. Griffiths, "A projection approach to robust adaptive beamforming," *IEEE Trans. Signal Processing*, vol. 42, pp. 867-876, Apr. 1994.
5. H. Cox, R. M. Zeskind, and M. H. Owen, "Robust adaptive beamforming," *IEEE Trans. Acoust., Speech, Signal Processing*, vol. 35, pp. 1365-1376, Oct. 1987.
6. A. B. Gershman, "Robustness issues in adaptive beamforming and high-resolution direction finding," chapter in *High-Resolution and Robust Signal Processing*, Y. Hua, A. B. Gershman, and Q. Cheng: Editors, Marcel Dekker, to appear in 2003.
7. A. B. Gershman, "Robustness issues in adaptive beamforming," keynote speech at RTA Symp. on Smart Antennas, Chester, UK, April 2003.
8. A. B. Gershman, G. V. Serebryakov, and J. F. Bohme, "Constrained Hung-Turner adaptive beamforming algorithm with additional robustness to wideband and moving jammers," *IEEE Trans. Antennas and Propagation*, vol. 44, no. 3, pp. 361-367, March 1996.
9. A. B. Gershman, U. Nickel, and J. F. Bohme, "Adaptive beamforming algorithms with robust-

- ness against jammer motion," *IEEE Trans. Signal Processing*, vol. 45, pp. 1878-1885, July 1997.
10. S. D. Hay ward, "Effects of motion on adaptive arrays," *IEE Proc. - Radar, Sonar and Navigation*, vol. 144, pp. 15-20, Feb. 1997.
11. A. B. Gershman, E. Nemeth, and J. F. Bohme, "Experimental performance of adaptive beamforming in a sonar environment with a towed array and moving interfering sources," *IEEE Trans. Signal Processing*, vol. 48, pp. 246-250, Jan. 2000.
12. B. D. Carlson, "Covariance matrix estimation errors and diagonal loading in adaptive arrays," *IEEE Trans. Aerospace and Electron. Syst.*, vol. 24, pp. 397-401, July 1988.
13. Y. I. Abramovich, "Controlled method for adaptive optimization of filters using the criterion of maximum SNR," *Radio Engineering and Electronic Physics*, vol. 26, pp. 87-95, March 1981.
14. O. Cheremisin, "Efficiency of adaptive algorithms with regularized sample covariance matrix," *Radiotechn. & Electron.*, no. 10, pp. 1933-1941, 1982.
15. L. Chang and C. C. Yeh, "Performance of DMI and eigenspace-based beamformers," *IEEE Trans. Antennas and Propagation*, vol. 40, pp. 1336-1347, Nov. 1992.
16. S. Vorobyov, A. B. Gershman, and Z.-Q. Luo, "Robust adaptive beamforming using worst-case performance optimization: a solution to the signal mismatch problem," *IEEE Trans. Signal Processing*, vol. 51, pp. 313-324, Feb. 2003.
17. R. J. Mailloux, "Covariance matrix augmentation to produce adaptive array pattern troughs," *IEE Electronics Letters*, vol. 31, no. 10, pp. 771-772, May 1995.
18. J. Riba, J. Goldberg, and G. Vazquez, "Robust beamforming for interference rejection in mobile communications," *IEEE Trans. Signal Processing*, vol. 45, pp. 271-275, Jan. 1997.
19. M. A. Zatman, "Production of adaptive array troughs by dispersion synthesis," *IEE Electronics Letters*, vol. 31, no. 25, pp. 2141-2142, Dec. 1995.
20. J. R. Guerci, "Theory and application of Covariance matrix tapers to robust adaptive beamforming," *IEEE Trans. Signal Processing*, vol. 47, pp. 977-985, Apr. 2000.
21. M. A. Zatman, "Comment on 'Theory and application of covariance matrix tapers for robust adaptive beamforming,'" *IEEE Trans. Signal Processing*, vol. 48, pp. 1796-1800, June 2000.
22. S. A. Vorobyov, A. B. Gershman, Z.-Q. Luo, and N. Ma, "Adaptive beamforming with joint robustness against signal steering vector errors and interference nonstationarity," in *Proc. ICASSP'03*, Hong Kong, Apr. 2003, vol. V, pp. 345-348.
23. S. A. Vorobyov, A. B. Gershman, Z.-Q. Luo, and N. Ma, "Adaptive beamforming with joint robustness against mismatched signal steering vector and interference nonstationarity," *IEEE Signal Processing Letters*, to appear.
24. S. Shahbazpanahi, A. B. Gershman, Z.-Q. Luo, and K. M. Wong, "Robust adaptive beamforming for general-rank signal models using worst-case performance optimization," in *Proc. 2nd IEEE Sensor Array and Multichannel Signal Processing Workshop*, Rosslyn, VA, Aug. 2002, pp. 13-17 (also to appear in *IEEE Trans. Signal Processing*, vol. 51, Sept. 2003).
25. S. Shahbazpanahi, A. B. Gershman, Z.-Q. Luo, and K. M. Wong, "Robust adaptive beamforming using worst-case SINR optimization: a new diagonal loading-type solution for general-rank signal models," in *Proc. ICASSP'03*, Hong Kong, Apr. 2003, vol. V, pp. 333-336.
26. R. Lorenz and S. P. Boyd, "Robust minimum variance beamforming," submitted to *IEEE Trans. Signal Processing*.
27. J. Li, P. Stoica, and Z. Wang, "On robust Capon beamforming and diagonal loading," in *Proc. ICASSP'03*, Hong Kong, Apr. 2003, vol. V, pp. 337-340.
28. N. Wong, T. S. Ng, and V. Balakrishnan, "A geometrical approach to robust minimum variance beamforming," in *Proc. ICASSP'03*, Hong Kong, Apr. 2003, vol. V, pp. 329-332.
29. J. F. Sturm, "Using SeDuMi 1.02, a MATLAB toolbox for optimization over symmetric cones," *Optim. Meth. Software*, vol. 11-12, pp. 625-653, Aug. 1999.

ON LOSSES OF COHERENT SIGNAL IN THE ADAPTIVE DETECTOR WITH NON-COHERENT INTEGRATION

D. I. Lekhovitsky ¹, P. M. Flekser, S. V. Polishko ²

¹ Scientific Center of Air Defence, Kharkiv, Ukraine
<David@rls.kharkiv.com>

² Kharkiv Military University, Kharkiv, Ukraine

Abstract

In the paper, there is compared the effectiveness of two types of adaptive detectors of Gaussian coherent signals against the background of Gaussian correlated interference – with coherent and non-coherent integration of output signals of an interference canceller. It is shown that at the maximum likelihood estimation of the adaptive canceller parameters, the detector with non-coherent integration can be not only simpler, but also more effective.

1. INTRODUCTION

The optimal, by the **Neuman-Pearson** criterion, detector of coherent signal of a point target against the background of Gaussian correlated interference should incorporate either a whitening or converting filter – an interference canceller (**IC**) and a coherent integrator (**CI**) matched with a determining parameter α (as parameter α , there can be a direction of arrival, a frequency or other) of the target signal [1-3]. Under typical for practice conditions, when parameter α is a priori unknown there should be provided either **CI** readjustment or an assortment of conditions for all the parameter values at possible range of its change. The first way often is unacceptable due to strong time limitations, the second one – because of great apparatus expenses.

By this reason, in practice, significantly simpler non-coherent integrators (**NCI**) of **IC** output signals are used. A great attention is paid in literature [1, 4-9 and other] to the analysis of losses associated with this. There is shown, in particular, that the more an interval (spatial, time, or space-time) of non-coherent integration, the higher their level.

However, in the mentioned works, as well as at a number of other ones, **NCI** losses are computed for non-adaptive detectors, wherein parameters of the receiving tract, including **IC** as well, are fixed. In adaptive detectors, **IC** parameters are formed over training samples with a finite volume and therefore are random. This randomness variously influences on the efficiencies of **CI** and **NCI**, and, as it is shown below, in certain situations, can change a steady notion of their comparative advantages.

The paper is arranged in the following manner. In item 2, the problems under solving and used assumptions

are formulated. In item 3, there are compared indices of optimum (with **CI**) and non-optimum (with **NCI**) detectors of coherent signal at **IC** with fixed parameters. In item 4, adaptive detectors with coherent and non-coherent integration of **IC** output signals with random parameters are compared.

2. PROBLEM FORMULATION

The problem under solving is in comparison of four versions of detectors differing in species of the used pre-threshold statistics, in the value of the probability of detection (**PD**)

$$D = \int_{x_0}^{\infty} p_{\xi_1}(x) dx \quad (1)$$

at the fixed, owing to choosing corresponding threshold x_0 , the probability of false alarm (**PFA**)

$$F = \int_{x_0}^{\infty} p_{\xi_0}(x) dx. \quad (2)$$

Here $p_{\xi_\gamma}(x)$ is the distribution density of compared statistics $\xi_\gamma = \xi(\mathbf{u}_\gamma)$ in the absence ($\gamma = 0$) and presence ($\gamma = 1$) of the useful (expected) signal $\mathbf{x}_s = \{x_{si}\}_{i=1}^M$ in an additive mixture

$$\mathbf{u}_\gamma = \{\mathbf{u}_{\gamma i}\}_{i=1}^M = \mathbf{y} + \gamma \cdot \mathbf{x}_s, \quad \gamma = 0, 1 \quad (3)$$

with interference $\mathbf{y} = \{\mathbf{y}_i\}_{i=1}^M$.

Terms in (3) are assumed to be independently complex, normal M -dimensional vectors

$$\mathbf{y} \sim CN(0, \Phi) \quad (4a)$$

$$\mathbf{x}_s = \beta \cdot \mathbf{x}, \quad \beta \sim CN(0, \sigma_s^2), \quad (4b)$$

with zero mean values ($\bar{\mathbf{y}} = \bar{\mathbf{x}}_s = 0$) and $M \times M$ correlation matrices (**CM**)

$$\Phi = \overline{\mathbf{y} \cdot \mathbf{y}^*}, \quad \text{rank } \Phi = M, \quad (5a)$$

$$\Phi_s = \overline{\mathbf{x}_s \cdot \mathbf{x}_s^*} = \sigma_s^2 \cdot \mathbf{x} \cdot \mathbf{x}^*, \text{rank } \Phi_s = 1,$$

where

$$\mathbf{x} = \{x_i\}_{i=1}^M = \mathbf{x} \quad (\alpha), \quad \mathbf{x}^* \cdot \mathbf{x} \leq M \quad (5b)$$

is the steering (non-random) M -dimensional vector of expected signal (4b) with power σ_s^2 , an over-scribed bar and (*) are symbols of statistical averaging and Hermitian conjugate, respectively.

In situations (4), (5), vector (3)

$$\mathbf{u}_\gamma \sim CN(0, \Phi_u) \quad (6)$$

has a zero mean value and **CM**

$$\Phi_u = \begin{cases} \Phi, & \gamma = 0, \\ \Phi + \sigma_s^2 \mathbf{x} \mathbf{x}^*, & \gamma = 1. \end{cases} \quad (7)$$

The pre-threshold statistics being analyzed are equal to

$$\xi_\gamma = |\eta_\gamma|^2, \quad \eta_\gamma = \mathbf{t}_\gamma^* \cdot \mathbf{x}, \quad \mathbf{t}_\gamma = \Psi \cdot \mathbf{u}_\gamma; \quad (8a)$$

$$\xi_\gamma = \mathbf{p}_\gamma^* \cdot \mathbf{p}_\gamma, \quad \mathbf{p}_\gamma = \{p_{\gamma i}\}_{i=1}^M = \mathbf{H} \cdot \mathbf{u}_\gamma; \quad (8b)$$

$$\mathbf{H}^* \mathbf{H} = \Psi = \Phi^{-1}. \quad (9)$$

$$\xi_\gamma = |\hat{\eta}_\gamma|^2, \quad \hat{\eta}_\gamma = \hat{\mathbf{t}}_\gamma^* \cdot \mathbf{x}, \quad \hat{\mathbf{t}}_\gamma = \hat{\Psi} \cdot \mathbf{u}_\gamma; \quad (10a)$$

$$\xi_\gamma = \hat{\mathbf{p}}_\gamma^* \cdot \hat{\mathbf{p}}_\gamma, \quad \hat{\mathbf{p}}_\gamma = \{\hat{p}_{\gamma i}\}_{i=1}^M = \hat{\mathbf{H}} \cdot \mathbf{u}_\gamma; \quad (10b)$$

$$\hat{\mathbf{H}}^* \hat{\mathbf{H}} = \hat{\Psi} = \hat{\Phi}^{-1}. \quad (11)$$

In the considered situations (4)–(7), the first of them (8a) corresponds to an optimal detector, wherein there is compared with a threshold a squared modulus of the coherent sum η_γ of elements of vector $\mathbf{t}_\gamma = \{t_{\gamma i}\}_{i=1}^M$ of output signals of a converting filter (with the $M \times M$ matrix impulse characteristic (**MIC**) equal to matrix Ψ (9) [3, p. 716]). The second statistics (8b) is formed of **NCI** (by summing squared modules) elements of vector $\mathbf{p}_\gamma = \{p_{\gamma i}\}_{i=1}^M$ of output signals of the whitening filter (with $M \times M$ **MIC** \mathbf{H} is the matrix “root” of matrix Ψ represented as in (9) [3, p. 714]).

Statistics (10) are “adaptive analogues” of statistics (8), wherein **CM** (a priori unknown) of interference Φ is replaced with its maximum likelihood (**ML**) estimate

$$\hat{\Phi} = K^{-1} \mathbf{A}, \quad \mathbf{A} = \mathbf{V} \mathbf{V}^* = \sum_{i=1}^K \mathbf{v}_i \cdot \mathbf{v}_i^*. \quad (12)$$

Here $\mathbf{V} = \{\mathbf{v}_i\}_{i=1}^K$ is the training sample of volume K of mutually independent M -dimensional vectors

$$\mathbf{v}_i \sim CN(0, \Phi), \quad i \in 1, K \quad (13)$$

being statistical equivalent to interference vector \mathbf{y} (4a), but not correlated with it, with the useful signal (4b) and, as a consequence, with their mixture (3):

$$\overline{\mathbf{v}_i \mathbf{u}_\gamma^*} = 0, \quad i \in 1, K; \quad \gamma = 0, 1. \quad (14)$$

Random matrix \mathbf{A} determining estimate (12) under such conditions has the **Wishart** complex distribution with a density [10]

$$p(\mathbf{A}) = C |\mathbf{A}|^\delta \exp \{-\text{tr } \Psi \cdot \mathbf{A}\}, \quad \delta \geq 0, \quad (15)$$

where C is the normalizing constant, $\delta = K - M \geq 0$ is the “effective” volume of training sample, $\text{tr } \mathbf{B}$ and $|\mathbf{B}|$ are the matrix \mathbf{B} trace and determinant, respectively.

For the formulated conditions (4)–(7), (12)–(15), there are defined below densities of the distribution $p_{\xi_\gamma}(\mathbf{x})$ of statistics (8), (10) and the following from them characteristics (1), (2) of the corresponding detectors.

3. COMPARISON OF POTENTIALITIES OF DETECTORS WITH CI AND NCI

Let us start from the well known and simplest statistics (8a) of an optimal detector. By virtue of (5)–(7), (9), vector

$$\mathbf{t}_\gamma \sim CN(0, \Phi_t), \quad \Phi_t = \Psi \Phi_u \Psi,$$

$$\eta_\gamma \sim CN(0, \bar{\xi}_\gamma),$$

$$\bar{\xi}_\gamma = \mathbf{x}^* \Phi_t \mathbf{x} = \begin{cases} \bar{\xi}_0 = \mathbf{x}^* \Psi \mathbf{x}, & \gamma = 0, \\ \bar{\xi}_1 = \bar{\xi}_0 (1 + \sigma_s^2 \bar{\xi}_0), & \gamma = 1, \end{cases} \quad (16)$$

and, consequently, statistics (8a) has the exponential distribution [11]

$$p_{\xi_\gamma}(\mathbf{x}) = \frac{1}{\bar{\xi}_\gamma} \exp \left\{ -\mathbf{x} / \bar{\xi}_\gamma \right\} \quad (17)$$

with the mean value $\bar{\xi}_\gamma$ (16). Therefore [1–3]

$$F = \exp \left\{ \frac{-x_0}{\bar{\xi}_0} \right\}, \quad D = \exp \left\{ \frac{-x_0}{\bar{\xi}_1} \right\} = F^{\frac{1}{1+\mu}}, \quad (18)$$

so at fixed PFA F , PD D is completely determined by the value

$$\mu = (|\bar{\xi}_1 - \bar{\xi}_0|) / \bar{\xi}_0 = \sigma_s^2 \mathbf{x}^* \Psi \mathbf{x} = \sigma_s^2 \bar{\xi}_0 \quad (19a)$$

having an evident meaning of the power signal / (interference + noise) ratio (**SINR**) at the **CI** output.

In the usually considered situation of equality of the own noise σ_n^2 and external interference σ_{in}^2 powers in all M receiving channels, when for **CM** Φ there is true the following representation

$$\Phi = \sigma_n^2 \cdot \mathbf{I}_M + \sigma_{in}^2 \cdot \Phi_{in} = \sigma_n^2 \cdot \Phi_N,$$

$$\Phi_N = \mathbf{I}_M + \eta \cdot \Phi_{in}, \quad \eta = \sigma_{in}^2 / \sigma_n^2, \quad \Phi_N^{-1} = \Psi_N,$$

where \mathbf{I}_M is the unit $M \times M$ matrix, **SINR** (19a) can be written as

$$\mu = M \cdot h \cdot \chi, \quad (19b)$$

where

$$h = \sigma_s^2 / \sigma_n^2 \quad \text{and} \quad \chi = \mathbf{x}^* \Psi_N \mathbf{x} / M \leq 1 \quad (19c)$$

are the signal to noise ratio (**SNR**) in the receiving channel and the “useful signal power utilization factor [2, 3]”.

The latter, at $\mathbf{x}^* \cdot \mathbf{x} = M$ is equal to unit in the absence of external interference ($\eta = 0$, $\Phi_N = \Psi_N = \mathbf{I}_M$), and otherwise is less than unit.

Let us proceed to the detector with NCI of output signals of the whitening filter. As it follows from (6), (7), (8b), the vector being formed by it

$$\mathbf{p}_\gamma \sim CN(0, \Phi_p) \quad (20)$$

has a zero mean value and CM

$$\Phi_p = \mathbf{H}\Phi_u\mathbf{H}^* = \begin{cases} \mathbf{I}_M, & \gamma = 0, \\ \mathbf{I}_M + \sigma_s^2 \mathbf{H}\mathbf{x}\mathbf{x}^* \mathbf{H}^*, & \gamma = 1, \end{cases} \quad (21)$$

Using the known [2, 3] representation

$$\mathbf{p}_\gamma = \mathbf{G}\Lambda^{1/2}\boldsymbol{\varepsilon}, \quad \mathbf{G}\Lambda\mathbf{G}^* = \Phi_p \quad (22a)$$

$$\boldsymbol{\varepsilon} = \{\varepsilon_i\}_{i=1}^M \sim CN(0, \mathbf{I}_M), \quad (22b)$$

$$\Lambda = \text{diag}\{\lambda_i\}_{i=1}^M, \quad \mathbf{G}\mathbf{G}^* = \mathbf{G}^*\mathbf{G} = \mathbf{I}_M \quad (22c)$$

of vector \mathbf{p}_γ (20) through eigenvalues (e.v.) $\lambda_i > 0$ and unitary (22c) matrix $\mathbf{G} = \{g_i\}_{i=1}^M$ of eigenvectors of its CM Φ_p (21), the statistics (8b) can be presented as

$$\xi_\gamma = \boldsymbol{\varepsilon}^* \Lambda \boldsymbol{\varepsilon} = \sum_{i=1}^M \lambda_i |\varepsilon_i|^2, \quad \gamma = 0, 1. \quad (23)$$

At $\gamma = 0$, as follows from (21), $\Lambda = \mathbf{I}_M$, therefore

$$\varepsilon_0 = \boldsymbol{\varepsilon}^* \boldsymbol{\varepsilon} = \sum_{i=1}^M |\varepsilon_i|^2. \quad (24)$$

For condition (22b), such a sum, as is known [11], has the Erlang distribution

$$p_{\varepsilon_0}(x) = x^{M-1} \exp\{-x\} / (M-1)! \quad (25)$$

and, consequently, the threshold x_0 fixing PFA F is the root of the equation

$$F = \varphi(M, x_0), \quad (26)$$

$$\varphi(m, x) = e^{-x} \sum_{i=0}^{m-1} \frac{x^i}{i!}. \quad (27)$$

At $\gamma = 1$ $\lambda_i = 1 + \ell_i$, where ℓ_i ($i \in 1, M$) are e.v. of matrix $\mathbf{S} = \sigma_s^2 \mathbf{H}\mathbf{x}\mathbf{x}^* \mathbf{H}^*$. Rank of this matrix equals 1 and, thereby, $\ell_i = 0$ for all $i \in 1, M-1$. A single non-zero e.v. ℓ_M in this case concurs with its trace $\text{tr} \mathbf{S} = \sigma_s^2 \mathbf{x}^* \mathbf{H}^* \mathbf{H} \mathbf{x} = \mu$. So,

$$\lambda_i = 1, \quad i \in 1, M-1; \quad \lambda_M = 1 + \mu, \quad (28)$$

and, in connection with this, statistics (23) at $\gamma = 1$ can be presented as a sum

$$\xi_1 = a + b, \quad a = \sum_{i=1}^{M-1} |\varepsilon_i|^2, \quad b = (1 + \mu) |\varepsilon_M|^2 \quad (29)$$

of two independent summands a and b with densities

$$p_a(x) = \frac{x^{M-2} e^{-x}}{(M-2)!}, \quad p_b(x) = \frac{e^{-x/(1+\mu)}}{(1+\mu)}. \quad (30)$$

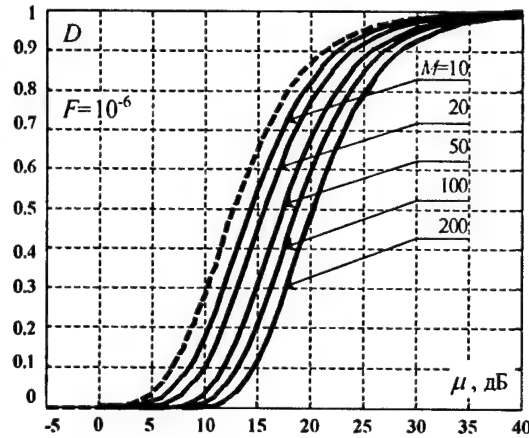


Fig. 1.

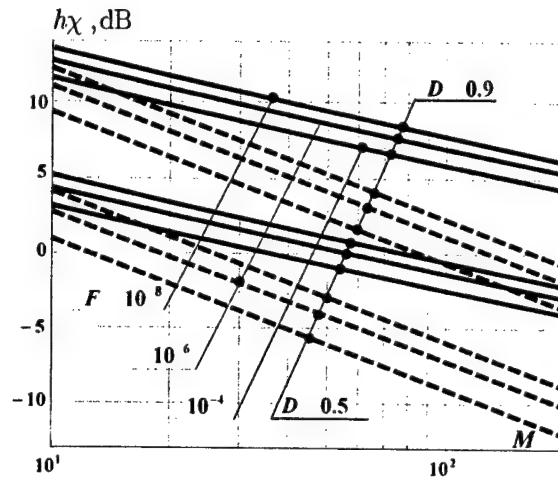


Fig. 2.

It is not difficult to show that the density of sum (29) in this case is equal to

$$p_{\xi_1}(x) = \lambda_M^{-1} b_M^{M-1} \exp\left\{-\frac{x}{\lambda_M}\right\} \left(1 - \varphi\left(M-1, \frac{x}{b_M}\right)\right), \quad (31)$$

$$b_M = 1 + \mu^{-1}.$$

Integrating it over (1), we obtain PD

$$D = b_M^{M-1} \left[\exp\left\{-\frac{x_0}{\lambda_M}\right\} - \lambda_M^{-1} \sum_{m=0}^{M-2} b_M^{-m} \varphi(m+1, x_0) \right] \quad (32)$$

for the detector with NCI of the whitening filter signals.

In Fig. 1, for FAP $F = 10^{-6}$, a family of detection curves $D(\mu)$ (32) at different values of the number M of processing channels is shown. The dashed curve here corresponds to the accounted by (18) PD of the optimal detector (8a). At arbitrary point $\mu = \mu_0$, the difference between the dashed curve ordinate and ordinates of solid curves characterizes a gain in optimal processing for PD D at this point. Difference of abscissas of the same curves at point $D = D_0$ characterizes its gain (in dB) in threshold SINR μ (19) at this point.

More readily it is seen in Fig. 2, where dependencies of M threshold values of product $h \cdot \chi = \mu / M$

(19b) of the optimal (dashed curves) and non-optimal (solid curves) processing for $D = 0.5$ and $D = 0.9$ at $F = 10^{-4}$, 10^{-6} , 10^{-8} are shown. Losses of the latter in the threshold SNR h (in dB) are determined here by the difference in ordinates of corresponding solid and dashed curves, which increases as M grows. Thus, at $F = 10^{-6}$ and $D = 0.9$, they constitute ≈ 2 dB at $M = 10$, and ≈ 7 dB at $M = 200$.

However, it should be outlined, that conclusions about advantages of coherent processing as compared with the non-coherent one, which follow from these pictures are valid only in the considered hypothetical situation of the exact knowledge of interference CM, which allows accurate forming the optimal statistics (8a). When replacing a priori unknown CM with this or that its (approximate) estimation, the relationship between them can turn into the opposite one making non-coherent processing preferable not only due to the considerably more simplicity, but and due to the higher effectiveness. This important for practice conclusion not reflected in the literature known for the authors is illustrated by the example of adaptive detectors (10) on the basis of ML CM estimates (12)–(15).

4. COMPARATIVE EFFECTIVENESS OF ADAPTIVE DETECTORS WITH CI AND NCI

The used in this part densities of the distribution $p_{\xi}(x)$ of adaptive statistics (10), which determine their statistical characteristics (1), (2) under conditions (12)–(15), are obtained and given in the prepared to publishing articles [12, 13]. Derivation of these densities is rather awkward and therefore is not being given here.

For statistics (10a), they are

$$p_{\xi}(x) = (K^2 \cdot \bar{\xi}_0)^{-1} \cdot p_{r_\gamma}(x / K^2 \bar{\xi}_0),$$

where $p_{r_\gamma}(x)$ is the distribution density of the normalized random value

$$r_\gamma = \xi_\gamma / (K^2 \cdot \bar{\xi}_0), \quad (33)$$

equal to

$$p_{r_\gamma}(x) = \begin{cases} \bar{\nu} \cdot \varphi(\delta) {}_3F_1(a, b, c; d; -4x), & \gamma = 0, \\ \varphi(\delta) \int_0^1 f(y) {}_2F_0\left(c, b; -\frac{4xy}{1+\mu y}\right) dy, & \gamma = 1. \end{cases} \quad (34)$$

Here ${}_3F_1(a, b, c; d; z)$ and ${}_2F_0(c, b; z)$ are corresponding hypergeometric functions [14],

$$a = \delta + 3, b = a/2, c = (a + 1)/2; d = K + 2;$$

$$\varphi(\delta) = (\delta + 1)(\delta + 2);$$

$$f(y) = yp_\nu(y)/(1 + \mu y),$$

$$\bar{\nu} = (K - M + 2)/(K + 1) = (\delta + 2)/(K + 1) \quad (35)$$

the mean value of the normalized to a maximum (19) estimating (random) SINR

$$\nu = \hat{\mu} / \mu \leq 1 \quad (36)$$

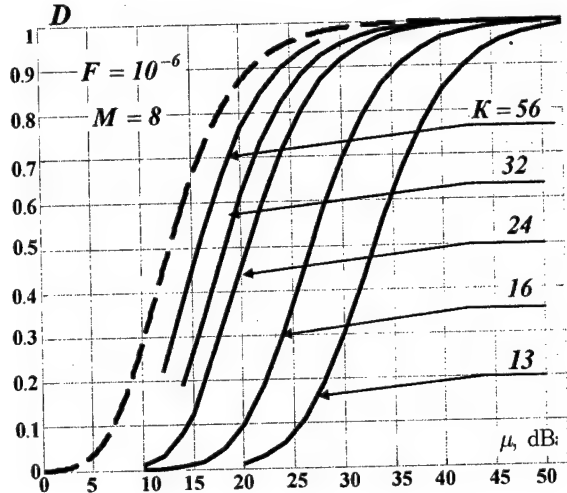


Fig. 3.

at the output of the adaptive detector (10a), (12) with the density of distribution [10]

$$p_\nu(y) = y^{\delta+1} (1-y)^{M-2} / B(\delta+2, M-1) \quad (37)$$

$$B(n+1, m+1) = n!m!/(n+m+1)!$$

Threshold x_0 fixing PFA $F(2)$ at a specified level is equal to [12]

$$x_0 = K^2 \cdot \bar{\xi}_0 \cdot x_1,$$

where x_1 is a root of the equation

$$F = {}_3F_1(\delta+2, (\delta+1)/2, (\delta+2)/2K+1; -4; x_1) \quad (38)$$

PD under condition (34) is determined by the integral

$$D = \int_0^1 p_\nu(y) {}_2F_0\left(\frac{\delta+2}{2}, \frac{\delta+1}{2}; -\frac{4x_1 y}{1+\mu y}\right) dy, \quad (39)$$

which in the general case is not expressed by neither elementary nor known special functions.

In Fig. 3, as an example, a family of dependencies $D = D(\mu)$ (38), (39) for $F = 10^{-6}$, $M = 8$ and different values of volume of training sample K in ML CM estimate is given (12). A dashed curve here, as well as in Fig. 1, corresponds to an optimal detector (8a).

The curves of this family link the sample volume with probability characteristics of detection and herewith determine statistical speed [12] of adaptive processing (10a), (12). It can significantly differ from the introduced in [10] and universally used "energetic" speed that correlates with this volume the mean value of energetic losses (36).

As follows from (35), already at $K = K_e = 2M - 3$ mean energetic losses constitute 3 dB ($\bar{\nu} = 1/2$), and therefore, for their compensation it is enough to double SNR h (19c). On this bases, a sample of such a volume is often considered practically sufficient for an adaptive detector (10a), (12).

However, such a sample can lead to prohibitively large losses in its statistical characteristics of detection,

which are not compensated at SNR doubling. For example, under conditions given in Fig. 3 ($M = 8$) at $K = K_e = 13$ it is practically inoperative ($D = D_a \leq 0.02$) until a value $\mu \approx 21$ dB, at which the optimal processing provides PD $D = D_0 = 0.9$. Doubling of SNR h , at which the mean value of its output SINR is equal to 21 dB as well, increases PD only until $D = D_a \leq 0.05$, that is continues keep it inoperative. In order to bring the value of PD to $D = D_a = 0.9$, in this case, SINR $\mu \approx 42$ dB is needed, i.e. the increase of SNR not by 3, but by 21 dB. For the requirements to an additional growth of threshold SNR h not exceeding 3 dB, under conditions in Fig. 3, there is necessary the training sample of significantly more volume $K = K_s \approx 56 = 7M$.

The reason of difference between "statistical" and "energetical" speeds (non-equalities $K_s > K_e$) is quite obvious. It is stipulated by the difference in the distribution laws (17) and (34) of pre-threshold statistics (8a) and (10a), (12) of optimal and adaptive detectors, by virtue of which, the equality of their energetic characteristics does not entail that of their statistical characteristics as well. This concerns also the detector (10b), (12) with non-coherent integration of output signals of the adaptive whitening filter, to whose analysis we now proceed.

For statistics ξ_γ (10b) under conditions (12)–(15)

$$p_{\xi_\gamma}(x) = K^{-1} p_{\tau_\gamma}(x/K),$$

where $p_{\tau_\gamma}(x)$ is the density of the random value distribution

$$\tau_\gamma = \xi_\gamma / K, \quad (40)$$

equal to [13]

$$p_{\tau_\gamma}(x) = \begin{cases} B^{-1}(M, \delta + 1) x^{M-1} / (1+x)^{K+1}, \gamma = 0, \\ f(x) {}_2F_1(M-1, K+1; M; -x), \gamma = 1, \end{cases} \quad (41)$$

$$f(x) = \frac{(1+\mu)^K}{B(M, \delta + 1)} \frac{x^{M-1}}{(1+\mu+x)^{K+1}},$$

$$z = \mu x / (1 + \mu + x).$$

Threshold x_0 fixing FAP F is equal to

$$x_0 = K \cdot x_1,$$

where x_1 is a root of the equation

$$F = B^{-1}(M, \delta + 1) \int_0^1 y^\delta (1-y)^{M-1} dy. \quad (42)$$

PD under condition (41) is determined by the integral

$$D = (B(M, \delta + 1)(1 + \mu))^{-1} J,$$

$J =$

$$J = \int_0^1 \frac{1}{(1+y)} y^\delta (1-y)^{M-1} {}_2F_1(1, K+1; M; z(y)) dy \quad (43)$$

$$z(y) = (1-y)\mu / (1 + \mu),$$

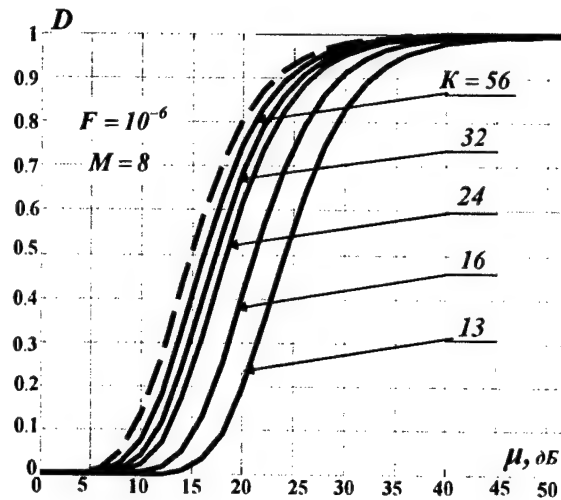


Fig. 4.

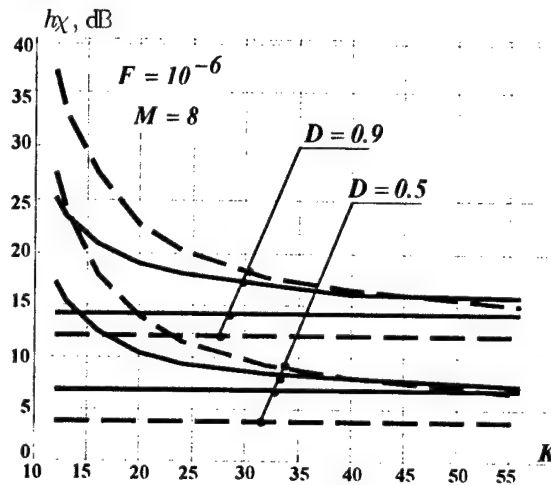


Fig. 5.

which in general case, as well as in (39), is not expressed neither by elementary nor known special functions.

Fig. 4 shows a family of characteristics $D = D(\mu)$ (42), (43) of the considered adaptive detector with NCI under the same condition ($F = 10^{-6}$, $M = 8$), as in Fig. 3. A dashed curve here is calculated by (32) and corresponds to its potentialities under these conditions.

It is seen from comparison of Fig. 4 and Fig. 3 that the detector with NCI (10b) has significantly higher "statistical" speed than that with CI (10a). For example, at $K = K_e = 13$, it provides PD $D = D_a = 0.9$ already at SINR $\mu \approx 32$ dB, i.e. at SNR h less by 10 dB. Two-fold (by 3 dB) growth h compensates losses of adaptive processing already at $K = K_s \approx 28 = 3.5 \cdot M$, what is half as much as with CI.

Fig. 5 visually illustrates the comparative efficiency of adaptive detectors with NCI and CI under considered conditions. Here, for $F = 10^{-6}$, $D = 0.5$ and $D = 0.9$, there are shown threshold values of product $h \cdot \chi$ for processing (10a) with CI (dashed curves) and (10b) with NCI (solid curves) at different volumes of

sample K . Horizontal straight lines show potentialities of corresponding detectors.

It is seen that under considered conditions, at any $K \leq 45 \approx 5.5 \cdot M$, the detector with NCI is more effective, and the less is volume of sample K the more is a gain in SNR h . In particular, at $K = K_e = 13$ it reaches ≈ 9 dB.

A formal reason of distinctions is connected with the difference in distribution laws (34) and (41) of pre-threshold statistics (10a) and (10b). Physically, the advantages of the latter statistics are originated by errors of interference estimation CM (12) due to finiteness of a volume of training sample. These errors change vectors \hat{t}_γ and \hat{p}_γ as compared with "ideal" vectors t_γ and p_γ both on length and direction. Statistics (10a) "feels" these both changes, whereas statistics (10b) depends only on length of vector \hat{p}_γ and does not "feel" its direction. Namely more "robustness" of statistics (10b) provides higher statistical speed and, hence, higher efficiency of adaptive detector with NCI at small volumes of training sample.

5. CONCLUSION

There have been compared efficiencies of two types of detectors of Gaussian coherent signals against the background of Gaussian correlated interference – with coherent (CI) and non-coherent (NCI) integration of output signals of the adaptive canceller of interference. It has been shown that at the maximum likelihood estimate of adaptive canceller parameters, the detector with NCI has roughly a double statistical speed, and therefore, at small volume of training sample provides a gain in detecting characteristics. In connection with this, the steady notion about "losses" at non-coherent integration of coherent signal is valid only for training samples of "large" ($K \geq (5 - 7)M$) volume. For many practical situations, where samples of such a volume are unachievable (due to non-stationarity of interference, limited productivity of hardware, etc.) transition to NCI not only simplifies processing, but can enhance its efficiency. In this case, there is made easier also solution of the important problem of stabilization of false alarm level (it is planned to devote a special publication to substantiation in detail of this statement).

Note in conclusion that the based on (35)–(37) universal **energetical** criterion of the adaptive processing speed, first introduced in [10], imposes the lowered requirements to volume of training sample, at which there can appear inadmissible large losses in **statistical** indices of detection. It is possible to specify the substantiated requirements to this volume owing to the introduced in [12, 13] and applied here **statistical** criterion of speed.

REFERENCES

1. P. A. Bakout, I. A. Bol'shakov et al. Questions of statistical radar theory. V.1.-M.: "Sovetskoe radio". Edited by G. P. Tartakovskiy 1963. – p. 424. (in Rus.)
2. Ya. D. Shirman, V. N. Manjos. Theory and techniques of processing radar information against the background of interference. M.: Radio i Svyaz', 1981. p.416. (in Rus.)
3. Radio electronic systems: foundations of construction and theory. Handbook / Edited by Ya. D. Shirman. M.: CJSC "MAKVIS"; 1998.- 828 p. (in Rus.)
4. D. Middleton. Introduction to the statistical communication theory, 1960.
5. L. A. Vainshtein, V. D. Zubakov. Signal selection against the background of random interferences. - M.: "Sovetskoe radio", 1960.- 448 p.
6. Okhrimenko A. E., Tosev I. T. The analysis of the Detection Characteristics of Interperiod Processing Systems. Radiotekhnika i elektronika, 1971, V.16, № 1, pp. 67 – 75.
7. Proskurin V. I. Probability distribution for the square functional of Gaussian random process. Radiotekhnika i elektronika, 1985, V.30, № 7, p. 1335-1340.
8. Fedinin V. V. Efficiency evaluation peculiarities of MTI systems with noncoherent pulse storage. Radiotekhnika i Elektronika, 1981, V.26, № 5, p. 955-961. (in Russian)
9. Kiselev A. Z. Theory of radar detection on the basis of using vectors of target scattering. M.: Radio i Svyaz, 2002., 272 p. (in Russian)
10. I. S. Reed, J. D. Mallett, L. E. Brennan. Rapid Convergence Rate in Adaptive Arrays, IEEE Trans. Aerosp. Electron. Syst., November 1974, Vol. AES-10, No. 6, pp. 853-863.
11. Hastings N. A. J. and Peacock J. B. Statistical Distributions. A Handbook for students and practitioners. London, Butterworths, 1975.
12. Lekhovitsky D. I., Flekser P. M. Speed of RMB adaptive filters by statistical criteria. In print
13. Lekhovitsky D. I., Flekser P. M. Speed of adaptive whitening filters with non-coherent integration of adaptive of output signals. In print.
14. Handbook of mathematical functions with Formulas, Graphs and Mathematical Tables, Edited by M. Abramowitz and I. Stegun National Bureau of standards, Applied mathematics series – 55. Issued June, 1964.

FOCUSING OF THE SPATIALLY SEPARATED ADAPTIVE ANTENNA ARRAYS ON MULTIPLE RADIATION SOURCES BY METHOD OF CORRELATION IDENTIFICATION OF THE BEARINGS

Yu. N. Sedyshev, P. Yu. Sedyshev, S. N. Rodenko

Abstract

The problems of space-time signal processing in coherent passive radar multistatic system with the adaptive antenna arrays (AAAs) in the receiving points are discussed. Stated that application of pair of spatially separated adaptive antenna arrays in self-focusing mode, which are involved in two-stage procedure of measurement of multiple jamming sources coordinates by base-correlation method, enables to solve bearing identification problem and to optimize the parameters of space-time processing system according to adaptation time. The problem of receiving of two-dimensional responses, which unequivocally characterize space position of each source being located, in the plane of base line - target is solved. The results of simulation are presented.

1. INTRODUCTION

Owing to multiplicity of jamming the signal detection is realized at high level of both correlated and uncorrelated noise. Radiation of electronic countermeasure systems, radio frequency unintended interference, ground clutter and natural noise sources background can be such interferences. High intensity of disturbing signals and their simultaneous influence are the strong reasons to use space-time processing systems on the basis of adaptive antenna arrays for the desired signals processing. Their main advantages [1] are the capability of jamming suppressing; multichanneling of suppression out of a boresight; accurate direction finding of radiation sources and localization of each one with the minimal error even under their close spacing. For the last years the research of methods of application of adaptive antenna arrays in multistatic passive radar systems has become widely spread. The works [2, 3, 4] synthesize optimal and quasi-optimal algorithms of detection of both deterministic and stochastic signals against the background of space-correlated jamming. Also those works give the estimation of signal-to-noise output ratio loss compare to optimal processing [3,5] and of the estimation of efficiency of focusing on the located radiation source in the bistatic system with AAA in one of the receiving points [3,6]. These works does not consider issues regarding application of joint adaptive aperture and correlation inter-aperture processing of noise signals in each position in order to increase efficiency of space localization of multiple radiation sources under limited time of space scanning.

Using of multistage measurement procedure in space-time processing systems with a great number of degrees

of freedom provided in [9,10] enables to eliminate difficulties as for detection, measurement and identification operations. In particular, the responses of space-time processing system under the influence of radiation sources signals can be received with the help of procedures of direction finding in adaptive antenna-arrays, spaced at a distance of a great number of wave lengths, and their self-focusing during correlation identification.

2. PRINCIPLE OF CREATION OF THE OPTIMAL SPACE-TIME FILTER ON THE BASIS OF SPATIALLY SEPARATED AAAS

Consider the possibility of increasing of efficiency of emitting targets space filtering by using of Keypon adaptive algorithm (minimization of external noise dispersion) separately in each antenna array of bistatic system and subject to correlation selection of the detected sources in the adaptive inter-aperture channel. The analysis will be carried out for the space-coherent system model (Fig. 1), which comprises the M_1 -elemental AAA in the central position and the M_2 -elemental AAA in the additional position put on the base b . Using of the AAA in the monostatic radar systems allows to localize the signal source in relation to it by the direction of radiation. Increasing of signal-to-noise ratio in the monostatic AAA due to the adaptation of the vector of weighting factors is typical at that. In this case AAA amplification factor hence the amplitude of signal source field) is a little bit reduced in relation to the direction of the maximal intensity of radiation of the desired signal. At the same time the nought in the jamming directions (Fig. 2) are formed.

If there is not one but some sources of radiation in the beam of the generated adaptive direction-finding

characteristic, their mutual moving in the plane, which is perpendicular to the boresight line, results in the fast fluctuations of the weight factors vector (noise of adaptation). In AAA of gradient type quality of adaptation depends on depth of a correlation feedback. However in this case the process of getting into the steady state is delayed and AAA space selection capabilities are reduced to the potential ones of not adaptive antenna array. It is possible to reduce the adaptation time and to raise quality of space selection by means of creation of information redundancy [5, 7]

If signal processing is realized in two adaptive arrays spaced by some base b , there is a possibility to locate the source radiation not only by its direction but also by difference of time of its arrival to the receiving points by means of focusing the second array on the source of the desired signal subject to the desired signal parallax. Presence of the additional information about radiation sources, particularly, about their selection by time of delay of the envelopes of the cross-correlation functions (CCF) of signals in AAs, which are spaced at a distance of a great number of wave lengths, allows to make additional selection of the chosen source and to make the amplitude-phase distribution (APD) more precise subject to these data. This process can be regarded as a next qualifying phase of localization, during which correction of the weight factors of adaptation is made due to the additional freedom degrees of a system and signal-to-noise relation is optimized due to the reduction of influence of the interfering sources of radiation in AAA's beam (Fig. 3).

In contrast to the system of space-time processing [6] adaptation of complex factors of amplification in each element of antenna arrays is carried out not by the way of gradient forming of the weighting vector but on the basis of the methods of direct conversion of the space correlation matrix of jamming. Besides, the survey on radiation sources propagation difference is carried out in the between-positions-delay-time matrix correlator (MC).

2.1. THE FIRST STAGE OF THE PROCEDURE OF MEASUREMENT OF RADIATION SOURCES COORDINATES WITHOUT ADAPTATION AA

Consider a special case of signal-jamming conditions when there are three stochastic signal sources in the AAA1 and AAA2 coverage sector (Fig. 4). Their searching is carried out in accordance with the optimal space processing algorithm without preliminary estimation of their number. As a result the bearing estimations vector (relative AAA1 - $\bar{\theta}_1$ and relative AAA2 - $\bar{\theta}_2$) is formed. Searching on the generated in both positions bearings by delay time is performed with the purpose of determining of amount of the targets on the bearing line.

The reradiating objects such as close located air ones or ground surface at small altitudes of flight can get in the illumination field. In other words there is an abnormal reproduction of sources in quantity to η (where η - quantity of objects in the illumination field) when multipath signal distribution. In this case these are objects O1 and O2. Moreover, as it is known [5], observation of radiation sources on the spatially separated apertures by the

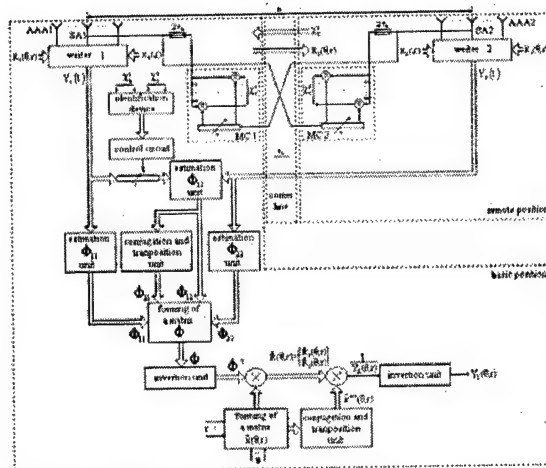


Fig. 1. Model of space-time processing system operation

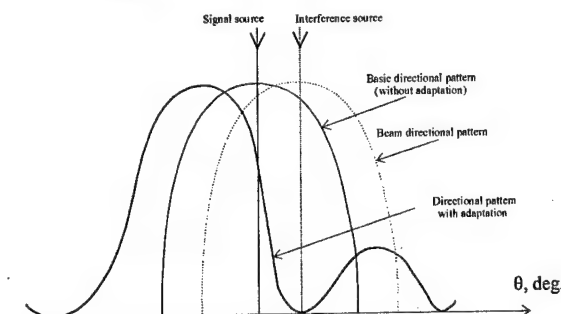


Fig. 2. Adaptation by direction in AAA

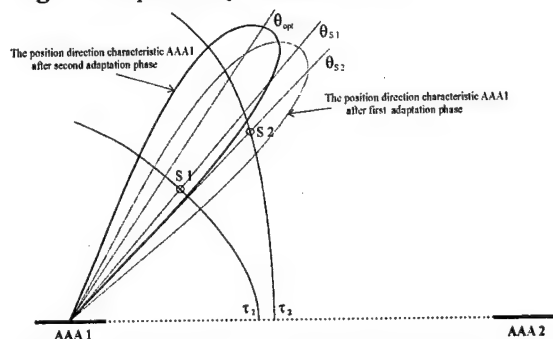


Fig. 3. Adaptation in the spatially separated AAAs by the time of delay of the envelopes of the signal cross-correlation functions (CCF)

methods of a passive location is accompanied with the false targets due to mutual crossing measuring beams. Generally number of false crossings is equal to $n^2 - n$, where n - true number of radiation sources. Thus information about signal and jamming conditions contains $n^2 - n + \eta$ false points, which as well as true ones can be considered by the space processing system as the coordinate measurement objects. Using of matrix correlators in the structure of model allows on the one hand to reduce the time of reception of the information about between-apertures complex envelope delay to the minimum in contrast to the procedure of consecutive focussing on the jamming sources in correlation interferometer [6]. And on the other hand there is possibility to realize a rule of an identification of the radiating targets in accordance with

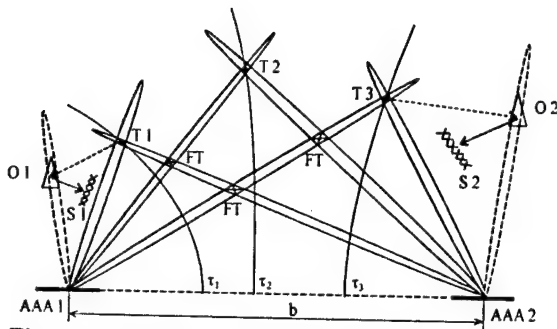


Fig. 4. A principle of space selection in the two AAAs system

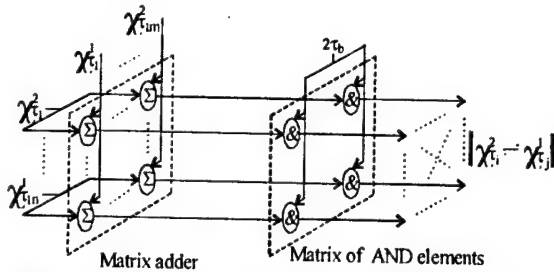


Fig. 5. The scheme of the feature identification device

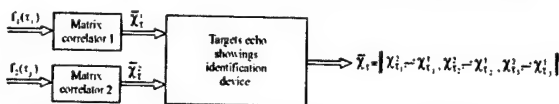


Fig. 6. The scheme of getting the information for focusing the main beams of AAA pair in the directions on the radiation source

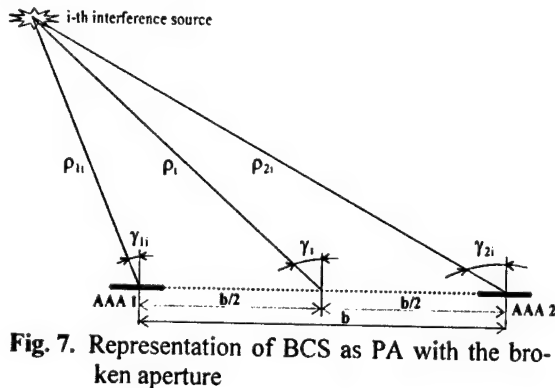


Fig. 7. Representation of BCS as PA with the broken aperture

the principle that the sum of signals delays between the positions in the direction of one source is always equal to $2\tau_b$. This is based on the exchanging of the current estimations of delays of signals from the targets ($\bar{\chi}_1^1$ and $\bar{\chi}_2^2$) between the positions. The device of the identification functioning in accordance with the given rule (Fig. 5) will not form a pair from the measurements $\|\chi_1^1 \Leftrightarrow \chi_2^2\|$ in the points O1 and O2, due to the presence of natural shielding factors S1 and S2 (Fig. 4) which do not allow to observe object O1 in the AAA2 position and object O2 in the AAA1 position.

The set of false targets {FT}, which are received due to crossing of bearings from the spatially separated antenna systems, do not form the vector of spatial position either,

when processing in the identification device, cause of the hyperbolas corresponding to their positions are not generated. Thus the correspondence of the numbers of targets received on the spatially separated apertures AAA1 and AAA2 is determined (Fig. 6) $\|\chi_1^1 \Leftrightarrow \chi_2^2\|$.

It is possible to associate each pair $\|\chi_1^1 \Leftrightarrow \chi_2^2\|$ with the amplitude-phase distribution (APD) $\dot{X}_1(\alpha_i)$ and $\dot{X}_2(\alpha_j)$ on the first and the second AAA apertures. Thus AAAs are focused on the chosen i -th source of radiation ($i = \overline{1, n}$).

2.2. THE SECOND STAGE OF AAA ADAPTATION RADIATION SOURCES COORDINATES MEASUREMENT PROCEDURE

As well as in the works [6, 9] the quality of system functioning can be estimated having concretized the space-time characteristics of signals on apertures of the spatially separated positions. At that consider the bistatic location system as the unique phased array (PA) comprised of the sub-arrays AAA1 and AAA2 spaced at a distance of a great number of wave lengths. In this PA the coordinates of radiation sources are estimated in relation to the centre of the base-correlation system (BCS) in the plane of the base line - target (Fig. 7).

Suppose there are N radiating sources in the BCS's coverage zone. Consider radiation of every i -th ($i = \overline{1, n}$) source to be stochastic signal. Considering the amplitude variety of a signal from the i -th source to be small within the range of aperture of one array, express the APD vectors in the following form:

- for the first antenna-array

$$\dot{X}_1(\gamma_{1i}) = \exp\left[jk \frac{2\pi}{\lambda} d_1 \sin(\gamma_{1i})\right], \quad (1)$$

$$k = \overline{-m_{11}, m_{11}},$$

where $|m_{11}| = |m_{12}|$, $m_{11} + m_{12} + 1 = M_1$ - odd number;

- for the second antenna array

$$\dot{X}_2(\gamma_{2i}) = \exp\left[jl \frac{2\pi}{\lambda} d_2 \sin(\gamma_{2i})\right], \quad l = \overline{-m_{11}, m_{11}}, \quad (2)$$

where $|m_{21}| = |m_{22}|$, $m_{21} + m_{22} + 1 = M_2$ - odd number;

d_1, d_2 - interelement distances in antenna array;
 λ - wave length;

Evaluate the values of $\sin(\gamma_{1i})$, $\sin(\gamma_{2i})$ in terms of γ_i and ρ_i :

$$\sin(\gamma_{1i}) = \frac{\rho_i \sin \gamma_i - b/2}{\sqrt{\rho_i^2 + (b/2)^2 - \rho_i b \sin \gamma_i}}, \quad (3)$$

$$\sin(\gamma_{2i}) = \frac{\rho_i \sin \gamma_i + b/2}{\sqrt{\rho_i^2 + (b/2)^2 + \rho_i b \sin \gamma_i}}. \quad (4)$$

Placing (3), (4) into (1) and (2) accordingly, the combined APD of the i -th signal source in the apertures of the first and the second antenna-array subject to their separation at the b value is expressed as the vector:

$$\dot{X}(\gamma_i, \rho_i) = \begin{bmatrix} \dot{X}_1(\gamma_i, \rho_i) \exp[j\phi_1(\gamma_i, \rho_i)] \\ \dot{X}_2(\gamma_i, \rho_i) \exp[j\phi_2(\gamma_i, \rho_i)] \end{bmatrix}, \quad (5)$$

where $\phi_1(\gamma_i, \rho_i)$, $\phi_2(\gamma_i, \rho_i)$ – the phase shift considering the delay of complex envelope of the mutually correlation function of a signal at its propagation from the i -th source up to the centre of the first and the second AA accordingly:

$$\phi_1(\gamma_i, \rho_i) = \frac{2\pi}{\lambda} [\rho_i^2 + (b/2)^2 - \rho_i b \sin(\gamma_i)]^{1/2},$$

$$\phi_2(\gamma_i, \rho_i) = \frac{2\pi}{\lambda} [\rho_i^2 + (b/2)^2 + \rho_i b \sin(\gamma_i)]^{1/2}.$$

Within the framework of such a model subject to before entered designations, the vector of complex amplitudes of the sum of the internal noises of the unique PA and a total signal from the n external sources received by the first and the second aperture may be expressed as follows:

$$\dot{N}(t) = \begin{bmatrix} \dot{N}_{10}(t) \\ \dot{N}_{20}(t) \end{bmatrix} + \sum_{i=1}^n \begin{bmatrix} N_i(t - t_{21i}) \dot{X}_1(\gamma_i, \rho_i) \times \\ \times \exp[j\phi_1(\gamma_i, \rho_i)] \\ N_i(t - t_{22i}) \dot{X}_2(\gamma_i, \rho_i) \times \\ \times \exp[j\phi_2(\gamma_i, \rho_i)] \end{bmatrix} =$$

$$= \begin{bmatrix} \dot{N}_{10}(t) \\ \dot{N}_{20}(t) \end{bmatrix} + \sum_{i=1}^n \begin{bmatrix} N_i(t - t_{21i}) \dot{X}_1(\gamma_i, \rho_i) \times \\ \times \exp[j\phi_1(\gamma_i, \rho_i)] \\ N_i(t - t_{21i} - \Delta t_i) \dot{X}_2(\gamma_i, \rho_i) \times \\ \times \exp[j\phi_2(\gamma_i, \rho_i)] \end{bmatrix},$$

where t_{21i} , t_{22i} – delay time of a signal at its propagation from the external i -th source up to the centre of the first and second antenna-array accordingly;

$N_{10}(t)$, $N_{20}(t)$ – correlation matrix of internal noise of the first and second antenna-array accordingly;

$$\Delta t_i = t_{22i} - t_{21i}.$$

Assume noises of each external radiation sources to be uncorrelated in time and to have uniform power spectral density in the receiver Π_{Π} 's band of frequencies. Then [10] according to Hinchin-Winner formula:

$$f_i(t, s) = N_i \Delta(t - s),$$

where N_i – spectral density of capacity of i -source of interferences,

$$\Delta(t - s) = \frac{\sin(\pi B[t - s])}{\pi[t - s]}.$$

Provided that the signal spectrum width is more than receiver B's bandwidth, it is possible to replace "quasi-white" noise with delta-correlated process. Then, by virtue of mutual independence of internal noises in the various reception channels, noises of internal and external sources, proportionality of correlation matrix elements to delta-function $\delta(t - s)$, – expression for the correlation matrix Φ of a mix of AAA's internal noises and signals of external sources looks like:

$$\dot{\Phi}(t, s) = \begin{bmatrix} N_{10} & 0 \\ 0 & N_{20} \end{bmatrix} \delta(t - s) +$$

$$+ \sum_{i=1}^n \begin{bmatrix} N_i \delta(t - s) \dot{\Phi}_{11i} & N_i \delta(t - s + \Delta t_i) \dot{\Phi}_{12i} \\ N_i \delta(t - s - \Delta t_i) \dot{\Phi}_{21i} & N_i \delta(t - s) \dot{\Phi}_{22i} \end{bmatrix},$$

where N_{10} , N_{20} – the internal noise spatial correlation matrix of the first and second antenna-array accordingly.

$$\begin{aligned} \dot{\Phi}_{11i} &= \dot{X}_1(\gamma_i, \rho_i) \dot{X}_1^{*T}(\gamma_i, \rho_i), \\ \dot{\Phi}_{21i} &= \dot{X}_2(\gamma_i, \rho_i) \dot{X}_1^{*T}(\gamma_i, \rho_i) \times \\ &\times \exp[j(\phi_2(\gamma_i, \rho_i) - \phi_1(\gamma_i, \rho_i))], \\ \dot{\Phi}_{12i} &= \dot{X}_1(\gamma_i, \rho_i) \dot{X}_2^{*T}(\gamma_i, \rho_i) \times \\ &\times \exp[-j(\phi_2(\gamma_i, \rho_i) - \phi_1(\gamma_i, \rho_i))], \\ \dot{\Phi}_{22i} &= \dot{X}_2(\gamma_i, \rho_i) \dot{X}_2^{*T}(\gamma_i, \rho_i), \end{aligned} \quad (6)$$

– the external noise spatial correlation matrixes of the first and second antenna-array. They characterize interrelation both inside one antenna-array and between aerials of the spatially separated receiving points.

For the i -th source chosen on the first stage the system is focused on the concrete target, for which $\Delta t_i = 0$.

Then

$$\begin{aligned} \dot{\Phi}(t, s) &= \begin{bmatrix} N_{10} & 0 \\ 0 & N_{20} \end{bmatrix} \delta(t - s) + \\ &+ \delta(t - s) \sum_{i=1}^n N_i \begin{bmatrix} \dot{\Phi}_{11i} & \dot{\Phi}_{12i} \\ \dot{\Phi}_{21i} & \dot{\Phi}_{22i} \end{bmatrix} = \dot{\Phi} \delta(t - s), \end{aligned}$$

here $\dot{\Phi}$ is the spatial correlation matrix of a mix of internal and external noises.

From expressions (6) it is clear that $\dot{\Phi}_{12i} = \dot{\Phi}_{21i}^*$. Thus consideration of a signal source in relation to the "virtual" centre allows to simplify processing of signals between positions because phases of signals which come into the spatially separated antenna-array aperture centers are equal modulo. Generally simplification of computing procedure is proportional to complexity of signal and jamming conditions $n \times (M_1 \times M_2)$ times. It allows the jamming space correlation matrix (JCM) of the unique adaptive system to be presented in the block form:

$$\dot{\Phi} = \begin{bmatrix} \dot{\Phi}_{11} & \dot{\Phi}_{12} \\ \dot{\Phi}_{12}^{*T} & \dot{\Phi}_{22} \end{bmatrix}, \quad (7)$$

where $\dot{\Phi}_{11}$ and $\dot{\Phi}_{22}$ sub-blocks of JCM are determined from signal and interference conditions relative to the first and second positions correspondingly; sub-blocks $\dot{\Phi}_{12}$ and $\dot{\Phi}_{21} = \dot{\Phi}_{12}^{*T}$ allow for correlation connections of signals sources between positions.

Considering that the space correlation matrix of references is defined by expression (7) the model of spatial distribution of the field caused by desired signal coming from θ direction and r range by analogy with (5) is given by:

$$\dot{X}(\theta, r) = \begin{bmatrix} \dot{X}_1(\theta, r) \exp[j\phi_1(\theta, r)] \\ \dot{X}_2(\theta, r) \exp[j\phi_2(\theta, r)] \end{bmatrix}. \quad (8)$$

Considering (7) and (8) optimal weight vector is given by:

$$\dot{R}(\theta, r) = \dot{\Phi}^{-1} \cdot \dot{X}(\theta, r),$$

where $\dot{\Phi}^{-1}$ – the inverse correlation matrix, and the expression for output effect according to Keypon algorithm will be:

$$Y_{\Sigma}(\theta, r) = \frac{1}{\dot{X}^{*T}(\theta, r) \dot{\Phi}^{-1} \dot{X}(\theta, r)}, \quad (9)$$

In turn the optimal space-time processing in effect is reduced to forming of the statistics as follows:

$$\dot{Y}(\theta, r, \bar{\gamma}, \bar{\rho}, t) = \dot{R}^{*T}(\theta, r, \bar{\gamma}, \bar{\rho}) \dot{Y}(t),$$

where $\dot{Y}(t) = \begin{bmatrix} \dot{Y}_1(t) \\ \dot{Y}_2(t) \end{bmatrix}$ – the vector of the accepted

realization; as before it consists of the subvectors with M_1 and M_2 lengths corresponding to each antenna array.

It is evident from (9), that the output effect of the considered system, which is based on algorithms appropriate to the optimal processing in AAA of monostatic system is two-parameter one namely the function of not only angular direction but the range relative to the system base centre (Fig. 8-10). While simulating the following assumptions were made: the wave-length was 0,03 m, signal-to-noise ration for both arrays was 2500, interelement distance in AA was 0,015 m, quantity of elements in each AA: $M_1 = M_2 = 15$, direction on the geometrical centre was 0° , on jammers was $+1^\circ$ and -1° , range to jammers was 50 km.

Thus, it is possible to realize the space discrimination with the chosen radiation source accuracy close to potential one. It can be achieved by optimal estimating of angular coordinates according to Keypon algorithm, which minimizes disturbing signal dispersion, and accepting the discreteness of matrix correlator to be $\delta\tau_c = (2...3)\tau_K$, where τ_K – the interval of correlation of the radiation source signal.

3. CONCLUSION

The presented results suggest the possibility of increasing of degree of radiation sources localization by means of multi-stage purposeful information interaction with the purpose of APD control in the spatially separated adaptive antenna subarrays. The multichanneling interposition exchange of radio signals and subsequent coherent space-time processing of them in matrix correlators and AAA adaptive processors when using correlation identification are required for that. The implemented simulation proves high space-time selection capability of such kind of systems.

REFERENCES

1. Colin J.-M. "Radars and EM Sensors for the Next Millennium" Proc. IEEE AES Systems Magazine, August 1999, P. 7-11.

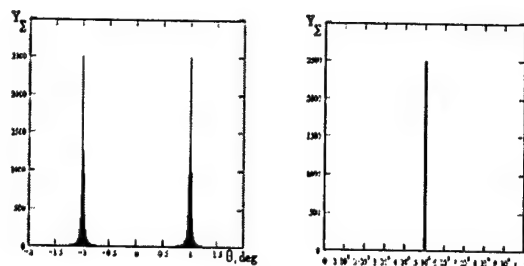


Fig. 8. Output effect for 6 km base

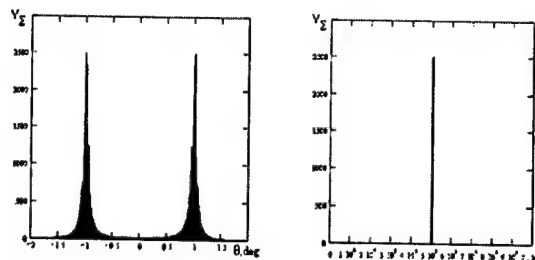


Fig. 9. Output effect for 3 km base

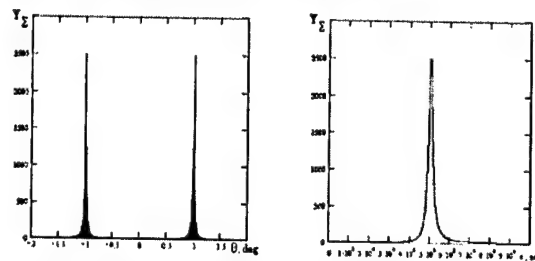


Fig. 10. Output effect for 1 km base

2. Chernyak W. S. Spatial frequency filtering of signals on a background of stochastic interferences in multi-way receiving systems // Radiotekhnika i Elektronika. – 1973. – № 5. – Vol. 18. – P.959-969. (in Russian)
3. Karavaev V. V., Sazonov V. V. The statistical theory of a passive detection and ranging. – M.: Radio i svjaz, 1987. 240 p. (in Russian)
4. Chernyak W. S. Fundamentals of Multisite Radar systems. Gordon and Breach Science Publishers. 1998.
5. Koval D. V., Koval V. M., Kovalenko M. V. Sharing of a correlation and adaptive spatial signal processing for increase of angular spectral estimation efficiency. // Transactions of scientific works GVIRE. Information systems. 2001. – № 4. – P. 105-114. (in Ukrainian)
6. Gabriel U. F. Spectral analysis and methods of the superresolution with usage of adaptive array. // IRE Trans. – 1980. – Vol. 68. – P. 19-31.
7. Shirman J. D. et al. Handbook on radio electronic systems // Shirman J. D. ed. M.: MACVIS, 1998. (in Russian)
8. Yu. N. Sedyshev, V. N. Gordienko "The Coherent Bistatic Radar With Multi-Stage Space-Time Adaptive Processing of Signals and Jamming". IEEE RADAR2000, 8-12 May, 2000, Alexandria, VA, USA, pp. 329-334.

EXPERIENCE OF ANTENNA COMPLEXES CREATION FOR THE RADARS OF DISTANT DETECTING AND SPACE AREA MONITORING

Evstropov G.A., Rogulyev V.A., Saprykin S.D., Sosulnikov V.P., Starostenkov E.A.

OAONPK NIIDAR, 1-st Bukhvostova st., 12/11, Moscow, Russia 107258
Tel. (095) 162-0387

In connection with creation in the fifties and taking up arms of missiles with small size war-heads in several states, as well as space area learning to handle for self-defense, there was necessity to create the radars of distant missile detecting and space area monitoring. Presented in that time the air defense radars, using reflector antennas with comparatively not great aperture and mechanical moving of antenna radiation pattern for area survey, were not found suitable for operating with the new targets. Antennas with great aperture surface and electrical beam moving were required.

In the fifties - sixties of last century the phase shifter manufacturing technology for phased antenna arrays was not yet elaborated sufficiently, but beam scanning methods with frequency change in linear running wave antenna array were learned to handle [1]. In this connection the first stations of distant missile detecting used active antenna arrays consisted of the linear running wave radiators. The stations with such antennas provide with the required survey velocity and needed target detection range. Wider frequency band usage, than the needed one for providing with the given radar range resolution, as well as possibility of adaptive jamming signal suppression only when forming elevation pattern, is a defect of such antennas.

Possibility to apply phased antenna array with full phase beam scanning with discrete commutation phase shifters [2] is appeared after completion of several radars creation with usage of frequency pattern scanning. Further development of antenna technique is connected with elaboration of digital beam forming methods for reception [3].

In NIIDAR antenna complexes elaboration had been gone suitable way.

1. THE ANTENNA COMPLEXES OF "DUNAI-3" AND "DUNAI-3U RADARS

The antenna complexes of "Dunay-3" and "Dunay-3U" radars operating in decimeter wave band consist of two antenna systems located in two sites - the transmitting one and the receiving one. The transmitting antennas scheme is shown in Fig. 1.

The antenna is an antenna array with linear radiators (linear antenna arrays) of moving wave.

Radiated signal is distributed between the linear radiators with help of an equi-pages power divider. Power amplifiers - phase shifters are installed between the divider and the linear radiator input. Azimuth beam is formed with the linear radiators, elevation beam is formed with the linear radiators array. Azimuth beam scanning is realized with radiated signal frequency change, elevation beam scanning is performed with use of phase shifters. Beam scanning elevation sector is 48° .

A ribbed waveguide is used as the linear radiator [4]. Ditch depth for the mean frequency is equal to a half of wave length in the waveguide. When frequency is decreased from its mean value, the waveguide operates in acceleration regimen and when frequency is increased, operating regimen is the delay one with respect to phase wave velocity into the waveguide without ribs. Energy is radiated from the waveguide through the longitudinal slots. Active waveguide part length is about 100 m. Group wave delay in the waveguide $\gamma_{gr} = 10$. Beam scan sector $\Delta\varphi = 53^\circ$.

Wide waveguide size is $0,66 \lambda_{av}$. Losses in the waveguide without the radiators is not more 3 dB per 100 m. Product of use surface coefficient and performance coefficient for the average frequency is equal 0,65 for the linear radiator. Carried power is not more 100 kW in continuous radiation regimen.

The ribbed waveguide is made from bimetal (copper and aluminum rolling), waveguide elements are connected between themselves with fuse method.

The waveguide section is shown in Fig. 2. The linear radiator end is a matched load made as a ferrite absorb-

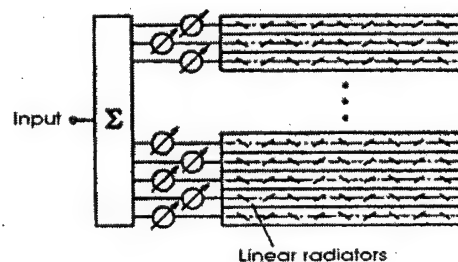


Fig. 1. The transmitting antennas scheme.

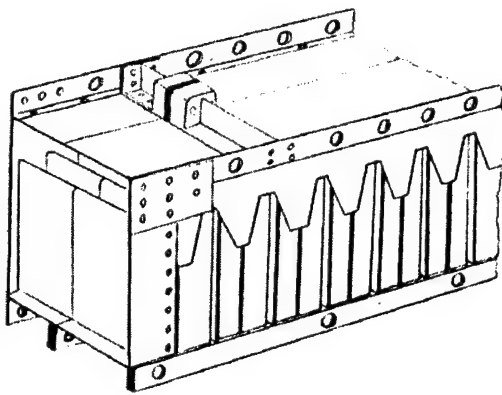


Fig. 2. Waveguide construction

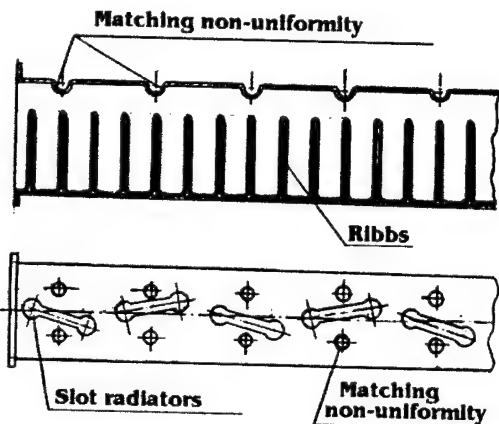


Fig. 3. Slots and matching non-uniformity in the ribbed waveguide.

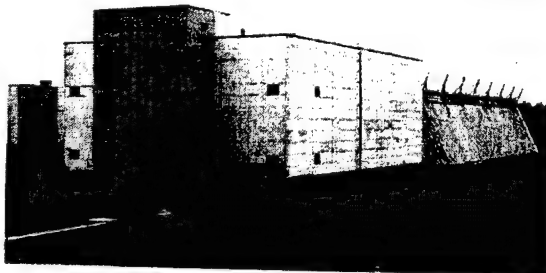


Fig. 4. "Dunay-3U" radar transmitting antenna.

ing plates stacked on the ribbed waveguide surface.

"Dunay-3" radar aperture consists of 13 linear radiators, there are 30 linear radiators in aperture of "Dunay-3U" radar. To perform linear polarization into the rotating one a filter - cover with inclined metal plates is used. Distinguishing "Dunay-3U" radar antenna peculiarity is change of the longitudinal slots with the inclined - displaced ones [5] and placing the vertical plates and an inclined strip (Fig. 3) between the linear radiators to decrease mutual coupling.

Slots matching is performed with small bottoms, which are put out in the upper waveguide surface in section going through the slot centre. When matched slots are used in waveguide slot antenna, there is not

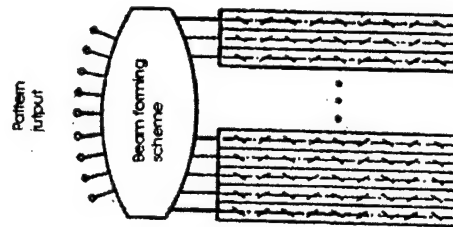


Fig. 5. "Dunay-3U" radar receiving antenna scheme

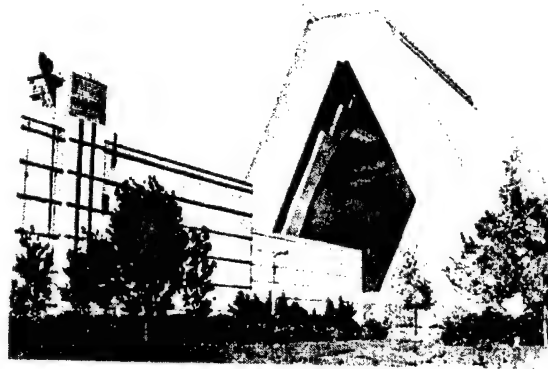


Fig. 6. "Dunay-3" radar receiving antenna.

the normal effect: standing-wave ratio increasing when beam going the antenna normal.

Photo of the transmitting "Dunay-3U" radar antenna is shown in Fig. 4.

In a building bordering upon the antenna, the amplifiers - phase shifters and equipment for forming and distribution of radiation signals are placed.

The waveguide is cut along the middle (neutral) line. The receiving antenna scheme of the radars is shown in Fig. 5.

The antenna also is an active array with the linear radiators. Active elements are low-noise amplifiers installed on the linear radiator output. For elevation survey in the vertical plane there is an intersected beams fan covering sector 48° . The beams fan is formed with a planar lens. The lens surface turned to the linear radiators has an elliptical cylinder form. If an exciter is situated in the ellipse focus, then there is a linear phase distribution on the ellipse. To form a beam fan the radiators are situated on circle arc connecting the ellipse focuses. Horns connected with the linear radiators outputs are situated on the refracting surface (of the ellipse).

The "Dunay-3" radar antenna uses 200 radiators, its aperture is 10^4 m^2 . Photo of the "Dunay-3" receiving antenna is shown in Fig. 6.

The "Dunay-3U" radar antenna consists of 100 linear radiators and its aperture is $0,5 \cdot 10^4 \text{ m}^2$. Connection of radar characteristics and such antennas characteristics was researched in [7], statistical antenna characteristics are shown in [8].

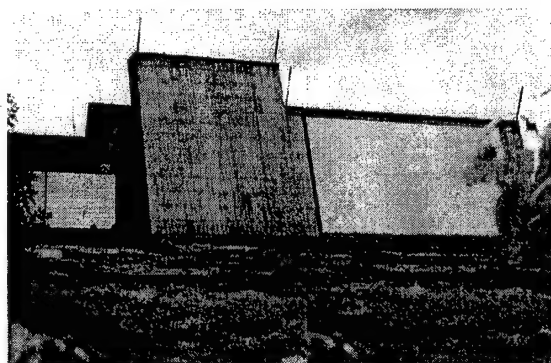


Fig. 7. "Dunay-3U" radar receiving antenna.

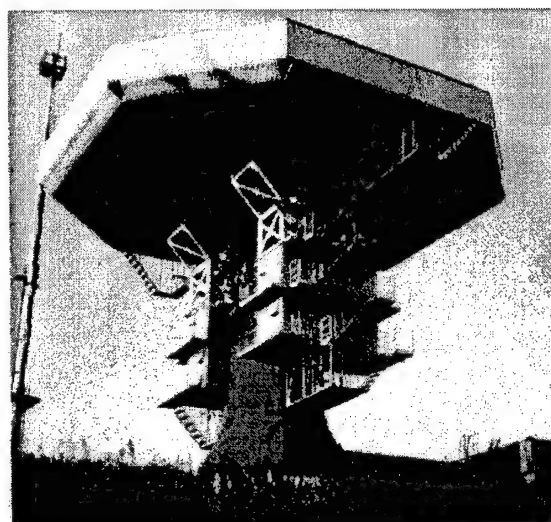


Fig. 8. Space objects tracking radar antenna.

Photo of the receiving "Dunay-3U" radar antenna is shown in Fig. 7. The highest building part corresponds to the lens antenna part. Receiving, measuring and digital equipment of the station is placed in a building bordering to the antenna.

2. TRANSMITTING-RECEIVING PHASED ANTENNA ARREY FOR THE PACE OBJECTS SURVEY SYSTEM RADAR

In the eighties according to the space area monitoring program in NIIDAR elaboration and manufacturing of the radar operating in the space objects survey system were fulfilled.

The main radar element is an antenna made as a phased antenna array on relatable system for the upper semi-sphere observation.

The phased antenna array has the following characteristics:

- operating wave band - decimeter band;
- band of operating frequencies - 5%;
- electron scanning sector - 40° ;
- beam width - $2,3^\circ$;

- operation regimen: transmission - reception with pore 2 and pulse duration 2...16 ms;
- polarization - elliptical with the left and right rotation, it is controlled with a special computer for reception and transmission;
- carried power - 800 KW;
- rotation angles of the relatable system :
for azimuth - $n * 360^\circ$,
for elevation - $0...180^\circ$;
- side lobe level - not less 25 dB;
- patterns number for reception: summary and two difference patterns;
- radiators number - 812;
- eight - edged with diameter 20 m;
- gain - 34,5 dB;
- pattern control - with a special computer located on the phased array frame;
- pattern switching time from transmission to reception - not less 100 μ s.

Photo of the antenna is shown in Fig. 8.

The main phased antenna array peculiarities:

- distance between radiators was increased from 0,745 to $0,875 \lambda$ and radiators number is decreased by 28%. It was the result of cross dipole radiator pattern forming as table type and diffraction lobes suppression when phased antenna array beam is deflected at 8° from the normal,
- multiple-series signal distribution system with power to 800 KW is created with the optimal amplitude distribution allowing to achieve the minimum of radiated power on the central radiators, when side lobe level is consecrated not more than minus 25 dB,
- pin-diode phase switches with 3 discrete were elaborated; they operate at the mean power level to 1 KW and the pulse one - to 2 KW with the maximum losses not more than minus 25 dB,
- switching lobes level not more minus 25 dB was conserved with the special given random phase errors distribution and further compensation of them in the special computer,
- total receiver protection level in transmission regimen is achieved minus 80...90 dB, when the direct losses are 0,5 dB, as a result of use of T-bridge decoupling and two switches with pin-diodes,
- cooling of all phased antenna array elements - air.

3. ANTENNA COMPLEX OF "VOLGA" DISTANT DETECTING RADAR

"Volga" radar is the new generation of distant detection stations operating in continuous radiation regimen: the radar illuminates a target and receives reflected signals simultaneously. The continuous radiation regimen allows to adapt simply to radioloca-

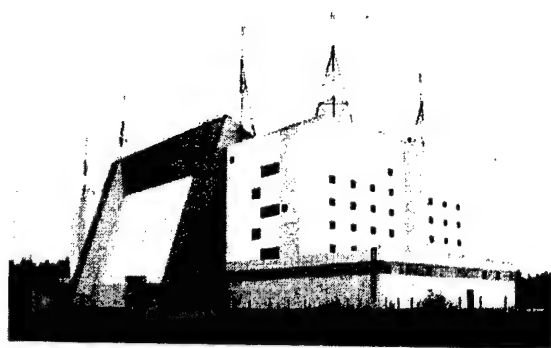


Fig. 9. "Volga" radar transmitting antenna.

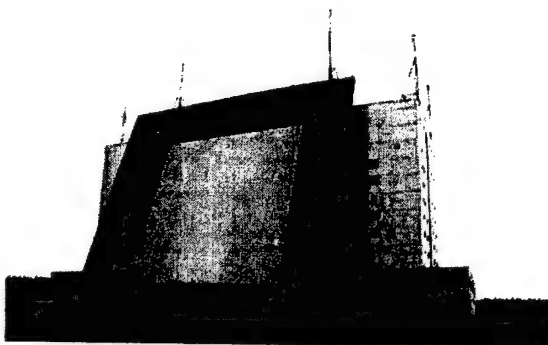


Fig. 10. "Volga" radar receiving antenna.

tion situation, to control energy at a target and range resolution for each angular direction as well as to operate with pore near 1, that is to radiate power near to average super-high frequency radar power.

To get the required decoupling between the transmitting and receiving antennas the antenna complex consists of two antennas located in transmitting and receiving sites.

The transmitting antenna is an active phased antenna array operating in long-wave part of dissymmetrical wave band. The distinguish peculiarity of active phased antenna array is use of phase shifters providing a continuous phase change (and frequency) of radiated signal in any limits with a great velocity diapason. It allows to scan the beam during signal radiation. The array consists of spiral radiators and provides with radar operation in wide frequency band when azimuth pattern swinging is 120° and more than 60° at elevation. Antenna aperture is $36 \times 20 \text{ m}^2$. Photo of the antenna is shown in Fig. 9.

As construction the antenna is combined with a building, where transmitting radar site equipment is contained. The array is surrounded with four lines of passive radiators and frame from ferrite absorbing materials. The receiving antenna array is also made from the spiral radiators with opposite spiraling to the transmitting ones. The receiving antenna distinguish peculiarity is application of full digital beam forming [3], offered by NIIDAR in 1976. In this method signal

from each radiator after amplification and frequency transformation has a number sequences form, then a parent system is formed. Digital pattern forming use allows to realize more completely the elaborated methods of adaptation to interference situation.

Antenna aperture is $36 \times 36 \text{ m}^2$. Antenna construction is analogous to the transmitting one. The active aperture part is also surrounded with four lines of passive radiators and special frame.

Antenna external view is shown in Fig. 10. The array is one of the building walls.

4. TRANSMITTING-RECEIVING ANTENNE-FEEDER SYSTEM OF THE CENTIMETER BAND

Transmitting - receiving antenna-feeder system is intended for operation amounting to a radar of low-orbit space objects parameters measurement.

The main antenna-feeder system technical characteristics:

- operating frequency band – 6995...7040 MHz;
- beam width in E and H planes – 30-40 angle min;
- antenna-feeder system amplification factor for transition – 44 dB, for reception – 46 dB;
- side lobe level - not more than minus 12 dB;
- electron scan sector in E and H planes – $\pm 10^\circ$;
- maximum pulse input power of super high frequency signal with pore 2 – 80 KW;
- maximum error of beam standing – 3 angle min.

The antenna-feeder system is a phased antenna array mounted on a relatable system for providing with operation zone along azimuth $\pm 270^\circ$ and elevation $0 - 90^\circ$. To simplify elaboration, manufacturing and tuning the phased antenna array is builder according to module type: all array is divided into 64 (8×8) sub-arrays (modules). Each module has aperture $0,53 \times 0,5 \text{ m}^2$. Open waveguide ends are used as elementary radiators. Radiators number in the module is $16 \times 10 = 160$ (16 – in H plane and 10 – in E plane). Discrete (90° and 180°) phase shifters with cross magnetization is used [7]. The general antenna system view is shown in Fig. 11. No equidistant module radiators displacement in E plane provides with diffraction lobes level decreasing to the level minus 15 dB.

A pyramidal horn is used to distribute signals to the module radiators. Antenna-feeder system module supply has multiple scheme with waveguide dividers using T-bridges.

The antenna-feeder system with relatable system are displaced under a radio transparent cover made as a truncated sphere; this allows to protect the antenna-feeder system from natural influence and to decrease antenna-feeder system wind loads with cover mounting on the its own base.

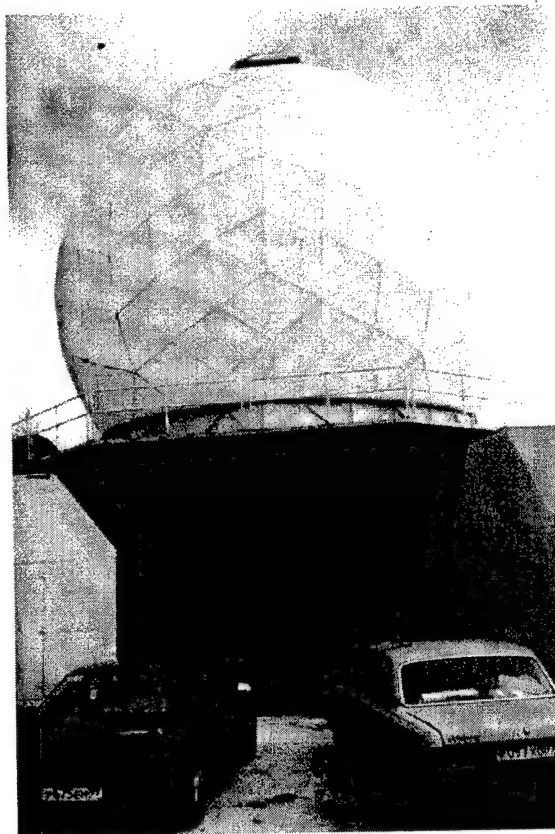


Fig. 11. General antenna-feeder system view of the centimeter band radar.

5. ANTENNA COMPLEXES FOR PERSPECTIVE DISTANT DEFLECTION RADARS

As analysis of manufacturing terms and expense for the distant detection radar creation shows, their main part is expense on the antenna complexes including the transmitting and receiving modules. The antenna complexes lead to the greatest exploiting expense, the main part of them is power consumption.

Earlier created radars equipment is placed in the buildings, this leads to great station creation term as a result of building construction, mounting and complex equipment tuning in the dislocation place.

Electronics development results in sharp equipment decreasing, its main part forms the antenna complex and must be distributed on a supported antenna complex metallic construction to provide with the minimum losses in the decimeter band. The transmitting and receiving modules (amplifiers with switching phase shifters), auxiliary apparatus, which is necessary for their operation, and thermo-stability system can be placed in the special "antenna" containers, these have manufacturing. The array fragment radiators served with equipment of the same container can be placed on the butt-end container wall. As a result, radar creation consists of metallic construction mounting, antenna containers placing into the specially created cells in the metallic construction, power supply connecting to the containers and link-

ing with equipment placed out the metallic construction.

Equipment to form signals and synchronization, that are required to radar operation, multi-channel reception system, that transforms signals receipted with antenna radiators to digital sequences, computer apparatus, providing with pattern form adaptive to interference situation, the first and second radiolocation signal processing, technical, functional control of the station equipment and functional monitoring, as well as service programs realization and communication with data transmitting apparatus and command communication are placed out the metallic construction. All this equipment can be placed into three standard ground containers, volume of each container is analogous to the antenna container volume. The ground containers with equipment are also manufactured and tuned in plants.

The given technology of distant detection radar creation allowed to increase essentially the stations creating terms was offered by NIIDAR in 1986 and named as the technology of distant detection radiolocation stations creation with high plant readiness.

To get the acceptable station value and limitations connected with computing technique, it is not proposed to use the full digital adaptive beam forming for the distant detection radars of the nearest perspective. The antenna array is divided at sub arrays with an analogue beam forming way and the full antenna pattern is formed with an adaptive digital way. The analogue sub arrays patterns are formed with equipment placed into the antenna containers.

REFERENCES

1. L.N. Deryugin, M.G. Kuznetsov. Frequency scan antennas common theory problems. In collection Scanning super high frequency antennas, edited by Mechanical engineering, 1964, pp. 5...17.
2. L.N. Deryugin, D.B. Zimin. Switching mode of beam control in antenna arrays //Radio engineering, Vol. 19, № 3. 1964, pp. 25...33.
3. G.A. Evstropov, I.L. Immoreev. Digital modes of receiving antenna arrays pattern forming.- Antenna technique problems edited by "Radio and communications", M., 1989, pp. 88...107.
4. G.A. Evstropov. Resonant slots in a ribbed waveguide. // Radio electronics problems, Vol. XII, No. 13, 1960, pp. 25...33.
5. I.E. Veshnikova, G.A. Evstropov. Matched slot radiators //Radio engineering and electronics, Vol. X, No 7, 1965, pp. 1182...1189.
6. G.A. Evstropov and A.I. Klimenko. Distance resolution for continuous radiation radar antenna characteristics. Proceedings of the XXVIII Moscow International conference on antenna and Technology, 22-24 September 1998, Moscow, Russia, pp. 243... 245.
7. G.A. Evstropov and A.I. Klimenko. Statistical characteristics research of the moving wave sectionalized linear radiators // Electrocommunications, edited by "Radio and communications", No 2, 1996, pp. 24...28.

HIGH-PERFORMANCE HORNS WITH OPTIMIZED WAVING TAPER

Hiroyuki Deguchi, Mikio Tsuji and Hiroshi Shigesawa

Department of Electronics, Doshisha University
Kyotanabe, Kyoto 610-0321, Japan
<hdeguchi@mail.doshisha.ac.jp>
<mtsui@mail.doshisha.ac.jp> and
<hshigesawa@mail.doshisha.ac.jp>

Abstract

We demonstrate here two types of high-performance horns with waving taper. These horns show a high efficiency and a compact low cross polarization. Our design method is based on the optimization technique, and we discuss the designed and fabricated horn antennas in X-band numerically and experimentally.

Keywords: Horn antennas, Optimization technique, Antenna radiation patterns, Aperture efficiency, Cross polarization.

1. INTRODUCTION

We have realized two compact horns with low cross polarization and high aperture efficiency, respectively, by introducing the waving taper (1), (2). The design method is based on the optimization technique combined with the mode-matching approach. This paper presents such horns with high performance.

2. DESIGN METHOD

The design parameters are defined by inner diameters D_n ($n = 1, 2, \dots, N$) and the axial length L . The continuous configuration of the taper is given by interpolating these dimensions through the third-order spline function (see Fig. 1). The scattering matrix for the whole structure of the interpolated taper is obtained by the cascade connection of step discontinuities and uniform waveguides with different diameters as shown in Fig. 2. The generalized scattering matrices for each discontinuity can be easily computed by the cylindrical mode-matching approach. To avoid much calculation time for step discontinuities in the optimization procedure, the dimension of the step discontinuities are kept same for all steps, and hence an arbitrary taper configuration is represented only by changing the lengths Δl_i of uniform waveguide between the adjacent step discontinuities as shown in Fig. 3. The objective function in the optimization procedure is defined by using the higher-order mode coefficients for high aperture efficiency or the radiation pattern by the dominant hybrid mode in corrugated horns, corresponding to the purpose of the horn use. Finally, the minimum length L is determined by iteration of the above procedure.

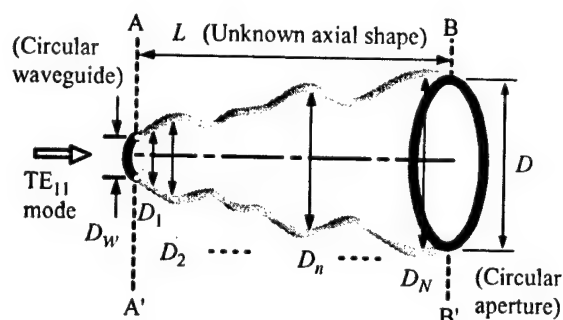


Fig. 1. Basic geometry of proposed horn antennas

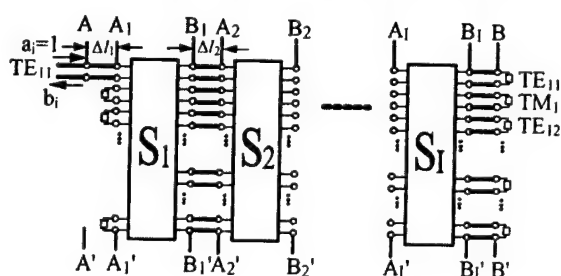


Fig. 2. Equivalent circuit represented by the generalized scattering matrices

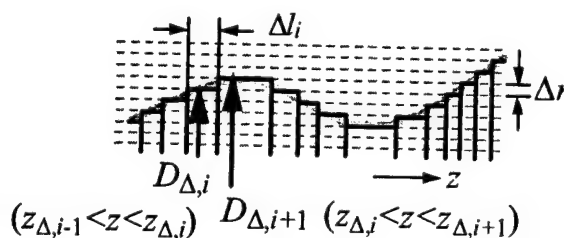


Fig. 3. Calculation model

3. DESIGN EXAMPLES AND EXPERIMENTS

3.1. HIGH EFFICIENCY HORN

Figure 4 (a) shows the waving taper configuration of the designed horn that realizes high efficiency, and its external view of the fabricated antenna is shown in Fig. 4 (b). The objective function ε_1 in this optimization is defined by the following equations.

$$\varepsilon_1 = \sum_{i=1}^{N_f} \left(w_r |S_{11,1}(\lambda_i)|^2 + \varepsilon_{m,i} \right)$$

with

$$\varepsilon_{m,i} = \sum_{k=1}^{N_m} \left(w_{t,k} \left| S_{21,k}(\lambda_i) / S_{21,1}(\lambda_i) - A_k \right|^2 \right),$$

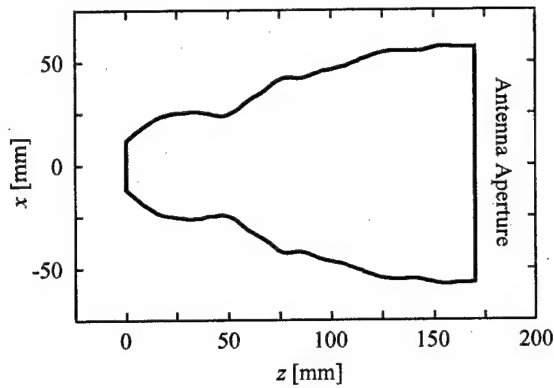
where λ_i is the sampling frequencies within the given frequency band, $S_{11,1}$ and $S_{21,1}$ are the reflection and the transmission coefficients of the TE_{11} mode for the whole structure of the horn. $S_{21,k}$ and A_k are the transmission coefficients and the desired coefficients of the k^{th} -order cylindrical waveguide modes at the horn aperture, respectively. N_f is the number of the sampling frequency points relating to the desired band and N_m is the number of expanded modes. Also w_r and $w_{t,k}$ are weighting functions. Table 1 gives the amplitude and phase of the mode coefficients A_k at the horn aperture used as the design goal in our optimization. The higher-order TE modes work to maximize the gain, while the TM modes work to reduce the cross polarization components.

The designed horn shown in Fig. 4 has approximately flat aperture distribution in both amplitude and phase, as shown in Fig. 5. The measured radiation patterns shown in Fig. 6 are in good agreement with the calculated ones in both the co-polar and the cross-polar fields.

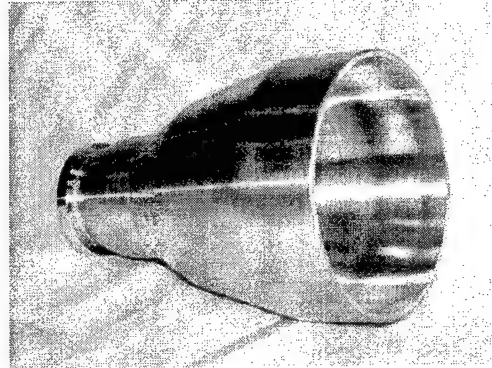
Figure 7 shows the comparison of the 3-dB and 10-dB beam widths between the measured and the calculated results as a function of the frequency. Both results agree well each other. Furthermore we evaluated the aperture efficiency from the antenna gain measured by means of the standard gain horn. High aperture efficiency is realized as shown in Fig. 8, comparing with a conventional TE_{11} mode horn. Although there are some scatters in measured results, they also agree well with the calculated ones.

Table 1. Coefficients of higher-order modes

Mode	Amplitude [dB]	Phase [rad]	Mode	Amplitude [dB]	Phase [rad]
TE_{12}	-10.6	π	TM_{11}	-23.4	0
TE_{13}	-14.8	0	TM_{12}	-23.3	π
TE_{14}	-17.6	π	TM_{13}	-22.9	0



a) Taper configuration of the designed horn



b) External view

Fig. 4. High efficiency horn

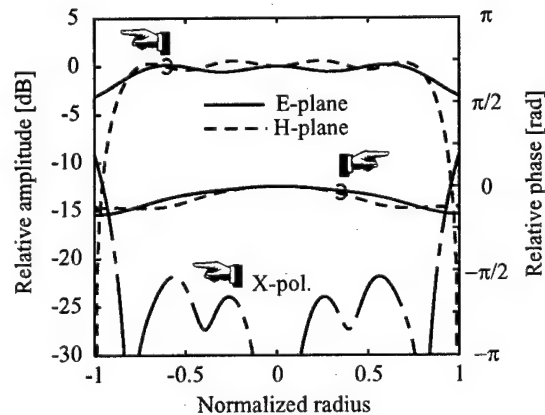
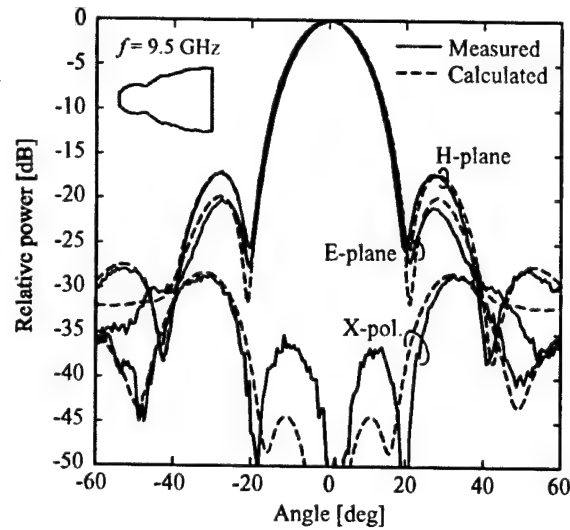


Fig. 5. Aperture distribution at center frequency of the high efficiency horn

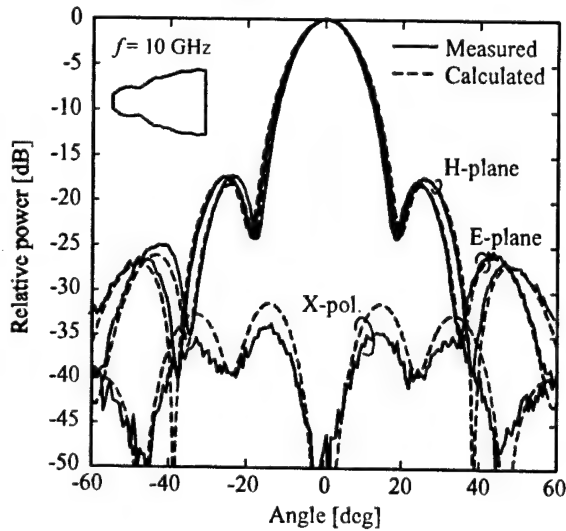
3.2. LOW CROSS-POLARIZATION HORN

Figure 9 (a) and (b) shows the waving taper configuration of the designed antenna with low cross polarization and its external view of the fabricated horn. The objective function ε_2 in this optimization is defined by considering both the far-field patterns and the return loss as follows.

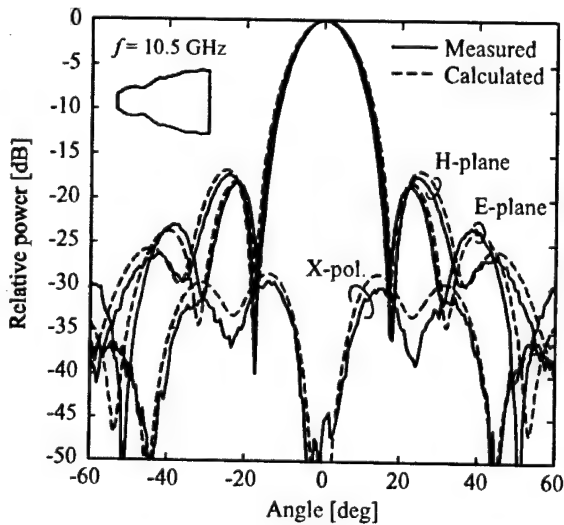
$$\varepsilon_2 = \sum_{i=1}^{N_f} \left(w_r |S_{11,1}(\lambda_i)|^2 + \varepsilon_{e,i} + \varepsilon_{h,i} + \varepsilon_{x,i} \right)$$



a) 9.5 GHz



b) 10 GHz



c) 10.5 GHz

Fig. 6. Radiation patterns of the high efficiency-horn

with

$$\begin{aligned}\epsilon_{e,i} &= \sum_{j=1}^{N_e} (w_e |F_{e,i}(u_{i,j}) - G(u_{i,j})|^2) \\ \epsilon_{h,i} &= \sum_{j=1}^{N_h} (w_h |F_{h,i}(u_{i,j}) - G(u_{i,j})|^2) \\ \epsilon_{x,i} &= \sum_{j=1}^{N_x} (w_x |F_{x,i}(u_{i,j}) - X_p|^2),\end{aligned}$$

where λ_i is the sampling frequencies within the given frequency band, $S_{11,i}$ is the reflection coefficient of the TE₁₁ mode at the horn throat. $F_{e,i}$ and $F_{h,i}$ are the E- and H-plane co-polar patterns, respectively. $F_{x,i}$ is the cross-polar pattern, G is the far-field pattern radiated by an ideal corrugated waveguide horn, X_p is the desired peak level of the cross-polar component, and $u_{i,j} = D \sin \theta_j / \lambda_i$. N_f is the number of the sampling frequency points relating to the desired band

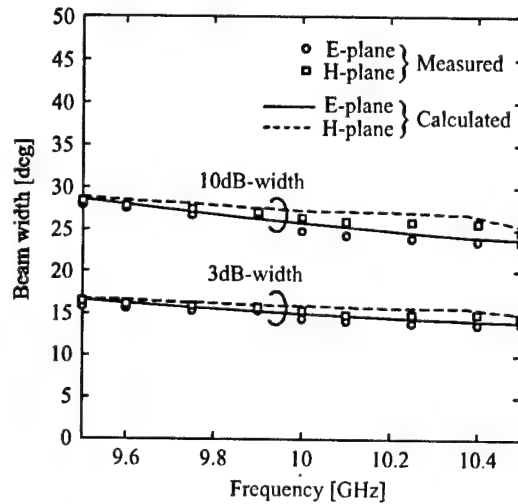


Fig. 7. Beamwidth as a function of frequency

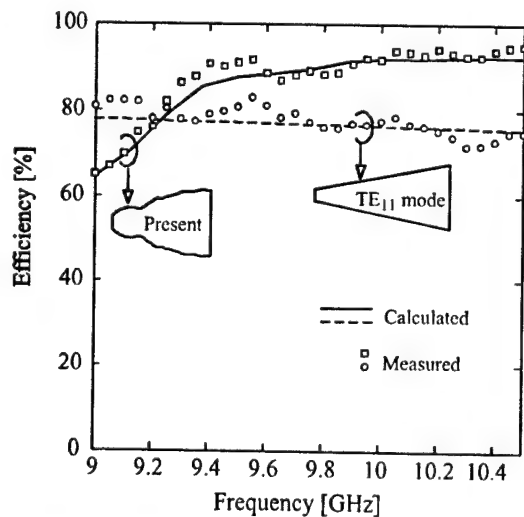
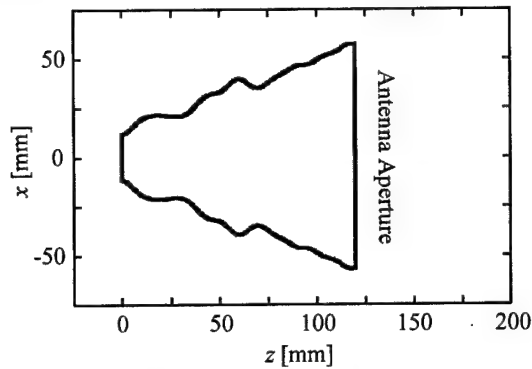
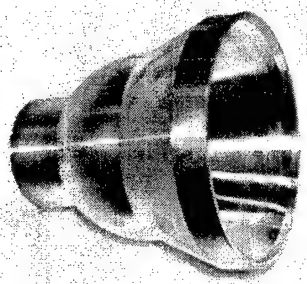


Fig. 8. Aperture efficiency as a function of frequency

and N_c and N_x are the numbers of the observation points on the co-polar and cross-polar patterns, respectively. Also w_r , w_e , w_h , and w_x are the weighting functions.

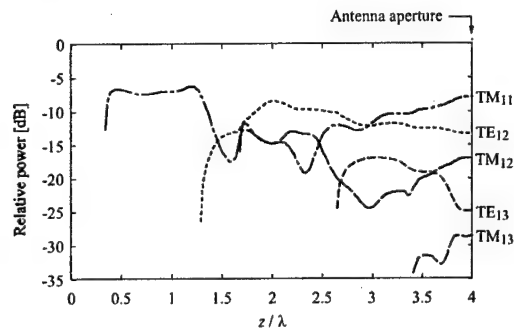


a) Taper configuration of the designed horn

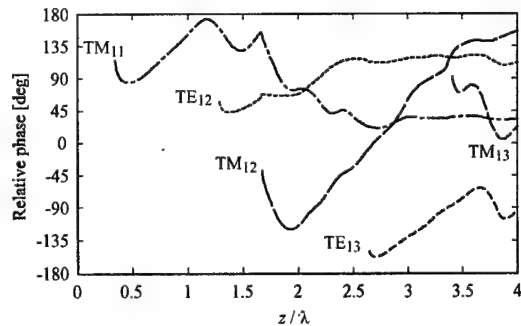


b) External view

Fig. 9. Compact low-cross polarization horn

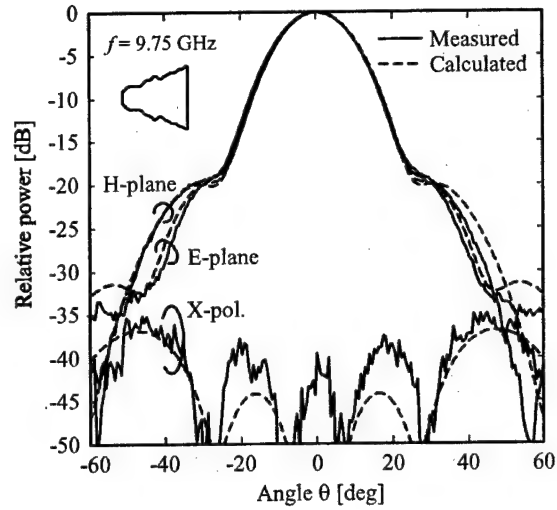


a) Amplitude

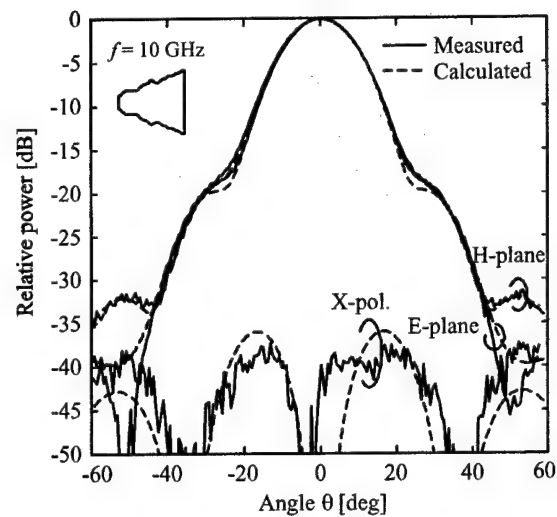


b) Phase

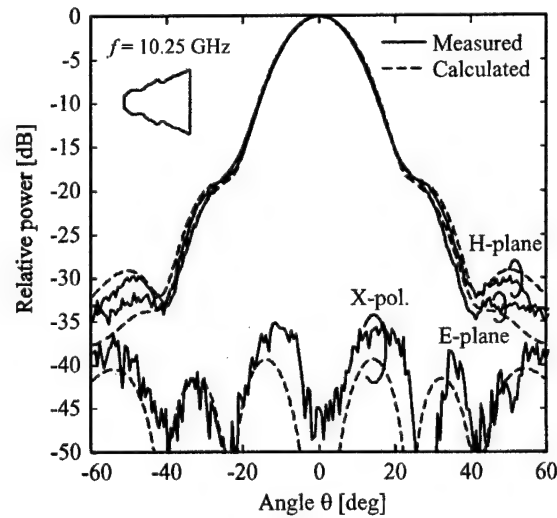
Fig. 10. Mode conversions in compact horn



a) 9.75 GHz



b) 10 GHz



c) 10.25 GHz

Fig. 11. Radiation patterns of compact horn

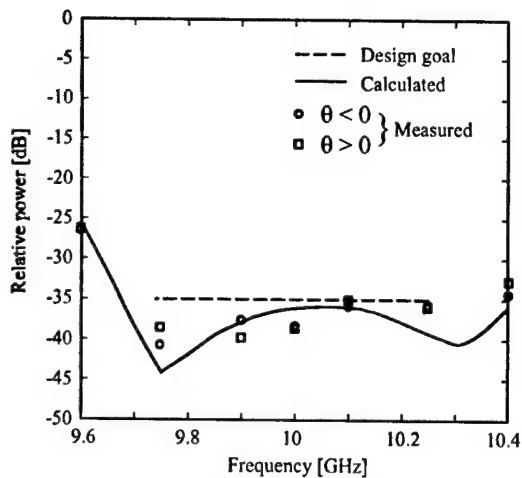


Fig. 12. Peak level of cross polarization component as a function of frequency

The behavior of the mode conversion caused by this taper is shown in Fig. 10. To achieve the low cross polarization characteristics in compact size, the five higher-order modes are successfully excited along the taper toward the aperture. Figure 11 shows the measured radiation patterns. The measured results are very good agreement with the calculated ones in both the co-polar and the cross-polar patterns. It is confirmed that our horn has ultra low cross polarization in very compact size.

Figure 12 compares the frequency characteristics of the peak level of the cross-polarization component

between the measured and the calculated results. The waving taper obtained here works well for the low cross polarization.

4. CONCLUSIONS

Two types of the horns with the waving-taper configuration have been developed under the optimization design method. The numerical and experimental discussions presented here have verified that such configurations work well to realize the horns with high performance.

ACKNOWLEDGEMENTS

This work was supported in part by a Grant-in Aid for Scientific Research © (13650439) from Japan Society for the Promotion of Science and by the Aid of Doshisha University's Research Promotion Fund.

REFERENCES

1. H. Deguchi, M. Tsuji and H. Shigesawa, "Synthesis of a high efficiency conical-horn antenna: Effect of the negative flare", European Microwave Conference Proceedings, 2001, Vol. 2, pp. 281-284.
2. H. Deguchi, M. Tsuji and H. Shigesawa, "A compact low-cross-polarization horn antenna with serpentine-shaped taper", IEEE Antennas Propagat. Symp. Digest. 2001, Vol. 2, pp. 320-323.

RADIO TELESCOPE RT-70 IN EVPATORIA AND SPACE INVESTIGATIONS

A. A. Konovalenko¹, L. N. Lytvynenko¹, C. G. M. van 't Klooster²

¹ Institute of Radio Astronomy of the National Ukrainian Academy of Sciences

4 Krasnoznamennaja St., 61002 Kharkov, Ukraine

Phone: +380-572-471134; E-mail: <akonov@ira.kharkov.ua>

² ESA - Estec, TOS-EEA

P.O. Box 299, 2200 AG Noordwijk, the Netherlands

Phone: +31-71-5653940; E-mail: <kvtkloos@estec.esa.nl>

Abstract

The current situation with the Evpatoria 70-m antenna is described. This unique 70-meter radio-telescope antenna (RT-70) was realised between 1973 and 1978 and was an important element in different missions as antenna in transmit-receive mode for instance for the missions like Venera, Granat, Interbol, etc. It was and is used in other modes like radar for planetary and asteroid investigations as well as radio telescope. Its current state is such that after and with the necessary maintenance the tasks can be continued and expanded. Technical activities are carried out today with involvement of the first author for the technical management on behalf of the Ukrainian Space Agency, in particular today the "Interferometer" - project be mentioned. The potential for future use is briefly indicated.

1. INTRODUCTION

Several ground-station antennas with a large diameter have been, or were planned to be constructed in Russia, Ukraine, Uzbekistan, Armenia and Baltic countries. A number of 32 meter antennas was realised, examples are the antennas in Ussurijsk (Russia), Evpatoria, Simferopol (both Ukraine), as well as the 32 m antenna in Ventspils, the latter is nowadays used by the Institute of Radio Astronomy in Riga. All 32 m antennas have a good surface quality, but they are currently not too much used. Another type of 32-meter antenna has been designed for the Quasar project and the 32m radio-telescope near Svetloe (near St. Petersburg) is an example of such type of antenna. Other antennas of the latter [11] type are realised in Zelensjuk and Badari (near Irkutsk) and potentially near Saryja Pustyn (near Nizhny Novgorod). Near Moscow the 64 m receiving antenna was realised in the early eighties (Bear Lakes) and a similar type of antenna has been constructed in the late nineties in Kalaizin (near Tver). The subject here concerns the impressive 70 m antenna (started in 1973, finished in the 1978) near Evpatoria. A similar type of antenna was realised later on near Ussurijsk in the far east of Russia and a start was made with the realisation of the large radio telescope antenna in Uzbekistan (Suffa plateau). The latter realisation was delayed by the political events and its current realisation is subject of collaborative efforts between Russia and Uzbekistan.

In this paper we concentrate on the situation with the Radio-Telescope (RT-70) in Evpatoria. The main plan was conceived in the late sixties, early seventies with strong support of Prof. Lev Davidovich Bakhrakh. Main designers of the RT-70 were V. B. Tarasov and A. N. Kozlov. Details are found (the reader is strongly recommended to learn some Russian....) in the Journal 'Antenni' nr 31 [1, 2], in 'Radiofysica' [3] and later on in [4, 5].

There were many design bureaux and institutes involved in this large project to realise the antenna, with to mention one of them: 'Special Construction Bureau for Machine building' from St. Petersburg (Tel: +7-812-245-3619). The latter organisation has currently the metal parts for the 'Suffa' antenna, waiting for realisation in Uzbekistan (some information might be found in the Astro Space Centre web pages, www.asc.rssi.ru). The design bureau for these antennas was involved in the early sixties in the realisation of more than 600 antennas with a diameter between 2.6 and 32 meter as well as the antennas on-board the 9 tracking vessels amongst which the 'Kosmonaut Vladimir Komarov', 'Kosmonaut Yuri Gagarin' and 'Academicik Serge Korolev'. Other involvements included a large thermal vacuum facility with a volume of 10000 m³ and launch facility aspects for the 'Byran' and 'Energia' rocket (the latter was transported horizontally and erected before launch).

The RT-70 antenna facility is unique in the sense, that it was the first shaped dual reflector antenna with such a large diameter, which had a homologue sup-

porting construction and which, thanks to the shaping of the reflector surfaces, realised an aperture efficiency of near to 80 %. Just to indicate the sizing aspect: the Westerbork radiotelescope consists of 14 antennas (25 m diameter) and has a collecting area of some 3500 to 4000 m², slightly smaller than the Effelsberg 100 meter radio telescope, but slightly larger than the collecting area of RT-70 (at a wavelength assumed to be 5 cm wavelength).

Such a type of reflector shaping exercises for high efficiency dual reflector antennas was ongoing in the early sixties already [6], slightly earlier than elsewhere [7]. Furthermore, in order to realise the capability to switch fast between different frequency bands, a dedicated feed system arrangement has been developed, in which 6 feeds were placed on a circle near the secondary focus. A small dual reflector assembly with two shaped nearly elliptical reflectors has been constructed with a possibility to rotate and so to select as a sort periscope one of the 6 feeds to the total large dual reflector assembly. The latter small dual-reflector assembly permits to use one of the 6 feeds at the time and – by rotation within a short time – permits to change frequency band. It is only 4 to 5 λ in size at the lowest frequency band. Such sizing is known for its diffraction losses, but special efforts were implemented (sort of spoilers) to reduce the effects of diffraction losses. The effect of small size reflectors and shaping was discussed later on in [8].

For the higher frequency bands these losses are less pronounced, as the relative sizes become larger in terms of wavelength. Today a comparable rotating dual reflector system is also considered for implementation in the 64 m radio telescope to be realised in Sardinia [9, 10].

As is indicated in [1–5], the effects of gravitational compensation have been thoroughly studied and approximate formulas were derived with radio astronomical methods to correct pointing as a function of elevation and azimuth, this leading to good diagrams for the different angular directions and a pointing knowledge for the best diagram was optimised. The Gregorian subreflector can be translated and can be axially displaced.

A decision for the Gregorian configuration was supported by investigations, from which a better noise temperature was apparent (less spill-over, better roll-off at the edge of the main reflector) and from which more complete correction possibilities for phase distortions were derived for gravity compensation. The RT-70 was constructed with upgrading to shorter wavelength in mind, as a very good demonstration of antenna design capabilities.

The ongoing developments today include the installation of receive capability at $\lambda = 21, 18, 13, 3.5$ and also 1.35 cm with sufficiently low noise temperature, while a wider bandwidth is achieved than in earlier measurements.

There are two new receivers installed in the RT-70 antenna, operating at 327 MHz and 4.8 GHz respec-

tively. The 'Saturn'-association in Kiev develops an 18 cm receiver, which will be installed this year (2002). The latter "Saturn"-association has very good experience in the realization of cryogenically cooled receivers at all wavelengths as considered for the "Radio-Astron"-project, as well as for other applications like in Ratan 600.

There is the interest to equip the RT-70 antenna with S- and X-band receivers, permitting the antenna to handle telemetry data in receive. With such a set of receivers, the total set of capabilities is more flexible, permitting the data downlinking for scientific missions as well as telecom missions. The latter reception capability would also be functional for the requirements for astrometry, as well as eventual support possibilities for other scientific missions like for example Mars-Express (exploring discussions between ESA and the Ukrainian Space Agency took place early April in 2001). Today the 'Saturn'-association is developing these receivers and may install them in the RT-70 during the years 2002-2003.

There is the possibility to use the feed for $\lambda = 18$ cm for both Right-hand and Left-hand circular polarization, with an overall effective area of 2300 m². The 327 MHz band ($\lambda = 92$ cm) is supported with a feed array with four helix antennas positioned around the secondary focus. The effective area at 327 MHz is 1400 m² and the associated antenna pattern has a Half Power Beam Width of $HPBW = 50$ arcminutes.

There is the plan to install also a 22 GHz ($\lambda = 1.35$ cm) receiver. With the capabilities then available, the Radio-Astron mission can be supported with a large ground-based radio telescope. The question about an eventual 32 GHz receiver is open, because the current surface accuracy should be re-assessed.

In the early beginning there have been carried out experiments even at a wavelength $\lambda = 8$ mm, with a resulting effective area of 900 m² [3]. As the RT-70 is rather well designed, some improvement might be anticipated from such an investigation, but this is somewhat at the limit. Also the pointing capability is then an aspect, which should be investigated, in combination with the capability to adapt the position of the movable sub-reflector.

2. RECENT ACHIEVEMENTS

In the last year the concept of a radio astronomy upgrade and use of RT-70 antenna as one of the largest centimeter-decimeter wavelength antennas, was proposed by the Institute of Radio Astronomy (IRA). The RT-70 antenna belongs to the National Control and Space Facilities Test Center (Evpatoria) under the Ukrainian Space Agency (Fig. 1).

This upgrading activity is supported by the National Ukrainian Space Agency (NSAU) with a number of Ukrainian and Russian organizations.

The principal purpose is the realisation of a set of high sensitive modern radio astronomy equipment, to put it into operation and to carry out scientific investigations with RT-70 for the most perspective fields of

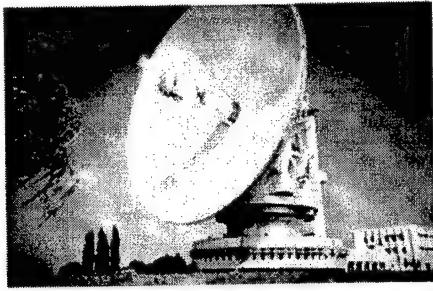


Fig. 1. The 70 meter Radio Telescope (RT-70)

RT-70, 327 MHz, 8.1998, $A_{\text{eff}} \sim 600 \text{ m}^2$, $\Theta_A \sim 50'$, $T_s \sim 100 \text{ K}$

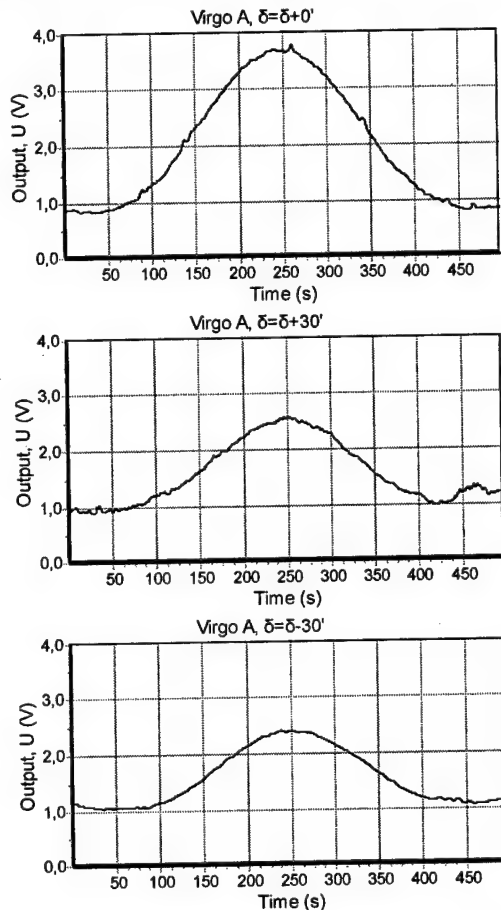


Fig. 2. Patterns, Virgo A as source, upper left: central scan, other scans at + and -30 angular minutes wrt peak

ground-space radio astronomy. The following topical areas are considered for this purpose:

- International very long base interferometer (VLBI) experiments including activities in the frame of ground-space interferometer projects (VSOP, VSOP-2, Radioastron) associated with the ultimate capability of angular resolution realization.
- Single-dish high sensitive broad band investigations of galactic and extragalactic objects in continuum and spectral lines for the study of physical and evolution processes in the Universe.

RT-70, 325 MHz, Cas A, DAC, 4×1024

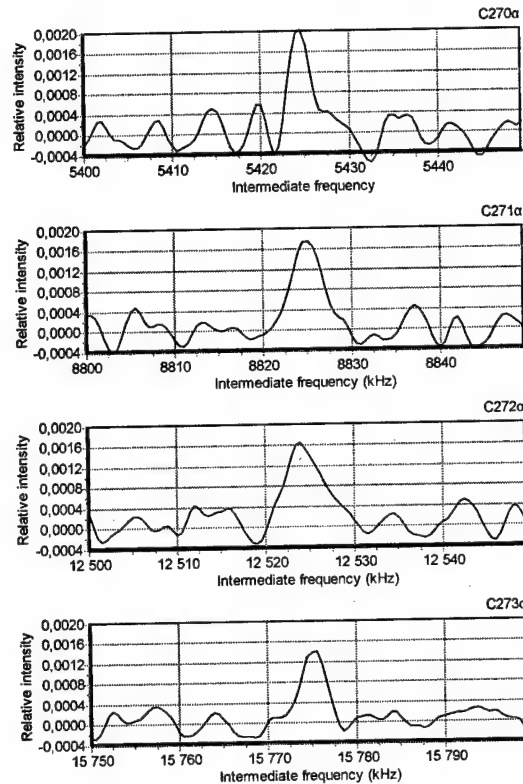


Fig. 3. Results at Evpatoria of reception of carbon recombination lines in four frequency bands. Cassiopeia as source.
4.8 GHz, 11.1998 $A_{\text{eff}} \sim 2100 \text{ m}^2$, $\Theta_A \sim 3.5'$,
 $T_s \sim 25\text{--}30 \text{ K}$, $\nu_{\text{IF}} \sim 100\text{--}600 \text{ MHz}$

- Radar investigations of natural and artificial solar system objects including the using of VLBI methods for planets, asteroids, meteors, space debris, satellites.
- Ground-space investigations of the interplanetary medium by signals transmission from deep space satellites and natural space radio sources.
- VLBI radio astrometry for coordinate-time tasks, geodynamics, precise space navigation.

During the years 1998-1999 a number of technical and scientific works was carried out.

The following new equipment was developed and installed into the RT-70 antenna for the 325 MHz frequency range: an antenna feed; a radio receiver including low noise preamplifier, high selective filters for interference rejection, frequency transformers and amplifiers, heterodynes, continuum radiometer, digital correlometers, the Mark II recording system. Antenna measurements show as system parameters: system temperature about 100 K; effective area 600 m^2 . The beam-width is 50 angular minutes.

Fig. 2 illustrates the registration of the antenna pattern with Virgo A as reference radio source. The upper-left pattern is the central scan, the other two scans correspond to the scans with a shift of ± 30 angular

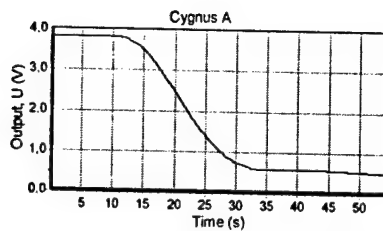


Fig. 4. Test result, Cygnus A as a source, different receiving stations involved

Exp: VLBP - 99.1
Base: Eupatoria - Svetloe
Src: 0745+241 (LCP)
Time: 9:159:11:38:00



Fig. 5. Response for an interferometer baseline. Reception at Eupatoria and Svetloe near St. Petersburg

minutes away from the main direction. The antenna pattern is symmetrical for both cross-sections and some pointing information is deduced from the patterns at + and -30 angular minutes.

Fig. 3 shows observations of carbon recombination lines observations with digital correlation-meters in four frequency bands towards Cassiopeia A. All four recombination lines were detected very reliably. During August and November 1998 a number of VLBI experiments have been carried out with the international low frequency VLBI net as a precursor for the future "Radio Astron" project. The magnetic tapes are processed in JPL laboratory in USA. New equipment for 4.8 GHz is a two-channel receiver with a micro-cryogenic closed cycle system cooled to a temperature of 6-8 K. The receiver can be used both for radio astronomy observations and for the radar-working regime. The intermediate frequency range is 100-600 MHz.

The S2 registration system was installed temporarily by the Institute of Applied Astronomy (St Petersburg, Russia [11]). The test have shown that the system total noise temperature is 25-35 K, the effective area is of an order of 2000 m² and the beam-width is about 3 angular minutes. With the given 2000 m² effective area, the reader should be in a position to estimate other parameters associated like G/T at 4.8 GHz as something like 53.5 dB/K.

Fig. 4 shows the result of a test experiment with Cygnus A as reference radio source. During the June 1999 a number of 4.8 GHz VLBI experiments were carried out. Fringes were detected with high reliability, for example, on the baseline Eupatoria (Ukraine) - Svetloe. For the information to the reader: Svetloe is near St. Petersburg, see [11] for a description of that 32 m antenna (QUAZAR) by V. Gratchev.

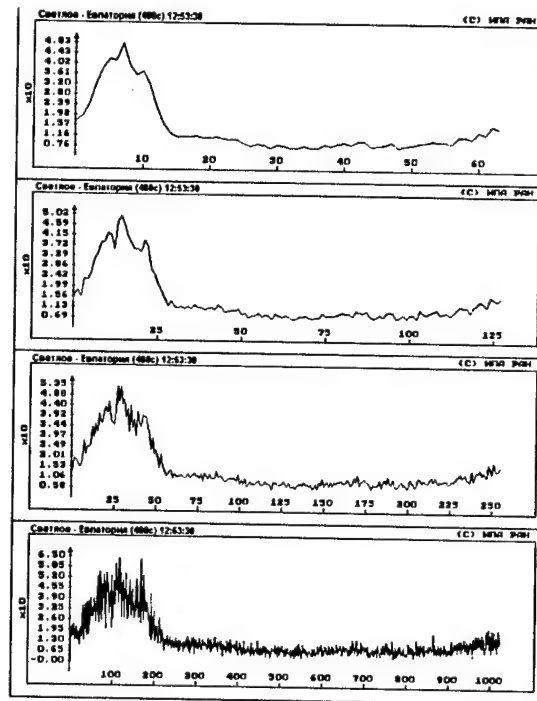


Fig. 6. Radar response spectra for the reflected spectra from Venus

Fig. 5 shows the interferometer response for this baseline (~ 2000 km) during the observations of quasar 0745+241. The horizontal axes correspond to the delay (0-8 mks) and power spectra (0-0.15 Hz). We can observe a strong localization of the signal for both parameters (time and frequency) with very high signal-to-noise ratio. It confirms the high reliability and quality of the experiment.

Furthermore, Fig. 6 shows mutual spectra of reflected signal from the Venus during radar experiments in VLBI mode for frequency band of 200 Hz. The signal-to-noise ratio is very high. Fringes were detected successfully. The processing was made by the Institute of Applied Astronomy, St. Petersburg, Russia.

Furthermore, the first test ground-space VLBI experiment was carried out on RT-70 antenna within the frame of the VSOP (Halca) project. The quasar 1351-145 was observed together with space radio telescope and with some ground-based antennas in southern part of the Earth. Now the S2 magnetic tapes are prepared for processing in Canada. With these achievements the first step in the creation of a modern ground-space radio astronomy center on the base of RT-70 antenna has ended. There are very good perspectives for future developments in this domain of research.

During the recent years the next steps in the development and upgrade of RT-70 antenna (Eupatoria) were carried out. It was connected with the installations of new equipment and methods as well as with the single-dish investigations, VLBI experiments, preparation of the participation in the ground-space interferometer projects and radar investigations of natural and artificial solar system objects with using of VLBI methods for planets, asteroids, meteors, space debris, satellites.

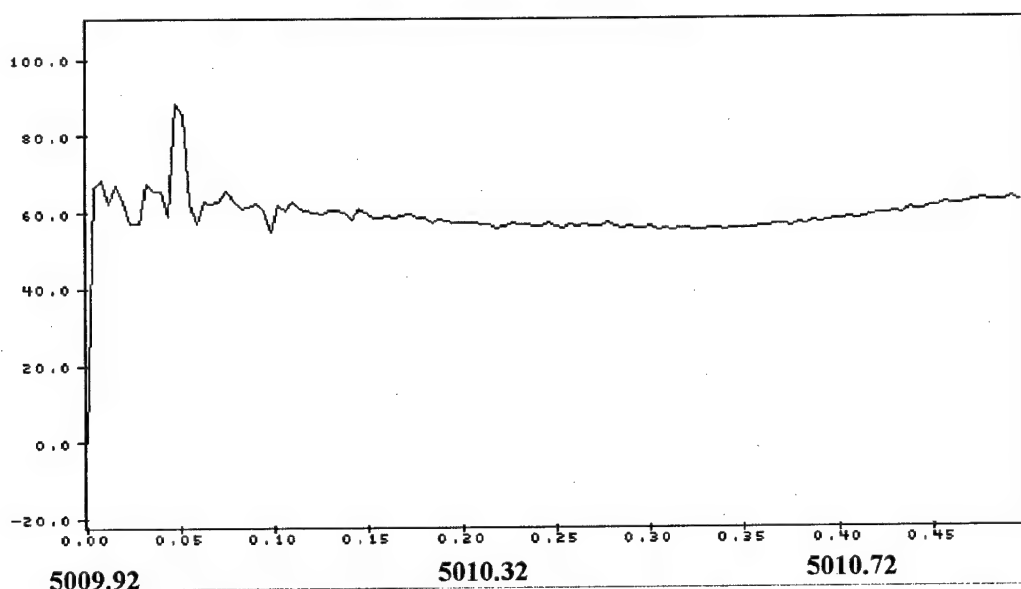


Fig. 7. Echo signal spectrum, to be further detailed in the workshop

3. SPACE DEBRI AND RADAR INVESTIGATIONS

New results are presented in this report involving the Evpatoria antenna, in the context of space debris research.

The RT-70 antenna, Evpatoria belongs to the world-largest antenna systems and is a "Europe-unique" receiving antenna capable of being fed with a high-power transmitter. The associated critical system parameters are given in Table 1.

Way back in the eighties the RT-70 antenna was repeatedly used in radar research of planets and asteroids. In recent years this transmit-receive system has been upgraded and equipped with new radio-astronomical facilities. This has enabled expansion of various radio-astronomical research and resuming radar experiments, including those employing the VLBI-methods. In 1999 the international 6-cm experiments for Venus and Mars were a success. There was radiation and reception in Evpatoria (Ukraine), reception in Svetloe (Russia) and

Shanghai (China). The interference lobes informative of the planet surface were recorded with high signal-to-noise ratio on all baselines.

When one considers the RT-70 power budget, the system, when used together with an available receiving antenna of 32-m in diameter, can be easily shown to be capable of detecting space debris-particles with a size of some mm on orbits to 400 km and accordingly some cm at geo-stationary orbits.

In 2001 an initial series of space-debris radar experiments was carried out, after a system upgrade and high-power transmitter repair. The transmitter tubes have been repaired in Kiev. The experiments consisted in radiating a continuous signal with a power level of roughly 100 kW at the frequency around 5 GHz (in some cases there was used a frequency modulation) towards the cataloged space vehicle fragments of about 1-m scattering cross-section, mainly in geo-stationary orbits. In testing also other targets like reference satellites in a high-elliptic orbit (apogee to 19,000 km) were considered as well. Different antennas in Russia and other countries (Svetloe, Kalyazin, Bear Lakes – Russia, MERLIN – Great Britain, Medicina – Italy, Torun – Poland, Shanghai – China, and others) were receiving the signals. In total more than 10 objects were explored. In silent intervals between the radiation sessions the above antennas were receiving the radio emission from quasi-stellar sources with coordinates very close to the debris objects. This allowed to monitor the antenna pointing accuracy, serviceability of receiving equipment and to utilize a new VLBI-radar method to essentially improve the positioning accuracy with the differential radio-astrometry method.

Practically all signals echoed from the studied objects were reliably detected with all antennas. As an example, Fig. 7 illustrates spectra of the echo signals recorded by the MERLIN and Bear Lakes antennas.

Table 1.

Main dish diameter:	70 m
Effective area at 6 cm wavelength:	2200 m ²
Transmitter output:	100–200 kW
PG-factor (product of antenna input and gain):	0.5–1 GW
Beam Width at 6 cm wavelength	3.5 arcmin.
Pointing accuracy:	~ 10 arc sec
System noise temperature with cryogenic 6-cm receiver:	40 K
Polarization	Circular

4. OTHER LARGE APERTURE ANTENNAS

Not far away from the RT-70 system there are some other large cm-wavelength antenna configurations in the Ukraine. These antennas are the RT-22 (Simeiz), the RT-32 (Evpatoria) and the RT-32 (Simferopol) antenna (Fig. 8). They all can well effectively receive the echoes of space debris echoes in the research sessions. Further improvement of the RT-70 transmit-receive system, in particular the increase of the transmitter output power and frequency deviation, is of current concern.

There has been accumulated a lot of data on meteor trails in the upper atmosphere, these data were acquired in the meter wavelengths. There are strong arguments to hold a remarkable part of the latter data as caused by space-debris particles. The radar searching of parent bodies in meteor streams at centimeter wavelength is of interest.

Further development of VLBI-radar of space bodies is of interest as it ensures an unprecedented positioning accuracy and thus fixes the actual traces of these bodies.

The Ukraine's radar system satisfies up-to-date requirements for supporting investigations into space debris problems.

The RT-70 space-object radar pilot experiments did already give evidence for promising prospects for expansion into this direction.

Many Ukrainian organizations (the Institute of Radio Astronomy of the National Academy of Sciences of Ukraine being the leading institution) participated in preparation and equipment of the RT-70 system, as well as in the research activity. Within the frame of a Ukraine-Russia cooperative agreement, several Russian organizations actively contribute to these efforts too – ASC FIAN, IRE RAS, (Moscow), IAA RAS (St.-Petersburg), NIRFI (NizhnyNovgorod), et al. It indicates the continuation and strong interest to maintain this unique instrument.

5. CONCLUSIONS

The radio telescope RT-70 has been described in outline and somewhat in history. It is a very elegant antenna design with at its time of construction very advanced solutions implemented for various technical problems.

Nowadays there is a continuous effort ongoing to maintain the operational capabilities of this unique instrument. A number of activities have been outlined. Recent results have been indicated and the interest to use such antenna for different applications related to space projects has become clearer.

REFERENCES

1. I. N. Knjasev, O. S. Viktorov, B. P. Riskov, L. M. Fedosejev, D. B. Roshdestvenski. "Antenna Facility with a 70 Meter Diameter Reflector (RT-70)," *Antenni*, (Russian) Issue 31, Publishing House Radio and Communication, Moscow 1984.
2. A. N. Kozlov, V. V. Tarasov, V. A. Grishmanovsky, B. G. Sergejev, "Summary and Experimental Investigations of the Radio Technical Characteris-



Fig. 8. The 32 meter antenna as built near Evpatoria and near Simferopol

tics of the Antenna RT-70", *Antenni*, (Russian) Issue 31, Publishing House Radio and Communication, Moscow 1984.

3. A. M. Aslanian, A. G. Gulian, A. N. Kozlov, V. B. Tarasov, P. M. Martirosian, V. A. Grishmanovskij, B. G. Sergejev, "Measurements of the Main Parameters of the Antenna RT-70," (Russian), *Radiofizika*, Issue XXVII, No 5, 1984.
4. V. A. Grishmanovsky, A. N. Kozlov, V. B. Tarasov, "The Main Principles of a 70-m Radio Telescope Reflecting System Design" (English...), *IEEE Transactions on Microwave Theory and Techniques*, Vol. 40 No. 6 June 1992.
5. R. V. Bakitko, M. B. Vasiljev, A. C. Vinitski, V. A. Grishmanovsky, A. L. Zaitsev, V. V. Kershakovits, E. L. Molotov, V. P. Oreshkin, G. M. Petrov, O. N. Rchiga, V. I. Rogalski, A. S. Selivanov "Radio Systems for Interplanetary Satellitesw" (Russian), ISBN 5-256-01054-9, Publishing House Radio and Communication, Moscow 1993.
6. V. Y. Kinber, "On Two Reflector Antennas", *Radio Eng. Electron. Physics*, Vol. 6, June 1962.
7. V. Galindo, "Design of Dual Reflectgor Antennas with Arbitrary Phase and Amplitude Distribution", *Proc. IEEE Antenna and Propagation Symposium*, Boulder Colorado, July 1963.
8. P. S. Kildal, "Comments on 'Synthesis of Offset Dual Shaped Subreflector Antennas for Control of Cassegrain Aperture Distributions", *IEEE Transactions on Antennas and Propagation*, Vol. AP-32, No 10, Oct 1984
9. R. Ambrosini, "Sardinia Radio Telescope (SRT), A Feasibility Study for a 64 m Active Surface Radio Telescope" Workshop on Large Antennas in Radio Astronomy, Feb. 1996 ESTEC, Noordwijk, The Netherlands. <http://www.estec.esa.nl/conferences/96002/prog.html>.
10. G. Cortes-Medellin, NAIC, USA, "The 64m Sardinia Radio Telescope Optics Design", *IEEE APS Conf. ernece*, San Antonio, Texas, USA, 2002
11. A. Finkelstein, E. Korkin, B. Poperechenko, S. Smolentzev, V. Gratchev, A. Ipatov, V. Kuzmin, E. Molotov, "VLBI Activity in IAA, St. Petersburg: New 32-m Radio Telescope for VLBI". Workshop on Large Antennas in Radio Astronomy, Feb. 1996 ESTEC, Noordwijk, the Netherlands. <http://www.estec.esa.nl/conferences/96002/prog.html>

NEEDS FOR GIGANTIC ANTENNAS FOR SPACE USE AND THEIR TECHNICAL PROBLEMS

Tadashi Takano

Institute of Space & Astronautical Science
Sagamihara, Japan
<ttakano@radionet.isas.ac.jp>
University of Tokyo

Abstract

Gigantic antennas for space use are needed in many potential applications such, and have different features from gigantic antennas for terrestrial use. This paper first enumerates the application fields and relevant requirements. The actual antenna for space VLBI and satellite Halca is described with our experiences in the development process. Current activities on gigantic antennas with diameter larger than several hundred meters are presented in relation with SPS.

Keyword: satellite communications, space radio astronomy, microwave power transmission, solar power satellites, gigantic antenna, aperture array

1. INTRODUCTION

Gigantic antennas for space use are needed in future satellite communications [1], space radio astronomy [2] or microwave power transmission from solar power satellites (SPS) [3]. The diameter of such antennas should be several tens meters or even one km.

The antenna is carried to space by a single launch to be deployed, or by several launches to be assembled. For these purposes, the mechanical structure of a gigantic antenna is of prime importance. Up to now, the structures suitable for a single launch have been proposed such as an umbrella type [4], a wrap rib type [5], and a hoop column type [6]. Another deployable antenna is a tension-truss type which was proposed by Dr. Miura [7]. This type of an antenna was actually applied to the antenna aboard Halca satellite for space VLBI in Japan [8].

The antenna with a larger diameter than several tens meters may be composed of a lot of radiators, and require several launches. Some concepts have been proposed and studied especially for a solar power satellite SPS [9-11]. The beam-scanning capability should be implemented to comply with the visible time of each revolution.

From the viewpoints of radiation characteristics, a gigantic antenna is associated with several difficulties: the appearance of grating lobes and pattern degradation due to antenna deformation. If the element radiator is a resonant half wavelength one, the spacing between the radiators can be made small enough to suppress the grating lobes. But the number of the radiators amounts to be enormous in order to cover a wide aperture of a gigantic antenna.

The gigantic antennas have been studied in Japan to be used in SPS systems. We proposed the concept of the array antenna of element apertures which can significantly reduce the number of the radiators [12]. But the design to suppress the grating lobes is needed [13].

This paper first presents the requirements of gigantic antennas and the conditions for their utilization in space. Then, the development of the 10 m antenna for Halca satellite is described with our experiences. Next, SPS systems which need satellite-borne antennas with a diameter larger than several hundred meters are presented. Our research results will be described in detail.

2. NEEDS FOR GIGANTIC ANTENNAS

Fixed satellite communication systems require gigantic antennas for the purpose of frequency reuse by narrowing zones. The half-power full-width angle θ_{HP} of a beam satisfies the following formula.

$$\theta_{HP} = 1.2 \lambda / D$$

$$D_{ZONE} = R_{SA} \tan \theta_{HP}.$$

where D : antenna diameter, λ : wavelength, D_{ZONE} : diameter of a ground irradiation zone, R_{SA} : distance between a satellite and an earth station.

If D_{ZONE} is 100 km at 4.6 GHz, an antenna of 30 m diameter is required. Mobile communications via a satellite aim to supply strong field on the ground in addition to narrowing zones.

Space VLBI systems aim high sensitivity. For example, ARISE of United States is assumed to carry the antenna of 30 m diameter at 80 GHz. Microwave

power transmission from a solar power satellite (SPS) requires an antenna of 1 km diameter at 2.45 GHz.

A gigantic antenna should satisfy the following electric conditions:

1. Beam width: narrow (high gain)
2. Beam direction stability
3. Frequency band
4. Transmission (T) / reception (R)
 SPS: T only
 Communication: T and R
 VLBI: R only
5. Sidelobes, noise and feeder loss

The items (1) and (2) are more general and common to many applications, but the items (3) to (5) are dependent on an application system. The frequency band may be narrow in SPS because a continuous wave is transmitted, but should be wide in VLBI because the radio wave from a radio star is almost a noise. Communications use a medium frequency band.

The following space conditions are also imposed on antennas for space use:

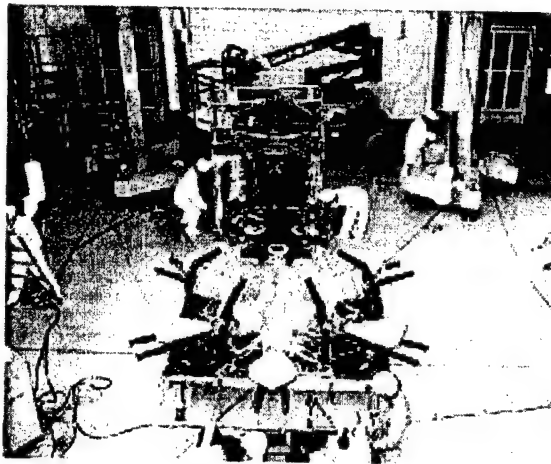
1. Weight and size of a unit: transportation.
2. Temperature: $+100^{\circ}\text{C}$ on the solar irradiation side, and -100°C shadow side
 Resultant deformation of the 1st order causes the beam deflection, and the 2nd order does the gain degradation.
3. Examination and test.
 As the antenna structure is flexible to lessen the weight, the compensation between the gravity of 1 G and 0 G is needed. Usually, Near Field Pattern (NFP) measurement as a whole is impossible.
4. Vibration conditions.

3. VSOP AND HALCA SATELLITE

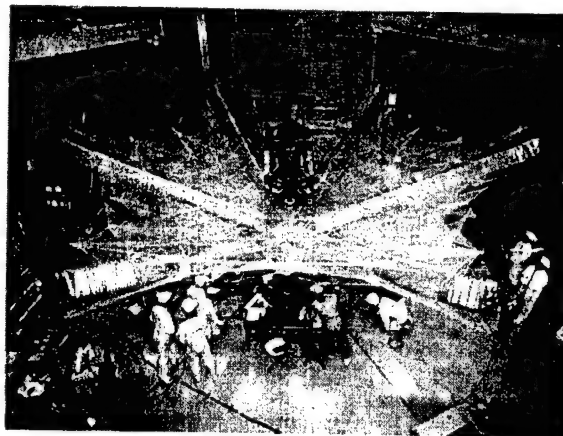
The VSOP stands for VLBI Space Observatory Project which uses a large antenna aboard a satellite in combination with a large antenna on the ground. This space VLBI system improves greatly the resolution of the radio wave interferometry by extending the baseline farther than the earth's diameter. The antenna on the dedicated satellite Halca has a maximum diameter of 10 m, and should operate at 1.7 GHz, 5 GHz and 25 GHz.

The antenna aboard Halca satellite is designed in the tension truss concept: Thousand of flexible cables are stretched by extensible masts to form a parabolic surface, and a reflecting mesh is attached on the cables, as shown in Fig. 1. As the concept is quite unique, we had many experiences with the deployable antenna of Halca.

In the development process, we suffered from difficulties of deployment. At the first stage, a deployment test model of the one-third reflector could not be deployed due to the entangling of cables with structures. The flight model mast in the deployment test was also hooked due to the interference of moving structures. We trimmed structural components in order to eliminate the trouble.



(a) Folded state



(b) Deployed state

Fig. 1. Structure of Halca antenna

Vibration test requires quite strong vibration level due to our launching rocket, so that the antenna itself and a shaker can not tolerate it. We contrived the method of frequency division excitation in analogy of frequency division multiplexing. First, the antenna was shaken at a lower level, and the modal analysis of the spectral response was carried out. Then, the total frequency bandwidth was divided to several bands each of which includes the coupled modes. As a result, the vibration level was kept within the tolerance of the shaker. We also had an interesting experience in the vibration test of the extensible mast in the folded state. When a random wave was imposed, the mast got longer gradually. We understood that the mast was extended by an exceptionally strong force, but could not move to the other side due to the mechanical stopper. As a result, random wave was rectified and caused a bias, analogous to electrical circuits. In order to overcome the situation, we attached a small spring which was quite effective to absorb spontaneous spikes, as is equivalent to a capacitor in the electrical circuit.

The analysis of radiation characteristics was also peculiar to a reflector composed of many flat facets. With the rigorous ray tracing to determine the field

Table 1. SPS Reference System Description

SPS generation capability (utility interface)	5 GW
Overall dimensions of the solar cell panel	5×10×0.5 km
Satellite mass	5·10 ⁴ ton
Construction location	GEO
Microwave transmission antenna diameter	1 km
DC-RF converter	Klystron
Frequency	2.45 GHz
Rectenna dimensions	10×13 km

distribution on the aperture, we had a wrong result. We should adopt an approximate ray tracing which ignores the Snell's law at the flat facet of the reflector. An electric model was manufactured to verify the validity of the analysis.

Concerning the electrical characteristics, I proposed a subreflector adjustment mechanism to compensate the antenna deformation. But the idea was rejected due to the severe limitation of the total weight, as happens often. Another concern was the connection of the antenna and LNA. I proposed to use a flexible waveguide, or to attach a small box of LNA to a large structure of the antenna. But it was finally decided to precisely install a bracket and connect the two components with a rigid waveguide of low-loss. This connection seemed to be broken by the shock during launch.

We learned the following lessons in the project:

1. During a research period prior to development, we should write papers as a researcher.
2. It is important for antenna engineers to give influence and powerful motivation for a project to adopt their ideas.
3. The interfaces should be flexible, and be deliberated by antenna specialists.

4. SOLAR POWER SATELLITE SYSTEM

4.1. REFERENCE SYSTEM

The energy consumption by the mankind has been greatly increased after the Industrial Revolution, but will be limited in a near future by the oil exhaust. The power generation in space and its transmission to the earth via a microwave beam is regarded as a possible solution of the energy crisis. The solar power satellite (SPS) concept was proposed by Dr. Peter Glaser in 1968. After the evaluation by NASA Office, the reference system description and preliminary environmental and societal assessments was published by Department of Energy of USA (DOE) in 1978.

The satellite and the microwave power transmission are illustrated in Fig. 2. Table 1 shows the main parameters of the SPS Reference System. An antenna of 1 km diameter is required to focus the beam within a rectenna

Table 2. SPS 2000 System antenna parameters

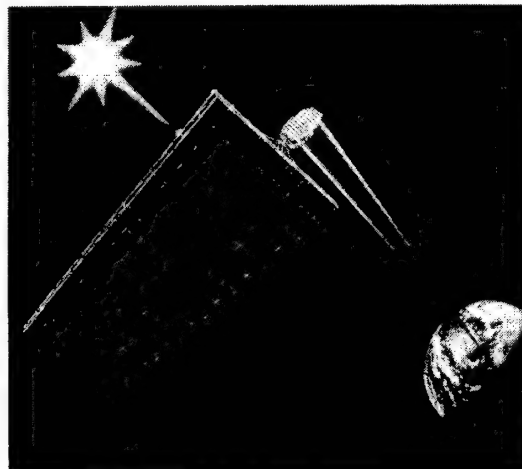
Satellite shape and dimensions	Triangular column, 336×303 m
Satellite mass	224 ton
Satellite orbit	Circular, 1100 km above the ground
Frequency	2.45GHz
Beam control	Retrodirective
Beam scanning angle	−30° ÷ +30° (east-west) −16.7° ÷ +16.7° (north-south)
Transmitting power	10 MW
Antenna shape and dimension	132×132 m square
Antenna mass	134 ton
Number of antenna elements	2.5·10 ⁸ units

(rectifier and antenna) on the ground from the Geostationary Earth Orbit of 36,000 km above the equator.

4.2. SPS 2000 SYSTEM

In Japan, the simplified version was proposed as SPS 2000 system which is shown in Fig. 3. The most significant difference is that the satellite flies 1100 km above the ground. Therefore, the power transmission antenna can be relatively small, but should be steered to point the beam to rectenna sites on the ground according to the satellite revolution.

The main parameters of SPS2000 are summarized in Table 2. The satellite mass and dimensions suggest easier realization than the Reference System. The antenna system, however, needs the control of a beam which will be realized by a large scale of a phased array antenna with 2.5 million elements. The mass and size of the antenna are still quite large.

**Fig. 2.** SPS Reference System

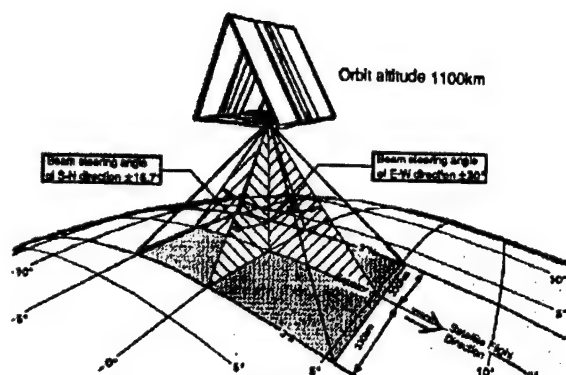


Fig. 3. SPS 2000 satellite and microwave beam-scanning control

5. GIGANTIC ANTENNAS WITH ABOUT 1 KM DIAMETER

A gigantic antenna with about 1 km diameter can be thought of in the three types, as shown in Fig. 4. A single aperture has a parabolic surface with possibly 300 m depth. The array of small radiators is the one proposed in the Reference System, and needs $2 \cdot 10^8$ elements.

We proposed the array of apertures each of which is much larger than a wavelength, for example 10 m diameter. The elements are 10^4 in number and can adjust the phase distribution as a whole. The beam scanning capability of this type is limited in ± 0.4 degree, which is sufficient for application to a GEO satellite. The total weight of the aperture array antenna is estimated to be 17 ton which can be carried by a single launch of a space shuttle. On the other hand, the small radiator array antenna needs 5 launches of a shuttle. Another merit of the aperture array antenna is found in the assembly process. Transportation, deployment and direction adjustment can be pursued according to the unit of an element aperture.

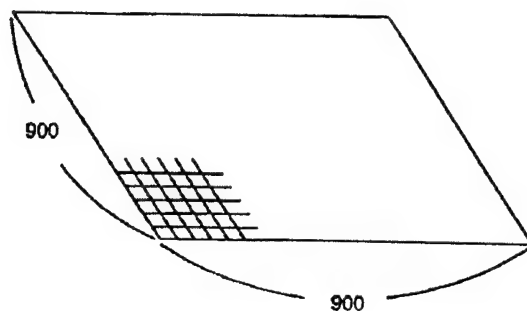
The aperture array antenna in the most densely-packed arrangement has the following technical subjects:

1. How to match the radiation pattern of a primary radiator with the shape of an element aperture.
2. How to suppress grating lobes.
3. How to patch the gap between apertures.

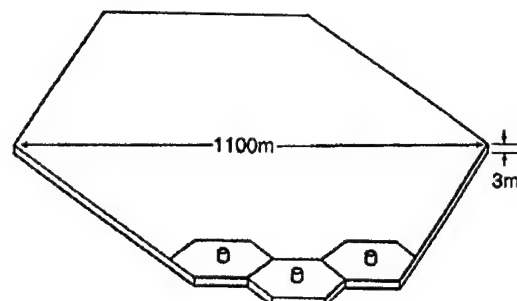
We developed a special horn to radiate a hexagonal beam for the term (1). The adjustment of the field distribution on both the element aperture and the total aperture is efficient to the term (2), as shown in Fig. 5.

For the term (3), a number of small parasitic radiators are installed to couple the adjacent apertures. The experimental system is shown in Fig. 6. The height of seventeen dipoles of a half-wavelength affects the gain of the total system, as shown in Fig. 7.

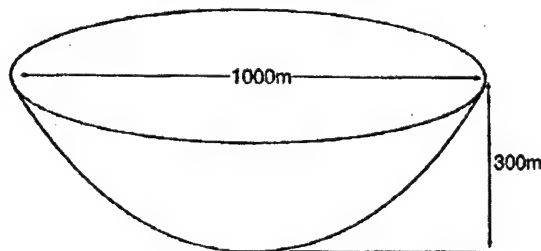
Finally, the height of each dipole was so optimized that the antenna gain in this case is 0.9 dB higher, and the first sidelobe level is 1.5 dB lower than the case



(a) Array of small radiators



(b) Array of apertures



(c) Single aperture

Fig. 4. Three concepts of gigantic antennas

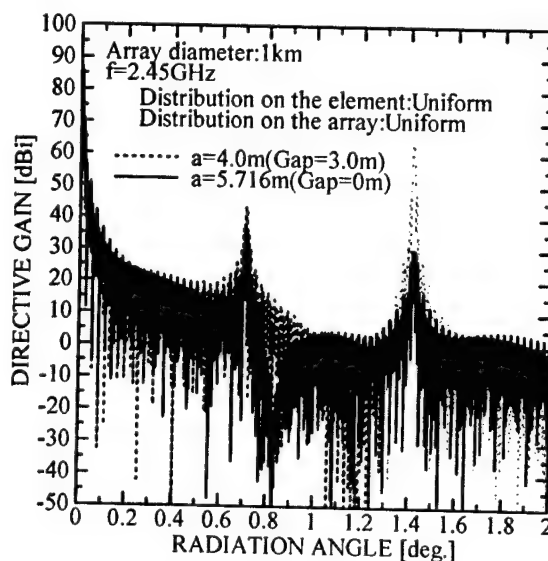


Fig. 5. The radiation pattern of the aperture array antenna

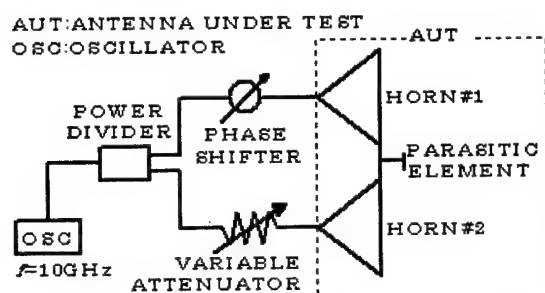


Fig. 6. Experimental system of electrical patching

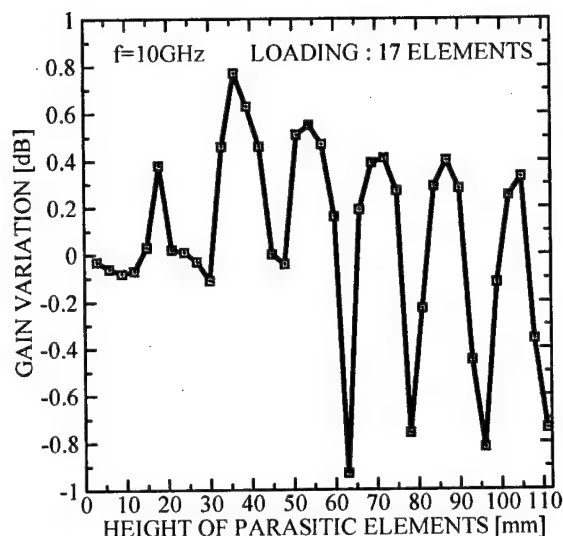


Fig. 7. Gain variation of the model antenna with 17 parasitic elements

without the dipoles. This system has been well analyzed assuming that the parasitic elements are irradiated by two pyramidal horns in the near field, and the current is induced on the parasitic elements.

6. CONCLUSION

- A gigantic antenna with a diameter of 100 m to 1 km is realizable.
- Its realization requires research activities and offers many research topics.
- Collaboration of electrical and mechanical engineers is inevitable.
- The tests should be studied for both of an antenna itself and its application system.

REFERENCES

1. Joseph N. Pelton, "New satellite communications architecture for the post 2010 time period", 21st Intn'l Commu. Satellite System Conf. & Exhibit, AIAA 2003-2356, April 2003.
2. H. Hirosawa and H. Hirabayashi, "VLBI space observatory programme (VSOP) satellite", IEEE Aerosp. Electron. Syst. Mag., vol. 10, no. 6, pp. 17-23, June 1995.
3. G. M. Hanley, "Satellite Power Systems (SPS) concept definition study: Vol. I-executive summary", NASA CR-3317, 1980.
4. W. M. Holmes, Jr., "NASA's tracking and data relay satellite system", IEEE Commun. Soc. Mag., vol. 16, pp. 13-20, Sept. 1978.
5. R. E. Freeland, N. F. Garcia and H. Iwamoto: "Wrap rib antenna technology development", NASA CP-2368, pp.139-166, Dec. 1984.
6. T. G. Campbell, D. H. Belvin, and B. B. Allen, "Development of the 15-meter hoop/column antenna system", NASA, CP-2368, pp.167-212, Dec.1984.
7. Koryo Miura, "Concept of tension truss lattice antenna", 37th Congress of the International Astronautical Federation, no. IAF-86-206, Oct. 1986.
8. T. Takano, K. Miura, M. Natori, E. Hanayama, T. Inoue, T. Noguchi, N. Miyahara, and H. Nakaguro, "Novel deployable antenna with 10 m maximum diameter for space use", IEEE Trans. AP (to be published).
9. M. Nagatomo, S. Sasaki and Y. Naruo, "Conceptual study of a solar power satellite SPS 2000", 19th International Symp. On Space Technology and Science, ISTS-94-e-04, May 1994.
10. Tadashi Takano, "Investigation on antennas in the concept of the most-dense packing", Symposium on SPS Technologies of Power Transmission and Reception", November 1994 (in Japanese).
11. T. Ohishi, et al., "Beam steering of an active integrated amplifier antenna array for microwave wireless power transmission in space", 2002 Asia-Pacific Microwave Conference, THO10, November 2002.
12. Sugawara, Y. Kami, T. Takano and E. Hanayama, "Investigation of the radiation characteristics of an ultra-large antenna for space use", 21st Intn'l Commu. Satellite System Conf. & Exhibit, AIAA 2003-2301, April 2003.
13. Sugawara, T. Takano, E. Hanayama and Y. Kami, "Investigation on an electrical patching method of a gap between apertures by loading parasitic elements", Trans. of Institute of Electronics, Information and Communication Engineers vol. J86-B, No.3, pp.519-526, 2003 (in Japanese).

TRACKING AND COMMUNICATION MEANS DEVELOPED AT THE SPECIAL MECHANICAL ENGINEERING DESIGN OFFICE

V. G. Himmelman, G. S. Kuchinsky

OAOKBSM (Special Mechanical Engineering Design Office), Russia, Saint-Petersburg
<kbsm@mail.admiral.ru>

Abstract

A brief review of the Special Mechanical Engineering Design Office activities in the sphere of tracking and communication means development – optical and radio telescopes – having, from the 50-s of the last century, provided for the implementation practically, of all the space studies and programs in the USSR, has been given in the report. The data on the problem trends in relevancy over the recent years has been given.

1. INTRODUCTION

The space studies, with the use of unmanned and the piloted spacecrafts, started in the middle of the last century, as well as the expansion of astronomical and radio physical studies of the Universe, have required the development of optical and radio telescopes of new generation.

The solution of this problem was entrusted to the Special Mechanical Engineering Design Office (KBSM), having acquired by that time a lot of experience in development of the alt-azimuthal mountings for the artillery systems to meet the increased requirements in respect to rigidity of constructions, accuracy of guidance and reliability. Thus, since 1954, the KBSM has become the leading company in the country in the designing of optical and radio telescopes.

2. OPTICAL TELESCOPES

In the period from 1956 to 1963, the optical telescopes AZT-10, AZT-11, AZT-12 with mirrors aperture, respectively, 1 m, 1.25 m, 1.5 m, as well as the largest in Europe telescopes ZTS with the mirror aperture of 2.6 m (Krymskaya and Byurokankaya Observatories), and the unique BTA telescope with the mirror diameter of 6 m for the Zelenchuk Observatory had been manufactured and commissioned.

All the mentioned telescopes have been in operation until present, although they do have a rather long length of service.

3. ANTENNA MOUNTINGS

3.1. STATIONARY AM

The contribution of the KBSM to the development of the antenna stock of the country is especially significant. Dozens of antenna mountings of various purposes, with the diameter of the reflecting surface from 2 to 70 m, with total quality of more than 600 units, ensuring the reception and transmission of data in the centimeter and decimeter bands, have been designed and commissioned for 50 years by the operation in this sphere.

In 1960, in Crimea (the region of Sevastopol), the first in the country large antenna mounting with the mirror diameter of 25 m was commissioned; which in 1962, was replaced by 32-meter one. This antenna has reliably provided for the communications of all first national space programs, including the flights of the first cosmonauts, control of automated self-propelled spacecrafts "Lunokhod-1" and "Lunokhod-2", and many more.

The further development of close and distant space has posed to the KBSM the problem to develop a unified communications contour and spacecraft flights control for the whole country. Within the frames of this program, in 1960-80, the ground-stationary, fully rotational antenna mountings (AM) dislocated throughout the whole of the country had been commissioned including:

- four AM with the mirror diameter of 32 m (in Crimea and Baltic by one, at Far East by two);
- twenty AM with the mirror diameter of 25 m;
- several dozens AM with the mirror diameter of 8-12 m and flat mirrors with area up to 150 m²;
- two antenna mountings, the largest in Europe and in the world, with the mirror diameter of 70 m (Crimea, Far East).

We need to make pause more closely on the antenna mounting with the 70-meter mirror, for its development had been an important stage in the development of the antenna engineering in our country.

The level of the requirements for this antenna had posed before the developers the problem to resolve new, and extremely complicated, research and engineering problems, stipulated, on the one hand, by the dimensions and the heavy loads on the metal constructions and mechanisms, and, on the other, by the high-output technical specifications. E.g. the mean square deviation of the parabolic surface of the 70-m mirror from the theoretical profile, at any point, is at most 0.7 mm; and the radio beam guidance accuracy is at least 30 angular sec.

To solve the whole set of problems, a lot of the research organizations were engaged, a significant number of research and experimental works was carried out. It took more than 10 years before the first antenna in the Deep Space Communications Crimea Center was commissioned in 1978.

The first tests carried out had exceeded all the expectations of the antenna developers; not only has the antenna surpassed, by many figures, the requirements of the request for proposal but became one of the best world instruments among the antennas of that class.

The commissioning of this antenna setup allowed the conducting in our country many radio astronomical studies, the implementation of which was simply impossible before.

3.2. THE SHIPBORNE AM

In order to maintain permanent communications with the spacecrafts along the whole flight trajectory, a series of 18 type dimensions of stabilized antenna systems of the shipborne-class with diameter mirrors from 5 to 25 meters were developed over these years. The 7 large science and research ships were equipped with them, including SRS "Vladimir Komarov", SRS "Academician Sergey Korolyov", SRS "Cosmonaut Yuri Gagarin" – the flagship of the space fleet with two antennas of 12 m in diameter and two antennas of 25 m in diameter.

The radio technical instrumentation for the majority of the mentioned stationary and shipborne antennas was developed by the Science Research Institute of Space Instrumentation Engineering (Moscow).

The antenna mountings designed by the KBSM have been taking part in all, without exception, national space studies, and in many international space programs; having thus shown, in doing so, the high reliability and communications ability.

3.3. THE MOBILE AND TRANSPORTABLE AM

Apart from ground and shipborne antennas, the KBSM has acquired much experience in developing the mobile and transportable AM with diameter mirrors from 2 to 7 meters, operating in the centimeter band and providing for the communications with the artificial sputniks of the Earth.

Set up upon the transport vehicles of a high cross-country ability, such antennas can be delivered to any point and brought into the operating state within 20-40 minutes (the mobile antennas) and within 24 hours (the transportable antennas).

Several dozens of the antennas of this class have been manufactured to the needs of various customers: Russian Aerospace Agency, Ministry of Communications, and other departments.

The chief Designers: A.I. Uokhov (the stationary antennas with mirrors of 25 m and 32 m in diameter), B. S. Korobov (the shipborne and the stationary antennas of the medium class), I.N. Knyazev (an antenna with the mirror of 70 m in diameter and the mobile antennas) were to manage the operations in designing of the above-mentioned antennas.

4. RADIO TELESCOPE RT-70

The task started in 80-s to the needs of the Russian Academy of Science in designing of a radio telescope of the millimeter radio wave band RT-70 with the mirror of 70 m in diameter is the whole trend.

The ensuring of exclusively high technical characteristics, practically by an order of and exceeding the analogous characteristics of any of the most accurate antenna mounting developed earlier is in the base of science and technical problems of the radio telescope development, namely:

- operating wave length – 1.2 mm;
- the MSD of the reflecting surface – 0.07 mm;
- guidance accuracy – at least 0.7".

The 70-meter antenna mounting of the KBSM development was adopted as the prototype, that allowed to borrow many mechanisms and metal constructions. The operations were conducted in a wide front; constructional operations were deployed in the Uzbekistan mountains, on the Suffa Plateau, at a height of 2500 m, plants proceeded to manufacture the material part, and the KBSM with the participation of a number of Research Institutions and Design Offices was carrying out the development of the design documentation of those mechanisms and assemblies, which were to provide for the increase of the precision characteristics. Up to 70% of mechanisms and metal constructions had been manufactured by 1990, and the installation operations had been implemented by 50% having approached to the mark of 60 m above the ground level.

However, in 1991 all operations to develop the radio telescope had been suspended for almost 10 years. And only for the last two years, the financing is renewed, although to a small extent, to continue the operations giving the ground to hope that the construction of this unique radio telescope, in the nearest years, will be definitely completed.

5. THE SUBJECTS OF TASKS OVER 1995-2003

Notwithstanding the known financial problems, in recent years the KBSM keeps on working to develop new, and modernize the current tracking and communications means:

- the first start-up phase (consisting of five stations) of the optical and electronic cosmic and air space observations system has been commissioned in the Tadzhikistan mountains, the second start-up phase, consisting of five stations as well, has already been installed and is passing through the integrated tests;
- the main control antenna bearing four mirrors each 6 m in diameter has been manufactured for the international program Sea Launch, installed on the Sea Launch Commander ship and participates successfully in the launches of the commercial sputniks;
- a series of the stationary and the mobile antennas of new generation with mirrors diameters from 3 to 6 m, including the tasks of the remote sounding, is being in the stage of designing and manufacturing;
- works to design, manufacture, commission several high-precision alt-azimuthal mountings, stationary and transportable, for the quantum and optical telescopes for the trajectory measurement of

spacecrafts and natural origin objects have been carried out;

- the development of the design documentation has been completed, the manufacturing and installation operations to create, in the Altai Laser Center, an informational telescope with the mirror aperture of 3.12 m have been conducted;
- a vast set of operations on the technical examination, defectation, maintenance, repairs and modernization of at least twenty antenna mountings being in the long-term operation of various customers and having worked out of their warranty periods is being carried out monthly;
- several science-and-research works in order to increase the engineering resource of the antenna mountings of different class have been implemented to the needs of the Russian Aerospace Agency.

6. CONCLUSIONS

The above-stated allows to make the conclusion that, notwithstanding the complex economical conditions, the KBSM having had a huge research and engineering work done, in advance, and over the many-year experience, is able to solve any of the engineering tasks to develop the instruments of various purpose; for space communications.

REMOTE SENSING OF TROPOSPHERE FOR AVIATION SAFETY: ANTENNA ASPECT

Felix J. Yanovsky

Department of Aeronavigation Systems, National Aviation University (NAU), Kiev, Ukraine

<yanovsky@nau.edu.ua>

International Research Centre for Telecommunications-Transmission and Radar

(IRCTR) Delft University of Technology, The Netherlands

<f.yanovsky@irctr.tudelft.nl>

Abstract

Techniques of microwave remote sensing of the atmosphere with the emphasis to the aviation applications are considered. Some results recently obtained are presented including joint research projects of NAU and IRCTR. Specificity of antennas is discussed. The paper mainly reflects the works, which were done with author participation, and does not aspire to saturation coverage.

Keywords: Radar, Remote Sensing, Antenna pattern, Polarization, Doppler-polarimetry, Dangerous meteorological phenomena.

1. INTRODUCTION

Weather information retrieval in particular the information about Dangerous Meteorological Phenomena (DMP) is an important application of remote sensing. Principal advantage of remote sensing is high velocity of data retrieval concerning large volumes of atmosphere, and also the possibility to derive information about the objects, which are practically inaccessible to be researched by other methods. Information about DMP is necessary for many fields, and aviation applications are probably the most obvious and important among them. From the aviation point of view, the notion of DMP includes aircraft icing, atmospheric turbulence, wind shear, an increased electric activity and lightning, hail, etc.

Remote sensing information is rather expensive. Nevertheless huge number of human lives, which were saved thanks to remote sensing information, proves high effectiveness of remote sensing in addition to the pure economic assessment of its importance. That is why ground-based and airborne weather radars and other weather sensors compose important part of airport facilities and airborne equipment.

The Weather Radar and Remote Sensing research group works during many years at the National Aviation University (NAU) in Kiev, Ukraine. The group cooperates with different research and design institutions, such as the International Research Centre for Telecommunications and Radar (IRCTR) at the Delft University of Technology (TU-Delft), the Research Institute "Buran" in Kiev, the Central Aerological Observatory in Moscow, etc.

Plenty different methods and devices for DWP detection and measuring were developed at NAU and in the framework of joint research projects.

Active and passive radars, radiometers, lidars and other sensors are considered as instruments for remote sensing of atmosphere. They can be installed on a ground-based platform, on aircraft or satellite. Really, antenna is one of key elements of any remote sensing system. In many respects, antenna defines main scope of a system. Various types of antennas are used in different remote sensing systems. Reflector antennas, including antennas with controlled polarization, lens, hybrid, slot antennas, antenna arrays, adaptive antennas, and others are among them.

The purpose of this paper is to give a general overview of the results achieved in the remote sensing of DMP using different types of antennas and to discuss some requirements to the antennas for remote sensing. However the paper mainly reflects the works, which were done with author participation, and does not aspire to saturation coverage.

2. MICROWAVE REMOTE SENSING

The remote sensing can be defined as means of getting information about objects, which are located on significant distance, without physical contact with the objects. The microwave remote sensing implies that information is carried by electromagnetic radiation, the object under observation exerts influence upon the characteristics or parameters of the radiation, and the information usually is derived by means of microwave technology and signal processing.

3. AIRBORNE FACILITIES

Airborne weather radar is necessary and obligatory standard equipment of any modern aircraft. Actually it is a multifunctional radar, which should enable to

detect clouds and precipitation, as well as zones of turbulence and wind shear, hail and icing. A major aspect of the operational efficiency of airborne weather radar is the reliability of DMP detection.

3.1. TURBULENCE

Detecting turbulence is difficult, because the reflectivity involved can be rather weak. Hence, noise and interference can essentially influence the reliability of the wanted information, resulting in very short detection ranges. At the same time, one of the major applications of turbulence detection is during cruise flight, at maximum airspeed. Finally, for aircraft in controlled airspace, often a significant lead-time is required before turbulence avoidance manoeuvres can be initiated. All these factors require large detection ranges if the turbulence detector is to be of any practical use [1].

The relationship between back-scattered signal parameters and singularities of the microstructure and dynamics of the scatterers (drops, crystals, snowflakes) in a single resolution volume or in an aggregate of resolution volumes is the physical basis of radar detection of turbulence in weather scattering objects. At present, amplitude and spectral techniques are in use for turbulence detection. A version of widely applied pulse-pair algorithm [2] is based on a direct evaluation of the sample inter-period correlation r^* on a signal sample x_1, \dots, x_n with n as sample size. Three developed algorithms are discussed in [2]. The first one is the parametrical algorithm [3], which is being used as a reference during the comparison of different developed algorithms. Two other synthesized algorithms are adaptive. First of them is one-sample and the second one is two-sample algorithm. The invariant one-sample algorithm is not sensitive to the power of the echo-signal and reacts only to changes in the correlation coefficient. More precise application of information originated from background scattering from Earth surface or from other fixed reflectors, being in the radar volume, is realized by construction of the two-sample decision rule.

The parametric algorithm gives the best results, as it must be. The two-sample adaptive algorithm comes most closely to the parametrical algorithm. Then one-sample adaptive algorithm follows. All three new algorithms provide significantly better reliability in comparison with pulse-pair algorithm. The difference is especially big in case of short samples. That is important for airborne radars.

Turbulence detecting from the board of aircraft requires antennas of limited size but with as narrow as possible main lobe. The level of side lobes should be rather low. Airborne X-band parabolic reflector antennas usually enable to provide side lobe level of -18 dB relative to the main lobe. In fact, it is not enough. That is why passive slot antenna arrays are in use in majority of modern airborne weather radars. Figure 1 shows Ukrainian airborne weather radar Buran A-140 with such kind of antenna.

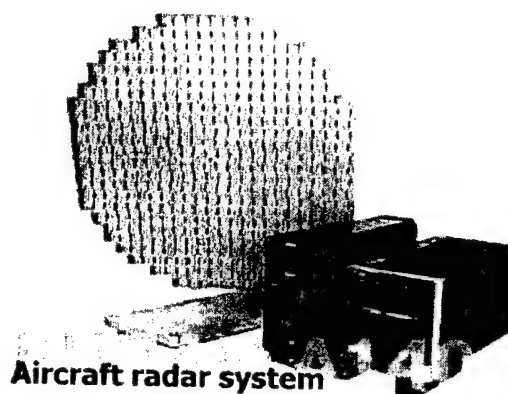


Fig. 1. Buran A 140 with slot array antenna

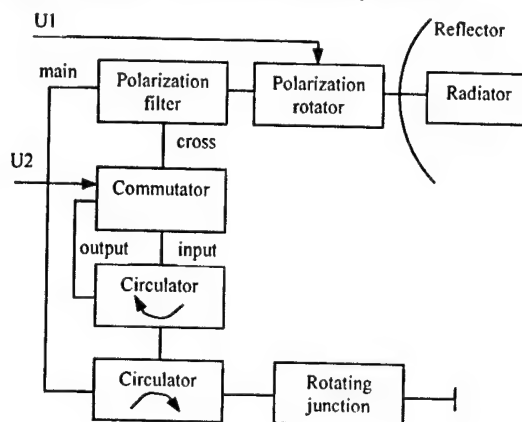


Fig. 2. Reflector antenna with controlled polarization

Such antenna provides at least -25 dB level of side lobe. Besides, the slot array antenna provides the beam width narrower than reflector antenna of the same size. That improvement is of $0.1^\circ - 0.2^\circ$ for antenna of $560 - 760$ mm diameter. Antenna gain is also $2 - 3$ dB higher for slot array antenna in comparison with reflector antenna.

3.2. HAIL

Several ways for microwave remote hail detection are known: multi- (dual-) wavelength methods with radar reflectivity as informative parameter [4], different polarization methods [5], radar-radiometric method, etc. Combinations of different methods are also possible. Polarization methods are the most suitable for airborne radar.

Hailstones are of irregular shape. That is why they differently reflect electromagnetic waves of two orthogonal polarizations, and they give considerable cross-polarization component of reflected signal. These properties are the basis for hail detection algorithms [6], [7].

Probably the only disadvantage of polarization approach for hail detection by airborne radar is associated with difficulties to change polarization of sounding signal when using slot array antenna. It is much easier to do with reflector antenna. Antenna with controlled polarization for airborne radar was

developed by [8]. The principle of the antenna is illustrated in Figure 2. Antenna operates as following. In the presence of the control pulse U1, horizontal polarization of the sounding wave is formed, and in the absence of U1, vertically polarized wave is radiated. Polarization filter separates the reflected components of main polarization (the same polarization as was radiated) and cross polarization (orthogonal one in respect to radiated polarization).

Both main and cross polarization components of a reflected signal come to the inputs of the commutator, and main component comes via circulators. The state of commutator is defined by the pulse U2, which is entered to its driving point. Then receiving signal from the output of commutator proceeds to antenna relay or duplexer via rotating junction.

Such antenna with controlled polarization was implemented in the research airborne weather radar on the basis of "Groza 26". Polarization radar equipped with this antenna was installed on the research airplane Ilushin 18 of the Central Aerological Observatory (Russia).

3.3. ICING

Supercooled water in atmosphere influences flight safety due to dangerous icing of aircraft. Strong icing not only makes worse the flight and aircraft performances but also can result in accident. The principal reason of icing during flight consists of the fact that the supercooled droplets collide with frontal parts of aircraft and become frozen. The character and intensity of icing depend on the temperature, water content, size of drops. The most intensive icing happen in zones of supercooled rain.

Polarization technique [9], [10] was proposed to increase the reliability of icing zone detection. Practically it is enough to detect supercooled water available in cloud to make a decision about high probability of icing. Water droplets have almost spherical shape; raindrops can be just a little flattened. Regular shape of droplets contrasts with irregular shape of ice crystals, which cannot cause icing.

Actually for the detection of icing, the same antennas can be used as was described above for hail detection. However, signal-processing algorithms are different.

3.4. INCREASED ELECTRIC ACTIVITY

Electric processes influence the forming of microstructure of clouds. Thus certain information about electric processes can be received using active remote sensing techniques (weather radars). The perspectives of active radiolocation applying for the detection of areas of increased electric activity are related with the adoption of polarization characteristics of signals for the estimation of regular component of scatterers orientation, which is associated with strong electric field [11]. For research in this direction the antenna with controllable polarization is suitable.

Different types of intensive self-radiation accompany electric activity in troposphere. That is why pas-

sive remote sensing of atmosphere electricity is especially envisaging further development.

Non-thermal, non-lightning pre-thunderstorm radiation is observed in a wide frequency band before the first lightning strikes, during the pauses between lightning discharges, and during some time after the termination of lightning. Statistical parameters of convective cloud self-radiation on different frequencies for three phases of thunderstorm were estimated by [12]. Three types of the EM self-radiation can be selected depending on the duration of pulse packages: 1) Pre-thunderstorm EM radiation with duration mode of 7 – 10 msec; 2) EM radiation of lightning with duration mode of 100 – 120 msec; 3) Continuous-noise EM radiation with duration mode of 0.8 – 2.0 msec. Data on non-lightning radiation of 1.7 MHz are presented in [13]. The method and apparatus for the detection of characteristic pre-thunderstorm self-radiation and estimating the coordinates of the radiant from the aircraft were developed by [14].

For receptions and primary processing of radiation of thunderstorm clouds, it is expedient to use the active antenna array. Active slot antennas can be used as the array elements. Their length appears 5 – 7 times less in comparison with conventional slot antennas. In considered range it is about 10 cm. This allows arranging of 50 elements on a leading edge of airplane. Spacing interval between the elements should be selected as equal to $\lambda/2$ where λ is wavelength. This allows avoiding appearance of the diffraction lobes at beam scanning in quadrant up to 90° . The use of slot radiators ensures a good anti-lightning protection and stability of the antenna at affecting static electricity. A wingspan of a modern passenger airplane is approximately 30 – 60 m, therefore at $\lambda = 3$ m minimum antenna pattern width can be about 2.5 – 5.0 degrees. As the characteristic radiation of electric cell in clouds exist also at higher frequencies (for example, at $\lambda = 1.0 - 1.5$ m), one can accept that the considered active antenna array is capable to provide a resolution angle about 2° in the perpendicular direction. It arises up to 4° at scan angle of 60° , and up to 7.7° at scan angle of 75° .

In order to provide automatic surveillance of the centers of increased thunderstorm hazard, it is expedient to apply self-focusing antenna arrays or arrays with variable parameters [15].

Proposed technique can detect thunderstorm centres 10 to 15 minutes before the beginning of active thunderstorm.

Distinct techniques are known for detection and ranging of sources of active lightning. Methods for determining coordinates of electric discharge source using lightning EM radiation are more developed because EM radiation of lightning is the most powerful in comparison with other types of non-thermal weather radiation. The task of lightning direction-finding is rather trivial. The difficulties are associated with estimating a distance up to a radiant of lightning especially when measurements should be produced

from one point, for example, from aircraft. Different approaches exist to design operational devices [16–20]. They are often based on measuring separately electric E and magnetic H components of lightning radiation. Loop antennas and conducting plates are in use for these purposes.

Both active and passive radar methods are not capable to detect zones of electric space charges when no thunderstorm activity appears as detectable radiation, for example, in nimbostratus clouds. However, it is known that lightning strokes into aircraft often occur just in such type of cloud. That happens due to the fact that electric charge of the aircraft itself activates the discharge if characteristic conditions exist. *The electrolocation method, based on solving of electrostatics inverse problem*, gives another way of deriving operative prognostic information about zones of electric activity. This method is associated with measuring of quasi-electrostatic field strength (EFS) along the route of aircraft. This way was developed, researched and realized as a method and apparatus by [21].

The inverse non-well-posed problem of determining the sources of electric field is solved by calculating of predictable values of EFS in the frameworks of adaptive models. Then values of EFS are measured during the flight, modeled and measured values are compared, and adaptive correction of the models is done to provide correspondence between modeled and measured values. The airborne weather radar data are used for previous detection of cloud cells and setting the initial models.

Determining space charges in atmosphere and estimating aircraft self-charge requires the use of not less than four EFS sensors, located at definite points of aircraft surface. These sensors can be considered as a kind of antennas of extremely low frequency. The working head of such sensor is practically out of the aircraft board. One of the key problems is creation of reliable EFS sensors for the use under extremely severe conditions. The technique for adaptive EFS measuring is described in [22].

4. GROUND-BASED RESEARCH RADAR

New possibilities of radar turbulence detection using Doppler-polarimetric radar were shown as a result of joint project of IRCTR at TU-Delft and NAU. The concept of mathematical modeling and computer simulation of Doppler-polarimetric spectra of radar signal from rain, which uses rain microstructure and turbulence parameters as initial data, was developed and implemented [23].

Experimental researches were done with S-band Transportable Atmospheric Radar (TARA) that was developed in IRCTR. The TARA system uses high-gain reflector antennas with beam-switching capabilities [24]. Figure 3 shows the complete antenna system of TARA.

The system consists of transmitting and receiving antennas with multiple beams. Antenna has extremely low level of side-lobes in the 90° directions. The multiple beams are used to measure three-dimensional

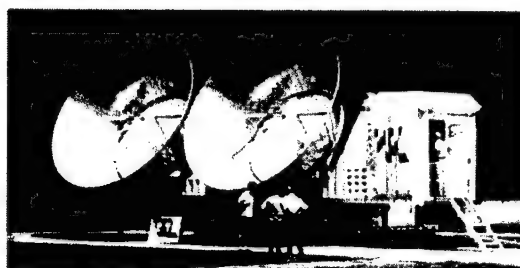


Fig. 3. Beam switching polarimetric TARA antenna

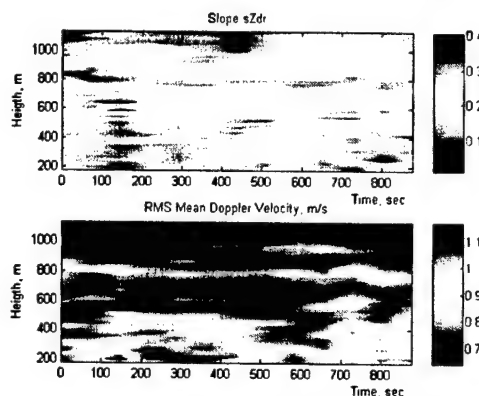


Fig. 4. Comparison of Doppler-polarimetric parameter 'Slope $sZdr$ ' and rms mean Doppler velocity

wind fields in quasi real time. Doppler measurements are performed in three independent directions. Beams are generated along the axis of rotational symmetry through the focus of the parabolic dish, the 0° beam, and in two orthogonal directions at 15° off axis by switching to a multiple beam feed system.

Specifications of the TARA antenna system are: diameter $D = 3$ m (or 33λ); focal length $F = 16.5\lambda$; $F/D = 0.5$; beam width $< 2^\circ$; gain > 37 dB; cross polarization < -30 dB (averaged over the beam); 1st side lobe < -25 dB; far side lobes < -80 dB. Being FM-CW radar system, TARA is very flexible and can provide extremely high range resolution Using high-resolution (15 m) mode, Doppler-polarimetric measurements were performed in rain.

As an example, Figure 4 demonstrates time-space distribution of slope $sZdr$ (upper panel) and rms of mean Doppler velocity (lower panel). These results are obtained by processing TARA data [25].

Slope $sZdr$ is new Doppler-polarimetric measurable variable introduced and researched by the international team in IRCTR [23, 26]. It can be calculated using measured Doppler spectra in resolution volume at two orthogonal polarizations. The value rms mean Doppler velocity represents independent estimate of turbulence with spatial scale more than radar resolution volume. Comparison of space-time distributions of the two parameters leads to the conclusion that the more turbulence intensity the less slope $sZdr$. This result corresponds completely to the theory and model developed previously [27, 28].

5. CONCLUSION

Dangerous meteorological phenomena (DMP) detection, is one of the most important applications of remote sensing in aviation. Active and passive radars, radiometers, lidars and other instruments are considered as sensors for remote sensing of DMP. They operate in extremely wide frequency band: from optics up to quasi electrostatics. They can be installed on ground-based platform, on aircraft or satellite.

The problems of DMP remote sensing are very diverse. That is why antennas of various types are in use for remote sensing. Applications of airborne reflector parabolic antennas, including antennas with controlled polarization, passive slot arrays, active arrays, adaptive antennas, loop antennas and conducting plates, as well as smart antennas with beam-switching capabilities have been considered in this paper.

Taking into account new sophisticated techniques of deriving meteorological information and signal processing, the qualifying standards are often quite rigorous on side lobes, cross-polarization isolation, identity of antenna pattern at orthogonal polarizations, and other critical parameters.

Multifunctionality of modern airborne and ground-based radars and other instruments for atmosphere remote sensing causes different types of adaptive, multipolarized, and smart antennas to be developed.

In many cases, the developed antenna with some new capabilities gives new possibilities for researchers in the field of remote sensing. New research facilities can be produced and unexpected achievements can be reached.

ACKNOWLEDGEMENTS

Author thanks the International Research Centre for Telecommunications-Transmissions and Radar at TU-Delft and its Director Prof. L. P. Ligthart for the possibility to work in Delft. He also thanks Dr. H. W. J. Russchenberg and Ms. C. H. M. Unal for fruitful collaboration.

REFERENCES

1. Ligthart, L.P., F.J. Yanovsky, and I.G. Prokopenko, Adaptive algorithms for radar detection of turbulent zones in clouds and precipitation. *IEEE Transaction on Aerospace and Electronic Systems*, Vol. 39, No 1, 2003, pp. 357-368.
2. Doviak, R.J., and D.S. Zrnic, Doppler radar and weather observations. Academic Press, inc., 1993, 562 pp.
3. Prokopenko, I.G., and F.J. Yanovsky, Integrated algorithm of hazardous turbulence areas detection with airborne radar, *Signal Processing Methods in Aviation Radio- and Electronic Equipment*, Kiev, KIUCA Press, 1995, pp. 29-35 (in Russian).
4. Abshaev, M.T., Radar detection and selection of hail centres. *Trudy VGI*, Issue 50, 1983, pp. 89-111 (in Russian).
5. Shupiatzky, A.B., and F.J. Yanovsky, Use of polarization and statistical characteristics of radar signals in detecting areas in clouds dangerous, for aircraft flying. 26 International Conf. on Radar Meteorology. 24-28 May 1993, Norman Okla, USA, pp.798-800.
6. Shupiatzky, A.B., and F.J. Yanovsky, Method for radar detection of hail zones in cloudiness, RU Patent application No 4943568, 1992.
7. Yanovsky, F.J., and V.A. Panits, Application of an antenna with controlled polarization for the detection of hail and icing zones. *Izvestiya Vuz: Radioelektronika*. Vol. 39, Oct 1996, pp.32-42 (in Russian).
8. Panits, V.A., A.B. Shupiatzky, and F.J. Yanovsky, Antenna with controllable polarization. SU Patent, No 1645918.
9. Shupiatzky, A.B., and F.J. Yanovsky, Method of aircraft icing areas radio-localization. Positive decision on Patent application No 4898827, Russia, 1991.
10. Yanovsky, F.J., Use of signal's polarization properties - the way to improvement of weather radar's parameters. *Proceedings of the Third International Workshop on Radar Polarimetry*, March 21-23, 1995, Nantes, France, pp. 578-589.
11. Shupiatzky, A.B., and F.J. Yanovsky, The influence of microphysical and electrical characteristics of troposphere's non-homogeneity on transformation of polarization parameters of radar signals. 16 All-Union Conference on Propagation of Radio-waves, Part 2. Kharkov, 1990, p.96.
12. Karmov, M.I. The use of some characteristics of an electromagnetic radiation for the assessment of thunderstorm and hail situations. *Trudi of All-Union Symposium on radio-physical methods in atmospheric researches*, Gidrometeoizdat, 1984, pp. 148-150 (in Russian).
13. Belotserkovsky A.V., L.I. Divinsky, H.K. Ekaterinicheva, L.G. Kachurin et al., Active and passive radiolocation of thunderstorm centers in clouds. *Gidrometeoizdat*, Sankt-Petersburg, 1992 (in Russian).
14. Ignatov, V.A., L.Y. Ilnitsky, B.E. Fishman, and F.J. Yanovsky, Method for the location of lightning dangerous zones from flying vehicle, SU Patent, No 1170877, 1984.
15. Drabkin A.L., V.L. Zuzenko, and A.P. Kislov, Antenna-feeder devices. - M.: Sov. Radio, 1974.- pp.425 - 430 (in Russian).
16. Ryan, P.A., and N. Spitser, Device for the detection of electric activity in atmosphere, US Patent, No 4023408, May 17, 1977.
17. Coleman, E.W., Storm warning method and apparatus, US Patent, No 4 672 305, June 9, 1987.
18. Yanovsky, F.J., and A.V. Korablev, Use of some propagation singularities for passive determination of the distance up to lightning source. *Millenium Conf. on Antennas & Propagation AP 2000*, Davos, Switzerland, 9-14 April 2000, 4 pp.

19. Yanovsky, F.J., and A.V. Korablev, Airborne Sensor for Passive Determination of the Distance Up to Lightning Source.. IEEE 2000 International Geoscience and Remote Sensing Symposium. Hilton Hawaiian Village Honolulu, Hawaii, 24-28 July 2000, Volume VII, pp. 3172-3174.
20. Korablev A.V., F.J. Yanovski, and L.P. Ligthart, New Method for Passive Determination the Distance up to Lightning Source, Proc. 2000 International Symposium on Antennas and Propagation (ISAP2000), Fukuoka, Japan, Vol 2., 2000, pp. 521-525.
21. Belkin, V.V., V.Y. Golubchik, B.E. Fishman, and F.J. Yanovsky, Method for determination of lightning hazards on aircraft. SU Patent, No 957629, 1981.
22. Yanovsky F., Methods and means of remote definition of clouds' electrical structure. Physics and Chemistry of the Earth. Vol.22, No. 3-4, 1997, pp. 241-245.
23. Yanovsky, F.J., H.W.J. Russchenberg, and L.P., Ligthart, Doppler and polarization parameters of radar signal from rain, IEEE Trans. GRS (In publication).
24. Heijnen S.H., and L.P. Ligthart, TARA: Transportable Atmospheric Radar, EUMWC 98 Conference Proceedings, October 1998, Vol. 2, pp.61-66.
25. Yanovsky F.J., C.H.M. Unal, and H.W.J. Russchenberg. Doppler - polarimetric radar observations of turbulence in rain, Report IRCTR-S-006-03, 2003, TU-Delft, The Netherlands, 102 pp.
26. Unal, C.M.H., D.N. Moiseev, F.J. Yanovsky, and H.W.J. Russchenberg, Radar Doppler polarimetry applied to precipitation measurements: introduction of the spectral differential reflectivity. 30th International Conf. on Radar Meteorology, 19-24 July 2001, Munich, Germany, American Meteorological Society, pp. 316 – 318.
27. Yanovsky, F.J., H.W.J. Russchenberg, L.P. Ligthart and V.S. Fomichev, Microwave Doppler-Polarimetric Technique for Study of Turbulence in Precipitation. IEEE 2000 International Geoscience and Remote Sensing Symposium. Hilton Hawaiian Village Honolulu, Hawaii, 24-28 July 2000, Volume V, pp. 2296-2298.
28. Yanovski, F.J., L.P. Ligthart, H.W.J. Russchenberg, and V.S. Fomichev, Comparison of Modeled and Measured Doppler-Polarimetric Parameters of Radar Signal Reflected from Rain, Proc. 2000 International Symposium on Antennas and Propagation (ISAP2000), Fukuoka, Japan, Vol 3, 2000, pp. 951-955.

BROADBAND PHASED ARRAY WITH WIDE-ANGLE SCANNING

Dmitry I. Voskresensky and Elena V. Ovchinnikova

Moscow Aviation Institute (state technical university), Moscow, Russia
<voskr@mai.ru>

Abstract

Wideband antenna arrays with wide-angle scanning are considered. The calculated characteristics of antenna arrays with 1D and 2D scanning are displayed. The possibility of the inter-element spacing increasing up to (2-3) wavelengths is shown. Considerable reduction of inter-element interaction simplifying matching under wide-angle scanning is obtained.

Keywords: Phased array antennas, ring concentric array antennas.

1. INTRODUCTION

Phased array antennas (PAA) are one of the most perspective types of the antennas. Planar PAA have limited sector of scanning, narrow band and small element distance. Conformal phased array antennas (CPAA) enable to overcome some shortcomings of planar array antennas [1]. However, practical realization of such antennas is connected with many difficulties. The necessity of far field control by phase, amplitude and polarization leads to considerable increasing of antenna element numbers and their cost. The comparison of necessary number of elements with minimal number shows considerable increasing number of antenna elements. Therefore one of the tasks is a research of ways of the construction antennas, possessing wide sector of scanning, a wideband and the number of elements which is coming nearer to the theoretically minimal ones. Ring concentric array antennas (RCAA) allow to solve the problem [2-4] to a certain degree are considered in the report.

The review of the literature on RCAA [5-12] shows the presence of significant number of works on the general questions of the calculation of such array antennas characteristics. However, there is no detailed research and recommendations on designing RCAA as electrically scanning array antennas with one-dimensional and bidimensional scanning.

The report shows considerable advantages of

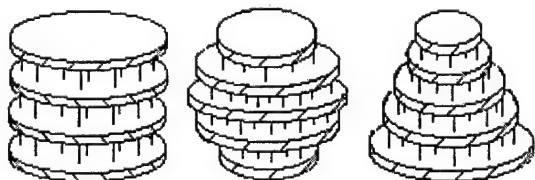


Fig. 1. Models of conformal phased antenna array construction

RCAA over planar and conformal array antennas. These advantages are: the reduction of the number of elements, the possibility of the wide-angle undistorted scanning and phase distribution control without commutation of radiation surface.

Ring concentric array antennas can be a component of conical, cylindrical and spherical array antennas with bidimensional scanning. Such antennas are shown in Fig. 1.

2. DIRECTIONAL CHARACTERISTICS

The results of numerical research of directional characteristics are presented in report to reveal the possibility of the reducing of the number of elements and increasing element distance. Element distance in RCAA depends on directivity and can be make some lengths of waves. The dependence of element distance on directivity is shown in Fig. 2. The elements distance increasing simplified matching under wide-angle scanning. In the case of such big distance of elements in the pencil-beam scanning array antennas there arises a question about appearance of diffraction lobe. The spatial patterns of RCAA are analyzed for this purpose on Fig. 3. Spatial patterns show the absence of the diffraction

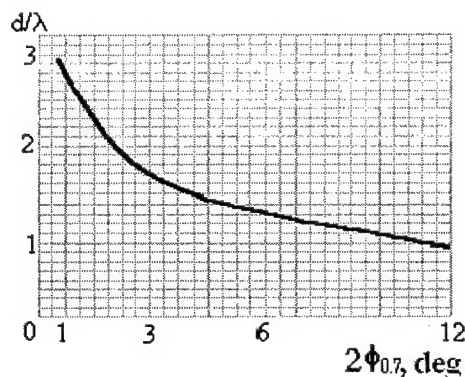


Fig. 2. Dependence of radiators distance on beam width

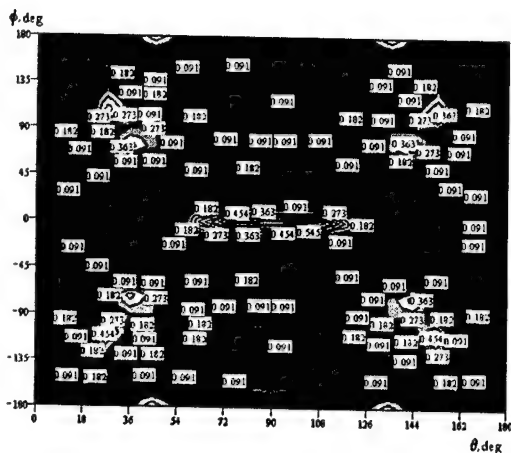


Fig. 3. Spatial pattern

lobe, but also quite a high side lobe level (SLL) of the return radiation which decrease with the increasing number of elements are investigated.

To define the influence of SLL on characteristics of RCAA, the dependences directivity factor (DF) on the beam width has been received by numerical methods. The gain of RCAA has been defined using well known relations for directivity factor (DF). The results providing high gain with minimum number of elements are presented. It is illustrated by Fig. 4.

3. FREQUENCY CHARACTERISTICS RCAA

Wideband operation possibility of RCAA is considered in the paper with both phase shifters of permanent phase shift in Figs. 5, 6 and on the basis of controlled delay lines in Figs. 7, 8.

Ring concentric array antennas for beam forming with wideband operation are especially interesting because of angle-frequency sensitivity absence and remarkable frequency band spreading under without changes of their performances.

4. INTERACTION OF RADIATORS

For the full analysis of the characteristics RCAA the decision of an internal problem is necessary. The most important problem is a coordination of the radiators at the wide-angle scanning. In the report research of interaction of the radiators by a method induced EMF is lead. The calculation by induced EMF showed satisfactory results for matching with an excitement system. On Fig. 9 dependences of the full entrance resistance on position of a radiator in array are shown. Fig. 10 shows the dependence of the average factor of reflection on azimuthal coordinate of a radiator.

5. CIRQUITS OF EXCITATION RCAA

The excitation of RCAA can be carried out both feeding and spatial way. Feeding excitation can be constructed on different lines of transfer and thus demands use of checkpoints phase switcher and the distributive systems providing necessary peak distribution.

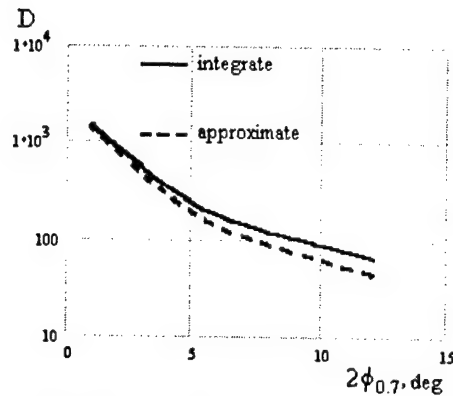


Fig. 4. Dependence of directivity factor on beam width

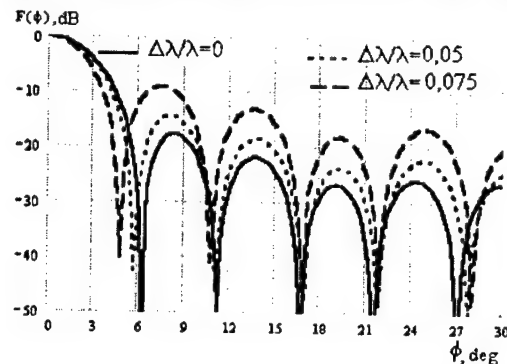


Fig. 5. Radiation pattern of RCAA in horizontal plane

At spatial excitation two variants are possible:

1. The central radiator is raised, and the others radiators become re-emitted with reflective phase shifters – Fig. 11a.

2. RCAA is a through passage array antennas which is irradiated with a primary irradiator and all its re-emitted elements – Fig. 11b.

Lacks both feeding, and a spatial way of the excitation which are shown as well for RCAA are well-known in radiation source. At drive one central radiator when thus the others - reflective the question wide-angle disappears coordination of a radiator with a falling stimulating wave which takes place at construction of the flat reflective lattices with a remote irradiator. Excitation of the central element allows to lower considerably also SLL due to peak distribution falling down to the edges. The spatial way of excitation in RCAA is realized by analogy to Luneberg lens and will consist in selection of such phase distribution of currents in vibrators at which the beam would be focused in the set direction and would allow to carry out sector scanning.

Array antennas with the wide-angle scanning in plane RCAA have above been considered. We shall consider models of array antennas which form convex array antennas of system RCAA and allow to carry out bidimensional scanning, having limited sector of scanning in a plane of a disk.

For the construction of two-dimensionally scanning antennas with the sector of scanning on an azimuth 360° from RCAA it is formed PAL, shown on Fig. 1.

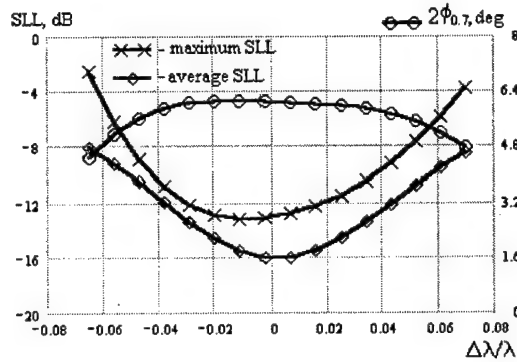


Fig. 6. Dependence of beam width and side lobe level on wavelengths

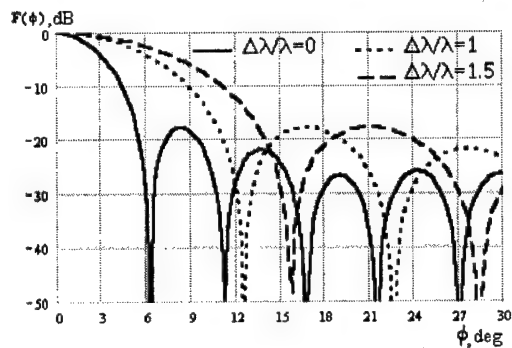


Fig. 7. Radiation pattern of RCAA in horizontal plane

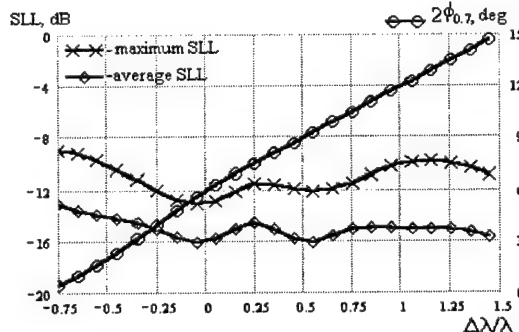


Fig. 8. Dependence of beam width and side lobe level on wavelengths

However, for their excitation and control of the phase distribution it is necessary RCAA to replace with the disk antenna (DA) [4]. Disk antenna is shown in Fig. 12. It consists of two conductive discs.

Between two conducting disks the radial wave guide which is raised by system of the concentric ring radiators is formed. For the basic wave phase speed coincides with speed of light, and for other types of waves the dispersion is observed. This circumstance specifies updating of the phase distribution resulted earlier. The lead calculations [4] show possible errors at phase excitation of the DA. The set of the DA allows to carry out scanning on an azimuth within the limits of 360° and on other coordinate in some limits, i.e. at the limited sector of scanning in other plane. In

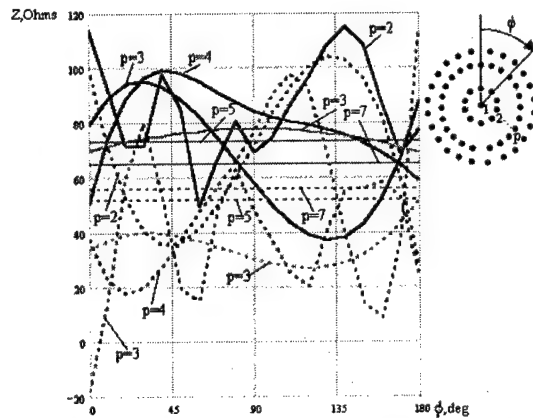


Fig. 9. Dependences of the entrance resistance on the number of a ring and azimuthal coordinate of a radiator

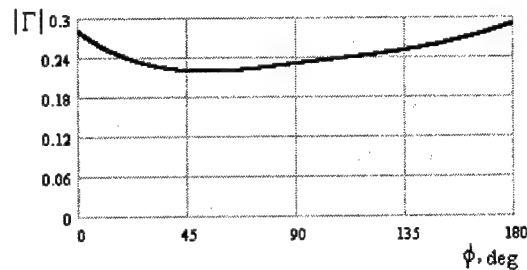


Fig. 10. Dependence of an average reflections factor on azimuthal coordinate of radiator

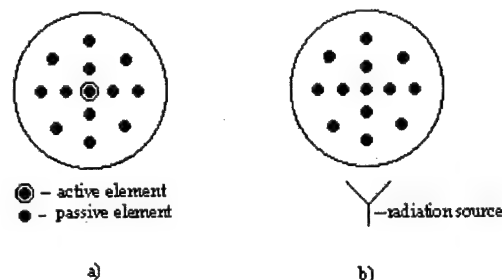


Fig. 11. Circuits of excitation RCAA

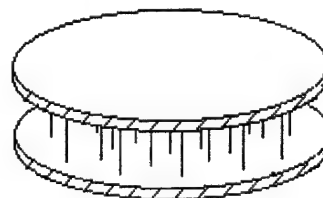


Fig. 12. Disk PAA

those problems, when the limited sector of scanning on azimuth; it is possible to consider the directed radiators and to construct modified RCAA with the minimum number of elements.

Such systems as RCAA have considerable advantages over planar arrays. These advantages are: decreased number of antenna radiators the wide-angle, 2D

distortion free scanning and broad band. Disk antenna represents also independent interest as the antenna or excitation system of cylindrical antenna, carrying out necessary sector excitation with the phase distribution control without commutation of radiation surface.

6. CONCLUSIONS

Thus, the directional characteristics RCAA as an array with wideangle scanning are presented.

The dependences of beam width and DF on number of elements are received.

Band and broadband properties RCAA which essentially exceed similar characteristics of the planar array antennas are revealed.

The possibility of bidimensional scanning which can be realized by disk PAA and set of disk PAA is shown.

REFERENCES

1. D. I. Voskresensky, L. I. Ponomarev, V. S. Filipov. Conformal scanning antennas – M. Sovetskoe Radio, 1970 (in Russian).
2. Voskresensky D. I., Ovchinnikova E. V., Proc. of the XXVIII Moscow International Conference on Antenna theory and technology Russia, Moscow, September, 1998.
3. D. I. Voskresensky, E. V. Ovchinnikova. Wide-band antennas with distortion-free and spreaded sector scanning. – Antennas, 1999, № 1 (42).
4. D. I. Voskresensky, E. V. Ovchinnikova. Disk antenna. – Antennas, 2001, № 4.
5. Woodward Oakley M., Rankin John Bruse. Steerable Antenna.[Radio Corp. of America]. Patent. USA, kl. 343–100, № 3090956, 21.05.63.
6. Array Antennas: the Review of foreign works /. L. S. Benenson. M. Sovetskoe Radio, 1966 (in Russian).
7. Goto Nachisa. Slot-hole array antennas with the round aperture., № 6457804, 6.03.89 // Sulfurs 7 (3.) – 1989–55 – with. 17–22.
8. L. I. Ponomarev, A. J. Pavlov. Dipole ring phased array antennas. High schools. Radio electronics, 1990 – 33, № 2. 33–37 p.
9. Dispersion of electromagnetic waves by antennas and array antennas.– M. MAI, 1992 (in Russian).
10. Stephanie L. Preston, David V. T. Mel, Trevor A. Smith, Steven G. O'Keefe, Jun Wei Lu. Base-Station Tracking in Mobile Communications Using a Switched Parasitic Antenna Array. IEEE Antennas Propagat. Vol.46, No.6, June 1998,
11. M. Vicente-Lozano, F. Ares-turnip, and E. Moreno. "Pencil-Beam Pattern Synthesis with a Uniformly Exited Multi-Ring Planar Antenna; IEEE Trans. Antennas Propagat., Vol.42, No.6, December 2000.
12. Yudin V. V. Theory and designing ring array antennas providing spatial multiplexing and the directed radiation not coherent signals. The dissertation on Ph. D degree. Samara, 2002.

MICROWAVE DEVICES WITH THE DISTRIBUTED NONLINEARITY

Yakov S. Shifrin and Anatoly I. Luchaninov

Department of Radio Engineering Foundations, Kharkiv National University of
Radio Electronics, Kharkiv, Ukraine (shifrin@kture.kharkov.ua)

Abstract

The paper is devoted to the based on the use of nonlinear boundary conditions (NBC) method of analysis of microwave devices with the distributed nonlinearity. There are considered two approaches to the formulation of nonlinear integral equations (NIE) for the distribution of the surface current density on elements of these devices. One of them is based on description of NBC in the space-time domain, another – on description of these conditions in the space-frequency domain. A procedure of numerical solution of NIE with the method of moments is set forth. Some results of modelling a nonlinear operating regime of two devices with the distributed nonlinearity stipulated by superconductive properties of material used in these devices are presented.

Keywords: antenna, microwave device, nonlinear boundary conditions, nonlinear effects, method of moments.

1. INTRODUCTION

One of important directions of the modern electromagnetics is the research of microwave devices comprising elements with the distributed nonlinearity. Especially it is topical for devices of the millimetre wave range, when dimensions of an area occupied by the nonlinearity become commensurable with a wavelength, or for devices whose surface is made of a material with nonlinear properties. An example of such devices is, in particular, an antenna made with the use of superconductors. Nonlinear properties of superconducting materials [1] caused a number of nonlinear effects that influence on device functioning.

The rigorous analysis of systems with the distributed nonlinearity necessitates a solution to the Maxwell equations with corresponding boundary conditions both for the area occupied by the nonlinearity and beyond it. This approach due to its complexity calls for great computational cost, and by today a limited number of problems are solved with its help [2].

However, in a whole number of cases, there is needed acknowledge of the electromagnetic field only in the area beyond the nonlinearity. In this case, the simplification of the general statement of the problem is possible. One of effective methods for this is that of nonlinear integral equations (NIE), which is based on the use of nonlinear boundary conditions (NBC). It enables to exclude from the consideration some area in space and the field within it by setting with NBC a certain relationship between its field vectors at its bound.

This method is applied, for example, for the investigations into electromagnetic waves scattering on bodies

with nonlinear contacts [3,4]. However, an essential restriction of similar works is the assumption of the polynomial approximation of the volt-ampere characteristic of a nonlinear contact. Such an assumption enables to study a case of the "weak" nonlinearity only.

In the paper, such a formulation of the problem is considered which enables to carry out the analysis of antennas and other microwave devices with the arbitrary nonlinearity.

2. STATEMENT OF THE PROBLEM

In the electromagnetic statement, a general problem of the analysis is formulated in [5,6] in the following way.

In homogeneous isotropic space with parameters (ϵ, μ) , a body V_1 (Fig.1), on whose surface Σ nonlinear boundary conditions are satisfied, is located. The surface is assumed to be smooth. Within volume V^i , external electric sources $\mathbf{J}^{e,i}$ and (or) magnetic sources $\mathbf{J}^{m,i}$ are enclosed. They create at point q on surface Σ intensities of fields $\mathbf{E}^i(q, t)$, $\mathbf{H}^i(q, t)$. It is required to determine the field in space beyond V_1 and V^i , i.e. in the region V_2 .

The first stage of the problem solution consists in determination of the current distribution on surface Σ . The formulation of integral equations, from whose solution the surface current density is being found, depends on in which domain the NBC and fields are written – in the space-time or in space-frequency domain. Therefore, in the beginning, let us dwell on the NBC representation.

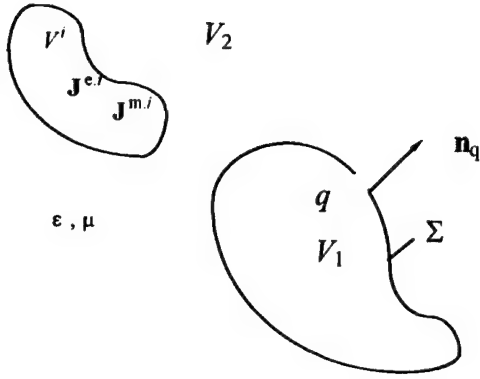


Fig. 1.

3. NONLINEAR BOUNDARY CONDITIONS IN SPACE-TIME AND SPACE-FREQUENCY DOMAINS

As the device under analysis is nonlinear, so in general case, it is impossible to manipulate with complex amplitudes, that is NBC must be formulated in the space-time domain. Correspondingly, we suppose that instantaneous values of tangential components of electric $\mathbf{E}(q, t)$ and magnetic $\mathbf{H}(q, t)$ fields intensity vectors on surface Σ are linked by the following relation

$$\mathbf{n}_q \times \mathbf{E}(q, t) = \hat{\mathbf{Z}}[\mathbf{n}_q \times \mathbf{H}(q, t)], \quad (1)$$

or in the equivalent form

$$\mathbf{J}^m(q, t) = -\hat{\mathbf{Z}}[\mathbf{J}^e(q, t)]. \quad (2)$$

Here \mathbf{n}_q is the external normal to the surface at point q ; $\mathbf{J}^m(q, t) = \mathbf{E}(q, t) \times \mathbf{n}_q$, $\mathbf{J}^e(q, t) = \mathbf{n}_q \times \mathbf{H}(q, t)$ are instantaneous values of the surface currents; $\hat{\mathbf{Z}}[\cdot]$ is the nonlinear operator depending on coordinates.

In general case, for the accurate determination $\hat{\mathbf{Z}}[\cdot]$, it is necessary to solve a boundary problem in the rigorous statement. However, there is no need in this: for a number of problems operator $\hat{\mathbf{Z}}[\cdot]$ can be determined from simpler (key) problems. Therefore, at the stage of statement of the problem – development of computational relations – that is where is possible, we do not concretize the form of this operator and use the boundary conditions in form (1) or (2).

However, when analyzing steady-state periodic or almost-periodic regimes, when a device is excited with external sources $\mathbf{E}^i(q, \omega_k)$ (or $\mathbf{H}^i(q, \omega_k)$) with different (in general case, not aliquot) frequencies ω_k ($k = \overline{0, K}$, $K+1$ is the total number of different frequencies of external sources), it is expedient to use NBC in space-frequency domain. The field intensities in (1) and surface current densities in (2) in this case may be written as

$$\left. \begin{aligned} \mathbf{E}(q, t) &= \sum_{n=-N}^N \delta_n \mathbf{E}(q, \nu_n) e^{j\nu_n t} \\ \mathbf{H}(q, t) &= \sum_{n=-N}^N \delta_n \mathbf{H}(q, \nu_n) e^{j\nu_n t} \\ \mathbf{J}^e(q, t) &= \sum_{n=-N}^N \delta_n \mathbf{J}^e(q, \nu_n) e^{j\nu_n t} \\ \mathbf{J}^m(q, t) &= \sum_{n=-N}^N \delta_n \mathbf{J}^m(q, \nu_n) e^{j\nu_n t} \end{aligned} \right\}, \quad (3)$$

where $\mathbf{E}(q, \nu_n)$, $\mathbf{H}(q, \nu_n)$, $\mathbf{J}^e(q, \nu_n)$, $\mathbf{J}^m(q, \nu_n)$ are, respectively, the complex amplitudes of intensities of electric and magnetic fields and of surface densities of electric and magnetic currents at frequency

$$\begin{aligned} \nu_n &= m_{0n}\omega_0 + m_{1n}\omega_1 + \dots + m_{Kn}\omega_K; \\ m_{kn} &= 0, \pm 1, \pm 2, \dots \end{aligned} \quad (4)$$

$$\delta_n = 1, \text{ if } \nu_n = 0 \text{ and } \delta_n = 1/2, \text{ if } \nu_n \neq 0.$$

Under these conditions, (1) and (2) are transformed to the following form

$$\begin{aligned} \mathbf{n}_q \times \mathbf{E}(q, \nu_n) &= \lim \left[\frac{1}{T} \int_{-T}^T \hat{\mathbf{Z}} \times \right. \\ &\times \left. \left[\sum_{i=-N}^N \delta_i (\mathbf{n}_q \times \mathbf{H}(q, \nu_i)) e^{j\nu_i t} \right] e^{-j\nu_n t} dt \right] \Bigg|_{T \rightarrow \infty} \\ &\forall \nu_n, \quad n = \overline{-N, N}, \end{aligned} \quad (5)$$

or

$$\begin{aligned} \mathbf{J}^m(q, \nu_n) &= \\ &= \lim \left[\frac{1}{T} \int_{-T}^T \hat{\mathbf{Z}} \left[\sum_{i=-N}^N \delta_i \mathbf{J}^e(q, \nu_i) e^{j\nu_i t} \right] e^{-j\nu_n t} dt \right] \Bigg|_{T \rightarrow \infty} \\ &\forall \nu_n, \quad n = \overline{-N, N}. \end{aligned} \quad (6)$$

These relations are nonlinear boundary conditions in the frequency domain. They represent a system of nonlinear equalities, which on surface Σ link complex amplitudes of all the frequency components of the magnetic field intensity ($\mathbf{H}(q, \nu_i)$, $(i = \overline{-N, N})$ with the amplitude of one frequency component of electric field $\mathbf{E}(q, \nu_n)$. Every condition of the system is defined at frequency ν_n , whereas dimension of the given system is equal to number of frequencies N being taken into account when reckoning the nonlinear operating regime of a device.

4. NONLINEAR INTEGRAL EQUATIONS IN SPACE-TIME AND SPACE-FREQUENCY DOMAINS

Representation of NBC in space-time and space-frequency domains allows obtaining the integral equations in two ways.

The first of them consists in that on basis of NBC (1) and (2), the integral equations are formulated in the space-time domain. Such an approach is realized in [6] with the resulting non-linear integral equations for electric and magnetic fields in the following form:

$$\begin{aligned} & \varepsilon \frac{\partial [\mathbf{n}_p \times \mathbf{E}^i(p, t)]}{\partial t} + \frac{1}{4\pi} \mathbf{n}_p \times \int_{\Sigma} \left[-\frac{\varepsilon \mu}{R} \frac{\partial^2 \mathbf{J}^e(q, \tau)}{\partial \tau^2} + \right. \\ & \left. + \text{grad}_p \text{div}_p \left[\frac{\mathbf{J}^e(q, \tau)}{R} \right] - \frac{\varepsilon}{R^2} \left(\frac{1}{R} \frac{\partial}{\partial \tau} + \frac{1}{c} \frac{\partial^2}{\partial \tau^2} \right) \times \right. \\ & \left. \times \hat{\mathbf{Z}} [\mathbf{J}^e(q, \tau)] \times \mathbf{R} \right] d\sigma_q = 0, \\ & \mu \frac{\partial [\mathbf{n}_p \times \mathbf{H}^i(p, t)]}{\partial t} + \frac{1}{4\pi} \mathbf{n}_p \times \int_{\Sigma} \left[-\frac{\varepsilon \mu}{R} \frac{\partial^2 \hat{\mathbf{Z}} [\mathbf{J}^e(q, \tau)]}{\partial \tau^2} + \right. \\ & \left. + \text{grad}_p \text{div}_p \left[\frac{\hat{\mathbf{Z}} [\mathbf{J}^e(q, \tau)]}{R} \right] + \frac{\mu}{R^2} \left(\frac{1}{R} \frac{\partial}{\partial \tau} + \frac{1}{c} \frac{\partial^2}{\partial \tau^2} \right) \times \right. \\ & \left. \times \mathbf{J}^e(q, \tau) \times \mathbf{R} \right] d\sigma_q = 0. \end{aligned} \quad (7)$$

Here $R = |\mathbf{R}| = |\mathbf{r}_p - \mathbf{r}_q|$; $\mathbf{r}_p, \mathbf{r}_q$ are radii-vectors of observation and integration points, respectively; $\tau = \sqrt{t - R/v}$ is the lag time; $v = 1/\sqrt{\varepsilon \mu}$.

It should be noted that the obtained equations enable to get insight into the non-linear regime of the device at any time dependency of the outer field. If, nevertheless, the investigations into the steady-state periodic or almost periodic regimes are intended, then it is expedient to carry out the analysis in the frequency domain. For transition to this domain it is necessary to use representation (3) and apply the Fourier transform to (7) or (8). Thus, e.g. the integral equation for the electric field in the space-frequency domain appears as [6]:

$$\begin{aligned} & [\mathbf{n}_p \times \mathbf{E}^i(p, \nu_n)] + \mathbf{n}_p \times \int_{\Sigma} \left\{ -j\nu_n \mu \mathbf{J}^e(q, \nu_n) G_n(p, q) + \right. \\ & \left. + \frac{1}{j\nu_n \varepsilon} \text{grad}_p \text{div}_p (\mathbf{J}^e(q, \nu_n) G_n(p, q)) - \right. \\ & \left. - \text{rot}_p \left\{ \hat{\mathbf{Z}} \left[\sum_{i=-N}^N \delta_i \mathbf{J}^e(q, \nu_i) e^{j\nu_i t} \right] \right\} G_n(p, q) \right\} d\sigma_q = 0, \quad \forall \nu_n, \quad n = \overline{1, N} \end{aligned} \quad (9)$$

where: $G_n(p, q) = \exp(-jk_n R)/(4\pi R)$ is the Green function of free space; $k_n = \nu_n/c$ is the wave factor; $\mathfrak{F}_n\{\cdot\}$ is the Fourier transform operator defined as:

$$\mathfrak{F}_n\{\cdot\} = \lim_{T \rightarrow \infty} \int_0^T \{\cdot\} e^{-j\nu_n t'} dt'.$$

There are two peculiarities of the obtained relations. First, (9) unlike the analogous equation in the space-time domain represents a system of equations with respect to complex amplitudes of the density of the surface electric currents $\mathbf{J}^e(q, \nu_n)$. Its dimension is equal to the number of frequencies being taken into account at computation. Second, at the development NIE in the

space-time domain it is necessary to know the Green function in the time domain for a boundary-value problem under consideration. In [6], as the Green function, there is used that of the homogeneous isotropic space. Therefore, systems of NIE, obtained as a result of (7), (8) transformation into the space-frequency domain, are valid, strictly speaking, only for microwave devices located in free space. This fact essentially restricts the applicability of the obtained systems of NIE.

The fact is that for a number of practically important problems, by today either there are absent expressions for the Green function in the time domain (for example, Green's function of stratified medium, which is needed when analysing microstrip devices) or the problem formulation itself loses its significance in the space-time domain (e.g., the periodic excitation of the infinite periodic structure).

Largely the mentioned restriction can be removed at the second way of NIE formation, which is possible for the periodic or almost periodic regimes of excitation. Its idea consists in that a stage of obtaining NIE in the time domain was excluded from a general procedure of NIE formation in the space-frequency domain. For this, NBC in the form of (5) and (6) are used. Thus, in [7,8] for electromagnetic structures made of thin wires or of thin microstrip conductors, NIE systems are developed in the following form:

$$\begin{aligned} & s_0 (\text{grad div} + k_n^2) \int_L \tilde{G}_n(p, q) \mathbf{I}(q, \nu_n) dl' - \\ & - \lim_{T \rightarrow \infty} \frac{j\nu_n \varepsilon}{T} \int_0^T \hat{\mathbf{Z}}_s \left[J(w) \sum_{i=-N}^N \mathbf{I}(\mathbf{r}, \nu_i) e^{j\nu_i t} \right] e^{-j\nu_n t} dt = \\ & = \begin{cases} -j\omega_k \varepsilon E_{tg}^i(p, \omega_k), & \text{at } \nu_n = \omega_k \\ 0, & \text{at } \nu_n \neq \omega_k \end{cases} \\ & \quad \forall n = \overline{0, N}. \end{aligned} \quad (10)$$

where $\tilde{G}_n(p, q)$ is the Green function of the region, within which the structure under analysis is located; $\mathbf{I}(q, \nu_n)$ is the distribution of the total current along conductors at frequency ν_n ; $k_n = \nu_n/c$ is the wave number of free space; s_0 is the ort tangent to the conductor axis at point p ; $E_{tg}^i(p, \omega_k)$ is the component of the external electric field intensity, which is tangent to a conductor; $J(w)$ is the function describing the distribution of current over the conductor cross-section. The integration is carried out along axial lines of conductors.

The obtained system of NIE enables to considerably expand a circle of analysed microwave devices. This is connected with the fact that when NIE are derived on basis of NBC in the form of (5) or (6), then in representation of fields through currents, there are used expressions for Green's function in the space-frequency domain, which by to-date are known for a number of electromagnetic structures. For example, with the use of the obtained system of NIE it is possi-

ble to analyze wire and microstrip structures located not only in free space, but in regions shaped in more complicated form, e.g., nearby a sphere, cylinder, on a stratified substrate, etc.

5. NUMERICAL SOLUTION OF NONLINEAR INTEGRAL EQUATIONS

Let us proceed to questions of solving NIEs. This is the most laborious stage of the analysis of antennas with the distributed nonlinearity.

Consider the NIE solution on an example of thin-wire antennas. For this purpose, let us write down relations (10) as [9]

$$\mathbf{L}[\mathbf{I}(l', \nu_n)] - \mathbf{N}[\mathbf{I}(l', \nu_n)] = \mathbf{E}_{ig}^i(l, \nu_i), \quad (11)$$

$$\forall \nu_n, \quad n = \overline{1, M},$$

where $\mathbf{L}[\mathbf{I}(l', \nu_n)]$ and $\mathbf{N}[\mathbf{I}(l', \nu_n)]$ are operators being respectively linear and non-linear parts of a system of NIE (10); l, l' are coordinates of points p and q counted along axis of conductors.

As usual, we shall seek the solution of the given system in the form of an expansion over some system of basis functions; as the latter, here functions of subregions will be used.

With this aim, we shall break up the conductor into M_L pieces and assume that within the limits of the μ -th piece the current distribution is approximated by some function $\Phi_\mu(l')$ which differs from zero only within the limits of this piece, whereas in its centre at $l' = l_\mu$ is equal to 1. Then the distribution along the entire conductor may be presented in the following manner:

$$\mathbf{I}(l', \nu_n) = \sum_{\mu=1}^{N_L} I_{\mu n} \Phi_\mu(l'), \quad (12)$$

where $I_{\mu n}$ is the amplitude of the current distribution at point $l_{\mu 0}$ at frequency ν_n . It should be noted that at all the frequencies, one system of basis functions is used. Distinction consists only in the approximation coefficients $I_{\mu n}$. Substitute (12) in (11) and take advantage of the method of moments choosing as weighting functions system $\Phi_\mu(l')$ for a linear operator and $\delta(l' - l_{\mu 0})$ - for non-linear. As a result, obtain

$$\mathbf{Z}_{Ln} \mathbf{I}_n - N_n \left[\sum_{i=-N}^N \delta_i I_i \right] e^{j\nu_i t} = U_n, \quad (13)$$

$$\forall \nu_n, \quad n = \overline{1, N},$$

where \mathbf{Z}_{Ln} is the matrix with elements $Z_{\lambda\mu} = \int \int \Phi_\mu(l) \mathbf{L}[\Phi_\lambda(l')] d\lambda_\lambda d\mu_\mu$; \mathbf{I}_n is the vector

with elements $I_{\mu n}$; $N_n \left[\sum_{i=-N}^N \delta_i I_i \right] e^{j\nu_i t}$ is the vector whose elements describe non-linear properties of

conductors; U_n - vector with elements $U_{\mu n} = \int \Phi_\mu(l) \mathbf{E}_{ig}^i(l, \nu_n) dl$.

System of equations (13) is that describing a non-linear circuit comprised of linear 2n-port being characterized by a matrix of eigen and mutual resistances \mathbf{Z}_{Ln} and a system U_n of acting at its inputs emf with connected to these inputs non-linear ports, whose characteristics are described by the function $u(t) = N_{\mu\mu}(i(t))$.

Thus, the solution of the NIE system for a radiator on whose surface nonlinear boundary conditions are met, consists of two stages.

At the first stage, the linear integral operator is reduced to the matrix form. Per se, this is the solution of the integral equation for a radiator similar to that under analysis, but with an ideally conducting surface. Therefore, all peculiarities of the latter problem are quiet inherent also to the considered by us task. Besides, when solving NIEs, it is needed to take into account a number of other factors with the aim of effective algorithms development. Apparently, the main of them is the necessity of the careful approach to a choice of systems of basis and weighting functions. The fact that account of radiator characteristics at high harmonics demands the correct approximation of the current distribution, i.e. leads to the enhancement of the number of basis functions, and, as a result, to the increase of the time of computation of matrix of eigen and mutual resistances. As accounts have shown, for wire and thin microstrip radiators, most acceptable remains the system of piecewise-sinusoidal functions of subregions, which was proposed by Richmond. It enables to develop the universal software package allowing to investigate characteristics of wire and microstrip radiators with NBC and with arbitrary complex geometry.

The second important stage of NIE solution consists in determination the device nonlinear regime of operation. This stage consists in equation (13) solution, i.e. in a vector \mathbf{I}_n determination. For this, the described in [9] effective enough two-level algorithm has been developed.

6. MODELLING RESULTS

The described above approach to modelling microwave structures with the distributed nonlinearity was finished by the software package, which has been widely used by us while analyzing the structures.

Let us consider briefly two examples.

In Fig.2, the taken from work [10] experimental dependence of the power of the third order intermodulation component at the output of the microstrip line (MSL) made as a piece of meander made of super high-temperature superconductor YBaCuO on the input power (curve 3). At the input of MSL with the wave resistance of 50 Ohm, there were inserted two sources of microwave oscillations of equal powers with frequencies of $f_1 = 4.69952$ GHz and $f_2 = 4.70052$ GHz. A value of the intermodulation component $2f_1 - f_2$ was controlled at the output of

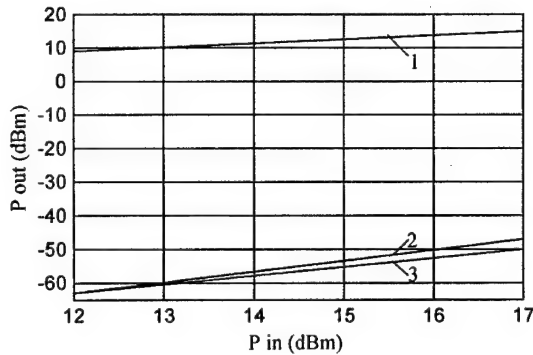


Fig. 2. Power at the output of MSL P_{out} as a meaner piece versus the input power P_{in} (1 – fundamental frequency; 2, 3 – intermodulation component of the third order (theory and experiment, respectively)).

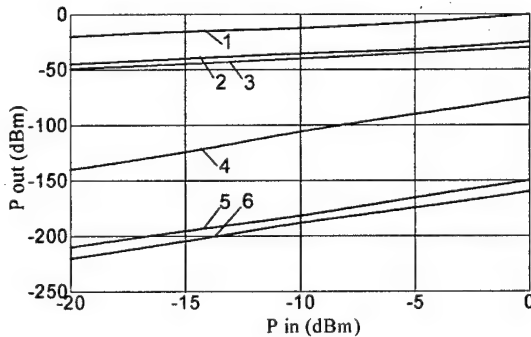


Fig. 3. The output power of the feed-through resonator at the fundamental and the third harmonic frequencies versus P_{in} at different values of the surface impedance linear part (curves 1, 2, 3 correspond to the first harmonic, L_0 are equal to 0.001, 0.0009, 0.0011; curves 4, 5, 6 – to the third harmonic, L_0 are equal to 0.001, 0.0009, 0.0011)

MSL. For this structure, we also carried out theoretical modelling under assumption that the nonlinearity of the surface impedance is of inductive nature and is described by the dependence [10] $L(I) = L_0 + L_2 I^2$ where L_0 and L_2 are the coefficients depending on the nonlinear properties of high-temperature superconductors. At first, by fitting coefficients L_0 and L_2 we were seeking the best coincidence of the experimental data with that of mathematical modelling for two values of the input power. As a result, the following values have been chosen $L_0 = 0.00043$ nH/m and $L_2 = 0.0001$ nH/A² m.

For these values of L_0 and L_2 , there were computed dependencies of the oscillations power at fundamental frequencies (they practically coincide – curve 1) and at the third order intermodulation component frequency on the input power. The latter (curve 2) is in a good agreement with an experimental (curve 3).

The results of simulation of a feed-through resonator excited at frequency $f_0 = 1.663$ GHz (wavelength

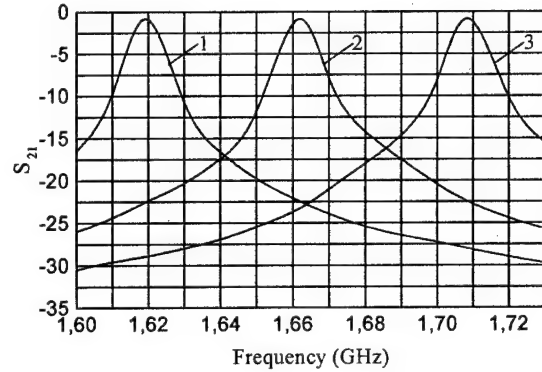


Fig. 4. Resonant characteristics of the feed-through resonator at different values of the surface impedance linear part (for curves 1, 2, 3, L_0 are, respectively, equal to 0.0009, 0.001, 0.0011)

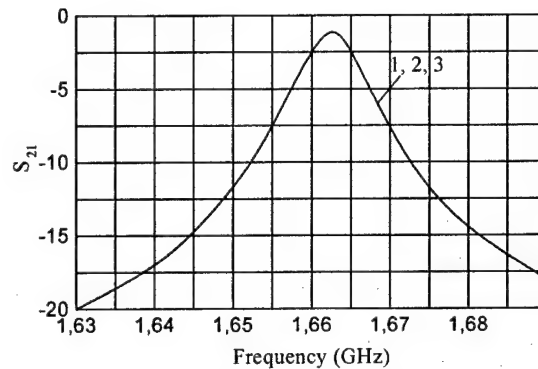


Fig. 5. Resonant characteristics of the feed-through resonator at different values of the surface impedance non-linear part (for curves 1, 2, 3 L_2 are, respectively equal to 0.0001, 0.0003, 0.0005)

$\lambda_0 = 0.18$ m) are shown in Figs.3-6. A wave resistance of MSL is 50 Ohm.

There was computed the power at the resonator output at fundamental frequency and frequency of the third harmonic at different parameters of linear and nonlinear parts of the surface impedance ($L_0 = 0.0009...0.0011$ and $L_2 = 0.0001...0.0005$). As is seen from Fig.3, change of L_0 entails considerable change of the resonator output signal at frequency f_0 , as well as at frequency $3f_0$. The reason of this is the change of the resonator resonance frequency as L_0 changes (the resonance curves for different L_0 are given in Fig.4).

Another situation is observed at the change of coefficient L_2 describing nonlinear properties of superconductive material. The change of L_2 within chosen limits does not lead to the change of resonance characteristics of the resonator shown in Fig.5. However, the change of L_2 influences on a level of the output power at the third harmonic frequency (Fig.6).

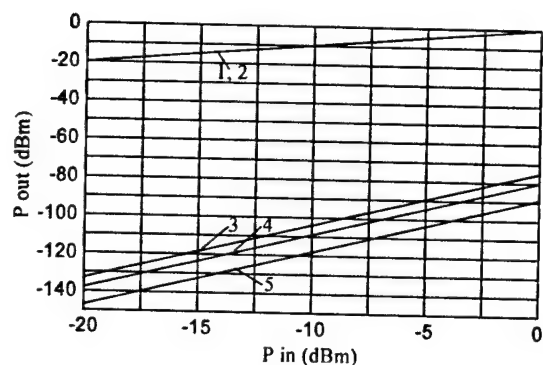


Fig. 6. The output power of the feed-through resonator at the fundamental and the third harmonic frequencies versus P_{in} at different values of the surface impedance non-linear part (curves 1, 2 correspond to the first harmonic, L_2 are equal, respectively, to 0.0001, 0.0005; curves 3, 4, 5 – to the third harmonic, L_2 are equal, respectively, to 0.0001, 0.0003, 0.0005)

ACKNOWLEDGMENT

The investigations considered in this paper have been carried out on the basis of the Radio Engineering Faculty of Kharkov National University of Radio Electronics. The authors would like to thank post-graduate students Gavva D. S. and Zhurbenko V. V., whose results were used when preparing the paper.

REFERENCES

1. IEEE Transactions On Applied Superconductivity.- 1999.- No 2.
2. Taflov A. Computational Electrodynamics: The Finite-Difference Time-Domain Method.- Boston-London, Artech House.- 1995.- 599 p.
3. Petrov B. M. Boundary conditions on nonlinear contacts // Scattering of electromagnetic waves.- Taganrog, 1991.- No. 8.- pp. 4-9. (in Rus.)
4. Petrov B. M., Semeniagina D. V., Panychev A. I. Effect of nonlinear scattering. – Taganrog, 1997. – P. 202. (in Rus.)
5. Shifrin Y. S., Luchaninov A. I. State-of-the-art of the antenna with nonlinear elements theory and techniques // Radiotekhnika. -1996.- V. 39. -№ 9-10. -pp.4-16.
6. Shifrin Y. S., Luchaninov A. I., Omarov M. A. Antennas with the distributed nonlinearity analysis. – Antenny / Ed. by L. D. Bahrah. – Moscow.: IPRZhR, 2000, No. 1(44). – pp. 70-83. (in Rus.)
7. Analysis of Strip Electromagnetic Structures with Nonlinear Surface Impedance / Luchaninov A. I., Omarov M.A., Zhurbenko V.V., Gavva D.S. Transactions of the 1-st International radio-electronic Forum « Applied radio electronics. State and future trend of development» IRF-2002. Kharkov, Ukraine, 2002. pp. 283-286. (in Rus.)
8. D.S. Gavva. Excitation of wire structures with distributed nonlinearity by various type sources // (In this issue).
9. Shifrin Y. S., Luchaninov A. I. Antennas with nonlinear elements //vol. X in: Antenna techniques handbook. V. 1./Ed. by L. D. Bahrah and E. G. Zelkin -Moscow: IPRZhR, 1997.- pp. 207-235. (in Rus.)
10. Shinho Cho, Cheon Lee Intermodulation measurements in superconducting meander lines // IEEE transactions on applied superconductivity.- 1999.- No2.- C. 3998 – 4001

MULTI-FACED AND MULTIBEAM DBF ANTENNA FOR HIGH ALTITUDE PLATFORM STATION STAGES OF ANTENNA DEVELOPMENT

Bon-Jun Ku¹, Yang-Su Kim¹, Byung-Su Kang¹, Do-Seob Ahn¹, A. S. Belyaev²,
Ye. N. Egorov², N. V. Vladimirov², S. A. Ganin², A. C. Reutov², Yu. A. Suserov²,
A. M. Shitikov², A. V. Shishlov², A. G. Shubov²

¹ Research Institute, Taejon, Republic of Korea,
<bjkoo@etri.re.kr>

² Joint-Stock Company "APEX", Moscow, Russia
<iscape@online.ru>

Abstract

Advantages of the multi-beam antenna for Stratospheric Communication System (or HAPS) with Digital Beam Forming (DBF) are demonstrated in comparison with Analogue Beam Forming (ABF). To cover the service area from nadir to a circle of radius 55 km by 199 beams, the antenna system of seven flat Active Phased Array Antennas (APAA) is proposed. Due to high accuracy of amplitudes and phases in channels of the APAA with DBF, optimal cell forming as well as high spatial isolation between cells is obtained. Stages of antenna creating are considered. Results of the work at initial stages are presented too.

1. INTRODUCTION

Global systems of personal communications become more and more popular today. It is very attractive to communicate with simple handheld phone anywhere, but there is a lot of difficulties in realization of such a system. For geostationary satellite, since a low power signal is obtained near the Earth surface, it would be impossible to use the simple handheld phone unit. One of the ways to solve this problem is to utilize intermediate-orbit (10000-14000 kilometers) or low-orbit (780-1800 kilometers) satellites. In addition to

them, a new concept, HAPS (High Altitude Platform Station), was proposed worldwide to provide high multimedia services with high capacities by obtaining more link margin than that of the satellite systems [1]. HAPS, the stratospheric airship with communication system equipment, would be located at about 20 kilometers altitude (Fig. 1). Conceptual design of stratospheric communication system is developed in different countries. In frame of US-Japan joint project, flight test of stratospheric experimental system were fulfilled in 2002 year at Kauai Island, Hawaii.

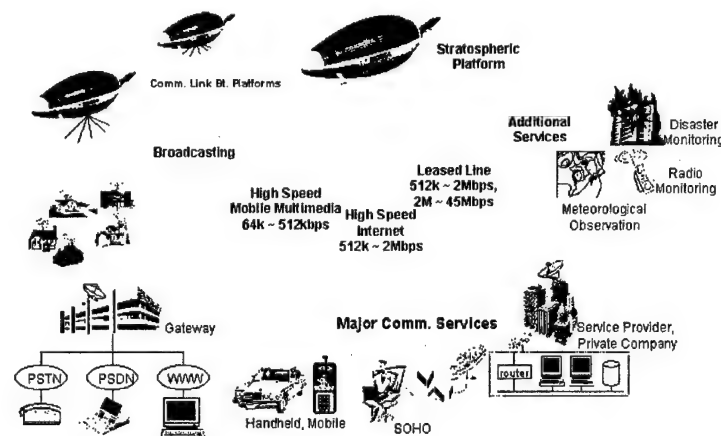


Fig. 1. Stratospheric communication system

To cover the wide area and provide the sufficient link margin to the users with the small and simple terminals, HAPS would adopt the multi-beam system. In consideration of HAPS airship, the elevation angle of about 20 degrees is assumed. The coverage angle of HAPS antenna is about ± 70 degrees, and the diameter of the coverage area on the ground is about 110 kilometers.

Some solutions for the multi-beam antenna in millimeter wave were proposed. For example, at 48/47 GHz, in V-band, different beams can be formed by independent apertures such as horns, each is connected with transmit and receive equipment respectively and directed to a specified point of the service area. For the lower frequency such as Ka-band (30/20 GHz) and S-band (2 GHz), independent apertures grow very strong, and multi-beam Active Phased Array Antenna (APAA) is preferable to independent apertures [2]. In this case, one APAA forms a bundle of beams at once. The experimental models of the Ka-band on-board receive (20.2-21.2 GHz) and transmit (30.0-31.0 GHz) antennas were developed in Japan [3].

Development of APAA with DBF opens up new possibilities in designing multi-beam antennas. It should be remembered, however, that such antennas could hardly be implemented in near future, due to present digital IC state-of-the-art. It is expedient to develop the communication system step-by-step. Some perspective antennas for the Stratospheric Communication System are considered below. The results of the work at initial stages are given too.

2. CONSIDERATION OF ANTENNA FEATURES

The APAA are applied in various Communication Systems [4, 5]. However a single-flat APAA is ineffective for wide service angles. The explanation of this fact is as follows. A multi-beam array antenna contains a system of simple radiators connected with a Beam Former. Usually, an antenna radiating element (for example, a horn, an open waveguide, a dipole, a spiral, etc.) has a radiation pattern beamwidth no more than $2 \times (40-50)^\circ$. The element gain outside of this angle is degraded rapidly. In fact, flat APAA's can be used up to $\pm 45^\circ$ from the boresight, rarely to $\pm 60^\circ$ scan angle.

Another important problem is connected with a distortion of antenna pattern cross-section within the coverage area. As the cell moves away from dirigible nadir, its dimensions grow and the energy is "smeared" on the Earth surface.

To reduce the effects mentioned above, a possible way is to use of multipanel antennas. Each panel of the antenna has its own partial coverage area, and all of them form the whole antenna coverage area. This engineering solution is successfully used, for example, in Iridium system [4] where the satellite has three separate APAA's. The problem of matching beams of several APAA arises in this case. To solve the problem, the ABF is used [4].

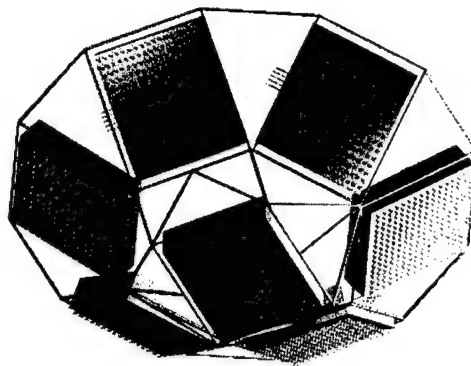


Fig. 2. Sketch of the seven-panel antenna

For the HAPS, due to the rigid requirements such as very low side lobe of radiation beam pattern, ABF is very complicated and it's hard to satisfy the requirements [6]. The DBF is preferable to ABF for HAPS because of its high capability and flexibility [2, 3, 7, 8].

In Fig. 2, antenna is shown above the Earth surface. Antenna axis is directed to the Earth center. To provide the required coverage area, it is necessary to determine the optimal number of the panels and the beam arrangement. There are several criterions for this choice. Actually, all the criterions are oriented on the achievement of a specified link budget and other parameters that are important for the communication system when the antenna cost is minimal.

The satisfactory value of the antenna gain should be obtained within the partial service area for each panel when the total number of panels is minimal. Also, a minimal irregularity in the cell arrangement should be provided to create a tight set of cells on the Earth surface without gaps (or holes) and overlapping the cells. A diverse picture takes a place when we used a multipanel antenna. Although the regular construction of the usual Beam Former provides a regular character of the beam arrangement within the partial coverage angle, distortions of the beam arrangement regularity are observed at the joints of the partial coverage angles. The reason of these distortions is connected with different positions of the phase centers for different panels relative to the Earth Surface. To overcome this problem, a small irregular Beam Former should be used. Moreover, the rigorous control of the side lobe level should be fulfilled [7]. Only the DBF Beam Former permits to solve this task (Fig. 3).

Antenna beams must have a high electromagnetic isolation. This leads to a strong limitation on off-axis antenna radiation. Especially low side lobe level (SLL) is required when Code Division Multiple Access (CDMA) standard is used. To satisfy these requirements [6] and to design the antenna with low side lobe level, it is necessary to realize with adequate accuracy a certain taper amplitude distribution in the antenna aperture. Amplitude errors should be less 0.2 dB and phase errors should be less 1.5° in order to

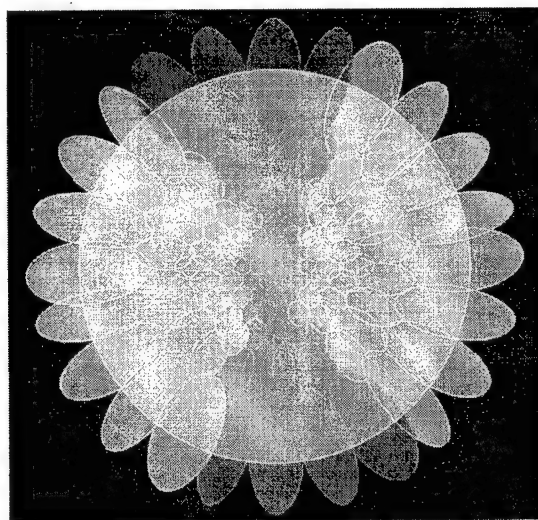


Fig. 3. Beam arrangement for the antenna with DBF

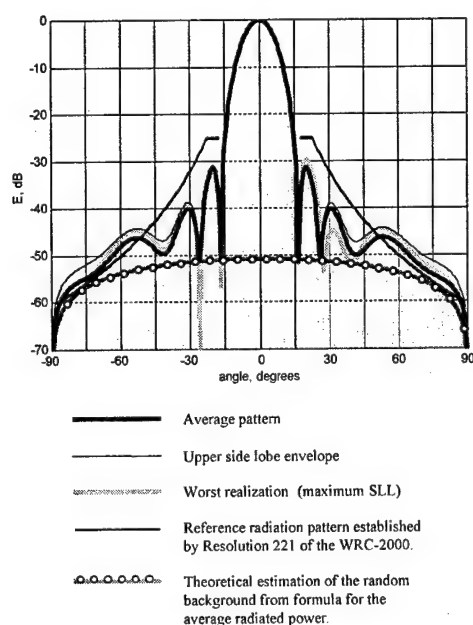


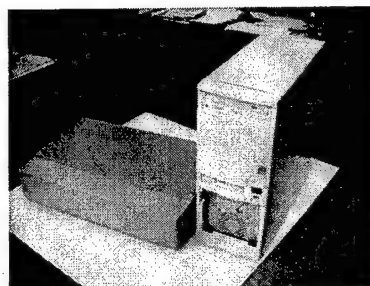
Fig. 4. Simulation patterns of the array [8]

suppress the side lobes of the HAPS antenna [8]. Due to the DBF, signals from the array radiators are converted directly to a digital form and translated to the digital signal processor where all the antenna beams are formed independently. An example of the APPA simulation is shown in Fig. 4.

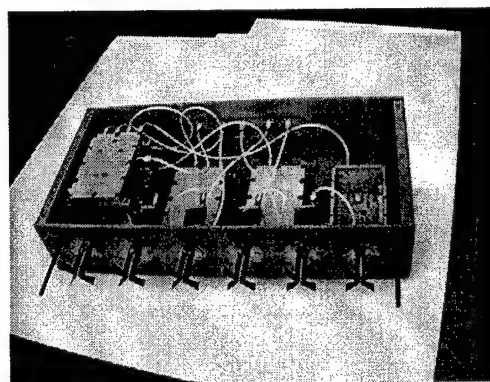
3. STAGES OF ANTENNA CREATING.

RESULTS OF EXPERIMENTAL MODELING

At present time, using of DBF is restricted by small arrays since there are no commercial chips to implement multi-element wideband digital beam former. However, this disadvantage is temporary. It is essential that new approaches and technologies will be required to create the antenna for Stratospheric Communication System. As the first approach, the



a)



b)

Fig. 5. a) Linear 4-element APAA with DBF
b) Radio-frequency subsystem of linear 4-element APAA with DBF

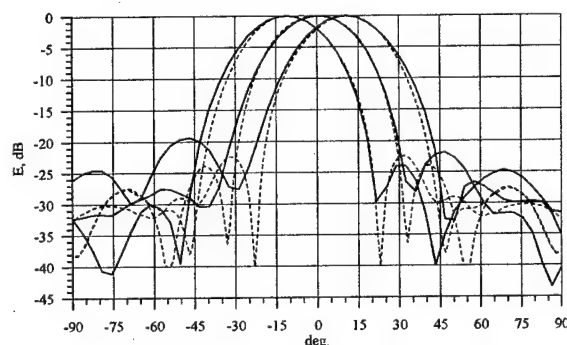


Fig. 6. Three beams of the linear APAA with DBF: calculated (dash) and measured results

development of the small sized antenna with DBF is initiated now for these purposes [3].

ETRI and JSC "APEX" developed and tested 4-element linear APAA with DBF in S-band (Fig. 5). Three beams are formed (Fig. 6). A good coincident of theoretical and experimental results has been obtained.

In addition, 19-element S-band APPA is developed and manufactured (Fig. 7). The antenna is assigned to form seven beams. Adjustment of the element and the antenna as a whole are carried out now.

The Ka-band APAA consisting of 7 elements and forming seven beams is developed too. Two main constructive units arrange the antenna channels: the module of Ka-band and module of S-band. It is necessary to create a special RF subsystem for the Ka-band antenna whereas the digital subsystem can be the same as for 19-element S-band antenna forming 7 beams. The architecture of the antenna and element

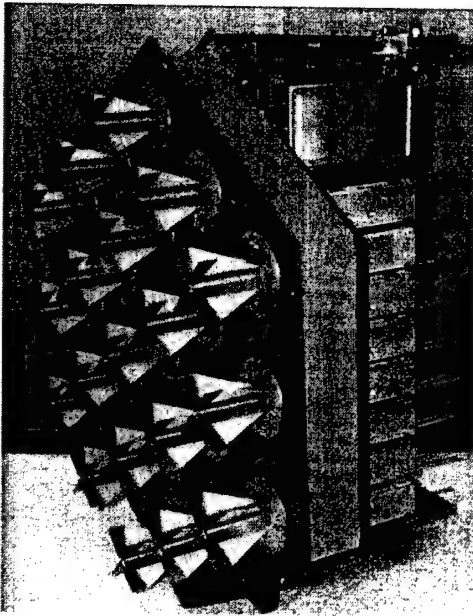


Fig. 7. Planar 19-element APAA with DBF

spacing of about 1.12 wavelength are similar to [3], except the radiation structure which is fulfilled to obtain a flat-topped element radiation pattern due to element mutual coupling. It is useful to suppress the grating lobes.

4. CONCLUSION

The requirements to the antenna for HAPS are extremely strong. It should be a new era of APAA. Only digital approach to beam forming in APAA and very stable active devices allow to meet these requirements. Development of multi-panel APAA with DBF is a perspective way to create antennas for HAPS.

REFERENCES

1. Do-Seob Ahn, Bon-Jun Ku, Dong-Cheol Baek, Kwang-Ryan Park, Seong-Pal Lee. "Conceptual Design of the Stratospheric Communication System in Korea". The *Second International Sym-*

- posium on Wireless Personal Multimedia Communications*, 1999, p. 74, Amsterdam.
2. R. Miura, M. Oodo, Y. Hase "Development of Multibeam Antennas in Millimeter-Wave Band on Board Stratospheric Platform" *Proc. of the Millennium Conference on Antennas and Propagation*, Paper 0436, 2000.
3. M. Oodo, R. Miura, Yo. Hase, T. Inaba, T. Sakamoto, M. Suzuki, "Real-time measurement results of digital beamforming array antenna of on-board Stratospheric Platform in the bands 31/29 GHz". *Proceedings of 25th ESA Antenna Workshop on Satellite Antenna Technology*, 18-20 September 2002. ESTEC, Noordwijk, the Netherlands.
4. J. J. Schuss, J. Upton, B. Myers, T. Sikina, A. Rohwer, P. Makridakas, R. Francois, L. Wardle, W. Kreutel, R. Smith "The Iridium Main Mission Antenna Concept". *IEEE Int. Symp. on Phased Array Systems and Technology*. 15-16 October. 1996. Boston, Massachusetts. P. 411-415.
5. Eli Brookner "Major Advances in Phased Arrays: Part 11". *Microwave Journal*. 1997, Vol. 40, No. 6, p. 84 - 92.
6. Resolution 221 (WRC-2000). Use of high altitude platform stations providing IMT-2000 in the bands 1885-1980 MHz, 2010-2025 MHz and 2110-2170 MHz in Regions 1 and 3 and 1885-1980 MHz and 2 110-2 160 MHz in Region 2. *The World Radiocommunication Conference 2000 (Istanbul, 2000)*.
7. B. J. Ku, J. M. Park, D. S. Ahn, A. V. Shishlov, A. M. Shitikov, S. A. Ganin, A. G. Shubov, "Multi-Beam and Multi-Faced DBF Antenna for HAPS (High Altitude Platform Station)," *Telecommunications Review*, Vol. 12, No. 5, pp. 756-769, 2002, 10.
8. B. J. Ku, D. S. Ahn, S. P. Lee, A. V. Shishlov, A. C. Reutov, S. A. Ganin, A. G. Shubov, "Radiation Pattern of Multi-beam Array Antenna with Digital Beam Forming for Stratospheric Communication System: Statistical Simulation," *ETRI Journal*. Vol. 24, No. 3, pp. 197-204, June 2002 ISSN 1225-6463.

WIDEBAND DUAL POLARIZED PLANAR ANTENNA ARRAYS

Fedir F. Dubrovka, Sergiy Y. Martynyuk

National Technical University of Ukraine "Kiev Polytechnic Institute"
Department of Theoretical Fundamentals of Radio Engineering
<dubrovka@tera.kiev.ua>, <mart_1974@yahoo.com>

Abstract

The paper presents a novel design of planar multilayered microstrip antenna arrays using aperture-coupled stacked patch radiating elements with dual polarization capability. Frequency bandwidth of up to 26 % (VSWR < 2:1), isolation between orthogonally polarized channels better than 30 dB and level of cross-polarization better than -30 dB have been achieved in both E- and H-planes of radiation pattern for the two orthogonal linear polarizations. Numerical results obtained by FDTD computer simulations are compared with measured characteristics of a manufactured antenna samples, operating in frequency bands from 0.9 to 15 GHz.

1. INTRODUCTION

Rapid development of digital satellite and cellular telecommunication systems goes the way of increasing the network capacity and possible useful data rate thus providing a new range of services to the customer (like image transfer or Internet connection). The next generation of the systems has to use spectral, code, polarization and space signal diversities in wide working band for achieving the maximal efficiency of allowed frequency resources. This cause a situation, that most of principal components in present systems should be modified under the long number of strict technical and economic requirements for the future ones. Very often these requirements come in contradiction. For instance, the technical specifications for GSM base station antenna arrays commonly include the following list: frequency bandwidth to be more than 25 %, dual polarization capability with levels of crosspolar radiation and isolation between orthogonally polarized channels better than -30 dB, possibly different values of beamwidth in elevation and in azimuth together with the limited levels of sidelobe and backward radiation, low weight and profile together with high mechanic reliability. For providing the space diversity (for example in 3G GSM) one need to choose and optimize the proper antenna configurations, that also help to avoid the problem of high mutual coupling of radiators in array, and propose appropriate multibeam signal processing algorithm. Great interest is also seen from the development of mathematical methods for quick and accurate electrodynamic modeling of planar radiating structures that take into account edge and mutual coupling effects and that connected with influence of the feeding network. More often antenna engineers prefer

to use versatile finite methods FEM or FDTD (the latter used here) in order to be able to analyze exact geometry of antenna array even with mounting devices or surrounding objects. Still the fulfillment of mentioned above system requirements for the planar base station antenna array is ideologically, computationally and technologically complicated that is why their market price stays high. This paper presents short description of state of the art in planar array configurations and technology from the point of view of their suitability for the application in mobile telecommunication systems. More detailed focus is made on the novel design of dual polarized planar antenna arrays, built of wideband aperture coupled stacked patch radiators. The proposed antenna arrays were optimized for the application in Ku-band (10.9–14.5 Hz) satellite telecommunication system and GSM mobile communication system (900 and 1800 MHz).

2. GENERAL ANTENNA DESIGN CONCEPT

Antenna arrays are considered being planar (or flat) if profile of their radiating structure is about $0,5\lambda$ or less. Nowadays technologies allow to built passive planar arrays 1) from radiating slots cut in close metal waveguide, 2) from different shaped patch (metal strips) placed over dielectric substrate; 3) from metal dipoles, placed in the uniform dielectric layer. None of them takes the absolute advantage over the others so that the final decision concerning their suitability is fully dependent on specific system requirements. Waveguide slot antenna arrays have simple series feeding network that is suitable for high power transmission in radar systems. One can use the combination of slots in narrow and wide walls in rectangular waveguide feeding system to achieve dual polariza-

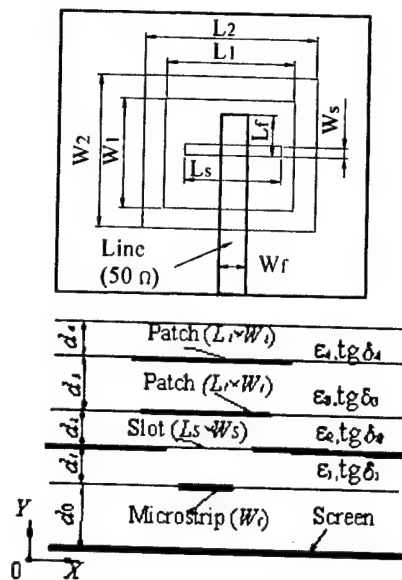


Fig. 1. Aperture slot coupled stacked patch antenna with single linear polarization operation.

tion capability with low levels of crosspolarisation. But nature of the series feeding limits possible frequency bandwidth ($< 5\%$) and produces frequency scan effect. Dipole antenna arrays with corporate feeding are widely used in telecommunication systems, that operate at frequencies less than 3 GHz. But they appear to be technologically complicated (not efficient) and sensitive to the manufacturing inaccuracies when the frequencies become higher. Moreover the significant difference in E- and H-planes radiation patterns of simple dipoles can cause additional problems for some dual-polarized applications (e.g. GSM base station).

The well-known microstrip patch antenna concept, based on the use of a rectangular conducting patch over a grounded substrate, usually leads to 1 to 3% of the input impedance bandwidth. Following the purpose of bandwidth expanding, one can implement an impedance matching microstrip network [1], directly coupled patch resonators placed on the same substrate [2] or U-shaped slots in the rectangular patch resonator [3]. However, these methods were found to be not effective for the design of dual-linearly polarized antenna arrays.

Aperture coupled stacked patch radiators (Fig. 1), in which parasitic element placed above lower patch, provides working frequency bandwidth more than 25%, better identity of beamwidth in E- and H-planes and perfect crosspolar characteristics, if use a symmetrical type of microstrip excitation. Here the dual resonator system formed by stacked patches is excited by a slot located in the metallic ground plane of an inverted microstrip feeding line [4]. Different dielectric permittivity of supported substrates cause a slight difference in resonant frequencies of highly radiation coupled patch resonators and, as a result, wider bandwidth performance of the composite antenna structure (up to 70% is

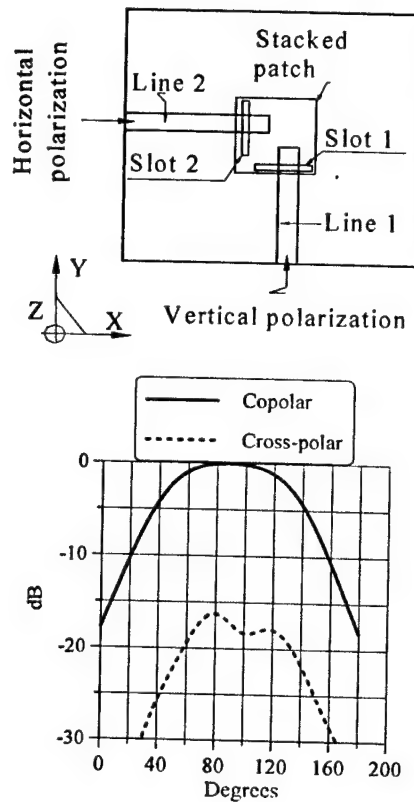


Fig. 2. Aperture slot-coupled stacked patch antenna with dual polarization capability and non-symmetrical location of slots: geometry (left) and radiation patterns (right).

achievable as shown in [4]). In addition, the microstrip feed network is separated from radiating surface by a ground plane, and therefore, does not influence the level of crosspolarization radiation.

The authors of [5] have reported dual polarized microstrip antennas that used two orthogonally coupled slots below the patch with two independent microstrip feeding lines (Fig.2). Each microstrip line is associated with either vertical or horizontal linear polarizations. However, the configuration of the antenna, shown in Fig. 2, still causes a significant level of parasitic crosspolar radiation. The level of crosspolarization radiation is in the order of $-15... -18$ dB and cannot be improved by varying the thickness or dielectric constants of dielectric layers (Fig. 2 right). Results of a full-wave FDTD analysis of the electromagnetic fields inside such a structure [6, 7] show that the high level of cross-polarization, which cannot be observed in the case of a single linearly polarized antenna (Fig. 1), occurs due to the electromagnetic coupling of two orthogonal slots with finite width located nearby. Consequently, the excitation of one slot inevitably leads to the excitation of also an orthogonally positioned slot and to generation of the unwanted crosspolar radiation [9].

In order to satisfy the strict requirements as mentioned above and to reduce the problems of electromagnetic interference of fields from adjacent slots, a

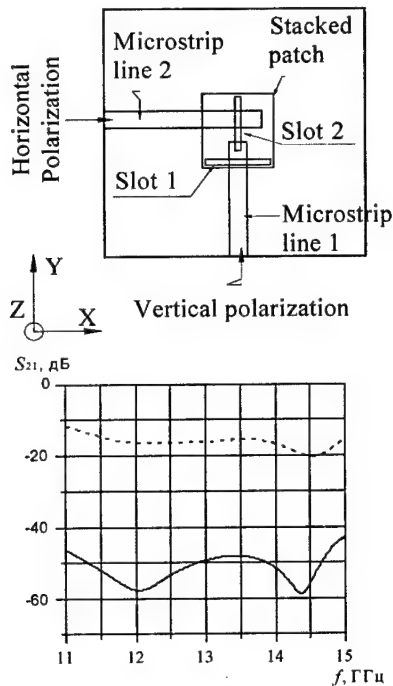
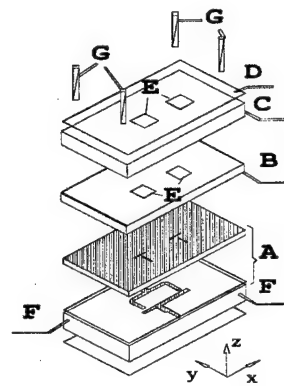


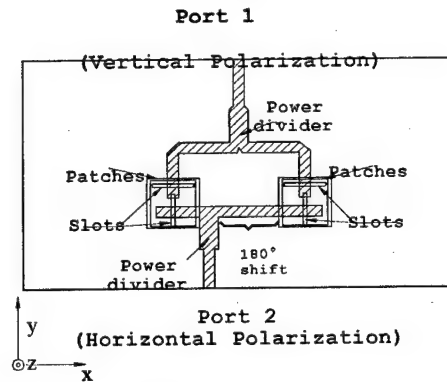
Fig. 3. Aperture slot-coupled stacked patch antenna with dual polarization capability and symmetrical location of slots: geometry (left) and radiation patterns (right)

combination of the stacked patch technique is proposed with a symmetrical positioning of the coupled slots [9], shown in Fig. 3. At the right hand of Fig. 3 one can observe a typical characteristic of two-port one for the cases of symmetric (single line) and nonsymmetric (dotted line) location of slots.

For the numerical simulation of the multilayered microstrip planar antenna structure we have chosen FDTD method. It's high flexibility and accuracy permits one to solve complex three-dimensional electromagnetic radiation problems without introducing additional assumptions and simplifications. Moreover this method is used to perform a multiparameter numerical optimization of antenna structure geometry and its feeding network. For this purpose the multilayered structure shown in Fig. 4 was incorporated into a Cartesian coordinate system with a non-uniform mesh configuration. The finest mesh resolution was taken to be better than $\lambda/100$ referring the radiating patch areas, microstrip feeding network and planar interfaces between different substrates. On the contrary, poor resolution (the sizes of cells were in the order of $\lambda/30$) refers to the homogeneous areas of dielectric layers and near absorbing boundaries. Stair-step approximations were used for the simulation of inclined metal strips used in feeding network. The total computational domain had sizes $190 \times 120 \times 95$ bounded by perfectly matched layer (PML) for absorption of the outgoing radiated electromagnetic waves. The Courant stability criteria was used as a limiting condition to select proper time step value. Finite losses in dielectric substrates were taken into



a) Perspective view.



b) Top schematic view

Fig. 4. Geometry of proposed dual-linearly polarized multilayer microstrip antenna

account. We tested aperture stacked patch radiators in several frequency bands ranging from 800 MHz to 15 GHz. The basic design of the proposed novel multilayered dual-polarized Ku-band (10.9...14.5 GHz) antenna is explained according to Fig. 4. The integrated antenna consists of two stacked aperture-coupled radiating elements and a microstrip feeding network, combining this radiators into a two-element antenna subarray. The spacing between elements was chosen to be equal of 0.8 of wavelength at the center of the frequency range (12.7 GHz). The stacked antenna structure is manufactured by using four low-loss dielectric layers with different thickness and dielectric constant. Each layer was separately manufactured. Parameters of the layers are given in Table 1. The composite sandwich structure assembly is situated quarter of a wavelength above the metallic screen at bottom side to suppress backward radiation. This dis-

Table 1. Parameters of layers

Layer	Substrate	Thickness, mm	ϵ_r	Loss tangent
A	Duroid 5880	0.508 mm	2.2	0.0009
B	Duroid 5880	0.765 mm	2.2	0.0009
C	Rohacell 51 IG	2.5 mm	1.07	0.001
D	Duroid 5880	0.25 mm	2.2	0.0009

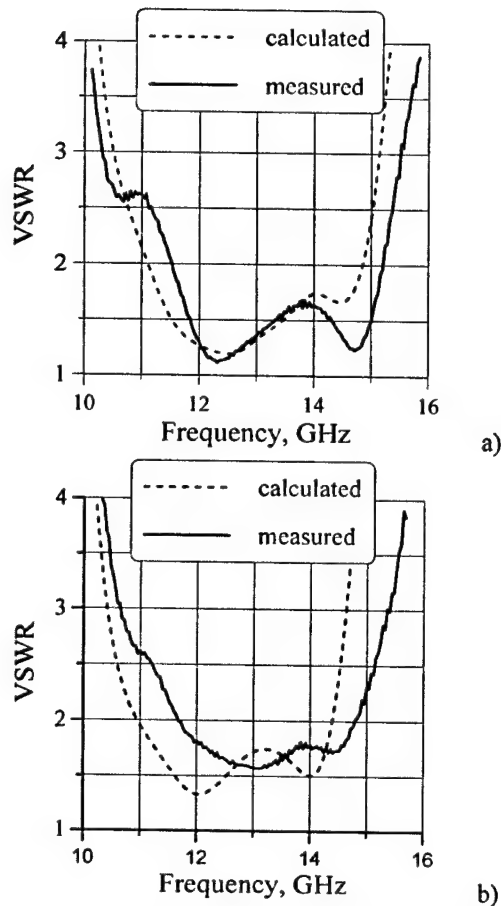


Fig. 5. Calculated and measured VSWR: a) horizontal polarization; b) right – vertical polarization.

tance is provided by special plastic holders that additionally contain rectangular plastic frames for making the whole assembly mechanically strong.

Fig. 5 contains calculated and measured characteristics of VSWR for two orthogonally polarized channel, that prove the wideband antenna subarray performance. In Fig. 6 measured and simulated far-zone radiation patterns for horizontal polarization channel at the center frequency (12,7 GHz) are presented, proving good dual linearly polarized performance with level of crosspolar radiation better than -30dB. From technological point of view the examined structure occurs to be very sensitive to the possible shift of dielectric substrates in horizontal plane. One can use corporate microstrip feeding network based on Wilkinson power dividers to built planar antenna arrays of the larger sizes as shown in Fig. 7.

Described principals were applied for the novel design of dual polarized GSM-900 and GSM-1800 base station array antennas with sector-shaped radiation patterns. Each array contain 4-aperture stacked patch radiating elements (fig. 7). Metal patches, strip feeding system and screen with slots were manufactured from metal sheet (thickness 1 mm) by milling technology. As a supporting low-loss dielectric material we used foam with $\epsilon = 1,2$. From the back and sides

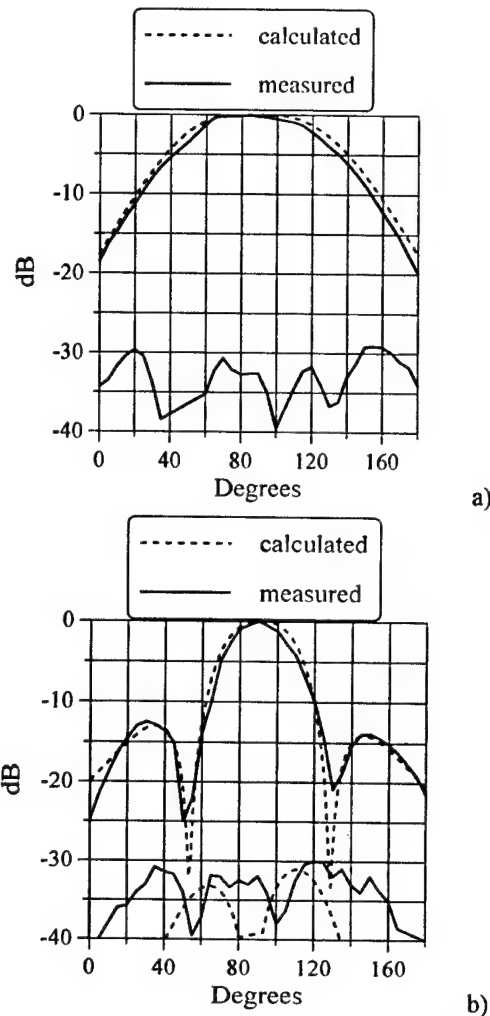


Fig. 6. Calculated and measured antenna radiation patterns (co- and cross-polarization) for the horizontal polarization channel at 12,7 GHz: a) YZ-plane; b) XZ-plane

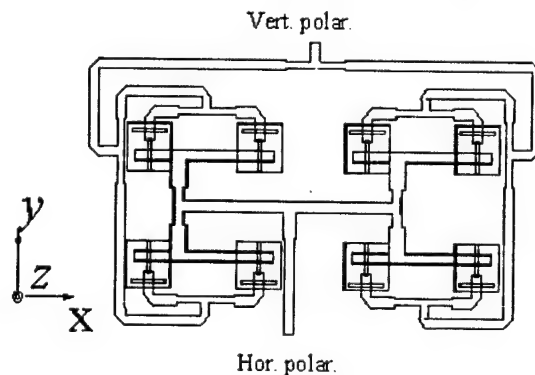


Fig. 7. Topology of a 4x2 element antenna array

the feeding network and radiating patches were closed by metal profile. Its has special form and was optimized by FDTD method together with the sizes of patches in order to provide low level of VSWR and in addition equal radiation patterns in horizontal planes for vertical (Fig. 9) and horizontal (Fig. 10) polariza-

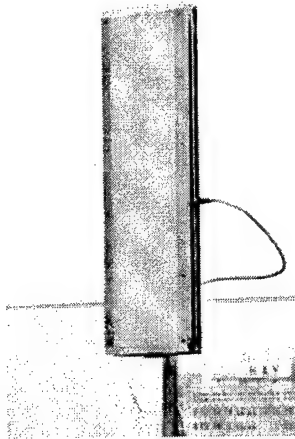


Fig. 8. (Photo of the antenna array for GSM-900 base station)

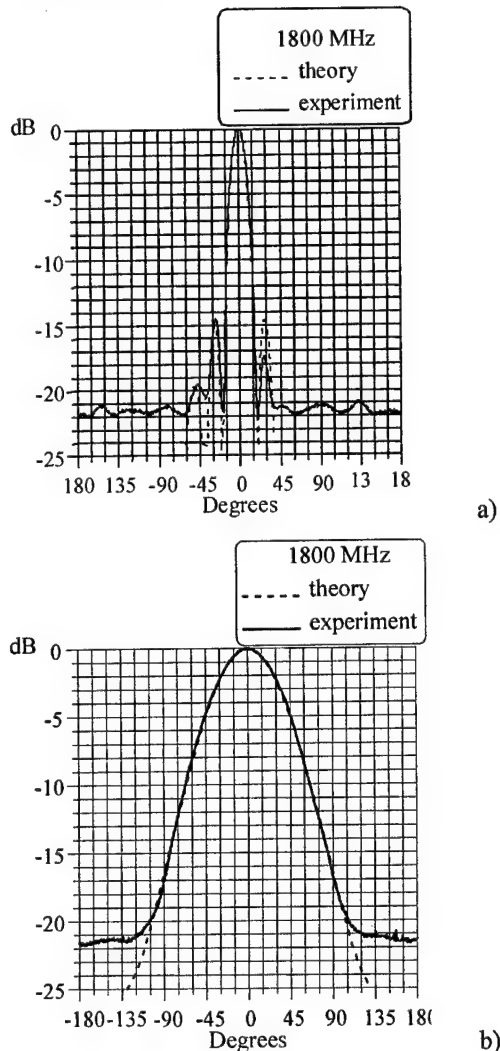


Fig. 9.

tion channels. In these figures letters with brackets a) and b) correspond to horizontal and vertical planes respectively. Symmetry in location of exciting slots

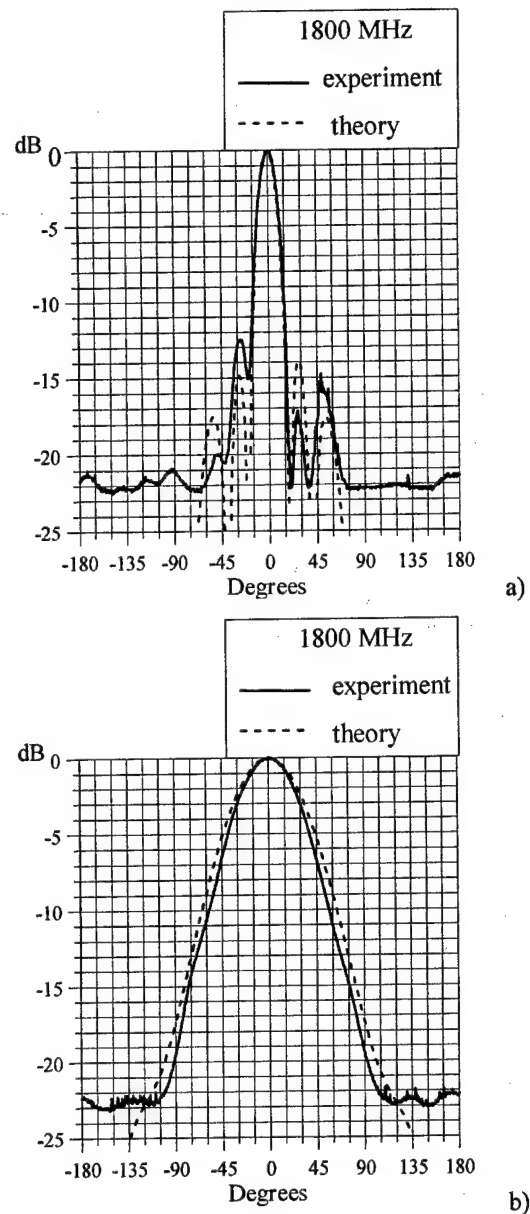


Fig. 10.

gives the opportunity to achieve the overall crosspolar isolation better than 33 dB. The last specifications plays a key-role for the realization of polarization processing of received signal from a mobile customer in modern GSM base stations. Radiating surface of array is protected from the climatic factors by thin low-loss fiber-glass cover with ergonomic design.

3. CONCLUSIONS

Novel design of planar antenna arrays built from aperture stacked patch elements and capable for operation in the frequency bands ranging from 0,8 to 15 GHz has been presented. It has been shown that symmetrical slot excitation of stacked patch radiators together with isolated strip feeding network allow to achieve crosspolar radiation level better than -30 dB and iso-

lation between orthogonally polarized channels > 33 dB in the frequency bandwidth more than 25 %. Due to dual polarization capability and the excellent crosspolar characteristics these antenna arrays are potential candidates for application in various radar and communication systems.

REFERENCES

1. H. F. Pues, A. R. van de Capelle, „An impedance matching technique for increasing the bandwidth of microstrip antennas“, IEEE Trans. On AP, vol.37, pp1345-1353, Nov. 1989.
2. G. Kumar, K. C. Gupta, „Directly coupled multiple resonators wideband microstrip antennas“, IEEE Trans. On AP, pp 588-593, June 1985.
3. T. Huynh, K. S. Lee, „Single layer single-patch wideband microstrip antenna“, Electron. Lett., vol. 31, No. 16, pp. 1310-1312 Aug. 1995
4. Targonski S. D., Waterhouse R. B., Pozar D. M. Design of wide-band aperture-stacked patch microstrip antennas // IEEE Trans.– 1998.–Vol. AP-46.–P. 1245-1250.
5. Shutie P. H., Aicher U., Sonn N. Dual polarised microstrip patch radiators for high resolution spaceborne SAR instruments // AP'2000 Millennium Conference on Antennas and Propagation.– Davos, Switzerland.–April 9-14.–2000.
6. K. S. Yee, „Numerical solution of initial boundary value problems involving Maxwell's equations in isotropic media“, IEEE Trans. Antenn. Propagat., vol. AP-14, pp.302-307, Mar. 1966.
7. Dubrovka F. F., Martynyuk S. Y. Analysis of the flat-layered metal-dielectric structures by FDTD // Izvestiya VUZ. Radioelectronika. – 2002. –Vol. 45, № 7.– P. 22–30. (In Russian).
8. Martynyuk S. Y., Dubrovka F. F., Adengofer P. Wideband bipolarization printed antenna sublatice Ku-band // Izvestiya VUZ. Radioelectronika. – 2002. – Vol. 45, № 8. – P. 3–12. (In Russian).
9. Martynyuk S. Y., Dubrovka F. F. Suppression cross-polar radiation of the bipolarization wide-band planar multilayered printed radiators// Izvestiya VUZ. Radioelectronika. – 2002. – Vol. 45, № 9. – P.3–10. (In Russian).

MODELING AND SIMULATION OF THE FUSED BAYESIAN-REGULARIZATION METHOD FOR REMOTE SENSING IMAGERY WITH SYNTHETIC APERTURE ARRAYS

Yuriy V. Shkvarko *, José Luis Leyva-Montiel, and Joaquin Acosta-Salas

CINVESTAV del IPN, Unidad Guadalajara,
López Mateos Sur 590, Guadalajara, Jal., C. P. 45090, MEXICO
<shkvarko@cts-design.com>

Abstract

A new fused Bayesian regularization (FBR) method for enhanced remote sensing imaging based on a new concept of aggregated statistical-deterministic regularization was developed recently. In this study, we present the results of modeling and extensive simulation of the FBR algorithms for enhanced reconstruction of the spatial spectrum patterns (SSP) of the point-type and spatially distributed wavefield sources as it is required for the remote sensing imagery with synthetic aperture arrays. The simulations were performed in the MATLAB computational environment for the family of the SAR imaging algorithms that employed different modifications of the FBR method. The presented results enable one to evaluate the operational performances of the FBR method that were not previously reported in the literature.

1. INTRODUCTION

This paper presents the results of the synthesized array-oriented modeling and extended simulation study of the family of the radar image formation algorithms that employ the recently developed fused Bayesian-regularization (FBR) method [6], for high-resolution estimation of the spatial spectrum pattern (SSP) of the wavefield sources distributed over the remotely sensing probing surface. The FBR method employs the idea of aggregating the Bayesian inference making strategy for high-resolution SSP estimation [2] with the descriptive regularization technique [5] that provides the rigorous formalism for incorporating the projection-type and metrics constraints imposed on the desired radar image. In applications related to SAR/radar remote sensing, this method was theoretically grounded and developed in [5, 6], whereas the operational performances that manifests the FBR method in its different modifications were not investigated in details. That is why, in this paper, we are going to present the results of modeling and extensive simulations of the family of FBR-based SSP estimation algorithms that were not previously reported in the literature. We use the MATLAB computational environment as simulation tools that provide the computational efficiency and flexibility in performing the simulation experiment.

2. SUMMARY OF THE FBR METHOD

The problem of enhanced radar/SAR imaging is to develop an antenna array (AA)/synthesized array (SA) based data processing method for performing the high efficient estimation of the SSP $B(x)$ as a function of the probing surface $X \ni x$ by processing the available data wavefield recordings $u(y)$ measured over the AA/SA trajectory $Y \ni y$. Such the estimate $\hat{B}(x)$ of the SSP $B(x)$ is referred to as the desired enhanced radar/SAR image of the probing surface [5]. In the conventional vector form, the estimate $\hat{\mathbf{B}}$ of the vectorized SSP model defines the desired discrete-form image of the remotely sensed scene in the adopted pixel image format [4]. The trajectory data is modeled by the equation of observation [5] $\mathbf{U} = \mathbf{S}\mathbf{E} + \mathbf{N}$, where \mathbf{E} is the original K -D vector of the discrete-form approximation of the random complex object scattering function (SF), K -by- M matrix \mathbf{S} is referred to as the linear signal formation operator (SFO) and \mathbf{N} is the observation noise (in this study we accept the robust white noise model, i.e. $\mathbf{R}_N^{-1} = (1/N_0)\mathbf{I}$, with the noise intensity N_0 pre-estimated by some means [2]. The SSP is related to the original complex random SF as, $\mathbf{B} = \{\langle \mathbf{E}\mathbf{E}^+ \rangle\}_{\text{diag}}$.

The family of the SSP estimation (reconstruction) algorithms that employ the FBR technique developed in [5, 6] comprises three following basic SSP estimators.

1. The general iterative *FBR* (*IFBR*) estimator of the SSP is defined as follows [6]

$$\hat{\mathbf{B}}_{IFBR} \rightarrow \hat{\mathbf{B}}^{(i+1)} = \hat{\mathbf{B}}^{(i)} + \zeta (\mathbf{W} [\mathbf{V}(\hat{\mathbf{B}}^{(i)}) - \mathbf{Z}_{\Sigma}(\hat{\mathbf{B}}^{(i)})] - (\hat{\mathbf{B}}^{(i)} - \mathbf{B}_{pr})) \quad (1)$$

with the initial iteration $\hat{\mathbf{B}}^{(0)}$ taken as some prior model of the SSP, e.g. $\hat{\mathbf{B}}^{(0)} = \mathbf{B}_{pr}$, where superscript $i = 0, 1, 2, \dots$ represents the iteration step number, ζ is the relaxation parameter, and

$$\mathbf{Z}_{\Sigma}(\hat{\mathbf{B}}^{(i)}) = \mathbf{T}(\hat{\mathbf{B}}^{(i)})\mathbf{B}_0 + \mathbf{Z}(\hat{\mathbf{B}}^{(i)}) \quad (2)$$

defines the total shift to the sufficient statistics (SS) at the i th iteration. In (1),

$$\mathbf{V} = \{\mathbf{F}\mathbf{U}\mathbf{U}^+\mathbf{F}^+\}_{\text{diag}} \quad (3)$$

represents the vector of (SS that is formed applying the SS formation operator

$$\mathbf{F} = \mathbf{F}(\mathbf{B}) = \mathbf{D}(\mathbf{B})(\mathbf{I} + \mathbf{S}^+\mathbf{R}_N^{-1}\mathbf{S}\mathbf{D}(\mathbf{B}))^{-1}\mathbf{S}^+\mathbf{R}_N^{-1} \quad (4)$$

to the trajectory data \mathbf{U} . Also in (1),

$$\mathbf{Z} = \mathbf{Z}(\mathbf{B}) = \{\mathbf{F}\mathbf{R}_N\mathbf{F}^+\}_{\text{diag}} \quad (5)$$

is the bias vector, $\mathbf{T} = \text{diag}\{\{\mathbf{S}^+\mathbf{F}^+\mathbf{F}\mathbf{S}\}_{\text{diag}}\}$, and

$$\mathbf{W} = \mathbf{P}\mathbf{\Omega} \quad (6)$$

defines the window operator, a composition of the smoothing filter $\mathbf{\Omega}$ and the projector \mathbf{P} onto the proper solution space, which must be designed to aggregate the corresponding metrics and projection constraints imposed on the solution (see [5] and [6] for details).

2. The robust spatial filtering (RSF) estimator

$$\hat{\mathbf{B}}_{RSF} = \mathbf{\Omega}\mathbf{V} \quad (7)$$

relates to (1) as its robustified version for the case of trivial priors, $\mathbf{B}_{pr} = \mathbf{0}$, $\mathbf{P} = \mathbf{I}$, and solution independent approximation

$$\mathbf{F} = (\mathbf{I} + \rho^{-1}\mathbf{S}^+\mathbf{S})^{-1}\mathbf{S}^+ \quad (8)$$

of the SS formation operator with the inverse ρ^{-1} of the SNR $\rho = \beta/N_0$ as a regularization parameter, where β represents the image average gray level preestimated by some means [5].

3. The *matched spatial filtering* (*MSF*) estimator is constructed as a further simplification of (7). Adopting the trivial a priori model information ($\mathbf{P} = \mathbf{I}$ and $\mathbf{B}_{pr} = \mathbf{0}$) and roughly approximating the SS formation

operator \mathbf{F} by the adjoint SFO, i. e. $\mathbf{F} \approx \gamma_0\mathbf{S}^+$ (where the normalizing constant γ_0 provides balance of the operator norms $\gamma_0^2 \text{tr}\{\mathbf{S}^+\mathbf{S}\mathbf{S}^+\mathbf{S}\} = \text{tr}\{\mathbf{F}\mathbf{S}\mathbf{S}^+\mathbf{F}^+\}$), the (7) is simplified to the *MSF* estimator

$$\hat{\mathbf{B}}_{MSF} = \mathbf{\Omega}\mathbf{H}, \quad (9)$$

where the rough SS, $\mathbf{H} = \gamma_0^2\{\mathbf{S}^+\mathbf{U}\mathbf{U}^+\mathbf{S}\}_{\text{diag}}$, is now formed applying the adjoint operator \mathbf{S}^+ , and the windowing of the rough SS \mathbf{H} is performed applying the smoothing filter $\mathbf{\Omega}$ that was constructed numerically in [5].

As it was shown in [5, 6], the *MSF* algorithm (9) coincides with the conventional aperture synthesis procedure [1, 4] with the matched filtering of the trajectory signal as the data processing method, whereas, the *RSF* and *IFBR* estimators (7) and (1), respectively, may be referred to as the enhanced imaging algorithms that provide the image improvement/reconstruction with respect to that formed using the conventional *MSF* method.

3. SIMULATION EXPERIMENT

3.1. SIMULATION DETAILS

The aim of the simulation experiment was to investigate the performances of three *FBR*-based SSP estimators (1), (7) and (9). We simulated a conventional side-looking SAR (i.e. the radar array was constructed by the moving antenna) with the SFO factored along two axes in the image plane: the azimuth and the range. The factorization of the SAR ambiguity function (AF) over the range and azimuth directions [4] implies that the SSP estimation algorithms presented above can be simulated independently over the corresponding axes in the image plain. In the azimuth direction x , the composition $\mathbf{S}^+\mathbf{S}$ defines matrix Ψ_a of the discretized model of the azimuth AF [6]

$$\Psi_a(\Delta x) \approx \exp(-\pi\Delta x^2/a^2), \quad (10)$$

where $a = \lambda_0\tau_0/2L_s$ is the fraction parameter that pertains to the partially (κ -fractional) effective synthesized aperture $L_s = \kappa L_{s\max} = \kappa(\lambda_0\tau_0/L_A)$ with the physical antenna of effective aperture L_A weighted with the Gaussian tapering function [6]. In the range direction y , the composition $\mathbf{S}^+\mathbf{S}$ corresponds to matrix Ψ_r that approximates the range AF $\Psi_r(\Delta y)$ [1].

In the simulations, in the y direction, the resolution cell was adjusted to the effective width of the range AF. In the x direction, the fraction parameter a in (10) was controlled to adjust different effective widths of the azimuth AF $\Psi_a(\Delta x)$. The second adjustable parameter, the SNR, was calculated as the ratio of the average signal component in the rough image formed using algorithm (9) to the relevant noise component in the same image, i.e. $\mu = (\beta/N_0)(\text{tr}\{\Psi_a\}\text{tr}\{\Psi_r\})^{-1} \cdot \text{tr}\{(\Psi_a)^2\}\text{tr}\{(\Psi_r)^2\}$, where β represents the average gray level of the original image. The matched SSP estimation algorithm (9) was applied to form the images over the vertical (range) axis while over the horizontal (azimuth) axis, three algorithms (9), (7) and (1) were tested. The window operator $\mathbf{W} = \mathbf{P}\mathbf{\Omega}$ was taken

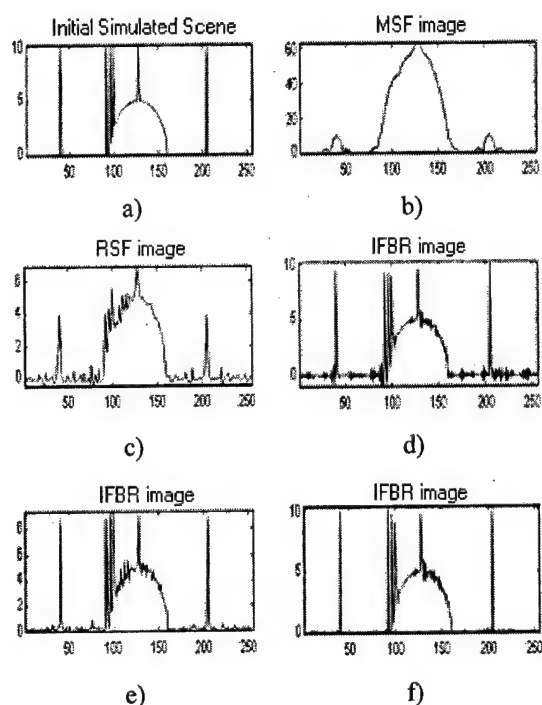


Fig. 1. Simulation results for 1-D scenario: a) original scene; b) *MSF* image; c) *RSF* image; d) *IFBR* image (10 iterations); e) *IFBR* image (4 iterations); f) *IFBR* image (40 iterations).

from [6] in which the projector \mathbf{P} was constructed to preserve the x -axis boundaries of the image formed using the *RSF* method (1) in each range gate and incorporated the projection-type constraints imposed on the desired SSP [6].

For the purpose of generality, in the simulations we considered two imaging scenarios: (i) 1-D imaging in the azimuth direction for a particular range gate with κ -fractionally synthesized aperture; (ii) 2-D imaging of the remotely sensed scenes in the x - y directions with κ -fractionally synthesized aperture.

3.2. SIMULATION RESULTS

We examined the behavior and performance indices of these estimators for different simulated scenes of the SSPs. The 1-D simulated image (for a particular range gate) is presented in Fig. 1a. The other pictures of Figure relate to three different SSP estimators (1), (7) and (9) for two different scenarios of fractional AS as specified in the Figure captions.

The examples of 2-D simulated images are presented in Fig. 2 for the same aperture synthesis scenarios as in the 1-D case. In the images depicted in Figs. 1 and 2 the parameter a in (10) was adjusted to provide the horizontal width of the discretized azimuth AF at a half of its peak level equal to 4 pixels. The quantitative measure of the improvement in the output signal-to-noise ratio (*IOSNR*) achieved with the enhanced imaging methods (1) and (7) for the two simulated aperture synthesis scenarios are presented in Tables 1 and 2, respectively. *IOSNR*⁽¹⁾ relates to

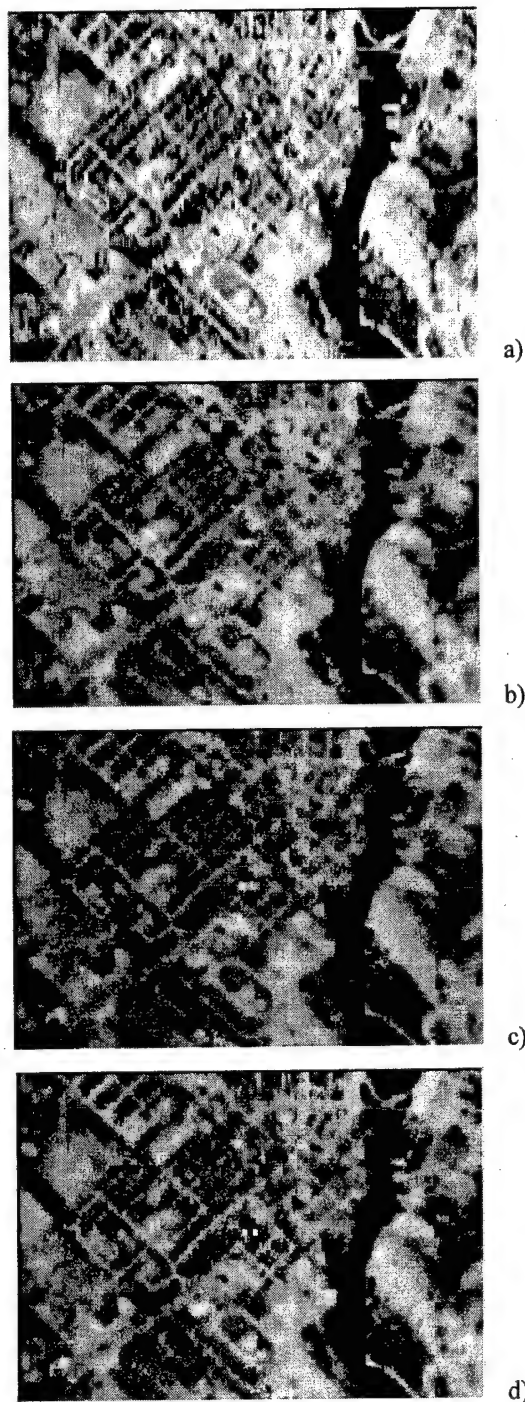


Fig. 2. Simulation results for 2-D scenario: a) original scene; b) *MSF* image; c) *RSF* image; d) *IFBR* image (40 iterations).

the *RSF* method, and *IOSNR*⁽²⁾ to the *IFBR* method, respectively.

4. CONCLUSIONS

In both SAR imaging scenarios, the *RSF* and *IFBR* estimators overperformed the conventional *MSF* method of AS, as the improvement in the image quality was observed. In addition, the estimates obtained

Table 1. IOSNR values provided with the two simulated methods: *RSF* and *IFBR*

Results are reported for the 1-D simulation scenario for two synthesized aperture models resolution parameters:

first system, $\Delta\Psi_A = 4$;

second system, $\Delta\Psi_A = 9$

SNR, μ (dB)	First system		Second system	
	IOSNR ⁽¹⁾	IOSNR ⁽²⁾	IOSNR ⁽¹⁾	IOSNR ⁽²⁾
15	2.28	3.93	8.42	9.53
20	3.89	4.09	10.85	12.81
25	5.52	7.39	14.64	17.06
30	7.28	9.41	18.37	20.22

with the *IFBR* algorithm outperformed those obtained with the *RSF* estimator. For the trivial a priori settings ($\mathbf{P} = \mathbf{I}$, $\mathbf{B}_0 = \mathbf{0}$), the latter corresponds to the previously developed Bayesian maximum entropy (*BME*) algorithm [5] thus, in summary, we conclude that the *IFBR* method overperforms also the *BME* estimator. Regions of interest and distributed object boundaries are better defined, whereas one can examine some ringing effect usually observed with filters based on inverse operations.

REFERENCES

1. L. G. Cutrona, "Synthetic Aperture Radar," in *Radar Handbook*, 2nd ed., M. I. Skolnik, Ed. in chief, MA: McGraw Hill, 1990.
2. S. Haykin and A. Steinhardt, Eds., *Adaptive Radar Detection and Estimation*. New York: Wiley, 1992.
3. J. Astola and P. Kuosmanen, *Fundamentals of Nonlinear Digital Filtering*. Boca Raton, FL: CRC, 1997.

Table 2. IOSNR values provided with the two simulated methods: *RSF* and *IFBR*

Results are reported for the 2-D simulation scenario for two synthesized aperture models resolution parameters:

first system, $\Delta\Psi_A = 4$;

second system, $\Delta\Psi_A = 9$

SNR, μ (dB)	First system		Second system	
	IOSNR ⁽¹⁾	IOSNR ⁽²⁾	IOSNR ⁽¹⁾	IOSNR ⁽²⁾
15	5.15	5.56	20.42	21.83
20	8.24	8.72	21.25	22.66
25	12.71	13.19	21.13	22.54
30	17.54	17.91	22.18	23.59

4. F. M. Henderson and A. V. Lewis, Eds., *Principles and Applications of Imaging Radar, Manual of Remote Sensing*, 3rd ed. New York: Wiley, 1998, Vol. 3.
5. Y. V. Shkvarko, "Estimation of wavefield power distribution in the remotely sensed environment: Bayesian maximum entropy approach" // *IEEE Trans. Signal Proc.*, Vol. 50, pp. 2333-2346, Sep. 2002.
6. Y. V. Shkvarko, "Towards the Bayesian-Regularization Method for Enhanced SAR Imaging" // *Proceedings of the SPIE Aero-Sense 2003 Int. Symp.*, Orlando, FL, USA, *SPIE Proceedings*, Vol. 5095, 2003.
7. Y. V. Shkvarko, "Theoretical Aspects of Unifying Regularization and Bayesian Estimation Methods for Enhanced Imaging with Remotely Sensed Data" // *IEEE Trans. Geoscience and Remote Sensing*, (to be published), 2003.

DEVELOPMENT OF MICROWAVE TECHNOLOGIES FOR THE OIL AND GAS EXTRACTION COMPLEX

Gennady A. Morozov, Oleg G. Morozov, Marat R. Galimov

Tupolev Kazan State Technical University, R&D of Applied Electronics
<root@kaiadm.kazan.su>

Abstract

Questions of microwave technologies development for the oil and gas extraction complex are considered. The data on the oil environments being object of microwave electromagnetic fields influence are resulted, the physical essence of carried out microwave technological processes is briefly discussed. Classification of the microwave technologies used and developed for the oil and gas extraction complex, the basic requirements is resulted for them, economic and ecological aspects of their application are marked.

Keywords: oil, mineral oil, processing, microwave technologies

1. INTRODUCTION

Modern world practice of oil deposits development is characterized by use of a wide set of various technical and technological decisions and means of extraction, gathering, preparation of oil, gas and water on crafts. Thus the high-efficiency block automated equipment working on deposits without constant presence of the attendants, different possible chemical reagents, etc. are widely applied in many technological processes.

At the same time a lot of problems in considered area wait for the decision. To them concern: development of effective ways and the equipment for deep dehydration of heavy and high-viscosity oil; preparation of oil, containing mechanical impurity; destruction of trap emulsion, forecasting of oil and water preparation technological parameters depending on their physical and chemical properties; increase of efficiency and reliability of the process equipment, etc.

The majority of the specified problems can be solved with use of microwave technologies (MWT). MWT possess a number of advantages in comparison with used technologies. First, it is volumetric heating of the processed environment with a various gradient for fractions of which it will consist; second, actually higher size of heating gradient (on the order, and sometimes, more).

Use of microwave processing results in more effective and productive separation of crude oil components (water and oil), allows to create installations as actually for their separation, and for definition of their quantitative ratio, provides automation of technological and measurement processes. And, at last, it is very important to note, that MWT are pollution-free technologies.

The examinations which have been carried out by authors and specialists from other regions of Russia and abroad prove, that use of MWT at the detailed account of physical and chemical properties and specific features of such composite heterogeneous disperse systems as water-oil emulsion (WOE) is a basis for the further perfection of oil, gas and water preparation technology and technical equipment in structure of oil and gas extraction complex (OGEC).

2. PROCESSES OF MICROWAVE INTERACTION WITH WOE

At microwave influence the classical phenomena of thermal conductivity, convection and radiation have secondary value in thermal balance of the processed environment, in comparison with the thermal heating caused by specific influence of used microwave electromagnetic fields (EMF). Microwave influence raises doublet rotation of environment molecules at presence of powerful intermolecular connections that results in occurrence of hysteresis between the enclosed field and the induced response, and reserved, thereof, energy is allocated at a relaxation as heat. Thus, molecules of environment should possess high enough doublet moment for maintenance of microwaves effective influence on environment.

One of WOE basic components is water. Because of significant asymmetry of the molecule it possesses exclusive polarization. Thus water is ideal material for microwave influence. Dielectric properties of water considerably change at addition of salts. In this case resulting permeability is influenced with number of hydration, i.e. number of the connected molecules of the water surrounding a molecule of salt. Thus the dielectric loss tangent insignificantly falls.

The mathematical models describing process of distribution in substance of electromagnetic fluctuations of various frequency ranges have essential distinctions. Spatial and time dispersion of dielectric permeability start to be shown at presence of microwave EMF. Maxwell's equations are inapplicable here in a classical kind, as the equation of connection between vector \vec{D} of electric displacement and vector of electric field intensity \vec{E} assumes the following form

$$\vec{D}(\vec{r}, t) = \int_{-\infty}^t \partial t' \int_V \epsilon(\vec{r}, \vec{r}', t, t') \vec{E}(\vec{r}', t') \partial V. \quad (1)$$

This expression shows, that the contribution to polarization of environment to the given point r and at present t is brought with the charges which are taking place earlier in the next points of space.

The molecular mechanism of this phenomenon is combined enough. As it mentioned above, it can be explained as the phenomenon of deduction at which rotation of dipoles is interfered by intermolecular connections that result in a hysteresis between the enclosed field and polarization of dipoles, i.e. to a stock of energy with its subsequent relaxation.

Heat, which has arisen inside material, is distributed with the help of mechanisms of conductivity, convection and radiation. As radiation is inherent only in surfaces, and convection is characteristic in an insignificant degree for liquids, we shall take into account only the mechanism of conductivity. Microwave heating can be described by the standard equation of thermal carry, including item of internal heat clearing

$$\frac{\partial^2 T}{\partial x^2} + \frac{\partial^2 T}{\partial y^2} + \frac{\partial^2 T}{\partial z^2} + \frac{P}{V\Lambda} = \frac{1}{a} \frac{\partial T}{\partial t}, \quad (2)$$

where Λ – thermal conductivity, a – factor of thermal diffusivity.

For the description of heat conductivity connection and other physical and chemical properties of WOE the various formulas are offered insignificantly distinguished in factors. As a rule, Predvoditelevs' formula is used

$$\Lambda = 4,28 \cdot 10^{-3} C_P \rho^{4/3} M^{-1/3}, \quad (3)$$

where C_P – thermal capacity at constant pressure; ρ – density; M – molecular weight. Under normal conditions the factor of heat conductivity of oil, gas and water changes within the limits of 0,14–0,16, 0,54–0,65 and 0,01–0,03 accordingly. The thermal capacity of oil can be determined under the formula

$$C_P = 107,325 \rho_H^{-1/2} (496,8 + t). \quad (4)$$

The specific thermal capacity of oil changes within the limits of 1,7–2,2 kJ/(kg·°K). A thermal capacity of water – 4,19 kJ/(kg·°K).

Factors of heat conductivity and thermal capacity depend on temperature and pressure. Usually at temperature rise on 10°K the factor of heat conductivity decreases for 1% on the average, and at pressure in-

crease on 10 MPa – insignificantly increases. At increase of pressure from 10 up to 80 MPa Λ increases on 5–10% and more.

3. THE BASIC MWT, USED IN OGEC, AND REQUIREMENTS TO THEM

Heating by means of microwave EMF possesses three prominent features determining its essential differences from other known ways. First of them will consist in volumetric character of material heating. The second feature of microwave heating consists in its selectivity. Oil products are non-uniform, have local inclusions (or are local inclusions) with distinguished dielectric permeability. According to above mentioned ratio allocation of heat on sites with various dielectric parameters will occur differently. The third feature of microwave heating is following. Control of EMF spatial distribution and intensity make possible to carry out heating as from the point of view of its uniformity in volume, and opposite, with the purpose of some part selective heating.

The listed features make microwave heating rather promising in the broad audience of appendices for OGEC. It is necessary to relate to them the following.

- Accelerated WOE separation with simultaneous destruction of hydrogen-sulfide bacterium in fractions of the unit.
- Decrease of oil, bitumen, firm sludge and other products viscosity.
- Dehydration of WOE with small contents of water.
- Clearing pipes from pyrobitumen and paraffin.
- Warming up sludge, natural bitumen, petroliferous sandstones with the purpose of oil feedback increase.

Besides it is necessary to pay attention to MWT heating application opportunity in oilchemistry. Today there are results of examinations and developments proving an opportunity of qualitative and quantitative changes of all oilchemistry technological processes parameters, using heating during an initial product processing. To them concern:

- Reduction of time, increase of productivity and improvement of quality of an end-product at vulcanization of rubber and thermoplastic materials, polymerization of various substances.
- Reception of substances with new physical and chemical properties due to influence of EMF at a level of their atomic condition.
- Disinfecting of industrial drains.
- Creation of essentially new technologies of metal surfaces painting due to their preliminary processing by microwave EMF (change of superficial oxides structure).
- Recovery of silica gel drier without technological processes shutdown.
- Drying of composites from various dielectrics on a glutinous basis.

The researches of last years, which have been carried out in the Research center of Applied Electrodynamics, have opened a new opportunity of properties change of various substances of nonmetallic character due to their processing by very small power level, so-called low-intensive, including information, EMF.

Under influence of such fields the destruction of various microflora, pathogenic mushrooms, various parasitic have been marked, that allows constructing today already economic and simple technological complexes with use of EHF-range energy. To them concern a complex for OGEC technical waters processing, a complex for laboratory waters processing in precision chemical technologies, etc.

One of the OGEC's major branches are technological processes of oil and WOE gathering, preparation and transport. These processes occur in conditions of changing parameters: pressure, temperature and debit. Besides, complicating factors are uncertainty of disperse structure and non-uniformity of its distribution in the volume, caused by features of structure of streams in oil pipelines.

Change of oil condition parameters results in its rheological parameters, electrophysical and other properties change. The specified characteristics rather essentially influence on processes of oil products microwave processing. It is represented expedient to consider oil as a conglomerate which parameters have casual character, and to use experimental methods of WOE parameters analytical control as the basic tool of research.

Features of microwave EMF and WOE interaction, marked above, cause application of the system approach as by development of new oil processing MWT, and of new microwave means for WOE parameters analytical control.

Historically developed approach to research WOE assumes division of a task into two stages: first, determination of components number forming a mix and its identification, establishing qualitative structure of a mix; and then, proceeding quantitative ratio between them from some characteristics of the components identified in a mix. In this case for definition of oil watering, for example, WOE microwave separation on components is possible at the first stage. Microwave measuring technologies can find application for research of oil medium-volume temperatures, both in a stream, and in tanks. And, at last, application of microwave gauges for definition of oil level and level of its phases is widely enough known.

Thus it is supposed to consider means of WOE analytical control both as independent informatics' measuring systems (IMS), and built - in IMS of MWT complexes. At creation of similar systems it is necessary to take into account the basic requirements of the modern concept for analytical systems construction, providing: contact free measuring process; the increased accuracy of measurement, use of microprocessor technical equipment; high dynamic characteristics; reliability of the data, simplicity of

service and flexibility of functioning; whenever possible the low price.

4. MWT CLASSIFICATION FOR OGEC

The classification resulted here is based on insignificant quantity of the publications found by authors and devoted to questions of MWT use in OGEC, and does not apply for exclusive completeness. However its use allows presenting the basic directions of application and prospect of MWT use in OGEC. MWT in OGEC are used basically for heating of oil environments.

First MWT class is intended for improvement of commodity oil preparation quality. Technologies of heating concern to them with the purpose:

- Decrease of oil viscosity.
- Dehydration of oil.
- Separation of WOE and trap oil.

Second MWT class is intended for processing OGEC waste products with the purpose of commodity oil allocation from them. Technologies of heating concern to them with the purpose:

- Allocation of oil from sludge.
- Allocation of oil from sandstones.
- Allocation of oil from bitumen.

Third MWT class is intended for restoration of the process equipment used at oil extraction, transportation and storage. Technologies of heating concern to them with the purpose:

- Melt of pyrobitumen and paraffin.
- Melt of oil adjournment on walls of tanks.

It is necessary to relate to the fourth MWT class MWT accompanying to the heating, used in technological processes of oilchemistry. Taking into account perspectives of the received results, we shall allocate technologies of heating with the purpose:

- Pyrolysis of automobile trunks.
- Acceleration of chemical reactions process course and improvement of their target products quality (vulcanization, polymerization, etc.).

It is necessary to relate to the fifth MWT class MWT for IMS. In this case it is necessary to make a reservation, that only some MWT for IMS use heating. Technologies of heating concern to such technologies with the purpose:

- Separations of WOE for the further definition of quantitative ratio of water, oil and gas;
- Sublimations of oil for the further definition of its fractional structure and other physical and chemical properties.

Other technologies of this class use microwave methods for measurements. To them, in particular, concern:

- Measuring instruments of oil level in parks.
- Measuring instruments of phase's level.
- Measuring instruments of medium-volume temperature (radiometers).

5. ECOLOGICAL AND ECONOMIC ASPECTS OF MWT APPLICATION IN OGEC

Russia is one of the largest oil-producing countries of the world. However existing technologies of extraction and oil refining actually do not provide recycling oil waste products. If to take into account already existing and potential pollution of subsoil waters, air, ocean, waterways becomes obvious, that such actions can lead to the most serious world ecological accident. The most significant on negative influence on ecology are accidents in Komi Republic in 1955, in area of Volgograd in 1996, in area of Saratov in 1997. Economic efficiency of microwave installations is based on influence by EMF energy on oil waste products which allows to destroy quickly and effectively intermolecular connections in WOE and sludge, and also on absence of expenses for purchase of raw material (waste products) as the oil companies agree to transfer them under the insignificant prices. It speaks by a high level of charges on storage and processing of waste products by other methods, penalties for environmental contamination.

Unfortunately, MWT do not provide the universal decision of all problems. However the opportunity of MWT application should be considered in all cases when other technologies do not allow achieving desirable result, and advantages of microwaves use be-

come unique and provide significant decrease in power and other expenses. MWT development for OGEC appreciably depends on size of required investments which for manufacture of MWT complex has the order \$750 on 1 kW against \$125 on 1 kW for manufacture of household microwave installation and \$50000 for manufacture of classical technological complexes of heating without taking into account unique advantages of MWT.

The estimation of economic feasibility of MWT application should include the detailed analysis of traditional technologies on which there is already saved up database, necessity of laboratory modeling, creation of pilot samples for definition of optimum parameters of technological processes and, at last, creations of monitoring means. In all cases the set of various factors, such as increase in volumes of manufacture, reduction of labor input, improvement of working conditions, a minimalism of thermal losses, economy of the resources spent on maintenance of technological process, its safety, ecology, etc. should be taken into account. Estimations should be carried out very critically, so that development of anyone MWT, under preliminary forecasts not adequate to expected economic characteristics, has been suspended right at the beginning.

**GENERAL
ANTENNA
THEORY**

THE DIFFER-INTEGRAL THEORY OF FRACTAL ANTENNAS

Volodymir M. Onufriyenko

Zaporizhzhia National Technical University
Zaporizhzhia, Ukraine
<onufr@zntu.edu.ua>

Abstract

The introduction of the so-called α -forms for studying the behaviour of electromagnetic field components in the vicinity of antennas with fractal properties is considered. To estimate the α -forms, some possible algorithms are formulated, namely a geometric one involving the evaluation of the Hausdorff measure and an analytical algorithm permitting the Hausdorff measure to be evaluated through the application of fractional derivatives and integrals. Far-field patterns of the fractal α -pole antennas are calculated.

Keywords: Fractal antenna, Hausdorff measure, differ-integral, α -forms, Maxwell (Abel) equations, vector and scalar potential, Green's function, turnstile α -poles, radiation pattern.

1. INTRODUCTION

"Fractals" were first defined by Benoit Mandelbrot in 1975 as a way of classifying structures whose dimensions were not integer numbers. These geometries have been used previously to characterize the unique occurrences in nature that were difficult to define with the Euclidean geometries, including the length of coastlines, the density of clouds, and the branching of trees [1].

Fractals represent a class of geometry with very unique properties that can be enticing for the antenna designer. Since the electrical lengths play such an important role in antenna design, this efficient packing can be used as a viable miniaturization technique.

The antenna design can benefit from studying these geometries. Looking at the geometries whose dimensions are not limited to integers may lead to the discovery of antennas with improved characteristics over these which exist today. The fractal antennas have shown possibility to miniaturize antennas and to improve the input matching. Certain classes of fractal antennas can be configured to operate effectively at various frequency bands [2].

There are three distinct advantages in using the fractal antennas: First, fractal geometries can be implemented to miniaturize the resonant loop and the dipole antennas. Also, the designing with fractal geometries can overcome the limitations to improve the input resistance of antennas that are typically hard to match to the feeding transmission lines. Furthermore, the self-similar nature in the fractal geometry can be utilized for operating a fractal antenna at various frequencies.

2. FORMULATION

The well known technique of approximating to non-coordinate boundaries through covering the surface with simple compacts (like rectangles, circles, or ellipses) permits application of numerical algorithms for solving boundary-value problems of electrodynamics. Let us extend the technique of covering the boundaries and domains of existence of the field to the case of a smooth contour possessing fractally distributed geometric points over its certain section (physically, a highly jagged (rough) portion of the contour). To that end, we will consider a model of the contour section showing the properties of local uniformity and local self-similarity. Let fractal portion of the contour be approximated to with a segmented line with the links $r_{i(k)}$ of constant length and the ends lying on the contour (k -number of covering generation). In this connection we are able to use the generalized measure of the manifold magnitude involving choice of a trial power function

$$h(r_{i(k)}) = \gamma(\alpha) \times r_{i(k)}^\alpha$$

with the weight factor $\gamma(\alpha)$ (geometrically: a rectangular segment, a square, a circle, a sphere, a cube, etc.), and covering of the multitude of points under study with elements B_i of length r_i , with formation of the Hausdorff α -measure

$$H^\alpha(E) = \lim_{\varepsilon \rightarrow 0} H_\varepsilon^\alpha(E) = \inf \left\{ \gamma(\alpha) \sum_i r_i^\alpha : \right. \\ \left. E \subset \bigcup B_i, r_i < \varepsilon \right\}.$$

That can serve as a measure of the extent and curvature of the continuous limiting line.

Instead of the complex procedure of each time constructing geometrically the fractal set and determining Hausdorff's measure with consequent limiting transitions, we will make use of the fractional integration and differentiation formalism, where

$$({}_a I_x^\alpha f)(x) = \frac{1}{\Gamma(\alpha)} \int_a^x f(t) \frac{dt}{(x-t)^{1-\alpha}},$$

with $x > a$ and $\alpha > 0$;

$$({}_a D_x^\alpha f)(x) = \frac{1}{\Gamma(1-\alpha)} \frac{d}{dx} \left(\int_a^x f(t) \frac{dt}{(x-t)^\alpha} \right),$$

with $x > a$ and $0 < \alpha < 1$.

Here $\Gamma(\alpha)$ is Euler's gamma-function and α is the order of the integro-differential operator (scaling factor).

Differintegral $D^\alpha f$ determines some the differintegral forms of a degree α on Ω with value in f (imaging Ω in $L^\alpha(\Omega \subset \vec{E}, \vec{F})$):

$$\vec{\omega}^\alpha(x) \cdot (\vec{X}) = (D^\alpha f)(x) \cdot \vec{X}.$$

If to crest factors

$$\omega^{\alpha+1} = \sum_i a_i(x) dx_i \wedge dx_i^\alpha$$

to put in correspondence vector $\vec{a} = \{a_i\}$ to coefficients of external differential $d\omega^\alpha$ there will correspond a curl of a vector \vec{a} on a fractal set.

The α -volume forms

$$d^\alpha V = d^\alpha x_1 \wedge \dots \wedge d^\alpha x_m$$

on a m -dimensional Riemannian manifold E induces a Borel measure, which coincides with the Hausdorff-measure $H^\alpha(U) = \int_U d^\alpha V$ for any open

set $U \subset E$. Hence, for any integrable α -forms f^α on E equality $\int_E f^\alpha = \int_E \langle f^\alpha, \tau_E \rangle dH^\alpha$, where τ_E

is a vector, defining tangential plane is valid. We have installed the formula of connection between integrals of the second type (from the α -forms) and integrals of the first type (in respect of Hausdorff's measure).

3. THE SOLUTION OF THE PROBLEMS

Electromagnetic field in fractal medium follows Maxwell (Abel) equations in the terms of α -forms

$$\begin{aligned} d^\alpha \vec{E}^{(\alpha)} &= -\frac{\partial}{\partial t} \vec{B}^{(\alpha)} - \vec{j}_m^{(\alpha)}, \\ d^\alpha \vec{H}^{(\alpha)} &= \frac{\partial}{\partial t} \vec{D}^{(\alpha)} + \vec{j}_e^{(\alpha)}, \\ d^\alpha \vec{D}^{(\alpha)} &= \rho_e^{(\alpha)}, \quad d^\alpha \vec{B}^{(\alpha)} = \rho_m^{(\alpha)}. \end{aligned} \quad (1)$$

The integral equation that is solved is the electrical field integral equation. The equation applies to fractal electri-

cal conductors. The currents are found by imposing the condition that tangential electric α -fields vanish on the fractal surface of the conductors (hereinafter $u^\alpha = ({}_a D_x^\alpha u^{(\alpha)})(x)$)

$$E_{\text{tang, gent, total}}^\alpha = E_{\text{tang, gent, incid}}^\alpha + E_{\text{tang, gent, scatt}}^\alpha \quad (2)$$

The incident field is the field that would exist if the conducting surfaces would be absent. The scattered fields are those that are generated from the induced surface currents. The equivalence theorem can be utilized to remove the conducting bodies and define a sheet of current that will excite the true scattered field, which is excited by the induced surface currents. The field from these equivalent currents can be computed from Maxwell's equations (10). The solution of Maxwell's equations for an electric field at an observation point r can be found using auxiliary potential functions, the magnetic vector α -potential, \vec{A} , and the electric scalar α -potential, Φ

$$E_{\text{scatt}}^\alpha = -j\omega \vec{A}^\alpha(r) - \nabla \Phi^\alpha(r). \quad (3)$$

Eq. (3) substituted into (2) results in the electric field integral equation

$$(-j\omega \vec{A}^\alpha(r) - \nabla \Phi^\alpha(r))_{\text{tangent}} = -E_{\text{tang, gent, incid}}^\alpha(r),$$

where,

$$\vec{A}^{(\alpha)}(r) = \mu \int_S \vec{J}(r') G(r, r') ds'^\alpha, \quad (4)$$

$$\Phi^{(\alpha)}(r) = -\frac{1}{j\omega\epsilon} \int_S \nabla' \cdot \vec{J}(r') G(r, r') ds'^\alpha, \quad (5)$$

$$G(r, r') = \frac{e^{-jkR}}{4\pi R}, \quad (6)$$

and $R = |r - r'|$ is the distance between an observation point r and the source point r' , and $k = 2\pi/\lambda$ with λ being the wavelength, $ds^\alpha = \delta^\alpha(r - r') ds$ is a surface that supports a sheet of current,

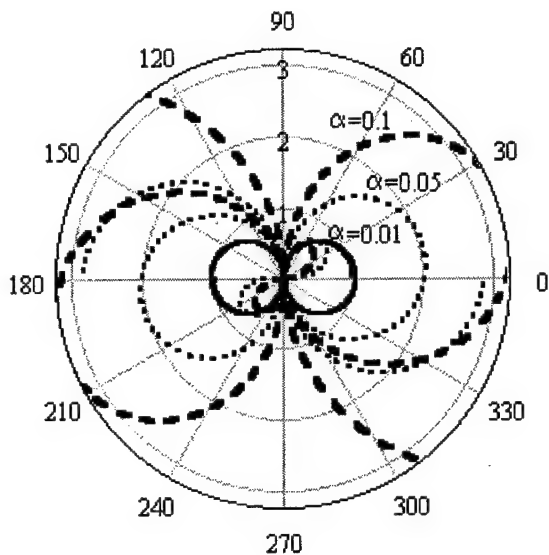
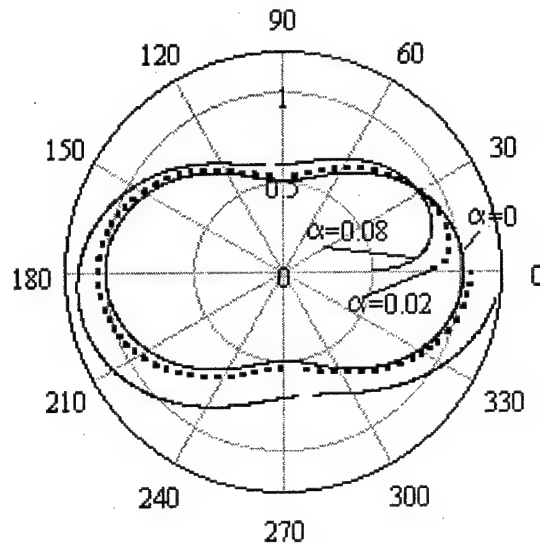
$$\delta^\alpha(r - r') = \frac{1}{\Gamma(\alpha)} \frac{1}{(r - r')^{1-\alpha}} \delta(r - r').$$

The sheet does not have to be continuous.

For wire radiators, the calculations can be simplified by using the thin wire approximation. This assumes that the wire radius, a , is much smaller than a wavelength, λ . Thus, the current density, $\vec{J}^{(\alpha)}$ is uniformly distributed around the circumference of the wire

$$\vec{J}^{(\alpha)} = \frac{I}{2\pi a^\alpha} \vec{l}^{(\alpha)},$$

where $\vec{l}^{(\alpha)}$ is a unit vector along the axis of the wire and I is the total current passing through a cross section of the wire.


Fig. 1. Far-field $E_{\theta}(\theta)$

Fig. 2. Radiation intensity $U(\theta, \varphi)$

4. THE RADIATION PATTERNS

The radiation patterns from the simulated antennas can be calculated by radiating the computed currents. The directivity of the antenna is calculated from

$$D(\theta, \varphi) = 4\pi \frac{U(\theta, \varphi)}{P}$$

where the radiation intensity, $U(\theta, \varphi)$, is a far field parameter that is independent of r . It can be found from both polarization components of the scattered electric field,

$$U(\theta, \varphi) = \frac{1}{2\pi} (|E_{\varphi}^{(\alpha)}|^2 + |E_{\theta}^{(\alpha)}|^2),$$

$$E_{\varphi}^{(\alpha)}(\theta, \varphi) \sim {}_0I_{\varphi}^{\alpha} \{ \cos(\theta) \exp(-j\varphi) \},$$

$$E_{\theta}^{(\alpha)}(\theta, \varphi) \sim {}_0I_{\theta}^{\alpha} \{ \cos(\theta) \exp(-j\varphi) \}.$$

The power P supplied to the antenna is computed from the sum of the applied voltage sources and the computed currents.

Three types of fractals were compared as dipoles: a Koch curve, a fractal tree, and a tree-dimensional fractal tree.

5. THE COMPUTED FAR-FIELD PATTERNS

Far-field $E_{\theta}(\theta)$ pattern of turnstile α -pole are shown in Fig. 1.

The computed directional diagram on power are plotted in Fig. 2.

6. CONCLUSION

The expected benefit of using a fractal as a dipole antenna is to miniaturize the total height of the antenna at resonance, where resonance means having no imaginary component in the input impedance.

REFERENCES

1. Mandelbrot B. The Fractal Geometry of Nature. - San Francisco: W. H. Freeman, 1982.
2. Cohen N. Fractal Antennas. Part 1. // Comm. Quarterly, Summer 1995, p.7-22.
3. Onufriyenko V. M. Physical and Geometric Interpretation of Electromagnetic Field's α -Characteristics // T&RE, V.53, N4-5, 1999, p.136-139.

EXACT 'ABSORBING' CONDITIONS IN INITIAL BOUNDARY-VALUE PROBLEMS OF THE THEORY OF PULSE WAVE RADIATION

Yuriy K. Sirenko¹, Vadim L. Pazynin¹, Anna I. Vyazmitinova¹, and Konstantin Yu. Sirenko²

¹Institute of Radiophysics and Electronics, National Academy of Sciences, Kharkov, Ukraine

²Kharkov National University, Kharkov, Ukraine

Abstract

The outcomes of a search for efficient and correct ways of the truncation of computational domain in finite-difference methods are presented. The relevant mathematical problem is resolved rigorously both for two-dimensional scalar model problems and for three-dimensional vector problems. In the framework of this abstract, we describe briefly only two typical two-dimensional situations. The peculiarities associated with a change to the analysis of three-dimensional vector problems are to be covered in the report.

Keywords: initial boundary-value problem, 'absorbing' boundary conditions, pulse wave radiation.

The analysis of pattern-forming structures with compact elements (whose parameters are given by the permittivity $\varepsilon(g)$, the conductivity $\sigma(g)$, $g = \{y, z\} \in \mathbf{R}^2$, and the boundaries S of perfectly conducting inclusions, see Fig. 1) excited by the 'current' sources $F(g, t)$ and 'momentary' sources $\varphi(g)$ and $\psi(g)$ is reduced to the solution of the initial boundary-value problems

$$\begin{cases} \left[-\varepsilon(g) \frac{\partial^2}{\partial t^2} - \sigma(g) \frac{\partial}{\partial t} + \frac{\partial^2}{\partial z^2} + \frac{\partial^2}{\partial y^2} \right] U(g, t) = \\ = F(g, t); \\ U(g, t)|_{t=0} = \varphi(g), \frac{\partial}{\partial t} U(g, t)|_{t=0} = \\ = \psi(g); g \in \bar{Q}; \\ E_{tg}(g, t)|_{g \in S} = 0; \quad t \geq 0; \\ g = \{y, z\} \in Q, \quad t > 0. \end{cases} \quad (1)$$

These equations describe transient states of E -polarized waves ($E_p = E_\phi = H_x = 0$, $U(g, t) = E_x(g, t)$) and H -polarized waves ($H_p = H_\phi = E_x = 0$, $U(g, t) = H_x(g, t)$) initiated by sources and objects located in the bounded region Q_L of the plane \mathbf{R}^2 of coordinates y and z , $\partial/\partial x \equiv 0$. Here $\varepsilon(g)$ and $\sigma(g)$ are piece-wise constant functions. The analysis domain $Q = \mathbf{R}^2 \setminus \text{int } S$ (S stands for the boundaries of the regions $\text{int } S$ occupied by perfect metal, \bar{G} is the closure of G and $Q = Q_L \cup LQ \cup L$) in problems (1) is not closed.

However, above (below, to the right of and to the left of) the boundary $z = L_1$ ($z = L_2$, $y = L_3$, and $y = L_4$) there are neither sources nor scatterers. The function $U(g, t)$ here corresponds to an outgoing wave crossing the respective boundary L in one direction only and satisfies homogeneous problems (1) with $\varepsilon(g) - 1 = \sigma(g) \equiv 0$. This fact allows one [1] to supplement problems (1) with the following exact 'absorbing' condition:

$$\begin{cases} \left[\frac{\partial}{\partial t} \pm \frac{\partial}{\partial z} \right] U(g, t) = \frac{2}{\pi} \int_0^{\pi/2} \frac{\partial V_1(g, t, \varphi)}{\partial t} \sin^2 \varphi d\varphi; \\ \left[\frac{\partial^2 V_1(g, t, \varphi)}{\partial t^2} - \frac{\partial^2 V_1(g, t, \varphi)}{\partial y^2} \right] = 0; \\ \left[\frac{\partial V_1(g, t, \varphi)}{\partial t} \right]_{t=0} = V_1(g, t, \varphi)|_{t=0} = 0; \end{cases} \quad (2)$$

$$L_4 \leq y \leq L_3, \quad \begin{cases} z = L_1; \\ z = L_2; \end{cases} \quad t \geq 0,$$

$$\begin{cases} \left[\frac{\partial}{\partial t} \pm \frac{\partial}{\partial y} \right] U(g, t) = \frac{2}{\pi} \int_0^{\pi/2} \frac{\partial V_2(g, t, \varphi)}{\partial t} \sin^2 \varphi d\varphi; \\ \left[\frac{\partial^2 V_2(g, t, \varphi)}{\partial t^2} - \frac{\partial^2 V_2(g, t, \varphi)}{\partial z^2} \right] = 0; \\ \left[\frac{\partial V_2(g, t, \varphi)}{\partial t} \right]_{t=0} = V_2(g, t, \varphi)|_{t=0} = 0; \end{cases} \quad (3)$$

$$L_2 \leq z \leq L, \quad \begin{cases} y = L_3; \\ y = L_4; \end{cases} \quad t \geq 0,$$

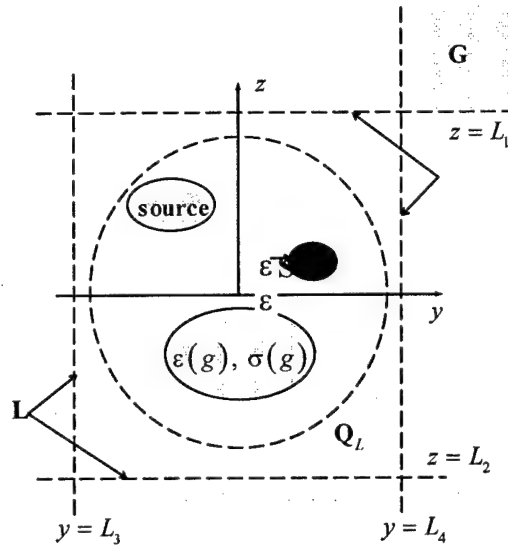


Fig. 1. Geometry of problems (1).

$$\begin{aligned} \left[\frac{\partial}{\partial t} \pm \cos \varphi \frac{\partial}{\partial y} \right] W_1 &= \frac{2 \cos \varphi}{\pi} \int_0^{\pi/2} R(\varphi, \gamma) \frac{\partial W_2}{\partial t} d\gamma \\ \left[\frac{\partial}{\partial t} \pm \cos \varphi \frac{\partial}{\partial z} \right] W_2 &= \frac{2 \cos \varphi}{\pi} \int_0^{\pi/2} R(\varphi, \gamma) \frac{\partial W_1}{\partial t} d\gamma \\ t \geq 0, \quad R(\varphi, \gamma) &= \frac{\sin^2 \gamma}{\cos^2 \varphi + \sin^2 \varphi \cos^2 \gamma}, \quad (4) \\ \begin{bmatrix} + \\ + \end{bmatrix} \rightarrow g = \{L_3, L_1\}, & \quad \begin{bmatrix} + \\ - \end{bmatrix} \rightarrow \{L_3, L_2\}, \\ \begin{bmatrix} - \\ + \end{bmatrix} \rightarrow \{L_4, L_1\}, & \quad \begin{bmatrix} - \\ - \end{bmatrix} \rightarrow \{L_4, L_2\}. \end{aligned}$$

In fact, only these three formulas taken together, define the exact local 'absorbing' condition for the entire rectangular virtual boundary L . Equations (4) fulfill the role of boundary conditions in the boundary value problems, inherent in (2) and (3), with respect to the auxiliary functions $V_j(g, t, \varphi)$ and $W_j(g, t, \varphi) = V_j(g, t, \varphi) \cos^2 \varphi + U(g, t)$, $j = 1, 2$.

The symbols « $\begin{bmatrix} + \\ + \end{bmatrix} \rightarrow g = \{L_3, L_1\}$ » stand for the rules governing the choice of a sign in the upper and the lower equations for different corner points $g = \{y, z\}$. Set of equations (2)–(4), being added to problems (1), restricts the analysis domain Q to the region Q_L . Problems (1) and (1)–(4) are equivalent: the additional conditions do not introduce any distortion in simulated physical processes of non-sinusoidal waves radiation.

The antenna near fields are determined in the immediate computational region Q_L of the finite-difference method, whereas the far fields are obtained by recalculation of $U(g, t)$ from the virtual boundary L onto the virtual boundary P , moved to the required

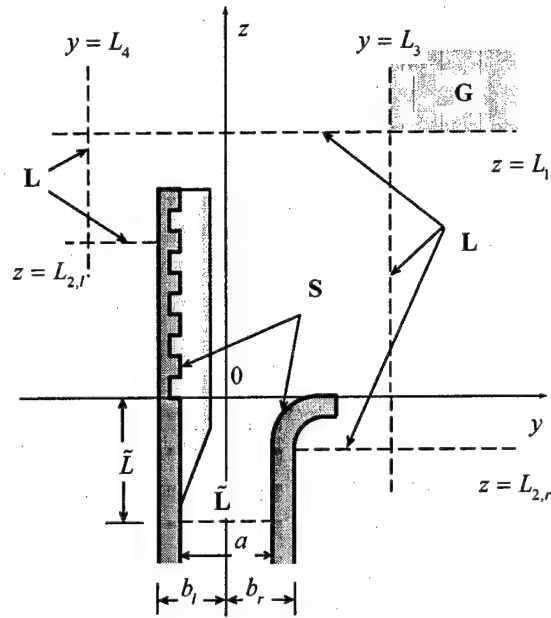


Fig. 2. Plane model of the antenna with a grating as dispersive element

distance from L : the exact radiation conditions (2)–(4) allow one to construct in an explicit form the 'transport' operator $Z_{p \in L \rightarrow g \in P}(t)$ such that $U(g, t) = Z_{p \in L \rightarrow g \in P}(t)[U(p, \tau)]$.

The above result can be easily extended to a case of pulse E - or H -polarized waves radiated from a plane-parallel waveguide with an aperture of arbitrary geometry (see, for example, Fig. 2). The rectangular boundary L closes the analysis domain in the region of free signal propagation, while the boundary \tilde{L} closes the domain in the supplying waveguide. The relevant original 'open' plane initial boundary-value problem (1) is reduced [1] to the equivalent 'closed' one with the analysis domain

$$Q_L = \left\{ g \in Q : L_4 < y < L_3; \right. \\ \left. \begin{aligned} & L_{2,l}; \quad y < -b_l \\ & -\tilde{L}; \quad |y| < a/2 \\ & L_{2,r}; \quad y > b_r \end{aligned} < z < L_1 \right\}$$

by adding local exact 'absorbing' conditions on \tilde{L}

$$\left\{ \begin{aligned} \left[\frac{\partial}{\partial t} - \frac{\partial}{\partial z} \right] U(y, z, t) \Big|_{z=-L} &= \frac{2}{\pi} \int_0^{\pi/2} \frac{\partial W(y, t, \varphi)}{\partial t} \sin^2 \varphi d\varphi, \\ t \geq 0, \quad |y| \leq a/2, \\ \left[\frac{\partial^2}{\partial t^2} - \cos^2 \varphi \frac{\partial^2}{\partial y^2} \right] W(y, t, \varphi) &= \frac{\partial^2 U(y, 0, t)}{\partial y^2}; \\ W(y, 0, \varphi) = \frac{\partial W(y, t, \varphi)}{\partial t} \Big|_{t=0} &= 0; |y| \leq a/2; t \geq 0 \\ W(\pm a/2, t, \varphi) = 0 \quad (E - \text{polarization}) \text{ or} \\ \partial W(y, t, \varphi) / \partial y \Big|_{y=\pm a/2} = 0 \quad (H - \text{polarization}); \end{aligned} \right. \quad (5)$$

and the following exact local conditions on L :

$$\left\{ \begin{aligned} \left[\frac{\partial}{\partial t} + \frac{\partial}{\partial z} \right] U(g, t) &= \frac{2}{\pi} \int_0^{\pi/2} \frac{\partial V_1(g, t, \varphi)}{\partial t} \sin^2 \varphi d\varphi, \\ t \geq 0; \\ \left[\frac{\partial^2 V_1(g, t, \varphi)}{\partial t^2} - \frac{\partial^2 W_1(g, t, \varphi)}{\partial y^2} \right] &= 0; t > 0; \\ \frac{\partial V_1(g, t, \varphi)}{\partial t} \Big|_{t=0} &= V_1(g, t, \varphi) \Big|_{t=0} = 0; \\ L_4 \leq y \leq L_3, \quad z = L_1, \\ \left[\frac{\partial}{\partial t} - \frac{\partial}{\partial z} \right] U(g, t) &= \frac{2}{\pi} \int_0^{\pi/2} \frac{\partial \tilde{V}_1(g, t, \varphi)}{\partial t} \sin^2 \varphi d\varphi, \\ t \geq 0; \\ \left[\frac{\partial^2 \tilde{V}_1(g, t, \varphi)}{\partial t^2} - \frac{\partial^2 \tilde{W}_1(g, t, \varphi)}{\partial y^2} \right] &= 0; t > 0; \\ \left\{ \begin{aligned} \tilde{V}_1(\tilde{b}, z, t, \varphi) &= 0; \quad E - \text{polar}; \\ \frac{\partial \tilde{V}_1(y, z, t, \varphi)}{\partial y} \Big|_{y=\tilde{b}} &= 0; \quad H - \text{polar}; \end{aligned} \right. \quad t \geq 0 \quad (7) \\ \frac{\partial \tilde{V}_1(g, t, \varphi)}{\partial t} \Big|_{t=0} &= \tilde{V}_1(g, t, \varphi) \Big|_{t=0} = 0; \end{aligned} \right.$$

$$\tilde{V}_1(y, z, t, \varphi) = \begin{cases} V_{1,r}(y, z, t, \varphi); \tilde{b} = b_r, \leq y \leq L_3, \\ z = L_{2,r}; \\ V_{1,l}(y, z, t, \varphi); L_4 \leq y \leq \tilde{b} = -b_l, \\ z = L_{2,l}; \end{cases}$$

$$\left\{ \begin{aligned} \left[\frac{\partial}{\partial t} \pm \frac{\partial}{\partial y} \right] U(g, t) &= \frac{2}{\pi} \int_0^{\pi/2} \frac{\partial V_2(g, t, \varphi)}{\partial t} \sin^2 \varphi d\varphi, \\ t \geq 0; \\ \left[\frac{\partial^2 V_2(g, t, \varphi)}{\partial t^2} - \frac{\partial^2 W_2(g, t, \varphi)}{\partial z^2} \right] &= 0; t > 0; \\ \frac{\partial V_2(g, t, \varphi)}{\partial t} \Big|_{t=0} &= V_2(g, t, \varphi) \Big|_{t=0} = 0; \\ \begin{cases} y = L_3, & L_{2,r} \leq z \leq L_1; \\ y = L_4, & L_{2,l} \leq z \leq L_1; \end{cases} \end{aligned} \right. \quad (8)$$

$$\left\{ \begin{aligned} \left[\frac{\partial}{\partial t} \pm \cos \varphi \frac{\partial}{\partial y} \right] Z_1 &= \frac{2 \cos \varphi}{\pi} \int_0^{\pi/2} R(\varphi, \gamma) \frac{\partial W_2}{\partial t} d\gamma; \\ \left[\frac{\partial}{\partial t} \pm \cos \varphi \frac{\partial}{\partial z} \right] W_2 &= \frac{2 \cos \varphi}{\pi} \int_0^{\pi/2} R(\varphi, \gamma) \frac{\partial Z_1}{\partial t} d\gamma; \end{aligned} \right.$$

$$R(\varphi, \gamma) = \frac{\sin^2 \gamma}{\cos^2 \varphi + \sin^2 \varphi \cos^2 \gamma}, \quad t \geq 0,$$

$$\left\{ \begin{aligned} + \\ + \end{aligned} \right\} \rightarrow g = \{L_3, L_1\} \text{ и } Z_1 = W_1, \quad (9)$$

$$\left\{ \begin{aligned} + \\ - \end{aligned} \right\} \rightarrow g = \{L_3, L_{2,r}\} \text{ и } Z_1 = W_{1,r},$$

$$\left\{ \begin{aligned} - \\ + \end{aligned} \right\} \rightarrow g = \{L_4, L_1\} \text{ и } Z_1 = W_1,$$

$$\left\{ \begin{aligned} - \\ - \end{aligned} \right\} \rightarrow g = \{L_4, L_{2,l}\} \text{ и } Z_1 = W_{1,l},$$

Here

$$W_j(g, t, \varphi) = V_j(g, t, \varphi) \cos^2(\varphi) + U(g, t),$$

$$j = 1, 2,$$

$$\tilde{W}_1(g, t, \varphi) = \tilde{V}_1(g, t, \varphi) \cos^2(\varphi) + U(g, t),$$

$$W_{1,r}(g, t, \varphi) = V_{1,r}(g, t, \varphi) \cos^2(\varphi) + U(g, t),$$

$$W_{1,l}(g, t, \varphi) = V_{1,l}(g, t, \varphi) \cos^2(\varphi) + U(g, t)$$

are auxiliary functions. For these functions, the initial boundary-value problems, entering into (6)–(8), are well-posed. The symbols like

$$\left\{ \begin{aligned} + \\ + \end{aligned} \right\} \rightarrow g = \{L_3, L_1\} \text{ and } Z_1 = W_1 \text{ stand for}$$

the rules governing the choice of signs in the upper and the lower equations (9) as well as the choice of the values of $Z_1(g, t, \varphi)$ for the corner points $g = \{y, z\}$.

REFERENCES

1. Sirenko Yu. K. 2003, Simulation and Analysis of transient Processes in Open Periodic, Waveguide, and Compact Resonators, EDENA, Kharkov.

ANALYSIS OF SCATTERING BY INHOMOGENEOUS DIELECTRIC OBJECTS USING HIGHER-ORDER HIERARCHICAL MOM

Oleksiy S. Kim¹, Erik Jørgensen², Peter Meincke¹, and Olav Breinbjerg¹

¹ Ørsted-DTU, Electromagnetic Systems, Technical University of Denmark
Ørsted's Plads, Building 348, DK-2800 Kgs. Lyngby, Denmark
<osk@oersted.dtu.dk>

² TICRA, Laederstraede 34, DK-1201 Copenhagen K, Denmark

Abstract

An efficient technique for the analysis of electromagnetic scattering by arbitrarily shaped inhomogeneous dielectric objects is presented. The technique is based on a higher-order method of moments (MoM) solution of the volume integral equation. This higher-order MoM solution comprises recently developed higher-order hierarchical Legendre basis functions for expansion of the electric flux density and a higher-order geometry modeling. An unstructured mesh composed by trilinear (8-node) and/or curved (27-node) hexahedral elements is used to represent the dielectric object accurately. It is shown that the condition number of the resulting MoM matrix is reduced by several orders of magnitude in comparison to existing higher-order hierarchical basis functions and, consequently, an iterative solver can be applied even for high expansion orders. Numerical results demonstrate excellent agreement with the analytical solutions for the dielectric sphere, as well as with results obtained by other numerical methods.

Keywords: volume integral equation, electromagnetic scattering, higher-order hierarchical basis functions, method of moments, inhomogeneous dielectric objects.

1. INTRODUCTION

Traditionally, scattering and radiation problems involving dielectric materials have been solved with surface integral equation formulations or by differential equation solvers such as the finite element method (FEM). A direct method of moment (MoM) solution of volume integral equations (VIE) has remained impractical due to its excessive CPU and memory requirements. Thus, various modifications of MoM have been developed to accelerate computations and relax computational demands for solution of VIE problems, e.g., the Conjugate-Gradient algorithm combined with Fast Fourier Transform (CG-FFT) [1] and the Fast Multipole Methods (FMM/MLFMM) [2]. Being relatively fast these methods also have disadvantages: the first requires rectangular discretization grid and the second is still memory consuming.

An alternative approach is to reduce the number of unknowns in MoM considerably by discretizing the integral equation with higher-order interpolatory or hierarchical basis functions. Hierarchical functions provide greater flexibility, enabling different expansion orders on different elements in the same mesh. The main bottleneck of existing hierarchical basis functions is the ill-conditioning of the MoM matrix which requires a direct solver to be employed [3].

This implies that the solution time of the MoM matrix is proportional to N^3 where N is the number of unknowns, whereas it is proportional to N^2 for iterative solvers. Thus, the application of an iterative solution method is essential for any efficient MoM tool for large-scale electromagnetic problems involving inhomogeneous dielectric materials.

Recently, a new type of higher-order hierarchical basis functions was proposed in [4], where they were applied to surface integral equations. Based on appropriately modified Legendre polynomials, the new basis functions are near-orthogonal and therefore provide low condition numbers of the MoM matrix. In this paper, we apply the new higher-order hierarchical Legendre basis functions to volume integral equations. The properties of the newly developed higher-order MoM solution are compared to existing higher-order formulations. Numerical examples for scattering by dielectric spheres demonstrate an excellent agreement between results of our higher-order hierarchical MoM and the Mie series analytical solution. A very low condition number of the MoM matrix allows the use of an iterative matrix solver even for high expansion orders. The memory requirements of the higher-order hierarchical MoM are compared with an existing multilevel fast multipole method (MLFMM) implementation [2].

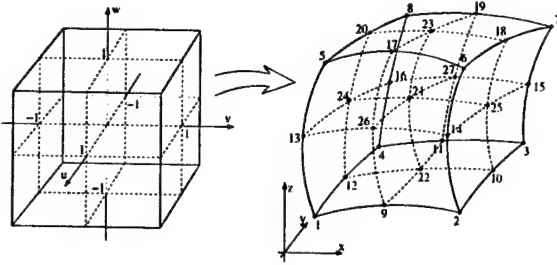


Fig. 1. Mapping between (u, v, w) and (x, y, z)

2. HIGHER-ORDER HIERARCHICAL MoM

The discretization of an electric field volume integral equation with higher-order MoM involves two steps. First, a volumetric dielectric object is accurately represented by trilinear and/or curved hexahedral elements, which are defined by 8 and 27 nodes, respectively. Lagrange interpolation is employed to define a unique mapping between a cube in a curvilinear coordinate system (u, v, w) and the hexahedron in the physical (x, y, z) space, see Fig. 1. The dielectric permittivity inside each element is not necessarily constant but may vary as a function of coordinates.

Second, the unknown electric flux density $\mathbf{D}(u, v, w)$ in each local curvilinear (u, v, w) -coordinate system is expanded as

$$\mathbf{D}(u, v, w) = \mathbf{a}_u D^u + \mathbf{a}_v D^v + \mathbf{a}_w D^w, \quad (1)$$

where \mathbf{a}_u , \mathbf{a}_v , and \mathbf{a}_w are the covariant unitary vectors. Each of the contravariant components (D^u, D^v, D^w) of \mathbf{D} are expanded in terms of the higher-order hierarchical Legendre basis functions [4] as

$$\begin{aligned} D^\xi = & \frac{1}{A} \sum_{n=0}^{N^\eta} \sum_{q=0}^{Q^\zeta} \left\{ C_0^\xi \left[b_{0nq}^\xi (1 - \xi) + \right. \right. \\ & \left. \left. + b_{1nq}^\xi (1 + \xi) \right] C_n^\eta P_n(\eta) C_q^\zeta P_q(\zeta) \right\} + \\ & + \frac{1}{A} \sum_{m=2}^{M^\xi} \sum_{n=0}^{N^\eta} \sum_{q=0}^{Q^\zeta} \left\{ b_{mnq}^\xi C_m^\xi \left[P_m(\xi) - \right. \right. \\ & \left. \left. - P_{m-2}(\xi) \right] C_n^\eta P_n(\eta) C_q^\zeta P_q(\zeta) \right\}, \end{aligned} \quad (2)$$

where (ξ, η, ζ) are (u, v, w) , (v, w, u) , or (w, u, v) . In (2), A is the Jacobian of the parametric transformation, $P_m(\xi)$ are Legendre polynomials, and b_{mnq}^ξ are unknown coefficients. M^ξ , N^η , and Q^ζ denote the expansion orders along the three parametric directions. The factors C_m^ξ , C_n^η , and C_q^ζ are chosen such that the Euclidean norm of each function is unity for a unit cubic element. The basis functions are divergence-conforming, i.e., they satisfy continuity of the normal component of the electric flux density flowing through a face shared by two adjacent elements. Despite the necessary modifications to enforce the continuity, the expansion (2) maintains almost perfect orthogonality of the basis functions.

Due to the hierarchical property of the basis functions the expansion order can be selected separately in each hexahedron depending on the electrical size of the element. This allows large smooth objects to be represented by rather large curvilinear hexahedra with high expansion orders while fine parts of the geometry are precisely modeled by small hexahedral elements with low expansion orders. In this way, the number of unknowns can be minimized as opposed to low-order discretization schemes (volume RWG, or rooftops) that require small elements throughout the mesh. Furthermore, independent selection of the expansion order along the direction of the electric flux density and along the transverse directions provides additional flexibility to the discretization technique. Consequently, even geometries represented by elements that are far from cubic in shape, for instance thin dielectric shells or antenna radomes, can be treated in an efficient manner without introducing unnecessary unknowns.

3. NUMERICAL RESULTS

First, consider a homogeneous dielectric sphere with dielectric constant $\epsilon_r = 4.0$. The sphere is placed at the origin of a rectangular xyz -coordinate system and illuminated by an x -polarized plane wave propagating in the z -direction. The size of the sphere is $k_0 a = 2.0$ where k_0 is a propagation constant in free space and a is the radius. The sphere is represented with 32 hexahedral elements, both trilinear and curved. The expansion order is varied from $M^\xi = 2$ to $M^\xi = 4$ and the resulting number of unknowns, root-mean-square (RMS) error, and condition number of the MoM matrix are listed in Table 1. Here, the RMS error is computed for the bistatic radar cross section (RCS) relative to an exact analytical solution (the Mie series expansion). The RMS error is defined as

$$RMS = \sqrt{\frac{\sum_{i=1}^{N_n} |\sigma_{MoM} - \sigma_{Mie}|^2}{\sum_{i=1}^{N_n} |\sigma_{Mie}|^2}}, \quad (3)$$

where N_n is the number of sampling points (observation angles), σ_{MoM} and σ_{Mie} are the MoM and the exact RCS, respectively. The results are obtained by sampling the bistatic RCS at 181 angles in the E- and H-planes. The convergence with the RMS error less than 1% was achieved with $M^\xi = 3$. A further increase of the expansion order yields a small improvement which probably indicates that geometrical modelling errors are dominating for $M^\xi = 4$.

In Table 1 the 2-norm condition numbers for our higher-order Legendre basis functions and the existing higher-order power basis functions [3] are compared. It is observed that the higher-order hierarchical Legendre basis functions presented here provide very well-conditioned MoM matrix system for all expansion or-

Table 1. Results for the homogeneous sphere

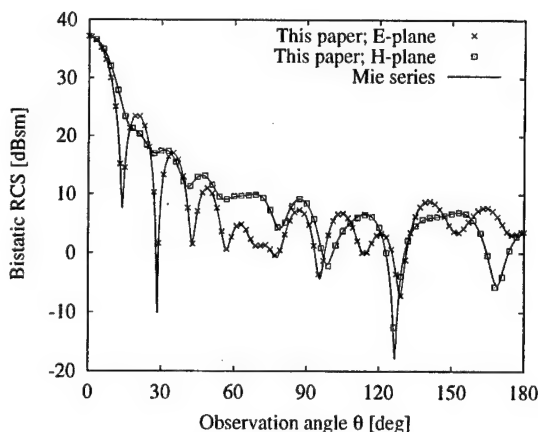
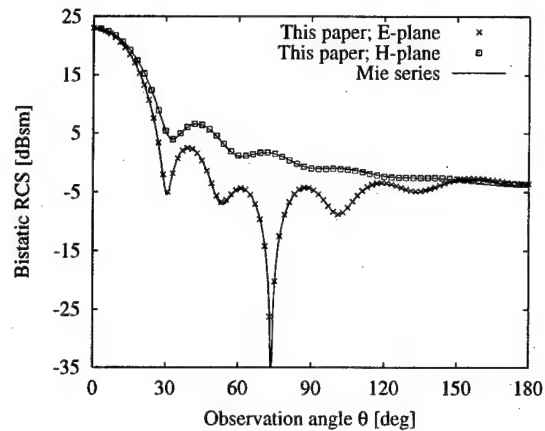
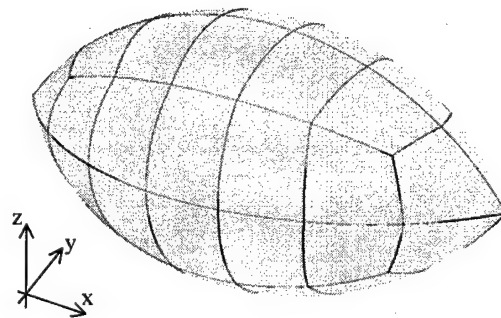
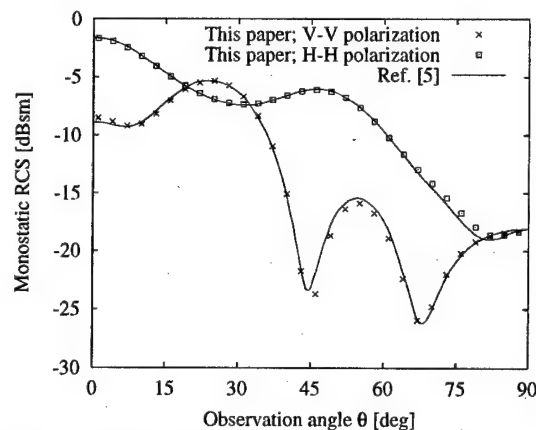
Exp. Order M^ξ		2	3	4
Unknowns		816	2700	6336
RMS error		$3.3 \cdot 10^{-2}$	$6.8 \cdot 10^{-3}$	$4.2 \cdot 10^{-3}$
Cond.	This paper	84	159	346
Number	[3]	1583	$1.23 \cdot 10^5$	$2.33 \cdot 10^7$

ders. However, the condition numbers for the power basis functions [3] increase rapidly, approximately two orders of magnitude for each expansion order.

In the second example, a spherical shell of radius $a = 2\lambda_0$ and thickness $0.2\lambda_0$ is analyzed. The dielectric constant of the shell is $\epsilon_r = 2.75 - 0.3j$. In contrast to the previous example, where the expansion order was fixed for all hexahedra in all directions, the expansion order is now changed depending on the electrical size of each element. Thus, the expansion orders are chosen to be $M^\xi = 4$ for the components tangential to the shell surface and $M^\xi = 2$ for the radial components. In total 96 curvilinear hexahedral elements are used to represent the geometry of the shell. The solution with 10752 unknowns requires 884 Mbytes of memory. The obtained bistatic RCS is plotted in Fig. 2. Excellent agreement with the corresponding exact result is observed.

For this example, the MLFMM analysis with first-order basis functions [2] requires 24642 hexahedra, 73962 unknowns, and 2GBytes of memory to achieve the same accuracy. Thus, despite the higher computational complexity of MoM ($O(N^2)$) in comparison to MLFMM ($O(N \log N)$), the large reduction in the number of unknowns provided by the higher-order technique results in a more efficient solution.

As an example of an inhomogeneous dielectric object, we consider the scattering by a two-layer dielectric sphere with the inner radius $a_1 = 0.8\lambda_0$ and outer radius $a_2 = 1.0\lambda_0$. The dielectric constant and conductivity are $\epsilon_{r1} = 4.0$, $\sigma_1 = 0.1 \text{ S/m}$, and $\epsilon_{r2} = 2.0$, $\sigma_2 = 0.05 \text{ S/m}$ for the inner and outer layer, respectively. 56 hexahedral elements and maximum expansion order $M^\xi = 4$ are used in the

**Fig. 2.** Bistatic RCS for the spherical shell**Fig. 3.** Bistatic RCS for the two-layer sphere**Fig. 4.** Dielectric ogive**Fig. 5.** Monostatic RCS for the dielectric ogive

solution. In Fig. 3, the bistatic RCS computed with 8640 unknowns at the frequency $f = 300 \text{ MHz}$ is compared to the exact Mie series solution. Again, both results are in excellent agreement.

The scattering by a dielectric ogive (Fig. 4) is presented in the last example. The ogive is made of homogeneous dielectric with dielectric constant $\epsilon_r = 4.0 - 0.1j$, and has a length 0.6 m and diameter 0.3 m. The monostatic RCS computed in the xz -plane at the frequency $f = 1 \text{ GHz}$ is shown in Fig. 5.

Our result obtained with 116 hexahedral elements, maximum expansion order $M^e = 3$, and 6480 unknowns is in good agreement with the reference [5], where the surface integral equation technique is employed.

4. CONCLUSION

A new higher-order discretization scheme for volume integral equation is presented. The technique is based on higher-order hierarchical Legendre basis functions [4] for expansion of the electric flux density and higher-order geometry modeling. Improved orthogonality of the basis functions allows the condition number of the resulting MoM matrix to be reduced by several orders of magnitude in comparison to existing higher-order hierarchical basis functions and consequently, an iterative solver can be applied even for high expansion orders. Trilinear (8-node) and curved (27-node) hexahedral elements are used for accurate representation of dielectric objects. Numerical examples for scattering by a dielectric sphere and a shell demonstrate an excellent agreement between results of our higher-order hierarchical MoM and the Mie series analytical solution. It is shown that for fairly large scattering problems the higher-order hierarchical MoM requires much fewer unknowns and less computer memory than low-order MLFMM.

REFERENCES

1. Catedra M. F., Gago E., Nuno L. A numerical scheme to obtain the RCS of three-dimensional bodies of resonant size using the conjugate gradient method and the fast Fourier transform // *IEEE Trans. Ant. and Prop.* 1989. Vol. AP-37. No 5, pp. 528-537.
2. Sertel K., Volakis J. L. Multilevel fast multipole method solution of volume integral equations using parametric geometry modeling // *Proc. IEEE AP-S.* 2001. Vol. 3, pp. 786-789. Boston, Massachusetts.
3. Notaros B. M., Popovic B. D., Weem J. P., Brown R. A., Popovic Z. Efficient large-domain MoM solutions to electrically large practical EM problems // *IEEE Trans. Microw. Theory Techn.* 2001. Vol. MTT-49. No 1, pp. 151-159.
4. Jørgensen E., Volakis J. L., Meincke P., Breinbjerg O. Higher-order hierarchical Legendre basis functions for iterative integral equation solvers with curvilinear surface modeling // *Proc. IEEE AP-S.* 2002. Vol. 4, pp. 618-621. San Antonio, Texas.
5. Liu G., Gedney S. D. High-Order Moment Method Solution for the Scattering Analysis of Penetrable Bodies // *Electromagnetics.* 2003. Vol. 23. No 4, pp. 331-345, 2003.

DECOUPLING OF APERTURE ANTENNAS WITH IMPEDANCE STRUCTURES

Essiben Dikoundou J.-F., Yukhanov Yuriy V.

Department of Antennas and Radio Transmitters, Taganrog State University of Radio Engineering
Taganrog, Russia
<airpu@tsure.ru>

Abstract

The observed issues concern provision for electromagnetic compatibility (EMC) of a receiving and a transmitting aperture antennas located in the same plane with the help of an impedance structure. The law of impedance Z distribution is found, which provides a required level of antennas decoupling.

Keywords: Electromagnetic compatibility, decoupling.

1. INTRODUCTION

One of the most effective and popular ways of providing a given level of decoupling between near-omnidirectional antennas, which are located on the same ideally conducting plane, is the use of impedance structures. A thick grate with rectangular riffles of definite depth can serve as a physical model of these structures. At present, rather the great number of works is devoted to development and research of such structures (for example [1]-[4]). As a rule, they consider the influence of different parameters of the structure (or their combination) on the degree of antennas decoupling, that is the tasks of analysis are solved. For effective solution of the task of electromagnetic compatibility it is necessary to state and solve the task of synthesis. Probably the only widely known work containing a solution of the task of synthesis of decoupling devices is the book [1], where as a the result of solving with a number of limitations, the law of purely reactive impedance (reactance) is obtained. This law allows the faster reduction of the field along the geodesic line which connects antennas, than the one with the ideally conducting surface.

The objective of this work is solution of the task of synthesis of the surface impedance and research of the achieved spatial decoupling of antenna devices located on the same plane.

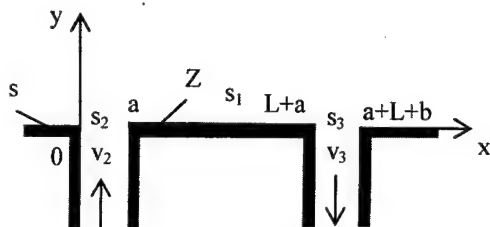


Fig. 1.

2. STATEMENT OF THE PROBLEM

Let us consider the solution of two-dimensional task in the following statement. Let two aperture antennas shaped as open ends of waveguides (the transmitting and the receiving ones) with the apertures dimensions a, b be located on the same plane at the distance of L from each other (Fig. 1). On the surface $S_1 (x \in [a, a+L])$, which separates antennas, the boundary impedance conditions are met:

$$[\mathbf{n}, \mathbf{E}] = -Z[\mathbf{n}, \mathbf{H}]. \quad (1)$$

It is required to define the distribution law of passive impedance $Z(x)$ ($\text{Re}(Z) \geq 0$) by the given law of magnetic field $H_z(x)$ alteration on the surface S_1 , and the degree of decoupling between antennas.

3. SOLUTION OF THE SYNTHESIS TASK

For the quantitative evaluation of decoupling they introduce [1] either the coefficient of antennas coupling

$$K_c = \frac{P_{rec}}{P_{tr}}, \quad (2)$$

where P_{rec}, P_{tr} are signal powers at the outputs of the receiving and transmitting antennas; or the inverse value – the coefficient of decoupling $K_d = -10 \log(K_c)$.

In practice, the task of synthesis [1] is solved, as a rule, in the absence of the second antenna – by the given law of electromagnetic field attenuation, while moving away from the source, placing further the receiving antenna at points with a minimum intensity of the “interfering” field. We solve the task of synthesis as in [1], for a single transmitting antenna by the given alteration of the entire field in the impedance area $x \in [-a; a+L]$ of the surface S , but without imposing the condition of the impedance pure reactivity.

Let the source of electromagnetic field be an infinite thread of in-phase magnetic current located in the beginning of coordinates along the z axis. It creates a magnetic field with the intensity of

$$H_z^i(x) = -\frac{kI_0^N}{4W} H_0^{(2)}(k|x|) \quad (I_0^N/W = 1A).$$

Let us write a magnetic field on the section $x \in [-L, L]$ as follows:

$$H_z(x) = 2H_z^i(x) e^{-\alpha|x|},$$

where α is the attenuation factor of $(\text{Re}(\alpha) \geq 0)$.

Then from the Laurence lemma we will obtain the of first kind Fredholm integral equation related to the entire field $E_x(x)$

$$\begin{aligned} \frac{k}{2W} \int_{-L}^L E_x(x') H_0^{(2)}(k|x-x'|) dx' = \\ = 2H_z^i(x) - H_z(x), \end{aligned} \quad (3)$$

where $H_0^{(2)}(k|x-x'|)$ is the Hankel function of the second kind of zero order $k = 2\pi/\lambda$.

The solution of the integral equation (3) is obtained numerically, with the Krylov-Bogolyubov method.

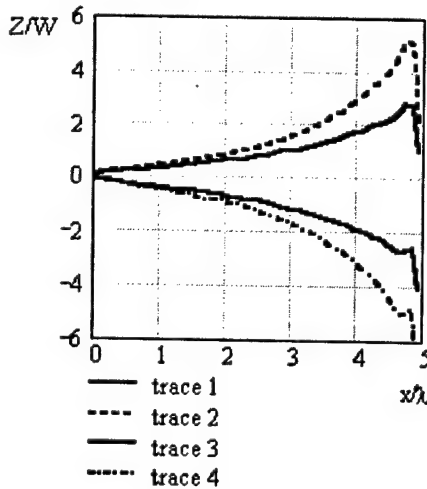


Fig. 2.

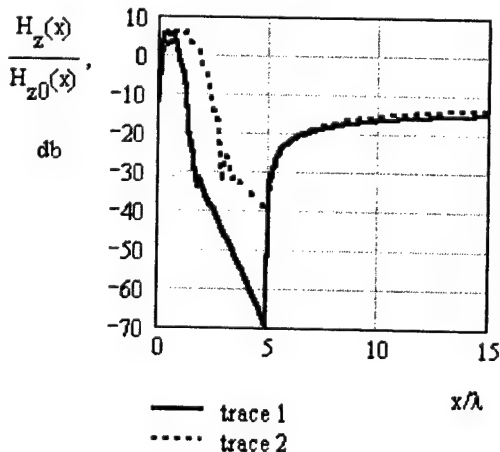


Fig. 3.

As an example, in Fig. 2, there is the law of synthesized impedance distribution for the values of attenuation coefficient $\alpha = 0.125k$ (curves 1, 3) and $\alpha = 0.25k$ (curves 2, 4) with the length of impedance structure $L = 5\lambda$. Curves 1, 2 correspond to $\text{Re}(Z)$, and curves 3, 4 $-\text{Im}(Z)$. As in work [1], the obtained results showed that large reduction of the field is accompanied with a large speed of impedance alteration. However, unlike [1], the obtained here impedance does not have not only a reactive component (curves 3, 4), but also an active (resistive) component ($\text{Re}(Z) \geq 0$) (curves 1, 2).

4. SOLUTION OF THE ANALYSIS TASK

The analysis task is solved by the method of integral equations (IE). These IE are obtained with the use of the Laurence lemma in the integral form [3] for each of the three areas: V_1, V_2, V_3 (see Fig. 1).

In order to evaluate a degree of the influence of resistive part ($\text{Re}(Z) \geq 0$) of impedance $Z(x)$ on the attenuation speed of the field along the impedance structure, in Figs. 3 and 4, there are shown laws of distribution of $H_z(x)$ related to the field $H_{z0}(x)$ above the ideally conducting plane ($H_z(x)/H_{z0}(x)$), for a $\alpha = 0.125k$ and $\alpha = 0.25k$ at $\text{Re}(Z) \geq 0$ (see Fig. 3) and at $\text{Re}(Z) = 0$ (see Fig. 4).

As we can see, the presence of a resistive part of impedance not only makes worse the level of decoupling between antennas as it is stated in [2], but, *visa versa* increases it additionally by 5..10 dB. These contradictions are probably conditioned by different laws of impedance distribution obtained in this work and analyzed in [2] (in [2], this law is uniform). The results of solution of the synthesis task show that the greater attenuation of the field is reached with the greater speed of impedance growth [1] (generally of its capacitance part) (see Fig. 2). However, the speed of impedance growth (steepness of the curves in Fig. 2) can not be made endlessly large because of construction constrains for the precision of structure manufacturing. In work [1], in order to increase the decoupling (increase the speed of impedance alteration), there is proposed to substitute the monotone growing impedance by its several periods.

The quantitative research have shown that the presence of areas with a zero impedance on the surface S_1 leads to the fast growth of magnetic field $H_z(x)$, like the behavior of the field above the heterogeneous radio line. This is seen from Figs 3 and 4 in the areas with $x \geq L$, where the impedance structure ends and the conducting surface begins. Similar phenomena are observed in all areas, where the values of reactance are close to zero or are positive ($0 < \text{Im} Z < 21$). Probably, the presence of a receiving aperture antenna will also lead to the undesirable reduction of antennas decoupling because of inhomogeneities created by the aperture receiving antenna itself.

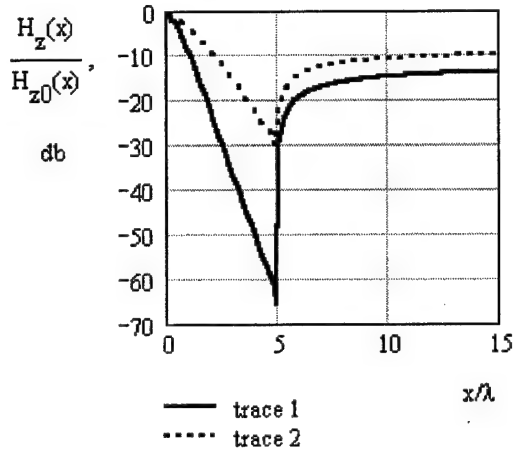


Fig. 4.

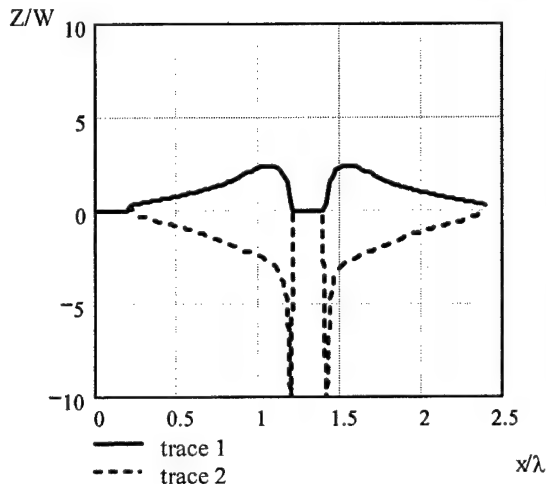


Fig. 5.

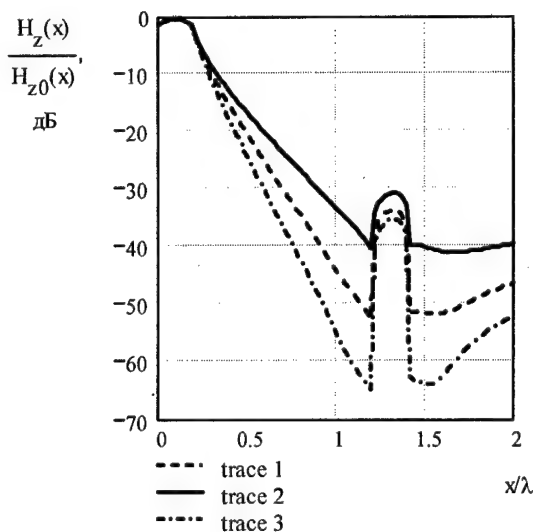


Fig. 6.

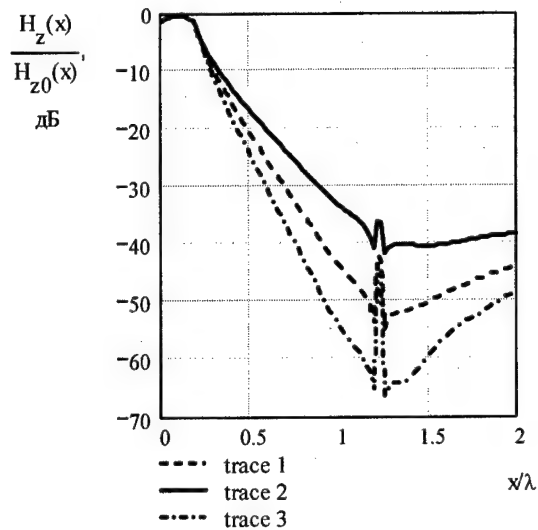


Fig. 7.

In Fig. 5, there is the law of complex impedance distribution, which provides falling of the field by the law (3) at $\alpha = 0.5k$ for antennas in the form of open ends of the waveguide (see Fig. 1) with aperture dimensions $a = b = 0.2\lambda$ and the distance between them $L = \lambda$. Behind the receiving antenna on the section, which equals to the wave length, impedance covering is realized. In Fig. 5, a zero impedance corresponds to the location of antenna apertures. For this geometry of antennas arrangement, in Fig. 6, there are graphs of distribution for different values of attenuation coefficient $H_z(x)/H_{z0}(x)$ α (of impedance). Here curve 1 corresponds to $\alpha = 0.5k$, curve 2 to $\alpha = 0.75k$ and curve 2 to $\alpha = k$. The analysis of the calculation results shows that the aperture of the receiving antenna significantly (by 10.30 dB) raises the level of the entire field in its aperture, remaining practically unchangeable for all the $\alpha > 0.75k$.

In addition, the area of the surface behind the receiving antenna practically does not influence on the behavior of the field between the antennas. Thus, the further increase of antennas decoupling with the help of impedance synthesized by the level of the complete field attenuation without taking into account the receiving antenna, is impossible. It is possible to additionally increase antennas decoupling by means of reducing the sizes of the receiving antenna aperture (b). In Fig. 7, there are graphs, which are similar to those in Fig. 6, but for $b = 0.02\lambda$. As we can see, this measure (reduction of the aperture heterogeneity) has led to additional reduction of the field by 10 dB.

It could be expected that the increase of decoupling between antennas can be achieved by means of directed properties of the transmitting antenna through the increase of its aperture dimension (dimension a , see Fig. 1). However, as the numerical research showed, the growth of the aperture dimension from $a = 0.2\lambda$ to $a = 2.2\lambda$ did not lead to significant falling of the field in the aperture of the receiving antenna. It is demonstrated in Fig. 8 for the task parameters: $a = 2.2\lambda$, $b = 0.2\lambda$, $L = \lambda$ and Fig. 9 for $a = 4.2\lambda$, $b = 0.2\lambda$, $L = \lambda$. In both cases $\alpha = k$.

Further research have shown that for effective reduction of coupling between closely located aperture antennas on the same plane, it is required to state and solve the task of synthesis of the surface impedance taking into account the presence of the receiving antenna aperture.

5. CONCLUSIONS

Thus, the task of synthesis of impedance structure has been solved. The structure provides the faster attenuation, than it is above ideally conducting surface. It has been shown that the presence of a resistive component in the impedance distribution law additionally increases the degree of antennas decoupling by 5..10 dB. It has been shown that depending on the aperture dimensions of the receiving antenna, antennas decoupling with the help of synthesized impedance without taking into account the receiving antenna, can not exceed -30..-50 dB, what is connected with the inhomogeneities caused by the aperture receiving antenna in the line of propagation of the wave radiated by the transmitting antenna along the plane where antennas are located. The growth of the dimensions of the aperture transmitting antenna (the increase of its directed properties) does not influence on the absolute level of the field in the receiving antenna aperture. In this case, decoupling grows only by means of the increase of the radiated electromagnetic wave power, which is proportional to a , at the unchangeable power of the received wave.

Thus, further increase of decoupling between antennas can be achieved only by means of solving the task of synthesis of the impedance surface in the presence of the receiving antenna.

The obtained laws of impedance distribution can be used as the independent solution of the task of EMC provision, as well as the first step in further optimization of the structure with the help of non-linear programming methods.

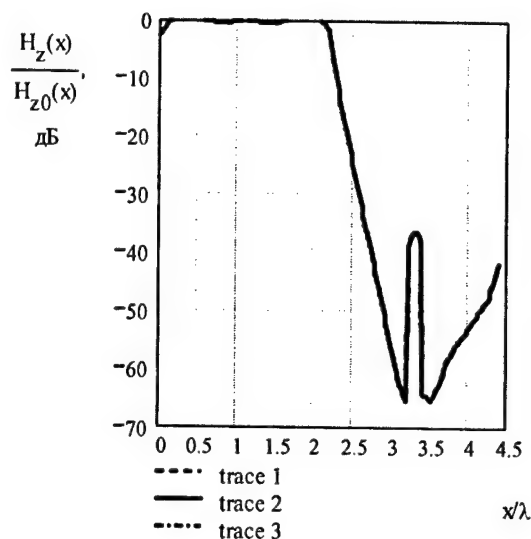


Fig. 8.

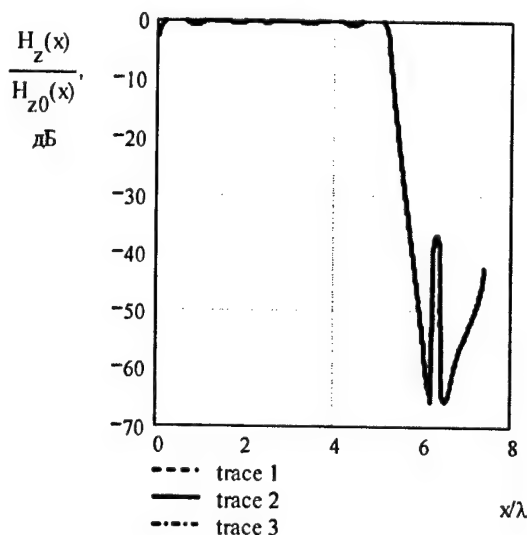


Fig. 9.

REFERENCES

1. Tereshin O. N., Sedov V. M., Chaplin A. F. Synthesis of Antennas on Decelerating Structures. Moscow: Svyaz, 1980. (in Russian)
2. Kurkchan A. G. Connection Between Antennas in the Presence of Ribbed Structures// Radiotekhnika i Elektronika).- 1977.- Vol. 7. (in Russian).
3. Martsafey V. V., Shvayko I. G. Influence of Ribbed Structures on Interaction of Near-Omnidirectional Antennas// Izvestiya Vuzov. Series Radioelektronika.- 1981.- Vol. 24, No. 5. (in Russian).
4. Tereshin O. N. Decoupling of Two slot Antennas with the Help of a Ribbed Structure Located in the Plane of slots // Radiotekhnika and Elektronika.- 1960.- Vol. 5, 12 p. 1944. (in Russian)

SYNTHESIS OF ANISOTROPIC IMPEDANCE PLANE

Y. V. Yukhanov

Department of Antennas and Radio Transmitters,
Taganrog State University of Radio Engineering, Russia
<airpu@tsure.ru; Yukhanov@tsure.ru>
<Yu_Yukhanov@tsure.ru>

Abstract

The aim of synthesis of anisotropic impedance plane reflecting a plane uniform wave in a given direction at the desired polarization is solved. The distribution of the impedance is expressed analytically and constitutes a periodic structure. The restrictions on the class of the allowable scattering patterns are formulated for the reactive values of impedance. The reflection coefficients of the no uniform anisotropic impedance plane are obtained. Numerical results are demonstrated.

The aim of the paper is to receive an impedance tensor and reflection coefficient of a heterogeneous anisotropic impedance plane that reflects an incident electromagnetic wave in the adjusted direction and on the required polarization in analytically closed form.

Let's consider the solution of the next problem. Suppose the flat electromagnetic wave $\mathbf{E}^i, \mathbf{H}^i$ falls to the heterogeneous anisotropic impedance plane S with impedance tensor \hat{Z} from the direction φ^i .

The Leontovich impedance boundary conditions are carried out on the surface S ($y = 0$):

$$[\mathbf{n}, \mathbf{E}] = -\hat{Z}[\mathbf{n}, \mathbf{H}]. \quad (1)$$

Let's consider the impedance as an often array of the orthogonal impedance strips Z_E, Z_M focused at angle of α to an axis z (fig. 1, б). It is necessary to find components Z_E, Z_M and α of \hat{Z} tensor of the passive impedance providing the adjusted mode of wave reflection from the surface $y = 0$.

Let's enter the local coordinate system (see Fig. 1б) with basis vectors $\mathbf{v}, \mathbf{u}, \mathbf{n}$ ($\mathbf{n} = [\mathbf{v}, \mathbf{u}]$; $(\mathbf{v}, \mathbf{i}) = \cos \alpha$;

$(\mathbf{u}, \mathbf{i}) = \sin \alpha$). In the given basis the impedance tensor \hat{Z} will take the next diagonal form:

$$\hat{Z} = \begin{pmatrix} Z_E & 0 \\ 0 & Z_M \end{pmatrix}, \quad (2)$$

where $E_u = -Z_E H_v$; $E_v = Z_M H_u$; \mathbf{v} and \mathbf{u} are the components of vectors \mathbf{E} and \mathbf{H} . They are connected by the next ratios:

$$\begin{cases} E_v \\ E_u \end{cases} = \begin{cases} \sin \alpha \\ -\cos \alpha \end{cases} E_x + \begin{cases} \cos \alpha \\ \sin \alpha \end{cases} E_z;$$

$$\begin{cases} H_v \\ H_u \end{cases} = \begin{cases} \sin \alpha \\ -\cos \alpha \end{cases} H_x + \begin{cases} \cos \alpha \\ \sin \alpha \end{cases} H_z.$$

If analytical performance of a required field (\mathbf{E}, \mathbf{H}) is known for $y \geq 0$ the required distributive law of the impedance can be received directly from boundary conditions.

Further let \mathbf{E} vector and tensor impedance elements Z_E, Z_M be normalized in relation to characteristic resistance of the free space W .

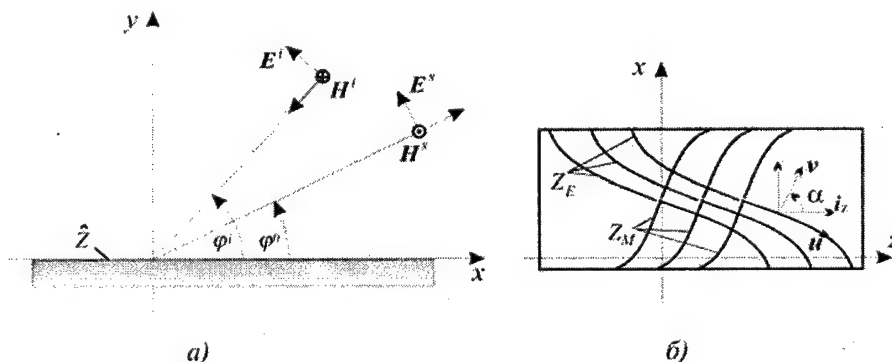


Fig. 1.

The feasibility of the passive impedance (2) ($\text{Re } Z_E \geq 0$; $\text{Re } Z_M \geq 0$) assumes the following form:

$$\begin{cases} \text{Re}\{\dot{H}_z E_x - \dot{H}_x E_z\} \geq 0; \\ \text{tg} 2\alpha \leq \frac{2 \text{Re}\{\dot{H}_z E_x\}}{\text{Re}\{\dot{H}_z E_z - \dot{H}_x E_x\}}. \end{cases} \quad (3)$$

The in equations (3) are the conditions of a physical reliability of the passive reflectors class.

Let's present the fields in the form:

$$H_z = |H_z(x, y)| e^{i\psi_H(x, y)}; \quad E_z = |E_z(x, y)| e^{i\psi_E(x, y)}.$$

When

$$E_x = \{\xi_H - i\Phi_H\} H_z; \quad H_x = -\{\xi_E - i\Phi_E\} E_z,$$

where $\xi_H = \frac{1}{k} \frac{\partial \psi_H}{\partial y}$; $\xi_E = \frac{1}{k} \frac{\partial \psi_E}{\partial y}$ - is a combination of cosines of the incident and reflection angles.

$$\Phi_H = \frac{1}{k|H_z|} \frac{\partial |H_z|}{\partial y}; \quad \Phi_E = \frac{1}{k|E_z|} \frac{\partial |E_z|}{\partial y} \frac{1}{|E_z|}.$$

As a result the in equations (3) have the next form:

$$\xi_H |H_z|^2 + \xi_E |E_z|^2 \geq 0; \quad (4)$$

$$\text{tg} 2\alpha \leq 2\sqrt{-\xi_E \xi_H} / [\cos \chi (1 + \xi_E \xi_H + \Phi_H \Phi_E) + \sin \chi (\Phi_E \xi_H - \Phi_H \xi_E)], \quad (5)$$

where $\chi = \psi_E - \psi_H$; $\xi_E \xi_H \leq 0$.

Let's consider the most practically interesting task - the synthesis of passive impedance. In this case the equations (3), (4) and (5) become equations.

The analysis of the conditions (5) shows that the orientation of the impedance strips on the surface is the function of coordinates $\alpha(x)$. Let's consider the conditions under which an angle α is constant for case when the incident and the reflective waves are flat uniform waves ($\Phi_E = 0$; $\Phi_H = 0$). In this case the equation (5) has the following kind:

$$\text{tg} 2\alpha = 2 \frac{\sqrt{-\xi_E \xi_H}}{\cos \chi (1 + \xi_E \xi_H)}.$$

As we see the angle α becomes a constant only in the next three cases:

1. $\alpha = 0.5 \arctg \left\{ 2 \frac{\sqrt{-\xi_E \xi_H}}{1 + \xi_E \xi_H} \right\}$, when $\chi = 0$;
2. $\alpha = \pi/4$, when $\xi_E \xi_H = -1$. It's the case of normal angle of the incident and reflected waves; $\alpha = \pi/4$, when $\chi = \pm \pi/2$ for any values of ξ_E and ξ_H under condition $\psi_E = \psi_H \pm \pi/2$, i. e. $\xi_H = -\xi_E$. The components of the tensor are constants for this case:

$$Z_E = -i; \quad Z_M = i.$$

Let the incident wave be H-polarized ($E_z^i = 0$):

$$H_z^i = H_0^i e^{ik(x \cos \varphi_i + y \sin \varphi_i)}.$$

Let the reflected field be the flat uniform wave as well but be E-polarized ($H_z^s = 0$):

$$E_z^s = E_0 e^{-ik(x \cos \varphi_0 + y \sin \varphi_0)},$$

where $E_0 = |E_0| e^{i\psi_0}$; $\psi_0 = \text{const}$; φ_0 - the angle of reflection.

Then $\Phi_E = \Phi_H = 0$; $\psi_H = k(x \cos \varphi_i + y \sin \varphi_i)$; $\psi_E = -k(x \cos \varphi_0 + y \sin \varphi_0) + \psi_0$; $\xi_H = \sin \varphi_i$; $\xi_E = -\sin \varphi_0$; $\chi = \psi_0 - kx(\cos \varphi_i + \cos \varphi_0)$.

As a result the conditions (4), (5) have the next form:

$$\sin \varphi_i |H_z^i|^2 = \sin \varphi_0 |E_z^s|^2; \quad (6)$$

$$\text{tg} 2\alpha = 2 \frac{\sqrt{\sin \varphi_i \sin \varphi_0}}{\cos \chi (1 - \sin \varphi_i \sin \varphi_0)}. \quad (7)$$

The equation (6) is the energy balance equation. According to the equation (7) the angle α is constant only in case of mirror reflection ($\cos \varphi_i + \cos \varphi_0 = 0$) $\chi = \psi_0 = \pi/2$. In this case α is equal to 45° .

Thus, the impedance structure does not depend on the incident direction in case of mirror reflection with plane-of-polarization rotation on 90° . The reflected and incident waves meet the next condition:

$$E_0 = i \sqrt{\frac{\sin \varphi_i}{\sin \varphi_0}} H_0^i.$$

Note, realization of often array of the orthogonal impedance strips with vary orientation is a very complex task. Therefore, let the angle α be constant and equal to 45° . Then the condition (3) becomes:

$$\text{Re}\{\dot{H}_z E_z - \dot{H}_x E_x\} = 0. \quad (8)$$

It is obvious that there must be a wave with the same polarization as incident wave in the reflected field, i.e.

$$H_y = H_0^i e^{ik(x \cos \varphi_i + y \sin \varphi_i)} + H_0^m e^{ik(x \cos \varphi_i - y \sin \varphi_i)}.$$

Under the equations (6) and (8) the waves amplitudes are meet the next equations

$$H_0^m = \frac{\sin \varphi_i \sin \varphi_0 - 1}{1 + \sin \varphi_i \sin \varphi_0} H_0^i; \quad E_0 = \frac{\pm 2 \sin \varphi_i}{1 + \sin \varphi_i \sin \varphi_0} H_0^i.$$

And tensor's components are:

$$Z_E = \frac{i}{\sin \varphi_0} \text{tg} \chi; \quad Z_E = -\frac{i}{\sin \varphi_0} \text{ctg} \chi. \quad (9)$$

According to expressions for H_0^m and E_0 the increasing difference between incident φ_i and reflecting angles φ_0 makes the efficiency of such reactance structure significantly decrease

$$\eta = \frac{\sin \varphi_0}{\sin \varphi_i} \left| \frac{E_z^s}{H_z^i} \right|^2 = \frac{4 \sin \varphi_i \sin \varphi_0}{(1 + \sin \varphi_i \sin \varphi_0)^2},$$

This result shows an imperfection of widely used polarizes consisted of parallel metal filaments system.

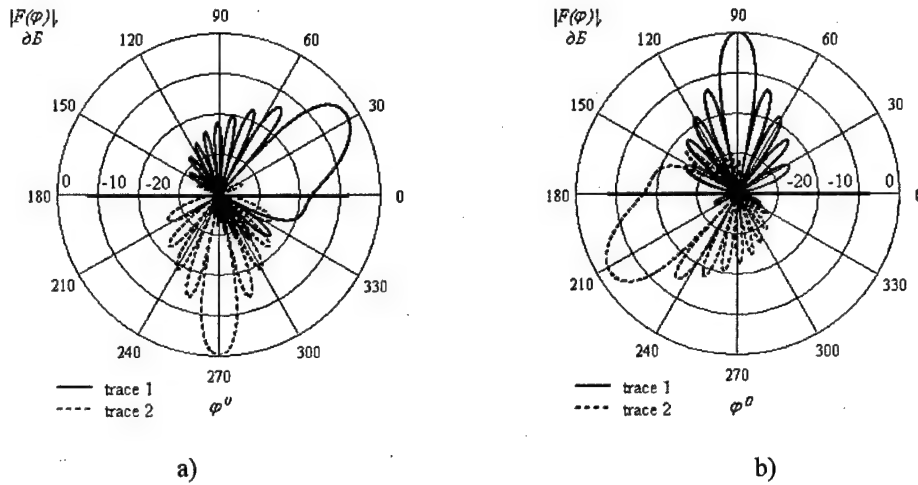


Fig. 2.

Reflection coefficient.

Let's consider the reflection coefficient of the system $P_{m,n}$ ($m, n = 1, 2$)

$$E_z^s = P_{11}E_z^i + P_{12}H_z^i; H_z^s = P_{21}E_z^i + P_{22}H_z^i. \quad (10)$$

According to the Maxwell's equations and equations (2) — (4) $P_{m,n}$ are the next:

$$\begin{aligned} P_{11} &= [Z_E Z_M \sin \varphi_i - \sin \varphi_0 + \\ &+ Z_E (\sin^2 \alpha \sin \varphi_i \sin \varphi_0 - \cos^2 \alpha) + \\ &+ Z_M (\cos^2 \alpha \sin \varphi_i \sin \varphi_0 - \sin^2 \alpha)] / \Delta; \\ P_{22} &= [\sin \varphi_i - Z_E Z_M \sin \varphi_0 + \\ &+ Z_E (\sin^2 \alpha \sin \varphi_i \sin \varphi_0 - \cos^2 \alpha) + \\ &+ Z_M (\cos^2 \alpha \sin \varphi_i \sin \varphi_0 - \sin^2 \alpha)] / \Delta; \\ P_{12} &= \sin \alpha \cos \alpha (\sin \varphi_i + \sin \varphi_0) \times \\ &\times (Z_H - Z_E) / \Delta; \\ P_{21} &= -P_{12}, \end{aligned} \quad (11)$$

where

$$\Delta = \sin \varphi_0 (1 + Z_E Z_H) + Z_E (\sin^2 \alpha \sin^2 \varphi_0 + \cos^2 \alpha) + Z_M (\cos^2 \alpha \sin^2 \varphi_0 + \sin^2 \alpha)$$

Reflected field. The reflected field is shown below:

$$\begin{pmatrix} E_z^s(r, \varphi) \\ H_z^s(r, \varphi) \end{pmatrix} = H_0^{(2)}(kr) \hat{F}(\varphi), \quad (12)$$

$$\text{where } \hat{F}(\varphi) = \begin{pmatrix} F_{\parallel E}(\varphi) & F_{\perp E}(\varphi) \\ F_{\perp H}(\varphi) & F_{\parallel H}(\varphi) \end{pmatrix}; F_{\parallel E}(\varphi), F_{\parallel H}(\varphi)$$

is the scattering pattern for the matched polarization, and $F_{\perp E}(\varphi), F_{\perp H}(\varphi)$ are for the cross polarization.

According to (11), (12) the scattering matrix \hat{F} is:

$$\hat{F}(\varphi) = \frac{k}{4} (\sin \varphi_0 + \sin \varphi_i) \int_{-\infty}^{\infty} \hat{U}(x) \Delta^{-1} e^{ikx(\cos \varphi - \cos \varphi_i)} dx,$$

where \hat{U} is a matrix 2×2 , which consists of the next elements:

$$\begin{aligned} u_{12} &= -u_{21} = \sin \alpha \cos \alpha (\sin \varphi + \sin \varphi_0) (Z_E - Z_M); \\ u_{11} &= P_{11} \Delta + (\sin \varphi - \sin \varphi_i) (Z_E Z_M + Z_{22} \sin \varphi_0); \\ u_{22} &= P_{22} \Delta + (\sin \varphi - \sin \varphi_i) (1 + Z_{22} \sin \varphi_0). \end{aligned}$$

Let's consider the case, if the impedance is passive, i.e. $Z_E = iX_E, Z_H = iX_H$.

The reflection factor P_{11} must be equal to zero to provide the full reflection of E-polarized wave with the necessary polarization rotation. P_{22} must be equal to zero in the case of H-polarized wave.

At that the tensor's components X_E, X_M and the angle α meet the next conditions:

$$\begin{cases} X_M = -\sin \varphi_{0,i} / X_E \sin \varphi_{i,0}; \\ \operatorname{tg}^2 \alpha = \frac{\sin \varphi_{i,0} (X_E^2 + \sin^2 \varphi_{0,i})}{\sin \varphi_{0,i} (1 + X_E^2 \sin^2 \varphi_{i,0})}, \end{cases} \quad (13)$$

where the first subscript is for the E-polarized wave, and the next is for the H-polarized wave.

The reflected field is the flat wave with cross polarization if

$$X_E(x) = 0.5 \left(-\xi \pm \sqrt{\xi^2 + 4 \sin \varphi_i \sin \varphi_0} \right) / \sin \varphi_{i,0}, \quad (14)$$

where $\xi = (1 + \sin \varphi_i \sin \varphi_0) \operatorname{ctg}[kx(\cos \varphi_i + \cos \varphi_0)]$.

Let's find out the components of the impedance tensor from the (13).

At that the scattering factors of the finite structure with L width (are not taking into account the edge effect) are

$$F_{\parallel}(\varphi) = 0.25kL(\sin \varphi - \sin \varphi_i) \frac{\sin U_i}{U_i}; \quad (15)$$

$$F_{\perp}(\varphi) = 0.25kL(\sin \varphi + \sin \varphi_0) \left(\frac{\sin \varphi_i}{\sin \varphi_0} \right)^{\pm 0.5} \frac{\sin U_0}{U_0}, \quad (16)$$

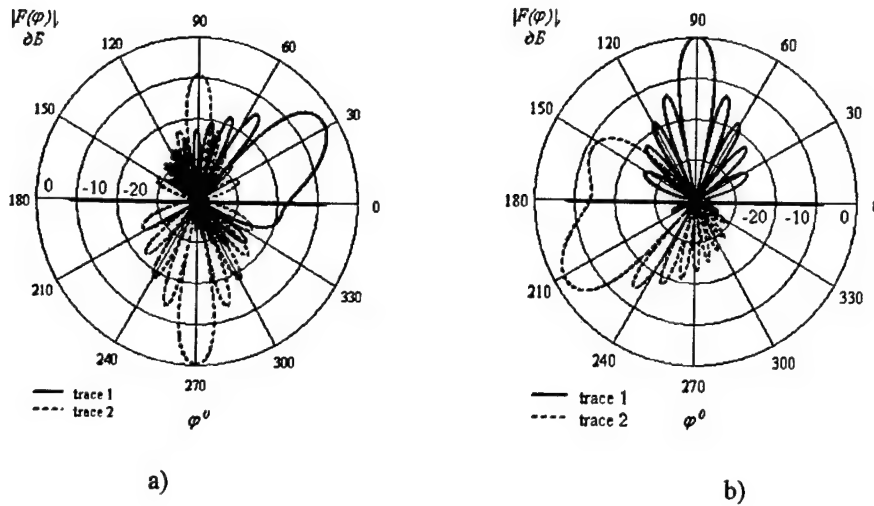


Fig. 3.

where $F_1(\varphi)$ is scattering factor for the matched polarization; $F_\perp(\varphi)$ is scattering factor for the cross polarization; $U_{i,0} = \frac{1}{2}kL(\cos \varphi \pm \cos \varphi_{i,0})$.

According to the formula (15) the involved structure is equivalent to the Kirgof's black body.

The scattering graphs calculated under the formulas (15), (16) are shown on figures 2a,b. Here the trace 1 is F_\perp , trace 2 is F_1 , $L = 5\lambda$, $\varphi_i = 90^\circ$, $\varphi_0 = 30^\circ$ (Fig. 2a) and $\varphi_i = 30^\circ$, $\varphi_0 = 90^\circ$.

There are the same graphs on the figures 3a,b for the case of structure with fixed orientation ($\alpha = 45^\circ$).

As is shown in the case of fixed angle $\alpha = 45^\circ$ the level of the main lobe for the cross polarization is

slightly smaller (on -0.5 dB) and the level of side lobe for the match polarization is greatly higher (upon to -10 dB) then the angle isn't fixed.

Thus the formula for the tensor of anisotropic impedance witch reflects an incident electromagnetic wave in the adjusted direction and on the required (cross) polarization is given in analytically closed form (13), (14). The obtained scattering factors of anisotropic impedance plane are different from what are known for a homogeneous plane. The restrictions on the class of the allowable scattering patterns are formulated (3)–(7), (8) for the reactive values of impedance.

The obtained scattering factors can be used while designing of complex form reflectors in approximate approaches (e.g. physical optics approximations).

ANALYSIS OF WAVEGUIDE-SLOT RADIATORS IN THE PRESENCE OF DISSIPATIVE MEDIUM

L. P. Yatsuk, A. A. Komyachko, Yu. V. Zhironkin, T. G. Nazarenko

V. N. Karazin Kharkov National University
4, Svobody Sq., Kharkov, 61077, Ukraine
Phone (0572)45-75-48, E-mail: <Ludmila.P.Yatsuk@univer.kharkov.ua>

Abstract

The scattering parameters of waveguide-slot radiators and coupling elements in the presence of ohmic losses in the system are under consideration. The problems of accounting dielectric losses and waveguide walls finite conductivity are solved in the cases when waveguides or slots are partially or fully filled with a lossy dielectric or are empty. The cases of dielectric slab position parallel to the narrow walls of a rectangular waveguide and broad ones are considered. The questions of eigenwaves orthogonality are discussed, the behaviour of eigenvalues of dominant wave and higher ones is studied. The ohmic losses of energy in the waveguide region containing a slot are investigated.

1. INTRODUCTION

Feeder lines with dielectric filling are used in purposes of devices miniaturisation. The theory of waveguide-slot radiators developed mainly under assumptions of an ideal dielectric and infinitely conducting waveguide walls. The slots electrodynamic characteristics in the presence of ohmic losses due to the dissipative dielectric and finite conductance of waveguide walls were not studied at all. The waveguides dielectric filling may be full or partial. The last one provides the additional degrees of freedom for the controlling the devices characteristics. In this paper the waveguide-slot radiators or coupling elements are considered with accounting losses in the dielectric, which fully or partially fills the waveguide or the slot, and losses in the imperfectly conducting waveguide walls. It is important to emphasize that not only the dominant wave but also the higher ones are responsible for energy losses. The slots scattering

characteristics are of interest. The main problems, which had to be solved, were as follows:

- investigation of full spectrum of eigenwaves in a waveguide partially filled with dissipative dielectric;
- clearing up the question of eigenwaves orthogonality;
- solving the excitation problems for slots in the waveguides with dissipative dielectric slabs and
- for slots, partly filled with dielectric;
- definition of energy losses in the vicinity of slot, caused by no ideal dielectric and waveguide walls.

2. EIGENWAVES.

Two types of a waveguide partial dielectric filling were considered (see Fig. 1).

The eigenwaves of such waveguides are the *LE*- and *LM*-modes relating the plane *yOz* in the case (a) and *xOz* in the case (b). The dominant waves in these cases are the *LE*₁₀-mode (a) and *LM*₁₁-one (b). The complex eigenvalues of these modes and higher ones can be found from the corresponding dispersion equations. The numerical realisation of a complex value problem for the structures having lossy dielectric is much more complicated then one in the case of an ideal dielectric. The power damping factor $2h''$, where $h = h' - ih''$ is a complex longitudinal wave number of a dominant mode, depends on permittivity $\epsilon' - i\epsilon''$, $\text{tg } \delta = \epsilon''/\epsilon'$, geometrical parameters and operating wavelength λ . The Napier per meter values of $2h''$, are presented in Fig. 2(a) and Fig. 2(b) for the cases (a) and (b).

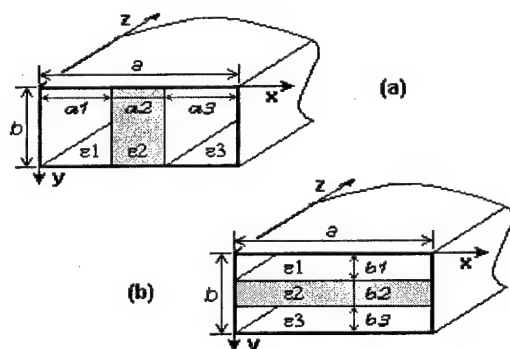


Fig. 1.

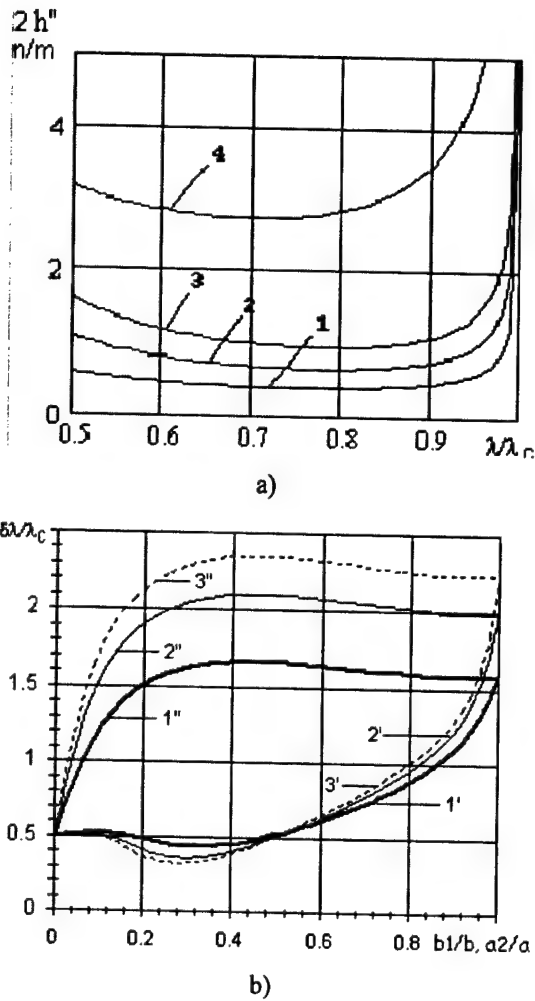


Fig. 2.

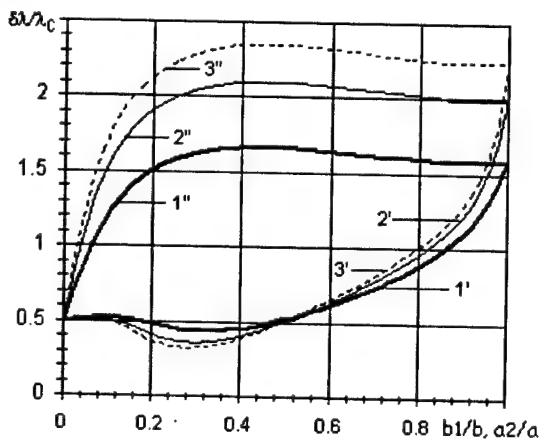


Fig. 3.

Here λ_c is a cut-off wavelength of the dominant mode when $\text{tg } \delta = 0$. The data in Fig. 2(a) are obtained for $\epsilon' = 16$, $\text{tg } \delta = 10^{-2}$ and various $a_2/a = 0.05; 0.25; 0.5; 0.7; 1$ (curves 1, 2, 3, 4, 5 correspondingly), in Fig. 2(b) — for the same $\text{tg } \delta$ but $\epsilon' = 5$ and $b_1/b = 0.1; 0.3; 0.4; 1.0$. The curves

$2h''$ as functions of λ/λ_c are not monotone. It is seen, that at the boundaries of operating band the damping factor increases in Fig. 2(a) more rapidly than in Fig. 2(b). This is probably because $\epsilon'(a) > \epsilon'(b)$ and the operating band in case (a) is sufficiently larger than in case (b). The last fact is illustrated in Fig. 3, where the differences $\delta\lambda$ between cut-off wavelengths of a dominant mode and nearest higher one normalised on $2a$ are presented (the curves 1,2,3 correspond to $\epsilon' = 10, 16, 20$, primed figures are used for the case (b), the double primed — for (a)).

In the case of higher modes, denoted with indexes μ, ν it is reasonable to investigate $\text{Re } h_{\mu\nu} = h'_{\mu\nu}$, which is equal to zero when $\text{tg } \delta = 0$. When $\text{tg } \delta = 10^{-3}, 10^{-2}, 10^{-1}$ it occurred enough to account the number of highest modes $r = \sqrt{\mu^2 + \nu^2}$ with approximately equals 1, 10, 25 correspondingly. This assertion is valid for both the *LE*- and *LM*-waves

3. PECULIARITIES OF BEHAVIOUR OF DISPERSION EQUATIONS FAR ROOTS

The far roots of dispersion equations for *LE*- and *LM*-waves behave in different ways. The transverse eigenvalue $\alpha_{\mu(\nu)}^{LE} = \sqrt{k^2 \epsilon - h_{\mu(\nu)}^2}$ of high-order *LE*-modes tend with increasing — μ and ν to $\mu\pi/a$ in (a)-case and to $\nu\pi/b$ in (b)-case, where μ and ν are numbers of the dispersion equations roots. So, starting with $\mu(\nu) > n_\gamma$, where n_γ depends on a concrete structure one can use $\alpha_\mu = \mu\pi/a$ or $\alpha_\nu = \nu\pi/b$ instead of the corresponding root of the dispersion equation. Some other situation takes place in the case of *LM*-waves. The far transverse eigenvalues α_ν^{LM} oscillate around the straight line $\alpha_\nu = \nu\pi/b$ not approaching asymptotically to it.

In Fig. 4, the solid and dotted lines show the behav-

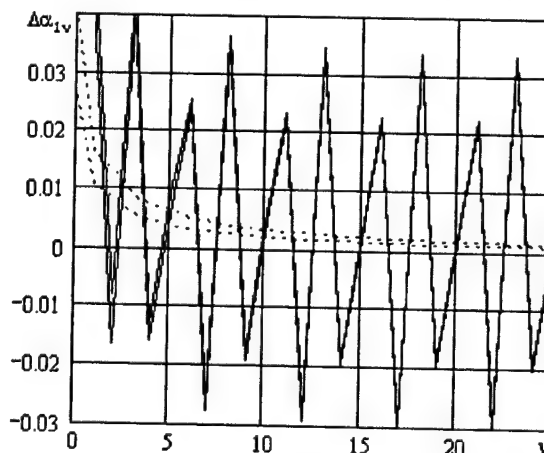


Fig. 4.

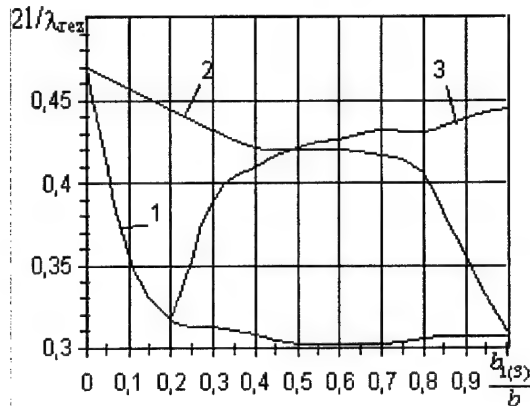


Fig. 5.

iour of the differences $(\alpha_{\nu}^{LM} - \nu\pi/b)$ and $(\alpha_{\nu}^{LE} - \nu\pi/b)$ depending on the number ν . The similar behaviour of LM -transverse eigenvalues causes complications in the process of determining the resonance length of a slot in a waveguide partially filled with dielectric. It was discovered some peculiar process of numerical results convergence. In order to obtain the stable result it is necessary to use the even number of "half-waves" in the α_{ν}^{LM} -dependence as a function of number ν . When the quantity of terms in the series is very large and the "half-wave" group of terms does not change the previous result, this rule may be neglected.

4. ORTHOGONALITY PROPERTY OF EIGENWAVES.

It is known that there are two aspects of orthogonality of eigenwaves in a waveguide — the energetic orthogonality and the mathematical one [1]. If \vec{E}^{μ} , \vec{H}^{μ} and $\vec{E}^{\mu'}$, $\vec{H}^{\mu'}$, the electric and magnetic fields of μ - and μ' -modes, satisfy the equality

$$\int_S [\vec{E}^{\mu}, \vec{H}^{\mu'*}] \vec{z}^0 dS = 0 \quad (1)$$

(\vec{z}^0 is unit vector along z -axis, S is a cross section of a waveguide), these modes are energetically orthogonal. If the equality

$$\int_S [\vec{E}^{\mu}, \vec{H}^{\mu'}] \vec{z}^0 dS = 0 \quad (2)$$

(without complex conjugation at $\vec{H}^{\mu'}$) is satisfied, the mathematical orthogonality takes place. Both kinds of orthogonality are typical for eigenwaves in waveguides fully filled with dielectric both ideal and dissipative. It was shown that in waveguides partially filled with dissipative dielectric only the energetic orthogonality is violated for the eigenwaves of the same type but various roots of dispersion equation. Both energetic and mathematical orthogonality are always saved between LE - and LM -modes.

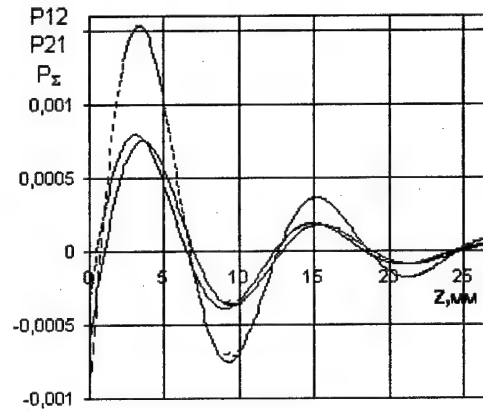


Fig. 6.

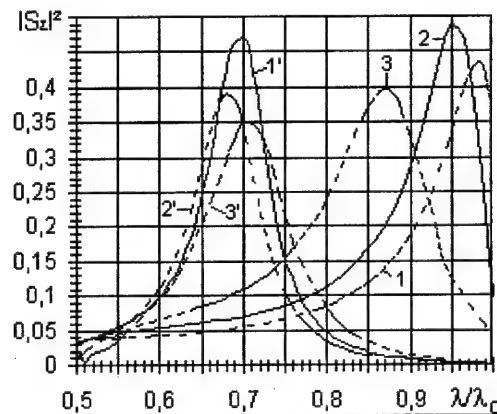


Fig. 7.

When two waves are not orthogonal their resulting flux of energy consists of sums of two own fluxes $P_{11} + P_{22}$ and two mutual ones $P_{12} + P_{21}$. The last sum changes its sign along z -axis (see Fig. 6). Due to this the resulting flux of energy decreases more or less rapidly along z -axis. It means that dielectric in the waveguide is heated inhomogeneously. At the steep parts of the line representing total flux it is heated more, at the slanting parts — less.

Here the flux $P_{12} + P_{21}$ is presented for LE_{10} and LE_{30} -waves interaction under assumption of 3-mode regime, $\epsilon' = 16$, $\text{tg } \delta = 10^{-2}$.

5. SLOTS IN A WAVEGUIDE PARTIALLY FILLED WITH DIELECTRIC

The case Fig. 1(b) was chosen for studying electrodynamics parameters of a transverse slot in a broad waveguide wall. The eigenwaves method was used for solving the excitation problem. The electrical length of resonance slot $2l/\lambda_{res}$ was analysed when dielectric slab with increasing width was situated under a slot (Fig. 5, curve 1 for b_1), on the opposite wall (curve 2 for b_3) and when the slab of thickness 2 mm was shifted from the upper wall where the slot is cut to the lower one (curve 3). It is seen that $2l/\lambda_{res}$ diminishes with in-

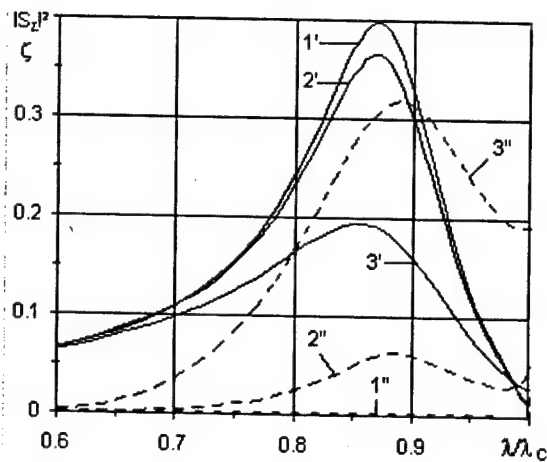


Fig. 8.

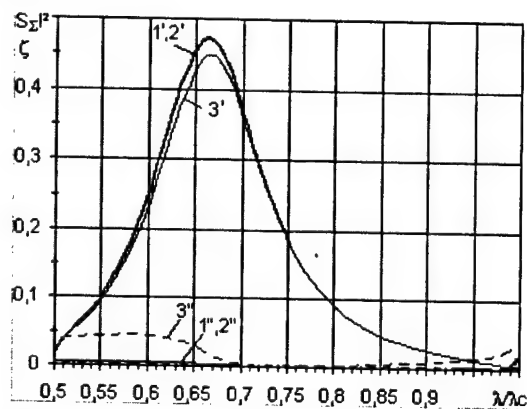


Fig. 9.

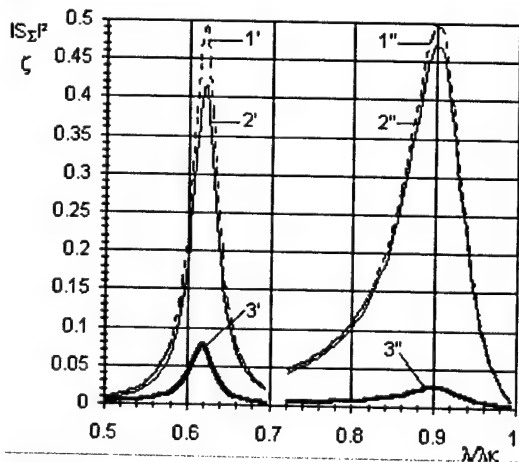


Fig. 10.

creasing the slab width. It happens very quickly when dielectric is near the slot and at first slowly enough and afterwards quickly, when the slab is against the opposite wall. The behaviour of radiation coefficient in the operating band is shown in Fig. 8 for slots of length $2l=16$ mm and $2l=10$ mm (primed numbers). The numbers 1,2,3 correspond to $b_1=2$ mm, 4 mm, 6 mm for both slots. These results are obtained for the case of an ideal dielectric ($\text{tg } \delta = 0$). When the losses appear in the slab situated near a slot the radiation coefficient noticeably

diminishes (Fig. 8, curves 1', 2', 3' for $\text{tg } \delta = 0, 10^{-2}, 10^{-1}$, $2l = 16$ mm, $b_1 = 4$ mm). Curves 1'', 2'' and 3'' show coefficient of losses ζ for these $\text{tg } \delta$. When the same dielectric slab adjoins to the opposite wall the losses with $\text{tg } \delta = 10^{-2}$ practically are not noticeable (Fig. 9).

The maximum ζ observed at the resonance frequency [2].

6. SLOTS PARTLY FILLED WITH DIELECTRIC

In slot antenna technique sometimes controlling elements (for example *p-i-n*-diodes) are put into a slot. This controlling element may be modelled as a lossy dielectric slab in the slot. It is interesting to know how much energy is spent in the dielectric slab.

The problem of two waveguides coupling through a transverse slot with dielectric slab has been solved. The waveguides were supposed to be rectangular, the slot was cut in their common broad wall. Elements of scattering matrix of the given coupling element were calculated using a set of LE_{q0} -functions for approximation the field in the slot. It has been shown that the slot resonance wavelength in the presence of dielectric slab is shifted to a more long wavelength and practically does not depend on $\text{tg } \delta$. Due to the losses in dielectric some part of energy is spent on its heating. The ohmic losses of energy ($\zeta = P_{\text{loss}} / P_{10}$) increase with permittivity ϵ . The character of this change is complicated enough. At full filling slots with dielectric having various ϵ and choosing slot lengths providing the resonance at the same frequency we have the following results when $\text{tg } \delta = 10^{-3}$. The values of ζ inside the intervals of ϵ from 1 to 2, 2 to 5, 5 to 20 do not exceed values 0.7 %, 7 %, 10 %. It is seen that in the last interval the growth of losses is slowing down because with increasing ϵ the slot length diminishes very much. The similar dependence of ζ as function of ϵ is saved at the partial filling of the slot with dielectric. Under condition of constant slot length and resonance frequency with increasing ϵ , are not changed. At the interval ϵ changing from 2 to 5 in spite of slab size decreasing ζ is growing like in the case of full filling. At the great ϵ the slab is very small but nevertheless the field is concentrated in dielectric. This causes increasing of ζ as by the full slot filling.

At the simultaneous variation of the slot length and resonance frequency (when the slab size is constant) the level of losses depends on the degree of slot filling with dielectric. The higher it is the greater are losses. It is well seen in Fig. 10 where the radiation coefficients $|S_{\Sigma}|^2$ (curves 1, 2) and coefficient of losses ζ (curves 3) are presented for $\epsilon' = 16$, slab width 1 mm. Primed and double primed numbers of curves are used correspondingly for the slots of length $2l = 10$ mm and $2l = 17$ mm. The curves 1, 2 are used for the ideal (1) and lossy (2) dielectric. It is seen that losses shown in Fig. 10, calculated for

$\text{tg} \delta = 10^{-2}$ at the resonance frequencies have the level about $\zeta = 7\%$ for the slot $2l = 10$ mm and $\zeta = 2,5\%$ for the slot $2l = 17$ mm (curves 3). Here the mode LE_{10} in the slot is resonance.

The frequency characteristics of radiation and loss coefficients when LE_{30} -mode is resonance are shown in Fig. 11. Here the slot is almost fully filled with dielectric (nearly 0,7 of its length) It is seen that the level of losses is much higher here. Even at $\text{tg} \delta = 10^{-2}$ they are noticeable ($\zeta = 7,5\%$ at resonance). When $\text{tg} \delta = 10^{-3}$, we have $\zeta = 25\%$ whereas $|S_{\Sigma}|^2$ is less than 15 %. The bands of radiation in these cases are very narrow. Thus, it means that if super-narrow high quality radiation band ($\zeta \leq 1\%$) is needed (which can be obtained at resonance of the third harmonic [3]) it is necessary to use a super high-quality dielectric with $\text{tg} \delta \leq 10^{-5}$.

7. OHMIC LOSSES IN A WAVEGUIDE WALLS NEAR A SLOT

Losses of power in waveguide walls due to their finite conductance were calculated in the region of longitudinal slot cut in the broad wall of a rectangular waveguide, excited with a wave H_{10} . The expressions for the field excited by the slot were modified using the complex longitudinal wave number according to [4]. The electric field inside a skin-layer was found using the approximate Leontovich boundary conditions. The problem was solved using the approach of approximation the field in the slot with the function $V \cos(\pi u / 2l) / d$, where u is a coordinate along the slot counted off its center, V is an amplitude coefficient having a sense of the voltage between slot edges where $u = 0$, d and $2l$ are the width and the length of the slot. The finite thickness of the waveguide wall was taken into account. The power lost in the copper walls of a waveguide with cross section 23×10 mm at scattering dominant mode field by slots of length 13, 16 and 19 mm is represented in Fig. 12 (the curves 1, 2, 3 correspondingly).

Here the ratio $\zeta = P_{\text{loss}} / P_{10}$ is shown in the operating band of the waveguide. It is seen that the losses increase at resonance frequencies of slots and near cut-off wavelength. These losses are appreciably greater than ones in the waveguide without a slot (curve 4). In systems having many slots these losses have to be taken into account.

8. CONCLUSION

As a result of investigations carried out it was shown the following. In a waveguide filled with layered lossy dielectric the orthogonality of eigenwaves is violated. In multimode regime it leads to an inhomogeneous dielectric heating along the waveguide axis. If $\text{tg} \delta \leq 10^{-3}$ this effect may be neglected. In the presence of inhomogeneities losses of energy grow due to higher-order modes. They grow with permittivity ϵ and with nearing dielectric layer to the slot.

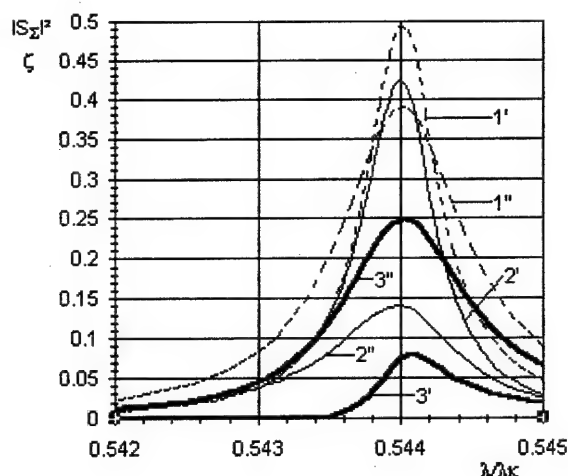


Fig. 11.

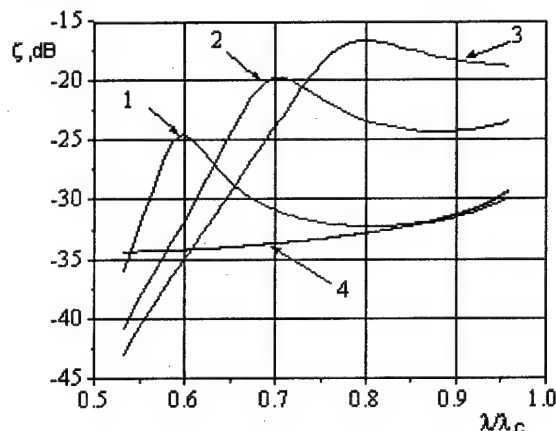


Fig. 12.

Losses in controlling elements put into radiating slot are much greater than ones in a waveguide filled with imperfect dielectric. Here $\text{tg} \delta = 10^{-3}$ in the case of $\epsilon > 10$ may cause losses up to 25 % of incident wave power if the slot is resonance at the third harmonic of distribution function of field in it. The losses due to the waveguide walls imperfect conductance are noticeable as well at the slot resonance frequency.

REFERENCES

1. Veselov G. I., Rayevskiy S. B. Layered metal-dielectric waveguides. M.: Radio and Svyaz', 1988, 247 p. (in Russian)
2. Yatsuk L. P., Nazarenko T. G., Scattering from the slots in a waveguide filled with a lossy dielectric // Radiophysics and Electronics. — 2002. — 7, Special issue. — P. 240-246 (in Russian).
3. Yatsuk L. P., Podcheko A. V., Reimer V. V. Waveguide waves scattering by narrow slots with stratified dielectric // URSI Proceedings of the International Symposium on Electromagnetic Theory. — St. Petersburg. — 1995. — P.39-41
4. Kisun'ko G. V. Electrodynamics of the Hollow Systems, L.: VKAS, 1949. — 426 p. (in Russian)

THE SYNTHETIC APERTURE METHOD IN THE ENVIRONMENT MICROWAVE INTERFEROMETER RADIOMETRY

B.G. Kutuza and G.K. Zagorin

Institute of Radio Engineering and Electronics, Russian Academy of Sciences (RAS),
Mokhovaya str. 11, 125009, Moscow, Russia <kutuza@mail.cplire.ru>

Abstract

The basic principles of space-borne two dimensional synthetic aperture microwave polarimetric interferometer function are considered. The main advantages of these systems over the well-known systems ESMR, SMMR and SSM/I are: a high rate of the observation scene image construction; the fine angular resolution; besides, they have no movable onboard construction elements on the spacecraft board, like the scanning antenna, and etc. The advantages of the synthetic aperture systems with hexagonally sampled interferometric radiometers are discussed.

Keywords: microwave emission; antenna configuration; synthetic aperture; spacecraft visibility function; angular resolution; radiometric sensitivity.

1. INTRODUCTION

The Earth both atmosphere and surface microwave emission Stokes vector measurements require both a high spatial resolution sources emission and a high radiometer receiver sensitivity [1]. A continuous progress in the digital signal processing device technology, as well as in the radiometric signal processing, allows one to hope that the combination of high sensitive polarimetric millimeter-wave radiometers and the techniques of digital synthesis two-dimensional aperture does provide both the space and radiometric resolution of the microwave sources. The microwave image of precipitation is obtained by means of the 2-D inverse Fourier transformation visibility function samples measured with the interferometer. The problems of a similar type in radio astronomy are solved successfully since long ago with the multi-element interferometers and the Earth rotation [2-4]. However, the observations of the Earth surface from satellites are characterized by much shorter integration time than in radio astronomy. Besides, it is not desirable to have movable onboard construction elements on a spacecraft board, like the scanning antenna, and etc.

Our aim is to show for some exemplary interferometer configurations, that the digital synthesis of two-dimensional aperture based on the modern signal processing technology allow one to provide both the space and the radiometry resolution of the microwave emission sources, which is necessary for the solution of remote sensing current problems in the parameter determination of precipitation, sea surface state and the ground cover by the observations from spacecraft.

2. THE BASIC PRINCIPLES OF A SPACE-BORNE RADIOMETRIC INTERFEROMETER OPERATION

Let us assume that \vec{B} is the base line; $\vec{s}(t)$ is the phase center position, \vec{b} is the projection of \vec{B} on the perpendicular to $\vec{s}(t)$ plane; $\vec{\sigma}$ is an elementary square position vector on the ground within the footprint; \vec{r}_j is the irradiator response function of the array element j ; \vec{E}, \vec{E}_u are the complex electric field strength vectors of the polarized and unpolarized part of the receiving wave, respectively; ϵ_j, ϵ are the ellipsis angles and ψ_j, ψ are the orientation angles of this j -th irradiator and the incident wave, respectively.

Then the polarimetric radiometry correlator response to a distributed source is [2]:

$$\vec{R}(t) = \exp[j2\pi(\vec{B}\vec{s}(t))] \vec{V}(\epsilon_m, \epsilon_n, \psi_m, \psi_n, u_m, v_n), \quad (1)$$

where the visibility function is as

$$\vec{V}(\epsilon_m, \epsilon_n, \psi_m, \psi_n, u_m, v_n) = \int_{-\infty}^{\infty} d\vec{\sigma} \exp[j2\pi\vec{b}\vec{\sigma}] \times \quad (2)$$

$$\times \vec{T}_B(\vec{\sigma}, \vec{b}, \epsilon, \epsilon_n, \psi, \psi_n),$$

and the vector of a brightness temperature

$$\vec{T}_B(\vec{\sigma}, \vec{b}, \epsilon, \epsilon_n, \psi, \psi_n) \propto \quad (3)$$

$$(\vec{r}_m \cdot \vec{E})(\vec{r}_n \cdot \vec{E})^* + \frac{1}{2}(\vec{r}_m \cdot \vec{r}_n) |\vec{E}_u|^2.$$

The problem of synthetic aperture polarimetric interferometry is the retrieval of the surface distribution $\vec{T}_B(\vec{\sigma}, \dots)$ from the measured up values of $\vec{V}(\dots)$ by means of resolution of the inverse problem for (2). In equations (2,3) $\vec{T}_B(\dots)$ is a combination of the bright-

brightness temperature Stokes vector components [5] $\{T_I, T_Q, T_U, T_V\}$.

On the other hand, in accordance with the Van Cittert-Zernike theorem [3], the visibility function samples $\bar{V}_{mn}(u, v)$ are the 2-D Fourier transform of the brightness temperature vector $\bar{T}_B(\xi, \eta)$ variations (where the direction cosine with respect to x, y axes $(\xi, \eta) = (\sin \theta \cos \phi, \sin \theta \sin \phi)$) within the image, it is found as the complex cross correlation between the analytic signals from two antennas $\bar{s}_m(t)$ and $\bar{s}_n(t)$. Let us assume here that the angle brackets $\{\}$ denote time averages (an ergodic process is assumed), K_m, K_n are constants depending on the properties of the corresponding receiver chain, the normalized baseline coordinates $(u, v) = (D_x, D_y)/\lambda$, $\Delta D = D_n - D_m$ - is the difference of distances from the two antennas to a point in direction (θ, ϕ) , $r_{mn}(\Delta D/c)$ is a function that describes the effect on the correlation when the difference in time between the signals is large, in radio astronomy it is called "delay", "bandwidth pattern", or "fringe-washing function", and it depends on the receivers band-pass voltage transfer functions $H_m(f), H_n(f)$ [3]:

$$r_{mn}(\Delta D/c) = F^{-1}[H_m(f - f_c)H_n^*(f - f_c)],$$

where f_c is the center frequency. For a rectangular shape filter response, $r_{mn}(\Delta D/c) = \sin c(\pi \Delta f \cdot \Delta D/c)$, where Δf is the receiver frequency bandwidth. The antenna pattern $F_m(\xi, \eta), F_n(\xi, \eta)$ includes the amplitude and phase ripples, that may differ from one antenna to another,

$$\Delta D/\lambda \approx u \sin \theta \cos \phi + v \sin \theta \sin \phi, \quad (4)$$

where λ is the wavelength,

$$\begin{aligned} \bar{V}(u_{mn}, v_{mn}) &= \frac{1}{2} E\{\bar{s}_m(t)\bar{s}_n^*(t)\} = \\ &= \iint_{\xi^2 + \eta^2 \leq 1} \bar{T}(\xi, \eta) \bar{r}_{mn}(\frac{\Delta D}{c}) \exp(-j2\pi \frac{\Delta D}{\lambda}) d\xi d\eta, \quad (5) \\ \bar{T}(\xi, \eta) &= \frac{\bar{T}_B(\xi, \eta) K_m K_n}{(1 - \xi^2 - \eta^2)^{1/2}} F_m(\xi, \eta) F_n^*(\xi, \eta). \quad (6) \end{aligned}$$

$\bar{T}(\xi, \eta)$ is the so-called «modified brightness temperature vector». An estimation of the modified brightness temperature vector is obtained by means of the inverse Fourier transform of the product of the visibility function and the weighing function $W(u, v)$ [6,7]:

$$\begin{aligned} \bar{T}(\xi, \eta) &= A \sum_m \sum_n W(u_{mn}, v_{mn}) \bar{V}(u_{mn}, v_{mn}) \times \\ &\times \exp[j2\pi(u_{mn}\xi + v_{mn}\eta)]. \quad (7) \end{aligned}$$

A is a pixel area in the (u, v) plane.

3. THE CHOICE OF THE ANTENNA CONFIGURATION

Mutual disposition of individual antenna within antenna configuration must provide whole and regular cover of (u, v) - plane, to synthesis maximal symmet-

ric synthetic aperture pattern. For example, «+» - shape configuration make sure whole cover of square (u, v) -plane. Another example is a "T"-shape configuration where one of the cross arms is absent, therefore it fills in only half (u, v) -plane, but that is enough, due to the symmetry property (l'Hermite condition) of the visibility function

$$\bar{V}(u, v) = \bar{V}^*(-u, -v). \quad (8)$$

It is shown in [3], there is simple antenna configuration which is formed by three equal length arms which have one common point and the equal angles between them. Besides, minimal abundance "Y"-shape individual antenna configuration possesses valuable qualities. For example, synthetic beam width (angular resolution) is just the same for its different cross-sections of the beam. The shape of (u, v) - plane, covered by such configuration is hexagon, it is particularly important for the processing, because one can cover the total spatial frequency (u, v) - plane by hexagonal cells without gaps. In the processing, due to property (8), it is enough to consider half (u, v) - plane only. "Y"-shape configuration is a simplest one, but not single. Examples of another synthetic aperture configurations with the total covering of hexagonal domain within (u, v) - plane are presented in [8]. It is shown that such a configuration is, for example, hexagon with the equal length of the sides $q+1$ ($q \geq 2$), five (of six) sides of it being filled by individual antenna, distributed equidistantly with distance z . In this case hexagonal spatial frequency domain of radius $2q$ is covered. The number of individual antennas in this configuration is $N = 5q + 1$, and the number of points within half baseline domain is $N_b = 3q(2q + 1)$. The synthetic beam shape in this case is determined by

$$\Phi(l, m) = \sum_{n=1}^{N_b} \cos\{(2\pi/\lambda)[lDu(n) + mDv(n)]\}, \quad (9)$$

where λ is the wavelength; $l = \sin \theta \sin \varphi$, $m = \sin \theta \cos \varphi$; θ is the angle with the interferometer plane normal; φ - azimuth; Du and Dv are the base projection to spatial frequency axes u and v . Let $a = 2qz$ is the hexagon side length within (u, v) plane, $\xi = a\pi l/\lambda$, $\eta = a\pi m/\lambda$, then expression for synthetic beam shape transformed to the following form

$$\begin{aligned} \Phi(\xi, \eta) &= (\xi \cos \xi \cos(\sqrt{3}\eta) - \sqrt{3}\eta \sin \xi \times \\ &\times \sin(\sqrt{3}\eta) - \xi \cos(2\xi)) / [12\xi(\xi^2 - 3\eta^2)], \quad (10) \end{aligned}$$

This configuration antenna pattern is close to antenna pattern of continue circular aperture of "average" radius $r_{cp} = (1 + \sqrt{3}/2)qz$:

$$\Phi_0(\xi) = J_1(2r_{cp}\xi)/(r_{cp}\xi), \quad (11)$$

where J_1 is the first order Bessel function. Eqs. (10) and (11) are distinguished only by side lobes. The main beam of circular aperture is close to hexagonal interferometer main beam.

The considered hexagonal configuration of individual antenna isn't the most effective. If some of antennas are transferred within inner domain of configuration then their number can be reduced. It is suggested to estimate the configuration efficiency by ϑ parameter, which equal to relation base quantity [8]:

$$N_{\max} = 2.5q(5q + 1), \quad (12)$$

$$\vartheta = N / N_{\max} = 0.48[1 + 0.3/q + O(q^{-2})], \quad (13)$$

The ϑ value of this configuration changes from 0.545 at $q = 2$ to 0.48 at large q . However if hexagon sides with length $2q$ are filled through one by three antennas, and one of antennas is placed in center, then this antenna configuration $\vartheta = 0.667$, and the total number of individual antennas is equal 10. It is possible to construct hexagonal configuration with more value of ϑ . From geometry it is known that if number of polygon sides is more than 6, it is impossible to cover plane without gaps. Consequently there are no configurations of more degree symmetry than hexagonal, which provide regular (equidistant) points accommodation within (u, v) plane. Configuration of individual antenna determines the necessary number of correlators for synthetic aperture. Thus in this case one can see advantages of hexagonal configuration, too. For example, abovementioned 10-elements configuration with $q = 2$, $\vartheta = 0.667$, which allow to measure 30 spatial harmonics, allows to have 5 correlators.

4. THE ADVANTAGES OF A HEXAGONAL GRID

Hexagonal samples produced by the hexagonal configuration of antenna comparably reduce both the computer memory volume and the number of arithmetic operations in computer processing of visibility samples. Other advantages of a hexagonal grid, in comparison with a rectangular one, are that in each record point of hexagonal lattice, there are six equidistant neighbouring points. Additional, it is shown [9], the hexagonal 2-D discrete fast Fourier transform (DFFT) may be determined and realized more effectively than the rectangular DFFT, because it needs 25% less operational memory volume and together with Rivard 2-D gives 25% economy in calculation time, too.

Thus antenna hexagonal configurations, for example, "Y", "+", or "Δ"-shaped, in synthetic aperture systems are optimal in construction sense and adequate optimal algorithms of measurement information massive processing are provided.

5. THE OPERATION PECULIARITIES

It can be shown that the interferometer observation scene radius r_c is limited by the relationship

$$r_c \leq \frac{3}{20} \left(\frac{H}{\cos \theta B_{\max} \Delta f} \right), \quad (14)$$

where H (km) is altitude of spacecraft, and Δf (GHz), B_{\max} (m) is array maximal baseline value. The individual antenna size d in mm (like λ) is determined by the condition

$$(\lambda/d)H \geq r_c. \quad (15)$$

For the integration time τ (sec) we obtain

$$\tau = r_c / (v_{sat} m \cos \theta), \quad (16)$$

where v_{sat} is the speed of satellite over ground (equal 7.2 km/s) and m is the number of polarization measurements conducted during the observation time of the scene.

6. THE ANGULAR RESOLUTION

In order to estimate the angular resolution of a synthetic aperture radiometer the ideal system array factor is introduced (or impulse response to the point source, that is point spread function) $AF^0(\xi, \eta)$ [6,7]

$$AF^0(\xi - \xi', \eta - \eta') = \iint_S W(u, v) \exp(j\Phi) du dv, \quad (17)$$

$$\Phi = 2\pi[u(\xi - \xi') + v(\eta - \eta')], \quad (18)$$

$$\phi' = (u\xi' + v\eta') / f_c.$$

An estimation of the modified brightness temperature vector is given by [6,7]

$$\tilde{T}(\xi, \eta) = \iint_{\xi^2 + \eta^2 \leq 1} AF^j(\xi, \xi', \eta, \eta') \tilde{T}(\xi', \eta') d\xi' d\eta'. \quad (19)$$

Angular resolution depends on frequency bandwidth [7]

$$\frac{\Delta\alpha_{-3dB}^f}{\Delta\alpha_{-3dB}^0} = \left(1 + \frac{W^2 \tan^2 \theta}{3(\Delta\alpha_{-3dB}^0)^2}\right)^{1/2}, \quad (20)$$

where $W = \Delta f / f_c$, $\Delta\alpha_{-3dB}^0$ is the 3 dB bandwidth. As a first approximation of $\Delta\alpha_{-3dB}^0$, we can use expression from [10]

$$\Delta\alpha_{-3dB}^0 = \lambda / B_{\max}. \quad (21)$$

The relationship for the pixel size is

$$p_{\perp} = \lambda H / (B_{\max} \cos \theta). \quad (22)$$

From this equation one can calculate the value of B_{\max} , if we assume that the other values are known.

7. THE RADIOMETRIC SENSITIVITY

If ΔT is radiometric sensitivity; and $T_{sys} = T_A + T_R$ is the total «system» noise, where T_A, T_R are the antenna temperature and the receiver's noise temperature, then [11]

$$\Delta T = \frac{T_{sys}}{(2\Delta f \cdot \tau_{eff})^{1/2}} \frac{1}{N_b} \frac{A_{syn}}{A}, \quad (23)$$

N_b^2 is a number of independent baselines, and τ_{eff} is the effective integration time, A_{syn} is the effective area of the synthesized beam, and the product $N_b A$ is the effective area of the antennas actually used in the array. Let us assume that L is the length of each arm of «T», «+» and «Y» arrays, and d is the width of arm (dimension of the individual antennas in the array). Taking into account also the possibility to improve the sensitivity by averaging pixels [11], we consider the attainable sensitivity of these type antennas at wavelength $\lambda = 22.5$ mm, 8.6 mm, and 3.3 mm. For «T»-

Table 1. Some calculated interferometer parameter values.

λ , mm	22.5	8.6	3.3
p_{\perp} , m	850	300	100
Δf , GHz	0.113	0.105	0.091
$\tau_{eff} \Delta f$	3.73E8	3.47E8	3E8
B_{max} , m	14.97	16.22	18.67
d , m	0.18	0.0688	0.0264

arrays ($A_{syn} = L^2, A = d^2, N_b = L/d$) with the pixel averaging [11] we obtain:

$$\Delta T = \frac{T_{sys}}{(\Delta f \cdot \tau_{eff})^{1/2}} \cdot \left(\frac{L}{2d}\right)^{1/2}, \quad (24)$$

and for «+» cross-shape arrays ($A_{syn} = L^2, A = d^2,$

$N_b = \frac{L}{2^{1/2}d}$) and «Y»-shape arrays ($A_{syn} = \frac{3^{3/2}}{2} L^2,$

$A = \frac{3^{1/2}}{2} d^2, N_b^2 = \frac{9}{2} \frac{L^2}{d^2}$) with the pixel averaging

the same expression with factor $\sqrt{2}$ is true as well for the «T»-shape arrays.

If we assume the following parameters: satellite altitude $H = 400$ km, angle of observation $\theta = 45^\circ$, radius of observed scene $r_c = 50$ km, number of polarization measurements $m = 3$, system noise temperature $T_{sys} = 1000$ K, then we obtain from (16) $\tau = 3.3$ s. Then if we would demand for the pixel size p_{\perp} , we obtain the values of $\Delta f, d, B_{max}, \Delta T$ for each wavelength presented in tables 1 and 2.

One can see from eqs. (14), (22), (23) that $\Delta T \propto H/L, \Delta f \propto H/L, p_{\perp} \propto H/L$, if $r_c = \text{const}$, therefore it is possible to improve sensitivity ΔT by making worse the spatial resolution p_{\perp} .

8. CONCLUSION

Here, a theoretical base is built for the interpretation of the measurement results, which uses the generalized Van Cittert-Zernike theorem. In accordance with this theorem, the visibility function samples $\tilde{V}_{mn}(u, v)$ are the 2-D Fourier transform of the brightness temperature vector $\tilde{T}_B(\xi, \eta)$ variations within the image. The visibility function is found as the complex cross correlation between the analytic signals from two antennas. The microwave image of spatial distribution of sources emission is obtained by means of the two-dimensional inverse Fourier transformation of the visibility function samples, measured with interferometer.

The optimal configurations of individual antenna, which allow to cover (u, v) plane by minimal abundance number of the visibility function samples, without overlapping in a best way, are produced. These antenna configurations divide spatial frequency plane by hexagonal cells. It gives a chance to obtain the maximal symmetrical synthesized beam with the minimal level of side lobes after a computer processing.

Table 2. Comparison of the sensitivity, calculated for several types of radiometers.

Array	λ , mm	22.5	8.6	3.3
«T»	L , m	10.6	11.47	13.2
«T»	ΔT , K	0.28	0.49	0.91
«+»	L , m	7.5	8	9.3
«+»	ΔT , K	0.33	0.58	1.09
«Y»	L , m	8.6	9.4	10.8
«Y»	ΔT , K	0.358	0.628	1.1

Synthetic aperture interferometer radiometric resolution may be improved by the computer processing, for example, with method of averaging pixels, or by receiver frequency bandwidth expansion.

For the computer processing of the hexagonal visibility samples, Revard's method 2-D DFFT (discrete fast Fourier transform) can be used. It allows one to reduce both the time of calculations and the necessary volume of computer memory considerably, due to the hexagonally sampled grid.

The results of the synthetic aperture microwave polarimetric interferometer parameter estimations show that it is possible to measure from space the first three Stokes vector components of sea and land microwave emission with a radiometric resolution of 1 K if the radiometer receiver bandwidth is 100 MHz. In this case a spatial resolution of 0.5-1.0 km can be reached at the wavelengths of 0.33-2.2 cm (frequencies of 90-13.5 GHz) with a length of 10-15 m for the interferometer arms. The «Y»-shape arrays configuration is the most perspective because of the constructive advantages and the minimal abundance of measurements.

REFERENCES

1. Zagorin G., *et al.* Proc. EUSAR' 2000, 23-25 May, 2000, Munich, pp.539-542, 2000.
2. Fomalont E.B. and Wright M.C.H. Interferometry and aperture synthesis, in Galactic and Extragalactic Radio Astronomy, pp.256-290, eds. G.L. Verschuur and K.I. Kellerman, Springer-Verlag, New York, 1974.
3. Thompson A.R., *et al.* Interferometry and Synthesis Radio Astronomy. John Wiley & Sons, New York, 1986.
4. Welch W.J., *et al.* Astronomy & Astrophysics, 59, 379-385, 1977.
5. Kutuza B.G., Zagorin G.K. Radio Science, 2003, v.38, No 3, 8055, doi: 10.1029/2002RS002651, MAR 20-1÷MAR 20-7.
6. Bara J., *et al.* Radio. Sci., 33(5), 1459-1473, 1998.
7. Camps A., *et al.* IEEE Trans. on Geos.&Remote Sens., 36 (5), 1835, 1998.
8. Sodin L.G. and Kopilovich L.E. Izv. VUZov, Radiophysika, vol. XLII, No 4, 345-349, 2000.
9. R.M. Mersereau IEEE Trans. 1979, v. 67, No 6, pp.930-949.
10. Peichl M. Radio Sci., 33(3), 781-801, 1998.
11. Le Vine D.M. Radio Sci. 25(4), pp.441-453, 1990.
12. Zagorin G.K., Kutuza B.G. in book: Voprosi perspektivnoi radiolokatsii, edit. A.V.Sokolov, Radio-tehnika, pp 464-486, 2003.

CALCULATING OF MUTUAL COUPLING COEFFICIENTS IN PRESENCE CYLINDER

M. Yu. Zvezdina

Rostov military institute of Missile Corps,
Rostov-on-Don, Russia
<zvezd@jeo.ru>

Abstract

The problem of the selection of the singularity of the Green's function spectral representation when calculating the mutual coupling coefficients of longitudinal electrical dipoles located near the impedance circular cylinder is solved. The current distribution in the dipoles is approximated by the generalized modes. The calculation results of both addition value caused by the singularity and the mutual coupling coefficients for the case when two longitudinal dipoles are located near the impedance circular cylinder are presented. It is shown that the Green's function singularity appear strongly in the case of calculating the reactive component of self impedance coefficients and mutual coupling coefficients of dipoles with moving off midpoints along the cylinder element to a distance equivalent to the length of the radiator.

Keywords: impedance circular cylinder; longitudinal dipole; selection of the singularity of Green's function spectral representation.

1. INTRODUCTION

In many applied problems for example in calculation of the reconciliation radiator characteristics the necessity to use the set of generalized modes for the current distribution approximation appears in order to increase the accuracy of obtained results. The load-carrying construction often represents a circular cylinder which surface area has an impedance.

The application of known calculation algorithms for mutual coupling coefficients for the electrical dipoles located at the cylindrical surface area as it is shown in papers [1-3] leads to the incorrect results for self impedance coefficients if we use the expression

$$I_n(\vec{r}) = \delta(\varphi - \varphi_n) \delta(\rho - \rho_n) / r \times \\ \times \sum_p \left\{ A_p \cos\left[\pi(p - 0.5) \frac{z - z_n}{\ell}\right] + B_p \sin\left[\pi p \frac{z - z_n}{\ell}\right] \right\}, \quad (1)$$

to determine current approximation $I_n(\vec{r})$ at n -radiator. In formula (1) following notations are used: $\vec{r} = \{\rho, \varphi, z\}$ is radius vector of an arbitrary point in the cylindrical coordinate system $0\rho\varphi z$; $\vec{r}_n = \{\rho_n, \varphi_n, z_n\}$ is coordinates of the midpoint of n -radiator; $\delta(\cdot)$ is Dirac delta-function; A_p, B_p are unknown complex magnitudes of current harmonics which are determined out of the boundary conditions on the surface of the electrical dipole.

The error mentioned above as it was shown in [4] is caused by the singularity of the Green's function spectral

representation. The singularity is being used for representing the electromagnetic field of the dipole placed near cylindrical body, and leads to an instable solution.

2. FORMULATION OF THE PROBLEM

The algorithm for calculation of mutual coupling coefficients for longitudinal electrical dipole placed near circular cylinder proposed in this paper is based on the selection of singularity of the Green's function spectral representation. This algorithm permits to exclude divergent integrals from the solution when using more general radiator current approximation by generalized modes.

2.1. MODEL

Let's carry out the analysis of the known expression from [1] for calculation of the mutual coupling coefficient $Z_{s_{nm}}$ of two longitudinal dipoles:

$$Z_{s_{nm}} = -\frac{1}{|I_0^n| |I_0^m|} \left\{ \int_L G_{\nabla}(\beta\rho, \beta\rho'; \varphi, \varphi') \times \right. \\ \times \int_{-\ell}^{\ell} I_n(z) \int_{-\ell+\Delta z}^{\ell+\Delta z} I_m(z') \left(k^2 + \frac{\partial^2}{\partial z^2} \right) \times \\ \times G_z(\gamma, z, z') dz' dz \gamma - \\ - 2\pi i \sum_g \text{Res} (G_{\nabla}(\beta_g \rho, \beta_g \rho'; \varphi, \varphi')) \times \\ \times \int_{-\ell}^{\ell} I_n(z) \int_{-\ell+\Delta z}^{\ell+\Delta z} I_m(z') \left(k^2 + \frac{\partial^2}{\partial z^2} \right) G_z(\gamma_g, z, z') dz' dz \Big\}, \quad (2)$$

where ℓ is the dipole arm length; $\Delta z = z_n - z_m$; $|I_0^n|$, $|I_0^m|$ are the current magnitude at feed points of the n -th and m -th radiator, respectively; $I_n(\cdot)$, $I_m(\cdot)$ are the functions that determine current distribution in radiators; G_∇, G_z are the transversal and longitudinal components of spectral representation of Green's function, respectively; $k = 2\pi/\lambda$; γ is the longitudinal wavenumber; β is the transversal wavenumber ($\beta^2 = k^2 - \gamma^2$); λ is the wave length; i is the imaginary unit; (ρ', φ', z') are the radius vector coordinates of integration point in the cylindrical coordinate system; $\text{Res}(\cdot)$ are the residues of the integrand calculated at the poles of the function G_∇ ; L is the integration contour. The integration contour form for the considering problem geometry and techniques applied to find poles are more detailed in [5, 6] so thus are not analyzed here.

2.2. EXPRESSION TRANSFORMATION

Next transformations in known algorithms are connected to the application of the operator $(k^2 + \partial^2/(\partial z^2))$ to the longitudinal component of Green's function $G_z(\cdot) = \exp(-i\gamma|z - z'|)$. However, in the case of the generalized current modes application the cofactor β^2 for $p = p' > 1$ causes the appearance of the poorly convergent integrals in (2). To improve the convergence we'll exclude the appearance of this cofactor by reducing the derivative order of the Green's function longitudinal component by implementation of the double integration by parts to the expression:

$$\int_{-\ell}^{\ell} I_n(z) \int_{-\ell+\Delta z}^{\ell+\Delta z} I_m(z') \left(k^2 + \frac{\partial^2}{\partial z^2} \right) G_z(\gamma, z, z') dz' dz. \quad (3)$$

This permits us to write (3) as the sum of single $K1$ and double $K2$ integrals determined by expressions:

$$K1 = \int_{-\ell+\Delta z}^{\ell+\Delta z} I_m(z') \left(\frac{\partial I_n(\ell)}{\partial z} \exp(-i\gamma|\ell - z'|) - \frac{\partial I_n(-\ell)}{\partial z} \exp(-i\gamma|-\ell - z'|) \right) dz', \quad (4)$$

$$K2 = \int_{-\ell}^{\ell} \int_{-\ell+\Delta z}^{\ell+\Delta z} I_m(z') \left(k^2 I_n(z) - \frac{\partial^2 I_n(z)}{\partial z^2} \right) \times \exp(-i\gamma|z - z'|) dz' dz. \quad (5)$$

Here the nm -th are mutual coupling coefficients matrix (2) element becomes block element:

$$Zs_{nm} = \int_L G_\nabla(\beta\rho, \beta\rho'; \varphi, \varphi') \begin{bmatrix} A1 & A2 \\ A2^T & A3 \end{bmatrix} d\gamma - 2\pi i \sum_g \text{Res} \left(G_\nabla(\beta_g\rho, \beta_g\rho'; \varphi, \varphi') \right) \begin{bmatrix} A1_g & A2_g \\ A2_g^T & A3_g \end{bmatrix} \quad (6)$$

and integrations $K1, K2$ for the block elements

$A1 - A3$ (the block matrix with dimension $P \times P$ describes the coupling of n -th and m -th dipoles at p -th and p' -th modes) can be written as:

$$K2_{A1} = \left(k^2 - \left(\frac{\pi(p-0,5)}{\ell} \right)^2 \right) G1(\gamma, \Delta z, \ell, p, p'),$$

$$K1_{A1} = (-1)^p \frac{\pi(p-0,5)}{\ell} G11(\gamma, \Delta z, \ell, p'), \quad (7)$$

$$\begin{bmatrix} K2_{A2} \\ K2_{A3} \end{bmatrix} = \left(k^2 - \left(\frac{\pi p}{\ell} \right)^2 \right) \begin{bmatrix} G2(\gamma, \Delta z, \ell, p, p') \\ G3(\gamma, \Delta z, \ell, p, p') \end{bmatrix}, \quad (8)$$

$$\begin{bmatrix} K1_{A2} \\ K1_{A3} \end{bmatrix} = (-1)^p \frac{\pi p}{\ell} \begin{bmatrix} -G12(\gamma, \Delta z, \ell, p') \\ G13(\gamma, \Delta z, \ell, p') \end{bmatrix} \quad (9)$$

In formulas (6)-(9) "T" is a transposition symbol; subscript "g" denotes the discrete component caused by surface wave field excited by harmonic β_g (g -th pole of function G_∇);

$$\begin{bmatrix} G1(\cdot) \\ G2(\cdot) \end{bmatrix} = \int_{-\ell}^{\ell} \int_{-\ell+\Delta z}^{\ell+\Delta z} \begin{bmatrix} \cos\left(\frac{\pi(p-0,5)z}{\ell}\right) \\ \sin\left(\frac{\pi pz}{\ell}\right) \end{bmatrix} \times \exp\left(\frac{\pi(p'-0,5)(z'-\Delta z)}{\ell}\right) \exp(-i\gamma|z - z'|) dz' dz; \quad (10)$$

$$G3(\cdot) = \int_{-\ell}^{\ell} \int_{-\ell+\Delta z}^{\ell+\Delta z} \sin\left(\frac{\pi pz}{\ell}\right) \sin\left(\frac{\pi p'(z'-\Delta z)}{\ell}\right) \times \exp(-i\gamma|z - z'|) dz' dz; \quad (11)$$

$$\begin{bmatrix} G11(\cdot) \\ G12(\cdot) \end{bmatrix} = \int_{-\ell+\Delta z}^{\ell+\Delta z} \cos\left(\frac{\pi(p'-0,5)(z'-\Delta z)}{\ell}\right) \times \begin{bmatrix} (\exp(-i\gamma|\ell - z'|) + \exp(-i\gamma|-\ell - z'|)) \\ (\exp(-i\gamma|\ell - z'|) - \exp(-i\gamma|-\ell - z'|)) \end{bmatrix} dz'; \quad (12)$$

$$G13(\cdot) = \int_{-\ell+\Delta z}^{\ell+\Delta z} \sin\left(\frac{\pi p'(z'-\Delta z)}{\ell}\right) \times (\exp(-i\gamma|\ell - z'|) - \exp(-i\gamma|-\ell - z'|)) dz'. \quad (13)$$

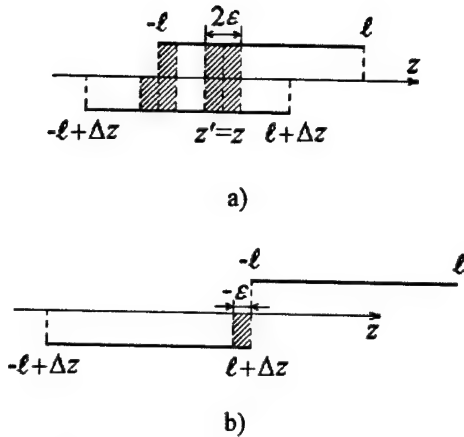


Fig. 1. Dislocation of singularity zones of Green's function

2.3. THE SEPARATION OF GREEN'S FUNCTION SINGULARITY

The expressions (10)-(13) analysis shows that the appearance of Green's function singularity is possible if the dipoles overlap along the axis Oz ($|\Delta z| \leq 2\ell$). Two variants of such dipoles disposition are shown in the Fig.1: the dipoles are partially overlapped (Fig.1a, $|\Delta z| < 2\ell$) and the dipoles are shifted at a distance equivalent to radiator length (Fig.1b, $|\Delta z| = 2\ell$). It is easy to notice that the dislocation and size of zones where Green's function singularities appear (ε or 2ε , where ε is a fixed small parameter) depend both on the integration multiplicity and on the size of dipoles overlapping.

Taking into account the dislocation of zones where Green's function singularities appear we'll represent the integrals (10)-(13) as a sum of the integrals of two types. In accordance with the fact of presence of such singularity these integrals realize the different calculation accuracy. The obtained integrals have analytical expressions and their closed forms are given in [7].

The preliminary investigations showed that the zone where Green's function singularity appears is connected to the dipole radius Ω by the formula

$$\varepsilon = n\Omega, \quad (14)$$

where the parameter n is an integer from the interval 3..7 for cylindrical bodies. In many cases it is sufficient to determine $n = 5$.

2.4. THE SIMULATION RESULTS

The results of calculating the self impedance and the mutual coupling coefficients $Z_{s_{nm}}^{pp'}$ for the generalized modes ($p, p' = \bar{1}, \bar{3}$) of two dipoles with the arm length $\ell = 0,25\lambda$ placed near circular cylinder with radius $a = 2\lambda$ are given in the tables 1, 2 for the cases of perfectly conducting and impedance surface of cylinder ($\tilde{Z}_H = 0 + 0i$, $\tilde{Z}_E = 0,3i$, where

Table 1. The mutual coupling coefficients of dipoles placed near the perfectly conducting cylinder

Modes	$Z_{s_{nm}}^{pp'}$	$\tilde{Z}_{s_{nm}}^{pp'}$
$n = m = 1$		
<i>A1</i>		
(1,1)	86,2+64,2i	0
(1,2)	-24,8-77,2i	0
(1,3)	14,76+67,6i	
(2,2)	7,4-1812i	-59,2-1429i
(2,3)	-4,4-111,3i	0
(3,3)	2,6-4538i	-174,8-4246
<i>A3</i>		
(1,1)	8,27-747,7i	-22,3-537,7i
(1,2)	-3,9-106,1i	0
(1,3)	2,5+101,6i	0
(2,2)	1,8-3070	-110,3-2669i
(2,3)	-1,2-134,3i	0
(3,3)	0,8-6144i	-251,9-6151i
$n = 1; m = 2$		
<i>A1</i>		
(1,1)	36,6+24,5i	0,1+1,6i
(1,2)	-13,5-38,6i	-0,3-4,7i
(1,3)	8,1+36,3i	0,5+7,8i
(2,2)	4,5+61,0i	0,8+14,1i
(2,3)	-2,7-66,9i	-1,4-23,4i
(3,3)	1,6+79,8i	2,3+38,8i
<i>A2</i>		
(1,1)	-17,6-46,1i	-0,2-3,1i
(1,2)	4,3+52,3i	0,4+6,3i
(1,3)	-2,3-49,9i	-0,6-9,4i
(2,2)	-2,1-65,3i	-1,1-18,8i
(2,3)	1,1+71,8i	1,7+28,1i
(3,3)	-0,8-83,8i	-2,8-46,58i
<i>A3</i>		
(1,1)	-1,4-54,7i	-0,4-6,3i
(1,2)	0,6+56,7i	0,7+12,5i
(1,3)	-0,4-56,2i	-1,1-18,8i
(2,2)	-0,2-71,1i	-1,5-24,9i
(2,3)	0,2+77,4i	2,2+37,4i
(3,3)	-0,1-88,7i	-3,3-55,7i

$\tilde{Z}_E = Z_E W_0^{-1}$; $\tilde{Z}_H = Z_H W_0^{-1}$; $W_0 = 120\pi$ Ohm; Z_E , Z_H are wave impedances in the classes of E - and H -waves, respectively). The radiators were located at $\rho_n - a = 0,25\lambda$ from cylinder surface. The values of Green's function singularity contribution $\tilde{Z}_{s_{nm}}^{pp'}$ into mutual coupling coefficients are also given in the same tables. The symmetry of the mutual coupling coefficients matrix relatively to the main diagonal is taken into account in the table compositions.

The functions given in [3, 7] were used as transversal Green's functions. The value of upper interval integration bounds along the imaginary contour was considered to be 13 for the calculation of integrals that

Table 2. The mutual coupling coefficients of dipoles placed near the impedance cylinder

Modes	$Z_{spp'}$	$\tilde{Z}_{spp'}$
$n = m = 1; \Delta z = 0$		
A1		
(1,1)	86,2+64,2i	0
(1,2)	-24,8-77,2i	0
(1,3)	14,76+67,6i	
(2,2)	7,4-1812i	-59,2-1429i
(2,3)	-4,4-111,3i	0
(3,3)	2,6-4538i	-174,8-4246
A3		
(1,1)	8,27-747,7i	-22,3-537,7i
(1,2)	-3,9-106,1i	0
(1,3)	2,5+101,6i	0
(2,2)	1,8-3070	-110,3-2669i
(2,3)	-1,2-134,3i	0
(3,3)	0,8-6144i	-251,9-6151i
$n = 1; m = 2; \Delta z = 2\ell$		
A1		
(1,1)	36,6+24,5i	0,1+1,6i
(1,2)	-13,5-38,6i	-0,3-4,7i
(1,3)	8,1+36,3i	0,5+7,8i
(2,2)	4,5+61,0i	0,8+14,1i
(2,3)	-2,7-66,9i	-1,4-23,4i
(3,3)	1,6+79,8i	2,3+38,8i
A2		
(1,1)	-17,6-46,1i	-0,2-3,1i
(1,2)	4,3+52,3i	0,4+6,3i
(1,3)	-2,3-49,9i	-0,6-9,4i
(2,2)	-2,1-65,3i	-1,1-18,8i
(2,3)	1,1+71,8i	1,7+28,1i
(3,3)	-0,8-83,8i	-2,8-46,58i
A3		
(1,1)	-1,4-54,7i	-0,4-6,3i
(1,2)	0,6+56,7i	0,7+12,5i
(1,3)	-0,4-56,2i	-1,1-18,8i
(2,2)	-0,2-71,1i	-1,5-24,9i
(2,3)	0,2+77,4i	2,2+37,4i
(3,3)	-0,1-88,7i	-3,3-55,7i

do not contain Green's function singularity and was considered to be 100 for the calculation of integrals containing Green's function singularity.

3. CONCLUSION

The analysis of the obtained results shows that the Green's function singularity appears strongly in the

case of calculating the reactive component of self impedance coefficients and mutual coupling coefficients of dipoles with moving off midpoints along the cylinder element to a distance equivalent to the length of the radiator length ($|\Delta z| = 2\ell$). The comparison of these results with results obtained by different algorithms for example as in [1, 8] permits to make a conclusion about the accuracy of the obtained solution sufficient for the practice.

The results obtained in this paper can be applied in the investigation of the antenna input resistance as well as in modeling the feeders and antenna reconciliation.

ACKNOWLEDGMENT

The author would like to thank prof. Dmitry Gabriel'yan for his advise and stimulating discussing during the revision phase of this paper.

REFERENCES

1. Aizenberg G.Z., Yampol'skii V.G., and Tereshin O.N. Ultrashort Wave Antennas. – M.: Svyaz', 1977, Vol.1 (in Russian).
2. Markov G.T., Chaplin A.F. Excitation of electromagnetic. – M.: Radio i svyaz', 1983 (in Russian).
3. Gabriel'yan D.D., Zvezdina M.Yu., Kostenko P.I. The excitation of a circular cylinder with anisotropic impedance by longitudinal electric dipole // Radiotekhnika i elektronika. 2001. Vol. 46. No 8. p. 875 (in Russian).
4. Felsen L., Marcuvitz N. Radiation and scattering of waves. – M.: Mir, 1978. (in Russian). Publish in English as "Radiation and Scattering of Waves", Englewood Cliffs, NJ, Prentice Hall, 1973.
5. Katsenelenbaum B.Z. High-frequency electrodynamics. – M.: Nauka, 1966 (in Russian).
6. Zvezdina M.Yu. The field of dipole placed near impedance circular cylinder // Elektromagnitnie volni i elektronnie systemi. 2002. Vol. 7. No 9. p. 49 (in Russian).
7. Zvezdina M.Yu. Modified algorithm for calculating of mutual coupling coefficients of longitudinal electrical dipoles located near the circular cylinder // Journal of radioelectronics 2002. No 2. <http://jre.cplire.ru/jre/aug02/3/text.html> (in Russian).
8. Gabriel'yan D.D., Zvezdina M.Yu. Mutual Coupling of Longitudinal Vibrators near Impedance Cylinder // Radiotekhnika. 2000. No 5. p. 67 (in Russian).

ACCOUNT OF CYLINDRICAL BODIES PECULIARITIES IN THE ANALYSIS OF DIPOLE CHARACTERISTICS

M. Yu. Zvezdina

Rostov military institute of Missile Corps,
Rostov-on-Don, Russia
<zvezd@jeo.ru>

Abstract

The method of analysis of radiation characteristics of electric dipole placed near impedance cylinder with arbitrary cross section is presented. The method is based on the account of cylindrical body peculiarities. This method is intended for the contours, which satisfy Lyapunov's conditions. The main considered property is the property of 2π periodic functions, describing the solution of the diffraction problem. The solution is presented as the Fourier series. The comparison of the given solution with solution obtained by the other known methods is carried out. It has been made the conclusion that the suggested method of calculation of scattered electromagnetic field guaranties the stability of the solution and satisfactory accuracy for practice.

Keywords: contour with arbitrary cross section; Lyapunov conditions; the property of 2π periodicity; method of integral equations.

1. INTRODUCTION

The radar-absorbing materials and coatings covering load-carrying constructions in order to control antennas characteristics have been widely used recently (see, e.g. [1, 2]). The account of such material parameters effect on the radiation and scattering antenna characteristics is realized by simulation of the structure of electromagnetic field excited in the presence of the object in near- and far-zones. In many cases while modeling the load-carrying construction can be approximated by a cylindrical body of arbitrary cross section, the radar-absorbing layer is simulated by the effective surface impedance. The distribution of excited surface electrical and magnetic currents is used as the investigated characteristic.

The special attention in the development of numerical algorithms for calculation of electromagnetic field structure in presence of the impedance body is given to solution stability [3, 4]. To increase stability of the obtained solution a priori information about the analytical properties of the solution should be taken into account, when developing the algorithm as in [5]. Thus, in the papers [6, 7] the rigorous solution of the problem is obtained on the basis of representation of the field as series by the set of metaharmonic functions. In this case the body contour is approximated either by a circle as in [6] or by a sphere as in [7]. This sphere contains scattered field nonanalyticity inside.

2. METHOD

The method of analysis of radiation characteristics of electric dipole located near impedance cylinder with arbitrary cross section proposed in this work is based on application of the property of 2π periodicity of functions which describe the diffraction problem solution. The method is meant for the contours which satisfy Lyapunov's conditions.

2.1. FORMULATION OF THE PROBLEM

The problem is formulated in the following way. Consider impedance cylindrical body homogeneous along the element of cylinder has an arbitrary star-shaped contour, i.e. in polar coordinate system its equation can be describe as $L = \rho(\varphi)$, where function $\rho(\varphi)$ is analytic function of the angle φ and has the period of 2π in the area of real angles, that determines the satisfaction of Lyapunov's conditions. In the absence of medium gyrotropy the body surface impedance is

described by tensor $Z = \begin{pmatrix} Z_E & 0 \\ 0 & Z_H \end{pmatrix}$, where $Z_E(\varphi)$,

$Z_H(\varphi)$ are wave impedance in the classes of E- and H-waves, respectively. Moreover, the impedance distribution is also 2π periodic function as it has been shown in [6].

The plane wave of arbitrary polarization excited by a point source located at a point with radius vector $\vec{r}_0 = \{R_0, \theta_0, \varphi_0\}$ falls on the body.

2.2. THE SET OF INTEGRAL EQUATIONS

When representing the wave as the composition of two linear polarization waves and taking into account incident wave depolarization, the solution of the diffraction problem in transversal plane can be described as two set of integral equations with respect to the density of a surface electric $J_z^{E(H)}(\vec{\rho})$ and magnetic $M_z^{E(H)}(\vec{\rho})$ currents as in [4, 6]. The sets are distinguished by right hand parts:

$$\int_L \left\{ ikWG(\vec{\rho}, \vec{\rho}') - \frac{Z_E(\varphi')}{\sin^2 \theta_0} \frac{\partial G(\vec{\rho}, \vec{\rho}')}{\partial n} \right\} J_z^{E(H)}(\vec{\rho}) - \frac{Z_E(\varphi')}{W \sin^2 \theta_0} \frac{\partial G(\vec{\rho}, \vec{\rho}')}{\partial \tau} M_z^{E(H)}(\vec{\rho}) \} d\ell = F_1^{E(H)}, \quad (1)$$

$$\int_L \left\{ \frac{-W \cos \theta_0}{\sin^2 \theta_0} \frac{\partial G(\vec{\rho}, \vec{\rho}')}{\partial \tau} J_z^{E(H)}(\vec{\rho}) + \left(\frac{1}{\sin^2 \theta_0} \frac{\partial G(\vec{\rho}, \vec{\rho}')}{\partial n} - Z_H(\varphi') k G(\vec{\rho}, \vec{\rho}') \right) \times \right. \\ \left. \times M_z^{E(H)}(\vec{\rho}) \right\} d\ell = F_2^{E(H)}, \quad (2)$$

$$F_1^{E(H)} = \\ = \exp[i(\vec{\tau}_0, \vec{\rho})] \left\{ E_0 \left(1 - \frac{Z_E(\varphi)}{k W \sin^2 \theta_0} (\vec{n}, \vec{\tau}_0) \right) \vartheta^E - \right. \\ \left. - H_0 \frac{Z_E(\varphi) \cos \theta_0}{k \sin \theta_0} ([\vec{n}, \vec{\tau}_0], \vec{i}_z) \vartheta^H \right\} \\ F_2^{E(H)} = \\ \exp[i(\vec{\tau}_0, \vec{\rho})] \left\{ H_0 \left(Z_H(\varphi) - \frac{W(\vec{n}, \vec{\tau}_0)}{k \sin \theta_0} \right) \vartheta^H - \right. \\ \left. - E_0 ([\vec{n}, \vec{\tau}_0], \vec{i}_z) \vartheta^E \right\} \quad (3)$$

where \vec{i}_z is a unit vector of cylindrical coordinate system; $W = 120\pi$ Ohm; \vec{n} , $\vec{\tau}$ are the basis vectors of normal and tangent respectively at a point with radius vector $\vec{\rho}' = \{\rho', \varphi'\}$ on the contour surface; $k = 2\pi/\lambda$ is the incident wavenumber in free space;

$$\vartheta^E = \begin{cases} 1 & \text{for E-pol.} \\ 0 & \text{for H-pol.} \end{cases}; \quad \vartheta^H = \begin{cases} 0 & \text{for E-pol.} \\ 1 & \text{for H-pol.} \end{cases};$$

λ is wavelength in free space; superscripts "E" and "H" correspond to the solutions of diffraction problems in the cases of E- and H- polarized waves respectively. The Green's function $G(\vec{\rho}, \vec{\rho}')$ is written taking into account the system regularity along Oz axis. The factor $\exp[i\omega t - ikz \cos \theta_0]$ is omitted.

2.3. APPLICATION OF THE PROPERTY OF 2π -PERIODICITY OF GREEN'S FUNCTION

The solution to the set of integral equations (1) can be easily reduced to the solution of infinite set of linear equations with respect to currents in the form of space spectrum of azimuth harmonics. For this case the

property of 2π -periodicity of functions in formulas (1) and (2) should be used. These functions are expanded in the Fourier series by the set $\{\exp(ip\varphi)\}$ and Green function and its derivatives are also expanded by the sets $\{\exp(ip\varphi)\}$ and $\{\exp(ip'\varphi')\}$.

The obtained expressions in contrast to the known solutions allow one to exclude singularities of integral equation kernel what leads to the guarantee of stability solution. This is achieved by using of "smoothed" distributions of surface impedance as in [6], allowing to reduce the number of harmonics in distribution.

In the particular cases when body contour is described by the function $r = \rho(\varphi) = a$ (circular cylinder) the form of the solution coincides with the representation obtained for this configuration as the Rayleigh series with zero surface impedance as in [9] and non zero surface impedance as in [10].

2.4. THE RESULTS OF SIMULATION

The distributions of the normalized magnitude of electric surface current excited by plane E-polarized wave incident from the direction $\theta_0 = 90^\circ$, $\varphi_0 = 135^\circ$ on a square with side $a = 4,8\lambda$ and surface impedance $0,3i$ are given in Fig. 1. The contour of impedance cylinder was considered as a function

$$\rho(\varphi) = \frac{a}{2} \begin{cases} \rho_1(\tilde{\varphi}(\varphi)) & \text{for } \tilde{\varphi}(\varphi) > \varphi_r, \\ \rho_2(\tilde{\varphi}(\varphi)) & \text{for } \tilde{\varphi}(\varphi) \leq \varphi_r, \end{cases} \quad (5)$$

where

$$\rho_1(\tilde{\varphi}(\varphi)) = \cos^{-1} \left(\frac{\pi}{4} - \tilde{\varphi} \right), \quad (6)$$

$$\tilde{\varphi}(\varphi) = \begin{cases} \varphi_1 & \text{for } \varphi_1 \leq 0,25\pi, \\ 0,5\pi - \varphi_1 & \text{for } \varphi_1 > 0,25\pi; \end{cases} \quad (7)$$

$$\varphi_1 = \varphi - 0,5\pi E(2\varphi\pi^{-1}); \quad (8)$$

$$\rho_2(\tilde{\varphi}(\varphi)) = \\ = \frac{\sqrt{2}}{\cos\left(\frac{\pi}{4} - \varphi_r\right)} \left\{ \cos \tilde{\varphi} \sin\left(\frac{\pi}{4} - \varphi_r\right) + \right. \\ \left. + \sqrt{\sin^2 \varphi_r + \sin^2 \tilde{\varphi} \sin^2\left(\frac{\pi}{4} - \varphi_r\right)} \right\}; \quad (9)$$

$E(\cdot)$ is an integer part of a number; φ_r is a half of the polar angle formed by initial point of union of a circle and a square. It is assumed in the calculations that $\varphi_r = 10^\circ$.

The results obtained by using the suggested method are denoted by the curve 1 in Fig. 1; the curve 2 denotes the results obtained by using the known algorithm based on the collocation method with the step basis functions as in [3]. The analysis of the obtained results shows sufficiently good convergence of the results. At the same time the order of linear equations set used by the proposed algorithm for calculation of unknown complex current magnitudes is $2^6 = 64$ against 204 in the collocation method. It should be

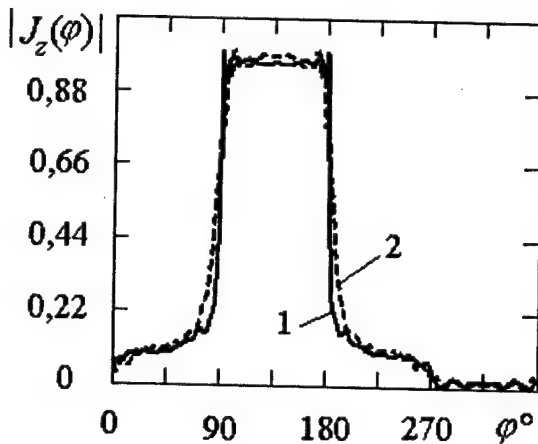


Fig. 1. Distribution of normalized magnitude of electric surface current

noted that the proposed method permits the application of the detailed discrete Fourier transform instrument for program realization of the algorithm.

Similar results were obtained in the case of the diffraction of H-polarized wave.

Using the known surface current distribution, the radiation characteristics of electric dipole located near cylindrical body are calculated.

3. CONCLUSION

Thus, the presented method for calculation of electromagnetic field scattered by object is based on taking into the account the cylindrical body contour peculiarity (which transverse plane contour is described as analytic function with 2π period; the radar-absorbing coating is described by the "smoothed" distribution of surface impedance with the same period) guarantees the accuracy of the solution sufficient for practice purpose and possesses solution stability.

ACKNOWLEDGMENT

The author is grateful to Prof. Dmitry D. Gabriel'yan for his useful suggestions regarding the improvement of material of this paper.

REFERENCES

1. Petrov B. M., Semenikhin A. I. Controlled impedance coverings and structures // *Zarubezhnaya radioelektronika*. 1994. No 6. p. 9 (in Russian).
2. Gabriel'yan D. D., Zvezdina M. Yu., Kostenko P. I. reducing of sidelobe level of antenna by using of impedance covers // *Izvestiya Vyssh. Uchebn. Zaved. Radioelektronika*. 2003. Vol. 46. No 2. p. 38 (in Russian).
3. Computer techniques for electromagnetics / Edit. by R. Mittra. - M.: Mir, 1977 (in Russian). Publish in English as "Computer technique for electromagnetics", Pergamon Press, Oxford, 1973.
4. Apeltsin V. F., Kyurkchan A. G. Analytical properties of wave fields. - M.: Izdat. MGU, 1990 (in Russian).
5. Kyurkchan A. G. Using the a priori information on analytical properties of the solution in problems of electrodynamics and acoustics // *Radiotekhnika i Elektronika*. 1996. Vol. 41. No 2. p. 162 (in Russian).
6. Petrov B. M., Yukhanov Yu. V. Inverse problem of scattering for the impedance cylinder of arbitrary cross section // *Izvestiya Vyssh. Uchebn. Zaved. Radioelektronika*. 1980. No 9. p. 78 (in Russian).
7. Avetisyan A. A. The generalized method of separation of variables and diffraction of electromagnetic waves on rotation bodies // *Radiotekhnika i Elektronika*. 1970. Vol. 15. No 1. p. 14 (in Russian).
8. Petrov B. M., Scharvarko V. G. Synthesis of a surface impedance of the circular cylinder under the given scattering pattern // In the Collect. of scientific-methodical works on applied electrodynamics - M.: Visshaya shkola, 1980. Vol. 3. p. 62 (in Russian).
9. Hönl H., Maue A., Westpfahl K. The theory of diffraction. - M.: Mir, 1964. (in Russian). Publish in German as "Theorie der beugung", Berlin, Göttingen, Heidelberg, 1961.
10. Gabriel'yan D. D., Zvezdina M. Yu., Kostenko P. I. The excitation of a circular cylinder with anisotropic impedance by longitudinal electric dipole // *Radiotekhnika i elektronika*. 2001. Vol. 46. No 8. p. 875 (in Russian).

FIELD OF A SURFACE ANTENNA BASED ON AN IMPEDANCE CYLINDER

Dmitri D. Gabriel'yan¹, Marina Yu. Zvezdina¹, and Oleg S. Labunko²

¹ Rostov military institute of Missile Corps,
Rostov-on-Don, Russia <zvezd@jeo.ru>

² Southern Russia Federal Okrug Radio Frequency Centre,
Rostov-on-Don, Russia <kan@rost.ru>

Abstract

The solution composed with a respect to longitudinal components of distribution of electric and magnetic current densities is obtained for the radiation problem of a surface antenna placed on the impedance cylinder using the integral equation method. Components of the antenna pattern (AP) are found by using the Lorentz lemma where auxiliary dipole is disposed ad infinitum. Current distribution densities for the corresponding AP components are defined basing on the solution of diffraction problems of plane E - and H - polarized waves incident on cylinder from direction allocating the AP observation point. The distribution of surface current density is approximated by step functions with unknown coefficients. The effect of surface impedance on singularities of excited electromagnetic field structure in far zone is analyzed. The results of numerical investigations are presented.

Keywords: contour with arbitrary cross section; impedance boundary condition; surface antenna; antenna pattern.

1. INTRODUCTION

The radiating aperture based on load-carrying construction is one of the fundamental antenna structures which have various practical applications. Many works are devoted to the investigation of radiation characteristics of such structures (see, for example, [1-4]). However, in the works mentioned above a generalized case of impedance cylinder with arbitrary cross section is not considered. At the same time it is the investigation of radiating aperture based on the cylindrical surfaces with impedance boundary conditions that is more interesting from the point of view of theory and urgent in technical application. The typical example is the open end of waveguide placed on the impedance surface with arbitrary cross section.

The solution to the problem of excitation electromagnetic field of surface antenna located at the impedance surface with an arbitrary cross section and satisfying Lyapunov conditions, proposed in this paper, is obtained in rigorous formulation. The method of integral equations composed with a respect to the longitudinal components of current densities distribution is used here.

2. SETTING THE PROBLEM

The setting of the problem is formulated in the following way. Let the antenna aperture be placed on the impedance cylindrical surface S with an arbitrary cross section L and satisfying Lyapunov conditions.

The distribution of tangential field component in aperture supposed to be known and is described by vectors \vec{E}_a and \vec{H}_a . The component χ ($\chi = \theta, \varphi$) of electric field strength at the arbitrary space point may be determined as it is shown in [1] by using the integral relations and Green's function spectral representation:

$$\vec{E}_\chi(\vec{r}) = \int_S \{ \vec{E}(\vec{r}') \vec{J}_\chi(\vec{r}, \vec{r}') - \vec{H}(\vec{r}') \vec{M}_\chi(\vec{r}, \vec{r}') \} d\vec{s} \quad (1)$$

Here $\vec{E}(\vec{r}')$, $\vec{H}(\vec{r}')$ are the impressed strength of electric and magnetic field respectively excited by the antenna on the cylindrical surface S ; $\vec{J}_\chi(\vec{r}, \vec{r}')$, $\vec{M}_\chi(\vec{r}, \vec{r}')$ are the densities of electric and magnetic currents excited on the cylindrical surface by auxiliary electrical dipole oriented along the unit vector $\vec{\chi}$. As it is shown in [1] in the case of an impedance cylindrical surface the impressed fields outside the aperture are connected by boundary conditions:

$$M_\tau^E(\vec{r}) = Z_E J_z^E(\vec{r}), \quad M_z^H(\vec{r}) = -Z_H J_\tau^H(\vec{r}), \quad (2)$$

where $Z = \begin{pmatrix} Z_E & 0 \\ 0 & Z_H \end{pmatrix}$ is the surface impedance tensor;

Z_E , Z_H are the wave impedance in the classes of E - and H - waves, respectively.

3. SOLUTION TO THE PROBLEM

3.1. COMMON EXPRESSIONS

Let's assume the cylinder surface S as a sum of the aperture area S_a and the outside area $S - S_a$. In this case if we superpose the same boundary conditions both with the impressed field and with the auxiliary source field then it is possible to pass from integral (1) to expression:

$$\vec{E}_\lambda(\vec{r}) = \int_{S_a} \left\{ \vec{E}_a(\vec{r}') \vec{J}_\lambda(\vec{r}, \vec{r}') - \vec{H}_a(\vec{r}') \vec{M}_\lambda(\vec{r}, \vec{r}') \right\} d\vec{s}. \quad (3)$$

Here \vec{E}_a , \vec{H}_a are the distributions of tangential field component of electrical and magnetic fields in antenna aperture, respectively.

In order to find the antenna pattern the auxiliary dipole is disposed ad infinitum and its disposition in the spherical coordinate system is determined by the radius vector $\vec{r} = \{R, \theta, \varphi\}$ (Fig. 1). In this case the calculation of currents distribution density can be carried out on the basis of diffraction problem of plane wave incident on the cylinder from direction defined by the determined angles. This corresponds to the approach proposed by [5, 6].

3.2. FIELDS REPRESENTATION

The determination of vector AP components of surface antenna in this case corresponds to the cases of E - and H - polarized waves diffractions as in paper [2]:

$$\begin{cases} E_z^{in}(x, y, z) \\ H_z^{in}(x, y, z) \end{cases} = \sin \theta \times \exp(i\alpha_0 x + i\beta_0 y) \exp(i\gamma_0 z) \begin{cases} E_0 \\ H_0 \end{cases} \quad (4)$$

where E_0 , H_0 are the strength of electrical and magnetic fields at the incident wave front; $\alpha_0 = k \sin \theta \cos \varphi$; $\beta_0 = k \sin \theta \sin \varphi$; $\gamma_0 = k \cos \theta$; $k = 2\pi/\lambda$ is the wave number of free space; λ is the wave length; i is an imaginary unit.

In each of these cases we'll suppose the presence of z -component of both electric and magnetic field in the scattering field at the same time. This corresponds to the exciting of longitudinal components of electrical

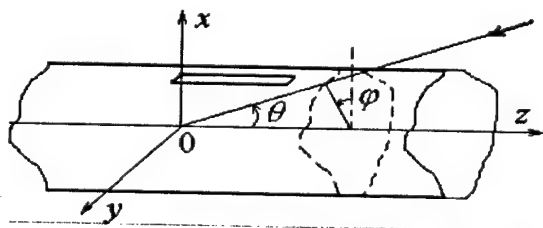


Fig. 1. Problem geometry

and magnetic currents on the cylinder surface. Since the geometrical and electromagnetic cylinder parameters are constant along the cylinder element, the principle of variation of the incident and scattering fields from such a coordinate determines the same factor $\exp(i\gamma_0 z)$. Using the interdependence of transversal electromagnetic field components, the set of integral equations with a respect to the longitudinal components of the electric $J_z^{E(H)}(\vec{\rho})$ and the magnetic $M_z^{E(H)}(\vec{\rho})$ currents is written. These currents are the solutions of the plane wave diffraction problem.

3.3. THE APPROXIMATION OF THE SURFACE CURRENT DENSITY

The solution of this integral equations set is based on the way of approximation of surface current density distribution. In order to find the unknown longitudinal components of electrical and magnetic current densities the initial contour L has the form P -gon in this paper. In this case the distribution of current densities in transversal plane is approximated by step functions

$$\begin{cases} J_z^{E(H)}(\vec{\rho}) \\ M_z^{E(H)}(\vec{\rho}) \end{cases} = \sum_{p=1}^P \begin{cases} A_p^{E(H)} \\ B_p^{E(H)} \end{cases} K_p(\ell - \ell_p), \quad (5)$$

where ℓ_p is the distance between the p -th corner of polygon and the initial point of reference along the contour ($p = 1, \dots, P$); Δ is the length of polygon side; $A_p^{E(H)}$, $B_p^{E(H)}$ are the unknown decomposition coefficients;

$$K_p(\ell - \ell_p) = \begin{cases} 1 & \text{at } \ell \in [\ell_p; \ell_p + \Delta], \\ 0 & \text{at } \ell \notin [\ell_p; \ell_p + \Delta], \end{cases}$$

Using the Krilov-Bogolyubov method with the disposition of P collocation points in the middle of the corresponding decomposition intervals as in Tikhonov and [7] further we transform the integral equations set to the linear algebraic equations set as

$$\begin{cases} (ikWT_{pq} - Z_E \sin^{-2} \theta D_{pq}) A_p^{E(H)} - \\ - Z_E (W \sin \theta)^{-1} C_{pq} B_p^{E(H)} = F_{1p}^{E(H)}, \\ -W \cos \theta \sin^{-2} \theta C_{pq} A_p^{E(H)} + \\ + (\sin^{-2} \theta D_{pq} - kZ_H T_{pq}) B_p^{E(H)} = F_{2p}^{E(H)}, \end{cases} \quad (6)$$

$$F_{1p}^{E(H)} = \exp[i(\vec{\tau}_0, \vec{\rho}_p)] \times \left\{ E_0 \left(1 - \frac{Z_E}{kW \sin^2 \theta} (\vec{n}_p, \vec{\tau}_0) \right) \vartheta^E - \right. \quad (7)$$

$$\left. - H_0 \frac{Z_E \cos \theta}{k \sin \theta} ([\vec{n}_p, \vec{\tau}_0], \vec{i}_z) \vartheta^H \right\}$$

$$F_{2p}^{E(H)} = \exp[i(\vec{\tau}_0, \vec{\rho}_p)] \times \left\{ H_0 \left(Z_H - \frac{W(\vec{n}_p, \vec{\tau}_0)}{k \sin \theta} \right) \vartheta^H - \right. \quad (8)$$

$$\left. - E_0 ([\vec{n}_p, \vec{\tau}_0], \vec{i}_z) \vartheta^E \right\}$$

$$\begin{Bmatrix} T_{pq} \\ C_{pq} \\ D_{pq} \end{Bmatrix} = 0,5i\pi \int_{\ell_q}^{\ell_q+\Delta} \begin{Bmatrix} \partial/\partial n \\ \partial/\partial \tau \end{Bmatrix} H_0^{(2)}(|\vec{\rho}_p - \vec{\rho}'|) d\ell' \quad (9)$$

$$\vartheta^E = \begin{cases} 1 & \text{for } E\text{-pol.}, \\ 0 & \text{for } H\text{-pol.} \end{cases}; \quad \vartheta^H = \begin{cases} 0 & \text{for } E\text{-pol.}, \\ 1 & \text{for } H\text{-pol.} \end{cases}$$

\vec{i}_z is the unit vector of cylindrical coordinate system; $W = 120\pi$ Ohm; \vec{n}_p is the basis vector of an exterior normal at the p -th collocation point; $H_0^{(2)}(\cdot)$ is the second-kind Hankel function of order 0.

3.4. RELATIONS OF THE DIAGONAL MATRIX ELEMENTS

When calculating the diagonal ($p = q$) coefficients in (9) the integrals become improper (see, [7]), because Green's function and its derivatives at $\vec{\rho}_p = \vec{\rho}'$ are discontinuous of second kind. However these integrals exist and after passing to the limit they may be written in closed form:

$$T_{pp} = \Delta \left\{ H_0^{(2)}(\tilde{\Delta}) + 0,5\pi \left(H_1^{(2)}(\tilde{\Delta}) H_0(\tilde{\Delta}) - H_0^{(2)}(\tilde{\Delta}) H_1(\tilde{\Delta}) \right) \right\} \quad (10)$$

$$C_{pp} = 0,5. \quad (11)$$

The coefficients D_{pp} in formula (9) are equivalent to zero in the meaning of main value. In expression (10) $\tilde{\Delta} = 0,5\Delta$; $H_0(\cdot)$, $H_1(\cdot)$ are Struve's functions; $H_1^{(2)}(\cdot)$ is the second-kind Hankel function of order 1 (see [8]).

3.5. RELATIONS FOR THE ANTENNA PATTERN

The solution of set (6) by using the expression (5) and by accounting the omitted factor $\exp(i\gamma_0 z)$ lets us determine the longitudinal components of both surface electrical and magnetic currents densities and transversal components corresponding to them.

The field distribution in surface antenna aperture is described by trigonometric functions aggregate in which we'll assume the complex amplitudes as known. In this case the expression for the antenna pattern looks like

$$E_\chi(\theta, \varphi) = \int_{S_a} \left(\vec{J}_\chi^{E(H)}(\theta, \varphi; \vec{r}') \times \{ \vec{E}_a(\vec{r}') - Z \vec{H}_a(\vec{r}') \} \right) ds \quad (12)$$

in which integrals of z value are tabular as it is shown in [9].

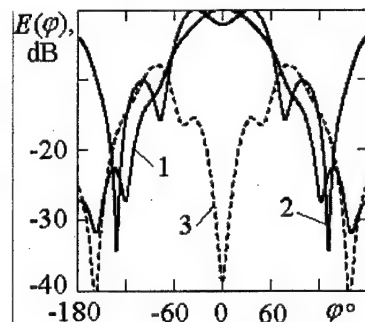
4. THE RESULTS OF THE SIMULATION

In this paper the obtained solution analysis is carried out. To illustrate the effect of geometrical and electromagnetic parameters of cylindrical surface on the sur-

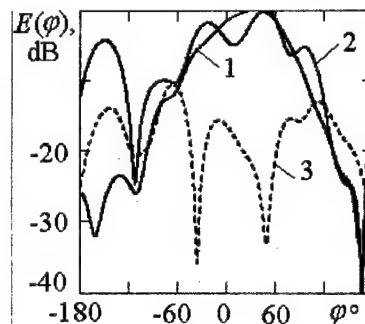
face antenna pattern, the realization of antenna as a rectangular waveguide with sides $a = 0,5\lambda$ (along the element of cylinder) and $b = 0,1\lambda$ placed on the cylinder with square cross section is considered. The side of square is equivalent to $1,2\lambda$. The distribution of the transversal field components in waveguide aperture is determined by fundamental type harmonic as in [10].

The results of the simulation are given in Fig. 2. The functions that were obtained under symmetrical concerning square corner disposition radiator are shown in Fig. 2,a. In Fig. 2,b the functions were obtained under the displaced waveguide at distance $0,3\lambda$ from the corner. Curves 1 in both cases illustrate the plane $\theta = 60^\circ$ section of AP excited by waveguide in case of a zero cylinder impedance ($Z = 0$). Curves 2 and 3 that were obtained in case of a surface impedance $Z_H/W = 0,1i$ represent the fundamental (E_φ -component) and cross-polarized (E_θ -component) components of waveguide AP. The reference of angle φ in both cases is chosen from the normal to the waveguide aperture plane. Cross-polarized AP component is normalized to maximum value of the fundamental AP component.

It is not difficult to note that the presence of surface impedance leads to the increase of fundamental AP component fluctuation. Cross-polarized component value that was obtained under the symmetrical radiator disposition vanishes at $\varphi = 0^\circ$. At the same time such effect does not occur under the radiator displacement.



a)



b)

Fig. 2. Antenna pattern of waveguide radiator based on cylinder with square cross section

5. CONCLUSION

The solution of the problem of excited electromagnetic field of surface antenna placed on the impedance surface with arbitrary cross section is obtained in rigorous formulation by using Lorentz lemma. The calculation of currents distribution density in this case may be carried out on the basis of diffraction problem of the plane wave incident on the cylinder from direction defined by AP observer angles. The determination of the vector AP components of surface antenna in this case corresponds to the cases of E - and H -polarized waves diffractions. The solutions of diffraction problems of these polarizations are described by two sets of integral equations with the respect to the unknown density of a surface electric and magnetic currents. In order to find the unknown longitudinal components of current densities, the initial contour has the form of P -gon and the distribution of current densities is approximated by step functions with unknown decomposition coefficients. These transformations make it possible to apply the Krilov-Bogolyubov method with the disposition of P collocation points in the middle of the corresponding decomposition intervals and to transform the set of integral equations to set of linear algebraic equations. The expressions in the closed form were obtained for diagonal matrix elements.

The received results show that the presence of a surface impedance leads to the increase of fundamental AP component fluctuation and to the appearance of cross-polarized AP component.

ACKNOWLEDGMENT

The author is grateful to Prof. Gennady P. Sinyavski for his useful suggestions regarding the improvement of material of this paper.

REFERENCES

1. Vasil'ev E. N. The excitation of revolution bodies. - M.: Radio i Svyav', 1983 (in Russian).
2. Galishnikova T. N., Il'inski A. S. The numerical methods in diffraction problems. - M.: Izdat. Mosk. GU, 1987 (in Russian).
3. Kyurkchan A. G. Antenna coupling in presence ridge structures // Radiotekhnika i elektronika. 1977. Vol.22. No 7. p. 1362 (in Russian).
4. Gabriel'yan D. D., Zvezdina M. Yu. The radiation of conformal radiating aperture placed on finite length cylinder // Radiotekhnika i elektronika. 1995. Vol. 40. No 1. p. 34 (in Russian).
5. Zakhar'ev L. N., Lemanski A. A., Scheglov K. S. The radiation theory of surface antenna. - M.: Sov. Radio, 1969 (in Russian).
6. Glisson A. W. Equivalent current excitation for an aperture antenna embedded in an arbitrary shaped impedance surface // IEEE Trans. Antennas and Propag. AP-50. 2002. № 7. P. 966.
7. Tikhonov A. N., Samarski A. A. Equations of mathematical physics. - M.: Nauka, 1980 (in Russian). Published in English as "Equations of Mathematical Physics" - Dover, N.Y., 1990.
8. Handbook of Mathematical Functions with Formulas, Graphs and Mathematical Tables. - National Bureau of Standard, US Gov., Printing Oce, Washington, 1964. Published in Russian as "Handbook of special functions with formulas, graphs and mathematical tables" - M: Nauka, 1979.
9. Prudnikov A. P., Brichkov Yu. A., Marichev O. I. Integrals and series. Special functions. - M.: Nauka, 1983 (in Russian).
10. Computer-aided design of antennas and SHF devices / D. I. Voskresenski, S. D. Kremenetski, A. Yu. Grinev, Yu. V. Kotov. - M: Radio i Sviaz', 1988 (in Russian).

SCATTERING OF ELECTROMAGNETIC FIELDS ON COMPLEX SPATIAL LATTICES OF MAGNETODIELECTRIC SPHERES

A. I. Kozar'

Kharkov National University of Radio Electronics, Kharkov, Ukraine
<Anatoliy.I.Kozar.fizika@kture.kharkov.ua>

Abstract

Solution to the problem of electromagnetic waves scattering by the complex spatial lattices of resonant magneto-dielectric spheres is given.

Expressions for the fields scattered by the lattices, which take into account the influence of the lattices' topological structure, are derived. These expressions can be used for studying the near and far zones of the scattered fields.

Keywords: magnetodielectrical sphere, integral equation, lattice.

Let us consider a complex spatial lattice consisting of C sub-lattices c ($c \in C$). These sub-lattices correspond to the coordinate representation having the following form in the Cartesian coordinate system:

$$\begin{aligned} x_{c,s} &= [s - 0,5\{(-1)^s - 1\}]d - (-1)^{s-1}x_{c,s=0} \\ &\quad (s = 0, \pm 1, \pm 2, \dots), \\ y_{c,t} &= [t - 0,5\{(-1)^t - 1\}]h - (-1)^{t-1}y_{c,t=0} \\ &\quad (t = 0, \pm 1, \pm 2, \dots), \\ z_{c,p} &= [p - 0,5\{(-1)^p - 1\}]l - (-1)^{p-1}z_{c,p=0} \\ &\quad (p = 0, \pm 1, \pm 2, \dots), \end{aligned} \quad (1)$$

where values d, h, l are defined by the conditions $x = 0, x = d; y = 0, y = h; z = 0, z = l$, and $x_{c,s=0}, y_{c,t=0}, z_{c,p=0}$ are coordinates of the node generating the sub-lattice c and being within the domain

$$\begin{aligned} 0 &\leq x_{c,s=0} \leq d, \\ 0 &\leq y_{c,t=0} \leq h, \\ 0 &\leq z_{c,p=0} \leq l. \end{aligned} \quad (2)$$

Coordinates $x_{c,s}, y_{c,t}, z_{c,p}$ define location of the lattice nodes c beyond the domain (2) limits and are the functions of the coordinates $x_{c,s=0}, y_{c,t=0}, z_{c,p=0}$. Each node of the c sub-lattice (1) is correlated with the ordered three numbers – $c(p, s, t)$, the chosen node of the lattice will be denoted by $c'(p', s', t')$. Setting the maximum value for the numbers (p, s, t) in (1), it is possible to consider the finite and infinite lattices.

The cell of the lattice is formed of C nodes within the domain (2), which will be repeated beyond the domain (2) limits by the coordinate representation (1) in the form of the spatial lattice.

A distance between the nodes (1) define as

$$r_{c'(p',s',t'),c(p,s,t)} = \sqrt{(x_{c',s'} - x_{c,s})^2 + (y_{c',t'} - y_{c,t})^2 + (z_{c',p'} - z_{c,p})^2}. \quad (3)$$

The nodes of sub-lattices (1) incorporate the centers of spheres with permittivities $\epsilon_{c(p,s,t)}$, and permeabilities $\mu_{c(p,s,t)}$, radii $a_{c(p,s,t)}$, volumes $V_{c(p,s,t)}$, which further on will be denoted by $\epsilon_c, \mu_c, a_c, V_c$. The lattice spheres are in the medium with permittivity ϵ_0 and permeability μ_0 .

For solving similar problems, it is convenient to use integral equations of electromagnetics [1, 2]. Here the integral equations presented in [2] will be used, and the problem will be solved in two stages. In the first stage, the internal field of the scattering spheres will be found. In the second stage, we will find the field scattered by the spatial lattice of spheres.

The field scattered on the lattice over the known internal field of scatterers will be defined through electric $\vec{\Pi}^e$ and magnetic $\vec{\Pi}^m$ Hertz potentials

$$\begin{aligned} \vec{E}_{pacc} &= (\nabla \nabla + k^2 \epsilon_0 \mu_0) \vec{\Pi}^e - ik\mu_0 [\nabla, \vec{\Pi}^m], \\ \vec{H}_{pacc} &= (\nabla \nabla + k^2 \epsilon_0 \mu_0) \vec{\Pi}^m + ik\epsilon_0 [\nabla, \vec{\Pi}^e]. \end{aligned} \quad (4)$$

Hertz potentials of the field scattered by separate spheres will be presented in the form

$$\begin{aligned}\bar{\Pi}_{c(p,s,t)}^0(\vec{r},t) &= \\ &= \frac{1}{4\pi} \int_{V_c} \left(\frac{\epsilon_c}{\epsilon_0} - 1 \right) \bar{E}_{c(p,s,t)}^0(\vec{r}',t) f_c(|\vec{r} - \vec{r}'|) dV, \\ \bar{\Pi}_{c(p,s,t)}^M(\vec{r},t) &= \\ &= \frac{1}{4\pi} \int_{V_c} \left(\frac{\mu_c}{\mu_0} - 1 \right) \bar{H}_{c(p,s,t)}^0(\vec{r}',t) f_c(|\vec{r} - \vec{r}'|) dV,\end{aligned}\quad (5)$$

where $\bar{E}_{c(p,s,t)}^0(\vec{r}',t)$, $\bar{H}_{c(p,s,t)}^0(\vec{r}',t)$ are the internal fields of the scatterer, V_c is the scatterer volume, the function $f(|\vec{r} - \vec{r}'|)$ is the solution of the equation

$$\Delta f(|\vec{r} - \vec{r}'|) + k^2 \epsilon_0 \mu_0 f(|\vec{r} - \vec{r}'|) = -4\pi \delta(|\vec{r} - \vec{r}'|),$$

that meets requirements of radiation on infinity and is written as

$$f(|\vec{r} - \vec{r}'|) = \frac{e^{-ik\sqrt{\epsilon_0\mu_0}|\vec{r} - \vec{r}'|}}{|\vec{r} - \vec{r}'|}. \quad (6)$$

It is possible to show that for the points beyond the sphere ($r > r'$), the sphere volume integral of Green function (6) has the form

$$\begin{aligned}W_{c(p,s,t)}(\vec{r}) &= \int_{V_c} \frac{e^{-ik\sqrt{\epsilon_0\mu_0}|\vec{r} - \vec{r}'|}}{|\vec{r} - \vec{r}'|} dV = \\ &= \frac{4\pi}{k_1^3} (\sin k_1 a_c - k_1 a_c \cos k_1 a_c) \frac{e^{-ik_1 r}}{r},\end{aligned}\quad (7)$$

where $k_1 = k\sqrt{\epsilon_0\mu_0}$, $k = 2\pi/\lambda_0$, r defines the distance from the center to the points beyond the sphere.

Let us present the field in the form

$$\bar{E}(\vec{r},t) = \bar{E}(\vec{r})e^{i\omega t}, \quad \bar{H}(\vec{r},t) = \bar{H}(\vec{r})e^{i\omega t}.$$

Assume that beyond the sphere $a_c/\lambda \ll 1$, where $\lambda = \lambda_0/\sqrt{\epsilon_0\mu_0}$ is the wavelength beyond the sphere, but within the sphere, there is possible the resonant case $a_c/\lambda_g \geq 1$, and $\lambda_g = \lambda_0/\sqrt{\epsilon_c\mu_c}$ is the wavelength in the sphere.

In the beginning, calculate the internal field of the scatterers for the case when inside the sphere $a_c/\lambda_g \ll 1$ and outside it $a_c/\lambda \ll 1$, and then generalize the results of calculations for the resonant case when $a_c/\lambda_g \geq 1$ within the sphere [3].

The internal field $c'(p',s',t')$ of the sphere will be found from the system of quasi-stationary inhomogeneous equations, which will be built on the basis of the integral equations [2]. The inhomogeneous equation for the internal electric field of the random sphere $c'(p',s',t')$ is as follows

$$\begin{aligned}\bar{E}_{0c'(p',s',t')}(\vec{r}',t) &= \left\{ \left[1 + \frac{1}{3} \left(\frac{\epsilon_{c'}}{\epsilon_0} - 1 \right) \right] \times \right. \\ &\times \bar{E}_{c'(p',s',t')}^0(\vec{r}',t) - \sum_p \sum_s \sum_t \left\{ \left(\nabla \nabla + k^2 \epsilon_0 \mu_0 \right) \times \right. \\ &\quad \left. \left. c'(p,s,t) \neq c'(p',s',t') \right) \times \right. \\ &\quad \times \frac{1}{4\pi} \left(\frac{\epsilon_{c'}}{\epsilon_0} - 1 \right) W_{c'(p,s,t)}^0(\vec{r}) \bar{E}_{c'(p,s,t)}^0(\vec{r}',t) - \\ &\quad \left. \left. - ik\mu_0 \left[\nabla, \frac{1}{4\pi} \left(\frac{\mu_{c'}}{\mu_0} - 1 \right) W_{c'(p,s,t)}^M(\vec{r}) \bar{H}_{c'(p,s,t)}^0(\vec{r}',t) \right] \right\} \right\} - \\ &- \sum_{c=1}^C \left(\sum_p \sum_s \sum_t \left\{ \left(\nabla \nabla + k^2 \epsilon_0 \mu_0 \right) \frac{1}{4\pi} \left(\frac{\epsilon_c}{\epsilon_0} - 1 \right) \times \right. \right. \\ &\quad \left. \left. (c \neq c') \right) \times W_{c(p,s,t)}^0(\vec{r}) \bar{E}_{c(p,s,t)}^0(\vec{r}',t) - ik\mu_0 \times \right. \\ &\quad \left. \left. \times \left[\nabla, \frac{1}{4\pi} \left(\frac{\mu_c}{\mu_0} - 1 \right) W_{c(p,s,t)}^M(\vec{r}) \bar{H}_{c(p,s,t)}^0(\vec{r}',t) \right] \right\} \right\} \quad (8)\end{aligned}$$

where $\bar{E}_{0c'(p',s',t')}(\vec{r}',t)$, $\bar{H}_{0c'(p',s',t')}(\vec{r}',t)$ is the field of the incident wave; $\bar{E}_{c'(p',s',t')}^0(\vec{r}',t)$, $\bar{H}_{c'(p',s',t')}^0(\vec{r}',t)$ is the internal field of a $c'(p',s',t')$ sphere; and $\bar{E}_{c(p,s,t)}(\vec{r}',t)$, $\bar{H}_{c(p,s,t)}(\vec{r}',t)$ are the internal fields of the other spheres.

The values $W_{c(p,s,t)}^0(\vec{r}')$, $W_{c(p,s,t)}^M(\vec{r}')$ are obtained from (3,7,8)

$$\begin{aligned}W_{c(p,s,t)}^0(\vec{r}') &= \frac{4\pi}{k_1^3} (\sin k_1 a_c - k_1 a_c \cos k_1 a_c) \times \\ &\times \frac{e^{-ik_1 r_{c'(p',s',t'),c(p,s,t)}}}{r_{c'(p',s',t'),c(p,s,t)}}, \\ W_{c(p,s,t)}^M(\vec{r}') &= -\frac{4\pi}{k_1^3} (\sin k_1 a_c - k_1 a_c \cos k_1 a_c) \times \\ &\times \frac{e^{-ik_1 r_{c'(p',s',t'),c(p,s,t)}}}{r_{c'(p',s',t'),c(p,s,t)}}.\end{aligned}$$

The equation for the internal magnetic field of the sphere $c'(p',s',t')$ looks like equations (8), if to replace the electric values by the magnetic ones.

Equations (8) represent an algebraic system of vector inhomogeneous equations $2N = 2 \sum_{c=1}^C N_c$, where N is the general number of the lattice spheres and N_c

is the number c of sub-lattice spheres. Solution of this system of equations for the sphere $c'(p', s', t')$ yields:

$$\begin{aligned} \bar{E}_{c'(p', s', t')}^0(\bar{r}', t) &= \frac{1}{\Delta^{3M}} \times \\ &\times \sum_{c=1}^C \left[\sum_u \left[\bar{g}_u^{3u'} \bar{E}_{0c(p, s, t)}(\bar{r}', t) + \bar{g}_u^{3u'} \bar{H}_{0c(p, s, t)}(\bar{r}', t) \right] \right], \\ \bar{H}_{c'(p', s', t')}^0(\bar{r}', t) &= \frac{1}{\Delta^{3M}} \times \\ &\times \sum_{c=1}^C \left[\sum_u \left[\bar{g}_u^{Mu'} \bar{H}_{0c(p, s, t)}(\bar{r}', t) + \bar{g}_u^{Mu'} \bar{E}_{0c(p, s, t)}(\bar{r}', t) \right] \right], \end{aligned} \quad (9)$$

where Δ^{em} is the determinant of the main matrix of the system of equations (8).

The obtained solutions (9) are true when $a_c/\lambda \ll 1$ outside and $a_c/\lambda_g \ll 1$ within the sphere. But they can be generalized for the resonant case $a_c/\lambda_g \geq 1$, if the effective permittivity and permeability [3,4,5] are introduced instead of ϵ_c and μ_c .

$$\begin{aligned} \epsilon_{cef} &= \epsilon_c F(k a_c \sqrt{\epsilon_c \mu_c}), \\ \mu_{cef} &= \mu_c F(k a_c \sqrt{\epsilon_c \mu_c}), \end{aligned} \quad (10)$$

where

$$\begin{aligned} F(k a_c \sqrt{\epsilon_c \mu_c}) &= \\ &= \frac{2(\sin k a_c \sqrt{\epsilon_c \mu_c} - k a_c \sqrt{\epsilon_c \mu_c} \cos k a_c \sqrt{\epsilon_c \mu_c})}{(k^2 a_c^2 \epsilon_c \mu_c - 1) \sin k a_c \sqrt{\epsilon_c \mu_c} + k a_c \sqrt{\epsilon_c \mu_c} \cos k a_c \sqrt{\epsilon_c \mu_c}}. \end{aligned}$$

Hertz potentials (4) of the field scattered by the lattice spheres can be presented taking into account (9) and (10) in the form of superposition of the lattice separate spheres' Hertz potentials (5)

$$\begin{aligned} \bar{\Pi}^0(\bar{r}, t) &= \sum_{c=1}^C \left[\sum_{p, s, t} \sum_{k_1} \frac{1}{k_1^3} (\sin k_1 a_c - k_1 a_c \cos k_1 a_c) \times \right. \\ &\times \left. \left(\frac{\epsilon_{cef}}{\epsilon_0} - 1 \right) \bar{E}_{c(p, s, t)}^0(\bar{r}', t) \frac{e^{-ik_1 r_{c(p, s, t)}}}{r_{c(p, s, t)}} \right], \\ \bar{\Pi}^M(\bar{r}, t) &= - \sum_{c=1}^C \left[\sum_{p, s, t} \sum_{k_1} \frac{1}{k_1^3} (\sin k_1 a_c - k_1 a_c \cos k_1 a_c) \times \right. \\ &\times \left. \left(\frac{\mu_{cef}}{\mu_0} - 1 \right) \bar{H}_{c(p, s, t)}^0(\bar{r}', t) \frac{e^{-ik_1 r_{c(p, s, t)}}}{r_{c(p, s, t)}} \right]. \end{aligned} \quad (11)$$

Here

$$r_{c(p, s, t)} = \sqrt{(x - x_{c, s})^2 + (y - y_{c, t})^2 + (z - z_{c, p})^2}, \quad (12)$$

where (x, y, z) are the coordinates of the observation point of the scattered field outside the lattice sphere,

$(x_{c, s}, y_{c, t}, z_{c, p})$ are the coordinates of the center point of the scattering sphere (1). Then, taking into account (10) and (11) and using (4) we will find the sought field scattered on the lattice spheres

$$\begin{aligned} \bar{E}_{scat} &= \sum_{c=1}^C \left[\sum_{p, s, t} \sum_{k_1} \frac{1}{k_1^3} (\sin k_1 a_c - k_1 a_c \cos k_1 a_c) \times \right. \\ &\times \left. \left\{ \left(\frac{\epsilon_{cef}}{\epsilon_0} - 1 \right) \bar{L}_c \bar{E}_{c(p, s, t)}^0(\bar{r}') - ik_1 \mu_0 \left(\frac{\mu_{cef}}{\mu_0} - 1 \right) \times \right. \right. \\ &\times \left. \left. (-1) \bar{P}_c \bar{H}_{c(p, s, t)}^0(\bar{r}') \right\} e^{i(\omega t - k_1 r_{c(p, s, t)})} \right], \\ \bar{H}_{scat} &= \sum_{c=1}^C \left[\sum_{p, s, t} \sum_{k_1} \frac{1}{k_1^3} (\sin k_1 a_c - k_1 a_c \cos k_1 a_c) \times \right. \\ &\times \left. \left\{ \left(\frac{\mu_{cef}}{\mu_0} - 1 \right) (-1) \bar{L}_c \bar{H}_{c(p, s, t)}^0(\bar{r}') + \right. \right. \\ &\times \left. \left. ik_1 \epsilon_0 \left(\frac{\epsilon_{cef}}{\epsilon_0} - 1 \right) \bar{P}_c \bar{E}_{c(p, s, t)}^0(\bar{r}') \right\} e^{i(\omega t - k_1 r_{c(p, s, t)})} \right], \end{aligned} \quad (13)$$

where \bar{L}_c and \bar{P}_c are functional matrices of the form

$$\begin{aligned} \bar{L}_c &= \begin{bmatrix} \Psi_{xxc} & \Psi_{xyc} & \Psi_{xzc} \\ \Psi_{yxc} & \Psi_{yyc} & \Psi_{yzc} \\ \Psi_{zxc} & \Psi_{zyc} & \Psi_{zcc} \end{bmatrix}; \\ \bar{P}_c &= \begin{bmatrix} 0 & \Psi_{zc} & \Psi_{yc}^0 \\ \Psi_{zc}^0 & 0 & \Psi_{xc} \\ \Psi_{yc} & \Psi_{xc}^0 & 0 \end{bmatrix}. \end{aligned} \quad (14)$$

The values making part of the functional matrices (14) have the form (1), (12)

$$\begin{aligned} \Psi_{xxc} &= \frac{1}{r_{c(p, s, t)}} k^2 \epsilon_0 \mu_0 + \frac{3(x - x_{c, s})^2 - r_{c(p, s, t)}^2}{r_{c(p, s, t)}^5} - \\ &- \frac{k_1^2 (x - x_{c, s})^2}{r_{c(p, s, t)}^3} + ik_1 \frac{3(x - x_{c, s})^2 - r_{c(p, s, t)}^2}{r_{c(p, s, t)}^4}, \\ \Psi_{yyc} &= \frac{1}{r_{c(p, s, t)}} k^2 \epsilon_0 \mu_0 + \frac{3(y - y_{c, t})^2 - r_{c(p, s, t)}^2}{r_{c(p, s, t)}^5} - \\ &- \frac{k_1^2 (y - y_{c, t})^2}{r_{c(p, s, t)}^3} + ik_1 \frac{3(y - y_{c, t})^2 - r_{c(p, s, t)}^2}{r_{c(p, s, t)}^4}, \\ \Psi_{zcc} &= \frac{1}{r_{c(p, s, t)}} k^2 \epsilon_0 \mu_0 + \frac{3(z - z_{c, p})^2 - r_{c(p, s, t)}^2}{r_{c(p, s, t)}^5} - \end{aligned}$$

$$\begin{aligned}
& -\frac{k_1^2(z-z_{c,p})^2}{r_{c(p,s,t)}^3} + ik_1 \frac{3(z-z_{c,p})^2 - r_{c(p,s,t)}^2}{r_{c(p,s,t)}^4}, \\
\Psi_{xyc} = \Psi_{yxc} &= \frac{3(x-x_{c,s})(y-y_{c,t})}{r_{c(p,s,t)}^5} - \\
& -k_1^2 \frac{(x-x_{c,s})(y-y_{c,t})}{r_{c(p,s,t)}^3} + ik_1 \frac{3(x-x_{c,s})(y-y_{c,t})}{r_{c(p,s,t)}^4}, \\
\Psi_{xzc} = \Psi_{zxc} &= \frac{3(x-x_{c,s})(z-z_{c,p})}{r_{c(p,s,t)}^5} - \\
& -k_1^2 \frac{(x-x_{c,s})(z-z_{c,p})}{r_{c(p,s,t)}^3} + ik_1 \frac{3(x-x_{c,s})(z-z_{c,p})}{r_{c(p,s,t)}^4}, \\
\Psi_{yyc} = \Psi_{zyc} &= \frac{3(y-y_{c,t})(z-z_{c,p})}{r_{c(p,s,t)}^5} - \\
& -k_1^2 \frac{(y-y_{c,t})(z-z_{c,p})}{r_{c(p,s,t)}^3} + ik_1 \frac{3(y-y_{c,t})(z-z_{c,p})}{r_{c(p,s,t)}^4}, \\
\Psi_{xc} &= \frac{(x-x_{c,s})}{r_{c(p,s,t)}^3} + ik_1 \frac{(x-x_{c,s})}{r_{c(p,s,t)}^2}, \quad \Psi_{xc}^0 = -\Psi_{xc}, \\
\Psi_{yc} &= \frac{(y-y_{c,t})}{r_{c(p,s,t)}^3} + ik_1 \frac{(y-y_{c,t})}{r_{c(p,s,t)}^2}, \quad \Psi_{yc}^0 = -\Psi_{yc}, \\
\Psi_{zc} &= \frac{(z-z_{c,p})}{r_{c(p,s,t)}^3} + ik_1 \frac{(z-z_{c,p})}{r_{c(p,s,t)}^2}, \quad \Psi_{zc}^0 = -\Psi_{zc},
\end{aligned}$$

The field at the random point of space outside the sphere will be presented in the form (13)

$$\vec{E}(\vec{r}, t) = \vec{E}_0(\vec{r}, t) + \vec{E}_{scat}(\vec{r}, t),$$

where $\vec{E}_0(\vec{r}, t)$ is the incident wave undisturbed field.

Expressions for internal and scattered fields of the magnetodielectric spheres lattice are derived in the considered problem, they are true when $a_c/\lambda \ll 1$ outside the spheres and $ka_c\sqrt{\epsilon_c\mu_c} \geq 1$ within the spheres.

The given solution can be useful when developing devices for antenna radiation field control and creating anisotropic composition materials.

REFERENCES

1. K. S. Shifrin. Scattering of light in the turbid medium. M.; L.: GITTL, 1951. P. 288. (In Russian)
2. N. A. Khizhniak. Integral equations of macroscopic electrodynamics. Kiev.: Naukova Dumka. 1986. P. 279 (In Russian).
3. A. I. Kozar'. Scattering of electromagnetic waves in the waveguide with homogeneous magnetodielectric spheres// Radiophysics and Electronics. - Kharkov: Institute of Radiophysics and Electronics of NAS of Ukraine. - 2002. - 7. - Special Issue. - P. 183-189 (in Russian)
4. L. Levin. Modern theory of waveguides. M.: Foreign Literature. 1954. P. 216 (In Russian).
5. A. I. Kozar', N. A. Khizhniak. Reflection of electromagnetic waves from the resonant dielectric sphere in the waveguide// Ukr.Phys.J. 1970. V. 15. P. 847-849 (In Russian).

METHOD OF GENERALIZED EIKONAL AND NEW 2-D SCATTERING ANALYTICAL SOLUTIONS

Michael V. Vesnik

Institute of Radio Engineering and Electronics of Russian Academy of Sciences
11 Mokhovaya Str., Bldg. 7, K-9, GSP-9, 101999, Moscow, Russia
<vesnik@mail.cplire.ru>

Recently a new method for analytical solving of 2-D diffraction problems was introduced in [1], [2]. As an example analytical solution for diffraction of electromagnetic wave on 2-dimensional perfectly conducting finite thickness half-plate based on this method was presented in [3]. In this paper main features of final version of the method are formulated.

The purpose of the method is to solve 2-D Helmholtz equation boundary value problem for perfectly conducting scatterers of arbitrary shape. Key point of the method lies in usage of integral representations received for special "generalized eikonal" function satisfying Laplace equation in one region (named here as "supplementary region") as a solution in another region (named here as "main region") of boundary value problem for Helmholtz equation with variable wavenumber. "Generalized eikonal" function is named in such way because it is developed from incident wave eikonal function by adding a supplementary radial coordinate. Usual radial coordinate with usual angular coordinate form "main region" while supplementary radial coordinate with the same angular coordinate form "supplementary region". In "main region" "generalized eikonal" function satisfies Helmholtz equation with variable wavenumber while in "supplementary region" it satisfies Laplace equation. "Main region" is a full complex plane. Upper and lower half - planes of this plane represent two copies of conformal transformation of scatterer exteriority on a half - plane. Upper and lower half - planes are "pasted" along horizontal axis which corresponds to the border of the scatterer. Non-scattered incident wave is defined in upper half - plane and non-scattered reflected wave is defined in lower half - plane. Scattered parts of both waves are defined in whole complex plane. "Supplementary region" represents similar full complex plane but with another dependence of "generalized eikonal" function on radial and angular coordinates. "Main region" and "supplementary region" intersect along the special curve. On this curve variable wavenumber from Helmholtz equation is a constant value. Also, on this curve values of incident wave function and "generalized eikonal" function are the same. This curve includes observation point as well as saddle points of "generalized eikonal" function. Applying Cauchy's residue theorem the value of "generalized eikonal" function in

observation point can be represented as an integral along a closed path in "supplementary region". Selecting in "supplementary region" parts of the closed path where incident wave function gets smaller while wavenumber gets higher one can construct solution for scattered wave in "main region" taking in account the fact that integrals over parts of the closed parts can be expressed in terms of values in saddle points of "generalized eikonal" function. Saddle points are common for "main region" and "supplementary region". Asymptotic expressions may be received in convenient compact form.

Fig. 1 depicts 2-D half-infinite perfectly conducting scatterer of arbitrary shape excited by plane wave $P(r_z, \varphi_z) = \exp[iS(r_z, \varphi_z)]$ where $S(r_z, \varphi_z) = -kr_z \cos(\varphi_z - \varphi_0)$ is eikonal function. Exteriority of the scatterer named as "region z ". P_1 and P_2 are incident and reflected waves. z_0 is observation point.

Fig. 2 depicts upper half-plane named as "region w ". Region w and region z are connected by conformal transformation $z = Z(w)$. w_0 is observation point.

Fig. 3 depicts "region d ", where $d = r_d \exp(i\varphi_d)$ determined by equation $dz/dw = d$. Condition $r_d = \text{const} = r_{d0}$ determines circle r_{d0} in region d and curves named as "curve r_{d0} " shown in Fig. 1 and Fig. 2.

Fig. 4 depicts region $\ln d$, d_0 is observation point.

Fig. 5 depicts introduction of additional radial vari-

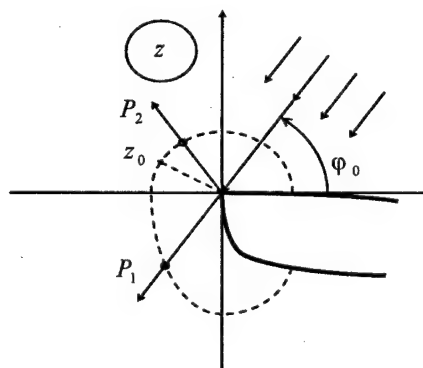


Fig. 1.

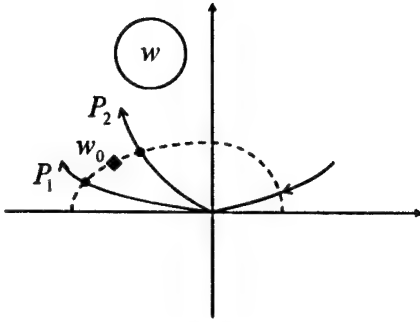


Fig. 2.

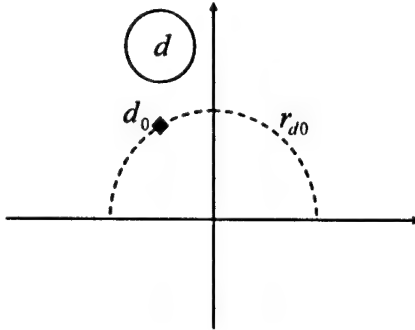


Fig. 3.

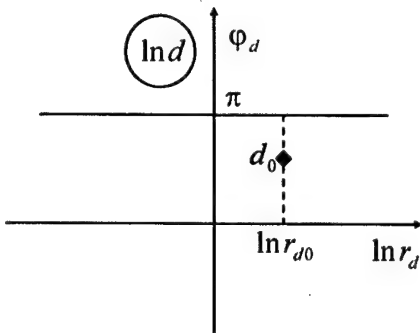


Fig. 4.

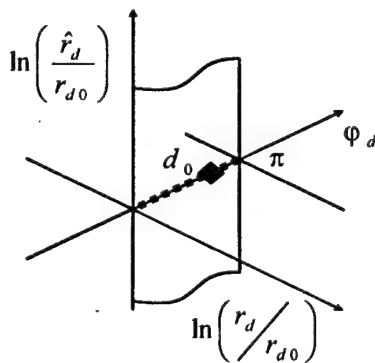


Fig. 5.

able \hat{r}_d . This variable is being included into angular variable φ_d by the following equation $\varphi_d^c = \varphi_d - i \ln(\hat{r}_d/r_{d0})$. Fixing $r_d = r_{d0}$ and replacing φ_d by φ_d^c in variable d one can get new variable

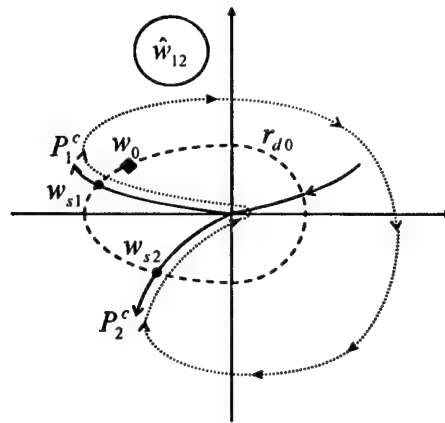


Fig. 6.

$\hat{d} = r_{d0} \exp(i\varphi_d^c)$ or what is the same $\hat{d} = \hat{r}_d \exp(i\varphi_d)$. Replacing φ_d by φ_d^c in eikonal function one can get so called "generalized eikonal function" $S^g(r_d, \hat{r}_d, \varphi_d)$ which gives the name to our method:

$$S[r_z(r_d, \varphi_d^c), \varphi_z(r_d, \varphi_d^c)] = -kr_z(r_d, \varphi_d^c) \times \cos[\varphi_z(r_d, \varphi_d^c) - \varphi_0] = S^g(r_d, \hat{r}_d, \varphi_d^c).$$

Fixing $\hat{r}_d = r_{d0}$ gives $\varphi_d^c = \varphi_d$ and $P^g(r_d, r_{d0}, \varphi_d) = P[r_z(r_d, \varphi_d), \varphi_z(r_d, \varphi_d)]$ while fixing $r_d = r_{d0}$ gives new function of complex variable φ_d^c :

$$P[r_z(r_{d0}, \varphi_d^c), \varphi_z(r_{d0}, \varphi_d^c)] = \exp\{-ikr_z(r_{d0}, \varphi_d^c) \times \cos[\varphi_z(r_{d0}, \varphi_d^c) - \varphi_0]\} = P^g(r_{d0}, \hat{r}_d, \varphi_d) = P^c(\varphi_d^c).$$

It may be shown [1], [2] that $P^c(\varphi_d^c)$ satisfies Laplace equation in region \hat{d} while $P(r_z, \varphi_z)$ satisfies Helmholtz equation with variable wavenumber in region d . Thus in accordance with Cauchy's residue theorem one can write:

$$\exp[iS^c(w_0)] = \frac{1}{2\pi i} \oint \frac{1}{\hat{w} - w_0} \exp[iS^c(\hat{w})] d\hat{w}$$

where connection between variables \hat{w} and \hat{d} is established by the same relations which connect variables w and d .

Fig. 6 depicts region \hat{w} with closed contour placed in this region. Extracting from closed contour pieces on which $P^c(\varphi_d^c)$ gets smaller while wavenumber k gets higher and integrating over these pieces one can receive asymptotic solution for scattered field:

$$U(k, r_{w0}, \varphi_{w0}, \varphi_0) = \sum_{n=1}^N \left[\sqrt{\frac{1}{2\pi [S^c(w_{sn})]''}} \frac{A_n}{w_{sn} - w_0} \times \exp[iS^c(w_{sn}) - i\frac{\pi}{4} + \psi_n] \right],$$

where parameters A_n and ψ_n depend on initial conditions of the problem. Here w_{sn} are saddle points of function $P^c(\varphi_d^c)$ which are disposed on the curve r_{d0} . Curve r_{d0} is common for regions w and \hat{w} .

Method of generalized eikonal makes it possible to use standard approach in wide range of diffraction problems and leads to analytical solutions with relatively simple analytical formulas.

REFERENCES

1. M. Vesnik, "An analytical solution of boundary problem for Helmholtz equation", *Journal of Communications Technology and Electronics*, vol. 45, No. 1, 2000, pp. 59-68. Translated from: "Analiticheskoe reshenie krajevoi zadachi dlja uravnenija Helmholtz'a" (in Russian), *Radiotekhnika i Elektronika*, vol. 45, No. 1, 2000, pp. 66-76.
2. M.V. Vesnik "Analytical solution for electromagnetic diffraction on 2-D perfectly conducting scatterers of arbitrary shape", *IEEE Trans. Antennas Propagat.*, vol. 49, pp. 1638-1644, Dec. 2001
3. M.V. Vesnik "Analytical solution for electromagnetic diffraction on 2-D half-plate with finite thickness", *12^{èmes} Journées Internationales de Nice sur les Antennes (12th International Symposium on Antennas) (JINA)*, 12-14 November 2002, Nice, France vol. 2, pp. 273-276.

THE VIDEOPULSE SCATTERING IN INHOMOGENEOUS MEDIA CONTAINING CONDUCTIVE CYLINDER OBJECTS

Varyanitzia-Roshchupkina L. A.

A. Ya. Usikov Institute of Radio Physics and Electronics of NASU, Kharkiv, Ukraine
<vla@ire.kharkov.ua>

Abstract

The results of the computer simulation of videopulse scattering on the conductive cylinder objects buried in inhomogeneous media are presented in this work. The finite difference time domain method (FDTD) and Mur's absorbing boundary conditions of second order were used to regularize the problem. The analysis and the comparison of the scattered electromagnetic fields obtained at different dielectric parameters of the media and different sizes of the conductive objects were carried out.

Keywords: videopulse, GPR, computer simulation, FDTD-method, profile.

1. INTRODUCTION

The ground penetrating radar (GPR) is of a great interest, and continues to attract more and more attention all over the world. The solution of the problems of detection and recognition of objects with different shapes buried in complex inhomogeneous dispersive and absorbing media, and the investigation of the composition and texture of the layered structures is a complex and, at the same time, actual problem for many spheres of the national economy (e.g. detection of pipes, cables, pipeline breaking, cavities, fractures, archeological findings and landmines in soil). The theoretical work in this area is carried out in two directions: the solution of direct problems of pulse diffraction by the subsurface objects and the inverse problems of determining the object shape and position from some existing echo.

The inverse problem solution is remarkable in that it answers the question of which shape and position the sought-for objects have. However, the methods of the problem solution are only under development. Therefore, the solution of the direct problems of diffraction takes on a special significance. Simulation of the desired situations and determination of regularities will help to understand the essence of existing processes and give answers to many questions of interest.

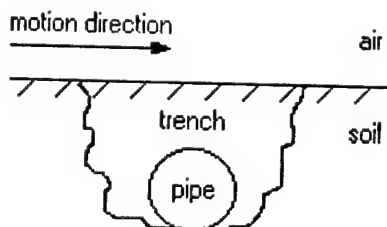


Fig. 1. The general geometry of the problem

2. THE PROBLEM DEFINITION

The objective of the given work is to simulate the process of a continuous survey of a flat country segment on the way cross backfilled trenches, which do not contain foreign objects, as well as ditches having a bottom pipeline (Fig. 1).

To simplify further analysis of the simulation results, we used the following assumptions:

1. The sounded ground surface is completely plane;
2. The trench, in its cross-section, has a trapezoidal form;
3. The ground inside the trench is
 - either homogeneous, and differs from the ground outside the trench in a higher or lower humidity;
 - or inhomogeneous, and represents an accumulation of ground blocks which differ, as in the previous case, from the ground outside the trench in their dielectric characteristics.

The sounding electromagnetic field, in the form of the Gaussian pulse time-derivative (Fig. 2), is excited by the point source located at the height h_1 above the ground. The pulse duration at the level of 3 dB equals 2.5 ns, and the amplitude is 1 Vpm.

The observation point is at the height h_1 over the ground and at the distance h_2 from the source.

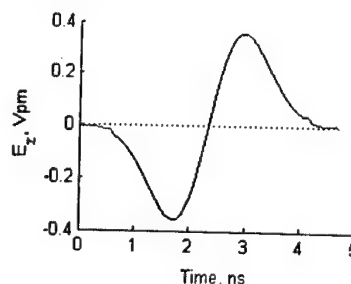


Fig. 2. The source field

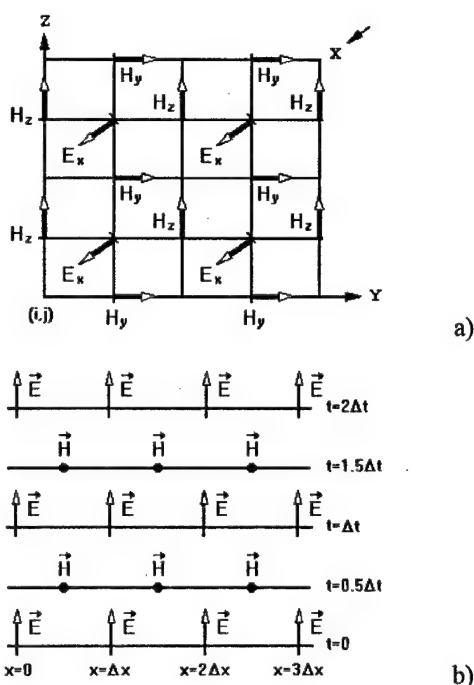


Fig. 3. a) Position of the electric and magnetic field vector components about a square unit cell of the Yee space lattice; b) Space-time chart of the Yee algorithm.

The calculation of the scattered fields is carried out by the finite-difference time-domain method (FDTD), which is one of the direct methods of solving Maxwell's differential equations [1, 2]. This method is used in the program Grider, developed by the author of the given work [3].

The main ideas of the used FDTD method:

1. All the calculations are performed using the space-time grid imposed upon the spatial and time-domains concerned; the grid cell sizes, in time and space, are in a special relationship providing numerical stability of the algorithm.
2. The spatial and time derivatives in Maxwell's differential equations are replaced by finite differences.
3. Yee algorithm realization [4].

The Yee algorithm centers its components E and H in the space in such a way that each component E is surrounded by four circulating components H , and each component H is surrounded by four circulating components E (Fig. 3a).

The Yee algorithm centers its components E and H in time in the so-called "leapfrog" order (Fig. 3b).

The Mur's conditions of second order [5] are used as the absorbing boundary conditions. To reduce the computer time and volume, we consider a two-dimensional spatial region, which should be quite wide nevertheless, in order that the absorbing boundary conditions could not influence the desired solution.

3. THE OBTAINED RESULT DESCRIPTION

In the course of the simulation, we examined several types of the ground inside and outside the trenches as well as the bottom pipelines with different diameters. Some of the most noteworthy and significant results are shown in Tables 1 and 2. The medium characteristics and object sizes are specified for every case in these Tables.

In the given examples the source is at the height $h_1 = 25$ cm above the ground, and the distance between the source and the point of observation is $h_2 = 60$ cm. The observation interval is 30 ns in all of the cases. The radar probing is carried out over the ground spot with length of 2.80 m, and with some structure of interest in the center (Fig. 1). The number of the signals falling down over this length equals 35.

The data visualization method utilizes the profiles plotted by means of the variable density method [6]. The color scale used to show the profile is represented in Fig. 4.

The zero level of the signal amplitude is represented by the gray color, the negative amplitude from 0 to -1 is shown by the light shades up to the white, the positive amplitude from 0 to 1 – by the dark shades up to the black.

The profile images were obtained by means of the georadar data processing program GPR ProView [7].

The data processing itself included only subtraction of a chosen signal (one of the first three signals) from the whole profile.

It follows from Table 1:

1. The profiles, which represent empty trenches, are characterized, first of all, by the distinct reflections from its upper and bottom boundaries. In the presented cases, the side boundaries are hardly noticeable.
2. The reflection pattern depends essentially on the ground humidity in the trench:
 - If the ground humidity in the trench is lower than the ground humidity out of it (Fig. 5.1.a, Fig. 5.2.a), the trench bottom boundary is represented, in the profile, by the hyperbolic reflection, which is rather oblate at the top on the full width of the ditch.
 - If the ground humidity in the trench is higher than the ground humidity out of it (Fig. 5.1.b, Fig. 5.2.b), the trench bottom boundary is represented in the profile by a more bright, than in the first case, almost plane reflection. In this case the ditch is a good resonator, therefore the "ringing" responses following the bottom-boundary reflection are clearly seen in the presented profiles.
3. Because of the media with different permittivity, the upper-boundary reflections come at different speed: they arrive faster in the ground with lower humidity (Fig. 5.1.a, Fig. 5.2.a), and, respectively, they arrive slower in the ground with higher humidity (Fig. 5.1.b, Fig. 5.2.b).

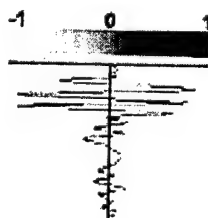
Table 1. Trenches without conductive objects

<p>1. Homogeneous trench.</p>		$d_{1t} = 80 \text{ cm},$ $d_{1b} = 60 \text{ cm},$ $d_2 = 60 \text{ cm};$ $\epsilon_1 = 1,$ $\epsilon_2 = 9,$ $\epsilon_3 = 6;$ $\sigma_1 = 0,$ $\sigma_2 = 0.005,$ $\sigma_3 = 0.005;$ $\mu_1 = \mu_2 = \mu_3 = 1;$	$d_{1t} = 80 \text{ cm},$ $d_{1b} = 60 \text{ cm},$ $d_2 = 60 \text{ cm};$ $\epsilon_1 = 1,$ $\epsilon_2 = 9,$ $\epsilon_3 = 12;$ $\sigma_1 = 0,$ $\sigma_2 = 0.005,$ $\sigma_3 = 0.005;$ $\mu_1 = \mu_2 = \mu_3 = 1;$
<p>Fig. 5.1.a</p>	<p>Fig. 5.1.b</p>		
<p>2. Trench, backfilled with blocky ground.</p>		$d_{1t} = 80 \text{ cm},$ $d_{1b} = 60 \text{ cm},$ $d_2 = 60 \text{ cm};$ $\epsilon_1 = 1,$ $\epsilon_2 = 9,$ $\epsilon_3 = 7;$ $\epsilon_4 = 8;$ $\sigma_1 = 0,$ $\sigma_2 = \sigma_3 = \sigma_4 =$ $= 0.005;$ $\mu_1 = \mu_2 = \mu_3 =$ $= \mu_4 = 1;$	$d_{1t} = 80 \text{ cm},$ $d_{1b} = 60 \text{ cm},$ $d_2 = 60 \text{ cm};$ $\epsilon_1 = 1,$ $\epsilon_2 = 9,$ $\epsilon_3 = 11;$ $\epsilon_4 = 10;$ $\sigma_1 = 0,$ $\sigma_2 = \sigma_3 = \sigma_4 =$ $= 0.005;$ $\mu_1 = \mu_2 = \mu_3 =$ $= \mu_4 = 1;$
<p>Fig. 5.2.a</p>	<p>Fig. 5.2.b</p>		

4. In case that the trench is backfilled with ground blocks, reflections between its upper and bottom boundaries have an explicitly random nature.

In case of trenches with a bottom iron-pipe, we have obtained the following results (Table 2):

1. The reflection from the upper boundary of the trench is clearly seen for trenches of different kinds;
2. The reflection from the pipe surface in the form of the classical or a little distorted hyperbola is clearly seen for trenches of different kinds;
3. Reflections from the bottom boundaries of trenches are overlapped by the reflection of a much higher amplitude from the pipe;
4. Reflections from the pipes with different diameters differ in their intensity and curvature of the hyperbolic curve (the larger diameter the higher in the intensity and the slighter in the curve).


Fig. 4. The color scale

Thus, we can conclude that the profiles which represent the trenches of different kinds with the bottom pipes inside are characterized, first of all, by a clearly visible reflection from the upper boundary of the trench and by the intense hyperbola from the pipe.

4. CONCLUSION

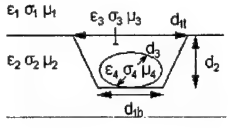

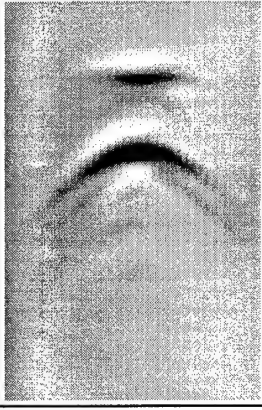
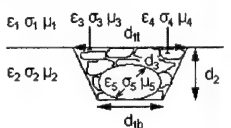

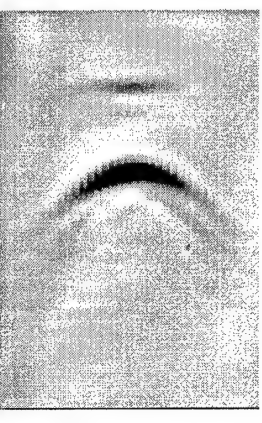
The considered above investigations will help to interpret a wave pattern, been obtained in the course of georadar ground investigations.

The presented results can be used as a sample for recognizing such objects as regions with a disturbed ground structure (trenches, ditches, pits), with or without a bottom pipe.

REFERENCES

1. Taflov. Computational electrodynamics. The Finite-Difference Time-Domain Method. Boston-London. Artech House, 1995.
2. F. Peterson, S. L. Ray, R. Mittra. Computational Methods for Electromagnetics. New York. IEEE PRESS. Oxford, Tokyo, Melbourne. Oxford University Press, 1997.
3. L. A. Varyanitz-Roshchupkina, V. O. Kovalenko. Pulse scattering on objects in the inhomogeneous

Table 2. Trenches having a bottom pipeline

<p>1. Homogeneous trench with a bottom pipe.</p> 	 <p> $d_{1t} = 80 \text{ cm},$ $d_{1b} = 60 \text{ cm},$ $d_2 = 60 \text{ cm},$ $d_3 = 10 \text{ cm};$ $\epsilon_1 = 1,$ $\epsilon_2 = 9,$ $\epsilon_3 = 6,$ $\epsilon_4 = 1;$ $\sigma_1 = 0,$ $\sigma_2 = 0.005,$ $\sigma_3 = 0.005,$ $\sigma_4 = 10^7;$ $\mu_1 = \mu_2 = \mu_3 = 1$ $\mu_4 = 1000;$ </p> <p>Fig. 6.1.a</p>	 <p> $d_{1t} = 80 \text{ cm},$ $d_{1b} = 60 \text{ cm},$ $d_2 = 60 \text{ cm},$ $d_3 = 30 \text{ cm};$ $\epsilon_1 = 1,$ $\epsilon_2 = 9,$ $\epsilon_3 = 6,$ $\epsilon_4 = 1;$ $\sigma_1 = 0,$ $\sigma_2 = 0.005,$ $\sigma_3 = 0.005,$ $\sigma_4 = 10^7;$ $\mu_1 = \mu_2 = \mu_3 = 1$ $\mu_4 = 1000;$ </p> <p>Fig. 6.1.b</p>
<p>2. Trench with a bottom pipe and backfilled with blocky ground.</p> 	 <p> $d_{1t} = 80 \text{ cm},$ $d_{1b} = 60 \text{ cm},$ $d_2 = 60 \text{ cm},$ $d_3 = 10 \text{ cm};$ $\epsilon_1 = 1,$ $\epsilon_2 = 9,$ $\epsilon_3 = 7;$ $\epsilon_4 = 8,$ $\epsilon_5 = 1;$ $\sigma_1 = 0,$ $\sigma_2 = \sigma_3 = \sigma_4 = 0.005,$ $\sigma_5 = 10^7;$ $\mu_1 = \mu_2 = \mu_3 = \mu_4 = 1,$ $\mu_5 = 1000;$ </p> <p>Fig. 6.2.a</p>	 <p> $d_{1t} = 80 \text{ cm},$ $d_{1b} = 60 \text{ cm},$ $d_2 = 60 \text{ cm},$ $d_3 = 30 \text{ cm};$ $\epsilon_1 = 1,$ $\epsilon_2 = 9,$ $\epsilon_3 = 7;$ $\epsilon_4 = 8,$ $\epsilon_5 = 1;$ $\sigma_1 = 0,$ $\sigma_2 = \sigma_3 = \sigma_4 = 0.005,$ $\sigma_5 = 10^7;$ $\mu_1 = \mu_2 = \mu_3 = \mu_4 = 1,$ $\mu_5 = 1000;$ </p> <p>Fig. 6.2.b</p>

- conducting medium. Kharkiv, Radio Physics and Radio Astronomy, 2002, v.7. No.4, pp.435-440.
- K. S. Yee. Numerical solution of initial boundary value problems involving Maxwell's equations in isotropic media. IEEE Trans. Antennas Propagat, vol. AP-14, May 1966.
- G. Mur, Absorbing boundary conditions for the finite-difference approximation of the time-domain electromagnetic field equations. IEEE Trans. Electromagnetic Compatibility, vol. EMC-23, Nov. 1981.
- M. L. Vladov, A. V. Starovoytov. Geo radar overburden investigations. Moscow University House, 1999. (in Russian)
- M. M. Golovko, G. P. Pochanin, V. O. Kovalenko. Presentation of the subsurface videopulse sounding. Kharkov, Radiophysics and electronics, vol. 5, No.2, 2000, pp.134-143. (in Russian)
- M. I. Finkelshtein, V. L. Mendelson, V. A. Kutev Layered ground surface radiolocation. Ed. by M. I. Finkelshtein. Moscow. "Soviet Radio", 1977. (in Russian)

THE LINEAR WIRE IN ANISOTROPIC MEDIUM

Evgueniy O. Yatsenko, Natalia M. Yatsenko

Department of Radiophysics and Electronics, Karazin Kharkiv National University,
Kharkiv, Ukraine
<Yatsenkok@rambler.ru>

Abstract

On the basis of a method of the integral equations of macroscopic electromagnetics concerning a uniaxial anisotropic medium the task of electromagnetic waves scattering of by a single wire and system of two parallel thin linear wires arbitrary situated relatively the axis of anisotropy of the medium is considered. From integral equations of electromagnetics the singular integral equations for density of currents is received and it is solved by a method of partial averaging. The analytical expressions for the electromagnetic fields and radiated power in far zone are obtained.

Keywords: linear wire, current, electromagnetic fields, anisotropic medium.

1. RADIATION OF THE LINEAR WIRE IN ANISOTROPIC MEDIUM

The task posing. In an anisotropic medium (monocrystal, plasma), described by permittivity tensor $\hat{\epsilon}$

$$\hat{\epsilon} = \begin{pmatrix} \epsilon_1 & 0 & 0 \\ 0 & \epsilon_1 & 0 \\ 0 & 0 & \epsilon_3 \end{pmatrix},$$

under any angle γ to the axis of anisotropy (optical axis, OZ axis), the thin linear wire of length $2L$, radius b , and complex surface impedance Z is located. One has to find the distribution of the current, the electromagnetic fields of radiation and the density of the power stream in far zone at a symmetric excitation of the wire, and to determine the conditions of the effective transfer of energy from the wire to medium.

The solution of the task is carried out within the framework of a method of the integral equations of macroscopic electromagnetics. It is shown that for any orientation of the wire the electromagnetic field in far zone represents two waves – the ordinary and unordinary ones. In the specific case of a wire parallel to the axis of anisotropy, the electromagnetic field is characterized only by the unordinary wave. With a symmetric excitation of the wire the power pattern in a plane perpendicular to axis of the wire, as well as in an isotropic medium, represents a circle whose radius is defined by the length of the wire and the equivalent permittivity

$$\epsilon_{eq} \equiv \epsilon_{eq}(\gamma) = \sqrt{\epsilon_3 \sin^2 \gamma + \epsilon_1 \cos^2 \gamma} \times \\ \times \left\{ \sqrt{\epsilon_3 \sin^2 \gamma + \epsilon_1 \cos^2 \gamma} \cos^2 \gamma + \sqrt{\epsilon_1} \sin^2 \gamma \right\}$$

Thus, the anisotropy of the medium alters the pattern shape only in the plane containing the wire. The effect

of the anisotropy of the medium on the patterns is a change in the level of the radiating power, in width and quantity of the lobes, a redistribution of the energy from one lobe to others; and is largely dependent on the length of the wire and its orientation in the medium. For example, for the wire located along the axis of anisotropy, the change of the component ϵ_3 in tensor $\hat{\epsilon}$ does not result in a change of the number of lobes in the pattern. At a deviation of the wire from this axis, the number of lobes in the pattern alters; which is caused by the dependence, in these cases, of the period of the function of the current distribution in the wire versus ϵ_3 . In the impedance wire, the essential influence on it pattern is performed by values of the real and imaginary parts of a surface impedance. The presence of the imaginary part renders the same influence on the pattern, as well as the variation of length of the wire, the anisotropy of the medium or the orientation of the wire in this medium. The real part of the surface impedance of the wire, caused by the thermal losses, results in the disappearance of zero in the pattern of the wire, both in an isotropic and in an anisotropic medium.

2. SYSTEM OF LINEAR WIRES IN ANISOTROPIC MEDIUM

2.1. PARALLEL WIRES

The task posing. In an anisotropic medium, two parallel thin linear wires and a component any angle γ with an axis of anisotropy are located. The lengths of wires are $2L_1$, $2L_2$, the radiuses b_1 , b_2 , the distance in between is d . One has to find the distributions of currents in each wire, electromagnetic fields of radiation and density of a stream of power in far zone.

It is shown that the anisotropy of the medium essentially alters the dependence of an input current (or

the distribution of it) in one wire against the length of other wire, and against the distance d between the wires. The effect of the anisotropy shows up in the change of the amplitude and period of these characteristics, which also depend on the orientation of system of the wires concerning the axis of anisotropy. The influence of the anisotropy of medium and of the orientation of wires in the medium on a period of function of distribution of currents established in each wire, is united in itself by such integral characteristic, as equivalent permittivity of medium ε_{eq} . In wires located under angle γ in uniaxial anisotropic medium, the distribution of a current is established, which the space period is the same as it were, if the wires were placed in an isotropic medium with permittivity $\varepsilon = \varepsilon_{eq}$.

It is known, that for wires located in isotropic medium, the amplitude of an input current of each wire is a periodic damped function of distance d between wires. In anisotropic medium the character of this dependence is kept up, but not for distance d , and for some equivalent distance d_{eq} , including, apart from distance d , the dielectric parameters $\varepsilon_1, \varepsilon_3$ of anisotropic medium and orientation of wires in this medium. For example, for wires laying in one plane with an axis of anisotropy, d_{eq} has the form

$d_{eq}^2 = d^2 \varepsilon_1 \varepsilon_3 \delta^2$. By each concrete system of wire with the given geometry in anisotropic medium can put in conformity some equivalent antenna system in isotropic medium, by choosing in appropriate way its geometrical sizes (this conclusion concerns only the currents, instead of the fields of radiation).

The electromagnetic field of antenna system in far zone represents ordinary and non-ordinary waves. The pattern on power in a plane, perpendicular to wires does not, practically, depend on the anisotropy of medium. Anisotropy has essential influence on the patterns in the plane of wires. The character of this influence is equivalent to change of distance between wires and depends on orientation of wires in medium.

2.2. PERPENDICULAR WIRES

The problem posing. In a uniaxial anisotropic medium two thin mutually perpendicular antennas of arbitrary length are placed, where γ is the angle between the axis of the first antenna and the axis of the anisotropy of medium. The antennas do not cross (have no common points). It is necessary to find the distribution of current in each antenna.

The solution of the problem is obtained on the basis of a method of integral equations of electromagnetics. The system of the integral equations for currents is solved by averaging. The simple expressions for currents are obtained at symmetric excitation of antennas.

It is shown, that the period distribution of a current in each antenna is determined by an equivalent permit-

tivity $\varepsilon_{eq}(\gamma)$. Parameter $\varepsilon_{eq}(\gamma)$ varies for each antenna, as it is determined not only by the permittivity of medium, but also by the orientation of the antenna concerning the axis of anisotropy of medium. Hence, in two identical antennas, the different distributions of current are established. The distribution of the current in the first antenna corresponds to the distribution of current in the antenna working in an isotropic medium with permittivity $\varepsilon_{eq}(\gamma)$; and the distribution of current in the second antenna corresponds to the distribution of current in the antenna working in the isotropic medium with permittivity $\varepsilon_{eq}(\gamma + 90^\circ)$. Thus, the distribution of currents are established in the antennas as if those worked in various media.

It is well known that two perpendicular antennas in an isotropic medium have no effect on the current in each of them. In an uniaxial anisotropic medium, a variation of distance between the perpendicular antennas results in a change of the amplitudes of current in the antennas, when the orientation of antennas does not coincide with the axis of anisotropy of the medium. If one of the antennas is focused along the anisotropy axis, the variation of distance between the antennas does not affect the distribution of current in them. The obtained result can be used for the revealing (indication) of the anisotropy.

3. CONCLUSION

The anisotropy of medium essentially alters all the characteristics of antennas. The functions of distribution of the currents along the antennas is determined by the equivalent permittivity ε_{eq} and the equivalent distance between antennas d_{eq} , which depend on the values of components $\varepsilon_1, \varepsilon_3$ of the permittivity tensor and on the orientation of the antenna system in the medium (angle γ). Hence, these factors determine the shape of patterns. It is possible to arrive at the conclusion on the two ways of the design of the antennas: the electrical (varying the working frequency, that is $\varepsilon_1(\omega), \varepsilon_3(\omega)$) and the mechanical (varying the orientation in the medium). It is known that if one of the components of the permittivity tensor is negative; then with a certain orientation of the antenna system relatively to the axis of anisotropy, the current in the perfectly conducting antenna is not excited. The excitation of significant currents in the impedance antenna in this case is possible, provided that the surface impedance is selected so that it does compensate the reaction of the surrounding plasma. If one puts $\varepsilon_1 = \varepsilon_3$ in the expressions for the fields of radiation and currents, we obtain the appropriate formulas for the isotropic medium. By removing one of the wires to infinity, we obtain the formulas for the single wire.

Thus in the present work, a high efficiency of the method of integral equations is shown up; which has enabled us to have solved the problem of the excitation of two linear wires in an anisotropic medium.

THE KONTOROVICH-LEBEDEV TRANSFORMS AND THE SEMI-INVERSION METHOD IN MODEL EXCITATION PROBLEMS FOR A SLOTTED CONICAL ANTENNAS

Vladimir A. Doroshenko

Department of Higher Mathematics, Kharkiv National University of
Radio Electronics, Kharkiv, Ukraine
<vlad_doroshenko@yahoo.com>

Abstract

The analytical and numerical method for solving a problem of electromagnetic waves scattering on a complex slotted perfectly conducting conical structure is proposed. This method uses the Kontorovich-Lebedev integral transforms and the semi-inversion method. By virtue of it the 3-D scattering problem is reduced to solving algebraic equations system of the second kind. The analytical solution is obtained for a single semi-transparent cone. The applying this method for solving an excitation problem for an imperfectly conducting cone is discussed.

Keywords: complex cone antenna, integral transforms, semi-inversion method, analytical solutions, imperfectly conducting cone.

1. INTRODUCTION

The separable variables method is the traditional one for solving electromagnetic boundary problems. Using the Kontorovich-Lebedev integral transforms simplifies solving boundaries problems for the wave equation in homogeneous cone region (an isotropic cone)[1]. Solutions of excitation problems for spiral and radial conducting cones have been obtained by these transforms in [2]. The method for solving electromagnetic boundary problems for 3-D slotted coaxial cone structures is proposed. This one is based on using the Kontorovich-Lebedev integral transforms and the semi-inversion method that was applied to investigating diffraction problems for 2-D unclosed screens [3].

2. STATEMENT OF THE PROBLEM

The cone structure Σ under consideration consists of two perfectly conducting thin circular infinite cones Σ_1 and Σ_2 ($\Sigma = \Sigma_1 \cup \Sigma_2$) with a common tip and periodical longitudinal N slots. We denote by $2\gamma_j$ the opening angle of the cone Σ_j ($j = 1; 2$), by $l = 2\pi/N$, the period of the cone Σ_j , by d_j the slot width of the cone Σ_j . In the spherical coordinate system r, θ, φ (the cones tip coincides with the origin) the cone Σ_j is defined by the equation $\theta = \gamma_j$. The field source (a harmonic dipole) is located at the point $M_0(r_0, \theta_0, \varphi_0)$.

The total electromagnetic fields those are sought satisfy Maxwell equations, the boundary conditions at the perfectly conducting cone structure, infinity conditions, the condition of finite stored energy. The electromagnetic fields may be written in terms of two scalar Debye potentials $v^{(1)}$ (an electrical potential) and $v^{(2)}$ (a magnetic potential) which satisfy:

- the scalar homogeneous 3-D Helmholtz equation

$$\Delta v^{(s)}(\vec{r}) - q^2 v^{(s)}(\vec{r}) = 0, \quad s = 1; 2;$$

where $\vec{r} \in R^3 \setminus \Sigma_j, \vec{r} \neq \vec{r}_0$; $q = -ik$ is for the time dependence $e^{-i\omega t}$, $q = ik$ is for the time depend-

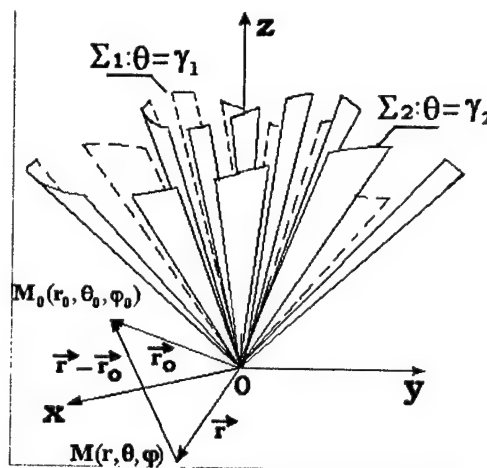


Fig. 1. A Complex Cone

ence $e^{i\omega t}$, k is a wave number;

- the boundary condition

$$\frac{\partial v^{(s)}}{\partial n^{s-1}}|_{\Sigma} = 0; \quad (1)$$

- the principle of ultimate absorption;
- the condition of finite stored energy.

Define the Debye potential $v^{(s)}$ of the total electric or magnetic field as

$$v^{(s)} = v_0^{(s)} + v_1^{(s)},$$

where $v_0^{(s)}$ corresponds the field in the absence of the cone structure, $v_1^{(s)}$ is the Debye potential for the scattered field.

The method of the Kontorovich-Lebedev integral transforms

$$G(\tau) = \int_0^{+\infty} g(r) \frac{K_{i\tau}(qr)}{\sqrt{r}} dr, \quad (2)$$

$$g(r) = \frac{2}{\pi^2} \int_0^{+\infty} \tau \operatorname{sh} \pi \tau G(\tau) \frac{K_{i\tau}(qr)}{\sqrt{r}} d\tau \quad (3)$$

is an effective one for solving boundary problems with cone geometries. By following the method developed in [4] we represent the potential $v_1^{(s)}$ in the form of the the Kontorovich-Lebedev integral (2), (3)

$$v_1^{(s)} = \frac{2}{\pi^2} \int_0^{+\infty} \tau \operatorname{sh} \pi \tau \hat{v}_1^{(s)} \frac{K_{i\tau}(qr)}{\sqrt{r}} d\tau,$$

where

$$\hat{v}_1^s = - \sum_{m=-\infty}^{+\infty} b_{m\tau}^{(s),p} U_{m\tau}^{(s)}(\theta, \varphi), p = 1, 2;$$

$U_{m\tau} =$

$$\begin{aligned} & \sum_{n=-\infty}^{+\infty} \alpha_{mn}^{(s)} P_{-1/2+i\tau}^{m+nN}(\cos \theta) e^{i(m+nN)\varphi}, 0 < \theta < \gamma_1 \\ & \sum_{n=-\infty}^{+\infty} [\beta_{mn}^{(s)} P_{-1/2+i\tau}^{m+nN}(\cos \theta) + \\ & + \xi_{mn}^{(s)} P_{-1/2+i\tau}^{m+nN}(-\cos \theta)] e^{i(m+nN)\varphi}, \gamma_1 < \theta < \gamma_2, \\ & \sum_{n=-\infty}^{+\infty} \zeta_{mn}^{(s)} P_{-1/2+i\tau}^{m+nN}(-\cos \theta) e^{i(m+nN)\varphi}, \gamma_2 < \theta < \pi, \end{aligned}$$

$K_\mu(z)$ is the Macdonald function, $P_{-1/2+i\tau}^M(\cos \theta)$

is the Legendre function, $b_{m\tau}^{(s),p}$ are given ($p = 1$ is for $\theta_0 < \gamma_1$ and $p = 2$ is for $\gamma_2 < \theta_0$) coefficients,

$\alpha_{mn}^{(s)}, \beta_{mn}^{(s)}, \xi_{mn}^{(s)}, \eta_{mn}^{(s)}$ are unknown coefficients.

After using boundary conditions (1) and field continuity across the slots we obtain the following two coupled systems of dual series equations for coefficients

$z_{mn}^{(s),j}$ (unknown coefficients are expressed via $z_{mn}^{(s),j}$):

$$\sum_{n=-\infty}^{+\infty} z_{mn}^{(s),j} e^{inN\varphi} = \hat{f}_{i\tau}^{(s),p}(\gamma_j) e^{im_0 N\varphi}, \text{ strips of } \Sigma_j, (5)$$

$$\sum_{n=-\infty}^{+\infty} [N(n+\nu)]^{\chi(s)} \frac{|n|}{n} (1 - \varepsilon_{nj}^{(s)}) \times \left\{ z_{mn}^{(s),1} [\hat{h}_{i\tau}^{(s),(n+\nu)N}(\pi - \gamma_2, \pi - \gamma_1)]^{j-1} - \text{slots of } \Sigma_j, (6) \right.$$

$$\left. z_{mn}^{(s),1} [\hat{h}_{i\tau}^{(s),(n+\nu)N}(\gamma_1, \gamma_2)]^{2-j} \right\} e^{imN\varphi} = 0,$$

$\hat{f}_{i\tau}^{(s),p}$ is defined by the source field, $\frac{m}{N} = m_0 + \nu$,

m_0 is the nearest to m/N , $-1/2 \leq \nu < 1/2$,

$$\chi(s) = (-1)^{s-1},$$

$$\hat{h}_{i\tau}^{(s),(n+\nu)N}(x, y) = \frac{\frac{d^{s-1}}{dx^{s-1}} P_{-1/2+i\tau}^{(n+\nu)N}(\cos x)}{\frac{d^{s-1}}{dy^{s-1}} P_{-1/2+i\tau}^{(n+\nu)N}(\cos y)}.$$

It should be noted that system coefficients independence on the wave parameter q guarantees unknown coefficients independence on this parameter. Investigation of the large-index behavior of the elements $\varepsilon_{nj}^{(s)}$ reveals that

$$\varepsilon_{nj}^{(s)} = O\left(\frac{1}{(n+\nu)^2 N^2}\right). \quad (7)$$

For the cone surface consisting of a slotted cone and an isotropic one, a symmetric bicone structure ($\gamma_2 = \pi - \gamma_1$), a single cone (Σ_1 or Σ_2) coupled systems of dual series equations (5), (6) become decoupled.

For the single cone Σ_2 that is excited by a magnetic dipole ($\gamma_2 < \theta_0$) dual series equations are transformed to the following ones ($s = 2, j = 2, p = 2$)

$$\sum_{n=-\infty}^{+\infty} z_{mn}^{(2),2} e^{inN\varphi} = e^{im_0 N\varphi}, \pi d_2/l < |N\varphi| \leq \pi, (8)$$

$$\sum_{n=-\infty}^{+\infty} z_{mn}^{(2),2} \frac{|n|}{n} (1 - \varepsilon_{n2}^{(2)}) e^{inN\varphi} = 0, |N\varphi| < \pi d_2/l, (9)$$

provided that

$$\sum_{n=-\infty}^{+\infty} z_{mn}^{(2),2} \frac{1}{n+\nu} \frac{|n|}{n} (1 - \varepsilon_{n2}^{(2)}) = 0. \quad (10)$$

Function equations (8)–(10) can be reduced to an infinite linear algebraic equations systems of the first kind like these

$$Ax = b. \quad (11)$$

The solution of (11) can be unstable. That is why one should find another way to solve it. It is the semi-inversion method, which was successfully applied to investigating 2-D electromagnetic diffraction problems [3]. By using this method we obtain an infinite linear algebraic equations system of the second kind

$$(I + B)x = b, \quad (12)$$

where B is a compact matrix operator in the space ℓ^2 , $x \in \ell^2$, $b \in \ell^2$. Hence, the needed solution exists, is unique and can be approximated by solving a truncated matrix equation. For semi-transparent cones, narrow slots, narrow conic strips the operator norm is less than the unity, $\|B\|_{\ell^2} < 1$, and the solution of the system (12) can be also derived with the iteration method [3, 4].

The main feature of the considered boundary problem is independence of the boundary problem spectrum on the wave parameter q . This is caused by the specific geometry of the problem.

3. RESULTS

For a single semi-transparent cone Σ_2 (a model of a wire cone antenna) that is excited by a radial magnetic dipole and is defined by existence of the limit

$$\lim_{N \rightarrow +\infty} \left[-\frac{1}{N} \ln \sin \frac{\pi d_2}{2l} \right] = IV > 0, \quad (13)$$

the Debye potential $v^{(2)}$ is represented in the form

$$v^{(2)} = g^{(2),1}(\theta, \varphi), \quad 0 < \theta < \gamma_2 \quad (14)$$

$$v^{(2)} = v_{\text{str}}^{(2)} + g^{(2),2}(\pi - \theta, \varphi), \quad \gamma_2 < \theta < \pi \quad (15)$$

$$g^{(2),\varsigma}(r, \theta, \varphi) = \frac{2}{\pi^2} \int_0^{+\infty} \tau \operatorname{sh} \pi \tau \hat{g}(\theta, \varphi) \frac{K_{i\tau}(qr)}{\sqrt{r}} d\tau,$$

$$\hat{g}(\theta, \varphi) = \sum_{m=-\infty}^{+\infty} \frac{a_{m\tau} A_{i\tau}^{(2),m}}{A_{i\tau}^{(2),m} + 2IV} \times$$

$$\times \left(\frac{\frac{d}{d\gamma_2} P_{-1/2+i\tau}^m(\cos \gamma_2)}{\frac{d}{d\gamma_2} P_{-1/2+i\tau}^m(-\cos \gamma_2)} \right)^{\varsigma-1} \times$$

$$\times P_{-1/2+i\tau}^m(-\cos \theta_0) P_{-1/2+i\tau}^m((-1)^\varsigma \cos \theta) e^{im\varphi};$$

$a_{m\tau}$, $A_{i\tau}^{(2),m}$ are given, $\varsigma = 1; 2$; $v_{\text{str}}^{(2)}$ is the Debye potential for total fields scattered by an isotropic perfectly conducting cone (a cone with no slots), $g^{(2),\varsigma}(r, \theta, \varphi)$ is caused by presence of the slots.

If $IV \rightarrow +\infty$ then the semi-transparent (13) becomes an isotropic perfectly conducting cone and the limiting expression for $v^{(2)}$ (14), (15) coincides with the solution for an isotropic perfectly conducting cone [1].

The potential $v^{(2)}$ satisfies the average boundary condition

$$\frac{\partial v^{(2)}}{\partial n} \Big|_{\Sigma} = \zeta(\vec{r}) [v^{(2)}] \Big|_{\Sigma}, \quad (16)$$

$$[v^{(2)}] \Big|_{\Sigma} = v^{(2)} \Big|_{\theta=\gamma_2+0} - v^{(2)} \Big|_{\theta=\gamma_2-0},$$

$$\zeta(\vec{r}) = \frac{1}{4rIV \sin \gamma_2}. \quad (17)$$

The boundary condition (16) can be treated as the third modified boundary condition. Thus, the solution for this type of a semi-transparent cone can be obtained by solving the third modified boundary problem for an infinite circular cone which surface properties is defined by the parameter $\zeta(\vec{r})$ (17). The boundary conditions like (16) are met in wave diffraction on resistive structures.

4. CONCLUSION

The method for solving the electromagnetic boundary problem for a complex perfectly conducting slotted cone have been presented. This one exploits the Kontorovich-Lebedev integral transforms and the semi-inversion method. By virtue of using this method the original problem is reduced to solving the linear algebraic equations system for Fourier coefficients of scattered field components. Analytical solutions have been derived for a semi-transparent cone. Taking into consideration results obtained one can conclude that this method is also applicable to solving wave diffraction problems for resistive cone surfaces.

REFERENCES

1. Felsen L. B., Marcuvitz N. Radiation and scattering of waves.- Prentice-Hall, Inc., Englewood Cliffs, New Jersey, Vol.2, 1973.
2. Goshin G. G. Boundary-value problems of electrodynamics in conic region.- Tomsk State University Public., Tomsk, 1987 (in Russian).
3. Shestopalov V. P. Summary equations in modern diffraction theory.- Kiev.Naukova dumka, 1983 (in Russian).
4. Doroshenko V. A., Kravchenko V. F. The scattering of plane electromagnetic waves from a cone with longitudinal slots // Journal of Communications Technology and Electronics, Vol.46, No.3, 2001, p.271. Translated from Radiotekhnika i Elektronika, Vol.46, No.3, p.296(in Russian).

MUTUAL RESISTANCES BETWEEN HORIZONTAL WIRE ANTENNAS NEAR AN INTERFACE

Peter L. Tokarsky

Department of Radio Engineering Foundations,
Kharkiv National University of Radio Electronics, Kharkiv, Ukraine
<tokarsky@ukr.net>, <tokarsky@kture.kharkov.ua>

Abstract

The problem of radiation of the coupled horizontal wire antennas with a specified current distribution, located near to a planar interface between two media is considered. Expressions for evaluation of a mutual impedance, mutual radiation resistance and mutual resistance of losses between dipoles above the ground are obtained. The results of numerical evaluations of the mutual resistances between two half-wave dipoles as functions against a distance between them are presented in graphical form.

Keywords: wire antennas, mutual impedance, radiation resistance, resistance of losses, interface between two media, imperfect ground.

1. INTRODUCTION

The impedance approach to the analysis of antenna arrays is an effective means of investigating various wire antenna systems [1]. It allows to present all powers, associated with a radiating system, as an Hermitian forms, coefficients of which are the appropriate mutual resistances between radiators and variables are complex amplitudes of the input currents [2, 3]. It enables simply to analyze power characteristics of the antenna arrays, in particular an antenna gain, a radiation efficiency and a polarization losses factor. The impedance approach is especially favorable when it is necessary to fulfill the multiple analysis of an antenna array at various distributions of the inputs currents exciting of the radiators. Such cases arise, for example, in the phased antenna arrays at a beam scanning. It appears also effective and at solving problems of optimizing the antenna arrays excitation for achievement of any power parameters maxima [4]. A necessary condition for application of the impedance approach to the analysis of a concrete antenna system is presence of the convenient mathematical expressions or an acceptable procedure for calculation of the mutual resistances between the array elements.

In full measure all of mentioned above can be applied to the antenna arrays located near to the interface between two media. Unfortunately, methods of calculation of the mutual resistances between elements of such arrays are developed not so well, as in a free space. In works [5, 6] the calculation procedure of the mutual resistances between the vertical dipoles [5] and between the horizontal Hertzian dipoles [6] located above interface is described. This paper presents a technique for calculation of the mutual impedance (including its components: the mutual radiation resistance and mutual

resistance of losses) between two horizontal linear radiators with specified current distributions, located above the interface between two media.

2. THEORY

2.1. STATEMENT OF THE PROBLEM

Let's consider radiation of two linear wire antennas 1 and 2, located in the infinite space divided in two by a plane $z = 0$ (Fig. 1). Upper the half-space, where antennas are located, contains a medium 1 which is a perfect dielectric (conductivity $\sigma_1 = 0$, permittivity ϵ_1 , permeability μ_1), and the medium 2, that fills the lower half-space, has the parameters $\epsilon_2, \mu_2, \sigma_2$. The wire 1 (2) has a length L_1 (L_2), its axis is placed in a plane $z = z_1$ ($z = z_2$) and is rotated through the angles φ_1 (φ_2) with respect to the x -axis.

Let a driving point Q_1 of antenna 1 is on the z -axis, and a driving point Q_2 of antenna 2 has coordinates x_2, y_2, z_2 . The antennas are excited by harmonic currents with complex amplitudes $I_{1,2}^0$ (a time de-

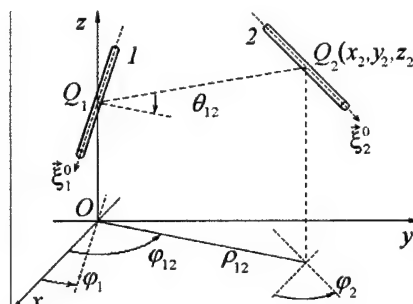


Fig. 1. Geometry for a radiating system

pendence $e^{j\omega t}$ is assumed). In this case the current distribution along the wires can be written in form:

$$\vec{I}_{1,2}(\xi) = \vec{\xi}_{1,2}^0 I_{1,2}^0 \chi_{1,2}(\xi),$$

where $\chi_{1,2}(\xi)$ are normalized functions of the current distributions; $\vec{\xi}_{1,2}^0 = \vec{x}^0 \cos \varphi_{1,2} + \vec{y}^0 \sin \varphi_{1,2}$ are the unit vectors of the wire axes; (\vec{x}^0, \vec{y}^0) are basis vectors of the Cartesian frame.

We restrict our attention to the mutual impedance Z_{12} between these antennas, and possibility to split its real part into the mutual radiation resistance $\Re_{\Sigma 12}$ and the mutual resistance of losses \Re_{d12} :

$$R_{12} = \text{Re}(Z_{12}) = \Re_{\Sigma 12} + \Re_{d12}.$$

The resistances of radiation are some kind of measures of the useful power P_{Σ} , which an antenna system radiates into the upper half-space, and the resistances of losses are measures of its power of losses P_d which transfers into the lower half-space and is scattered in medium 2.

2.2. PROBLEM SOLUTION

2.2.1. Fields Representation.

The strengths of electric and magnetic fields in the upper half-space due to dipole n ($n = 1, 2$) may be written as the sums:

$$\vec{E}_n = \vec{E}_n^\infty + \Delta \vec{E}_n, \quad \vec{H}_n = \vec{H}_n^\infty + \Delta \vec{H}_n, \quad (1)$$

where the augends correspond to a case, when the medium 2 is an perfect conductor ($\sigma_2 \rightarrow \infty$), and the addends are the correction terms which are taking into account real parameters of the lower medium.

We present the electromagnetic field due in the upper half-space to the n -th wire as a spectrum of planar waves [7] and separate out the correction terms $\Delta \vec{E}_n$ and $\Delta \vec{H}_n$ [6]:

$$\Delta E_{n \ x,y,z} = \int_{-\infty}^{\infty} \int_{-\infty}^{\infty} \Delta e_{n \ x,y,z} e^{-j\vec{\Psi}} d\nu_x d\nu_y, \quad (2)$$

$$\Delta H_{n \ x,y,z} = \int_{-\infty}^{\infty} \int_{-\infty}^{\infty} \Delta h_{n \ x,y,z} e^{-j\vec{\Psi}} d\nu_x d\nu_y, \quad (3)$$

where

$$\Delta e_{n \ z} = Z_{01} K_n \nu_y T_\varepsilon; \Delta h_{n \ z} = -j K_n \frac{\nu_x}{\gamma_1} \tilde{T}_\mu;$$

$$\Delta e_{n \ x} = j Z_{01} K_n \frac{\nu_x \nu_y (\gamma_1^2 T_\varepsilon + k_1^2 \tilde{T}_\mu)}{k_1 \gamma_1 (\nu_x^2 + \nu_y^2)};$$

$$\Delta h_{n \ x} = K_n \frac{\nu_y^2 T_\varepsilon + \nu_x^2 \tilde{T}_\mu}{k_1 \gamma_1 (\nu_x^2 + \nu_y^2)};$$

$$\Delta e_{n \ y} = j Z_{01} K_n \frac{\nu_y^2 \gamma_1^2 T_\varepsilon - \nu_x^2 k_1^2 \tilde{T}_\mu}{k_1 \gamma_1 (\nu_x^2 + \nu_y^2)};$$

$$\Delta h_{n \ y} = -K_n \frac{\nu_x \nu_y (T_\varepsilon - \tilde{T}_\mu)}{\nu_x^2 + \nu_y^2};$$

$$K_n = \frac{k_1^2 l_{en}}{8\pi^2} s_n(\alpha, \nu) e^{j\Psi_n};$$

$$T_\varepsilon = \frac{2\gamma_2 \varepsilon_1}{\gamma_1 \varepsilon_2 + \gamma_2 \varepsilon_1}; \quad T_\mu = \frac{2\gamma_2 \mu_1}{\gamma_1 \mu_2 + \gamma_2 \mu_1};$$

$$\tilde{T}_\varepsilon = \frac{2\gamma_1 \varepsilon_2}{\gamma_1 \varepsilon_2 + \gamma_2 \varepsilon_1}; \quad \tilde{T}_\mu = \frac{2\gamma_1 \mu_2}{\gamma_1 \mu_2 + \gamma_2 \mu_1};$$

$$j\Psi = jk_1(\nu_x x + j\nu_y y) + \gamma_1 z;$$

$$j\Psi_n = jk_1(\nu_x x_n + j\nu_y y_n) - \gamma_1 z_n;$$

$$k_{1,2} = \omega \sqrt{\varepsilon_{1,2} \mu_{1,2}}; \quad \gamma_{1,2} = \sqrt{k_1^2 \nu^2 - k_{1,2}^2};$$

$$\nu = \sqrt{\nu_x^2 + \nu_y^2}; \quad \tilde{\varepsilon}_{1,2} = \varepsilon_{1,2}(1 - j\sigma_{1,2}/\omega\varepsilon_{1,2}).$$

l_{en} is effective length of wire antenna n ; $s_n(\alpha, \nu)$ is a spectral density function of the current in wire n , viz.

$$s_n(\alpha, \nu) = \frac{1}{l_{en}} \int_{L_n} \chi_n(\xi) e^{jk_1 \xi \nu \cos(\alpha - \varphi_n)} d\xi. \quad (4)$$

In particular, for a dipole antenna having the sine-wave current distribution, viz.:

$$\chi_i(\xi) = \begin{cases} \sin k_1(l_i + \xi) / \sin k_1 l_i, & -l_i \leq \xi < 0; \\ \sin k_1(l_i - \xi) / \sin k_1 l_i, & 0 \leq \xi \leq l_i, \end{cases}$$

the function $s_n(\alpha, \nu)$ can be written as:

$$s_i(\alpha, \nu) = \frac{\cos[\nu k_1 l_i \cos(\alpha - \varphi_i)] - \cos k_1 l_i}{[1 - \nu^2 \cos^2(\alpha - \varphi_i)](1 - \cos k_1 l_i)}. \quad (5)$$

2.2.2. Mutual Resistances

The mutual impedance Z_{mn} between wire antennas m and n can be estimated, using the induced EMF method, viz.

$$Z_{nm} = -\frac{1}{I_n} \int_{L_n} \vec{E}_n \vec{\xi}_m^* \chi_m^*(\xi) d\xi = -\frac{1}{I_n} \int_{L_n} (\vec{E}_n^\infty + \Delta \vec{E}_n) \vec{\xi}_m^* \chi_m^*(\xi) d\xi = Z_{nm}^\infty + \Delta Z_{nm} \quad (6)$$

To find the addend we substitute (2) - (3) into (6). After needed manipulation a result can be expressed in the following manner:

$$\Delta Z_{mn} = -j \frac{Z_{01} k_1^2 l_{en} l_{em}}{4\pi} \int_0^\infty (\gamma_1 T_\varepsilon \cdot I_\varepsilon(\nu) - \frac{1}{\gamma_1} \tilde{T}_\mu \cdot I_\mu(\nu)) e^{-\gamma_1 k_1 (z_m + z_n)} \nu d\nu, \quad (7)$$

where

$$\left. \begin{aligned} I_\varepsilon(\nu) &= \frac{1}{2\pi} \int_0^{2\pi} s_m^*(\nu, \alpha) s_n(\nu, \alpha) \times \\ I_\mu(\nu) &= \frac{1}{2\pi} \int_0^{2\pi} s_m^*(\nu, \alpha) s_n(\nu, \alpha) \times \\ &\times \left\{ \begin{aligned} &\cos(\alpha - \varphi_m) \cos(\alpha - \varphi_n) \\ &\sin(\alpha - \varphi_m) \sin(\alpha - \varphi_n) \end{aligned} \right\} e^{jk_1 \nu \rho_{mn} \cos(\alpha - \varphi_{mn})} d\alpha; \\ \rho_{mn} &= \sqrt{(x_m - x_n)^2 + (y_m - y_n)^2}; \end{aligned} \right\} \quad (8)$$

$$\varphi_{mn} = \arctg \frac{y_m - y_n}{x_m - y_n}.$$

To avoid the numerical integration in (7), we represent a product $s_{mn}(\nu, \alpha) = s_m^*(\nu, \alpha) \cdot s_n(\nu, \alpha)$ in (8) as a Fourier series:

$$s_{mn}(\nu, \alpha) = c_0 + \sum_{i=1}^{\infty} (a_i \sin i\alpha + b_i \cos i\alpha). \quad (9)$$

Using (9), equation (8) reduces to the following form:

$$\begin{aligned} \begin{Bmatrix} I_\varepsilon(\nu) \\ I_\mu(\nu) \end{Bmatrix} &= c_0 J_0(u) \begin{Bmatrix} \cos \varphi'_m \cos \varphi'_n \\ \sin \varphi'_m \sin \varphi'_n \end{Bmatrix} + \\ &+ \frac{1}{2} \cos(\varphi'_m - \varphi'_n) \mp c_0 \frac{J_0(u)}{u} \cos(\varphi'_m + \varphi'_n) \mp \\ &\mp \frac{1}{4} \sum_{i=1}^{\infty} (-1)^i \{ b_{2i} [J_{2i+2}(u) - J_{2i-2}(u)] \} \cos(\varphi'_m + \varphi'_n) \pm \\ &\pm \frac{1}{4} \sum_{i=1}^{\infty} (-1)^i \{ a_{2i} [J_{2i+2}(u) - J_{2i-2}(u)] \} \sin(\varphi'_m + \varphi'_n). \end{aligned} \quad (10)$$

$$\varphi'_m = \varphi_m - \varphi_{mn}; \quad \varphi'_n = \varphi_n - \varphi_{mn}; \quad u = k_1 \nu \rho_{mn};$$

$J_i(u)$ is being the Bessel function of order i . In expression (10) the upper sign relates to I_ε , but the lower sign relates to I_μ .

Now we find the mutual resistance of losses \Re_{dmm} and the mutual radiation resistance $\Re_{\Sigma mn}$, using the following relation [4]:

$$\Re_{\Sigma, d mn} = \frac{1}{2I_n I_m^*} \int_{S_{\Sigma, d}} ([\vec{E}_m, \vec{H}_n^*] \vec{s}^0 + [\vec{E}_n^*, \vec{H}_m] \vec{s}^0) ds,$$

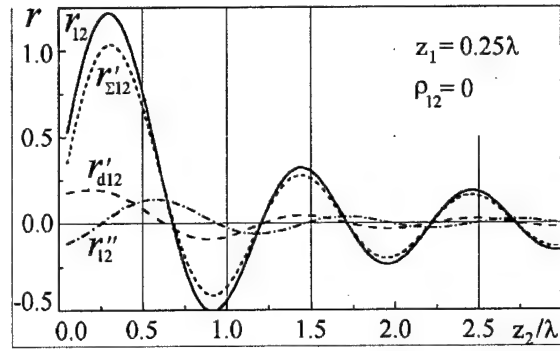
where S_Σ is a hemispherical surface of radius $R \rightarrow \infty$, which cover over the radiating system from above, and its centre is coincided with an origin of the coordinates; S_d is a surface conterminous to the plane interface xOy , \vec{s}^0 is a unit normal to these surfaces.

Applying the expression (10)–(11) in the last equation, it is easy to determine the required resistances:

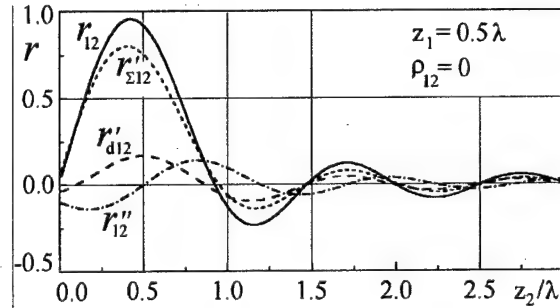
$$\Re_{\Sigma mn} = \text{Re}(Z_{mn}^\infty) + \Delta \Re_{\Sigma mn}^{\theta\theta} + \Delta \Re_{\Sigma mn}^{\varphi\varphi}, \quad (11)$$

where $\Delta \Re_{\Sigma mn}^{\theta\theta}$ and $\Delta \Re_{\Sigma mn}^{\varphi\varphi}$ are the parts of ΔZ_{mn} , which are caused by radiation of the wires into the upper half-space on the E - and H -polarized waves respectively, viz.

$$\begin{aligned} \Delta \Re_{\Sigma mn}^{\theta\theta} &= \frac{Z_{01} k_1^2 l_e m l_n}{4\pi} \int_0^1 I_\varepsilon(\nu) \left\{ \text{Re}(T_\varepsilon e^{-\gamma_1 k_1 (z_m + z_n)}) - \right. \\ &\quad \left. - \left[\text{Re}(T_\varepsilon) - \frac{1}{2} |T_\varepsilon| \right] e^{-\gamma_1 k_1 (z_m - z_n)} \right\} \frac{\gamma_1 \nu}{ik_1} d\nu; \\ \Delta \Re_{\Sigma mn}^{\varphi\varphi} &= \frac{Z_{01} k_1^2 l_e m l_n}{4\pi} \int_0^1 I_\mu(\nu) \left\{ \text{Re}(\tilde{T}_\mu e^{-\gamma_1 k_1 (z_m + z_n)}) - \right. \\ &\quad \left. - \left[\text{Re}(\tilde{T}_\mu) - \frac{1}{2} |\tilde{T}_\mu| \right] e^{-\gamma_1 k_1 (z_m - z_n)} \right\} \frac{ik_1 \nu}{\gamma_1} d\nu; \end{aligned}$$



a)



b)

 Fig. 2. The mutual resistances versus z_2 / λ

$$\begin{aligned} \Re_{d mn} &= \frac{Z_{01} k_1^2 l_e m l_n}{4\pi} \int_0^\infty \left\{ I_\varepsilon(\nu) \text{Im} \left(\frac{\gamma_1}{k_1} T_\varepsilon T_\varepsilon^* \right) - \right. \\ &\quad \left. - I_\mu(\nu) \text{Im} \left(\frac{k_1}{\gamma_1} \tilde{T}_\mu T_\mu^* \right) \right\} e^{-\gamma_1 k_1 z_m - \gamma_1^* k_1 z_n} \nu d\nu \end{aligned} \quad (12)$$

The obtained expressions are a solution of the considered problem. The integrals in (7) and (12) enough fast converge, because their integrand quickly decrease with growth ν due to the factor $\exp\{-\gamma_1 k_1 (z_m + z_n)\}$. Indeed, if $z_1 + z_2 > \lambda_0 / 2$, then its module falls more than three order already at $\nu = 10$. In the sums (9) it is required to take into account no more than 2ν items for achievement of the same accuracy.

3. NUMERICAL EXAMPLES

Here we apply the considered procedure for analyzing the mutual resistances between two horizontal half-wave dipoles located in air near to the surface of a imperfect ground as functions of a distance between them. The results of calculations reduced below accomplished for frequency of 6 MHz under the assumption that the ground has the following parameters: $\varepsilon_{r2} = 10$, $\sigma_2 = 0.01 (\Omega \cdot m)^{-1}$, $\mu_{r2} = 1$.

In Fig. 2 a,b the components of the mutual impedance between parallel half-wave dipoles, centers of which are on the z -axis, are plotted against a height of dipole 2 when the height of dipole 1 is fixed: $z_1 = \lambda/4$ (Fig. 2a) and $z_1 = \lambda/2$ (Fig. 2b). It is necessary to note, that here all resistances are normal-

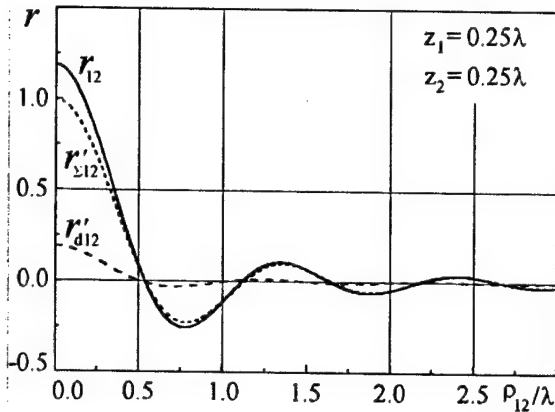


Fig. 3. The mutual resistances versus ρ_{12} / λ

ized to the resistance of the single radiator in the free space, viz.

$$\begin{aligned} R_{12} / R_{00} &= r_{12} = r_{\Sigma 12} + r_{d12}; \\ R_{\Sigma 12} / R_{00} &= r_{\Sigma 12} = r'_{\Sigma 12} + jr''_{12}; \\ R_{d12} / R_{00} &= r_{d12} = r'_{d12} - jr''_{12}. \end{aligned}$$

Fig. 3 shows the components of the normalized mutual impedance between two half-wave dipoles, both of which are parallel to the y-axis, as functions of the radial distance $\rho_{12} = |x_2 - x_1|$ between them. In this figure the curve r''_{12} is absent ($r''_{12} = 0$), because here $z_1 = z_2$.

It is interesting to compare the mutual impedance between two half-wave dipoles and between two Hertzian dipoles [6]. Fig. 4 gives the plots of the normalized components of the additional term $\Delta Z_{12} / R_{00} = \Delta r_{12} + j\Delta x_{12}$ (7) for both types of radiators. Here the components relating to the mutual impedance between two half-wave dipoles are indicated by solid curves and components relating to the Hertzian dipoles are indicated by dashed curves.

From the figure follows, that the curves Δr_{12} (and Δx_{12}) are close to each other for two compared cases, however their components differ among themselves, what especially noticeably on a curve r'_{d12} near to a point $z_1 = z_2$.

4. CONCLUSION

The offered technique may be useful to analyzing effect of the imperfect ground on the mutual resistances between elements of wire antenna arrays, including antenna arrays for HF-band communication systems.

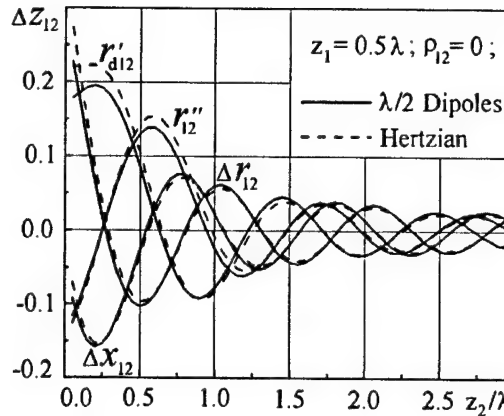


Fig. 4. A comparison of the mutual resistances between two half-wave dipole and between two Hertzian dipoles

REFERENCES

1. Microwave Scanning Antennas / Ed. by R. C. Hansen. Vol. II. Academic Press, New York, 1966.
2. Tokarskiy P. L. Mutual Coupling in a System of Radiators with Joule Losses // Soviet J. of Communicat. Techn. and Electron. 1987. No. 3, p. 9.
3. Tokarskiy P. L. Impedance Approach to Analysis of Polarization Losses in Antenna Arrays // Soviet J. of Communicat. Techn. and Electron. 1992. No. 16, p. 17.
4. Tokarskii P. L., Rybalko A. M., Sinepup A. V. Optimization of the Power Parameters of Antenna Arrays with Suppressed Level of Cross-Polarized Radiation // Radio Electron. and Communicat. Systems. 2000. Vol. 43, No. 4, p. 7.
5. Tokarskiy P. L. Coupling Impedances and Electric Efficiencies of Vertical Dipoles above the Ground // Telecom. and Radio Eng. 1999. Vol. 53. No. 7-8, p. 43.
6. Tokarsky P. L. Coupling Impedances and Radiation Efficiencies of Horizontal Electric Dipoles Placed above the Earth Surface // Telecom. and Radio Eng. 2002. Vol. 57. No. 4, p. 35.
7. Markov G. T., Chaplin A. F. Excitation of Electromagnetic Waves. - Moscow: Energiya, 1967 (in Russian).

EFFECT OF MUTUAL COUPLING IN CRUCIFORM DIPOLE ON SCATTERING PERFORMANCES

Tatyana V. Peretyatko

Rostov military institute of Missile Corps, Rostov-on-Don, Russia
<zvezd@jeo.ru>

Abstract

The expressions for determination of characteristics of radiation and scattering by symmetrical cruciform electrical dipole are found on the basis of mathematical model of this radiator. The influence of excitation of asymmetrical harmonics of current in other arm of radiator in stimulation of cruciform dipole one arm is considered. The results of numerical research of the current distribution on the dipole arms and the pattern of scattering are considered for various lengths of arms and directions of wave falling.

Keywords: the cruciform electrical dipole, the current distribution, the pattern of scattering, the characteristics of scattering, length of dipole arm.

1. INTRODUCTION

The development of antenna theory and techniques and more wide application of antennas in the radio engineering systems of various purposes leads to the necessity of new parameters in addition to well-known generally accepted performances. One of the new parameters is the effective surface of scattering (ESS). The symmetrical cruciform electrical dipole is widely used both as an independent antenna and as an element of the phased antenna array.

Consequently creation of new mathematical model and methods of calculation of various characteristics including the used characteristics of scattering of this type radiators is very important problem.

2. FORMULATION OF THE PROBLEM. MATHEMATICAL MODEL

The mathematical model of the cruciform electrical dipole from [1] is used for realization of investigations. The geometry of the problem is presented in Fig. 1.

Let the system of N cruciform electrical dipoles be excited by plane electromagnetic wave. The direction of wave falling is defined by angles θ_0, φ_0 . It is necessary to define scattering performances of this system of radiators.

2.1. MATHEMATICAL MODEL

The current distribution in the cruciform electrical dipole excited by the incident plane electromagnetic wave is found in accordance with the mathematical model from [1].

The current distribution in the cruciform electrical dipole excited by plane electromagnetic wave in every

arm may be determined as a sum of trigonometrical harmonics with unknown coefficients.

If the current distribution in radiators is known, the vector pattern in free space may be determined with well known expressions.

The final formula for components of vector pattern may be presented in the following form

$$F_\theta(\theta, \varphi) = \sum_{n=1}^N \left\{ \cos \theta \cos \varphi \sum_{m_x}^{M_x} [A_{m_x}^n C_{m_x}^n + B_{m_x}^n S_{m_x}^n] + \right. \\ \left. + \cos \theta \sin \varphi \sum_{m_y}^{M_y} [A_{m_y}^n C_{m_y}^n + B_{m_y}^n S_{m_y}^n] \right\}, \quad (1)$$

$$F_\varphi(\theta, \varphi) = \sum_{n=1}^N \left\{ -\sin \varphi \sum_{m_x}^{M_x} [A_{m_x}^n C_{m_x}^n + B_{m_x}^n S_{m_x}^n] + \right. \\ \left. + \cos \varphi \sum_{m_y}^{M_y} [A_{m_y}^n C_{m_y}^n + B_{m_y}^n S_{m_y}^n] \right\}, \quad (2)$$

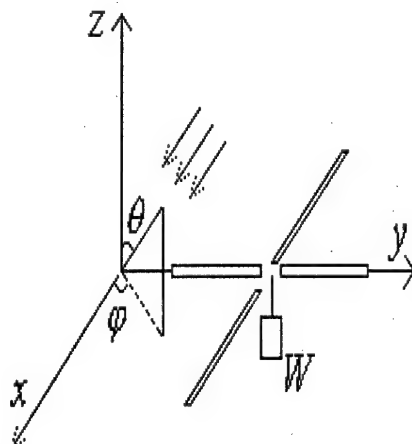


Fig. 1. Problem geometry

where

$$\begin{aligned}
 C_{m_x}^n &= \exp(ik(x_n \sin \theta \cos \varphi + y_n \sin \theta \sin \varphi)) \times \\
 &\times \int_{-\ell/2}^{\ell/2} \cos\left(\frac{\pi(m_x - 0.5)x'}{\ell}\right) \exp(ikx' \sin \theta \cos \varphi) dx', \\
 S_{m_x}^n &= \exp(ik(x_n \sin \theta \cos \varphi + y_n \sin \theta \sin \varphi)) \times \\
 &\times \int_{-\ell/2}^{\ell/2} \sin\left(\frac{\pi m_x x'}{\ell}\right) \exp(ikx' \sin \theta \cos \varphi) dx', \\
 C_{m_y}^n &= \exp(ik(x_n \sin \theta \cos \varphi + y_n \sin \theta \sin \varphi)) \times \\
 &\times \int_{-\ell/2}^{\ell/2} \cos\left(\frac{\pi(m_y - 0.5)y'}{\ell}\right) \exp(iky' \sin \theta \sin \varphi) dy', \\
 S_{m_y}^n &= \exp(ik(x_n \sin \theta \cos \varphi + y_n \sin \theta \sin \varphi)) \times \\
 &\times \int_{-\ell/2}^{\ell/2} \cos\left(\frac{\pi m_y y'}{\ell}\right) \exp(iky' \sin \theta \sin \varphi) dy'.
 \end{aligned}$$

In expressions (1) and (2), $A_{m_x}^n$, $B_{m_x}^n$ and $A_{m_y}^n$, $B_{m_y}^n$ are complex amplitudes of components of current in x -arm and y -arm, respectively, in the n -th radiator. This complex amplitudes are defined by correlations from the solution of the system of linear algebraic equations given in [1]; x_n, y_n are the coordinates of center of the n -th radiator; $k = 2\pi/\lambda$ is the wave number; ℓ is the length of dipole arm.

3. RESULTS OF RESEARCH

These correlations can be used for calculation of the current distribution and the pattern of scattering of the cruciform electrical dipole for various lengths of arm and directions of wave falling. The number of radiators in the considered case equals one. If the length of arm is 0.25λ , the current distribution is independent of the direction of wave falling. The current amplitude only depends on this direction.

In accordance with this, the pattern of scattering in this case preserves its form. In the case of larger length of electrical dipole arm, when the wave falls not normally, changes of the current distribution both in shape and amplitude are observed. The results of calculations for the case of incidence of θ -polarized plane wave are presented in Figs. 2–5 by curves 1–4. To calculate the performances of the current distribution in arms of dipole and the pattern of scattering the cruciform electrical dipole with $\ell = \lambda$ is considered. The number of considered harmonics in every dipole arms of the cruciform electrical dipole is chosen to be equal to 10. Fig. 2 illustrates the dependencies of the current distribution in the x -arm of the dipole and Fig. 3 – in the y -arm of dipole.

The θ -component of the pattern of scattering in case $\varphi = 0^\circ$ is presented in Fig. 4 and in case $\varphi = 90^\circ$ – in Fig. 5.

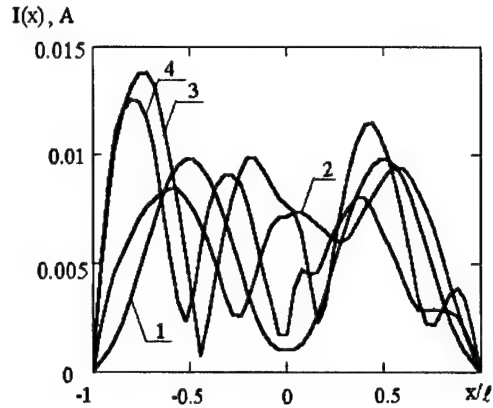


Fig. 2. The current distribution in x -arm of dipole

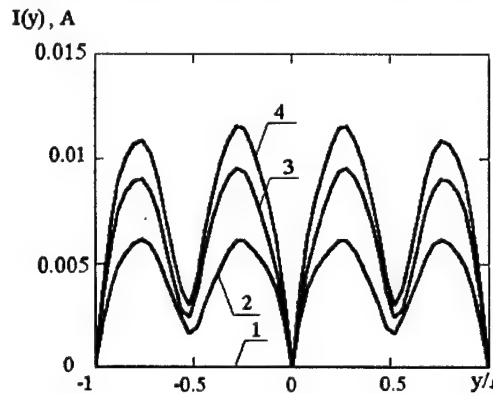


Fig. 3. The current distribution in y -arm of dipole

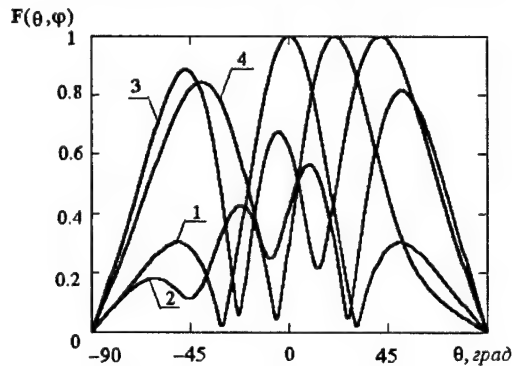


Fig. 4. The pattern of scattering in case $\varphi = 0^\circ$

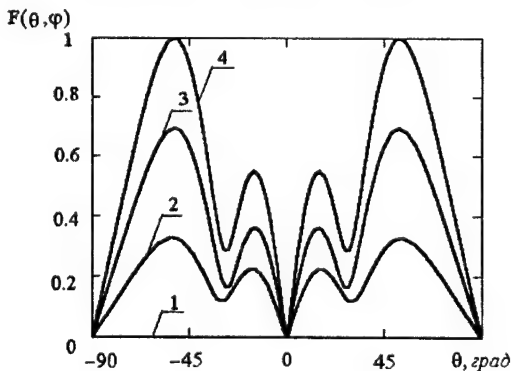


Fig. 5. The pattern of scattering in case $\varphi = 90^\circ$

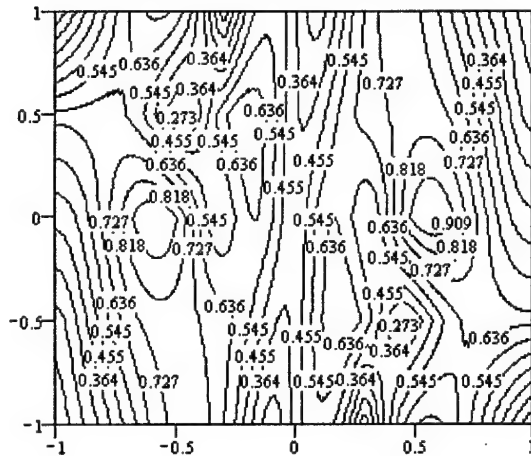


Fig. 6. The power scattering pattern in case $\theta_0 = 60^\circ$, $\varphi = 0^\circ$

In these pictures, the curve 1 corresponds to the case of the direction of θ -polarization wave falling $\theta_0 = 0^\circ$, $\varphi_0 = 0^\circ$, curve 2 – $\theta_0 = 20^\circ$, $\varphi_0 = 0^\circ$, curve 3 – $\theta_0 = 40^\circ$, $\varphi_0 = 0^\circ$, curve 4 – $\theta_0 = 60^\circ$, $\varphi_0 = 0^\circ$.

The given results are normalized to a maximum value of scattering field, which is obtained in the case of $\theta_0 = 0^\circ$, $\varphi_0 = 0^\circ$.

The carried out research demonstrates that in the case of $\theta_0 = 90^\circ$, $\varphi_0 = 0^\circ$ of wave falling, the current distribution in x -arm has symmetrical character, but in perpendicular arm (y -arm) is equal to zero. If the angle θ_0 differs from 90° , the current distribution changes its character and becomes nonsymmetrical, but in y -arm, current appears and has asymmetrical character. Accordingly its contribution to the output voltage of dipole is equal to zero.

The current distribution in x -arm has parameters coinciding with those for linear dipole from [2]. In the same time, the occurrence of the current in perpendicular arm changes the scattering pattern and scatter-

ing performances of a cruciform dipole as compared with a linear dipole.

In support of this, the results of investigations of power scattering pattern of the cruciform electrical dipole are illustrated in Fig. 6.

4. CONCLUSION

In the process of the research it has been revealed, that in the case of the direction of wave falling in plane of one dipole arms (in plane xOz) appearance of the asymmetrical component in the current distribution along this arm causes appearance the asymmetrical component in perpendicular of dipole arm, what leads to changes in the pattern of scattering and cross-section.

Thus, the presented results demonstrate that in the time of studying the characteristics of scattering of cruciform electrical dipole the consideration of the mutual coupling between the arms of radiator is necessary for obtaining correct results.

The results presented in this paper can be applied in the investigations of the antenna input resistance as well as in modeling the feeders and antenna scattering performances.

ACKNOWLEDGMENT

The author would like to thank Prof. Dmitry Gabriel'yan for his advise and encouraging discussions during the revision phase of this paper.

REFERENCES

1. Gabrielyan D. D., Peretyatko T. V. Scattering of plane electromagnetic wave by cruciform electrical dipole with load // Proceedings of the 3-rd International Conference on Antenna Theory and Techniques, Sevastopol, Ukraine, 8-11 Sept. 1999.
2. Brikker A. M., Zernov N. A., Martinova T. E., Shkil V. M. The scattering of electromagnetic wave by dipole antenna with an arbitrary angle of incidence // Radiotekhnika i elektronika, Vol. 43, 1998, No. 5, pp. 574-579. (in Russian).

THE STATISTICAL TESTS METHOD APPLICATION FOR CALCULATING OF THE AXISYMMETRIC ANTENNAS CHARACTERISTICS

Levagin G. A., Bondarenko I. N., Chepiga V. N.

Kharkov military university, Kharkov Ukraine
<leo-gi@rambler.ru>

Abstract

The paper considers the expediency of using of method of statistical tests for calculation of statistical characteristics of axisymmetric antennas. The analysis of average performance of circular antenna arrays is carried out.

Keywords: antennas, circular antenna arrays, directional diagram, amplitude phase distribution

Modern aircraft performance characteristics are the reasons of high requirements to quality of rate of updating of the environment information. It causes applying of the active antenna arrays (AAs) and new methods of area survey, used in survey systems.

In the most of modern radars with electronic scanning the plane antenna arrays are used, which have a number of disadvantages at omnidirectional scanning, and so plane antenna arrays are proposed to be substituted for axisymmetric ones, specifically circular antenna arrays (CAAs). Such arrays are preferred for realization of such survey methods as parallel survey or ultra high-speed scanning.

The question arises as to level of technical requirements to manufacturing accuracy and operating conditions of antennas systems with CAA.

The founder of the antennas statistical theory is Shifrin I. S. The problems as for linear AAs [1, 2, 3, 4, 5] are widely covered in his works and works of his followers. However, the issues of this theory as applied to CAA are not studied enough.

Antenna arrays with the great relation L/λ and complicated multichannel feed system are usually used in such systems. As a result the role of factors, which are generating the random spread of antennas parameters, considerably increases, thus causing the necessity of study of their statistical characteristics.

The various statistical methods are used to study real antenna characteristics. The characteristic functions method is the most fully developed and mostly used one. It is rather universal and suitable at analytical study when the errors are multiplicative. It is reasonable to use a spectral representations method when the errors are additive. If a source of errors is some specific mechanism (for example, inaccuracy of mounting of feed element in reflector antenna) or unknown characteristic of directional diagram (DD) is expressed by the functional equations (which are un-

solvable in general form), the canonical decomposition method or asymptotic approximation method are respectively used.

When using the characteristic functions method for the complicated antennas types (e.g., convex) analysis, the obtained expressions are intricate and this complicates their correct physical interpretation. Therefore, for such antennas at the presence of primary formulae, which describe antenna field with errors, it is reasonable to use the statistical tests method by entering data about the amplitude phase distribution (APD) errors or antenna design parameters by means of random-number generators with desired distribution laws.

Arisen unstability can cause the errors (amplitude, phase and frequency) both in whole antenna system and in its separate elements. Thus, the errors can have different correlation radiuses that should be taken into account when analysing the system.

The phase errors exert essential influence on the characteristics of antenna systems.

When considering the main issues of statistics of CAA field with occasional phase errors, the average antenna characteristics such as average DD, average directivity factor (DF), dispersion of principal maximum direction drift as well as some fluctuation characteristics, particularly the errors of angular coordinates measurement were analyzed.

The following primary formulae for undistorted DD were used:

- when parallel survey:

$$f_0(\varphi) = \sum_{n=-N}^N a_n e^{jkr(\cos(n \cdot \delta\alpha - \varphi) - \cos(n \cdot \delta\alpha - \varphi_0))} \times \cos(n \cdot \delta\alpha - \varphi) \cdot \cos(n \cdot \delta\alpha - \varphi_0), \quad (1)$$

where $\cos(n \cdot \delta\alpha - \varphi_0)$ is the DD shift in relation to the center in 0.7 of it's width,

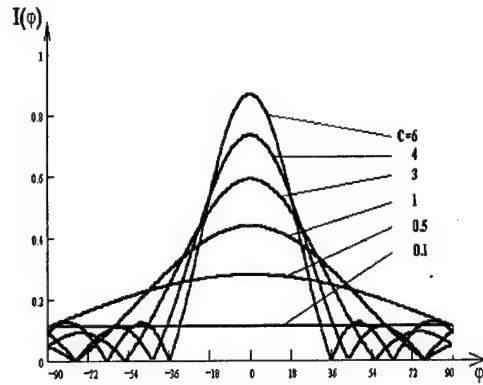


Fig. 1. Dispersion diagram $I(\varphi)$ at different values of errors correlation radius

the expression under the sign of sum is determined as follows:

- for MQS:

$$f_0(\varphi) = \sum_{n=-N}^N a_n e^{jn(\varphi + \Omega \cdot t)} \quad (2)$$

- for real DD:

$$f(\varphi) = \sum_{n=-N}^N a_n e^{j\sigma \Delta \varphi_n} e^{jkr[\cos(n \cdot \delta \alpha - \varphi) - \cos(n \cdot \delta \alpha)]} \times \cos(n \cdot \delta \alpha - \varphi) \cdot \cos(n \cdot \delta \alpha) \quad (3)$$

$$f(\varphi) = \sum_{n=-N}^N a_n e^{jn(\varphi + \Omega \cdot t + \Delta \varphi_n)}, \quad (4)$$

where $\Delta \varphi_n$ – the occasional phase error in the n -th CAA's element.

The analysis of average directional diagram makes possible to determine the influence of error on the DD form, to what extent the magnitude of power emitted in the main maximum direction decreases and how average DD changes when errors correlation radius varying.

$$|\overline{f(\varphi)}|^2 = (1 - \sigma^2) |f_0(\varphi)|^2 + \sigma^2 I(\varphi) \quad (5)$$

When $\overline{\Delta \varphi_n^2} \ll 1$ the average power DD represents the sum of undistorted DD with the coefficient $k - (1 - \sigma^2)$ and dispersed power diagram $I(\varphi)$ at different relative correlation radiuses C , given in Fig. 1.

As one can see, at small correlation radiuses C , the dispersion diagram $I(\varphi)$ is insignificant and “directional characteristics” of this function are poorly expressed, i.e. $I(\varphi)$ represents almost constant “background” of lateral radiation. The magnitude of this background at the specified magnitude of error dispersion is determined by the relation of the error correlation radius to the length of system. When correlation radius increasing the magnitude and “directivity” of $I(\varphi)$ function increases.

In order to find out the “mechanism” of reduction of the antenna average DF it is expedient to take into

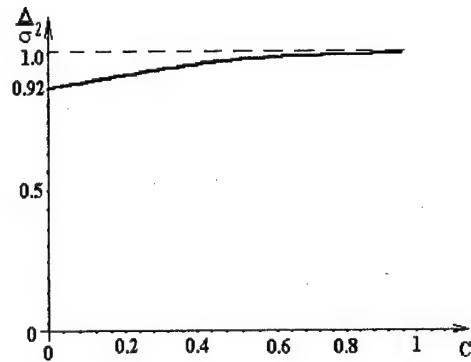


Fig. 2. Reduction of the average DF at different correlation radiuses

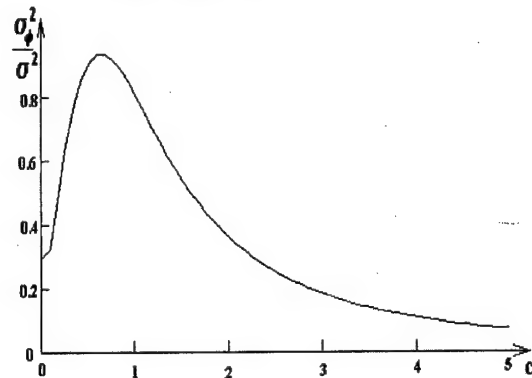


Fig. 3. The dependency of the main maximum direction dispersion from the correlation radius

account the character of the main lobe width dependency on the error correlation radius. Here, system average DF dependency on the error correlation radius is presented on Fig. 2.

This figure shows that magnitude of the average DF relative reduction is reduced at correlation radius increasing. Thus, DF reduction is equal to the reduction of power which is being emitted to the main maximum direction.

At uncorrelated errors magnitude of Δ depends on the amount of emitters and error dispersion. At correlated errors the average DF reduction depends on the correlation radius as well. The obtained dependencies of the the DF reduction at errors presence can be explained by two effects which are the main petal broadening and lateral radiation level increasing. DF reduction caused by the first effect is insignificant in the considered case. So, lateral radiation average level increasing brings the main contribution into DF reduction.

The most essential effect at phase distribution distortion along the antenna is the main maximum directions shift. This effect is one of the most unpleasant results of the phase error presence, which further leading to the angular coordinates measurement errors. Therefore, antenna fluctuation parameters analysis is the next step of antenna field statistic analysis after antenna average characteristics consideration. The results of estimation are presented on Fig. 3.

The researches of the error correlation radius influence to the main maximum direction dispersion revealed as one would expect that error dispersion tends to zero when correlation radius tends to zero or to infinity.

It's physical sense is explained in the following way: at very small radius the number (N) of harmonics, in which DF is decomposed, is great enough. It is on symmetry reasons that direction of field maximum $\Delta\varphi$ is highly close to the direction $\varphi = 0$ in this case. The system is practically in-phase at very big radiuses and for the in-phase systems $\varphi = 0$. The maximal main maximum shift dispersion is to be observed when aperture is comparable to the correlation radius.

The research of the influence of phaseshifters discreteness on the pelengation sensitivity (PS) is accomplished also. The obtained results had been compared with the PS of flat AA and with the PS of CAA of the same size.

The results received shows that when using the phaseshifters with great discreteness (discreteness – 0° – 22.5°) pelengation sensitivity in CAA is worse than in the equidistant AA. This inadequate is smoothed when phaseshifters with smaller discreteness (discreteness – 0° – 11.25°) are used.

Thus, it is possible to conclude that there are two basic mechanisms of errors formation in circular antenna arrays depending on used survey mode.

- At the parallel survey the resulting error comprises of errors in each channel and common error in the CAA aperture.
- At superfast scanning the resulting error comprises of diagram-forming unit' errors and terminal antenna waveguide channel errors.

The feature, which connected with applying of the statistical theory to the CAA, is substitution of generalized angle " ψ ", which is used for the linear antenna arrays for the real one " φ ".

The statistical analysis results allow to claim the following:

- different mechanisms of errors differently influence on the circular antenna arrays statistical characteristics;
- the character of these dependences differs somewhat from the similar dependences for the linear antenna arrays;
- these differences are comparatively insignificant at small errors and at the big antennas radius to wave length ratio.

Thus, the errors in CAA elements affect its statistical characteristics the same way as in the linear antennas, so requirements to manufacture accuracy and elements stability are the same as for the linear antennas.

Applying of the statistical tests method allows to simplify the complex types antennas statistical characteristics estimation and analysis to the maximum degree.

REFERENCES

1. Shifrin Ja. S. Antennas statistical theory problems.– M.: Radio and communication, 1970.
2. The antennas technique directory. Under. Redaction of J. N. Feld and E. G. Zelkin. Vol.1.– M.: "Radio engineering" magazine press.
3. Shifrin Ja. M. Antennas statistical theory (modern state, basic development ways). Kh.: Dep. in Ukr. 09.09.85 № 2098.
4. Tikhonov V. I. Statistical radio engineering.– M.: Radio and communication, 1982г.
5. Suharevskij I. V., Zamjatin V. I. Stochastic functions orthogonal decomposition method using to some antenns statistics problems. - Radio engineering and electronics, 1967, v.12 № 7.

THE USE OF THE RELATIVISTIC EFFECT FOR OBTAINING NEGATIVE PERMITTIVITY

K.N. Klimov¹, B.V. Sestroretsky¹, V.A. Ruchenkov¹, T.V. Kamishev¹, S.M. Godin²,
V.V. Roshchin²

¹ Lavochkin Association, Leningradskay st. 24, Chimki-2 Moscow Area 141400,
Russia, ph. (095) -575-50-69 <const0@laspace.ru>

² Neotek, Moscow, Russia

Abstract

It is shown that owing to the relativistic effect, there is the electrical field opposite in the direction of the impressed field inside the moving conductor that is possible to treat as the negative permittivity. The evaluation of the effect being used and conclusions concerning its practical value are given in the present work.

Keywords: Negative permittivity, relativistic effect.

Let's consider the system represented in Fig. 1. As one can see from this figure, it is a flat capacitor – two parallel XOZ metal planes, the distance between which is equal to D . The surface charge density on the bottom and the top plates is equal to $+\sigma$ and $-\sigma$ respectively. This surface charge density creates the homogeneous electrical field E_y between the capacitor plates, which size is determined by the expression [1]:

$$E_y = \sigma / \epsilon_0.$$

There is a metal plane with a thickness d placed also inside the capacitor (see Fig. 1). The given plane moves along the axis x with the speed V_x . With the coordinate axes $X'Y'Z'$, on which the conductor is fixed, the homogeneous electrical field E'_y being created inside the capacitor plates will be equal to:

$$E'_y = \sigma' / \epsilon_0,$$

where $\sigma' = \gamma\sigma = \sigma / \sqrt{1 - V_x^2/c^2}$ is the surface

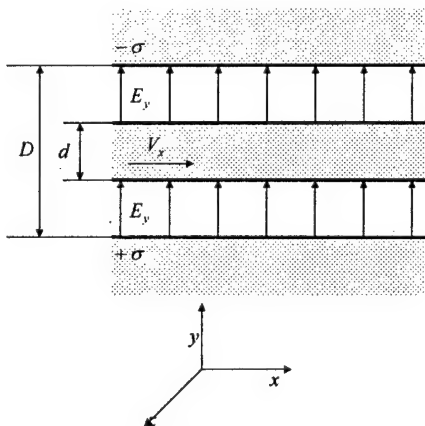


Fig. 1. The flat capacitor with a moving metal plate in a gap.

charge density on the capacitor plates in the coordinate system $X'Y'Z'$, that has changed according to the Lorentzian length reduction in the moving frame, c is the light speed. In addition to the electrical field, the magnetic field with the intensity H'_z is also generated between the capacitor plates.

Knowing the surface density of electrical charges σ'_m in the coordinate system $X'Y'Z'$, it is possible, using the invariant property of an electrical charge and Lorentz transforms, to find the surface density of electrical charges σ_m on the metal plane surface in the coordinate system XYZ :

$$\sigma_m = \gamma\sigma'_m = \gamma^2 \cdot \sigma = \sigma / (1 - V_x^2/c^2).$$

Using the expression for σ_m , we can write down ratios for calculation of values of the electrical and magnetic fields in coordinate system XYZ inside the moving metal plane:

$$E_\Sigma = -E_y \cdot (V_x^2/c^2) / (1 - V_x^2/c^2) \quad (1)$$

$$H_\Sigma = E_y / W \cdot (V_x/c) / (1 - V_x^2/c^2) \quad (2)$$

$$B_\Sigma = E_y / c \cdot (V_x/c) / (1 - V_x^2/c^2) \quad (3)$$

Thus, inside the moving metal plate the electrical field is non-zero and directed opposite to the external impressed electrical field. Generally, the value, that shows how much the electrical field inside the material is weakened, in comparison with the electrical field in vacuum, is named the relative permittivity of the given material. In other words, it is possible to speak about the appearance of the relative permittivity ϵ of the moving metal:

$$\epsilon = \frac{E_y}{E_\Sigma} = 1 - \frac{c^2}{V_x^2} \quad (4)$$

As we can see the negative permittivity ϵ has the negative sign, and its value depends only on the metal

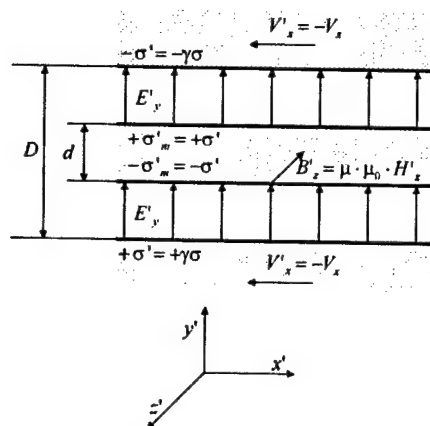


Fig. 2. The investigated capacitor in the coordinate system, in which the metal plate is fixed.

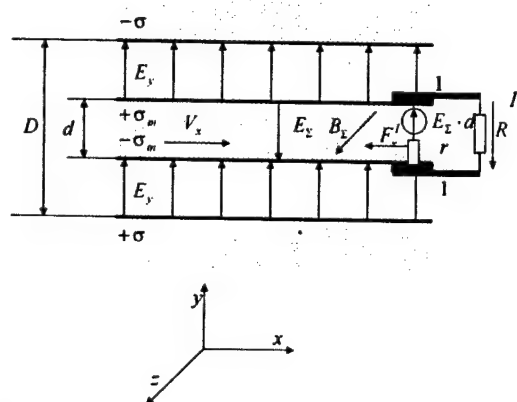


Fig. 3. The electrostatic relativistic dynamo-machine.

speed and varies from $-\infty$ to 0 at changing the speed V_x from 0 to c . The appearance of the additional magnetic field makes a bianisotropic medium out of the moving metal [2]. The negative frequency-independent permittivity means that the medium has changed from passive, in which only a signal propagation occurs, into active, in which a signal amplification is possible. Since ϵ is the velocity function, it is possible to assume

that the medium becomes active because of the presence of the metal speed. That is, the energy of mechanical motion by means of this mechanism can be transformed into the electrical energy.

Such transformation can be carried out, for example, in the system shown in Fig. 3, where the considered above capacitor creating the homogeneous electrical field E_y is presented.

The metal plane is placed between the capacitor plates and moves perpendicularly to the electrical field with the speed V_x . As a result, in the fixed coordinate system XYZ we observe the EMF $U = E_y \cdot d$ between the top and bottom boundaries of the metal plane. The given EMF is taken off with the help of sliding contacts 1 (see Fig. 3.). We shall describe the resistance of the most metal plane r as the internal resistance of the voltage source, and the external circuit will be characterized by the resistance R . Let's estimate the possibility of using the suggested converter of the mechanical energy into the electrical one. As a moving conductor at the room temperature we shall take a copper plate with the thickness $d = 10$ mm and the area 0.001 m². In that case, the internal resistance of the chosen metal plate is $r = 1.56 \cdot 10^{-7}$ Ohms. At the external electrostatic field intensity $E_y = 20$ kV/m the EMF obtained at the speed 10 m/s will make $0.22 \cdot 10^{-14}$ V, that results in the smallest useful electrical power. Nevertheless, in principle it is possible to measure the current and thereby to confirm or deny the presence of the electrical field in the moving metal.

REFERENCES

1. Parcell E. Electricity and magnetism. – Moscow: Nauka, 1983. – (the Berkleevskii lecture on physics). – 416 p.
2. Serdyukov A.N., Semchenko I.V., Tretyakov S.A., Shihvola A.H. Electromagnetics of bi-anisotropics materials: Theory and applications. – Amsterdam: Gordon and Breach Science Publishers, 2001. – 216 p.

THE MODEL OF CREATION OF ROTATING STATIONARY ELECTROMAGNETIC FORMATIONS IN VACUUM

B. V. Sestroretsky¹, K. N. Klimov¹, S. M. Godin², V. V. Roshchin², T. V. Kamishev¹, V. A. Ruchenkov¹

¹ Lavochkin Association, Leningradskaya st. 24, Chimki-2 Moscow Area 141400, Russia
Phone: (095) -575-50-69, E-mail: <const0@laspace.ru>

² Neotek, Moscow, Russia

Abstract

The hypothesis of creation of $R\tau$ -electromagnetic formations around rotating cylindrical nonuniform magnets is considered in the given work. During investigations devices of stream $R\tau$ -grids, Lorentz transforms and hysteresis effects in magnets are used.

Keywords: Negative permittivity, relativistic effect.

1. INTRODUCTION

According to the literature [1] stationary magnetic cylindrical formations of small thickness with a sharp recession of the magnetic field intensity at borders are formed around rotating nonuniform magnetic systems. In the given work it is assumed that similar cylindrical formations can be considered as quasistatic concentrators of the electromagnetic energy that arise in layers of the 3D stream $R\tau$ -grids [4], simulating the electrodynamics processes in time domain. In the stream $R\tau$ -grids, in contrast to finite-difference grids, not the E and H fields are modeled by some point pattern in a small volume, but the vacuum as an infinite grid of volumes Δ^3 (Fig. 1a) with small dispersion of the flat wave velocity during their distribution to any directions. An operator of the 3D stream $R\tau$ -grid is the 12-ports circuit in the volume Δ^3 , formed of the system of ideal transformers and video signal delay elements $\tau = \Delta/(4c)$, where Δ is the volume size, $c = 1/\sqrt{\epsilon_0\mu_0}$ is the light speed (see Fig. 2). The operator is matched in all 12 ports, has no signal of direct leakage and transmits an input videopulse with unit amplitude duration τ to four neighboring inputs with the amplitude double reduction. Similar pulses are transmitted with the double light speed.

Owing to balancing properties of the circuit of elementary volume the stream $R\tau$ -grid allows one to form energy-isolated stationary electromagnetic formations in net vacuum that cannot be detected by external observers. In physics the stationary electromagnetic formations have been investigated as elementary particles (an electron, a positron, a proton, neutrino, etc.) that are characterized by a specified value of energy, weight and other parameters.

In the $R\tau$ -stationary electromagnetic formations the energy storage level is not limited, since the intensity of macroscopic fields E and H is not quantized.

In the present work it is supposed that because of the weak connection with the $R\tau$ -stationary cylindrical electromagnetic formation the rotating nonuniform magnet can create a rotating electromagnetic field and transform noise external fields into the ponderomotive energy of magnet rotation.

2. CREATION OF STEADY ELECTROMAGNETIC FORMATIONS IN THE $R\tau$ GRID PLANAR LAYER

A simplified version of the full stream $R\tau$ -circuit (Fig. 2) is shown in Fig. 3a. The circle with the designation M represents a system of 12 ideal transformers, which internal windings are crossed at 6 points (black circles in Fig. 2). Thick lines designate pairs of orthogonal two-wire lines, which input terminals are shown in Fig. 3a by thin lines with indexes from 1 to 12, in conformity with Fig. 2. A layer of the infinite three-dimensional grid in the plane XZ (Fig. 3b) is formed of circuits Fig. 3a. Projected dual lines focused along the axis Y are shown in the center of the circles M .

If to apply unit in-phase pulses having the duration $\tau = \Delta/(2\sqrt{\epsilon_0\mu_0})$ from the inputs 1 and 3 to the circuit Fig. 3a, then unit in-phase pulses will also appear in the

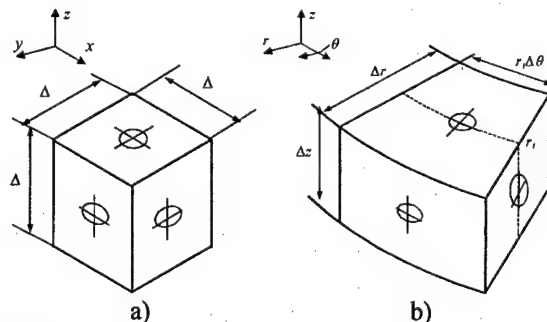


Fig. 1.

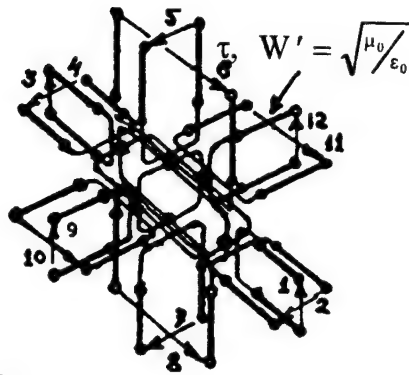


Fig. 2.

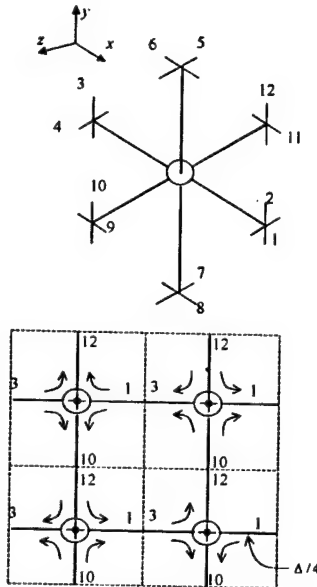


Fig. 3.

shoulders 10 and 12 with the time shift $\tau/2$ (see Fig. 2). There will be no pulses at the output of all other shoulders of the circuit Fig. 3b. The pulse propagation from the shoulder 1 to the shoulder 12, and from the shoulder 3 to the shoulder 10 is shown in Fig. 3b by bent arrows. Since the power is divided into halves, the pulse amplitudes for the arrows will decrease by factor of $1/\sqrt{2}$. It is essential also that pulses in the shoulders 6 and 8 will be absent, which determines the power isolation of the layer of volumes Δ^3 in the section XZ (see Fig. 3b).

On the circuit Fig. 3b unit pulses approach in pairs to the units M as on a chess-board. As a result, it is possible to reduced the circuit Fig. 3b to the circuit Fig. 4, in which one can see closed circuits with the geometrical length 4Δ and the electric perimeter 2Δ (taking into account the pulse motion with the double light speed). As the drive pulses had the time length $\tau = \Delta/(2\sqrt{\epsilon_0\mu_0})$, the video pulses with duration of 2τ are along the length of the closed circuits in Fig. 4 (thick lines with arrows).

"Ring" videopulses have the identical intensity of the electric E and magnetic H fields ($E/H = \sqrt{\mu_0/\epsilon_0}$) along the whole length. The ring videopulse contains an identical quantity of the stored electrical $W_E = \epsilon_0 E^2 \Delta^3$ and magnetic $W_H = \mu_0 H^2 \Delta^3$ energy.

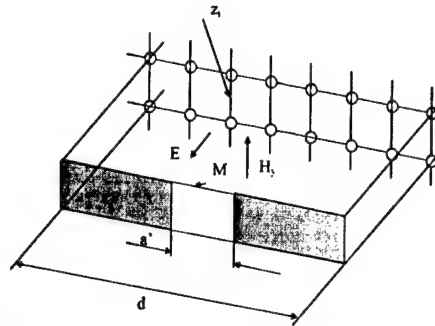


Fig. 4.

As for the ring videopulse the E and H fields phase does not change along the ring, it can be considered as a stationary electromagnetic formation. The pulse energy motion with the double light speed cannot be directly detected. It becomes apparent only in the direction of the magnetic field H . Granting this the circular arrows show the direction of the Poynting Π vector for orthogonal E and H fields (see Fig. 3b).

Hanging ring videopulses are placed on the whole surface of the layer of volumes Δ^3 in Fig. 3b. For all electromagnetic formations in Fig. 3b the direction of the electric field E_y is identical, and the fields H_x , H_z have the ring direction with "chess" coloring. The constancy of the field E_y direction allows one to assume that this field can be connected with the external electrostatic field focused along the axis Y .

3. CREATION OF CYLINDRICAL ELECTROMAGNETIC FORMATIONS

As concentric rings are formed around the rotating magnet, the elementary volume form should be properly changed (see Fig. 1b). The volume sizes Δr_i , Δz_i and $r_i \Delta \Theta$ in coordinates R , Z and Θ should be determined by the ratio:

$$\Delta r = \Delta; \Delta z = \Delta; r_i \Delta \Theta \cdot \frac{\sqrt{\mu_i \epsilon_i}}{\sqrt{\mu_0 \epsilon_0}} = \Delta \quad (1)$$

$$\Delta \Theta = 2\pi/n \quad (2)$$

$$\sqrt{\mu_i/\epsilon_i} = \sqrt{\mu_0/\epsilon_0} \quad (3)$$

When going from the circuit Fig. 1a to the circuit Fig. 1b it is supposed that the equivalent $R\tau$ -circuit of the stream cubic element Fig. 2 remains constant in form. The time delay conservation $\tau/2$ for lines along the axis $r_i \Delta \Theta$ is attained by introducing the anisotropy with respect to ϵ and μ only in this coordinate. The values $\epsilon_0 \mu_0$ remain unchanged in coordinates r and z . The ratio (1) provides the equating of the volume electric length $r_i \Delta \Theta$ Fig. 1b to the value Δ . The ratio (3) provides the wave resistance identity along all axes.

When meeting the condition (2) the whole n number of elementary volumes Fig. 1b is along the length of the ring circle $2\pi r_i$ in a circle with any r_i . Substituting (3) into (1) we shall obtain the ratio in order to determine r_i

$$r_i \Delta \Theta \sqrt{\epsilon_i/\epsilon_0} = \Delta \quad (4)$$

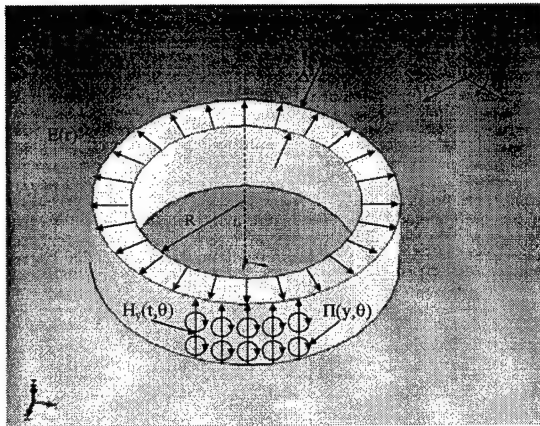


Fig. 5.

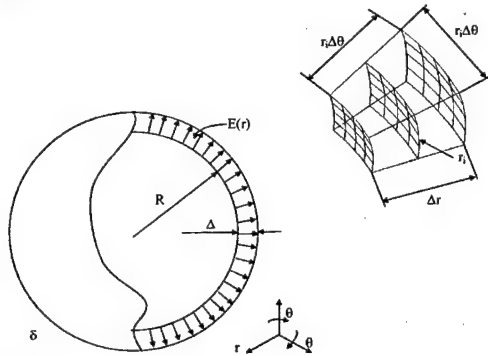


Fig. 6.

It follows from (4) that when $r_i \Delta \theta > \Delta$ it is required to introduce a dielectric with $\epsilon_i < \epsilon_0$ and a magnetic with $\mu_i = \epsilon_i \mu_0 / \epsilon_0$ along the axis $r_i \Delta \theta$.

The considered approximate model of bend adjustment along the axis $r_i \Delta \theta$ allows one to save the equivalent circuit Fig. 2 and its unique balancing property. Taking into account the possibility of formation of sector elementary volumes Δ^3 (see Fig. 1b), the plane ZX can be bent with the radius R , forming a cylindrical surface Fig. 5 with the electrostatic field $E(r)$ directed along the axis r . The magnetic field $H(y, \theta)$, dependent on coordinates Y , $r\theta$ forms loops, alternating in the direction, on the cylinder surface (see Fig. 5). The electric field $E(r)$ intensity does not depend on time, as well as the electrostatic field according to the Coulomb equation for a charged metal string located on the cylinder axis.

However, the electrostatics cannot answer how the field $E(r)$ was created, because the energy along the field is not transferred. The energy through the ring thickness Δ for static fields can "be caught" only by inserting two metal cylinders with the diameter difference Δ .

In case of the model Fig. 5 the energy though the thickness Δ is "caught" without metal cylinders. In our case these metal cylinders act as the balancing $R\tau$ -operator Fig. 2 and create a divide wall between the layer of elementary volumes Δ^3 and the external space.

If to enter a tapered compression into the cubic volume (see Fig. 4a) not along one axis (Fig. 1b), and along two ones (Fig. 4a), going to spherical coordinates, then the volume layer Fig. 4a will permit to form a spherical object (Fig. 4b) with thickness Δ .

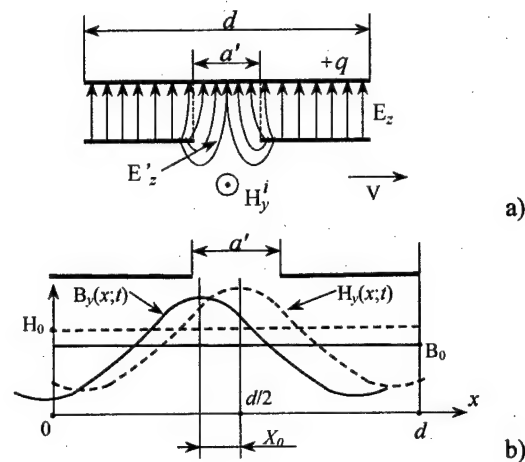


Fig. 7.

4. EXCITATION OF THE AXIAL MAGNETIC FIELD IN THE CYLINDRICAL RING

To simplify the analysis we shall turn round the cylindrical surface Fig. 7 with the radius R and present it as a section of the planar grid with the length $d = p\Delta$ that is formed of p elements like in Fig. 3a. The whole number of q sections is along the cylinder circle Fig. 5 with the length $2\pi R$, i.e. $d = 2\pi R / q = p\Delta$.

Let's assume that some heterogeneity M , moving along the segment d on the axis X with the speed V , changes the wave resistance Z_i in the line directed along the axis Y , for example, for one i -th element of the grid layer. When changing $Z_i = \sqrt{\mu_i / \epsilon_i}$ we shall keep the videopulse delay time along the line with the length Δ constant with $\tau = \Delta 2\sqrt{\mu_i \epsilon_i} = \Delta / 2\sqrt{\mu_0 \epsilon_0}$. The equality violation $Z_i \neq Z_0 = \sqrt{\mu_0 / \epsilon_0}$ in one of the grid elements Fig. 6 will lead to some structure disturbances of stationary fields in the ring grid Fig. 5 that will be periodic along the cylinder circle with the period $q = 2\pi R / p\Delta$. A similar field disturbance in the steady state mode will move along the circuit of the cylindrical resonator Fig. 5 with the speed V , i.e. with the cylinder speed P .

The change of Z_i will lead to radiation of a part of the electromagnetic energy through the element sections $\Delta \times \Delta$ on either side of the ring surface.

We can suppose that it is due to the presence of a component of the electric field E_z^i in the radiated fields that moves along the ring surface on the axis X with the speed V and stimulates the field H_y^i .

To simplify the analysis the three-dimensional problem of the flat layer Fig. 3b, in which electromagnetic fields are isolated, will be replaced by the two-dimensional problem of the electrostatic condenser Fig. 7. The electromagnetic field isolation is provided by metal surfaces with a charge surface density of $\pm q$. The electric field is equal to $E_z = q / \epsilon_0$. If there is a gap d in the bottom surface (that is equivalent to the change of Z_i in the layer Fig. 3b), the field E_z^i with a smaller intensity will appear outside of the aperture

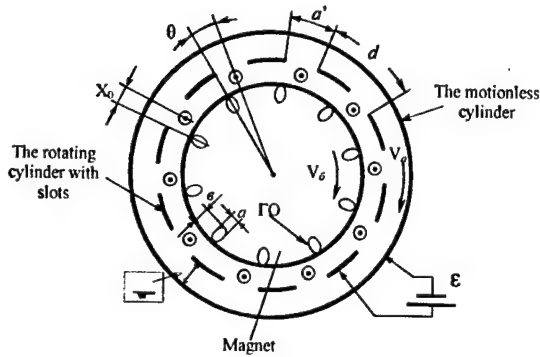


Fig. 8.

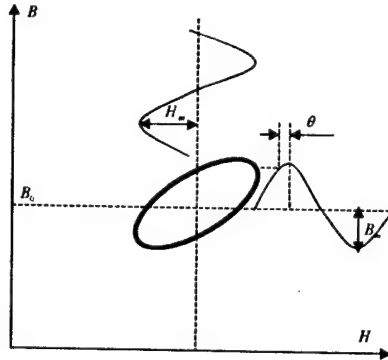


Fig. 9.

(Fig. 7). As both surfaces of the condenser move with the speed V , then according to the Lorentz ratio the magnetic field will appear near the aperture:

$$H_Y^i = \gamma \cdot E_2^i; \quad \gamma = V/c$$

It is possible to assume that in rings like in Fig. 5 the electric field intensity can considerably exceed fields of the electric breakdown in the air that allows one to receive very high values of the field H_Y^i when $V/c \sim 10^{-6}$, which is characteristic of mechanical systems.

5. DYNAMICS OF SYNCHRONIZATION PROCESSES OF CYLINDER AND MAGNET ROTATION SPEEDS

On the basis of approximation of the $R\tau$ -cylinder Fig. 5 by the condenser-type cylinder Fig. 7a we shall form a design like in Fig. 8 where the electrode of the condenser cylinder with slots d rotates with the speed V_a around the magnet rotating with the speed V_b . We shall connect the constant-voltage source ε creating the radial constant electric field E_2 to two electrodes of the condenser cylinder. The non-uniform magnetic field H_Y^i rotating as the electrode with the speed V_a is excited in a gap between the magnet and the electrode with slots. The field H_Y^i maximums being near slots excite domain formations HO (hysteresis areas) in the magnet, in which the field B_Y^i intensity changes in comparison with the average value of the field B_0 in the magnet volume.

It can be supposed that the fields H_Y and B_Y are described by cosinusoidal functions like in Fig. 7b:

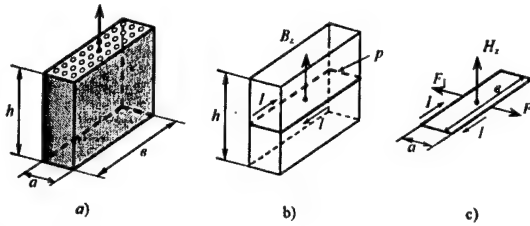


Fig. 10.

$$H_Y = H_0 + H_m \cos \frac{2\pi}{d}(x) \quad (5)$$

$$B_Y = B_0 + B_m \cos \frac{2\pi}{d}(x - x_0) \quad (6)$$

where H_0 and B_0 are average values of the fields, H_m and B_m are cosinusoid amplitudes, d is the distance between apertures, $V = V_a = V_b$ is the synchronous speed of rotation of the ring and domain areas in the stationary mode, x_0 is the geometrical displacement of the field B_Y curve with respect to the field H_Y curve because of the delay under hysteresis magnetic reversal. In (5) it is supposed that the field H_Y maximums are in centers of the slots d . The angular displacement of sinusoids equals to $\Theta_0 = 2\pi/d \cdot x_0$.

In the work [2] the degree of the angle Θ is estimated by the formula:

$$\Theta = \arcsin(P_{cT}/H_m B_0) \quad (7)$$

where

$$P_{cT} = kH_c B_m / \pi \quad (8)$$

– is the energy dissipated in the magnet for one time cycle of the sine-wave magnetic reversal T in a unit of the magnet volume, $T = 1/f = d/V_1$; H_m is the amplitude of the magnetic field modulation; B_0 is the average value of the magnetization induction; H_c is the coercive force by induction.

The hysteresis characteristic like in Fig. 9 corresponds to the magnetic field approximation and magnetization in the form of sinusoids (5) and (6). We introduce a similar approximation by analogy with [2] allowing for constant components B_0 and H_0 .

It is supposed that the field H_Y of cosinusoidal form penetrates into the magnet and changes the field B_Y there according to the curve in Fig. 9. We shall assume that the size a of the hysteresis area is equal to the width of the slot a and much less than d , and the value of B_Y in the magnet volume is practically constant and equal to B_0 .

Any point of the curve $B = f(H)$ in Fig. 9 corresponds to the steady-state mode of magnetization. The dynamics of interaction of the moving field H_Y and moving magnetization areas is similar to the dynamics of interaction of the moving electromagnetic wave and bundles of electrons moving in the same direction in travelling-wave tubes. In the steady-state mode of the flow velocity of two streams, $V_a = V_b$ are equalized. Each of the streams can be a source of the energy transferred to the second stream. For example, if magnets are accelerated by applying the mechanical force then the moving field B_Y excites a wave with the field H_Y , accumulating the magnetic energy in this wave.

The stream H_Y , influencing the field B_Y , creates the ponderomotive force F , which will rotate the magnet. To describe the specified processes we shall set up a differential equation connecting the mechanical force F with the speed $V_a = V_b$ and the fields H_Y and B_Y .

To simplify the analysis we shall replace hysteresis areas (Fig. 10a) with the section $a \times b$ and the height h by the wire loop of the same section with the current I .

For ferromagnets the intensity of the magnetic polarization M exceeds essentially the intensity of the regulating field H_Y . The value of M for the magnet is equal to the product of the number of focused dipoles (domains) in a volume unit and the magnetic moment m of each dipole [2]. At that, it is not important what keeps the dipole direction save: applying the external field H_Y or spontaneous self-organization of domains. In our case the magnetic polarization intensity can be considered equal to the field B_Y , i.e.:

$$M \approx B_Y \quad (9)$$

The change of the internal field M of the magnet material and accordingly B_Y is regulated by the hysteresis curve Fig. 11.

If the field B_Y is supposed to be equal in the section $a \times b$ both for the hysteresis area and for the loop, then the value of the current I is determined by the ratio:

$$I = B_Y h \quad (10)$$

The input field H_Y tends to move apart the loop wires with the opposite current I (see Fig. 10c). If the sinusoid H_Y is located symmetrically to the magnet center, the resultant force $F = (F_1 - F_2)$, effecting on the loop, will be equal to zero. For other positions ($x \neq 0$ in Fig. 7b) the resultant force F is not equal to zero and can have various directions on the axis X , accelerating or slowing down the structure rotation velocity Fig. 8. Taking into account the small value a in comparison with the sinusoid period d , the value of the force F (the Lorentz force) is determined by the ratio:

$$F = I \cdot a \cdot b (\partial H_Y / \partial x)_{x=x_0} \quad (11)$$

Differentiating (6) with respect to x we shall obtain the force effecting on one domain area:

$$F = H_m \cdot I \cdot 2\pi / d \cdot a \cdot b \cdot \sin 2\pi(x - x_0) / d \quad (12)$$

Substituting the value of the current I from ratios (10) and (6) into (12) we shall obtain:

$$F = a \cdot b \cdot h [B_0 + B_m \cos 2\pi / d(x - x_0)] \times \\ \times H_m 2\pi / d \sin 2\pi(x - x_0) / d \quad (13)$$

In turn the force F is determined by weight and acceleration of the structure with magnets:

$$F = m \partial v / \partial x \quad (14)$$

where $m = \gamma abhN$ is the total weight of the magnet in the system Fig. 8; γ is the relative density of the magnet material; v is the system speed of rotation Fig. 8.

From (13) and (14) we shall obtain the differential equation describing the interaction of two moving elements of the system Fig. 8 with close speeds $V_a \approx V_b$:

$$\gamma \partial v / \partial t = 2\pi / d H_m \sin 2\pi / d(x - x_0) \\ [B_0 + B_m \cos(2\pi x / d)] \quad (15)$$

where $x = v_1 t$; $x_0 = \Theta_0 d / 2\pi$; d , γ are specified parameters.

According to (7), (8) and taking into account the fact that the period $T = d / v$, we shall obtain the additional ratio:

$$\Theta = \arcsin(k H_c B_m d / \pi H_m B_0 v) \quad (16)$$

The quantity H_0 does not obviously appear in (15) and (16). Granting this, specifying the fixed quantity H_m is enough to solve the differential equation (15), subject to (16), entering some speed value v_i as an initial condition.

6. THE POSSIBLE MECHANISM OF FORMATION OF THE RADIAL ELECTRIC FIELD

To provide a constant rotation of the ring with slots in the system Fig. 7 that is in the stationary mode of rotation ($V_a = V_b$) it is necessary to sustain a certain level of the radial electric field. It is possible to assume that in the radial $R\tau$ -ring (Fig. 5) the rotating heterogeneities M (Fig. 6) excite the rotating magnetic field H_Y not only on the internal surface of the ring about the magnet (Fig. 8), but also on the external surface. We can assume that the field H_Y will stimulate the input of some electromagnetic field formations moving chaotically in vacuum and self-organizing into radially directed fields to the radial $R\tau$ -ring. Thereby the stationary mode of rotation is sustained near the external area of the ring. A similar mechanism of self-excitation of the magnetic field in a conducting medium (with zero density of the distributed charge) is considered in [3]. The effect is named «the turbulent dynamo». In the loop in the conducting medium it is spontaneous because of small casual distortions being accompanied with the occurrence of weak electric and magnetic fields, can intensify on the average owing to the whirl and at the medium certain sizes and microturbulences, and create the constant magnetic field.

7. CONCLUSION

The considered self-sustaining mechanisms of rotation in systems with magnets should be regarded as theoretical hypotheses that require an experimental check and more detailed mathematical simulation, in particular on the basis of programs of the $R\tau$ -grid analysis taking into account the body motion and hysteresis effects in magnets.

REFERENCES

1. V. V. Roshchin, S. M. Godin. Experimental investigation of physical effects in the dynamic magnetic system. - Letters to JTP, Vol. 26, №24 - 2000, pp. 70-75.
2. E. S. Kuharkin. Principles of engineering electrophysics. - "Higher school", M.: 1969.
3. L. D. Landau, E. M. Lifshits. Electrodynamics of continuous environments. Theoretical physics, Vol. 8. - "Fizmat", M.: 2001.
4. B. V. Sestroretsky. Balance RLC and $R\tau$ schemes of elementary volume of space. Questions of Radioelectronics, "General questions of radioelectronics", Vol. 5, M.: 1983, pp. 127-158.

MODELING OF PLANE ELECTROMAGNETIC WAVE DIFFRACTION ON A CONICAL ANTENNA

Elena K. Semenova, Vladimir A. Doroshenko

Department of Higher Mathematics, Kharkiv National University of Radio Electronics
Kharkiv, Ukraine

<h_semenova@yahoo.com>, <vlad_doroshenko@yahoo.com>

Abstract

The problem of plane electromagnetic wave diffracted by a conical structure with longitudinal slots is considered. The plane wave propagates along the cone axis. The problem solution method uses the Kontorovich-Lebedev transform and the analytical regularization procedure. It is shown, that electromagnetic problem is equivalent to the solution of the linear algebraic equations system for Fourier coefficients of scattered field components. The numerical algorithm for solving this system is constructed. Two cases of electromagnetic plane wave polarization are considered. Scattered field patterns are given to investigate slot effects.

Keywords: conical antenna, slots, plane wave diffraction, scattered field patterns.

1. INTRODUCTION

Conical structures have some special features. They are omnidirectional and super-wide-band in radiation pattern and matching.

The excitation problems of this structure by radial dipoles have been considered in the previous works [1]. However, the solution of the diffraction problem for such structure is of a great interest from the standpoint of antenna technique and radar applications.

The task of this paper is to find numerical solution for plane wave field diffraction problem and to analyze slot effects on scattering characteristics.

2. PROBLEM FORMULATION AND SOLUTION METHOD

Let a homogeneous plane electromagnetic wave be incident on a thin perfectly conducting semi-infinite circular cone with N longitudinal slots (Fig. 1). Plane wave propagates along the cone axis. The time dependence is given in the form $e^{-i\omega t}$. In the employed spherical coordinate system (r, θ, φ) , with the origin at the cone tip, the conical surface Σ is defined by the equation $\theta = \gamma$. The period $l = 2\pi/N$ and the slot width d are angular values.

The presence of a cone with longitudinal slots leads to arising of a scattered field $\vec{E}^{(sc.)}, \vec{H}^{(sc.)}$. The total field for \vec{E}, \vec{H} has the form:

$$\vec{E} = \vec{E}^{(in.)} + \vec{E}^{(sc.)}, \vec{H} = \vec{H}^{(in.)} + \vec{H}^{(sc.)}, \quad (1)$$

where $\vec{E}^{(in.)}, \vec{H}^{(in.)}$ denote the primary plane wave field. We will express the components of the electro-

magnetic field in terms of the electric U_1 and magnetic U_2 Debye potentials and then reduce the initial electromagnetic problem to two scalar boundary-value Dirichlet and Neumann problems for the U_1 and U_2 potentials.

We will treat two cases of polarization of the primary field, namely,

$$\vec{E}^{(in.)} = (E_x^{in.}, 0, 0), \quad \vec{H}^{(in.)} = (0, H_y^{in.}, 0), \quad A$$

$$E_x^{(in.)} = H_y^{(in.)} = e^{ikz};$$

$$\vec{E}^{(in.)} = (0, E_y^{in.}, 0), \quad \vec{H}^{(in.)} = (H_x^{in.}, 0, 0), \quad B$$

$$H_x^{(in.)} = -E_y^{(in.)} = e^{ikz};$$

2.1. CASE A

In accordance with the representation of Debye potential $U_j^{(inc.)}$ ($j = 1, 2$) for plane wave field we will

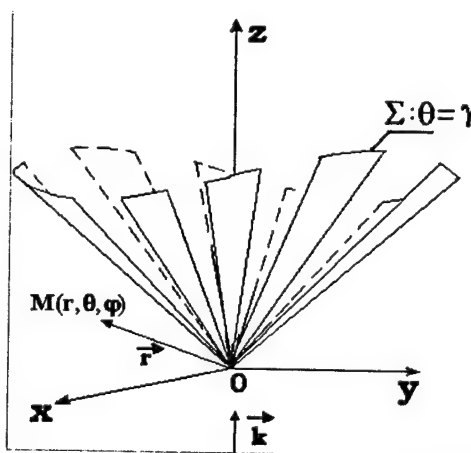


Fig. 1. Cone geometry

look for the solution in the Kontorovich-Lebedev integral transform [2]:

$$U_j^{(sc.)} = U_{j,div.}^{(sc.)} + U_{j,env.}^{(sc.)} \quad (2)$$

$$U_{j,div.}^{(sc.)} = - \int_0^{+\infty} \frac{H_{i\tau}^{(1)}(kr)}{\sqrt{r}} \sum_{m=-1;1} \left(-i \frac{|m|}{m} \right)^{j-1} \times \quad (3)$$

$$\times \frac{d^{j-1}}{d\gamma^{j-1}} P_{-1/2+i\tau}^m (\cos \gamma) U_{m\tau}^{(j)} d\tau$$

$$U_{m\tau}^{(j)} = \sum_{n=-\infty}^{+\infty} x_{m+nN}^{(j)} \times \frac{P_{-1/2+i\tau}^{m+nN} (\pm \cos \theta)}{d^{j-1}} e^{i(m+nN)\varphi}, \quad (4)$$

$$U_{j,env.}^{(sc.)} = - \frac{i}{2k^2} \frac{\sin kr}{r} \frac{d^{j-1}}{d\gamma^{j-1}} \left(tg \frac{\gamma}{2} \right) \times \sum_{m=-1;1} \left(-i \frac{|m|}{m} \right)^{j-1} U_m^{(j)}, \quad (5)$$

$$U_m^{(j)} = \sum_{n=-\infty}^{+\infty} \xi_{m+nN}^{(j)} \times \frac{P_0^{-|m+nN|} (\pm \cos \theta)}{d^{j-1}} e^{i(m+nN)\varphi}, \quad (6)$$

where $P_m^m(\cos \theta)$ is the associated Legendre function, $x_p^{(j)}$ and $\xi_p^{(j)}$ are unknown coefficients related by expression:

$$\xi_p^{(j)} = \lim_{i\tau \rightarrow 1/2} x_p^{(j)}. \quad (7)$$

The upper signs in (4), (6) correspond to the $0 < \theta < \gamma$ range, and the lower signs correspond to the $\gamma < \theta < \pi$ range.

The boundary condition imposed on the cone and the field continuity condition on the slots yield a system of dual series equations:

$$\sum_{n=-\infty}^{+\infty} x_{m,n}^{(j)} e^{imN\varphi} = e^{im_0N\varphi}, \quad \pi d/l < |N\varphi| \leq \pi, \quad (8)$$

$$\sum_{n=-\infty}^{+\infty} [N(n+\nu)]^{\alpha(j)} \frac{|n|}{n} (1 - \varepsilon_{m,n}^{(j)}) x_{m,n}^{(j)} e^{imN\varphi} = 0, \quad (9)$$

$$|N\varphi| < \pi d/l,$$

where $\varepsilon_{m,n}^{(j)}$ are known coefficients:

$$[N(n+\nu)]^{\alpha(j)} \frac{|n|}{n} (1 - \varepsilon_{m,n}^{(j)}) = \frac{(-1)^{(n+\nu)N+j-1} ch\pi\tau}{\pi(\sin \gamma)^{1-\alpha(j)}} \frac{\Gamma(1/2+i\tau+(n+\nu)N)}{\Gamma(1/2+i\tau-(n+\nu)N)} \times \quad (10)$$

$$\times \frac{1}{d^{j-1}} \frac{P_{-1/2+i\tau}^{(n+\nu)N}(\cos \gamma)}{d^{j-1}} \frac{d^{j-1}}{d\gamma^{j-1}} P_{-1/2+i\tau}^{(n+\nu)N}(-\cos \gamma)$$

$\frac{m}{N} = m_0 + \nu$, $-1/2 \leq \nu < 1/2$, m_0 is an integer closest to m/N , $\alpha(j) = (-1)^{j-1}$. Coefficients $\varepsilon_{m,n}^{(j)}$ are independent of the wave number k and are estimated at $(n+\nu)N \gg 1$,

$$\varepsilon_{m,n}^{(j)} = O\left(\frac{1}{(n+\nu)^2 N^2}\right) \quad (11).$$

The coefficients $x_{m,n}^{(j)}$ do not depend on the wave number, and this is convenient for studying field patterns.

One should modify the system (8), (9) of paired equations to apply a regularization procedure that exploits the Riemann-Hilbert problem method. After using this procedure we obtain the two independent Fredholm infinite system of linear algebraic equations (ISLAE) of the second kind for $x_{m,n}^{(j)}$ ($j = 1, 2$) in the following form:

$$D_\nu(u) y_{m,0}^{(1)} = V^{m_0}(u) + \sum_{p=-\infty}^{+\infty} \frac{|p|}{p} \delta_{m,p}^{(1)} V^p(u) y_{m,p}^{(1)} \quad (12)$$

$$y_{m,n}^{(1)} = V_{n-1}^{m_0-1}(u) + \sum_{p=-\infty}^{+\infty} \frac{|p|}{p} \delta_{m,p}^{(1)} V_{n-1}^{p-1}(u) y_{m,p}^{(1)} + y_{m,0}^{(1)} P_n(u), \quad (13)$$

where

$$y_{m,n}^{(1)} = (-1)^{n-m_0} \cdot \frac{n+\nu}{m_0+\nu} \cdot \frac{|n|}{n} (1 - \varepsilon_{m,n}^{(1)}) x_{m,n}^{(1)}, \quad (14)$$

$$D_\nu(u) = \frac{2P_{\nu-1}(-u)}{\nu(P_\nu(-u) + P_{\nu-1}(-u))},$$

$$\text{and } 1 - \delta_{m,n}^{(1)} = \frac{1}{1 - \varepsilon_{m,n}^{(1)}}, \quad u = \cos \frac{l-d}{l} \pi,$$

$V_{n-1}^{p-1}(u)$, $V^p(u)$, $V_{n-1}^{-1}(u)$ are known functions.

The infinite system of linear algebraic equations of the second kind for $x_{m,n}^{(2)}$ is obtained in [2].

The solution of the matrix equation exists, is unique, and can be approximated by solving a truncated matrix equation for arbitrary problem parameters.

2.1.1. Numerical results

To demonstrate the slot effect on the far field scattering patterns, we place patterns for an isotropic cone (a perfectly conducting cone without slots) and a slotted cone both. Thus, Fig.2 depicts a pattern for an isotropic cone ($\gamma = 45^\circ$, $\theta = 99^\circ$). Patterns for this cone with one slot are shown in Fig.3. It is observed that the slot width varying leads to the transformation of the scattered field. The narrow slot ($d < 5^\circ$) has little effect on the scattering pattern.

2.2. CASE B

The structure of the potentials and their representation in the form of the Kontorovich-Lebedev integral are analogous to (2)–(7), as in case A. The unknown Fou-

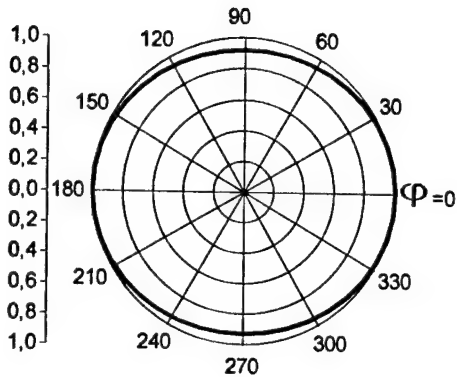


Fig. 2. φ -plane scattering pattern for an isotropic cone ($\gamma = 45^\circ$, $\theta = 99^\circ$)

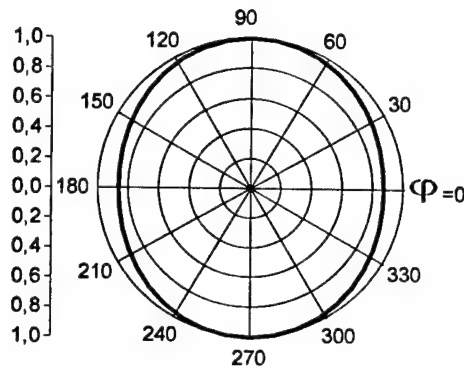


Fig. 4. φ -plane scattering pattern for an isotropic cone ($\gamma = 22,5^\circ$, $\theta = 54^\circ$)

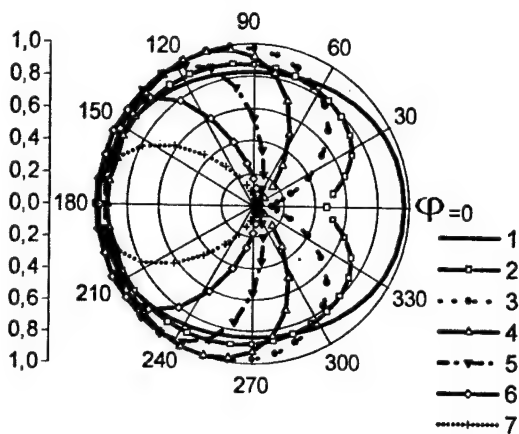


Fig. 3. φ -plane scattering patterns. Scattered far field dependence on the slot width d ($\gamma = 45^\circ$, $\theta = 99^\circ$) 1. $d = 5^\circ$, 2. $d = 30^\circ$, 3. $d = 60^\circ$, 4. $d = 120^\circ$, 5. $d = 180^\circ$, 6. $d = 240^\circ$, 7. $d = 300^\circ$

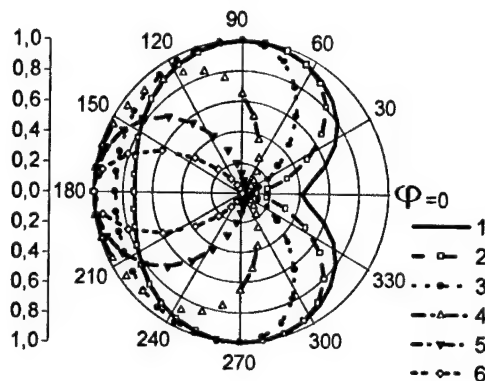


Fig. 5. φ -plane scattering patterns. Scattered far field dependence on the slot width d ($\gamma = 22,5^\circ$, $\theta = 54^\circ$) 1. $d = 5^\circ$, 2. $d = 60^\circ$, 3. $d = 120^\circ$, 4. $d = 180^\circ$, 5. $d = 240^\circ$, 6. $d = 300^\circ$

rier coefficients $x_{m,n}^{(j)}$ satisfy the same dual series equations (8)–(9) and two ISLAEs (12)–(13).

2.2.1. Numerical results

The φ -plane scattering patterns for the case of H -polarized plane wave are shown in the Figs. 4–5. Thus, Fig. 4 depicts pattern for an isotropic cone ($\gamma = 22,5^\circ$, $\theta = 54^\circ$). Patterns for this cone with one slot are shown in Fig. 5.

3. CONCLUSION

The solution to the problem of electromagnetic plane wave diffraction on a conical structure has been obtained with the Kontorovich-Lebedev integral transform and the analytical regularization procedure. Numerical results have been presented to show the variation of the scattering patterns when the slot width is varied. Results show that a narrow slot has little effects on scattering patterns.

REFERENCES

1. Doroshenko V. A., Evsyukova E. K. (Semenova), Kravchenko V. F., Excitation of a conical slot antenna // *Journal of Communications Technology and Electronics*, Vol. 46, No. 8, 2001, pp. 879-885.
2. Doroshenko V. A., Kravchenko V. F. The scattering of plane electromagnetic waves from a cone with longitudinal slots // *Journal of Communications Technology and Electronics*, Vol. 46, No. 3, 2001, pp. 271-278

ANTENNA SYNTHESIS

THE THEORY OF FRACTAL ANTENNA ARRAYS

Victor F. Kravchenko

Institute of Radio Engineering and Electronics of Russian Academy of Sciences
11 Mokhovaya st., Center, GSP-3, Moscow, 103907, Russia
Phone: +7 (095) 203 47 93, Fax: +7 (095) 203 84 14, E-mail: kravchenko_vf@fromru.com

Abstract

Foundations of measure theory, the Hausdorff-Besicovitch measure, fractal nowhere differentiable Boltzmann, Weierstrass, Cantor, Riemann, Darboux, Van-der-Waerden, Koch, Sierpinski, Besicovitch, and Weierstrass-Mandelbrot functions, and also some atomic functions possessing fractal properties are considered. For the first time, the atomic-fractal functions are constructed. The theory proposed and justified is illustrated on problems of synthesis of fractal radiating structures by means of modeling the corresponding physical processes.

Keywords: fractals; antenna arrays; antenna theory; antenna radiation patterns; low-sidelobe antennas; array signal processing; atomic functions; R-functions.

1. INTRODUCTION

The name 'fractal', from the Latin 'fractus' meaning broken, was given to highly irregular sets by Benoit Mandelbrot in his foundational essay in 1975 [1]. Since then, fractal geometry has attracted widespread, and sometimes controversial, attention. The subject has grown on two fronts: on the one hand many 'real fractals' of science and nature have been identified. On the other hand, the mathematics that is available for studying fractal sets, much of which has its roots in geometric measure theory, has developed enormously with new tools emerging for fractal analysis. This paper concerned with the mathematics of fractals and application to antenna theory [2-9].

Various attempts have been made to give a mathematical definition of a fractal, but such definition has not proved satisfactory in a general context. Here we avoid giving a precise definition, preferring to consider a set E in Euclidean space to be a fractal if it has all or most of the following features:

(i) E has a fine structure, that is irregular detail at arbitrarily small scales.

(ii) E is too irregular to be described by calculus or traditional geometrical language, their locally or globally.

(iii) Often E has some sort of self-similarity or self-affinity, perhaps in a statistical or approximate sense.

(iv) Usually the 'fractal dimension' of E (defined in some way) is strictly greater than its topological dimension.

(v) In many cases of interest E has a very simple, perhaps recursive, definition.

(vi) Often E has a 'natural' appearance.

Examples of fractals abound, but certain classes have attracted particular attention. Fractals that are invariant under simple families of transformations include self-similar, self-affine, approximately self-similar and statistically self-similar fractals. Certain self-similar fractals are especially well-known: the middle-third Cantor set, the von Koch curve, the Sierpinski triangle (or gasket) and the Sierpinski carpet, see Fig. 1. Fractals that occur as attractors or repellers of dynamical systems, for example the Julia sets resulting from iteration of complex functions, have also received wide coverage. Fractal geometry is the study of sets with properties such as (i)-(vi). Many of the questions that are of interest about fractals are parallel to those that have been asked over the centuries about classical geometrical objects. These include:

a) *Specification.* We seek efficient ways of defining fractals. For example, iterated functions systems provide one way of specifying fractal of certain classes.

b) *Local description.* Locally a smooth curve looks like a line segment. Whilst fractals do not have such simple local structure, notions such as densities and tangent measures provide some local information.

c) *Measurement of fractals.* The usual way of 'measuring' a fractal is by some form of dimension. Nevertheless dimension provides only limited information and other ways of quantifying aspects of fractality are being introduced. For example, 'lacunarity' and 'porosity' are used to describe the small-scale preponderance of 'holes' in a set. For such quantities to have more than just descriptive use, their definitions and properties need a sound mathematical foundation.

It may be argued that there is too much emphasis on dimension in fractal analysis. Certainly, dimension (with its various definitions) tends to be mathematically tractable and can often be estimated experimentally. Moreover, the dimension of an object is often

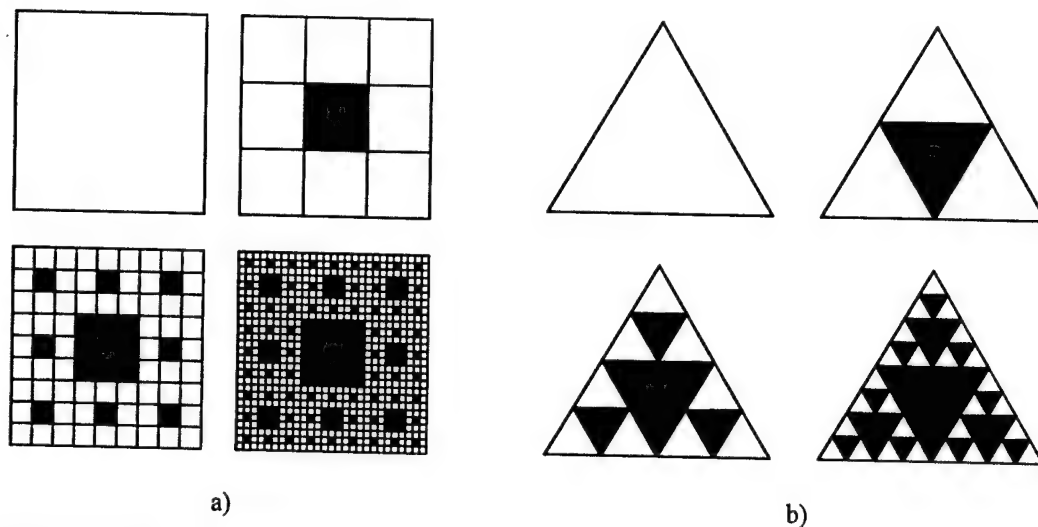


Fig. 1. First four stages of constructing the Sierpinski carpet (a) and Sierpinski gasket (b)

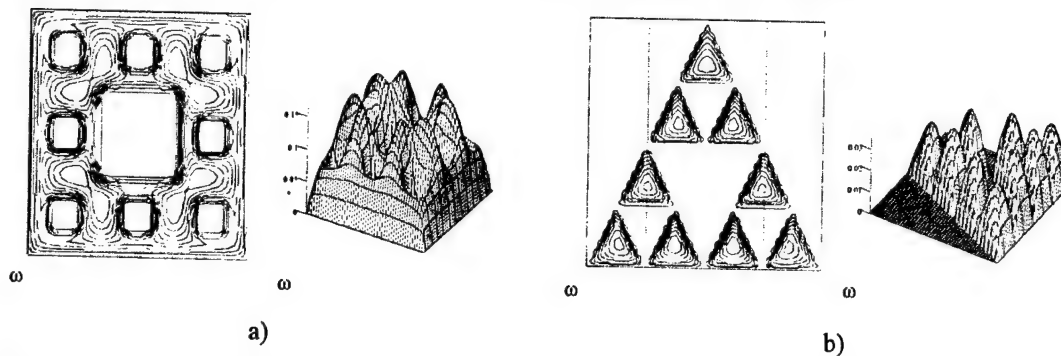


Fig. 2. Contour and surface plots for equations of the Sierpinski carpet (a) and gasket (b) constructed by the R-function method

related to other features, for example the rate of heat flow through the boundary of a domain depends on the dimension of the boundary, and the dimension of the attractor of a dynamical system is related to the dynamical parameters such as the Liapunov exponents. However, many fractal aspects of n object are not reflected by dimension alone and other suitable measure of fractality are much needed.

d) *Classification*. We seek ways of classifying fractals according to significant geometrical properties. One approach is to regard two sets as 'equivalent' if there is a bi-Lipschitz mapping between them (just as in topology two sets are considered equivalent if they are homeomorphic) and to seek 'invariants' for equivalent sets. For example two sets that are bi-Lipschitz equivalent have the same dimension, but dimension is far from a 'complete invariant' in that, except for certain rather specific classes of sets, there can be many non-equivalent sets of the same dimension.

e) *Geometrical properties*. Properties of orthogonal projection, intersections, products, etc., are often of interest.

f) *Occurrence in other areas of mathematics*. Fractals arise naturally in many areas of mathematics, for example, dynamical systems or hyperbolic geometry.

The general theory of fractals ought to relate easily to these areas.

g) *Use of fractals to model physical phenomena*. There are many 'approximate fractals' in physics and nature, and these can often be modeled by 'mathematical' fractals. Ideally the mathematical theory should then tell us more about the physical situations. One of the effective methods for description of objects with fractal properties of boundaries is the method of R-functions [10]. For the first time, it was applied for constructing equations of boundaries of the Sierpinski carpet and gasket (Fig. 2).

So, last years of the last century were marked by intensive investigation in fractal geometry. It should be mentioned that fractals appeared more than one hundred years ago were met with caution as it was also many times in the history of other new mathematical ideas. The report consists of some parts. First four of them are devoted to the foundation of measure theory, measure of Hausdorff-Besicovitch [1-4], fractal nowhere differentiable functions constructed by Boltzono, Besicovitch, and some AF possessing fractal properties. The effectiveness of application of both classical fractal functions and new atomic-fractal functions [5, 9] in problems of antenna synthesis is shown in the last part by means of the numerical experiment.

2 ATOMIC AND ATOMIC-FRACTAL FUNCTIONS

By definition, AF are the compactly supported infinitely differentiable solutions of differential equations with a biased argument,

$$Lf(x) = \lambda \sum_{k=1}^M c(k) f(ax - b(k)), |a| > 1, \quad (1)$$

where L is a linear differential operator with constant coefficients. Main classes of AF, their properties and applications are described in [5-9]. Using the aforementioned results and taking into account ideas and results presented in [5-9], let us consider the construction of the new class of atomic-fractal functions (AFF). To understand the proposed approach we will describe its main stages. The operation of multiplying the distribution (for example, $up(x)$, $\pi_m(x)$) by a number or an ordinary function (in our case, the Boltzmann, Van-der-Waerden, Besicovitch, and Weierstrass-Mandelbrot functions) is well-known. Note that a multiplication of AF by the classic fractal function is a direct product of two or more functions. This implies the following statement.

Statement 1. Let R^n and R^m be two Euclidean spaces of dimensions n and m respectively, and $x \equiv (x_1, x_2, \dots, x_n)$ and $y \equiv (y_1, y_2, \dots, y_m) \in R^m$ be the points in these spaces. Then the Cartesian product of these spaces $R^n \times R^m = R^{n+m}$ is a new Euclidean space of dimension $n + m$. The pairs $(x, y) = (x_1, x_2, \dots, x_n, y_1, y_2, \dots, y_m)$ are the points of these spaces, and coordinates are written in the proper order.

Statement 2. Let $f(x)$ and $g(y)$ be two numerical functions, and $x \in R^n$, $y \in R^m$. By definition, the function

$$u(x, y) = f(x) \times g(y) = f(x) \cdot g(y), \quad (2)$$

defined on R^{n+m} , is called the direct product of functions $f(x)$ and $g(y)$.

Therefore, the direct product of two functions coincides with an ordinary product, and is commutative, associative, and distributive with respect to the sum of functions defined on the same space. Note that if, particularly, functions $f(x)$ and $g(y)$ are locally integrable from R^n into R^m , then their direct product $u(x, y)$ is a function that is locally integrable on R^{n+m} . Taking into account the statements 1 and 2 (the strictly justification demands a separate investigation), we constructed AF multiplied by classical fractal functions [9].

3 SYNTHESIS OF ATOMIC-FRACTAL RADIATION PATTERNS

Unlike the traditional techniques [4, 9], when smooth antenna RP are synthesized, the fractal synthesis is based on the idea of realization of radiation characteristics with a repeating structure in arbitrary scales. Such an approach allows the new regimes of operating to be constructed in fractal problems of antenna

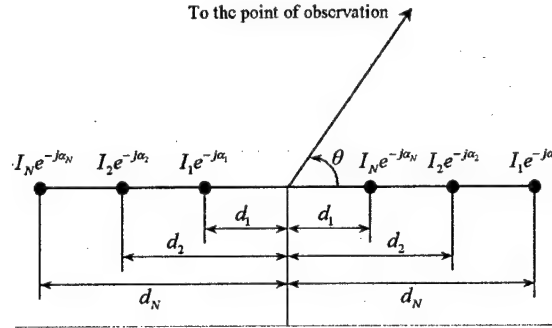


Fig. 3. The linear antenna array with $2N$ equally-spaced elements

synthesis [4-9]. A family of functions, called the generalized Weierstrass functions [2-5] are known to play a pivotal role in the theory of fractal radiation pattern synthesis. These functions are everywhere continuous but nowhere differentiable and exhibit fractal behavior at all scales. This class of functions can be represented by

$$f(x) = \sum_{n=1}^{\infty} \eta^{(D-2)n} g(\eta^n x), \quad (3)$$

where $1 < D < 2$, g is a suitable bounded periodic function, and $\eta > 1$.

The element spacing provides a third variable, in addition to the amplitude and phase of the array excitation currents, with which we can control the radiation pattern. The array factor for the nonuniformly but symmetrically spaced linear array of $2N$ elements illustrated in Fig. 3 may be expressed in the form

$$f(\theta) = 2 \sum_{n=1}^N I_n \cos(k d_n \cos \theta + \alpha_n). \quad (4)$$

Here, $k = 2\pi/\lambda$, I_n and α_n are amplitude and phase excitations, respectively, d_n represents the array element locations. Suppose the factor of an array with infinite number of elements to be expressed by the generalized Weierstrass function (3) with cosine function g and random phase α_n as

$$f(u) = 2 \sum_{n=1}^{\infty} \eta^{(D-2)n} \cos(a\eta^n u + \alpha_n), \quad (5)$$

where a is a constant. The current amplitude and element location satisfy the following conditions:

$$I_n = \eta^{(D-2)n}, \quad k d_n = a\eta^n, \quad (6)$$

where $u = \cos \theta$. The fractal RP defined by (5) possesses the self-similarity at the infinite range of scales. In practice, physically realizable arrays consist of a finite number of elements, i.e., here, we have a truncated series

$$f_N(u) = 2 \sum_{n=1}^N \eta^{(D-2)n} \cos(a\eta^n u + \alpha_n). \quad (7)$$

Expression (7) represents the array factor for a non-uniform linear array of $2N$ elements with current amplitudes and phases given by (5). Thus, in this case the Weierstrass partial sum (7) may be classified as band-limited since the resulting RP only exhibits frac-

tal behavior over a finite range of scales with lower bound $2\pi/a\eta^N$. The range of scales may be controlled by the number of elements N in the array. That is, the addition of two or more elements to the array has the effect of enhancing the fine structure in the RP. The maximum value (7) for angle θ_0 is

$$f_N(u_0) = 2 \sum_{n=1}^N \eta^{(D-2)n}, \quad (8)$$

and is determined by the choice of the excitation current phase $\alpha_n = -a\eta^n u_0$ for $u_0 = \cos \theta_0$. Series (8) represents a geometric progression, therefore,

$$f_N(u_0) = 2\eta^{(D-2)} \left[\frac{1 - \eta^{(D-2)N}}{1 - \eta^{(D-2)}} \right], \quad (9)$$

and a normalized form of the Weierstrass array factor can be obtained by dividing (13) by (15) that yields

$$g_N(u) = \left[\frac{1 - \eta^{(D-2)N}}{1 - \eta^{(D-2)}} \right] \sum_{n=1}^N i_n \cos(a\eta^n u + \alpha_n), \quad (10)$$

where the normalized excitation current amplitude is

$$i_n = \eta^{(D-2)(n-1)}. \quad (11)$$

Comparing (6) and (11), we can see that the fractal dimension of the RP can be controlled by the array element current distribution. The distance between any two consecutive array elements is given by

$$d_{n+1} - d_n = \left[\frac{a(\eta - 1)\eta^n}{2\pi} \right] \lambda, \quad n = 1, 2, \dots, N-1. \quad (12)$$

Since $\eta > 1$, it follows that $\eta^n > \eta$ for $n > 1$. Therefore,

$$d_{n+1} - d_n > d_2 - d_1, \quad n = 2, 3, \dots, N-1. \quad (13)$$

Let τ be a constraint which is imposed on the minimum separation between any two consecutive elements of the array. There are two possible cases satisfying the given condition,

$$\begin{aligned} d_2 - d_1 &= \tau & \text{and} & \quad d_1 \geq \tau/2 \quad (\text{case 1}), \\ d_1 &= \tau/2 & \text{and} & \quad d_2 - d_1 \geq \tau \quad (\text{case 2}). \end{aligned} \quad (14)$$

From (13) it follows that if (14) is satisfied, then the spacing between all other pairs of consecutive array elements will automatically satisfy the minimum separation criterion τ . An expression for a as a function of τ and η can be derived by solving (6) and (14). The result is

$$a = \frac{k\tau}{\eta(\eta - 1)}, \quad 1 < \eta \leq 3, \quad a = \frac{k\tau}{2\eta}, \quad \eta \geq 3. \quad (15)$$

Note that the parameter η governs the convergence of the Weierstrass array factor. The closer η is to one, the slower the array factor will converge and the more elements will be required in the array. At the same time, the spacing between consecutive array elements is decreasing as η approaches unity. On the other hand, it should be noted here that amplitudes I_n and phases α_n of the excitation current, as well as spacings d_n between elements may all be obtained by an iterative procedure

$$\begin{aligned} I_n &= \eta^{(D-2)} I_{n-1}, & I_1 &= \eta^{(D-2)}, \\ \alpha_n &= \eta \alpha_{n-1}, & \alpha_1 &= -a \eta u_0, \\ d_n &= \eta d_{n-1}, & d_1 &= a \eta / k, \end{aligned} \quad (16)$$

where $n = 2, 3, \dots, N$.

Further, we shall consider the Weierstrass array with $\tau = \lambda/2$, $\tau = \lambda/8$. Then, from (15) for $a = 1$ it follows that $\eta = 2.34$, and for $a = 2$ parameter $\eta = 1.3$. Values of η for other τ and a are presented in [9] and used in (15) for determining the spatial locations of array elements. Let us investigate now, the long radiating system L with continuous current $I(z)$. For a linear source of infinite length, characteristics of radiation $F(u)$ and current distribution $I(z)$ are connected by the pair of Fourier transforms

$$\begin{aligned} F(u) &= \int_{-\infty}^{\infty} I(s) \exp(i \cdot 2\pi u s) ds, \\ I(s) &= \int_{-\infty}^{\infty} F(u) \exp(-i \cdot 2\pi S u) du, \end{aligned} \quad (17)$$

where $s = z/\lambda$. Any fractal function is constructed by using recursive algorithms with an appropriate generating function. Suppose that the RP of a linear radiator of infinite length may be represented as a band-limited generalized Weierstrass function of the form

$$F(u) = \sum_{n=0}^{N-1} \eta^{(D-2)n} g(\eta^n u) \quad (18)$$

with generating function $g(u)$. Here, we assume that $g(u)$ is periodic and even, i.e., $g(u+2) = g(u)$, $g(-u) = g(u)$. In our case, the newly obtained family of generating functions has the following form:

1. $g_K(u) = \pi_m(u)$ is a compactly supported AFF (V.F. Kravchenko function),
2. $\tilde{g}_K(u) = \pi_m(u) \cdot \text{up}(x)$ is a V.F. Kravchenko function (the product of fractal function $\pi_m(u)$ with "mother" AF $\text{up}(x)$),
3. $g_{KB}(u)$ V.F. Kravchenko-Boltzono function (the product of "mother" AF $\text{up}(x)$ with the Boltzono function),
4. $g_V(u)$ is the classical Van-der-Waerden fractal function.

Any of these synthesized functions (1-4) can be expressed by series

$$g(u) = \frac{a_0}{2} + \sum_{m=1}^{\infty} a_m \cos(m\pi u), \quad (19)$$

whose Fourier coefficients are determined as

$$a_m = 2 \int_0^1 g(u) \cos(m\pi u) du.$$

Then, substituting (19) into (18), we get the expression for the RP in the form

$$\begin{aligned} F(u) &= \frac{a_0}{2} \frac{\eta^{(D-2)N} - 1}{\eta^{(D-2)} - 1} + \sum_{m=1}^{\infty} \sum_{n=0}^{N-1} a_m \eta^{(D-2)n} \times \\ &\times \cos(m\pi \eta^n u). \end{aligned} \quad (20)$$

In (20) one may substitute $u + 1$ for u . The result is

$$F(u) = \frac{a_0 \eta^{(D-2)N} - 1}{2 \eta^{(D-2)} - 1} + \sum_{m=1}^{\infty} a_m \left\{ \sum_{n=0}^{N-1} \eta^{(D-2)n} \cos(m \pi \eta^n (u + 1)) \right\} \quad (21)$$

$$a_m = 2 \int_0^1 g(u-1) \cos(m \pi u) du,$$

where $\eta > 1$ and $1 < D < 2$. Expression (21) represents the Fourier expansion of the fractal RP $F(u)$ with respect to the basis of AFF in combination with the band-limited cosine Weierstrass function. This representation is called the Fourier-Weierstrass expansion. The current distribution for a linear source, required for obtaining the given RP, using (17) is written as

$$I(s) = \int_{-1}^1 F(u) \exp(-i 2 \pi s u) du. \quad (22)$$

Here, $F(u)$ for AFF is found with the help of series (21). Thus, we have

$$I(s) = a_0 \frac{\eta^{(D-2)N} - 1}{\eta^{(D-2)} - 1} \text{sinc}(2 \pi s) + \sum_{m=1}^{\infty} \sum_{n=0}^{N-1} a_m \eta^{(D-2)n} \left\{ \exp(i m \pi \eta^n) \times \text{sinc}(2 \pi s - m \pi \eta^n) + \exp(-i m \pi \eta^n) \text{sinc}(2 \pi s + m \pi \eta^n) \right\}. \quad (23)$$

Expression (23) represents the required current distribution for an infinite line source. For a finite line source,

$$\tilde{I}(s) = I(s), |s| \leq \frac{L}{2\lambda}, \quad \tilde{I}(s) = 0, |s| > \frac{L}{2\lambda}. \quad (24)$$

Corresponding expressions for the synthesized AFF RP for linear radiating system L are expressed by using (17) and (24) as

$$\tilde{F}_{AFF}(u) = \frac{a_0 \eta^{(D-2)N} - 1}{2 \pi \eta^{(D-2)} - 1} \times \left\{ \text{Si} \left[\pi \frac{L}{\lambda} (1 + u) \right] + \text{Si} \left[\pi \frac{L}{\lambda} (1 - u) \right] \right\} + \frac{1}{2 \pi} \sum_{m=1}^{\infty} \sum_{n=0}^{N-1} a_m \eta^{(D-2)n} \times \left\{ \cos[m \pi \eta^n (u + 1)] S_{nm}(u) + \sin[m \pi \eta^n (u + 1)] C_{nm}(u) \right\}, \quad (25)$$

where functions $S_{nm}(u)$ are $C_{nm}(u)$ are defined in [9] and

$$\text{Si}(x) = \int_0^x \frac{\sin t}{t} dt, \quad \text{Ci}(x) = -\int_x^{\infty} \frac{\cos t}{t} dt = \gamma + \ln x + \int_0^1 \frac{\cos t - 1}{t} dt, \quad \gamma = 0.57721 \dots$$

It can easily be shown that $\lim_{L \rightarrow \infty} \tilde{F}(u) = F(u)$ and $\text{Si}(\infty) = \pi/2$, $\text{Ci}(\infty) = 0$, $S_{nm}(ki) = 2\pi$, $C_{nm}(\infty) = 0$.

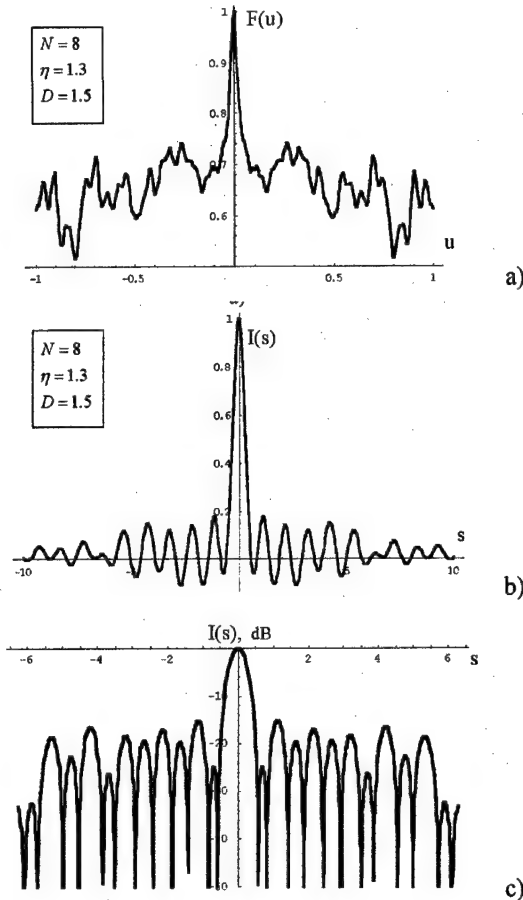


Fig. 4. The fractal array RP (a) and current distribution in ordinary (b) and logarithmic (c) scales. The Kravchenko generating function $g_K(u) = \pi_6(u)$.

To illustrate the synthesis procedure for the linear radiation source, we considered some examples with the generating distribution [9]. The directivity of the atomic-fractal array with generating functions of V.F. Kravchenko, V.F. Kravchenko-Boltzono, and Van-der-Waerden, are expressed by formulas (14) and (15),

$$G_{AFF}(u_0) = \frac{2 f_N^2(u_0)}{\int_{-1}^1 f_N^2(u) du}, \quad (26)$$

where $f_{N AFF}(u)$ is determined from (21), and coefficients a_m are those for the expansion of AFF with respect to the basis of band-limited cosine Weierstrass functions.

To illustrate the synthesis procedure for the linear radiation source, we considered some examples with the generating distribution.

Using the properties of the AFF generating functions (the V.F. Kravchenko, V.F. Kravchenko-Boltzono, and Van-der-Waerden functions), let us present examples of normalized RP for linear sources $F(u)$ with given D , η , and N shown in Fig. 4 (V.F. Kravchenko generating function $g_K(u)$).

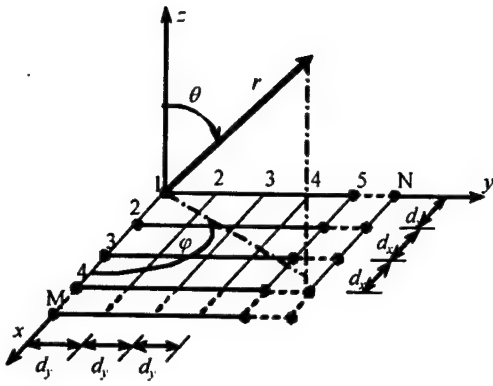


Fig. 5. Linear two-dimensional antenna array with $M \times N$ equally-spaced elements.

4. TWO-DIMENSIONAL FRACTAL ARRAYS

Consider the case of a two-dimensional flat symmetric phased antenna array with radiators equally-spaced at distances d_x along x axis and d_y along y axis. We shall study two-dimensional antenna arrays constructed on the base of combinations between atomic function and classical fractal functions. Such arrays belong to the class of non-equally-spaced arrays with non-uniform amplitude distribution. The expression for evaluating radiation pattern $F(\psi_x, \psi_y)$ has the following form [5, 9]:

$$F(\psi_x, \psi_y) = \begin{cases} I_{11} + 2 \sum_{m=2}^M (I_{m1} \cos(m\psi_x) + I_{1m} \cos(m\psi_y)) + \\ 4 \sum_{n=2}^M \sum_{m=2}^M I_{nm} \cos(m\psi_x) \cos(n\psi_y) \\ \text{for } (2M-1)^2 \text{ elements;} \\ 4 \sum_{n=1}^M \sum_{m=1}^M I_{nm} \cos((m-1/2)\psi_x) \times \\ \times \cos((n-1/2)\psi_y) \\ \text{for } (2M)^2 \text{ elements,} \end{cases}$$

where

$$\psi_x = kd_x (\sin \theta \cos \varphi - \sin \theta_0 \cos \varphi_0);$$

$$\psi_y = kd_y (\sin \theta \sin \varphi - \sin \theta_0 \sin \varphi_0).$$

Further we calculate a $(2M)^2$ -element array. Here, the latter expression will take the form

$$F(\psi_x, \psi_y) = 4 \sum_{n=1}^M \sum_{m=1}^M I_{nm} \cos((m-1/2)\psi_x) \times \cos((n-1/2)\psi_y),$$

with parameter I_{nm} defined by a form of a fractal function

$$I_{nm} = \begin{cases} 1, & B_{ni} < 0; \\ 0, & B_{ni} > 0. \end{cases}$$

Some antenna arrays (the Van-der-Waerden and Kravchenko-Van-der-Waerden functions f_{VDV} and

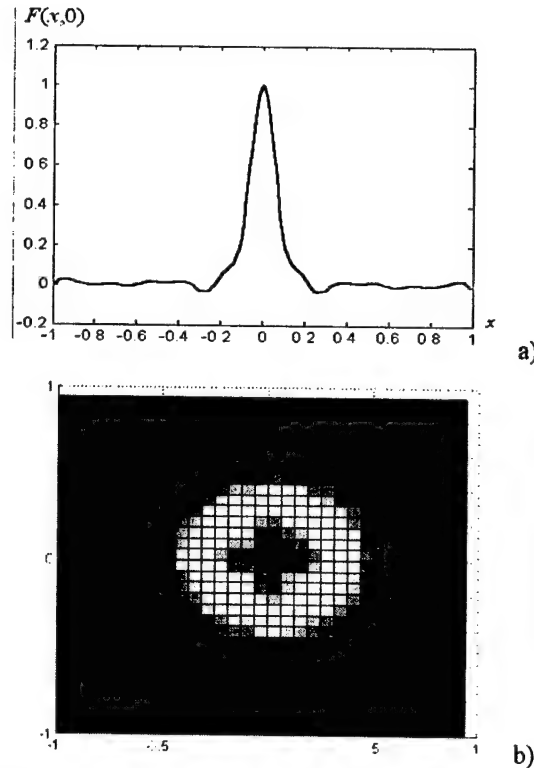


Fig. 6. Section of RP by OX plane (a) and current distribution for the function $f_{KVDV}(x, y)$

f_{KVDV3}) have narrow main lobe and low, for fractal antennas, sidelobe level (up to -30 dB).

Non-equally-spaced arrays, based for example on the Kravchenko-Besicovitch function, allow one to increase $d > \lambda/2$ at small values of the aperture mean-square width, i.e., additionally enlarge directivity without increasing number of elements. Such effect is useful for antennas with electrical scanning.

Table 1 represents the aperture mean-square width L_s , the ratio between first sidelobe level and maximum sidelobe level ξ , dB, and directivity for some two-dimensional distributions.

5. CONCLUSION

Fractal antenna engineering based on atomic-fractal functions represents a relatively new field of research that combines attributes of fractal geometry and theory of functions with antenna theory. Research in this area yielded a rich class of new designs for antenna elements as well as arrays. The overall objective of this report has been to develop the theoretical foundation required for analysis and design of fractal arrays. It has been demonstrated here that there are several desirable properties of atomic-fractal arrays, including frequency-independent multi-band behavior, schemes for realizing low-sidelobe design, systematic approaches to thinning, and the ability to develop rapid beam-forming algorithms by exploiting the recursive nature of fractals and properties of atomic functions.

Table 1.

Function	N	L_s	Directivity dB	ξ
$f_{KB}(x, y)$	32	2.0467	33.3642	-13.8
$f_{VDV}(x, y)$	32	1.6977	33.8851	-21.94 / -18.41
$f_{KVDV}(x, y)$	32	1.0722	30.9002	-29.7090
$f_{KVDV2}(x, y)$	64	1.7685	41.3202	-33.15 / -15.9
$f_{KVDV3}(x, y)$	64	1.7488	41.5400	-21.41 / -17.39
$f_{KBz2}(x, y)$	128	1.5975	46.4948	-12.58
$f_{Han}(x, y)$	128	2.1833	49.5705	-14.99
$f_{Han2}(x, y)$	128	1.4756	47.1863	-29.79

REFERENCES

1. Mandelbrot B. B., *The Fractal Geometry of Nature*, San Francisco: Freeman, 1982.
2. Falconer K. J., *Fractal Geometry. Mathematical Foundations and Applications*, New York: John Wiley and Sons, 1997.
3. Falconer K. J., *Techniques in Fractal Geometry*, New York: John Wiley and Sons, 1997.
4. Werner D. H., Haupt R. L., and Werner P. L., *Fractal Antenna Engineering: The Theory and Design of Fractal Antenna Arrays*, IEEE Antennas and Propagation Magazine, 1999, vol.41, No. 5, pp. 37-59.
5. Kravchenko V. F., *Lectures on the Theory of Atomic Functions and Their Some Applications*, Moscow: Radiotekhnika, 2003.
6. Kravchenko V. F. and Basarab M. A., *A New Class of Self-similar Antenna Arrays*, Doklady Physics, 2002, vol.47, No. 3, pp. 209-214.
7. Kravchenko V. F., *Application of the Boltzmann Function to the Theory of Fractal Antennas*, Doklady Physics, 2002, vol.66, No. 2, pp. 294-300.
8. Kravchenko V. F., *New Class of Atomic-Fractal Functions for Antenna Synthesis*, Doklady Physics, 2002, vol.47, No. 8, pp. 605-612.
9. Kravchenko V. F. and Masyuk V. M., *Modern methods of Approximation in Antenna Theory. Book 3: New Class of Fractal Functions in problems of Antenna analysis and Synthesis*, Moscow: Radiotekhnika, 2002.
10. Basarab M. A. and Kravchenko V. F., *The Construction of Equations for Boundaries of Fractal Domains with the Use of the R-function Method*, Telecommunications and Radio Engineering, 2001, vol.6, No. 6, pp. 31-37.

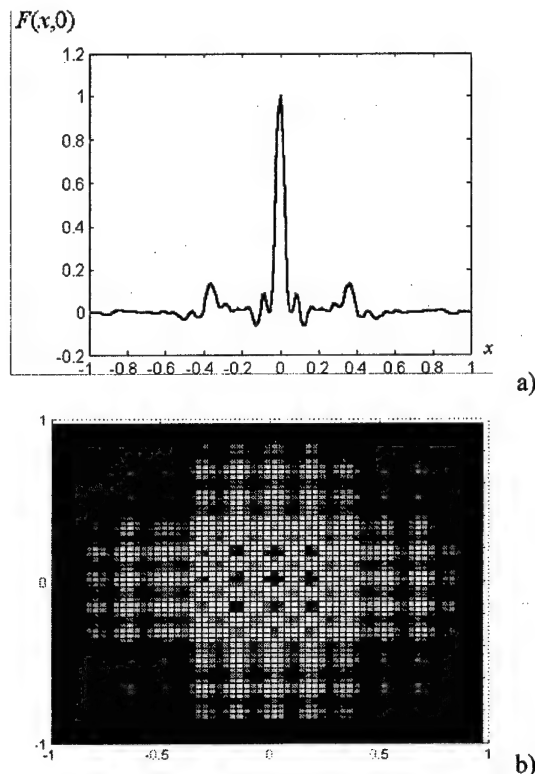


Fig. 7. Section of RP by OX plane (a) and current distribution for the function $f_{KVDV3}(x, y)$ (b)

R-FUNCTION THEORY IN PROBLEMS OF ELECTROMAGNETIC WAVE RADIATION FROM ARBITRARILY SHAPED WAVEGUIDES

Victor F. Kravchenko¹, Michael A. Basarab²

¹Institute of Radio Engineering and Electronics of the Russian Academy of Sciences,
11 Mokhovaya st., Center, GSP-3, Moscow, 103907, Russia
Phone: +7 (095) 203 47 93, Fax: +7 (095) 203 84 14, E-mail: <kravchenko_vf@fromru.com>

²Bauman Moscow State Technical University
5 Vtoraya Baumanskaya st., Moscow, 107005, Russia
Phone: +7 (095) 263 62 16, E-mail: <bmic70@pochtamt.ru>

Abstract

The problem of electromagnetic wave radiation from an arbitrarily shaped waveguide is studied. The solution process consists of two stages. At the first stage, the internal electromagnetic problem inside a waveguide is solved with the use of the R-function method and the field in the waveguide open end is determined. At the second stage, the fields in the far, intermediate, and near zones are evaluated using the Kirchhoff approximation.

Keywords: open-ended waveguide, Ritz-Galerkin method, R-function method, general solution structure, electromagnetic field radiation.

1. INTRODUCTION

An open end of a waveguide can be considered as a basic antenna structure [1]. The radiation from open rectangular and circular waveguides is well studied unlike the case of complex-shaped apertures. That is why it is of some interest to examine radiation characteristics of waveguides with arbitrary cross-sections (H-shaped, cross-shaped, etc.). This needs solving the Dirichlet (for longitudinal E-waves) and Neumann (for longitudinal H-waves) eigenvalue problems with corresponding boundary conditions that can be done with the help of numerical approaches only. The variational Ritz-Galerkin method with an appropriate set of basic functions is one of the most universal variational techniques for solving boundary-value problems. The main difficulty is to choose basic functions satisfying boundary conditions exactly. V.L. Rvachev [2] solved the inverse problem of analytical geometry and developed the R-function method (RFM) for constructing the implicit real-valued function of an arbitrarily-shaped domain boundary. Given such a function, we can obtain basic functions for the Ritz-Galerkin scheme, satisfying boundary conditions exactly.

Our algorithm consists of two stages. At the first stage, we evaluate eigenfunctions of TE- and TM-fields by solving the internal electrodynamic problem for a waveguide. To satisfy boundary conditions exactly, the RFM general solution structure is used. Given approximate eigenvectors and eigenvalues, at the second stage, we can evaluate external radiation from an open end of a waveguide and study its main radiation characteristics.

2. THE R-FUNCTION METHOD

Consider the domain $\Omega \subset R^2$ with piecewise smooth boundary $\partial\Omega$. The inverse problem of analytical geometry is in finding the function $\omega(x, y)$ positive inside Ω , negative outside Ω , and vanishing on $\partial\Omega$. So, $\omega(x, y) = 0$ implicitly determines the boundary equation. Let Ω be composed of original domains $\Omega_1, \dots, \Omega_m$ with the help of theoretical-set operations of intersection « \cap », join « \cup », and negation « \neg », i.e.,

$$\Omega = F(\{\Omega_1, \dots, \Omega_m\}, \{\cap, \cup, \neg\}). \quad (1)$$

Suppose original domains have simpler geometry than Ω , and equations of their boundaries $\omega_i(x, y) = 0$ ($i = 1, \dots, m$) are known. The R-function method [2] allows one to obtain the analytical expression $\omega(x, y) = 0$ for the domain Ω boundary on the base of its theoretical-set description. The function whose sign is totally determined by signs of its arguments is called the R-function corresponding to the partition of the real axis on intervals $(-\infty; 0)$ and $[0; \infty)$. Each R-function corresponds to an accompanying Boolean function with the same number of arguments. So, the function $z = f(x, y)$ can be called the R-function if a Boolean function F exists such that $S[z(x, y)] = F[S(x), S(y)]$, where the two-valued predicate $S(t) = 0$ for $t < 0$ and $S(t) = 1$ for $t \geq 0$. The most popular in practice system of R-functions is

$$\begin{aligned} x \wedge y &\equiv x + y - \sqrt{x^2 + y^2}, \\ x \vee y &\equiv x + y + \sqrt{x^2 + y^2}, \quad \neg x \equiv -x. \end{aligned} \quad (2)$$

Substituting in (1) Ω for $\omega(x, y)$, Ω_i for $\omega_i(x, y)$ ($i = 1, \dots, m$), and symbols $\{\cap, \cup, \neg\}$ for symbols of R-operations $\{\wedge_\alpha, \vee_\alpha, \neg\}$, we obtain the analytical expression determining the equation of boundary $\partial\Omega$,

$$\omega(x, y) = 0. \quad (3)$$

Equation of boundary (3) is called normalized if $\partial\omega/\partial\vec{n}|_{\partial\Omega} = -1$, where \vec{n} is the vector of the external normal to $\partial\Omega$. The normalized function $\tilde{\omega}(x, y)$ can be constructed on the base of an ordinary function $\omega(x, y)$ in the following way:

$$\tilde{\omega} \equiv \frac{\omega}{\sqrt{C\omega^2 + |\nabla\omega|^2}} = 0, \quad (4)$$

where $C = \text{const} > 0$. It is important to note that the function $\omega(x, y)$ constructed from normalized functions $\omega_i(x, y)$ with the help of R-operations of system (2) will also be normalized. This fact allows us to simplify the process of constructing the normalized equation of a boundary composed of segments of lines, circles and other algebraic curves of the second order whose normalized equations are well-known. Let us find the solution of an operator equation inside a bounded domain $\Omega \subset R^2$ with given boundary conditions on $\partial\Omega$. The general solution structure (GSS) of a boundary value problem is determined by the expression

$$u = F(\Phi, \omega, \omega_i, \varphi), \quad (5)$$

satisfying the boundary conditions exactly under an arbitrary choice of the undetermined component Φ . Here, F is the operator depending on the geometry of the domain Ω and parts of its boundary $\partial\Omega_i$, and φ is the known function entering the right part of the boundary condition. Thus, the GSS is a continuation of boundary conditions inside the domain. GSSs for the Dirichlet ($u|_{\partial\Omega} = \varphi(x, y)$) and the Neumann ($\partial u/\partial\vec{n}|_{\partial\Omega} = \varphi(x, y)$) boundary value problems are

$$u = \omega\Phi + \varphi$$

and

$$u = (1 - \omega D)\Phi - \omega\varphi,$$

respectively. Here, the operator

$$D \equiv \left(\frac{\partial\omega}{\partial x} \frac{\partial}{\partial x} + \frac{\partial\omega}{\partial y} \frac{\partial}{\partial y} \right) \Big|_{\partial\Omega} = \frac{\partial}{\partial\vec{n}} \Big|_{\partial\Omega},$$

and the equation $\omega(x, y) = 0$ for the Neumann condition must be normalized. Structures for boundary conditions of other types (3rd kind, for example) are also developed. The undetermined component Φ in (5) is approximated by a series

$$\Phi = \sum_{n=1}^M c_n \psi_n, \quad (6)$$

where $\psi_n(x, y)$ are elements of any full system of basic functions (see Appendix), such as algebraic or trigonometric polynomials, splines, atomic functions [3], etc., and c_n are unknown coefficients found with

the help of one of variational or projective methods.

R-functions also can be used for smoothing sharp corners of domains. The expression $f_1 \wedge_\alpha f_2 - \varepsilon$ is not the R-conjunction because there exist points inside the domain Ω such that $f_1 > 0$ and $f_2 > 0$ but $f_1 \wedge_\alpha f_2 - \varepsilon < 0$. At the same time, the function $f_1 \wedge_\alpha f_2 - \varepsilon$ is positive inside a subdomain Ω' of the domain Ω , i.e., on a set contained together with its closure in Ω ; if $\varepsilon < f_1 \wedge_\alpha f_2$ then the set $\partial\Omega'$ where $f_1 \wedge_\alpha f_2 - \varepsilon = 0$ is not empty. The function whose sign everywhere in R^2 differs from the sign of an R-function on a set Ω^* of sufficiently small measure $\mu\Omega^*$ is called the almost R-function. The almost R-conjunction $f_1 \wedge_\alpha f_2 - \varepsilon$ and almost R-disjunction $f_1 \vee_\alpha f_2 - \varepsilon$ are denoted by $f_1 \wedge_\alpha^\varepsilon f_2$ and $f_1 \vee_\alpha^\varepsilon f_2$, respectively. Here, a constant ε determines measure of the set Ω^* . The almost R-functions converge to corresponding R-functions as $\varepsilon \rightarrow 0$, i.e., $\lim_{\varepsilon \rightarrow 0} f_1 \wedge_\alpha^\varepsilon f_2 = f_1 \wedge_\alpha f_2$, $\lim_{\varepsilon \rightarrow 0} f_1 \vee_\alpha^\varepsilon f_2 = f_1 \vee_\alpha f_2$.

Instead of using the almost R-operations, one can construct an equation of a smoothed boundary directly as

$$\omega_\varepsilon(x, y) \equiv \omega(x, y) - \varepsilon = 0. \quad (7)$$

The latter function vanishes on the boundary of the domain $\Omega_\varepsilon \subset \Omega$ and positive inside it. The function ω_ε is smooth on $\partial\Omega_\varepsilon$. Analogously to (4), the normalized equation for the boundary of the domain Ω_ε has the form

$$\tilde{\omega} \equiv \frac{\omega - \varepsilon}{\sqrt{C(\omega - \varepsilon)^2 + |\nabla\omega|^2}} = 0. \quad (8)$$

As an example, let us smooth the corner formed by two lines intersecting under an arbitrary angle. Let the original domains be

$$\Omega_1 = (x \geq 0), \quad \Omega_2 = (y - kx \geq 0),$$

where $k > 0$. Applying the almost R-conjunction to normalized equations of these domains, we get a new domain with boundary described by the equation

$$y = k(x - \varepsilon) + \varepsilon(k + \sqrt{1 + k^2}) + \frac{\varepsilon^2}{2} \sqrt{1 + k^2} \frac{1}{x - \varepsilon}. \quad (9)$$

Equation (9) have asymptotes $x = \varepsilon$ and $y = kx + \varepsilon\sqrt{1 + k^2}$. Maximum curvature is achieved at the point $(x_0, (k + \sqrt{1 + k^2})x_0)$, where $x_0 = \varepsilon(1 + 1/\sqrt{2})$. Here, the minimum curvature radius is

$$\rho_{\min} = \varepsilon(k^2 - k\sqrt{1 + k^2} + 1)^{3/2} / \sqrt{1 + k^2}, \quad (10)$$

and the curvature center is situated at the point with coordinates

$$x_c = \varepsilon \left[1 + \frac{1}{\sqrt{2}} (1 + (\sqrt{k^2 + 1} - 1)^2) \right],$$

$$y_c = \varepsilon [k + (1 + \sqrt{2})\sqrt{k^2 + 1}].$$

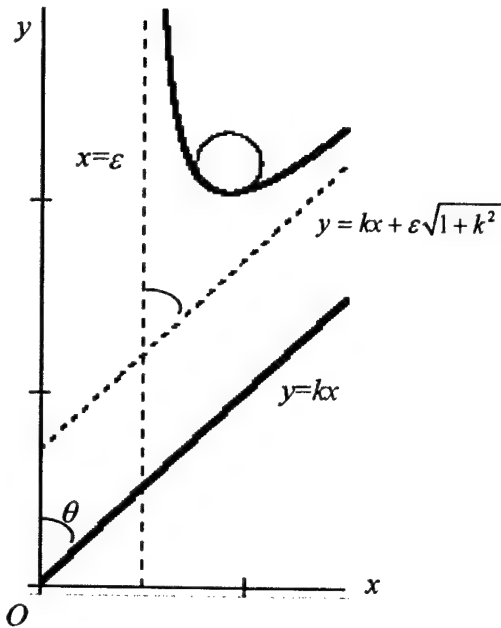


Fig. 1. Smoothing the angle between two lines

From (10) it follows that $\rho_{\min} \approx \varepsilon$ at $k \ll 1$ and $\rho_{\min} \approx \varepsilon/k$ at $k \gg 1$. Taking into account the fact that k is the cotangent of the angle θ between original lines, expression (10) can be rewritten as

$$\rho_{\min} = \varepsilon \sqrt{1 - \cos \theta} / (1 + \cos \theta). \quad (11)$$

Fig. 1 illustrates the aforementioned process of smoothing the angle between two intersecting lines.

3. RADIATION FROM A WAVEGUIDE

In the theory of regular waveguides the partial solutions to the homogeneous Maxwell equations are studied. They are obtained for the internal part of a waveguide under the condition of vanishing tangential electric field on waveguide walls. These solutions are separated into two main groups: H-waves or TE_{mn} -modes and E-waves or TM_{mn} -modes. In the first case, the longitudinal component of the magnetic field \tilde{H}_z is given and $\tilde{E}_z = 0$. Here, $\tilde{H}_z = H_z(x, y)e^{-i\gamma z}$; axes Ox and Oy are oriented in the plane of the waveguide open end (aperture) and axis Oz is perpendicular to this plane. The amplitude H_z satisfies the Helmholtz equation

$$\Delta H_z + g^2 H_z = 0 \quad (12)$$

with Neumann boundary condition on edges of the aperture $\partial\Omega$

$$\partial H_z / \partial \vec{\nu} |_{\partial\Omega} = 0. \quad (13)$$

In the second case, we know the longitudinal component of the electric field $\tilde{E}_z = E_z(x, y)e^{-i\gamma z}$, $\tilde{H}_z = 0$, and

$$\Delta E_z + g^2 E_z = 0, \quad (14)$$

$$E_z |_{\partial\Omega} = 0. \quad (15)$$

In (12), (14) $g = \sqrt{k^2 - \gamma^2}$ and $k = 2\pi/\lambda$. Represent the unknown solution u to problems (12)-(13) and (14)-(15) in the form of a corresponding GSS. Using the Ritz-Galerkin technique, we obtain the generalized eigenvalue problem with respect to the vector C of undetermined coefficients of expansion (6):

$$AC = -g^2 BC. \quad (16)$$

Solving (16), we obtain eigenvalues g_k ($k = 0, 1, \dots$) and corresponding eigenvectors

$$u_k = \begin{Bmatrix} \omega \\ 1 - \omega D \end{Bmatrix} \sum_{j=1}^M C_j^k \psi_j.$$

Other components of electrical and magnetic fields are found from the Maxwell equations. Now we can evaluate radiation from the aperture taking into account reflection by the waveguide aperture edges. The approximate expression for reflectance is

$$\Gamma = (k - \gamma)/(k + \gamma). \quad (17)$$

We must multiply the found electric and magnetic field components by $(1 + \Gamma)$ and $(1 - \Gamma)$, respectively. The tangential components of the radiated far-zone field are evaluated as

$$E_\theta(\theta, \varphi) = \frac{i}{4\pi} \int_{\Omega} (\omega \mu_0 H_s \cos \theta \sin \varphi + k E_s \sin \varphi) \times \exp[-ik(x \sin \theta \cos \varphi + y \sin \theta \sin \varphi)] dx dy, \quad (18)$$

$$E_\varphi(\theta, \varphi) = \frac{-i}{4\pi} \int_{\Omega} (\omega \mu_0 H_s \cos \varphi + k E_s \cos \theta \cos \varphi) \times \exp[-ik(x \sin \theta \cos \varphi + y \sin \theta \sin \varphi)] dx dy, \quad (19)$$

where θ, φ are the spherical coordinates; $\omega = ck$, c is the velocity of light; H_s and E_s are tangential field components in the aperture.

4. WAVEGUIDES WITH LOSSES.

IMPEDANCE BOUNDARY CONDITIONS

In the case of finite (but relatively large) conductance σ , the non-zero tangential component of the electric field \tilde{E}_τ presents on the boundary between two media. Here, the approximate impedance boundary conditions must be satisfied:

$$\tilde{E}_\tau = Z_S \tilde{H}_\tau, \quad (20)$$

where $Z_S = R_S - iX_S = (1 - i)\sqrt{\omega \mu_0 / (2\sigma)}$ is the surface impedance. Condition (20) for E- and H-waves takes the form

$$\left(\frac{\partial E_z}{\partial \vec{\nu}} - i\eta_E E_z \right) \Big|_{\partial\Omega} = 0 \quad (21)$$

and

$$\left(\frac{\partial H_z}{\partial \vec{\nu}} + i\eta_H H_z \right) \Big|_{\partial\Omega} = 0, \quad (22)$$

respectively, where $\eta_E = g^2 Z_0 / (k Z_S)$ and $\eta_H = g^2 Z_S / (k Z_0)$.

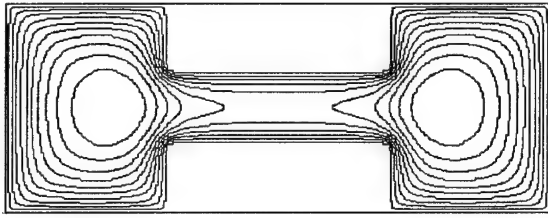


Fig. 2. Contour plot for the normalized equation (30)

Spectral problems with impedance (3rd kind) boundary conditions (21) and (22) are non-self-adjoint in $L_2(\Omega)$. For arbitrary domains, the existence of eigenvalues and eigenfunctions can be proven but, in general case, the systems of such functions may be incomplete in $L_2(\Omega)$. It can be shown that if $\sigma \gg 1$ then the non-self-adjoint operators can be considered as small regular perturbations of self-adjoint ones. Their spectrum is also discrete and has the only limit point at infinity, and their eigenfunctions form functional systems complete in $L_2(\Omega)$. The only difference is that eigenvalues of non-self-adjoint operators are shifted in the complex plane.

Under presence of attenuation in the waveguide walls, the longitudinal wave number is complex-valued, i.e.,

$$\gamma = \beta - i\alpha, \quad (23)$$

where α is the attenuation factor. The transversal wave number is also complex-valued and

$$g = g' + ig''. \quad (24)$$

Since conditions (21) and (22) depend on the unknown wave number g , the solution of a boundary value problem for the Helmholtz operator becomes more complicated. The simpler procedure is usually used in practice, when one assumes approximately that the tangential component of the magnetic vector \vec{H}_τ coincides with the analogous component evaluated on a perfectly conducting surface. For majority of metals the error caused by such assumption is very small. This approach is called the energetic method. It is correct when $\alpha \ll \beta$ in (23). An approximate expression for the attenuation factor has the form

$$\alpha = P_l / (2P), \quad (25)$$

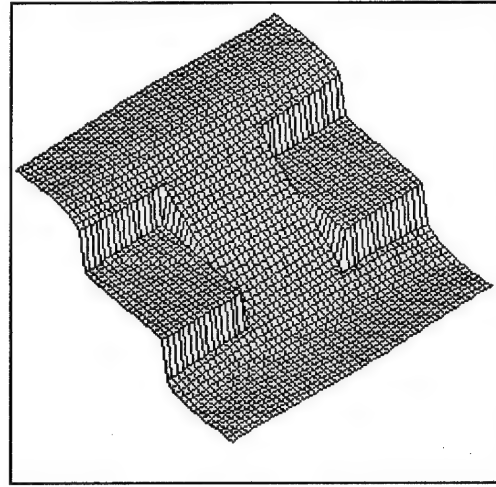
where

$$P_l = \frac{R_s}{2} \oint_{\partial\Omega} |\vec{H}_\tau| ds \quad (26)$$

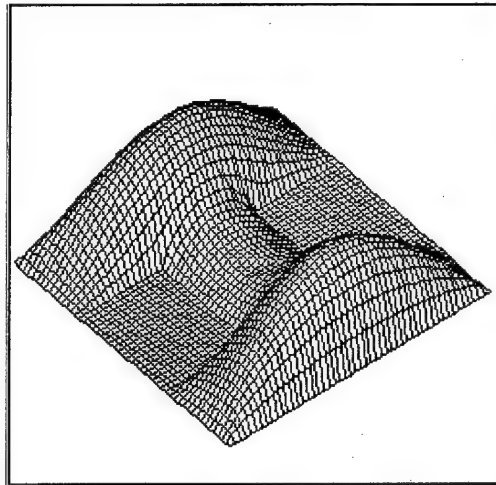
is the power of losses in metal per unit length of a waveguide and

$$P = \frac{\text{Re} Z_c}{2} \int_{\Omega} |\vec{H}_\perp|^2 dx dy \quad (27)$$

is total power carried over a waveguide. Here, \vec{H}_τ and \vec{H}_\perp are the vectors of tangential to the boundary and transversal components of the magnetic field, respectively. Expanded expressions for the attenuation factor



a)



b)

Fig. 3. Surface plots of the membrane functions for H_{10} (a) and E_{11} (b) modes

can be rewritten in the form

$$\alpha^E = \frac{R_s}{2Z_0} \frac{k}{\beta} \frac{\oint_{\partial\Omega} |\partial u^e / \partial \nu|^2 ds}{\int_{\Omega} |\nabla u^e|^2 dx dy} \quad (28)$$

for E- and TEM-waves and

$$\alpha^H = \frac{R_s}{2Z_0} \frac{\beta}{k} \left(\frac{\oint_{\partial\Omega} |\partial u^m / \partial \tau|^2 ds}{\int_{\Omega} |\nabla u^m|^2 dx dy} + \frac{g^2}{\beta^2} \frac{\oint_{\partial\Omega} |u^m|^2 ds}{\int_{\Omega} |\nabla u^m|^2 dx dy} \right) \quad (29)$$

for H-waves. Values β and g are found from solutions of problems (12), (13) or (14), (15). It should be mentioned that the attenuation factor sharply increases at frequencies close to critical ones. Here, the condition of applicability of the energetic method ($\alpha \ll \beta$) is not satisfied and expressions (28) and (29) have no sense.

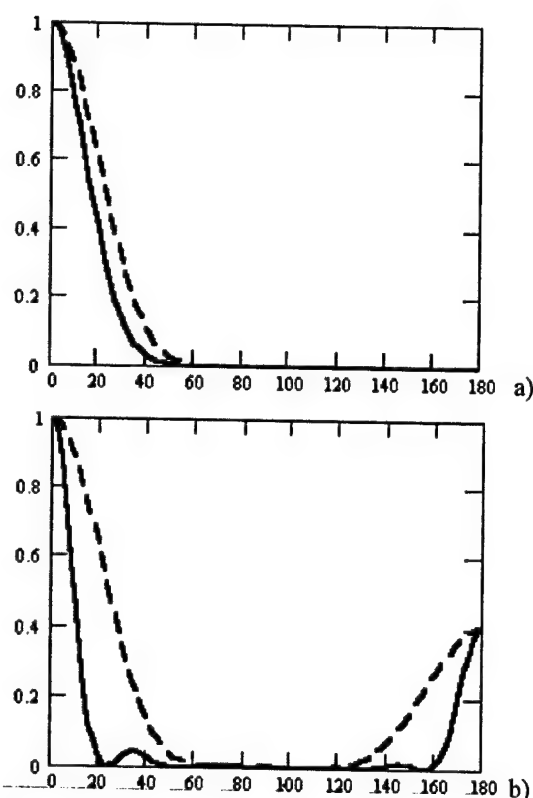


Fig. 4. Radiation patterns in H- (solid line) and E- (dashed line) planes for H_{10} (a) and E_{11} (b) modes

5. NUMERICAL EXAMPLE

Consider the symmetrical H-shaped waveguide with length $2l$, height $2h$, whose cross-connection has length $2a$ and height $2p$. The normalized equation of its boundary can be written as

$$\omega(x, y) = [(l^2 - x^2)/(2l) \wedge (h^2 - y^2)/2h] \wedge [- (a^2 - x^2)/2a \vee (p^2 - y^2)/2p]. \quad (30)$$

Fig. 2 demonstrates the contour plot of the function $z = \omega(x, y)$. First, we solve problems (12)-(13) and (14)-(15) by the R-function method to evaluate TE- and TM- waves in the waveguide. The set of trigonometric polynomials is used in the capacity of basic functions $\{\psi_j\}$. The H-shaped waveguide has parameters $l = 11.5$ mm, $h = 5$ mm, $a = 4.6$ mm, and $p = 1.81$ mm. Calculated critical wavelengths are $\lambda(H_{10}) = 71.353$ mm and $\lambda(E_{11}) = 11.319$ mm. Fig. 3a,b shows surface plots of the membrane functions for H_{10} and E_{11} modes, respectively. These results are in good agreement with those obtained experimentally. Fig. 4a,b illustrates radiation patterns for H_{10} and E_{11} modes, respectively, calculated by formulas (18)-(19).

Table 1. The polynomial function set for $L = 3$

i					
3	y^3				
2	y^2	xy^2			
1	y	xy	x^2y		
0	1	x	x^2	x^3	
	0	1	2	3	j

6. CONCLUSION

Results of numerical experiments performed for different types of waveguides with complex-shaped cross-sections proved the efficiency of the new method in comparison with other numerical and numerical-analytical techniques.

REFERENCES

1. Collin, R.E., Antennas and Radiowave Propagation, New York, McGraw-Hill, 1985.
2. Rvachev, V.L., The R-Function Theory and Its Some Applications, Kiev, Naukova Dumka, 1982.
3. Kravchenko, V.F., Lectures on the Theory of Atomic Functions and Their Some Applications, Moscow: Radiotekhnika, 2003.

APPENDIX

Application of multidimensional polynomials in practice yields some computational difficulties connected with necessity of their ordering. Consider an algebraic polynomial basis $\{\psi_k\} = \{x^i y^j\}$, $i, j \geq 0$, $i + j \leq L$, where L is the degree of a polynomial space. Such a set for $L \leq 3$ is shown in Table 1.

It is naturally to introduce the ordering of the sequence $\{x^i y^j\}$ terms along diagonals of the table, along which $i + j = \text{const}$, i.e.,

$$1, x, y, x^2, xy, y^2, x^3, x^2y, xy^2, y^3, \dots$$

(Here, the ordering with priority with respect to x variable is used). With this ordering it is possible to enlarge the degree of a given space by 1 by simply labeling the diagonal of terms of degree $L + 1$ with the next $L + 2$ integers. This procedure does not upset the previous ordering. Thus, the number of any element (the ordering function) of the sequence $\{\psi_k\}_{k=0}^K$ is expressed via indexes i and j in the following way:

$$k(i, j) = (i + j)(i + j + 1)/2 + j, \quad (A1)$$

and $K = (L^2 + 3L)/2$.

Consider the inverse problem of finding indexes i and j by known integer k . The commonly used approach is in organizing the loop with respect to i and

Table 2. The $k \leftrightarrow (i, j)$ mapping for $L = 2$

k	0	1	2	3	4	5
(i, j)	(0, 0)	(0, 1)	(1, 0)	(0, 2)	(1, 1)	(2, 0)

j where at each step condition (A1) is checked. Another variant is to store a matrix determining a mapping from a linear ordering variable k into the set of ordered pairs (i, j) as given by (A1). For example, the mapping for $L = 2$ can be constructed simply by inspection of Table 1 (see Table 2).

For large values of L such approaches are not convenient. The analytical relations between k and pairs (i, j) , i.e., the inverse analog of formula (A1), can be established. The proposed method consists of three stages:

- i) finding the diagonal number: $l = i + j$;
- ii) finding the index j : $j = k - l(l + 1)/2$;
- iii) finding the index i : $i = l - j$.

The latter two stages are obvious. It can be shown that

$$(l^2 + l - 2)/2 = [(l - 1)^2 + 3(l - 1)]/2 < k \leq (l^2 + 3l)/2$$

Taking into account that $l \geq 0$, after solving this system of inequalities, we get

$$(\sqrt{9 + 8k} - 3)/2 \leq l < (\sqrt{9 + 8k} - 1)/2$$

or, because l is integer,

$$l = \lceil (\sqrt{9 + 8k} - 3)/2 \rceil, \quad (\text{A2})$$

where $\lceil p \rceil$ means "the smallest integer greater than p ". Analogously, using the evident inequalities

$$(l^2 + l)/2 \leq k < (l + 1)(l + 2)/2,$$

we obtain another estimate for l :

$$(\sqrt{1 + 8k} - 3)/2 < l \leq (\sqrt{1 + 8k} - 1)/2,$$

i.e.,

$$l = \lfloor (\sqrt{1 + 8k} - 1)/2 \rfloor, \quad (\text{A3})$$

where we use $\lfloor p \rfloor$ to mean "the greatest integer less than p ". One can establish more general expressions for l :

$$l = \lceil (\sqrt{p + 8k} - 3)/2 \rceil \text{ if } (1 < p \leq 9)$$

and

$$l = \lfloor (\sqrt{p + 8k} - 1)/2 \rfloor \text{ if } (1 \leq p < 9).$$

SOLVING AN ARBITRARILY SHAPED FLAT RADIATOR SYNTHESIS PROBLEM BY THE R-FUNCTION METHOD

Michael A. Basarab

Bauman Moscow State Technical University,
5 Vtoraya Baumanskaya st., Moscow, 107005, Russia
Phone: +7 (095) 263 62 16, E-mail: <bmic70@pochtamt.ru>

Abstract

A numerical method for solution of the problem of a planar radiator synthesis is proposed. The specific property of the problem is in the requirements posed on the aperture field which must satisfy boundary conditions so that equivalent electrical and magnetic currents in the aperture do not generate pointwise or linear charges.

Keywords: planar radiator, radiation conditions, method of moments, R-function method.

1. STATEMENT OF THE PROBLEM

As is known [1], the main equation of the problem of a planar radiator synthesis has the following form:

$$\mathbf{E} = i \frac{k}{2\pi} \frac{e^{-ikr}}{r} [\mathbf{j}_r [\mathbf{PN}]], \quad (1)$$

$$\mathbf{N} = \int_S \mathbf{F} e^{ik \sin \theta (x \cos \psi + y \sin \psi)} dx dy, \quad (2)$$

$$\mathbf{P} = \mathbf{n} - \frac{1}{a} \sqrt{\frac{\mu}{\epsilon}} \mathbf{j}_r, \quad (3)$$

where S is the aperture surface; r is the distance between the radiator and an observation point; $\mathbf{j}_r, \psi, \theta$ are the unit vector and coordinate angles of an observation point; \mathbf{n} is the unity normal to the aperture; a is the coefficient proportional to the wave impedance; μ and ϵ are the magnetic and dielectric constants; $k = 2\pi/\lambda$ is the wave number, λ is the wavelength; \mathbf{F} is the component of the electric field, tangential to the aperture plane, or the aperture current vector; x and y are coordinates of a point on the aperture. The factor $i \frac{k}{2\pi} \frac{e^{-ikr}}{r}$

is not essential that is why we omit it. Denote the expression in square brackets (1), which is the RP of a flat aperture, by \mathbf{D} . Introducing the far-zone coordinate system with orts $\mathbf{q}_1, \mathbf{q}_2, \mathbf{q}_3$, connected with orts of the spherical coordinate system $\mathbf{j}_r, \mathbf{j}_\theta, \mathbf{j}_\psi$, with formulas

$$\begin{aligned} \mathbf{q}_1 &= \mathbf{j}_\theta \cos \psi - \mathbf{j}_\psi \sin \psi, \\ \mathbf{q}_2 &= \mathbf{j}_\theta \sin \psi + \mathbf{j}_\psi \cos \psi, \\ \mathbf{q}_3 &= \mathbf{j}_r, \end{aligned} \quad (4)$$

we obtain the following expression for the RP:

$$\mathbf{D} = (1 + \cos \theta) (N_x \mathbf{q}_1 + N_y \mathbf{q}_2). \quad (5)$$

Assume for simplicity that $a = \sqrt{\mu/\epsilon}$. Thus, the problem of a planar antenna synthesis with arbitrary polarization is reduced to two independent simpler problems of synthesis of planar systems with fields linearly polarized both in the aperture (with respect to $\mathbf{j}_x, \mathbf{j}_y$) and in the far zone (with respect to $\mathbf{q}_1, \mathbf{q}_2$). Represent a RP as a function of angles α and β between an observation point direction and planes xz and yz , respectively:

$$\sin \alpha = \sin \theta \cos \psi, \quad \sin \beta = \sin \theta \sin \psi. \quad (6)$$

Then

$$\begin{aligned} N_x(\alpha, \beta) &= \int_S F_x(x, y) e^{ik(x \sin \alpha + y \sin \beta)} dx dy, \\ N_y(\alpha, \beta) &= \int_S F_y(x, y) e^{ik(x \sin \alpha + y \sin \beta)} dx dy. \end{aligned} \quad (7)$$

Substituting variables by the formulas

$$\begin{aligned} \xi &= \frac{L}{\lambda} \sin \alpha, \quad \eta = \frac{L}{\lambda} \sin \beta, \quad u = \frac{2\pi x}{L}, \quad v = \frac{2\pi y}{L}, \\ R_{x,y} &= N_{x,y} L^2, \end{aligned} \quad (8)$$

we obtain the equation

$$\begin{aligned} R(\xi, \eta) &= \frac{1}{(2\pi)^2} \int_{\Omega} F(u, v) e^{i(u\xi + v\eta)} du dv, \\ \xi, \eta &\in [-L/\lambda, L/\lambda]. \end{aligned} \quad (9)$$

Here, $R(\xi, \eta)$ is the RP of a planar radiating system (polarization indexes x and y are omitted), L is the characteristic scale of the aperture, and Ω is the scaled domain S . To solve planar aperture RP synthesis problem (9) it is important to define conditions

when the RP can be reconstructed exactly. A RP $R(\xi, \eta)$ is realizable if it satisfies the conditions of the Plancherel-Polya theorem [2] which is a multidimensional generalization of the Wiener-Paley theorem. In this case, the surface current distribution is connected with the RP by the inverse Fourier transform

$$F(u, v) = \int_{R^2} R(\xi, \eta) e^{-i(u\xi + v\eta)} d\xi d\eta, \quad (10)$$

where $R(\xi, \eta) \in W_{\pi, \pi}$, i.e. belongs to the class of entire functions of exponential type with indicator π . The field in the aperture $F(u, v)$ must satisfy the radiation conditions [3], i.e. it is necessary that equivalent electrical and magnetic currents in the radiator aperture do not generate pointwise or linear charges because of their connection with infinitely large power. Such requirements are satisfied by an everywhere continuous function $F(u, v)$ vanishing together with its derivative on the aperture boundary $\partial\Omega$, i.e.

$$F(u, v)|_{\partial\Omega} = 0, \quad \partial F(u, v)/\partial \mathbf{n}|_{\partial\Omega} = 0. \quad (11)$$

Note that a piecewise constant aperture current distributions often used in synthesis problems do not satisfy conditions (11). In the case of rectangular apertures, the method based on atomic functions was proposed [3] to synthesize patterns by current distributions satisfying (11). In the general case of arbitrarily shaped apertures, the stated problem becomes to be more complicated.

2. THE METHOD FOR SOLUTION

The main idea is based on the following result of I. Yu. Kharrif [4, 5]. Let the function u together with its partial derivatives up to order $(r-1)$ vanish on the boundary $\partial\Omega \in C^\infty$ of the domain $\Omega \subset R^n$. If we have a function $\omega \in C^k(R^n)$ such that $\omega > 0$ in Ω , $\omega < 0$ outside Ω , $\omega = 0$ on $\partial\Omega$, $\text{grad } \omega \neq 0$ on $\partial\Omega$, and its partial derivatives of order k satisfy the Lipschitz condition ($\text{Lip}_M 1$) then a polynomial P_N of degree no greater than N with respect to each variable can be found such that

$$\|u - \omega^r P_N\|_{C^p(\Omega)} = O\left\{\frac{\tilde{\omega}(u, N^{-1})_{C^k(\Omega)}}{N^{k-p}}\right\}, \quad (12)$$

$$p = \overline{0, k},$$

where $\tilde{\omega}(u, \varepsilon)_{C^k(\Omega)}$, $\varepsilon > 0$, is the modulus of continuity of u in the space $C^k(\Omega)$. In particular, the system of functions $\omega^2 x^m y^n$, $m, n = 0, 1, 2, \dots$ is complete in the space of differentiable functions satisfying conditions (11). Undetermined coefficients of the polynomial P_N can be found with the help of one of variational methods, for example, by the method of moments (MoM) or the Galerkin method [4, 5]. It can easily be checked that if we approximate the exact current distribution F by an expression $\omega^2 P_N$, so that

$$\|F - \omega^2 P_N\| \leq \varepsilon, \quad (13)$$

then, according to (9), we obtain

$$\|R - \tilde{R}\| \leq S_\Omega \|F - \omega^2 P_N\| \leq \varepsilon S_\Omega, \quad (14)$$

where \tilde{R} is the approximate pattern and S_Ω is the square of Ω .

The function ω satisfying the aforementioned conditions can be constructed by the R-function method (RFM) [6] in the following way. Consider the domain $\Omega \subset R^2$ with piecewise smooth boundary $\partial\Omega$. The problem is in finding the function $\omega(x, y)$ positive inside Ω , negative outside Ω , and vanishing on $\partial\Omega$ so that $\omega(x, y) = 0$ implicitly determines the boundary equation. Let Ω be composed of original domains $\Omega_1, \dots, \Omega_m$ with the help of theoretical-set operations of intersection, join, and negation. Suppose the original domains have simpler geometry than Ω and equations of their boundaries $\omega_i(x, y) = 0$ ($i = 1, \dots, m$) are known. The RFM allows one to obtain an analytical expression $\omega(x, y) = 0$ for the domain Ω boundary on the base of its theoretical-set description and specific algebraic operations called the R-functions. The most popular in practice system of R-functions is

$$\begin{aligned} x \wedge y &\equiv x + y - \sqrt{x^2 + y^2}, \\ x \vee y &\equiv x + y + \sqrt{x^2 + y^2}, \quad -x \equiv -x. \end{aligned} \quad (15)$$

Having the function ω constructed, we can find the approximate current distribution \tilde{F} in the form

$$\tilde{F}(u, v) = \omega^2(u, v) \sum_{m+n=0}^N c_{k(m,n)} u^m v^n, \quad (16)$$

where $k(m, n) = (m+n)(m+n+1)/2 + n$ is the ordering function. Substituting (16) in (9), we get

$$\begin{aligned} \tilde{R}(\xi, \eta) &= \frac{1}{(2\pi)^2} \times \\ &\times \sum_{m+n=0}^N c_{k(m,n)} \int_{\Omega} \omega^2(u, v) u^m v^n e^{i(u\xi + v\eta)} du dv. \end{aligned} \quad (17)$$

Coefficients c_{mn} are found by any variant of the MoM (collocation, the least squares, Galerkin, etc.) method.

3. CONCLUSION

For the first time, a new method for an arbitrarily-shaped planar radiator RP synthesis based on the R-function theory is proposed and justified. The specific property of the considered problem of synthesis is in the presence of radiation conditions posed upon the aperture current distribution. The method proposed for a planar radiator RP synthesis allows obtaining RPs approximating the required RP more exactly in comparison with other known analogous methods. Numerical experiments prove efficiency of the novel approach in antenna synthesis.

REFERENCES

1. E. G. Zelkin and V. G. Sokolov, *Methods of Antenna Synthesis*. Moscow: Sov. radio, 1980. (in Russian)
2. B. M. Minkovich and V. P. Yakovlev, *The Theory of Antenna Synthesis*. Moscow: Sov. radio, 1969. (in Russian)
3. V. F. Kravchenko, *Lectures on the Theory of Atomic Functions and Their Some Applications*. Moscow: Radiotekhnika, 2003. (in Russian)
4. S. G. Mikhlin, *Variational Methods in Mathematical Physics*. New York: Macmillan, 1974.
5. M. H. Shultz, *Rayleigh-Ritz-Galerkin Methods for Multidimensional Problems*. SIAM J. Numer. Anal., 1969, vol.6, no.4, pp.523—538.
6. V. L. Rvachev, *The R-Function Theory and Its Some Applications*. Kiev: Naukova Dumka, 1982. (in Russian)

SYNTHESIS OF RESONANT ANTENNAS WITH SEMITRANSSPARENT EXTERNAL BOUNDARIES

M. I. Andriychuk, O. F. Zamorska

Pidstryhach Institute of Applied Problems of Mechanics and Mathematics, NASU
3 "B" Naukova St., 79601, Lviv, Ukraine
Phone: +380 322 651944, e-mail: <andr@iapmm.lviv.ua>

Abstract

The synthesis problem of resonant antennas according to the prescribed amplitude radiation pattern is considered. Variational statement of the synthesis problem is used. The functional, that allows one to minimize a mean-square deviation of the prescribed and received amplitude radiation patterns as well as taking into account the restrictions on a field in the given areas of a near zone is used as criterion of optimization. The appropriate nonlinear equations having the nonunique solution are obtained. The developed approach of solving these equations gives the possibility to determine the antenna parameters, which are more acceptable for practical use. Results of numerical modeling are presented.

Keywords: Resonant Antenna, Amplitude Radiation Pattern, Variational Approach, Constructive Synthesis

1. INTRODUCTION

Resonant antennas are new type of radiating systems, which allow one to form the radiation characteristics satisfying the widest spectrum of practical requirements. Such antennas are formed by several surfaces, one of which is semitransparent. Thus the additional opportunities arise in comparison with use of usual metal or metal-dielectric surfaces. Using the semitransparent surface properties we obtain one more parameter to change the structure of the electromagnetic field, including the radiation pattern (RP). Antennas with one semitransparent and other metal boundary are considered here.

Resonant antenna, as well as any other radiating system, should form the required radiation characteristic. We consider the RP as such a characteristic. The synthesis problem consists in determination of such parameters of antenna (the geometry of internal boundary and transparency of the external boundary), which form the amplitude RP close to the prescribed one. Use of the variational approach allows one to adjust both a degree of proximity of the amplitude RPs and to set restrictions on the field in the given areas of a near zone, i.e. to solve a problem of electromagnetic compatibility.

2. STATEMENT OF PROBLEM

The mathematical basis of solution of the excitation and synthesis problems for resonant antennas is the generalized method of eigenoscillations [1]. The solution of a direct problem is carried out using one of its variants, namely method of eigen transparency (ρ -method). The two-dimensional model of resonant

antennas (the case of E -polarization) is considered. Since statement of the synthesis problems according to the prescribed amplitude RP is used we should receive the explicit expression for RP as a result of solution of the direct problem at the given geometrical parameters of antenna.

2.1. DIRECT PROBLEM

The main (constructive) parameter of resonant antennas is the inphase field on external surface. This field can be considered as real because the constant phase shift of field does not change the amplitude RP. The direct problem is to determine the RP $f(\varphi)$ by the known field $v(S)$ on the external boundary S of the given form. Generally, the RP created by this field can be written as follows

$$f = \mathbf{A}v, \quad (1)$$

where \mathbf{A} is the integral (or matrix) operator with kernel that represents the asymptotic of function $\partial G / \partial N$, G is the Green function of external domain with condition $G|_S = 0$.

In the case of circular external boundary, the operator \mathbf{A} can be written in explicit form [2]

$$\mathbf{A}v = \int_0^{2\pi} K(\varphi, \varphi') v(\varphi') d\varphi', \quad (2)$$

where

$$K(\varphi, \varphi') = \sum_{n=0}^{\infty} \frac{i^n \cos n(\varphi - \varphi')}{(1 + \delta_{0n}) H_n^{(2)}(ka)}, \quad (3)$$

δ_{0n} is Kronecker symbol, $H_n^{(2)}(ka)$ is the Hankel function of the second kind, a is the circle radius.

In the case of resonant antenna with arbitrary external boundary, the method of auxiliary sources [3, 4, 5] is used for determination of the RP f by the field v . In this method the field $u(r, \varphi)$ outside of antenna is represented approximately as the finite sum

$$u(r, \varphi) = \sum_{n=1}^N a_n H_0^{(1)}(kR_n), \quad (4)$$

where $R_n = \sqrt{r^2 + r_n^2 - 2rr_n \cos(\varphi - \varphi_n)}$ is the distance from a point of observation up to n -th auxiliary source, r, φ and r_n, φ_n are the polar coordinates of a point of observation and n -th source accordingly.

If the field on the contour S is given by the values v_j in some system of N points, then we receive the system of linear equations

$$\sum_{n=1}^N a_n H_0^{(1)}(kR_{nj}) = v_j, \quad j = 1, 2, \dots, N \quad (5)$$

for determination of unknown factors a_n . Here R_{nj} is the distance between n -th source and j -th point on a contour S . The system (5) can be written down in matrix form

$$\mathbf{H}\mathbf{a} = \mathbf{v}, \quad (6)$$

where \mathbf{a} and \mathbf{v} are vectors with elements a_n and v_j ,

\mathbf{H} is matrix with elements $H_0^{(1)}(kR_{nj})$.

Directing to a limit (at $r \rightarrow \infty$) in the formula (4), we receive expression for the RP

$$f(\varphi) = \sqrt{\frac{2}{\pi}} e^{i\pi/4} \sum_{n=1}^N a_n e^{ikr_n \cos(\varphi - \varphi_n)} = \mathbf{H}_\infty \mathbf{a}. \quad (7)$$

Solving (6) relatively \mathbf{a} , we receive

$$\mathbf{a} = \mathbf{H}^{-1} \mathbf{v}. \quad (8)$$

Using (7) and (8), the explicit expression for the RP f by the factors a_n can be written in the form (1), where the operator \mathbf{A} represents a product of two matrixes

$$\mathbf{A} = \mathbf{H}_\infty \mathbf{H}^{-1}. \quad (9)$$

Thus the explicit expression for the operator \mathbf{A} is received. It allows one to calculate the RP f by the field v on the external boundary S .

2.2. INVERSE PROBLEM

Solving the inverse problem (synthesis problem), the field on external boundary of the antenna and transparency of this boundary, that form amplitude RP $|f(\varphi)|$ close to the prescribed amplitude RP $F(\varphi)$ are determined. Additionally, the restrictions on a field in some areas of a near zone may be prescribed. The following functional

$$\sigma = \int_0^{2\pi} p(\varphi) [F(\varphi) - |f(\varphi)|]^2 d\varphi + \sum_{i=1}^M p_i(S) [U_i(S) - |u_i(S)|]^2 dS + \alpha \int_0^{2\pi} v^2(\varphi) d\varphi \quad (10)$$

allows one to take into account these requirements. Here $U_i(S)$ are prescribed values of the amplitude of the field in the areas of restriction, $u_i(S)$ are the received values of the field. Functions $p(\varphi)$, $p_i(S)$ are the weight functions, allowing to adjust a degree of proximity of the given and received values of field, α is the parameter limiting norm of the field v . This limitation allows one to exclude the occurrence of the fast oscillated summands which influence little few on the RP.

3. METHOD OF SOLUTION

At the first stage of solution of the synthesis problem, the field v on external boundary S is determined from a condition of the functional (10) minimum. Minimization of functional can be carried out using the gradient methods, or by the solution of the appropriate Euler equation.

In the first case, the generalized gradient method [6]

$$v_{n+1} = \delta_n^{(1)} v_n + \delta_n^{(2)} z_n + \delta_n^{(3)} h_n \quad (11)$$

is used. Thus the gradient z of the functional (10) (in view of the requirement of reality of field) has form

$$z = \alpha v - \text{Re } \mathbf{A}^* [F \exp(i \arg f) - f] - \sum_{i=1}^M \text{Re } \mathbf{B}_i^* [U_i \exp(i \arg u_i) - u_i], \quad (12)$$

where \mathbf{A}^* and \mathbf{B}_i^* are the operators adjoined to \mathbf{A} and \mathbf{B}_i accordingly [2]. Each step of iterative process (11) reduces the functional σ value. Since σ is limited from below ($\sigma \geq 0$), the process (11) is convergent one.

In the second case, using a necessary condition of the functional extremum (equality to zero of its first variation or derivative Gateaux), we receive the Euler equation concerning the field v

$$\alpha v = \text{Re } \mathbf{A}^* [F \exp(i \arg f) - f] + \sum_{i=1}^M \text{Re } \mathbf{B}_i^* [U_i \exp(i \arg u_i) - u_i] \quad (13)$$

Equation (13) is the nonlinear integrated equation of the Hammerstein type. This equation can have the nonunique solution; the number of these solutions depends on the characteristic parameter k , which is contained in its kernel. In order to search the number of solutions and their branching it is more convenient to use the equation relatively the RP $f(\varphi)$

$$\begin{aligned} \alpha f + \text{Re } \mathbf{A} \mathbf{A}^* f + \sum_{i=1}^M \text{Re } \mathbf{B} \mathbf{B}_i^* u_i = \\ = \text{Re } \mathbf{A} \mathbf{A}^* [F \exp(i \arg f)] + \\ + \sum_{i=1}^M \text{Re } \mathbf{B} \mathbf{B}_i^* [U_i \exp(i \arg u_i)] \end{aligned} \quad (14)$$

In equation (14) nonlinear part is transferred to the right hand part. From such a form of writing, it is apparently that the method of successive approximations is convenient one for its solution. Setting the various types of initial approximations, we can receive different solutions of this equation.

At the second stage of solution of the synthesis problem (after determination of real field v on the boundary S), the transparency ρ of this boundary and the form of internal metal boundary S_0 are determined.

For the antenna with circular external boundary, the transparency distribution can be presented in the explicit form

$$\rho(\varphi) = \pi k v(\varphi) / (2 \sum_{n=0}^N \frac{a_n \cos n\varphi}{J_n^2(ka) + N_n^2(ka)}), \quad (15)$$

where J_n and N_n are the Bessel and Neuman functions.

In the case of antenna with arbitrary external boundary, similarly to [2], the distribution of transparency is determined by the formula

$$\rho(\varphi) = 1 / \left[\frac{\partial \psi(S(\varphi))}{\partial N} \right], \quad (16)$$

where $\frac{\partial \psi(S(\varphi))}{\partial N}$ is the growth rate of phase of the external field u while approaching to S normally, N is the external normal to S .

4. NUMERICAL RESULTS

The numerical calculations are carried out for the resonant antennas with the given external elliptic boundary. The prescribed amplitude radiation pattern is the following $F(\varphi) = \sin^8(\varphi/2)$. In Fig. 1, these results are presented for the antenna with parameters $kb = 15$ and different ka : $ka = 12.75, ka = 14.25$, where b and a are the big and small semiaxes of ellipse. For such antennas the level of side lobes is smaller than -20 dB, and distribution of transparency is smoother in the direction of main radiation (solid lines in Figs. 1a, 1b correspond to $ka = 12.75$, and the dashed ones to $ka = 14.25$). The external elliptic boundaries (dashed lines), the found form of internal metallic boundaries (solid lines), and internal contour of placement of the auxiliary sources (dash-and-dot lines) are shown in Figs. 1c, 1d.

The numerical results for solution of the synthesis problem with restrictions on the field in a near zone are given for the antenna with circular external boundary. The prescribed amplitude RP is the following $F(\varphi) = \sin^8(\varphi/2)$, $ka = 15$. Minimization of a field was carried out in two points $\varphi = \pi/2, 3\pi/2$ on the additional circle with radius $kb = 20$. These points were allocated in the second summand of the functional (10) using the weight function $p_1(\varphi) = \delta(\pi/2, 3\pi/2)$, $p(\varphi) \equiv 1, \alpha = 0.01$. In Fig. 2a, the prescribed F (fat solid line) and synthe-

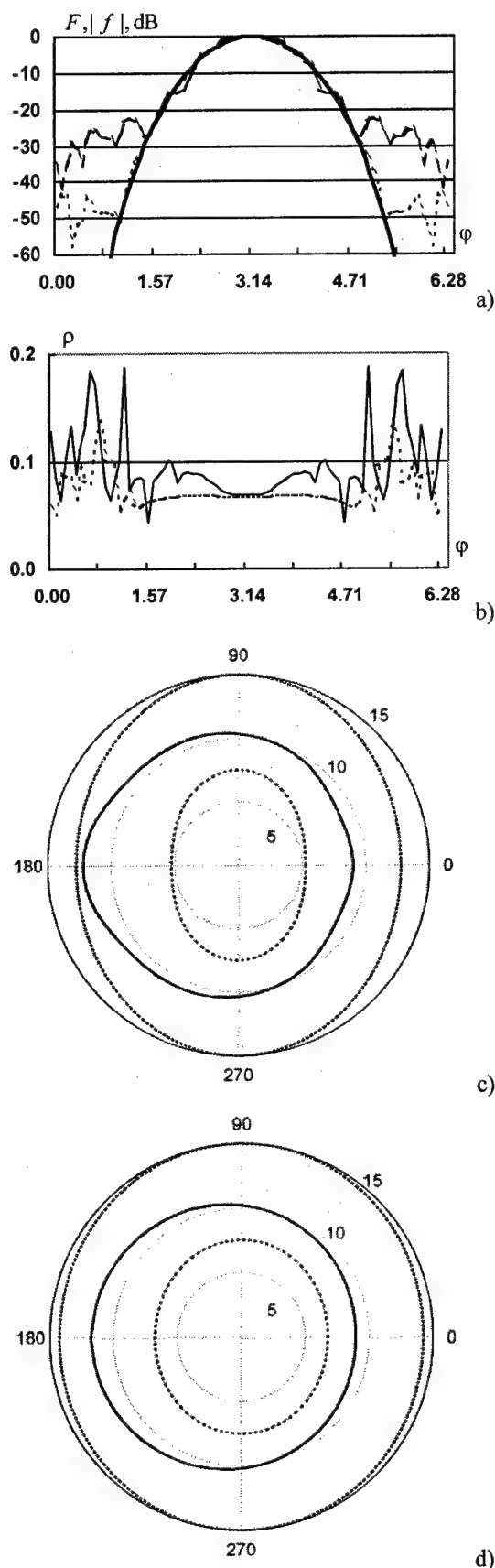
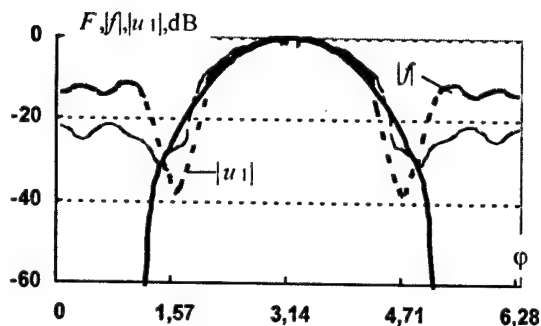
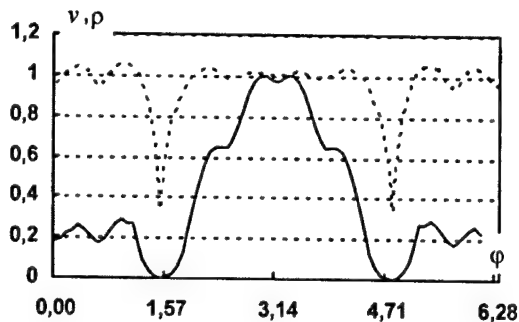


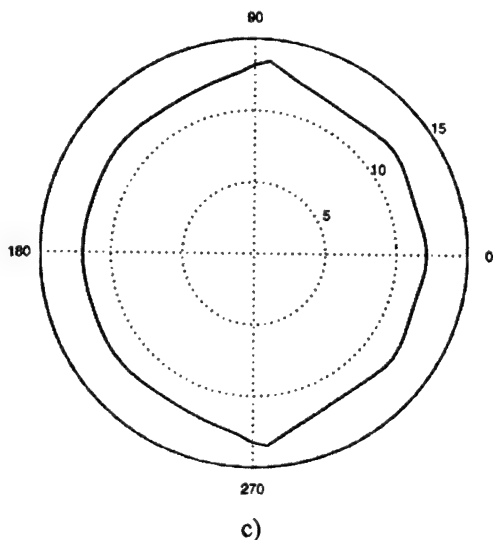
Fig. 1.



a)



b)



c)

Fig. 2.

sized $|f|$ (thin solid line) amplitude RP are shown. The amplitude $|u_1|$ of obtained field on the circle of restrictions is shown by dashed line.

It can be seen that the value of field in points of restrictions is reduced up to the level -37 dB. The syn-

thesized field v (solid line) and transparency ρ (dashed line) are presented in Fig. 2b.

The geometry of the antenna is shown in Fig. 2c. The external circular semitransparent boundary is designated by dashed line; the internal synthesized metallic boundary is designated by solid line.

5. CONCLUSION

The proposed approach for solving the synthesis problems of resonant antennas is highly universal, and it provides the possibility to synthesize antennas with the arbitrary form of external boundary. The calculation time of the RP of antenna is enough small that it is very important in the process of solution of the synthesis problem. For example, in the case of antenna with noncircular external boundary, for the effective solution of the synthesis problems it is enough to be limited by the number of auxiliary sources approximately equal to the electrophysical size of antenna (parameter kb).

The used variational statement of the synthesis problem allows one alongside with achievement of the best approximation to the prescribed amplitude RP to take into account restrictions on the field in the given points (areas) of a near zone.

REFERENCES

1. M. S. Agranovich, B. Z. Katsenelenbaum, A. N. Sivov, N. N. Voitovich, *Generalized Method of Eigenoscillations in Diffraction Theory*, Wiley-VCH, Berlin, 1999.
2. N. N. Voitovich, B. Z. Katsenelenbaum, E. N. Korshunova, and all, *Electrodynamics of antennas with semitransparent surfaces*, Nauka, Moscow, 1989. (in Russian).
3. V. D. Cupradze, "About Approximate Solution of Mathematical Physics Problem." *Uspekhi Mat. Nauk*, vol. 22, pp. 59—107, February 1967. (In Russian).
4. M. A. Alexidze, *Solution of boundary problems by decomposition on non-orthogonal functions*, Moscow, Nauka, 1978. (In Russian).
5. D. I. Kaklamani, H. T. Anastassiou, "Aspects of the Method of Auxiliary Sources (MAS) in Computational Electromagnetics." *IEEE Antennas & Propagation Magazine*, vol. 44, pp. 48-64, June 2002.
6. M. I. Andriychuk, N. N. Voitovich, P. A. Savenko, V. P. Tkachuk, *The antenna synthesis according to the amplitude radiation pattern. Numerical methods and algorithms*, Nauk. Dumka, Kiev, 1993. (in Russian).

THE USE OF ATOMIC FUNCTION FOR INNER PROBLEM SOLUTION FOR WIRE ANTENNAS

Yuri Y. Bobkov

Belorussian State University of Informatics and Radioelectronics
Minsk, Belarus
<bkyuri@mail.ru>

Abstract

The comparison of computing efficiency of primary atomic functions $Up(x)$ and piecewise sinusoidal functions for the inner problem solution of wire problem, used as the basis function, was executed. The ways to increase the computing efficiency were considered.

Keywords: antenna modelling, Method of Moment, basis function.

1. INTRODUCTION

The solution of integral or integro-differential equations is at the heart of the wire antenna analysis with the use of thin wire (axled) approximation. One of the equation of this type is the Poklington's equation. It is more universal with respect to the use of different basis function in case of their solution by the Moment Method (MoM). The selection of the kind of the basic function is important for MoM, as the speed and accuracy of calculation depend on this selection. The atomic function and piecewise sinusoidal functions have high approximating property and can be used as the basic function in MoM [2, 3]. This paper is devoted to comparison of the computing efficiency of MoM when using both primary atomic and piecewise sinusoidal functions as the basic functions.

2. USING RICHMOND'S EQUATION

The symmetrical half-wave vibrator was used as a test antenna in the numerical experiment, since the inner problem for this antenna obtained by other methods is well known.

It is known, that the Poklington's equation for rectilinear wire can be transformed to the Richmond's equation [2]:

$$\vec{E}_{ct} = \int_{-L/2}^{L/2} I(l_q) \frac{e^{-ikr}}{r^5} \times \times [(1 + ikr)(2r^2 - 3a^2) + k^2 a^2 r^2] dl_q \quad (1)$$

Replacing in (1) current $I(l_q)$ by the sum of the kind:

$$I(l_q) = \sum_{m=1}^{\infty} I_m(l_q) \quad (2)$$

where: $I_m(l_q)$ is the basic function: piecewise sinusoidal functions [2, p.21] or the basic function obtained on the basis of atomic function $up(x)$:

$$I_m(l_q) = \begin{cases} I_{m-1} Up\left(\frac{l_q - l_{m-1}}{dL}\right) + \\ + I_m Up\left(\frac{l_m - l_q}{dL}\right), l_{m-1} \leq l_q \leq l_m, \\ 0 \quad \text{otherwise.} \end{cases} \quad (3)$$

and combining additives with equal coefficients $I_m(l_q)$, the expressions for coefficients of generalised impedance matrix (CGIM) are result. Introducing the weight (test) functions, as MoM contemplate, the equation (1) is reduced to the system of linear algebraic equations (SLAE). In the numerical experiments of the presented work the Dirac function was used as the weight function. The results of current distribution along half-wave vibrator having radius $a/\lambda = 0.005$ and 26 segments at the antenna (52 segments at the wavelength) with use of the piecewise sinusoidal basic functions (so-called Sin-D method, dotted line) and atomic basic functions (3) (so-called Up-D method, solid line) are illustrated in Fig. 1. The antenna feed-impedance with the current distribution equals $Z = 103.24 + 30.993i$ Ohm (Sin-D method) and $Z = 94.32 + 19.58i$ Ohm (Up-D method).

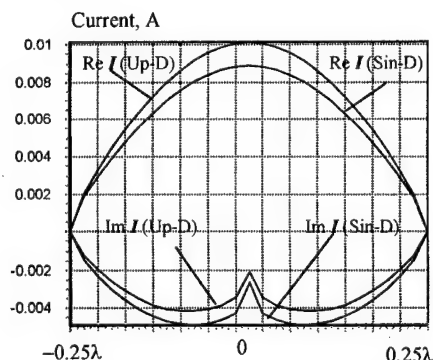


Fig. 1. The current distribution along half-wave vibrator

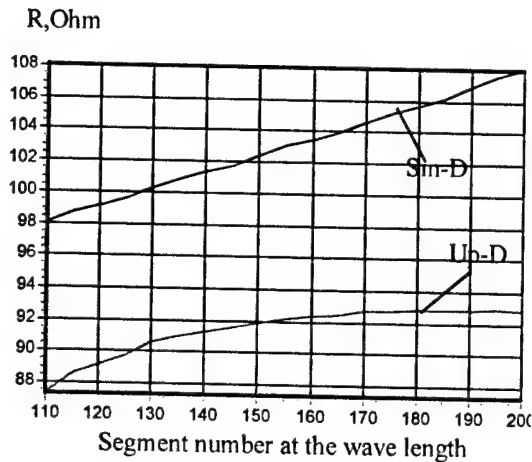


Fig. 2. The convergence of the real part of the antenna feed impedance, $a/\lambda = 0.005$

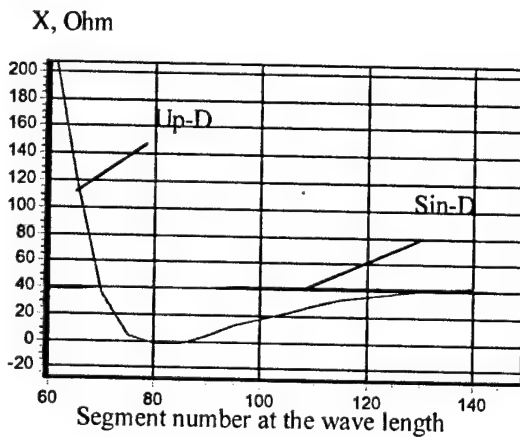


Fig. 3. The convergence of the imaginary part of the antenna feed impedance, $a/\lambda = 0.005$

Dependence of the real and imaginary parts of the antenna feed-impedance from segment number at the antenna, based on which the computing efficiency can be evaluated, is illustrated in Fig. 2 and 3.

As the results of numeric experiments prove and as Fig. 2 and 3 indicate, the atomic functions provide convergence of the real part of the antenna feed impedance at a smaller segment number than the piecewise sinusoidal functions. For the Sin-D method the convergence of the real part of the antenna feed impedance appears at a big number of segments (about 350). However, convergence for the imaginary part of the antenna feed-impedance in case of the Sin-D method appears early than in case of Up-D method.

It is necessary to draw attention to the fact that when solving the Richmond's equation the antenna impedance convergence with different ratio, of a/λ is observed in different segment number range. The calculation results are reviewed in Table 1.

The errors in determination of the SLAE elements are the cause for such a great limits scattering of the convergence limits.

Table 1.

a/λ	Range of impedance convergence, segments			
	Real impedance part		Imaginary impedance part	
	Sin-D	Up-D	Sin-D	Up-D
0.01	120-130	80-100	30-50	165-180
0.005	≈ 350	180-200	90-140	130-140
0.001	230-350	>400	150-350	>400

3 USING POKLINGTON'S EQUATION

Different results are observed if the Poklington's equation transformed to kind, in what the derivatives of the Green's function are absent under the radical because the great rounding error at the phase of their calculation. The transformation is achieved by integration part-by-part method of all the additives including derivatives of the Green's function.

Replacing the sought desired function by the sum of the basic functions with some coefficients and combining additions with same coefficients, the expressions for CGIM as the sum of similar-type integral are obtained:

$$A(l_q) = \int_a^b G(l_q, l_p) \cdot \left\{ f(l_q) + \frac{1}{k^2} \frac{\partial^2 f(l_q)}{(\partial l_q)^2} \right\} dl_q + \frac{1}{k^2} \left\{ \left(f(l_q) \frac{\partial G(l_q, l_p)}{\partial l_q} \right)_a^b - \left(\frac{\partial f(l_q)}{\partial l_q} G(l_q, l_p) \right)_a^b \right\} \quad (4)$$

where $f(l_q)$ is either the right or the left parts (the first or the second additional) of the basic function; for the first additional $a = l_m$ $b = l_{m+1}$; for the second additional $a = l_{m-1}$ $b = l_m$.

Taking into account the values of the functions and their derivatives at the segment ends l_{m-1} , l_m , l_{m+1} , the expressions for CGIM using the piecewise sinusoidal basic functions (Sin-D method) and atomic basic functions (Up-D method) are obtained:

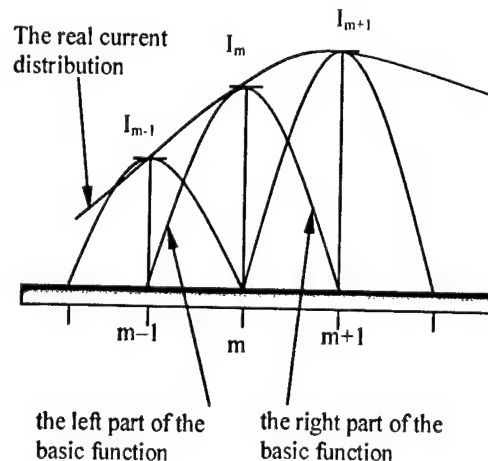


Fig. 4. To the explanatory of the formula (4)

$$K_m(l_n) = \frac{1}{k \sin(k\Delta L)} \left(G(l_{m-1}; l_n) + \right. \quad (5)$$

$$\left. + G(l_{m+1}; l_n) - 2G(l_m; l_n) \cos(k\Delta L) \right)$$

$$K_m(l_n) = \int_{l_{m-1}}^{l_m} G(l_q; l_n) \left(up \left(\frac{l_q - l_{m-1}}{\Delta L} \right) + \right. \quad (6)$$

$$\left. + up^{(2)} \left(\frac{l_q - l_{m-1}}{\Delta L} \right) \right) dl_q +$$

$$+ \int_{l_m}^{l_{m+1}} G(l_q; l_n) \left(up \left(\frac{l_m - l_q}{\Delta L} \right) + \right.$$

$$\left. + up^{(2)} \left(\frac{l_m - l_q}{\Delta L} \right) \right) dl_q$$

Comparing these expressions, it is possible to assert that the Sin-D method is more effective because of absence of the integration operations for calculation CGMI of congruent segments. The computing efficiency of the piecewise sinusoidal functions in this option of their application is illustrated in Fig. 5. In this figure the dependence of the real part of the antenna feed-impedance on the number of the segments at the antenna is given for $a/\lambda = 0,001$.

As it is apparent from figure, the convergence of the real part of impedance is already observed at 35 segments at the antenna (the real part of impedance is equal to $R = 73.1$ Ohm). Other calculations prove that the converging of the imaginary part of impedance is observed at 70 segments at the antenna (the imaginary part of impedance is equal to $X = 40.6$ Ohm); for steady convergence in field (coincidence of beam patterns) it is necessary 10 segments at antenna. The beam pattern $f(\theta)$ of the half wave vibrator calculated by the current distribution, obtained at solution the integral Poklington's equation by the use of the piecewise sinusoidal functions as the basis functions and the δ -functions as the weight (test) functions, is presented in Fig. 6. The beam pattern calculated by the analytic formula (7) that obtained by the sinusoidal current distribution is also illustrated in Fig. 6.

$$f(\theta) = \frac{\cos\left(\frac{\pi}{2} \cos \theta\right)}{\sin(\theta)} \quad (7)$$

Absence of the integration operation in the expression for CGIM (4) for congruent segments considerably increases the computational efficiency of MoM. Moreover, the use of the functions as the basis functions for the congruent wire systems, as consequence of the absence of the integration operation, makes possible to exactly solve the inner problem for the ratio of the wire diameter to the wavelength equalling 0.01–0.00001, by 120–150 segments at the wavelength. The real (R) and imaginary (X) parts of the antenna feed impedance practically are not changed up to 800–900 segments at wavelength.

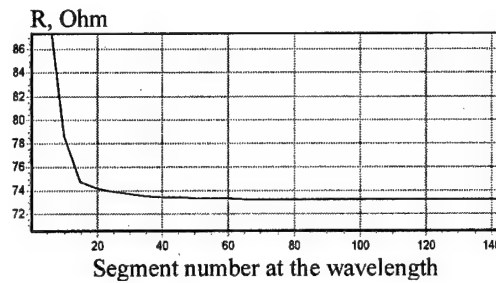
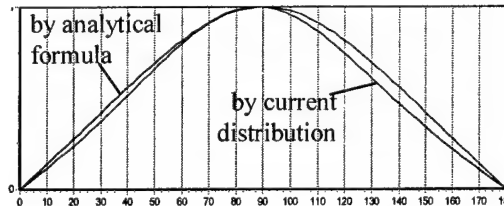
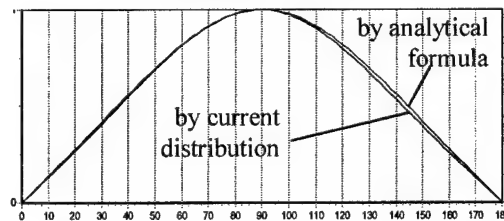


Fig. 5. The convergence of the real part of the antenna feed impedance



a) at 3 segments at the antenna



b) at 10 segments at the antenna

Fig. 6. The beam patterns of half wave vibrator

4 CONCLUSION

Use of the piecewise sinusoidal functions in MoM to solve inner problems makes it possible to avoid integration operations, their increasing the computational efficiency of MoM if the antenna or they item constitute the system of the congruent wires.

ACKNOWLEDGEMENT

The author expresses gratitude to doctor of technical sciences, Professor Oleg Anatolevich Jurcev for the help, valuable remarks and the general management of the work.

This work was prepared within the bounds of the republican program "The Problems of The Electrodynamics of Millimetre range (Microwaves)", The Republic of Belarus.

REFERENCES

1. Mittra R. Computer techniques for electromagnetics— M. Mir, 1977 (in Russian) Published in English as "Computer techniques for electromagnetics," Pergamon Press, Oxford etc., 1973.
2. Kravchenko V. F. Rvachev V. A. Rvachev V. L. Mathematics method for signal processing // Radioengineering and electronics. 1996. No 9, pp. 1385–1406.

AN OVERVIEW OF APPLICATIONS OF THE APERTURE ORTHOGONAL POLYNOMIALS METHOD IN THE DEVELOPMENT OF ANTENNA SYSTEMS

V.I. Gusevsky, the member of IEEE

FGUP OKB MEI, Moscow, Russia <Vgysevsky@mail.ru>

Abstract

The aperture orthogonal polynomials (AOPs) method, a new technique for phase control of antenna systems, is reviewed; and several problems solved with this method are considered. It is demonstrated that phase control algorithms that ensure the beam orientation of linear and planar phased arrays (PAs) with various geometrical parameters in the prescribed directions and simultaneous beam nulling in the directions of jamming signals are more accurate in comparison with traditional phase control algorithms. The criterion is obtained that provides for suppression of broadband jamming signals by forming the sector-shaped nulls of linear and planar PAs beams. Algorithms for determining the laws of optimal elements arrangement in non-uniformly spaced PAs, thus securing against parasitic side lobes of high intensity in wide-angle scan and for an extended (up to 2-3 octaves) frequency band, are considered.

Keywords: aperture orthogonal polynomials; antenna array; phase distribution; weighting function; phase shifter; nonuniform phased array; interference.

1. INTRODUCTION

In the last 10-15 years, the aperture orthogonal polynomials (AOPs) method has turned into a powerful tool for developing the phase control algorithms of linear and planar antenna arrays with various geometrical parameters.

Its fundamental distinction from traditional phase control algorithms based on the criterion of a uniform approximation of phase distribution functions in antenna apertures to ideal ones, is that optimal phase distribution functions are sought from a mean-square criterion, taking into account the actual amplitude distribution and geometric shape of a planar aperture, which may be of multilinked form [1].

The AOPs method has appeared as a generalization of the least squares method, which was used to estimate the slope of mean-square linear phase front of an antenna aperture field in the presence of a nonlinear initial phase distribution caused by some inhomogeneous phase distortions in the aperture field.

With the AOPs method, several theorems of antenna theory have been proved. First, it has been demonstrated that the amplitude-distribution fluctuations of an antenna aperture field impact on the angular position of a main lobe only when an initial phase distribution is nonlinear. When changing the amplitude and phase distributions, the expressions for a quantitative estimate of main lobe displacement have been found. For a planar aperture of arbitrary shape, they are written in the following form:

$$\begin{aligned}\cos \gamma_x &= a_{11}c_{10} + b_{01}c_{01} \\ \cos \gamma_y &= b_{11}c_{01}\end{aligned}\quad (1)$$

where $\cos \gamma_x$ and $\cos \gamma_y$ are the directional cosines of the normal to the plane of the linear mean-square phase front;

$$\begin{aligned}p_{10}(x, y) &= a_{11}x + a_{10}; \\ p_{01}(x, y) &= b_{11}y + b_{01}x + b_{10}\end{aligned}\quad (2)$$

are the first-order orthogonal polynomials, whose coefficients are determined by the weighting function that is identical with the amplitude distribution $\rho(x, y)$ and by the planar aperture geometry Ω ; and

$$\begin{aligned}c_{10} &= \int_{\Omega} \Phi(x, y) p_{10}(x, y) \rho(x, y) d\Omega, \\ c_{01} &= \int_{\Omega} \Phi(x, y) p_{01}(x, y) \rho(x, y) d\Omega,\end{aligned}\quad (3)$$

where c_{10} and c_{01} are the Fourier coefficients of the phase distribution $\Phi(x, y)$ when it is projected onto the subspace of linear orthogonal polynomials.

It should be emphasized that a conventional estimation of the impact of aperture field phase distortions on the antenna pattern, which is performed through the power-series expansion of the phase distribution, is incorrect. The fact is that the power-series expansion terms are nonorthogonal within the aperture. For example, all the odd-degree terms of the phase distribution involve distortions of lower degrees, which, in particular, cause an angular

rotation of the main lobe; even-degree terms also involve distortions of all lower degrees.

The representation of phase distribution in terms of the segment of Fourier series with respect to orthogonal functions is not a subject to this drawback. It describes refined distortions of a pattern that are only intrinsic to appropriate harmonics of the aperture field distribution.

The following relationship obtained with the help of AOPs method makes it possible to estimate the relative degradation of the gain of a linear or planar antenna aperture in the presence of inhomogeneous phase distortions. In the case of a linear array, the formula for estimating this gain degradation is found by calculating the level of power radiated in the main direction using the part of the Taylor-series expansion of the exponential factor that characterizes the phase distribution of field.

$$\frac{G}{G_0} = 1 - (k\ell)^2 \alpha \sum_{n=2}^N C_n^2 + 0 \left\{ \sum_{n,m} C_n^2 C_m^2 \right\}, \quad (4)$$

where $k\ell$ is the electrical size of the semiaperture of antenna; $\alpha = 1/\int_{-1}^1 \rho(x) dx$ is the coefficient taking into account the character of the amplitude distribution (for a uniform distribution, $\alpha = 1/2$); and C_n are the Fourier coefficients of the expansion of phase distribution function in terms of orthogonal polynomials.

An explicit expression for the remainder term, which allows for the third and fourth degrees of the expansion of an exponential factor, is written as follows

$$0 \left\{ \sum_{n,m} C_n^2 C_m^2 \right\} \approx \frac{(k\ell)^4 \alpha}{4!} \left[6 \sum_{n=2}^N \sum_{m=2}^N C_n^2 C_m^2 + \sum_n \sum_m \sum_r \sum_q C_n C_m C_r C_q \cdot \beta_{0rq}^{n,m} \right]. \quad (5)$$

Here $\beta_{0rq}^{n,m}$ is the Fourier coefficient of the zeroth-degree term obtained from the expansion of the multiplication of four orthogonal polynomials into series in terms of the same polynomials. Comparative calculations show that formula (4) enables the degradation of gain to a level of 70% from the nominal value to be determined with an accuracy of 2-3%. Formula (5), which allows for the remainder term, provides the same accuracy in determining the relative degradation of gain to 50%. These estimates can be used in the process of testing before communication sessions, thus providing the operative control of PAs on the basis of the known actual amplitude-phase distribution (APD) of the aperture field.

The AOPs method was further employed for evaluating the phase center of linear and planar arrays with an arbitrary APD. It has been found that the slope of a far-field phase characteristic reaches its zeroth level only when the origin of coordinates coincides with the center of gravity of the field amplitude distribution with respect to copolarization.

The coordinates of the center of gravity of amplitude distribution are associated with the position of a partial phase center. When being rigorously defined,

this center degenerates into the antenna's phase center for even amplitude and odd phase distributions [2].

The most important results have been obtained by applying the AOPs method for deep nulling in the direction of arrival of jamming signals. Although an initial problem is nonlinear and multiextremal by its nature, synthesized phase distribution functions may have a global extremum. This is explained by the following reasons.

- First, the synthesis algorithm, based on the search for the Fourier coefficients of the higher harmonics of the aperture phase distribution, does not change the mainlobe orientation owing to the orthogonality between the linear part and higher harmonics of the wave front.
- Second, the choice of optimal harmonics set according to the Lagrange objective functional guarantees the minimal gain degradation with simultaneous nulling in the directions of jamming signal arrival.
- Third, on exposure to broadband jamming signals, for linear and planar PAs with various amplitude distributions, the deepest sector nulls are formed only when phase distributions are synthesized relative to a partial phase centre.

For planar PAs with various geometrical parameters, including nonuniform PAs, the fundamental proportionality relationship has been found, which connects the relative band of a jamming signal to relative size of the sector null, from which, in particular, follows that the sector null size should be increased when the angular distance between the boresight and the direction of arrival of broadband jamming signals increases [3].

Fig. 1 demonstrates the radiation patterns of PAs consisting of 20 elements with a uniform amplitude distribution and sector nulls in the directions of maxima of the first, second and third sidelobes. The broadband jamming signal suppression is achieved by synthesis of the sector nulls of different width. The quantization of the synthesized phase distribution functions with a step of the order of $\pi/8$ supports the depth of nulls at -30 dB level, fully complying with practical requirements.

The following problem, which has been solved with the AOPs method, makes it possible to design the linear and planar nonuniform PAs with enlarged average spacing between elements. The major advantage of this method is the possibility to define the laws of antenna element arrangement for planar PAs with arbitrary number of elements.

The following problem, which has been solved with the AOPs method, makes it possible to design the linear and planar nonuniform PAs with enlarged average spacing between elements. The major advantage of this method is the possibility to define the laws of antenna element arrangement for planar PAs with arbitrary number of elements.

In this case, the sidelobes of higher level, which are analogous to diffraction lobes, are certainly lacking both in the mode of wide-angle scan and in the extended frequency band as much as 2 - 3 octaves and more. The total gain of the PA with dispersed elements decreases proportionally to the number of

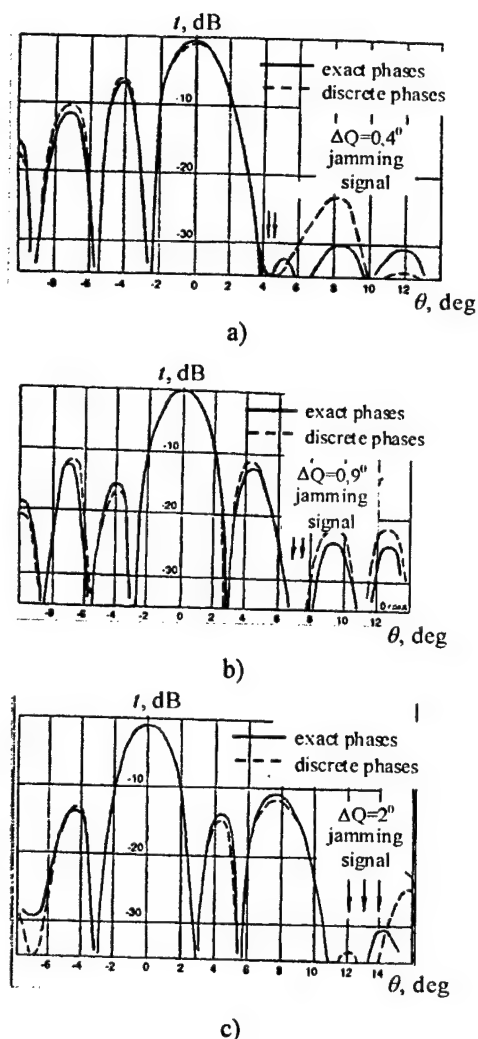


Fig. 1.

The relative gain as a function of the average element spacing for a PA having the same current (field) amplitudes of antenna elements.

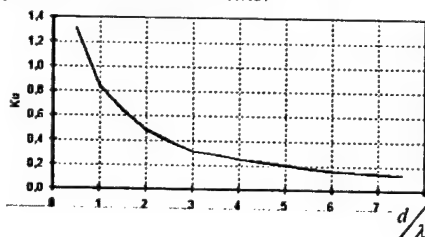


Fig. 2.

eliminated elements. Nevertheless, the preservation of the accuracy of defining the main beam angle position, although the total level of sidelobes is growing up, allows one to use such arrays in the antenna systems designed, for example, to determine, the angle position of target with higher accuracy. Numerical-simulations have shown that the location of antenna elements at the orthogonal polynomials zeros or at the extremal points of products of the orthogonal polynomials and weighting function eliminates the appearance of the higher level sidelobes.

Thus, any far-field phase distribution at the antenna aperture can be represented by the generic Fourier series in terms of orthogonal polynomials in the following form:

$$\begin{aligned} \Phi(x, y) &= \Phi_0 + \sum_{n=1}^{\infty} \sum_{m=1}^{\infty} C_{nm} p_{nm}(x, y) = \\ &= \Phi_0 + C_{10} p_{10}(x, y) + C_{01} p_{01}(x, y) + \\ &+ \sum_{n=2}^{\infty} \sum_{m=2}^{\infty} C_n C_m \prod_q^n (x - x_q) \prod_r^m (y - y_r) \end{aligned} \quad (5)$$

where Φ_0 is the constant phase shift; $C_{10} C_{01}$ are the Fourier coefficients of first-order polynomials, which determine the angular tilt of the phase front, x_q, y_r are the zero coordinates of the n, m -degree polynomials.

The expression in the form of the double sum of higher harmonics is orthogonal to the linear component of phase front at the aperture. There are no conditions at which such a part of the phase distribution can have another linear component of the phase front, which is different from initial component.

Fig. 2 illustrates the relative gain degradation of the linear nonuniform PA as function of average element spacing [4]. In the design nonuniform PAs, one can find trade-off solutions that would allow the total element quantity to be reduced 2 – 3 times and more at an acceptable level of gain degradation and preserving the main-beam angle resolution. As the total cost of a PA is directly dependent on the quantity of antenna elements (400÷1000\$ per each element), the above stated approach makes it possible to reduce significantly the total cost of the PA.

Finally, using the AOPs method, the problem of local zone definition at the aperture of a planar antenna with arbitrary amplitude distributions has been solved, whose phase perturbations contribute significantly to the distortions of certain far-field harmonics. This allows the optimal strategy for the real – time control of the surface of PAs and reflector antennas to be defined.

REFERENCES

1. V. I. Gusevsky «Method of aperture orthogonal polynomials and its application in antenna techniques»//Zarubezhnaya radioelektronika. Uspekhi sovremennoy radioelektroniki, 2001, № 3, pp. 52-72. (in Russian)
2. V. I. Gusevsky «Phase characteristic and phase center of linear and plane PAs»// Radiotekhnika i elektronika, 1991, № 3, 433-441 pp. (in Russian).
3. V. I. Gusevsky «Formation of sector gap in PAA RP at suppression of wideband interference»// Izv. vuzov, ser. Radioelektronika, 1991, № 5, pp. 23-34. (in Russian)
4. Lavrent'ev M.V. «On calculation of NPAA energetic characteristics characteristics»// Radiotekhnicheskie tetradi, 2002, № 25, pp. 41-44.(in Russian).
5. V. I. Gusevsky, Chadov S. E. «On a choice of optimal positions of control points inapertures of linear and plane antennas»// Radiotekhnicheskie tetradi, 1999, № 20, pp. 52-57.(in Russian).

EMPLOYING THE APERTURE ORTHOGONAL POLYNOMIALS METHOD IN THE DESIGN OF SPARSE UNEQUALLY SPACED PHASED ARRAYS

V. I. Gusevsky, M. V. Lavrentiev

Moscow, FGUP OKB MEI
<Vgusevsky@mail.ru>, <lavrem@mail.ru>

Abstract

A new method is considered for designing the linear and planar unequally spaced phased arrays (USPAs) in which the number of elements may be practically unlimited. This method is based on aperture orthogonal polynomials and enables one to find the law by which elements are positioned in the array aperture so as to eliminate parasite sidelobes similar to diffraction lobes in the scanning sector or over a wide operating frequency band. A sparse USPA is shown to have an increase in the level of side lobe radiation and a decrease in the array gain, while the array resolution remains unaltered. The behavior of USPA directivity is numerically estimated and the dependence of the degree of USPA directivity reduction on the average distance between elements is presented.

Keywords: aperture orthogonal polynomials, array, phase distribution, weighting function, phase shifter, unequally spaced phased array, interference.

At all times, the potentialities of unequally spaced phased arrays (USPAs) have attracted the particular attention of the designers of antenna systems because they make it possible to operate in a wider waveband, apply the sparse configurations of array elements and reduce the probability that diffraction lobes will arise. However, the absence of valid deterministic algorithms of array element positioning in the aperture that ensures the lack of sidelobes of higher level restrains the evolution of this investigation line.

Existing classical methods of USPAs designing use either random laws of element positioning or procedures of numerical optimization of USPAs parameters by varying the positions of array elements. Moreover, they also employ combinations of element spacings that are related as ratios of mutually prime integers.

The principle difference of the aperture orthogonal polynomials (AOPs) method used to develop the phase control algorithms of linear and planar apertures from conventional phase control algorithms is that any phase distribution can be expressed as a segment of the generalized Fourier series in orthogonal polynomials of the aperture. As the weighting function $\rho(x)$ and $\rho(x,y)$ (for a planar array), an amplitude distribution function of the aperture field with respect to copolarization is used that takes into account an actual field distribution over the whole aperture and in the local zone around every array element.

At the same time, the phase distortions in the aperture field, which are described by different terms of the Fourier series, are mutually orthogonal. First of all, it is necessary to emphasize that, if the linear

phase front described by the linear term of series is formed in the antenna aperture, then the best mean-square approximation to the ideal linear phase control law is provided.

The proposed method can be used to design either linear or planar arrays with amplitude-phase distributions of different kind and with a large number of array elements. Consider the construction of this algorithm.

The far-field pattern of planar aperture is expressed via the following integral:

$$f(u, v) = \frac{1}{4} \iint_{\Omega} e^{ik(\ell_x u x + \ell_y v y - \ell \Phi(x, y))} \rho(x, y) d\Omega \quad (1)$$

Here, $u = \cos \varphi \cdot \sin \theta$, $v = \sin \varphi \cdot \sin \theta$ are the directional cosines of wave front; $k = 2\pi/\lambda$ is the wave number of the propagation medium; $\rho(x, y) > 0$ is the amplitude distribution; $\rho(x, y) \in L_2$; phase distribution $\Phi(x, y) \in L_2$; and ℓ_x, ℓ_y are a half of the length and the width of the rectangular aperture, respectively, where the domain Ω , $l = \max(\ell_x, \ell_y)$ is inscribed.

The phase distribution function $\Phi(x, y)$ is presented as Fourier series in orthogonal polynomials with the weighting function equal to the amplitude distributions in the aperture.

As $\rho(x, y) > 0$ is the strictly positive function, such orthogonal polynomials always exist:

$$\Phi(x, y) = \sum_{n=0}^{\infty} \sum_{m=0}^{\infty} C_{nm} \cdot P_{nm}(x, y), \quad (2)$$

where,

$$\begin{aligned} \iint_{\Omega} P_{nm}(x, y) P_{kl}(x, y) \cdot \rho(x, y) d\Omega &= \delta_{nl} \delta_{mk} \\ P_{nm}(x, y) &\in L_{ort} \{ \Omega \mid \rho(x, y) > 0 \} \\ C_{nm} &= \iint_{\Omega} \Phi(x, y) P_{nm}(x, y) \rho(x, y) d\Omega \end{aligned} \quad (3)$$

These polynomials that are orthogonal in the domain Ω have properties of eigenfunctions of the integral operator (1).

The main property of such orthogonal representation of the field in array apertures lies in the fact that phase distortions described by individual harmonics are mutually orthogonal. They are in correspondence with the certain distortions of a far-field pattern shape, which are intrinsic to these orthogonal harmonics only. For example, when phase distortions are described by the third-degree orthogonal polynomial, an angular displacement of the mainbeam is lacking in contrast to the usual power-type description of phase distortions in the antenna aperture that shows such a displacement.

In the design process of USPAs and sparse USPAs in particular, the central problem is the derivation of the nonperiodical law of element positioning in the aperture which provides the absence of the high-level side lobes in the mode wide-angle scanning. Such sidelobes similar to diffraction lobes are caused by the periodicity of discrete element arrangement with a step of $d > \lambda/2$ and, as a consequence, the presence of a quasilinear component of the phase distribution in the aperture field which is distinct from the basic linear component of the field.

Consider such a nonperiodical law of antenna element positioning in the linear normalized aperture under which every element is located at the point corresponding to the root of an orthogonal polynomial from the collection of N polynomials. In this case, any phase distribution can be expressed in the following form:

$$\begin{aligned} \Phi(x) &= C_0 p_0 + C_1 p_1(x) + \sum_{n=2}^{\infty} C_n p_n(x) \approx \\ &\approx C_0 a_0 + C_1 a_{10} + C_1 a_{11}(x) + \sum_{n=2}^N C_n \prod_{q=1}^n a_q(x - x_q) \end{aligned} \quad (4)$$

where $\{C_0, C_1, \dots\}$ are the Fourier coefficients, $\{x_q\}$ is the set of roots n th-power polynomial, $p(x) = a_1 x + a_{10}$ is the linear polynomial, $p_0 = a_0$ is the zero-power polynomial.

The orientation of the linear phase front in the antenna aperture that corresponds to the best mean-square approximation is determined by the coefficient $C_1 a_{11}$ for the variable x , where the linear part of the Fourier series is orthogonal to the sum of another harmonics. All harmonics do not depend on frequency and the point of observation at the far zone. The condition of physical realizability requires that, in the relationship (4), the finite number of harmonics N in the expansion of phase distribution should be used because the minimal distance d between adjacent

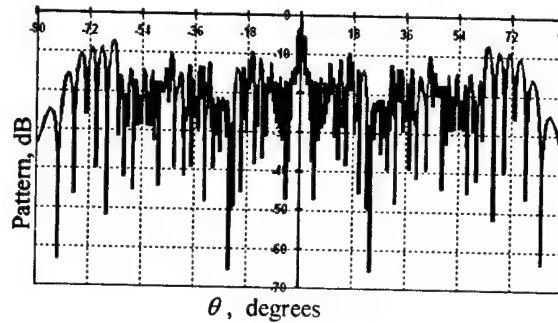


Fig. 1. A pattern of the USPA with uniform amplitude distribution. The total number of element is 35. The average element spacing is 2λ . The element positioning is determined by (5).

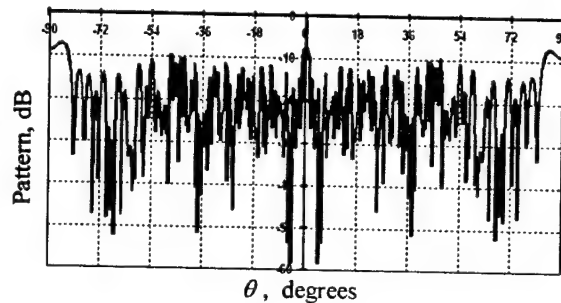


Fig. 2. A pattern of the USPA with uniform amplitude distribution. The total number of elements is 43. The average element spacing is 2λ . Elements are located at AOP zero points.

radiating elements should be more or equal to a specified value, for example, $d > \lambda/2$.

This approach may readily be generalized to the planar USPAs with the amplitude distribution function $\rho(x, y) = \rho_1(x) \rho_2(y)$ presented in the multiplicative form.

In this case, the set of two-dimensional orthogonal polynomials is expressed as $p_{nm}(x, y) = p_n(x) p_m(y)$. If such a representation is impossible, then the computational constraints of determining the two-dimensional orthogonal polynomials and their roots are sharply growing.

There is another way of positioning the element with unequal spacing in the antenna aperture by which the elements are located at the extremal points of orthogonal polynomials or at the extremal points of multiplication of orthogonal polynomials by the weighting function. It follows from the fact that, first, the above-mentioned points have the properties of maximal influence on the pattern shape of respective harmonics under local phase perturbations in these points [1] and, second, extremal points are located between the adjacent roots of orthogonal polynomials and do not significantly change the mechanism of unequal positioning of elements.

Figs. 1 and 2 demonstrate the far-field patterns of USPAs that has been designed with the help of two algorithms discussed above. Picture 1 presents the pat-

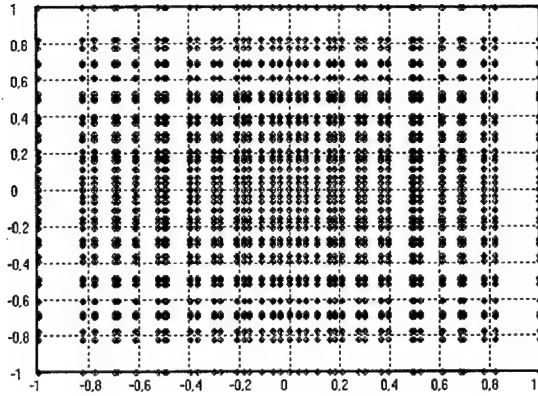


Fig. 3. The arrangement of the USPA element in the normal aperture. The total amount of elements is 40×40 .

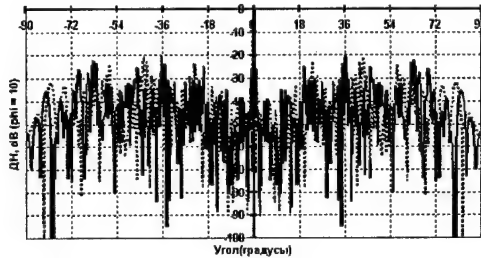


Fig. 4. $\varphi = 10^\circ$.

tern of the USPA, which consists of 35 isotropic elements. This array has the uniform amplitude distribution. This means that the well-known Legendre polynomials play the role of AOPs and antenna elements are located at the extremal points of corresponding Legendre polynomials. The Legendre polynomials of less than and equal to 10th order were taken as an example. Fig. 1 illustrates the pattern of the array with an average element spacing of 2λ (the aperture length is 70λ). The pattern analysis shows that the mean level of sidelobes does not exceed -10 dB.

The nearest sidelobes have the maximal values (about -6 dB). Furthermore, it should be noted that the sidelobes do not taper. This behavior is predictable and typical for most USPAs. However, it is possible to decrease the level of nearest sidelobes when using the falling-down amplitude distribution and the special procedure of inversion of the antenna elements positioning points relative to the array center.

Fig. 2 shows the far-field pattern of the same array with elements located at zeros of AOPs. It should be emphasized that there are no significant differences in the behavior of patterns that were built with the help of the first and second algorithms.

When designing the planar USPAs we observe that the mean level of sidelobes significantly depends on the value of φ because, in case of multiplicative representation of the weighting function, there are only two critical directions $\varphi = 0$ and $\varphi = 90^\circ$. In these directions, the pattern of the planar USPA is equivalent

to the pattern of the linear USPA. Fig. 3 illustrates the arrangement of elements in the aperture of the planar USPA with a total element amount of 40×40 and average element spacing of $\sim 4.4\lambda$.

Fig. 4 shows the pattern of this USPA at the angle $\varphi = 10^\circ$. It follows from Fig. 4 that the mean level of sidelobes is reduced by at least 10 dB in the non-critical direction in comparison with a critical one.

For sparse USPAs it is necessary to estimate the degree of reduction of the gain or directivity as compared with those of conventional uniformly spaced arrays with a complete configuration of elements ($d \approx 0.5\lambda$). This procedure is carried out by estimating the directivity and radiation power of the array aperture using the well-known formula:

$$G = \frac{4\pi f(\theta_0, \varphi_0) f^*(\theta_0, \varphi_0)}{I} \quad (5)$$

where

$$I = \int_0^{\pi/2} \int_0^{2\pi} f(\theta, \varphi) f^*(\theta, \varphi) \sin \theta d\varphi d\theta \quad (6)$$

The initial array pattern can be presented by the following expression:

$$f(u, v) = \sum_{i=0}^{N_x} \sum_{j=0}^{N_y} \rho(x_i, y_j) \exp[ik(l_x(u - u_0) + l_y(v - v_0))] \quad (7)$$

where $\rho(x_i, y_j)$ is the amplitude distribution function in the array aperture, $x_i \in (-1, 1)$, $y_j \in (-1, 1)$ are the coordinates of array elements located in the normal aperture $\Omega \subset [-1, 1] \otimes [-1, 1]$. $N_x \times N_y$ is total amount of elements in the array.

The mainbeam direction is defined by $u_0 = \cos \varphi_0 \cdot \sin \theta_0$ and $v_0 = \sin \varphi_0 \cdot \sin \theta_0$. Substituting the expression (7) into the integral (6) and using the Poisson formula, we obtain:

$$\int_0^{\pi} \int_0^{2\pi} f[\mu \sin \theta \cos \varphi + \nu \sin \theta \sin \varphi + \xi \cos \theta] \times \sin \theta d\varphi d\theta = 2\pi \int_{-1}^1 f(u \sqrt{\mu^2 + \nu^2 + \xi^2}) du \quad (8)$$

after simple but tedious computations, we can obtain the final expression for determination of the planar USPA directivity in the direction of maximal radiation ($u_0 = 0$, $v_0 = 0$).

$$G = 2 \cdot \left\{ \sum_{i=0}^{N_x} \sum_{j=0}^{N_y} \rho(x_i, y_j) \right\}^2 \times \left\{ \sum_{i=0}^{N_x} \sum_{j=0}^{N_y} \sum_{m=0}^i \sum_{n=0}^j \rho(x_i, y_j) \rho(x_m, y_n) \varepsilon_{im} \varepsilon_{jn} \right\} \times \left\{ \frac{\sin \left\{ k \cdot \sqrt{l_x^2 \cdot (x_i - x_m)^2 + l_y^2 \cdot (y_j - y_n)^2} \right\}}{k \cdot \sqrt{l_x^2 \cdot (x_i - x_m)^2 + l_y^2 \cdot (y_j - y_n)^2}} \right\}^{-1} \quad (9)$$

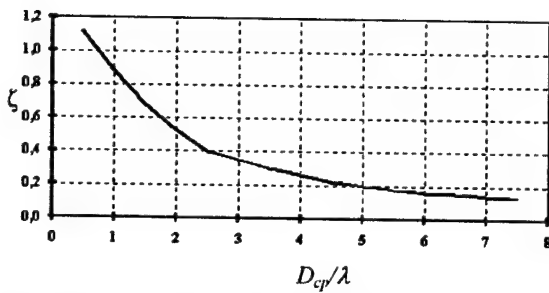


Fig. 5. The degree of reduction of the directivity for the USPA with a uniform amplitude distribution

where $\varepsilon_{ij} = \begin{cases} 1, & i = j \\ 2, & i \neq j \end{cases}$

When passing from the two-dimensional array to the one-dimensional one, the formula (10) is reduced to:

$$G = 2 \cdot \left\{ \sum_{i=0}^{N_x} \rho(x_i) \right\}^2 \times \left\{ \sum_{i=0}^{N_x} \sum_{j=0}^i \rho(x_i) \rho(x_j) \varepsilon_{ij} \frac{\sin(k l_x |x_i - x_j| u)}{k l_x |x_i - x_j| u} \right\}^{-1} \quad (10)$$

The directivity of USPAs in comparison with the directivity of uniformly spaced arrays is very important in the design of USPAs. This reduction can be evaluated by introducing the relative coefficient of directivity reduction, which shows the degree of reduction of the USPA directivity in comparison with the directivity of a corresponding uniformly spaced array. This relative coefficient is introduced by the formula:

$$\zeta = G / G_e, \quad (11)$$

where G is the USPA directivity, G_e is the directivity of a uniformly spaced array.

Fig. 5 illustrates the dependence for linear arrays. It has the decaying character and is practically independent from the type of amplitude distribution.

Thus, the new method of designing the linear and planar USPAs makes it possible to:

- Use the deterministic procedure of element positioning in the antenna aperture.
- Eliminate the restriction on the total number of antenna elements.
- Provide the mode of wide-angle scanning and operation in the broad frequency band without high levels of sidelobes because the law of element positioning does not depend on frequency.
- Use sparse USPAs with the controlled degree of directivity reduction and ensure unchanging resolution and, simultaneously, reduce expenses by decreasing the number of receiving-transmitting modules.

REFERENCES

1. Gusevsky V. I., Chadov S. E. "About choice of optimal location of control points at the linear and planar antennas apertures" // M.: Radio copy-books, special edition, 1999, № 18, pp. 34-37.
2. Lavrentiev M. V. "To solve the energetical parameters of nonuniformly spaced phased array antennas" // M.: Radio copy-books, 2003, № 25, pp. 41-45.

ABOUT ONE GRADIENT PROCEDURE OF DETERMINATION OF THE BRANCHING POINTS OF NONLINEAR INTEGRAL EQUATION ARISING IN THE THEORY OF ANTENNA SYNTHESIS

Podlevskyi B. M.

Pidstryhach Institute of Applied Problems of Mechanics & Mathematics, NASU,
3-b Naukova Str. Lviv, 79000 Ukraine
<podlev@iapmm.lviv.ua>

Abstract

The problem of building a numerical algorithm for determination of branching points of one nonlinear integral operator, which arises in the theory of antennas synthesis according to the given amplitude radiation pattern, is considered. The basic difficulty consists in that the kernel of an integral operator nonlinearly depends on two parameters, which play role of the spectral ones. For such problems, except a special case, the existing numerical algorithms are not applicable. For building an algorithm for solving such problems, the equivalent variational statement is used. The problem is reduced to a sequence of linear two-parameter eigenvalue problems with application of one gradient procedure for simultaneous evaluation of two spectral parameters being the branching points of an initial nonlinear integral operator.

Keywords: antennas synthesis, branching points, nonlinear integral operator, two-parameter eigenvalue problem, numerical algorithm, eigenvalue, gradient procedure.

1. INTRODUCTION

When investigating the nonlinear equations as

$$A(\lambda, f) = f,$$

where operator $A(\lambda, f)$ nonlinearly depends both on parameter λ and function f , the formalistic approach based on a linearization, is applied. The application of this approach shows that the branching points of equation can be only those values of parameter λ , for which unit is the eigenvalue of the appropriate homogeneous equation [1]

$$A(\lambda)f = f$$

with the operator-valued function $A : C \rightarrow X(H)$ (where $X(H)$ is a set of linear operators, $\lambda \in C$ is the spectral parameter) nonlinearly depending on the parameter λ . If $A(\lambda) \equiv A$ is the linear operator, its eigenvalues will be the branching points of an input equation. In general case, there are curves of eigenvalues $\nu(\lambda)$ and then branching points will be those values of a parameter λ of the problem

$$A(\lambda)f = \nu(\lambda)f,$$

for which $\nu(\lambda) = 1$.

The application of the cited above approach to the nonlinear integral operator arising at the synthesis of the antenna systems in accordance with the given amplitude RP leads to the nonlinear eigenvalue problem $T(\lambda, \mu)f = f$ with an integral operator $T(\lambda, \mu)$ analytically depending on two spectral parameters λ and μ .

In the given work, the variational approach to building the numerical algorithm for solving such eigenvalue problems is offered. It consists in replacement of the nonlinear operator of function $T(\lambda, \mu)$ with a linear operator of function on both parameters and application of the gradient procedure for simultaneous evaluation of a gang of spectral parameters λ, μ of obtained two-parameter eigenvalue problem.

2. STATEMENT OF THE PROBLEM

The variational statement of the problem of antennas synthesis with flat aperture according to the given amplitude directivity pattern reduces to the nonlinear equation [2]

$$f(\xi_1, \xi_2) = \iint_{\Omega} F(\xi'_1, \xi'_2) K(\xi_1, \xi_2, \xi'_1, \xi'_2, k) e^{i \arg f(\xi'_1, \xi'_2)} d\xi'_1 d\xi'_2, \quad (1)$$

where

$$K(\xi_1, \xi_2, \xi'_1, \xi'_2, k) = \iint_D e^{i k [x(\xi_1 - \xi'_1) + y(\xi_2 - \xi'_2)]} dx dy \quad (2)$$

is a kernel considerably depending on the form of aperture, and $\Omega \subset R^2$ is the area, in which the amplitude RP is given.

For the rectangular aperture of antenna $D = \{ |x| \leq a, |y| \leq b \}$ the kernel (2) is possible to be presented as [2, page 247]

$$K(\xi_1, \xi_2, \xi'_1, \xi'_2, c_1, c_2) = \frac{\sin c_1(\xi_1 - \xi'_1)}{\pi(\xi_1 - \xi'_1)} \cdot \frac{\sin c_2(\xi_2 - \xi'_2)}{\pi(\xi_2 - \xi'_2)}, \quad (2')$$

where c_1, c_2 are the fundamental physical parameters describing electrical sizes of the antenna and solid angle of area Ω , which also looks like some rectangle $\Omega: \{ |\xi_1| \leq 1, |\xi_2| \leq 1 \}$.

The equation (1) has a non-unique solution, and as one of its possible solutions (we shall name it as trivial) is the following one

$$f_0(\xi_1, \xi_2, c_1, c_2) = \iint_{\Omega} F(\xi'_1, \xi'_2) K(\xi_1, \xi_2, \xi'_1, \xi'_2, c_1, c_2) d\xi'_1 d\xi'_2. \quad (3)$$

It corresponds to RP with a phase center ($\arg f(\xi_1, \xi_2) \equiv 0$) and takes place for arbitrary $c_1 > 0$ and $c_2 > 0$. But in most cases, just nontrivial solutions branching from $f_0(\xi_1, \xi_2, c_1, c_2)$ with the increase of parameters c_1 and c_2 are of physical interest.

Thus, the problem of determination of points c_1 and c_2 , in which there appear solutions different from trivial $f_0(\xi_1, \xi_2, c_1, c_2)$, is reduced to definition of the eigenvalues of the integral operator

$$T\omega(\xi_1, \xi_2, c_1, c_2) \equiv \iint_{\Omega} F(\xi'_1, \xi'_2) K(\xi_1, \xi_2, \xi'_1, \xi'_2, c_1, c_2) \times \frac{\omega(\xi'_1, \xi'_2, c_1, c_2)}{f_0(\xi_1, \xi_2, c_1, c_2)} d\xi'_1 d\xi'_2. \quad (4)$$

The appropriate eigenfunctions of this operator are used when solving equation (1).

Since the parameters c_1 and c_2 play a role of spectral parameters, we actually have come to the generalized two-parameter eigenvalue problem

$$\omega(\xi_1, \xi_2, c_1, c_2) = T(c_1, c_2)\omega(\xi_1, \xi_2, c_1, c_2). \quad (5)$$

Note, that in a specific case, when it is possible to separate variables in function $F(\xi_1, \xi_2)$, i.e. to present $F(\xi_1, \xi_2)$ as

$$F(\xi_1, \xi_2) = F_1(\xi_1) \cdot F_2(\xi_2),$$

the equation (5) is decomposed into two independent one-parameter (but nonlinear with respect to the parameter) equations, i.e.

$$\omega_j(\xi_j, c_j) = T(c_j)\omega_j(\xi_j, c_j), \quad j = 1, 2.$$

For such equations both the numerical methods (see, for example, [3], [4]) and the numerical analytical methods of their research [2] are developed.

In the given work, the numerical algorithm for solution of more complicated problem when the variables are not separated, is offered. The essence of it consists in that the solution of the nonlinear two-parameter eigenvalue problem (5) is reduced to solution of some sequence of linear two-parameter eigenvalue problems, for solution of which the gradient procedure is used.

3. BASIC EQUATION AND ALGORITHM OF THE SOLUTION

At first we shall reduce with a standard method operator (4) to a self-adjoint form.

Introducing a new function

$$\varphi(\xi_1, \xi_2, c_1, c_2) = \sqrt{w(\xi_1, \xi_2, c_1, c_2)} \omega(\xi_1, \xi_2, c_1, c_2),$$

where $w(\xi_1, \xi_2, c_1, c_2) = F(\xi_1, \xi_2) / f_0(\xi_1, \xi_2, c_1, c_2)$, we come to the integral equation

$$\varphi(\xi_1, \xi_2, c_1, c_2) = \int_{-1}^1 \int_{-1}^1 \Phi(\xi_1, \xi_2, \xi'_1, \xi'_2, c_1, c_2) \varphi(\xi'_1, \xi'_2, c_1, c_2) d\xi'_1 d\xi'_2 \quad (6)$$

with the symmetrical kernel

$$\Phi(\xi_1, \xi_2, \xi'_1, \xi'_2, c_1, c_2) = K(\xi_1, \xi_2, \xi'_1, \xi'_2, c_1, c_2) \sqrt{w(\xi_1, \xi_2, c_1, c_2) w(\xi'_1, \xi'_2, c_1, c_2)}.$$

In order to get rid of a continuous spectrum, we shall select from the kernel the trivial solution (3), which corresponds to the eigenvalue $\eta(c_1, c_2) = 1$ for any positive c_1 and c_2 . In this case, equation (6) will be transformed into the equation

$$\varphi(\xi_1, \xi_2, c_1, c_2) = \int_{-1}^1 \int_{-1}^1 E(\xi_1, \xi_2, \xi'_1, \xi'_2, c_1, c_2) \varphi(\xi'_1, \xi'_2, c_1, c_2) d\xi'_1 d\xi'_2. \quad (7)$$

with the symmetric kernel

$$E(\xi_1, \xi_2, \xi'_1, \xi'_2, c_1, c_2) = \sqrt{w(\xi_1, \xi_2, c_1, c_2) w(\xi'_1, \xi'_2, c_1, c_2)} \times \left[K(\xi_1, \xi_2, \xi'_1, \xi'_2, c_1, c_2) - \frac{f_0(\xi_1, \xi_2, c_1, c_2) f_0(\xi'_1, \xi'_2, c_1, c_2)}{\| \varphi_0(\xi_1, \xi_2, c_1, c_2) \|^2} \right]$$

Decomposing the kernel E of the operator T by Taylor series in the neighbourhood of point $(c_1 = \mu, c_2 = \nu)$, and taking up the linear terms of expansion, we come to the two-parameter eigenvalue problem of the form

$$\tilde{T}\varphi \equiv \tilde{A}\varphi - \lambda_1 \tilde{B}_1\varphi - \lambda_2 \tilde{B}_2\varphi = 0. \quad (8)$$

In view of bulky size of the formulas, the expressions for operators here are not written.

Now we shall consider the functional

$$\tilde{F}(\varphi) = \frac{1}{2} \|\tilde{A}\varphi - \lambda_1 \tilde{B}_1\varphi - \lambda_2 \tilde{B}_2\varphi\|^2. \quad (9)$$

It is not difficult to show that equality $\tilde{F}(\varphi) = 0$ holds if and only if $\nabla \tilde{F}(\varphi) = 0$, where $\nabla \tilde{F}(\varphi)$ is the gradient of functional (9). And, obviously, $\nabla \tilde{F}(\varphi) = 0$ if and only if both φ and $\Lambda(\varphi) = \{\lambda_1, \lambda_2\}$ are the eigenvector and eigenvalue of the problem (8).

This result allows us to construct the gradient procedure, as the algorithm of numerical determination of eigenvector as

$$\begin{aligned} \psi_{k+1} &= \varphi_k - \gamma(\varphi_k) \nabla \tilde{F}(\varphi_k), \quad k = 0, 1, 2, \dots, \\ \varphi_{k+1} &= \psi_{k+1} / \|\psi_{k+1}\|, \end{aligned} \quad (10)$$

$$\gamma(\varphi_k) = \frac{\|\nabla \tilde{F}(\varphi_k)\|^2}{\|\tilde{T} \nabla \tilde{F}(\varphi_k)\|^2},$$

and the eigenvalue $\Lambda(\varphi) = \{\lambda_1, \lambda_2\}$ is uniquely determined according to the obtained φ from a set of equations

$$\alpha(\varphi) = \Lambda(\varphi) \beta(\varphi), \quad (11)$$

where $\alpha(\varphi) = \{\alpha_1(\varphi), \alpha_2(\varphi)\}^T$ is a column vector, and $\beta(\varphi) = \{\beta_{ij}\}_{i,j=1}^2$ is matrix with components $\alpha_i(\varphi) = (\tilde{A}\varphi, \tilde{B}_i\varphi)$ and $\beta_{ij} = (\tilde{B}_i\varphi, \tilde{B}_j\varphi)$, respectively, and (\cdot, \cdot) is a scalar product in space L_2 .

Thus, the algorithm consists in the following:

1. For some initial approximation ($i = 0$) of parameters $c_1^{(i)} = \mu$, $c_2^{(i)} = \nu$ the operators $\tilde{A}, \tilde{B}_1, \tilde{B}_2$ are defined using expansion of kernel of operator (4) into a Taylor series.

2. Using the iterative process (10) with some initial approximation φ_0 the eigenvector φ_k and gangs of eigenvalues $\Lambda(\varphi_k) = \{\lambda_1, \lambda_2\}$ by (11) of linear two-parameter problem (8) are defined.

3. If c_1^{i+1} and c_2^{i+1} are not defined with a necessary accuracy, i.e. $|c_1^{(i)} - c_1^{(i+1)}| > \varepsilon_1$ and $|c_2^{(i)} - c_2^{(i+1)}| > \varepsilon_2$, this approximation is fixed and giving $c_j^{(i)} = c_j^{(i+1)}$, $j = 1, 2$ we pass to item 1.

4. NUMERICAL RESULTS

For the cases, when in function $F(\xi_1, \xi_2)$ describing the amplitude directivity pattern of antenna, the variables are separated and not separated, the numerical experiments on application of the described above algorithm for determination of the first branching point were carried out.

Table 1.

$F(\xi_1, \xi_2)$	Branch. points		Branch. points from [2]	
	c_1	c_2	c_1	c_2
const $\equiv 1$	3.141592	3.141592	π	π
$\cos \frac{\pi \xi_1}{2} \cos \frac{\pi \xi_2}{2}$	4.712543	4.712543	4.712	4.712
$\sin \pi \xi_1 \sin \pi \xi_2$	3.141591	3.141591	π	π
$\sqrt{1 - \frac{1}{2}(\xi_1^2 + \xi_2^2)}$	3.464286	3.464286		
$1 - \frac{1}{2}(\xi_1^2 + \xi_2^2)$	3.797263	3.797263		

In the table, the first branching points for three given functions, when the variables are separated, also for two, when the variables are not separated, are given. For three first functions the branching points obtained by other method (by a solution of transcendental equations) from [2] also are given.

From the table it is seen, that for the case, when variables of $F(\xi_1, \xi_2)$ are separated, the results obtained by two different approaches completely coincide.

5. CONCLUSION

The approach offered in the work, for construction of iterative processes, can be applied to determination of generalized eigenvalues of nonlinear two-parameter (multiparameter) eigenvalue problems.

In particular, for definition of branching points of the nonlinear integral equation considered in the work, it can effectively be applied in the most common case, i.e., when variables in function $F(\xi_1, \xi_2)$ are not separated and for which the existing algorithms are not applicable.

REFERENCES

1. Vainberg M.M., Trenogin V.A. Branching theory of the solution of nonlinear equations. Moscow. Nauka, 1969. [in Russian].
2. Savenko P.O. Nonlinear problems of radiating systems synthesis (theory and methods of solution). Lviv: IAPMM NASU, 2002. [in Ukraine].
3. Podlevskyi B.M. Numerical method for solution of one class of nonlinear spectral problems. Math. Methods and Physicomechanical Fields. – 2001. 44, No 2. – P. 34-38 [In Ukraine].
4. Savenko P.O. Numerical algorithm for solution of a generalized eigenvalue problem for compact self-adjoint operators with a nonlinear spectral parameter. Math. Methods and Physicomechanical Fields. – 1997. 40, No 1. – P. 146-150 [In Ukraine].

APPLICATION OF THE KRAVCHENKO-DARBOUX AND KRAVCHENKO-BESICOVITCH TWO- DIMENSIONAL FRACTAL FUNCTIONS IN ANTENNA THEORY

Vladimir M. Masyuk

Bauman Moscow State Technical University
5 Vtoraya Baumanskaya st., Moscow, 107005, Russia
Phone: +7 (095) 263 66 40, E-mail: <masyuk77@hotmail.ru>

Abstract

One of the methods for fractal antenna array synthesis, based on the use of fractal current distributions is considered. Analysis of both equally-spaced and non-equally-spaced antenna arrays constructed with using the Kravchenko-Darboux and Kravchenko-Besicovitch functions is shown.

Keywords: antenna arrays; antenna theory; antenna radiation patterns; low-sidelobe antennas; fractals; atomic functions; linear array; Darboux function; Besicovich function.

1. INTRODUCTION

Recently, new approaches in antenna system analysis and synthesis, based on ideas of fractal geometry become more popular. [1, 2]. Antenna radiators were constructed on the base of fractal sets and their properties were investigated [3]. Two approaches in the fractal antenna array design may be distinguished:

- arrays undemanding to accuracy of radiator placement and possessing low directivity and a sufficiently high sidelobe level. Such arrays are similar to randomly spaced arrays [3];
- arrays with a low sidelobe level and high directivity. Their properties are close to those of classical arrays but sometimes it is possible to realize simple algorithms for synthesis of such fractal arrays.

Here, the class of two-dimensional antenna arrays constructed with using the Darboux and Besicovitch classical fractal functions and atomic functions. Such an approach for the first time was realized by V.F. Kravchenko [3].

Consider two-dimensional antenna arrays constructed on the base of different combinations of atomic functions and classical fractal functions. They belong to the class of equally-spaced arrays with non-uniform amplitude distribution complicating the synthesis algorithms. The lack of such an approach is in the fact that separate elements of an antenna array operate in different working regimes and can fault due to overheating. It also known that arrays with nonuniform current distribution have lower values of aperture efficiency in comparison with arrays having uniform amplitude distribution. But here it is possible to decrease the sidelobe level by an appropriate choice of the current distribution.

2. PLANAR ANTENNA ARRAYS

Consider the case of a planar two-dimensional symmetric non-equally-spaced FAA with spaces d_x along axis x and d_y along axis y (Fig. 1).

The formula for evaluating the radiation pattern $F(\psi_x, \psi_y)$ for a $(2M)^2$ -element array has the form

$$F(\psi_x, \psi_y) = 4 \sum_{n=1}^M \sum_{m=1}^M I_{nm} \cos\left(\left(m - \frac{1}{2}\right)\psi_x\right) \cos\left(\left(n - \frac{1}{2}\right)\psi_y\right),$$

where

$$\psi_x = kd_x(\sin \theta \cos \varphi - \sin \theta_0 \cos \varphi_0);$$

$$\psi_y = kd_y(\sin \theta \sin \varphi - \sin \theta_0 \sin \varphi_0).$$

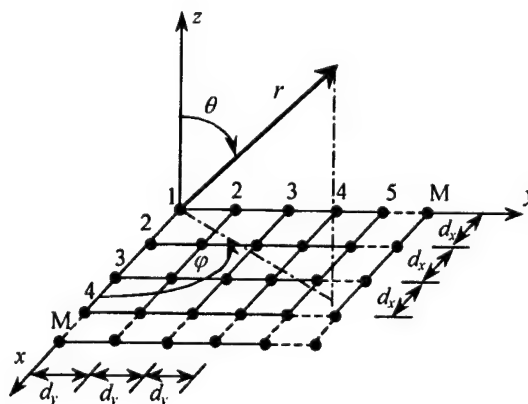


Fig. 1. Linear two-dimensional antenna array with $M \times N$ equally-spaced elements

Current distribution amplitudes obey the following rule:

$$I_{mn} = f(\psi_{x_m}, \psi_{y_n}),$$

where $f(\psi_{x_m}, \psi_{y_n})$ are values of the atomic-fractal function at corresponding points x_m and y_n .

3. ATOMIC FUNCTIONS

Foundations of the theory of atomic functions are considered in [3]. Here, we shall present some information about less known atomic functions. Another often used function is $up_m(x)$, the generalization of the atomic function $up(x)$, satisfying the functional-differential equation

$$y'(x) = a \sum_{k=1}^m (y(2mx + 2m - 2k + 1) - y(2mx - 2k + 1)),$$

$m = 2, 3, 4, \dots$. All properties of functions $up_m(x)$ are presented in [3]. Let us discuss one of them, using for evaluating the function at rational points in the domain of definition. Let $\mu_n^{(m)}$ be the moment of order n of the function $up_m(x)$, where

$$\mu_n^{(m)} = \int_{-1}^1 x^n up_m(x) dx, \quad \mu_{2n-1}^{(m)} = 0, \quad \text{because}$$

$up_m(x)$ is even for any m . even moments $\mu_{2n}^{(m)}$ are rational numbers found by the recurrent formula

$$\mu_{2n}^{(m)} = \frac{(2n)!}{m^2 ((2m)^{2n} - 1)} \sum_{k=1}^n \frac{\sum_{l=1}^m (2l-1)^{2k+1}}{(2n-2k)!(2k+1)!} \mu_{2n-2k}^{(m)},$$

($n = 1, 2, 3, \dots$). The following remark takes place. From the theory of AFs it follows that $x_{m,n,s} = -1 + \frac{s}{m(2m)^n}$, $s = 0, 1, \dots, (2m)^n + 1$. The points $x_{m,n,s}$ form an everywhere dense set on the interval $[-1, 1]$. Note that values of $up_m(x)$ at points of this set are rational and can be determined explicitly as

$$up_m(x_{m,n,s}) = \frac{2^{n+1}}{n!(2m)^{\frac{(n+1)(n+2)}{2}}} \times \sum_{j=1}^s \delta_j^{(m)} \sum_{k=0}^{\lfloor n/2 \rfloor} \binom{n}{2k} (2s - 2j + 1)^{n-2k} \mu_{2k}^{(m)},$$

where $[a]$ is the integral part of the number a .

Other often used functions are $y_r(x)$ determined as

$$y_r(x, \bar{o}) = \frac{1}{2\pi} \int_{-\infty}^{\infty} e^{-i\bar{o}t} F_r(t) dt, \quad r = 1, 2, 3, \dots,$$

where

$$F_r(t) = \prod_{k=r}^{\infty} \Phi_k(t) = \prod_{k=r}^{\infty} \frac{\sin^2(m_k t / m_{r,k})}{(m_k^2 t / m_{r,k}) \sin(t / m_{r,k})}.$$

The function $y_r(x)$ satisfies the system of functional-differential equations

$$y'_r(x) = 2 \sum_{k=1}^{2m_r} (-1)^{\lfloor \frac{k-1}{m_r} \rfloor} y_{r+1}(x_{k,r}), \quad r = 1, 2, 3, \dots,$$

where

$$x_{k,r} = 2m_r x + 2m_r - 2k + 1, \quad x \in R^1, \quad k = \overline{1, 2m_r}.$$

The function $\pi_m(x)$ is defined as

$$\pi'_m(x) = a [\pi_m(x_1(m)) + \sum_{k=2}^{2m-1} (-1)^k \pi_m(x_k(m)) - \pi_m(x_{2m}(m))],$$

$$m = 3, 4, 5, \dots,$$

where

$$x_k(m) = 2mx + 2m - 2k + 1, \quad x \in R^1, \quad k = \overline{1, 2m}.$$

As in the case of the function $up_m(x)$, fast algorithms for evaluating these functions exist [4].

4. FRACTAL FUNCTIONS

4.1. THE DARBOUX FUNCTION.

In spite of the fact that the term «fractal» was introduced by Mandelbrot only in 1975, examples of self-similar functions were known earlier. In 1872 Darboux generalized the Hankel function and constructed his original nowhere differentiable function

$$f(x) = \sum_{n=1}^{\infty} \frac{\sin[(n+1)!x]}{n!}. \quad (1)$$

Later on, he obtained the following expression:

$$\varphi(x) = \sum_{n=1}^{\infty} \frac{f(a_n b_n x)}{a_n}, \quad (2)$$

where a_n and b_n are some real-valued sequences; $f(x)$ is a continuous bounded together with its second derivative function. If the sequences $\{a_n\}$ and $\{b_n\}$ are chosen so that, at fixed k ,

$$\lim_{n \rightarrow \infty} \frac{a_n}{a_{n+1}} = 0,$$

$$\lim_{n \rightarrow \infty} \frac{a_1 b_1^2 + a_2 b_2^2 + \dots + a_{n-k} b_{n-k}^2}{a_n} = 0,$$

then series (2) everywhere converges to a some continuous function $\varphi(x)$. If $b_n = n + 1$, $k = 3$, and $f(x) = \sin x$, then expression (2) coincides with (1). The plot of function (1) is presented on Fig. 2.

4.2. THE BESICOVITCH FUNCTION.

This function is an example of nowhere differentiable continuous function. Its construction procedure consists of the following stages. At the first stage, the interval of length $2a$ is constructed. Then, because this function is symmetrical with respect to the point a , it is enough to

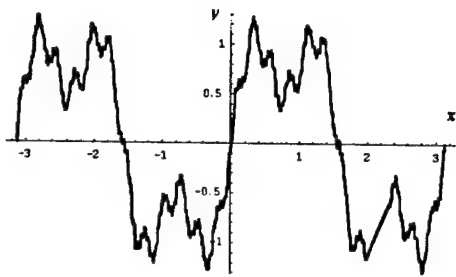


Fig. 2. The Darboux function

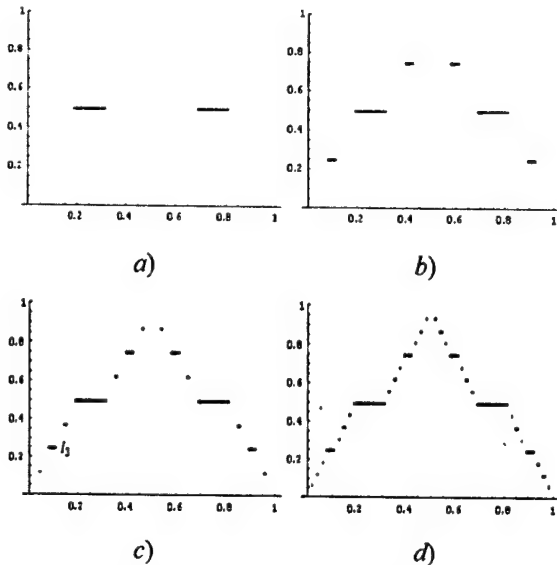
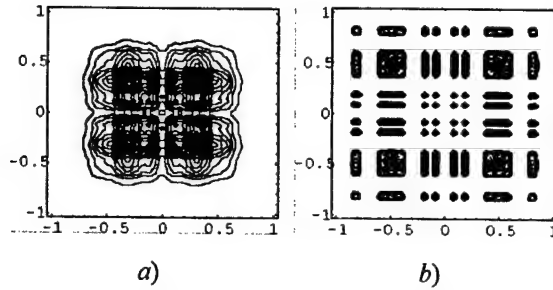


Fig. 3. The first four iterations of the Besicovitch function

construct it on the interval $(0, a)$. Later on, we construct the interval of length $l_1 = a/4$ in the central part of this interval. The interval $(0, a)$ is divided by the segment l_1 onto two equal parts; new intervals of length $l_2 = a/2^4$ are placed at their centers. Thus, we obtain four equal intervals with segments of lengths $l_3 = a/2^6, \dots, l_i = a/2^{2i}$ at their centers. As a result, the infinite set of intervals l_1, l_2, l_3, \dots , is constructed on the base of the interval OC ; their join L is an everywhere dense set of total length $a/2$. A continuous function constructed in this way is nowhere differentiable. Its plot after the first four iterations is presented on Fig. 3.

5. EXAMPLES OF ANTENNA ARRAYS BASED ON THE KRAVCHENKO-DARBOUX AND KRAVCHENKO-BESICOVITCH FUNCTION

Consider some examples of antenna arrays with current distributions I_{nm} corresponding to the Kravchenko-Darboux and Kravchenko-Besicovitch function. Fig. 4 shows plots of the functions $up_1(x, y)D(x, y)$ and $up_3(x, y)Bez(x, y)$.

Fig. 4. Plots of the functions $up_1(x, y)D(x, y)$ (a) and $up_3(x, y)Bez(x, y)$ (b)

6. CONCLUSION

Fig. 4 and Table 1 present plots and main physical parameters (RP, directivity) of 128-element fractal arrays constructed on the base of combinations of the synthesized Kravchenko-Darboux and Kravchenko-Besicovitch functions with spacing $d_x = d_y = \lambda/2$ between elements, for $\theta_0 = 90^\circ$.

The following designations are introduced in the table: L_s is the aperture mean square width; ξ_{\max} is the sidelobe level. Analysis of these parameters shows that arrays based on the aforementioned fractal current distributions have lower values of aperture efficiency in comparison with arrays with smooth distributions. The aperture efficiency values depend on the form of a fractal function (for example, arrays on the base of the Darboux function possess greater values of efficiency).

This effect is caused by the fact that fractal current distributions have large numbers of maximums and minimums and their integration yields low aperture efficiency. Since the obtained arrays are less sensitive to separate elements currents, they (especially those based on the Kravchenko-Besicovitch function) may be considered non-equally-spaced, with large numbers of excluded elements. Their analysis becomes to be more complicated but their aperture efficiency increases sufficiently.

Non-equally-spaced arrays have small values of L_s and allows one to enlarge the spacing $d > \lambda/2$, i.e., additionally, without increasing the number of radiators, to increase directivity and to narrow down the main lobe width. This effect is necessary for antennas with *electrical scanning*.

Table 1. Physical parameters of fractal antenna arrays

Function	L_s	Directivity, dB	ξ_{\max} , dB
$Bez(x, y)$	2.29	48.28	-8.68
$Bez(x, y)y_6(x, y)$	2.32	48.24	-8.11
$Bez(x, y)up_6(x, y)$	1.59	46.49	-12.58
$Bez(x, y)\pi_5(x, y)$	2.19	47.56	-8.41
$D(x, y)$	2.83	51.29	-15.29
$D(x, y)\pi_5(x, y)$	2.50	50.04	-11.44

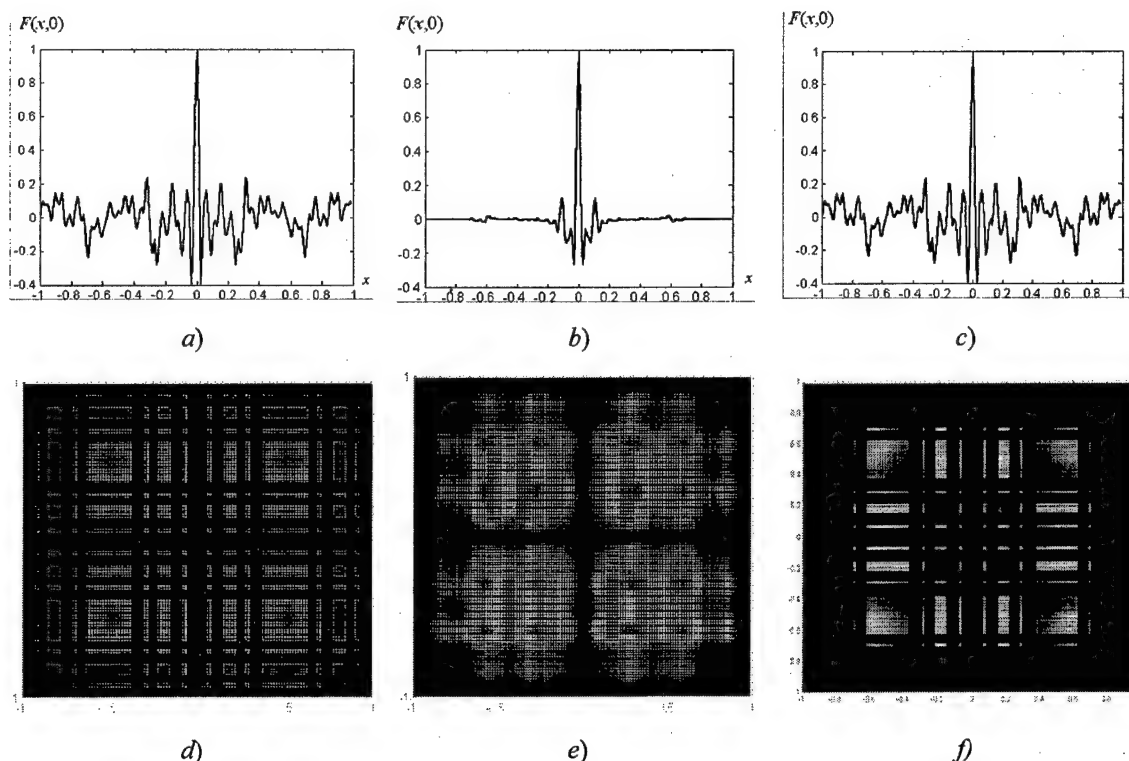


Fig. 5. Cross-sections of the RP by the plane Ox and current distributions $up_6(x,y)Bez(x,y)$ (a, d), $D(x,y)\pi_5(x,y)$ (b, e), and $\pi_5(x,y)Bez(x,y)$ (c, f) in the 128-element array

REFERENCES

1. Mandelbrot B. B. *Fractals: form, chance and dimension*. San Francisco: Freeman, 1977.
2. Werner D. H., Haupt R. L., Werner P. L. *Fractal Antenna Engineering: The Theory and Design of*
3. *Fractal Antenna Arrays*, IEEE Antennas and Propagation Magazine, vol. 41, no.5, pp. 37-58.
3. Kravchenko V. F. *Lectures on the Theory of Atomic Functions and Their Some Applications*, Moscow: Radiotekhnika, 2003.

METHODS FOR MATHEMATICAL MODELING OF FRACTAL ANTENNA ARRAYS

Vladimir M. Masyuk

Bauman Moscow State Technical University
5 Vtoraya Baumanskaya st., Moscow, 107005, Russia
Phone: +7 (095) 263 66 40, E-mail: <masyuk77@hotmail.ru>

Abstract

One of the methods for constructing fractal antenna arrays, based on ideas of fractal geometry is considered. General algorithms for synthesis of fractal arrays are presented. Results of using the atomic functions in algorithms of ring fractal antenna array analysis and synthesis are shown.

Keywords: antenna arrays; antenna theory; antenna radiation patterns; low-sidelobe antennas; fractals; atomic functions; circular subarray; linear array.

1. INTRODUCTION

Let us consider one of the methods for constructing the mathematical model of fractal antenna arrays, based on the use of generating concentric circular ring arrays with centers located at distances r_m from the origin.

The generating array factor for the concentric circular ring array may be expressed in the form [1]

$$F(\theta, \varphi) = \sum_{m=1}^M \sum_{n=1}^{N_m} I_{mn} e^{j\psi_{mn}(\theta, \varphi)}, \quad (1)$$

where $\psi_{mn}(\theta, \varphi) = kr_m \sin \theta \cos(\varphi - \varphi_{mn}) + \alpha_{mn}$, $k = 2\pi/\lambda$ is the wave number, M is the total number of concentric rings, N_m is the total number of elements on the m th ring, r_m is the m th ring radius, I_{mn} is the excitation current amplitude of the n th element on the m th ring located at $\varphi = \varphi_{mn}$, and α_{mn} is the excitation current phase of the n th element on the m th ring located at $\varphi = \varphi_{mn}$.

The technique for constructing such fractal arrays is based on the results of [1-3] and is sufficiently flexible in comparison with other approaches. It ensures obtaining required results in fractal antenna array design without complicated mathematical algorithms.

A wide variety of simple recursive schemes may be constructed using expression (1). The fractal array factor for a particular stage of growth P may be derived directly from (1) by a procedure similar to that outlined in [2, 3]. Thus, the resulting expression for the array factor was found to be

$$F_P(\theta, \varphi) = \prod_{p=1}^P \left\{ \sum_{m=1}^M \sum_{n=1}^{N_m} I_{mn} e^{j\delta^p \psi_{mn}(\theta, \varphi)} \right\}, \quad (2)$$

where δ represents the scaling or expansion factor associated with the fractal array.

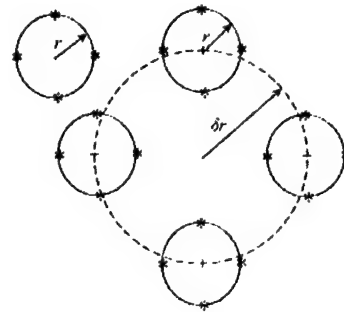


Fig. 1. Elements of stages 1 and 2 of a circular array of radius r

Let us present main stages of constructing fractal arrays defined by (1). Consider a unit element of a circular ring array of radius r (Fig. 1). It can be interpreted as a generating subarray of level 1 for the fractal array. The next stage of the construction is also represented on Fig. 1. On the first stage of the construction process, a four-element generating subarray with factor δ must be obtained. The algorithm has the following form: at the second stage, each of the elements of the array is replaced by an exact copy of the original unscaled four-element circular subarray generator. The entire process is then repeated in a recursive fashion, until the desired stage of growth for the fractal array is reached.

This process is convenient for analysis and modeling. It allows us to express the fractal array factor (2) in the following normalized form:

$$F_P(\theta, \varphi) = \prod_{p=1}^P \left(\frac{\sum_{m=1}^M \sum_{n=1}^{N_m} I_{mn} e^{j\delta^p \psi_{mn}(\theta, \varphi)}}{\sum_{m=1}^M \sum_{n=1}^{N_m} I_{mn}} \right). \quad (3)$$

Taking the magnitude of both sides of Eq. (3) leads to

$$|F_P(\theta, \varphi)| = \prod_{p=1}^P \left| \frac{\sum_{m=1}^M \sum_{n=1}^{N_m} I_{mn} (e^{j\delta^{p-1} \psi_{mn}(\theta, \varphi)})}{\sum_{m=1}^M \sum_{n=1}^{N_m} I_{mn}} \right|, \quad (4)$$

which has a corresponding representation in terms of decibels given by

$$|F_P(\theta, \varphi)|_{\text{db}} = 20 \sum_{p=1}^P \lg \left| \frac{\sum_{m=1}^M \sum_{n=1}^{N_m} I_{mn} (e^{j\delta^{p-1} \psi_{mn}(\theta, \varphi)})}{\sum_{m=1}^M \sum_{n=1}^{N_m} I_{mn}} \right|. \quad (5)$$

Another unique property of Eq. (3) is the fact that the conventional co-phased excitation [2],

$$\alpha_{mn} = -kr_m \sin \theta_0 \cos(\varphi_0 - \varphi_{mn}), \quad (6)$$

where θ_0 and φ_0 are the desired main-beam steering angles, can be applied at the generating subarray level.

To see this, we recognize that the position of the main beam produced by Eq. (3) is independent of the stage of growth P (i.e., when $\theta = \theta_0$ and $\varphi = \varphi_0$), since it corresponds to a value of $\psi_{mn} = 0$.

Consider some examples of different recursively generated arrays discussed in detail in [1].

These arrays have in common the fact that they may be constructed via a concentric circular ring subarray generator of the type considered in the previous section. Hence, the mathematical expressions that describe the radiation patterns of these arrays are all special cases of Eq. (3).

2. LINEAR ARRAYS

Suppose we consider the two-element concentric circular subarray generator with a radius of $r = \lambda/4$. If the excitation-current amplitudes for this two-element generating subarray are assumed to be unity, then the general fractal array factor expression given in Eq. (3) will reduce to the form

$$F_P(\varphi) = \frac{1}{2^P} \prod_{p=1}^P \sum_{n=1}^2 e^{j\delta^{p-1} \left[\frac{\pi}{2} \cos(\varphi - \varphi_n) + \alpha_n \right]}, \quad (7)$$

where, without loss of generality, we have set $\theta = 90^\circ$ and

$$\varphi_n = (n-1)\pi, \quad (8)$$

$$\alpha_n = -\frac{\pi}{2} \cos(\varphi_0 - \varphi_n). \quad (9)$$

Substituting Eqs. (8) and (9) into Eq. (7) results in a simplified expression for the fractal array factor, given by

$$F_P(\varphi) = \prod_{p=1}^P \cos \left[\delta^{p-1} \frac{\pi}{2} (\cos \varphi - \cos \varphi_0) \right]. \quad (10)$$

If we choose an expansion factor equal to one (i.e., $\delta = 1$), the Eq. (9) may be written as

$$F_P(\varphi) = \cos^P \left[\delta^{p-1} \frac{\pi}{2} (\cos \varphi - \cos \varphi_0) \right]. \quad (11)$$

This represents the array factor for a uniformly spaced ($d = \lambda/2$) linear array with a binomial current distribution, where the total number of elements, N_P for a given stage of growth, P , is $N_P = P + 1$.

The general rule in the case of overlapping array elements is to replace each of those elements by a single element that has a total excitation-current amplitude equal to the sum of all the individual excitation-current amplitudes.

For example, we consider the case when $\delta = 3$. This particular case results in the family of the triadic Cantor arrays which (the Cantor sets) were considered in [1, 3]. The total number of elements in these sets is $N_P = 3^P$, and these elements have equal excitation-current amplitudes I_{mn} corresponding to uniform distributions, i.e., $I_{mn} = 1$. The resulting arrays are equally-spaced. Their array factors have the form

$$F_P(\varphi) = \prod_{p=1}^P \cos \left[3^{p-1} \frac{\pi}{2} (\cos \varphi - \cos \varphi_0) \right]. \quad (12)$$

The latter expression follows directly from Eq. (11) when $\delta = 3$.

3. PLANAR SQUARE ARRAYS

Consider an example of planar square arrays that can be constructed using the uniformly-excited four-element circular subarray generator shown in Fig. 2.

The radius of the circular array is chosen to be $r = \lambda/2\sqrt{2}$, in order to ensure that the spacing between the elements of the circumscribed square array would be a half-wavelength (i.e., $d = \lambda/2$). It can be shown that the general expression for the fractal array factor given in Eq. (2) reduces to

$$F_P(\theta, \varphi) = \frac{1}{4^P} \prod_{p=1}^P \sum_{n=1}^4 e^{j\delta^{p-1} \left[\frac{\pi}{\sqrt{2}} \sin \theta \cos(\varphi - \varphi_n) + \alpha_n \right]}, \quad (13)$$

where $\varphi_n = (n-1)\frac{\pi}{2}$, $\alpha_n = -\frac{\pi}{\sqrt{2}} \sin \theta_0 \cos(\varphi_0 - \varphi_n)$.

If we define

$$\psi_n(\theta, \varphi) = \frac{\pi}{\sqrt{2}} [\sin \theta \cos(\varphi - \varphi_n) - \sin \theta_0 \cos(\varphi_0 - \varphi_n)],$$

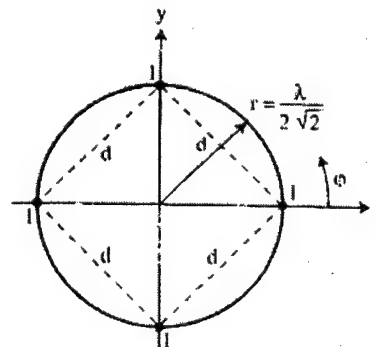


Fig. 2. The geometry for a four-element generating subarray with $r = \lambda/2\sqrt{2}$

then Eq. (13) may be rewritten in the convenient form

$$F_P(\theta, \varphi) = \frac{1}{4^P} \prod_{p=1}^P \sum_{n=1}^N e^{j\delta^{p-1} \psi_n(\theta, \varphi)},$$

where $\psi_n(\theta_0, \varphi_0) = 0$.

Consider the case when $\delta = 1$, i.e.,

$$F_P(\theta, \varphi) = \left[\frac{1}{4} \sum_{n=1}^4 e^{j\psi_n(\theta, \varphi)} \right]^P.$$

The resulting array is a family of square arrays obtained with uniformly spaced elements ($d = \lambda/2$) and binomially distributed currents. For a given stage of growth P , the corresponding array will have a total of $N_P = (P+1)^2$ elements.

The radiation patterns for these arrays have no sidelobes, which is a feature characteristic of binomial arrays [4].

At $\delta = 3$, we get the expression for the Sierpinski carpet [1, 3]. The generating subarray for this Sierpinski carpet consists of a uniformly excited and equally spaced ($d = \lambda/2$) 3×3 planar array with the center element removed. It may also be represented by two concentric four-element circular arrays, i.e.,

$$F_P(\theta, \varphi) = \frac{1}{8^P} \prod_{p=1}^P \sum_{m=1}^M \sum_{n=1}^4 e^{j3^{p-1} \psi_{mn}(\theta, \varphi)},$$

where

$$\begin{aligned} \psi_{mn}(\theta, \varphi) &= \sqrt{m}\pi [\sin \theta \cos(\varphi - \varphi_{mn}) - \\ &\quad - \sin \theta_0 \cos(\varphi_0 - \varphi_{mn})], \\ \varphi_{mn} &= \left(\frac{mn-1}{m} \right) \frac{\pi}{2}, N_P = 2^{3P}. \end{aligned}$$

4. OTHER TYPES OF PLANAR ARRAYS

4.1. PLANAR TRIANGULAR ARRAYS

This three-element circular array of radius $r = \lambda/2\sqrt{3}$ can also be interpreted as an equilateral triangular array, with half-wavelength spacing on a side. The fractal array factor associated with this triangular generating subarray is

$$F_P(\theta, \varphi) = \frac{1}{3^P} \prod_{p=1}^P \sum_{n=1}^N e^{j\delta^{p-1} \left[\frac{\pi}{\sqrt{3}} \sin \theta \cos(\varphi - \varphi_n) + \alpha_n \right]}, \quad (14)$$

where $\varphi_n = (n-1)\frac{2\pi}{3}$, $\alpha_n = -\frac{\pi}{\sqrt{3}} \sin \theta_0 \cos(\varphi_0 - \varphi_n)$.

The second category of triangular arrays is shown in Fig. 3. This generating subarray consists of two three-element concentric circular arrays, with radii $r_1 = \lambda/2\sqrt{3}$ and $r_2 = \lambda\sqrt{3}$. The excitation current amplitudes on the inner three-element array is twice as large as those on the outer three-element array. The dimensions of this generating subarray were chosen in such a way that it forms a non-uniformly excited six-element triangular array with half-wavelength spacing between its elements (i.e., $d = \lambda/2$).

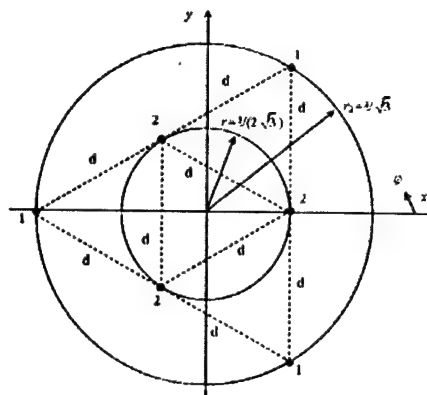


Fig. 3. The geometry for a six-element generating subarray

Expression for the fractal array factor in this case may be expressed as

$$F_P(\theta, \varphi) = \frac{1}{9^P} \prod_{p=1}^P \sum_{m=1}^2 \sum_{n=1}^3 I_{mn} e^{j\delta^{p-1} [kr_m \sin \theta \cos(\varphi - \varphi_{mn}) + \alpha_{mn}]}, \quad (15)$$

where $I_{mn} = 2/m$, $kr_m = \frac{m\pi}{\sqrt{3}}$, $\varphi_{mn} = (2n+m-3)\frac{\pi}{3}$, $\alpha_{mn} = -kr_m \sin \theta_0 \cos(\varphi_0 - \varphi_{mn})$, or

$$F_P(\theta, \varphi) = \frac{1}{9^P} \prod_{p=1}^P \sum_{m=1}^2 \sum_{n=1}^3 I_{mn} e^{j\delta^{p-1} \psi_{mn}(\theta, \varphi)},$$

if

$$\begin{aligned} \psi_{mn}(\theta, \varphi) &= \frac{m\pi}{\sqrt{3}} [\sin \theta \cos(\varphi - \varphi_{mn}) - \\ &\quad - \sin \theta_0 \cos(\varphi_0 - \varphi_{mn})]. \end{aligned}$$

These arrays have non-uniform current distributions, therefore, low-sidelobe level arrays can be obtained. Thus, the sidelobe level of -20 dB can be reached at large P .

4.2. HEXAGONAL ARRAYS

These arrays are becoming increasingly popular, especially for their applications in the area of wireless communications. The standard hexagonal arrays are formed by placing elements in an equilateral triangular grid with spacing of $d = \lambda/2$. The resulting expression for the array factor, in the normalized form, is given by

$$\begin{aligned} F_p(\theta, \varphi) &= \frac{I_0 + \prod_{p=1}^P \sum_{m=1}^M \sum_{n=1}^N I_{pnm} e^{j[kr_{pm} \sin \theta \cos(\varphi - \varphi_{pmn}) + \alpha_{pmn}]} }{I_0 + \prod_{p=1}^P \sum_{m=1}^M \sum_{n=1}^N I_{pnm}}, \end{aligned}$$

where $r_{pm} = d\sqrt{p^2 + (m-1)^2 - p(m-1)}$,

$$\varphi_{pmn} = \cos^{-1} \left[\frac{r_{pm}^2 + d^2 p^2 (m-1)^2}{2r_{pm} dp} \right] + \frac{n\pi}{3},$$

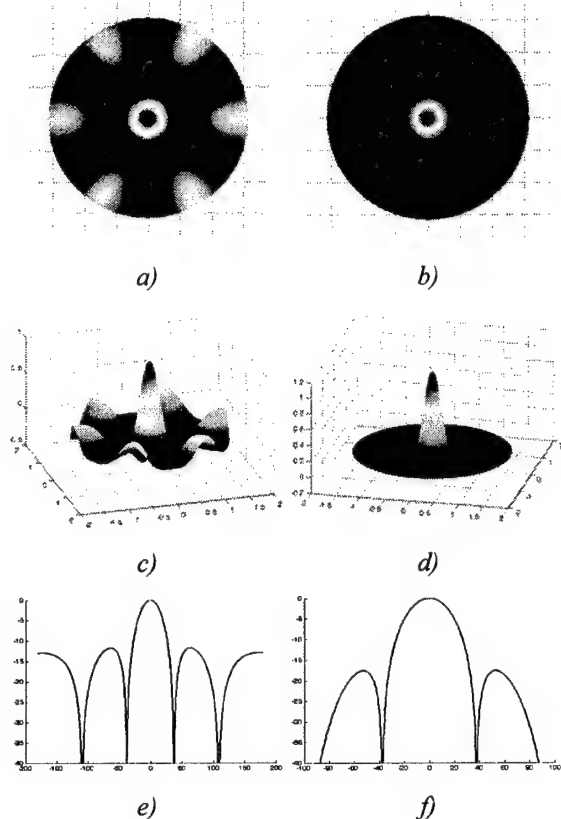


Fig. 4. Radiation patterns for the triangular antenna subarray with uniformly distributed currents (a, c, e) and with currents distributed by the law $I_{mn}(\theta, \varphi) = \text{up}(\theta)$, $P = 3$, $\delta = 2$

$$\alpha_{pmn} = -kr_{pm} \sin \theta_0 \cos(\varphi_0 - \varphi_{pmn}),$$

and P is the number of concentric hexagons in the array. Hence, the total number of elements contained in an array with P hexagons is $N_P = 3P(P + 1) + 1$.

Hexagonal arrays have some elements missing, i.e., they are thinning. This is a potential advantage from the design point of view, since they may be realized with fewer elements. Another advantage of these arrays is that they possess low sidelobe levels at $\varphi = 90^\circ$. Finally, it should be noted that the compact product form of the array factor for some particular cases. This offers a significant advantage in terms of computational efficiency, especially for large arrays, and may be exploited to develop rapid beam-forming algorithms.

5. FRACTAL SUBARRAYS WITH NON-UNIFORMLY DISTRIBUTED CURRENTS. ATOMIC FUNCTIONS.

Another way for decreasing sidelobe levels is the use of non-uniform amplitude distributions. Here, in most cases, we cannot apply effective computational algorithms developed by using ideas of fractal geometry.

Table 1. Main parameters of antenna arrays

Current distribution	Main lobe width at the 3 dB level	Sidelobe level, dB	Directivity, dB
Ring array ($P = 3$, $\delta = 2$)			
Uniform	13.2	-25.6	61.85
$\text{up}(x)$	13.5	-32.2	63.17
Triangular array ($P = 3$, $\delta = 2$)			
Uniform	14	-11.75	54.7
$\text{up}(x)$	16	-17.61	59.8
Triangular array (2nd variant) ($P = 3$, $\delta = 2$)			
Uniform	5.7	-16.7	74.05
$\text{up}(x)$	5.72	-16.9	77.56

However, using some types of distributions, we can combine both approaches.

We shall use atomic functions for forming current distributions I_{mn} ; these functions, namely, $\text{up}(x)$, $\text{up}_m(x)$, $y_r(x)$, and $\pi_k(x)$, were efficient in the design of planar antenna arrays [3]. All of them are the solutions to functional-differential equations but they can easily be evaluated by using fast iterative algorithms [5].

Consider some examples. Evaluations were carried out according to formulas (2)–(6), (7), and (13)–(15) for fractal subarrays with different geometry. Let $I_{mn}(\theta, \varphi) = \text{up}(\varepsilon\theta)$. Using the non-uniform current distribution, we complicate the algorithm but significantly decrease the sidelobe level (from -12 dB to -17 dB). Here, the main lobe width widens. Changing the parameter ε , one can obtain a variety of intermediate results.

REFERENCES

1. Werner D. H., Haupt R. L., Werner P. L. *Fractal Antenna Engineering: The Theory and Design of Fractal Antenna Arrays*, IEEE Antennas and Propagation Magazine, vol. 41, no.5, pp. 37–58.
2. Ma M. T. *Theory and application of antenna*, New York, Wiley, 1974.
3. Kravchenko V. F., Masyuk V. M. *Antennas* (in Russian).
4. Stutzman W. L., and Thiele G. A., *Antenna Theory*, New York, Wiley, 1997.
5. Kravchenko V. F. *Lectures on the Theory of Atomic Functions and Their Some Applications*, Moscow: Radiotekhnika, 2003.

THE METHOD FOR APPROXIMATION OF A TWO-DIMENSIONAL FIELD DISTRIBUTION BY ATOMIC FUNCTIONS

Michael V. Golubin

Bauman Moscow State Technical University,
5 Vtoraya Baumanskaya street, Moscow, 107005, Russia
Phone: +7 (095) 263 66 40, e-mail: <michael_golubin@inbox.ru>

Abstract

The method for approximation by atomic functions of a two-dimensional antenna aperture current amplitude distribution is proposed.

Keywords: antenna arrays; antenna theory; antenna radiation patterns; low-sidelobe antennas; atomic functions; circular subarray; linear array.

1. INTRODUCTION

According to [1-4], we shall present a method for two-dimensional antenna aperture current amplitude approximation by atomic functions (AFs).

2. MAIN PHYSICAL PARAMETERS OF AN ANTENNA

The following physical parameters were used in the numerical experiment [3,4]:

- Radiation pattern maximum

$$F_m \equiv F(0) = \omega \int_{-1/2}^{1/2} g(x') dx';$$

- Total radiated power

$$P_{rad} \equiv \int_{-\infty}^{\infty} |F(u)|^2 du = \int_{-\omega/2}^{\omega/2} |g(x)|^2 dx;$$

- Aperture efficiency

$$\eta_x = \frac{|F_m|^2}{\int_{-\infty}^{\infty} |F(u)|^2 du} = \frac{\left| \int_{-1/2}^{1/2} g(x') dx' \right|^2}{\int_{-1/2}^{1/2} |g(x')|^2 dx'};$$

- Noise beam width (radians)

$$\theta_n = \frac{\lambda \int_{-\infty}^{\infty} |F(u)|^2 du}{\omega |F_m|^2} = \frac{\lambda}{\eta_x \omega};$$

- Noise aperture width (in units of coordinate x)

$$\omega_n = \frac{\omega \int_{-1/2}^{1/2} |g(x')|^2 dx'}{|g_m(x')|^2};$$

- Ratio between the curve steepness in the center of the beam and the slope of a linear odd amplitude distribution

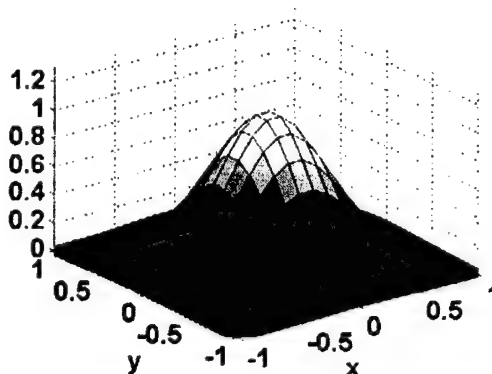


Fig. 1. Two-dimensional current amplitude distribution $fup_1^4(x) \cdot fup_1^4(y)$

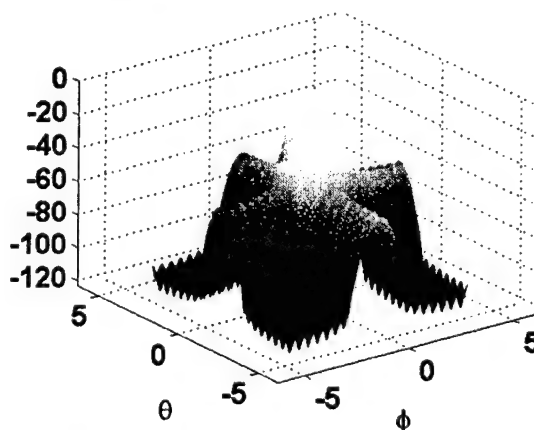


Fig. 2. Radiation pattern corresponding to the distribution shown on Fig. 1

$$K_r = \sqrt{12} \int_{-1/2}^{1/2} x' \cdot g(x') dx' / \left[\int_{-1/2}^{1/2} |g(x')|^2 dx' \right]^{1/2};$$

- The first sidelobe level of the RP (dB);

Let us compare two-dimensional amplitude distributions of Kravchenko in the antenna aperture [4] with the following classical amplitude distributions:

- the cosine distribution

$$G_n(x, y) = \cos^n(\pi x) \cos^n(\pi y);$$

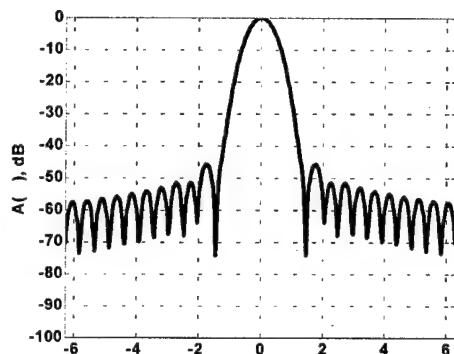


Fig. 3. RP corresponding to the Kravchenko-Bessel amplitude distribution ($\text{fup}_2^2(x) J_0^2(x)$)

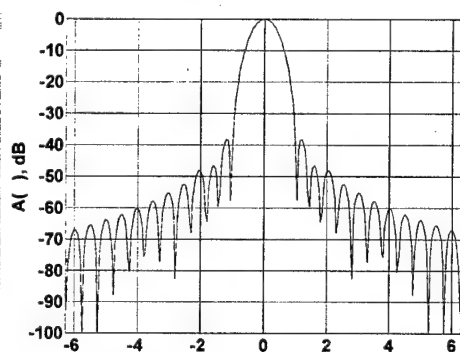


Fig. 4. RP corresponding to the Kravchenko-Bernstein amplitude distribution ($\text{fup}_2(x) \text{br}(x)$)

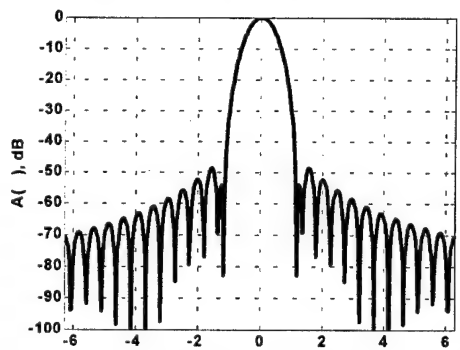


Fig. 5. RP corresponding to the Kravchenko-Bernstein amplitude distribution ($\text{fup}_4^2(x) \text{br}(x)$)

- the truncated Gaussian distribution

$$G_n(x) = \exp(-1,382(nxy)^2);$$

- the Taylor even distribution with the first sidelobe levels equal to 20, -25, -30, -35, -40, and -45 dB.

3. COMPARISON OF THE CLASSICAL TWO-DIMENSIONAL AMPLITUDE DISTRIBUTIONS WITH THE KRAVCHENKO AMPLITUDE DISTRIBUTIONS

3.1. TWO-DIMENSIONAL COSINE DISTRIBUTIONS AND KRAVCHENKO DISTRIBUTIONS.

Results of numerical experiments show that the new Kravchenko distributions exceed known ones with respect to main parameters. At comparable sidelobe levels, they possess better values of aperture efficiency and greater RP maximums. The sidelobe level of the RP generated by the Kravchenko-Bessel function $\text{fup}_2^2(x) J_0^2(x) \text{fup}_2^2(y) J_0^2(y)$ is -46 dB and corresponding aperture efficiency is equal to 0.41; the two-dimensional distribution $\cos^4(\pi x) \cos^4(\pi y)$ forms the RP with sidelobe level -47 dB and aperture efficiency equals 0.26. Analogous physical situation is observed for other new distributions.

The RP maximum for the Kravchenko-Bernstein distribution $\text{fup}_2(x) \text{br}(x) \text{fup}_2(y) \text{br}(y)$ equals 0.25 at the sidelobe level -38 dB; the RP for the distribution $\cos^4(\pi x) \cos^4(\pi y)$ has maximum 0.07 at the sidelobe level -47 dB.

3.2. TWO-DIMENSIONAL GAUSSIAN DISTRIBUTIONS AND KRAVCHENKO DISTRIBUTIONS.

Numerical experiments and analysis of physical results showed that the new Kravchenko distributions do not concede known ones with respect to main parameters. They possess the same or even more radiated power at the analogous level of the first sidelobe. For instance, the Kravchenko distribution $\text{fup}_4^2(x) \text{br}(x) \text{fup}_4^2(y) \text{br}(y)$ RP has maximum 0.21 at the sidelobe level -54 dB. At the

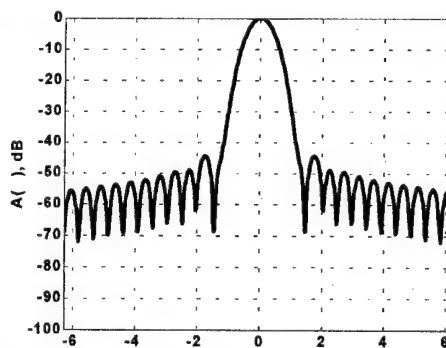


Fig. 6. RP corresponding to the Kravchenko-Bessel amplitude distribution ($\text{fup}_2^2(x) J_0^2(x)$)

same time, the RP of the distribution $G_{3,2}(x)G_{3,2}(y)$ has the first sidelobe level -46 dB and the same value of the RP maximum.

The Kravchenko distribution $fup_2^2(x)J_0(x)fup_2^2(y)J_0(y)$ RP maximum is 0.23 and the first sidelobe level is -45 dB.

3.3. TWO-DIMENSIONAL TAYLOR DISTRIBUTIONS AND KRAVCHENKO DISTRIBUTIONS.

Taylor [5] proposed a new class of current distributions in a linear radiator, widely used in antenna theory. The essence of these distributions is in the fact that they generate RPs with equal sidelobe levels and main lobe having the least possible width from all equiphase aperture distributions. It should be noted that, unlike the Kravchenko amplitude distributions based on AFs, the Taylor expressions are heuristic. Considering parameters of the Taylor two-dimensional field distributions, one can note that they possess sufficient RP maximums at the given sidelobe level and the Kravchenko distributions are close to them with respect to physical parameters. However, the latter are more convenient in engineering computations.

For example, the RP corresponding to the distribution $(fup_1^2(x)J_0^2(x)fup_1^2(y)J_0^2(y))$ has the sidelobe level -37 dB, i.e., significantly greater than that of the similar Taylor distribution $(T_{35}(x)T_{35}(y))$. At the same time, the new distribution RP maximum is 0.29 and the Taylor distribution generates a RP with maximum 0.36. The Kravchenko-Bessel distributions $(fup_1^2(x)J_0^4(x)fup_1^2(y)J_0^4(y))$ form a RP with the sidelobe level 44 dB and maximum 0.25. Corresponding values for the Taylor distribution $T_{45}(x)T_{45}(y)$ are -45 dB and 0.29, respectively. The total radiated power of the Kravchenko distribution $\Xi_3(x)\Xi_3(y)$ at the sidelobe level -45 dB is 0.22 against 0.15 of the distribution $T_{45}(x)T_{45}(y)$.

4. CONCLUSION

Physical analysis of numerical experiments showed that the new method of approximation based on amplitude distributions of Kravchenko is efficient and reliable. It is not worse than techniques based on the classical distributions and even exceeds them with respect to some parameters. Such an approach is of definite theoretical and practical interest for computation of the aperture current distribution and for synthesis of antennas by their given RPs.

REFERENCES

1. Kravchenko V. F., Lectures on the Theory of Atomic Functions and Their Some Applications, Moscow: Radiotekhnika, 2003. (in Russian)
2. Kravchenko V. F., The New Method for Approximation of the Antenna Aperture Current Amplitude Distribution, Doklady RAN, 2003, vol. 388, no.4, pp. 472-476.

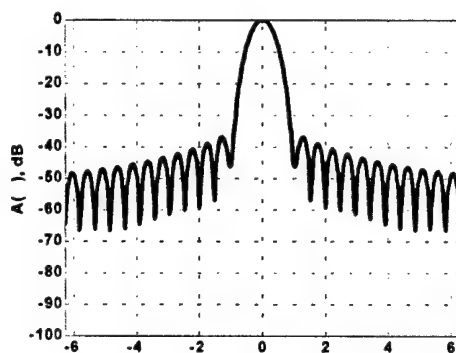


Fig. 7. RP corresponding to the Kravchenko-Bessel amplitude distribution $(fup_1^2(x) J_0^2(x))$

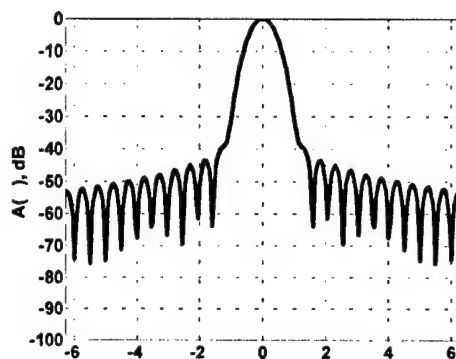


Fig. 8. RP corresponding to the Kravchenko-Bessel amplitude distribution $fup_1^2(x) J_0^4(x)$

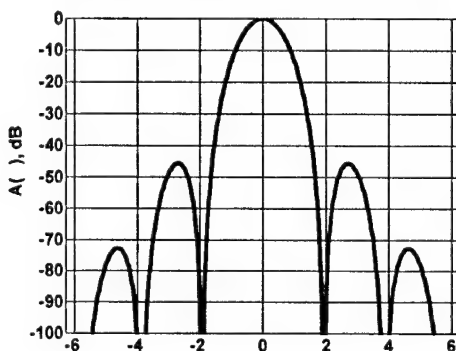


Fig. 9. RP corresponding to the Kravchenko amplitude distribution $(\Xi_3(x))$

3. Zelkin E. G. and Kravchenko V. F., Modern Methods of Approximation in Antenna Theory. 1. Problems of Antenna Synthesis and New Methods for Their Solution, Moscow: Radiotekhnika, 2002. (in Russian)
4. Kravchenko V. F. and Golubin M. V., Spectral Properties of New Weighting Functions in Digital Signal Processing, Electromagnetic Waves and Electronic Systems, 2002, vol. 7, no.2, pp.25-37.
5. Barton D., Vard G. Handbook on radiolocation measurements / Trans. from English. — M.: Sov. Radio, 1976.
6. Balanis C. A., Antenna Theory. Analysis and Design, New York: John Wiley and Sons., Inc, 1997.

REFLECTOR AND LENS ANTENNAS

ANALYSIS OF PARTIALLY DIELECTRIC-LOADED COAXIAL HORN ANTENNAS

F. F. Dubrovka, O. O. Krupnov, Ya. O. Rospopa

National Technical University of Ukraine "Kiev Polytechnic Institute"
Department of Theoretical Fundamentals of Radioengineering
<dubrovka@tera.kiev.ua>

Abstract

The paper presents a mode matching solution for a hybrid-mode dielectric-loaded coaxial horn, which is a generalized structure for axially symmetrical types of feeds such as smooth-wall horns, corrugated horns, disc-o-cone antennas and partially dielectric-loaded horns.

Keywords: non-uniform dielectric loaded coaxial horn, hybrid-mode feeds, mode-matching technique analysis.

1. INTRODUCTION

In radioelectronic systems with polarization signal processing, in particular, in satellite telecommunication systems with polarization diversity corrugated horn are widely used. They differ from smooth horns by low level crosspolar radiation and low sidlobes [1,2]. However corrugated horns are limited to a continuous bandwidth performance of 2.4:1 [2], because of presence of the fixed geometrical periodicity of corrugations. Moreover corrugated horns are technologically complex and expensive.

An alternative to corrugated horns can be smooth-wall horn with non-uniform (partially) dielectric filling. It allows to expand considerably an operating bandwidth due to absence of resonant elements inside the structure, e.g. in [3] a bandwidth ratio 30:1 was achieved. Besides partially dielectric horns are technologically much more simple and cheap. A level of crosspolarization that provide dielectric-loaded horns are the same or even better in a wide bandwidth in comparison with corrugated horns. Besides horns without corrugations can be simply made profiled with smaller longitudinal size without essential deterioration of their characteristics. Certainly all these advantages in a near future will result in increase of popularity of dielectric-loaded horn as feeds for reflector antennas.

In this work a generalized horn with two dielectric layers and metal inner conductor is analyzed. Changing a profile and sizes of the horns and dielectric and an inner conductor it is possible to obtain a great number of particular horn structures, including all known types of corrugated horns, disc-o-cones, profiled horns and horns without a central conductors. Thus the obtained solution and algorithm are suitable for analysis of all these horn antennas.

2. FULL WAVE SOLUTION, NUMERICAL AND EXPERIMENTAL RESULTS

Geometry of the coaxial horn under analysis is shown in Fig. 1.

The horn has exterior and interior conductors and also two dielectric layers. Let's use a letter *e* (*exterior*) for designation of the exterior dielectric layer, and letter *i* (*interior*) to denote the exterior layer.

To obtain a solution of propagation problem the mode matching technique [4] is used. According to this method a horn is divided into a great number of short cylindrical sections with small increment steps. Further at each of junction of the sections, a scattering problem is to be solved. In a result a generalized scattering block matrix of the junction is calculated. The final stage of the method is a procedure of progressively cascading the obtained generalized scattering matrices of all junctions and short regular waveguides in order to obtain the overall generalized scattering matrix of the structure, which allows to calculate distribution of a transverse field at the horn aperture and a reflected field in the horn input.

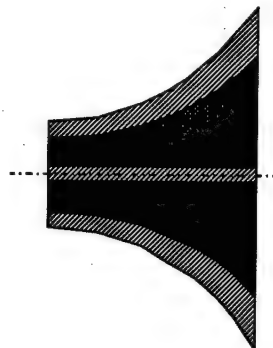


Fig. 1. Profiled partially dielectric-loaded coaxial horn

The matching of modes occurs at each junction of any two sections of regular waveguides and consists in the condition of a continuity of transverse components of fields at the junction. Fixing this condition, we present transverse field at the junction of two sections by a sum of own functions of the left and right sections and then we find a matrix that determines unknown coefficients in both sections, that is the generalized scattering matrix.

In order to determine modes that can propagate in sections of dielectric-loaded cylindrical coaxial waveguides it is necessary to solve the Maxwell equations with proper boundary conditions at all boundaries of the media.

Let's denote the radius of an interior conductor by letter a_i , exterior conductor a_e , a radius of the boundary of the layers – a , parameters of the interior dielectric layer – ϵ_i, μ_i , the exterior layer – ϵ_e, μ_e . As one can see in Fig. 2 three radial discontinuities (boundaries 1,2,3) provide two areas in the waveguide, where the modes can propagate.

In a result, we find the following expressions for all components of the modes in both dielectric layers:

$$\begin{aligned} \dot{E}_z^{i,e} &= (\dot{C}_m^{i,e} J_m(p_{i,e} r) + \dot{D}_m^{i,e} Y_m(p_{i,e} r)) \cos m\varphi \cdot e^{-\gamma z}, \\ \dot{H}_z^{i,e} &= (\dot{A}_m^{i,e} J_m(p_{i,e} r) + \dot{B}_m^{i,e} Y_m(p_{i,e} r)) \sin m\varphi \cdot e^{-\gamma z}, \\ \dot{E}_r^{i,e} &= -\frac{1}{2} \left[\gamma \tilde{p}_{i,e} \left(\dot{C}_m^{i,e} J'_m(p_{i,e} r) + \dot{D}_m^{i,e} Y'_m(p_{i,e} r) \right) + \right. \\ &\quad \left. + \frac{i\omega\mu_{i,e} m}{r} \left(\dot{A}_m^{i,e} J_m(p_{i,e} r) + \dot{B}_m^{i,e} Y_m(p_{i,e} r) \right) \right] e^{-\gamma z} \cos m\varphi \\ \dot{E}_\varphi^{i,e} &= \frac{1}{p_{i,e}^2} \left[\frac{\gamma m}{r} \left(\dot{C}_m^{i,e} J_m(p_{i,e} r) + \dot{D}_m^{i,e} Y_m(p_{i,e} r) \right) + \right. \\ &\quad \left. + i\omega\mu_{i,e} \tilde{p}_{i,e} \left(\dot{A}_m^{i,e} J'_m(p_{i,e} r) + \dot{B}_m^{i,e} Y'_m(p_{i,e} r) \right) \right] e^{-\gamma z} \sin m\varphi \\ \dot{H}_r^{i,e} &= -\frac{1}{p_{i,e}^2} \left[\frac{i\omega\epsilon_{i,e} m}{r} \left(\dot{C}_m^{i,e} J_m(p_{i,e} r) + \dot{D}_m^{i,e} Y_m(p_{i,e} r) \right) + \right. \\ &\quad \left. + \gamma \tilde{p}_{i,e} \left(\dot{A}_m^{i,e} J'_m(p_{i,e} r) + \dot{B}_m^{i,e} Y'_m(p_{i,e} r) \right) \right] e^{-\gamma z} \sin m\varphi \\ \dot{H}_\varphi^{i,e} &= -\frac{1}{p_{i,e}^2} \left[i\omega\epsilon_{i,e} \tilde{p}_{i,e} \left(\dot{C}_m^{i,e} J'_m(p_{i,e} r) + \dot{D}_m^{i,e} Y'_m(p_{i,e} r) \right) + \right. \\ &\quad \left. + \frac{\gamma m}{r} \left(\dot{A}_m^{i,e} J_m(p_{i,e} r) + \dot{B}_m^{i,e} Y_m(p_{i,e} r) \right) \right] e^{-\gamma z} \cos m\varphi \end{aligned} \quad (1)$$

where

$$p_{i,e}^2 = k_{i,e}^2 + \gamma^2, \quad k_{i,e} = \omega \sqrt{\epsilon_{i,e} \mu_{i,e}}. \quad (2)$$

Using boundary conditions, we obtain the system of equations, that describes modes propagation in the partially dielectric-loaded coaxial waveguide:

$$\begin{aligned} \dot{C}_m^i J_m(p_i a_i) + \dot{D}_m^i Y_m(p_i a_i) &= 0 \\ \dot{C}_m^e J_m(p_e a_e) + \dot{D}_m^e Y_m(p_e a_e) &= 0 \\ \dot{C}_m^i J_m(p_i a) + \dot{D}_m^i Y_m(p_i a) &= \dot{C}_m^e J_m(p_e a) + \dot{D}_m^e Y_m(p_e a) \\ \dot{A}_m^i J'_m(p_i a_i) + \dot{B}_m^i Y'_m(p_i a_i) &= 0 \\ \dot{A}_m^e J'_m(p_e a_e) + \dot{B}_m^e Y'_m(p_e a_e) &= 0 \end{aligned}$$

$$\begin{aligned} \dot{A}_m^i J_m(p_i a) + \dot{B}_m^i Y_m(p_i a) &= \dot{A}_m^e J_m(p_e a) + \dot{B}_m^e Y_m(p_e a), \\ \frac{1}{p_i^2} \left(\frac{\gamma m}{a} \left(\dot{C}_m^i J_m(p_i a) + \dot{D}_m^i Y_m(p_i a) \right) + \right. \\ &\quad \left. + i\omega\mu_i \tilde{p}_i \left(\dot{A}_m^i J'_m(p_i a) + \dot{B}_m^i Y'_m(p_i a) \right) \right) = \\ &= \frac{1}{p_e^2} \left(\frac{\gamma m}{a} \left(\dot{C}_m^e J_m(p_e a) + \dot{D}_m^e Y_m(p_e a) \right) + \right. \\ &\quad \left. + i\omega\mu_e \tilde{p}_e \left(\dot{A}_m^e J'_m(p_e a) + \dot{B}_m^e Y'_m(p_e a) \right) \right) \\ &\cdot \frac{1}{p_i^2} \left(i\omega\epsilon_i \tilde{p}_i \left(\dot{C}_m^i J'_m(p_i a) + \dot{D}_m^i Y'_m(p_i a) \right) + \right. \\ &\quad \left. + \frac{\gamma m}{a} \left(\dot{A}_m^i J_m(p_i a) + \dot{B}_m^i Y_m(p_i a) \right) \right) - \\ &- \frac{1}{p_e^2} \left(i\omega\epsilon_e \tilde{p}_e \left(\dot{C}_m^e J'_m(p_e a) + \dot{D}_m^e Y'_m(p_e a) \right) + \right. \\ &\quad \left. + \frac{\gamma m}{a} \left(\dot{A}_m^e J_m(p_e a) + \dot{B}_m^e Y_m(p_e a) \right) \right) \end{aligned} \quad (3)$$

The equation system (3) concerning unknown coefficients $\dot{A}_m^{i,e}, \dot{B}_m^{i,e}, \dot{C}_m^{i,e}, \dot{D}_m^{i,e}$ is a system of eight linear homogeneous equations with eight unknowns. Such a system has an untrivial solution in the only one case when the determinant of the system is equal zero. This condition gives dispersion equation of the structure that must be solved concerning propagation constant γ .

The last two equations in (3) give coupling between the pairs of coefficients $\dot{C}_m^{i,e}, \dot{D}_m^{i,e}$ and $\dot{A}_m^{i,e}, \dot{B}_m^{i,e}$, therefore coefficients of longitudinal components $\dot{E}_z^{i,e}$ and $\dot{H}_z^{i,e}$ are dependent. It means that modes are hybrid that is the mode has simultaneously all six components of an electromagnetic field. In the case $m = 0$ the mode breaks up in two modes: E- and H- mode.

However it is obvious, that not taking into account decomposition of a hybrid mode into two independent modes it is possible to use the system of equations (3) for calculation the propagation constant γ and the coefficients $\dot{A}_m^{i,e}, \dot{B}_m^{i,e}, \dot{C}_m^{i,e}, \dot{D}_m^{i,e}$ in the case $m = 0$.

The obtained dispersion equation is transcendental. It has infinite number of solutions, which corresponds to infinite number of modes from the spectrum of the own modes of the waveguide under consideration.

It should be noted that except γ the p_i and p_e are variables in the dispersion equation, the latter's being

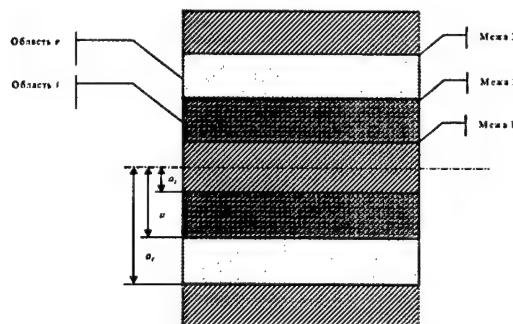


Fig. 2. Two dielectric-layer coaxial waveguide

unequivocally related with γ

$$p_{i,e}^2 = k_{i,e}^2 + \gamma^2, \quad k_{i,e}^2 = \omega^2 \varepsilon_{i,e} \mu_{i,e}. \quad (4)$$

Speaking in another way at a fixed frequency and parameters of dielectrics to every γ corresponds the only values of p_i and p_e . With identical success it is possible to solve the dispersion equation both rather p_i in a case $\varepsilon_i \mu_i > \varepsilon_e \mu_e$ (dielectric rod) and rather p_e in a case $\varepsilon_i \mu_i < \varepsilon_e \mu_e$ (dielectric cartridge). Then the following ratios take place:

- Case $\varepsilon_i \mu_i > \varepsilon_e \mu_e$:

$$p_e = \sqrt{\omega^2(\varepsilon_e \mu_e - \varepsilon_i \mu_i) + p_i^2}, \quad (5)$$

$$\gamma = \sqrt{p_i^2 - \omega^2 \varepsilon_i \mu_i}.$$

- Case $\varepsilon_i \mu_i < \varepsilon_e \mu_e$:

$$p_i = \sqrt{\omega^2(\varepsilon_i \mu_i - \varepsilon_e \mu_e) + p_e^2}, \quad (6)$$

$$\gamma = \sqrt{p_e^2 - \omega^2 \varepsilon_e \mu_e}.$$

On calculated values p_i or p_e (in a result of the numerical solutions of the dispersion equation) we determine the propagation constant γ of a separate mode in the dielectric-loaded coaxial waveguide. Then we determine the coefficients $\dot{A}_m^{i,e}, \dot{B}_m^{i,e}, \dot{C}_m^{i,e}, \dot{D}_m^{i,e}$ from the system of equations (3).

In such a way, all unknowns are calculated. It means that vector functions of electromagnetic fields in the coaxial waveguide with two dielectric layers are determined.

Further following the mode matching method [4] we shall obtain a system of equations, that is a solution of the scattering problem for $\bar{B}^O = \bar{S}_{21}^O \bar{A}^I$ a junction of two sections of partially dielectric-loaded coaxial waveguides:

$$\bar{B} = \bar{S} \bar{A}, \quad (7)$$

where

$$\bar{B} = \begin{pmatrix} \bar{B}^I \\ \bar{B}^{II} \end{pmatrix}, \quad \bar{A} = \begin{pmatrix} \bar{A}^I \\ \bar{A}^{II} \end{pmatrix}, \quad (8)$$

\bar{S} is a generalized scattering matrix with elements

$$\begin{aligned} \bar{S}_{11} &= (\bar{R} + \bar{P}^T \bar{Q}^{-1} \bar{P})^{-1} (\bar{R} - \bar{P}^T \bar{Q}^{-1} \bar{P}), \\ \bar{S}_{12} &= 2(\bar{R} + \bar{P}^T \bar{Q}^{-1} \bar{P})^{-1} \bar{P}^T, \\ \bar{S}_{21} &= 2(\bar{Q} + \bar{P} \bar{R}^{-1} \bar{P}^T)^{-1} \bar{P}, \\ \bar{S}_{22} &= -(\bar{Q} + \bar{P} \bar{R}^{-1} \bar{P}^T)^{-1} (\bar{Q} - \bar{P} \bar{R}^{-1} \bar{P}^T). \end{aligned} \quad (9)$$

where \bar{A}^I, \bar{B}^I are vectors of the size M , that contain the unknown coefficients forward ($A_1^I \dots A_M^I$) and reflected ($B_1^I \dots B_M^I$) modes in the section I. Simi-

larly, $\bar{A}^{II}, \bar{B}^{II}$ are vectors of the size N , containing unknown coefficient of forward ($A_1^{II} \dots A_N^{II}$), and reflected ($B_1^{II} \dots B_N^{II}$) modes in the section II. \bar{P} is a matrix of the size $N \times M$, \bar{Q} is a diagonal matrix of the size $N \times N$, \bar{R} is a diagonal matrix of the size $M \times M$. The elements of these matrices are determined by the formulas [4]:

$$\begin{aligned} P_{mn} &= \int_S \vec{e}_m^I \times \vec{h}_n^{II} \cdot d\vec{s}; \\ Q_{nn} &= \int_S \vec{e}_n^{II} \times \vec{h}_n^{II} \cdot d\vec{s}; \\ R_{mm} &= \int_S \vec{e}_m^I \times \vec{h}_m^I \cdot d\vec{s}. \end{aligned} \quad (10)$$

where \vec{e}_i^I, \vec{h}_i^I are own functions of transverse electric and magnetic fields of a mode with a radial index m accordingly. Finally the integral (10) are reduced to the double Lommel's integrals that have been integrated analytically.

Final expressions for P, Q, R are not presented here because they are quite cumbersome.

To receive the overall scatterings matrix \bar{S}^O of the horn it is necessary to cascade progressively scattering matrices of junctions between sections and the selections of regular.

The regular waveguides

$$\bar{B} = \bar{S}^O \bar{A}. \quad (11)$$

Voltage standing wave ratio for a stimulating mode is:

$$VSWR = 20 \log B_{m_0}^I. \quad (12)$$

Transverse fields at the aperture of the horn are:

$$\vec{E}_r^O = \sum_{n=1}^{N_0} B_n^O \vec{e}_n^O, \quad (13)$$

$$\vec{H}_r^O = \sum_{n=1}^{N_0} B_n^O \vec{h}_n^O. \quad (14)$$

Then coefficients of reflected modes at the input of the horn and forward modes at the output of the horn are defined by the formulas:

$$\bar{B}^I = \bar{S}_{11}^O \bar{A}^I \quad (15).$$

The field at the aperture of the horn is a sum of fields of modes with known amplitudes in the last waveguide sections. Besides each mode is determined in two dielectric layers. Therefore applying a principle of a superposition it is possible to calculate a field in a far zone as a linear combinations of fields that are created separately by each mode in each medium, that is:

$$E_\theta = \frac{ikc e^{-ikR}}{2\pi R} \sum_{n=1}^N B_n^O \times \left[\int_0^{2\pi} \int_{a_i}^a [E_{ri}^n \cos(\Phi - \varphi) + E_{\varphi i}^n \sin(\Phi - \varphi)] \times e^{ikr \sin \theta \cos(\Phi - \varphi)} r dr d\varphi + \right. \quad (16)$$

$$+ \int_0^{2\pi} \int_a^{a_e} [E_{re}^n \cos(\Phi - \varphi) + E_{\varphi e}^n \sin(\Phi - \varphi)] \times e^{ikr \sin \theta \cos(\Phi - \varphi)} r dr d\varphi \left. \right] \\ E_\Phi = \frac{ikc e^{-ikR}}{2\pi R} \sum_{n=1}^N B_n^O \times \left[\int_0^{2\pi} \int_{a_i}^a [-E_{ri}^n \cos(\Phi - \varphi) + E_{\varphi i}^n \sin(\Phi - \varphi)] \times e^{ikr \sin \theta \cos(\Phi - \varphi)} r dr d\varphi + \right. \quad (17)$$

$$+ \int_0^{2\pi} \int_a^{a_e} [E_{re}^n \sin(\Phi - \varphi) + B_n^O E_{\varphi e}^n \cos(\Phi - \varphi)] \times e^{ikr \sin \theta \cos(\Phi - \varphi)} r dr d\varphi \left. \right]$$

where B_n^O is a coefficient of a mode n in the last section of the horn.

We have carried out the analytical integration and the following formulas for components of the radiated field in the far zone have been obtained

$$E_\theta = -\frac{i^m k c e^{-ikR} \tilde{p}}{R} \cos m\Phi \times \left[\begin{aligned} &KE_1 \cdot \Lambda_m^{J,J}(p, kr \sin \theta, z) + \\ &+ KE_2 \cdot \Lambda_m^{Y,J}(p, kr \sin \theta, z) + \\ &+ KE_3 \cdot \Lambda_m^{J,J'}(p, kr \sin \theta, z) + \\ &+ KE_4 \cdot \Lambda_m^{Y,J'}(p, kr \sin \theta, z) \end{aligned} \right]_{a_1}^{a_2}$$

$$E_\Phi = \frac{i^m k c e^{-ikR} \tilde{p}}{R} \sin m\Phi \cdot \cos \theta \times \left[\begin{aligned} &KE_1 \cdot \Lambda_m^{J',J}(p, kr \sin \theta, z) + \\ &+ KE_2 \cdot \Lambda_m^{Y',J}(p, kr \sin \theta, z) + \\ &+ KE_3 \cdot \Lambda_m^{J,J}(p, kr \sin \theta, z) + \\ &+ KE_4 \cdot \Lambda_m^{Y,J}(p, kr \sin \theta, z) \end{aligned} \right]_{a_1}^{a_2}$$

where Λ_m are the double Lommel's integrals.

As an example the results of calculations (dotted curve) and measurements (continuous curve) of radiation pattern of a model of the partially dielectric-

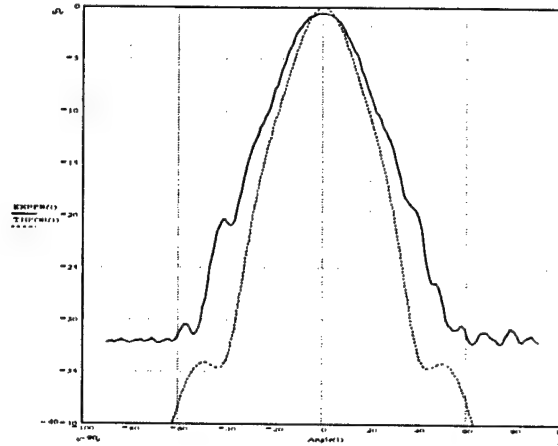


Fig. 3. Radiation pattern of the partially dielectric-loaded coaxial horn

loaded coaxial horn with semi-flare angle 34° at frequency 6 GHz are compared in Fig. 3

A divergence between the theoretical and experimental results are explained by using Fourier Transform for calculation of the far field of the wide flare angle horn and an approximate value of dielectric permeability of the used dielectric material.

3. CONCLUSION

We have carried out the full-wave analysis of the dielectric - loaded hybrid mode coaxial horn using mode-matching technique. The obtained generalized solution includes the whole of known solutions for axially symmetric horns and is particularly aimed for research and development of ultra-wideband hybrid - mode feeds for advanced reflector antennas.

REFERENCES

1. P.J. B. Clarricoats, A. D. Oliver. Corrugated horns for microwave antennas.-Peter Peregrinus., London, UK 1984.-p.231.
2. T. S. Bird, G. L. James. Design and practice of reflector antennas and feed systems in the 1990 // Review of Radio Science 1996 - 1999.-Oxford University Press.-1999.-pp. 81-117.
3. P. R. Clark, G. L. James. Ultra-wideband Hybrid - Mode Feeds.// Electronic letters, Vol. 31, № 23, pp. 1968-1969.
4. G. L. James. Analysis and Design of TE_{11} to H_{11} Corrugated Cylindrical Waveguide Mode Converters // IEEE Trans., Vol. MTT-29.-1981/-pp. 1059-1066.
5. Watson G. N. The theory of Bessel functions / trans. from second eng. Izd. for red. V. S. Berman's.-1949.- 800 pp.

SYNTHESIS OF OFFSET-FED GREGORIAN VSAT ANTENNAS

F. F. Dubrovka¹, R. F. Dubrovka¹, O. S. Kim¹, V. H. Syrotyuk², H. P. Khymych²

¹ National Technical University of Ukraine "Kyiv Polytechnic Institute"
Department of Theoretical Fundamentals of Radio Engineering, Kyiv, Ukraine
<dubrovka@tera.kiev.ua>

² State Scientific – Production Enterprise "Promin", Ternopil, Ukraine.

Abstract

The paper presents results of synthesis, design, development, manufacturing and testing prototypes of 1.2 m, 1.8 m and 2.4 m Gregorian shaped offset dual-reflector antennas with low crosspolar radiation for VSAT applications.

Keywords: VSAT antennas, offset-fed Gregorian antennas, spherical wave analysisIntroduction.

In the recent years corporate VSAT networks have become one of the most dynamically developing branches of satellite communication systems. A key constituent part of any VSAT earth station is an antenna. In order to be suitable for application in VSAT networks an antenna has to meet the stringent CCIR requirements on crosspolar radiation level, i.e., crosspolar radiation level in –1 dB contour in copolar radiation main lobe must be less than –35 dB and the side lobe envelope must be lower of that one required by CCIR to transmitting earth station antennas. For VSAT application offset reflector antennas are more attractive than axially symmetrical reflector antennas because of their capability to obtain lower side lobes, higher efficiency and absence of de-icing problem. The only disadvantage of offset antennas is the higher level of crosspolar radiation. But properly optimized Gregory type offset dual-reflector antennas allow to obtain the low level of crosspolar radiation that meets CCIT requirements to earth stations antennas.

In this paper a new approach to fast and accurate synthesis of offset dual-reflector antennas is considered. Results of synthesis, design, manufacturing and testing the 1.2 m, 1.8 m and 2.4 m prototype antennas for VSAT application are presented.

1. OUTLINE OF ANALYSIS AND SYNTHESIS

Synthesis of Gregorian shaped offset dual-reflector antennas (Fig. 1) has been carried out using the novel efficient iterative method of synthesis [1,2] that could be called "false objectives method". There are three constituent key points of this method of synthesis that determine its extremely fast convergence and accuracy: 1) the idea and the way of generating false objectives; 2) using a fast reliable approximate analytical or numerical method of synthesis; 3) using an accurate

rate analysis. The first point is given in detail in [1,2]. The approximate synthesis of the offset dual-reflector antenna under consideration we have carried out using the solution of the geometrical optics first-order partial differential equations [3].

Accurate analysis of the offset dual-reflector antenna has been carried out as follows:

- *Feed horn analysis using Mode Matching Technique* [4]. To calculate the radiation fields of the horn at an arbitrary distance from the source, we have used the method of expansion into spherical waves [5]

$$\vec{E}(r, \theta, \varphi) = -\sum_m \sum_n a_{e_{mn}} \vec{m}_{e_{mn}} + b_{e_{mn}} \vec{n}_{e_{mn}}; \quad (1)$$

$$\vec{H}(r, \theta, \varphi) = \frac{k}{j\omega\mu} \sum_m \sum_n a_{e_{mn}} \vec{n}_{e_{mn}} + b_{e_{mn}} \vec{m}_{e_{mn}}.$$

The functions $\vec{m}_{e_{mn}}$ and $\vec{n}_{e_{mn}}$ represent the

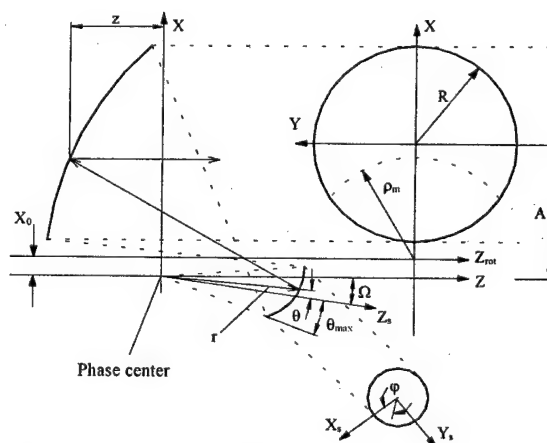


Fig. 1. Geometry of Gregory offset dual-reflector antenna.

spherical wave solutions of the Maxwell equation in the form:

$$\vec{m}_{e_{mn}} = \mp z_n(kr) \frac{m P_n^m(\cos \theta) \sin}{\sin \theta} m \varphi \vec{i}_\theta -$$

$$- z_n(kr) \frac{\partial}{\partial \theta} P_n^m(\cos \theta) \frac{\cos}{\sin} m \varphi \vec{i}_\varphi,$$

$$\vec{n}_{e_{mn}} = n(n+1) \frac{z_n(kr)}{kr} P_n^m(\cos \theta) \frac{\sin}{\cos} m \varphi \vec{i}_r +$$

$$+ \frac{1}{kr} \frac{\partial}{\partial r} [r z_n(kr)] \frac{\partial}{\partial \theta} P_n^m(\cos \theta) \frac{\sin}{\cos} m \varphi \vec{i}_\theta \pm$$

$$\pm \frac{1}{kr} \frac{\partial}{\partial r} [r z_n(kr)] \frac{m P_n^m(\cos \theta)}{\sin \theta} \frac{\cos}{\sin} m \varphi \vec{i}_\varphi,$$

where we assume the time-dependent relation of $\exp(j\omega t)$, (r, θ, φ) are spherical coordinates, $z_n(kr)$ is any solution to the Bessel equation, $P_n^m(\cos \theta)$ is the associated Legendre function while the indices e and o denote selection of the dependence \sin or $\cos \varphi$.

• *Calculation of the spherical wave expansion coefficients for the electromagnetic field at the horn aperture.* The coefficients $a_{e_{mn}}$ and $b_{o_{mn}}$ for the horn

radiation field are obtained with the aid of orthogonality of the spherical wave functions $\vec{m}_{e_{mn}}$ and $\vec{n}_{e_{mn}}$

and previously calculated fields \vec{E}_a , \vec{H}_a at the horn aperture (1):

$$a_{e_{mn}} = -\frac{k\omega\mu}{2\gamma_{mn}} \int_{S_a} \left(-\vec{m}_{e_{mn}} \times \vec{H}_a + \frac{k}{j\omega\mu} \vec{n}_{e_{mn}} \times \vec{E}_a \right) d\vec{S},$$

$$b_{o_{mn}} = -\frac{k\omega\mu}{2\gamma_{mn}} \int_{S_a} \left(-\vec{n}_{e_{mn}} \times \vec{H}_a + \frac{k}{j\omega\mu} \vec{m}_{e_{mn}} \times \vec{E}_a \right) d\vec{S},$$

where S_a is the aperture surface while

$$\gamma_{0n} = 4\pi \frac{n(n+1)}{2n+1},$$

$$\gamma_{mn} = 4\pi \frac{n(n+1)(n+m)!}{2n+1 (n-m)!}, m \neq 0.$$

Due to analytical integration with respect to azimuth in the cylindrical system of coordinates, we have reduced the surface integrals (2) to linear integrals of the products of the Bessel functions and their derivatives over radius for each waveguide mode at the horn aperture.

• *Calculation of the currents at the subreflector surface induced by the feed horn field using physical optics (PO) approach, which is an approximation that expresses \mathbf{J}_s at any point on the reflector in terms of*

Table 1.

D, m	$F = 11.95 \text{ GHz}$	$F = 14.125 \text{ GHz}$
1.2 m	42.1 dB	43.5 dB
1.8 m	45.8 dB	47.3 dB
2.4 m	48.3 dB	49.7 dB

the incident magnetic field intensity \mathbf{H}_i at that point. Specifically, it is assumed that

$$\mathbf{J}_s = 2\mathbf{u}_n \times \mathbf{H}_i \quad (3)$$

where \mathbf{u}_n is the unit normal to S . Note, if the radius of curvature is large in terms of wavelength, equation (3) is very accurate except near the edges and in the shadow zone.

• *Calculation of the fields near the main reflector surface by PO method using subreflector currents.* Note, if the source consists of simply an induced current density \mathbf{J}_s on a perfectly conducting surface S , and the surface current density \mathbf{J}_s is known at every point on the reflector surface S , the scattered field in both near and far-field zones can be calculated as [5]

$$\mathbf{E}_s = -\frac{j}{\omega\epsilon} \int_S [(\mathbf{J}_s \cdot \nabla) \nabla + k^2 \mathbf{J}_s] G dS, \quad (4)$$

which is exact and valid at all points in space exterior to the source region (on the actual sources the Green's function G has a singularity).

• *Calculation of the currents on the main reflector surface induced by the subreflector field using (3).*

• *Calculation of the far-field of the main reflector by PO method.* In far-field region, along the direction \mathbf{u}_r , equation (4) simplifies to

$$\mathbf{E}_s = -\frac{jk^2}{\omega\epsilon} \frac{e^{-jk r}}{4\pi r} (\tilde{\mathbf{I}} - \mathbf{u}_r \mathbf{u}_r) \bullet$$

$$\bullet \int_S \mathbf{J}_s(r') \exp(kr' \bullet \mathbf{u}_r) dS, \quad (5)$$

where $\tilde{\mathbf{I}}$ is the unit dyadic.

• *Calculation of the far-field radiation pattern of the offset dual-reflector antenna by superposition the radiated fields of the main reflector, subreflector and feed horn.*

2. RESULTS

Theoretical gains of the synthesized Gregorian shaped offset dual-reflector antennas with equivalent diameters 1.2, 1.8 and 2.4 m are presented in Tab. 1.

Theoretical crosspolar radiation levels in -1dB contour for the antennas are presented in Tab. 2.

Table 2.

D, m	$F = 11.95 \text{ GHz}$	$F = 14.125 \text{ GHz}$
1.2 m	-38 dB	-39 dB
1.8 m	-38 dB	-39 dB
2.4 m	-39 dB	-40 dB

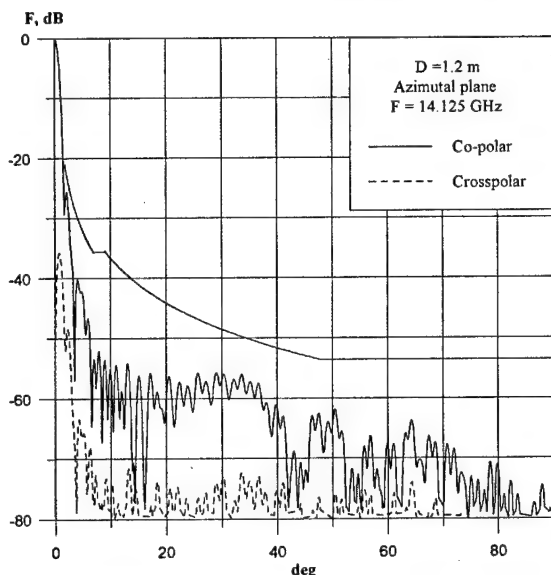


Fig. 2. Radiation pattern of the synthesized 1.2 m Gregorian shaped offset dual-reflector antenna.

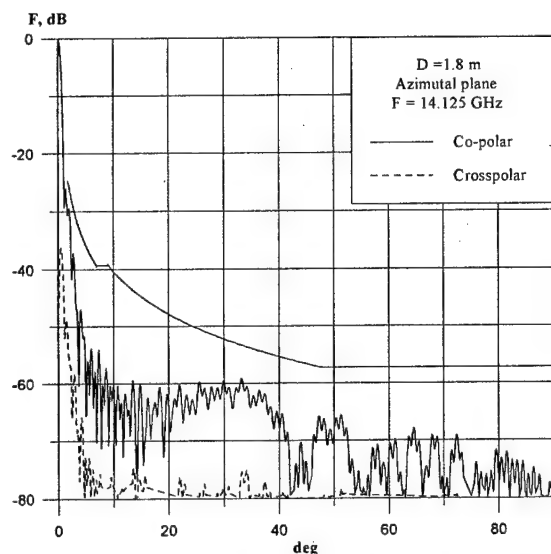


Fig. 3. Radiation pattern of the synthesized 1.8 m Gregorian shaped offset dual-reflector antenna

Calculated radiation patterns of the antennas at the center transmit mode frequency 14.125 GHz are shown in Fig. 2-4. It should be noted that calculated co- and crosspolar radiation patterns of the synthesized antennas fully meet CCIR requirement to earth stations.

A production samples of the synthesized antennas have been manufactured (photo of the 2.4 m antenna is shown in Fig.5) and tested.

Excellent agreement between calculated and measured results have been obtained. All three prototypes antennas have crosspolar radiation level less then –

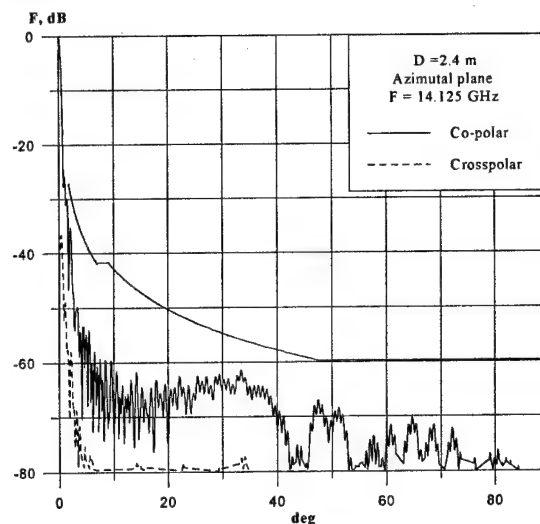


Fig. 4. Radiation pattern of the synthesized 2.4 m Gregorian shaped offset dual-reflector antenna

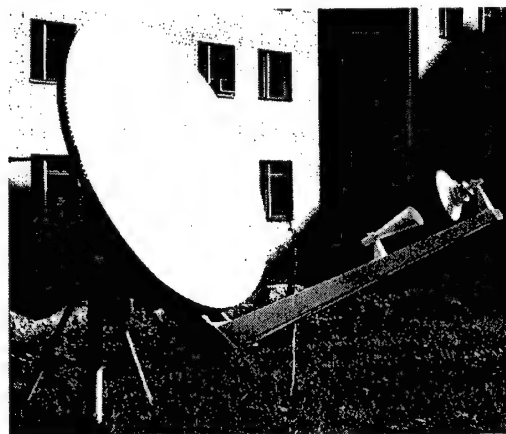


Fig. 5. 2.4 m Gregorian shaped offset dual-reflector antenna design.

38 dB in -1 dB contour and their sidelobe envelopes are below the envelope recommended by CCIR to earth station antennas.

3. CONCLUSION

Results of synthesis, design and testing prototypes of 1.2 m, 1.8 m and 2.4 m Gregory offset dual-reflector antennas with very low crosspolarization have been presented. The results of testing have demonstrated that the synthesized novel antennas fully meet stringent CCIR requirements to earth station antennas and therefore are suitable for application in satellite telecommunication systems.

REFERENCES

1. Dubrovka F.F. An Extremely Fast-Convergent Iterative Method of Synthesis and its Application to Design of High Performance Antennas and Microwave Components // Proc. of the 3-d Int. Conf. on Antenna Theory and Techniques ICCAT'99.- Sevastopol, 8 – 12 September 1999. – P. 17-26.
2. Dubrovka F.F. Quick-convergent iterative method of synthesis // Radioelectronika. – 2000. - №11. – P. 15-20 (Izvestiya VUZov) (In Russian).
3. V. Galindo-Israel, W. Imbriale, R. Mittra. On the theory of the synthesis of single and dual offset shaped reflector antennas // IEEE Trans., vol. AP-35, no. 8, pp.887-896, 1987.
4. G.L. James. Analysis and design of TE₁₁-to-H₁₁ corrugated cylindrical waveguide mode converters // IEEE Trans. on MTT. – vol HTT – 29, №10. – pp. 1059-1066.
5. A.W. Rudge, K. Milne, A.D. Olver, and P. Knight: "The handbook of antenna design", Chaps.2 and 3 (Peter Peregrinus Ltd., 1983).

SIMULATIONS OF THE ESA PLANCK HFI BEAMS OF POLARIZED AND MULTI-MODE HORNS

Vladimir B. Yurchenko¹, John A. Murphy¹ and J.-M. Lamarre²

¹ Experimental Physics Department, National University of Ireland,
Maynooth, Ireland
<v.yurchenko@may.ie>

² Observatoire de Paris, 61 Av. de l'Observatoire, 75014,
Paris, France

Abstract

We report on rigorous physical optics simulations of the ESA PLANCK dual-reflector telescope being designed for measuring the temperature anisotropies and polarization characteristics of the Cosmic Microwave Background. Both polarized mono-mode and non-polarized multi-mode beams covering the frequency range from 100 GHz to 857 GHz ($D/\lambda_{\min} \sim 5000$) are computed by using a specially developed ultra-fast physical optics code propagating the source field mode-by-mode from the apertures of profiled corrugated horns simulated by the scattering matrix approach. Polarization characteristics of the broad-band incoherent beams have been computed for the purpose of the analysis of systematic errors in polarization measurements.

Keywords: ESA PLANCK Surveyor, CMB radiation, HFI instrument, PO simulations, polarization systematic errors.

1. INTRODUCTION

The ESA PLANCK Surveyor is the deep-space satellite being designed for the accurate measurements of temperature anisotropies and polarization characteristics of the cosmic microwave background (CMB). The satellite will carry a dual-reflector multi-beam telescope equipped with two focal plane instruments (the Low-Frequency and High-Frequency Instruments) for detecting the radiation in a wide frequency range extending from 30 GHz to 1000 GHz [1].

The High-Frequency Instrument (HFI) will operate in six frequency channels centered at 100, 143, 217, 353, 545 and 857 GHz. The HFI consists of 36 corrugated horn antennas feeding cryogenically cooled bolometric detectors. Channels operating at 100, 143, 217 and 353 GHz use diffraction-limited mono-mode quasi-Gaussian horns. Half of these channels will be used for polarization measurements by utilizing polarization-sensitive micromesh bolometers developed by Turner *et al.* [2].

The higher frequency channels (545 and 857 GHz) are non-polarized and incorporate non-diffraction-limited profiled multi-mode horns. All the HFI horns are broad band, with the bandwidth being about 30 % of central frequency. The horns are specifically designed to meet extremely constrain requirements on both the primary mirror edge taper (~ 25 -30 dB) and the angular resolution on the sky (about 5 arcminutes at the frequencies of 217-857 GHz).

Since both the temperature anisotropy $\varepsilon = \delta T/T$ and the degree of polarization d of the CMB radiation are extremely small ($\varepsilon \sim 10^{-5}$ and $d < 10^{-6}$), the CMB measurements require an exquisite accuracy of the instrument and a tight control of possible sources of systematic errors. To achieve the goal, thorough simulations and testing of the instrument are needed at every stage of the design.

Optical simulations are particularly challenging because of multi-beam dual-reflector geometry of the telescope, significant refocus of elliptical mirrors, rather large primary mirror having projected diameter $D = 1.5$ m ($D/\lambda_{\min} \sim 5000$), strict requirements on the accuracy and, generally, multi-mode structure of the feed horn antenna fields. Physical optics (PO) is the most appropriate technique for this kind of simulations. Conventional software cannot, however, cope efficiently with the electromagnetic problem of this size.

As an alternative, a special ultra-fast PO code has been developed for the PLANCK simulations [3, 4]. It allowed us to perform rigorous PO simulations of the main beams of the telescope in a few minutes for mono-mode HFI beams at a single frequency and in half an hour for the complete broad-band polarization-averaged multi-mode beams. Available comparisons of the results with much more resource-consuming GRASP8 simulations prove the accuracy and the advantages of this approach.

The aim of this paper is to summarise the results of our simulations of the ESA PLANCK HFI beams and to consider the implications of the beam imperfections on systematic errors of polarization measurements.

2. SIMULATIONS OF THE HORN FIELD

The electric field at the aperture of corrugated horns has been simulated by the scattering matrix approach. The effective modes of the electric field at the horn aperture, \mathbf{E}_{nm} , are represented via the canonical TE-TM modes ϵ_{nj} of a cylindrical waveguide as follows

$$\mathbf{E}_{nm}(\rho, \varphi) = \sum_{j=1, \dots, 2M} S_{nmj} \epsilon_{nj}(\rho, \varphi) \quad (1)$$

where S_{nmj} is the scattering matrix computed by Gleeson *et al.* [5] for each particular horn at various frequencies f (S_{nmj} is used as an input in this work), $n = 0, 1, \dots, N$ is the azimuthal index and $m, j = 1, 2, \dots, 2M$ are the radial indices accounting for both the TE ($m, j = 1, \dots, M$) and TM ($m, j = M + 1, \dots, 2M$) modes.

Spatial structure of the \mathbf{E}_{nm} aperture modes is essentially different from the structure of canonical modes ϵ_{nj} . It depends on the horn design and varies with varying the frequency within the bandwidth of the channel.

Notice that the terms TE and TM in application to \mathbf{E}_{nm} (unlike ϵ_{nj}) are mere notations since, generally, none of the \mathbf{E}_{nm} modes is perfectly transverse. Notice also that the total power of the horn field is the sum of powers of \mathbf{E}_{nm} modes.

Fig. 1 shows the power contribution of different \mathbf{E}_{nm} modes to polarized mono-mode beams HFI-143 and non-polarized multi-mode beams HFI-545. In multi-mode beams, both the power contribution and the shape of \mathbf{E}_{nm} modes vary significantly within the bandwidth, with many modes being rejected at the lower frequency edge.

In case of mono-mode horns, all the aperture modes have the same shape and effectively sum up to a single mode which is of one unit of total power, almost perfectly Gaussian and linearly polarized on the horn aperture. Broad-band and mono-frequency far-field power patterns of the HFI-143 and HFI-545 horns are shown in Fig. 2.

To minimize polarization errors due to mismatch of different beams, the pairs of orthogonal polarization channels have been incorporated into the same horn by using the polarization sensitive bolometers [2]. In this case, the difference of power patterns of two channels is minimal (typically, less or about 1%). It arises only due to minor asymmetry of the polarized modes propagating through the horn and a slight difference in propagation of different polarizations along the same path via the telescope (the mismatch of different beams is much greater and depends on the horn location in the focal plane).

3. SIMULATIONS OF MULTI-MODE BEAMS

Simulations of multi-mode beams require the propagation of each mode for a few times with different polarization angle for proper averaging of polariza-

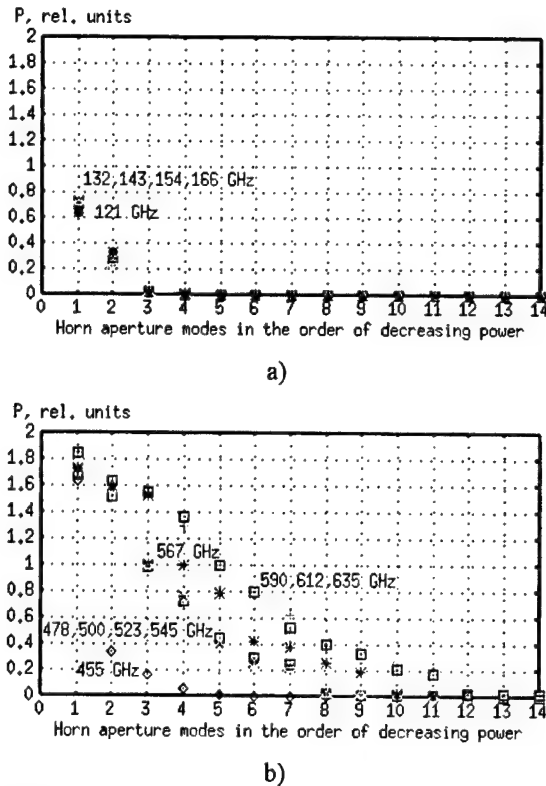


Fig. 1. Contribution of \mathbf{E}_{nm} modes to (a) HFI-143 and (b) HFI-545 beams in units of power of a single polarized mode

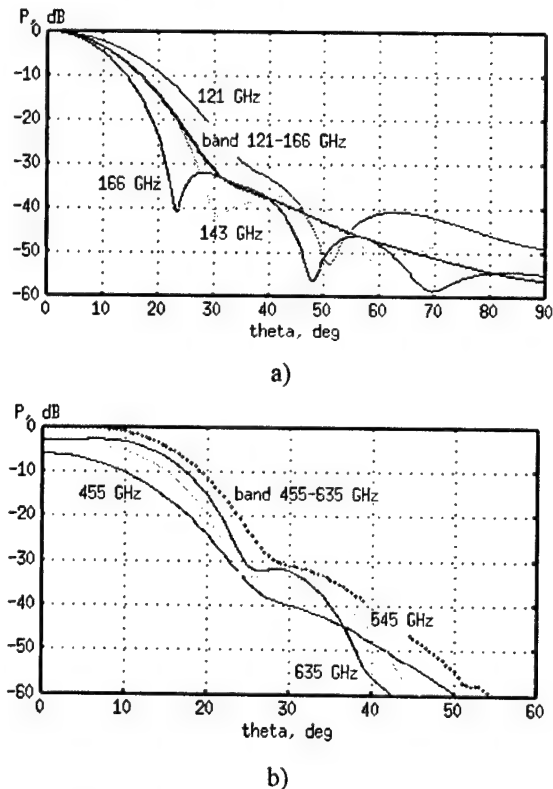


Fig. 2. Broad-band and mono-frequency far-field power patterns of (a) HFI-143 and (b) HFI-545 horns

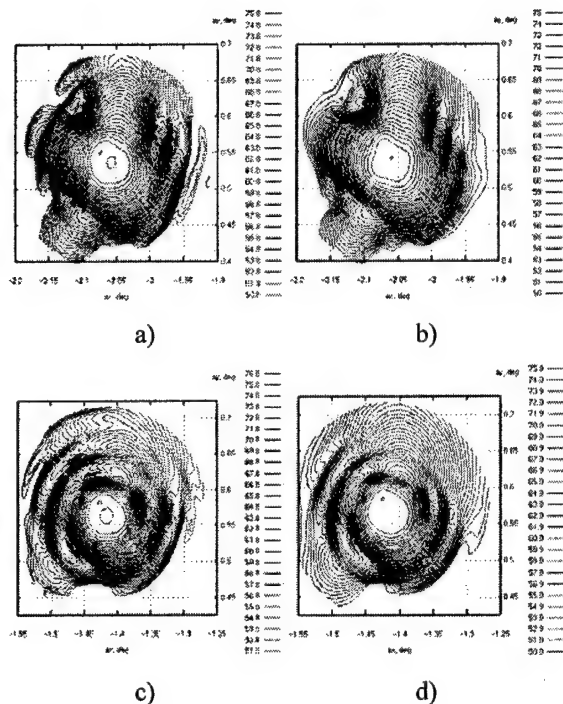


Fig. 3. Power patterns of (a,c) mono-frequency and (b,d) broad-band telescope beams from the multi-mode horns (a,b) HFI-545-1 and (c,d) HFI-545-2 computed by the scattering matrix approach

tion. The reason is that, unlike the field of a conical or Gaussian horn, the modes of the profiled horns are not axially symmetric and the mode pattern in the sky depends on the polarization angle on the horn aperture. Also, because of broad frequency bands ($\sim 30\%$), averaging over frequency is needed as well.

Fig. 3 shows the mono-frequency ($f = 545$ GHz) and broad-band ($f = 455 - 635$ GHz) power patterns of the telescope beams from the profiled corrugated horns HFI-545-1 and HFI-545-2 computed by the scattering matrix approach with averaging over polarization angle. Each horn is placed at the best refocus providing both the maximum gain and the best resolution of the telescope. The best refocus is found by repeated PO simulations of the broad-band beams with different locations of the horn. For these multi-mode horns with the aperture radius $a = 4.298$ mm, the best refocus corresponds to the effective focal centre located at $R_C = 5.0$ mm inside the horn as measured from the horn aperture.

The beams in Fig. 3 are computed with the horns optimized for the required angular resolution of the telescope (the full beam width on the sky $W = 5$ arcminutes) when satisfying the edge taper requirements on the primary mirror. The distortion of the beams at this level of resolution is mainly due to coma (aberrations of the wider beams are mainly due to astigmatism). Each beam has a well-defined flat top of the angular diameter $W = 4.8$ arcminutes when measured at the level of -3 dB which appears to be

just the edge of the flat top. At the level below -10 dB, the beams, however, are rather complicated because of significant aberrations of the telescope. The aberrations are different for different modes and vary significantly when sweeping the frequency across the bandwidth of the frequency channel.

4. SIMULATIONS OF POLARIZED BEAMS

Polarized mono-mode beams of channels $f = 100, 143, 217$ and 353 GHz are produced by profiled corrugated horns rather similar to multi-mode ones. These horns are also simulated in a general way as multi-mode ones. However, due to Gaussian-like profile, selection of modes and sensitivity of the bolometers to only one linear polarization, the aperture field of these horns consists of just two effective modes TE_{11} and TM_{11} (Fig. 1,a) producing almost the same pattern on the sky both in terms of power and polarization.

Because of these properties, the aperture field of the polarized horns can be well simulated by a clipped Gaussian source field with some curvature of the wave front. This model allowed us to find the required orientation of the polarization vector on the aperture of each horn by computing the orientation of the polarization ellipse on the axis of the coherent telescope beam at the central frequency of each channel [4].

More rigorous approach requires the scattering matrix simulations with averaging of the polarization data over all the contributing modes and over all the frequencies of incoherent beam. The averaging of this kind is computed by representing the polarization data in terms of Stokes parameters of the telescope beams.

We compute Stokes parameters defined with respect to the parallels and meridians of the spherical frame on the sky with the pole being the geometrical spin axis of telescope (the spherical frame of spacecraft). This definition has an advantage that the polarization data of this representation can be easily converted into the invariant E-B representation which is independent of the coordinate frame on the sky. Also, this spherical frame does not have artificial singularities in the field of view of telescope and the beam patterns are directly superimposed and compared on the sky when the telescope is spinning about its geometrical axis.

Fig. 4 shows the broad-band power patterns computed in this way for two pairs of beams, HFI-143-2a and HFI-143-4a of one pair, and HFI-217-6a and HFI-217-8a of another pair. It is the beams of each pair that are directly superimposed on the sky when spinning the telescope. The patterns in Fig. 4 are plotted as projected on the plane normal to the line of sight of telescope.

Accurate polarization measurements require identical power patterns and perfect superposition of two beams on the sky. In reality, as shown in Fig. 4, the beams are distorted in different manner because of different locations of horns on the focal plane, and the

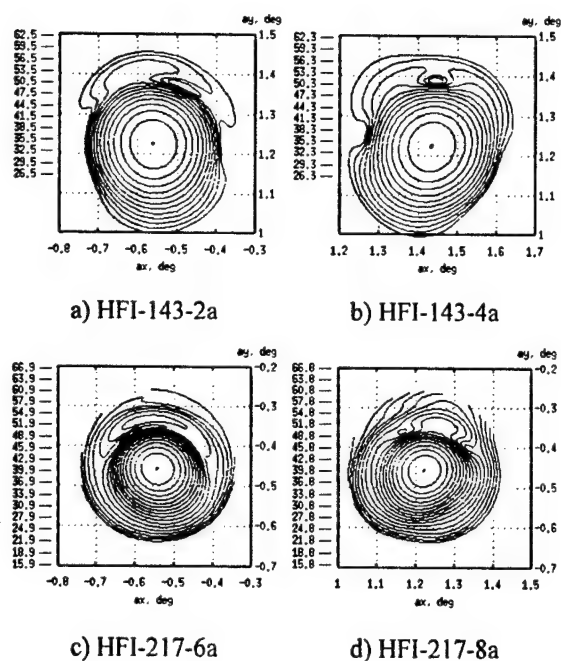


Fig. 4. Power patterns of the pairs of beams to be superimposed on the sky (a with b and c with d) for polarization measurements when spinning the telescope (broad-band channels (a, b) $f = 121\text{--}166\text{ GHz}$ and (c, d) $f = 182\text{--}252\text{ GHz}$)

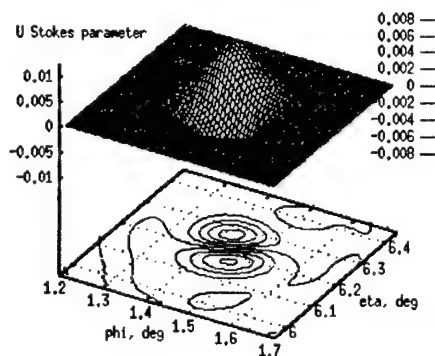


Fig. 5. The U Stokes parameter pattern of the broad-band beam HFI-143-4a

difference of power patterns provides an important estimate on the level of possible systematic errors in the measurements of CMB polarization.

Fig. 5 shows the U Stokes parameter pattern of the broad-band beam HFI-143-4a (the V pattern is rather similar, although greater in magnitude and slightly twisted about the beam axis).

As one can see, positive and negative values of the U parameter are well balanced over the beam pattern and the average value is very close to zero. It proves that the chosen direction of polarization of the horn field as found by Yurchenko [4] for a simplified model of a coherent mono-frequency quasi-Gaussian beam is really an optimum (ideally, U should be zero in this polarization).

The amplitude values of both the U and V parameters are small enough ($|U| < 1\%$ and $|V| < 4\%$ of maximum beam intensity) that ensures a sufficiently small magnitude of the cross-polarized power ($P_{\text{cross}} < -30\text{ dB}$) as required by the telescope specification.

Recent simulations of the HFI-100 channels show that even these rather low-frequency beams are sufficiently perfect (difference of power patterns of orthogonal polarization of the same beam is about 1%) and the cross-polarized power is well below -30 dB (e.g., for the HFI-100-3a beam, $P_{\text{cross}} < -37\text{ dB}$).

4. CONCLUSION

Polarized mono-mode and non-polarized multi-mode HFI beams of the ESA PLANCK telescope have been computed by physical optics propagation of the horn aperture field simulated by the scattering matrix approach. Beam patterns of Stokes parameters have been computed and the required polarization angles on the horn apertures have been found. Beam patterns have been studied for the estimate of systematic errors in polarization measurements.

ACKNOWLEDGEMENTS

This work was supported by the Enterprise Ireland Basic Research Grant and by the Ulysses Research Visit Grants 2002 and 2003.

REFERENCES

1. Tauber J. A. The PLANCK mission: overview and current status // *Astrophys. Lett. Comm.* 2000. Vol. 37. p. 145–150.
2. Turner A. D. et al. Silicon nitride micromesh bolometer array for submillimeter astrophysics // *Applied Optics*, 2001. Vol. 40. p. 4921–4932.
3. Yurchenko V. B., Murphy J. A., and Lamarre J.-M. Fast physical optics simulations of the multi-beam dual-reflector submillimeter-wave telescope on the ESA PLANCK Surveyor // *Int. J. Infrared and Millimeter Waves*, 2001. Vol. 22. No. 1. p. 173–184.
4. Yurchenko V. B., Murphy J. A., and Lamarre J.-M. PLANCK HFI beam simulations for polarized and multi-moded horns // *25th ESA Antenna Workshop on Satellite Antenna Technology*, 18–20 September, 2002, ESTEC, Noordwijk, The Netherlands. K. van't Klooster and L. Fanchi, Eds. 2002. p. 281–286.
5. Gleeson E., Murphy J. A., Maffei B., Lamarre J.-M., and Wylde R. J. Definition of the multi-mode horns for the HFI instrument on PLANCK // *ibid.* p. 649–655.
6. Yurchenko V. B. Measuring CMB polarization with ESA PLANCK submm-wave telescope // *Experimental Cosmology at Millimetre Wavelengths: 2K1BC Workshop*, Breuil-Cervinia, Italy, July 9–12, 2001. M. De Petris, P. A. Moro, and M. Gervasi, Eds. AIP Conf. Proc. 2002. Vol. 616. p. 234–238.

DIRECTIVITY OF RECTANGULAR APERTURE ELECTROMAGNETIC RADIATION

S. V. Butakova

Kharkov Institute of Air Force of Ukraine
Tel.: +380 0572 272409 <svetvik@ukr.net>

Abstract

On the basis of an analytical solution for a reflectance and a gain of the open-ended waveguide having cross-section $a \times b$ with wave H_{10} it is shown for $a \geq 0,7\lambda$, $b \geq a$ or $a \geq 4\lambda$, $b > 0,4a$, where λ is a wavelength in free space, what the gain dependence of the open-ended waveguide on a/λ at $a/b = \text{const}$ corresponds to generalized gain dependence of optimal plane horns in plains E or H on a dimension of the horn aperture. The calculation of an effective area and an area use factor of open-ended waveguide and optimal plane horn apertures are made.

Keywords: open-ended rectangular waveguide, optimal plane horn, reflectance, gain, effective area, area use factor.

1. INTRODUCTION

At analysis of the open-ended rectangular waveguide, H -plane horn and E -plane horn excited by wave H_{10} the following heuristic conjectures are used:

- 1) field distribution in the waveguide aperture coincides a field distribution of a travelling wave;
- 2) field distribution in a horn of final length coincides with the field in the applicable part of an infinite horn. The wave front in a horn is considered as a part of a surface of the cylinder, the axis which one coincides an edge of a dihedron formed by divergent walls of the horn. The obtained formulas for calculation of the radiation of these three devices are not tied one with another, see, for example, [1, 2, 3].

In the paper [4] H_{10} mode of the rectangular waveguide with cross-section $a \times b$ is reviewed as the sum of magnetic and electric modes H_{01} , E_{00} of two orthogonal flat waveguides with spacing interval between plates a and b and then with usage of a stringent solution [5] of diffraction problem on the flat waveguide opened end the analytical proportions for the reflectance R_{10} and gain D_0 of the open-ended rectangular waveguide are obtained.

In progressing such an approach in this paper for optimal horns in H and E plains a generalized analytical gain dependence on aperture dimensions, an effective area and an area use factor are retrieved.

2. REFLECTANCE AND GAIN OF OPEN-ENDED RECTANGULAR WAVEGUIDE

Let us write down a gain of the open-ended waveguide with cross-section $a \times b$ in the direction of a radiation maximum at $\theta = 0$ on wavelength λ as [4]

$$D_0 = \frac{8 \cdot F(0)}{R_{\text{lenk}}}, \quad (1)$$

where $F(0) = \frac{8q^2\gamma^2 \exp[\pi(q-\gamma)]}{\pi(q+\gamma)}$ is a power radiating in simple solid angle $(\Delta\theta)^2$ at $\theta = 0$;

$$q = a/\lambda, \quad \gamma = \sqrt{q^2 - 0,25}, \quad \nu = b/a;$$

$$R_{\text{lenk}} = \gamma q \left\{ 1 + \frac{4\gamma \exp[\pi(q-\gamma)]}{\pi(q+\gamma)} \right\} (1 - |R_{10}|^2)$$

is an active loss power of wave H_{10} in the rectangular waveguide, $|R_{10}|$ is its opened end reflectance modulus.

Plots of function D_0 are shown in Fig. 1.

Let us re-arrange Eq. (1) for the case of large aperture dimensions, i.e. when $\gamma \rightarrow q$. Then

$$F(0) \rightarrow \frac{4q^3}{\pi}, \quad R_{\text{lenk}} \rightarrow q^2 \left(1 + \frac{2}{\nu\pi} \right) (1 - |R_{10}|^2).$$

Fig. 2 and Fig. 3 show reflectance R_{10} of the current, calculated by formulas of paper [4]. It is seen from Figs. 2, 3, that $|R_{10}| \approx 0$ at $a \geq 0,7\lambda$, $b \geq a$ or at $a \geq 4\lambda$, $b > 0,4a$.

At $|R_{10}| \approx 0$ we receive an approximate formula for a gain of the large aperture rectangular waveguide with wave H_{10}

$$D_{\text{ap}} \approx \frac{32\nu}{\nu\pi + 2} q + C. \quad (2)$$

Values of coefficient C calculated under formulas (1), (2) are shown in a table.

Table 1.

$\nu = b/a$	1	1.5	2	2.5	3	4
C	1.49	1.969	2.30	2.539	2.72	2.98

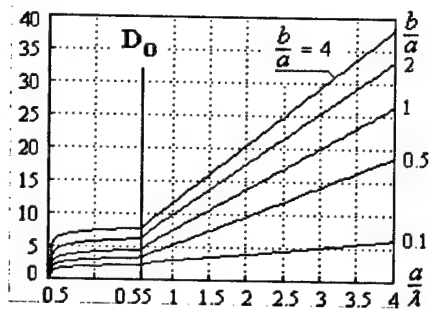


Fig. 1. Gain of the open-ended rectangular waveguide.

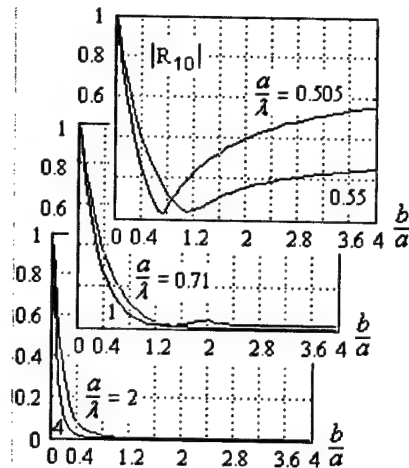


Fig. 2. Reflectance modulus of the open-ended rectangular waveguide

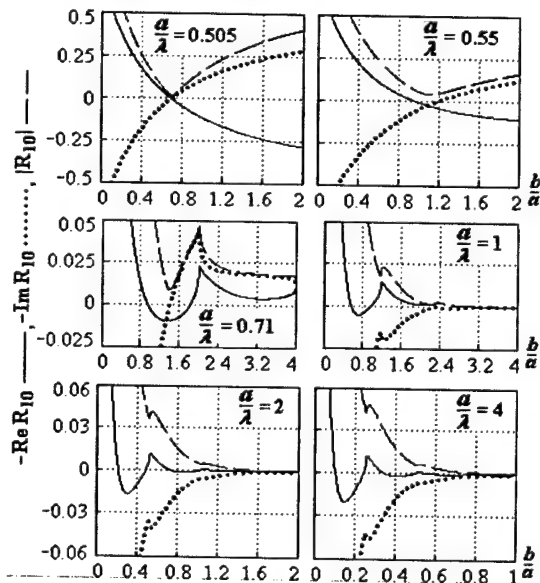


Fig. 3. Reflectance of the current of the open-ended rectangular waveguide

3. OPTIMAL PLANE HORN GAIN

Plane horns are formed by the extension of a waveguide cross-section dimension in the H or E plain (Fig. 4).

Supposing, that in the horn aperture wavelength $\Lambda_{10} = \lambda$ and characteristic resistance $Z_{c10} = 120\pi\Omega$, H - and E -plane horn gains are counted under formulas [1]:

$$D_H = \frac{4\pi b R_H}{\lambda A} \{ [C(u) - C(u1)]^2 + [S(u) - S(u1)]^2 \}; \quad (3)$$

$$D_E = \frac{64a R_E}{\pi \lambda B} [C^2(u2) + S^2(u2)], \quad (4)$$

where $C(t) = \int_0^t \cos\left(\frac{\pi x^2}{2}\right) dx$, $S(t) = \int_0^t \sin\left(\frac{\pi x^2}{2}\right) dx$

are the Fresnel's integrals;

$$u = \frac{1}{\sqrt{2}} \left(\frac{\sqrt{\lambda R_H}}{A} + \frac{A}{\sqrt{\lambda R_H}} \right);$$

$$u1 = \frac{1}{\sqrt{2}} \left(\frac{\sqrt{\lambda R_H}}{A} - \frac{A}{\sqrt{\lambda R_H}} \right); \quad u2 = \frac{1}{\sqrt{2}} \frac{B}{\sqrt{\lambda R_E}};$$

R_H , R_E are the horn length from an dihedron edge inside the waveguide to an aperture with dimensions $A \times b$ or $a \times B$ (Fig. 4).

In Fig. 5 functions $D_0(\alpha = q, \nu = 2)$ (1),

$D_H \frac{\lambda}{b}(\alpha = A/\lambda)$ (3), $D_E \frac{\lambda}{a}(\alpha = B/\lambda)$ (4) are shown.

We see from Fig. 5, that plot $D_0(\alpha = q, \nu = 2) = D_0(\alpha)$, determined from the problem solution of open-ended rectangular waveguide, traverses maximums of plane horn gains $D_H \frac{\lambda}{b}$, $D_E \frac{\lambda}{a}$, applicable to plane horns optimal in gain.

Curve $D_0(\alpha)$ represents a generalized gain dependence on the aperture dimensions of an optimal plane horn in any of plains H or E and taking into account (2) and table function $D_0(\alpha)$ is approximated at $\alpha \geq 2$ as

$$D_0(\alpha) \approx \frac{32 \cdot 2}{2\pi + 2} \alpha + 2,3 \approx 7,726\alpha + 2,3. \quad (5)$$

Using plot $D_0(\alpha)$ it is possible to determine parameters of any optimal plane horn on the given gain. For example, for preset GAIN = 100 of a plane horn it is necessary to find aperture dimensions and length of H -, E -horns R_H , R_E . On a function scale (Fig. 5) we tag dot Gain = 100, under plot $D_0(\alpha)$ or under formula (5) we discover argument $\alpha = 12,646$. From here we determine the horn aperture dimensions by

$$A \times b = 12,646\lambda \times \lambda \text{ and } a \times B = \lambda \times 12,646\lambda.$$

For H -, E -optimal horns the greatest lagging on aperture edges is equal to

$$\psi_{H \max} = \frac{2\pi}{\lambda} \sqrt{R_H^2 + (A/2)^2} - R_H = \frac{3\pi}{4};$$

$$\psi_{E \max} = \frac{2\pi}{\lambda} \sqrt{R_E^2 + (B/2)^2} - R_E = \frac{\pi}{2}.$$

then obtain

$$R_H = \frac{4}{3} [(\alpha/2)^2 - (3/8)^2] = 53,1\lambda, \quad (6)$$

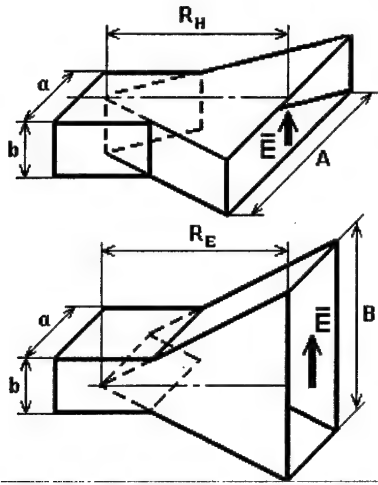
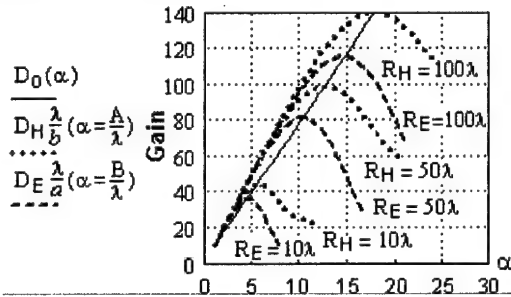
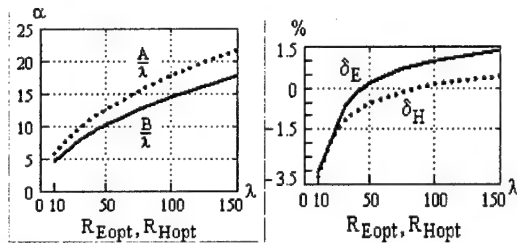


Fig. 4. H-, E-plane horns.


 Fig. 5. Optimal plane horn gain $D_0(\alpha)$; H-plane, E-plane horn gains D_H , D_E

 Fig. 6. The relation of optimal plane horn dimensions and offsets δ_H and δ_E . (8)

$$R_E = 2[(\alpha/2)^2 - 0,25^2] = 79,8\lambda. \quad (7)$$

That corresponds to values of functions (3), (4)

$$D_H \frac{\lambda}{b} = 101,98, \quad D_E \frac{\lambda}{a} = 103,01.$$

We instituted lengths of optimal horns for GAIN=100 and have obtained a little bit other gain values. A reason, probably, is the assumptions adopted at the deduction of functions (3), (4). In Fig. 6 dependences on optimal horn length R_{Hopt} , R_{Eopt} of dimensions A/λ at $b = \lambda$ and B/λ at $a = \lambda$ are shown. Also offset magnitudes δ_H , δ_E of generalized dependence $D_0(\alpha)$ on maximums of functions (3), (4) are given.

$$\delta_H = \frac{\max(D_H \frac{\lambda}{b}) - D_0}{D_0}; \quad \delta_E = \frac{\max(D_E \frac{\lambda}{a}) - D_0}{D_0}. \quad (8)$$

From Fig. 6 it is possible to see the almost proportional dependence of the aperture dimensions of an optimal plane horn on its length.

In a interval of lengths of a H-planar horn of $10\lambda \leq R_{Hopt} \leq 150\lambda$ magnitudes of offsets δ_H between curve $D_0(\alpha)$ and maximums of function $D_H \frac{\lambda}{b}(\alpha = A/\lambda)$ lay in limits from -3,228 % up to 0,442 %, offsets δ_E for function $D_E \frac{\lambda}{a}(\alpha = B/\lambda)$ at $10\lambda \leq R_{Eopt} \leq 150\lambda$ lay in limits from -3,091 % up to 1,402 %.

Plots $\frac{A}{\lambda}(R_{Hopt})$ and $\frac{B}{\lambda}(R_{Eopt})$ in Fig. 6 allow, passing calculations under formulas (6), (7), to find required length of an optimal horn R_{Hopt} or R_{Eopt} after the determination of magnitude α on Fig. 5. Then on retrieved horn length it is possible to evaluate offsets, having taken advantage curves $\delta_H(R_{Hopt})$ or $\delta_E(R_{Eopt})$.

4. EFFECTIVE AREA AND AREA USE FACTOR (AUF) OF RECTANGULAR APERTURE

The geometrical and effective areas (S, A_e) of an antenna aperture, antenna gain D_0 along an electrical axis and area use factor K_S are connected by proportions

$$A_\lambda = A_e/\lambda^2 = D_0/(4\pi); \quad K_S = \lambda^2 D_0/(4\pi S). \quad (9)$$

Let for two optimal H- and E-horns

$$D_H \frac{\lambda}{b}(\alpha = \frac{A}{\lambda}) = D_E \frac{\lambda}{a}(\alpha = \frac{B}{\lambda}) \quad \text{and also} \quad \frac{A}{\lambda} = \frac{B}{\lambda}. \quad (10)$$

Taking into account (9) for these horns

$$A_\lambda(\alpha) = D_0(\alpha)/(4\pi), \quad K_S(\alpha) = D_0(\alpha)/(4\pi\alpha). \quad (11)$$

Taking into account (5)

$$K_S(\alpha) = (7,726\alpha + 2,3)/(4\pi\alpha). \quad (12)$$

In Fig. 7 dependences (11) and $S_\lambda = S/\lambda^2 = \alpha$ for H- and E-horns (10) and for comparison normalized effective area $A_\lambda(a/\lambda)$ and area use factor $K_S(a/\lambda)$ (13) of standard waveguide IEC-14 with mode H_{10} are shown.

$$A_\lambda(a/\lambda) = D_0/4\pi; \quad K_S(a/\lambda) = \lambda^2 D_0/(4\pi ab). \quad (13)$$

For the standard waveguide in a long wavelength part of the operating range we have area use factor $K_S(a/\lambda) \geq 1$. A range with $K_S(a/\lambda) \geq 1$ is the

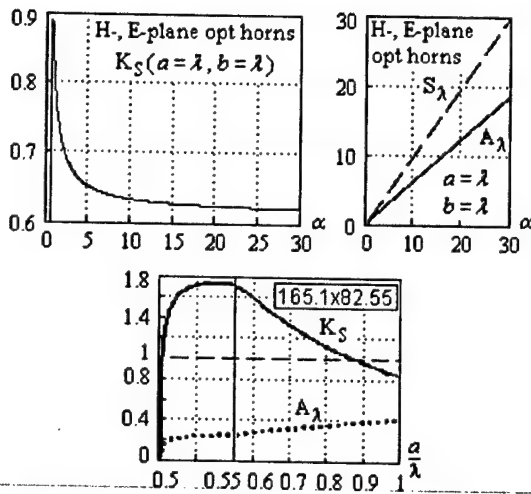


Fig. 7. The area use factor K_S and the effective area A_λ of rectangular apertures

more widely, than it is less ratio b/a (compare with [4]). Area use factor $K_S(r/\lambda) \geq 1$ is obtained also for the opened end of a circular guide with wave H_{11} near to extreme value of radius r [5].

For the open-ended rectangular waveguide in the literature value $AUF \approx 0.81$ is given. It follows from conjecture 1, reduced in the introduction, see, for example, [2, 3].

For optimal H - and E -horn with the identical aperture dimensions $\alpha = A/\lambda = B/\lambda$, $a = b = \lambda$, is receivable the identical effective areas and AUF. At variation α (and normalized geometrical area S_λ) from 2 up to 30 magnitudes of AUF $K_S(\alpha)$ receives values from 0,704 up to 0,621 and has maximum of 0,889 at $\alpha = 0,56$.

In the literature on antennas different values of the area use factor of optimal horns are given:

$$\begin{aligned} AUF_H = AUF_E = 0.64 [1], \\ AUF_H = 0.66, AUF_E = 0.52 [2], \end{aligned}$$

$$AUF_H = 0.64, AUF_E = 0.8 [3].$$

5. CONCLUSION

It is shown, that the reflectance modulus of wave H_{10} from the opened end of the waveguide with cross-section $a \times b$ becomes negligible small at $a \geq 0,7\lambda$, $b \geq a$ or at $a \geq 4\lambda$, $b > 0,4a$. Thus the gain dependence of the open-ended waveguide on a/λ at $a/b = \text{const}$ corresponds to generalized gain dependence of optimal H -, E -plane horns on the horn aperture dimensions.

Designed formulas (11), (12) of an effective area and an area use factor of the optimal horns are obtained. At variation of geometrical aperture area S from $2\lambda^2$ up to $30\lambda^2$ the area use factor of optimal horns receives values from 0,704 up to 0,621. For the open-ended standard waveguide the area use factor is more or equal to unit at the long wavelength part of the operating range.

REFERENCES

1. Aizenberg G. Z. Antennas of ultra-short waves. Moscow: State Publishing House on link and wireless. 1957. (in Russian).
2. Microwellenantennen. Rudolf Kühn. Veb Verlag Technik, Berlin, 1964.
3. Markov G. T. and Sazonov D. M. Antennas. Moscow: Energy. 1975. (in Russian).
4. Butakova S. V. Usage of solutions for the flat waveguide at analysis of the open-ended rectangular waveguide radiation. // Moscow: Publishing House of the Journal «Radiotekhnika». Antennas, № 12 (67), p. p. 48-54. 2002 (in Russian)
5. Weinstein L. A. The diffraction theory and factorization method. Moscow: Soviet Radio, 1966. (in Russian).

THE INVESTIGATION OF RADIATION CHARACTERISTICS OF FRESNEL ANTENNA FOR Q-BAND

Magro V. I., Morozov V. M.

Dnepropetrovsk National University,
13 Naukova st., Dnepropetrovsk, Ukraine, 32050,
<morozovavu@mail.ru> tel. 0562-467995

Abstract

The general approach to analysis of zonal Fresnel antenna is considered. The frequency characteristics of Fresnel antenna are analyzed. The radiation characteristics of the Fresnel antenna are considered.

Keywords: Fresnel antenna, focus, radiation pattern.

1. INTRODUCTION

Recently the interest to investigation of the plane zonal antennas has increased notably [1, 2]. The printed antennas are widely used in the systems of satellite television. In some cases these antennas may compete with classic parabolic reflector. The printed plane antenna has advantages in construction, exploitation and value.

The results of investigations of plane sounded antenna radiation characteristics are presented. This plane structure named the Fresnel antenna has been considered (Fig. 1).

2. ANALYSIS OF DIFFRACTION ON PLANE RING STRUCTURE

Let us consider the diffraction problem on ringing structure by the method of integral equation. In the

general case, the diffraction problem on conducting unclosed surface S can be solved as the boundary problem of Helmholtz equation. The unknown function (vector of secondary field A_m) must satisfy the Helmholtz equation, boundary condition, edge condition and condition of radiation.

Another approach to this problem is known. The diffraction problem under study can be solved by integral equation for current density j . The current density j is induced on the surface S [3].

Let surfaces S_1, S_2, \dots, S_n be the plane rings $a_q \leq r \leq b_q$, $0 \leq \varphi \leq 2\pi$, $z = z_q$. Denote r_q , φ_q , z_q and ρ_p , ψ_p , ς_p as the spherical coordinates of the points $M_0 \in S_q$, $q = 1, 2, \dots, n$, and $M \in S_p$, $p = 1, 2, \dots, n$. The vector of current density components j_{xq} and j_{yq} induced on surface S_q , $q = 1, 2, \dots, n$ can be expanded in the Fourier series

$$j_v(\rho, \psi) = \sum_{m=-\infty}^{\infty} j_v^{(m)}(\rho) e^{im\psi}; v = x, y$$

In this case, the secondary vector potential A at the point $M \in S_q$ is created by the currents leaking on S_q and on the other surfaces. Then we have

$$\begin{aligned} & \frac{i\omega\mu}{4\pi} \sum_{p=1}^{p=n} \int_{a_p}^{b_p} j_{xp}^{(m)}(\rho_p) \rho_p d\rho_p \times \\ & \times \int_0^{2\pi} \frac{e^{-ikL_{pq}}}{L_{pq}} \cos(m\beta) d\beta = \\ & = -i\omega \hat{A}_{xq}^{(m)}(r_q) + C_{1q}^{(m)} J_m(kr_q) + \\ & + C_{2q}^{(m)} N_m(kr_q) - g_{1q}^{(m)}(r_q) + g_{2q}^{(m)}, \\ & a_q \leq r_q \leq b_q \end{aligned} \quad (1)$$

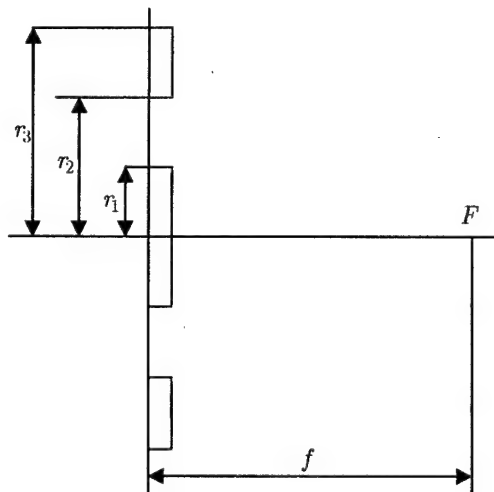


Fig. 1.

$$\begin{aligned} & \frac{i\omega\mu}{4\pi} \sum_{p=1}^n \int_{a_p}^{b_p} j_{yp}^{(m)}(\rho_p) \rho_p d\rho_p \times \\ & \int_0^{2\pi} \frac{e^{-ikL_{pq}}}{L_{pq}} \cos(m\beta) d\beta = \\ & = -i\omega \hat{A}_{yq}^{0(m)}(r_q) - id_{1q}^{(m)} J_m(kr_q) - \\ & - id_{2q}^{(m)} N_m(kr_q) + ig_{1q}^{(m)}(r_q), \quad a_q \leq r_q \leq b_q, \end{aligned} \quad (2)$$

where

$$L_{pq} = \sqrt{r_q^2 + \rho_p^2 - 2r_q\rho_p \cos \beta + (z_p - z_q)^2};$$

$A_{xq}^{0(m)}(r_q)$ and $A_{yq}^{0(m)}(r_q)$ are the Fourier components of the initial vector potential. The vector potential is calculated at the point of surface S_q . The functions $g_{1q}^{(m)}(r_q)$ and $g_{2q}^{(m)}(r_q)$ are written in the following form

$$g_{1q}^{(m)} = \frac{1}{2} \left[\frac{m-1}{r_q} P_{1q}^{(m-1)}(r_q) - \frac{dP_{1q}^{(m+1)}(r_q)}{dr_q} \right];$$

$$g_{2q}^{(m)} = \frac{1}{2} \left[\frac{m-1}{r_q} P_{2q}^{(m-1)}(r_q) + \frac{dP_{1q}^{(m+1)}(r_q)}{dr_q} \right];$$

$$\begin{aligned} P_{1q}^{(m)} &= \frac{\pi}{2} \left\{ J_m(kr_q) \int_{r_q}^{b_q} f_q^{(m)}(\rho_q) N(k\rho_q) \rho_q d\rho_q + \right. \\ & \left. + N_m(kr_q) \int_{a_q}^{r_q} f_q^{(m)}(\rho_q) J_m(k\rho_q) \rho_q d\rho_q \right\}. \end{aligned}$$

The function $f_q^{(m)}$ represents the coefficients of expansion into the Fourier series of function $f_q(r, \varphi)$

$$f_q(r, \varphi) = \sum_{m=-\infty}^{\infty} f_q^{(m)}(r) e^{im\varphi}.$$

The constants $C_{1q}^{(m)}, C_{2q}^{(m)}, d_{1q}^{(m)}, d_{2q}^{(m)}$ can be expressed in terms of constants $b_1^{(m\pm 1)}$ and $b_2^{(m\pm 1)}$. The constants $b_1^{(m)}$ and $b_2^{(m)}$ are defined from the following condition

$$j_{rq}^{(m)}(a_q) = j_{rq}^{(m)}(b_q) = 0,$$

where $j_{rq}^{(m)}$ is the m -th harmonic of the Fourier radial component of the vector of current density. These currents are induced on the surface S_q .

In general case, the numerical solution of double integrals of oscillation function (1), (2) is very difficult. The integrals like (1) and (2) can be reduced to the single integrals only for the cases when plane wave impinges normally the plane of ring location. Therefore, it is more expedient in most practical cases to consider this problem by geometrical optics approximation.

3. ANALYSIS OF FREQUENCY PROPERTIES OF FRESNEL ANTENNA

Let us consider the zonal Fresnel antenna. This antenna is being constructed by the way of hiding of the halves of the Fresnel zones, which make the antiphase contribution to the field. The condition of coherence summation addition of radiation at the focal point f is

$$f + \frac{k\lambda}{4} = f^2 + r_k^2,$$

where k is equal to $1, 3, \dots, N$.

The expression for radius of the Fresnel zone may be written as

$$r_k = \sqrt{\frac{k\lambda f}{2} + \frac{k^2\lambda^2}{16}}.$$

The position of focus of the Fresnel antennas changes as

$$f = \frac{r_N^2}{2k\lambda} + \frac{N\lambda}{2}. \quad (3)$$

Thus, as the wavelength λ and the number of rings change, the focus distance f also changes. The role of the second term grows with the increase of the wavelength λ , when the first term decrease, whereas the second one increases. In the second term of the expression (3) becomes more than the first term, then the antenna turns to the scattering one.

The value of f is equal to zero when $\lambda_0 = \frac{r_N}{N}$.

Fresnel antenna becomes scattering one, when $\lambda > \lambda_0$. Fresnel's antenna becomes converging one, when $\lambda < \lambda_0$. Taking into account the denotations equation (3) can be written in the following form

$$f = \frac{N\lambda}{2} \left[\left(\frac{\lambda_0}{\lambda} \right)^2 + 1 \right].$$

The significant part in the frequency performances of the Fresnel antenna is played by the value of relative aperture diameter D/λ ($D = r_N$). From the results shown in paper [4] the condition of unselectivity is

$$\frac{D}{f} \leq \frac{1,856}{\sqrt[3]{D/\lambda}}.$$

4. RESULTS OF EXPERIMENT

The structure of diffracted field on the Fresnel antenna with number of rings $N = 3, 5, 7, 10$ has been investigated. The Fresnel antenna has been calculated for frequency band 10.7...11.7 GHz. The field distribution along axle of antenna is analyzed. It is established that maximum of radiation intensity along axis of antenna depends on wavelength. The analysis of the field distribution has shown that focus ("real focal point") is shifted along the axis. The transversal distribution of the field amplitude in the focus plane has been investigated.

The radiation pattern of antenna with number of rings $N = 3, 5, 7, 10$ has been measured. It is established that the position of intensity maximum on the longitudinal axis depends on the wavelength. The results of measurement are in a good agreement with other available data [5, 6]. It is determined that width of radiation pattern of the Fresnel antenna lies within $8-10^\circ$. The measurements of different types of horn feed have been carried out. A maximum of antenna directive gain is 19.6. It has been shown that as the number of the Fresnel antennas elements N increases, the width of the radiation pattern changes insignificantly (no more than 20 %), whereas the value of the directive gain increases significantly. The increase of the element number N in the Fresnel antenna leads to some narrowing of the operating frequency band.

5. CONCLUSION

The general approach to the analysis of diffraction phenomena on the Fresnel antenna based on the method of integral equation has been considered. The analysis of frequency characteristics of the Fresnel antenna has been carried out. The Fresnel antenna for Q-band has been investigated.

REFERENCES

1. Fresnel antenna // IEEE Electronics and Wireless World. – 1989. – Vol. AP-24. – No. 9. – 8127 p.
2. Kronkevich V.P., Palchikova L.G. Modern zone plate // Avtometrija. – 1992. – №1. – P. 57-61 (in Russian).
3. Zakcharov E.V., Pimenov Y.V. Numerical analysis of wave diffraction. Moscow: Radio I svjaz, 1982. – 184 p. (in Russian).
4. Bazarskij O.V., Kolesnikov A.I., Hljavich J.L. Band characteristics of Fresnel antenna // Radio-technika i elektronika. – 1980. – №12. – P. 2492-2497 (in Russian).
5. Voloshin O.I., Tsaliev T.A. Investigation of frequency characteristics of Fresnel antenna // Radioelectronika. – 1995. – №9. – P. 43 – 46 (Izv. vuzov) (in Russian).
6. Leschuk I.I., Tsaliev T.A. Numerical analysis of lens antenna of Fresnel // Radioelectronika. – 1998. – №5. – P. 3 – 8 (Izv. vuzov) (in Russian).

CALCULATION OF NON-AXISYMMETRICAL PARABOLIC REFLECTOR ANTENNAS

A. V. Alpatova, A. M. Gorin, I. N. Kad'kalo

Federal State Unitary Enterprise Taganrog Research Institute of Communication
(Russia) <beletsky@style.tgn.ru>

Abstract

An aperture method is used for calculation of non-axisymmetrical parabolic reflector antennas. The possibility of scanning of horizontal-plane pattern at rotation of reflector at fixed radiator is investigated. The results of numerical and measurement experiments are presented in the paper.

Keywords: Non-axisymmetrical parabolic reflector antenna, pattern, aperture method.

1. INTRODUCTION

Today many books and papers on calculation of parabolic reflector antennas are published, for example [1-3], however calculation of non-axisymmetrical parabolic reflector antennas is not quiet considered in the literature known for the authors.

In the paper, mechanical beam scanning of the pattern of a non-axisymmetrical parabolic reflector antenna is researched at rotation of reflector in main planes with respect to a fixed radiator. The use of the mechanical method of scanning allows excluding rotating joints from a transmitting tract of radio-electronic equipment and diminishing dimensions and cost of rotating devices, as well as improving adjustment of the tract at wide frequency band [4].

2. THEORETICAL PART

Calculation of the pattern of a non-axisymmetrical parabolic reflector antenna (Fig.1) is carried out with the aperture method.

If to neglect currents leaking to a shady side, it is possible to define the field intensity at any point of

space by the field distribution on a surface of an antenna aperture.

A method of geometric optics is used for approximate determination of the field distribution in the aperture plane. According to the method, every radiator beam incident on the surface of parabolic antenna corresponds to a beam reflected by this surface.

On the way from the radiator to an aperture of antenna paraboloid, an amplitude of beams decreases inverse proportional to a distance. Thus, if the antenna radiator with radiation pattern (RP) $F_{fn}(\psi, \varphi)$ is disposed in the focus of paraboloid, the field distribution in the aperture is defined by the formula

$$E(\psi, \varphi) = \frac{F_{fn}(\psi, \varphi) \cdot 2f}{l_t}, \quad (1)$$

where f is the focal distance, $l_t = l_i + l_r$ is the length of beam path from radiator to paraboloid aperture.

RP of aperture with distribution (1) is determined as follows

$$F(\theta, \phi) = \iint_S E(\psi, \varphi) \cdot F_1(\theta) \cdot e^{-i\Phi(\psi, \varphi, \theta, \phi)} dS,$$

where

$$\Phi(\psi, \varphi, \theta, \phi) = \Phi_a(\psi, \varphi) - \frac{2\pi}{\lambda} \sin \theta (y_a \cos \phi + z_a \sin \phi)$$

is the spatial phase coefficient of pattern of non-axisymmetrical parabolic antenna, λ is the wavelength, $F_1(\theta) = \left(\frac{1 + \cos \theta}{2} \right) \cos \theta$ is the factor that

takes into account directive properties of elementary square and diminution of aperture at beam scanning,

$\Phi_a(\psi, \varphi) = \frac{2 \cdot \pi \cdot l_t}{\lambda}$ is the phase distribution in the

aperture of a parabolic reflector antenna, S is aperture plane of a non-axisymmetrical parabolic reflector antenna, angles θ, ψ are counted as Fig.2 shows,

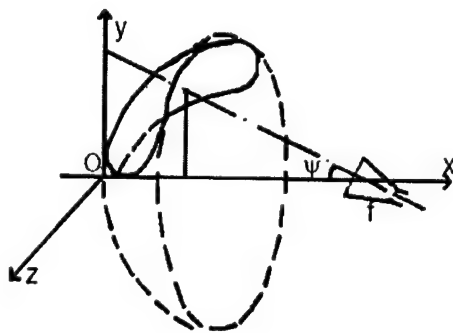


Fig. 1.

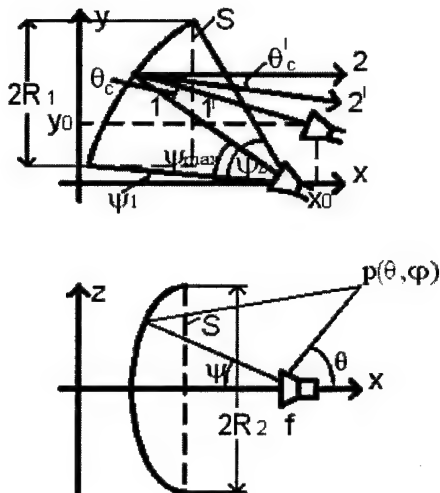


Fig. 2.

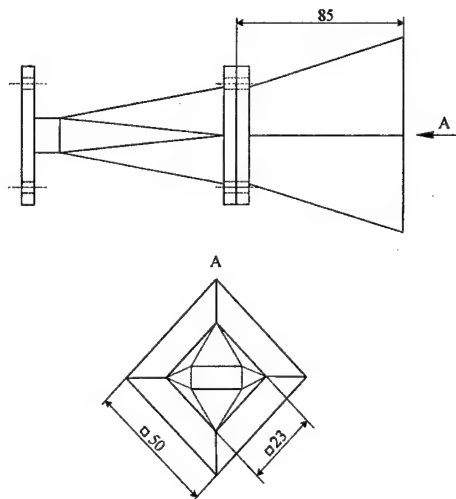


Fig. 3.

angles ϕ , φ are counted from axis Oy in plane of aperture of parabolic reflector antenna.

Beam scanning (deviation of irradiation maximum by angles θ'_c , φ'_c , Fig.2) takes place as a result of change of inclination angles of paraboloid in azimuthal or elevation planes (or displacement of antenna radiator along line by some angles).

Computer programs were developed and carefully tested. Testing of programs was realized by experimental data.

Two pyramidal horns were considered as antenna radiators:

- 1) with the aperture of 55×55 mm, length of 150 mm, horizontal polarization, frequency of 5 GHz,
- 2) with squared output 23×23 mm and transition to the rectangular section of 23×10 mm at an angle of 45° , horn aperture of 50×50 mm, length of 85 mm, horizontal polarization, frequency of 8 GHz, Fig.3.

The first horn excited a non-axisymmetrical parabolic reflector antenna 1 ($\psi_{\max} = 49^\circ$ is the direction of

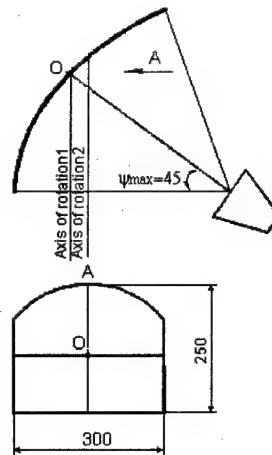


Fig. 4.

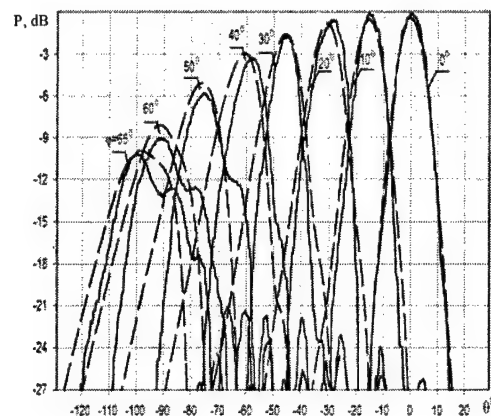


Fig. 5.

maximum radiation of antenna radiator) with parameters of reflector $\psi_1 = 20^\circ$, $\psi_2 = 80^\circ$, $f = 16$ cm, $R_1 = 10.604$ cm, $R_2 = 17.674$ cm, the second horn was used for irradiation of non-axisymmetrical parabolic reflector antenna 2 (Fig.4) ($\psi_{\max} = 45^\circ$) with parameters of reflector $\psi_1 = 0^\circ$, $\psi_2 = 76^\circ$, $f = 16$ cm, $R_1 = 12.5$ cm, $R_2 = 15$ cm.

Usually, it is accepted to use not the volumetric RP, but its sections in fixed main planes. For that, first, elevation RP (main vertical pattern) was plotted, then, after angle θ'_c is defined, calculation of RP of non-axis-symmetric parabolic reflector antenna in azimuthal plane (perpendicular plane xOy and passing through maximum pattern) was carried out.

3. RESULTS OF RESEARCH

The investigations of non-axisymmetrical parabolic reflector antenna RP were carried out at rotation of reflector in vertical and horizontal planes.

Fig. 5 shows the good agreement of the obtained results (long dashed line) to the measured data (solid line) for the RP of non-axisymmetrical parabolic re-

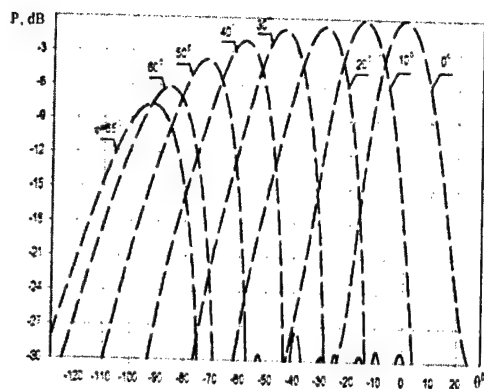


Fig. 6.

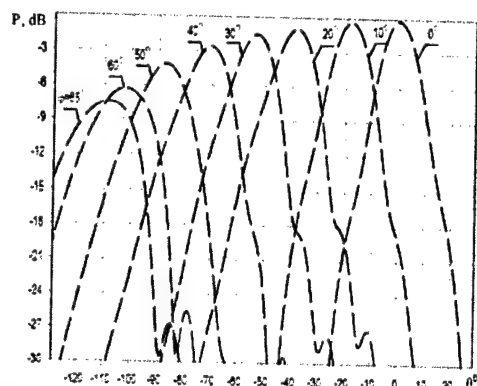


Fig. 7.

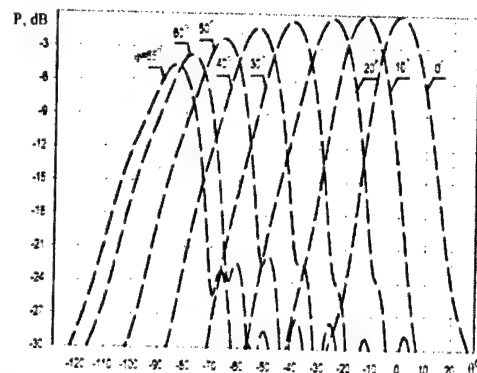


Fig. 8.

reflector antenna 2 at scanning in azimuth plane (E-polarization pattern).

Radiator antenna 2 was in the focus of parabolic reflector. Scanning was performed at azimuthal rotation of reflector by angle ψ . Possibly, some noncoincidence of patterns for $\psi = 40^\circ..65^\circ$ is explained by the fact that the aperture of reflector was approximated for calculation either by a rectangle or an ellipse and additionally points of reflector turning were different in calculation (axis 1, Fig.4) and measurement (axis 2, Fig.4).

Figs.6-8 show the calculated RPs of non-axisymmetrical parabolic reflector antenna 1 with first radiator by azimuth scanning (E-polarization pattern), angle of rotation is attributed to every pattern. In addition,

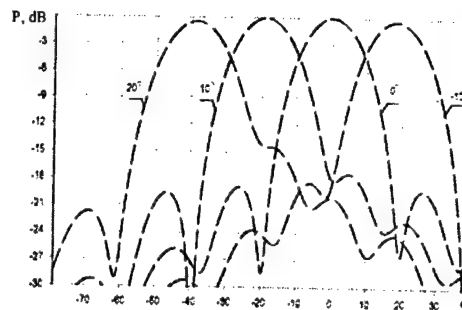


Fig. 9.

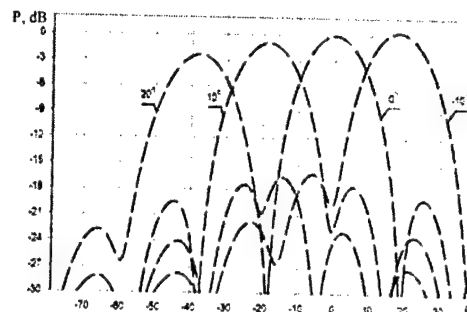


Fig. 10.

tion, elevation turning of reflectors were 0° (Fig.6), 30° (Fig.7), -10° (Fig.8) in the vertical plane.

Figs.9-10 show the calculated elevation patterns of non-axisymmetrical parabolic reflector antenna 1 with first radiator, angle of rotation is attributed to every pattern. Azimuthal turn was 0° (Fig.9), -10° (Fig.10).

4. CONCLUSION

The presented results show that it is possible to build non-axisymmetrical parabolic reflector antennas with scanning of pattern at a wide sector of angles ($\pm 90^\circ$ in azimuthal plane with diminution of signal to -7 dB). An angle of deviation of pattern from direction $\theta = 0^\circ$ conforms to angle of turn of reflector about with factor 1.5. The elevation pattern is much wider than the azimuthal pattern and deviation of pattern is performed close to angle 2ψ with turn of reflector to some angle ψ .

REFERENCES

1. Izenberg G.Z., Yampol'sky V.G., Teryoshin O.N. USW Antennas. - M.: «Svyaz'» - 1977. (in Rus.)
2. Kyun R. Microwave antennas. - L.: "Sudostroenie", 1967. (in Russ.)
3. Vood P. Analysis and design of reflector antennas - M.: «Radio i svyaz'» - 1984. (in Rus.)
4. Borisov A.A., Smirnov E.A., Fabryy A.A., Yukhanov Yu.V. Reflector antenna with mechanical beam scanning - Radioelektronika - V.45. - Issue.3. - 2002. (in Rus.)

COMBINED REFLECTOR – LENS MONOPULSE ANTENNA

Mikhail P. Natarov^{1,2}, Vladimir V. Glamazdin², Valery N. Skresanov^{1,2},
Alexander I. Shubny²

¹Institute of Radio Astronomy NAS of Ukraine;

²Institute of Radiophysics and Electronics NAS of Ukraine 12 Acad. Proskura Str.,
Kharkov, 61085, Ukraine Tel. +38(0572)-44-84-55, Fax +38-(0572)-441105,
<valery@ire.kharkov.ua>

Abstract

The combined reflector-lens antenna having the common monopulse feed system is proposed for changing the sum and difference patterns width by turning of lamellate subreflector. Such an antenna allows one to improve a target detection probability with the same tracking accuracy. Information for antenna designing is done. The prototype antenna measurements are discussed.

Keywords: Monopulse antenna, monopulse feed system, Cassegrain antenna.

1. INTRODUCTION

The monopulse reflector antennas designed according to Cassegrain scheme possess a high directivity. That provides adequate tracking accuracy [1,2]. At once detection probability for high-speed targets, existing at small distances is inadequate in view of speed limitation of the antenna drive mechanism. Proposed combined reflector-lens monopulse antenna allows this collision.

In combined antenna design beside two-reflector Cassegrain antenna exists a lens antenna, which has a wider beam. Apparently that in case of the wide-beam scanning target search duration decreases. After the hold of the target by the lens antenna pattern, take place commutation to the sum-difference pattern of the Cassegrain antenna. Thus the adequate detection probability and tracking accuracy are provided.

2. COMBINED ANTENNA PRINCIPLE

Principle and structure of the combined monopulse antenna are illustrated by the photo and scheme in Fig. 1. The feed horn phase center is situated in the point F_1 , which is the focus of hyperbolic subreflector 2, and the focus of lens 3. According to the classic Cassegrain scheme [1] the focus F_2 of the parabolic reflector 4 is combined with the far focus of the hyperbolic subreflector 2. Subreflector is made as a grid consisting of lamellas and mounted with possibility of rotation around the OZ axis of the antenna.

In Fig. 1 antenna version for H-polarized subreflector setting (H field vector is parallel to the lamellas of the grid) is shown. In this case the wave radiated by the feed horn passes thorough the subreflector to the lens, which forms a wide pattern (see ray 1).

If the subreflector is turned to angle 90° the wave, radiated by the feed horn, is reflected by the subreflector to the reflector, which forms a narrow pattern (see ray 2).

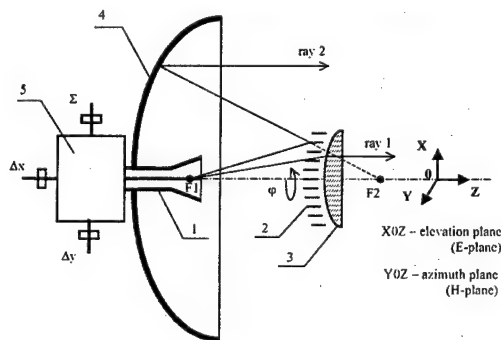
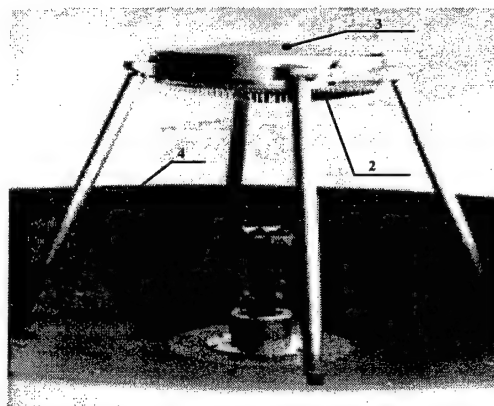


Fig. 1. Reflector-lens monopulse antenna: 1 - feed horn; 2 - hyperbolic grid subreflector; 3 - dielectric lens; 4 - parabolic reflector; 5 - sum-difference waveguide system.

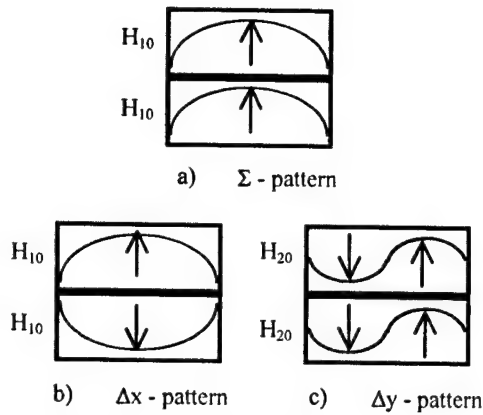


Fig. 2. Scheme of monopulse feed system excitation.

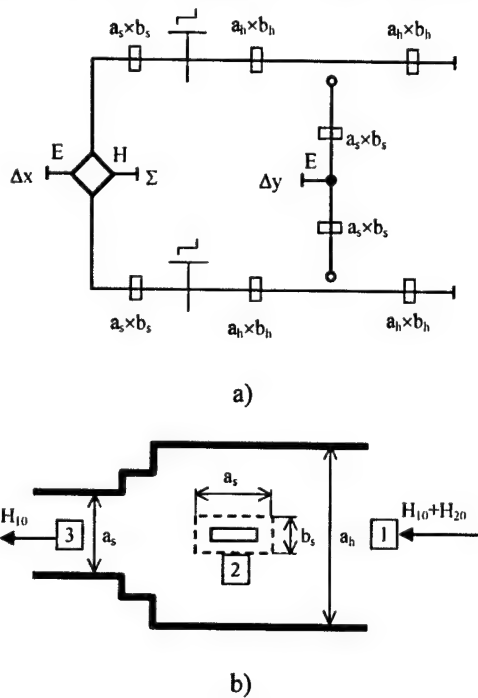


Fig. 3. Sum-difference waveguide system. a) scheme; b) wave types selector.

Thus proposed combined reflector-lens antenna has a pleasing individuality – common feed system for both reflector and lens antennas.

Monopulse feed system consists of the double-mode pyramidal horn 1 and the sum-difference waveguide system 5. There are three waveguide ports, marked as Σ , Δx , Δy .

We have developed the original design of the monopulse feed system albeit many technical solutions are described in literature (see, for example, [3]). The double-mode horn contains the metal baffle-board symmetrically mounted in H-plane. As a result we have two horns with throat cross-section $a_h \times b_h$ which are connected to sum-difference system ports. Waveguide cross-section is chosen so that H_{10} and H_{20} modes could propagate. For inphase H_{10} signals

in the both horns (see Fig. 2a) we obtain the sum pattern, for antiphase – the difference elevation pattern (see Fig. 2b). For inphase H_{20} signals (see Fig. 2c) we obtain the difference pattern in azimuth plane.

The sum-difference system scheme is illustrated in Fig. 3a. For separation H_{10} and H_{20} wave types in the two-mode waveguide with cross-section $a_h \times b_h$ we have designed the wave types selector (see Fig. 3b). It consists of stepped transition from the waveguide with cross-section $a_h \times b_h$ (port 1) to the waveguide with standard cross-section $a_s \times b_s$ (port 3) and rectangular slot for coupling to the standard waveguide (port 2). The coupling slot is manufactured in the center of the wide waveguide wall a_h . It has minimal width and does not disturb the H_{10} mode. The stepped transition reflects the H_{20} mode. Its dimensions and the distance from the slot were calculated to obtain maximum transition coefficients T_{13} and T_{12} from the two-mode waveguide to the port 3 for the H_{10} mode and to the port 2 for the H_{20} mode.

Difference signal Δy is obtained by summation of signals from the side ports of the selectors in a matched E-tee. Sum signal and difference signal Δx are obtained by separation of inphase and antiphase components of the sum of the H_{10} modes in the E-H-tee (see Fig. 3a).

3. COMPUTATION AND PROTOTYPE ANTENNA MEASUREMENTS

The basic parameters for designing of horn-lens and reflector antennas are directivities and side-lobe levels. Diameter of parabolic reflector was predefined. Calculation of radiation patterns of reflector antenna and lens antenna was done by aperture method [4] for the different parameters of subreflector, horn and lens. As a result optimum design of both antennas was found by heuristic method.

Field explanation on the horn aperture was assumed as sum of H_{10} and H_{20} modes and horns radiation field:

$$F(\theta, \varphi) = F0(\theta, \varphi)(A_1 F1(\theta, \varphi) + A_2 F2(\theta, \varphi))AF(\theta, \varphi),$$

where A_1 , A_2 – amplitudes of H_{10} and H_{20} modes on the horn aperture; $F0$, $F1$, $F2$ – are the patterns of rectangular aperture with dimensions $a \times b$ which is excited by one of the such modes:

$$F0(\theta, \varphi) = \frac{1 + \cos(\theta)}{2\lambda} \frac{b}{2} \frac{\sin\left(\frac{\pi b}{\lambda} \sin(\theta) \sin(\varphi)\right)}{\frac{\pi b}{\lambda} \sin(\theta) \sin(\varphi)},$$

$$F1(\theta, \varphi) = \frac{\pi a}{2} \frac{\cos\left(\frac{\pi a}{\lambda} \sin(\theta) \cos(\varphi)\right)}{\left(\frac{\pi}{2}\right)^2 - \left(\frac{\pi a}{\lambda} \sin(\theta) \cos(\varphi)\right)^2},$$

$$F2(\theta, \varphi) = -j\pi a \frac{\sin\left(\frac{\pi a}{\lambda} \sin(\theta) \cos(\varphi)\right)}{\pi^2 - \left(\frac{\pi a}{\lambda} \sin(\theta) \cos(\varphi)\right)^2};$$

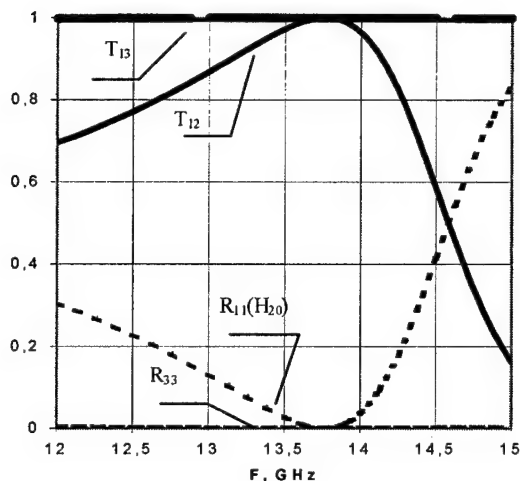


Fig. 4. Transmission coefficient T_{ij} and reflection coefficient R_{ij} ; $i, j = 1, 2, 3$ – waveguide selector ports (see Fig. 3).

AF is grid factor for the two rectangular plates, which is separated one from the other by metal partition with the thickness $2h$ and with excitation amplitudes ratio ΔA :

$$AF(\theta, \varphi) = \exp\left(\frac{-j\pi(b+h)}{\lambda} \cdot \sin \varphi\right) + \Delta A \cdot \exp\left(\frac{j\pi(b+h)}{\lambda} \cdot \sin \varphi\right)$$

For the defining of antenna directivity obtained pattern is normalized to the coefficient:

$$DG = \frac{1}{4\pi} \iint |F(\theta, \varphi)|^2 \sin \theta d\varphi d\theta$$

Having analyzed the result of calculations we have chose such antenna parameters:

- parabolic reflector with aperture 1200 mm and focal length 500 mm;
- feed horn with aperture in E-plane 44 mm, in H-plane 62 mm, partition thickness 1.6 mm;
- hyperbolic subreflector with aperture 230 mm, focal length 82,6 mm, eccentricity 2.25;
- single surface dielectric lens with hyperbolic surface, aperture 230 mm, focal length 66 mm, eccentricity 1.73, dielectric constant $\epsilon = 3$.

Selector parameters were calculated by accurate methods. Computation programs were worked out in the department of computational electromagnetics IRE NASU. Fig. 4 shows transmission and reflection coefficients vs. frequency. Central frequency of the selector is 13.75 GHz.

Calculated H-plane patterns of the horn, lens antenna, reflector antenna are explained in Fig. 5, Fig. 6, Fig. 7, correspondingly. Measured patterns are shown in the same place.

It is a good correspondence of the calculations and measured results for the H-plane within the patterns

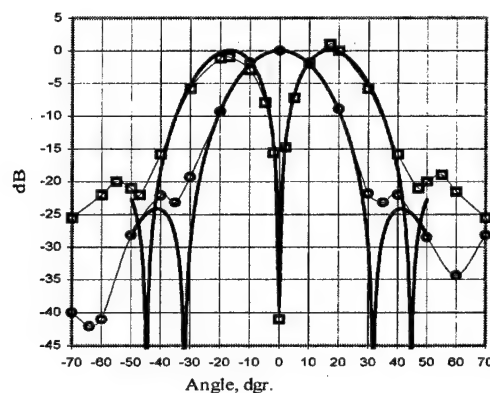


Fig. 5. Monopulse feed horn H-plane patterns. — - calculation, \circ - sum pattern, (measurement), \square - difference pattern (measurement).

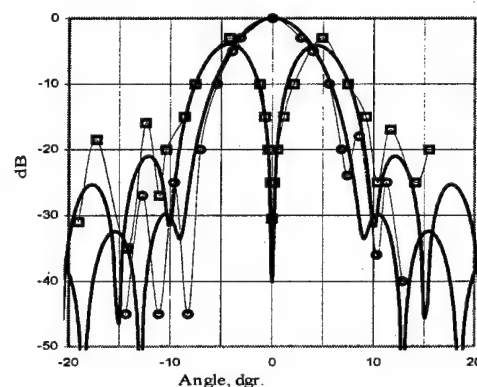


Fig. 6. Horn-lens antenna H-plane patterns. — - calculation, \circ - sum pattern, (measurement), \square - difference pattern (measurement).

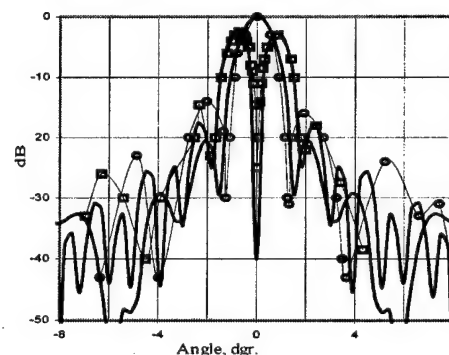


Fig. 7. Cassegrain antenna H-plane patterns. — - calculation, \circ - sum pattern, (measurement), \square - difference pattern (measurement).

main beam. Measured side-lobes for the lens antenna and the reflector antenna are higher then calculated levels. Additional scattering and aperture blockage of designs units that did not take into account in calculations cause it.

For the E-plane patterns it is the same correspondence of the calculations and measurements within the patterns main beam. Measured side-lobes for the E-plane is less then for the H-plane by 2...3 dB.

Finally let us describe the grid subreflector design procedure. Functional destination of the grid is absolute reflection of the E-polarized wave and absolute transmission of the H-polarized wave in bandwidth. Grid consists of metal rectangular lamellas in air ($\epsilon = 1$). Calculation of the geometrical parameters was made with help of the model: we replaced incident wave beam by the plane wave and hyperbolic reflecting surface by the plane surface. For such replacing we went by the small variation of reflection coefficients and transmission coefficients within the confines of the small incidence angles [5]. For chosen grid pitch – 5 mm and lamella thickness – 1 mm was calculated grid high – 10.3 mm. In this case reflection coefficient for E-polarized wave and transmission coefficient for H-polarized wave were not less than 99.99% in bandwidth. Measurement for the plane grid model had a good correspondence with the calculation. Thus the subreflector was manufactured as grid consists of lamellas having hyperbolic top and bottom edges 10.3 mm distant. Difference of the measured Cassegrain antenna patterns for the cases of solid subreflector and grid subreflector lies within the confines of measurement inaccuracy.

ACKNOWLEDGMENTS

The authors would like to thank Prof. D. Vavriv and V. Bormotov for statement of problem and Prof. A. Kirilenko, D.Sc. L. Rud', Ph.D. V. Tkachenko for waveguide units and grid subreflector computation programs.

REFERENCES

1. P. Bhartia, I.J. Bahl Milimeter. Wave Engineering and Applications, John Wiley & Sons, New York, 1984.
2. E.L. Holzman, R.L. Eisenhart, R.S. Robertson and L.A. Kihm. A Low-Cost Ka-Band Cassegrain Colormetric Tracking Antenna, IEEE AP-S International Symposium, Vol. 1, pp.16-19, 1992 Digest.
3. Skolnik M., editor, Radar Handbook, McGraw-Hill, 1970.
4. G.Z. Ayzenberg, V.G. Yanpolskiy, O.N. Terehin Microwave antenna. M.: Svyas, part 2, 1977, - 288p. (in Russian)
5. Diffraction of the waves on array/ V.P. Shestopalov, V.G. Sologub. Kharkov. Izdatelstvo Kharkovskogo universiteta, 1973, -278p.

AN ULTRA-WIDEBAND FEED FOR AXISSYMMETRICAL REFLECTOR ANTENNA

M. M. Bilanovskij², V. M. Glushenko¹, G. O. Ena², M. M. Litvin¹, S. M. Litvin¹,
O. E. Shrenk¹

¹ Department of Theoretical Foundations of Radio Engineering, National Technical
University of Ukraine "Kiev polytechnical institute", Kiev, Ukraine
<Alexandr_Shrenk@yahoo.com>

² State Scientific Research Institute of Radar-tracking Systems
"Kvant-radiolokatsia", Kiev, Ukraine

Abstract

Results of modelling of an ultra-wide feed built on a basis on log-periodic dipole antenna by a finite differences time domain method have been submitted. Structurally the feed is the H-plane array of single log-periodic antennas. Numerical results have been verified by experimental data.

1. INTRODUCTION

Wideband and ultra-wideband log-periodic dipole antennas (LPDA) are widely used as feeds for reflector antennas for various purposes. Advantages of the feeds are the capability of maintenance of the radiator pattern in all operating frequency bandwidth [1]. In this paper the results of synthesis of geometry of the ultra-wideband feed built as a H-plane array of two log-periodic structures as well as experimental results are presented.

2. CALCULATION OF IRRADIATOR BY THE FINITE DIFFERENCES TIMEDOMAIN METHOD

The LPDA consists of antennas of linear vibrators (Fig. 1). Lengths and distances between vibrators are changed in a geometrical progression with a parameter $\tau < 1,0$. The parameter S represents the distance (in lengths of waves) between the half-

wave and next (smaller) vibrator. The size S is related to τ as $S = 0,25(1 - \tau) \text{ctg } \alpha$, where α is the angle between an axis of the aerial and a line which is pass through the ends of vibrators. Vibrators are raised with a variable phase a symmetric line of constant wave resistance. Geometry of the LPDA (lengths of vibrators and distances between them) are defined under the known formulas:

$$l_1 = \lambda_{\text{max}} / 4, r_n = 4l_n \sigma, l_n = l_{n-1} \tau.$$

Calculation of characteristics of radiation is carried out with the help of method FDTD [2] which represents the direct numerical solution of the system of the differential Maxwell equations concerning electric and magnetic fields under the boundary conditions and conditions of excitation of structure in time. Thus completely closed algorithm provides modelling of excitation, distribution, scattering and radiation of an electromagnetic field by considered metal-dielectric structure in time domain. The subsequent application of the discrete or the fast Fourier transformation (DPF or BPF accordingly) gives the full characteristic of behaviour of object in the interesting range of frequencies at the set of presented type of excitation. Results of calculations of feed radiation patterns for two frequencies are shown in Fig. 2. The LPDA radiation patterns at high frequencies appear deformed as a result of excitation of the higher harmonics of a current at the LPDA structure.

Besides one can see in the Fig.2 that beamwidth in the H-plane is essentially wider, than in the E-plane. In order to obtain axissymmetrical radiation pattern the feed is built as the array of two optimized single LPDA. The general view of the synthesized feed is shown in Fig. 3.

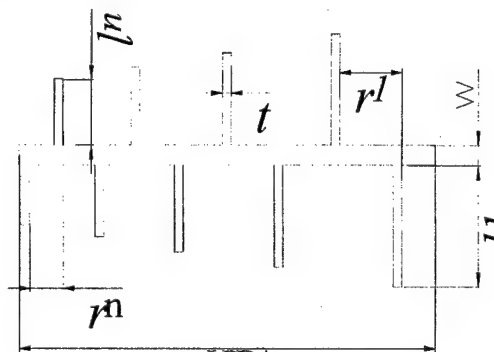


Fig. 1. Structure of the LPDA.

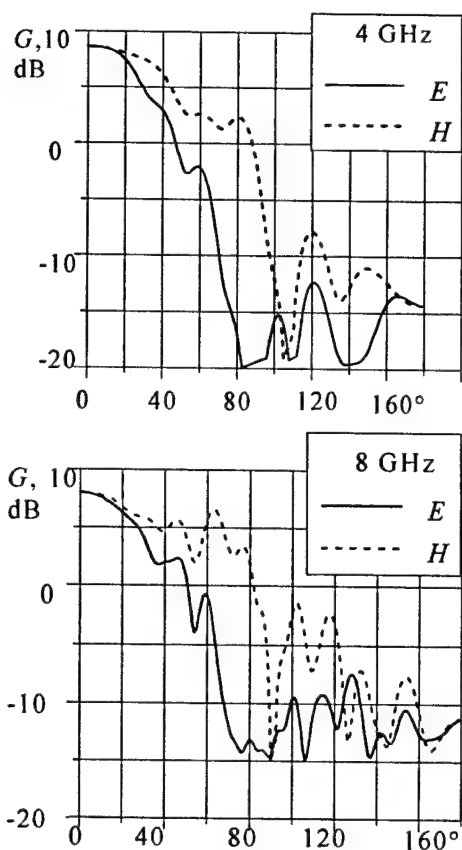


Fig. 2. Calculated radiation patterns.



Fig. 3. A general view of the feed.

3. RESULTS OF EXPERIMENTAL RESEARCHES

Results of measurements of radiation patterns of the developed feed at various frequencies are shown in Fig. 4-7. Apparently in these figures, the feed provides the radiation patterns close to axissymmetrical with the required width of the main lobe.

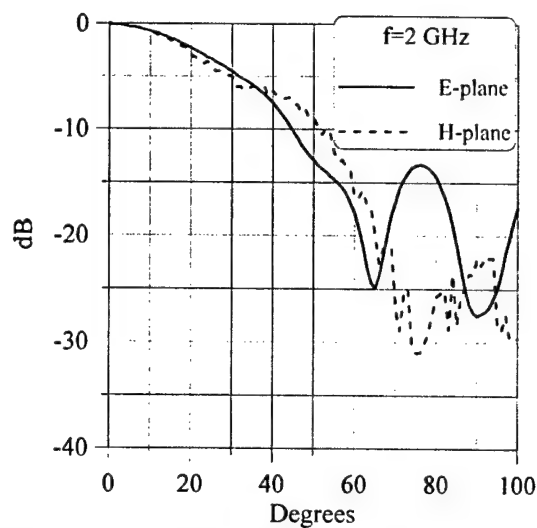


Fig. 4 The measured radiation patterns.

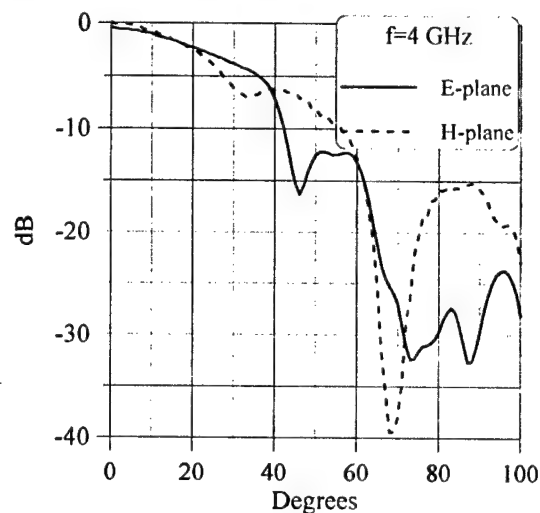


Fig. 5 The measured radiation patterns.

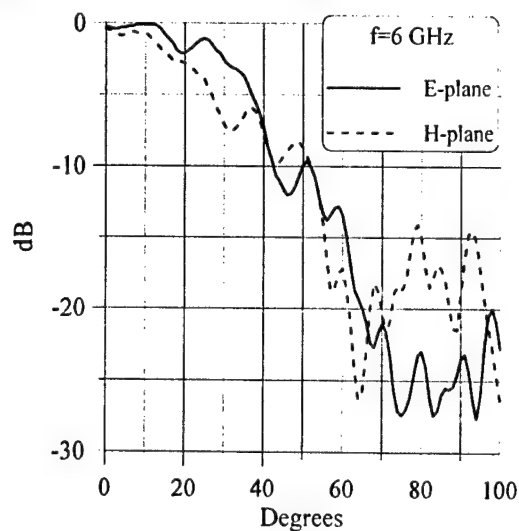


Fig. 6 The measured radiation patterns.

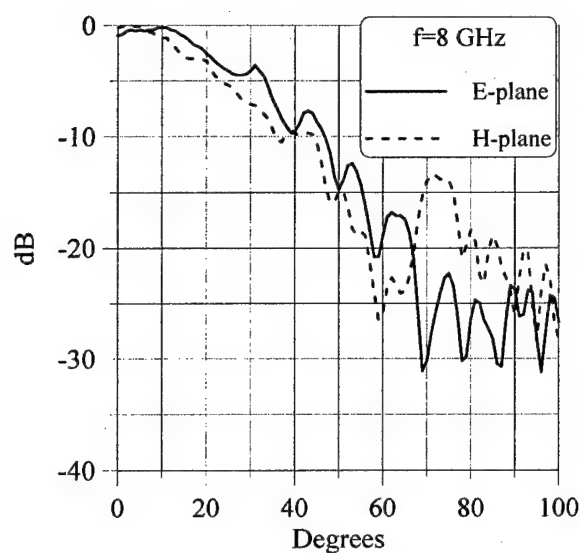


Fig. 7 The measured radiation patterns.

4. CONCLUSION

The developed feed composed of the two LPDA meets the requirements to ultra-wideband feeds for axiallysymmetrical reflector antennas, providing both a uniform symmetric irradiation of a reflector and a necessary low level of an irradiation at his edges in all operating bandwidth.

REFERENCES

1. V. N. Hlushenko, F. F. Dubrovka, A. M. Kuprii, S. E. Martynyuk, and A. E. Shrenk. New Log-Periodic and Quasi-Periodic Dipole Antennas of the VHF-UHF Range // *Radioelectronics and Communications Systems*, Vol. 41, No. 8, pp. 7-17, 1998.
2. Dubrovka F. F., Shrenk A. E. Analysis log-periodic dipole antennas a finite differences time domain method // [6] V. N. Hlushenko, F. F. Dubrovka, A. M. Kuprii, S. E. Martynyuk, and A. E. Shrenk. New Log-Periodic and Quasi-Periodic Dipole Antennas of the VHF-UHF Range // *Radioelectronics and Communications Systems*, No. 8, 2000.-№ 11.

COMPARISON OF THE EFFICIENCY OF VARIOUS OPTIMIZATION METHODS IN THE PROBLEMS OF THE FOCUSED APERTURE

Potapova O. V.

Kazan State Technical University, Kazan, Russia
<potapova_olga@mail.ru>

Abstract

Comparison of the efficiency of various optimization methods in the problems of the focused aperture was performed. The microwave installations of exposed-type with a coherent and a non-coherent excitation of the radiators are considered. The problems of two types (the focusing in a small and in an extended area) are solved.

Keywords: efficiency, focusing aperture, numerical optimization, criterion of optimization

1. INTRODUCTION

The researches on the expansion of the spheres of application of microwave electromagnetic fields are actively carried out in recent years. In a number of works [1, 2], the advantages of the use of the microwaves fields in medicine, biology, agriculture and industry are proven. However, the questions of the increase of the uniformity of the excitation of electromagnetic fields in a given area and of the decrease of the level of the electromagnetic radiation outside the focused area are not solved.

In the report, the exposed-type microwave installations (with an unlimited volume) are considered. Linear antenna array with N radiators are used as a device of excitation of the microwave fields. The radiators are located on the borders of a media in the process and radiate inside the media. Two essentially different ways of the radiator excitation (coherent and non-coherent) are considered.

By analogy to the antenna array theory, it is possible to assume that by varying the parameters of radiating system (complex amplitudes of currents and the geometry of antenna array) it is possible to increase the level and supply the more uniform distribution of the power in a given area.

In the work, the optimization of radiating system is understood as such a choice of the number, the complex amplitudes of currents, and the coordinates, of the sources at which the distribution of power of electrical field tends to the given. Using the terms by the antenna engineering, the tasks of this type are classified as a task of creation of the focused apertures. Two variants of similar tasks are considered (focusing in small area (point) and focusing in extended area) depending on the size of the focusing area.

In the report, the basic attention is given to a quantitative rating of the efficiency of focusing at various methods of optimization. In the practical recommendations, besides the absolute value of the received effect, the simplicity of a realization of the recommended way of optimization is taken into account.

2. THE BASIC QUESTIONS

In many technological processes of microwave processing it is desirable to supply allocation of the maximal power within the limits of focusing area. If the focusing area has the extended enough sizes, besides the requirement of absorbed of maximal power, there is a requirement of uniformity of power distribution inside of the specified area.

In work [3] a task of optimization of excitation in case of the small sizes of focusing area is submitted as follows:

$$\int_V P_{\text{provided}}(|\dot{I}|, |r'|, r) dV \rightarrow \max_{|\dot{I}|, |r'|}, \quad (1)$$

where V – is the volume of focusing area.

Criterion of the solution of (1), named criterion of power efficiency, is the value

$$Q_1 = \int_V P_{\text{provided}}(|\dot{I}|, |r'|, r) dV. \quad (2)$$

The task of the increase of the uniform distribution of absorbed power in case of enough extended sizes of focusing area is submitted as follows [3]:

$$P_{\min}(|\dot{I}|, |r'|, r) \rightarrow \max_{|\dot{I}|, |r'|}, \quad (3)$$

where P_{\min} – minimal value of absorbed in focusing area power. Criterion of the solution of (1), named criterion of increase of uniformity, is the value Q_2 :

$$Q_2 = P_{\min}(|\dot{I}|, |r'|, r). \quad (4)$$

The following condition is considered as a restriction at the solution of problem (4):

$$\|\dot{I}\| = \sum_{i=1}^N |\dot{I}_i|^2 = P_{\text{supply}} = \text{const} \quad (5)$$

The condition (5) allows to increase the uniformity of the absorbed power in focusing area.

The controlled variables in the optimization of excitation devices are the coordinates of radiators determining geometry of system, and complex amplitudes of currents of radiators ($I_i, i = 1, \dots, N$).

At a coherent excitation of radiators the general task of optimization is solved for special cases: Optimization of amplitude (amplitude optimization), phases (phases optimization), amplitude-phases (amplitude-phases optimization), and elements locations definitions (geometry optimizations). At noncoherent excitation of radiators are optimized the amplitudes and geometry of antenna array.

In general case the solution of problems (1), (3) by analytical methods is impossible, therefore optimization was realized by numerical methods.

3. THE CALCULATION RESULTS

At realization of calculations, the device of excitation is represented as set of sources, each of which creates elementary electromagnetic fields in a supervision point. The exact definition of elementary electromagnetic fields represents a rather difficult electrodynamic task, which can be solved only for a concrete variant of microwave installation.

In work [4] for calculations of elementary electromagnetic fields inside plane-layered semiconductor media, the field created by electrical dipole are considered. After finished the transients, in each layer of structure are present two flat arbitrary polarized waves – falling and reflected. However the obtained in [4] formulas are not so convenient for realization of large volume of calculations by the COMPUTER because they too large.

In work [3] are used the simplified model of elementary electromagnetic fields. In this case elementary electromagnetic field is as a field created by elementary electrical dipole disposed on the border air-media inside infinite semiconductor media. Electromagnetic field is represented as a fading spherical wave.

In a distant zone ($r \gg \lambda_m / 2\pi$), the results obtained from the exact and the approached model, have a good degree of concurrence. Therefore, if the focusing area is located in a distant zone of radiation, the use of the approached model is quite justified.

The model of exposed-type installation for coherent excitation of radiators is shown in Fig. 1. For the case of noncoherent excitation each radiator is connected to the separate generator.

The calculations was carried out for a fatty fabric having typical electrical parameters among processable medias. The quantity of radiators was various from 3 up to 19, distance between them (except for cases of optimization of geometry) gets out equal $\lambda_m / 2$. The depth of location of focusing area inside absorbed media was equal 10 cm.

The results of investigations have shown, that analytically can be solved only task of phases optimization (for coherent excitation) and task of amplitude optimization (for non-coherent excitation) in case focusing at point. All other tasks have no analytical solution, are multi-extreme and the values of local maximums appropriate of various quasi-optimal kinds of excitation differ rather considerably. The found results depend on a ratio of the sizes of focused area and antenna array, kind of semiconductor media, start point of optimization.

At coherent excitation of radiators the increasing of absorbed power in focusing point is equal from 6.6 up to 9 dB for different optimization methods in comparison with excitation of radiators with equal amplitudes and

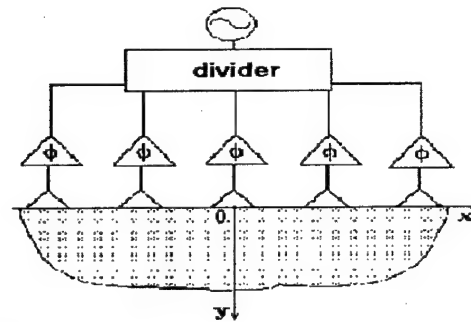


Fig. 1.

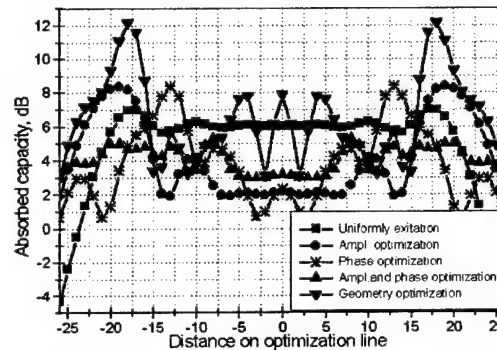


Fig. 2.

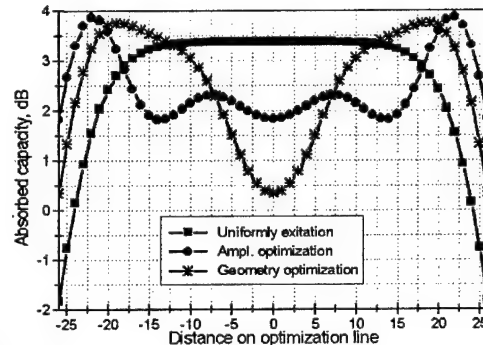


Fig. 3.

phases (uniformly excitation). At non-coherent excitation of radiators the increasing of absorbed power in focusing point makes about 6 dB. Thus, at case of focusing in a point the efficiency of coherent excitation is higher.

The distribution of absorbed power on focusing line for various quasi-optimal kinds of coherent excitation of radiators is shown in Fig. 2, for non-coherent excitation – in Fig. 3.

Comparison of efficiency of various methods of optimization for coherent excitation of radiators is shown in Fig. 4. The obtained results showed that optimization of amplitudes and phases allows to increase P_{\min} and distribution of absorbed capacity in focusing area becomes more uniform, however effect from amplitude optimization more. The consecutive amplitude and phase optimization allows a little to increase P_{\min} in comparison with amplitude optimization, but this increasing is insignificant. The optimization of radiators location by efficiency is comparable, but more often surpasses all other kinds of optimization. The increase of P_{\min} , absorbed on a focusing area are equal from 0.4 up to 8.0 dB for different medias, ratio of the sizes of focusing line and antennas array, start points of optimization. At absence of the additional

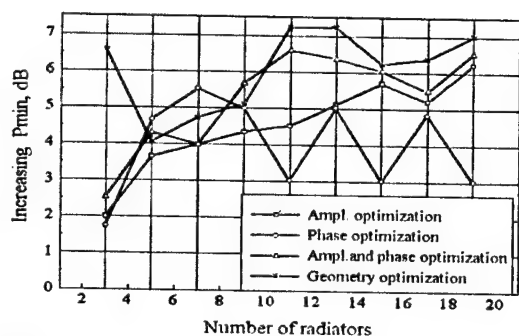


Fig. 4.

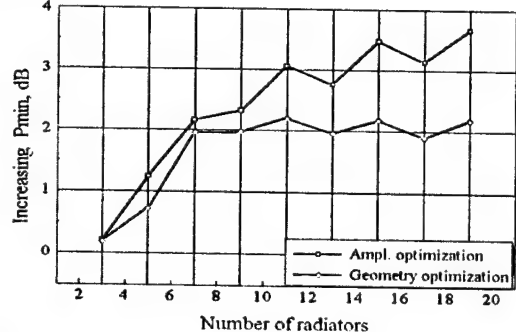


Fig. 5.

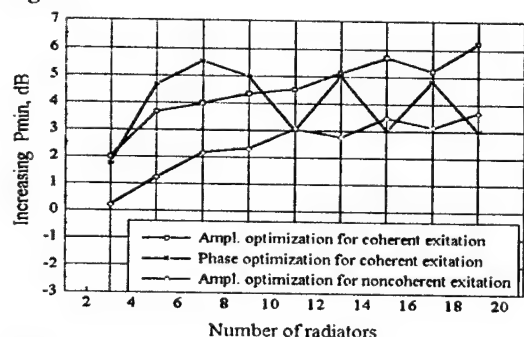


Fig. 6.

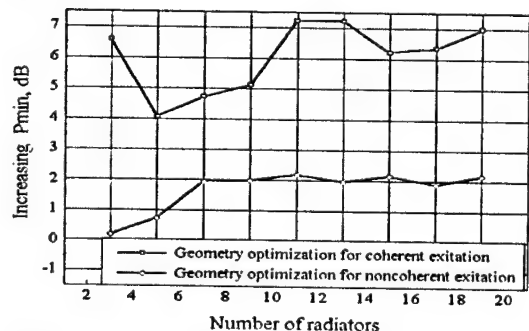


Fig. 7.

information, as a start point of numerical optimization it is expedient to use location of radiators with equal distance, amplitudes and phases.

The basic conclusions obtained for non-coherent excitation of radiators practically coincide with a case of coherent excitation of radiators. The range of increase of values P_{min} , absorbed on focusing line, equal from 0.25 up to 7.5 dB (Fig. 5) for different semiconductor medias, of sizes of focusing area and start points of optimization. The comparison of the efficiency of optimization for coherent and non-coherent excitation of radiators (Figs. 6, 7) shows

advantage of coherent excitation. The largest distinction between coherent and non-coherent excitation of radiators is obtained in case of optimization of geometry of antenna array. P_{min} in the case of coherent excitation exceeds similar value for non-coherent excitation more than 3 dB. The difference in values P_{min} by optimization of complex amplitude currents equal from 1.5 up to 2.5 dB.

4. CONCLUSION

The carried out investigation showed the efficiency of the use of the methods of the focused apertures for increase of the level and uniformity of distribution of power inside limited area. Thus, the level of power outside focusing area decreased. It enables to reduce the time of processing and also to improve the quality of production.

On the basis of the investigations the practical recommendations for designing technological microwaves installations are produced. Comparison of efficiency of optimization for coherent and noncoherent excitation of radiators shows advantage of coherent excitation in case of focusing in point. At the extended sizes of focusing area also more expediently using coherent excitation of radiators. The exception from this statement is two cases, at which efficiency of optimization for coherent and noncoherent excitation of radiators approximately equal: case of phases optimization and size of focusing line a little more length of antenna array (Fig. 6), and also case of optimization of geometry and size of focusing line approximate equal a half of antenna array length with step $\lambda_m / 2$.

At comparison of various ways of excitation of working chambers it is necessary to take into account and cost factor: now cost of 1 W of MICROWAVE ENERGY for magnetron with middle power approximate in 2...5 times are lower in comparison with powerful magnetrons, therefore cost of installation of equal power assembled by a principle of coherent excitation will be in some times more perspective, than constructed on a principle of non-coherent summation.

ACKNOWLEDGEMENT

In summary, the author expresses gratitude to Prof. Sedelnikov Yu. E. for discussion and useful councils, and to Prof. Morozov G. A. for support in work.

REFERENCES

1. Anfinogentov V.I., Sedelnikov Yu.E., Stepanov V.V., Potapova O. V. Multielement excitation of electromagnetic fields for microwave industrial installations // Proc. of 7th Intern. Crimean Conf. "Microwave & Telecommunication Technology". - Crimea, Sevastopol, 1997, pp.200-201.
2. Morozov G. A., Sedelnikov Yu. E., Potapova O. V. Improvement of microwave equipment excitation efficiency using methods of focused arrays // Proc. of III Intern. Conf. on Antenna Theory and Techniques, Kyiv, Ukraine, 1999.
3. Potapova O. V. Investigation of methods of the focused aperture for increase of efficiency of a exposed type MICROWAVE-technological installations, Kazan, 1998.
4. Dautov O. Sh. et. all The report on investigation "Excitation of plane-layered structure by a local source such as dipole", Kazan, 1997.

ON A PROBLEM OF IMPLEMENTATION OF MONOPULSE SELF-STEERING ON AN INFORMATION SIGNAL

A. V. Usichenko, A. S. Soroka, Y. A. Umzar, A. G. Rudnik

Ukraine. Ak. Pavlova-str., 271, Kharkov, 61054
OJSC "AO Scientific Research Institute For Radiotechnical Measurements"
(OJSC "AO NIIRI") <common@niiri.kharkov.com>
Ukraine. Textilnaya-str., 38 Ternopol
State scientifically technical manufacture "Texas-K" <sat@saturn.te.ua>

Abstract

The most widespread ways of guidance of antenna system on a space vehicle (SV) provide for usage of additional equipment (radio beacon) onboard of space vehicle, that reduces in additional expending of its power resources. In the paper it is offered to abandon GPS receiver and transmitter of a radio beacon at the expense of usage of improved antenna system, which ensures its self-steering on a signal of an information channel in a monopulse mode. It is offered to use for this aim a multimirror antenna system as large module antenna consisting of 4 not rotationally symmetric mirror antennas, which allows one to provide reliability of the useful information receiving with desired quality.

Keywords: the antenna system, monopulse self-steering, self-steering on an information signal.

1. INTRODUCTION

The space-communication systems, navigation systems (GPS, NavStar etc.), satellite television etc. are widely used in the life of a modern society. The near-earth space saturated with the satellites of the different countries solving different tasks. Thus all space vehicles require controlling, adjusting of a trajectory in on-ground servers by receiving information. However, the growth of SV quantity is not fundamental problem yet. The tasks, which are solved by modern SV, require implementation of more and more high-speed streams of information. In this view the problem of development of a different kind of on-ground servers which allows one to satisfy growing requirements to quality and reliability of a receiving stream of information are very actual [1].

The growth of a receiving information stream requires boosting a signal to noise ratio. Magnifying of this ratio on an antenna system input is possible only by reduction of a width of antenna patterns, that considerably diminish the direction-finding characteristics of the on-ground server and can reduce in impossibility of capture of space vehicle and increase of probability of failure of attending during a session [3]. This problem is solved in the on-ground servers, in which the program guidance for SV under the information from GPS receiver installed onboard is implemented.

In the paper another approach for solving this problem is developed, namely, to implement a monopulse

self-steering on an information signal, and thus, it is possible to expect reduction of losses in a feeder circuit and reduction of interferences, which act in a receiving system on side lobes.

2. FORMULATION OF THE PROBLEM

As is known, monopulse self-steering can be realized by an amplitude and phase method. The distinctive difference of methods is as follows:

- the amplitude method – it is necessary overlap phase centers of two radiating units for which the antenna pattern are separated from each other on an angle equal to their width on a level of a half of power;
- the phase method – the identical patterns are necessary and diversity of phase centers of two radiating units on some removal d have to be equal to half of an aperture of radiating unit (if radiating unit - aperture type) is necessary.

Usually, amplitude method of direction-finding is implemented as one aperture antenna with a system consisting of 4 feed antennas. In a monopulse method, of matching of amplitudes for determination of an error in one coordinate plane two overlapped pattern of an antenna are used. Such two beams can be shaped by one reflector, or lens antenna irradiated with two feed antennas. The sum patterns are used for transmitting, and for receiving the sum and difference pattern are used.

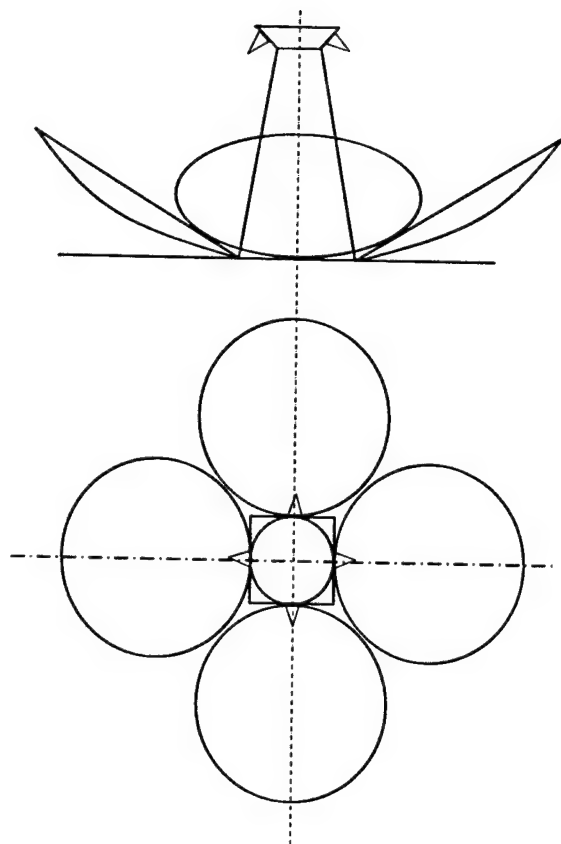


Fig. 1. The scheme of multimirror antenna system for amplitude monopulse self-steering.

Though the phase comparison is the constituent of a monopulse method of amplitude matching, the signal of an angular error is gained mainly as a result of matching amplitudes of reflected pulses simultaneously received by displaced beams. The ratio of phases between signals received by displaced beams is not determined and is not used. The sign of an error signal is determined by a phase-sensitive detector. Such a solution is not optimal one, as the system of high-frequency sum-differenced processing appears rather complicated.

For solving this contradictory task for creation of a monopulse self-steering system operating on an information signal, it is necessary to satisfy a number of the requirements that are able to provide the necessary accuracy of detection and attending of SV, and also organization of a reliable information radio link with a high dataflow.

This task can be solved using mirror antennas or phased antenna arrays. Now, receiving on-ground servers with one-mirror and two-mirror antenna systems are commonly used [2]. The virtues and drawbacks of such types of antenna systems are well known. Therefore there was a necessity of the development of such a construction of the antenna, which would integrate virtues of two-mirror AS (namely, small losses in an information channel) and one-mirror AS (ease of implementation, low minor-lobe level etc.).

Let's consider a construction of such a multimirror system as large modular antenna array consisting of four rotationally nonsymmetrical (offset) mirror antennas with equivalent diameter of an aperture of 1,8 m. The scheme of such ACE represented in Fig. 1.

Such an engineering solution of an AS ensures compact arrangement of feed antennas by partial channels, that allow one to optimize a system by criterion of a maximum noise Q-factor, as in two-mirror variant with one-piece reflector element.

Small level of losses of receiving information signal is provided by two ways. At first, the design of the multimirror AS has allowed up to reduce to a minimum of blockage of reflector elements, that essentially has lowered a level of side radiation; secondly, it's exist the possibility of arrangement of pattern forming system and first stages of the receiver in near proximity from feed antennas, that allows decreasing losses in a feeder circuit

Simultaneously in such AS is reached:

- increasing of common square of the aperture of the antenna without magnifying its total mass, that allows warranted to implement a required high amplification;
- increasing of a moment of inertia (almost on 50 %) at the expense of reallocation of masses;
- increasing on 20 % of wind loads;
- ease of implementation of each radiating element of an array with possibility of an independent alignment of channels for providing a mode of monopulse self-steering.

The phase method of direction-finding can be realized at the expense of the complication of the aerial system. The target sight lines for each antenna are parallel, owing to that each antenna irradiates (in a far-field region) the same size of space. The amplitudes of signals reflected from the target for each antenna beam are practically identical, but the phases are different. The method of measurement of an angle of arrival by matching phase relations of signals in diverse antennas of a radio interferometer is widely used in radio-astronomy. The on-ground server of attending operating on the basis of usage of the information on a phase of signals is similar to an active interferometer and can be called as direction-finding interferometer.

For angle tracking in two orthogonal planes it is possible to use four antennas located on pair. One of them is intended only for transmission, and three last for receiving. One antenna is joined to the receiving channel of an elevation angle, another – to the receiving channel of a Az, and third – to the common receiver to ensure the control of a reference signal as for elevation, and azimuth receiver, Fig.2

The radars of attending based on a principle of phase comparison, were implemented in practice and satisfactorily executed tasks, however this method has not found wide application. It can be explained by following. At first, the minor-lobe levels, available in real antennas, can appear above than minor-lobe lev-

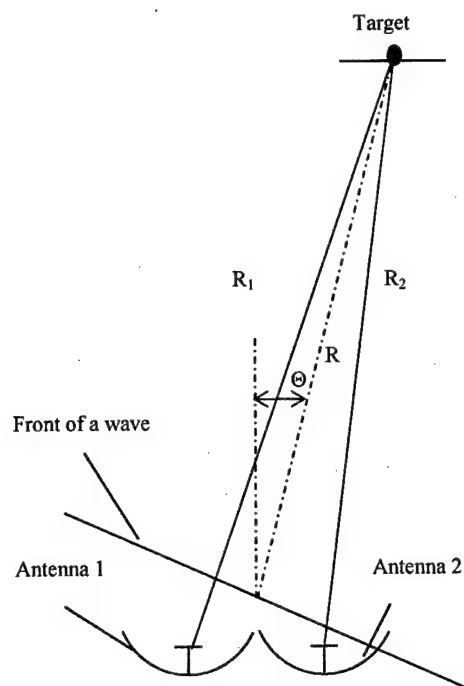


Fig. 2. Phase ratio in a monopulse direction finder with comparison of phases.

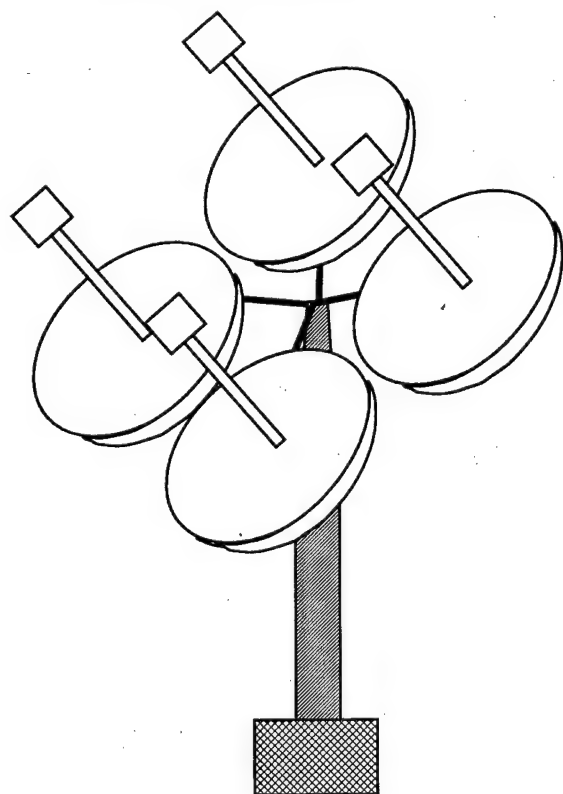


Fig. 3. The scheme of multimirror antenna system for phase monopulse self-steering.

els at usage of a single reflector; secondly, in radar with a phase comparison the common antenna aperture usually is used ineffectively.

Offered AS for a phase monopulse self-steering on an information signal provides for usage of four mirror antenna system installed on the uniform common support-rotating device (SRD), Fig. 3. As elements of such AS it is possible to use a two-mirror AS located on controlled movable rods and facilitating adjusting.

Using two-mirror antenna system allows one to have the first cascades of the receiver in immediate proximity from irradiators. It results in reduction of losses in a feeding path.

Simultaneously in such an AS we can reach the following:

- outcome between reception and transmitting channels as the receiver and the transmitter work on various aerials;
- decrease in the moment of inertia, in connection with redistribution of weights, on with a uniform reflector;
- increasing of wind loads.

3. CONCLUSION

Applying of the monopulse antenna system for self-steering on an information signal in the on-ground server for receiving of an information from a space vehicle allows to refuse power-intensive equipment on space vehicle (radio beacon, GPS receiver) saving excellent level of reception of large dataflow, and also stable detection and attending of space vehicle during a session.

REFERENCE

1. Belyanskiy P. V., Sergeev B. G. Control of ground antennas and radiotelescopes. Moscow: Sov. Radio, 1980. – 280 p. (in Russian)
2. Korostilev A. A., Kluev N. F., Melnik Y. A. Theory of radiolocation. Uchebnoe posob. Dlya VUZov. Moscow: Sov. Radio, 1978. – 608 p. (in Russian)
3. M. Skolnik. Introduction in the radiolocation techniques. Moscow: Mir, 1965. (in Russian)

HYBRID ANTENNAS WITH SHAPED REFLECTORS FOR LIMITED BEAM STEERING

A. S. Reutov, A. V. Shishlov

JSC "Apex", JSC "Radiofizika", Moscow, Russia
<jscapex@online.ru>

Abstract

In the paper, a numerical optimization algorithm for the hybrid antenna reflector shaping is considered. As an example, the algorithm is applied to a hybrid antenna with linear feeding array for one-dimensional beam steering in limited sector.

Keywords: hybrid antennas.

1. INTRODUCTION

In the paper, the method of reflector shaping for hybrid antennas (HA) with one-dimensional limited beam steering is presented. The method is based on the algorithm of synthesis of a shaped reflector, forming a contour beam pattern.

The considered antenna has a feed array that is significantly smaller than the reflector. A beam steering sector represents a two-dimensional area, in which the HA should form a beam. The area determines a desired contour pattern of the antenna element partial beam. This desired pattern is constant in the area of beam steering and equals zero out of it. The reflector of HA is synthesized by using the following procedure. Each element of the feeding array jointly with the reflector forms its partial pattern. The reflector is synthesized so that each partial pattern coincides with the desired pattern. This approach allows to minimize a number of controls for the selected beam steering sector. The pattern coincidence means the minimization of the patterns difference (in a some normalized space).

The proposed method of reflector shaping is based on the algorithm of contour beam synthesis. Therefore, a beam steering sector can be both one- and two-dimensional, and not only a linear but of any arbitrary form (Fig. 1).

Below the algorithm of reflector shaping for HA is presented. For demonstration of the algorithm, we consider two examples: 1) the offset HA with linear array, scanning in the sector of $\pm 10^\circ$ (beamwidth equals 1°), 2) HA with curved steering sector (with the same linear array).

In addition, reflector aperture efficiency of the HA is considered. The equation, which shows the limitation on the maximal efficiency of the single reflector HA, is presented.

2. REFLECTOR PARAMETRISATION

In order to have a possibility of varying a reflector shape it is necessary to give a parametric representation of the reflector surface.

In this case, optimization of the reflector means the search of optimum parameters (an optimum parametric vector) for the reflector shape representation. The following method of reflector parameterization is used in this work [1].

An antenna aperture is covered by a rectangular grid (see Fig. 2). The central node of this grid is fixed. All other nodes can move along OZ toward and back. A reflector surface is determined by the two-dimensional cubic spline on this rectangular grid. Z-coordinates of moving nodes constitute reflector parametric vector, denoted as $\mu = [z_1, z_2, \dots, z_L]^T$. This vector is searching during the optimization procedure of reflector shaping. If it is necessary to increase a number of freedoms, the current spline is recalculated on a more fine rectangular grid (with larger number of nodes).

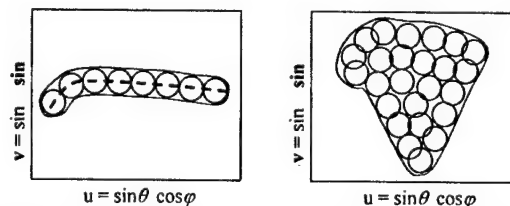


Fig. 1. One- and two- dimensional steering sectors.

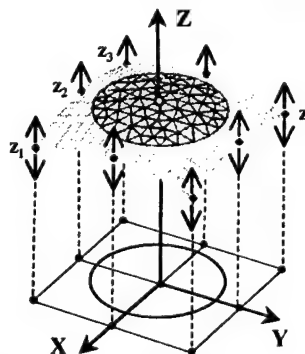


Fig. 2. Reflector parameterisation.

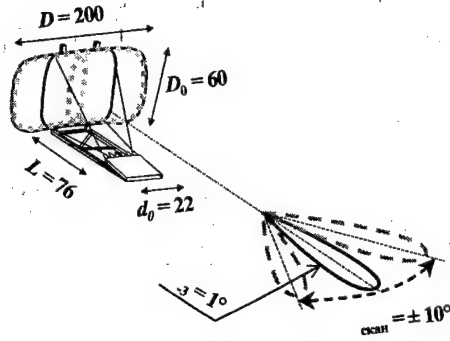


Fig. 3. Scheme of HA.

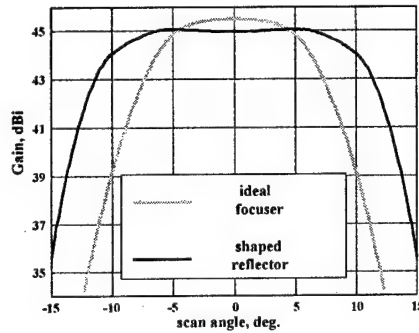


Fig. 4. Scan dependence.

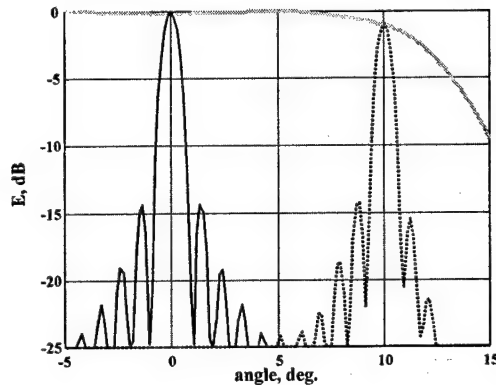


Fig. 5. Antenna patterns in the plane of the beam steering.

3. HYBRID ANTENNA REFLECTOR SHAPING

Each element of the feeding array forms its partial pattern $G^e(\mathbf{p}, \mu)$, where $\mathbf{p} = [p_1, p_2, \dots, p_n]^T$ is an arbitrary system of points in the far zone, $e = 1 \dots N$ is an element number. Let us demand the coincidence of each partial pattern with the desired pattern $G_d(\mathbf{p})$, determined by the beam steering sector, so

$$G^e(\mathbf{p}, \mu) = G_d(\mathbf{p}), e = 1 \dots N.$$

Combining all this equations, we have:

$$G^{total}(\mathbf{p}, \mu) = \begin{bmatrix} G^{(1)}(\mathbf{p}, \mu) \\ G^{(2)}(\mathbf{p}, \mu) \\ \dots \\ G^{(N_e)}(\mathbf{p}, \mu) \end{bmatrix} = \begin{bmatrix} G_d(\mathbf{p}) \\ G_d(\mathbf{p}) \\ \dots \\ G_d(\mathbf{p}) \end{bmatrix} = G_d^{total}(\mathbf{p}).$$

To find a solution of this system we minimise the norm of the distance between two patterns:

$$\min_{\mu} \|G^{total}(\mathbf{p}, \mu) - G_d^{total}(\mathbf{p})\|. \quad (1)$$

Components of the reflector parametric vector represent optimisation parameters. For solution of (1), we sequentially use two optimisation algorithms: non-linear least squares algorithm, which minimises square norm $\|\cdot\|_2$, and minimax algorithm, which minimise the norm of the maximum deviation $\|\cdot\|_\infty$ [1].

4. EXAMPLE OF THE SYSTEM SYNTHESIS

As a first example, let us consider the synthesis of a HA with beamwidth 1° and steering angle $\pm 10^\circ$ (see Fig. 3). The antenna is fed by the linear array of E-plane open-end rectangular waveguides with $a = 1.9\lambda$ and $b = d_0/N$, where $d_0 = 22\lambda$ is the array length, and $N = 32$ is the total element number.

As an initial approximation for the reflector shaping, the surface of ideal focuser is used [2].

Dependence of the maximum antenna gain on beam steering angle before and after optimization is shown in Fig. 4.

According to geometrical optics, HA with focuser reflector can scan in the sector of $\pm 10^\circ$. Owing to aperture phase errors, steering sector is limited down to $\pm 6.5^\circ$.

A HA with shaped reflector can scan up to $\pm 10^\circ$ with 1 dB gain variations, and 0.5 dB gain decrease in centre of the steering sector.

It is necessary to note that HA with shaped reflector has the element use factor of the value $N/N_{min} = 1.7$, which is a good result for the hybrid antennas.

Antenna patterns for the different location of the steering beam are shown in Fig. 5.

The considered above results were obtained by using least squares algorithm. This means that in equation (1) we use a square norm $\|\cdot\|_2$. It is necessary to continue optimization of the HA reflector by applying minimax algorithm.

The obtained gain/scan dependence is shown in Fig. 6. In this case, the gain variation in the sector of the beam steering is equal to 0.3 dB.

5. CURVILINEAR SECTOR OF BEAM STEERING

It is possible to use the approach described above for reflector shaping of a HA with curvilinear sector of beam steering.

In the second example, we use the same structure of HA as in the first example (see Fig. 3). But the de-

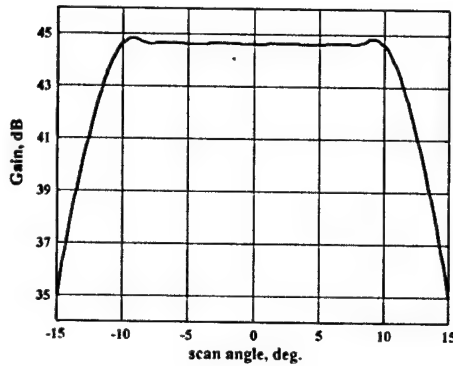


Fig. 6. Gain/scan dependence after minimax optimization.

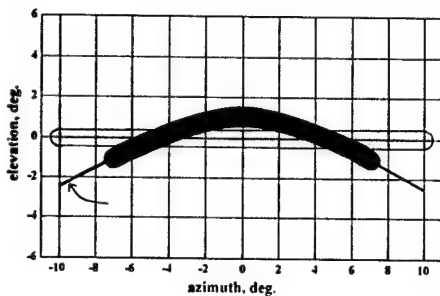


Fig. 7. Curvilinear beam steering sector.

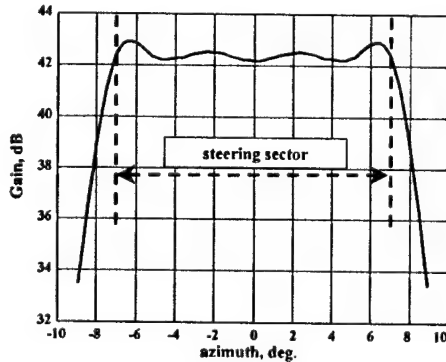


Fig. 8. Gain/scan dependence in the curvilinear steering sector.

sired sector of beam steering in this case is shown in Fig. 7.

In this figure, a grey colour denotes a rectilinear beam steering sector, while black colour denotes a desired curvilinear beam steering sector.

It is necessary to note that the beam steering in this sector is done only due to shaped reflector while the same linear array (as in the first example) is used. The antenna gain vs. scan angle after reflector shaping is shown in Fig. 8. In this case, the antenna focuses its beam in different points of the curve γ (see Fig. 7).

In Fig. 8, x-axis corresponds to the beam azimuth on the curve γ , and y-axis corresponds to appropriate antenna gain values.

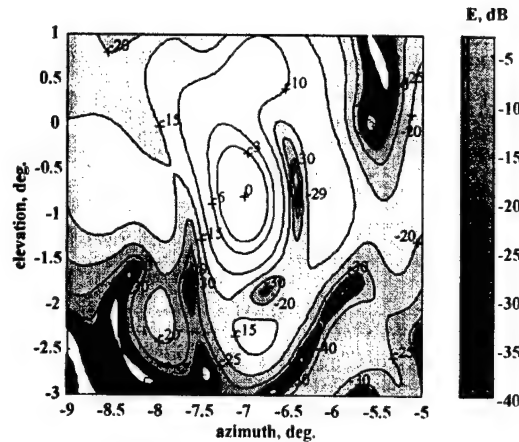


Fig. 9. Antenna beam in the end point of the steering sector.

The antenna gain variations in considered curvilinear sector constitutes 0.7 dB.

The pattern colormap for the HA with obtained shaped reflector is shown in Fig. 9. The point of the beam maximum is 7° in azimuth and 1° in elevation.

It can be seen from this figure that the beam has slightly different widths in azimuth and elevation planes (the beam has an elliptical cross-section). In addition, the maximum of antenna pattern is gently displaced from the focusing point $(-1^\circ, -7^\circ)$ to the point $(-0.8^\circ, -7^\circ)$. The maximum antenna gain is 42.7 dBi.

The considered HA with curvilinear steering sector can be used, for example, as a satellite antenna for the service of Russia. If a satellite is located in the point of 100°W , the considered curvilinear sector (from -5° to $\pm 5^\circ$ by azimuth) provide a good coverage of the Russia territory. So, this HA with active phased array feed can be used as a multibeam antenna for the communication system.

6. LIMITATION ON THE EFFICIENCY OF THE HYBRID ANTENNAS

Let us consider the efficiency of HA with single reflector.

Let the feed array dimension and the beamwidth are fixed, then there is a minimum HA reflector dimension, which provides a beam steering in a given sector. To understand this limitation let us consider the following.

A field on the reflector surface is formed by a small array, i.e. has a finite spectra. In addition, the reflector itself has limited dimensions. Therefore, there is a limited number of functions (excitations), which can effectively transfer the energy from the array through reflector to far zone of the antenna. Let us consider the following evaluations.

For the simplicity, we assume that the reflector is located in far zone of the array. The dimension of the array beam is $\Delta\Omega_{-3} = \lambda/d_x \cdot \lambda/d_y = \lambda^2/A$, where

$d_x d_y = A$ is the array area. The flare angle of the reflector is S/L^2 , where S is the reflector area, L is the mean distance from the array to the reflector.

The number of orthogonal array beams (Kotelnikov's samples) allocated on the reflector is

$$N \approx (S/L^2)/(\lambda^2/A) = A \cdot S/(\lambda \cdot L)^2.$$

The N can be considered as number of independent excitations that can effectively transfer the energy of antenna.

Let's Ω is a solid angle of the beam steering sector. The dimension of the antenna beam is $\Delta\Omega = \lambda^2/S_0$, where S_0 is effectively excited reflector area, which forms the beam. The number of independent (orthogonal) beams in the steering sector is

$$N_{beam} = \Omega/\Delta\Omega = \Omega/(\lambda^2/S_0) = \Omega \cdot S_0/\lambda^2.$$

This number can not be more than the number of independent excitations which can form the HA, i.e.

$$N_{beam} \leq N,$$

therefore,

$$S_0/S \leq A/(\Omega \cdot L^2) = A/S_0 \cdot (S_0/L^2)/\Omega.$$

Denote as $\Omega_D = S_0/L^2$ the flare angle of the effectively excited area. For the HA with limited sector of scanning, the condition $\Omega_D/\Omega \leq 1$ is always true. Therefore, we have

$$S_0/S \leq A/S_0. \quad (3)$$

Equation (3) shows that the decrease of the array aperture A in comparison with the area S_0 forming the beam leads to necessity to increase the reflector area S in comparison with S_0 at least by the same value. The value $\varepsilon = S_0/S$ means the efficiency of the HA. So, we have

$$\varepsilon \leq A/S_0. \quad (4)$$

The last equation represents the final limitation on the efficiency of the HA with single reflector.

Thus one can understand that small efficiency of the HA is an inevitable consequence of the wish to use a small feeding array.

The equation (4) can be obtained in a more formalised manner. In addition, one can obtain that equation (4) takes place if the following two conditions are true:

1) steering sector is rather large one, and includes at least more than ten independent (orthogonal) beams;

2) HA is able to form a complete set of orthogonal beams in the steering sector.

In the case of one-dimensional beam steering, the above equation is transformed in the following manner. The total dimension of the reflector D in the plane of scanning, the dimension of the effectively excited part of reflector D_0 that forms the beam, and the length of the feeding array are bound by the relation:

$$D_0/D \leq d_0/D_0,$$

and accordingly, we have for the antenna efficiency:

$$\varepsilon \leq d_0/D_0.$$

Equation (5) was confirmed by a number of numerical simulations of the HA, considered in this paper.

REFERENCES

1. A. S. Reutov, A. V. Shishlov, "Features of the Stepwise Contour Beam Reflector Antenna Synthesis Using Cubic Spline Representation of Reflector Surface", *Electromagnetic waves and electric systems*, Moscow, № 2, 2003, pp. 4-14.
2. A. S. Reutov, A. V. Shishlov, "Focuser-Based Hybrid Antennas For One-Dimensional Beam Steering", *Proceedings of the 2000 IEEE International Conference on Phased Array Systems and Technology*, Dana Point, California 2000, pp. 411-414.

REFLECTIVITY OF ROUGH METAL SURFACES OVER MILLIMETER WAVE RANGE

Ruslan V. Vorobjov

Kharkov Air Force Institute, Kharkov, Ukraine
<vorbut@ukr.net>

Abstract

Calculations of the reflection factor over the millimeter wave range are made on the basis of the theory of black body, the skin-effect theory and the electrodynamic criterion of smoothness obtained in our previous works. The results of these calculations are compared with experimental data. Errors are estimated. The application area and capabilities of this technique are noted.

Keywords: reflectivity, rough metal surface, millimeter waves, electrodynamic criterion of smoothness.

1. INTRODUCTION

The reflection loss decreasing by appropriate surfacing is one of actual problems of electrodynamics of large powers of millimeter and submillimeter ranges. There is a divergence between calculated and measured values of reflection losses appearing as a result of mechanical or chemical treatment of the metal surface. These stray-load losses lead to the surface thermal degradation and increasing of the same losses. The given work is devoted to the development of the method of calculation of reflectivity of rough metal surfaces with a definite profile of average irregularity on the basis of investigations [1, 2]. The simulated results are compared with experimental data [3].

2. SPECTRAL HEMISPHERICAL REFLECTIVITY OF A ROUGH METAL SURFACE

According to the paper [4], the spectral hemispherical reflectivity R_λ is determined by

$$R_\lambda = rA / (1 - r(1 - A)), \quad (1)$$

where r is the smooth metal surface reflectivity; A is the smoothness factor.

$$A = s / S, \quad (2)$$

where s is the irregularity aperture area; S is the area of the effective reflecting interior rough surface. For refractory metals the value of r at $\lambda > 1 \mu\text{m}$ can be determined by Eq. [6]

$$r = 1 - 5.8 \cdot 10^{-5} \sqrt{\frac{T}{\lambda \cdot \delta}}, \quad (3)$$

where T is the heating metal thermodynamic temperature, K; δ is the thermal conductivity, W/(m·K).

For calculating the spectral hemispherical reflectivity of the rough metallic surface it is necessary to determine its smoothness factor depending on the average irregularity profile. The real roughness often has no regular geometric shape, but to some extent it verges towards this [4]. To a first approximation it is enough to investigate V-shape grooves on the metal surface as a result of its primary treatment [5]. The finishing of the metal surface, been brought up to size, leads to the irregularity top cutting and trapezoidal groove formation on the surface [1]. The smoothness factor of metal surfaces with V-shape and trapezoidal grooves was obtained in papers [1, 8]. The irregularity profiles acquired due to the blade processing of metal is described more precisely by the Gaussian curve [9]. The expression for the smoothness factor of the Gaussian groove was derived in the paper [9]. However, there was no comparison of calculated results with experimental data presented in papers [1, 2, 8]. Besides there is no estimation of errors arising at the use of obtained expressions.

3. FIELD PROPAGATION CONSTANTS INSIDE ELEMENTARY VOLUMES OF THE GAUSSIAN GROOVE

The 3D image of the Gaussian average groove with metal walls is shown in Fig. 1. A nonpolarized plane wave (wave with random polarization) is incident on its aperture (in the plane xy) from the half-space $z < 0$. On corrugation ridges located along the y -axis the nonpolarized wave is decomposed into a pair of uncorrelated waves with orthogonal polarizations and identical average amplitudes: the E -wave with the polarization vector H_y and H -wave with the polarization vector E_y . The E - and H -waves, separately from each other, excite the field inside the groove whose sides form a waveguide with variable wave impedance dependent on z .

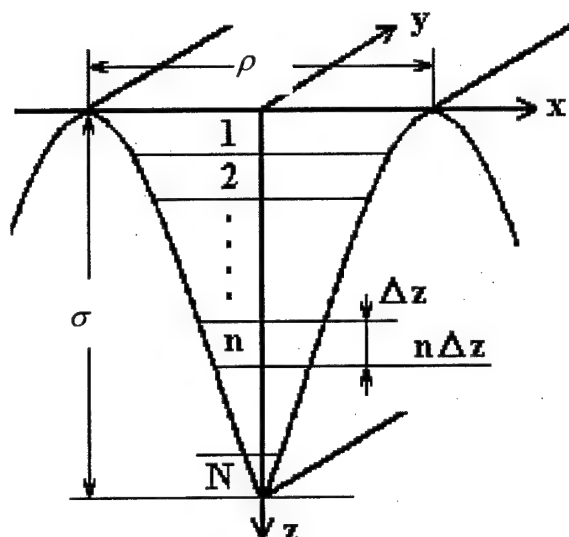


Fig. 1. Groove with Gaussian profile

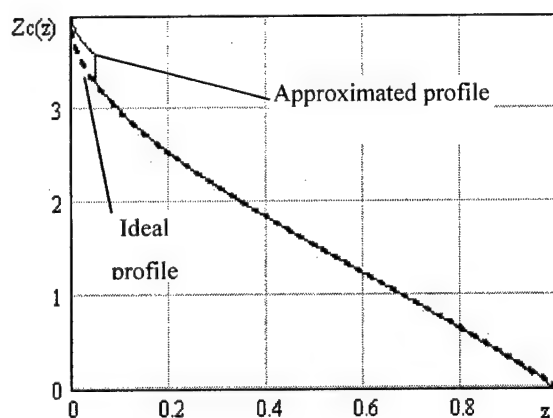


Fig. 2. Ideal and approximated profile of the Gaussian groove

Let's divide the groove into N volumes by planes, parallel to the plane xy and arranged at a distance of Δz from each other. Between planes $z = n\Delta z$ and $z = (n+1)\Delta z$ ($n = 0, 1, \dots, N-1$) we enter the moving coordinate ζ . In each of N volumes the groove walls is approximated by the exponential transmission line, so that in each elementary volume for the wave propagating along the z -axis the wave impedance is determined by

$$Z_c(\zeta) = Z_{c(\zeta=0)} \exp\{c\zeta\} \text{ when } 0 < \zeta < \Delta z. \quad (4)$$

The Gaussian groove profile and its approximation by exponential sections are shown in Fig. 2. On partitioning the groove into 20 elementary volumes the arithmetic average error of the wave impedance along the full groove does not exceed 5%. The error distribution into volumes is irregular (Fig. 3). The increase of the number of volumes results in the decrease of the approximation error in the first layer. Values of the wave impedance errors in last and penultimate layers do not depend on the quantity of elementary volumes and have the peak value. However the con-

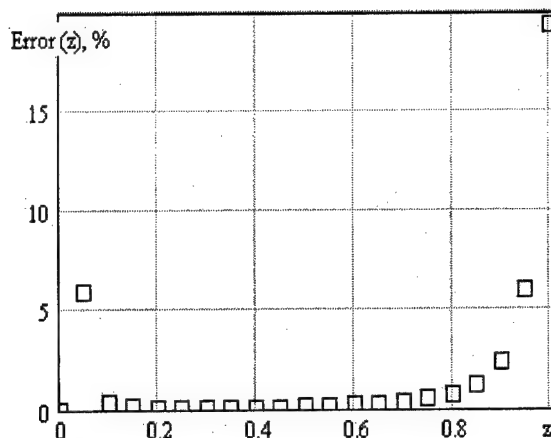


Fig. 3. Wave impedance error in the elementary volume

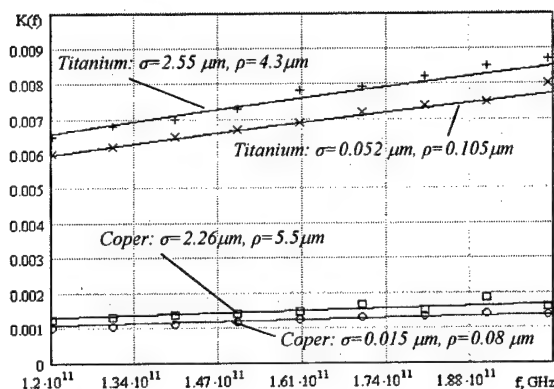


Fig. 4. Dependence of the reflection loss on frequency

tribution of these two layers to the magnitude of the reflection factor is negligible that allows excluding them from consideration.

As the interval Δz inside the elementary volume is small, the longitudinal wave number γ is considered constant. The expression of the factor c , see (4), corresponding to the Gaussian groove, was obtained in the paper [2]:

$$c = \frac{-(1 - e^{-1})}{2[L - z(1 - e^{-1})]\xi(1 - \xi)}. \quad (5)$$

Propagation coefficients of the current Γ_i and the voltage Γ_u inside the interval Δz are determined by characteristic equations

$$\Gamma_u = c/2 \pm jp \mp \chi, \quad \Gamma_i = -c/2 \mp jp \mp \chi. \quad (6)$$

where χ is the attenuation coefficient of the waveguide field. The parameter p depends on the wavelength λ and is determined by the expression

$$p = \sqrt{\left(\frac{2\pi}{\lambda}\right)^2 - \frac{c^2}{4}}. \quad (7)$$

A part of the groove which reflects effectively the incident wave can consist of two areas: the area with the propagating wave ($\text{Re}(p) \neq 0$) and another area without the propagating wave ($\text{Re}(p) = 0$), but the field strength is not attenuated yet by factor of e (in

accordance with the skin-effect theory). All irregularities can be subdivided into three classes depending on their parameters: into grooves of the first class with the propagating wave area, and grooves of the second class without propagating wave area and where the field is attenuated more than e times, and into grooves of the third class without the propagating wave area and where the field is attenuated less than e times.

4. COMPARISON OF CALCULATED VALUES OF THE REFLECTION LOSS FACTOR WITH EXPERIMENTAL DATA

The experimental data [3] correspond to the last case of irregularity classification. Consequently the whole inside surface of the groove reflects effectively the incident field. The calculated values of the reflection loss factor and experimental data are shown in Fig. 4. At a definite ratio of the irregularity aperture ρ to its height σ the calculated values coincide with experiment data.

5. CONCLUSION

The method of calculation of the reflection coefficient of a rough surface developed in this paper gives good coincidence of the calculated results with experimental data. The errors arising during implementation of this method, are small enough and can be minimized. The method can be applied to estimate parameters of rough surfaces and their radiation properties in the millimeter, submillimeter and infra-red waveband. It should be noted that the known method [3] of calculation of the reflection loss on rough metal surfaces has limitations in a shortwave part of the millimeter waves and for shorter waves.

REFERENCES

1. R. V. Vorobjov, S. V. Butakova. Electrodynamics criterion of smoothness as expanded Raleigh's criterion // Proceedings of 27th General Assembly "International Union of Radio Science".- Maastricht: "MECC", 2002, p. 0116.
2. R. V. Vorobjov, S. V. Butakova. Electrodynamics criterion of smoothness of a surface with asperities as Gaussian grooves for E waves // Proceedings of 12th International Conference "Microwave and Telecommunication Technology" (CriMiCo'2002). Sevastopol: "Weber", 2002, p.317-318.
3. S. E. Myasnikova, A. A. Bogdashov, V. V. Parshin, Yu. V. Rodin. Metal reflectivity investigation at 110-200 GHz // Proceedings of 12th International Conference "Microwave and Telecommunication Technology" (CriMiCo'2002). Sevastopol: "Weber," 2002, pp. 538-539.
4. S. G. Agababov, Influencing of a surface roughness of a solid on its radiation properties and methods of their experimental definition // Thermal Physics of Heats. 1968. V.6, № 1. pp. 78-88.
5. O. R. Popova, Radiation of roughness surface and its polarization features. 1. Calculation method // Thermal Physics of Heats. 1983. V. 21, № 1. pp. 66-72.
6. G. F. Mutshnik and I. B. Rubashov, Methods of the heat exchange theory. Heat radiation.- Moscow: The Highest School, 1974. 272 p.
7. J. Ruze. Antenna tolerance theory - A review // Proc. IEEE. 1966. Vol. 54, № 4. pp. 633-642.
8. S. V. Butakova, R. V. Vorobjov. Electrodynamics criterion of smoothness // Radiotekhnika: All-Ukr. Sci. Interdep. Mag. 2002. № 124. pp. 61-67.
9. A. G. Suslov. Technological ensuring of parameters of surface layer state of machine elements. M.: Engineering, 1987. 208 p.

ANTENNA ARRAYS

CLOSELY SPACED TRANSVERSE SLOTS IN RECTANGULAR WAVEGUIDE

Sergey L. Berdnik, Victor A. Katrich, Valentina A. Lyaschenko

Department of Applied Electrodynamics,
V.N. Karazin Kharkiv National University, Kharkiv, Ukraine
<sergey.l.berdnik@univer.kharkov.ua>

Abstract

The leaky-wave antennas in the form of closely spaced transverse slots cut in a broad wall of rectangular waveguide were investigated. The thickness of waveguide walls and interaction between slots were taken into account in numerical calculations.

Keywords: Leaky-wave antenna, rectangular waveguide, transverse slot set.

1. INTRODUCTION

There are no exact analytical investigations of leaky-wave slotted-guide antennas. Often a simplified model of antenna is used or equivalent circuit theory is applied. In some case, it is made a guess that the radiating array is infinite periodic one with half-wave approximation of field within a single slot. The thickness of waveguide walls is not taken into account in such investigations.

The proposed below method allows one to investigate multielement slotted-guide antenna sufficiently rigorously and to solve inner and outer problem for antenna in the form of closely situated transverse slots cut in the broad wall of a rectangular waveguide.

2. PROBLEM DEFINITION AND SOLUTION METHOD

The set of closely spaced transverse slots is cut in the broad wall with thickness t of rectangular waveguide. The slots may be with different dimensions in length and width and can be situated arbitrary as to the centerline of the broad wall of rectangular waveguide (Fig. 1).

The unknown fields in the surfaces of slot with a number n which verge on inner and outer spaces of waveguide ($\vec{E}_n^{(1)}$ and $\vec{E}_n^{(2)}$ respectively) is represented in expanded form of linear-independent vector-function of slot $\vec{e}_{n,q}$ with complex coefficients $\dot{V}_{n,q}^{(1)}$ and $\dot{V}_{n,q}^{(2)}$ [1].

Then the field in the aperture of multislot system may be written as follow:

$$\vec{E}^{(2)} = \sum_{n=1}^N E_n^{(2)} = \sum_{n=1}^N \sum_{q=1}^Q \dot{V}_{n,q}^{(2)} \vec{e}_{n,q} \quad (1)$$

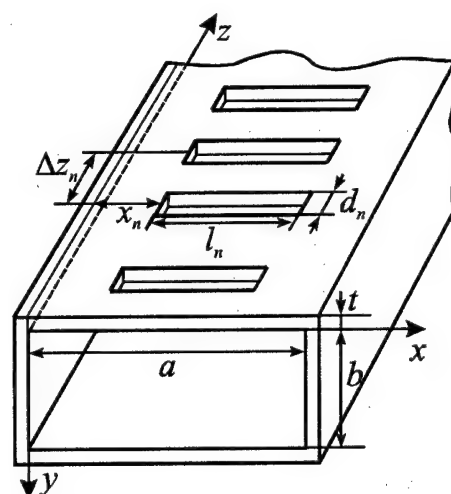


Fig. 1. Transversely slotted waveguide geometry

Considering narrowness of slots it is made a guess that the field \vec{E} has across slot direction and does not depend on transverse coordinate. Then the vector fundamental functions of slot can be written as

$$\vec{e}_{n,q} = \frac{\vec{z}^0}{d_n} \sin \frac{q\pi}{l_n} (x - x_n) \quad (2)$$

where x, z are the coordinates along and across of a slot respectively, \vec{z}^0 is a unit vector.

After substitution of (1) in to the continuity equations of magnetic field tangential components on exterior and interior surfaces of slots, we obtain the set of algebraic equations for unknown $\dot{V}_{n,q}^{(1)}$ and $\dot{V}_{n,q}^{(2)}$, as in [1].

Self and mutual, inner and exterior conductivities of slots and conductivities of slot volume space are coefficients of the obtained set of equations.

After determination of the electric field in antenna aperture according to the expression (1), we determine radiation and directional characteristics of antenna, as in [1].

3. CALCULATION RESULTS

First of all consider the properties of a single transverse slot in the broad wall of rectangular waveguide should be investigated. This information is necessary to design multielement antennas.

Fig. 2 shows the radiation coefficients $|\Gamma_\Sigma|^2$ for slots of the electrical length $l/\lambda = 0.469$ and differing width d/l versus thickness of waveguide walls t . The slots are cut in the waveguide of cross-section $a \times b = 23 \times 10 \text{ mm}^2$. For the case of narrow slots, the energetic coefficients strongly depend on walls thickness t . Changing the proportion by d and t it is possible to change $|\Gamma_\Sigma|^2$. This is very important for design of antenna array with a great number of radiators.

Consider the leaky-wave antenna consisting of 20 slots cut symmetrically regarding centerline of a wide wall of the waveguide. The slots placed at a distance $\Delta z = 0.375\lambda$ and excited by field of H_{10} wave with $\lambda = 32 \text{ mm}$ have identical length ($l/\lambda = 0.4$) and width ($d/l = 0.077$). The magnitude field distribution in the aperture of such an antenna is shown in Fig. 3 (curve 1)

The radiation pattern of the antenna is presented in Fig. 4 (curve 1). Sidelobe level of the radiation pattern is -10 dB . Therefore, we shall create in the given antenna such magnitude distribution, which would shape radiation pattern with an acceptable sidelobe level, for example, decreasing distribution to the edges of the system. Such a distribution can be obtained if to select length of each slot in appropriate way. Magnitude distribution shown in a Fig. 3 (curve 2) is shaped in a set of slots, which length varies according to the graph

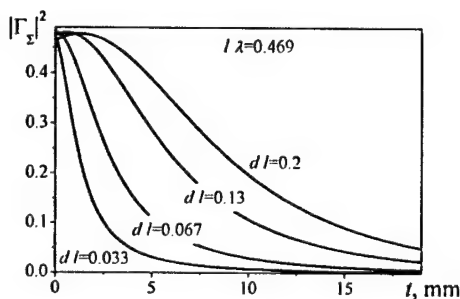


Fig. 2. Radiation coefficient versus thickness of waveguide walls.

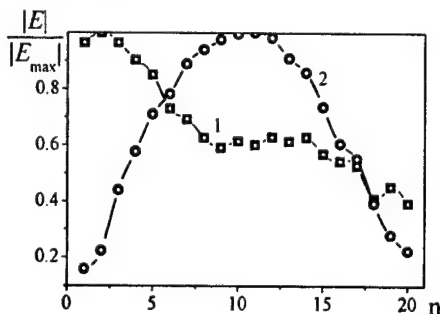


Fig. 3. Magnitude distribution.

in Fig. 5. Corresponding radiation pattern is shown in Fig. 4 (curve 2). As evident, sidelobe level decreased to -19 dB . In this case $|\Gamma_\Sigma|^2 = 0.89$.

In practice exterior dielectric covers of antennas in the form of one or more layers with finite width of different dielectrics have often used. This implies that the characteristics of antennas are change. The problem about radiation of an antenna with exterior dielectric in layers is more complicated mathematically than radiation in space filled by dielectric. As follows from [2] the radiation from a slot covered by a dielectric layer of $0.5\lambda_e$ (λ_e is the wavelength in space filled by dielectric with permittivity ϵ^e) practically does not differ from the case of radiation of an antenna in space completely filled by such a dielectric.

Fig. 6 shows directivity, gain and radiation coefficients (D , G and $|\Gamma_\Sigma|^2$ respectively) of the above-considered antenna versus permittivity ϵ^e of outside dielectric.

The functions $D = f(\epsilon^e)$ and $G = f(\epsilon^e)$ reach maximal values at certain value of ϵ^e . Moreover the main lobe of the radiation pattern is sharpened and is

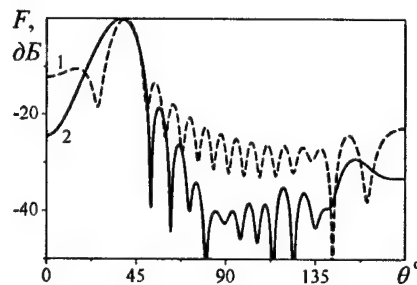


Fig. 4. Radiation patterns.

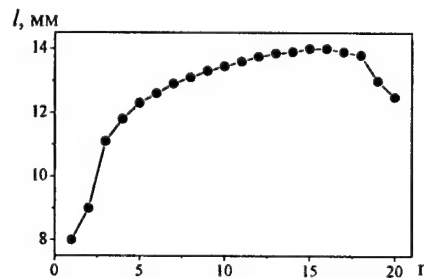


Fig. 5. Length of slots versus slot number

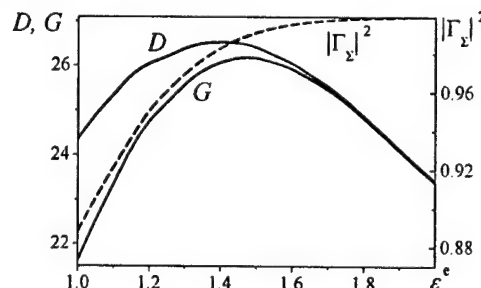


Fig. 6. Directivity, gain and radiation coefficients versus permittivity ϵ^e .

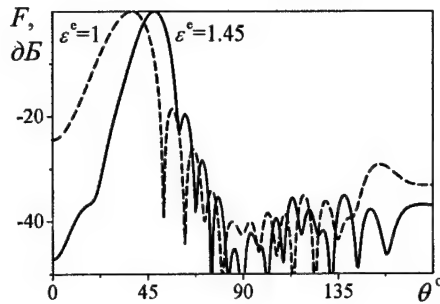


Fig. 7. Radiation patterns.

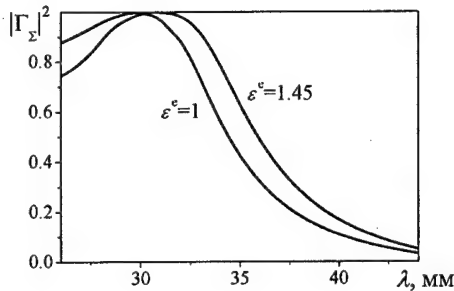


Fig. 8. Radiation coefficient versus wavelength.

deflected from waveguide axis at location of the dielectric as contrasted to case $\epsilon^e = 1$. Fig. 7 shows the radiation pattern of antenna with $\epsilon^e = 1.45$ at which maximum of function $G = f(\epsilon^e)$ is reached. In this figure the radiation pattern of the antenna with $\epsilon^e = 1$ is shown. The directivity coefficient of the antenna covered by the dielectric has increased by 8.8 % and the gain has increased by 21 % whereas the radiation coefficient has also increased.

Consider frequency properties of the given type of antennas. The operating frequency band is restricted to the following factors. With decreasing wavelength sidelobe level of radiation pattern increases and with increasing wavelength radiation coefficient decreases. Fig. 8 shows the radiation coefficient versus wavelength for the investigated antenna of 20 slots with dielectric cover and without it.

Application of dielectric cover makes it possible to increase directivity coefficient over the broad frequency band and to increase radiation coefficient over long-wave band. It allows one to extend operating frequency band. Fig. 9 shows the radiation patterns of the antenna covered by dielectric with $\epsilon^e = 1.45$ at different values of wavelength: $\lambda = 30$ mm (curve 1), $\lambda = 35$ mm (curve 2), $\lambda = 40$ mm (curve 3).

Decreasing of sidelobe level of the radiation pattern can be achieved by using antennas array with space tapering of radiators. Fig. 10 shows the radiation patterns of the antenna of length 13.44λ consisting of 50 slots with $l = 0.33\lambda$ with constant distance between slots $\Delta z = 0.27\lambda$ (curve 1) and the radiation pattern of the given slot set, in which distance between slots $\Delta z_n = z_{n+1} - z_n$ varies sinusoidally versus number n . It is shown that sidelobe level

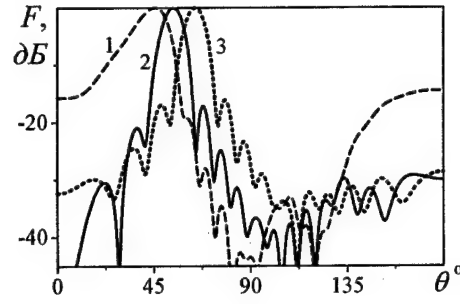


Fig. 9. Radiation patterns.

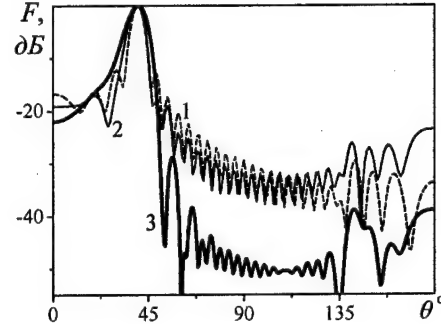


Fig. 10. Radiation patterns.

managed to decrease. Radiation coefficient of antenna is $|\Gamma_S|^2 = 0.88$.

Calculations have shown that it is possible to improve considerably the radiation pattern, when using slot set in which the slot length l_n , the distances between slot Δz_n and position of slots in a wide wall of the waveguide x_n are functions of the number of slots. Fig. 10 (curve 3) shows the radiation pattern of antenna with length 13.44λ consisting of 50 slots. In this antenna dependences l_n , Δz_n , and x_n versus number of slots n vary similar to half-wave of sinusoidal function.

4. CONCLUSION

The problem of radiation of leaky-wave antennas in the form of closely situated transverse slots cut in a broad wall of rectangular waveguide has been solved.

The numerical calculations have shown that in such slotted-waveguide antennas the shaping of the given magnitude-phase distribution is possible by selection of sizes of slots, distance between them and position of slots in a wide wall of the waveguide. Therefore it is possible to create antenna with radiation pattern of necessary shape and sidelobe level.

REFERENCES

1. Feld Ya. N. and Benenson L. S. Antenna-Feeder Devices.— M., 1959, vol.2, 551 p. (in Russian).
2. Whetten F. L. and Balanis C. A., "Effects of a Dielectric Coating on Leaky-Wave Long-Slot Waveguide Antennas", IEEE Trans. Antennas Propag., vol. AP-44, pp. 1166–1171, Aug. 1996.

LEAKY-WAVE ANTENNA WITH INCLINED SLOTS IN A WAVEGUIDE

Victor A. Katrich, Sergey A. Martynenko, Svetlana V. Pshenichnaya

V. N. Karazin Kharkiv National University, Kharkiv, Ukraine
<Sergey.A.Martynenko@univer.kharkov.ua>

Abstract

The expression for the inner mutual admittance of inclined slots in a narrow wall of a rectangular waveguide with broad wall penetration was obtained. The expression for the radiation pattern was obtained. The radiation patterns and magnitude distributions of antenna with closely spaced slots are presented. It is shown the possibility to create magnitude distributions in aperture by means of variation of tilt and dimensions of cut in the broad walls of a waveguide for each slot.

Keywords: Antenna, leaky-wave, waveguide, slot, radiation pattern, magnitude-phase distribution, mutual admittance.

1. INTRODUCTION

Narrow slots in a side surface of a waveguides have widely used in SHF techniques as independent radiators and as functional elements of equipment of antenna-feeder sections and guide-slotted arrays. Designing of antenna arrays with titled slots in a narrow wall of a rectangular waveguide is complicated because no adequate theory exists regarding the behaviors of a single slot.

In the work [1], expression for a slot admittance including broad wall penetration was obtained. It has been found from this expression that the slot resonant length is $0.4625\lambda_0$ (λ_0 is the wavelength in free space) for arbitrary angles of inclination. This is not in agreement with the experimental and computed data obtained by the other authors.

The difficulty with applying the method of moments approach to the study of such slots is that the form of the Green's function outside the waveguide is not known analytically. Therefore some type of approximation must be used, for example, such as wedge type external Green's function proposed by Jan *et al.* [2]. However, the moment method analysis with such a complicated external the Green's function is quite time consuming and the results are found to be rather susceptible to the numerical errors. In the work [3], the problem of titled slot in the narrow wall of the rectangular waveguide using the finite-difference method is solved. Method is not require knowledge of Green's function, and is simple to program. However, large amounts of computer memory and calculations time are fully restricted of a practical using of this method.

The purpose of this paper is to build a mathematical model to calculation of characteristics slotted-guide leaky wave antenna with inclined slot in a narrow wall of a rectangular waveguide.

2. FORMULATION OF THE PROBLEM

There are N of inclined slots in the narrow wall of infinite waveguide with wall thickness t , cross section $a \times b$ with medium parameters of a waveguide cavity ϵ, μ (Fig. 1). Let us denote as $L_j, l_j, d_j, \vartheta_j$ respectively slot length inside a waveguide, broad wall penetration, width of slot, angle of slot title and z_j is the shift along waveguide center of the slot with number j ($j = 1, 2 \dots N$).

Waveguide is excited by dominant mode H_{10} of wavelength in free space λ_0 . Aperture of the slot is considered as three linear parts and distribution function of electric field $e_{sl}(u)$ in a slot is presented by cosine half-wave as in [6]. Assume slots to be narrow and electric field in aperture each of slot $\vec{e}_{sl j}$ has transverse component predominantly ($\vec{e}_{sl j} = \vec{v}_j^0 e_{sl j}(u_j)$), where \vec{v}_j^0 is

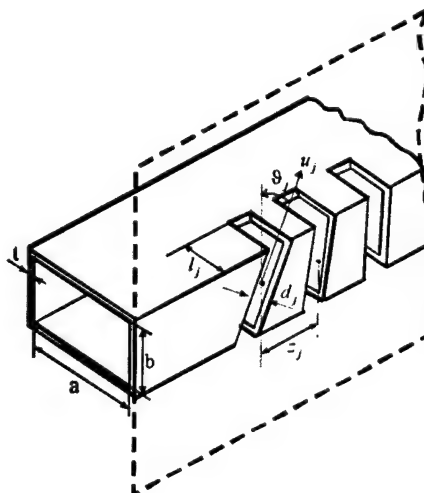


Fig. 1. Geometry of the antenna

the basis vector across slot, u_j is the local coordinate along part of the slot from center each of part).

3. THE MUTUAL ADMITTANCE

Inner mutual admittance of the slots in the general form according to [4] is defined as:

$$Y_{1,2}^{\text{int}} = \frac{1}{d_2} \int_{S_{sl2}} e_{sl2}(u_2) H_u^{\text{int}}(\vec{e}_{sl1}) dS, \quad (1)$$

where S_{sl2} is the square of aperture of the second slot; $H_u^{\text{int}}(\vec{e}_{sl1})$ is the projection on the second slot axis of the magnetic field, excited by the first slot inside a waveguide. Considering that areas of the slot location are not overlapped along the waveguide, magnetic field in this area can be presented as Fourier series expansion on a complete set of rotational eigenfunctions of a waveguide volume occupied by a slot [5]:

$$\vec{H}_{\pm u}^{\text{int}}(\vec{e}_{sl1}) = \sum_{m,n} C_{\pm mn}^e \vec{H}_{\pm mn}^e + \sum_{m,n} C_{\pm mn}^h \vec{H}_{\pm mn}^h, \quad (2)$$

where $\vec{H}_{\pm mn}^h, \vec{H}_{\pm mn}^e$ are the rotational eigenfunctions of a waveguide, $C_{\pm mn}^e$ and $C_{\pm mn}^h$ are traveling waves magnitudes of E_{mn} - и H_{mn} - types respectively, that propagating from the first slot to $z < 0$ (sign «-») and $z > 0$ (sign «+»), as in [4]:

$$C_{\pm mn}^{e(h)} = \frac{1}{N_{mn}} \frac{V_{01}}{d_1} \int_{S_{sl1}} e_{sl1}(u_1) H_{\mp u}^{e(h)} dS, \quad (3)$$

where N_{mn} is the normalization factor; V_{01} is the voltage between edges of the first slot. Using (2), (3) from (1) the inner mutual admittance expression is obtained:

$$\begin{aligned} Y_{1,2}^{\text{int}} &= -\sqrt{\frac{\epsilon_a}{\mu_a}} \frac{k}{2\gamma ab d_1 d_2} \sum_{m=0}^{\infty} \sum_{n=0}^{\infty} e^{-i\gamma z_0} \times \\ &\times \left[\frac{\epsilon_m \epsilon_n}{2} (F_1^h - V_1^h)(F_2^e - V_2^e) - \right. \\ &\quad \left. - (F_1^e - V_1^e)(F_2^h - V_2^h) \right]; \\ F^h &= -2jJ^h - 2\frac{\kappa_x \gamma}{\kappa k} [1 + (-1)^n] G^S; \\ V^e &= 2D^e - \frac{2\kappa_y}{\kappa} [(-1)^n + 1] G^S; \\ F^e &= -2J^e; V^h = -2D^h; \\ G^S &= \frac{4L/\pi}{1 - (2L\kappa_x/\pi)^2} \times \\ &\times \left[\sin \Lambda \left(C + D \frac{2L\kappa_x}{\pi} - \cos \frac{l\pi}{4L} \right) + \right. \\ &\quad \left. + \cos \Lambda \left(A - B \frac{2L\kappa_x}{\pi} + \sin \frac{l\pi}{4L} \right) \right] \frac{\sin \gamma \frac{d}{2}}{\gamma}; \\ J^e &= \frac{\kappa_x}{\kappa} j \cos \vartheta \cos \kappa_y \frac{b}{2} \left[M \frac{\sin \chi \frac{d}{2}}{\chi} - N \frac{\sin \Psi \frac{d}{2}}{\Psi} \right]; \end{aligned}$$

$$J^h = \cos \kappa_y \frac{b}{2} \left[\alpha N \frac{\sin \Psi \frac{d}{2}}{\Psi} - \beta M \frac{\sin \chi \frac{d}{2}}{\chi} \right];$$

$$D^e = \frac{\kappa_x}{\kappa} \cos \vartheta \sin \kappa_y \frac{b}{2} \left[N \frac{\sin \Psi \frac{d}{2}}{\Psi} + M \frac{\sin \chi \frac{d}{2}}{\chi} \right];$$

$$D^h = \sin \kappa_y \frac{b}{2} \left[\alpha N \frac{\sin \Psi \frac{d}{2}}{\Psi} + \beta M \frac{\sin \chi \frac{d}{2}}{\chi} \right];$$

$$M = \frac{\sin(\varphi - \zeta)}{\frac{\pi}{2L} - \eta} + \frac{\sin(\varphi + \zeta)}{\frac{\pi}{2L} + \eta} \quad B = \cos \frac{l\pi}{4L} \sin \kappa_x l;$$

$$\alpha = \frac{\gamma \kappa_y}{k \kappa} \cos \vartheta + \frac{\kappa}{k} \sin \vartheta; \beta = \frac{\gamma \kappa_y}{k \kappa} \cos \vartheta - \frac{\kappa}{k} \sin \vartheta;$$

$$N = \frac{\sin(\varphi + f)}{\frac{\pi}{2L} + \xi} + \frac{\sin(\varphi - f)}{\frac{\pi}{2L} - \xi};$$

$$C = \cos \frac{l\pi}{4L} \cos \kappa_x l;$$

$$A = \sin \frac{l\pi}{4L} \cos \kappa_x l; D = \sin \frac{l\pi}{4L} \sin \kappa_x l;$$

$$\chi = \kappa_y \sin \vartheta - \gamma \cos \vartheta; \Psi = -\kappa_y \sin \vartheta - \gamma \cos \vartheta;$$

$$\eta = -\kappa_y \cos \vartheta - \gamma \sin \vartheta; \xi = \kappa_y \cos \vartheta - \gamma \sin \vartheta;$$

$$\Lambda = \frac{\pi}{4L} \left(\frac{b}{\cos \vartheta} + l \right); f = \frac{\xi b}{2 \cos \vartheta}; \varphi = \frac{\pi b}{4L \cos \vartheta};$$

$$\zeta = \frac{\eta b}{2 \cos \vartheta}; k_i = \sqrt{\kappa_x^2 + \kappa_y^2 + k_z^2};$$

$$\kappa = \sqrt{\kappa_x^2 + \kappa_y^2}; \gamma = \sqrt{k^2 - \kappa^2};$$

$$c = \frac{d}{\cos \vartheta} + b \tan \vartheta; \kappa_x = \frac{m\pi}{a}; \kappa_y = \frac{n\pi}{b};$$

$$k = \frac{2\pi}{\lambda_0};$$

$$\epsilon_m = \begin{cases} 1, & m = 0 \\ 2, & m \neq 0 \end{cases};$$

$$\epsilon_n = \begin{cases} 1, & n = 0 \\ 2, & n \neq 0 \end{cases}; z_0 = z_2 - z_1. \quad (4)$$

In (4) $F_1^h, V_1^h, F_1^e, V_1^e$ and variables included in it are calculated by the first slot geometry. The $F_2^h, V_2^h, F_2^e, V_2^e$ are calculated by the second slot geometry, $\epsilon_a = \epsilon_0 \epsilon$, $\mu_a = \mu_0 \mu$, where ϵ_0 and μ_0 are an electrical and magnetic constant.

To define the exterior own and mutual admittances the approximation formulated in [6] can be used, presenting the exterior surfaces of the investigated slots as equivalent linear slots, which radiate in a half-space limited by an infinite plane. In this case slots length is defined as $2L_j^{\text{ext}} = \frac{b + 2t}{\cos \vartheta_j} + 2l_j + 2t$.

4. RADIATION PATTERN

Consider slots to be linear and radiate in a half-space limited by an infinite plane. Then electric field in the slot is presented as

$$e_{sl\ j}(u_j) = \frac{V_{0j}}{d_j} \cdot \cos \frac{\pi u_j}{2L_j}, \quad (5)$$

where V_{0j} is the complex field magnitude in a center of j -th slot.

Observation point M (Fig. 2) is characterized by coordinates of the spherical system ϑ, φ, r with center point in center of the slot.

The electrical field intensity that created in observation point as in [4] is

$$\bar{E}_j(\theta, \varphi, r) = \frac{ike^{-ikr}}{4\pi r} \int_{S_{sl}} [\bar{r}^0, \bar{J}_j^m] e^{ik\bar{r}^0 \cdot \bar{r}_s} dS, \quad (6)$$

where $\bar{r}_s = \bar{u}_j^0 u_j + \bar{v}_j^0 v_j$, $\bar{J}_j^m = \bar{u}_j^0 e_{sl\ j}$.

After integration procedure of the expression (6) per the slot square the intensity field expression created by the j -th slot in the observation point is obtained:

$$\begin{aligned} \bar{E}_j(\theta, \varphi, r) = & \frac{iV_{0j}}{2\lambda_0\pi} \frac{L_j}{r} e^{-ikr} \cdot \frac{\cos(\chi)}{1 - \left(\frac{2\chi}{\pi}\right)^2} \times \\ & \times \frac{2 \sin\left(k\gamma_v \frac{d_j}{2}\right)}{k\gamma_v} (\alpha_u \bar{\varphi}^0 - \beta_u \bar{\theta}^0), \end{aligned} \quad (7)$$

where $k = \frac{2\pi}{\lambda_0}$, $\chi = k\gamma_u L_j$,

$\alpha_u = \cos\theta \cos(\varphi - \vartheta_j)$, $\gamma_u = \sin\theta \cos(\varphi - \vartheta_j)$,
 $\beta_u = \sin(\vartheta_j - \varphi)$, $\gamma_v = \sin\theta \sin(\varphi - \vartheta_j)$.

The electrical field intensity created by a set of slots in the observation point is defined by the follow-

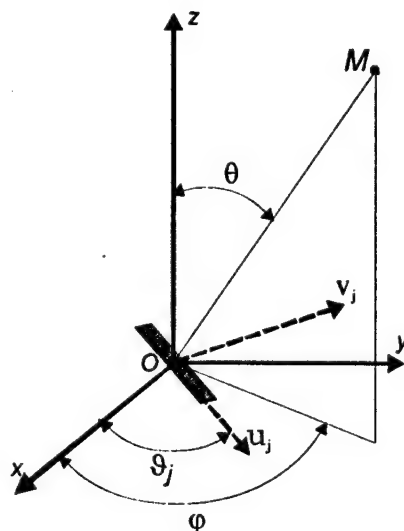


Fig. 2. To definition of radiation pattern of the slot

ing expression:

$$\bar{E}(\theta, \varphi, r) = \sum_{j=1}^N \bar{E}_j(\theta, \varphi, r) e^{ikz_j \sin\theta}, \quad (8)$$

where j is slot number in array.

To define values of the voltage magnitudes on the slots V_{0j} method of magnetic motive force in accordance with [4] is used.

In this case, inner mutual admittance is computed using the formula (4). Expression $F(\theta, \varphi) = \left| \frac{\bar{E}(\theta, \varphi, r)}{\bar{E}_{\max}(\theta, \varphi, r)} \right|$ defines the radiation pattern of the set of slot.

5. CALCULATIONS RESULTS

The radiation patterns and magnitude-phase distributions of antenna of 30 slots with width $d_j = 1.5$ mm in narrow wall of the rectangular waveguide with wall thickness $t = 1$ mm and cross section 23×10 mm² were computed by expression (4), (7). In this case, all slots were titled in the same direction and the distance between slots was 13 mm.

Waveguide is excited by dominant mode with frequency $f = 8.0$ GHz.

In Fig. 3 the radiation pattern of antenna is presented, when title angle of all the slots are the same $\vartheta_j = 30^\circ$ and value of slot penetrations in broad walls of a waveguide is changed along aperture as cosine function.

The radiation pattern has side lobe of about -20 dB. Radiation coefficient of such an antenna is about 0.8 and reflection coefficient is $4.0 \cdot 10^{-4}$. The major lobe of the radiation pattern deviates from normal to aperture as far as a linear phase distribution of the electric field in aperture is formed. In this case as shown in Fig. 4 magnitude distribution drops down to the edge of aperture. A symmetric magnitude distribution can be created if decreasing of last slots excitation be compensated by increasing of their title angles.

The radiation patterns are presented in Fig. 5. The corresponding magnitude distribution of antenna for

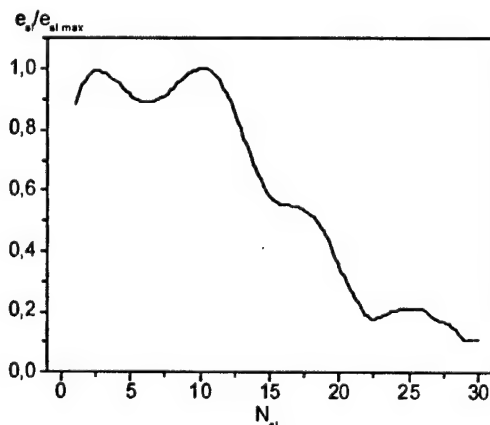


Fig. 3. Radiation pattern

the case, when title angles of the slots vary along aperture of antenna as cosine-square (curve 1) and cosine-cubic (curve 2) functions is presented in Fig.6.

In the second case, it possible to create radiation pattern with lower side lobes level. In this case radiation coefficient within the limits $|S_{\Sigma}|^2 = 0.82 \dots 0.85$ and reflection coefficient is $|\Gamma_1|^2 = (2.3 \dots 2.5) \cdot 10^{-9}$.

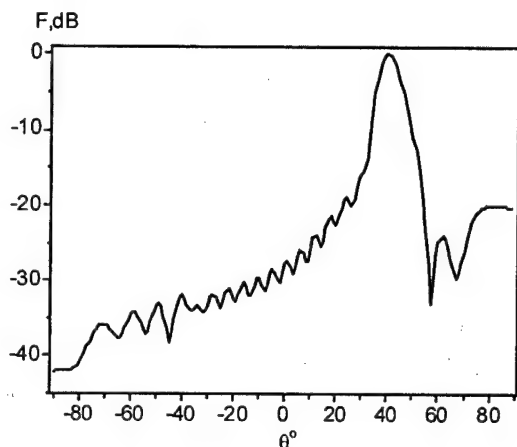


Fig. 4. Magnitude distribution

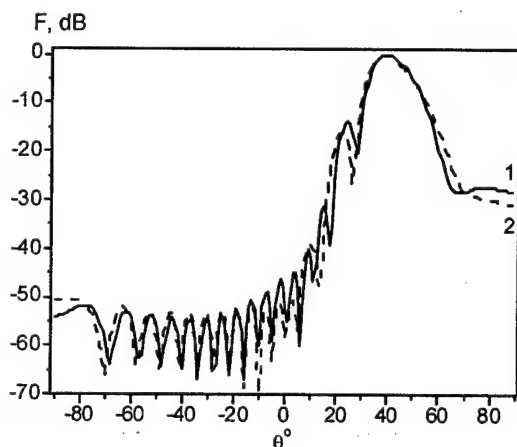


Fig. 5. Radiation patterns

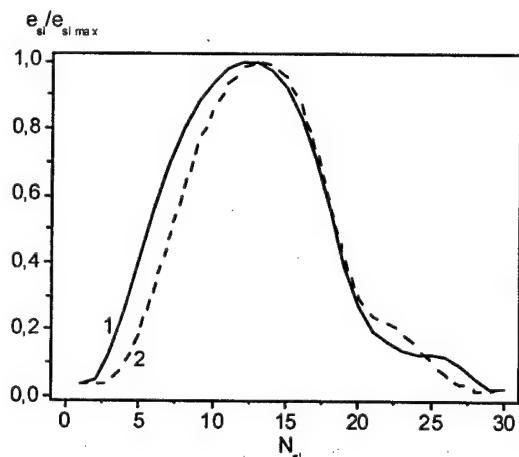


Fig. 6. Magnitude distributions

6. CONCLUSION

In the present work, a mathematical model to calculate the characteristics of antenna with inclined slots in a waveguide is developed. The method of magnetic motive force is used. It has been shown that magnitude distribution in the antenna aperture can be created by variation of title angle and penetration depth of the slots into broad walls of waveguide. In this case, it is possible to obtain high value of the radiation coefficient and low value of the reflection coefficient in a waveguide section.

REFERENCES

1. B.N. Das, J. Ramakrishna, and B.K. Sarap, "Resonant conductance of inclined slots in the narrow wall of a rectangular waveguide", IEEE Trans. Antennas Propagat., vol. AP-32, pp. 759-761, July 1984.
2. C.G. Jan, P. Hsu, R.B. Wu, "Moment method analysis of sidewall inclined slots in rectangular waveguides", IEEE Trans. Antennas Propagat., vol. 39, pp. 68-73, Jan 1991.
3. E.A. Kraut, J.C. Olivier, J.B. West "FDTD solution of Maxwell's equations for an edge slot penetrating adjacent broadwalls of a finite wall thickness waveguide", IEEE Trans. Antennas Propagat., vol. 42, pp. 1646-1648, Dec 1994.
4. Feld Ya.N., Benenson L.S. Antenna-Feeder devices. - M., 1959, vol. 2, p. 551 (in Russian).
5. Yatsuk L.P., Zhironkina A.V., Katrich V.A. Exciting of a rectangular waveguide by inclined and crossed slots // Antennas (M.), 1975. Vol. 22, p. 46-60 (in Russian).
6. Katrich V.A., Martynenko S.A., Yatsuk L.P. Tilted slot in a narrow wall of a rectangular waveguide. // Radiotechnics. Kharkiv. Sci. Interdep. Mag. 2001. No 110. P. 100-105 (in Russian).

ASYMPTOTIC SOLUTION OF INTEGRAL EQUATION INTO A PROBLEM OF COUPLING BETWEEN WAVEGUIDES THROUGH NARROW SLOTS

M. V. Nesterenko and V. A. Katrich

Karazin Kharkov National University, Kharkov, Ukraine
<Mikhail.V.Nesterenko@univer.kharkov.ua>

Abstract

On a basis of the asymptotic method of averaging the approximate analytical solution of the integral equation concerning a magnetic current in slot-hole coupling apertures of electrodynamic volumes was obtained. There are presented some expressions for currents and scattering characteristics of the transverse and longitudinal slots in the common broad and narrow walls of rectangular waveguides. The comparison with the results obtained by other methods is carried out.

Keywords: narrow slots, waveguides, integral equation, asymptotic solution.

1. INTRODUCTION

The problem of electromagnetic coupling of two waveguides through apertures in their common walls is the classical problem, which starting with paper [1] has been attracting attention of many researchers. Particular place among coupling apertures occupies the narrow slots a length $2L$ of which is commensurable with operating wavelength λ . The investigation of such slots located both in the broad and in the narrow walls of rectangular waveguides were carried out by various methods, namely: analytical [2, 3], variational [4, 5], numerical [6] and also equivalent circuits method [7, 8].

However, all the mentioned methods have some drawbacks. The numerical techniques have not sufficient clearness and simplicity to understand the physical processes. The analytical solutions have the limited range of applicability ($kL \cong \pi/2$, where $k = 2\pi/\lambda$). The variational method and the method of equivalent circuits suppose the presence of the information a priori about distribution function of the equivalent magnetic slot current, which in some cases is even approximately unknown (for example in the case of electrically long slots).

In this paper the asymptotical method of averaging is employed to obtain the general analytical expression for a magnetic current in the slot. This expression can be applied both for adjusted ($kL = n\pi/2$, $n = 1, 2, 3, \dots$) and for unadjusted ($kL \neq n\pi/2$) slots coupling two waveguides with different cross-section sizes in the general case under exciting ones with arbitrary fields of impressed sources.

2. THEORY

Let two volumes limited with ideally conducting flat surfaces be coupled between ones with an aperture cut in the common infinitely thin wall. Using the discontinuity of tangential magnetic field on the boundary surface S_{sl} of the coupling aperture the following integral equation for an equivalent magnetic current can be obtained:

$$\begin{aligned} (\text{grad div} + k^2) \int_{S_{sl}} \hat{G}_m^{\Sigma}(\vec{r}, \vec{r}') \vec{J}^m(\vec{r}') d\vec{r}' = \\ = -i\omega \vec{H}_0^{\Sigma}(\vec{r}) \end{aligned} \quad (1)$$

Here \vec{r} and \vec{r}' are the radius-vectors of observation point and source; $\vec{J}^m(\vec{r})$ is the surface density of magnetic current on the aperture; $\hat{G}_m^{\Sigma}(\vec{r}, \vec{r}') = \hat{G}_m^e(\vec{r}, \vec{r}') + \hat{G}_m^i(\vec{r}, \vec{r}')$, $\hat{G}_m^e(\vec{r}, \vec{r}')$ are the magnetic dyadic Green's functions; $\vec{H}_0^{\Sigma}(\vec{r}) = \vec{H}_0^i(\vec{r}) - \vec{H}_0^e(\vec{r})$ are the fields of impressed sources in the internal (index "i") and external (index "e") volumes.

Functions $\hat{G}_m^e(\vec{r}, \vec{r}')$ may be represented as follows [9]:

$$\hat{G}_m^e(\vec{r}, \vec{r}') = \hat{I}G(\vec{r}, \vec{r}') + \hat{G}_{0m}^e(\vec{r}, \vec{r}'), \quad (2)$$

where \hat{I} is the unit dyadic, $G(\vec{r}, \vec{r}') = e^{-ik|\vec{r}-\vec{r}'|} / |\vec{r}-\vec{r}'|$ is the Green's function of the free space, $\hat{G}_{0m}^e(\vec{r}, \vec{r}')$ are the regular dyadic functions providing satisfaction of boundary

conditions for $\hat{G}_m^{e,i}(\vec{r}, \vec{r}')$ on the internal surfaces of coupled volumes.

Equation (1) is sufficiently complicated for analysis. However for narrow slots ($d/2L \ll 1$, $d/\lambda \ll 1$, d is the slot width) it is simplified. In this case the current in the slot can be represented as follows (index "m" is omitted):

$$\vec{J}(\vec{r}) = \vec{e}_s J(s) \chi(\xi), \quad J(\pm L) = 0, \quad \int_{\xi} \chi(\xi) d\xi = 1, \quad (3)$$

where s and ξ are the longitudinal and transverse local slot co-ordinates; $\chi(\xi)$ is the set function, accounting features of electrostatic field on the slot edges; \vec{e}_s is the unit vector. Thus, a problem of finding the current $\vec{J}(\vec{r})$ by given field $\vec{H}_0^{\Sigma}(\vec{r})$ is reduced to determining the current distribution function $J(s)$.

Let us assume further that the slot is rectilinear and the impressed field in external volume is absent: $\vec{H}_0^e(\vec{r}) = 0$. Then, substituting expressions (3) into (1), we obtain:

$$\left(\frac{d^2}{ds^2} + k^2 \right) \int_{-L}^L J(s') [G_s^e(s, s') + G_s^i(s, s')] ds' = -i\omega H_{0s}^i(s) \quad (4)$$

$$G_s^{e,i}(s, s') = 2 \frac{e^{-ikR(s, s')}}{R(s, s')} + G_{0s}^{e,i}(s, s'), \quad (5)$$

$$R(s, s') = \sqrt{(s - s')^2 + (d/4)^2}.$$

It is accounted here that for sources on the surface $\hat{G}^{e,i}(s, \xi; s', \xi') = 2\hat{I}G(s, \xi; s', \xi') + \hat{G}_0^{e,i}(s, \xi; s', \xi')$ and

$$G(s, s') = \int_{\xi} G(s, \xi; s', \xi') \chi(\xi') d\xi', \quad (6)$$

$$\hat{G}_0^{e,i}(s, s') = \int_{\xi} \hat{G}_0^{e,i}(s, \xi; s', \xi') \chi(\xi') d\xi'.$$

It should be noted that in kernel (5) of the integral equation (4) the approximate expression of R was used, namely dependence on transverse coordinate was chosen in form of $(\xi - \xi')^2 \cong (d/4)^2$, as it was used in the vibrator antenna theory [10]. This is correct with the satisfactory accuracy for slots in the metal surfaces [11].

Isolating the logarithmic singularity in equation (4) we obtain integral-differential equation with small parameter:

$$\frac{d^2 J(s)}{ds^2} + k^2 J(s) = \alpha \{ i\omega H_{0s}(s) + F[s, J(s)] + F_0[s, J(s)] \}, \quad (7)$$

in which $\alpha = 1/(8 \ln(d/8L))$ is the natural small parameter of the problem ($|\alpha| \ll 1$), $H_{0s}(s)$ is the

component of the field of impressed sources along the axis of the slot,

$$F[s, J(s)] = 4 \left[-\frac{dJ(s')}{ds'} \frac{e^{-ikR(s, s')}}{R(s, s')} \right]_{-L}^L + \left(\frac{2dJ(s)}{ds} + J(s) \frac{d}{ds} \right) \frac{1}{R(s, s')} + 4 \int_{-L}^L \frac{1}{R(s, s')} \left[\left(\frac{d^2 J(s')}{ds'^2} + k^2 J(s') \right) e^{-ikR(s, s')} - \left(\frac{d^2 J(s)}{ds^2} + k^2 J(s) \right) \right] ds' \quad (8)$$

is the own field of the slot in an infinite screen;

$$F_0[s, J(s)] = -\frac{dJ(s')}{ds'} [G_{0s}^e(s, s') + G_{0s}^i(s, s')] \Big|_{-L}^L + \int_{-L}^L \left(\frac{d^2 J(s')}{ds'^2} + k^2 J(s') \right) \times [G_{0s}^e(s, s') + G_{0s}^i(s, s')] ds' \quad (9)$$

is the slot own field repeatedly reflected from the walls of coupled volumes.

Further, following the variation method of arbitrary constants, execute the change of variables:

$$J(s) = A(s) \cos ks + B(s) \sin ks, \quad (10)$$

By the latter the equation (7) is transformed into the next system of integral-differential equations concerning unknown functions $A(s)$ and $B(s)$

$$A'(s) = -\frac{\alpha}{k} \{ i\omega H_{0s}(s) + F_N[s, A(s), A'(s), B(s), B'(s)] \} \sin ks, \quad (11)$$

$$B'(s) = +\frac{\alpha}{k} \{ i\omega H_{0s}(s) + F_N[s, A(s), A'(s), B(s), B'(s)] \} \cos ks,$$

where $A'(s) = dA(s)/ds$, $B'(s) = dB(s)/ds$,

$F_N = F + F_0$ is the full own field of the slot.

The obtained equations are complete equivalent of equation (7). These equations represent the system of integral-differential equations of standard type, unresolved in derivative. The right-hand side of these equations are proportional to the small parameter α . Therefore the functions $A(s)$ and $B(s)$ in the right-hand parts of the equations (11) can be considered as slowly varying functions. To solve the system of equations (11) it is possible to use the asymptotic method of averaging. Substantiation of applicability of this method to the systems like (11) and the technique of its solution are grounded by Philatov [12]. Then, associate the system of equations (11) with the simplified system, at which in the right-hand sides of

equations (11) $A'(s) = 0$ and $B'(s) = 0$. Performing in this system the partial averaging by explicitly entering variable s , we obtain two equations of the first approximation:

$$\begin{aligned} \bar{A}'(s) &= -\alpha \left\{ \frac{i\omega}{k} H_{0s}(s) + \bar{F}_N[s, \bar{A}, \bar{B}] \right\} \sin ks, \\ \bar{B}'(s) &= +\alpha \left\{ \frac{i\omega}{k} H_{0s}(s) + \bar{F}_N[s, \bar{A}, \bar{B}] \right\} \cos ks, \end{aligned} \quad (12)$$

in which $G_s^\Sigma(s, s') = G_s^e(s, s') + G_s^i(s, s')$,

$$\begin{aligned} \bar{F}_N[s, \bar{A}, \bar{B}] &= \\ &= [\bar{A}(s') \sin ks' - \bar{B}(s') \cos ks'] G_s^\Sigma(s, s') \Big|_{-L}^L. \end{aligned} \quad (13)$$

Integrating the system (12) and substituting the obtained values $\bar{A}(s)$ and $\bar{B}(s)$ as a approximating functions of $A(s)$ and $B(s)$ in (10), the most general asymptotic expression of the current in the narrow slot at its any position concerning the walls of the coupled volumes is obtained in the following form:

$$\begin{aligned} J(s) &= \bar{A}(-L) \cos ks + \bar{B}(-L) \sin ks + \\ &+ \alpha \int_{-L}^s \left\{ \frac{i\omega}{k} H_{0s}(s') + \bar{F}_N[s', \bar{A}, \bar{B}] \right\} \times \\ &\times \sin k(s - s') ds'. \end{aligned} \quad (14)$$

To define the constants $\bar{A}(\pm L)$ and $\bar{B}(\pm L)$ it is necessary to use boundary conditions (3) and conditions of symmetry, which are uniquely connected with the way of the slot excitation. Then, taking in consideration symmetrical (index "s") and antisymmetrical (index "a") components of the current under arbitrary slot excitation the $H_{0s}(s) = H_{0s}^s(s) + H_{0s}^a(s)$ with accuracy not more than terms of an order α^2 we have definitively:

$$\begin{aligned} J(s) &= J^s(s) + J^a(s) = \\ &= \alpha \frac{i\omega}{k} \left\{ \int_{-L}^s H_{0s}(s') \sin k(s - s') ds' - \right. \\ &\quad \left. \frac{\sin k(L + s) \int_{-L}^L H_{0s}^s(s') \sin k(L - s') ds'}{\sin 2kL + \alpha N_s(kd, 2kL)} - \right. \\ &\quad \left. - \frac{\sin k(L + s) \int_{-L}^L H_{0s}^a(s') \sin k(L - s') ds'}{\sin 2kL + \alpha N_a(kd, 2kL)} \right\}, \end{aligned} \quad (15)$$

where $N_s(kd, 2kL)$ and $N_a(kd, 2kL)$ - the functions of the own field of the slot, are accordingly equal

$$\begin{aligned} N_s(kd, 2kL) &= \\ &= \int_{-L}^L [G_s^\Sigma(s, -L) \pm G_s^\Sigma(s, L)] \sin k(L - s) ds, \end{aligned} \quad (16)$$

and which are completely defined with Green's functions of coupled volumes (infinite or half-infinite waveguides, resonators etc.)

As an example, let us consider the coupling of two identical rectangular waveguides with cross-sectional dimensions $a \times b$ through the symmetrical transverse slot cut in the common broad wall and through the longitudinal slot in the common narrow wall.

2.1. SYMMETRICAL TRANSVERSE SLOT IN BROAD WALL

In this case $H_{0s}(s) = H_{0s}^s(s) = H_0 \cos(\pi s/a)$ and

$$\begin{aligned} J(s) &= -\alpha H_0 \times \\ &\times \frac{i\omega \{ \cos ks \cos(\pi L/a) - \cos kL \cos(\pi s/a) \}}{\gamma^2 [\cos kL + \alpha N(kd, kL)]}, \end{aligned} \quad (17)$$

where $\gamma^2 = k^2 - (\pi/a)^2$, H_0 is the amplitude of the incident wave, falling from $z = -\infty$ (region 1), $N_s(kd, 2kL) = 2 \sin kLN(kd, kL)$.

Reflection (in region 1) and transmission (in region 2) coefficients ($|S_{11}|$ and $|S_{12}|$ accordingly) in the first waveguide and forward (in region 4) and backward (in region 3) coupling coefficients $|S_{14}|$ and $|S_{13}|$ into the auxiliary waveguide are equal to

$$\begin{aligned} |S_{11}| &= |S_{13}| = |S_{14}| = \\ &= \left| \frac{4\pi\alpha f(kL, \pi L/a)}{abk\gamma [\cos kL + \alpha 2N(kd, kL)]} \right|, \\ |S_{12}| &= |1 + i|S_{11}|, \\ f(kL, \pi L/a) &= \end{aligned} \quad (18)$$

$$\begin{aligned} &2 \cos \frac{\pi}{a} L \frac{\sin kL \cos \frac{\pi}{a} L - \frac{\pi}{ka} \cos kL \sin \frac{\pi}{a} L}{1 - (\pi/ka)^2} \\ &- \frac{\cos kL}{(2\pi/ka)} \left(\sin \frac{2\pi L}{a} + \frac{2\pi L}{a} \right). \end{aligned}$$

2.2. LONGITUDINAL SLOT IN NARROW WALL

For a longitudinal slot the component of the field of impressed sources along slot axis equals $H_{0s}(s) = H_0 \exp(-i\gamma s)$ and

$$\begin{aligned} J(s) &= J^s(s) + J^a(s) = \alpha H_0 \frac{i\omega}{(\pi/a)^2} \times \\ &\times \left\{ e^{-i\gamma s} - \frac{\cos ks \cos \gamma L}{\cos kL + \alpha N^s(kd, kL)} + \right. \\ &\quad \left. + i \frac{\sin ks \sin \gamma L}{\sin kL + \alpha N^a(kd, kL)} \right\}. \end{aligned} \quad (19)$$

$$N_s(kd, 2kL) = 2 \sin kLN^s(kd, kL),$$

$$N_a(kd, 2kL) = 2 \cos kLN^a(kd, kL).$$

For reflection, transmission and coupling coefficients the following expressions were obtained:

$$\begin{aligned}
 |S_{11}| &= |S_{13}| = \\
 &= \left| \frac{4\pi\alpha}{abk\gamma} \left\{ f^s(kL, \gamma L) + f^a(kL, \gamma L) - \right. \right. \\
 &\quad \left. \left. - 2kL \frac{\sin 2\gamma L}{2\gamma L} \right\} \right|, \\
 |S_{12}| &= \\
 &= \left| 1 + \frac{i4\pi\alpha}{abk\gamma} \left\{ f^s(kL, \gamma L) - f^a(kL, \gamma L) - \right. \right. \\
 &\quad \left. \left. - 2kL \right\} \right|, \\
 |S_{14}| &= |S_{12} - 1|, \\
 f^s(kL, \gamma L) &= \\
 &= 2 \cos \gamma L \frac{\sin kL \cos \gamma L - (\gamma/k) \cos kL \sin \gamma L}{[1 - (\gamma/k)^2][\cos kL + \alpha N^s(kd, kL)]}, \\
 f^a(kL, \gamma L) &= \\
 &= 2 \sin \gamma L \frac{\cos kL \sin \gamma L - (\gamma/k) \sin kL \cos \gamma L}{[1 - (\gamma/k)^2][\sin kL + \alpha N^a(kd, kL)]}.
 \end{aligned} \tag{20}$$

3. NUMERICAL RESULTS

In Fig. 1 the plots of dependencies of coupling coefficient $C_{13} = 20 \log |S_{13}|$ on the length of the symmetrical transverse slot cut in the common infinitely thin broad wall of two identical rectangular waveguide are represented for various methods of the calculation. It is seen that the averaging method, the variational method and the method of moments give the slot resonance length $2L \cong 0.47\lambda$ ("shortening" of slot). On the other hand quasi-static antenna method and equivalent circuits method ("reaction" method) provide the resonance value of length $2L = 0.5\lambda$ that does not correspond to reality. The difference between values of C_{13} calculated with the averaging method

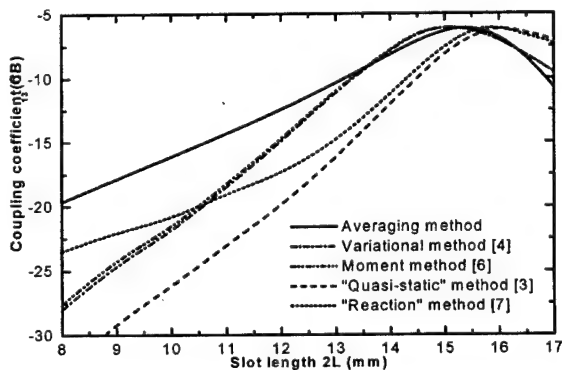


Fig. 1. Coupling versus slot length for a symmetrical transverse slot in the common broad wall between a pair of rectangular waveguides, with $a = 22.86$ mm, $b = 10.16$ mm, $d = 1.5875$ mm, $\lambda = 32.0$ mm.

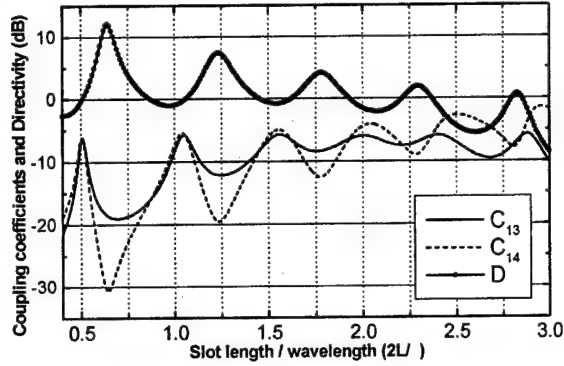


Fig. 2. Coupling and directivity versus relative slot length for a longitudinal slot in the common narrow wall between a pair of rectangular waveguides, with $a = 23.0$ mm, $b = 10.0$ mm, $d = a/15$, $y_0 = b/2$ is the slot axis position, $\lambda = 28.75$ mm.

and other methods for short slots is explained evidently with increasing the small parameter α , that leads to increasing the inaccuracy, when solving the equation (7).

In Fig. 2 the plots of dependence of coupling coefficients C_{13} and $C_{14} = 20 \log |S_{14}|$ and directivity $D = 20 \log (|S_{13}|/|S_{14}|)$ versus $2L/\lambda$ for the longitudinal slot, coupling two rectangular waveguides through the common narrow wall of the finite thickness, are shown.

It is seen from the plots that increase of the electrical slot length leads to increase of the differences between values C_{13} and C_{14} near resonances ($kL \approx n\pi/2$, $n = 1, 2, 3, \dots$) and to change of the sign of D on the opposite one. It should be noted that in paper [8] the incorrect conclusion about equality of C_{13} and C_{14} for such coupling the waveguides was made on the basis of the equivalent circuits method. This discrepancy can be explained by using in [8] the symmetrical function for the current $J^s(s) = J_0 \sin k(L - |s|)$ for obtaining formulas of parameters of the equivalent circuit, whereas the asymptotic solution of equation (7) gives the expression (19), where $J(s) = J^s(s) + J^a(s)$.

4. CONCLUSION

The obtained asymptotic solution of the integral equation for a magnetic current in slot-hole coupling apertures allows one to obtain even for a first approximation the current analytical expressions, which is valid for the various ratio between the wavelength and the longitudinal size of the slot.

The carried out numerical results demonstrate efficiency and effectiveness of such a solution.

REFERENCES

1. Bethe H.A. Theory of diffraction by small holes // Phys. Rev. 1944. Vol.66. p.163.
2. Stevenson A.F. Theory of slots in rectangular wave-guides // J. Appl. Phys. 1948. Vol.19. p.24.
3. Lewin L. Some observations on waveguide coupling through medium sized slots Proc. IEE. 1960. Vol.107C, p.171.
4. Sangster A.J. Variational method for the analysis of waveguide coupling // Proc. IEE. 1965. Vol.112. No.12, p.2171.
5. Levinson I.B., Fredberg P.Sh. Slot couplers of rectangular one mode waveguide equivalent circuits and lumped parameters // Radio Eng. and Electron. Phys. 1966. Vol.11. No.1, p.717.
6. Khac T.Vu. Solutions for some waveguide discontinuities by the method of moments // IEEE Trans. 1972. Vol.MTT-20. No.6, p.416.
7. Pandharipande V.M., Das B.N. Coupling of waveguides through large apertures // IEEE Trans. 1978. Vol.MTT-26. No.3, p.209.
8. Pandharipande V.M., Das B.N. Equivalent circuit of a narrow-wall waveguide slot coupler // IEEE Trans. 1979. Vol.MTT-27. No.9, p.800.
9. Khizhnyak N.A. Integral equations of macroscopical electrodynamics - Kiev: Naukova dumka, 1986 (in Russian).
10. King R.W.P. The Theory of Linear Antennas - Cambr.-Mass.: Harv. Univ. Press, 1956.
11. Naiheng Y., Harrington R. Electromagnetic coupling to an infinite wire through a slot in a conducting plane // IEEE Trans. 1983. Vol.AP-31. No.2, p.310.
12. Philatov A.N. Asymptotic methods in the theory of differential and integral-differential equations - PHAN: Tashkent, 1974 (in Russian).

FORMING A PARTIALLY POLARIZED WAVE BY NON-COHERENT SOURCES OF THE NOISE FIELD

L. G. Kornienko, V. A. Kovalchuk

Kharkov Military University

Abstract

Polarization parameters of the wave formed by noise radiation of two non-coherent sources in far zone are considered. The directional properties of system of radiators concerning a degree of polarization of a wave and their dependence on a ratio of intensity partial fields and mutual orientation of antennas are analyzed.

In this paper, we research a polarization condition of the noise radiation formed by superposition of two independent partial completely polarized noise fields extending in a certain direction. Such a radiation can be created, for example, by two closely standing and unresolvable on angular coordinates onboard stations of electronic warfare. Research of a polarization condition of a summary noise wave is necessary, in particular, for an efficiency estimation of methods of polarization and spatial rejection of jammings with fluctuating polarization [1].

A complex amplitude of the intensity of the electric field vector for a separate harmonic component of the i -th radiation source in the direction of ort \vec{u}

$$\vec{E}_i(\vec{u}, f) = A_i(f) \vec{F}_i(\vec{u}, f) S_i(f), \quad (1)$$

$$A_i = \frac{\sqrt{30 R_{\Sigma i} D_i}}{r_i} e^{-j\omega t_{di}},$$

depends on radiation resistance $R_{\Sigma i}$, directive gain

D_i , the normalized vector radiation pattern (RP) \vec{F}_i of the antenna excited by a current with spectral density $S_i(f)$, delay interval $t_{di} = r_i / c$ of partial wave past a distance r_i ($\omega = 2\pi f$ is the circular frequency of oscillations).

For studying a polarization condition of a summary wave from two sources of noise radiation

$$\vec{E}(\vec{u}, t) = \vec{E}_1(\vec{u}, t) + \vec{E}_2(\vec{u}, t), \quad \text{where}$$

$$\vec{E}_i(\vec{u}, t) = \int_{\Omega} \vec{E}_i(\vec{u}, f) e^{j2\pi f t} df, \quad i = 1, 2 \quad \text{are limits}$$

of integration $f_0 - 0,5\Pi \leq \Omega \leq f_0 + 0,5\Pi$, f_0 , Π are the central frequency and effective width of a radiation spectrum, it is convenient to use a method of a coherence matrix [2]

$$J = \begin{bmatrix} \sigma_x^2 & \sigma_x \sigma_y r_{xy} \\ \sigma_x \sigma_y r_{yx} & \sigma_y^2 \end{bmatrix}, \quad (2)$$

whose elements depend on dispersions σ_x^2 , σ_y^2 and mutual correlation factors r_{xy} , r_{yx} of projections of a field E_x , E_y on the axis of the cartesian coordinates system placed in a plane, perpendicular to a direction of wave propagation, and $r_{xy} = r_{yx}^*$. Taking into account, that for stationary processes the spectral density of currents is delta-correlated, we can obtain

$$\sigma_x \sigma_y r_{xy} = \int_{\Omega} [|A_1|^2 F_{1x} F_{1y}^* N_1(f) + |A_2|^2 F_{2x} F_{2y}^* N_2(f)] df, \quad (3)$$

where $N_i(f)$ is a power spectrum of the i -th antenna current, F_{ik} , $i = 1, 2$, $k = x, y$ are coordinate projections of vector pattern for each of antennas.

If combining in appropriate way indices x and y , it is possible to obtain from (3) the expressions for elements of a matrix (2). Because of the mutual independence of partial fields, elements of matrix J do not depend on waves delay interval t_{di} . Stocks' parameters of a summary random field $s_0 = \sigma_x^2 + \sigma_y^2$,

$$s_1 = \sigma_x^2 - \sigma_y^2, \quad s_2 = 2\sigma_x \sigma_y |r_{xy}| \cos(\arg r_{xy}),$$

$$s_3 = 2\sigma_x \sigma_y |r_{xy}| \sin(\arg r_{xy}) \quad \text{allow calculating a}$$

wave polarization degree $m = \sqrt{s_1^2 + s_2^2 + s_3^2} / s_0$, an ellipticity angle $\sin 2\chi = s_3 / \sqrt{s_1^2 + s_2^2 + s_3^2}$ and an orientation angle of the ellipse big axis $\tan 2\psi = s_2 / s_1$ of completely polarized wave component with the intensity $\sqrt{s_1^2 + s_2^2 + s_3^2}$. The indicated parameters characterize a wave polarization condition.

Let's apply the described technique for the analysis of the summary field parameters excited at an observation point with a pair of elementary electric dipoles turned from each other by angle γ . For these antennas, RP and DG do not depend on the field oscillations fre-

quency. The radiation impedance of dipoles depends on frequency. Antennas radiate the waves completely polarized with linear polarization. Because of full intensity of a summary wave s_0 , polarization degree m and ellipticity angle χ are invariant concerning system coordinates rotation, it is convenient to combine a vector \vec{F}_1 , for example, with an Ox -axis. Then $F_{1x} = F_1$ and $F_{1y} = 0$. Under the specified conditions the expression for Stocks' parameters get a kind

$$s_0 = a_1 F_1^2 + a_2 F_2^2; \quad s_1 = a_1 F_1^2 + a_2 (F_{2x}^2 - F_{2y}^2); \quad (4)$$

$$s_2 = 2a_2 F_{2x} F_{2y}; \quad s_3 = 0,$$

where factors a_i , $i = 1, 2$, define the mean field intensity of the i -th antenna in the direction of RP main maximum. As $s_3 = 0$, a completely polarized component of a summary field is linearly polarized ($\chi = 0$).

Let's study parameters of summary radiation in a magnetic plane of the first vibrator. Then $|F_1| = 1$, $F_{2x} = \cos \gamma$, $F_{2y} = \sin \gamma \sin \varphi$. Polarization degree m and inclination angle ψ of vector \vec{E} are determined in accordance with the expressions

$$m = \frac{\sqrt{1 + bF_2^4 + 2b(F_{2x}^2 - F_{2y}^2)}}{1 + bF_2^2};$$

$$\psi = \frac{1}{2} \arctg \frac{2bF_{2x}F_{2y}}{1 + b(F_{2x}^2 - F_{2y}^2)},$$

where $b = a_2/a_1$.

First, consider parameters of a summary wave in direction $\varphi = \pi/2$. For $\gamma = 0$ (axes of dipoles are parallel), and also for $b \rightarrow 0$ or $b \rightarrow \infty$ the summary wave is completely polarized ($m = 1$). Thus, vector \vec{E} is oriented either along an Ox -axis, or $\psi = \gamma$ (for $b \rightarrow \infty$). At $\gamma = \pi/2$ (axes of dipoles are perpendicular) and $b = 1$, the wave is non-polarized ($m = 0$), a vector \vec{E} in a cross-section plane occupies an equiprobable position through time intervals $\tau_K \sim 1/\Pi$. In all other cases, the summary wave is partially polarized ($0 < m < 1$) [3].

We research the dependence of a wave polarization degree on angle φ . For this purpose, introduce a notion of RP of the system of radiators in polarization degree $m(\varphi)$. Such an RP $m(\varphi)$ of the fluctuating field does not depend on the distance between the phase centers of dipoles. This distance defines the far zone of a dipole pair, where parameters of a summary field are studied.

In Fig. 1, the dependencies of the full intensity of the wave $s_0^n(\varphi)$ normalized to the intensity of the first dipole radiation for cases $\gamma = \pi/2$ (a continuous line) and $\gamma = \pi/4$ (a dotted line) at $b = 1$ are

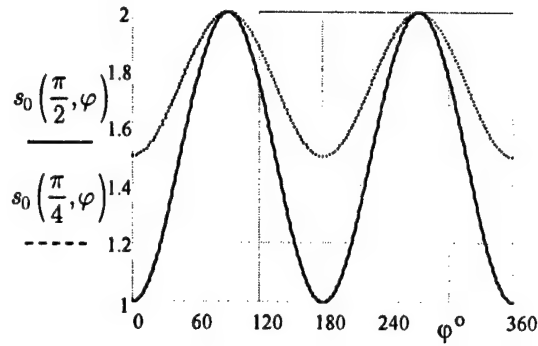


Fig. 1. The full normalized intensity of two non-coherent radiators system field

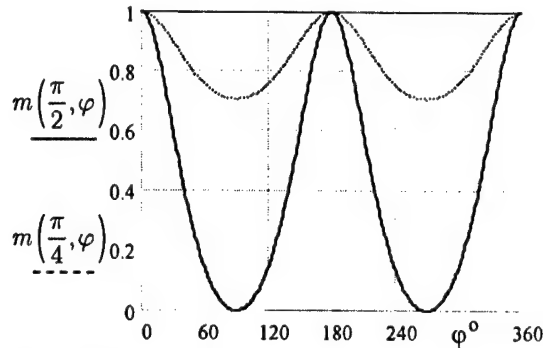


Fig. 2. RP in a polarization degree of system of two radiators of noise fields

shown. In Fig. 2, dependencies $m(\varphi)$ for the same cases are presented.

At $\gamma = \pi/2$, the full intensity of radiation and a polarization degree of a summary field essentially depends on an angular direction φ . In directions $\varphi = 0^\circ$ and 180° (both dipoles are in one plane with an observation point), only one dipole radiates ($s_0^n = 1$, Fig. 1), therefore, the field is completely polarized ($m = 1$, Fig. 2). In directions $\varphi = 90^\circ$ and $\varphi = 270^\circ$ two dipoles are located in a picture plane concerning an observer and radiate non-coherent fields of orthogonal polarization and equal intensity. Therefore, the full intensity is doubled ($s_0^n = 2$, Fig. 1), and the summary field is completely non-polarized ($m = 0$, Fig. 2). At other angles φ , the full intensity lies in the limits of from 1 to 2, the degree of polarization changes from 0 up to 1.

At $\gamma = \pi/4$, the full intensity and a polarization degree has weaker direction. At any angle φ both dipoles radiate, therefore, $s_0^n > 1$. The field is polarized much stronger (the minimal polarization degree $m = 0.707$), what is stipulated by the greater intensity of a x -component of the summary field. The angular dependence $s_0^n(\varphi)$ is determined by the directed radiation of the second dipole.

Thus, in the common case, two sources of independent noise radiations of linearly polarized waves

create partially polarized field in the far zone. The completely polarized component has a linear polarization. The polarization degree and orientation angle of vector \vec{E} depend on relationship of intensities of radiated fields in the specified direction and mutual orientation of dipoles. Parameters of the partially polarized field do not depend on partial fields delay interval. These fields are summarized non-coherently at an observation point, what reduces the directional properties of the system of radiators.

REFERENCES

1. Kornienko L. G., Mysik F. F. Feature and potentialities of coherent compensation of partially polarized jams. In Journal "Antennas", issue 1(47), 2001. - P. 55-63. [in Russian].
2. M. Born, E. Volf. Foundations of optics. M.: Nauka, 1970, 856 p. [in Russian].
3. Kornienko L. G., Mysik F. F. Polarization characteristic of the jamming created by a pair of angularly unresolvable jammings. - Kharkiv: (KAI), issue. 22, 2001.-P. 268-272. [in Russian].

A NOVEL APPROACH TO SCANNING ANTENNAS DESIGN

Konstantin A. Lukin

LNDES

Institute of Radiophysics and Electronics,
National Academy of Sciences of Ukraine, Kharkiv, Ukraine
<lukin@ire.kharkov.ua>

Abstract

A new concept for design of scanning antennas is suggested. The concept is based upon a combination of a single radiating element movement with antenna aperture synthesizing. The radiator movement may be either real or virtual one. In turn, the latter may be either mechanical or electronic one. In the paper, the case of electromechanical motion is preferably considered. Various realizations of real and virtual movements of the radiator are shortly described. Examples of the concept implementing are presented. Advantages and drawbacks of the concept are briefly discussed.

Keywords: Scanning Antenna, Synthetic Aperture, Radiator, Electromechanical Scanning, MEMS

1. INTRODUCTION

Development of scanning antennas is still a challenge for radar engineers. There are several design problems to be solved for providing of scanning antenna performance, such as low sidelobes levels, smoothness of antenna amplitude and phase patterns, large number of antenna beam positions, low power consumption, etc. Many technical approaches have been suggested for design of scanning antennas [1]. They may be split into two big classes: (a) electromechanical (mechanical) scanning and (b) electronically scanning: phased-array antenna (PAA). A fast scanning and flexibility in resetting of scanning program are basic advantages of the latter approach. However, that concept poses numerous drawbacks as well: strong parasitic coupling of the radiating elements, big losses, roughness of the phase antenna pattern, restricted scanning angles, etc. With this respect, mechanical scanning may provide much better performance, but it is much slower. Recently, a compromise approach has been elaborated to go around some of the above drawbacks: application of Micro-Electro-Mechanical System (MEMS) switches for proper connections/ disconnections of patch elements in PAA. Combination of a real aperture antenna with virtual movement of a patch radiator for aperture synthesizing on receive only has been suggested in [2]. Similar idea, but suitable for design of transmit/receive antennas with electro-mechanical scanning has been suggested in [3].

In the paper, a new concept for designs of scanning transmit/receive antennas is suggested. The concept is based upon a combination of a single radiating element movement with antenna aperture synthesizing. Physically, the radiator movement may be either real or virtual one. In turn, the virtual movement may be

either mechanical or electronic one. The case of electro-mechanical motion is preferably considered. Various realizations of real and virtual movements of the radiating element are considered. Examples of the concept implementing are presented. Advantages and drawbacks of the concept are briefly discussed.

2. GENERAL DESCRIPTION OF THE APPROACH

The basic idea of the suggested approach consists in the following [4]. For antenna beam forming and scanning, we use the principles of 1D-PAA, but using radiation/reception of electromagnetic pulses at each position of a *single radiating element* rather than simultaneous radiation/reception by all elements of the 1D-PAA, as usually. In other words, we use the concept of synthetic aperture radar being applied in the situation of a 1D-PAA having a real aperture. Generally, this approach enables application of both various types of radiating elements and methods for implementing of its movement along the antenna aperture. The following parameters are of the most interest: (1) antenna beam width, (2) number of beam positions, (3) antenna pattern sidelobes and (4) time of full scan. In the scanning antenna suggested, the beam width is defined by its real aperture, while the number of beam positions is defined by that of measurement positions for the radiating element. The sidelobes level will depend on the phase-amplitude distribution (weighting function) along the real aperture of the antenna. Finally, the time of full scan is defined by both radiating element shift time to a neighboring position and numbers of those positions. This parameter is limited by the required data acquisition time at each position.

Besides, in order to implement a full scan in real time scale one has to perform both range and azimuth compressions in quasi-real time scale. The latter is to be implemented with help of an appropriate digital signal processor, which is nowadays feasible for many short range applications.

3. TECHNICAL IMPLEMENTATIONS

We have suggested, elaborated and tested several antennas for implementing of the suggested concept.

3.1. HELICAL-SLOT SPINNING ANTENNA

This antenna should consist of two hollow co-axial cylinders. The outer cylinder has a longitudinal slot parallel to the cylinders axis, while another one contains a helically shaped waveguide with either a single longitudinal slot or set of half-wavelength slots properly oriented with respect to the slot of the outer cylinder. When rotating, the inner cylinder will cause movement of the longitudinal slot and helical waveguide cross-point along the slot. In this way, we realize a linear motion of the radiating element provided radiation suppression by other half-wavelength slots. Scanning rate of such antenna is defined by rotation rate of the inner cylinder and may be rather high provided a properly fast SAR processor. This type of scanning antennas is described in [4] in more details. It should be noticed that the principle of linear motion of a cross-point of helical slot and linear one because of helical slot rotation has been used in so called helical scanner [1]. However, both the function and design of that scanner cardinally differ from those in the suggested scanning antenna.

3.2. SLOT-IN-TAPE SCANNING ANTENNA

Another technical approach to realization of the suggested principle represents itself the following. As a real aperture antenna, one has to use a waveguide with a not-radiating half-wavelength longitudinal slot in its wider wall. When covering this wall by a metallic tape with a half-wavelength transverse slot one provides condition for resonant radiation of the wave traveling inside the waveguide. In order to enhance its efficiency one has to place a short circuit at the proper distance from the radiating slot. The tape is to be self-connected into a ring and rotated with a certain speed. Scanning rate depends on the tape ring rotating speed and also may be rather high provided a properly fast SAR processor. Unlike the previous case, this antenna does not need a rotary joint. This type of antenna has been also developed and tested in LNDES. The tests showed excellent results concerning its suitability for scanning antenna design on the basis of aperture synthesizing principle.

3.3. FLIP-FLOP SLOT WAVEGUIDE ANTENNA

In that type of scanning antennas a virtual movement of the radiating element is suggested. The antenna consists of a waveguide with a linear array of equally spaced resonant radiating slots. Each slot is covered

by a three-state-screening strip (TSSS) having three different states: (1) open, (2) close and (3) chop. The first/second state is used to open/close each radiating slot according to the control signal, while the third state is used to stop propagation of the feeding wave through the waveguide for enhancement of the radiation efficiency. Flip-Flop operation is to be implemented by electro-mechanical switches, e.g. combination of springs with electro-magnets. A linear virtual motion of the radiating slot is performed via switching of the TSSSs in the way enabling for each slot a sequential alternation of the following states: chop-state, open-state and close-state. The scanning rate of that antenna will be defined by time of TSSS electro-mechanical switching.

3.4. FLIP-FLOP PATCH SCANNING ANTENNA

Similar design may be implemented for patch antennas. With this aim, one has to prepare a linear array of radiating patches at the upper row and chop patches at the lower row while feeding strip-line is to be placed between them. Each patch should be fed through a flip-flop switch. A linear virtual motion of the radiating patch is performed via connecting/disconnecting of the radiating patches and chop patches in the way similar to that in the previous case: (1) "radiating patch disconnected" and "chop patch connected"; (2) "radiating patch connected" and "chop patch disconnected"; (3) "radiating patch disconnected" and "chop patch disconnected". In order to provide high efficiency, low cross-talk, high decoupling of the radiating patches one has to use either electronic switches having small losses and high rate isolation, or electromechanical flip-flop switches possessing similar performance.

ACKNOWLEDGMENTS

This work has been supported in part by Intermap Technologies GmbH (Former AeroSensing Radar Systeme GmbH) – STCU Project P-050.

REFERENCES

1. Barton D. K. and Leonov S. A. 2001. Radar Technology Encyclopedia. Artech House Publishers.
2. Venot Y., Younis M., Wiesbeck W. 2000, Compact Forwardlooking SAR using Digital Beam Forming on Receive Only, *Proc. EUSAR2000*, Munich, 795-8.
3. Lukin K.A., Skresanov V.N., et al. 2001. FLAR Design. Technical Report. STCU Project P-050.
4. Lukin K.A., Natarov M.P. and Skresanov V.N. 2003, Synthetic Aperture Antenna for Near Field Applications, *Proc. Intl. Conf. Antenna Theory & Techniques*, Kharkiv.

SYNTHETIC APERTURE ANTENNA FOR NEAR FIELD APPLICATIONS

Konstantin A. Lukin, Mikhail P. Natarov, and Valery N. Skresanov

Institute of Radiophysics and Electronics NAS of Ukraine
12 Acad. Proskura St., Kharkov, 61085, UKRAINE
<lukin@ire.kharkov.ua> or <valery@ire.kharkov.ua>

Abstract

Preliminary results of implementation of a new approach to design of scanning antennas are presented. Combining mechanical movement of a simple radiator along a real aperture of a stationary antenna with the concept of the antenna aperture synthesizing is the main idea of that approach. Helical-Slot Synthetic Aperture Antenna has been suggested, designed and tested in Ka-band. The tests shown a good agreement with theoretical evaluations, as well as a high efficiency of the suggested antenna in transmit/receive operating mode. A high azimuth resolution is provided by the antenna in the near-field zone for relatively small real antenna apertures.

Keywords: scanning antenna, near-field and far-field zones, antenna pattern, Helical-Slot Synthetic Aperture Antenna, azimuth resolution, remote sensing

1. INTRODUCTION

Scanning antennas are used for radar design when both resolution in range and azimuth are required, e.g. various surveillance radars. Nowadays, designs of fast scanning antennas having a large number of beam positions is a big challenge, specifically design of transmit/receive antennas of that type. A promising approach has been recently suggested in [1]. Combining mechanical movement of a simple radiator along a real aperture of a stationary antenna with the concept of antenna aperture synthesizing is the main idea of that approach. Actually, in that approach, observation of a territory via real beam scanning in azimuth and range scanning due to pulsed waveform is substituted with mapping of the same area using synthetic aperture radar concept. It turned out that this approach enables a designer to implement antenna having capability of virtual azimuth beam scanning with the number of beam positions not available for standard methods. Similar approach, but with electronic switching of the receiving elements has been investigated in [2]. It is worth to note, that capability of scanning in near field (for the whole real aperture) range is another essential advantage of such scanning antennas.

In the paper we describe one of the methods for implementing of the above approach and present the preliminary results of design and development of helical-slot synthetic aperture antenna in Ka-band. In the antenna design, electromechanical movement of the transmit/receive resonant slot antenna is provided along the real aperture of a stationary antenna. For that, we used well known idea of fast motion of a cross-point of a helix and linear waveguide [3], but in a different and

new implementation. The antenna suggested is to be used in combination with a coherent radar capable of preserving the phase ratios between transmitted and received signals during the mapping period of an area. The latter is required for application of the synthetic aperture radar concept [4] to provide scanning of the virtual antenna beam over the mapped area. High azimuth resolution is equivalent to a large number of antenna beam positions for real scanning antenna.

2. HELICAL-SLOT SYNTHETIC APERTURE ANTENNA

The Helical-Slot Synthetic Aperture Antenna (HSSAA) suggested is made of two metal hollow cylinders, one of which is coaxially inserted into another with the minimal backlash between their surfaces. The appearance of the suggested antenna and some details of its design are shown in Fig. 1, while Fig. 2 shows (schematically) the fragment of its cross section (flattened version).

The inner cylinder is mounted with a possibility of its rotation around the cylinders axis OX . It is referred to as the HSSAA rotor. The outer cylinder, referred to as the HSSAA stator, contains a longitudinal slot supplied with 2D-horn, i.e. plane-parallel waveguide with smoothly increasing cross-section. A helically formed rectangular waveguide (HFRW) is incorporated into the rotor body, Fig.1b. In the HFRW narrow wall, the rectangular resonant slots are cut with the required period, δz and parallel to the OX axis. Hence, when rotating the rotor, the HFRW slots will be serially overlapping with the slot of the 2D-horn. The overlapping of the slots will occur at the equally spaced positions along the OX axis, at the

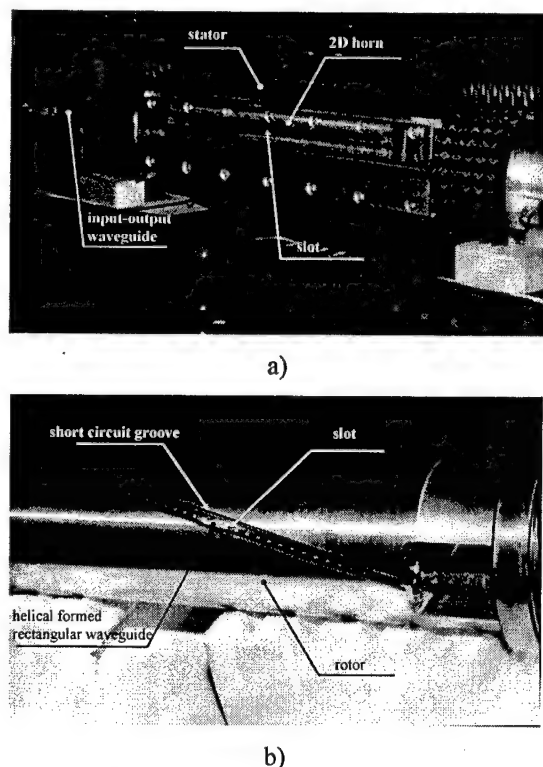


Fig. 1. Helical-Slot Synthetic Aperture Antenna:
a) General view and antenna stator;
b) Antenna rotor with array of resonant slots in the helically formed rectangular waveguide

consecutive moments of time t_n . The period of the HFRW slots spacing is taken in the way that the excitation of the 2D-horn is possible through one and only one slot in a time. The transceiver of the synthetic aperture radar is to be connected to the HFRW via waveguide rotary join.

The resonant slots in the HFRW narrow wall may excite a parasitic propagating wave inside the backlash between the rotor and stator of the antenna, which, in fact, is a slightly curved plane-parallel waveguide. In order to prevent excitation of that wave short circuit grooves (chokes) are to be made in the rotor body along both sides of the HFRW.

Maximal power, radiated by a resonant slot in a rectangular waveguide, is no more than 50 % of the power of the propagating waveguide wave. That radiation can be increased up to 100 %, when a reflecting load will be placed at the certain distance from the slot [5]. In order to enhance the HSSAA radiating efficiency we have used the idea of reflecting load that increases radiation efficiency of each slot exciting the 2D-horn at any given moment.

We have used the following design: when the n^{th} HFRW slot excites the 2D-horn, the next HFRW slot is shielded by the HSSAA stator inner surface and, hence, does not radiate. If exactly in that place of the HSSAA stator body to place a resonator it will interact with the $(n+1)^{\text{th}}$ slot of the HFRW ensuring the required reflection rate inside the HFRW. As the slots

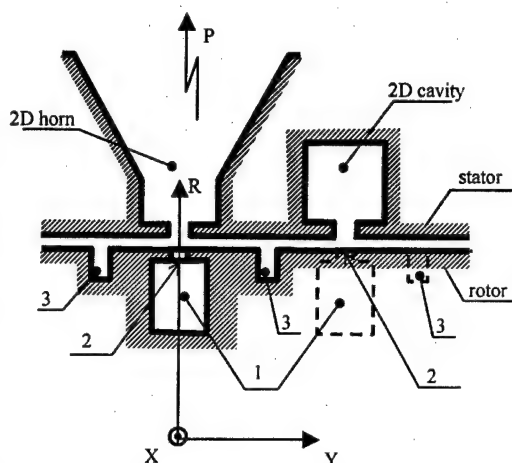


Fig. 2. Cross-Section (flatted version) of the Helical-Slot Scanning Antenna. Waveguide slot radiator arrangement: 1 – HFRW, 2 – resonant slots, 3 – resonant chokes

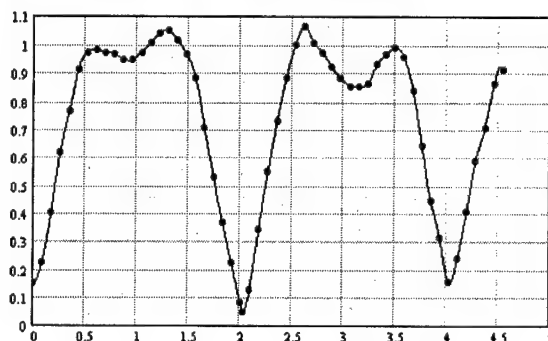


Fig. 3. Dependence of HSSAA radiation power as function of the HSSAA rotor turn angle

are located periodically, the increase in the radiation efficiency is achievable for any slot. The reflecting resonator represents a groove of a rectangular cross section in the HSSAA stator body (see 2D-cavity in Fig. 2). The radiation efficiency of the HSSAA achieved experimentally was 96 % at the error of measurements $\pm 4\%$.

Excitation of the 2D-horn will take place not only at the moments of symmetrical overlapping of the HFRW resonant slots and the slot of the 2D-horn, but also within some range of mutual displacements of the rotor and stator slots. Indeed, Fig. 3 shows the dependence of the power, radiated by HSSAA under investigation as a function of the HSSAA rotor turn angle. The angular size of both slots equals to 0.9° , while their mutual angular displacement is 2.1° when scanning the antenna via rotor spinning. The case of consecutive passages by two slots is illustrated. It is clearly seen the shielding effect by the HSSAA stator. In the antenna suggested, the radiation of probing pulses and reception of radar returns occur for different positions of resonant slots equally spaced by spatial period Δx at the consecutive moments of time $t_n = (n + N)\Delta y / (R\Omega)$, where Ω is the angular fre-

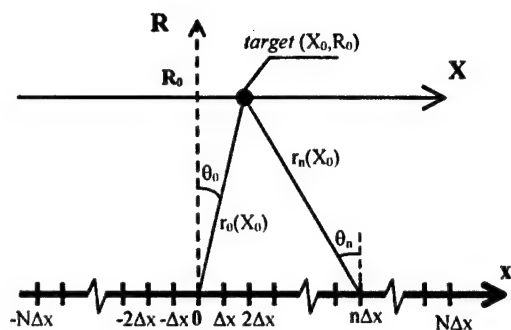


Fig. 4. Geometry for calculation of the synthetic aperture antenna pattern in the near-field zone

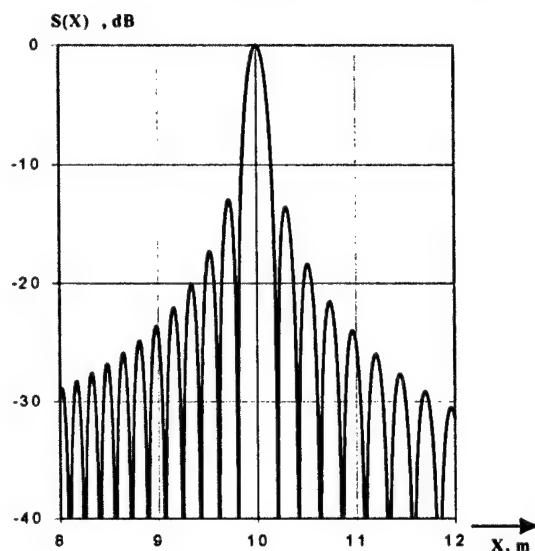


Fig. 5. Synthetic aperture antenna pattern for HSSAA in its near-field zone

quency of the HSSAA rotor spinning; $\Delta y = \Delta x \tan \alpha$ is spacing between resonant slots along OY axis; R is the radius of the rotor; α is the helix angle; $n = -N, \dots, -1, 0, 1, \dots, N$ and $2N + 1$ is the number of the resonant slots. The HSSAA real aperture equals $L = 2N\Delta x$.

Taking into account geometry and notations of Fig. 4, one can calculate [4] the antenna pattern for the HSSAA from the following equation:

$$S_F(X, X_0) = \sum_{n=-N}^N F(X_0, n\Delta x) \cdot s(X, X_0, n\Delta x)$$

where $F(X_0, n\Delta x) = e^{i\frac{4\pi}{\lambda} r_n(X_0)}$; $r_n(X) = \sqrt{R_0^2 + (X - n\Delta x)^2}$; $s(R_0, X, n\Delta x, t) = kA(t - \tau_n) \cdot e^{i\omega_0 t} e^{-i\frac{4\pi}{\lambda} r_n(X)}$ are radar returns having a delayed amplitude $kA(t - \tau_n)$; $\tau_n = 2r_n(X)/c$; $\omega_0 = 2\pi c/\lambda$; λ is the wavelength of the probing signal; c is velocity of light. The rest of the notations are to be seen in Fig. 4.

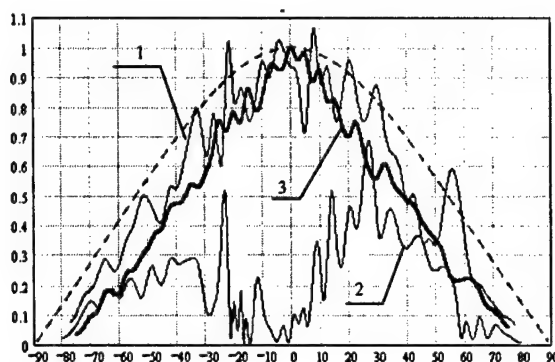


Fig. 6. HSSAA antenna patterns in a H-plane: 1 – measured resulting HSSAA antenna pattern; 2 – radiation from chokes only; 3 – no chokes, resonant slot only; dashed line – theory

The above equations are valid not only for the HSSAA far-field zone, but also for its near-field zone. Evaluation of the HSSAA pattern using these equations has shown its capability of a high azimuth resolution in the near-field zone. Fig. 5 shows the HSSAA pattern for the following set of parameters:

$$\lambda = 0.01 \text{ m}; L = 0.7 \text{ m}; R_0 = X_0 = 10 \text{ m}; N = 100.$$

It is seen, that with these parameters we may achieve -3 dB azimuth resolution of $\Delta X = 0.10 \text{ m}$ in the near-field zone.

In this way, the design suggested enables implementing of HSSAA with the real aperture L for stationary (non-moving) installation of the equipment, provided synchronization of the pulse repetition period of the probing signal with that of resonant slot flashing in the longitudinal slot of the stator: $\Delta t = \Delta y / (R\Omega)$, when scanning the antenna via spinning of its rotor.

3. PRELIMINARY RESULTS OF THE HELICAL-SLOT SYNTHETIC APERTURE ANTENNA TESTS

Using results of theoretical and experimental modeling of the suggested antenna elements [5, 6] the experimental model of the HSSAA was designed and tested. We have studied linear azimuth resolution of the HSSAA at distances from ten to hundred meters within azimuth scanning sector of 120 degrees by a method of antenna aperture synthesizing. The measurements were carried out at the radar working frequency $f = 30.1 \text{ GHz}$. In the whole, the test has confirmed the azimuth resolution expected from theoretical evaluations. However, more careful studying of the antenna pattern fine structure has revealed a significant departure of the antenna pattern from its theoretical expectation. It is seen rather strong roughness of the antenna pattern. Let's discuss the most probable reason for that distortion. The antenna pattern in elevation plane (E-plane) is formed by the 2D-horn and agrees with theory within the limits of measurements

errors. In azimuth plane (H-plane), the 2D-horn does not strongly affect the antenna pattern and it approximately corresponds to the antenna pattern of a resonant slot in a screen. In Fig.6 theoretical antenna pattern is shown with dashed line. The measured HSSAA antenna pattern in azimuth plane is presented in Fig. 6 by curve 1. It is seen a rather strong roughness of the HSSAA antenna pattern. The additional studying has shown, that along with the radiation from the resonant slot there is additional parasitic radiation from chokes (see curve 2 in the Fig. 6). If to leave the resonant slot open and to put an absorber into the choke grooves the roughness decreases significantly, as it is seen from the curve 3 in Fig. 6.

The most probable reason for that is the wave excited in the space between the antenna rotor and stator surfaces which propagates along HFRW and causes the partial radiation when it crosses the interaction area of the 2D-horn. The interference of that parasitic radiation with the main interference from the resonant slot causes the roughness of the antenna pattern. Preventing excitation of that parasitic wave via properly choosing of working frequency one may improve significantly the HSSAA pattern smoothness.

4. CONCLUSIONS

We have presented preliminary results of implementation of a new approach to virtual scanning antennas design. The main idea of that approach consists in combining of mechanical movement of a simple transmit/receive antenna along aperture of a stationary antenna and the concept of the antenna aperture synthesizing. The Helical-Slot Synthetic Aperture Antenna has been suggested, designed and tested in Ka-band. The tests have shown a good agreement with theoretical evaluations, as well as a high efficiency of the suggested antenna in transmit/receive operating mode. A high azimuth resolution is provided by the antenna in its near-field zone for relatively small real antenna apertures. In order to realize virtual beam scanning in real time scale using the antenna suggested one has to use rather fast SAR-imaging algorithms and DSPs. However there are many applications where a real time scale is not required. For instance, the HSSAA is very suitable for development of remote sensing systems for monitoring of

structural and other changes in natural and manmade objects [7, 8], such as large buildings, bridges, dams, etc., as well as monitoring of objects with intensive movement of vehicles, such as airport, seaports, crossroads of highways, etc. Usage of radar systems instead of or in addition to optical ones is forced by the requirement of day & night data acquisition under difficult weather conditions.

ACKNOWLEDGMENTS

This work has been supported in part by Intermap Technologies GmbH (Former AeroSensing Radar Systeme GmbH) – STCU Project P-050.

REFERENCES

1. Lukin K. A. A Novel Approach to Scanning Antenna Design. *Proc. Int. Conf. Antenna Theory & Techniques*, Kharkiv.
2. Venot Y., Younis M., Wiesbeck W. 2000, Compact Forward Looking SAR using Digital Beam Forming on Receive Only, *Proc. EUSAR2000*, Munich, 795-8.
3. Barton D. K. and Leonov S. A. 2001, Radar Technology Encyclopedia. Artech House Publishers.
4. Cutrona L. J. 1970, 'Synthetic aperture radars, chapter 8' In.: Radar Handbook. McGRAW-HILL Book Company. Ed. M. I. Skolnik
5. Lukin K. A., et al. 2001. FLAR Design. Technical Report. STCU Project P-050.
6. Natarov M. P., Glamazdin V. V., Sresanov V. N., Tkachenko V. I., 2001, 'A waveguide longitudinal narrow wall slot radiating between baffles. Matching analysis', *Proc. 4th Int. Kharkov Symp. Phys. and Eng. of mm and submm Waves*, Vol.2, Kharkov, 607-609.
7. Tarchi D., Leva D., Lukin K. A., Mogyla A. A., Nesti G., Sieber A. J., 2000, 'Short range imaging applications using noise radar technology', *Proc. EUSAR'2000, 3rd European Conf. on Synthetic Aperture Radar*, Munich, Germany, pp. 361-364.
8. Tarchi D., Leva D., Lukin K. A., Mogyla A. A., Sieber A. J. 2002, 'SAR imaging using CW and pulsed noise radar', *Proc. The First Int. Workshop on the Noise Radar Technology*, Yalta, Crimea, Ukraine, pp. 97-104.

LASER SEISMO-ACOUSTIC ANTENNA ARRAY

Mstislav N. Dubrov and Rostislav F. Matveev

Institute of Radio-engineering and Electronics, Russian Academy of Sciences
Fryazino, Moscow Region, Russia
<mnd139@ire216.msk.su>

Abstract

The determination problem of wide band wave field parameters in continuous mechanical media is considered. The problem is solved by means of the accurate measurements of displacements and strain of the certain number of medium elements together with subsequent numeric development and data processing.

Keywords: laser interferometer, seismic array, acoustic wave, earth strain

The oscillations which are excited by the source of any physical nature in the continuous mechanical medium can be presented as some superposition of relative spatial displacements of medium particles. These displacements cause the variations of pressure or tension in the medium depending on their mechanical properties.

The simple problem of the acoustic wave tests in the liquid or gas medium is usually solved by measurements of the temporal pressure variations $dp(t)$ at some point \mathbf{x} within this medium. In the three-dimensional case, the space-time distribution of the scalar pressure field is the function of four variables:

$$p = p(x_k, t), \quad k = 1, 2, 3;$$

where t is time.

The equation of such a medium motion is expressed as follows:

$$i\omega\rho\mathbf{v} = \text{grad } p, \quad (1)$$

where: \mathbf{v} is the velocity vector of the particle spatial displacements $\xi_k (v_k = \partial\xi_k / \partial t, k = 1, 2, 3)$; p is the scalar pressure; ω is the frequency of the complex amplitudes of wave field, $i = \sqrt{-1}$.

One pressure sensor can measure the intensity of the wave oscillations. For determination of the spatial wave field parameters (the direction to a source of oscillations and its localization), the acoustic array of N sensors has to be used [1]:

$$p_n = p_n(t), \quad n = 2, 3, \dots, N$$

Another situation occurs when the wave field distribution is probed in the elastic continuous medium. The basic equation of motion in such a medium is expressed as [2]:

$$\rho \partial^2 \xi_k / \partial t^2 = \kappa \partial^2 \xi_m / \partial x_k \partial x_m + q \partial^2 \xi_m / \partial x_1^2 \quad (2)$$

The left part of this equation includes the temporal derivations of particle displacement vector ξ_k :

$$\xi_k = \xi_k(\mathbf{x}, t), \quad k, m = 1, 2, 3,$$

whereas the right one represents the combinations of the spatial displacement derivations in some given plain $x_1 = 0$; κ and q are the combinations of Lamé's constants, which determine the elastic medium properties. This kind of media motions usually are detected by three-component accelerometers, which measure every component of the acceleration vector $\partial^2 \xi_k / dt^2$.

A three-component accelerometer alone, in addition to the wave intensity, is able to determine the direction to the oscillations source. The source localization is defined when using the velocities difference of refining longitudinal and transversal components of the elastic waves (the so called primary and secondary seismic waves). One can see that the amount of information has been increased here in comparison with the above acoustic methods (1) of the wave field parameters determination.

We resort to the next approach of the elastic wave detection improvement in continuous media. It is based on application of the precise laser interferometers for measurements of the medium strains in the wave field distribution to be studied. This technique deals with the values in the right part of equation (2), which actually relate to the strain tensor P_{km} of the tested medium. This tensor has 9 components, and 6 of them are pair-wise ones equal to [2]:

$$P_{km} = P_{mk}, \quad k, m = 1, 2, 3$$

In such a way we can significantly increase the amount both of calculating parameters and equations for their determination. In addition, we suggest to apply the multi-component laser strainmeter system [3] to realize the advantages of this method.

The technique consists in measuring the small increments of strain sensor base-lengths L_k :

$$dL_k = \xi_k(\mathbf{x}_a) - \xi_k(\mathbf{x}_b), \quad k = 1, 2, 3,$$

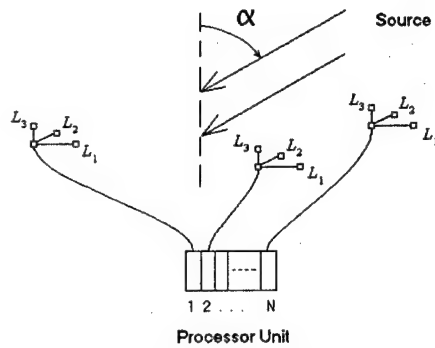


Fig. 1. Seismo-acoustic antenna-array

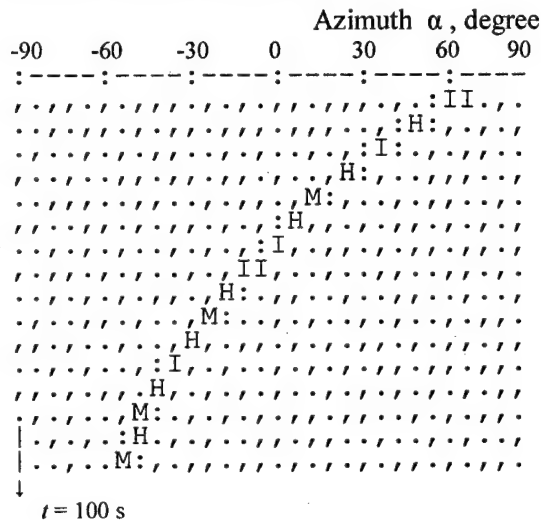


Fig. 2. The result of antenna data processing

\mathbf{x}_a and \mathbf{x}_b are the vector points of the laser interferometer arms.

In this procedure, the spatial derivative is recorded:

$$\partial \xi_k / \partial x_k = dL_k / L_k,$$

if $L_k = |\mathbf{x}_a - \mathbf{x}_b| \rightarrow 0$. As we have earlier shown [4], this condition is satisfied when the strainmeter base-length is much less than the wave-length Λ of seismic disturbance $L_k \ll \Lambda$. For arbitrary relation between Λ and L_k , the azimuth diagram of strain sensor have been found [4].

Having the number of strainmeter components, one can determine both the intensity of wave oscillations and field spatial characteristics: the direction to the signal source, its localization, and motion.

In Fig. 1 the diagram of the proposed antenna set is shown.

It consists of N spatially distributed strain sensors. Each of them is the multi-component laser interferometer with the horizontal and vertical measuring arms [5]. Every laser sensor measures the strain components of the seismo-acoustic field. In this way we obtain the $k \times N$ strain amplitudes:

$$dL_{kn}, \quad k = 1, 2, 3, \quad n = 2, \dots, N$$

Our technique implies also the capability of phase-difference measurements:

$$d\Phi_{kn}, \quad k = 1, 2, 3, \quad n = 2, \dots, N - 1$$

The calculation method [3] is used to obtain the wave amplitudes and the azimuth angle which determines the direction to the source. If the processor unit (Fig. 1) operates permanently, the dynamic azimuth diagram (Fig. 2) can be displayed in real time.

We have applied seismo-acoustic antennas to detect both the acoustic and seismic sources of signals.

Our recent experiments are directed to the precise recording of the seismic waves with spatially distributed laser interferometers. We apply remote instruments with base-length $L_k = 1 \dots 300$ m [6] which are placed apart at a distance of up to 140 km with respect to each other for investigations of unusual wave propagation appearances.

ACKNOWLEDGEMENTS

This work is supported by the Russian Foundation of Basic Research, Project N02-05-64720.

REFERENCES

1. Telyatnikov V. I., Zarubezhnaya radio-elektronika, 1978, No 4, pp. 66–86. (in Rus.)
2. Jeffreys H., The Earth: Its Origin, History, and Physical Constitution, Cambridge Univ. Press, 1959.
3. Dubrov M. N. and Matveev R. F., Journal of Communications Technology and Electronics, 1998, v.43, No 9, pp. 1068–1073.
4. Dubrov M. N. and Matveev R. F., The Problems of Theory of Long Laser Strainmeters for Seismic Investigations, Preprint IRE RAS, Moscow, 1994.
5. Dubrov M. N. and Alyoshin V. A., Journal of Radio Electronics, www journal, 2000, N 10, <http://jre.cplire.ru/jre/oct00/4/text.html>
6. Dubrov M. N., Matveev R. F., and Medvedev V. P., Issledovano v Rossii, 2002 (187) 2077–2085 (in Rus.) <http://zhurnal.apelarn.ru/articles/2002/187.pdf>

PHASED ARRAY ANTENNA ON A RADIAL WAVEGUIDE

Voronin E. N., Emel'chenkov F. I., Kotov Yu. V., Luk'yanov A. S.

Moscow Aviation Institute (the State Technical University)
<voskr@mai.ru>

Abstract

Numerical and research results of investigation and optimization of the distributive system of the monopulse Phased Array Antenna (PAA) with circular aperture based on the radial waveguide are presented. The research was carried out with decomposition technique using a one term approximation of the induced EMF.

Keywords: monopulse PAA, radial waveguide, collector array, coaxial probes, amply-phase distribution (APD), aperture efficiency factor (AEF), side-lobe level (SLL), parameter synthesis, iterative algorithm.

1. INTRODUCTION. THE PRESENT STATE AND FUTURE OF THE AIR-BORNE PAAS FOR RADAR SYSTEMS

There is a big interest as for the modern aircraft in the flat mono-pulse PAA designs with circular aperture, minimal longitudinal sizes, integrated construction (including radiating elements, phase shifters, sum-difference and distributive microwave subsystems) and high techno-economical performance. For the urgent air-borne radar frequency-band around ~10 GHz, the above-mentioned requirements are satisfied to a fullest measure by mono-pulse PAAs on the basis of radial distributive waveguides.

The basic advantages of the radial lines are the radio mode of excitation and their plane geometry. The urgent problem for the air-borne radars is also size-incorporation of the antenna into the aircraft cross-section. The radial wavelines correspond in most ways to these geometry requirements with the connection links under the given law in radial dimension, which in electrodynamic sense means a parallel (ether, space) feed of PAA elements. Such a design concept is very technologic and also compact. Another its advantage is a small longitudinal size. Its drawback is the constructive complexity of the directive energy coupling. Nevertheless, even when nondirective coupling is realized, the energetically effective microwave circuits of power distribution for multi-element PAAs with the circular aperture is possible, using the rigorous account of electrodynamic properties of distributive microwave subsystems on the radial waveguide basis. The strict electrodynamics approach allows evaluating such PAAs with their interference taken into account. The effective development in this direction is the experimental model of PAA, which was widely investigated in practice, having increased electrical durability in the transmitting mode due to a non-conventional feed of

the radial waveguide from its circular perimeter by converging radial waves. The quite large number of PAA's elements ($N \approx 10^3 \dots 10^4$), the quasi-regular (close to a hexagonal one) and dense ($d \sim 0,7\lambda$) character of their distribution in the PAA aperture do result in an appreciable interference. The latter is the basic reason for practically insuperable difficulties of direct experimental operational development of such PAAs up to the given performance. In particular, there are some developments of Russian "Phazotron" organiza-

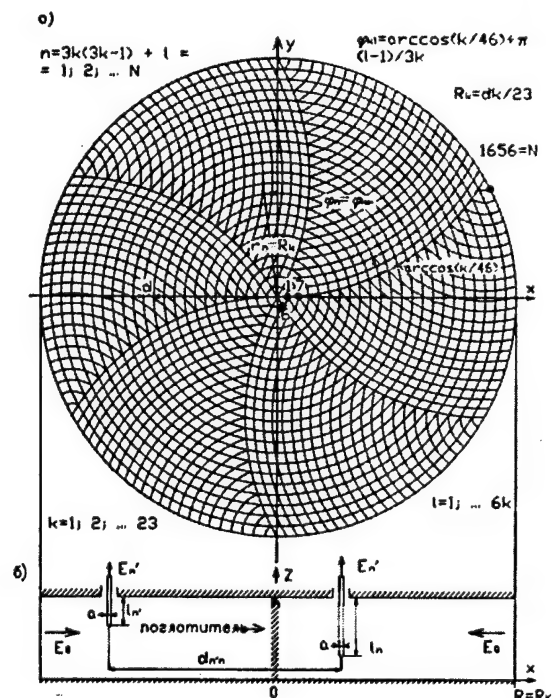


Fig. 1. Phased array geometry: *a* – the aperture elements distribution; *b* – the collector array based on a radial waveguide.

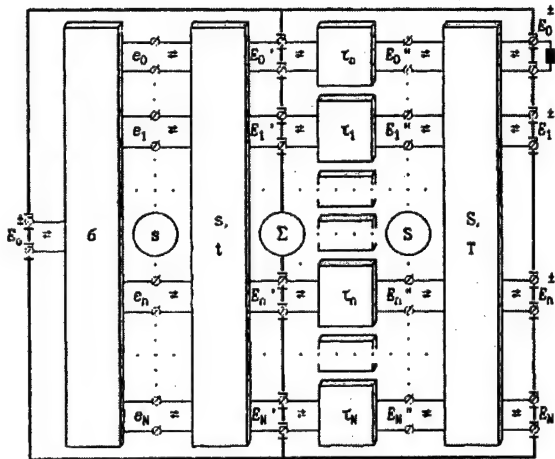


Fig. 2. Block-scheme

tion, such as "Zhuk-radar-MSFE". Here, the key ways of theoretical overcoming of the above difficulties are presented, using strict and approximation approaches to PAA elements interference effects both in its internal and external paths. At the same time, by virtue of the specified reasons, the electrodynamic solution of the formulated problem is a very difficult one.

2. THE DECOMPOSITION OF THE PROBLEM

Using the decomposition technique of the task, there was developed a complete real scattering matrix of the given PAA sum-channel as regards all the features of its microwave circuit (Fig. 2).

$$\Sigma = \begin{bmatrix} \Gamma & < T_n \\ T_n > & \Sigma' \end{bmatrix}. \quad (1)$$

Here

$$\Gamma = s_0 + < s_n \cdot (E - \tau S \tau \cdot s')^{-1} \cdot \tau S \tau \cdot s_n > \quad (2)$$

is the reflection factor of the monopulse PAA's sum channel;

$$< T_n = < s_n \cdot (E - \tau S \tau s')^{-1} \cdot \tau \cdot (E - S S^*)^{0.5} \quad (3)$$

is the transfer factor a E_0 field of the PAA's sum channel in its aperture;

$$\Sigma' = -S^* + \tau(E - S S^*)^{0.5} \times \\ \times (E - s' \tau S \tau)^{-1} \cdot s_0 \cdot (E - S S^*)^{0.5} \tau \quad (4)$$

is the scattering matrix of PAA's elements in its aperture.

The problem decomposition of the given PAA allows making the following conclusions: the circuit essentially is not matched to a common input and has non-zero reflection factor (2); it is theoretically possible to realize the given APD $< \alpha_n$ in the form of factors, proportional to it of transfer coefficients (3), controlled by the expedient choice, of probe lengths; the influence of the "well designed" (conditionally matched) PAA elements on the circuit operation is minimal and has an effect only for separate elements patterns.

3. THE REDUCTION PROBLEM

The feed system of the given PAA includes a collector array in the radial waveguide form, which is excited at its sum channel by the converging (from its perimeter) cylindrical TEM, given by the Hankel function of the first kind

$$E_z(r) = \frac{E_0 \cdot H_0^{(1)}(k_0 r)}{H_0^{(1)}(k_0 R)}. \quad (5)$$

The initial field (5) excites the $N + 1$ collector probes array with cylindrical coordinates r_n, φ_n electric forces, which are transferred through a cascade of three multipole circuits with transfer matrixes t, τ and T of the $N + 1$ rank in the following output fields:

$$< E_n = E_0 < e_n \cdot T. \quad (6)$$

Here

$$T \approx t \cdot \tau \cdot T \quad (7)$$

is the "through" square transfer matrix of the $N + 1$ rank for the field (5) in the PAA aperture.

As a matter of fact the T -matrix in (7) is a quasi-diagonal one, i.e. the PAA's edge effects can be neglected and its product with the complex vector of normalized element patterns may quite lawfully be approximated as follows:

$$T f(\theta, \varphi) > = \hat{f}_{n_{\infty}}(\theta, \varphi) > \approx f_{\infty}(\theta, \varphi) \times \\ \times \exp[-ik_0 r_n \sin \theta \cdot \cos(\varphi - \varphi_n)] > \quad (8)$$

where $f_{\infty}(\theta, \varphi)$ is an element pattern within of an infinite hexagonally regular PAA.

Elements distribution the PAA circular aperture has 60° -periodicity and coaxial-ring character in azimuth and radial dimensions. These attributes of PAA geometrical symmetry are to be used for elements order numeration and for providing a convenient mathematical symmetry to numerical calculation of non-normalized PAA's patterns. The most effective is the polar (radial and circular) numbering, which allows any (from 0 up to $N = 1656$) n -element of the PAA is placed on k -ring ($k = 1; 2; \dots; 23$) and in m -position of an azimuth angle ($m = 1; 2; \dots; 6k$). At those positions $3k(k-1) + m = n \neq 0$, and their polar coordinates are equal to:

$$r_n = R_k = kR/23 = kd \\ \varphi_n = \varphi_{km} = \arccos\left(\frac{k}{46}\right) + \frac{\pi(m-1)}{3k}. \quad (9)$$

The chosen law of radial-circular numeration (9) simplifies the calculation of the transfer matrix in (7), describing phase shifters, which assignment is double: the compensation of cone-shaped phase distribution of complex waves amplitudes, leaving the collector array, E_n^- (Fig. 1) and PAA beam forming in accordance with the given scanning law.

The polar grid of PAA elements distribution (8) in full takes into account its azimuth (coaxial) symmetry in respect to z -axis (Fig. 1). For the case of in-phase PAA scanning in the axial direction $\theta_0 = 0$, there is the identity of $6k$ variables in each k -ring and in all input-output planes of the multipole circuits, and also in block-circular character all the matrix multiples in (7), uniformly ordered in the grid (8), including the transfer matrix of the $N + 1$ rank of the collector array based on coaxial probes in radial waveguide (Fig. 1,a)

$$t = [t_{nn'}] = [t_{3k(k-1)+m, 3k'(k'-1)+m'}] = [t_{n'n}] = [t_{3k'(k'-1)+m', 3k(k-1)+m}], \quad (10)$$

where the indexes $k(k')$ are numbers of horizontal (vertical) matrix blocks, starting from the 0-th (they are just numbers t_{0n} , t_{n0}) and finishing at 23-th (by rectangular matrixes with the $6k \times 6K$ and $6K \times 6k$ sizes), and the indexes $m(m')$ correspond to column (row) element numbers in the matrix blocks with numbers $k(k')$, beginning from 1 and up to $6k(6k')$ and $m(m') = 0$, if $k(k') = 0$.

Relations (6), $E_n \equiv E_{3k(k+1)} = E_k$ and $e_n \equiv e_{3k(k+1)} = e_k$ at $3k(k-1) + 1 \leq n \leq 3k(k+1)$ (i.e. $6k$ variables in each k -ring are equal each other in all input-output multipole planes) are carried out simultaneously, if their following matrix consequence of much lower order ($K + 1 \ll N + 1$): takes place

$$\langle E_k = E_0 \langle e_k \cdot \Xi \rangle. \quad (11)$$

Here

$$\Xi = G \cdot T \cdot g = [\zeta_{k'k}] \quad (12)$$

is the square matrix of the $K + 1$ rank, formed from the square t -matrix of the $N + 1$ rank by rectangular matrixes of under-pressure g and duplication G [with the according sizes $(N + 1) \times (K + 1)$ and $(K + 1) \times (N + 1)$]. The first one is $g = [\delta_{n, 3k(k+1)}]$ ($\delta_{n,n'}$ is the Kroneker symbol), which is everywhere with exceptions of "rare units", placed on crossings of $3k(k + 1)$ -th lines and k -th columns of the matrix. The second matrix is

$$G = [\delta_{n-3k(k-1), k} + \delta_{n-3k(k-1), k+K} + \delta_{n-3k(k-1), k+2K} + \delta_{n-3k(k-1), k+3K} + \delta_{n-3k(k-1), k+4K} + \delta_{n-3k(k-1), k+5K}],$$

i.e. It has $6k$ of units in every k -th line in columns with numbers $3k(k-1) + 1 \leq n \leq 3k(k+1)$.

Due to inter-block circularity of the (10) matrix, any column (row) in blocks is acquired by the cyclic shift of the neighbor one. The formal calculation of the reduced matrix elements (12) is reduced to the following sum:

$$\zeta_{k'k} = \sum_{m'=1}^{6k'} T_{3k(k-1)+1, 3k'(k'-1)+m'}, \quad (13)$$

where the factors are $T_{n'n} = t_{n'n}$.

At last, the $(K + 1)$ -dimensional non normalized radial APD (11) considerably reduces calculations resources thanks to essentially smaller dimension [in $(N + 1)/(K + 1) = 1657/24 = 69.041666$ times at presence of the central element and in $N/K = 1656/23 = 72$ times at its absence] in comparison with APD (6). It allows to determine and to estimate in a very fast way a number of important PAA's characteristics. For example, the vector and non-normalized pattern of the in-phase PAA with partial element patterns (8) is expressed by the following way:

$$\begin{aligned} E(\theta, \varphi) &= E_0 \langle E_k | \cdot G \cdot \hat{f}_{n_x}(\theta, \varphi) \rangle = \\ &= E_0 f_{\infty}(\theta, \varphi) \cdot \langle E_k | \cdot f_k(\theta, \varphi) \rangle = \\ &= E_0 f_{\infty}(\theta, \varphi) \cdot \left[1 + \sum_{k=1}^K |E_k| \cdot f_k(\theta, \varphi) \right] \end{aligned} \quad (14)$$

Here

$$\begin{aligned} f_k(\theta, \varphi) &= \\ &= \sum_{m=1}^{6k} \exp[-ik_0 R_k \sin \theta \cdot \cos(\varphi - \varphi_{km})] \approx \\ &\approx 6k J_0(k_0 R_k \sin \theta) \end{aligned} \quad (15)$$

is the non-normalized multiplier of PAA's k -ring, which is approximated as the pattern of a continuous ring radiator with in radius equal to R_k : $R_k J_0(k_0 R_k \sin \theta)$, where $J_0(\dots)$ is Bessel function of the zero order.

4. CALCULATIONS OF PAA'S EXTERNAL CHARACTERISTICS

There were considered various APDs of PAA and was chosen as an optimal one the Taylor distribution. For the AEF estimation there was adapted the general relation for any coaxial-ring PAA with the radial APD (11)

$$\begin{aligned} \text{AEF} &= \\ &= \frac{\left| E_0 + 6 \sum_{k=1}^K k \cdot E_k \right|^2}{3K(K+1) \left[|E_0|^2 + 6 \cdot \sum_{k=1}^K k \cdot |E_k|^2 \right]} \leq 1. \end{aligned} \quad (16)$$

In the sense of the compromise between AEF and SLLs, the most delicate one is the Taylor distribution:

$$\alpha_k = \Delta + (1 - \Delta) \cdot [1 - (k/K)^2]^3, \quad (17)$$

where $0 \leq \Delta \leq 1$ is the so-called "distribution pedestal". For the case of the PAA with the central element the relations of PAA's SLL and AEF (16) with

pedestal levels are presented in figures 3 and 4, correspondingly, where $d/\lambda = 0,6410256$ and $K = 23$. It can be seen that the most compromise combination of the basic PAA parameters (AEF = 87,5 %, SLL = 28.51 dB and pattern width = 2.2) is achieved at $\Delta_{opt} = 0,333...$

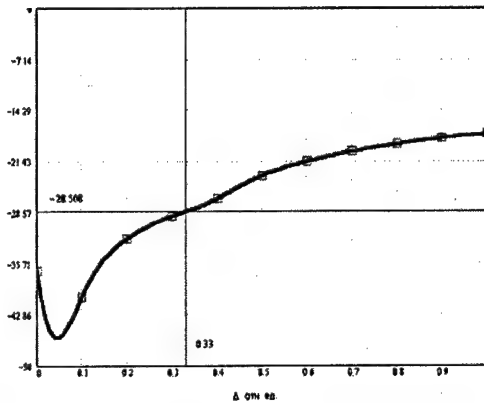


Fig. 3. The SLL relation with t various pedestals of the Taylor distribution

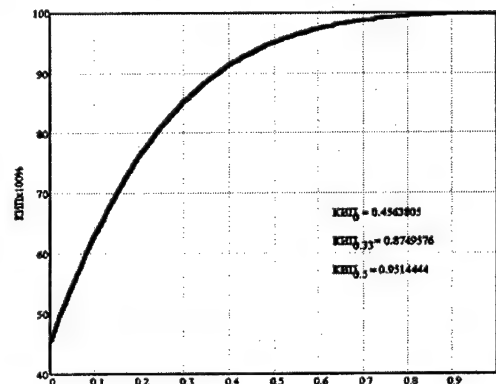


Fig. 4. The PAA's AEF relation with Taylor distribution pedestals

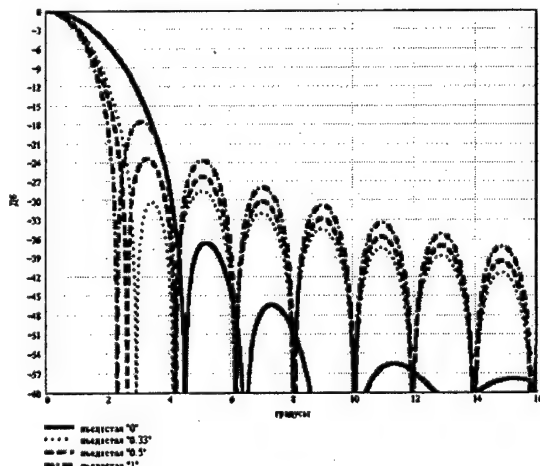


Fig. 5. The PAA patterns with the Taylor APD

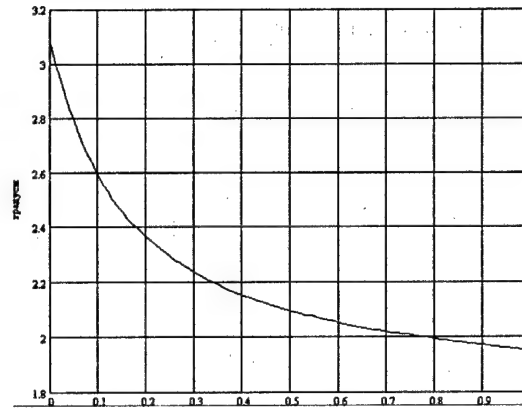


Fig. 6. Relation of PAA's patterns widths with pedestal levels

REFERENCES

1. Takada J., Takahashi M., Ando A., Ito K., Goto N. The optimum aperture illumination design in single-layered radial line slot antennas // Proc. IEICE Fall Conf. B-73. 1992/ Sept., pp. 2...73.
2. Williamson A. G. // Radial-line/coaxial-line junctions: analysis and equivalent, circuits, Int. J. Electron., 1985, Vol. 58, No 1, pp. 91...104.
3. Sazonov D. M., Gridin A. N., Mishustin B. A., Microwave Devices / Under red. D. M. Sazonov.- M.: higher school, 1981.- 295 with.
4. Amitey N., Galindo V., Wu C. Item. The theory and analysis phased antenna array/trans. with Engl. Under red. A. F. Chaplin- M.: Mir, 1974.- 455 p.
5. Markov G. T., Chaplin A. F. Excitation of electromagnetic waves.- M.: Energy, 1967.- 376 p.
6. Markov G. T., Sazonov D. M., Antennas.- M.: Energy, 1975.- 528 p.
7. Antennas and microwave devices. Designing phased array antennas: The manual for high schools / V. S. Filippov, L. I. Ponomarev, A. Y. Grinev etc.; Under red. D. I. Voskresensky.- M.: Radio and Communication, 1994.- 592 p.
8. Collin R. E. Field Theory of Guided Waves. 2nd ed., Piscataway, NJ, IEEE Press, 1991, p. 313.

AN ANTENNA SYSTEM OF A CONTINUOUS WAVE RADAR

S. D. Andrenko, I. A. Vyazmitinov, and Y. B. Sidorenko

Department of Radio Physic Introspect, Usikov Institute for Radio Physics and Electronics
Kharkov, Ukraine
<ire@ire.kharkov.ua>

Abstract

The given work describes an antenna system of a continuous wave decimeter radar. The transmitting and receiving antennae are cylindrical spirals with the oppositely directed windings, where the distance between the axes is comparable with the wavelength. The main antenna parameters have been experimentally determined. It is shown that the reception-transmission channel isolation coefficient is 75–80 dB in the frequency band ranging $\pm 18\%$ relative to the central value.

Keywords: spiral antenna, beam width, oppositely sensed circularly, polarized antenna, isolation

1. INTRODUCTION

It is common knowledge [1] that the continuous wave radars have a number of advantages as compared to pulse radars. Thus, if operating at small (meters – tens of meters) distances, it becomes extremely difficult to realize the pulse-operating mode, especially at low frequencies (tens of megahertz – units of megahertz). Hence, in such conditions, the continuous wave radar operating mode becomes the only possible one. At the same time, alongside with all its merits, the continuous wave radars are far from being devoid of essential drawbacks, whose removal requires tackling the complex scientific-and-engineering problems. One of such problems consists in a "leakage" of transmitter's power onto receiver's input directly through the antenna system, which constrains fundamentally the possibilities of the radar potential increase. "As a matter of fact, the whole history of continuous wave radar development is connected with persistent efforts to develop unconventional methods which provide necessary receiver's sensibility as a compensation for the effect of a direct "leakage" of power from transmitter" [1]. The above said is still urgent today. It is worth noting that alongside with the development of the methods of compensation for the transmitter's power "leakage" onto receiver's input, it is a search for the ways to decrease the level of this power using the optimal design of a radar receiving-transmitting antenna system is not less important, in other words, a search for the ways of solving the problem of electromagnetic compatibility of a high-sensitive receiver with an inherent radar transmitter by using electromagnetic methods under the conditions of their operation at one and the same carrier frequency and practically in one and the same frequency band with the observance of the requirements to minimize antenna system sizes.

It is well known that this is not an easy task and a lot of theoretical and experimental works [2] are devoted to it.

The present report gives the results of development and study of an antenna system of a continuous wave decimeter radar with circular polarization (polarization plane rotation directions "to transmission" and "to reception" are mutually opposite) that could provide high isolation coefficient (not less than 60 dB) between reception and transmission channels in a 10 % frequency band at minimum weight and overall dimensions.

2. STATEMENT OF THE PROBLEM AND METHODS OF ITS SOLUTION

Let us write the isolation coefficient (dB) between two antennae using the ideal radio transmission formulae:

$$\chi = 22.6 + 6 \cdot n - G_{12} - G_{21} + \mu_{12} + A,$$

where the first term is the isolation of two isotropic radiators, the spacing between which equals one wavelength; G_{12} , G_{21} are the amplification coefficients of antennae in the direction towards each other; μ_{12} is the polarization coefficient; n is the exponent when spacing between antennae is written as $R_{12} = 2^n$; A is the "effective area" of the isotropic radiator. Despite the fact that this expression is valid only for the far zone and free space, it allows one to assess the qualitative effect of various factors upon the isolation value. Thus, for example, it is seen that a two-fold increase of spacing between the antennae results in increase of isolation by just 6 dB and, consequently, it is not an effective means to suppress a "parasitic" coupling between transmission and reception antennae. Inefficiency of the above method of enhancing the isolation makes itself the more evident,

the lower is the operating frequency and it may often become unacceptable already in the decimeter wavelength range. From the given expression it follows that reducing the polarization coefficient μ_{12} to zero enables one to totally decouple the antennae. However, even for the far zone this opportunity is still hypothetical, since it is practically impossible to control the field polarization structure in the area of sidelobes, especially of the far ones, which are, as a rule, responsible for formation of coupling channels between the transmission and reception antennae of one and the same system. This is the more so in the case, when it is necessary to reduce the distance between antennae as much as possible.

Thus, even in the above-mentioned ideal case, the most effective method of suppression of "parasitic" coupling between the transmission and reception antennae incorporated in continuous wave radar consists in a decrease of their gainable coefficients in the direction towards each other. The latter is equivalent to decreasing the levels of sidelobes, especially of the far ones. In actual practice, when it is not possible to have the antennae spaced apart for a considerably great distance, in the sense stated, this demand means the necessity to terminate all coupling channels between the radar antennae, which are not due to interaction of the sounding radiation with a search target.

As a rule, the known methods of termination or, at least, decrease of efficiency of the "parasitic" channels of coupling between the transmission and reception antennae [2] are cumbersome enough and, what appears to be much worse, they operate in a relatively narrow frequency band. At the same time, sometimes it is easier to eliminate the reason than to fight with consequences. As can be easily noticed, the main reason of appearance of these channels under the mentioned conditions is a mismatch of antennae with feeder lines and free space. This is just the fact that has determined the choice of the method of solving the stated problem and directions of the research. The results of the above method are presented in the given report.

A laboratory scale model of the antenna system represented two cylindrical regular one arm spiral antenna with parallel axes and mutually opposite direction of windings. A fastener assembly allowed the variation of distance between the antennae' axes at their orientation preserved.

The spirals were made of a copper wire 1.6 mm in diameter and were stuck with glue on a polyvinyl acetate base to cylindrical tubular expanded polystyrene frames having the dielectric constant of $\epsilon \approx 1.18$ in such a way that the coil's diameter was $2a = 86$ mm and the increment was 64 mm. So the angle of winding of each spiral was equal to $\alpha \approx \pm 13.5^\circ$. This provided a primary excitement of the fundamental (T_{+1} or T_{-1} depending on the sign of α) wave at the central frequency 940 MHz ($ka \approx 0.85$, $\kappa = 2\pi/\lambda$, λ is the wavelength) and, consequently, the mode of axial radiation at the frequency overlapping coefficient being close to the maximum [3]. Each spiral

consisted of 6 coils and had a square counterbalance (counter reflector) with the side 250 mm. The dielectric cylinders serving as spiral's bases were fastened to the counterbalances through polystyrene inserts ($\epsilon \approx 2.5$) with metal pins 8 mm in diameter. They served as the elements of antennae fastening to a common cross bar, equipped with a shifting device which provided variation of the distance between the antennae axes at their orientation and counterbalance coplanarity preserved.

So much attention is paid to the description of the fastening units because the experiment mainly concerned matching of the antenna with the coaxial feeder path having the wave resistance of 50 Ohm at feeding "from below", i.e. just close to the fastening elements. The slightest mismatch in this field gives rise to parasitic channels of coupling between antennae and, consequently, restricts their isolation value.

In contrast to the matching devices being conventional for this range [4], there has been used a matching transformer in the form of an irregular "strip" line with the purpose to minimize a possible mismatching in the point of coupling of a 50 Ohm coaxial feeder path with the spiral antenna having, as is well known [3], the input resistance of $140 \div 150$ Ohm. One current-carrying line element was represented by the antenna counterbalance, to which a cable loom was attached, and another one was a conductor segment that served as an extension of the first spiral coil. So, the first spiral coil together with the conductor extending from the cutoff point to the spiral represented a resistance transformer with the constantly varying parameters. The angle of winding of this part of the coil was smoothly varying from zero (relative to the counterbalance plane) to the value of α at the origin of the first coil.

The approximate formula [5] is valid for characteristic impedance of this irregular line:

$$Z_0 \approx (138/\sqrt{\epsilon}) \lg(4h/d), \text{ (Ohm)}.$$

Here d is the conductor diameter, h is the distance between the conductor and screen (the antenna counterbalance).

In our case, when $\epsilon = 1$, the gaps between the conductor and screen were approximately equal 0.5 mm in the point of coupling with the feeder and approximately equal 4 mm at the origin of the first coil.

Such a resistance transformer does not involve any resonance elements and operates in the relatively wide frequency band.

3. RESULTS OF EXPERIMENTS

The experimental study of antennae has been carried out using the methods based on the techniques which proved themselves to be effective for antenna measurements [6], involving determination of matching using a panoramic standing-wave coefficient meter, radiation pattern measurement by the method of two antennae, polarization characteristic measurement using an auxiliary linear polarization antenna capable of rotating around a longitudinal (horizontal) axis.

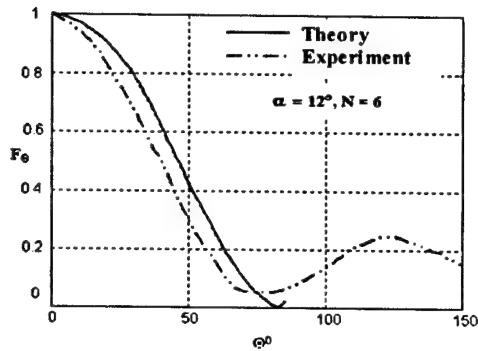


Fig. 1.

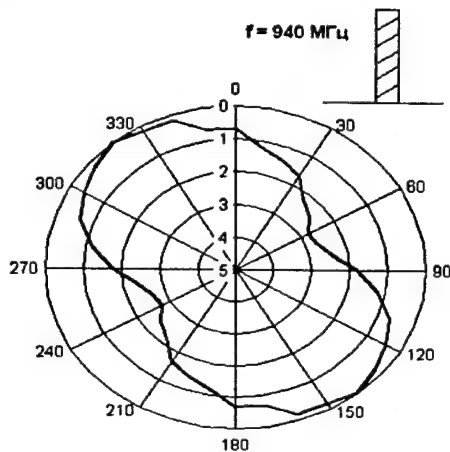


Fig. 2.

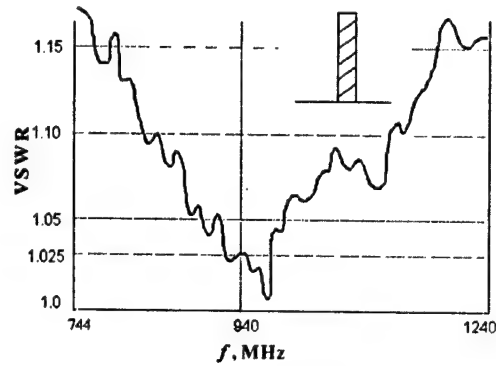
The measurement of the transmission-reception channel isolation coefficient has been performed using a method of replacement in an anechoic chamber, equipped by a "Bamboo"-type absorber. Here the location and orientation of the studied antenna system were chosen such as to provide that the coefficient of back scattering from the planes confining the anechoic chamber was not exceeding (90÷100) dB.

Fig. 1 shows the radiation patterns of a spiral antenna with the mentioned above parameters – the experimentally measured at the frequency $f = 940$ MHz and the calculated one [3]. The presented radiation patterns indicate a satisfactory agreement of the calculated results with the experimental ones.

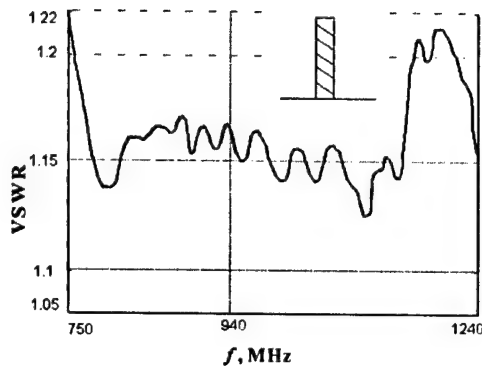
The radiation pattern of a spiral antenna (a "dumb-bells-shaped curve") is given in Fig. 2. It allows one to conclude that the antenna polarization is elliptical with the ellipticity coefficient $r \geq 0.75$.

The degree of matching of the transmitting and receiving antennae is shown in Fig. 3, where the VSWR dependence on frequency in the frequency range 50÷1240 MHz is given. The presented dependences show good matching of antennae in the frequency range ($VSWR \leq 1.2$).

The imperfect identity of the given dependences for transmission and reception channels is explained by non-identity of the resistance transformers by the channels.



a)



b)

Fig. 3.

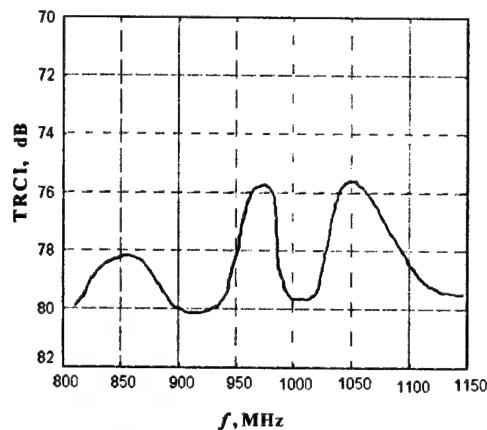


Fig. 4.

The measurements of the radiation pattern, polarization characteristic and degree of matching have been carried out not inside the antenna system but separately by the channels. Taking into account rather high isolation between channels (see below), this becomes quite admissible.

The behavior of transmission-reception channel isolation (TRCI) in the frequency band 800÷1150 MHz measured by the method of replacement is given in Fig. 4. The results obtained show rather high realized isolation between channels (75÷80) dB in the stated frequency band.

The availability of oscillations of the VSWR curve (Fig. 3) at $1.05 \div 1.1$ level is explained by the polarization vector rotation in the frequency band towards the coupling of the transmission and reception antennae, i.e. by small variations in the polarization coefficient μ_{12} . On the one hand, this evidences that assumptions are valid as to the random character of the polarization ellipse orientation not only in the field of sidelobes in the far antenna zone, but at comparatively small ($\sim 1.7\lambda$) distances and as to incomplete suppression of the "parasitic" coupling channels, on the other hand, this allows assessment of the "efficiency" of these channels.

4. CONCLUSION

Thus, the results of development and experimental study of the decimeter antenna system consisting of two orthogonally polarized spiral antennas testify that one of the most important factors which entail appearance of parasitic channels of coupling between antennae is a mismatch in their feeding points.

It is shown that the use of the simplest irregular microwave power transmission lines together with orthogonal circular polarized transmission and reception channels as the matching devices appears to be rather effective in fighting the appearance of these coupling channels and allows one to obtain high values of the isolation coefficient in the given frequency band.

In the considered case the antenna system having the distance between the antenna axes of $\sim 1.7\lambda$ is characterized by the following parameters:

- $\chi \geq (75 \div 80)$ dB.
- $\text{VSWR} \leq 1.2$.
- Central operating frequency value $f_0 = 940$ MHz.

- Operating frequency band $\Delta f = (800 \div 1150)$ MHz.
- Maximum gains $G_{\max 1,2} \approx 10$ dB.
- Sidelobe Level ≤ 3 dB
- Ellipticity coefficients in the direction of the main maxima of the radiation pattern $\eta_{1,2} \geq 0.75$.
- Orientation of large axes of polarization ellipses of the transmission and reception antennae to the direction of the main maxima of the radiation pattern is mutually orthogonal.

The developed antenna system can be used in low power continuous wave radars designed for location of objects having rather pronounced depolarizing effect in the operating frequency band.

REFERENCES

1. M. Skolnik, Radar Handbook, v.3, Moscow: Sov. Radio Publishers, 1979.
2. Y.N.Feld, E.G. Zelkin (Ed.), Antenna Technology Handbook, v. 1, Moscow: Radiotekhnika Publishers, 1997 (in Russian).
3. O. A. Yurtsev, A.V.Runov, and A.N.Kazarin, Spiral Antennae, Moscow: Sov. Radio Publishers, 1974.
4. Super-Wide Band Antennae, Moscow: MIR Publishers, 1964 (translated from English).
5. M. A. Ganston, A Handbook on Wave Resistances of Microwave Feeder Lines (Ed. A.Z. Fradin), Moscow: Svyaz Publ., 1976 (translated from English)
6. A.Z. Fradin, E.V. Ryzhkov, Antenna Parameter Measurement, Moscow: State Publ. (communication and radio), 1962.

IN-PHASE EXCITATION OF INFINITE PHASED ANTENNA ARRAY

Svetlana V. Chumachenko

Kharkov National University of Radio Electronics,
Kharkov, Ukraine
<ri@kture.kharkov.ua>

Abstract

The accurate solution of the problem of scattered field in a phased antenna array made of semi-bounded flat wave-guides at in-phase excitation is proposed. The Functional Expansion Method over Selected Values in Hilbert space with a reproducing kernel is used. Alternative representations for amplitude coefficients in the analytical form without series and infinite products are derived.

Keywords: phased antenna array, Functional Expansion Method on Selected Values.

1. ACTUALITY OF INVESTIGATIONS

There are a lot of methods for calculation of phased antenna arrays. They are based on the classical theory [1, 2], analytical methods [3-5], numerical and experimental results [6]. Analytical methods frequently are approximate. Numerical methods imply time expenses. It is connected with computational complexity and an increasing accuracy of results. The accurate analytical solution must be convenient for the numerical analysis. The investigations and development of effective analytical methods of solving boundary problems, which allow obtaining accurate solutions, keep being topical in all fields of science.

2. STATEMENT AND GEOMETRY OF THE PROBLEM

The problem of phased antenna array formed by parallel endless planes semi-bounded wave-guides is considered. The wave-guide planes are assumed extremely thin and ideally conducting, a is the distance between them. The incident field in every of wave-guides has the same amplitude and for every two contiguous of them is phase shifted by the same angle (in-phase excitation). Let θ_0 be the counted out from the x -axis angle of inclination of the antenna RP main lobe. Then a phase of the incident field in the m -th waveguide should be described by multiplier $\exp(imu)$, where $u = ka \sin \theta_0$. Suppose that the incident field in wave-guide area consists only of a main wave of TEM type. For each wave-guide the field components are presented as follows:

$$H_y = \Psi = e^{ikr} e^{imu}, \quad (1)$$

$$E_x = \frac{1}{i\omega\epsilon} \frac{\partial}{\partial z} \Psi, \quad (2)$$

$$E_z = \frac{1}{\omega\epsilon} \frac{\partial}{\partial x} \Psi, \quad (3)$$

where $x < 0$ and $ma < z < (m+1)a$.

It is necessary to obtain the field radiated in free space and reflected to wave-guides. The main goal of this paper is to obtain analytically expressions for electromagnetic field amplitude coefficients by Functional Expansion Method over Selected Values.

3. METHOD OF SOLVING THE PROBLEM AND THE MAIN THEORETICAL RELATIONS

The formulated problem is solved by the method of partial areas with the use of the Floquet harmonics. The method is applied for investigations of volumetric complex structures, which are decomposed into two or more simple adjacent areas. For each of them it is possible to get a solution by variable division. The first step consists in presenting unknown fields for each partial area in the form of expansion into eigenfunctions. In the rectangular co-ordinate system, components of the electromagnetic field constitute solutions of the Helmholtz equation in the corresponding area. Building the periodical solution of the Helmholtz equation satisfying boundary conditions is the matter of the Floquet theorem. Orthonormal functions of transverse co-ordinates form the system of scalar spatial harmonics (Floquet modes). On their basis, full systems of vector harmonics are built [2]. The explicit representations for inter-orthogonal functions are known. Thus, the problem is reduced to obtaining amplitude coefficients to eigenfunctions for the field expansion in every partial area. For this purpose, it is necessary to satisfy boundary conditions of the field. As a result, one can obtain an infinite system of linear algebraic equations (SLAE) relatively to

unknown eigen wave amplitudes. In general case, it is impossible to find the accurate solution of this infinite system. Usually it is confined by the rough solution obtained with the help of methods of reduction or sequential approximations [3]. But in particular cases, it is possible to obtain the accurate solution either with the functional-theoretical method (a method of residues [1], a modified method of residues [1, 4]) or with the Wiener-Hopf method [1, 5]. In the method of residues, an integral over a special analytical function is introduced, and then residues of the sub-integral function are associated with unknown coefficients.

There is a class of boundary problems, for which infinite SLAE yields the accurate solution. Functional Expansion Method over Selected Values allows expanding it. This method is based on the following statements [7].

Let A be some class of functions defined on a T set. Function $f \in A$ can be expanded into a series over sSelected values at points $t_i \in T$, if there exists a set of sSelected functions $\psi_i(s, t_i)$, such that:

$$1) \psi_i(s, t_i) \in A, \quad 2) \psi_i(t_i, t_j) = \begin{cases} 1, & i = j, \\ 0, & i \neq j; \end{cases}$$

3) for each function $f \in A$, a series $f(s) = \sum_i f(t_i) \psi_i(s, t_i)$ converges uniformly for $s \in T$. There is the following theorem [8].

Let H be abstract Hilbert space with a reproducing kernel $K(s, t)$ defined on the T -set. Let $\{\varphi_i(s, t_i)\}$, $t_i \in T$ be a complete orthonormal system in H . If there exist nonzero real constants c_i such that

$$\varphi_i(s, t_i) = c_i K(s, t_i), \quad |K(t, t)| \leq c_i < \infty, \quad t \in T, \quad (4)$$

then expansion by complete orthonormal system for every $f \in A$, where

$$f(s) = \sum a_i \varphi_i(s, t_i), \quad s \in T, \quad a_i = (f, \varphi_i), \quad (5)$$

is a series over sSelected values.

The fundamental research of the problem of expansion over sSelected values have been carried out by K. Shannon and V. A. Kotelnikov.

4. THE PROBLEM SOLUTION

From the continuity condition for tangent field components on a surface of the area $x = 0$, the following system of functional equations holds

$$e^{imu} + \sum_{n=0}^{\infty} A_n^m \cos \left[\frac{n\pi}{a} (z - ma) \right] = \sum_{p=-\infty}^{\infty} B_p e^{i\alpha_p z}, \quad (6)$$

$$ik e^{imu} + \sum_{n=0}^{\infty} \omega_n A_n^m \cos \left[\frac{n\pi}{a} (z - ma) \right] = \sum_{p=-\infty}^{\infty} (-\Omega_p) B_p e^{i\alpha_p z}, \quad (7)$$

$$\text{where } ma < z < (m+1)a, \quad \alpha_p = (2p\pi + u)/a, \quad \Omega_p = (\alpha_p^2 - k^2)^{1/2}, \quad \omega_n = [(n\pi/a)^2 - k^2]^{1/2}.$$

To define unknown coefficients, rewrite (6), (7) as follows

$$1 + \sum_{n=0}^{\infty} (A_n^m e^{-imu}) \cos \left[\frac{n\pi}{a} (z - ma) \right] = \sum_{p=-\infty}^{\infty} B_p e^{i\alpha_p (z - ma)}, \quad (8)$$

$$ik + \sum_{n=0}^{\infty} \omega_n (A_n^m e^{-imu}) \cos \left[\frac{n\pi}{a} (z - ma) \right] = \sum_{p=-\infty}^{\infty} (-\Omega_p) B_p e^{i\alpha_p (z - ma)}, \quad (9)$$

$$ma < z < (m+1)a$$

Let us introduce designation: $z' = z - ma$. Then from the given equations there follows a relation for amplitudes of eigenwaves in different wave-guides:

$$A_n^m = (-1)^n A_n^0 e^{imnu}, \quad (10)$$

where $n = 0, 1, 2, \dots; m = 0, \pm 1, \pm 2, \dots$. It is easy to show that with $m = 0$ formulas (8), (9) can be given as:

$$1 + \sum_{n=0}^{\infty} (-1)^n A_n^0 \cos \frac{n\pi}{a} z = \sum_{p=-\infty}^{\infty} B_p e^{i\alpha_p z}, \quad (11)$$

$$ik + \sum_{n=0}^{\infty} (-1)^n A_n^0 \omega_n \cos \frac{n\pi}{a} z = \sum_{p=-\infty}^{\infty} (-\Omega_p) B_p e^{i\alpha_p z}, \quad (12)$$

$$0 < z < a.$$

Thus, the problem is reduced to consideration of one period $m = 0$. From (11), (12) one can obtain the system of algebraic equations with respect to unknown coefficients $\{A_n\}$. For this, let us multiply both parts by $e^{-i\alpha_q z}$ and integrate the result with respect to z , $z \in (0, a)$. This yields

$$\sum_{n=0}^{\infty} (-1)^n A_n^0 \frac{1 - (-1)^n e^{-iu}}{\omega_n^2 - \Omega_q^2} + \frac{1 - e^{-iu}}{\omega_0^2 - \Omega_q^2} = \frac{a}{i\alpha_q} B_q, \quad (13)$$

$$\sum_{n=0}^{\infty} (-1)^n A_n^0 \omega_n \frac{1 - (-1)^n e^{-iu}}{\omega_n^2 - \Omega_q^2} - \omega_0 \frac{1 - e^{-iu}}{\omega_0^2 - \Omega_q^2} = \frac{a}{i\alpha_q} B_q (-\Omega_q), \quad (14)$$

$$q = 0, \pm 1, \pm 2, \dots$$

where $\omega_0 = -ik$. Further, equation (13) is multiplied by Ω_q and added with (14), what gives

$$\sum_{n=0}^{\infty} (-1)^n \frac{1 - (-1)^n e^{-iu}}{\omega_n - \Omega_q} A_n^0 = \frac{1 - e^{-iu}}{\omega_0 + \Omega_q}, \quad (15)$$

$$\sum_{n=0}^{\infty} (-1)^n \frac{1 - (-1)^n e^{-i\omega_n}}{\omega_n + \Omega_q} A_n^0 - \frac{1 - e^{-i\omega_0}}{\omega_0 - \Omega_q} = \frac{i2a\Omega_q}{\alpha_q} B_q, \quad (16)$$

$$q = 0, \pm 1, \pm 2, \dots$$

From the problem statement it follows that $\{A_n^0\}$ are independent of q . Thus, from subsystem (15) for $q = 0$ one can obtain

$$\sum_{n=0}^{\infty} (-1)^n \frac{1 - e^{-i\omega_n} \cos \pi n}{\omega_n - \Omega_0} A_n^0 = \frac{1 - e^{-i\omega_0}}{\omega_0 + \Omega_0}. \quad (17)$$

Let's search unknown amplitude coefficients $\{A_n^0\}$ in the following form

$$A_n^0 = \frac{A \varepsilon_n}{a(\omega_n + \Omega_0)(1 - e^{-i\omega_n} \cos \pi n)}, \quad (18)$$

where A is some constant, which is independent of n . Substituting (18) in (17), obtain

$$A = \frac{u(e^{-i\omega_0} - 1) \sin u}{a(\omega_0 + \Omega_0)}.$$

Thus, from subsystem (15) unknown amplitudes $\{A_n^0\}$ have been obtained in the form

$$A_n^0 = \frac{(e^{-i\omega_n} - 1) \varepsilon_n u \sin u}{a^2(\omega_0 + \Omega_0)(\omega_n + \Omega_0)(1 - e^{-i\omega_n} \cos \pi n)}, \quad (19)$$

ε_n is the Neumann number. It should be noted that representation (19) transforms (15) into identity [8, 5.139, p. 350]. After this, the coefficient B_q is defined from (16) and (19). For this purpose, it is necessary to define sum of series in (16). Application of reproducing summing operator yields

$$B_q = \frac{\alpha_q}{2ia\Omega_q} \frac{e^{-i\omega_0} - 1}{\omega_0 - \Omega_q}, \quad q = 0, \pm 1, \pm 2, \dots \quad (20)$$

5. RESULTS AND DISCUSSIONS

Thus, the accurate solution of the problem of the field in a phased antenna array made of semi-bounded flat waveguides at in-phase excitation is obtained. The formulated problem is solved with the use of the linking method with application of Floquet harmonics in co-operation with the Functional Expansion Method over Selected Values in Hilbert space with reproducing kernel. The latter one allows deriving alternative representations for unknown amplitude coefficients in explicit form in terms of more elementary functions. The considered problem was solved in [1] by method of residues. Amplitude coefficients have the following form

$$A_n^0 = \frac{\text{Res } f(\omega_n)}{1 - (-1)^n e^{-i\omega_n}}, \quad n = 1, 2, 3, \dots, \quad (21)$$

$$B_q = \frac{\alpha_q}{i2a\Omega_q} f(-\Omega_q), \quad q = 0, \pm 1, \pm 2, \dots \quad (22)$$

where $f(w)$ is the analytical function:

$$f(w) = \frac{1 - e^{-i\omega_0}}{w + \omega_0} \exp \left[\frac{(w + \omega_0)a}{\pi} \ln 2 \right] \frac{2}{1 - w/\omega_0} \times \\ \times \prod_{m=1}^{\infty} \frac{(1 + \omega_0/\omega_m)(1 - w/\Omega_0)}{(1 - w/\omega_m)(1 + \omega_0/\Omega_0)} e^{-\frac{(w + \omega_0)a}{m\pi}} \times \\ \times \prod_{m=1}^{\infty} \frac{(1 - w/\Omega_m)(1 - w/\Omega_{-m})}{(1 + \omega_0/\Omega_m)(1 + \omega_0/\Omega_{-m})} e^{-\frac{(w + \omega_0)a}{m\pi}}.$$

Apparently, there are infinite products in equations for amplitude coefficients (21), (22). Therefore, it is possible to obtain only approximate results for A_n^0 and B_q . The comparison of expressions (19), (20) and (21), (22) yields the following formula for infinite products

$$\text{Res } f(\omega_n) = \varepsilon_n \frac{u \sin u}{a(\omega_n + \Omega_0)} \frac{e^{-i\omega_n} - 1}{a(\omega_0 + \Omega_0)},$$

$$f(-\Omega_q) = \frac{e^{-i\omega_0} - 1}{\omega_0 - \Omega_q}.$$

The obtained solutions are accurate. It is applicable for the numerical analysis of waveguides of different sizes. Since the different types of series occur when solving similar waveguide problems, for radiation from the flanged parallel plate waveguide [10], the investigations in this scientific direction are very perspective.

REFERENCES

1. Mittra R., Lee S. W. Analytical techniques in the theory of guided waves. The Macmillan Company-New-York Collier-Macmillan Ltd-London. 1971.
2. Amitey N., Halindo B., Wu C. Theory and Analysis of Phased Antenna arrays. New York: Wiley, 1972.
3. Shestopalov V. P., Litvinenko L. N., Masalov S. A., Sologub V. G. Wave diffraction on arrays. Kharkov: Kharkov's Univ. Press, 1973. (in Russian).
4. Shestopalov V. P., Kirilenko A. A., Masalov S. A. Convolution-type Matrix Equations in the theory of diffraction. Kyiv: Naukova Dumka, 1984. (in Russian).
5. Nobl B. Methods based on Wiener-Hopf technique. New-York: Pergamon Press. 1958.
6. Sergey P. Skobelev. Shaping of Flat-Topped Element Patterns in an Array of Slow-Wave Strip Structures Excited by Parallel-Plate Waveguides // IEEE Transactions on antennas and propagation. Vol. 49, N12, December 2001. P.1763-1768.
7. Curant R., Gilbert D. The methods of mathematical physics. M.: Postechizdat, 1951.
8. Buchholz H. Elektrische und magnetische Potentialfelder. Berlin-Yottingen-Heidelberg. Springer-Verlag. 1957.
9. Veliev E. I., Oksasoglu A. Bessel functions series in two dimensional diffraction problems / J. of Electromagnetic and Applications. 1996. Vol. 10. N4. P. 493-507.

THE SCANNING ANTENNA FOR A 3-MM MULTICHANNEL RADIOMETER

Anatoliy P. Yevdokymov and Volodymyr V. Kryzhanovskiy

A. Ya. Usikov Institute of Radiophysics and Electronics NAS of Ukraine
12 Ac. Proskura st., Kharkov, 61085, Ukraine
Phone: 0572-448326, Fax: (380-572) 44-11-05, E-mail: <yevdok@ire.kharkov.ua>

Abstract

The millimeter-wave planar antenna of present concern is distinguished for the development of a two-dimensional radiometric image by the combined scanning through a not ordinary mechanical scanning in one plane and frequency scanning in the other.

Keywords: diffraction grating, planar dielectric waveguide, dispersion, parabolic horn taper, dielectric lens.

1. THE ELECTROMAGNETIC CIRCUIT OF THE SCANNING ANTENNA

For the purpose of a radiometric visualization of two-dimensional objects, a single-channel radiometer does make the beam scanning in two orthogonal directions. An alternative approach is by using a multichannel radiometer equipped with an antenna which electromechanically scans in one plane, and has pronounced dispersion properties in the orthogonal plane, Fig. 1. A multifrequency radiometer incorporated with such antenna provides a parallel-sequential scanning of a two-dimensional area.

The antenna of present concern is intended for the scanning of a 2.5m high, 1.3m wide, and 5m distant area. The operating frequency band is 86 to 100GHz. The aperture diameter is 280mm. The in-space resolution power is enhanced with a beam-focusing lens.

The electromechanically scanning antenna (Fig. 1) consists of a planar dielectric waveguide 1 accommo-

dated in the yOz plane and the reflection diffraction grating 2 on a metal disk. The grating is set parallel to the planar dielectric waveguide some distance apart. In reception mode, the grating converts the volume waves from the object into the surface waves propagating through the dielectric waveguide. Afterwards in a planar parabolic horn taper, the eigenwave set of the planar dielectric waveguide is transformed to a broadband signal passing down a hollow metal waveguide to the radiometer input.

The coordinate system employed in Fig. 1 is related to the planar dielectric waveguide position. The grating generating lines are oriented at arbitrary angle α to the direction of the surface wave propagation in the planar dielectric waveguide. In general, the electromagnetic circuit, as shown, can receive as many as n rays, in keeping with a chosen number of the grating diffraction harmonics. But for the considered antenna class [1], it is sufficient to take the first space harmonic which satisfies the reception condition. The direction of the space wave reception is given by the angles Θ_n and φ_n . These follow from the relationships wherein Θ_n is the angle which the xOz - projection of wave vector \vec{K} of the reception field makes with the Oz axis; φ_n is the angle between wave vector \vec{K} of the particular reception harmonic and its xOz - projection

$$\cos \Theta_n = \frac{[U + (n/\chi) \cos \alpha]}{\cos \varphi_n},$$

$$\sin \varphi_n = -(n/\chi) \sin \alpha,$$

where $n = -1, -2, \dots$ is the number of the grating diffraction harmonic, $\chi = \ell/\lambda$, ℓ is the grating period, λ is the wavelength, U is the wave deceleration factor in the planar dielectric waveguide.

The scanning in the xOy plane is performed by turning the grating-carrying disk 2 round its axis

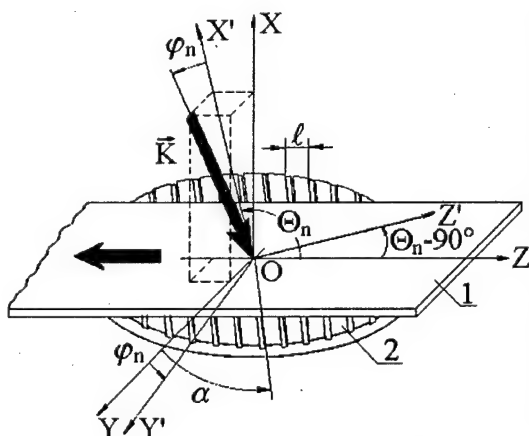


Fig. 1. The electrodynamic circuit of the scanning antenna

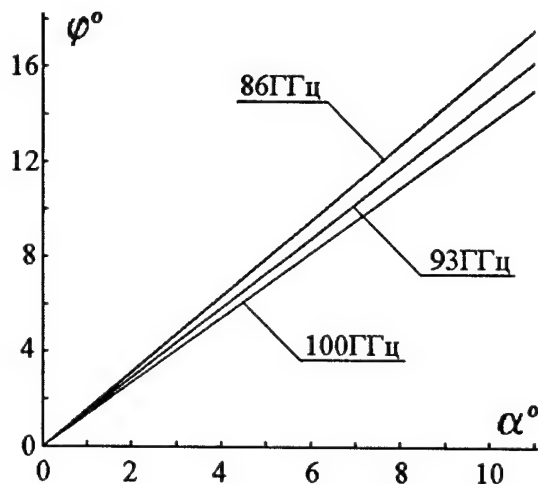


Fig. 2. The chosen sector of the antenna mechanical scanning in the xOy plane.

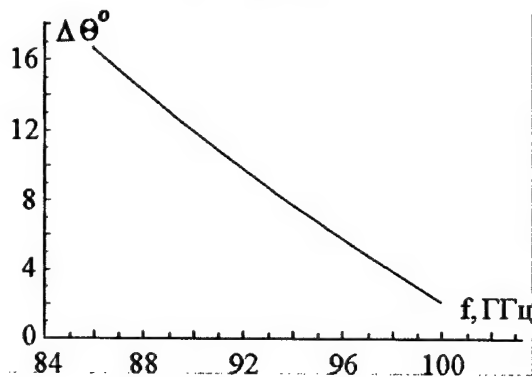


Fig. 3. The obtained angular sector of the frequency scanning in the xOz plane

through angle α . The corresponding α -dependencies of the scanning angle φ_{-1} are presented in Fig. 2. At the 100 GHz frequency, the grating turn through $\pm 10.25^\circ$ makes the scanning within $\pm 14^\circ$. In general, the mechanical turn of the disk in the antenna-type provides the scanning sector as wide as $\pm 60^\circ$. In the present design, the scanning frequency is 1 Gz, the scanning sector is $\pm 14^\circ$.

The parallel scanning in the xOz plane is performed with a 16 – channel 14 – GHz radiometer. The dispersion characteristics of the antenna are viewed in Fig. 3 as a beam position in the xOz plane depending on the signal frequency. A signal band of 14 GHz provides a scanning sector of 14.6° . In order to do away with a slight nonlinearity of this characteristic, the radiometer passbands should be better matched. Also an optimum antenna positioning relative to the scanning area helps it.

2. THE ANTENNA DESIGN

A view of the in-plane scanning antenna is in Fig. 4. Planar dielectric waveguide 1 represents a rectangular shaped Teflon plate measuring $320 \times 320 \times 2.25 \text{ mm}^3$. On the three sides, the waveguide is locked on the in-

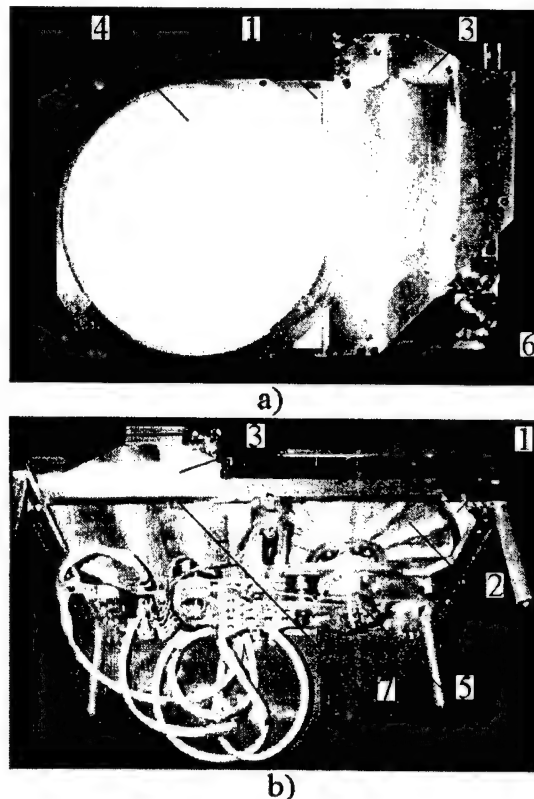


Fig. 4. A view of the in-plane scanning antenna of the multichannel radiometer

side of the antenna aluminum metalwork 7. The fourth side is attached to the horn taper of excitation unit 3 of the planar waveguide. Excitation unit 3 is the parabolic horn taper from the hollow metal waveguide of standard $2.4 \times 1.2 \text{ mm}^2$ cross section to the overdimensional hollow metal waveguide of $280.0 \times 3.0 \text{ mm}^2$ cross section. It serves the function of effective excitation of planar dielectric waveguide 1 and develops a proper field distribution in the antenna aperture in the xOy plane.

The diameter of grating carrying disk 2 is 280 mm. This value comes from a desired size of the 5 m distant field spot after being focused with the aid of dielectric lens 4. The grating carrying disk, the disk turning shaft, the shaft bearing, and the antenna drive make up scanning unit 5 mounted on a T-shaped frame and locked to antenna metalwork 7 at three points. The mounting is such as to provide the adjustment of the diffraction grating plane with dielectric waveguide 1 in both planes toward getting a desired field distribution in the xOz plane. The scanner T-frame carries also the antenna electrical components: step motor ДШИ-200-1-1, step-motor damping resistors, the board with magnetic hermetic contact detectors of grating 2 position, adapting panel toward antenna electrical circuits. The antenna drive is a reducing step motor between the step motor and the grating disk shaft. The antenna beams are spatially related to the observation plane by means of unmatched laser pointers 6 placed on the antenna facial surface.

3. THE ANTENNA PARAMETERS

- The operating frequency band at the 1 dB level covers 14.0 GHz from 86.0 to 100.0 GHz.
- In the 14 GHz band, the observation field is kept to be a rectangular area 2.5 m high, 1.28 m wide, and 5.0 m distant.
- The resolution power depends on the aperture diameter, operating frequency, and scanning angle. The monochromatic – signal best resolution (at the observation field center) is $70 \times 70 \text{ mm}^2$. Toward the observation field ends the resolution power goes down to $100 \times 100 \text{ mm}^2$. The antenna resolution is susceptible both to the lens astigmatism for off-axis rays and the difference between the focal distance and the off-axis ray distance.
- Due to angle – frequency sensitivity, the scanning antenna develops an actual multibeam radiation pattern in the xOz plane. The reception unit specifies the number of the beams that the antenna forms, and it is 32.
- For the operating frequency band and observation angle sector, the active loss because of the energy absorption in antenna components does not exceed 1.4 dB, including 0.8 dB in the planar parabolic horn taper and 0.6 dB in the dielectric waveguide.
- The antenna provides linear polarization of the reception radiation.
- Over the operating frequency band, the VSWR is as good as 1.25.

Compared to the mirror antenna, the planar design is an unusual and compact one. The testing of the scanning antenna, as part of an experimental radiometrical set, does encourage its multi-purpose applications.

REFERENCES

1. A. P. Yevdokimov and V. V. Kryzhanovsky, A new direction in antenna array technology, *Izv. VUZov. Radioelektronika*, 1996, Vol. 39, No. 9 – 10, pp. 54 – 61 (in Russian).

METHOD OF ELIMINATING INTERFERENCE NOUGHTS OF RADIATION PATTERN OF BASE STATION ANTENNA ARRAY

Vladimir Yatskevich, Yevgeniy Bulikov

Vologda State University, Vologda, Russia
<bulikov@vologda.ru>

Abstract

A simple method of excitation of the base station antenna array eliminating interference noughts of the radiation pattern in vertical plane has been proposed. Characteristics of the panel antenna containing collinear dipoles have been theoretically studied.

Keywords: radio communication base station antenna; collinear dipoles; directive gain.

1. INTRODUCTION

For basic stations with a big coverage area it is reasonable to use a linear vertically oriented dipole array with a high gain and with the main beam orientated to the area boundary. The increase of the gain is achieved by increasing the vertical size of the antenna and the number of dipoles, however at the same time the width of the main beam of the radiation pattern in vertical plane is reduced and the number of interference noughts increases, that causes the appearance of zones of weak reception. The noughts, nearest to the main beam, which correspond to remote receiving points are especially detrimental to the quality of reception.

The known method of eliminating interference noughts means excitation of dipoles with small out-phasing, however this method for multielement arrays doesn't let to eliminate all noughts and causes close tolerances to realization of transmission lines phasing sections.

2. DESCRIPTION OF THE METHOD

Let's take the linear antenna array of N identical radiators (N is odd). We accept that the radiators are excited with equal amplitudes and phases (or with linear phase shift), that, evidently, gives the maximum directive gain of an array, provided the mutual coupling can be neglected. We suppose the input currents in all radiators are equal to units. The corresponding radiation pattern in vertical plane is marked as $F_0(\theta)$.

We change the central radiator input current making it equal to

$$I_c = 1 \pm j\alpha, \quad (1)$$

where α is a real number. Then radiation pattern becomes equal to

$$F(\theta) = F_0(\theta) \pm j\alpha f(\theta), \quad (2)$$

and its module

$$|F(\theta)| = \sqrt{F_0^2(\theta) + \alpha^2 f^2(\theta)}, \quad (3)$$

where $f(\theta)$ is the radiation pattern of the central radiator, which we consider near-omnidirectional and having no noughts in the coverage area.

It's obvious that new noughts don't appear in the pattern (3) and in directions there is no former noughts for which $F_0(\theta_m) = 0$, value (3) equals to $F(\theta_m) = \alpha f(\theta_m)$. The relative value of the radiation pattern in former noughts directions, nearest to the main beam, will be

$$|F(\theta_m)|/|F_{\max}| \approx \alpha/N.$$

We take into account here that $F_{\max} \approx Nf$.

Evidently, the parameter α defines the depth of minimums in the array radiation pattern.

Thus, in the suggested method all interference noughts are eliminated due to the change of excitation of only one radiator. According to (1), at the input of the central radiator the current module should be multiplied by $\sqrt{1 + \alpha^2}$ and the current phase should be increased by $\Delta\varphi = -\arctg \alpha$, where the parameter α should be taken from the ratio, where δ is the predetermined minimal radiation pattern level near the main beam. The reduction of the array directive gain can be evaluated by the formula

$$G/G_0 = (1 + \delta^2)/(1 + N\delta^2). \quad (4)$$

While deducing (4), we suggested that mutual coupling could be neglected.

The panel antenna containing the array of collinear dipoles ($N = 7$) with a period of $d = 0.75\lambda$ is considered as an example (Fig. 1). The dipoles are placed at a distance of 0.308λ from the flat screen, marked by the dashed line in the figure. The dipole's length is 0.44λ .

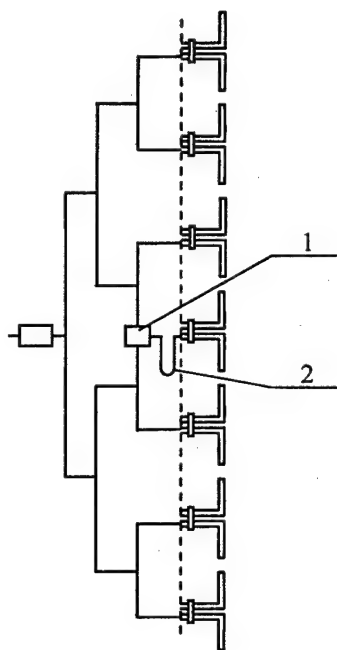


Fig. 1. The scheme of the antenna-feeder device

Taking the value $\delta = 0.14$ (-17 dB) we get $\alpha = 1$; $|I_c| = \sqrt{2}$; $\Delta\varphi = \pm 45^\circ$. Such excitation is achieved by the feeder (Fig.1) obtained from the standard feeder, usually used for the 8-element array in which we inserted the microwave adder 1 and the transmission line section 2. This allows to excite the central dipole by the amplitude, which exceeds amplitudes of the rest dipoles by $\sqrt{2}$. The necessary phase shift 45° is received due to the proper choice of the section length 2.

The six-pole of the ring structure [2] is used as a microwave adder 1. So, taking into account the fact that the additional phase shift made by the adder is equal to 180° we get the section 2 having the electrical length $5/8\lambda$.

The theoretical analysis was made with the help of MMANA program, which realizes the well-known

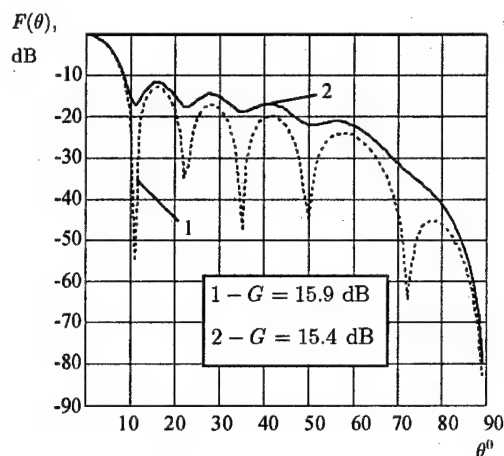


Fig. 2. Radiation pattern in vertical plane

algorithm of the electrodynamic analysis of thin wires using of piecewise - sinusoidal basis functions. Fig. 2 gives the vertical plane radiation pattern of the array for: 1 – excitation by equal amplitudes and phases of dipoles; 2 – excitation, suggested here. In the second case the width of the main beam of the radiation pattern in vertical plane is 9° , in horizontal plane – 100° . VSWR at the antenna input doesn't exceed 1.5 and the antenna gain reduction is 0.5 dB.

3. CONCLUSION

The suggested method of eliminating interference noughts doesn't require complex preliminary calculations. It is simple to realize, not sensitive to the device parameter disturbance and to frequency variation.

REFERENCES

1. Buzov A.L. VHF antennas for mobile radio, broadcasting activities. – M.: Radio and Communication, 1997. – 293 P.
2. Sazonov D.M. Microwave antennas and devices. – M.: Higher School, 1988. – 432 P.

INVESTIGATION OF PERIODICAL SEQUENCES OF CIRCUMFERENTIAL SLOTS IN CIRCULAR WAVEGUIDES

Sergey A. Pogarsky and Vyacheslav A. Chumachenko

Department of Physics of Ultra High Frequencies, Kharkov National University,
Kharkov, Ukraine <Sergey.A.Pogarsky@univer.kharkov.ua>

Abstract

A wide range of diffraction wave problem by semi-infinite equidistant succession of identical obstacles with axial symmetry has been considered. The numerical-analytical method for this problem solution has been suggested. It is based on the idea of the partial inversion of diffraction problem operator by the extraction of the simple part of the semi-infinite sequence of obstacles for which the scattering operator is known. The desired total operator is then constructed using specific symmetry of the semi-infinite structure on the basis of the above mentioned operator allowing one to take into account the wave interaction by the obstacle components.

Keywords: circumferential slot, circular waveguide, periodical structure, semi-infinite periodical.

1. INTRODUCTION

During the last years one can observe in many branches of modern radiophysics (from traditional microwave and super high frequencies to the optical band) the growing interest to the devices based on periodical and «quasi-periodical» discontinuities. This interest can be explained by the non-trivial properties of such systems. Based on these structures, the waveguide systems are used for the fabrication of different types of leaky-wave slot antennas for telecommunication, industrial purposes, etc. Using special properties by proper control of the period and duty-cycle it is possible to realize a wide range of novel components.

It is evident, that all physical phenomena in periodical structures in different frequency bands satisfy to the common principles. In a whole, the properties of periodical, semi-infinite periodical and «quasi-periodical» structures can be characterized with the help of scattering operator \hat{R} (in the case of multi-wave propagation) and with the help of scattering coefficient (in the case of single-wave propagation). This method was suggested by L.N. Lytvinenko [1]. Below, one can find the development and realization of this idea as applied to the circular waveguide with semi-infinite and limited periodical sequence of circumferential slots.

2. THEORY

Let us investigate the interaction process between one of the E_{op} -modes in circular waveguide with semi-infinite periodical sequence of circumferential slots. There is no doubt that the scattered fields in this prob-

lem have continuous spatial spectrum but it is possible to construct approximate solution by use the matrix operator rather than the integral operator. For simplicity let us suppose a negligible quantity of the slot's interference, which is caused by the slot's radiation into free space. In such an approximation radiated from any slot fields don't change complex magnitudes of waves in the space with the other slots. The error of such an approximation will be negligible in the case of narrow slots and large period of the slot's displacement comparing with the wavelength.

Following the mentioned method let us formulate the boundary problem for the key-structure (single circumferential slot). Assume that one of the E_{op} wave ($p = 1, 2, \dots$) propagates towards a single slot. Let d be the width of slot, $2a$ be the diameter of the waveguide in cylindrical co-ordinate system. Let us suppose that the ratio between frequency and diameter allow to propagate everyone from m E_{op} -waves ($1 \leq m \leq p$, $n \leq m$, $m = 1, 2$); $\beta_n = \sqrt{\xi^2 - \mu_n^2}$, $\xi = ka$, μ_n is the n -th root of Bessel's function $J_0(x)$.

The solution of this boundary problem can be found using the Fourier's transformation. The single nonzero component of magnetic field H_φ can be represented in the form:

$$H_\varphi^{(12)}(r, z) = \begin{cases} \frac{ikh}{a} \int_{-\infty}^{\infty} F(\beta) J_1(hr/a) \times \\ \times \exp(i\beta z/a) d\beta; & r \leq a, \\ \frac{ikh}{a} \int_{-\infty}^{\infty} F(\beta) \frac{J_0(h)}{H_0^{(1)}(h)} H_1^{(1)}(hr/a) \times \\ \times \exp(i\beta z/a) d\beta; & r \geq a. \end{cases} \quad (1)$$

The function's presentation in the form (1) satisfies to the Helmholtz's equation and provides the continuity of electric field in the whole space. It is possible to obtain the system of pair integral equations under conditions that the tangential component of the total electric field is equal to zero on the waveguides surface; the electric current on slots is absent and if one takes into account the Wronskian determinant for the Bessel's functions as:

$$J_0(x)H_1^{(1)}(x) - J_1(x)H_0^{(1)}(x) = 2/\pi ix. \quad (2)$$

These systems can be written as:

$$\int_{-\infty}^{\infty} \frac{X_n(\beta)}{h^2 J_0(h)H_0^{(1)}(h)} \exp(i\beta z/a) d\beta =$$

$$= -\frac{i\pi a^3}{2\mu_n} J_1(\mu_n) \exp(i\beta z/a), \quad |z| < d/2$$

$$\int_{-\infty}^{\infty} X_n(\beta) \exp(i\beta z/a) d\beta = 0, \quad |z| > d/2 \quad (4)$$

where $X_n(\beta) = F_n(\beta)h^2 J_0(h)H_0^{(1)}(h)$. One can derive that unknown functions $X_n(\beta)$ are equal to Fourier's transformation from the tangential components of electric field E_z on the slot (with range of accuracy to constant factor):

$$E_z|_{\rho=a} = \int_{-\infty}^{\infty} X_n(\beta) \exp(i\beta z/a) d\beta.$$

The systems of equations (3), (4) allow one to find the solution of the boundary problem with arbitrary parameters of structure. The most interesting case for practical applications is the case of narrow slots. The solution for this case can be obtained with the use of the method of moments [2].

It is well known that electric field E_z has root singularity at the edge of slots so it is appropriate to choose the Chebyshev's polynomials of the first kind with weight as basic functions $T_n(z) \left[1 - (2z/d)^2\right]^{-1/2}$. Introducing the parameter of so called narrowness of slots $\zeta = d/2a$, transform equations (3)-(4) using $t = 2z/d$:

$$\int_{-\infty}^{\infty} \frac{X_n(\beta)}{h^2 J_0(h)H_0^{(1)}(h)} \exp(i\beta \zeta t) d\beta +$$

$$+ \frac{i\pi a^3}{2\mu_n} J_1(\mu_n) \exp(i\beta_n \zeta t) = 0, \quad |t| \leq 1; \quad (5)$$

$$\int_{-\infty}^{\infty} X_n(\beta) \exp(i\beta \zeta t) d\beta = 0, \quad |t| \geq 1.$$

In such a way, the function E_z can be presented as:

$$f(t) = E_z(t) = \frac{1}{a^3} \int_{-\infty}^{\infty} X_n(\beta) \exp(i\beta \zeta t) d\beta =$$

$$= \begin{cases} T_n \frac{1}{\sqrt{1-t^2}}; & |t| < 1, \\ 0; & |t| > 1. \end{cases} \quad (6)$$

As far as the unknown function $X_n(\beta)$ is the Fourier transformation from $E_z(t) = f(t)$ and as it is well known [3] the Fourier transformation from Chebyshev's polynomials can be represented as the series of Bessel's functions and its derivatives up to N order, the unknown function $X_n(\beta)$ can be represented as series of Bessel's functions with unknown coefficients as:

$$X_n(\beta) = \frac{\zeta a^3}{2\pi} \int_{-1}^1 \frac{T_N(t)}{\sqrt{1-t^2}} \exp(i\beta \zeta t) dt =$$

$$= \frac{\zeta a^3}{2} \sum_{k=0}^N M_k J_k(\beta_n \zeta) \quad (7)$$

Taking into account the linear independence of the basic functions on interval $[-1,1]$ one can obtain the system of linear algebraic equations of the first kind:

$$\frac{\zeta a^3}{2} \sum_{k=0}^N M_k \int_{-\infty}^{\infty} \left(\frac{J_k(\beta \zeta) J_m(\beta \zeta)}{h^2 J_0(h)H_0^{(1)}(h)} d\beta + \right.$$

$$\left. + \frac{i\pi a^3}{2\mu_n} J_1(\mu_n) J_m(\beta_n \zeta) \right) = 0; \quad (m = 0, 1, \dots, N).$$

The "defined field" approximation can be used in the case of narrow slots, so one can take into account only finite quantity of M_k . It is caused that the "defined field" approximation provides correct field's characteristics in far zone (including scattering matrices) up to the second approximation of the narrowness of slots parameter [3,4]. This phenomenon is connected with stationary dependence of the far zone characteristics of field distribution on slot.

Defined functions $X_n(\beta)$ allow one to determine the surface current density:

$$j_z = A \left[\exp(i\beta_n z/a) + \frac{2\mu_n}{\pi J_n(\mu_n)} \int_{-\infty}^{\infty} \frac{X_n(\beta)}{h^2 J_0(h)H_0^{(1)}(h)} \cdot \exp(i\beta z/a) d\beta \right], \quad (9)$$

where $A = C\xi J_1(\mu_n)/4\pi\mu_n$ is the magnitude current density of E_{op} wave. Using the well known methods of integration in the complex plane it is possible to define j_z as:

$$j_z = A \left[\exp(i\beta_n z/a) + \sum_{p=1}^m R_{np} \exp(-i\beta_p z/a) \right], \quad (10)$$

$$z \ll -d/2,$$

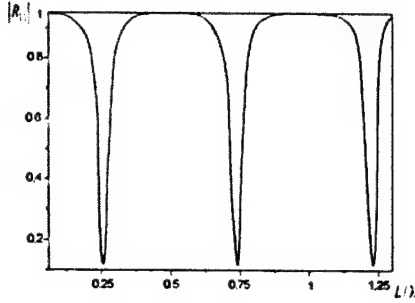


Fig. 1.

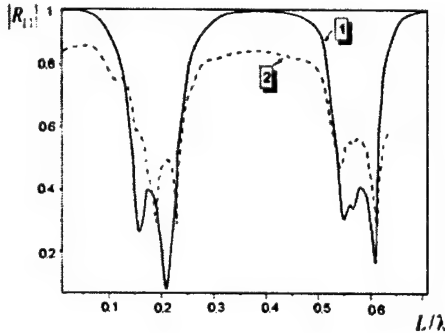


Fig. 2.

$$j_z = A \sum_{p=1}^m T_{np} \exp(i\beta_n z/a), \quad z \gg d/2, \quad (11)$$

where the notations are used:

$$R_{np} = \frac{i\pi\mu_n}{J_1(\mu_n)} \frac{\mu_p}{\beta_p} X_n(-\beta_n),$$

$$T_{np} = \delta_{np} + \frac{i\pi\mu_n}{J_1(\mu_n)} \frac{\mu_p}{\beta_p} X_n(\beta_n), \quad n, p \leq m \quad (12)$$

δ_{np} is Kronecker's function. The R_{np} and T_{np} define matrix operators of reflection and propagation "by current" correspondently.

3. SIMULATION. EXPERIMENT. DISCUSSION

Thus, the solution of the key-problem has been described in the previous section. Following the method [1] one can find the total reflection operator \hat{R} of the semi-infinite structure from the operator equation of the second kind:

$$\hat{R} = \hat{r} + \hat{t} [I - \hat{\varphi} \hat{R} \hat{\varphi} \hat{r}]^{-1} \hat{\varphi} \hat{R} \hat{\varphi} \hat{t}, \quad (13)$$

where \hat{r} is defined by R_{np} and \hat{t} is defined by T_{np} ; $\hat{\varphi}$ is operator, which defines phase-shift between neighboring slots. This equation can be solved by different methods, but Newton's method is the most preferable, especial, if the initial approximation is far from root or if function $R(r, t)$ has irregular regions. The functional dependence $|R_{11}|$ upon L/λ is represented at Fig.1. One can observe quasi-periodical character of this curve.

The solution for semi-infinite structure is key-problem for analysis of bounded periodical sequence structures. It is possible to obtain the partial reflection and transmission operator (coefficients) of s -th slot (discontinuities) as:

$$\hat{\rho}_s = \frac{(r - R) e^{-ik_n L}}{1 - r e^{ik_n L} R e^{-ik_n L}}; \quad (14)$$

$$\hat{\tau}_s = (1 + R e^{ik_n L} \rho) e^{ik_n L} t. \quad (15)$$

Using the circuit theory there is no any problem to obtain the summary operators (coefficients) for bounded periodical structures. This procedure was realized for the bounded sequence, which includes 10 circumferential slots. The results of simulation for this case can be found in Fig. 2 (straight line). It is evident that characteristic is quasi-periodical. The period is connected with L/λ parameter and it is approximately equal to 0.5.

The series of experiments were carried out with aim to confirm the main concept of these investigations. This concept lies in idea that integral reflection operator may substitute for matrix reflection operator under some condition. The main requirement is absence mutual influence of slots. This requirement can be realized by two ways: it is necessary to have narrow slots and the distance between neighboring slots must be more than wavelength.

In Fig.2 dash curve reflects the experimental data. It is obvious that the theoretical and experimental central frequencies of stop-band and pass-band are in good agreement. Moreover, the form of curves is very similar. One can detect the difference in magnitudes but it can be explained by errors of experimental model manufacturing and errors of the experimental method.

Thus, the undertaken experiments show the possibility of transformation integral scattering operator into matrix scattering operator under certain conditions. The results of these investigations can be used in antenna technique and in the design of new types of functional elements in SHF techniques.

REFERENCES

1. Lytvinenko L.N., Reznik I.I., Lytvinenko D.D. 'Wave diffraction by semi-infinite periodical structures', Reports of the Ukrainian Academy of Sciences, 1991, No 6, P. 62-66.
2. Bateman G., Erdelyi A. 'Higher transcendental functions', N.Y.: McGraw Hill,
3. Mittra R., Lee S. 'Analytical methods in waveguide theory'
4. Lapta S.I., Sologub V.G. 'The influence of narrow slot in circular waveguide into propagation of E_{0p} -waves', Digest of the Ukrainian Conference 'The main directions in development of radioelectronics, computational technique and communication', Kiev, 1973, p.30.
5. Nefedov E.I., Sivov A.N. 'Electrodynamics of periodical structures', M.: Nauka, 1977, 208 p.

SWITCHING HEMISPHERICAL ANTENNA ARRAY

E. V. Lukashuk, Y. V. Kolosova

271, Akademika Pavlova str., Kharkov, Ukraine, 61054
Open Joint Stock Company "Jsc Scientific Research Institute Of Radioengineering
Measurements" (OJSC "JSC SRIRM")
<common@niiri.kharkov.com>

Abstract

All known radio engineering systems, including of flight vehicles (FV) landing systems, (for example, airplanes, lowered space vehicles etc.) have one essential defect: in order to implements FV tracking the antenna systems (AS) should mechanically change the own azimuth and elevation, and radiation pattern (RP) should move in space with large speed reaching 40 Hz. It is known, that any mechanical movement is connected both with the power expenses, and with operational expenses.

Evidently solution of a problem is: FV tracking by means of phased antenna arrays (PAA) meet the troubles caused their very high cost. In present article it is offered to combine rather low cost of mechanical moving antennas with fast non-mechanical steering of RP by development of switching hemispherical PAA (HPAA) which characteristics are identical to the characteristics of antenna with mechanical steering of RP.

1. INTRODUCTION

The proposed antenna array is made of the ring antenna arrays with variable radius both in azimuth and in elevation. We shall consider the principle of the operation of the offered antenna on an example of one-ring switching antenna array (OSAA).

The proposed variant of the ring antenna array (RAA) concerns to the commutative class of ones. Distinctive feature of RAA is that the commutative (discrete) phase shifters (PS) are not used in it. The necessary phase ratios are provided by fixed PS's, which sequentially connected to the group of antenna elements (AE) by means of electronic commutator, thus forming required RP in defined direction. If it is required to find only one angular coordinate, for example azimuthal one, the offered variant of RAA can consist of one ring [1]. If it is required to increase an amplification factor, RAA can consist of two and more rings. If it is required to determine both angular coordinates, the offered variant of RAA should have two co-perpendicular ring arrays, which place on a spherical surface, as it was proposed in [2]. In difference from RAA offered in [3], in which for the circle scanning the expensive Battler matrix is used, in offered RAA the set of fixed PS representing set of simple and cheap microstrip delay lines is used. Rather close prototype offered RAA is the circle antenna array [4]. However in it the principle of feeding in pairs of opposite AE and controlled PS that has high price used. Ring antennas offered in [5] and [6] have also the similar disadvantages. Therefore, taking into account advantages and disadvantages of already developed ring (commutative and analogue) antenna arrays, the following variant of RAA is offered.

2. FORMULATION OF THE PROBLEM

In order to bearing FV, the width of a main lobe of RP on a level minus 3 dB β_A , ε_A should be:

- If scanning is carried out only in horizontal plane:

$$\begin{aligned}\beta_A &\leq \beta_{Ac} \\ \varepsilon_A &= \varepsilon_{AE}\end{aligned}\quad (1)$$

- If scanning is carried out only in vertical plane:

$$\begin{aligned}\beta_A &\leq \beta_{AE} \\ \varepsilon_A &= \varepsilon_{Ac}\end{aligned}\quad (2)$$

where ε_{A3} , β_{A3} are the specific angular sectors on azimuth and elevation defined by the requirements to accuracy of coordinates calculation, ε_{AE} is the width of RP of antenna element.

As the expressions (1) and (2) correspond to fan-shaped RP, for their implementation is not necessarily to excite antenna elements (AE) on all hemispherical surface of HPAA, but it is enough to excite two orthogonal ring AA(RAA) (Fig. 1).

The radius of RAA can be calculated from conditions:

- Required accuracy of positioning of a main lobe RP;
 - Required accuracy of a bearing determination.
- If to limit by known ways of scanning by means of controlled PS, then for overlap, for example, sectors $\beta_c \times \varepsilon_c = \pm 60^\circ \times 20^\circ$ are necessary to have not less $n_k \times 1200$ phase discrete (can be recurring), and also the same number of AE and PS, where n_k is the

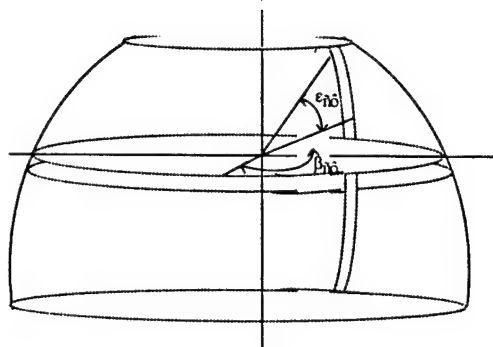


Fig. 1.

number of rings AE. Therefore to estimate n_k parameter it is expedient to evaluate the selectivity in space of RAA, which has not the controlled PS. An evaluation of selectivity of developed RAA we shall make on one-ring AA as an example. Consideration other RAA will differ only by frequency band and accordingly by radius.

It is known, that RP formed by OSAA with a main lobe direction $\theta = \theta_0$ and $\varphi = \varphi_0$ can be expressed as [5]:

$$F(\theta, \varphi) = \left| \sum_{n=1}^{N_{AE}} f_n(\theta, \varphi) I_n \exp[-jka(\sin \theta_0 \times \right. \quad (5)$$

$$\left. \times \cos(\varphi_0 - \varphi_n) - \sin \theta \cos(\varphi - \varphi_0)) \right|,$$

where N_{AE} is AE number; $f_n(\theta, \varphi)$ is the RP of separate n -th AE; I_n is a current amplitude of n -th AE; $a = r_i$ is a ring radius.

If AE are identical [$f_n(\theta, \varphi) = \text{const}(r)$], isotropic [$f_n(\theta, \varphi) = 1$], and are excited by currents with identical amplitudes ($I_n = 1$), the RP of OSAA is expressed as:

$$F(\theta, \varphi) = \left| N_{AE} \sum_{m=-\infty}^{\infty} J_{mN} (k\rho^{-jmN(\pi/2+\chi)}) \right|, \quad (6)$$

where

$$\rho = a\sqrt{(\sin \theta \cos \varphi - \sin \theta_0 \cos \varphi_0)^2 + (\sin \theta \sin \varphi - \sin \theta_0 \sin \varphi_0)^2};$$

$$\chi = \arccos \frac{a(\sin \theta \cos \varphi - \sin \theta_0 \cos \varphi_0)}{\rho}.$$

If the number of N_{AE} is rather great ($N_{AE} > 10$), and diameter of a ring $2a$ not so large, then RP of OSAA is well described by the first member of the sum from (6), i.e.

$$F(\theta, \varphi) \approx J_0(k\rho). \quad (7)$$

To improve accuracy it is possible to take into account the correction members

$$F(\theta, \varphi) \approx J_0(k\rho) + \Delta F, \quad (8)$$

where

$$\Delta F = \begin{cases} 2J_{N_{AE}}(k\rho) \cos[(\pi/2 - \chi)N_{AE}], \\ j2J_{N_{AE}}(k\rho) \cos[(\pi/2 - \chi)N_{AE}]. \end{cases} \quad (9)$$

Width of RP in a horizontal plane depends a little on angles θ_0 and φ_0 , and, with increasing N_{AE} , the

more poorly this dependence appears. However in vertical plane the width of RP θ_A^B varies significantly:

$$F(\theta, \varphi = 0) = J_0[ka(\sin \theta - \sin \theta_0)]. \quad (10)$$

From expressions (5-9) follows, that the OSAA selectivity is worse than selectivity of a linear AA (LAA), which has the same overall dimensions.

These caused by the following reasons:

- appearance of square-law(quadratic) phase distribution on LLA aperture, being an equivalent to sector AA, i.e. part of a ring RAA;
- increasing of side lobes level and decreasing of amplification because of various orientation of main lobes of AE, which are forming OSAA;
- non-equidistant allocation of AE projections over the LAA aperture, resulting to increasing the density of these projections on the ends of the LAA that is equivalent to appearance of amplitudes distribution (AD), increasing on edges of the aperture.
- All listed above results to RP extension (θ_A) and to growth of side radiation (Fs) of OSAA in comparison with LAA.

To improve OSAA selectivity in a horizontal plane it is proposed:

- in order to decrease the side radiation caused by non-parallelisms of main lobes of AE, which forms OSAA, we propose to realize the AE as antenna units (AU), consisting of two antenna radiators (AR), which are remote from each other on distance d_E . On input of one AR is attached fixed phase shifter ensuring FD over the AU aperture, which provides the turn of AU main lobe to θ_i angle, thus ensure a parallelism of θ_{mi} directions;
- the quadratic-law phase distribution is eliminate through the connection of i -th AU output to phase shifter with the fixed phase (Φ_i);
- to decrease influence of non-equidistant AU allocation over LLA aperture, the so-called RP digital steering is implemented; this approach is similar to [6] and presume to install the low-noise amplifiers (LNA), which have regulated, but fixed amplification.

The offered OSAA allows one to improve the RAA selectivity in comparison with known ones.

It is known that in air motion control (AMC) service the plenty of radio electronic systems is used. In particular, it is possible to use OSAA, in which one of HPAA rings is used as elevation radio beacon (ERB). At the same time, if the radius of sphere is calculated, then the calculation of geometrical parameters OSAA for ERB is reduced to calculation only of moving elevation sector ϵ_{se} , within of which RP with specific width of a main lobe(on a level of minus 3 dB) is formed. Analytically factor of RP OSAA, composed from AE (for example, as vibrators with improved selectivity), is written as:

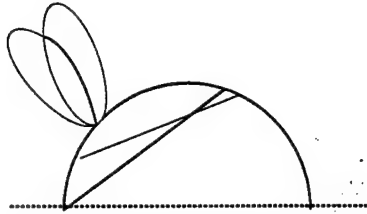


Fig. 2.

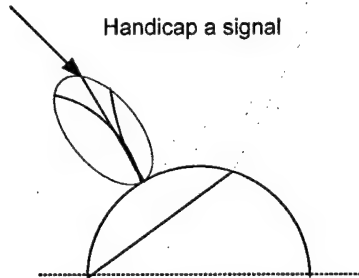


Fig. 3.

$$F_C = \sum_{i=0}^{N_m-1} a_i F_{h_i} \exp(-jk d_{ki} \sin \theta) \quad (11)$$

where: a_i is the weight coefficients of amplitude distribution on LAA.

$$\begin{aligned} F_{1i} &= \sum_{q=0}^1 \exp(-jk d_{E q} |(\sin \theta - \sin \theta_i)|) = \\ &= 1 + \exp(-j0,5 \kappa d_E |(\sin \theta - \sin \theta_i)|) = \\ &= \cos(0,5 \kappa d_E (\sin \theta - \sin \theta_i)); \end{aligned} \quad (12)$$

$d_{ri} = R(1 - \cos \beta_i)$ – distance between AU phase centers on LAA aperture; β_i is the angle from radius-vector of 1-st AU up to radius-vector of i -th AU; d_{\bullet} is the distance between phase centers of AR, formed AU: $d_E = \iota_B + 0,1\lambda$; ι_B is the length of the radiator (for example, vibrator) in a plane of a circle; the value $0,1\lambda$ undertakes from a condition of weakening of mutual influence AI and geometrical placement of AI within the antenna unit; θ_i is the angle, on which it is necessary to turn a main maxima of RP AU; ($\theta_i = \beta_i - 90^\circ$), to ensure parallelism of their directions.

For numerical assessments the ratio (11) and following parameters (Fig. 1) was taken:

$$N_M = \begin{cases} 105 & \text{– in a horizontal plane,} \\ 6 & \text{– in a vertical plane,} \end{cases}$$

$f = 5$ GHz ($\lambda = 60$ mm); $\iota_B = 0,48\lambda$; $d_E = 0,58\lambda$; d_{ri} are depends on R and, are determined in RP calculation process.

The executed calculations have shown, that:

1. RP in horizontal and vertical planes is symmetric relative to it's main maxima.
2. Width of RP main lobe lies in bounds:

- In a horizontal plane: $\varphi_A^\beta < 1^\circ$;
- In a vertical plane: $\theta_A^\beta < 20^\circ$.

3. The maximum level of aside lobes has the value:

- In a horizontal plane:
at uniform amplitude distribution: $F_\sigma^\beta < -11$ dB;
at digital (optimal) method of amplitude distribution steering: $F_{\sigma opt}^\beta < -17,63$ dB; the optimal amplitude distribution given to one from possible functions:

$$A_i = 20 \left[1 - (1 - t) \left(i/52 - 1 \right)^2 \right],$$

where t is the value of 'pedestal' on the edge of OSAA.

- In a vertical plane:
at uniform amplitude distribution $F_\sigma^\epsilon < -12$ dB;
at digital (optimal) method of amplitude distribution steering: $F_{\sigma opt}^\epsilon < -35,6$ dB; the optimal amplitude distribution is prescribe with the following coefficients: $A_{1,6} = 1$; $A_{2,5} = 7$; $A_{3,4} = 14,5$.

RP OSAA for ERB is described in a vertical plane by the same expression (11) and is similarly to RP OSAA ARB in a horizontal plane. In a vertical plane because of uses one ring SAA, it RP coincides with RP of a single AE.

3. CONCLUSION

The speed of action offered RAA does not concede modern phased AA, but its cost is significantly cheaper. If to use multi-entry AE, the creation two-beam RP is possible, which main maximum are biased on a half of RP width (on a half power level). It indicates possibility of implementation of a monopulse amplitude direction-finding (Fig. 2), as it is offered in [7, 8], and the possibility of creation of nulls in interference direction, as is offered in [9] (Fig. 3).

REFERENCES

1. Patent SU 1238182 A1. 3827527/24-09/ 19.12.84 15.06.86, № 22. A.F. Chaplin, M.D. Buchackiy/ 4H OIQ 21/20 ring dipole antenna (in Russian).
2. D. I. Voskresenskiy, L. I. Ponamarev, V. S. Filipov. Convex scanning antenna (in Russian) M.: Sovetskoe radio. – 1978. -302 pp.
3. A circular array configuration for simplifying multiplexing in radiocommunication antennas. Daires D.E.N., Guy J.R. F "Jnt. Symp. Dig. Antennas and propag., Albuguergue, N.M., may 24-28, 1982"
4. Japan A 62-69505 MKI HOIQ 3/24, 3/246, 21/20 Circular antenna system.
5. Inventors certificate, SU 1462440 A1. HOIQ 3/26 26.05.86, 28.02.89, № 8 Ring antenna (in Russian).
6. Japan A 63-217702 MKI HOIQ 3/30, 3/24, 21/06 Antenna system.
7. Japan MKI 4HOIQ 25/02, GOIS 13/44, HOIQ 21/24 Monopulse antenna.
8. Inventors certificate, SU 14642 25(JI) HOIQ 3/26 04.06.84, 07.03.89, № 9. V. A. Landman, A. A. Piotrovsky. Formirovanie mnogoluchevoy diagrammi s nezavisimim skanirovaniem luchey (in Russian)

A LINEAR DOLPH – CHEBYSHEV ANTENNA GRID FOR SPEAKING-TRUMPET RADIATORS

V. N. Bakhvalov, V. F. Kulishenko, E. V. Lukashuk

Joint stock venture "Scientific Research Institute For Radiotechnical Measurements"

<niri@cnti.kharkov.ua>

Abstract

The technical solution of the design of a linear Dolph-Chebyshev antenna grid of the speaking-trumpet radiators is proposed. This proposition is based on the application of special waveguide non-absorbing power elements used for installation of Dolph-Chebyshev amplitude distribution in the grid speaking-trumpets.

The receiving-transmitting antennas with narrow direction diagram (DD) on azimuth and relatively wide DD on location angle are widely used in radiolocation and other radiotechnical systems. For example, linear antenna grid which looks like horizontal line of pyramidal speaking-trumpet radiators could be used as such antenna.

The development of a technical solution to decreasing the side radiation level on horizontal surface for such grid is the objective of our research.

The linear grid looks like horizontal line composed of N radiating elements of pyramidal shape, which operate on gap. Antenna operates in X – band on $\lambda = 0.032$ m wavelength. The size of grid aperture is equal to $A = 1.0725$ m (width) and $a_p = 0.1143$ m (length). The size of speaking-trumpet radiating element aperture is equal to $b_p = 0.0268$ m (width) and $a_p = 0.1143$ m (length). The grid consists of $N = 40$ elements.

The grid is installed in the aperture of large E - sectors speaking-trumpet of relatively short length $B = 0.5$ m. This speaking-trumpet is required for optical supply of grid elements. At such relatively short length of large E - sector speaking-trumpet phase distortions of a field on aperture edges are inevitable. However, such distortions are not hazardous and do not have any significant meaning, because they can be easily compensated by the selection of appropriate parameters of rectangular waveguide of each speaking-trumpet radiating elements.

Because of that, we can apply E - sector speaking-trumpet, which length is significantly smaller than the horizontal size of the grid aperture. Large E - sector speaking-trumpet is supplied by mutual rectangular waveguide. In addition, polarization of radio waves is horizontal.

Our calculations show that such sin-phase grid with almost uniform amplitude distribution on its length has quite poor direction performance. Even though DD on azimuth of 1.6° of this grid is relatively narrow, such result is obtained at the expense of unacceptably high level of side radiation of -16 dB. Grid DD in vertical surface has 20° width and appropriate level of side radiation of -24 dB, which is quite satisfying.

Our calculations demonstrate the need in development of new technical solution on decreasing of side radiation level of linear grid on horizontal surface. One of the ideas on such development is discussed below.

The idea is based on the application of well-known Dolph – Chebyshev amplitude distribution [1, 2], used in sin-phase vibrator linear antenna grid. Currents in vibrators are set based on that distribution, so the required low level of side radiation is obtained with their help. However, it is difficult to apply directly this well-known solution to the considered linear speaking-trumpet grid. The explanations of those difficulties are provided below. Radiating elements of linear grid do not have any devices for weakening of currents (fields) amplitude in them. Additional introduction of fields weakening devices could lead to big loss in transmitter power; therefore, it is not expedient to use those devices based on design and energy reasons.

The goal is to obtain low level of side radiation on horizontal surface in the considered linear grid by installing Dolph – Chebyshev amplitude distribution in its radiating elements. We need to develop special devices, which will pass to radiating grid elements only part of energy falling on them without absorbing the heat of residual energy in those devices. Therefore, we need the devices, which change the general load of waveguide-feeder device without energy absorption.

The design of the device for passing to radiating grid elements only part of energy falling on it is presented below.

The simplified design of proposed radiating grid element is presented on Fig. 1.

Radiating grid element is pyramidal of b_p aperture size (width) and a_p (length). This speaking-trumpet is supplied by rectangular wave-guide. Polarization of radio waves is horizontal.

Signal amplitude changing device in radiating grid element is mobile section of waveguide. This device can rotate along vertical axis of the grid radiator. Basic section of this device is designed as rectangular waveguide part. That section is bounded on its edges

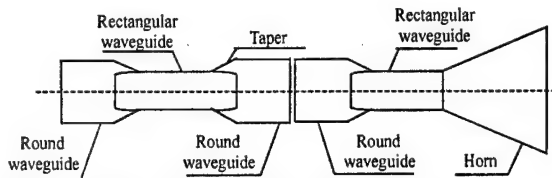


Fig. 1. Draft of the element of the antenna array.

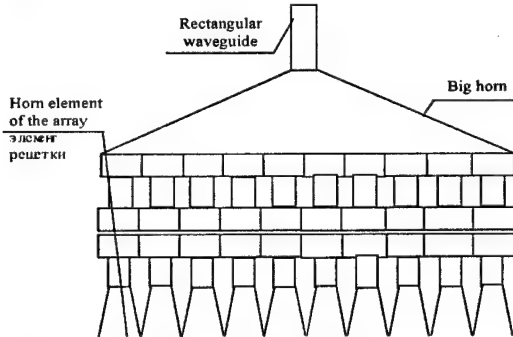


Fig. 2. Draft of the antenna array.

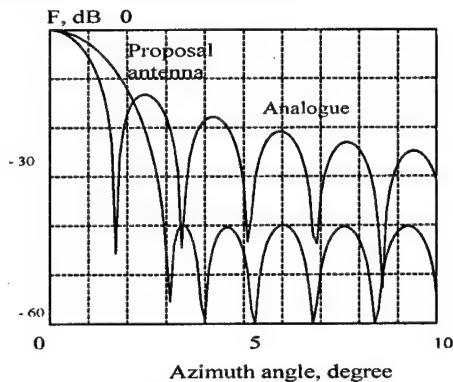


Fig. 3. Patterns of the antenna arrays.

with two section of round waveguide of d diameter. The bound is implemented through regular waveguide transitions from rectangular waveguide to round one.

In the end of the rectangular waveguide of speaking-trumpet grid element, a part of circular waveguide (the transition from rectangular waveguide to circular one is used again) is also installed. Circular waveguides are needed for a connection of the immobile element part with mobile one.

The connection between the mobile and the immobile parts of the element can be either contact or contact-less. We should note that the mobile section of waveguide should be rotated only if it is needed for antenna tuning during its manufacturing; after that, it can be soldered (welded) to the immobile section.

If the mobile section of rectangular waveguide is not tilted to the vertical axis, then waveguide will pass all energy to radiating element. If waveguide is tilted on 90° , then it will not pass any energy. If we choose pitch to α_m vertical axis, then we can change field amplitude on aperture of radiating grid element in long interval starting from zero to maximal possible value.

We propose to set α_m pitch angles of mobile waveguide sections to vertical axis in a way that field amplitude on apertures of radiating grid elements are distributed according to Dolph – Chebyshev distribution law.

So we need to set α_m pitch angles in compliance to the formula:

$$\alpha_m = \arccos \sqrt{\frac{\sqrt{B^2 + b_p^2 (m - 1/2)^2}}{\sqrt{B^2 + b_p^2 / 4}}} A_m,$$

where b_p is the horizontal aperture size of radiating grid element; m is the number of radiating grid elements (we define numbers by counting from aperture center to the right and left; overall number of grid elements is equal to $2M$); B is the length of large; E is the sector speaking-trumpet of grid radiation; A_m is the normed coefficient of Dolph – Chebyshev distribution [1, 2].

Simplified design of proposed linear speaking-trumpet grid with low level of side radiation on horizontal surface is presented on Fig. 2. We install additional mobile waveguide sections, which angles of pitch to vertical axis are defined by the formula given above, in the proposed grid between radiating element and large E - sector speaking-trumpet of grid radiation.

DD on horizontal surface of proposed linear speaking-trumpet grid is defined approximately by the following formula

$$F(\beta) = \frac{1 + \cos \beta \sin \left(\frac{\pi b_p}{\lambda} \sin \beta \right)}{2 \frac{(\pi b_p / \lambda) \sin \beta}{\sin \beta}} \times \sum_{m=1}^M A_m \cos \left\{ \left(\frac{\pi b_p}{\lambda} \right) (m - 0,5) \sin \beta \right\},$$

in which all of acronyms are explained above.

Example of calculations for DD of proposed linear grid on horizontal surface is presented on Fig. 3.

Calculations are made for the linear grid containing 40 radiating elements ($M = 20$) on wavelength $\lambda = 0.032$ m, and the grid size is given above. The same figure also shows DD of a similar grid which has a uniform amplitude distribution, for the comparison purposes.

Fig. 3 shows that the side radiation level of the proposed linear grid on horizontal surface E does not exceed -40 dB. It is a much better parameter than the parameter of the grid with a uniform amplitude distribution. The DD width of the proposed grid on a horizontal surface is equal to 2° , which is slightly wider than for analog grid, but it is a trade-off for the low level of side radiation.

A similar antenna may be used, for example, in ship impulse radio-location system, designed for the detection of targets on sea surface, and the prevention of sea collisions. The low level of side radiation in such antenna is needed for elimination of false bearings on the side petals of DD antenna, because errors in direction-finding can lead to ships collisions.

Thus, the proposed technical solution of the design of linear speaking-trumpet antenna grid can be implemented in practice, and provide for the side radiation on horizontal surface which is not worse, than -40 dB. It can become a widely used design in radiolocation and other radio technical systems.

REFERENCES

1. Shifrin Ya.S. Antennae. – Kharkov: VIRT, 1976.
2. Aizenberg G.Z. USW antennae. M.: Svyazizdat, 1957.

LINEAR PHASED ANTENNA ARRAY WITH LOW LEVEL OF SIDE RADIATION

V. N. Bakhvalov, V. A. Burmasov, Yu. V. Klonova, Yu. V. Kolosova

Joint stock venture "Scientific Research Institute For Radiotechnical Measurements"
(JSC "NIIRI") <niiri@cnti.kharkov.ua>

Abstract

Technical solution of design of linear phased antenna array consisting of speaking-trumpet radiating elements with controlled phase-rotators and uniform amplitude distribution along the array is proposed. Low level of side radiation is provided by special shift of phase-rotators phases, which does not require any changes in grid design.

Receiving-transmitting antennas with narrow direction diagram (DD) on azimuth and relatively wide DD on location angle are widely used in radiolocation and other radiotechnical systems. For example, linear phased antenna array (PAA), which looks like horizontal line of speaking-trumpet radiating elements can be used as such an antenna.

Each element of PAA has controlled phase-rotator that provides electrical scanning on azimuth of DD beam.

Development of new technical solution for decreasing of side radiation level on horizontal surface for such PAA is the objective of our research.

Simplified design of PAA in two projections is presented on Fig. 1.

Linear PAA looks like horizontal line composed of N radiating elements of H-sector speaking-trumpets, which operate on gap. PAA operates in X-band on $\lambda = 0.032$ m wavelength. Each PAA element has the

phase-rotator installed, for example, ferrite phase-rotator. The size of PAA aperture is equal to $A = 0.9143$ m (width) and $a_p = 0.1143$ m (length). The size of speaking-trumpet radiating element aperture is equal to $b_p = 0.01145$ m (width) and $a_p = 0.1143$ m (length). PAA consists of $N = 80$ elements.

The linear PAA is installed in the aperture of large E-sectors speaking-trumpet of relatively short length $B = 0.5$ m. This speaking-trumpet is required for optical supply of array elements. At such a relatively short length of large E-sector speaking-trumpet, phase distortions of a field on aperture edges are inevitable. However, such distortions are not hazardous and do not have any significant meaning, because they can be easily compensated by controlled phase-rotators of the elements. Because of that, we can apply E-sector speaking-trumpet, which length is significantly smaller than horizontal size of PAA aperture. Large E-sector speaking-trumpet is supplied by rectangular waveguide with wide wall size $a = 0.0229$ m and narrow wall $b = 0.01145$ m. mutual rectangular waveguide. In addition, polarization of radio waves is horizontal.

Controlled phase-rotators are used in the elements of linear PAA for the following purposes:

- electrical scanning on azimuth of antenna DD;
- compensation of phase distortions of a field on aperture edges (that allows one to use large but short E-sector speaking-trumpet for radiation of PAA elements).

Our calculations show that directed parameters of such a linear PAA are mediocre. Even though DD on azimuth of 2° of such a PAA is relatively narrow one, such a result is obtained at the expense of unacceptably high level of side radiation of -15.5 dB. For example, almost the same level has sin-phase vibrator antenna array with uniform amplitude distribution, which means that worse parameters simply do not exist. PAA DD in

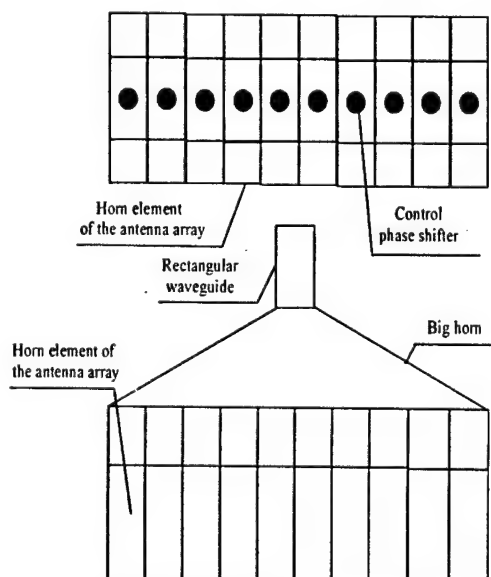


Fig. 1. Draft of the antenna array.

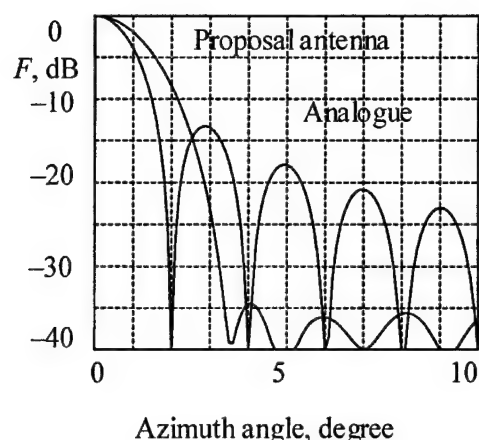


Fig. 2. Patterns of the antenna arrays

vertical surface has 20° width and appropriate level of side radiation of -24 dB, which is quite satisfying.

Our calculations demonstrate the need to develop a new technical solution to decrease side radiation level of linear PAA on horizontal surface. One of the ideas of such a development is discussed below.

The idea is based on the application of well-known Dolph-Chebyshev amplitude distribution [1, 2], used in sin-phase vibrator linear antenna array. The currents in vibrators are set based on that distribution, so the required low level of side radiation is obtained with their help. However, it is impossible to apply directly this well-known solution to the considered linear PAA. The explanations of those difficulties are provided below. The elements of linear PAA have only phase-rotators, and do not have any devices for weakening of currents (fields) amplitude in them. Additional introduction of fields weakening devices can lead to big loss in transmitter power; therefore, it is not expedient to use those devices based on design and energy reasons. Therefore, application of Dolph-Chebyshev distribution is still just a good idea, which is difficult to apply to the considered linear PAA.

The goal is to obtain low level of side radiation on horizontal surface in the considered linear PAA without any change in currents (fields) amplitude and radiation power of each PAA element by the use of only existing controlled phase-rotators. At first it seems to be impossible.

The scope of Dolph-Chebyshev distribution application is that this is radiation fields' intensity in the direction of element's axis, but not currents (fields) amplitude in PAA elements, which needs to be set in compliance to that distribution.

We propose to implement this idea as follows.

Elements of linear PAA are conditionally broken down into pairs, and number of pair is counted starting from the mid-point of aperture to the right and left. Shifts of phases are equal to

$$\varphi_m = \pm \arccos \left[\frac{\sqrt{B^2 + b_p^2 (2m-1)^2}}{\sqrt{B^2 + b_p^2}} A_m \right] + \frac{2\pi}{\lambda} \left[\sqrt{B^2 + b_p^2 (2m-1)^2} - \sqrt{B^2 + b_p^2} \right]$$

and are installed in each pair of elements with the help of controlled phase-rotators, where φ_m is the phases shift of controlled phase-rotator of m -pair of PAA radiating element (in the left half of PAA: "+" sign is assigned for the left element of the pair, "-" sign is assigned for the right element of the pair; in the right half of PAA it goes vice versa: "+" sign is assigned for the right element of the pair, "-" sign is assigned for the left element of the pair); m is the number of pair of radiating PAA elements (number of pair is counted starting from the mid-point of PAA aperture to the right and left; overall there are $2M$ of pair elements in PAD, $N = 4M$); B is the length of large E - sector speaking-trumpet of PAA radiation; λ is the wavelength; b_p is the size of PAA element measured on horizontal line of aperture; A_m is normed coefficient of Dolph-Chebyshev distribution [1, 2].

The idea of proposed technical solution on decreasing of side radiation of PAA can be easily explained from physics point of view.

With the help of controlled phase-rotators of PAA elements' pair DD beam of that pair can be slightly shifted to the right (left half of PAA) or left (right half of PAA), so that intensity of radiation field in the direction of PAA axis decreases slightly and receives a value which is proportional to appropriate Dolph-Chebyshev distribution coefficient. That allows one to apply effectively Dolph-Chebyshev distribution without loss in radiation power and change of field amplitude in the elements. Except for controlled phase-rotators installed in each PAA radiation elements, other elements are not needed for the implementation of our proposal.

A shift of beams of elements' pair to the right or left (depending on PAA half) does not lead to symmetry distortions of PAA DD and beam deviation of all PAA DD on azimuth.

Controlled phase-rotators are used for the following purposes in considered linear PAA:

- electrical scanning on azimuth of antenna DD;
- compensation of phase distortions of a field on aperture edges;
- development of Dolph-Chebyshev distribution of radiation intensity in the direction of element's axis by slight deviation of DD beam of elements' pair on azimuth.

Proposed linear PAA is an exact analog to PAA - analog on their design, which is demonstrated on Fig. 2. The only difference is in shifts of phases set in controlled PAA phase-rotators.

DD on horizontal surface of proposed linear PAA is defined approximately by the following formula:

$$\begin{aligned}
F(\beta) = & \frac{1 + \cos \beta}{2} \frac{\sin\left(\frac{\pi b_p}{\lambda} \sin \beta\right)}{\frac{\pi b_p}{\lambda} \sin \beta} \times \\
& \times \sum_{m=1}^M A_m \left\{ \cos\left(\frac{k b_p}{2} \sin \beta\right) \cos[k(2m-1)b_p \sin \beta] - \right. \\
& - j \operatorname{tg} \arccos \left[\frac{\sqrt{B^2 + b_p^2 (2m-1)^2}}{\sqrt{B^2 + b_p^2}} A_m \right] \times \\
& \times \sin\left(\frac{k b_p}{2} \sin \beta\right) \sin[k(2m-1)b_p \sin \beta] \Big\}.
\end{aligned}$$

Example of calculations for DD of proposed linear PAA on horizontal surface is presented in Fig. 3. Calculations are made for linear PAA of exactly the same design as of analog PAA mentioned above. The only differences are set phases in controlled phase-rotators. For comparison purposes the same figure also shows DD of analog PAA.

Fig. 2 shows that side radiation level of proposed linear PAA on horizontal surface E is equal to -35 B.

It is much better parameter than parameter of analog PAA. DD width of proposed PAA on horizontal surface is equal to 2.4° , that is slightly wider than for analog PAA, but that is a trade-off for low level of side radiation.

Thus proposed new technical solution can be implemented in practice, and provide for side radiation on horizontal surface which is not worse than -35 dB, and provide for acceptable level of side radiation on vertical surface of -24 dB. It can be become widely used design in radiolocation and other radio technical systems. This proposal can become widely used device in radiolocation and other radio technical systems.

REFERENCES:

1. Shifrin Ya.S. Antennae. - Kharkov: VIRT, 1976.
2. Aizenberg G.Z. USW antennae. - M.: Svyazizdat, 1957.

SUPPRESSION OF MUTUAL INFLUENCE OF ANTENNA CHANNELS, WHICH ACCOMPLISH SELF-POINTING GUIDED BY INFORMATION SIGNAL THROUGH GEOMETRIC RATIOS OPTIMIZATION OF IRRADIATORS CONSTRUCTION

Y. V. Kolosova, V. N. Rudenko, V. A. Burmasov

271, Akademika Pavlova str., Kharkov, Ukraine, 61054
Open Joint Stock Company "Jsc Scientific Research Institute of Radioengineering
Measurements" (Ojsc "Jsc Srim")
<common@niiri.kharkov.com>

Abstract

For realization of self-pointing with the help of mirror antennas of ground stations by an information signal it is necessary to have 4 irradiators minimum. All irradiators, as it is known, should be placed on a small distance from focal axis of a mirror for displacement of partial radiation patterns, which are forming direction-finding characteristic with the help total-differential systems. Therefore irradiators are in a zone of significant mutual influence, which can complicate both bearing and accuracy of self-pointing. Really, at exact pointing of the radiation patterns of the antenna on the flying device on one angular coordinate the interfering signal because of mutual influence of pair of irradiators, which define other angular coordinates, can appear and this will result in a failure of auto-support on first angular coordinate. Therefore, the development of ways of lessening mutual influence of antenna channels, which realize self-pointing by an information signal, is urgent. Usually, the mutual influence is estimated either as a factor of connection, or mutual resistance, concerned to it [1]. In the given work we shall consider a dependence of factor of connection (mutual resistance) from geometrical parameters and from mark of polarization of regular spiral antennas, and also from their mutual orientation.

Keywords: irradiator, spiral antenna, factor of connection.

1. INTRODUCTION

At realization of self-pointing by the information channel there is very important question of a mutual outcome both channels of self-pointing among themselves, and outcome between channels of self-pointing and basic receiving-transmitting information channel.

One of the main questions of easing of mutual influence is the choice of irradiator type both for the decision of a task of self-prompting, and in view of easing mutual influence of channels of self-pointing and basic information channels.

For realization of self-pointing by the information channel it is important to choose irradiators both by criterion of formation required radiation pattern (RP), and by criterion of a minimum of mutual influence.

The application of waveguide-horn antennas is limited by the following defects: the horns turn out bulky; they have linear polarization. The single dipole antennas have not directed RP in a plane H, that as is

essential defect. The dipoles with reflector are usually used for removal of this defect (such antennas widely applied as irradiator of mirrors and lenses). Advantage of the dipole irradiators is its small sizes, hence, insignificant shadowing of aperture. The dipole with reflector provides wide required RP ($70-100^\circ$). Spiral and log-periodic antennas are low- and middle-directed wide-band antennas of elliptic and linear polarization. They can be used as irradiators. However, dipole and log-periodic antennas have linear polarization, and realization of required circular polarization needs difficult system of summation and phasing. Therefore, it is expedient to use spiral aerials. The advantages of spiral antennas are: the rather small sizes; simplicity of the feeding; the good coordination; they provide radiation and reception of elliptical polarized fields in a wide range of frequencies. Thus, as irradiators of mirror antennas for reception of waves of elliptic polarization, that is typical for ground stations of reception of the information from a space vehicle, the application of spiral aerials is most

expedient. Therefore, we shall stop on consideration of a question of easing of mutual influence of antenna's channels, which realize self-pointing by an information signal by means of optimization of geometrical proportions of irradiator design.

2. FORMULATION OF THE PROBLEM

The mutual connection between irradiators of a mirror in the form of spiral antennas with various parameters can be essential. Let's consider the ways of reduction of mutual connection between irradiators in form of spiral antennas. In the given work we shall consider dependence of connection factor (mutual resistance) from geometrical parameters and from polarization mark of regular spiral antennas, and also from their mutual orientation.

For reception of parities, which establish interrelation of connection factor from d/λ and from geometrical parities of regular spiral antennas, the method, according to which the RP to each of the interconnected antennas can be submitted by function as $(\cos)^m$, where m – parameter of RP approximation of the single antenna, is used [4].

From [3] it is known, what RP width on half-capacity level is concerned with geometrical sizes (diameter of a spiral d , number of coils N , corner of winding α) by following parity:

$$(2\theta_{0.5})^\circ \cong \frac{85}{\sqrt{N \cdot k \cdot a \cdot \operatorname{tg} \alpha}}, \quad (1)$$

where $k = \frac{2 \cdot \pi}{\lambda}$.

If to show RP of the regular spiral antenna as $(\cos)^m$ and to use parities (1), it is possible to receive [1]:

$$m = \frac{-0.1506}{\lg \left[\cos \frac{0.74}{\sqrt{N \cdot k \cdot a \cdot \operatorname{tg} \alpha}} \right]}. \quad (2)$$

The expression for connection factor in a general form can be received, using [1 and 3]:

$$|Z_{vz}| = \frac{\Gamma(m+3/2)}{(kd/2)^{\frac{m+1}{2}+\frac{1}{4}}} \left(\left[J_{m+\frac{1}{2}}(kd) \right]^2 + \left[(kd/2)^{m-1/2} \frac{1}{\sqrt{\pi} \Gamma(m+1)} - H_{m+\frac{1}{2}}(kd) \right]^2 \right)^{1/2}, \quad (3)$$

where m is defined by a equation (2); $\Gamma(x)$ is the gamma-function; $J_\nu(x)$ is the Bessel function of ν -th order; $H_\nu(x)$ is the Struve function of ν -th order.

Obviously, the equation (3) taking into account with (2) establishes dependence of connection factors both from geometrical parameters, and from a mutual arrangement of two spiral antennas.

The equation (3) is exact one, however its analysis is difficult. With the purpose of simplification of the analysis we shall consider a sort of connection factor for asymptomatic cases of distance between elements.

At small distances between elements

$$\left(0 < \frac{d}{\lambda} < \frac{1}{2\pi} \right) \\ |Z_{vz}| \cong (kd/2)^{\frac{m+1}{2}+\frac{1}{4}} \sqrt{1 + \left((2/kd) \frac{\Gamma(m+\frac{3}{2})}{\sqrt{\pi} \Gamma(m+1)} \right)^2} \cong \\ \cong (kd/2)^{\frac{m+1}{2}+\frac{1}{4}} \frac{2}{kd} \frac{\Gamma(m+\frac{3}{2})}{\sqrt{\pi} \Gamma(m+1)} \times \\ \times \left[1 + \frac{1}{2} \left(\frac{kd}{2} \frac{\Gamma(m+1)\sqrt{\pi}}{\Gamma(m+\frac{3}{2})} \right)^2 \right] \quad (4)$$

From a equation (4) it is apparent that at a weak orientation of the spiral antenna ($m=1$) connection factor $|Z_{vz}|$ with growth of d/λ , i.e. distance between elements (not exceeding, however $1/2\pi$), decreases very slowly, not faster then $(kd)^{-1/4}$. If the orientation of the spiral antenna is characterized by value $m > 1$, then in limits $0 < \frac{d}{\lambda} < \frac{1}{2\pi}$ the value $|Z_{vz}|$ even little grows with a growth of d/λ .

At distances between elements, which are significant large than $1/2\pi$, which more often occur in practice (i.e. $d/\lambda \geq 0.4$), the equation (3) can be transformed to:

$$|Z_{vz}| = \frac{\Gamma(m+3/2)}{\sqrt{\pi} \cdot (kd/2)^{\frac{m+3}{2}+\frac{1}{4}}} \quad (5)$$

From a equation (5) it is visible, what even at a weak orientation of the spiral antenna ($m < 1$) connection factor decreases absolutely not more slowly, than $(kd)^{5/4}$. With an increasing of an orientation the mutual connection decreases even faster.

As parameter m is unequivocally associated to geometrical parameters of the spiral antenna by the equation (2), it is obvious, what with growth of N , ka and $\operatorname{tg} \alpha$ the value $|Z_{vz}|$ decreases.

The experiment has shown good concurrence of the settlement and experimental data of dependence $|Z_{vz}|$ from d/λ and N [1].

The technique of experiment organization consists in usage of the Kirgoff equations for measurement of connection factor.

It is known, that for two cooperating antennas, one of which is active, and other is passive, the Kirgoff equa-

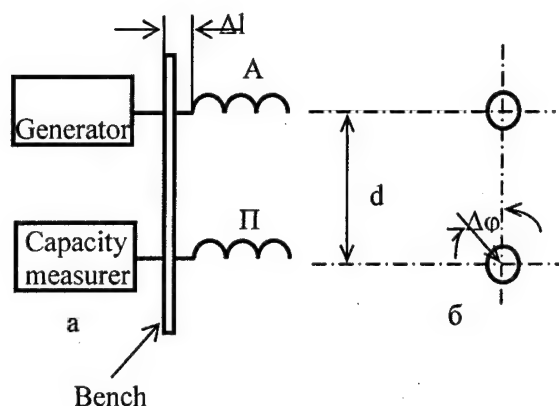


Fig. 1.

tions can be written down as follows:

$$\begin{aligned} U_A &= J_A \cdot Z_A + J_{II} \cdot Z_{vz}, \\ 0 &= J_A \cdot Z_{vz} + J_{II} \cdot Z_P, \end{aligned} \quad (6)$$

where U_A is equivalent to a feeding voltage on an input of the active aerial; J_A is the established current on the active antenna when passive antenna is present; J_{II} is the induced current in the passive antenna; $Z_{A(II)}$ is the own resistance of the single active (passive) antenna; Z_{vz} is the resistance to interrelation, which module is connection factor.

Obviously, the capacities, radiate (reradiate) by the active (passive) antenna, are proportional to squares of currents. If two cooperating antennas are identical, the parity is fairly:

$$\frac{P_{II}}{P_A} = \frac{J_{II}^2}{J_A^2} \quad (7)$$

Using equation (6) and (7), it is possible to obtain:

$$\frac{P_{II}}{P_A} = \left| \frac{Z_{vz}}{Z_{A(II)}} \right|^2, \text{ e.g. } |Z_{vz}|^2 \equiv \frac{P_{II}}{P_A} \quad (8)$$

From (8) it is evident, that if $Z_{A(II)}$ is known and if ratio of capacities $\frac{P_{II}}{P_A}$, have been measured, it is possible to obtain unequivocally the value of a square of connection factor.

The experimental plant is assembled from the generator, capacity measuring device, test bench with two moving from each other spiral antennas (Fig. 1). In the same figure the basic geometrical parameters of spiral antennas are shown:

Δl is the length of stimulating junction;

$\Delta\varphi$ is the corner of mutual orientation of the first coils of active and passive spiral antennas;

d is the distance between active and passive antennas.

For reduction of P_A and P_{II} measurement errors both capacities were measured with the help of the same measurer in power feeder by measuring of maximal and minimum levels of field intensity with the subsequent of calculation arithmetic-mean.

The results of experiments are processed and it is possible to make the following conclusions:

1. At measuring of dependence $|Z_{vz}|^2$ from distance between spiral antennas, when $\Delta l/\lambda = 0,2$, $N=7$, from various orientation of the first coil ($\Delta\varphi = 0, 90, 180^\circ$) and from a various polarization mark of active and passive antennas. Is founded, what at identical orientation of the first coils ($\Delta\varphi = 0$) the square of connection factor decreases with accuracy of constant multiplier when d/λ is growth, and it repeat a theoretical parity (5). When $\Delta\varphi = 180^\circ$ connection factor decreases not monotonously, and it has some rise in area $\Delta l/\lambda = 1,5$; however, in all range $0,4 \leq \Delta l/\lambda \leq 1,8$ where it changing it remains less, than when $\Delta\varphi = 0^\circ$.

2. Square of connection factor accepts the least value when $\Delta\varphi = 90^\circ$, it is more then in 6 times less when $\Delta\varphi = 0^\circ$, it is more then in 2times less when $\Delta\varphi = 180^\circ$ in all range of change $\Delta l/\lambda$.

3. Change of polarization mark simultaneously at both antennas does not result in appreciable changes of $|Z_{vz}|^2$.

4. We measured the dependences $|Z_{vz}|^2$ on quantity of spiral coils for a case when connection is maximal and $\Delta\varphi = 0^\circ$ at the following values: $d/\lambda = 0,72; 1,27$, $\Delta l/\lambda = 0,2$. It has been obtained, that when $d/\lambda = 0,72$ and $N = 5 \div 7$, some increase of connection is observed, and when $d/\lambda = 1,27$ such an increase of connection is observed in area $N = 3 \div 6$, and the connection of hetero-polarized antennas is stronger, than in spiral antennas with the same mark of polarization (one-polarized antennas).

5. We measured the dependences $|Z_{vz}|^2$ on length of stimulating transition $\Delta l/\lambda$. It has been obtained, that the minimal connection is observed when $\Delta l/\lambda \approx 0,3$, both for hetero- and for one-polarized antennas. Maximal connection is observed, when $\Delta l/\lambda = 0,2$ and $0,4$.

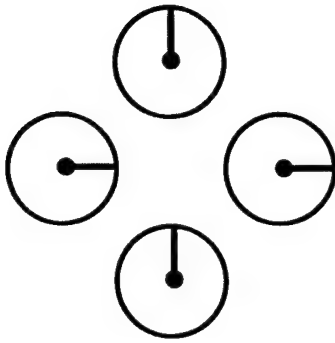


Fig. 2.

6. We measured the dependences $|Z_{\text{vz}}|^2$ on mutual orientation of the first coil of spiral antennas. It has been obtained, that minimal connection of hetero-polarized antennas is observed when $\Delta\varphi = 90^\circ$, and of one-polarized antennas at 135° (-45°) for right-polarized and at $+45^\circ$ for left-polarized antennas.

3. CONCLUSION

In this work the theoretical equations of dependence of the mutual resistance module (connection factor) from the geometrical sizes, mutual orientation and mark of polarization of two regular spiral aeri-als are obtained. The carried out experiment has confirmed the received settlement equations. As a result of experiment it has been established, that the mutual connection essentially depends on length of stimulating junction and from mutual orientation of the first coil

of a spiral. It has been marked, that the minimal connection is observed when size of stimulating junction is $\Delta l/\lambda = 0,3$, and orientation of the first coil of a spiral is 90° for the one-polarized antennas. With a growth of number of coils the mutual connection tends to decrease.

Hence, at easing of mutual influence of antenna channels, which realize self-pointing on an information signal by optimization of geometrical parities of irradiator design, it is expedient to set irradiators as shown in a Fig. 2.

Such an orientation allows one, at first, to keep phase synchronism of irradiator pairs, which realize a monopulse method of direction-finding in each channel of self-pointing, and secondly, to reduce mutual influence between channels up to a minimum.

REFERENCES

1. V. N. Rudenko, L.F. Korzh. L.F. Korbut / Vzaimnaya svyaz mezhdu regul'yarnymi spiral'nymi antennami. Voprosi postroeniya fazirivannih antennih reshotok. Minsk. -1972. 57 pp. (in Russian)
2. V. N. Loverov, V.E. Yamaykin, V.N. Kovalev, O.A. Yurcev, V.N. Rudenko, A.V. Runov. Osnovi proektirovaniya anrennih ustroystv SHF. part.1, Minsk, -1970, 545pp.
3. V. N. Yurcev, A.V. Runov, A.N. Kazarin. Spiral Antennas. Moscow: Sov. Radio. -1974.
4. O. G. Vendik. Antenny s nemehanicheskim dvizheniem luchu. Moscow: Sov. Radio 1965.

PERISCOPE ANTENNA RERADIATOR BASED ON TWO COUPLED ARRAYS

V. I. Zamiatin, A. V. Perekaty, Y. V. Yefimova

Ukraine, 61054, Kharkov, Ak. Pavlova-str., 271, <common@niiri.kharkov.com>
OJSC «AO Scientific research institute of radio measurements», (OJSC «AO NIIRI»)

Abstract

Planar structures reradiating electromagnetic waves are widely used now. Such structures can be seen as planar analogues of reflector antennas. One of perspective variants of their application may be a planar horizontal reradiator of periscope antenna system. The present paper suggests a variant of reradiating structure with longitudinal-broadside radiation. The suggested structure is simple and manufacturable. Its application as horizontal reradiator for periscope antenna system (PAS) will simplify the design considerably due to load reduction.

Periscope antenna systems (PAS), used in radio communication, are large stationary structures. But application of horizontal reradiating array in such structure as reradiator allows simplifying reradiator bearing-lifting gear. At that, basic requirement is capability of reradiator to re-emit power in direction longitudinal to its plane. The second part of the paper introduces PAS reradiator structure on the basis of two coupled antenna arrays. The suggested methods of calculation are supported by experimental investigation of model of the reradiating structure.

Keywords: planar antenna, reradiating structure.

INTRODUCTION

Now various planar antenna systems are widely used. For instance, planar analogues of reflector antennas based on phased arrays are applied in satellite television systems, Internet and communication systems [1]. Such arrays are structures with radiators placed on the plane. Changing the shape and features of reradiators it is possible to make the structure reradiate arriving electromagnetic wave in the required direction. Often it is necessary to reradiate the wave in direction longitudinal to structure plane. For instance, in periscope systems replacement of vertical reradiator with horizontal one with longitudinal reradiation provides significant gain in reradiator lifting gear.

The suggested reradiating structure may be a considerable support in accomplishing this task. Operation principle of the suggested reradiating structure consists in capability to reradiate the received electromagnetic wave (EMW) in the specified direction. One of features of the described structure is the capability to reradiate normally falling EMW in direction, which is longitudinal relative to the structure plane. Such reradiation scheme is often used in conformal antenna structures.

PART 1

Let us consider reradiating structure, which consists of half-wave dipoles, placed on plane dielectric surface (Fig.1). It is a planar equispaced array with half-wave diode as elementary radiator. Array spacing is similar in rows and columns and equals a half of wave length.

Number of radiators in columns is N , number of rows is M . At that, adjacent dipoles in rows are turned to opposite sides at angle $\alpha = 45^\circ$ (Fig. 2), and in columns they are oriented in a similar way. Antenna array is radiated by E-sector horn, placed in the same plane.

Antenna array directional pattern calculation is not possible according to Bonch-Bruyevich law, i.e. sepa-

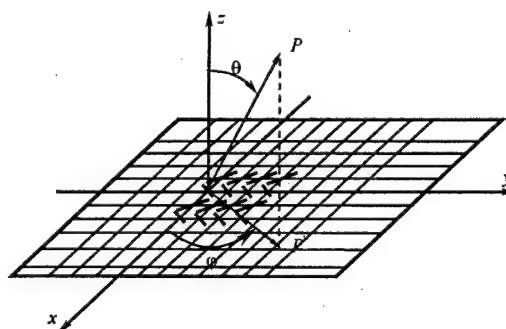


Fig. 1.

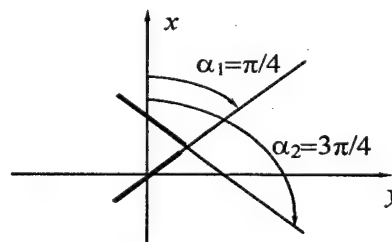


Fig. 2.

rate radiators are oriented unequally. That's why we will consider the system containing two nested arrays, placed in plane XOY .

Each array is a two-dimensional equispaced array, which consists of half-wave dipoles. Elements of each array are placed in straight-line graticube nodes with spacing dx , dy . Array spacing is equal, centers of one and other arrays are shifted from coordinate origin by $dx1$, $dy1$, $dx2$, $dy2$. The elements are turned relative to axis X by angles α_1 and α_2 .

Let's add spherical coordinates system r , θ , φ , where r – range from coordinate origin to sighting point, θ – angle between axis Z and direction to sighting point, and φ – angle between X axis and sighting point projection to plane XOY Fig. 1.

To determine directional pattern of a separate subarray element we will use the known ratio [3]. Let's consider that dipole is characterized by certain current vector located in plane XOY .

This current vector can be represented as:

$$\vec{i}_1 = (\vec{x}_0 \cos \alpha_1 + \vec{y}_0 \sin \alpha_1) \cos \alpha_1 \quad (1)$$

for the first subarray and

$$\vec{i}_2 = (\vec{x}_0 \cos \alpha_2 + \vec{y}_0 \sin \alpha_2) \cos \alpha_2 \quad (2)$$

for the second subarray. At that, functions of \cos and \sin in brackets determine dipole position at XOY plane, and \cos out of brackets – dipole position relative to electric field vector, inducing current in it.

Let us use the method based on vector and scalar potential to estimate the field in the dipole far zone. We know, that vector potential can be specified as [3]:

$$\vec{A} = \frac{\mu_a}{4\pi} \int_{-1/2}^{1/2} \frac{\vec{i} dl}{r} \approx \frac{\mu_a \vec{i}}{4\pi r} \quad (3)$$

where: μ_a is the absolute magnetic permeability; \vec{i} is the dipole with induced current i ; r is the range to sighting point.

Performing the known conversions [3] we obtain:

$$\vec{H} = \frac{1}{\mu_a} \text{rot} \vec{A} = \text{const}(r) \vec{r}^0 \times \vec{i}. \quad (4)$$

As we are interested only in directional pattern, multiplier, depending on range from sighting point ($\text{const}(r)$), can be omitted. Hence, after normalization and designating the normalized vector of magnetic intensity as \vec{h} , we receive:

$$\vec{h} = \vec{r}^0 \times \vec{i}, \quad (5)$$

where: $\vec{r}^0 = \vec{x}_0 \sin \theta \cos \varphi + \vec{y}_0 \sin \theta \sin \varphi + \vec{z}_0 \cos \theta$ – direction to sighting point.

We determine dipole field of the first subarray:

$$\vec{h}_1 = \begin{vmatrix} \vec{x}_0 & \vec{y}_0 & \vec{z}_0 \\ \sin \theta \cos \varphi & \sin \theta \sin \varphi & \cos \theta \\ \cos \alpha_1 & \sin \alpha_1 & 0 \end{vmatrix} \quad (6)$$

The same way we determine dipole field of the second subarray

$$\vec{h}_2 = \begin{vmatrix} \vec{x}_0 & \vec{y}_0 & \vec{z}_0 \\ \sin \theta \cos \varphi & \sin \theta \sin \varphi & \cos \theta \\ \cos \alpha_2 & \sin \alpha_2 & 0 \end{vmatrix}. \quad (7)$$

Let's determine subarray system multipliers.

$$f_{sis_1}(\theta, \varphi) = \sum_{m=0}^{M-1} \sum_{n=0}^{N-1} \exp(jk \vec{\rho}_{mn} \vec{r}_0), \quad (8)$$

where $k = 2\pi/\lambda$; $\vec{\rho}_{mn} = \vec{x}_0 [dx1 + m dx] + \vec{y}_0 [dy1 + n dy]$ – for the first subarray and $\vec{\rho}_{mn} = \vec{x}_0 [dx2 + m dx] + \vec{y}_0 [dy2 + n dy]$ – for the second subarray.

Correspondingly subarray vector diagrams

$$\begin{cases} \vec{f}_1(\theta, \varphi) = \vec{h}_1 f_{sis_1}; \\ \vec{f}_2(\theta, \varphi) = \vec{h}_2 f_{sis_2}. \end{cases} \quad (9)$$

To determine scalar expression for subarray directional pattern it is necessary to perform coordinatewise addition of subarray fields and take a module of it:

$$\begin{cases} f_x = h_{x1} \cdot f_{sis1} + h_{x2} \cdot f_{sis2}, \\ f_y = h_{y1} \cdot f_{sis1} + h_{y2} \cdot f_{sis2}, \\ f_z = h_{z1} \cdot f_{sis1} + h_{z2} \cdot f_{sis2}, \end{cases} \quad (10)$$

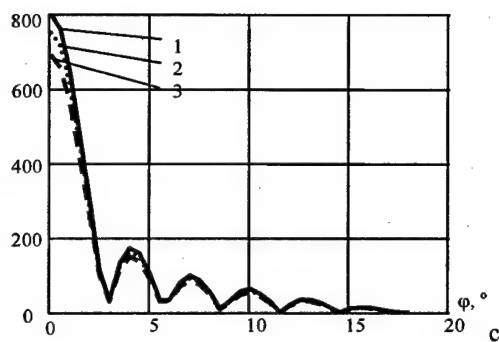
$$F = \sqrt{f_x^2 + f_y^2 + f_z^2}. \quad (11)$$

According to the stated methods directional pattern calculation of subarray, including 20 rows and 40 columns, was carried out. Fig.3 represents subarray directional patterns for three variants of dipole positions.

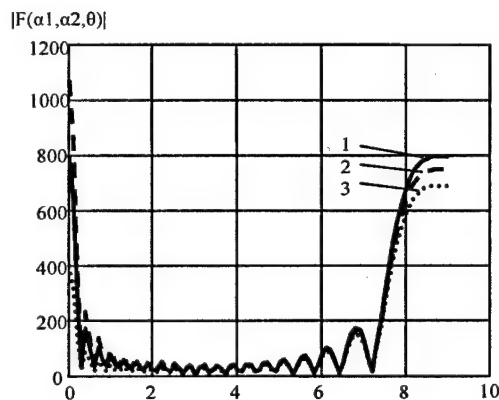
In the first case adjacent dipoles are turned relative to each other by the angle of 45° . At that, directional pattern main lobe is jammed to array surface and has narrow shape in horizontal plane and wide shape in vertical plane (Fig. 4). Back lobe has the same size as main one. There is also a narrow diffraction maximum, directed vertically in normal direction relative to array plane. In the case, stated in Fig. 3 with number 2, adjacent dipoles have an angle of 70° between each other. At that, as per the first case, array directional pattern has the same shape, but DP main lobe is lower in amplitude. Amplitude value of diffraction maximum is higher. In the third case, the angle between dipoles is 110° . DP shape is similar to the first and second variants, though it is lower in amplitude.

Hence, dipoles orientation change relative to the first variant of position when the degree of 45° between them leads to DP decrease, as part of power changes to diffraction maximum or to lobe at cross polarization.

Availability of high diffraction lobe, equal to main lobe in level, makes the structure of little use at single-layer application. The percent of power leakage (not intercepted by the structure). This lack can be corrected using additional layer of the same structure mixed relative to the first one at the range of $\lambda/4$.



a)



b)

Fig. 3. Nonstandardized directional pattern of subarray includes 1600 dipoles: a) in horizontal plane, b) in vertical plane. Angles between adjacent dipoles: 1 – 90°; 2 – 70°; 3 – 110°.

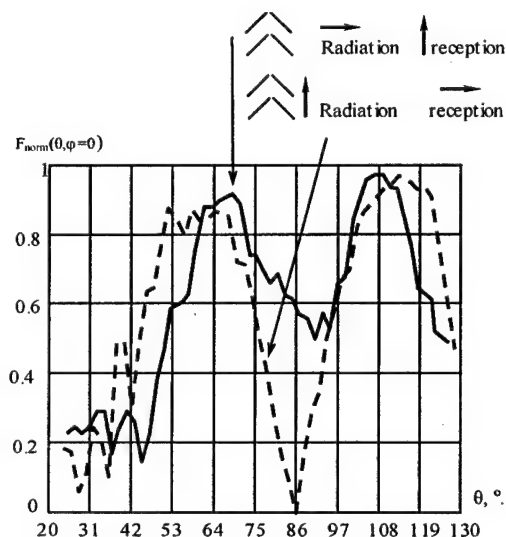


Fig. 4.

Experimental research of fragment of such structure was carried out for practical check of theoretical calculations and comparative evaluation of the se-

lected reradiating structure. Structure fragment DPs were read by way of measurements in free space.

Fig. 4 represents experimental DP in vertical plane and Fig. 5 in horizontal plane of the structure.

It is seen, that reradiating structure has pronounced directional features. Frequency bandwidth, evaluated on gain decrease by 2 times, is approximately 8% of frequency carrier.

Dependence of the structure model DP main maximum direction on radiation frequency has been obtained during the experiment, which can be used for creation of systems with frequency scan or creation of double-diagram arrays.

PART 2

The suggested reradiator design includes two interconnected arrays. The first one is an array of wave dipole quarter. The second one – is an array of one-thread spiral elements Fig. 6. Both arrays are coupled bit-by-bit by feeder line, which is a part of wire. The same type of wire is used at creation of spirals and loop dipoles.

Let us consider one dipole, coupled with spiral, as a separate integrated element of reradiator. Reradiator element operation mechanism determines the necessity to have metallic shield, which shall separate loop dipole and spiral. Electromagnetic wave (EMV), received by spiral element, is partly reradiated in direction, determined with phasing, and partly it is transmitted to loop dipole, which transmits it finally.

Array phasing shall be performed for reradiation to pass in longitudinal direction relative to reradiator surface. Reradiator phasing with such design is performed by way of establishing the corresponding angle of spiral element turn. Depending on the selected inclination angle of DP main angle and its azimuth orientation, relative to reradiation array, diffraction maximums may occur in DP. The analysis of diffraction maximums occurrence in arrays with various variants of element arrangement was carried out in the monograph [2]. It was outlined, that during selection of phasing direction in azimuth plane it is possible to find a direction, at which the required level of diffraction maximums is obtained.

To check the above, reradiator model was manufactured and experimentally examined. First, reradiator element design variants were checked using special stand with method of measuring electric parameters in waveguides. Then, DPs of reradiator-model, manufactured on the basis of finalized element design, were read by method of measurement in a free space. Array elements were arranged within metal circle with thickness of 5 mm and radius $a = 15,5$ cm, in nodes of triangular grid with step $b = c = \lambda/2$ Fig. 7.

By way of reradiator lower array spirals turn, it was possible to check reradiator adjustment with directional pattern maximums of reradiator both arrays (higher and lower) phased at angle $\theta = 82^\circ$ relative

to axis, perpendicular to reradiator plane. Reradiator elements were calculated for wave length of 3 cm.

Fig. 8 and Fig. 9 represent PAS model directional patterns, one measured during experimental examination and one calculated, in vertical and horizontal planes.

CONCLUSION

1. The suggested reradiating structure with feature of longitudinal-broadside radiation is much cheaper in manufacturing and more comfortable for application as conformal antenna. Application of the second layer in the structure will give the opportunity to compensate the large back lobe, which is a characteristic of single-layer design.

2. Experimental examinations of periscope antenna reradiator on the basis of two coupled arrays proved the possibility to create a structure with longitudinal reradiation. The suggested design of electrically coupled antenna arrays can be considered as one variant of such a structure.

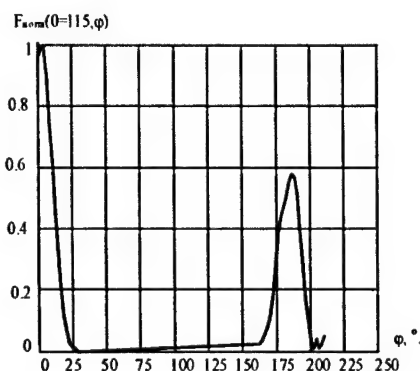


Fig. 5.

REFERENCES

1. Zamiatin V. I., Perekaty A. V., Baturin O. V., Tolokneev E. A., Pereguda G. B. "Feedthrough array as low-flying target detection radar station periscope antenna reradiator". Collected studies. Issue 2 (28). - Kharkov; KMU. 2000. - pp.17-23.
2. Voloshin O. I., Leshchuk I. I., Tsaliyev T. A. Planar reflector antennas for satellite communication systems. /Book.: Materials of 3-rd Crimean conference. "SHF device and satellite reception". Sevastopol: SPI, 1993. - book 5.- pp. 82-85.
3. Alekseev M. A., Bogoslovskiy G. S., Cherniayev L. K., Shtitelman B. I. "Theory of electromagnetic field and SHF technology". Kharkov: VIRTU, 1974.
4. Sokolov P. V. Effect of element geometry of two-dimensional periodic structure on frequency selective features. Radiotekhnika, 1996., № 7, pp. 31-33.
5. Automated design of antennas and SHF devices. / D. I. Voskresenskiy, S. D. Kremenetskiy, A. Y. Griniov, Y. V. Kotov/ Tutorial for institutes of higher education. - M.: Radio i sviaz, 1988. - p. 240.



Fig. 6.

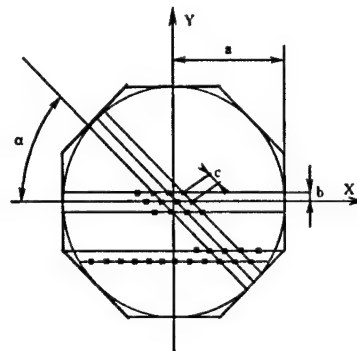


Fig. 7.

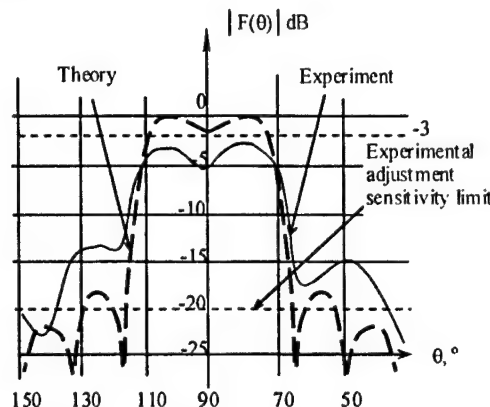


Fig. 8.

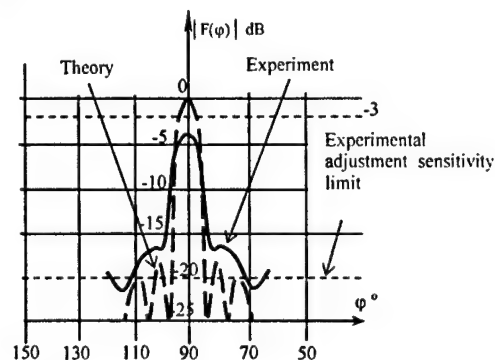


Fig. 9.

6. Viktorov B. V., Ishmametov I. A., Sadykov V. I. Microstrip module of Feedthrough phased array. In collection "Calculation and designing of stripe lines", Sverdlovsk, 1986, p. 145.
7. Shanberg O. H., Ferrar F. G., Sindorig A., Hages S. T. Microstrip antennas with frequency agility and polarization diversity. IEEE Trans. Antennas and Propagation 1981, 29, N 1, pp. 118-123.

**ADAPTIVE
ANTENNA
ARRAYS AND
SIGNAL
PROCESSING**

WEIGHT ERROR LOSS IN MIMO SYSTEMS WITH ADAPTIVE TRANSMIT AND RECEIVE BEAMFORMERS

V. T. Ermolayev, A. G. Flaksman, I. P. Kovalyov, and I. M. Averin

MERA scientific-technical company, Nizhny Novgorod, Russian Federation
<ermol@mera.ru>, <flak@mera.ru>, <kovalyov@mera.ru>, <ave@mera.ru>

Abstract

The effects of non-ideal channel estimation in multiple-input-multiple-output (MIMO) wireless communication systems using the eigenchannel technique for the independent symbol transmission are investigated in this paper. Analytical expression is derived for the Shannon capacity for arbitrary signal-to-noise ratio (SNR), training sequence length (TSL), transmit and receive antenna numbers. The weight error loss (WEL) that quantifies the increase in signal-to-noise ratio (SNR) required to meet a given capacity target due to weight jitter are investigated.

Keywords: MIMO systems, adaptive beamformer, channel estimation, eigenchannels, capacity, weight error loss, training sequence.

1. INTRODUCTION

One of the main problems of the communication systems is a significant increase of the data rate in the different environments, especially in the deep Rayleigh fading which is caused by the multipath propagation. The data rate can be increased significantly due to the use of the multiple-input-multiple-output (MIMO) systems with antenna arrays at both the transmit and receive link ends.

Recently, MIMO systems with the parallel spatial eigenchannels for the independent symbol transmission have drawn considerable attention [1], [2]. These eigenchannels are orthogonal decoupled channels and the symbol detection at the outputs of eigenchannels is carried out independently. Such MIMO system increases the data rate considerably [3], but the transmitter must have the channel knowledge that gives the possibility to form the eigenchannels.

In the case of the MIMO system the training sequence of each transmit antenna must be differ from the others, in order to allow each transmit antenna to be identified at the receive antennas and to estimate the channel coefficients between all pairs of transmit and receive antennas. The time channel variations mean that only finite number of the training signals can be used for channel estimation at any time. Noise will be present in the estimated channel coefficients causing so-called "weight jitter" [4].

The imperfect channel estimation leads to the errors of the eigenvectors of both the transmit and receive adaptive beamformers. Therefore the orthogonality of the eigenchannels is destroyed and the crosstalk between eigenchannels appears. With the

increase of the channel estimation error the crosstalk gain between the eigenchannels is increased and the eigenchannel gains are decreased. If MIMO system must attain a certain level of the capacity averaged over the fading then we can introduce the weight error loss (WEL) that quantifies the increase in signal-to-noise ratio (SNR) required to meet a given capacity target due to weight jitter. This paper is devoted to the investigation of the capacity and WEL of MIMO system using the eigenchannel technique.

2. POWER AND CROSSTALK GAINS OF EIGENCHANNELS

We consider the MIMO system with M transmit and N receive antennas. Let h_{ij} be the channel coefficient for j^{th} transmit and i^{th} receive antennas and \mathbf{H} be a $(N \times M)$ -matrix of the channel coefficients. This matrix has a singular-value decomposition of the form $\mathbf{H} = \mathbf{U}\mathbf{\Lambda}^{1/2}\mathbf{V}^H$, where the matrix $\mathbf{V} = (\mathbf{V}_1, \mathbf{V}_2, \dots, \mathbf{V}_K)$ consists of the matrix $\mathbf{H}^H\mathbf{H}$ eigenvectors and the matrix $\mathbf{U} = (\mathbf{U}_1, \mathbf{U}_2, \dots, \mathbf{U}_K)$ consists of the matrix $\mathbf{H}\mathbf{H}^H$ eigenvectors; $\mathbf{\Lambda}$ is the $(K \times K)$ -diagonal matrix of non-zero eigenvalues λ_j of the matrix $\mathbf{H}^H\mathbf{H}$ or $\mathbf{H}\mathbf{H}^H$; $K = \min\{M \times N\}$; $(\cdot)^H$ - is Hermitian conjugate. We assume that for the Rayleigh fading the matrix \mathbf{H} has independent identically distributed, complex, Gaussian, zero-mean entries h_{ij} and $|h_{ij}|^2$ is a chi-squared random variable with two degrees of freedom normalised so $\langle |h_{ij}|^2 \rangle = 1$ ($\langle \dots \rangle$ means the statistical average).

The orthogonal beam sets at both the transmitter (with the help of matrix \mathbf{V}) and the receiver (with the help of matrix \mathbf{U}) are formed in order to create parallel eigenchannels. The signal vector \mathbf{S} at the transmit beamformer \mathbf{V} output can be written as $\mathbf{S} = \mathbf{P}^{1/2} \mathbf{V} \mathbf{C}$, where $\mathbf{C} = (c_1, c_2, \dots, c_K)^T$ is the vector of K symbols simultaneously transmitted over K eigenchannels; $\mathbf{P} = (p_1, p_2, \dots, p_K)^T$ is the diagonal matrix of powers at eigenchannel inputs; $(\cdot)^T$ is transpose. The optimal power allocation between eigenchannels that maximises the capacity is found on the base of the so-called 'water-filling' algorithm [5].

The signal vector at the receive beamformer input is $\mathbf{X} = \mathbf{P}^{1/2} \mathbf{A}^{1/2} \mathbf{V} \mathbf{C} + \mathbf{Z}$, where \mathbf{Z} is the vector of complex, additive white Gaussian noise (AWGN) that is assumed as independent in different antennas, has zero mean and variance σ_0^2 . The output signal vector is equal to $\mathbf{Y} = \mathbf{P}^{1/2} \mathbf{A}^{1/2} \mathbf{C} + \tilde{\mathbf{Z}}$, where $\tilde{\mathbf{Z}} = \mathbf{U}^H \mathbf{Z}$. The statistical properties of the transformed noise $\tilde{\mathbf{Z}}$ and non-transformed noise \mathbf{Z} are the same. Therefore the eigenchannels are the orthogonal decoupled channels and can be used for the independent symbol transmission. The block diagram of MIMO systems is shown on Fig. 1.

The SNR at the k^{th} eigenchannel output is equal to $SNR_k = \rho_k \lambda_k$, where $\rho_k = p_k / \sigma_0^2$. The mean Shannon capacity $\langle C \rangle$ is the sum of the mean capacities of all individual eigenchannels and given by [1], [3]

$$C = \sum_{k=1}^K \langle \log_2(1 + \rho_k \lambda_k) \rangle. \quad (1)$$

This formula is true for the case of the perfect channel knowledge when the TSL L is unlimited ($L = \infty$). Assume that each element h_{ij} of the exact channel matrix \mathbf{H} is estimated by means of the training sequence, which has length L of symbols. Then we have the channel matrix $\hat{\mathbf{H}} = \mathbf{H} + \Delta \mathbf{H}$ instead of the matrix \mathbf{H} . If the maximum likelihood estimate is used then the matrix $\Delta \mathbf{H}$ elements are independent normal complex random values with a zero mean and variance equals to

$$\sigma_h^2 = \frac{M}{\rho L}, \quad (2)$$

where the SNR $\rho = P_0 / \sigma_0^2$, P_0 is the full transmit

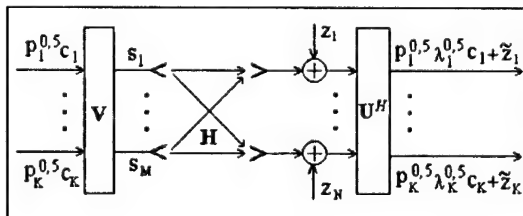


Fig. 1. The diagram of MIMO systems with adaptive transmit and receive beamformers

power. Formula (2) takes into account that the power, radiated by i^{th} antenna for the measurement of the channel matrix, is $p_i = P_0 / M$.

The error matrix $\Delta \mathbf{H}$ leads to errors of the eigenvectors of the transmit and receive beamformers (the matrices $\hat{\mathbf{V}}$ and $\hat{\mathbf{U}}$ instead of the matrices \mathbf{V} and \mathbf{U}). Therefore the orthogonality of the eigenchannels is destroyed and the crosstalk appears. It decreases the SNR and capacity.

Let's write the transformations of the transmitted symbols in the transmit beamformer, spatial channel and receive beamformer. As a result, we obtain that the signal at the i^{th} eigenvector output is

$$y_i(t) = \sqrt{p_i} (\hat{\mathbf{U}}^H \hat{\mathbf{H}} \hat{\mathbf{V}})_{ii} c_i + \sum_{k=1, k \neq i}^K \sqrt{p_k} (\hat{\mathbf{U}}^H \hat{\mathbf{H}} \hat{\mathbf{V}})_{ik} c_k + \tilde{z}_i \quad (3)$$

The first item gives the useful signal. The second term characterises the crosstalk since the ij^{th} element $(\hat{\mathbf{U}}^H \Delta \mathbf{H} \hat{\mathbf{V}})_{ij}$ ($i \neq j$) gives the crosstalk in the i^{th} eigenchannel, caused by the j^{th} eigenchannel. The matrices $\hat{\mathbf{V}}$ and $\hat{\mathbf{U}}$ are unitary and don't change statistic properties of the matrix $\Delta \mathbf{H}$. Therefore the elements of the matrix $\hat{\mathbf{U}}^H \hat{\mathbf{H}} \hat{\mathbf{V}}$ are independent complex random values with zero mean and the variance given by (2).

It follows from (3) that the SNR at the k^{th} eigenchannel output given by

$$\eta_k = \frac{\rho_k |(\hat{\mathbf{U}}^H \hat{\mathbf{H}} \hat{\mathbf{V}})_{ii}|^2}{1 + \sum_{j=1, j \neq i}^K \rho_k |(\hat{\mathbf{U}}^H \hat{\mathbf{H}} \hat{\mathbf{V}})_{ij}|^2}. \quad (4)$$

For the capacity averaging we must find the probability density function of random SNR at each eigenchannel output taking into account the formula (4). But it is a very difficult problem. Therefore the approximate expressions for the mean SNR and mean capacity will be obtained for arbitrary σ_h^2 , M and N . These formulas will be derived on the base of two limited cases ($\sigma_h^2 = 0$ and $\sigma_h^2 \gg 1$) and verified for the intermediate σ_h^2 with the help of the Monte Carlo simulation.

The eigenchannel gains equal to eigenvalues of the exact matrix \mathbf{H} with the perfect channel knowledge ($\sigma_h^2 = 0$). With the big error of the channel estimation ($\sigma_h^2 \gg 1$) the gain of all the eigenchannels tends to unity. Such behaviour of the average power gain of the i^{th} eigenchannel can be described with the function

$$\langle |(\hat{\mathbf{U}}^H \hat{\mathbf{H}} \hat{\mathbf{V}})_{ii}|^2 \rangle = \frac{\langle \lambda_i \rangle + \sigma_h^2}{1 + \sigma_h^2}. \quad (5)$$

The crosstalk gain between eigenchannels equals to zero with the perfect channel estimation ($\sigma_h^2 = 0$). For large errors ($\sigma_h^2 \gg 1$), the eigenchannels are destroyed and all the average crosstalk gains tend to unity. Such a behaviour of the average crosstalk gains is described with the function

$$\langle |(\hat{\mathbf{U}}^H \mathbf{H} \hat{\mathbf{V}})_{i,j}|^2 \rangle = \frac{\sigma_h^2}{1 + \sigma_h^2} \quad (i \neq j). \quad (6)$$

It can be seen that the crosstalk gains are the same for the different transmit and receive numbers and depend only on the variance σ_h^2 of the channel estimation error.

The theoretical results for the eigenchannel and crosstalk gains obtained on the base of (5) and (6) were compared with the Monte Carlo simulation results obtained with the help of (4) for Rayleigh fading channel. Fig. 2 and 3 show the mean power gains of all the eigenchannels and two mean eigenchannel crosstalk gains versus the variance σ_h^2 for $M = 4$ and $N = 4$. It can be seen that the simulation results match very well with the theory. Analogous results were obtained for other values of M and N . Therefore formulas (5) and (6) are a good approximation for the mean eigenchannel gains and eigenchannel crosstalk gains.

3. MEAN CAPACITY WITH IMPERFECT CHANNEL KNOWLEDGE

Formulas (5) and (6) allow us to obtain the mean SNR at the eigenchannel outputs. As a result the mean SNR in the i^{th} eigenchannel is

$$\langle \rho_i \rangle = \frac{\langle \lambda_i \rangle + \sigma_h^2}{1 + \sigma_h^2} \quad (7)$$

For the use of this result we make the following approximation: the averaging of logarithmic functions in (1) is replaced by the averaging of arguments of these functions. This approximation is exact for the case of static channel without fading and has the largest inaccuracy for the Rayleigh fading channel. Taking into account (2) we obtain that

$$\langle C \rangle \approx \sum_{i=1}^K \log_2 \left[1 + \frac{\langle \rho_i \rangle \left(\langle \lambda_i \rangle + \frac{M}{\rho L} \right)}{1 + (\rho - \langle \rho_i \rangle + 1) \frac{M}{\rho L}} \right]. \quad (8)$$

Formula (8) is valid in the case of the arbitrary (small and big) error of the channel estimation or in the case of the arbitrary SNR and TSL. It takes into account eigenchannel crosstalk and the change of the useful signal due to imperfect channel estimation.

If the uniform power allocation is used instead of the 'water-filling' algorithm then $\rho_i = \rho/K$ and it is follows from (8) that

$$\langle C \rangle \approx \sum_{i=1}^K \log_2 \left[1 + \frac{\frac{\rho}{K} \left(\langle \lambda_i \rangle + \frac{M}{\rho L} \right)}{1 + \frac{(K-1)M}{KL} + \frac{M}{\rho L}} \right]. \quad (9)$$

Now we consider the case of the small error variance, when $\sigma_h^2 \ll 1$ or $\rho L \gg M$. This is the case of high SNR ρ or long TSL L . Let's take into account that only the eigenchannels with $\lambda_i \geq 1$ give the main contribution into the capacity. Then the capacity is given by

$$\langle C \rangle \approx \sum_{i=1}^K \log_2 \left[1 + \frac{\rho}{K} \frac{\langle \lambda_i \rangle}{1 + \frac{(K-1)M}{KL}} \right]. \quad (10)$$

The key formula (8) for the mean capacity was detailed verified on the base of the comparison with Monte Carlo simulation results for the different σ_h^2 , N and M . Fig. 4 shows the simulation and the theoretical results for $M = 4$ and $N = 2$ when the TSL $L = 1$ and $L = 100$. Analogous results were obtained for other N and M . Thus the obtained formula (8) is a good approximation for the mean capacity of the MIMO systems for the arbitrary SNR ρ , TSL L , the number of the transmit (M) and receive (N) antennas.

4. WEIGHT ERROR LOSS ANALYSIS

WEL quantifies the increase in SNR required to meet a given mean capacity C due to weight jitter arising from noisy channel estimates. WEL w can be obtained from the equation

$$C(L = \infty, \rho) = C(L, w\rho). \quad (11)$$

The capacity $C(L, \rho)$ for the arbitrary TSL L is given by (8). The substitution of $w\rho$ instead of ρ must be done in this formula. Then we must substitute TSL $L = \infty$ into (8). A closed form solution for WEL w can be found only in the case of the uniform power allocation between eigenchannels and of small channel estimation errors when the variance $\sigma_h^2 \ll 1$, i.e. $\rho L \gg M$. As a result we have that the WEL w is given by:

$$w = 1 + \frac{(K-1)M}{KL}. \quad (12)$$

Thus if the number N of transmit antennas is increased then the TSL L at each antenna must be increased proportionally to M to prevent the WEL increasing.

The WEL w versus SNR ρ for the different TSL L and for MIMO system with $M = 4$, $N = 2$ in Rayleigh fading channel are shown on Fig. 5.

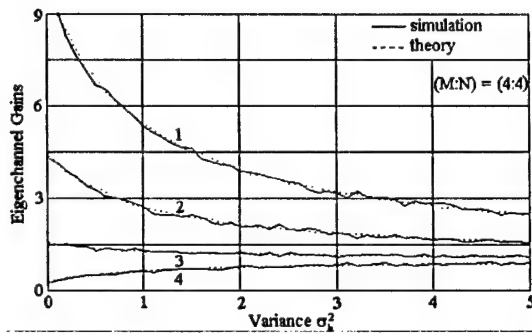


Fig. 2. Theoretical and simulation results for the eigenchannel gains versus the variance σ_h^2 .

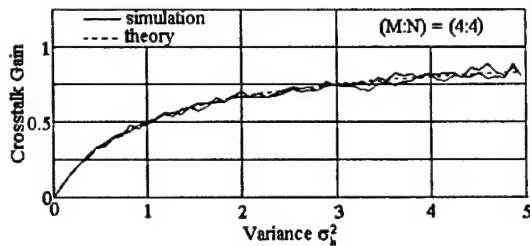


Fig. 3. Theoretical and simulation results for the eigenchannel crosstalk gains versus the variance σ_h^2 .

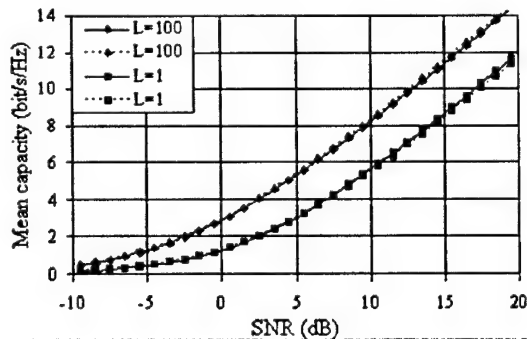


Fig. 4. Mean capacity for MIMO system with $M = 4$, $N = 2$ when TSL $L = 1, 100$. Solid and dotted curves correspond to theoretical and simulation results, respectively.

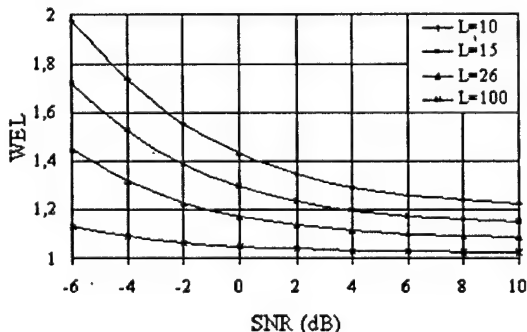


Fig. 5. WEL versus SNR for MIMO system with $M = 4$, $N = 2$ and for the different TSLs.

5. CONCLUSIONS

The effects of non-ideal channel estimation in MIMO wireless communications systems using the parallel spatial decoupled eigenchannels are investigated in this paper. The imperfect channel estimation leads to errors of the eigenvectors of both the transmit and receive beamformers. Therefore the orthogonality of the eigenchannels is destroyed and the crosstalk between eigenchannels appears. Analytical approximate formulas have been derived for the mean eigenchannel and crosstalk gains and for the mean Shannon capacity in the general case of the arbitrary transmit and receive antennas numbers, SNR and TSL. These formulas give the results that are matched very well with the Monte Carlo simulations. The obtained results show that when the number M of transmit antennas is increased then the TSL L at each antenna must be increased proportionally to M to prevent the WEL increasing. WEL depends weakly on the receive antennas number N .

REFERENCES

1. Andersen J. B. Antenna Arrays in Mobile Communications: Gain, Diversity, and Channel Capacity // IEEE Antennas and Propagation Magazine, 2000. Vol. 42, No 2, p. 12.
2. Shiu D, Foschini G. J, Gans M. J. and Kahn J. M. Fading Correlation and Its Effect on the Capacity of Multielement Antenna System // IEEE Trans. Commun., 2000. Vol. 48, No 3, p. 502.
3. Telatar I. E. Capacity of Multi-antenna Gaussian Channels // European Trans. Telecommun, 1999. Vol. 10, No 6.
4. Bevan D. D. N., Ermolayev V. T. and Flaksman A. G. Analysis of Weight Error Loss with a multichannel beamformer processor // IEE Proceedings Radar, Sonar and Navigation, 1998. Vol. 145, No 1, p. 63.
5. Gallager R. G. Information Theory and Reliable Communication – New York: Wiley, 1968.

ORTHOGONALIZED ALGORITHMS FOR FIR ANC ADAPTIVE SYSTEMS

Daniel Tapia-Sanchez, Rogelio Bustamante Bello,
Héctor Perez-Meana and Mariko Nakano-Miyatake

SEPI ESIME Culhuacan, National Polytechnic Institute of Mexico
<hmpm@calmecac.esimecu.ipn.mx>

Abstract

Active Noise Cancellation algorithms (ANC) based on modification of filtered-x least mean squares (FxLMS) and filtered-x recursive least squares (FxRLS) algorithms are proposed, which are a direct consequence of using an orthogonal transform for decomposing the filter input into a number of finite and mutually near orthogonal signal components. The most important advantage of this approach is that it admits processing schemes in which each signal component can be independently processed. Computer simulation results are given to show the desirable features of proposed schemes.

1. INTRODUCTION

Unwanted acoustic noise is a problem that becomes more and more important as the applications of electronic communication systems increase, because their effects represent an important source of annoyances for the end user and they may considerably reduce the efficiency, the quality and the reliability of this type of systems. Active noise cancellation (ANC) is an attractive alternative to noise reduction in which a secondary noise source that destructively interferes with the unwanted noise is introduced.

Because the characteristics of the acoustic noise source and the environment are time varying, the frequency content, amplitude, phase, and sound velocity of the undesirable noise are non-stationary, the ANC system must be adaptive in order to cope with these variations. On the other hand, in real time signal processing, a significant amount of computational effort can be saved if the input signals are represented in terms of a set of orthogonal signal components. Taking this fact into account, this paper proposes a parallel form adaptive noise cancellation algorithm using a single sensor, in which the input signal is split into a set of approximately orthogonal signal components by using the discrete cosine transform. Subsequently these signal components are feed into a bank of adaptive transversal filters (FIR-ADF) whose parameters are independently updated to minimize a common error. The proposed scheme can be considered as an alternative form of the filtered-x least mean square and filtered-x recursive least square algorithms that allow to improve their performance, either by increasing their convergence rate or reducing the operations number necessary to obtain the optimal adaptive filter output.

2. ADAPTIVE ANC ALGORITHMS

A widely used adaptive algorithm in active noise cancellation is the filtered-x least mean square (FXLMS), which is motivated by the simple noise cancelling system shown in Fig. 1.

First, if we consider the LMS algorithm as the adaptation method for $W(z)$, the introduction of a secondary-path transfer function into the noise controller will generally cause instability [1]. This is because the error signal is not correctly "aligned" in time with the reference signal, due to the presence of $S(z)$. There are a number of possible schemes that can be used to compensate for the effect of $S(z)$. The first solution is to place an inverse filter, $1/S(z)$, in cascade with $S(z)$ to remove its effect. The second solution is to place a filter, whose impulse response is an estimation of $S(z)$, in the reference signal path used by either the LMS or RLS algorithms to update the coefficients vector of $W(z)$. These approaches result in the so-called filtered-x LMS (FXLMS) or filtered-x RLS (FXRLS) algorithms.

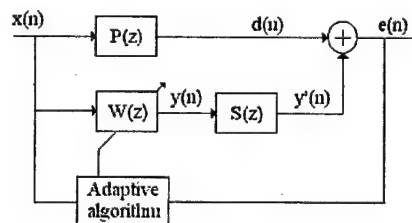


Fig. 1. Simplified active noise cancellation system.

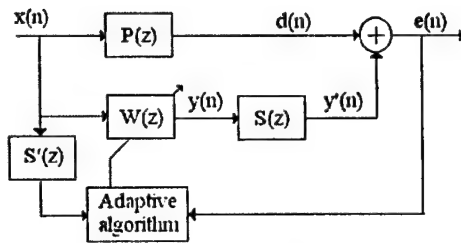


Fig. 2. Block diagram of FXLMS and FXRLS active noise cancel algorithms.

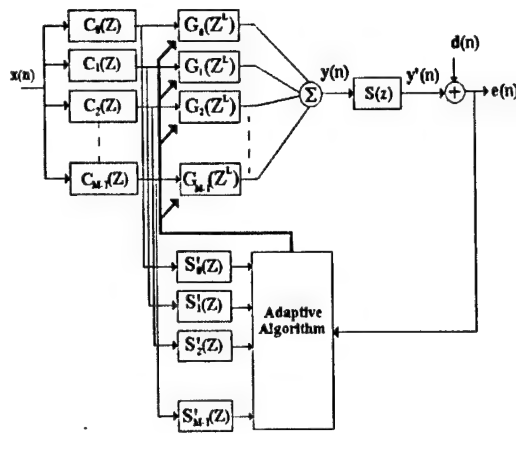


Fig. 3. Proposed structure of adaptive filtering structure based on subband decomposition.

Because an inverse does not necessarily exist for $S(z)$, the FXLMS and FXRLS algorithms, whose block diagram is shown in Fig. 2, are generally the most effective approaches.

2.1. FXLMS ALGORITHM

When the LMS algorithm is used to update the coefficients vector of $W(z)$, shown in Fig. 4, $W(n)$ is given by

$$W(n) = W(n-1) + \mu X'(n) e(n). \quad (1)$$

where

$$e(n) = d(n) - W^T(n) X'(n) \quad (2)$$

is the output error, n is the time index,

$$X'(n) = s(n) * X(n). \quad (3)$$

$s(n)$ is the impulse response of secondary path and $*$ denotes the linear convolution

2.2. FXRLS ALGORITHM

When the filtered-x RLS algorithm is used to update the adaptive filter coefficients vector, $W(n)$ at time instant n is given by

$$W(n) = W(n-1) + \mu K(n) e(n), \quad (4)$$

where μ is the convergence factor

$$P(n) = \frac{1}{\lambda} [P(n-1) - K(n) X'(n) P(n-1)] \quad (5)$$

$$K(n) = \frac{P(n-1) X'(n)}{\lambda + X'^T(n) P(n-1) X'(n)} \quad (6)$$

$e(n)$ is the output error given by eq. (2), $X'(n)$ is given by eq. (3), λ is a "forgetting factor" that enables RLS-type algorithms to track the statistics of the input signal (filtered-reference signal in this case) if it is time-varying.

3. PROPOSED STRUCTURE

Consider the transfer function $W(z)$ of an NN order transversal filter structure which is given by

$$H(z) = \sum_{i=0}^{N-1} h_i z^{-i}, \quad (9)$$

which by using a subband decomposition approach can be represented in terms of M parallel subfilter bank as shown in Fig. 3

Its output signal is given by

$$y(n) = \sum_{r=0}^{M-1} W_r^T X_r(n), \quad (10)$$

where

$$W_r = [w_r(0, n), w_r(1, n), w_r(2, n), \dots, w_r(2, L-1)]^T \quad (11)$$

$$X_r(n) = [x_r(n), x_r(n-M), \dots, x_r(n-(L-1)M)]^T \quad (12)$$

$$x_r = 2 \cos\left(\frac{\pi r}{N}\right) x_r(n-1, r) - x_r(n-2, r) - \cos\left(\frac{\pi r}{2N}\right) \{x[n-N-1] - x[n-1](-1)^r - x(n-N) + x[n](-1)^r\}. \quad (13)$$

3.1. MODIFIED FILTERED-X LMS ALGORITHM (MFXLMS)

When a LMS-like adaptive algorithm is used, the adaptive filter coefficient vectors is updated as follows

$$W_r(n) = W_r(n-1) - \beta \frac{\partial e^2(n)}{\partial W_r}, \quad (14)$$

where $e(n)$ is the output error given by

$$e(n) = d(n) - \left(\sum_{r=0}^{M-1} W_r^T X_r(n) \right) * s(n). \quad (15)$$

Taking the derivative of (15) with respect to W_r from eq. (12) it follows that

$$W_r(n) = W_r(n-1) + \beta_r e(n) X'_r(n), \quad (16)$$

where, assuming that the DCT components are near orthogonal among them,

$$\beta_r = \frac{\alpha}{|X'_r|^T}, \quad (17)$$

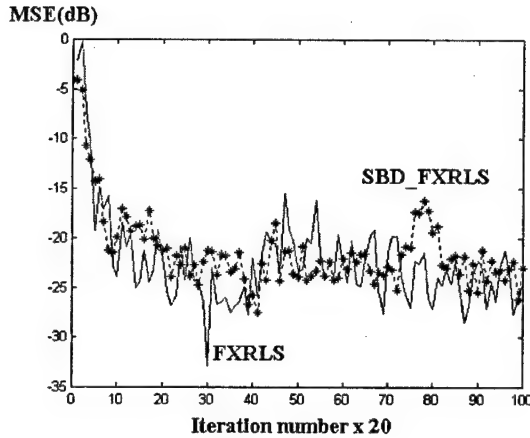


Fig. 4. Convergence performance of proposed MFXRLS algorithm.

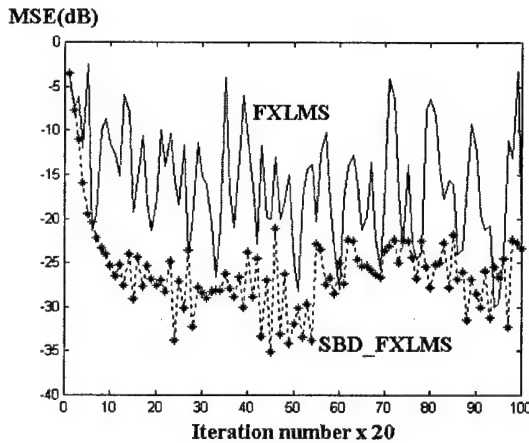


Fig. 5. Convergence performance of proposed MFXLMS algorithm.

$$\mathbf{X}_r(n) = [x_r(n), x_r(n-M), \dots, x_r(n-(L-1)M)]^T, \quad (18)$$

$0 < \alpha < 2$, and

$$x_r(n) = s(n) * x(n). \quad (19)$$

These equations allow to implement filtered-x LMS algorithm with band-partitioning in order to improve the convergence performance of the convergence performance of the filtered-x LMS.

3.2. MODIFIED FILTERED-X RLS ALGORITHM (MFXRLS)

The FXRLS algorithm used to update the filter coefficients is a modified form of the filtered-x recursive least square (FXRLS) algorithm derived by assuming that the DCT coefficients of input signal are fully decorrelated. Under this assumption each sparse FIR filter can be updated independently, and then the $N \times N$ autocorrelation matrix of the parallel form FXRLS algorithm, $\mathbf{R}(n)$, can be replaced by a $N \times N$ block diagonal matrix, where each block has

a rank equal to L . Then, under this assumption the proposed adaptive filter coefficients becomes

$$\mathbf{W}_r(n) = \mathbf{W}_r(n-1) + \mu \mathbf{K}_r(n) e(n), \quad (20)$$

where

$$\mathbf{R}_r^{-1}(n) = \mathbf{P}_r(n) = \left(\frac{1}{\lambda} \right) \times [\mathbf{P}_r(n-1) - \mathbf{K}_r(n) \mathbf{X}_r'(n) \mathbf{P}_r(n-1)], \quad (21)$$

$$\mathbf{K}_r(n) = \frac{\mathbf{P}_r(n-1) \mathbf{X}_r'(n)}{\lambda + \mathbf{X}_r'^T(n) \mathbf{P}_r(n-1) \mathbf{X}_r'(n)}, \quad (22)$$

and $\mathbf{X}'(n)$ is given by eqs. (12) and (13). The modified FXRLS algorithm allows to reduce the computational cost associated with its conventional from about $2M^2L^2 + ML$ multiplications per sampling period to $2M(L^2 + 2L) + 6M$. Thus, keeping L constant the computational complexity becomes linear instead of quadratic as in the conventional FXRLS algorithm.

4. COMPUTER SIMULATIONS RESULTS

Fig. 4 shows the convergence performance of proposed MFXRLS algorithm when it is required to cancel an actual bell noise, where the convergence performance of conventional FXRLS algorithm is shown for comparison. The figure displays that the proposed algorithm provides the convergence performance similar to the conventional FXRLS algorithm with much less computational cost.

Figure 5 shows the convergence performance of proposed MFXLMS when it is required to cancel an actual bell sound, where the convergence performance of conventional FXLMS algorithm is shown for comparison. Simulation results show that proposed algorithm improves the performance of conventional algorithm with a similar computational complexity.

5. CONCLUSIONS

In this paper, there have been proposed alternative structures for the filtered-x LMS and the filtered-x RLS algorithms based on subband decomposition in which the input signals are split into M near orthogonal signal components using the discrete cosine transform. This approach allows a reduction of the computational complexity of conventional FXRLS algorithm, while keeping similar convergence performance. When an LMS-like algorithm is used, the proposed structure also allows improving the convergence performance of the noise cancellation system, because it is possible to optimize the convergence factor at each subband. Besides, the correlation between consecutive taps at each subband becomes weakened, the sparse factor increases.

ACKNOWLEDGEMENTS

The authors thank for the support of the National Council of Science and Technology (CONACYT) to the investigation that gives origin to this paper.

REFERENCES

1. Sen M. Kuo and Dennis R. Morgan, "Active noise control: A tutorial review", *Proceedings of the IEEE*, Vol. 87, No. 6, June 1999.
2. B. Widrow *et al.*, "Adaptive noise canceling: Principles and its applications", *Proc. IEEE*, vol. 63, pp. 1692-1716, Dec. 1975.
3. J. Makhoul, "Linear Prediction: A tutorial review", *Proc. IEEE*, vol. 63 pp. 561-580, Apr. 1975.
4. L. Griffiths, "Rapid measurement of digital instantaneous frequency", *IEEE Trans. Acoust., Speech, Signal Processing*, vol. ASSP-23, pp. 209-222, Apr. 1975.
5. B. Widrow, "Adaptive filters", in *Aspects of Network and System Theory*, R. Kalman and N. DeClaris, Eds. New York: Holt, Rinehart, and Winston, 1971, pp. 563-587.
6. E.R. Ferrara, "Fast implementation of LMS adaptive filters", *IEEE Trans. Acoust., Speech, Signal Processing*, vol. ASSP-28, pp. 474-475, Aug. 1980.
7. S. Haykin, "Adaptive Filter Theory", Prentice Hall, Englewood Cliffs NJ, 1991.
8. H. Pérez Meana and S. Tsujii, "A System Identification Using Orthogonal Functions", *IEEE Trans. on Signal Processing*, vol. 39, No. 3, March 1991.
9. S. Shankar Narayan, A. Peterson, and J. Narasimha, "Transform domain LMS Algorithm", *IEEE Trans. Acoust., Speech, Signal Processing*, vol. ASSP-31, no.3, pp. 609-615, June 1983.
10. H. Pérez-Meana, M. Nakano-Miyatake, L. Niño-de-Rivera, "Adaptive Filtering Based on Subband Decomposition", *Proceedings of The International Workshop of Mathematical Modeling of Physical Processes in Homogeneous Media*, pp. 14-16, Guanajuato, Mex, March. 2001.
11. Daniel Tapia Sánchez, H. Pérez Meana y Mariko Nakano Miyatake, "Filtrado Adaptable usando la Transformación Coseno Discreta". 12º. Congreso Internacional de Electrónica y Comunicaciones (CONIELECOMP'2002). Acapulco, Gro. México.
12. Daniel Tapia Sánchez, H. Pérez Meana y Mariko Nakano Miyatake, "A Fast Parallel Form Filtered-x LMS for Active Noise Control". 2th. International Workshop on Control, Virtual Instrument and Digital Systems (CICINDI'2002). Pachuca, Hgo. México.
13. Daniel Tapia Sánchez, H. Pérez Meana y Mariko Nakano Miyatake, "A scheme for Active Noise Control based on Filtered-x RLS algorithm". 2-th International Workshop on Random Fields Modeling and Processing in Inhomogeneous Media (RFMPIM'2002). Guanajuato, Gto. México.

DECISION FEEDBACK EQUALIZERS FOR HIGH SPEED DATA COMMUNICATIONS

Edith González Lee, José Ambrosio Bastián,
Mariko Nakano Miyatake, Héctor Pérez Meana

Sección de Estudios de Posgrado e Investigación
Escuela Superior de Ingeniería Mecánica Eléctrica, Unidad Culhuacán.
Av. Santa Ana N° 1000, Col. San Francisco Culhuacán, 04430 México, D.F.
Tel./Fax: 56562058 <hmpm@prodigy.net.mx>

Abstract

This work shows the performance of different Decision Feedback Equalizers (DFEs) for high speed data transmission over a telephone line. The analyzed structures are: the Interference Intersymbol-predictive Decision Feedback Equalizer (ISI-DFE), the Decision Feedback Equalizer with Noise Predictor (NP-DFE) and the Hybrid-type DFE (H-DFE).

1. INTRODUCTION

Digital information over a communications channel is distorted mainly by the *Intersymbol Interference (ISI)*. In practical communications systems designed to allow high speed of transmission over band limited channels, the knowledge of frequency response of the channel is not enough to design a fixed demodulator (time-invariant) in order to reduce the *ISI*, as a consequence, an adaptive filter approach (equalizer) must be used [1,2,4]. Adaptive filters and adaptive signal processing algorithms are called adaptive equalizers and adaptive equalization algorithms, respectively. The purpose of both adaptive equalizers and adaptive equalization algorithms is to achieve an enhancement on the received signal. So, an equalizer is a filter used to compensate the non-ideal frequency response of a communications channel [1,3].

2. TELEPHONE CHANNEL CHARACTERISTICS

The *ISI* is caused by non-ideal characteristics of frequency response of the communications channels. Fig. 1 shows the frequency response characteristics of a telephone channel of medium range. It can be seen that it is not a flat response on the entire frequency range, and hence, there is a distortion in the amplitude and delay as well [1][4].

3. DISCRETE CHANNEL MODELS

Fig. 2 shows the discrete channel models for some communication channels; channel 1 represents the discrete channel model for a telephonic channel of 'good quality', channel 2 is the discrete channel

model that is affected by *ISI* and channel 3 is a channel that is affected by *ISI* in higher degree[1][3].

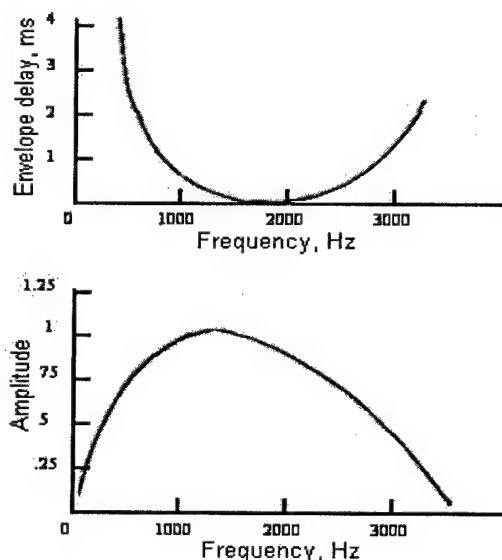


Fig. 1. Characteristics of Amplitude and Average Delay of a Telephone Channel of Medium Range.

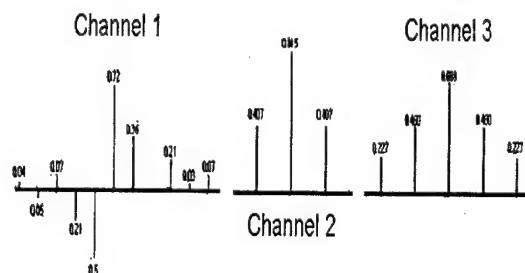


Fig. 2. Coefficients for the Discrete Channels Models.

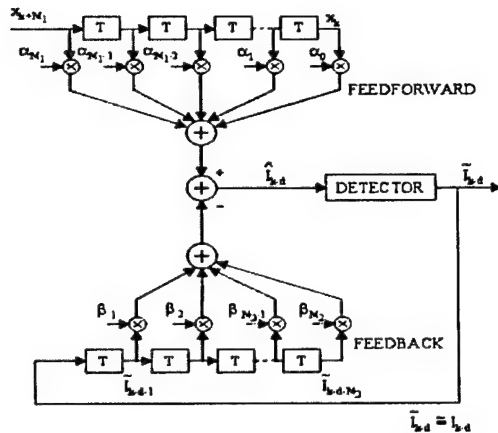


Fig. 3. Decision Feedback Equalizer (DFE).

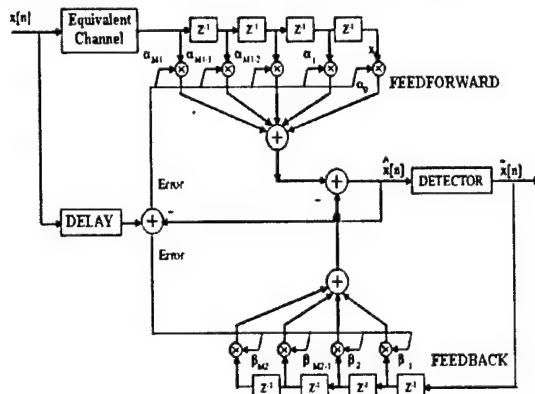


Fig. 4. ISI-predictive DFE (ISI-DFE).

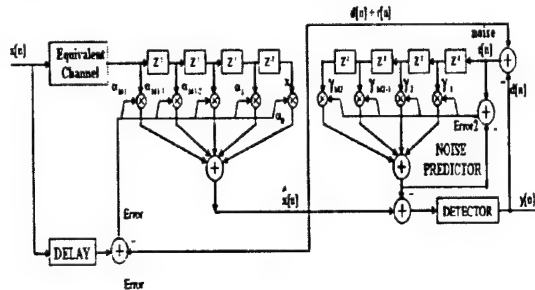


Fig. 5. Noise-predictive DFE (NP-DFE).

4. DECISION FEEDBACK EQUALIZER (DFE)

The *decision feedback equalizer* (DFE), shown in the Fig. 3, consists of two sections, a feedforward section and feedback section. The feedforward section is identical to previous linear transversal equalizer with $N - 1$ taps. The feedback section, on the other hand, is also a transversal equalizer with $N - 2$ taps whose function is to remove the intersymbol interference portion due to the previously detected symbols [1]. The output is given in [1, 5]:

$$\hat{I}_{k-d} = \sum_{j=0}^{M_1} \alpha_j x_{k+j} - \sum_{j=1}^{M_2} \beta_j \hat{I}_{k-d-j}, \quad (1)$$

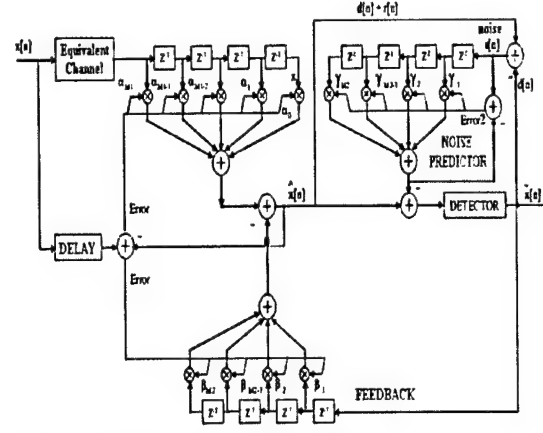


Fig. 6. Hybrid-type DFE (H-DFE).

where \hat{I}_k is an estimate of the k -th information symbol; $\hat{I}_{k-1}, \dots, \hat{I}_{k-M_2}$ are previously detected symbols; α_j are tap weight coefficients of the feedforward section; β_j are tap weight coefficients of the feedback section; d is a delay; x_k is the input sequence at instant k -th.

5. ANALYZED DFE STRUCTURES

Figs 4, 5 and 6 show the analyzed DFE structures: ISI-predictive DFE (ISI-DFE), noise-predictive (NP-DFE) and hybrid-type (H-DFE) [6].

All the filters are adapted by NLMS (Normalized Least Mean Squares) algorithm equation [5]:

$$\alpha_j(n+1) = \alpha_j(n) + \frac{\mu}{|X(n)|^2} e(n)x(n), \quad (2)$$

where: μ is a convergence factor $0 < \mu < 1$; α_j are tap weight coefficients of the corresponding section; $x(n)$ is the input sequence at instant n -esimo; $e(n)$ is the error signal.

6. ADAPTIVE ECHO CANCELLATION USING A FINITE IMPULSE RESPONSE (FIR) AT THE USER'S TERMINAL AND THE STATION

Fig. 7 shows a block diagram for the connections of a user to the local station, the 2 to 4 wires conversion is made by the hybrid, since this device is not perfectly balanced, there are several possible paths for the signal that flows from the user to the local station. The model shown in Fig.7 is used to evaluate the performance of the three structures of Decision Feedback Equalizers, the ISI-DFE, NP-DFE and H-DFE, considering the cancellation of an additional voice signal from transmitter 2 (T2), since the objective is to recover the signal transmitted by T1 at R1.

The three structures were evaluated considering 2 possibilities:

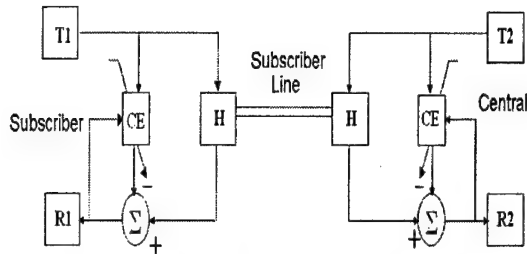


Fig. 7. Adaptive Echo Cancellation Model. There: T1, R1: Transmitter and Receiver at the User's Place. T2, R2: Transmitter and Receiver at the Local Station's Place. EC: Adaptive Echo Canceller. H: Hibrid.

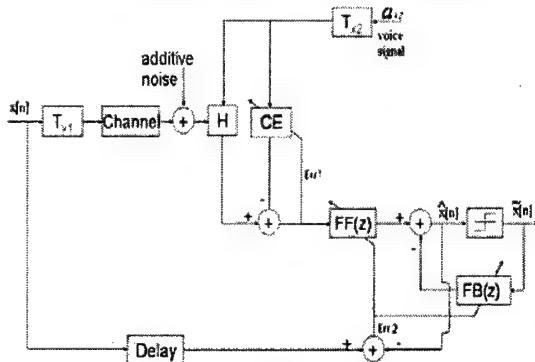


Fig. 8. ISI-DFE with Adaptive Echo Cancellation Model.

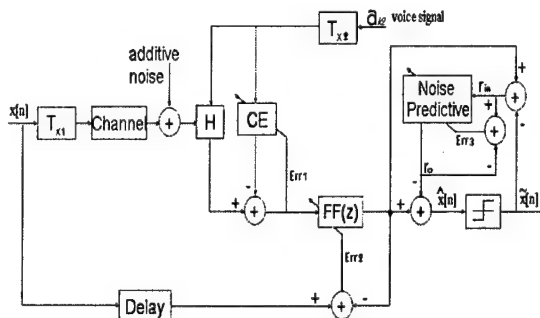


Fig. 9. NP-DFE with Adaptive Echo Cancellation Model.

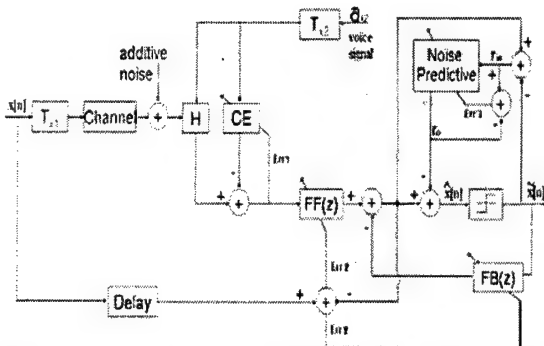


Fig. 10. H-DFE with Adaptive Echo Cancellation Model.

First proposal: Echo canceller is adapted independently to the DFE equalizer.

Table 1. Comparison of erroneous bits

ERRONEOUS BITS			
S/N	DFE-ISI	DFE-NP	DFE-H
1	2997	3642	3601
1.2	2587	3008	3044
1.4	2220	2553	2495
1.6	1869	1958	1947
1.8	1634	1482	1523
2	1332	1141	1142
2.2	1116	811	856
2.4	854	635	618
2.6	648	486	455
2.8	567	353	343
3	398	276	302
3.2	324	241	252
3.4	275	211	253
3.6	271	176	211
3.8	231	159	179
4	218	149	163
4.2	198	159	133
4.4	180	145	132
4.6	166	122	127
4.8	153	117	112

Thus, the received sequence is distorted by a signal generated by the second transmitter (voice signal), so, the echo is reduced by placing the canceller before the equalization process, and the filters are adapted independently among them as shown in Figs 8, 9, and 10.

Simulation results with additive noise at the output of the channel block and a voice signal at the second transmitter are shown in Table 1.

The total number of samples used to obtain the results is 20000, with 3000 samples only considered for training and the second channel was employee.

Second Proposal: The Echo canceller and the DFE equalizer are adapted simultaneously.

Thus, the received sequence is distorted by the signal generated by the second transmitter, thus, the echo effect is reduced by placing the echo canceller in the middle of the equalizer's structure, then, the adaptation process is accomplished simultaneously as shown in figures 12, 13, and 14.

Simulation results under the same previous considerations are shown in table 2.

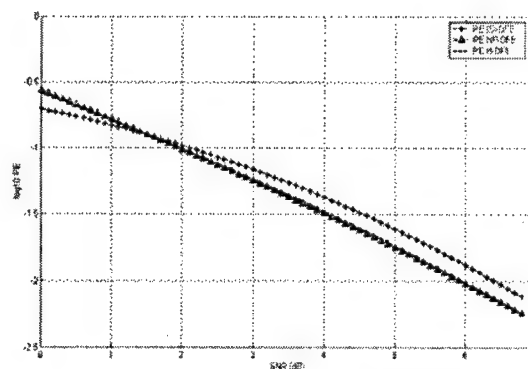


Fig. 11. Error Rate Performance.

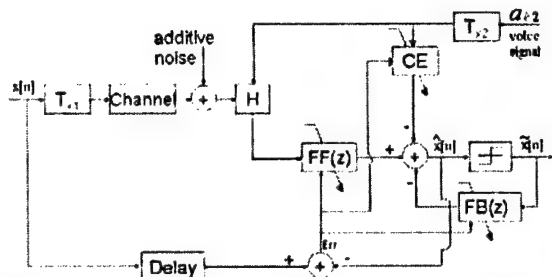


Fig. 12. ISI-DFE with Adaptive Echo Cancellation Model.

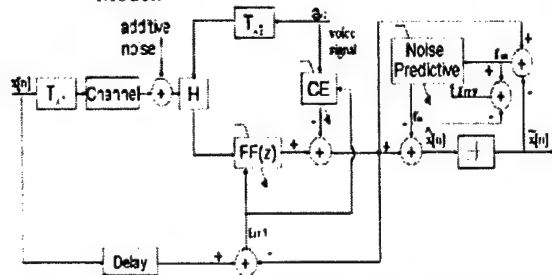


Fig. 13. NP-DFE with Adaptive Echo Cancellation Model.

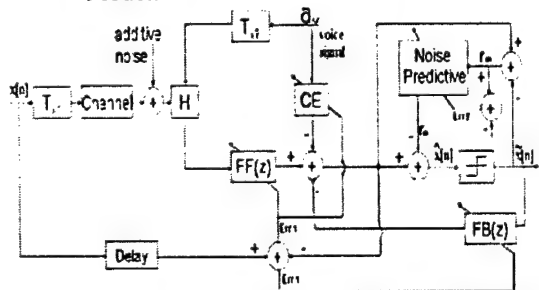


Fig. 14. H-DFE with Adaptive Echo Cancellation Model.

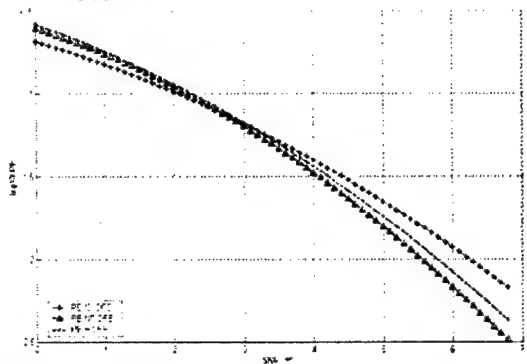


Fig. 15. Error Rate Performance.

7. CONCLUSIONS

The computer simulation show that the both structures NP-DFE and H-DFE provides a little better performance than conventional ISI-DFE under distortion conditions of ISI and a colored signal such as a voice signal at the receiver, generated it for own transmitter, due to that the NP-DFE structure doesn't propagate a symbol not well detected to the output (feedback) as the ISI-DFE structure. The H-DFE is a structure that combines the characteristics of DFE-ISI and DFE-NP (ISI reduction and noise reduction). According to the results is better to adapt simultaneously the echo canceller and the equalizer.

Table 2. Comparison of erroneous bits.

ERRONEOUS BITS			
S/N	DFE-ISI	DFE-NP	DFE-H
1	2998	3617	3808
1.2	2582	3177	3243
1.4	2240	2463	2616
1.6	1961	1977	2088
1.8	1636	1526	1742
2	1307	1233	1315
2.2	1076	903	961
2.4	856	757	711
2.6	608	531	637
2.8	489	370	448
3	383	311	298
3.2	275	231	225
3.4	253	173	226
3.6	221	140	171
3.8	193	115	151
4	189	93	132
4.2	179	92	107
4.4	170	81	103
4.6	154	74	97
4.8	141	77	99

ACKNOWLEDGEMENT.

Our thanks to the Science and Technology Council of Mexico (CONACyT) and The National Polytechnic Institute of Mexico (IPN).

REFERENCES

1. John G. Proakis, Digital Communications, "Digital Signaling over a Channel with Intersymbol Interference and Additive Gaussian Noise", cap. 6, McGraw-Hill 1985.
2. Juan Carlos Sánchez-García, Mariko Nakano Miyatake y Hector M. Pérez-Meana, "A Modified Hopfield Network Based Analog Decision Feedback Equalizer for Land Mobile Communications", Journal of Signal Processing, Vol. 3, No 5, pp 347-356, Septiembre 1999.
3. José Ambrosio Bastián, "Algoritmo Neurodifuso para Ecuación de Canales" cap. 1,4 Tesis de Maestría de la Sección de Estudios de Posgrado e Investigación de ESIME del IPN, Agosto del 2001.
4. C.F.N Cowan y P.M. Grant, "Adaptive Filters", cap 1, 3, 8, Prentice Hall 1985.
5. Arthur A. Giordano, Frank M. Hsu, "Least Square Estimation with Applications to Digital Signal Processing", cap. 6, Wiley Interscience 1985.
6. Gi-Hong Im, Kyu-Min Kang, "Performance of a Hybrid Decision Feedback Equalizer Structure for CAP-Based DSL Systems", IEEE Transactions On Signal Processing, Vol.49 No.8, Julio 2001.

EXPERIMENTAL INVESTIGATIONS OF AN INTERFERENCE CANCELLER WITH THE MODULATION ALGORITHM OF THE WEIGHING COEFFICIENTS GENERATION

Sergey V. Artuynov, Anatoliy V. Kobzev, Valeriy R. Khachaturov

Kharkiv Military University, Kharkiv, Ukraine
<niiret@kharkov.com>

Abstract

The principle of operation of the interference canceller with the gradient method of the weighing coefficients estimation is considered. Experimental data obtained from investigations of the breadboard model are given.

1. INTRODUCTION

The modulation algorithms of adaptive multi-channel signal processing at the conditions of external interference are known for a long time [1, 2]. These pertain to the gradient algorithms, and their main distinction from the other algorithms for similar purpose is the possibility to simplify essentially the hardware (to reduce number of parallel channels of reception) at the expense of modulation of weighting summation coefficients. If weighing summation (interference cancellation) is realized at the carrier frequency, the mentioned positive property becomes especially appreciable. In this case it is not necessary to apply the additional receiving channels with reducing frequency converters in circuits of correlation feedback of interference canceller [3].

Among numerous works devoted to practical realization of cancellers the modulation-type devices are not represented. The aim of this work is the acquaintance with one of the versions of practical realization of a multi-channel canceller with the modulation method of weighing coefficients estimation, realized on the modern analog and digital elements.

2. THE SCHEME AND THE PRINCIPLE OF OPERATION OF THE CANCELLER WITH THE MODULATION METHOD OF ADAPTIVE ADJUSTMENT

The simplified scheme of the interference canceller is shown in Fig. 1.

There are the main receiving antenna "0" and N additional antennas in the canceller. Complex enve-

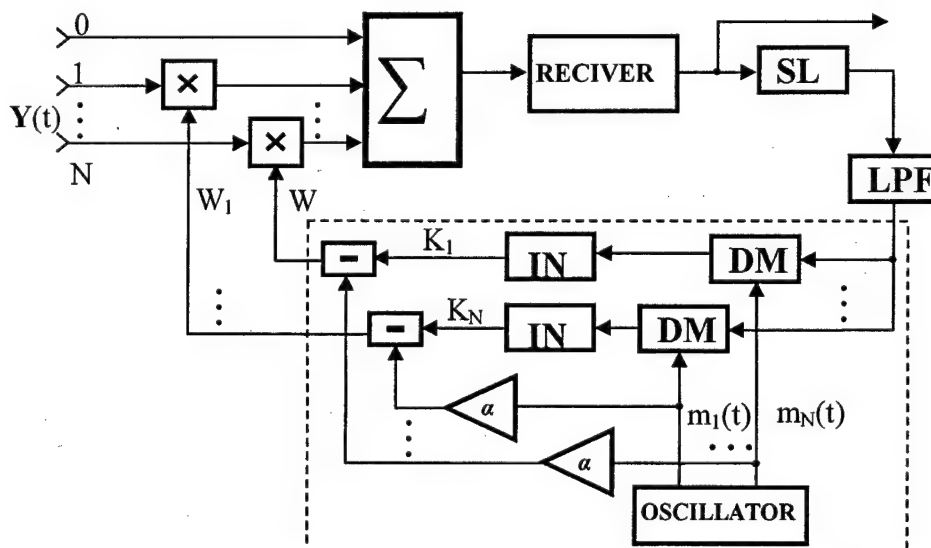


Fig. 1. The simplified scheme of the interference canceller

lopes of received oscillations we'll designate accordingly $y_0(t)$ and vector $\mathbf{Y}(t)$. The weighing summation is carried out at the carrier frequency with the vector coefficient \mathbf{W} . One receiving channel with a reducing frequency converter, an amplifier and band-pass filter at an intermediate frequency is included in the output of the adder. The square-law detector (SLD), low-pass filter (LPF) and the elements, dotted-line enclosed, pertain to devices of weighing coefficients estimation.

The weighing regulators and all the elements put in after the low-pass filter perform the operations with complex oscillations, i.e. consist of two quadrature channels. For the sake of simplicity in the scheme, the feedback only for one quadrature component of each channel is shown.

The weighing coefficients $\mathbf{W}(t)$ represent the difference

$$\mathbf{W}(t) = \alpha \mathbf{M}(t) - \mathbf{K}(t), \quad (1)$$

where $\mathbf{K}(t)$ are slowly changing coefficients, which cause the interference cancellation at the summation, $\mathbf{M}(t)$ is the vector of modulating voltages $m_1(t) \dots m_N(t)$, α is a constant coefficient ($\alpha \leq 1$), which influences the convergence rate, as will be pointed out farther.

The modulating functions $m_i(t)$ ($i = 1 \dots N$) are mutually orthogonal and should not change power of accepted oscillations. It is possible, for example, to use as these functions the processes with phase manipulation $m_i(t) = \exp[j\varphi_i(t)]$, where phase $\varphi_i(t)$ can take only two values 0 and π , so that the functions $\varphi_i(t)$ also are mutually orthogonal.

In the output of the adder, the oscillation consists of two components

$$\begin{aligned} y_\Sigma(t) &= (y_0(t) - \mathbf{K}^*(t) \cdot \mathbf{Y}(t)) + \\ &+ \alpha \cdot \mathbf{M}^*(t) \cdot \mathbf{Y}(t) = \\ &= Z_0(t) + Z_M(t) \end{aligned} \quad (2)$$

The asterisk means transposition and complex conjugation. The first summand $Z_0(t)$ pertains to the useful component for further processing (detection, parameter measurement), and it is the result of interference cancellation. The second summand $Z_M(t)$ is the sum of the modulated oscillations received by the additional antenna. The square-law detector in the output, except for square of summands (2), contains also results of their multiplication, which is used farther on for weighing coefficients estimation \mathbf{K} . Demodulators (DM) and the integrators (INT) allow selecting necessary component for generation of weighing coefficients \mathbf{K} .

Let's take into account that the ratios for the average values of uncorrelated processes $\mathbf{Y}(t)$ and $\mathbf{M}(t)$ hold true

$$\begin{aligned} \langle |Z_{0,M}(t)|^2 \cdot \mathbf{M}(t) \rangle &= \mathbf{0}_N, \\ \langle \mathbf{M}(t)^* \cdot \mathbf{M}(t) \rangle &= \mathbf{E} \end{aligned} \quad (3)$$

Here $\mathbf{0}_N$ is zero vector of size N , \mathbf{E} is the identity matrix. Then average value of signals in the outputs of the integrators is possible to present as

$$\begin{aligned} \mathbf{K} &= \langle Z_0(t) \cdot Z_M^*(t) \cdot \mathbf{M}(t) \rangle = \\ &= \alpha \gamma \langle Z_0(t) \cdot \mathbf{Y}^*(t) \rangle \end{aligned} \quad (4)$$

which coincides with the similar ratios for the cancellers constructed on the traditional scheme [4]. Here γ is a transmission coefficient of circuit from an output of the adder up to outputs of the integrators. For an approximation of weights \mathbf{K} to the optimal values it is necessary to ensure $\alpha \gamma \gg 1$ [4].

The interference power in the output of the adder in a stationary condition is equal to

$$\begin{aligned} P_\Sigma &= \langle |Z_0(t)|^2 \rangle + \langle |Z_M(t)|^2 \rangle = \\ &= P_O + P_M \end{aligned} \quad (5)$$

The second summand P_M caused by presence of the sum of the modulated component and equals

$$P_M = \alpha^2 P_\Pi, \quad (P_\Pi = \langle \mathbf{Y}(t)^* \cdot \mathbf{Y}(t) \rangle), \quad (6)$$

makes a hindering influence for further processing. Selecting coefficient α to be small (for preservation of condition $\alpha \gamma \gg 1$), it is possible to make the summands in (5) close to each other. Other way is most expedient in order to eliminate the influence of modulated component $Z_M(t)$. It is to divide in time the stages of adjustment of weights $\mathbf{K}(t)$ and the further processing. For example, as applied to the pulse radar, the adjustment of weights ($\alpha \neq 0$) is possible to realize at the end of sounding period (at the non-working parts of the distance), then to fix obtained weights and to use them at $\alpha = 0$ for interference cancellation for the operational range of distances.

3. THE EXPERIMENTAL BREADBOARD MODEL AND ITS PERFORMANCES

The breadboard model of the modulation canceller was created on the basis of the scheme of the Fig. 1. The weight summation was carried out at the frequency $f_0 = 150$ MHz. The number of channels of cancellation is equal to 2. The weighting regulators are made using AD835. The intermediate frequency of the receiving channel is equal to $f_{if} = 24$ MHz, and the passband of its linear part $\Delta f = 2.5$ MHz. The passband of the low-pass filter in the output of the square-law detector had the value $\Delta f_{LPF} = 1.2$ MHz. The dotted-line enclosed block of elements is realized on basis of programmed logic arrays such as Xilinx. Therefore after the low-pass filter the AD 8-digit converter is installed.

The program for fulfillment of all operations on calculation of the weighing coefficients, generation

of modulating voltages, integrations etc is developed. Outputs of the digital part were completed by the registers of memory for a storage of weighting coefficients and by the AD converters. The integrators are low-pass filters with a band $\Delta f = 1$ kHz.

The test of efficiency of the breadboard model of the canceller with a modulation method of weighting summation coefficients was conducted in the laboratory conditions. The generator of a harmonic signal and generator of a noise were used as interference sources. The generator of a harmonic signal with frequency tuning in a passband was applied both to preliminary adjustment of the canceller, and for the estimation of limiting coefficient of interference suppression in the dynamic range of stability. Since there is no influence of such factors as a non-identity of frequency characteristics and electrical lengths of channels at that. The maximal coefficient of cancellation of a harmonic interference after recording of the weighting coefficients and eliminating of the modulation was about 50 dB. In case of noise interference at the same conditions the cancellation was 32 dB. As modulating functions were used phase-shift keyed oscillations under the periodic law

$$m_i(t) = \exp[j\nu_i(t)] \quad (7)$$

where $\nu_i(t)$ represented impulses as meander with frequencies f_1 and $f_2 = 2f_1$. These magnitudes do influence the choice of pass-bands of the receiving channel up to the detector $\Delta f > 4f_1 + \Delta f_n$ and low-pass filter $\Delta f_{LPF} > 2f_1 + \Delta f_n$. (Δf_n is breadth of interference spectrum). At $\Delta f_1 > \Delta f_n$ the convergence rate is differed a little from the cancellers constructed on the traditional scheme.

The experiment was conducted at various frequencies of the modulating functions ($f_1 = 60 \dots 500$ kHz). In case of a violation of the above condition ($\Delta f_1 > \Delta f_n$), the delay of transients was observed, as then the spectrum of the modulated and not modulated component of interference were overlapped and the estimation of a gradient had become less precise.

It is established during the experiment that it is allowed to select such α that the power of the residuals of interference at the output P_O is commensurable

with the power of modulated component P_M at the condition of the preservation $\alpha\gamma = \text{const} \gg 1$. The further decrease of magnitude α would result in violation of efficiency of the canceller. As it should be expected, the modification of the coefficient $\alpha\gamma$ did vary the processing speed of the canceller. The choice of this magnitude influences also the level of fluctuation of the weighing coefficients in the steady mode, which is intrinsic to all types of the canceller with a feedback.

4. CONCLUSION

The presented experimental breadboard model of the modulation-type canceller can practically be used to protect the radio engineering means from masking jamming when any possibility for the signals branching-off in the carrier frequency tract for the weighing coefficients estimation is excluded because of specific construction of the antenna system. The best performance is to be expected in the narrow-band interference case, whose spectrum's breadth does not exceed that one of the modulating functions. The interference cancellation on the carrier frequency of the canceller with modulation of the weighing coefficients permits a considerable reduction as to the hardware costs.

REFERENCES

1. M. H. Myers. Adaptive Processing Apparatus. US Patent 4442433, April, 1984.
2. A. A. Cavelos. Controllable Saturation on Sidelobe Canceller. US Patent 4204211 May, 1980.
3. A. V. Kobzev, V. R. Khachaturov. Application of Channeling Principles of Estimating Weighting Coefficients in Antennas With Adaptive Spatial Signal Processing Against the Interference Background // Proc. of 3rd Int. Conf. on Antenna Theory and Techniques, Sevastopol, Ukraine, 8—11 September, 1999. pp. 272-275.
4. Shirman Ya. D. and V. N. Manzhos. Teoriya i tekhnika obrabotki radiolokatsionnoy informatsii na fone pomekh (Theory and Technique of Processing Radar Data on Noise Background), Radio i Svyaz Press, Moscow, 1981.

OPTIMAL ARRAY MULTIMODE SIGNAL PROCESSING IN THE PRESENCE OF MODAL MISMATCH

E. Yu. Gorodetskaya, D. M. Kharlamov, A. I. Malekhanov

Institute of Applied Physics, Russian Academy of Science
Nizhny Novgorod, Russia
<almal@hydro.appl.sci-nnov.ru>

Abstract

Modal mismatch effects on the output SNR of linear and quadratic array processors under the conditions of multimode propagation in a waveguide are presented. The modal mismatch is modelled by the distortion in the sound speed profile, which leads to unaccurate estimation of modal shapes at the array input. Numerical results are presented for the case of 16-element vertical array receiving the multimode signal in the background of spatially-white and modal noise. The channel of signal propagation is simulated for typical shallow-water environments from the Barents sea and the source frequency of 300 Hz. The scenarios when modal mismatch induces considerable array SNR loss are demonstrated. It is shown that the key factors of mismatch effects are the spatial modal resolution of the signal-carrying modes and intermodal phase shifts.

Keywords: array signal processing, modal mismatch, linear and quadratic processors, signal-to-noise ratio, signal coherence

1. INTRODUCTION

Recent developments of the array signal processing have been stimulated by the research and applied interest to the problems of the signal detection and estimation in random-inhomogeneous multimode waveguides with linear arrays. The most actuality of these problems was found with application to low-frequency underwater sound. As is well known, underwater sound channels allow long-range propagation of acoustic signals in the ocean. This leads to the two specific features of the array processing. The first is multimode spreading of the signal spatial spectrum even for a point source. The second, the loss of the signal coherence in space which results from multiple signal scattering by random inhomogeneities of the channel. The both features are critical factors of the large-array beamforming and gain [1,2]. It is known from a general theory that optimization of the array processing of perfectly coherent signals (with a regular wave front) is achieved among linear processing techniques and results in a weight summation of the array inputs in the array output. A more complicated scheme, quadratic array processing is optimal under the conditions of signal coherence degradation and is expressed in a weight summation of quadratic (by power) outputs of partial spatial filters, or beamformers [1-3]. The number of the partial beamformers is easily estimated by the ratio of array size to the signal coherence length.

In the both cases, both in the linear and quadratic processing schemes, mismatch problem is considered as one of the key issues of optimal array performance analysis. The appearance of mismatch in estimation of the signal shape (amplitude and phase distribution along the array) is an intrinsic feature of array operation in complex media that makes the array processor to decline from the optimal one. Thus, mismatch in the input signal field leads to decreasing of the output SNR and array gain. In the most of the literature dedicated to mismatch problem for the arrays in multimode channels, the perfectly coherent signals and, therefore, linear beamforming processors, or so called matched-field beamformers, are considered [4].

This article is focused on the study of the optimal array processors, both linear and quadratic ones, in the presence of modal mismatch, or mismatch in the signal modal shapes. Mismatch effects on the output SNR of linear and quadratic array processors are examined and compared. Numerical results are presented for the case of multimode signal in the background of spatially-white and modal noise, which is simulated for typical shallow-water environments from the Barents sea and vertical array. The most attention is paid to the scenarios when modal mismatch induces a considerable array SNR loss.

2. BASIC FORMULATIONS

Signal and noise fields in a multimode waveguide can both be expressed as a superposition of the discrete

spectrum normal modes. The signal \mathbf{s} and additive noise background \mathbf{n} have following vector representation at the array input:

$$\mathbf{s} = \sum_{m=1}^M a_m \mathbf{u}_m, \quad \mathbf{n} = \mathbf{n}_0 + \sum_{m=1}^M b_m \mathbf{u}_m \quad (1)$$

where $\mathbf{u}_m(\mathbf{r}, z) = (u_m(\mathbf{r}_1, z_1), u_m(\mathbf{r}_2, z_2), \dots, u_m(\mathbf{r}_N, z_N))^T$ is the m -th modal shape vector (modal vector) at the array input (the superscript "T" denotes transpose); a_1, a_2, \dots, a_M are coefficients of signal \mathbf{s} decomposition by mode vectors \mathbf{u}_m , also called signal modal amplitudes; similarly, b_1, b_2, \dots, b_M are the noise modal amplitudes; M is a total number of the discrete spectrum modes; \mathbf{n}_0 is the vector of non-modal noise which includes nearest noise sources and the array elements noise. We suppose in the further analysis, that \mathbf{s} and \mathbf{n} are random and statistically independent vectors, \mathbf{n} is a Gaussian vector, and \mathbf{n}_0 is a spatially-white noise.

We define here the output SNR as the deflection ratio in the array processor output [1-3]:

$$q = \frac{\langle P(\mathbf{s} + \mathbf{n}) \rangle - \langle P(\mathbf{n}) \rangle}{[\langle P^2(\mathbf{n}) \rangle - \langle P(\mathbf{n}) \rangle^2]^{1/2}} \quad (2)$$

The expression (2) is also known as a detection index or generalized SNR. It is known that maximum of the SNR (2) leads to (i) the small-signal asymptotic of the optimal processor from the maximum likelihood criterion and (ii) to the same optimal processor as it follows from maximum of the ratio of the output signal power to the noise one in a particular case of coherent signal.

When the signal is a coherent superposition of modal shapes, the optimal array processor is achieved by the known equation for the array weight vector:

$$\mathbf{w}_{opt} = \mathbf{R}_{nn}^{-1} \mathbf{s}^* \quad (3)$$

where $\mathbf{R}_{nn} = \langle \mathbf{n}^* \mathbf{n}^T \rangle$ is a spatial covariance matrix of the noise field (superscript "*" denotes conjugation). When the signal is a partially coherent modal superposition, arising from random modal amplitudes in Eq. (1), the optimal signal processor is achieved by the array weight matrix from the following equation:

$$\mathbf{W}_{opt} \mathbf{W}_{opt}^+ = \mathbf{R}_{nn}^{-1} \mathbf{R}_{ss} \mathbf{R}_{nn}^{-1} \quad (4)$$

where $\mathbf{R}_{ss} = \langle \mathbf{s}^* \mathbf{s}^T \rangle$ is the signal covariance matrix and the index "+" denotes conjugate transpose. Equation (4) was exploited for the recent study of large-array beamformers under the conditions of coherence-degraded signals in various environments [1-3].

As it follows from Eqs. (3, 4) the optimal array processing requires *a priori* known or measured amplitude and phase shapes and covariance matrixes of the signal and noise. Mismatch arises when the typical fluctuation time of the input shapes is less than typical time required for their estimation and processor optimization or when the reference signal shape differs from the real one. The problem above was widely

formulated in literature as the mismatch problem; the term "mismatch" can relate either to the channel parameters estimation or to the array weight coefficients forming. In scope of the model (1) one of the mismatch scenario is modal mismatch which is caused by the errors in the modal structure estimation at the array input. In short, this mismatch appears as a result of an inaccurate estimation of the modal vectors for the signal-carrying modes. Another type of mismatch scenario within the framework of a basic model (1) is an inaccurate estimation of the signal modal amplitudes, which was studied by many authors (see, for example, [5]).

We define the modal mismatch by the following model:

$$\tilde{\mathbf{u}}_i = \mathbf{u}_i + \delta \mathbf{u}_i, \quad i = 1, 2, \dots, M$$

Let the relative mismatch value to be defined for a single m -th mode by:

$$\xi_m = \frac{|\delta \mathbf{u}_m|^2}{|\mathbf{u}_m|^2} \quad (5)$$

The value that shows mismatch effects on the array performance is defined as the ratio of the output SNR in the presence of mismatch to the output SNR of fully optimal processor [6]:

$$\rho = \frac{q_{mismatch}}{q_{opt}} \quad (6)$$

where the SNR q is determined from Eq. (2).

Preliminary analytical results based on Eqs. (5),(6) were obtained from the mismatch study in the framework of two-mode signal model ($M = 2$) [6]. It was shown that mismatch leads to the array gain loss with increasing of relative value (5) in the case of both coherent and partially coherent signal. Specific value of ρ is dependent on the set of parameters. The most critical ones are the spatial mode resolution by the array (modal orthogonality), the intermodal phase shift, and the modal SNR. Also it was shown that mismatch effects reduces with decreasing of the mode amplitudes correlation. The SNR loss becomes less with mutual mode correlations decreasing for the signals with similar modal SNR and doesn't depend on mutual mode phases.

Some numerical results which show the output SNR loss in the presence of modal mismatch are presented below.

3. NUMERICAL SIMULATIONS

For numerical simulations, we assume some typical shallow-water environments from the Barents sea. The accurate and mismatched sound-speed profiles are drawn on Fig. 1 by solid and dot lines, respectively. The vertical equidistant array consists of 16 half-wavelength elements. The simulation parameters are the following: the total channel depth is of 120 m; the source frequency is of 300 Hz; $M = 30$. The modal shapes are calculated both for the accurate and dis-

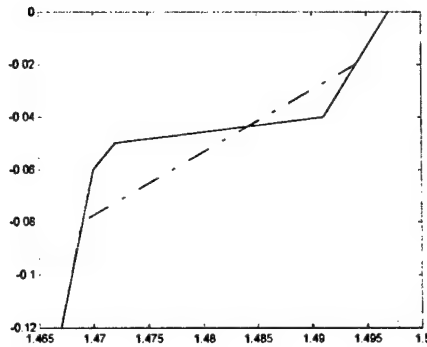


Fig. 1. Sound-speed profiles for the accurate (solid) and mismatched (dots) estimations

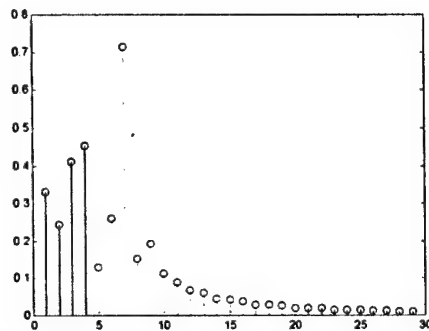


Fig. 2. Relative mismatch values (5)

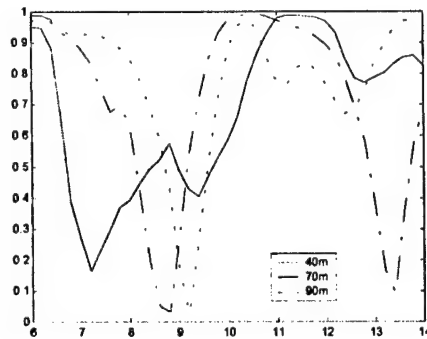


Fig. 3. Mismatch-induced SNR loss of linear processor

torted profiles, and the values (5) are estimated for each mode.

For the modal noise covariances we take the model of surface-generated noise [7]:

$$\{R_{mn}\}_{ij} = \frac{1}{p_q} \sum_{m=1}^M \frac{[u'_m(0)]^2}{h_m \operatorname{Im}(h_m) H} u_m(z_i) u_m(z_j) \quad (7)$$

where p_q is the intensity of spatially-white noise, h_m is a modal wavenumber, and H is a depth of the water channel. We note that high-order modes in the noise spectrum appear to be the most intensive modes due to their excitation by the surface sources. Therefore, optimal filter is adjusted to receive low-order modes (about 15 modes) in the absence of mismatch.

Computations of the relative mismatch value ξ (5) for the three different source depths in a waveguide and for the three depths of the first array element ($z_1 = 5, 35, 75$ m) reveal that mismatch is essential only for the first ten modes. Figure 2 shows the modal distribution $\xi^2(m)$ for the array arranged at the middle part of channel ($z_1 = 35$ m).

3.1. COHERENT SIGNAL (CORRELATED MODES)

For the near-surface array ($z_1 = 5$ m) mismatch effects become noticeable when the source excites low-order modes in which the relative mismatch values (5) are the most significant. It is important to note that low-order modes are not orthogonal at the array input. But low-order modes have small modal SNRs since its projections on the near-surface array are practically negligible, so the output SNR is slightly decreased (for about two times).

For the array centered in the channel ($z_1 = 35$ m) significant mismatch appears in the first ten modes (see Fig. 2). The dependence of ρ on the source distance is shown in Fig. 3 for the three different depths of the source. The particular case of dramatic mismatch-induced SNR degradation is illustrated here. A group of modes (starting from 5-th) with strong mismatch are partially orthogonal and have the biggest modal SNRs. Clearly, the mismatch leads in this case to essential suppression of the desired signal. It can be compared with array beamforming in a free space when beam pattern is deflected from direction-of-arrival of the plane-wave signal, and the signal moves to the side lobes or even null of the beam pattern.

This case confirms earlier resume formulated from the two-mode analysis [6]: the output SNR loss depends on the mode spatial resolution and mode phases. We also emphasize that considerable SNR degradation takes place for the small SNR values at the array input.

For the near-bottom arranged array ($z_1 = 75$ m) mismatch effects are weak because most intensive modes are practically orthogonal at the array input. Output SNR loss is caused by large relative mismatch values (5) in first five modes.

3.2. PARTIALLY COHERENT SIGNAL (UNCORRELATED MODES)

To simulate the partially coherent signal at the array input the following exponential model of the cross-modal correlations was used [2]:

$$\langle a_m a_n^* \rangle = |a_m| |a_n| \exp\left(-\frac{|m-n|}{\Delta}\right)$$

where Δ is the scale of cross-modal correlations. Numerical results for ρ were obtained for three values of this scale: $\Delta = 0, 3, 10$. We note here that this model does not include "residual" intermodal phase shifts so there is no any influence of the source range on the array SNR.

Table 1. Mismatch-induced SNR loss for the quadratic array processor.

	$\Delta = 0$	$\Delta = 3$	$\Delta = 10$
$h = 40$ m	0.78	0.71	0.54
$h = 70$ m	0.97	0.98	0.94
$h = 90$ m	0.97	0.94	0.76

Table 1 shows the dependence $\rho(\Delta)$ for the middle-depth array ($z_1 = 35$ m) and three various depths of the source.

In comparison with the optimal linear processing of the coherent signal, in this case mismatch effects decrease, and the output SNR loss depends only on the relative mismatch values. For example, for the near-bottom and near-surface arrays the loss doesn't exceed 10 % for the all scales Δ . For the middle-depth array the output SNR loss achieves up to 50 % that corresponds to the largest values (5). With increasing of the cross-modal correlation scale the influence of the mismatch increases because the signal becomes more coherent. But the loss level remains relatively small because the modal phase shifts are neglected.

Thus, optimal array processing of the partially coherent signal is essentially more robust to the modal mismatch as compared to the case of coherent signal. We note, however, that the coherence-induced SNR loss in this case is significant even for the optimal processor so the total effect of the signal coherence degradation leads to the rather poor SNR performance.

4. CONCLUSION

In this paper, we analyzed optimal array processing of the multimode signal against the modal noise background in the presence of mismatch in modal shapes estimation. Numerical results were presented for the vertical array in shallow-water environments from the Barents sea.

Specific effects of modal mismatch on optimal linear and quadratic array processors were demonstrated. It was shown that the key factors of mismatch effects are the spatial modal resolution of the signal-carrying modes and intermodal phase shifts. They are essentially significant for the case of coherent signal when the signal modes are well correlated. This case corresponds to relatively short distances in random channels. Contrary, optimal quadratic processing of partially coherent signals consisting of the uncorrelated modes is much more robust to the mismatch effects. In this case, the output SNR loss has a weak

dependence on the source range due to random phase shifts of the signal modes.

Therefore, modal mismatch should be taken into account when the optimal array processors are evaluated for the practical sonar systems operating in the underwater sound channels. Some special efforts can be considered with the aim to minimize the mismatch effects especially for linear beamformers. For example, as it follows from the results obtained, one of the recommendations is to arrange the vertical array elements in a channel in such a way that to resolve (to make orthogonal) the modes with the largest SNRs and in any case to minimize the values (6) for the signal-carrying modes.

ACKNOWLEDGEMENTS

This work was supported in part by the Russian Foundation for Basic Research (grant # 03-02-17035) and the Russian Ministry for Industry and Science (project # NSh-1637.2003.2).

REFERENCES

1. Gorodetskaya E.Yu., Malekhanov A.I., and Talanov V.I. Modelling of optimal array signal processing in underwater sound channels // *Akust. Zhur.* 1992. Vol. 38. No. 6. p. 1044 (in Russian).
2. Gorodetskaya E.Yu., Malekhanov A.I., Sazontov A.G., and Vdovicheva N.K. Deep-water acoustic coherence at long ranges: Theoretical predictions and effects on large-array signal processing // *IEEE J. Oceanic Eng.* 1999. Vol.24. No. 2, p. 156.
3. Morgan D.R. and Smith T.W. Coherence effects on the detection performance of quadratic array processors, with application to large-array matched-field beamforming// *J. Acoust. Soc. Am.* 1990. Vol. 87. No. 2. p. 737.
4. Tolstoy A. Matched Field Processing for Underwater Acoustics. – World Scientific, Singapore. 1993.
5. Malekhanov A.I. and Serebryakov G.V. Detection performance of optimal array signal processing of the discrete spectrum signals // *Radiotekhnika i Elektronika.* 1993. Vol. 38. No.6. p. 1069 (in Russian).
6. Kharlamov D.M. Optimal array signal processing of partially coherent signals in the presence of modal mismatch // *Proc. 5th Conf. on Radiophysics (Univ. of Nizhny Novgorod, 2001).* p. 41 (in Russian).
7. Kuperman W.A. and Ingenito F. Spatial correlation of surface generated noise in a stratified ocean // *J. Acoust. Soc. Amer.* 1980. Vol. 67. No. 6. 1988.

THE OPTIMIZATION OF A SIGNAL PROCESSING IN RADAR WITH SCANNING ANTENNA ARRAY

Anatoly D. Pluzhnikov and Elena N. Pribludova

Information Radiosystems department, State Technical University of Nizhny Novgorod
Nizhny Novgorod, Russia
<pluzhnikov@nntu.nnov.ru>

Abstract

It is shown that the scanning radar antenna is an instrument of a selection of echoes from target with intended range and an instrument of a suppression of intensive close clutter. The obtained result is useful to a case of a continuous or quasi-continuous transmitted signal.

Keywords: Space-time processing, resolution, selection, clutter, antenna, array.

1. INTRODUCTION

Continuous or quasi-continuous radar radiation is an effective way to improve a time (Doppler) selection of moving targets in clutter [1]. However, here an ability to receive weak useful signals from maximally distant targets is hampered by intense clutter originating at a close range. In this case it would be tempting to perform a clutter suppression by a spatial processing of signals (by a receiving antenna). This suppression is impossible without a spatial resolution of radar echoes originating at different distances. The known theory [2] does not mention about using of similar resolution in monostatic systems and suggests the widening of the antenna aperture and the narrowing of the antenna pattern (AP) as the only way of the spatial suppression of clutter. However, these recipes ignore scanning. Some results of the development of the mentioned theory with the scanning are presented below. In particular, new capabilities of a radar echo resolution and selection of continuous or quasi-continuous signals on clutter background are described.

2. THE SPATIAL ATTENUATION OF THE CLUTTER

We will consider a linear antenna system, rotating around its center at a fixed rate Ω rad/sec in the scanning plane (α, R) , where α is the angular coordinate (azimuth), R is the radial coordinate (range) measured from the center of the rotation. The zeros of the time t and angle α are taken so that the value Ωt of this angle defines the normal to the receiving antenna. For such a system the criterion of the spatial-distance resolution (the generalized Woodward constant [3]) is determined by the formula [4]:

$$\delta = \lambda \Pi^{-1} \Omega^{-1} \approx \theta_w \Omega^{-1}, \quad (1)$$

where $\theta_w \approx \lambda \Pi^{-1}$ is the width of the receiving AP in the scanning plane, λ is the operating wavelength, Π is the aperture antenna.

According to the expression (1) the spatial-distance resolution is improved not only with the increasing of the antenna aperture or with the narrowing of the AP (this is accustomed for a spatial resolution) but also with the increasing of the scanning rate.

We consider (see above) the continuous or quasi-continuous radar radiation and the problem of the selection of the signal on a clutter background. Moreover, according to the peculiarity of the problem, the signal and a clutter are reflected at different distances. Namely the signal originates at the range R_s , and the clutter originates at the range $R \ll R_s$. Consequently, in our case it is needed

$$\delta_R \leq R_s \text{ or } \delta \leq t_s = 2R_s/c. \quad (2)$$

In accordance with (1) and (2) the scanning rate should be so increased that

$$\varepsilon_{bw} = \Omega t_s \geq \theta_w \text{ or } \varepsilon_{bw} = \Omega t_s = \gamma \theta_w,$$

where the relative scanning rate

$$\gamma = \varepsilon_{bw} / \theta_w = \Omega t_s / \theta_w \geq 1.$$

In other words, during signal delay t_s , the antenna, its transmitting AP and receiving AP, rotate through an angle ε_{bw} which exceeds the width θ_w of the receiving AP in the scanning plane.

The obtained results and their use for the solution of the discussed problem of the spatial selection of the signals on a clutter background with continuous and quasi-continuous radiation can be interpreted in the following way. Assume that an antenna system has the separate transmitting AP (the dashed curve in Fig. 1) and receiving AP (the solid curves – the optimization result with conditions indicated below in the Section 3). While scanning, the main lobes of these APs are dis-

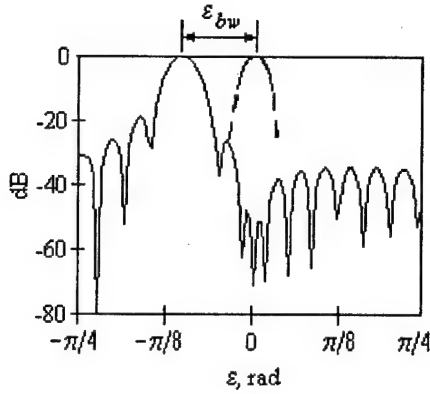


Fig. 1. Transmitting AP and receiving AP

placed by the constant angle ε_{bw} with respect to each other. Moreover, the scanning rate Ω is so high that during a delay of the signal from the farthest target every scanning AP rotates through an angle ε_{bw} which exceeds the AP width. However, these APs have not time for a turn between moments of the probing and of the echo reception from nearby land or water surfaces. Then clutter will be reached at angles corresponding to the main lobe of the transmitting AP and, consequently, to sidelobes of the receiving AP. I.e., the most intense clutter from nearby interfering reflectors will be attenuated with the reception. During delay of the useful signal from a far target the APs rotate so that the signal is received by the main lobe of the receiving AP. This reception will lead to a signal gain.

3. THE OPTIMIZATION EFFICIENCY OF A SIGNAL PROCESSING

The boundless increasing of the scanning rate (increasing of the value Ω or γ) is not reasonable, since it leads to the spectrum broadening of the radar echoes, their time (Doppler) resolution degradation and, as a consequence, degradation of the Doppler selection of moving targets on a clutter background. Therefore it is tempting to define the clutter suppression efficiency in the optimal system of the space-time signal processing. Assume that such a system is realized on an array base. Herewith the optimal space-time signal processing is defined by a weight vector column \mathbf{W} , which satisfies [5] the Wiener-Hopf equation and its solution (the so-called Wiener's solution):

$$\mathbf{H}\mathbf{W} = \chi\mathbf{S}^*,$$

$$\mathbf{W} = \chi\mathbf{H}^{-1}\mathbf{S}^*,$$

where χ is an arbitrary complex constant, the $NK \times NK$ noise correlation matrix

$$\mathbf{H} = E\{\mathbf{U}^*\mathbf{U}^T\} = \begin{bmatrix} \mathbf{H}_{a11} & \mathbf{H}_{a12} & \cdots & \mathbf{H}_{a1K} \\ \mathbf{H}_{a21} & \mathbf{H}_{a22} & \cdots & \mathbf{H}_{a2K} \\ \vdots & \vdots & \ddots & \vdots \\ \mathbf{H}_{aK1} & \mathbf{H}_{aK2} & \cdots & \mathbf{H}_{aKK} \end{bmatrix},$$

the $N \times N$ block

$$\mathbf{H}_{akl} = E\{\mathbf{U}^*(t_k)\mathbf{U}^T(t_l)\},$$

$E\{\cdot\}$ denotes the statistical expectation, N is the element quantity of the linear equidistant antenna array, K is the quantity of the processed signal samples, $k, l = \overline{1, K}$, the space-time noise vector column

$$\begin{aligned} \mathbf{U} &= \|\mathbf{U}^T(t_1), \mathbf{U}^T(t_2), \dots, \mathbf{U}^T(t_K)\|^T = \\ &= \sum_{k=1}^K \mathbf{I}_K^{(k)} \otimes \mathbf{U}(t_k), \end{aligned}$$

$\mathbf{I}_K^{(k)}$ is the k -th column of the unit matrix \mathbf{I}_K of order K , the symbol \otimes denotes the Kronecker multiplication, space noise vector

$$\mathbf{U}_a(t_k) = \|u_1(t_k), u_2(t_k), \dots, u_N(t_k)\|^T$$

$u_n(t_k)$ is the value of the complex envelope of the noise (clutter and intrinsic noise) in the n -th array element, $n = \overline{1, N}$, the used presentation of the space-time signal vector is

$$\mathbf{S} = \mathbf{I}_K^{(Z)} \otimes \mathbf{S}(t_{\max}),$$

Z is the integer part of the number $(K+1)/2$, with the Doppler shift ω and the target direction α the space signal vector

$$\begin{aligned} \mathbf{S}(t) &= \|s_1(t), s_2(t), \dots, s_N(t)\|^T = \\ &= \mu_s \exp(j\omega t) G_{b0} \{\alpha - \Omega(t - t_s)\} \Phi\{\alpha - \Omega t\}, \end{aligned}$$

$s_n(t)$ is the complex envelope of the signal in the n -th array element, a complex $\mu_s = \text{const}$, $G_{b0}(\varepsilon)$ is the normalized transmitting AP with the direction of the principal maximum $\varepsilon = \varepsilon_{b0}$, $\varepsilon = \alpha - \Omega t$ is the angle measured from the normal to the receiving antenna in the scanning plane, vector column

$$\Phi\{\varepsilon\} = \|\varphi_1\{\varepsilon\}, \varphi_2\{\varepsilon\}, \dots, \varphi_N\{\varepsilon\}\|^T,$$

$$\varphi_n\{\varepsilon\} = \exp\left\{j2\pi \frac{a}{\lambda} \left(n - \frac{N+1}{2}\right) \sin \varepsilon\right\},$$

$\pi = 3.14\dots$, a is the distance between neighboring elements. For the indicated notations the time of the signal maximum

$$t = t_{\max} \approx t_s + \frac{\alpha - \varepsilon_{b0}}{\Omega}.$$

In our case the space-time correlation noise matrix \mathbf{H} cannot be represented as a Kronecker multiplication of the space and time correlation matrices (even neglecting the intrinsic noise of the array elements). Consequently, even with the assumption of a space-time narrowband signal it is not possible to divide the processing routine into space and time processing: it is necessary to combine the array element outputs by means of the using of different Doppler filters in the spatial channels. This result can be interpreted by different linear velocities of the array elements during array rotation.

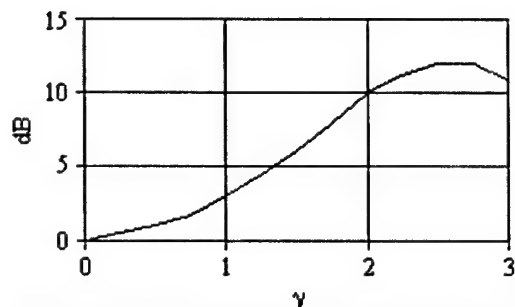


Fig. 2. Signal-to-noise improvement

Fig. 1 (mentioned above) and Fig. 2 show numerical results of the space-time processing analysis. They are obtained with using of the brought vector-matrix equations for a real noise situation and such system parameters: $\lambda = 0.2$ m, $\varepsilon_{b0} = 0$, $\gamma = 3$, $N = 20$, $a = 0.5\lambda$, the clutter level in each element equals 30 dB relatively to the intrinsic noise, the radar maximum-range equals $3 \cdot 10^5$ m, the order of the Doppler filter equals 2 ($K = 3$). This Doppler filter is a transversal filter, which there is in the each space channel of the array and accomplishes the optimal weighted summation of the signal samples equally spaced in time by 100 μ s (transmitted pulse repetition period with quasi-continuous radar radiation). The receiving AP (the solid curve in Fig. 1) is optimized for the indicated conditions. Fig. 1 shows that a dip is formed in the receiving AP in the vicinity of the value of $\varepsilon = 0$, corresponding to the maximum of the transmitting AP and, consequently, to the arrival direction of the highest intensity clutter from the close reflectors. At Fig. 2 the signal-to-noise improvement (compared to the traditional case of the low-velocity scanning when $\gamma \ll 1$) is presented. As one can see (Fig. 2), there is an optimum scanning rate ($\gamma \approx 2.7$): the efficiency of the space-time process-

ing is reduced with a decrease in the scanning rate due to degraded spatial suppression of the clutter and with an increase due to degraded time (Doppler) suppression. With $\gamma \approx 2.7$ the signal-to-noise improvement equals 12 dB.

4. CONCLUSIONS

Thus, the spatial-distance signal resolution and the spatial-distance signal selection are improved not only by the increasing of the antenna aperture or by the narrowing of the AP (this is a well-known recipe) but also by the increasing of the scanning rate. In this sense the increasing of the scanning rate is equivalent to the antenna aperture increasing and to the antenna pattern narrowing.

For the maximization of the efficiency of the space-time signal processing on a clutter background not only the antenna system parameters and the parameters of Doppler filters should be optimized but also the scanning rate should be optimized.

REFERENCES

1. Long, III W. H., Harriger K. A. Medium PRF for the AN/APG-66 Radar // Proc. IEEE. 1985. Vol. 73. No 2, p. 301.
2. Skolnik M. I. Radar Handbook - New York. McGraw-Hill Book Company, 1970.
3. Cook C. E., Bernfeld M. Radar Signals - New York, London. Academic Press, 1967.
4. Pluzhnikov A. D., Pribludova E. N., Torgushin E. I. Woodward constant with space-distance resolution in radar scanning system // Signal Processing. 1998. Vol. 65, p. 129.
5. Monzingo R. A., Miller T. W. Introduction to adaptive arrays - New York, Chichester, Brisbane, Toronto. John Wiley & Sons, Inc., 1980.

SPACE-TIME PROCESSING IN THREE-DIMENSIONAL FORWARD SCATTERING RADAR

Myakinkov A.V., Ryndyk A.G.

Information Radiosystems department, State Technical University of Nizhny Novgorod
<redvillage@mail.ru>

Abstract

The space-time processing algorithm for bistatic forward scattering radar is considered, which is based on application of antenna arrays with beamforming after amplitude detection in receive channels of non-directional (slightly directional) elements. It is shown that ambiguity of measured angles of arrival can be easily worked out. Mathematical modeling results are obtained.

Keywords: bistatic forward scattering radar, antenna array, space-time processing, beamforming, amplitude detection.

1. INTRODUCTION

Bistatic forward scattering radars (BFSR) provide effective detection and coordinates measurement of very small radar cross section (RCS) targets due to bistatic RCS rises (up to 20..40 dB in relation to monostatic RCS) in narrow region close to the base line between transmit and receive positions [1-3]. In practice, systems using continuous quasi-harmonic probe signal are applied [1-7]. Receive position location signal is a sum of powerful direct transmitter signal and target return. As a result, a receive antenna input signal is amplitude modulated, and modulation frequency is determined by the target return Doppler shift. Therefore, quasi-harmonic Doppler shift frequency signal can be obtained by the amplitude detection.

An angle of arrival of a target return can be measured by the way of forming partial beams. It can be realized, for example, with reflector antennae [4]. The significant disadvantage of this technique is in that a direct transmitter signal level in each channel significantly influence on transfer coefficients of receive channels. In the channel of center beam (directed to the transmitter), high level of a direct signal leads to the channel overload. At the same time, in the channels of side beams, a level of direct signal is determined by their radiation pattern side lobes and therefore, it is random.

This disadvantage can be eliminated by space-time processing on the base of the antenna array with beamforming after amplitude detection in receive channels of non-directional elements [8]. Direct signal levels are the same in all channels and do not influence on the channels transfer coefficients relation. Besides, under conditions of the powerful direct signal presence, amplitude detectors perform target return synchronous detection with quasi-harmonic Doppler shift frequency signal (real envelope) extraction, what provides the

latter without non-linear distortions. In addition, there is no need in transmission of the transmitter reference signal to the receive site or in its extraction from received signals. Due to this circumstance, technical realization of the system is considerably simplified as compared with that of systems based on phased antenna arrays with coherent signal processing [8].

Nowadays mostly developed radars are two-dimensional forward scattering radars that determine moving target coordinates in horizontal plane by measurements of target return Doppler shift and azimuth angle [4-7]. Application of three-dimensional forward scattering radars will permit improving the accuracy of determination of target coordinates. This can be achieved due to elimination of the inherent to two-dimensional radar systematic measurement errors. Besides, additional information about target altitude can be obtained.

The main purpose of this paper is to propose an effective and inexpensive space-time processing (STP) algorithm for three-dimensional forward scattering radar built on basis of two orthogonal linear equispaced antenna arrays with beamforming after amplitude detection in receive channels of non-directional elements.

2. SPACE-TIME PROCESSING ALGORITHM

A functional scheme of the azimuth antenna array STP algorithm is presented in Fig. 1. The STP algorithm of the elevation angle antenna array is fully analogous. In Fig.1 AD means amplitude detectors, RF – rejection filters, ADC – analog-to-digital converters, \hat{f}_D , $\hat{\alpha}$ – Doppler shift and azimuth estimations.

Equation (1) gives the value of n -th sample of the process at the AD output in receive channel of i -th azimuth antenna array element (or i -th azimuth channel, briefly) [8]:

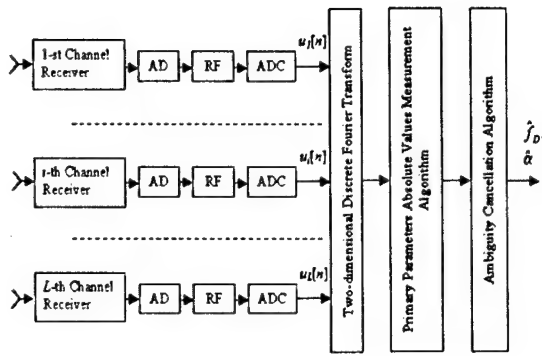


Fig. 1. STP functional scheme.

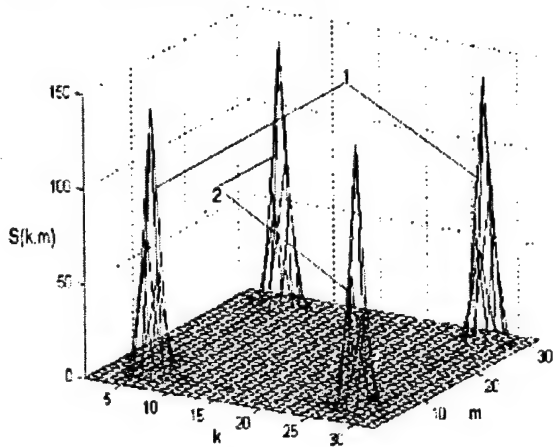


Fig. 2. Two-dimensional space-time spectrum.

$$u_{hor,i}[n] = u_0 + u_S \cos\{\varphi_D[n] + i2\pi(d/\lambda)\sin\alpha[n] + \varphi_0\} + \xi_i[n], \quad (1)$$

where u_0 is the constant component caused by the presence of direct transmitter signal, $\varphi_D[n]$ is the phase delay caused by the target return Doppler shift; u_S and φ_0 are, respectively, the amplitude and the random initial phase of quasi-harmonic Doppler frequency signal in the i -th azimuth channel; $i2\pi(d/\lambda)\sin\alpha[n]$ is the phase shift between the 1-st and i -th element, which is determined by the target azimuth; d is the constant array spacing; λ is the transmitter wavelength; α is the target azimuth; $\xi_i[n]$ is the i -th channel noise.

A phase delay between elevation angle antenna array elements $i2\pi(d/\lambda)\sin\beta[n]$ is determined by the target elevation angle $\beta[n]$. Besides, the elevation angle antenna array (AA) is inclined with respect to the vertical in order to reduce the influence of ground surface upon AA radiation pattern. Therefore, the expression for signals at the AD output in i -th elevation angle channel can be written as

$$u_{ver,i}[n] = u_0 + u_S \cos\{\varphi_D[n] + i2\pi\frac{d}{\lambda}[\sin(\beta[n] + \beta_0) - \sin\beta_0] + \varphi_0\} + \xi_i[n], \quad (2)$$

where angle $\beta_0 < 0$ corresponds to the elevation of antenna array normal towards the azimuth plane by the angle $|\beta_0|$.

Rejection filters suppress constant component u_0 arising at the AD output as a result of the direct signal presence. Application of analog rejection filters included before ADC (Fig. 1) enables to reduce ADC dynamic range requirements as compared with application of digital rejection filters.

The amplitude distribution over antenna array aperture at each instant of time has a form of spatial harmonics [9] whose frequencies are determined by azimuth α and elevation β angles. In order to obtain a result of unit measurement of return Doppler shift and angular coordinates of the target, the two-dimensional Fourier transform (3) over two-dimensional files of signal samples in azimuth and elevation channels is to be performed

$$S(k, m) = \sum_{i=0}^{L-1} \sum_{n=0}^{N-1} u[i, n] e^{-j(2\pi/L)ik} e^{-j(2\pi/N)nm}, \quad (3)$$

$$i, k \in [0, L-1], \quad n, m \in [0, N-1],$$

where i is the channel (azimuth or elevation) number, n is the signal sample number in the i -th channel, L is the number of antenna array elements, N is the number of signal samples per measurement interval in one channel.

Absolute values of function $S(k, m)$ for the cases when of Doppler shift and angle (azimuth or elevation) have the same and different signs are plotted in Fig. 2 (graphs 1 and 2, respectively). Values of Doppler shift and angle can be estimated by coordinates of function (3) maximum.

The need in concatenated space-time processing is a principal feature of the considered system. As indicated in [8], initial phases of spatial harmonics fluctuate with Doppler shift frequency when target moves along its trajectory. Since spatial harmonics after amplitude detection are real, the fluctuations of spatial harmonics lead to significant fluctuations of spatial filters response. In addition, the amplitude spectrum of real spatial harmonic is the even function of spatial frequency. This leads to the ambiguity with respect to angular coordinate sign. Noted circumstances do not permit obtaining instantaneous angular measurement independently of time processing. At the same time, concatenated space-time processing provides averaging of spatial spectrum for the measurement interval [8]. Due to this fast, the fluctuations of spatial filters responses are cancelled.

Ambiguity in sign of obtained azimuth angle α , which can be easily cancelled in the process of target tracking [8]. A positive Doppler shift corresponds to the target movement toward the base line. In this case, the Doppler shift decreases. A negative Doppler shift corresponds to the target movement away from the base line. In this case, the Doppler shift absolute value increases. Therefore, when measuring during target

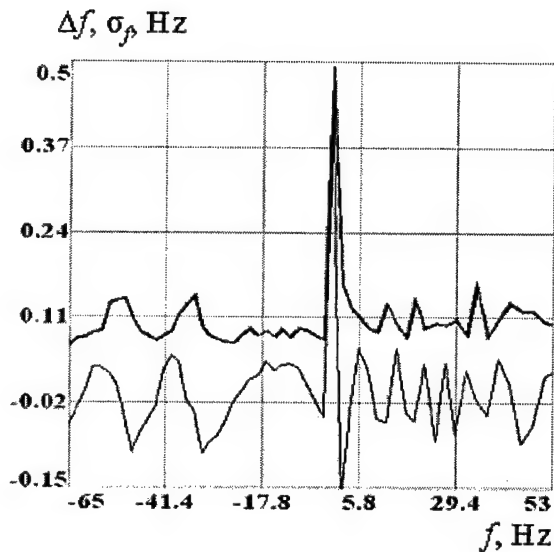


Fig. 3. Doppler shift measurement errors.

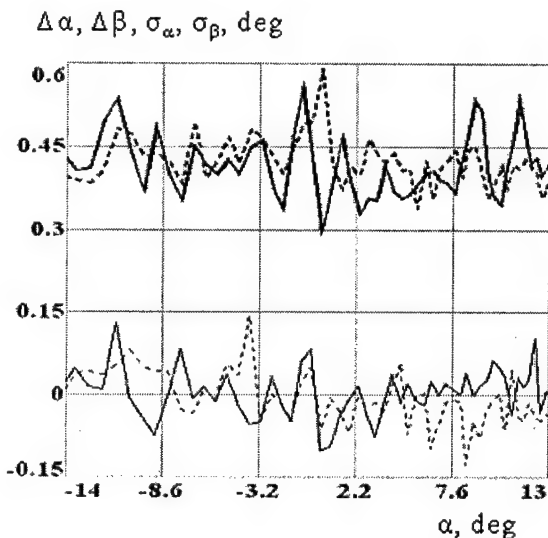


Fig. 4. Angles measurement errors.

tracking the first derivative of the Doppler shift absolute value, it is possible to obtain unambiguously the Doppler shift sign. If the elevation angle is always positive, the algorithm of ambiguity cancellation is considerably simplified, for in this case, Doppler shift sign is determined unambiguously for one measurement interval by mutual location of maxima of two-dimensional DFT in elevation angle channels.

3. PERFORMANCE ANALYSIS

When two-dimensional DFT in azimuth and elevation channels is executed, there are measured Doppler shift and angle (azimuth or elevation) by response amplitudes in five spatial-temporal filters. Filter with maximum response amplitude and two adjacent filters in both Doppler and spatial frequency dimensions are used. At the spectral analysis, two-dimensional

space-time weight processing is performed to improve characteristics. It provides both suppression of side lobes and reduction of instrumental errors of measurements. Besides, in order to improve an accuracy of angles measurement at the expense of the increase of the spatial filters number, files of the data obtained at the outputs of receive channels of azimuth and elevation AAs were added by zeroes [10].

Numerical estimations of an accuracy of Doppler shift and angles measurements are obtained with the mathematical modeling. To form signal samples in azimuth and elevation channels, target movement at the constant altitude of 1000 m was simulated. Receive channels noise at the two-dimensional DFT input was modeled as the discrete white Gauss noise.

In Fig.3, estimations of Doppler shift measurement errors versus Doppler shift values are shown. Thin line indicates an estimation of error Mean Δf (caused by the presence of measurement instrumental error). Thick line shows an estimation error Root Mean Square (RMS) σ_f of Doppler shift measurement.

Fig.4 shows estimations of angles (solid line – of the azimuth angle, dotted line – of the elevation one) measurement errors in dependence on target azimuth. True elevation angle values varied from about 3.5° to about 4.5° . Thin line represents error Mean $\Delta\alpha$, $\Delta\beta$ estimations. Thick line represents angles measurement errors RMS σ_α , σ_β estimations. One can see that azimuth and elevation angle measurement errors have close statistics.

Measurement error statistics were estimated by averaging of 100 independent experiment results. System parameters were assumed to have the following values: the distance between transmit and receive positions (base) $b = 40$ km; transmitter wavelength $\lambda = 1$ m; measurement interval $T = 1$ s; the number of receive channel signal samples per measurement interval is $N = 2048$ (corresponds to the number of Doppler filters with bandwidth of 1 Hz); the number of antenna array (both azimuth and elevation) elements $L = 16$; array spacing $d = 0.7\lambda$; the number of spatial filters formed in both azimuth and elevation angle dimensions $M = 32$. Amplitude detector output signal-to-noise ratio was assumed to be equal $q = 0.1$.

Instrumental errors of Doppler shift and angular coordinates measurements at the chosen system parameters (errors Mean, the same) do not exceed, in modulus, values of $\Delta f = 0.1$ Hz, $\Delta\alpha = 0.1^\circ$, $\Delta\beta = 0.1^\circ$ (Fig. 3, 4). The specified signal-to-noise ratio roughly corresponds to the minimum ratio providing the absence of abnormal (huge) measurement errors. Under these conditions, measurement errors of RMS are about $\sigma_f = 0.1..0.2$ Hz, $\sigma_\alpha \approx \sigma_\beta = 0.3..0.5^\circ$ for different targets trajectories.

A certain increase of measurement errors is possible if values of Doppler shift and angles are close to zero (Fig. 3, 4). It is caused by the central-axis symmetry of two-dimensional amplitude spectrum of real two-dimensional signal. If maxima of the two-

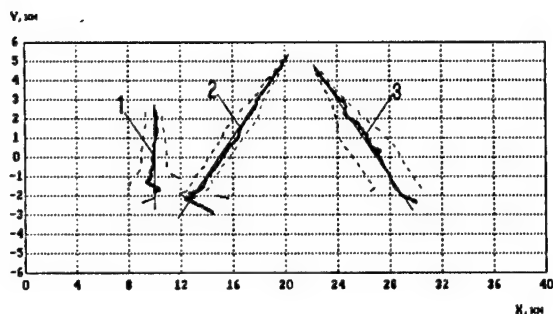


Fig. 5. Tracking results.

dimensional DFT over both Doppler and spatial frequencies dimensions fit in zero-tuned filters, Doppler shift and angle can be measured with the accuracy determined, respectively, by the space-time filter bandwidths of Doppler and spatial frequencies dimensions. In this case, relations between amplitude responses of space-time filters do not provide obtaining an accurate estimation of coordinates of a two-dimensional DFT maximum.

The obtained accuracy of primary parameters (Doppler shift, azimuth and elevation angle) measurement provides enables one to construct trajectories of moving targets with a high enough accuracy. This statement is proved by the results of mathematical modeling. Some target trajectories built by tracking algorithm are shown in Fig. 5.

The iteration Gauss-Newton algorithm on basis of maximum likelihood method [4,5] was used. The input of tracking algorithm is a primary parameters vector obtained by the space-time processing technique under consideration. It is assumed that a receive position location has coordinates (0,0), transmit position location is (40,0). Thin lines correspond to the true trajectories. Thick lines correspond to tracking-built trajectories. Dotted lines show errors regions of $\pm 3\sigma_X$. Statistics of the coordinates measurement errors were estimated by the results of 100 independent experiments. System parameters and receive channels noise statistics correspond to described above.

4. CONCLUSION

Space-time processing algorithm on basis of antenna arrays with beamforming after the amplitude detection in receive channels of non-directional elements is considered to be applied in three-dimensional bistatic

forward scattering radar. It is shown that the proposed technique provides unambiguous measurement of target return angle of arrival and tracking with a high accuracy. The results of mathematical modeling are presented. Principal advantages of the discussed STP algorithm as compared with conventional forward scattering radar STP approaches are discovered. These advantages make the considered technique attractive for the practice implementation.

REFERENCES

1. Willis N.Y. Bistatic Radar. Technology Service Corporation, Silver Spring, 1995.
2. Howland P.E. A Passive Metric Radar Using a Transmitter of Opportunity. International Conference of Radar, Paris, May 1994, pp.370-375.
3. Blyakhman A.B. Forward Scattering Bistatic Radar. PIERS Workshop on Advances in Radar Methods, Italy, July 1998, pp. 107-113.
4. Blyakhman A.B., Ryndyk A.G., Sidorov S.B. Forward Scattering Radar Moving Objects Coordinates Measurement. The record of the IEEE 2000 International Radar Conference. Alexandria, USA, May 7-12, 2000.
5. A.G. Ryndyk, S.B. Sidorov, A.B. Blyakhman, and F.N. Kovalev Accuracy of Estimating the Target Position by the Maximum Likelihood Method Using a Transmittive Radar // Radiotekhnika i Elektronika, 1999, No 12, pp.1436-1440. (in Rus.)
6. Blyakhman A.B., Kovalev F.N., Ryndyk A.G. Target Location Method in Forward Scattering Bistatic Radar // Radiotekhnika, 2001, No 1, pp.4-15.
7. Blyakhman A.B., Ryndyk A.G., Kovalev F.N. The equipment for object movement parameter measurement. Russian Federation Patent N2124220 with priority of 29.10.97, registered 27.12.98.(in Rus.)
8. Blyakhman A.B., Myakinkov A.V., Ryndyk A.G. Phased Antenna Arrays in Bistatic Forward Scattering Radar System // Progress in Electromagnetics Research Symposium Proceedings, Cambridge, Massachusetts, July 2002, p.163.
9. Korostelev A.A. Space-Time Theory of Radio Systems. Moscow, Russia, 1987. (in Rus.)
10. S. Lawrence Marple, Jr. Digital Spectral Analysis with Applications. Prentice-Hall, Inc., Englewood Cliffs, NJ 07632, 1987.

THE ROBUST SPATIOTEMPORAL FILTERING OF SIGNALS IN CORRELATED NOISE

O. V. Sytnik

Institute for Radiophysics and Electronics of NAS of Ukraine,
12 Acad. Proskura St., 61085, Kharkov, Ukraine
<vigor@ire.kharkov.ua>

Abstract

A new approach is considered for solving the problem of spatiotemporal signal processing in adaptive antenna arrays working in conditions of intensive correlated noise processes. The method of synthesis of robust algorithms is based on the game-theoretical principle of searching a minimum of the root-mean-square error that characterizes the quality of received estimations of existential spectra. The signal processing algorithms, constructed on this principle, relate to the class of minimax algorithms being invariant with respect to the prior uncertainty concerning noise distribution.

Keywords: Adaptive antenna array, algorithm, robust method, minimax rule, probability density.

1. INTRODUCTION

The noise depending on a probing signal arises in many applied radar and acoustic problems. Such noise can appear, for example, because of the multipath propagation of probing signal fluctuations and reflections from local objects or it can be specially caused for counterradio measures. The adaptive antenna arrays [2] used in radar systems with existential signal processing algorithms [2,3] that optimize parameters of radar systems in conditions of the Gaussian or any other given models of noise distribution at the presence of correlated noise processes, reduce the operating efficiency, and in some cases are unable to form an acceptable directional pattern.

This dependence of properties of optimal algorithms of existential signal processing on noise characteristics forces the developers of radar systems with adaptive antenna arrays to build not optimal but stable (robust) algorithms [1, 4-6] having the high, though yielding to optimal algorithms, efficiency under nominal conditions and the acceptable efficiency in conditions when the signal and noise properties can vary within the limits of the given classes of possible characteristics.

2. STATEMENT OF THE PROBLEM

Let's consider the response model of one of identical channels of the M -element linear antenna array

$$y(t) = S(t) + N(t), \quad (1)$$

where $S(t), N(t)$ are random processes representing a signal and noise.

Let's designate the power spectral density of a signal and noise as F_S, F_N . If the path pulse characteristic is $h(t)$, the signal evaluation at its output turns out to be convoluted realizations (1) with the following pulse characteristic

$$\hat{S}(t) = \int_{-\infty}^{\infty} h(t - \tau) y(\tau) d\tau. \quad (2)$$

The quality of signal evaluation (2) is usually [3, 5, 6] characterized by the size of the root-mean-square error that is determined by the expression

$$E\{|S(t) - \hat{S}(t)|^2\} = \frac{1}{2\pi} \int_{-\infty}^{\infty} [1 - |H(\omega)|^2] F_S(\omega) + |H(\omega)|^2 F_N(\omega) d\omega = \varepsilon(F_S, F_N, H) \quad (3)$$

where $H(\omega)$ is the Fourier transform of $h(t)$.

If the functions F_S and F_N are unknown and can assume any form within the limits of classes \mathfrak{S} and \mathfrak{R} , the upper boundary of possible solutions will be determined by

$$\sup_{(F_S, F_N) \in \mathfrak{S} \times \mathfrak{R}} \{\varepsilon(F_S, F_N, H_0)\}, \quad (4)$$

where H_0 is the optimal characteristic of the path.

Hence, the synthesis of the robust algorithm means a solution of the problem of minimization of the H degree of the filter efficiency decrease in the worst case, namely the search of the criterion minimum

$$\min_H \left\{ \sup_{(F_S, F_N) \in \mathfrak{S} \times \mathfrak{R}} \{\varepsilon(F_S, F_N, H_0)\} \right\}. \quad (5)$$

We shall consider the algorithm that satisfies the criterion (5) as robust with respect to the uncertainty classes $\mathfrak{S}, \mathfrak{R}$.

3. GENERAL APPROACH TO SOLVING THE PROBLEM OF THE ROBUST ALGORITHM SYNTHESIS

If to assume that the signal and noise in (1) are jointly stationary (in wide sense) random processes, their correlation structure is completely determined by the matrix D of spectral density

$$D(\omega) = \begin{bmatrix} F_S(\omega) & F_{SN}(\omega) \\ F_{NS}^*(\omega) & F_N(\omega) \end{bmatrix}, \quad (6)$$

where the symbol $*$ denotes the operation of complex conjugation, and the bottom indexes SN, NS mean the cross-spectra of processes $S(t), N(t)$.

In case of obtaining a signal evaluation at the antenna element output in conformity with (2), we can immediately write down the expression for the root-mean-square error:

$$E\{|S(t) - \hat{S}(t)|\} = \frac{1}{2\pi} \int_{-\infty}^{\infty} \|1 - H(\omega)\|^2 F_S(\omega) + |H(\omega)|^2 F_N(\omega) - 2H(\omega) F_{SN}(\omega) + 2|H(\omega)|^2 \operatorname{Re}\{F_{SN}(\omega)\} d\omega = \varepsilon(F_S, F_N, F_{SN}, H) \quad (7)$$

The characteristic of the optimal filter that minimizes the root-mean-square error depending on the expression (7) is determined by the expression

$$H_0 = \frac{F_S + F_N}{F_S(\omega) + 2\operatorname{Re}\{F_{SN}(\omega)\} + F_N(\omega)} \quad (8)$$

but the corresponding minimal value of the root-mean-square error is equal to

$$\varepsilon(F_S, F_N, F_{SN}, H) = \frac{1}{2\pi} \int_{-\infty}^{\infty} F_S(\omega) - \frac{|F_S + F_{SN}|^2}{F_S(\omega) + 2\operatorname{Re}\{F_{SN}(\omega)\} + F_N(\omega)} d\omega \quad (9)$$

If the matrix D (6) is absolutely unknown, but it is known that it belongs to some class \mathcal{N} , then the criterion function is replaced by its upper boundary of this class [1], and as the estimation \hat{D} of the matrix D we take the matrix that satisfies the criterion

$$\hat{D} = \arg \left\{ \min_{D \in \mathcal{N}} \varepsilon(F_S, F_N, F_{SN}) \right\}. \quad (10)$$

This approach provides the solution of the problem of synthesis of signal processing quasioptimal algorithms in conditions of uncertainty with respect to F_S, F_N, F_{SN} .

4. REALIZATION OF THE ALGORITHM IN THE LINEAR ADAPTIVE ANTENNA ARRAY

We shall consider the realization of the algorithm by an example of the linear narrow-band antenna array containing M identical elements. For simplicity, we will consider the distance between adjacent elements equal to $d = \lambda/2$, where λ is the wave length, corresponding to the central frequency of the probing

signal spectrum. The signal source and the noise sources are in the antenna far zone.

It is known [2, 7, 8] that the sample covariance matrix of signals from m interfering noise sources located in directions $\theta_1, \theta_2, \dots, \theta_m$ at the presence of the white noise with the dispersion σ^2 is determined by

$$R_{l,k} = \sigma^2 \delta_{l,k} + \sum_{i=1}^m R_i e^{j(2\pi d/\lambda) \sin \theta_i}, \quad (11)$$

where R_i is the power of the i -th source and $\delta_{l,k}$ is the delta function.

For the useful signal source the response of the i -th element of the array will be

$$S_i = S e^{j(2\pi d/\lambda) \sin(\theta)}. \quad (12)$$

The weight vector of the spatiotemporal filter, which maximizes the signal-to-noise merit, is put down as

$$\vec{W}(\theta) = \mu \vec{R}^{-1} \vec{S}_0^*(\theta), \quad (13)$$

where μ is the normalizing constant.

It can be shown that for the class of possible signals $\vec{S}(\theta)$ that satisfy the condition

$$\sum_{i=1}^M |S_i(\theta) - S_{i0}(\theta)|^2 \leq \nu \quad (14)$$

the vector of weight coefficients of the robust spatiotemporal filter is expressed by the simple ratio

$$\vec{W}_r(\theta) = \mu (\vec{R} + \alpha_0 \vec{I})^{-1} \vec{S}_0^*(\theta), \quad (15)$$

where \vec{I} is the unitary matrix and α_0 is the constant that depends on ν .

Moreover, as it follows from (15), the signal-to-noise merit at the adaptive antenna output with the weight vector \vec{W}_r is dependent on the value of ν .

5. EXPERIMENTAL INVESTIGATIONS OF THE ALGORITHM

The antenna directional pattern at the fixed direction to the useful signal source θ_0 is determined by [2]

$$G(\theta, \theta_0) = \left| \sum_{i=1}^M W_i(\theta_0) S_{i0}(\theta) \right|. \quad (16)$$

The directional patterns, calculated according to (13), (15) and (16), of the 9-element linear antenna array are shown in Fig. 1 and Fig. 2. The correlated noise sources were at corners $\theta_1 = 32^\circ$ and $\theta_2 = 36^\circ$ during calculation. At that the power and spectral density of noise were identical. The direction to the useful signal corresponded to the corner $\theta_0 = 0^\circ$. The directional pattern of the nonadaptive 9-element equispaced array with the uniform field distribution on the aperture is showed with a dotted curve (the curve 1) in Fig. 1 and Fig. 2.

As is obvious from Fig. 1 the directional pattern of the adaptive antenna designed for uncorrelated noise (the curve 2) cannot be formed at the presence of two neighboring powerful sources of correlated noise. In

this case the optimal algorithm does not only improve the signal-to-noise merit at the antenna output, but also it reduces essentially the efficiency of this antenna even with respect to the usual nonadaptive antenna. The fading nulls in directions to the noise sources are practically absent, and the main lobe providing the useful signal reception is strongly deformed. The directional pattern of the same antenna (the curve 2 in Fig. 2), which works using the robust algorithm, has strongly pronounced fading nulls in the field of side lobes in directions to the noise sources, and the form of the main lobe practically coincides with the form of the main lobe of the nonadaptive antenna (the curve 1). At that, the signal losses of the order of 10 dB, been caused by the reduction of the gain factor of the robust antenna, are insignificant with respect to the increase of the resulting signal-to-noise merit that makes, at worst, approximately 40 dB.

6. CONCLUSIONS

Thus, the application of the robust methods of synthesis of signal processing algorithms in adaptive antenna arrays results in the opportunity of obtaining quasioptimal algorithms which are stable against noise statistical characteristics of the given class. The inevitable losses of the useful signal in robust algorithms with respect to classical optimal algorithms are insignificant in comparison with the advantage of the signal-to-noise merit for the case of correlated noise. And also these losses can be regarded as an original "charge" for the reliability improvement of the algorithm under prior uncertainty. Therefore, in essential multifunctional systems using the adaptive antenna arrays it is reasonable to use the robust approach to synthesis of existential signal processing algorithms.

The considered class of narrow-band signals can be expanded into the generalized class which is specified by the constraint set $\nu_1, \nu_2, \dots, \nu_n$. The broadband signal processing using the robust algorithms is possible, provided that a signal of each antenna element passes through the multidrop delay line. It results in increasing the reversible matrix size by factor of k^2 , where k is the number of tapplings of the delay line. And, though the volume of calculations increases, there is an additional advantage of the robust algorithm. Namely, the smaller sensitivity to interchannel mismatches and the spread of parameters of the channel-delay lines. While for realization of the optimal algorithm the rigid restrictions on characteristics of multidrop delay lines [2] are required.

It should be noted that the considered example of the quasioptimal algorithm does not take into account the technique of analog-digital conversion. The adaptive algorithms of signal processing in antenna arrays are built, as a rule, on the basis of some preset statistical model of quantized data [9,10]. As it is impossible to specify such an adequate model in real conditions, it is necessary to use adaptive or so-called asymptotic robust quantizers [10] when constructing the robust algorithms of existential signal processing in adaptive antenna arrays.

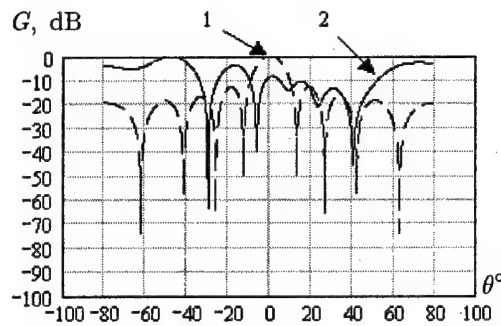


Fig. 1. The directional pattern of the antenna with an optimal vector of weight coefficients

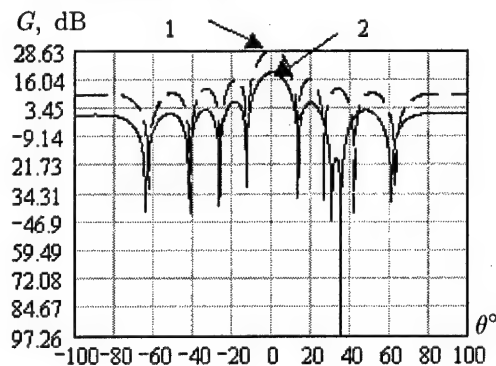


Fig. 2. The directional pattern of the antenna with a robust vector of weight coefficients

REFERENCES

1. Huber P. J. Robust Statistics.— New York, Chichester, Brisbane, Toronto. 1981.
2. Monzingo R. A., Miller T. W. Introduction to Adaptive Arrays.— New York, Chichester, Brisbane, Toronto. 1980.
3. Marpl Jr. S. L. Digital Spectral Analysis with Applications.— Prentice-Hall, Englewood Cliffs, New Jersey. 1987.
4. Hollander M., Wolfe D. A. Nonparametric Statistical Methods.— New York, London, Sydney, Toronto. 1973.
5. Kassam S. A., Poor H. V. Robust Signal Processing for Communication systems // IEEE Commun., Mag., 1983. Vol. 21, No 1, p. 20-28.
6. Poor H. V. The Rate-distortion Function Classes of Sources determined by Spectral Capacities // IEEE Trans. Inform. Theory 1982. Vol. IT-26, p. 19-26.
7. Wirth W. D. Fast and Efficient Target Search with Phased Array Radars // Proc. IEEE Int. Radar Conf., 1975, p. 198-203.
8. Wirth W. D. Signal Processing for Target Detection in Experimental Phased-array Radar ELRA // IEE Proc. F., Commun., Radar & Signal Proc., 1981, 128 (5), p. 311-316.
9. Bucklew J. A., Wise G. L. Multidimensional Asymptotic Quantization Theory with Power Distortion Measures // IEEE Trans. Inform. Theory. 1982. Vol. IT-28, p. 239-247.
10. Aazhang B., Poor H. V. On Optimum and Nearly Optimum Data Quantization for Signal Detection // IEEE Trans. Commun. 1984. Vol. COM-32, p. 745-751.

HYBRID OPTOELECTRONIC PROCESSOR FOR DETECTION, DIRECTION FINDING AND RECEPTION OF COMPLEX SIGNALS

A. Yu. Grinev¹, D. V. Bagno¹, V. V. Rozdobudko², V. S. Temchenko¹

¹ Moscow Aviation Institute (State Technical University), Moscow, Russia
<antenna@mai.ru>

² Taganrog State Radiotechnics University, Taganrog, Russia
<fep@tsure.ru>

Abstract

Results of research of multifunctional hybrid optoelectronic processor of spatial-temporal signals are presented. The processor provides detection, essential parameters measurement and reception of complex signal with pseudo-random frequency hopping.

Keywords: electro-optic, acousto-optic, array antenna, interferometer, optical beam-forming, spread-spectrum, pseudo-noise, correlation, bearing.

1. INTRODUCTION

The modern radio systems widely use complex signals with $\Delta F \Delta T$ product of one thousand to one million and over with bandwidth ΔF of hundreds of MHz. These are the pseudo-noise signals with phase manipulation, frequency modulation, pseudo-random frequency hopping and others. The use of these signals allows increasing interception immunity for radio systems, so the investigation of effective means of detection, angle-of-arrival estimation and reception is topical.

In the present time, the traditional approaches to complex signals processing by using both analog and digital techniques does not provide satisfactory solution in the case that $\Delta F \Delta T$ product exceeds one thousand. Digital processors still face with difficulties with power consumption, weight and dimensions. If the necessary bandwidth is more than 300 MHz or $\Delta F \Delta T$ product is close to 1 million, then the required processing rate exceeds the abilities of digital means.

The solution may be in creation of heterogeneous data processing systems which is based on integration of traditional electronic components and processors based on different principals and architectures. This approach meets present and probably future requirements.

One of the most prepared techniques for this is hybrid optoelectronic processors (HOEPs) [1], which successfully unite wide band analog acousto-optical processors and digital means of post-processing and control. It is known that time-domain integrating acousto-optical correlators (TIAOCs) allow ultra long time spread-spectrum signals processing of tenths and more milliseconds. Acousto-optic phase-modulated pulse signal analyzers and demodulators are able to process the single pulse with a phase measurement accuracy of the order of 10° . HOEPs of array antenna

(electro-optical arrays) are capable to process space-time signals. The use of multi-channel acousto-optic modulator (AOM) as radio frequency signal to coherent light transducer allows 50...100 parallel spatial channels, each operates at the central frequency of 1 GHz with the bandwidth of up to 500 MHz [2].

2. THE HYBRID OPTOELECTRONIC PROCESSOR

The structure of multi-functional HOEP of receiving antenna system signals is shown in Fig. 1. The HOEP provides detection, bearing finding, pulse structure analysis and reception of complex signal originating from communication system. The signal features are the following: use of pulse packets; pulse-to-pulse frequency hops with the rate of 0.1 million hops/s within 300 MHz bandwidth; continuous-phase manipulation waveform with minimal phase shift; data transfer by the use of relative cyclic shift of binary code which is used for internal pulse modulation.

The HOEP includes the following structural modules: detection module (for parallel (panoramic) radio scene survey, detection and angle-of-arrival estimation of low-power source(s) of spread-spectrum signal); beam forming module (for receiving array antenna pattern maximization toward the source of interest); structure analysis module (for restoration of binary code used for pulse manipulation) and demodulation module (for binary data extraction).

The HOEP antenna system incorporates small inline array WA2 and the single element distant antenna WA1. Due to special signal processing in the HOEP, the antenna system acts as an integration of interferometer with base d (Fig. 2) and array antenna. Space-time signals registered with the antenna system are amplified, transformed to the intermediate frequency

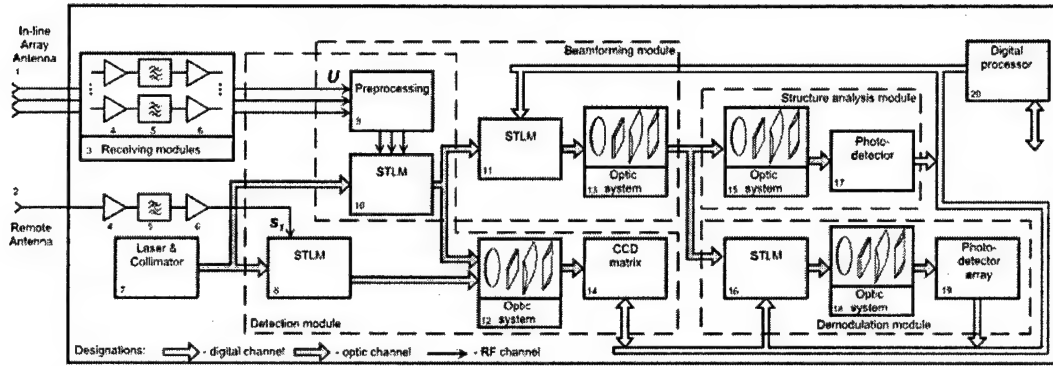


Fig. 1. HOEP structure

and entered the coherent optical processor (COP) by the use of acousto-optic space-time light modulators (STLM) 8 and 10 (Fig. 1).

2.1. DETECTION MODULE

The structure of detection module is shown in Fig. 2. Elements of WA2 can be aligned either along the base d (WA2X) or across the d (WA2Y). The COP of the module includes AOM 1 and 2, laser with collimator (not shown), lenses and astigmatic pairs L1-L4, space filters T, and CCD matrix as output transducer.

In the XOZ plane, the COP functions as quadrature TIAOC (Fig. 3 a) whose AOMs operates in Bragg mode. The special illumination of AOMs with crossed beams (designated as "a" and "b" in Fig. 3 b) is implemented for heterodyne spatial frequency transformation [3]. One of the beams ("a") is used as reference source for the AOM2 and is not deflected by the AOM1 due to special regime of acousto-optic interaction and special geometry of T_{π_1} space filter. In case of signal bandwidth $\Delta F \sim 300$ MHz, the strongest interfering diffracting order ("1st" order of "a" beam - "a-"), shown as dash line in Fig. 3b), which appears in the passband window of T_{π_1} , is suppressed down to -25 dB and over by insufficient (< 3 dB) reduction of intensity in the useful light order (b+). The same technique is implemented for the diffraction on the AOM2.

In the YOZ plane, the COP shown in Fig. 2 functions as in-line electro-optical array [2]. The COP transforms space-time radio frequency signal registered by the array antenna WA2 and visualizes an angular distribution of radio sources (radio scene) in form of appropriately aligned light strips.

So the CCD matrix (Fig. 2) detects the combination of the two coherent light distributions which represent space-time signals in the two AOMs:

- in OY direction: Fourier-image of signal in AOM2 (the radio scene formed by electro-optical array antenna) and Fourier-image of AOM2 (quasi-homogeneous light illumination);
- in OX direction: an image of AOM1 and upside-down image of AOM2.

The CCD matrix integrates the total light distribution in time domain. Collected charge relief Q reads out periodically and enters the digital processor where the post-processing is performed.

The 2D integral transform of the space-time signal registered by the array antenna is defined as

$$Q(x, y) \sim \beta(y) \otimes \text{Re} \left\{ \hat{R}_{\hat{s}_{1m}} \hat{S}_{\{U_m\}} \left(\frac{2x}{V} \right) \right\} = \\ = \text{Re} \left\{ \sum_{i=1}^N \hat{R}_{\hat{s}_{1m} \hat{s}_{m_i}} \left(\frac{2x}{V} - \frac{d}{c} \cos \varphi_i \right) \times \right. \\ \left. \times F \left(y - \lambda_{ig} f_L \frac{\nu_i}{m} \right) \right\},$$

where $\beta(y)$ is the COP image kernel; \otimes , \hat{R} and \hat{S} are the convolution, cross-correlation and Fourier transform operators; index m and asterisk (*) designate complex amplitude and complex conjugation, respectively; V is the ultrasound velocity in the body of AOM; N is the quantity of radio sources; s_i is the signal of i -th source; c is the light speed; $F(y) = F_{AA} \left(m (\lambda_{ig} f_L)^{-1} y \right) \otimes \beta(y)$ and m are the image kernel and scale ratio of the electro-optical array, respectively; F_{AA} is the WA2 array antenna pattern; f_L is the focal length of lenses and astigmatic pairs L1-L4; $\nu_i = \lambda_0^{-1} \cos \varphi_i$ for the WA2^X and $\nu_i = \lambda_0^{-1} \cos \theta_i$ for the WA2^Y are the spatial frequency; other symbols are disclosed in the figure. In parallel mode, the HOEP forms the cross-correlation function of the group signal s_1 with the signals received from every direction of the radio scene. HOEP provides the signal/(noise + jammer) ratio increasing due to space-domain processing in elevation plane, signal/noise ratio increasing due to space-time correlation processing (interferometric) of complex signals [4], and parallel forming of azimuth and elevation coordinates estimations of multiple radio frequency sources.

The format of 2D output signal of CCD matrix is shown in Fig. 4. In case of WA2Y (Fig. 4 a), the envelope of auto-correlation function (ACF) of every source is formed along OX. The position of ACF peak is determined by the azimuth position of source.

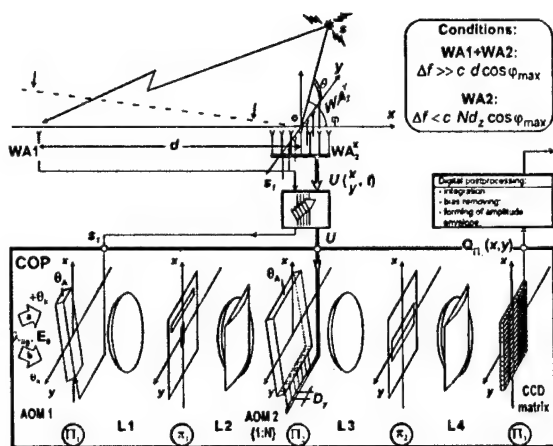


Fig. 2. Detection module

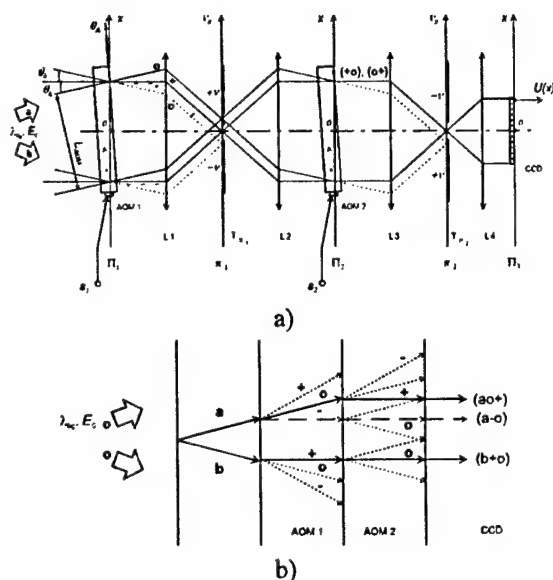


Fig. 3. Configuration a) and beams b) in the TIAOC

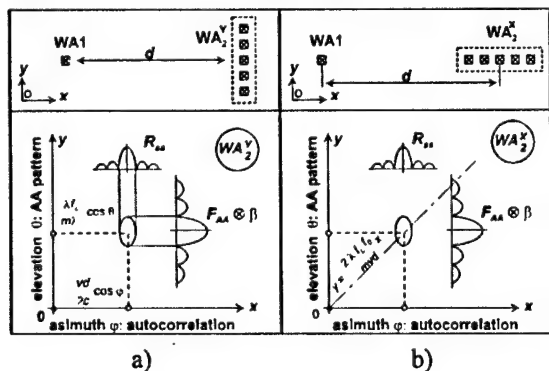


Fig. 4. Format of the HOEP 2D output

Along OY , the distribution of radio sources is formed in elevation plane.

In case of $WA2X$ (Fig. 4b) the peak of optical image of source lies on a line originating from the center of coordinates; the processor surveys the radio scene in single plane (the azimuth plane) but has the ability to detect both wide band and narrow band signals with extended ACF.

2.2. BEAM FORMING MODULE

The information about the state of radio scene supplied by the detection module is used in the beam forming module to select the desired signal source. The module realizes algorithm [5] of signal/(noise + jammer) ratio maximization. The algorithm was modified for implementation in HOEP [3]. The COP uses parallel beam forming method. In the front focal plane Π of positive lens the coherent light distribution is formed by use of multi-channel STLM. The complex amplitude $\dot{E}_{\Pi}(y)$ of light corresponds to current distribution $\dot{J}(y)$ in the array antenna $[WA_2^Y]$. As a result, the diffracted light distribution $\dot{E}_{\pi}(my/\lambda_{ij}f_L)$ ($m \gg 1$ – scale coefficient) in the rear focal plane π of lens is defined by the spatial spectrum of radio signals registered by the array antenna. So the angular distribution of radio sources (the radio scene) is visualized. The algorithm of space-time signal transformation in the COP is:

$$\hat{L}\{\dots\} = \hat{S}\left[\Psi_0^{-1}(y)\left[1 - \text{rect}\left(\frac{y}{\Delta y}\right)\right] \times \right. \\ \left. \times \hat{S}\left[\hat{\tau}_{\psi}(\theta - \theta_s)\hat{S}\left[\Psi_0(y)\text{rect}\left(\frac{y}{\Delta y}\right)\dot{E}(my, t)\right]\right]\right] \quad (2)$$

where Ψ_0 is the light amplitude in the COP input plane defined by the extended wave spherical function of the zero order [3]; Δy is the STLM aperture size; θ_s is the radio source bearing; $\hat{\tau}_{\psi}$ is the transfer function of the spatial filter (controlled binary phase transparent).

The action of (2) is in the disturbance of optical image of the signal of interest by the controlled filter with the transfer function $\hat{\tau}_{\psi}$. This filter is optimized in terms of minimal losses of laser light energy, the simplicity of realization by the dynamic transparent and minimal distortion of signals. Filter has the following structure of $\hat{\tau}_{\psi}$: $|\hat{\tau}_{\psi}| = 1$ in the whole surface, but in the position of useful source in σ_0 rectangular region it inserts 180° shift. The size of $\sigma_0 = c_0\lambda_{ij}f_L/\Delta y$ where c_0 is the Ψ_0 parameter, $c_0 = 0.54$ for in-line array antenna. As a result of the disturbance, most part of the source energy is pushed out to the transparent window of high pass spatial filter $(1 - \text{rect}(\dots))$ diaphragm while the rest part of the optical image of the radio scene (including jammers) is rejected. Further, the signal is processed in time domain and is used as feedback for controlling the $\hat{\tau}_{\psi}$ filter.

2.3. TIME-DOMAIN PROCESSING MODULES

After space-domain filtering, the signal goes to the structure analysis module where the by-element demodulation of continuous-phase manipulated waveform is performed. The signal parameters are determined (pulses quantity, amplitude, duration,

repetition time, type of packet), and phase modulating binary sequence is extracted. The main difficulty is the pulse-by-pulse random frequency hopping. The module realizes autocorrelation algorithm which is invariant to the carrier frequency (including frequency hops), but requires high signal-to-noise ratio $\gg 1$.

The module is based on space-integrating acousto-optic correlator (SIAOC). The function of one-element delay line is performed by the AOM itself (STLM 11 in Fig. 1). The optical system 15 combines images of upper and lower parts of the AOM on the aperture of photodetector 17 which performs multiplication and integration of signal. Photodetector output compares with the threshold, and the decision is made on the code element value.

The signal with the low signal-to-noise ratio (down to -15 dB) is processed in demodulation module which realizes pulse compression and multi-channel frequency reception. The necessary initial information is the pulse modulating binary code. The code is obtained previously by the structure analysis module. Some different optical schemes were designed for demodulation module based on SIAOC with programmable transient characteristic. The transient characteristic is set up by small-element liquid-crystal device matrix (16 in Fig. 1) and special phase filter. A photodiode array 19 is used for light detection, each photodiode corresponds to the frequency channel of the frequency hopping pattern. The photodiode output can be used for adjoining purposes: for pulse packet

type estimation, for instant spectrum measurements and for the time of arrival determination.

3. CONCLUSIONS

The antenna system with multifunctional hybrid optoelectronic processor realizes detection, space- and time domain selection, structure analysis and reception of complex signals with pseudo-random frequency hopping and $\Delta F \Delta T$ product of up to one million.

REFERENCES

1. Transition of Optical Processors into Systems. Proc. SPIE, vol.1958 (1993), 2236 (1994), 2489 (1995).
2. Vosresenskii D. I., Grinev A. Yu., Voronin E. N. Electrooptical Arrays. – Springer-Verlag, New York, 1989. – 318 p.
3. Yu. V. Egorov, K. P. Naumov, V. N. Ushakov. Acousto-Optic Processors and Spectrum Analyzers: New Techniques for Signal Processing. SPIE Optical Engineering Press, Vol. PM33, August 1997. – 174 p.
4. A. W. Houghton, C. D. Reeve. Detection of spread-spectrum signals using the time-domain filtered cross spectral density // IEE Proc. Radar, Sonar Navig. – 1995. – Vol. 142, № 6. P. 286-292.
5. A. Yu. Grinev, D. V. Bagno. Hybrid electrooptic processor of space-time signals. // Radiotekhnika, 2001, № 3, pp. 42-51. (In Russian)

ANTENNA ARRAY SIGNAL PROCESSING WITH SUPERRESOLUTION BY 2-D UNITARY TLS-ESPRIT WITH STRUCTURE WEIGHTING

Volodymyr I. Vasylyshyn

Kharkov Air Force Institute
Klochkovskaya street 228, Kharkov, Ukraine
<vladvas@ukr.net>

Abstract

In this paper we extend the recently proposed algorithm of direction-of-arrival (DOA) estimation named as Unitary TLS-ESPRIT with structure weighting (SW) for a uniform rectangular array (URA). The obtained two-dimensional (2-D) Unitary TLS-ESPRIT algorithm with SW provides automatically paired estimates of source azimuth and elevation angle (or spatial frequencies), and conserves inessential computational load inherent for the 2-D Unitary TLS-ESPRIT algorithm. Simulation results verifying the efficiency of the algorithm are presented.

Keywords: Antenna array, TLS-ESPRIT, Unitary transformation, Structure weighting

1. INTRODUCTION

There are many signal processing applications for which a set of unknown parameters must be estimated from measurements collected in time and/or space through an antenna array. For example, high-resolution DOA estimation is important in radar, sonar, wireless mobile communications, and so on.

The DOA estimation could be implemented with any one of a number of the popular high-resolution methods [1], but the most suitable and frequently used are ESPRIT-like algorithms. One of them is the Unitary TLS (Total Least Squares) – ESPRIT algorithm, being a low-complexity modification of conventional ESPRIT formulated in terms of real-valued computations [2]. This algorithm provides source DOA estimates via a closed-form procedure when using the uniform linear array (ULA) or the URA. The term "closed-form" means that under using the ULA (URA) the algorithm does not require a 1-D (2-D) spectral search as in the case of the MUSIC algorithm or an iterative optimization procedure as in cases of 1-D (2-D) IQML algorithm or multiple invariance ESPRIT [2]. The algorithm used in conjunction with URA yields automatically paired source azimuth and elevation angle estimates and permits resolve the sources having one common spatial frequency.

The 1-D Unitary TLS-ESPRIT algorithm with SW for a ULA [3] extends the Unitary TLS-ESPRIT ideas using the structure (row) method [4]. In this paper we introduce generalization of this algorithm, a 2-D Unitary TLS-ESPRIT algorithm with SW for a 2-D antenna array. The computer simulations show that the proposed algorithm enables to increase an accuracy of DOA estimation of radiation sources in the domain of mean and great values of signal-to-noise ratio (SNR).

2. 1-D UNITARY TLS-ESPRIT WITH SW

The problem of finding the DOA's of V narrow-band plane waves impinging on ULA of M sensors can be reduced to that of estimating the spatial frequencies (SF) $\omega = [\omega_1, \dots, \omega_V]^T$ in the following model

$$\mathbf{x}(t) = \mathbf{A}(\omega)\mathbf{s}(t) + \mathbf{n}(t), \quad (1)$$

where parameter $\omega = 2\pi d_x \sin \theta / \lambda$ specifies the source arrival angle, d_x is the interelement spacing, λ is the wave length, $(\cdot)^T$ stands for transpose. The $M \times V$ matrix $\mathbf{A}(\omega) = [\mathbf{a}(\omega_1), \dots, \mathbf{a}(\omega_V)]$ contains the array response vectors, $\mathbf{a}(\omega)$ is the $M \times 1$ steering (array response) vector, $\mathbf{s}(t)$ is the $V \times 1$ vector of source complex envelopes, $\mathbf{n}(t)$ is the $M \times 1$ vector of sensor noise. The source signals are zero-mean, complex Gaussian, temporally white processes with the covariance matrix $\mathbf{S} = E[\mathbf{s}(t)\mathbf{s}^H(t)]$, where $E[\cdot]$ and $(\cdot)^H$ stand for expectation operator and hermitian transpose, respectively. The sensor noise $\mathbf{n}(t)$ is also the zero-mean complex Gaussian process and is assumed to be both temporally and spatially white with the variance σ^2 .

The array response vectors are conjugate centrosymmetric due to the choice of ULA center as the phase reference [2].

$$\mathbf{a}_M(\omega) = [e^{-j\frac{M-1}{2}\omega}, \dots, e^{j\frac{M-1}{2}\omega}]^T. \quad (2)$$

The array output covariance matrix \mathbf{R} is defined by the relation

$$\mathbf{R} = E[\mathbf{x}(t)\mathbf{x}^H(t)] = \mathbf{A}(\omega)\mathbf{S}\mathbf{A}^H(\omega) + \sigma^2\mathbf{I}, \quad (3)$$

where \mathbf{I} is the $M \times M$ identity matrix. As an estimate of \mathbf{R} it is common to use the sample covariance matrix, obtained from N snapshots

$$\hat{\mathbf{R}} = \frac{1}{N} \sum_{t=1}^N \mathbf{x}(t) \mathbf{x}^H(t) = \frac{1}{N} \mathbf{X} \mathbf{X}^H, \quad (4)$$

where $\mathbf{X} = [\mathbf{x}(t_1), \dots, \mathbf{x}(t_N)]$ is the $M \times N$ data matrix. The eigendecomposition (ED) of $\hat{\mathbf{R}}$ is of the following form

$$\hat{\mathbf{R}} = \hat{\mathbf{E}}_s \hat{\mathbf{\Lambda}}_s \hat{\mathbf{E}}_s^H + \hat{\mathbf{E}}_n \hat{\mathbf{\Lambda}}_n \hat{\mathbf{E}}_n^H, \quad (5)$$

where the $\hat{\mathbf{V}} \times \hat{\mathbf{V}}$ and $(M - \hat{\mathbf{V}}) \times (M - \hat{\mathbf{V}})$ diagonal matrices $\hat{\mathbf{\Lambda}}_s$ and $\hat{\mathbf{\Lambda}}_n$ contain $\hat{\mathbf{V}}$ and $M - \hat{\mathbf{V}}$ sample signal and noise subspace eigenvalues, whereas $M \times \hat{\mathbf{V}}$ matrix $\hat{\mathbf{E}}_s = [\hat{\mathbf{e}}_1, \dots, \hat{\mathbf{e}}_{\hat{\mathbf{V}}}]$ and $M \times (M - \hat{\mathbf{V}})$ matrix $\hat{\mathbf{E}}_n = [\hat{\mathbf{e}}_{\hat{\mathbf{V}}+1}, \dots, \hat{\mathbf{e}}_M]$ contain the corresponding eigenvectors, and $\hat{\mathbf{V}}$ is an estimate of number of sources.

For the standard ESPRIT scenario, an M -element antenna array incorporates two identical subarrays separated by a common displacement Δ . Let $\mathbf{J}_1 = [\mathbf{J}_{m \times m} \mathbf{0}_{m \times 1}]$ and $\mathbf{J}_2 = [\mathbf{0}_{m \times 1} \mathbf{J}_{m \times m}]$ be $m \times M$ selection matrices, which assign the elements of $\mathbf{x}(t)$ (rows of \mathbf{A}) to subarrays 1 and 2, respectively. Here $\mathbf{0}_{m \times 1}$ is the $m \times 1$ zero matrix, and m is the number of elements in each subarray. For example, under $m = M - 1$ the first $M - 1$ and last $M - 1$ elements of ULA can be used for forming two identical overlapping subarrays with displacement $\Delta = d_x$.

Under the SW method [4], the generalization of overlapping structure is used. In this case, pairs of subarrays of m_s ($m_s < m$) elements are used. Let $\mathbf{J}_{1s} = [\bar{\mathbf{J}}_{q \times m} \mathbf{0}_{q \times 1}]$ and $\mathbf{J}_{2s} = [\mathbf{0}_{q \times 1} \bar{\mathbf{J}}_{q \times m}]$ be the corresponding selection matrices, $q = m_s(M - m_s)$ be the total number of elements in each subarray for the given case, and $\bar{\mathbf{J}} = [\bar{\mathbf{J}}_1^T, \bar{\mathbf{J}}_2^T, \dots, \bar{\mathbf{J}}_{M-m_s}^T]^T$, where $\bar{\mathbf{J}}_i = [\mathbf{0}_{m_s \times (i-1)} \mathbf{I}_{m_s \times m_s} \mathbf{0}_{m_s \times (M-i-m_s)}]$. The $m_s \times m$ matrix $\bar{\mathbf{J}}_i$ picks m_s sequential rows of the matrix \mathbf{E}_s : $i, i + 1, \dots, i + m_s - 1$. The key moment in realization of the TLS-ESPRIT algorithm with SW [3] is that at the final stage of algorithm, the ED of matrix product $[\mathbf{J}_1 \mathbf{E}_s \mathbf{J}_2 \mathbf{E}_s]^H \Sigma [\mathbf{J}_1 \mathbf{E}_s \mathbf{J}_2 \mathbf{E}_s]$ is being calculated instead of finding ED directly for matrix product $[\mathbf{J}_{1s} \mathbf{E}_s \mathbf{J}_{2s} \mathbf{E}_s]^H [\mathbf{J}_{1s} \mathbf{E}_s \mathbf{J}_{2s} \mathbf{E}_s]$ (which is equal to the first one). Here $\Sigma \bar{\mathbf{J}}^T \bar{\mathbf{J}}$ is the $(M - 1) \times (M - 1)$ weighting matrix, $\Sigma = \text{diag}[1 \ 2 \dots w \dots w \dots 2 \ 1]$, $w = \min(m_s, M - m_s)$, parameter m_s under maximum overlapping of subarrays in [4] is recommended as $m_s \approx (M/2)$. Elements of the diagonal matrix Σ indicate how many times each row of \mathbf{A} is used.

When using the unitary transformation method, the vector of array data and covariance matrix are transformed into vector $\mathbf{y}(t) = \mathbf{U}_M^H \mathbf{x}(t)$ and matrix $\mathbf{R}_u = E[\mathbf{y}(t) \mathbf{y}^H(t)] = \mathbf{U}_M^H \mathbf{R} \mathbf{U}_M$, respectively. For odd M , the unitary matrix \mathbf{U}_M is defined as [2]

$$\mathbf{U}_{2K+1} = (1/\sqrt{2}) \begin{bmatrix} \mathbf{I}_K & \mathbf{0} & \mathbf{j}\tilde{\mathbf{I}}_K \\ \mathbf{0}^T & \sqrt{2} & \mathbf{0}^T \\ \tilde{\mathbf{I}}_K & \mathbf{0} & -\mathbf{j}\tilde{\mathbf{I}}_K \end{bmatrix}, \quad (6)$$

where matrix $\tilde{\mathbf{I}}_K$ is an $(M - 1)/2 \times (M - 1)/2$ exchange matrix (with ones on its antidiagonal and zeros elsewhere).

The ESPRIT algorithm invariance property in the case of applying the unitary transformation method and SW may be presented as [3]

$$\text{tg}(\omega/2) \mathbf{K}_{1s} \mathbf{g}_M(\omega) = \mathbf{K}_{2s} \mathbf{g}_M(\omega), \quad (7)$$

where $\mathbf{K}_{1s} = \text{Re}(\mathbf{U}_q^H \mathbf{J}_{2s} \mathbf{U}_M)$, $\mathbf{K}_{2s} = \text{Im}(\mathbf{U}_q^H \mathbf{J}_{2s} \mathbf{U}_M)$, $\mathbf{g}_M(\omega) = \mathbf{U}_M^H \mathbf{a}_M(\omega)$. Equation (7) is the basis for the development of 1-D Unitary TLS-ESPRIT with SW.

A summary of the 1-D Unitary TLS-ESPRIT algorithm with SW and maximum subarray overlapping is as follows [3]. First, compute the $M \times \hat{\mathbf{V}}$ matrix $\hat{\mathbf{E}}_{su}$ via $\hat{\mathbf{V}}$ the "largest" eigenvectors of matrix $\text{Re}(\mathbf{U}_M^H \hat{\mathbf{R}} \mathbf{U}_M)$ or $\hat{\mathbf{V}}$ "largest" left singular vectors of the real-valued matrix $[\text{Re}\{\mathbf{Y}\}, \text{Im}\{\mathbf{Y}\}]$, where $\mathbf{Y} = \mathbf{U}_M^H \mathbf{X}$. Second, define the $(M - 1) \times M$ matrices $\mathbf{K}_1 = \text{Re}(\mathbf{U}_{M-1}^H \mathbf{J}_2 \mathbf{U}_M)$, $\mathbf{K}_2 = \text{Im}(\mathbf{U}_{M-1}^H \mathbf{J}_2 \mathbf{U}_M)$ and calculate the eigendecomposition of matrix product $[\mathbf{K}_1 \hat{\mathbf{E}}_{su} \mathbf{K}_2 \hat{\mathbf{E}}_{su}]^H \mathbf{U}_{M-1}^H \Sigma \mathbf{U}_{M-1} [\mathbf{K}_1 \hat{\mathbf{E}}_{su} \mathbf{K}_2 \hat{\mathbf{E}}_{su}]$, i.e. $[\mathbf{K}_1 \hat{\mathbf{E}}_{su} \mathbf{K}_2 \hat{\mathbf{E}}_{su}]^H \Sigma_{un} [\mathbf{K}_1 \hat{\mathbf{E}}_{su} \mathbf{K}_2 \hat{\mathbf{E}}_{su}] = \hat{\mathbf{E}}_0 \hat{\mathbf{E}}_0^H$, where $\Sigma_{un} = \mathbf{U}_{M-1}^H \Sigma \mathbf{U}_{M-1}$ is the weighting matrix, such that $\Sigma_{un} = \text{diag}[1 \ 2 \dots w \ w \ 1 \ 2 \dots w]$, $\hat{\mathbf{E}}_0$ is the eigenvectors matrix. Third, calculate the eigenvalues $\hat{\lambda}_v, v = 1, \dots, \hat{\mathbf{V}}$ of matrix $\hat{\Pi}_w$, such that $\hat{\Pi}_w = (-\hat{\mathbf{E}}_{12} \hat{\mathbf{E}}_{22}^{-1})$, where $\hat{\mathbf{E}}_{12}$ and $\hat{\mathbf{E}}_{22}$ are the upper right and lower right $\hat{\mathbf{V}} \times \hat{\mathbf{V}}$ submatrices of $\hat{\mathbf{E}}_0$. Fourth, determine the source SF as $\hat{\omega}_v = 2 \arctg(\hat{\lambda}_v), v = 1, \dots, \hat{\mathbf{V}}$.

3. 2-D UNITARY TLS-ESPRIT WITH SW

Consider a $M \times L$ element URA, centered at the origin lying in the $x - y$ plane and equi-spaced by $d_x = d_y = \lambda/2$ in the x and y directions. In addition to the SF $\omega = \frac{2\pi}{\lambda} d_x u$, where $u = \cos \theta \sin \phi$ (ϕ is the source elevation angle, θ is the source azi-

muth angle) we define another parameter $\mu = \frac{2\pi}{\lambda} d_y \vartheta$, where $\vartheta = \sin \theta \sin \phi$.

The array response to a source arriving from the direction (θ, ϕ) (or (ω, μ)) is given by the $M \times L$ matrix $\mathbf{A}(\omega, \mu) = \mathbf{a}_M(\omega) \mathbf{a}_L^T(\mu)$, where $\mathbf{a}_L(\mu)$ is defined by (2) with M replaced by L and ω replaced by μ . Owing to using the column stacking operator $\text{vec}(\cdot)$ [2] this response matrix can be vectorized and presented as $\mathbf{a}(\omega, \mu) = \text{vec}(\mathbf{A}(\omega, \mu))$.

The array output at time t may be presented as $\mathbf{x}(t) = \tilde{\mathbf{A}}(\omega, \mu) \mathbf{s}(t) + \mathbf{n}(t)$, where $\mathbf{x}(t)$ is the $ML \times 1$ vector formed by stacking the columns of the URA outputs, $\tilde{\mathbf{A}}(\omega, \mu)$ is the $ML \times V$ DOA matrix. Assumptions as for signals and noise for URA are the same as for the ULA. The columns of $\tilde{\mathbf{A}}(\omega, \mu)$ have the form $\text{vec}[\mathbf{a}_M(\omega) \mathbf{a}_L^T(\mu)] = [\mathbf{a}_L(\mu) \otimes \mathbf{a}_M(\omega)]$, and symbol \otimes denotes the Kronecker matrix product.

The matrix form of real-valued manifold denoted as $\mathbf{G}(\omega, \mu)$, is related to the matrix form of the array manifold as $\mathbf{G}(\omega, \mu) = \mathbf{U}_M^H \mathbf{A}(\omega, \mu) \mathbf{U}_L^*$, where \mathbf{U}_L is defined similarly to \mathbf{U}_M with M replaced by L , superscript $*$ denotes conjugation. Obviously

$$\mathbf{G}(\omega, \mu) = \mathbf{U}_M^H \mathbf{a}_M(\omega) \mathbf{a}_L^T(\mu) \mathbf{U}_L^* = \mathbf{g}_M(\omega) \mathbf{g}_L^T(\mu) \quad (8)$$

where $\mathbf{g}_L(\mu) = \mathbf{U}_L^H \mathbf{a}_L(\mu)$. Since $\mathbf{g}_M(\omega)$ meets the invariance relationship in (7), we have \mathbf{K}_2 . After applying the property of the operator $\text{vec}(\cdot)$, i.e. $\text{vec}(\mathbf{ABC}) = (\mathbf{C}^T \otimes \mathbf{A}) \text{vec}(\mathbf{B})$, we find that the $ML \times 1$ stacked real-valued manifold vector \mathbf{K}_1 satisfies

$$\text{tg}(\omega/2) \mathbf{K}_{\omega 1s} \mathbf{g}(\omega, \mu) = \mathbf{K}_{\omega 2s} \mathbf{g}(\omega, \mu), \quad (9)$$

where $\mathbf{K}_{\omega 1s} = \mathbf{I}_L \otimes \mathbf{K}_{1s}$ and $\mathbf{K}_{\omega 2s} = \mathbf{I}_L \otimes \mathbf{K}_{2s}$ are the $qL \times ML$ matrices.

Similar manipulations can be performed for the 1-D real-valued manifold $\mathbf{g}_L(\mu)$.

The 1-D real-valued manifold $\mathbf{g}_L(\mu)$ satisfies the corresponding invariance property presented as $\text{tg}(\mu/2) \mathbf{K}_{3s} \mathbf{g}_L(\mu) = \mathbf{K}_{4s} \mathbf{g}_L(\mu)$, where $z \times L$ real-valued matrices \mathbf{K}_{3s} and \mathbf{K}_{4s} are defined as $\mathbf{K}_{3s} = \text{Re}(\mathbf{U}_z^H \mathbf{J}_{2s} \mathbf{U}_L)$ and $\mathbf{K}_{4s} = \text{Im}(\mathbf{U}_z^H \mathbf{J}_{2s} \mathbf{U}_L)$, and $z = l_s(L - l_s)$, $l_s \approx (L/2)$. If we use this fact in equation (8) then obtain the following expression: $\text{tg}(\mu/2) \mathbf{G}(\omega, \mu) \mathbf{K}_{3s}^T = \mathbf{G}(\omega, \mu) \mathbf{K}_{4s}^T$. Application of the stacking property now results in

$$\text{tg}(\mu/2) \mathbf{K}_{\mu 1s} \mathbf{g}(\omega, \mu) = \mathbf{K}_{\mu 2s} \mathbf{g}(\omega, \mu), \quad (10)$$

where $\mathbf{K}_{\mu 1s}$ and $\mathbf{K}_{\mu 2s}$ are the $zM \times ML$ matrices, $\mathbf{K}_{\mu 1s} = \mathbf{K}_{3s} \otimes \mathbf{I}_M$, $\mathbf{K}_{\mu 2s} = \mathbf{K}_{4s} \otimes \mathbf{I}_M$.

Application (9) to the $ML \times V$ dimensional real-valued DOA matrix $\tilde{\mathbf{G}} = [\mathbf{g}(\omega_1, \mu_1), \dots, \mathbf{g}(\omega_V, \mu_V)]$ leads to

$$\mathbf{K}_{\omega 1s} \tilde{\mathbf{G}} \mathbf{P}_\omega = \mathbf{K}_{\omega 2s} \tilde{\mathbf{G}}, \quad (11)$$

where $\mathbf{P}_\omega = \text{diag}[\text{tg}(\omega_1/2), \dots, \text{tg}(\omega_V/2)]$.

Similarly, if we use (10) to the DOA matrix $\tilde{\mathbf{G}}$ then obtain

$$\mathbf{K}_{\mu 1s} \tilde{\mathbf{G}} \mathbf{P}_\mu = \mathbf{K}_{\mu 2s} \tilde{\mathbf{G}}, \quad (12)$$

where $\mathbf{P}_\mu = \text{diag}[\text{tg}(\mu_1/2), \dots, \text{tg}(\mu_V/2)]$. Asymptotically (assuming the number of snapshots N to be large) $\mathbf{E}_{su} = \tilde{\mathbf{G}} \mathbf{T}$, where \mathbf{T} is a non-singular real-valued matrix. Substitution of $\tilde{\mathbf{G}} = \mathbf{E}_{su} \mathbf{T}^{-1}$ in (11) and (12) yields the following relationships

$$\mathbf{K}_{\omega 1s} \mathbf{E}_{su} \mathbf{\Pi}_\omega = \mathbf{K}_{\omega 2s} \mathbf{E}_{su}, \text{ where } \mathbf{\Pi}_\omega = \mathbf{T}^{-1} \mathbf{P}_\omega \mathbf{T} \quad (13)$$

$$\mathbf{K}_{\mu 1s} \mathbf{E}_{su} \mathbf{\Pi}_\mu = \mathbf{K}_{\mu 2s} \mathbf{E}_{su}, \text{ where } \mathbf{\Pi}_\mu = \mathbf{T}^{-1} \mathbf{P}_\mu \mathbf{T} \quad (14)$$

All the quantities in (13) and (14) are real-valued. Automatic pairing of the spatial frequency estimates ω_i and μ_i is achieved by computing the eigendecomposition of the "complexfield" matrix $\mathbf{\Pi}_\omega + j \mathbf{\Pi}_\mu = \mathbf{T}^{-1} (\mathbf{P}_\omega + \mathbf{P}_\mu) \mathbf{T}$.

Similarly to the 1-D case [4], when solving matrix equations (13) and (14) by the TLS method, it is necessary to calculate ED of matrix equation

$$\mathbf{F}_\omega^H \mathbf{F}_\omega = \Phi_\omega^H [\mathbf{I}_L \otimes (\mathbf{U}_{M-1}^H \Sigma \mathbf{U}_{M-1})] \Phi_\omega,$$

where matrix $\mathbf{F}_\omega = [\mathbf{K}_{\omega 1s} \mathbf{E}_{su} \quad \mathbf{K}_{\omega 2s} \mathbf{E}_{su}]$ and matrix $\Phi_\omega = [\mathbf{K}_{\omega 1s} \mathbf{E}_{su} \quad \mathbf{K}_{\omega 2s} \mathbf{E}_{su}]$, in order to find estimate ω and the equation

$$\mathbf{F}_\mu^H \mathbf{F}_\mu = \Phi_\mu^H [(\mathbf{U}_{L-1}^H \Sigma \mathbf{U}_{L-1}) \otimes \mathbf{I}_M] \Phi_\mu,$$

where matrix $\mathbf{F}_\mu = [\mathbf{K}_{\mu 1s} \mathbf{E}_{su} \quad \mathbf{K}_{\mu 2s} \mathbf{E}_{su}]$ and matrix $\Phi_\mu = [\mathbf{K}_{\mu 1s} \mathbf{E}_{su} \quad \mathbf{K}_{\mu 2s} \mathbf{E}_{su}]$, in order to find estimate μ . Here matrices $\mathbf{K}_{\omega 1} = \mathbf{I}_L \otimes \mathbf{K}_1$, $\mathbf{K}_{\omega 2} = \mathbf{I}_L \otimes \mathbf{K}_2$, and $\mathbf{K}_{\mu 1} = \mathbf{K}_3 \otimes \mathbf{I}_M$, $\mathbf{K}_{\mu 2} = \mathbf{K}_4 \otimes \mathbf{I}_M$, where $\mathbf{K}_3 = \text{Re}(\mathbf{U}_{L-1}^H \mathbf{J}_2 \mathbf{U}_L)$, $\mathbf{K}_4 = \text{Im}(\mathbf{U}_{L-1}^H \mathbf{J}_2 \mathbf{U}_L)$.

A summary of 2-D Unitary TLS-ESPRIT with structure weighting is as follows:

- 1) obtain the data matrix $\mathbf{Y} = (\mathbf{U}_M^H \otimes \mathbf{U}_L^H) \mathbf{X}$;
- 2) compute the $ML \times \hat{V}$ matrix $\hat{\mathbf{E}}_{su}$ via \hat{V} the "largest" left singular vectors of matrix $[\text{Re}\{\mathbf{Y}\}, \text{Im}\{\mathbf{Y}\}]$ or as "largest" eigenvectors of real-valued matrix $\text{Re}(\hat{\mathbf{R}}_Y)$, where $\hat{\mathbf{R}}_Y = (1/2N) \mathbf{Y} \mathbf{Y}^H$;
- 3) determine matrices \mathbf{K}_1 and \mathbf{K}_2 , $\mathbf{K}_{\omega 1}$ and $\mathbf{K}_{\omega 2}$ and calculate the ED of matrix product $\Phi_\omega^H \Sigma_1 \Phi_\omega = \hat{\mathbf{E}}_0 \hat{\Lambda} \hat{\mathbf{E}}_0^H$, where $\Sigma_1 = [\mathbf{I}_L \otimes \Sigma_{un}]$, $\hat{\Lambda}$ is the eigenvalue matrix of this product, and $\hat{\mathbf{E}}_0$ is the eigenvectors matrix. Partition the $2\hat{V} \times 2\hat{V}$ matrix $\hat{\mathbf{E}}_0$ into submatrices of size $\hat{V} \times \hat{V}$ and calculate the matrix $\hat{\Pi}_\omega$ that is formed similarly to the 1-D case, i.e. $\hat{\Pi}_\omega = (-\hat{\mathbf{E}}_{12} \hat{\mathbf{E}}_{22}^{-1})$;

- 4) implement step 3 for matrix $\hat{\Pi}_\mu$ (when using the corresponding matrices);
- 5) compute $\hat{\lambda}_v, v = 1, \dots, \hat{V}$ as eigenvalues of the matrix $\hat{\Pi}_w + j\hat{\Pi}_\mu$;
- 6) determine spatial frequencies of sources as $\hat{\omega}_v = 2 \arctg(\text{Re}(\hat{\lambda}_v))$, $\hat{\mu}_v = 2 \arctg(\text{Im}(\hat{\lambda}_v))$, $v = 1, \dots, \hat{V}$.

4. SIMULATION RESULTS

In this section we present the results of the experiment (consisted of a batch of Monte-Carlo trials) carried out in order to evaluate the relative performance of the presented in this paper algorithm and the original one, i.e. 2-D Unitary TLS-ESPRIT. The main objective of these simulations was evaluation of the root mean square errors (RMSE) between the true source spatial frequencies and the estimated ones obtained with the above-mentioned algorithms.

In the experiment, we assumed that two equipowered, uncorrelated sources were impinging on URA. Their directional cosines relative to x and y axes are $(u_1, \vartheta_1) = (0, 0.05)$ and $(u_2, \vartheta_2) = (0, 0.087)$. So, the sources have the same u coordinate.

The presented results are averaged over 500 trials, and the number of data samples was taken $N = 64$. The 12×12 URA ($M = L = 12$) was used, and for the presented algorithm $m_s = l_s = 5$. Fig. 1 displays the RMSE versus the SNR. The sample RMSE (Q) was computed as

$$Q = \sqrt{\frac{1}{2BV} \sum_{v=1}^V \sum_{b=1}^B [(\hat{u}_v(b) - u_v)^2 + (\hat{\vartheta}_v(b) - \vartheta_v)^2]},$$

where $\hat{u}_v(b)$ ($\hat{\vartheta}_v(b)$) denote the coordinate estimates of the v^{th} source obtained from a particular algorithm at the b^{th} run, whereas u_v (ϑ_v) is the corresponding true spatial frequency.

The figure shows that the obtained algorithm outperforms the 2-D Unitary TLS-ESPRIT algorithm in the domain of mean and large values of SNR. At small SNR, the former algorithm does not yield a gain. It is explained (as in [3]) by the inadequacy (when realizing it) of the used subarray aperture for the high accuracy DOA estimation with a given distance between sources.

5. CONCLUSION

A new ESPRIT-like algorithm of parameter estimation — the 2-D Unitary TLS-ESPRIT algorithm with SW for DOA estimation with 2-D antenna array has been presented. The obtained algorithm possesses all the attractive features (such as low computational complexity, ability to provide automatically paired

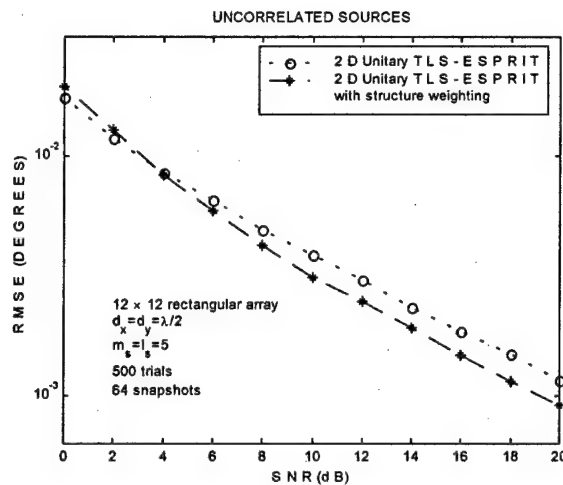


Fig. 1. RMSE characteristics of 2-D Unitary TLS-ESPRIT and proposed algorithm versus SNR

source azimuth and elevation angle estimates) of the 2-D Unitary TLS-ESPRIT. By using techniques similar to those in [2], a beamspace version of 2-D Unitary TLS-ESPRIT with SW for URA can be derived.

Note, that the proposed algorithm also may be used for estimation of sinusoid frequencies in white noise in much the same manner as it is used for estimation of DOA. Besides, the very interesting application of the 2-D Unitary TLS-ESPRIT with structure weighting is a multiple-input-multiple-output vector radio channel sounding as in [5], where the necessity of joint superresolution estimation of direction of departure, time delay of arrival, Doppler shift, and DOA of propagating waves arises.

REFERENCES

1. Godara L. C. Application of antenna arrays to mobile communications, Part II: Beam-forming and DOA considerations // Proc. IEEE. 1997. vol. 85, pp. 1195–1245.
2. Zoltowski M. D., Haardt M., Mathews G. P. Closed-form 2-D angle estimation with rectangular arrays in element space or beamspace via unitary ESPRIT // IEEE Trans. on SP. 1996. vol.44, pp. 316–328.
3. Vasilishin V. I. DOA estimation via unitary TLS-ESPRIT algorithm with structure weighting // Proc. XXVIIth URSI GA.— Maastricht, the Netherlands, 2002, CD, report 0086.
4. Ottersten B., Viberg M., Kailath T. Performance analysis of the TLS ESPRIT algorithm // IEEE Trans. on SP. 1991. vol.39, pp. 1122–1135.
5. Richter A., Hampicke D., Sommerkorn G., Thomä R. S. Joint Estimation of DoD, Time-Delay, and DoA for high resolution channel sounding // Proc. IEEE Vehicular Technology Conference (VTC2000-Spring), Tokyo, 2000.

QUALITATIVE INDICES OF THE METHOD OF DETERMINING THE NUMBER OF SIMULTANEOUSLY ACTING SIGNALS

N. M. Nikitin, L. G. Shatsman

Kiev, Ukraine

Abstract

In the paper, there is discussed a method of determining the number of signals, which are resolved only by an angular coordinate, with the use of ratio of modified likelihood functions, and its qualitative indices in the form of statistical characteristics.

Keywords: Signal source, resolution, likelihood function, antenna array, probability of true detection.

1. INTRODUCTION

The task of determination of the number of simultaneously acting signals, which are resolved only by one parameter, arises in multichannel receiving systems while processing a total output response. There are different approaches to such a problem solution.

In a number of well-known methods, determination of a number of simultaneously acting signals is realized without estimation of their parameters. Methods based on analyses of eigen values of the correlation matrix [1] and methods based on equation factors, whose solution results in the signal parameters estimation, are among them. The latter ones are subdivided by ways of obtaining the equation factors into two groups: (1) – the statistical method [1], in which factors are formed from estimation of cross-correlation functions H_m and H_{m+1} , (2) – the deterministic one [3], in which one or several samples of the output instantaneous values of multichannel system are used for factors forming.

In other methods, the task of determination of the number of simultaneously acting signals is solved together with tasks of detection and estimation of the parameters. To them there are concerned actual methods of the spectral estimation, based on the analysis of various functions of correlation matrix [1, 4–6] and methods of maximization the vector of likelihood functions ratio [7].

It is expedient to compare qualitative indices of any of the proposed methods with the attainable ones.

2. STATEMENT OF THE PROBLEM

In order to estimate the multichannel system performance, consider a simultaneous effect of signals excited by M sources, on the linear equidistant antenna array

(AA) of R elements. Assume that directions to each source α_m , $m = 1, 2, \dots, M$ are known.

$M + 1$ hypotheses H_0, H_1, \dots, H_M are put forward, hypothesis H_0 corresponds to the absence of signal. Hypothesis H_k assumes an action of signals excited by any m sources from total assembly M . The problem is in making a decision corresponding to one of $M + 1$ hypotheses and rejecting another one, basing on results of measurement of AA output voltages \dot{U}_r , ($r = 1, 2, \dots, R$):

$$\begin{aligned} H_0 (m = 0) : \quad & \dot{U}_r = \dot{n}_r \\ H_1 (m = 1) : \quad & \dot{U}_r = \dot{a}_1 \dot{\beta}_{1,r} + \dot{n}_r \\ H_2 (m = 2) : \quad & \dot{U}_r = \sum_{m=1}^2 \dot{a}_m \dot{\beta}_{m,r} + \dot{n}_r \\ & \vdots \\ H_M (m = M) : \quad & \dot{U}_r = \sum_{m=1}^M \dot{a}_m \dot{\beta}_{m,r} + \dot{n}_r \end{aligned} \quad (1)$$

where \dot{a}_m is an instantaneous value of the m th signal complex amplitude; $\dot{\beta}_{m,r} = \exp(jx_{m,r})$,

$x_{m,r} = (\frac{2\pi}{\lambda} d \sin \alpha_m)(r - \frac{R+1}{2})$, λ is the wavelength; d is the distance between AA adjacent elements, α_m is the direction of the m -th signal arrival with respect to the array normal, \dot{n}_r is the noise instantaneous complex value in the r th channel.

To verify $M + 1$ hypotheses, it is necessary [8, 9] to form an M -dimensional vector of likelihood ratios

$$l(\dot{U}_r) = [l_1(\dot{U}_r), l_2(\dot{U}_r), \dots, l_M(\dot{U}_r)],$$

whose m th component is

$$l_m(\dot{U}_r) = w(\dot{U}_r | H_m) / w(\dot{U}_r | H_0), \quad (2)$$

where

$$w(\dot{U}_r | H_m) = (2\pi\sigma^2)^{-\frac{R}{2}} \exp\left(-\frac{1}{2\sigma^2} L_m\right)$$

is the likelihood function for Gaussian and signal-independent noises in channels with the variance $\sigma_r^2 = \sigma^2$,

$$L_m = \sum_{r=1}^R \left\{ \left[U_r^c - \sum_{k=1}^m (a_k^c \cos x_{k,r} - a_k^s \sin x_{k,r}) \right]^2 + \left[U_r^s - \sum_{k=1}^m (a_k^c \sin x_{k,r} + a_k^s \cos x_{k,r}) \right]^2 \right\} \quad (3)$$

$$\dot{U}_r = U_r^c + jU_r^s, \dot{a}_k = a_k^c + ja_k^s.$$

It is possible to reduce a multichoice problem of hypotheses testifying, whose solution *a priori* uncertain conditions is difficult, to the sequential examination of two-alternative situations using formation of the extending number of series of competing hypotheses H_m and H_{m+1} [7]. In this case, the Neuman-Pearson criterion can be used as the algorithm of the problem solution. According to this criterion, solution γ_{m+1} concerning simultaneous $m+1$ signals action against alternative γ_m of m signals action is accepted by comparison of a likelihood ratio with threshold l_0 :

$$\frac{l_{m+1}(\dot{U}_r)}{l_m(\dot{U}_r)} = \frac{w(\dot{U}_r | H_{m+1})}{w(\dot{U}_r | H_m)} \underset{\gamma_m}{\overset{\gamma_{m+1}}{>}} l_0 \quad (4)$$

At the next stage, two competing hypotheses H_{m+1} and H_{m+2} are considered. If the newly formed likelihood ratio doesn't exceed the threshold at this stage, then the final decision in favour of the hypothesis about $m+1$ signals is made. Otherwise an incompletely defined decision about $m+2$ or more signals acting is made. This decision is a subject of revision at the next stage.

Let's obtain a rule for the problem solution using the modified likelihood function [3] (in such a sense that in this function, unknown components of signal complex magnitudes a_k^c, a_k^s are excluded using substitution of formal estimates):

$$w_M(\dot{U}_r | H_M) = (2\pi\sigma^2)^{-\frac{R}{2}} \exp\left[-\frac{1}{2\sigma^2} \left(\sum_{r=1}^R U_r^2 - \frac{1}{D_M} \sum_{m=1}^M D_m \right) \right] \quad (5)$$

Here determinant

$$D_M = \begin{vmatrix} f_{11} & f_{12} & f_{13} & \cdots & f_{1M} \\ f_{21} & f_{22} & f_{23} & \cdots & f_{2M} \\ f_{31} & f_{32} & f_{33} & \cdots & f_{3M} \\ \cdots & \cdots & \cdots & \cdots & \cdots \\ f_{M1} & f_{M2} & f_{M3} & \cdots & f_{MM} \end{vmatrix} \quad (6)$$

is constituted of values of the channels directional characteristics formed as a result of the phased voltages summation on the array components in such a way that the largest values of these directional characteristics coincided with known directions to the sources of radiation:

$$f_{km} = \sum_{r=1}^R \left[\cos(x_m - x_k) \left(r - \frac{R+1}{2} \right) \right] = \frac{\sin[R/2(x_m - x_k)]}{\sin[1/2(x_m - x_k)]} \quad (7)$$

Determinants D_m are obtained from the determinant D_M by replacement of row $(f_{m1}, f_{m2}, \dots, f_{mM})$ with the one of scalar voltage products $\{(\dot{V}_m \cdot \dot{V}_1^*), (\dot{V}_m \cdot \dot{V}_2^*), \dots, (\dot{V}_m \cdot \dot{V}_M^*)\}$ calculated for specified directions to signal sources

$$\dot{V}_m = V_m^c + jV_m^s = \sum_{r=1}^R \dot{U}_r \exp(-jx_{mr}). \quad (8)$$

Proceeding from (4) to the statistics of the modified likelihood function logarithm (5), we obtain:

$$L_{M+1} = \ln \left[\frac{w_{M+1}(\dot{U}_r | H_{M+1})}{w_M(\dot{U}_r | H_M)} \right] = \frac{1}{2\sigma^2} \left(\frac{1}{D_{M+1}} \sum_{m=1}^{M+1} D_m - \frac{1}{D_M} \sum_{m=1}^M D_m \right) \quad (9)$$

The expression in parentheses being a subject of maximization, after transformation is reduced to the view:

$$F_{M+1} = \frac{1}{D_M \cdot D_{M+1}} [(d_{M+1}^c)^2 + (d_{M+1}^s)^2], \quad (10)$$

where

$$d_{M+1}^{(s)} = \begin{vmatrix} f_{11} & f_{21} & \cdots & f_{M+1,1} \\ f_{12} & f_{22} & \cdots & f_{M+1,2} \\ \cdots & \cdots & \cdots & \cdots \\ f_{1,M} & f_{2,M} & \cdots & f_{M+1,M} \\ V_1^{(s)} & V_2^{(s)} & \cdots & V_{M+1}^{(s)} \end{vmatrix} \quad (11)$$

Substituting values of voltages in the secondary channels formed as a result of a phased summation (8) into (11)

$$V_k^{(s)} = \sum_{m=1}^{M+1} a_m^{(s)} \cdot f_{k,m} + N_k^{(s)}, \quad (12)$$

and opening determinations $d_{M+1}^{(s)}$ by the lower row, we obtain:

$$F_{M+1} = \frac{1}{D_{M+1} D_M} \times \left[(D_{M+1} a_{M+1}^c + D_n^c)^2 + (D_{M+1} a_{M+1}^s + D_n^s)^2 \right] \quad (13)$$

where determinants

$$D_n^{(s)} = \begin{vmatrix} f_{11} & f_{21} & \cdots & f_{M+1,1} \\ f_{12} & f_{22} & \cdots & f_{M+1,2} \\ \cdots & \cdots & \cdots & \cdots \\ f_{1,M} & f_{2,M} & \cdots & f_{M+1,M} \\ N_1^{(s)} & N_2^{(s)} & \cdots & N_{M+1}^{(s)} \end{vmatrix} \quad (14)$$

are caused by noises in the secondary channels

$$\dot{N}_k = N_k^c + jN_k^s = \sum_{r=1}^R \dot{n}_r \exp(-jx_{kr}).$$

Obtained expression (13) shows that calculation of value F_{M+1} for $M+1$ -th signal detection corresponds to forming of channel with characteristic directed with "zeroes" to other M sources.

A digital antenna array enables to determine the number of acting signals with known directions of arrival in a one time sample. For this, channels are formed according to (10) in turn by fixed instantaneous values of voltage quadrature components at the outputs of primary channels. Determinant D_M is constructed of values f_{k1} except f_{m1} and f_{km} for the m th detected signal. In determinants $d_{M+1}^{(s)}$ the row with values of characteristics of channel f_{m1} , directed to the source of the detected signal, is excluded. A decision about the m -th signal activity is made as a result of comparison L_{M+1}^m with threshold. The number of the threshold crossings corresponds to the estimated number of acting signals.

From (13) it follows that the distribution of random F_{M+1} subjects to a noncentral χ^2 distribution with 2 degrees of freedom and with a noncentrality parameter $A_{M+1}^2 = a_{M+1}^2 (D_{M+1}/D_M)$ [10]:

$$p_L(x) = \frac{1}{2\sigma^2} \exp\left(-\frac{x + A_{M+1}^2}{2\sigma^2}\right) \cdot I_0\left(\frac{\sqrt{A_{M+1}^2 \cdot x}}{\sigma^2}\right), \quad (15)$$

where $I_0(\cdot)$ is the zeroth order modified Bessel function. Using the asymptotic expansion at large values of an argument

$$I_0(z) \approx \frac{e^z}{\sqrt{2\pi \cdot z}} \left(1 + \frac{1}{8z} + \frac{1}{128z^2} + \cdots\right)$$

and restricting ourselves with its first component, we arrive to an approximate expression for L_{M+1} density function at sufficiently great signal-to-noise ratio $q^2 = A_{M+1}^2/\sigma^2$

$$p_L(x) \approx \frac{1}{2\sigma \cdot \sqrt{2\pi \cdot \sqrt{A_{M+1}^2 \cdot x}}} \times \exp\left(-\frac{(\sqrt{x} - \sqrt{A_{M+1}^2})^2}{2\sigma^2}\right) \quad (16)$$

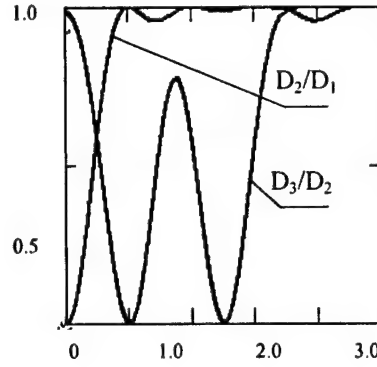


Fig. 1.

It should be noted that the squared coefficient of the signal amplitude $k(a_m) = D_{M+1}/D_M$, is stipulated by positional relationship of the detected $M+1$ -th source and other M sources in space. It corresponds to the introduced in [11] conception of an available power utilization factor.

In the absence of signal, the distribution (16) is transformed into the exponential one:

$$p_L(x|a_{M+1}=0) = \frac{1}{2\sigma^2} \exp\left(-\frac{x}{2\sigma^2}\right), \quad (17)$$

and for the given probability of false alarm

$$P_F = \int_{x_0}^{\infty} p_L(x|a_{M+1}=0) dx = \exp(-x_0/2\sigma^2) \quad (18)$$

threshold $x_0 = 2\sigma^2 \ln(1/P_F)$. This allows calculating the probability of true detection of the signal from the $M+1$ -th source using equation (17):

$$P_D = \int_{x_0}^{\infty} p_L(x) dx. \quad (19)$$

Ratios D_{M+1}/D_M and a_{M+1}/σ are the basic data for calculation of working detection characteristics for the $M+1$ -th signal against other ones according to formula (19).

The coefficient $k(\alpha_m)$ characterizes positional relationship of signal sources in space and it affects the total signal-to-noise ratio. It's dependence on an arbitrary angular position α of the detected signal source (in parts of half a main lobe width by zero level), as an example, is shown in Fig. 1. In this figure, there are two cases: $M=2$, $\alpha_1=0$, and $M=3$, $\alpha_1=1.0$, $\alpha_2=2.5$.

3. TWO SOURCES CASE

Such a case is of practical interest from the point of view of the problem solution. According to (4, 10), taking into account obvious relations $f_{12} = f_{21}$, $D_1 = f_{11} = R$, $D_2 = R^2 - f_{21}^2$, it is clear that it is necessary to compare with threshold the following values:

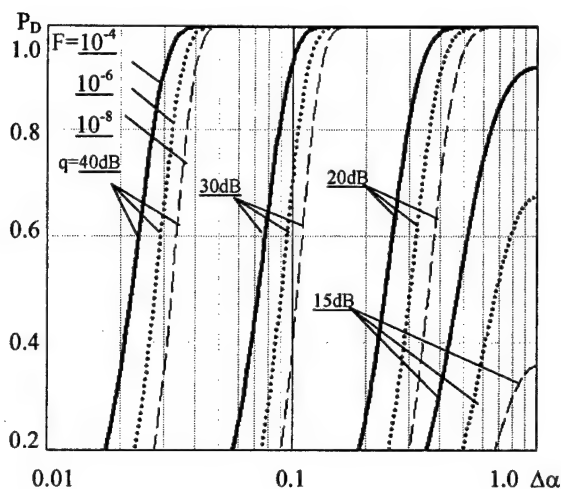


Fig. 2.

a) at detection of the first signal against the background of the second one

$$F_2^{(1)} = \left| \begin{matrix} f_{12} & R \\ V_1^c & V_2^c \end{matrix} \right|^2 + \left| \begin{matrix} f_{12} & R \\ V_1^s & V_2^s \end{matrix} \right|^2,$$

b) at detection of the second signal against the background of the first one

$$F_2^{(2)} = \left| \begin{matrix} R & f_{12} \\ V_1^c & V_2^c \end{matrix} \right|^2 + \left| \begin{matrix} R & f_{12} \\ V_1^s & V_2^s \end{matrix} \right|^2.$$

Estimation of the potential solution for detection of two signals excited by sources located at a certain angular distance can be carried out with characteristics shown in Fig. 2. There are shown here the dependencies of the true detection probability versus the angular distance between the sources for fixed signal-to-noise ratios and for three values of probability of false alarm (taking into account the normalized antenna beam pattern).

REFERENCES

1. Very-large-scale integration circuits and modern signal processing: Trans. from Engl./ edited by S. Ghun., H. Whiteous, T. Kailate. - Moscow.: Radio i svyaz', 1989. - pp. 45...123. (in Rus.)
2. Tsarkov N. M. Multichannel radar meters. - Moscow.: Sov.Radio, 1980, 192 p. (in Rus.)
3. Variuhin V. A. Fundamental multichannel analysis theory. - Kiev: MA AD of LF, 1993, - 171 p.; with ill. (in Rus.)
4. Kapon G. / TIHER. - 1969. - v.57, No 8.-pg.69.
5. Gabriel V. F. / TIHER - 1980. - v.68, No 6 - p.19.
6. Key S. M., Marple S. L. / TIHER - 1981. - v.69, No. 11.- p. 5.
7. Juravlev A. K. Determination of number and coordinates of point radiators non-resolved by Rayleigh criterion. - Radiotekhnika, 1995, No11. (in Rus.)
8. Van-Triss G. Detection, estimations and modulation theory. In 3 volumes. Trans. from Engl./ edited by Tihonov V. I. - Moscow.: Sov. Radio, 1972. - V.1./ (in Rus.)
9. Levin B. R. Statistic radio engineering theory. 3-rd revised and suppl. edit., - Moscow.: Radio i svyaz', 1989. - 656 p.; with ill. (in Rus.)
10. Handbook on the probability theory and mathematical statistics / V. S. Korolyuk, Portenko N. I., Skorohod A. V. Turbin A. F. - Moscow.: Nauka, 1985. (in Rus.)
11. Shirman J. D. Signals resolution and compression. Moscow., Sov.Radio, 1974. (in Rus.)

CORRECTION OF SMART ANTENNAS RECEIVING CHANNELS CHARACTERISTICS FOR 4G MOBILE COMMUNICATIONS

V. I. Slyusar, I. V. Titov¹

Central Research and Development Institute of Armament and Military Engineering
Kyiv, Andruschenko Street, 4, e-mail: swadim@profit.net.ua

¹The Kharkov military university,
maidan Svobody, 6, Kharkov, 310043, Ukraine

Abstract

The paper considers a way of correction of the reception channels characteristics for smart-antennas in 4G mobile communications.

Keywords: smart-antenna, mobile communications, digital beam formings, correction coefficients, digital antenna array, calibrating source, base station.

The key technology of 4G mobile communications systems is adaptive digital beam forming for smart antennas. Adaptive array technology provide for high gain systems, in turn optimizing handset size and power consumption, and at the same time reduce possible interference effects from other terminals in the same cell area. Software radio technology of smart antennas also enable multimode and multi band operation for base stations [1].

For errors minimization of digital beam formings communications systems with nonidentical channels of antenna arrays arises a problem of correction of the reception channels characteristics.

For the solution of the given problem it is proposed to operate by a special external submission of the pilot-signal. To minimize the hardware expenditures it is proposed to use as a the pilot-signal a signals from other base stations in the same cell area (Fig. 1).

When applied a pilot-signal from only one base station, as a correction procedures for square smart an-

tennas is proposed to use a method [2]. In the general case the correction process is consisted in weighing the digital voltages in receiving channels by complex weight coefficients:

$$\begin{aligned} \dot{U} \cdot \dot{\alpha}_{cor} &= (U^c + j \cdot U^s)(\alpha_{cor}^c + j \cdot \alpha_{cor}^s) = \\ &= (U^c \alpha_{cor}^c - U^s \alpha_{cor}^s) + j(\alpha_{cor}^s U^c + U^s \alpha_{cor}^c), \end{aligned} \quad (1)$$

where $\alpha_{cor}^c, \alpha_{cor}^s$ – quadratic components of correction coefficient, U^c, U^s – quadratic components of response of the primary digital antenna arrays (DAA) channels.

In the case of square smart antennas with $R \times Q$ elements the quadratic components of correction coefficient must be calculated for a set of N readings of pilot-signal from base station with number "m":

$$\begin{aligned} \alpha_{rqm}^c &= \frac{\sum_{n=1}^N \{U_{rqn}^c \beta_{rqm,n}^c + U_{rqn}^s \beta_{rqm,n}^s\}}{\sum_{n=1}^N (U_{rqn}^{c^2} + U_{rqn}^{s^2})}, \\ \alpha_{rqm}^s &= \frac{\sum_{n=1}^N \{U_{rqn}^c \beta_{rqm,n}^s - U_{rqn}^s \beta_{rqm,n}^c\}}{\sum_{n=1}^N (U_{rqn}^{c^2} + U_{rqn}^{s^2})}, \end{aligned} \quad (2)$$

where $\beta_{rqm,n}^s, \beta_{rqm,n}^c$ – quadratic components of a measurement standards response of the rq -th primary smart antennas channels in the n -th time interval, $\alpha_{rqm}^s, \alpha_{rqm}^c$ – quadratic components of correction coefficient for rq -th primary smart antennas channels, which calculate for a pilot-signal from base station with number "m", U_{rqn}^s, U_{rqn}^c – quadratic compo-

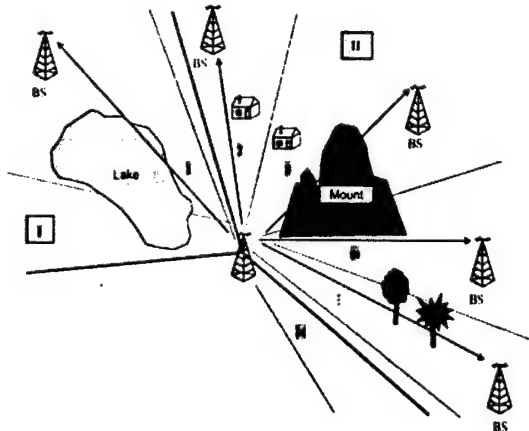


Fig. 1.

nents of response of the rq -th primary smart antennas channels in the n -th time interval,

$$\beta_{rqm,n}^c = a_n^c \cos(X) - a_n^s \sin(X),$$

$$\beta_{rqm,n}^s = a_n^s \cos(X) + a_n^c \sin(X), \quad X = x_{rm} + x_{qm},$$

x_{rm}, x_{qm} – generalized coordinates of calibrating source (base station with number "m") with respect to DAA normal,

$$x_{rm} = \frac{2\pi}{\lambda} d_r \left(r - \frac{R+1}{2} \right) \sin \theta_m \cdot \cos \varepsilon_m,$$

$$x_{qm} = \frac{2\pi}{\lambda} d_q \left(q - \frac{Q+1}{2} \right) \sin \theta_m \cdot \sin \varepsilon_m,$$

λ – wavelength of calibrating source carrier, d_r, d_q – the distance between array's elements in a row and in a column correspondingly, R, Q – number of array's elements in a row and in a column, θ, ε – angle coordinates of the calibrating source with respect to DAA normal, $a_n^c = U_{sT_n}^c, a_n^s = U_{sT_n}^s$ – quadratic components of response of the standard primary smart antennas channel in the n -th time interval.

In the case of linear digital antenna array use a correction coefficients only for one angle plane:

$$\alpha_{rm}^c = \frac{\sum_{n=1}^N \{ U_{rn}^c \beta_{rm,n}^c + U_{rn}^s \beta_{rm,n}^s \}}{\sum_{n=1}^N (U_{rn}^c + U_{rn}^s)},$$

$$\alpha_{rm}^s = \frac{\sum_{n=1}^N \{ U_{rn}^c \beta_{rm,n}^s - U_{rn}^s \beta_{rm,n}^c \}}{\sum_{n=1}^N (U_{rn}^c + U_{rn}^s)}, \quad (3)$$

where $\beta_{rm,n}^c, \beta_{rm,n}^s$ – quadratic components of a measurement standards response of the r -th primary smart antennas channels in the n -th time interval, $\alpha_{rm}^c, \alpha_{rm}^s$ – quadratic components of correction coefficient for r -th primary smart antennas channels, which calculate for a pilot-signal from base station with number "m", U_{rn}^c, U_{rn}^s – quadratic components of response of the r -th primary smart antennas channels in the n -th time interval,

$$\beta_{rm,n}^c = a_n^c \cos(x_{rm}) - a_n^s \sin(x_{rm}),$$

$$\beta_{rm,n}^s = a_n^s \cos(x_{rm}) + a_n^c \sin(x_{rm}),$$

x_{rm} – generalized coordinate of calibrating source (base station with number "m") with respect to DAA normal,

$$x_{rm} = \frac{2\pi}{\lambda} d \left(r - \frac{R+1}{2} \right) \sin \theta_m,$$

λ – wavelength of calibrating source carrier, d – the distance between array's elements in a row and in a column correspondingly, R – number of array's elements, θ – angle coordinate of the calibrating source with respect to DAA normal.

When applied a pilot-signal from more base stations, for a correction procedures can be used a average correction coefficient:

$$\alpha_{cor}^{c(s)} = \frac{1}{M} \sum_{m=1}^M \alpha_{rqm}^{c(s)}. \quad (4)$$

The most effective way of correction is use of a more pilot-signals from M base stations in the one time interval. In this case must be used a correction coefficients:

$$\alpha_{rq}^s = \frac{\sum_{n=1}^N \left\{ U_{rq_n}^c \sum_{m=1}^M \beta_{rqm}^s - U_{rq_n}^s \sum_{m=1}^M \beta_{rqm}^c \right\}}{\sum_{n=1}^N (U_{rq_n}^c + U_{rq_n}^s)},$$

$$\alpha_{rq}^c = \frac{\sum_{n=1}^N \left\{ U_{rq_n}^c \sum_{m=1}^M \beta_{rqm}^c + U_{rq_n}^s \sum_{m=1}^M \beta_{rqm}^s \right\}}{\sum_{n=1}^N (U_{rq_n}^c + U_{rq_n}^s)}, \quad (5)$$

where

$$\beta_{rqm}^c = a_m^c \cos(x_{rm} + x_{qm}) - a_m^s \sin(x_{rm} + x_{qm}),$$

$$\beta_{rqm}^s = a_m^s \cos(x_{rm} + x_{qm}) + a_m^c \sin(x_{rm} + x_{qm}),$$

$$a_m^c = \text{Re}[A_m], \quad a_m^s = \text{Im}[A_m],$$

$$[A_m] = [P^* P]^{-1} P^* \vec{U},$$

$$P = \begin{bmatrix} f_1(\omega_1) & f_1(\omega_2) & \dots & f_1(\omega_M) \\ f_2(\omega_1) & f_2(\omega_2) & \dots & f_2(\omega_M) \\ \vdots & \vdots & \ddots & \vdots \\ f_N(\omega_1) & f_N(\omega_2) & \dots & f_N(\omega_M) \end{bmatrix} \quad - \text{matrix of}$$

amplitude-frequency characteristics meanings of N FFT-filters for a measurement standards reception channels;

$$f_n(\omega_m) = \frac{\sin N(\omega_m - \omega_n)}{\sin(\omega_m - \omega_n)},$$

ω_n – the central frequency of n -th FFT-filter, U – vector of voltages of the responses channels.

REFERENCES.

1. The Path to 4G Mobile. – Communications Week International. – Issue 260. – 5 March 2001. – P. 16–17.
2. Patent of Russ. Fed. N 2103768 H 01 Q3/36, G 01 R 29/10. A way of amplitude-phase characteristics correction of primary channels of plane digital antenna array. Slyusar V. I., Pokrovskij V. I., Sakhno V. F., priority 16.10.92, publ. 27.01.98.

THE VARIANT OF EQUATION OF DIRECTION FINDING CHARACTERISTIC OF THE AMPLITUDE SUM-DIFFERENCE DIRECTION FINDER

V. A. Kryachko

Kharkov Military University, Kharkov 61204, Ukraine
Phone: (0572) 40-41-41 (2-88).
<promk@lin.com.ua>

Abstract

The equation of the direction finding characteristic of the amplitude sum-difference direction finder with parameters similar to those of the equation of the phase sum-difference direction finder characteristic has been received to simplify the comparative analysis of these direction finders.

Keywords: direction finding characteristic, sum-difference direction finder, angular coordinate.

When using a pencil-beam antenna, the equation of the direction finding characteristic (DFC) of the phase sum difference direction finder (PSDDF) is known [1, 2] to look like

$$S_{ph}(\theta) = \operatorname{tg}\left(\frac{\pi d}{\lambda} \theta\right), \quad (1)$$

where d is the linear base of the phase centers of antennas 1 and 2 (see Fig. 1); θ is the angle with respect to equiphase direction (EPD) of a direction finder; λ is the electromagnetic wavelength.

The formula (1) allows estimating the value of a signal error at the direction finder output depending on the target direction error angle θ with regard to EPDF. The formula parameter is the linear base relation of the base phase centers d to the electromagnetic wave length λ of a radio signal.

The DFC equation of the sum-difference direction finder near the equisignal direction (ESD) is of the following form [2]

$$S_{pt}(\theta) = \mu \theta, \quad (2)$$

where μ is the steepness of the DFC at the ESD of the direction finder; θ is the angle with respect to ESD of the direction finder.

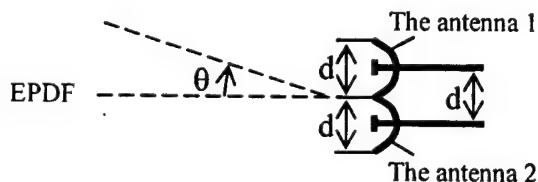


Fig. 1. The relation between the aperture size of the antennas and the base of phase centers of PSDDF antennas

The value μ is defined by the equation [2]

$$\mu = \frac{d}{d\theta} \left| \frac{F_1(\theta) - F_2(\theta)}{F_1(\theta) + F_2(\theta)} \right|_{\theta=0}, \quad (3)$$

where $F_1(\theta)$, $F_2(\theta)$ are the amplitude radiation patterns (RP) (see Fig. 2) of the direction finder antennas.

The DFC equation of ASDDF (2) differs from that of PSDDF (1). Therefore, while measuring the target angular coordinates, the analysis of these direction finders is made with the use of different methods.

The proposed variant of the DFC equation of ASDDF with parameters analogous to those of PSDDF, enables to provide the research of these direction finders with the use of a common method. This allows simplifying essentially the analysis of direction finders.

The purpose of the publication is to derive the conclusion of the equation of DFC with parameters similar to those of the PSDDF DFC equation.

Amplitudes of input signals of ASDDF will be

$$u_1(t, \theta) = U \cdot F_1(\theta) \cdot \cos(\omega_0 t + \varphi_0); \quad (4)$$

$$u_2(t, \theta) = U \cdot F_2(\theta) \cdot \cos(\omega_0 t + \varphi_0), \quad (5)$$

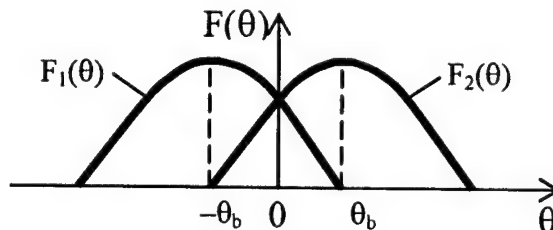


Fig. 2. The main lobes of ASDDF antennas amplitude RPs: θ_b is a bias of RPs $F_1(\theta)$ and $F_2(\theta)$ with regard to ESD

where U is the amplitude of a signal received in the direction of the antenna amplitude RP maximum; ω_0 is a carrier frequency of a radio signal; φ_0 is the initial phase of a radio signal; the output signals of the sum and difference devices are equal, respectively, to

$$u_t(t, \theta) = \frac{\sqrt{2}}{2} U \cdot F_t(\theta) \cdot \cos(\omega_0 t + \varphi_0); \quad (6)$$

$$u_r(t, \theta) = \frac{\sqrt{2}}{2} U \cdot F_r(\theta) \cdot \cos(\omega_0 t + \varphi_0), \quad (7)$$

where $F_t(\theta) = F_1(\theta) + F_2(\theta)$ and $F_r(\theta) = F_1(\theta) - F_2(\theta)$ are the antenna system sum and difference amplitude RP of the DD.

The main amplitude RP lobes in the direction finder plane (Fig. 2) may be approximated by functions given in [3]

$$F_1(\theta) = \cos[k_{dd} \cdot (\theta_b - \theta)]; \quad (8)$$

$$F_2(\theta) = \cos[k_{dd} \cdot (-\theta_b - \theta)], \quad (9)$$

where k_{dd} is the multiplier describing the directive properties of the antenna in the plane of direction finding.

The k_{dd} size can be defined by the formula

$$k_{dd} = \frac{\pi}{2\Delta\theta_{0.5P}}, \quad (10)$$

where $\Delta\theta_{0.5P}$ is the angular width of the half power amplitude RP of the antenna.

The size θ_b (Fig. 2) is defined by the equality [2]

$$\theta_b = \frac{\Delta\theta_{0.5P}}{2}. \quad (11)$$

Substituting (10) in (8) and (9) and taking into account (11), we have

$$F_1(\theta) = \cos\left(\frac{\pi}{4} - \theta_b\right); \quad (12)$$

$$F_2(\theta) = \sin\left(\frac{\pi}{4} - \theta_b\right), \quad (13)$$

where $\theta_b = k_{dd}\theta$ is a generalized direction finder angle with respect to direction finder ESD.

The sum and difference RPs of the direction finder antenna system are equal, respectively, to

$$F_t(\theta) = \sqrt{2} \cos(\theta_b); \quad (14)$$

$$F_r(\theta) = \sqrt{2} \sin(\theta_b). \quad (15)$$

Substituting (14) and (15) in (6) and (7), correspondingly, we shall obtain intermediate frequency signals of the sum and difference channels at the inputs of the phase detector:

$$u_{tin}(t, \theta) = KU \cos(\theta_b) \cos(\omega_{in} t + \varphi_{0in}); \quad (16)$$

$$u_{rin}(t, \theta) = KU \sin(\theta_b) \cos(\omega_{in} t + \varphi_{0in}), \quad (17)$$

where K is the receiver gain; ω_{in} are the signal intermediate frequencies; φ_{0in} are the initial signal phases at the outputs of the receiver.

At the output of the direction finder phase detector, the signal, after filtration of its low frequency component, with account of the receiver automatic gain control (the DFC equation of ASDDF), is described by the expression

$$S_t(\theta) = \frac{u_{tin}(t, \theta)u_{rin}(t, \theta)}{[u_{tin}(t, \theta)]^2} = \operatorname{tg}\left(\frac{\pi}{2\Delta\theta_{0.5P}}\theta\right). \quad (18)$$

Taking into account that [1]

$$\Delta\theta_{0.5P} = \frac{\lambda}{2d}, \quad (19)$$

where d is the dimension of the antenna aperture in the plane of direction finding, we shall obtain

$$S_t(\theta) = \operatorname{tg}\left(\frac{\pi d}{\lambda}\theta\right). \quad (20)$$

The identity of equations (1) and (20) gives a possibility to make a conclusion that the DFC equation of ASDDF (18) is similar to that of PSDDF (1). Application of analogous DFC equations enables one to carry out the research of these direction finders with common methods, what essentially simplify their comparative analysis.

REFERENCES

1. Theoretical foundations of radar / Edit. by. Yakov D. Shirman. School-book for high school.- M.: Sovetskoe radio, 1970.- 560 p.(in Russian)
2. Leonov A. I., Fomichev K. I. Monopulse radar.- M.: Sovetskoe radio, 1970.- 392 p. (in Russian)
3. D. Barton and G. Vard. Handbook on radar measurements. Translated from English under edition of M. M. Veysman.- M.: Sovetskoe radio, 1976.- 392 p. (in Russian)

THE PERSPECTIVE DIRECTIONS OF THE TECHNICAL MODERNIZATION OF INTER-PERIOD SIGNAL PROCESSING SYSTEMS OF PULSE ATC RADARS

D. I. Lekhovitsky, V. I. Zaritsky, I. G. Kirillov, S. I. Burkovsky

Scientific centre of anti-aircraft defense forces
(Kharkiv Military University), Kharkov
<zarja@asape.kharkiv.com>

Abstract

The engineering solutions improving detection of air targets against the clutter background in pulse radars of ATC are substantiated and analyzed.

Keywords: pulse modernization, inter-period signal processing systems, pulse radars, adaptive lattice filters.

1. INTRODUCTION

Detection of signals reflected by air targets moving with arbitrary radial speeds against the background of clutters of different nature is one of the major problems for the broad class of pulse ATC radars. In the majority of them, it is solved at the expense of using the spectral-correlation distinction between the reflected useful and unwanted signals, which is conditioned by differences in speeds of moving, and in the spatial characteristics of targets and sources of clutter.

The inter-period processing IPP systems of present radars accomplishing these differences were mostly elaborated in "the pre-numerical epoch," the technical abilities of the above mentioned stations did not allow them to approach theoretically optimal systems of IPP. The modern standard and fast paces of the advance in digital signal processing technology allow to essentially reduce a gap between the IPP achieved possibilities and its potentialities. The paper is devoted to the substantiation and analysis of the perspective directions of this problem solution.

2. PERSPECTIVE DIRECTIONS

The main direction consists in the successive approximations of the present IPP systems to statistically optimal ones. The latter are synthesized by the given distribution laws of random M -dimensional vectors $U = \{ u_i \}_{i=1}^M$ of complex amplitudes of M radio-echoes received at adjacent periods of sounding (M - element packets of radio echoes) from each element of a resolution range processed by the IPP system.

The extensive theoretical and experimental investigations show that the Gaussian approximation of mutually independent item addends of the additive

mixture $U = Y + \gamma \cdot X$ ($\gamma = 0, 1$) of the pack of a target $X = \{ x_i \}_{i=1}^M$ and clutter $Y = \{ y_i \}_{i=1}^M$ with the identical (zero) average values $\bar{X} = \bar{Y} = 0$, but generally with the different correlation matrices (CM) of the inter-period fluctuations $\Phi_X = \overline{X \cdot X^*}$ and $\Phi_Y = \overline{Y \cdot Y^*}$, proved to be well-grounded for the broad class of pulse radar ATC stations of the decimetre and centimetre wave bands.

For such conditions, as is well-known, the procedure of the optimum detection, by the criterion of Neumann-Pearson, of a useful signal (making decision about the value of a parameter $\gamma \in 0, 1$) includes stages of the linear and non-linear processing.

At the first of them, the power signal / (interference + noise) ratio (SINR) for each of $m \leq M$ coherent components $\beta_l \cdot X_l$ generally ($m > 1$) of non-coherent useful signal $X = \sum_{l=1}^m \beta_l \cdot X_l$ with the Gaussian complex independent multipliers β_l with $\bar{\beta}_l = 0$ and $|\bar{\beta}_l|^2 = h_l^2$, $l \in 1, m$, is maximized. Such a maximum is provided by the bilinear forms $p_l = h_l \cdot U^* \cdot \Psi_l \cdot X_l = h_l \cdot (H \cdot U)^* \cdot (H \cdot X_l)$, $l \in 1, m$, which are formed by transforming a vector of the processed signals U and (or) reference vectors $h_l \cdot X_l$ in inverting or whitening filters with matrix pulse characteristics (MPC) $\Psi_l = \Phi_l^{-1}$ or "root square" H from them, which satisfy the equation $H^* \cdot H = \Psi_l$.

The second stage presumes summation of modulus squares (non-coherent integration) of results of linear processing, and comparison of the obtained sum $\xi = \sum_{l=1}^m |p_l|^2$ with a threshold level, which ensures the given false alarm probability F .

In a particular case of the non-coherent signals with independent ("fast") fluctuations of pulses of a pack ($x_i \cdot x_j^* = 0$, $i \neq j$, $|x_i|^2 = h^2$, $i, j \in 1, M$), optimal pre-threshold statistics $\xi_1 = \mathbf{W}^* \cdot \mathbf{W} = \sum_{i=1}^M |w_i|^2$ or $\xi_2 = \mathbf{V}^* \cdot \mathbf{V} = \sum_{i=1}^M |v_i|^2$ are formed by non-coherent integration of signals $\mathbf{W} = \{w_i\}_{i=1}^M = \mathbf{\Psi} \mathbf{I} \cdot \mathbf{U}$ or $\mathbf{V} = \{v_i\}_{i=1}^M = \mathbf{H} \cdot \mathbf{U}$ from all M outputs of the inverting or whitening filters, respectively.

In the case that is more characteristic for conditions of ATC radars with coherent commonly - "amicably fluctuating" packs of useful signals ($m = 1$) squared modulus of the result of coherent integration $p = \mathbf{W}^* \cdot \mathbf{X}$ of output signals of the inverting or, with insignificant losses, the whitening filters must be compared with a threshold. More simple non-coherent integration of output signals of the latter is accompanied with the loss of energy of a threshold signal, if $F = 10^{-6}$ and $M \gg 1$ does not exceed $(1.5 + M/35)$ times.

As a rule, exact realization of all stages of the optimal processing is impossible because of lack of *a priori* knowledge of various and dynamically changing in time CMs of useful signals and interferences. In present systems of IPP, which can be conditionally subdivided into the filter and compensating filter ones, only some approaches to them are realized.

3. IPP FILTER SYSTEMS

The squared modules of the output signals $q_l = \mathbf{U}^* \cdot \mathbf{X}(f_l)$ of the comb filters of the integration which are linked to M anticipated coherent signals $\mathbf{X}(f_l)$ to the Doppler frequencies f_l , $l \in 1, M$ are used in a role of the pre-threshold statistics in the IPP filter systems. Such matched processing is far from optimal because of the absence of the whitening or inverting comb filters, which ensure the suppression of interferences. The losses, conditioned by it, under conditions of powerful clutter can make tens of dB. They decrease at the coherent integrating of a kind $q_l = \mathbf{U}^* \cdot \mathbf{D} \cdot \mathbf{X}(f_l)$ with a specially diagonal matrix of "weighing" \mathbf{D} , but can be inadmissibly large in this case as well.

4. IPP COMPENSATING FILTER SYSTEMS

IPP compensating-filter systems of ATC radar usually contain non-adaptive systems of inter-period equalization IPE of clutter with different multiplicity and integrations (coherent or non-coherent) of pulses of the useful signal pack at their output. Such a construction is closer to optimal, but has serious practical defects due to the imperfection of the used IPE systems, which have a fixed MPC differing from MPC of whitening or inverting filters of clutters.

In this paper, some technical solutions of the modernization of present systems of the IPC on the basis of their analysis are offered. They consist in the stabilization of the clutter power at the input and outputs of IPC all stages, the refusal of equilibrium subtraction in them for the benefit of non-equilibrium, the integration (coherent or non-coherent) of signals not only at the input of the latter, but also at the input and outputs of IPC all stages. At the expense of these measures in standard radars with wobble of the period of sounding, the quality of the detection of moving targets against the clutter from fixed local subjects improves (the gain can constitute 5..10 dB), and the detection of useful signals, whose power is higher than the interference power, from the targets with zero radial speed, is also possible. The latter of mentioned problems is solved in this case without usage of known enough complex systems of scan-to-scan processing.

The problem of the detection of air targets against the background of passive interferences with a complex spectrum of inter-period fluctuations, which are conditioned by combination of reflections from fixed local subjects and travelling hydrometeors, is actual for the ATC radars of both centimetre and decimetre wave bands. Its solution demands further approaching of IPP to the optimal at the expense of transition of non-adaptive or partially adaptive (items 5) systems of IPC to the adaptive inverting or whitening filters with variables MPC, which are proportional to the "good" estimates $\hat{\Psi}_l$ or $\hat{\mathbf{I}}$ of *a priori* unknown and time-varying matrices $\mathbf{\Psi}_l = \Phi_l^{-1}$ or $\hat{\mathbf{I}}$ respectively.

The authors of this paper have worked out lattice filters (LF) representing regular association of "the elementary lattice filters (ELF)" - two-input-output filters with cross connections, which can be practically expediently used as a structural basis of such filters. The adapting of the whitening and inverting LF as a whole doesn't demand the direct forming of matrices $\hat{\mathbf{I}}$ or $\hat{\mathbf{\Psi}}_l = \hat{\mathbf{I}}^* \cdot \hat{\mathbf{I}}$ and is reduced only to the parameter estimation of ELF of the whitening LF. There have been designed different algorithms of the formation of maximum likelihood (ML) estimations of these parameters by readings of the entrance process in the distance sliding "window", including recurrent algorithms, whose computational complexity doesn't depend on dimensions of "window" (a volume of a training sample). It is shown that on the basis of these ML estimations, the close to the potential efficiency of the adaptive IPP is provided in a quite accessible to the majority of practical situations volume of a training sample, which exceeds the multiplicity of the intra-period compensation of interferences in 3-5 times (an order of the adaptive whitening LF).

Numerous theoretical, as well as semi-full-scale experiments, which have been carried out so far, have confirmed the essential advantages of the developed adaptive systems of IPP on the basis of the adaptive LF as compared with existing filter and compensating-filter systems of IPP of pulse ATC radars.

References

1. White W. D. Cascade processors for adaptive antennas // IEEE Trans. Antennas Propag., 1976, v.AP-24, № 5, P.670-684.
2. Lev-Ari H., Kailath T. Schur and Levinson algorithms for nonstationary processes // Proc. IEEE Int. Conf. Acoust, Speech and Signal Process (Atlanta, CA, March 1981), P.860-864.
3. Brennan L. E., Reed I. S. An Adaptive array signal Processing Algorithm for Communications // IEEE Trans on Aerosp. and Electr System, v.AES-18, N1, January 1982.
4. Fridlander B. Lattice filters for the adaptive processing of data // Proc. IEEE.- 1982.- Vol.70.- N8.- P.54-97.. (in Russian)
5. Juravlev A. K., Lukoshkin A. P., Poddubny S. S. Signal processing in adaptive antenna array.- L.: 1983.- 240 p.. (in Russian)
6. Sharman K. C., Durrani T. S. A triangular adaptive lattice filter for spatial signal processing.- ICASSP 83, Proc. IEEE Int. Conf. Acoust., Speech and Signal Process., Boston, Mass., 14-16 Apr., 1983, v.1 New York, 1983, P.348-351.
7. Zaritsky V. I., Kokin V. N., Likhovitsky D. I., Salamatov V. V. Recursive algorithm of adaptive processing at the central symmetry of spatial-time channels of receiving // Izv. vuzov. Radiophysika.- 1985.- N7.- P.863-871.. (in Russian)
8. Likhovitsky D. I., Zaritsky V. I., Rakov I. D., Sverdlov B. G., Ratinsky M. V. Methods of adaptive lattice filtration in problems of spatial-time signal processing // Preprint 8610. - M.: RTI AS USSR, 1987.- 30 p. [in Russian]
9. Munje J., Delil J. Yu. Spatial analysis in passive location systems with help of adaptive methods // Proc. IEEE.- 1987.- Vol.75.- N11.- P.21-37. [in Russian]
10. Adaptive Filters /Trans. from eng. /Under editorial of K. Kouen and P. M. Grant. - M.: Mir, 1988.- 392 p. [in Russian]
11. Likhovitsky D. I. Levinson generalized algorithm and universal lattice filters // Radiophysika.- 1992.- Vol. 35.- № 9-10.- P.790-808. [in Russian]
12. Likhovitsky D. I., Milovanov S. B., Rakov I. D., Sverdlov B. G. Universal adaptive lattice filters. Part 2. Adaptation by given root from estimated correlation matrix // Izv. vyzov. Radiophysika.- 1992.- № 11-12.- P.969-992. (in Russian)
13. Shirman Ya. D., Losev Yu. D., Minervin N. N., Moskvitin S. V., Likhovitsky D. I. etc. Radio-electronic units: fundamentals of construction and theory / Under editorial of Shirman Ya.D. - M.: JS "Makvis", JSC "Ream-Building", 1997.. (in Russian)
14. Likhovitsky D. I., Atamansky D. V., Kirillov I. G., Flexer P. M. Problems and new results of spectral estimation and antenna arrays superresolution techniques. - Proc. of the 3rd International Conference Antenna Theory and Techniques, 8-11 September 1999, Sevastopol, Ukraine, P.62-68. (in Russian)
15. Likhovitsky D. I., Atamansky D. V., Kirillov I. G., Zaritsky V. I. Effectiveness compare of adaptive processing in arbitrary and central-symmetric PAA // Antenna. - M., 2000.- Issue 1 (44).- P.99-103. (in Russian)
16. Likhovitsky D. I., Flexer P. M., Atamansky D. V., Kirillov I. G. Statistical analysis of some "super-resolution" noise direction finding methods in array antenna at finite number of snapshots // Antenna. - M., 2000.- Issue 2 (45).- P.23-39. (in Russian)
17. Likhovitsky D. I., Atamansky D. V., Kirillov I. G. Variety of "superresolution" analyzers of spatial-temporal random signals' spectrum based on whitening adaptive lattice filters // Antenna. - M., 2000.- Issue 2 (45).- P.40-54.. (in Russian)

MEASUREMENTS OF RECEPTION DIRECTION OF DETERMINISTIC SIGNAL AGAINST SPATIALLY-CORRELATED INTERFERENCES WITH THE USE OF THE ADAPTIVE ANTENNA ARRAY

S. T. Bagdasaryan, V. A. Tarshin, V. A. Vasilyev

Kharkov Military University, maidan Svobody, 6, Kharkiv 61043, Ukraine

Abstract

The variant of creation of a measurer of reception direction of a signal against the spatially-correlated interference by the maximum likelihood method with the use of the adaptive antenna, which simultaneously provides minimum values of the variance and biases, is given. The minimization of errors is achieved without the automatic correction of the array radiation pattern after adaptive compensation of interference and without the increase of the variance of the biased estimate.

1. INTRODUCTION

The adaptation of antennas to external interferences essentially complicates the problem of measuring angular coordinates of target-sources of useful deterministic signals [1-4]. In this case, the maximum likelihood estimates are biased [3-5], what requires special correction measures. Frequently [4-5 etc.], the bias of estimate is being eliminated by the automatic correction of the adaptive array radiation pattern (RP) by normalization of the output by a detection parameter. However, this results in the increase of the measurement error variance. Optimal measurers are characterized by simultaneously minimum values of the estimate variance and bias [6].

The purpose of the paper is the substantiation of a structure of a multichannel measurer of direction of signal reception (DSR) in radar with an adaptive an-

tenna array (AAA), which simultaneously provides minimum variance and bias of the estimate. It is shown that it is possible to derive the algorithm of the unbiased estimate from the maximum likelihood equation.

The adaptation to the external interference influences on results of current and tracking measurements. The influence on the latter displays itself through results of the current measurements. In this case, the increase of the current measurement variance leads to the increase of duration of the transient process and the variance of a tracking measurer in steady mode. In Fig. 1, the ratio of the tracking measurement variance to the maneuver variance versus the number of a measurement cycle for fixed values of current measurement variances is shown. Therefore hereinafter main attention is paid to the research of the accuracy of current measurements of the angular position under conditions of correlated interferences impact.

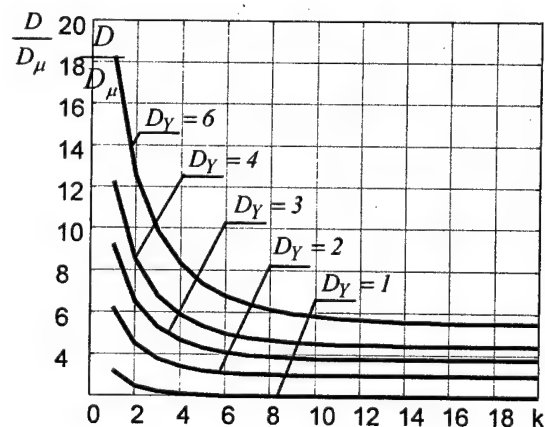


Fig. 1.

2. ALGORITHMS OF DETERMINATION OF MAXIMUM LIKELIHOOD ESTIMATES

The maximum likelihood estimate of direction of signal α reception usually is found by the following: maximum of logarithm of the likelihood ratio $\ln L(\alpha)$ obtained after averaging over random amplitude and initial phase of the deterministic signal [2, 4]; maximum of the module of a weight integral $|\dot{Z}(\alpha)|$; maximum of the module of the normalized weight integral $|\dot{Z}_l(\alpha)|$ [4]:

$$\ln L(\alpha) = \frac{q^2(\alpha) |\dot{Z}_l(\alpha)|^2}{4(1 + q^2(\alpha)/2)} - \ln(1 + q^2(\alpha)/2), (1)$$

$$|\dot{Z}(\alpha)| = \left| \frac{1}{2} \int_{-\infty}^{\infty} \dot{Y}^T(t) \dot{R}^*(t, \alpha) dt \right| \quad (2)$$

$$|\dot{Z}_i(\alpha)|^2 = |\dot{Z}(\alpha)|^2 / q^2(\alpha) \quad (3)$$

where $q^2(\alpha) = \frac{1}{2} \int_{-\infty}^{\infty} \dot{X}^T(t, \alpha) \dot{R}^*(t, \alpha) dt$ is the detection parameter; $\dot{Y}(t)$, $\dot{X}(t, \alpha)$, $\dot{R}(t, \alpha)$ are the column vectors of complex amplitudes of the received oscillation, the expected signal and the weighting functions, respectively; and $\dot{X}(t, \alpha)$, $\dot{R}(t, \alpha)$ are divided into space $\dot{X}(\alpha)$, $\dot{R}(\alpha)$ and time $\dot{X}(t)$, $\dot{R}(t)$ multipliers; the star * denotes transposition and complex conjugation; α is the generalized angular parameter expressed in shares of the half-width RP of the array.

As a result of application of statistics (1) and (2) for measurements, the estimate of DSR is biased, but with the variance smaller, than that of the unbiased estimate obtained with statistics (3) [7]. Therefore for the optimization of measurements, it is expedient to choose the algorithm (1) or (2) and to provide minimization of bias.

Further, the optimization of DSR measurements for maximum $|\dot{Z}(\alpha)|$ is considered. It is stipulated both by simplicity of the technical realization of $|\dot{Z}(\alpha)|$ and by wide application in the measurers for estimation of signal parameters against the background of uncorrelated noise.

3. MEASURER OF DIRECTION OF SIGNAL RECEPTION WITH MINIMIZATION OF THE ESTIMATE VARIANCE AND BIAS

A possible version of the block diagram of the DSR measurer to be constructed for radar with a linear equidistant array is presented in Fig. 2.

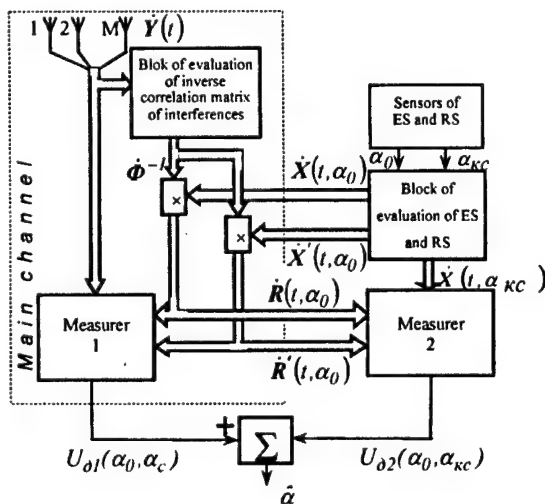


Fig. 2.

The given measurer incorporates a main channel and an additional measurer. The main channel represents a typical system for many radars with sum-difference signal processing. It includes: the antenna array; the block of evaluation of inverse correlation matrix of interferences; the matrix multipliers for shaping a space weight vector $\dot{R}(\alpha_0) = \dot{\mathbf{O}}^{-1} \dot{\mathbf{O}}(\alpha_0)$ (for a sum channel) and its derivative $\dot{R}'(\alpha_0) = \dot{\mathbf{O}}^{-1} \dot{\mathbf{O}}'(\alpha_0)$ (for difference channels). Assemblage of these elements, and also the sensor of directions of the expected signal (ES) and the reference signal (RS), the block of evaluation of these signals provide shaping of the DSR estimate at the output of the measurer 1 (the direction-finder) according to the algorithm

$$U(\alpha) = \frac{\text{Re}(\dot{Z}'(\alpha) \dot{Z}^*(\alpha))}{|\dot{Z}(\alpha)|^2} \quad (4)$$

The measurer 2 is intended for obtaining an estimate of direction of RS reception, which is assumed to be arbitrary known value α_{kr} . Algorithms of measurers 1 and 2 are identical and determined by the expression (4). The value of the output signal of measurer 1 $U_{01}(\alpha_0, \alpha_c)$ corresponds to the biased estimate of the reception direction. At the output of the measurer 2, the direction-finding performance with RS biased zero is formed. Signals at outputs of measurers 1 and 2 take identical values under overlapping of ES and RS directions. Therefore at the output of the adder, the adjusted direction-finding performance is formed, whose zero corresponds to ES reception direction. This is illustrated by the results of the mathematical simulation. It was conducted for the linear equidistant array consisted of ten elements, taking into account various interference situations and different DSRs, with respect to the fixed RP. The interference represents the additive mixture of internal noise and external correlated interference.

Fig. 3 shows direction-finding performances being the results of simulation for various positions of a signal source without the bias compensation and after it. In Fig. 4, the analogous direction-finding performances for various positions of the interference source are presented. It is seen from these figures that the zero position of the adjusted direction-finding performance corresponds to DSR. Figs 3, 4 are depicted for the known interference environment. The carried out analysis of operation of the offered device with the array adaptation to the varying interference environment has shown that the residual value of the bias constitutes the thousandth proportion of the RP width, what is much less than the fluctuation measurement error. It means that the measurement accuracy is determined by the value of the fluctuation error. Note also, that compensation of the bias does not result in modification of the steepness of the direction-finding performance, and consequently, it does not change the variance of the measurement error with respect to the

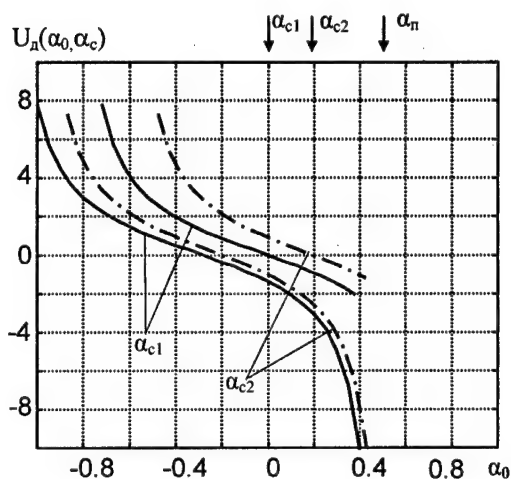


Fig. 3.

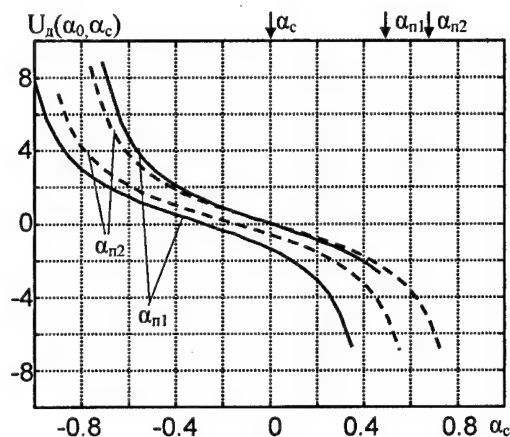


Fig. 4.

one of the bias estimate. In the offered measurer, as distinct from [7], we succeeded in eliminating the bias at the array fixed RP.

4. CONCLUSION

- It is shown, that, when receiving with AAA a signal against the background of spatially-correlated interference, it is possible to use effectively the algorithm of the maximum likelihood estimate over the maximum of the complex weight integral module with consequent compensation of bias.
- The structure of the DSR measurer using AAA is offered, which provides the estimate minimum variance and bias.

REFERENCES

1. Devis R. C., Brenan L. E., Reed I. S. Angle estimation with adaptive arrays in external noise fields.— IEEE Trans. 1976, vol. AES-12, № 2, p. 179-186.
2. Shirman Ya. D. and V. N. Manzhos. Teoriya i tekhnika obrabotki informatsii na fone pomekh, Radio i Svyaz Press, Moscow, 1981 (in Rus.)
3. Zuravlev A. K., Lukoshkin A. P. and S. S. Poddubny. Obrabotka signalov v adaptivnykh anten-nykh reshetkakh, Leningrad university Press, Leningrad, 1983. (in Rus.)
4. Radioelektronnye sistemy: osnovy postroeniya i teoriya. Spravochnik /Shirman Ya. D., Losev U. I., 1998. (in Rus.)
5. Bagdasaryan S. T., Belov A. A., Ryabuha V. P., Tarshin V. A. Nesledyashee izmerenie v RLS s adaptivnoy AR informativnykh parametrov signala so sluchajnymi amplitudoy i nachalnoy fazoy na fone pomekh., Antenni, 2000, vipusk №2(45), p. 78-83 (in Rus.)
6. Kuz'min S. Z. Tsifrovaya radiolokatsiya. Vvedenie v teoriyu. Kiev: Izd. KVITH, 2000.— 428. (in Rus.)
7. Tarshin V. A., Vasilyev V. A. Povyshenie tochnosti izmereniya uglovykh koordinat v radiolokatsionnoy stantsii s antennoj reshetkoj na fone pomekh. Sistemi obrabotki informatsii. Zbirnik naukovikh prats. Vip. 3(19)— Kharkiv p. 113-118. (in Ukr.)

ALGORITHM OF SPATIAL SELECTION OF UNCORRELATED SIGNALS

Oleg Z. Sultanov

Rostov Military Institute of Missile Corps, Rostov-on-Don, Russia
<zvezd@jeo.ru>

Abstract

The opportunity of using supersolution algorithm in radar-location system to spatial selection of signals scattered from targets is considered in the r. The analysis of rate of signal correlation in temporal and space parameters is given. The conditions which signals are uncorrelated or rate of correlation is less than the given value are defined. The algorithm of treatment of radar signals is proposed on the base of the given expressions and its efficiency is evaluated. The results of numerical simulations of spatial selection of signal reflected from various targets performed on the basis of both classical algorithm and suggested algorithm are carried out.

Keywords: radar-location system; vector of weight coefficients; covariance matrix; space signal selection.

1. INTRODUCTION

One of the basic peculiarities of functioning of the modern radar-location systems (RLS) is a necessity of simultaneous discoveries and distinguishing a great number of signals, reflected from different targets. For discriminating by angular direction the radiators system can be used united in antenna array (AA) output signals of which sum up then with some weights as in Bakhrakh and Voskresensky (1989). However, the classical method based on in-phase summarizing with equal weights has a number of shortcomings the principal of which is the "undistinguishing" of weaker by power signals as in Monzingo and Miller (1980).

2. FORMULATION OF THE PROBLEM

One of the methods of approach to overcome this drawback is the using algorithms of supersolution which are considered as in Monzingo and Miller (1980) and in Gabriel'an *et al.* (2002). The possibility of using this method for distinguishing uncorrelated signals in RLS is determined by the weak correlation of signals reflected from the different targets. The justification of weak correlation of radar-locating signals will be shown below.

2.1. SETTING THE PROBLEM

Let us consider antenna array of M -elements which is subjected to the acting of L signals from different targets. It is necessary to develop the algorithm of treatment of signals reflected from various targets signals guaranteeing resolution of signals independently from their levels.

2.2 DESCRIPTION OF ANTENNA SIGNALS

The output signal of antenna array $U(t)$ can be put down as

$$U(t) = Y(t)W^T, \quad (1)$$

$$Y(t) = N(t) + \sum_{l=1}^L S_l U_l(t), \quad (2)$$

where $Y(t)$ is M -element row vector of output signals of AA radiators; S_l is a row vector of dimension $1 \times M$ the elements of which are defined by the correlation

$$S_{ml} = \exp\{-i2\pi\lambda^{-1}\phi(x_m, y_m, z_m, \theta_l, \varphi_l)\}, \quad (3)$$

$$U_l(t) = \begin{cases} P_l^{1/2} \exp(i\frac{2\pi c}{\lambda}t), & 2\frac{R_l}{c} \leq t \leq 2\frac{R_l}{c} + \tau, \\ 0, & \text{in opposite case,} \end{cases} \quad (4)$$

that corresponds to the use of impulse signals duration τ in operating radar-location system.

In expressions (3), (4) $U_l(t)$ is the function describing the temporary dependence of signal reflected from l -th target; W is row vector of weights coefficients (VWC):

$$W = \{\omega_1, \omega_2, \dots, \omega_M\};$$

$$\phi(x_m, y_m, z_m, \theta_l, \varphi_l) = (x_m \cos \varphi_l + y_m \sin \varphi_l) \cos \theta_l + z_m \sin \theta_l;$$

c is the velocity of light; τ is the duration of radiated impulses; x_m, y_m, z_m are coordinates of m -th radiator; λ is the operating wave length; R_l, θ_l, φ_l are coordinates of l -th target in spherical coordinate system ($l = 1, \dots, L$);

$$N(t) = \{n_1(t), n_2(t), \dots, n_M(t)\}, \quad (5)$$

$N(t)$ is a row vector of signals of thermal noises in radiators.

2.3. THE ALGORITHM OF WEIGHT SUMMARIZING

For realizing weight summarizing of signals in AA channel the vector of weight coefficients will be chosen on the basis of correlation as in Monzingo and Miller (1980)

$$W = (A^* R^{-1} A^T)^{-1} R^{-1} A^T, \quad (6)$$

in which

$$R = \{Y^T(t)Y^*(t)\}. \quad (7)$$

In formula (7) R is the covariance matrix of signals dimension of $M \times M$, $\{\bullet\}$ is operation of averaging by time.

Direction of vector A (row vector $1 \times M$) defines the orientation of the main lobe of pattern of a receiving antenna in direction θ_0, φ_0 in the space and its elements are defined by formula:

$$a_m = \exp\{i2\pi\lambda^{-1}\phi(x_m, y_m, z_m, \theta_0, \varphi_0)\}. \quad (8)$$

In the case of selection of vector of weight coefficients are based on correlation

$$w_m = a_m, \quad (9)$$

the algorithm of treatment coincides with the classical algorithm. This case is realized by substituting covariance matrix R by unity matrix. Physical interpretation of this replacement consists in refusal of account of spatial correlation of output signals of antenna array radiators.

2.4. EVALUATION OF RATE OF SIGNAL CORRELATION

The output signal of m -th radiator caused by l -th target on the basis of radar equation as in Scolnik (1970) is defined using formula (3) by equality

$$P_l = B(\theta_l - \theta_0, \varphi_l - \varphi_0) D_m \lambda^2 \sigma_l R_l^{-4}, \quad (10)$$

in which $B(\theta_l - \theta_0, \varphi_l - \varphi_0)$ is a factor considering static coefficients and parameters of a radiating antenna; σ_l is effective surface of scattering of l -th target; D_m is directivity coefficient of m -th element.

Expressions (2), (3), (7) and (10) allow to present the elements of covariance matrix R as

$$\begin{aligned} r_{mt} = & \sum_{l=1}^L \sum_{q=1}^L \exp[-i2\pi\lambda^{-1}(\phi(x_m, y_m, z_m, \theta_l, \varphi_l))] \times \\ & \times \exp[i2\pi\lambda^{-1}(\phi(x_t, y_t, z_t, \theta_q, \varphi_q))] \times \\ & \times B(\theta_l - \theta_0, \varphi_l - \varphi_0) B^*(\theta_q - \theta_0, \varphi_q - \varphi_0) \times \\ & \times \frac{D_m D_t \lambda^4 \sigma_l \sigma_q}{R_l^4 R_q^4} \times \{u_l(t)u_q^*(t)\} + \{n_m(t)n_t^*(t)\}, \\ m = 1, \dots, M; \quad t = 1, \dots, M. \end{aligned} \quad (11)$$

From the correlation (11) it follows that $\{u_l(t)u_q^*(t)\} \neq 0$ only if $|R_l - R_q| < \frac{c\tau}{2}$. In the case of targets which distances satisfy condition $|R_l - R_q| > \frac{c\tau}{2}$ the correlation scattered from these

targets signals is zero $\{u_l(t)u_q^*(t)\} = 0$. The last condition corresponds to resolution targets in distance.

For items from (10) corresponding to targets that have different angular positions the following inequalities are correct

$$|B(\theta_\chi - \theta_0, \varphi_\chi - \varphi_0) B^*(\theta_\xi - \theta_0, \varphi_\xi - \varphi_0)| \ll B(0, 0), \quad \chi = 1, \dots, L; \quad \xi = 1, \dots, L. \quad (12)$$

Formula (12) shows that the rate of spatial correlation of signals reflected from various targets is evaluated by the level of sidelobes of pattern of transmitting antenna of radar-location system. As a rule this level is less than -10 dB.

Thus on the base of the fulfilled analysis we can consider that signals from the different targets received by AA are uncorrelated. Consequently the elements r_{mt} in supposition that thermal noises present a white Gaussian noise are defined by equals

$$\begin{aligned} r_{mt} = & \sum_{l=1}^L \exp[-i2\pi\lambda^{-1}(\phi(x_m, y_m, z_m, \theta_l, \varphi_l))] \times \\ & \times \exp[i2\pi\lambda^{-1}(\phi(x_t, y_t, z_t, \theta_l, \varphi_l))] \times \\ & \times |B(\theta_l - \theta_0, \varphi_l - \varphi_0)|^2 \frac{D_m D_t \lambda^4 \sigma_l^2}{R_l^8} + P_n \delta_{mt}, \\ m = 1, \dots, M; \quad t = 1, \dots, M, \end{aligned} \quad (13)$$

in which δ_{mt} is a Kronecker symbol; $P_n = \overline{\{n_m^2(t)\}}$

2.5. THE RESULTS OF SIMULATION

By using the given correlations a numeral simulating of power dependence of antenna array output signal $P(\theta_0, \varphi_0) = \overline{\{U(t)\}^2}$ was fulfilled on the basis of application of both classical algorithm and considered algorithm of supersolution consequently. The results of simulation are demonstrated on Fig. 1 and Fig. 2. In the first case the elements of vector weight coefficients are chosen by expression (9) that corresponds to formula $W = A$. In the second case vector weight coefficients are defined by formula (6). It is considered that both transmitting antenna and receiving antenna are circular antenna array with 32 radiators. The radius of circle is 3λ . The distance between radiator is 0.6λ . The level of sidelobe of pattern of transmitting antenna in these parameters is -11 dB. The relations of power of reflected from various targets signals to power of thermal noise based on expressions (3), (4) and (10) are defined by the following values:

$$P_l/P_n = 10^3, \theta_l = 15^\circ, \varphi_l = 40^\circ;$$

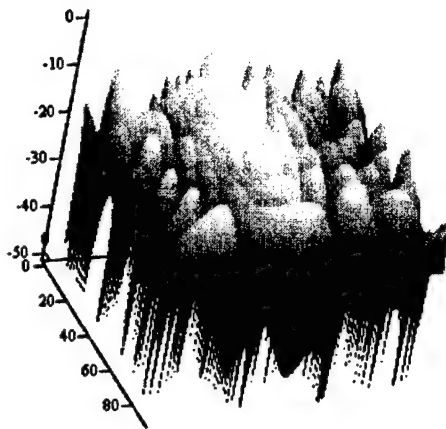


Fig. 1. Antenna array output signal by using classical algorithm.

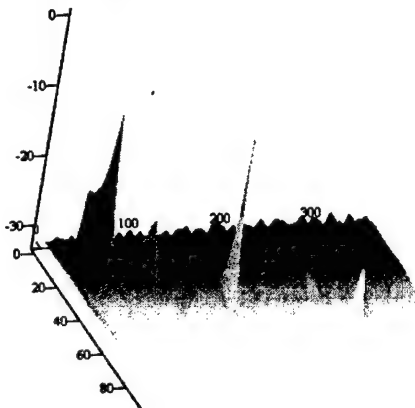


Fig. 2. Antenna array output signal by using super-resolution algorithm.

$$P_2/P_n = 40, \theta_2 = 25^\circ, \varphi_2 = 80^\circ;$$

$$P_3/P_n = 10^4, \theta_3 = 40^\circ, \varphi_3 = 160^\circ;$$

$$P_4/P_n = 10^2, \theta_4 = 75^\circ, \varphi_4 = 240^\circ.$$

Given results demonstrate that application of classical algorithm doesn't make it possible to select targets which signals have significantly distinguishing

levels. In an opposite way application of suggested algorithm based on the method of superresolution makes it possible to select signals from various targets. This opportunity is independent from relations of power of signals reflected from various targets.

3. CONCLUSION

In the paper the opportunity of application of super-resolution method to distinguishing signals reflected from various targets is demonstrated. It is exhibited that an application of impulse signals in operating radar-location systems and directive transmitting antenna permits to supply decreasing of correlation level to the necessary value. Consequently signals reflected from the various targets may be considered as invariable signals. The receiving results demonstrate that proposed algorithm in the difference from the classical algorithm allows one to distinguish signals reflected from various targets independently from the correlation of their power.

ACKNOWLEDGMENT

The author would like to thank Doctor of Engineering Science, Professor Dmitry Gabriel'yan and Candidate of Engineering Science Marina Yu. Zvezdina for their advice and stimulating discussing during the revision phase of this paper.

REFERENCES

1. The problems of antennas technique / Editor-In-Chief Edit. Bakhrah L.D. and Voskresensky D.I. – M.: Radio and Svyaz, 1989 (in Russian).
2. Monzingo R.A., Miller T.W. Introduction to Adaptive Arrays. – John Wiley & Sons, Inc., 1980.
3. Gabriel'an D.D. *et al.* Application of an adaptive method for distinguishing uncorrelated signals // *Avtomatika i vychislitel'naya tekhnika*. 2002. No 4. p.79 (in Russian).
4. Radar Handbook / Editor-In-Chief M.I. Scolnik. McGraw-Hill book company, 1970. V.I.

THE METHOD OF DETERMINATION OF THE AMPLITUDE AND PHASE DISTRIBUTION IN ANTENNA APERTURE PLANE

I. B. Shirokov

Sevastopol National Technical University, Sevastopol, Ukraine
<shirokov@stel.sevastopol.ua>

Abstract

This paper presents the method of determination of the amplitude and phase distribution in antenna plane aperture. This method is based on homodyne one, where the initial microwave oscillation is heterodyne one. The mobile probe unit consists of proper antenna probe and reflecting controlled phase shifter. The initial microwave oscillation is shifted on low frequency with reflecting controlled phase shifter. The initial phase and frequency of microwave oscillations are eliminated. Low frequency feeder with arbitrary phase stability is used to carry the low frequency oscillations to mobile probe unit. The initial phase of low frequency oscillations is transferred on microwave.

Keywords: homodyne method, reflecting controlled phase shifter, low frequency feeder with arbitrary phase stability.

1. INTRODUCTION

The creation of antenna pattern measurement usually assumes the using of far-field one. Furthermore, the anechoic chamber is preferable. In any case, the lengthy antenna pattern range is necessary for far-field measurements.

On the other hand, it can carry out antenna near-field measurements and then determine the aerial patterns. However, in a number of cases, there are many difficulties to be dealt with when determining the antenna pattern. So, the two plane rotating of testing plane aperture antenna results in great disparity of measured and real data, because of the mutual position of testing plane aperture and probe antenna is changed during rotating. Furthermore, the phase centre position of testing antenna is usually unknown. So, it is impossible to interpret measured data adequate.

The scanning of testing antenna aperture with antenna probe in a plane of testing antenna aperture, or displacement of testing antenna in a plane of its aperture allows determine the amplitude and phase distribution in testing aperture plane. The converting of measured data gives good accordance to real antenna pattern. The using of anechoic chamber and lengthy antenna pattern range is not obligatory in this case. However, the same measurement assumes the solving of a main problem. That is the ensuring of amplitude and especially phase stability of mobile antenna feeding. Such arrangements make the antenna measurements very complex and expensive.

In this paper it is proposed to simplify a problem with certain arrangements.

2. METHOD DESCRIPTION

In this paper it is proposed to use the homodyne method of amplitude and phase measurements, where the initial microwave is heterodyne one. This method let us to eliminate the influence of uncertainty of microwave oscillation initial phase on phase measuring accuracy.

The main problem of all phase measurements on microwave is a transmitting of initial phase of microwave to the point of phase difference measuring without any addition phase shift. Any flexible antenna feeder does not have phase stability, so it is impossible to feed mobile antenna probe with one.

It is proposed to make amplitude and phase measurements in a point of placing of microwave oscillator and testing antenna, which are set hard. The phase stability of hard and short feeder is enough for phase measurements on microwave.

On the other hand, the phase stability of any feeder for low frequency is not taken into account, because of feeder length is incomparably smaller than low frequency oscillations wavelength. The only task had to be solved is the transferring of the initial phase of the low frequency oscillations on microwave. Such task can be solved by heterodyne method, which, however, results in additional problems related to the heterodyne synchronization.

In this paper it is suggested to abandon the synchronization of the microwave by low frequency oscillations and to use the origin microwave as heterodyne oscillations with the same initial phase and a frequency shift. This frequency shift is put into microwave in terms of a monotonous phase delay [1].

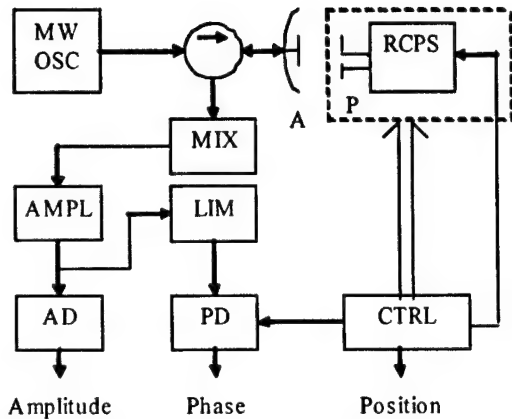


Fig. 1. Equipment scheme for amplitude and phase distribution measurements

The change of the microwave phase over the period T of the low frequency oscillations by 2π is tantamount to the frequency shift of the microwave by the frequency $\Omega = 2\pi/T$. In this case, the initial phase of the low frequency oscillations is transferring on microwave [2].

The equipment for determination of amplitude and phase distribution in antenna aperture plane consists of (Fig.1) microwave oscillator MW OSC, microwave circulator, testing antenna A, mixer MIX, low frequency amplifier AMPL, limiter LIM, amplitude and phase detectors AD and PD, controller CTRL, antenna probe P and reflecting controlled phase shifter RCPS. It can describe the microwave oscillations, which are generated with microwave oscillator, as

$$u_1(t) = U_0 \cdot \sin(\omega t + \varphi_0), \quad (1)$$

where U_0 is the amplitude, ω is the frequency, φ_0 is the initial phase. The received with antenna probe oscillations are characterized by following expression

$$u_2(t) = U_0 \cdot R \cdot \sin(\omega t + \varphi_0 + \Delta\varphi), \quad (2)$$

where R is the generalized multiplier, taking into account all feeder transferring coefficients, $\Delta\varphi$ is the phase shift which characterizes the phase distribution in certain point of antenna aperture. In the mobile unit reflecting phase shifter realizes the phase change law, described above. Controller forms the low frequency oscillations and creates the movement of mobile unit.

Thus, the microwave obtains frequency shift according to the law

$$u_3(t) = U_0 \cdot R \cdot \sin((\omega + \Omega)t + \varphi_0 + \Delta\varphi + \varphi_1), \quad (3)$$

where φ_1 is the initial phase of the low frequency oscillation. Transformed with the frequency and phase microwave are radiated back and are received with testing antenna. The received oscillations are characterized by the expression

$$u_4(t) = U_0 \cdot R^2 \cdot \sin((\omega + \Omega)t + \varphi_0 + 2\Delta\varphi + \varphi_1), \quad (4)$$

and are mixed with the origin microwave with the mixer. The difference of these microwave oscillations is described by the expression

$$u_5(t) = U_0 \cdot R^2 \cdot \sin(\Omega t + 2\Delta\varphi + \varphi_1). \quad (5)$$

From (5) it is shown that the frequency ω and the initial phase φ_0 of the origin microwave oscillations are missing, the factor R^2 defines the amplitude in certain point of antenna aperture, $2\Delta\varphi$ is characterized the phase in that point. This difference is selected and amplified with low frequency amplifier.

The amplitude detector picks up signal $U_a(x, y)$, which is in a common case changed in dependence on antenna probe position as follows $U_a(x, y) = U_0^a \cdot R^2(x, y)$, where U_0^a is the generalized amplitude factor which is not changed over a time band and takes into account transfer ratios of the all parts of the equipment, $R^2(x, y)$ characterizes the amplitude distribution in antenna aperture plane XOY .

The phase detector with the low frequency controller signal picks up the $U_p(x, y)$, which is changed in dependence on antenna probe position in a common case too. This signal is changed according to the law $U_p(x, y) = U_0^p(2\Delta\varphi(x, y) + \varphi_2 - \varphi_1)$, where φ_2 is the initial phase of the low frequency controller oscillations, U_0^p is phase detector transfer constant, $2\Delta\varphi(x, y)$ characterizes the phase distribution in antenna aperture plane.

3. CONCLUSION

Thus, it is possible to determine the amplitude and phase distribution in antenna aperture plane. No rotary microwave adapters or flexible microwave feeders are used according to presented method. The cost of measurement equipment is low, because of all signal processing is carried out on low frequencies.

The antenna probe and reflecting phase shifter dimensions, which arrange the mobile unit, are small. The low frequency feeder thickness can be chosen as small as possible. All of mentioned above results does not significantly change in real amplitude and phase distribution in antenna aperture plane. So, the antenna pattern can be calculated with high accuracy.

REFERENCES

1. J. S. Jaffe, R. C. Mackey, "Microwave Frequency Translator" IEEE Trans. MTT, vol. MTT-13, May 1965, pp 371- 378.
2. I. B. Shirokov "Amplitude and Phase Difference Measurements Device" AC SU 1486942 G 01 R 19/04, 25/00.

COMPUTER SIMULATION OF TARGET BACKSCATTERING AS ELEMENT OF PERSPECTIVE RADAR DESIGN

S. P. Leshchenko, V. M. Orlenko, Y. D. Shirman

Kharkov Military University (KMU), Kharkov, Ukraine
 <cliver@bestnet.kharkov.ua, vorlenko@vl.kharkov.ua>
 <ysh@vl.kharkov.ua>

Abstract

Method of computer simulation of aerial target backscattering is described. It is used for comparative study of wideband and narrowband radar signals in application to radar recognition, detection, coordinate measurement, and tracking. It is shown on the basis of examples that computer simulation becomes an important element of the perspective radar design.

Keywords: computer simulation, radar backscattering, bodies of simple shape (simple components), aerial targets, radar detection, radar recognition, radar tracking.

1. PURPOSE AND METHOD OF THE SIMULATION

The radar problem solutions convictive for the radar designer can be usually obtained by field tests. However, large-scale comparative field tests are not carried out yet for recognition, detection, and tracking variants with various signal bandwidths. Pure theoretical consideration of such problems (recognition especially) is often impossible due to lack of necessary initial data on the target backscattering. Therefore, simulation methods have to be used.

The target backscattering model must account for the target shape, presence of fast rotating elements (compressor, turbine, and prop blades), polarization features, and dynamics of flight in turbulent atmosphere. This model happens to be much more complex than those commonly used to study the detection and tracking of a point target.

It can be assumed in quasi optical waveband that a target (especially conductive) contains limited number of local reflectors (LR) [1, 2]. Calculation of the target's scattering characteristics can be reduced to determining the coordinates and polarization scattering matrices of these LRs.

The surface of complex target is decomposed into a set of the bodies of relatively simple shape. In the process of decomposition some simple bodies approximating the target's surface can be clipped by means of the so called limiting surfaces. Local reflectors not shadowed by others are used then for calculating the backscattered signals. The most common limiting surface is a pair of parallel planes. This is illustrated in Fig. 1a, b [3]. In Fig. 1a the simplest aircraft model is shown that is composed from the

main components: clipped ellipsoid, cylinder, plate, wedge etc. Fig. 1b shows the pair of limiting planes.

There are different coordinate systems introduced for backscattering simulation: 1) Cartesian and spherical coordinate system originated at radar; 2) Cartesian coordinate system originated at target; and 3) Cartesian coordinate systems originated at simple bodies (local coordinate systems).

Aerial target position is determined by the coordinates of the target mass center X_t, Y_t, Z_t in radar coordinate system O_rXYZ , and by orientation angles of the target coordinate system $O_t\xi\eta\zeta$ in the radar one (course angle ψ , pitch angle θ , and roll angle γ).

Each simple body and corresponding limiting surfaces are described in their local coordinate systems $O_\nu xyz$, $\nu = 1, 2, \dots, N_\Sigma$, where N_Σ is the number of approximating bodies and limiting surfaces used to compose the target model. Origins $\xi_\nu, \eta_\nu, \zeta_\nu$ of local coordinate systems and orientation angles $\psi_\nu, \theta_\nu, \gamma_\nu$ of their axes are set in such a way that corresponding simple approximating bodies can be described by canonical equations.

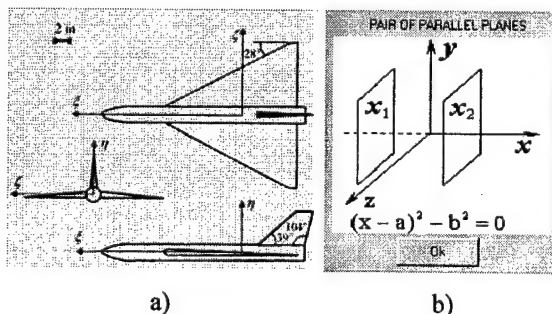


Fig. 1.

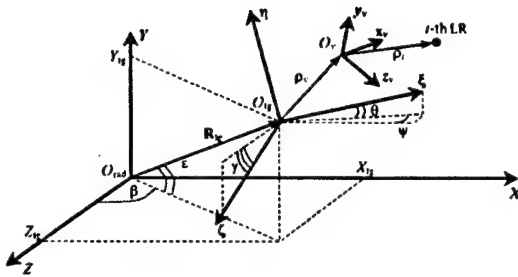


Fig. 2.

All these coordinate systems, used for simulating the different kinds of movement of target and their elements and their backscattering, are shown in Fig. 2.

The following values are found in the process of calculation:

- a) vector of the wave propagation direction \mathbf{r}^0 taking into account the target orientation;
- b) the number of LR and their coordinates taking into account the effects of their possible shadowing by other target's surfaces;
- c) elements of the polarization scattering matrix of each LR in own polarization basis.

The differential peculiarity of aerial target is the presence of fast rotating elements on it. These elements are: propeller and rotor blades of turboprop aircraft and helicopters as well as air compressor and turbine blades of turbojet aircraft. The radar signal backscattered from such elements receives peculiar rotational modulation that influences on the characteristics of target detection, tracking, and recognition.

The expression of complex amplitude of the radar signal backscattered from aerial target at the antenna input has the form

$$\dot{X}(t) = \sum_{i=1}^N \mathbf{A}_i(\mathbf{r}^0, t) \mathbf{S}_i U \left(t - \frac{2\rho_i \mathbf{r}^0}{c} \right) e^{-\frac{j4\pi f_0 \rho_i \mathbf{r}^0}{c}} \frac{Q_i}{10^{20}}.$$

Here $\mathbf{A}_i(\mathbf{r}^0, t)$ is the polarization scattering matrix of i -th LR accounting for its possible nonstationary nature for the fast rotating elements; \mathbf{S}_i is the polarization vector of the incident wave; N is the number of illuminated LR; \mathbf{r}^0 is the unit vector of the incident wave direction; $U(t)$ is the complex signal envelope at the output of matched processing device; ρ_i is radius vector of the i -th LR phase center; Q_i is the absorption factor of the i -th LR; f_0 is the carrier frequency; c is the light velocity.

Since all the compressor and turbine blades are identical, the rotational modulation corresponds to periodical change in amplitude and phase of sinusoidal signals with the period of $1/NF_{rot}$. Here N is the number of blades, F_{rot} is the rotation frequency.

Amplitude of backscattered signal is described by the equation

$$E(t) \equiv \sum_{\nu=0}^{N-1} \sqrt{\sigma_{\nu} \left(t - \frac{\nu}{NF_{rot}} \right)} \times \cos \left\{ 2\pi f_0 t + C_{\nu} \sin \left[2\pi F_{rot} \left(t - \frac{\nu}{NF_{rot}} \right) + \phi_{\nu} \right] \right\}.$$

Here $\sigma_{\nu}(\bullet)$ is the RCS of a single blade as a function of time; f_0 is the carrier frequency; ϕ_{ν} are the constant initial phases; C_{ν} are the constants.

Propeller as a rotating structure differs from the air compressor and turbine by the fewer number of blades and slower rotation. In the computer simulation model each propeller's blade is approximated by the ellipsoid with unequal half axes.

Simulated turbine and propeller modulation for narrowband signals coincided with that of real targets obtained in experiments. Examples of such modulation obtained by simulation can be heard using the computer multimedia capability.

Simulation of target's random movement in turbulent atmosphere is provided by the corresponding mathematical model of the aircraft as a dynamic system.

The simulation method as a whole allowed to obtain not only RCS of point aerial targets (where the target is much smaller than the range resolution interval), but also their range profiles, which begin to appear when the range resolution interval is comparable with the target size.

The dynamic of these range profile change can be seen too. Both orientation change and turbine modulation contribute to this dynamic of range profiles.

2. THE FIRST SIMULATION PROGRAM OF REAL TARGETS' BACKSCATTERING

Our works on backscattering simulation were partly accomplished by creation of the computer program published by Artech House [3]. This program is capable of calculating backscattering of eleven aerial targets. They are: Tu-16, B-52, B-1B bomber aircraft, An-26 transport aircraft, Mig-21, F-15, Tomado tactical fighter aircraft, ALCM and GLCM cruise missile, AH-64 fire support helicopter, and decoy missile. The decoy missile model is based on the ALCM cruise missile on which the Lunenburg lens reflector with radar cross-section of 10 m^2 was installed. One more model of the surface-to air guided missile of the S-200 antiaircraft complex was recently designed.

Our program doesn't embrace all the target types, newly built ones especially. But it provides a good tool to study gains in quality of recognition, detection and tracking when narrowband radar signals are replaced by wideband ones [2-6]. Besides, it operates fast enough to be run on personal computer.

3. APPLICATION OF SIMULATION TO RADAR RECOGNITION

Simulation method allows considering and comparing different variants of Bayesian and neural recognition algorithms for both narrowband and wideband illumination signals. Recognition of both aerial target class and type was considered.

As it has been shown by simulation [7], the recognition signatures of narrowband illumination can be ordered by increase of information as follows:

- normalized polarization signatures in own polarization basis (obtained by diagonalization and normalization of polarization scattering matrix (PSM));
- frequency diversity of illumination signal with two carrier frequencies;
- amplitude of backscattered signal;
- elements of non-diagonalized and non-normalized PSM;
- rotational (propeller, rotor, or turbine) modulation spectra.

High potential probabilities of recognition by rotational modulation signature decrease sharply if rotation frequencies of turbojet engine rotors are changed. Besides, the use of this signature requires high signal-to-noise ratio (higher than 40 dB).

If only narrowband signatures are used, the reliability and information measure of target type recognition are not very high in the whole. The reliability and information measure of wideband signatures are much higher.

The main recognition signature in the last case is the target's range profile (RP). If the signal-to-noise ratio is asymptotically high, the single RP provides practically certain (with probability higher than 0.9) target type recognition for the signal bandwidths exceeding the 60 MHz.

Given the signal bandwidth larger than 100 MHz and signal-to-noise ratio higher than 24 dB, the probability of correct recognition of eleven target types that can be achieved is higher than 0.85.

Wideband illumination signals allow also obtaining the recognition signatures that are usually used for a narrowband illumination signals (target RCS and elements of PSM). The use of these signatures in common improves the recognition quality, especially when the signal's bandwidth is not very high. If these wideband and narrowband signatures are used together then, depending on conditions, the information measure of the target type radar recognition may be greatly improved. Additional involvement of trajectory signatures helps to provide practically certain recognition of the target type even for the signal-to-noise ratio of 20 dB.

Correlation recognition algorithm commonly used and mentioned above is an approximation of additive Bayesian algorithm. It is optimal only if the signal-to-noise ratio is high.

Bayesian recognition algorithm with direct estimation of the conditional probability distributions of target range profiles was also introduced. The distributions themselves were estimated for various targets using the Parzen window method [2]. Applicability of such algorithm wouldn't be grounded if the simulation wasn't used.

Neural recognition algorithms are other algorithms studied with the help of simulation. They provide a natural way of adaptation to various interfering factors such as uncertain target range and aspect relative to radar, unknown signal-to-noise ratio, etc. We have chosen a common algorithm based on a feedforward network with back propagation training. The algorithm was applied to recognition of target classes and types for different signal-to-noise ratios.

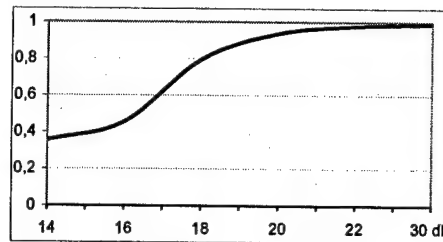


Fig. 3.

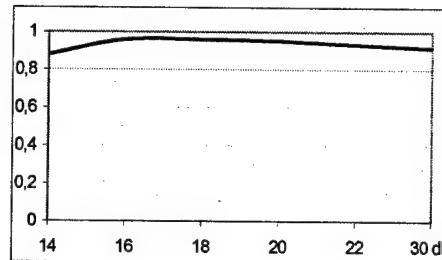


Fig. 4.

The best way to recognize the target type proved to be the use of two-stage neural algorithm [8, 9]. It recognizes the target class first and then elaborates the target type within the class recognized only. The network used for the first stage – class recognition – consisted of 60 input elements, 50 hidden elements, and 3 output elements. It was trained to recognize single RPs of Tu-16, B-52, and B-1B aircraft as those of the first (large-sized) class targets; Mig-21, F-15, and Tornado aircraft – as those of the second (medium-sized) class targets; and ALCM, GLCM, and Decoy cruise missiles – as those of the third (small sized) class targets. The RPs were obtained using the chirped illumination of 80 MHz bandwidth. The network was trained using 200 RPs of each target type. Fig. 3 shows the dependence of probability of correct class recognition on the signal-to-noise ratio.

Three additional neural networks were used to elaborate target type within each class. They differed by the lower number of hidden elements, 20 instead of 50. Fig. 4 shows the dependence of the probability of correct type recognition within the class of large-sized targets listed above.

It is evident from Fig. 3 and Fig. 4 that class recognition is more affected by low signal-to-noise ratio than the type recognition.

4. APPLICATION OF SIMULATION TO RADAR DETECTION

For the case of narrowband signals commonly used in radar the target size is much smaller than the range resolution interval. Quality of detection of such "point" targets depends primarily on the probability distribution of the target RCS. The simplified models of the RCS fluctuations such as Swerling, log-normal and other distributions are commonly used for the detection analysis in this case. However, such distributions can vary not only from one target type to another, but also from one aspect sector to

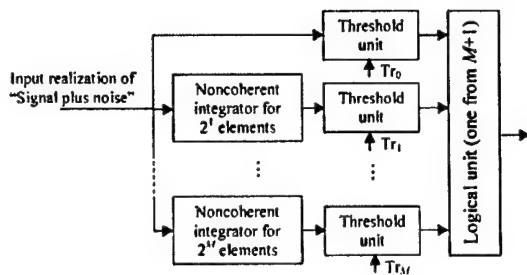


Fig. 5.

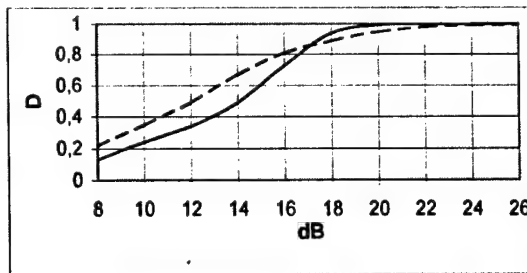


Fig. 6.

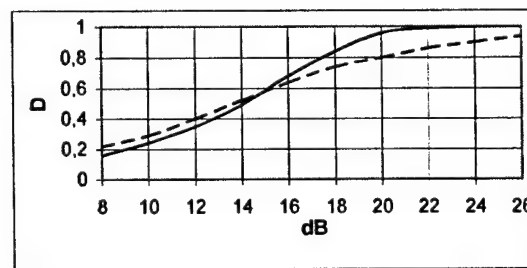


Fig. 7.

another for the same target. The use of simulation program can reveal such differences in the RCS distributions [2].

So long as the signal's bandwidth doesn't allow resolution of the target elements, the detection threshold signal (and, consequently, the detection losses) rises by not more than 0.4 dB for each decade of resolution increase [10].

For the case of wideband signals used all the more frequently in recent times the targets become non point that has to be accounted for in detection. Detection of a non point target presumes non coherent integration of the backscattered signal. Target RCS's *fluctuations after non-coherent integration are essentially reduced*.

Optimal non coherent integration of the backscattered signals becomes somewhat complicated by the ambiguity of their form and extension. But this ambiguity can scarcely be assumed complete because at least extensions of real targets are limited. Assumption of the target reflectivity function evenly spread within the presumed target length leads to quasi optimal "log-scale" detector scheme (Fig. 5).

The name "log-scale" is connected with the logarithmic dependence of the integration intervals in different channels.

Probabilities of wideband (80 MHz) signal detection using the "log-scale" detector via signal-to-noise ratio

were simulated for the large-sized aircraft (Tu-16) and small sized missile (ALCM). This probabilities (solid lines in Fig. 6 and Fig. 7 respectively) are shown together with probabilities of narrowband (5 MHz) detection (dashed lines in Fig. 6 and Fig. 7).

There is a gain in the detection threshold for probabilities $D = 0.6 \dots 0.8$ if a wideband (about 80 MHz) illumination signal and the "log-scale" detector are used [10]. For the detection probability $D = 0.9$ this gain is about 2 to 6 dB depending on the type of the target being detected. For the detection probability $D = 0.5$, for which the detection range of surveillance radar is usually estimated, the wideband signals introduce additional power losses just of 0.5 to 3 dB. It can be claimed that inside the detection zone $D \geq 0.5$ target tracking will be more reliable for wideband signals than for narrowband ones due to lower probability of the echo dying out.

Wideband echo signals can be detected without use of non coherent integration (cumulative detection). Such detection provides lower detection probability, but for the bandwidths lower 80 MHz the difference from the "log-scale" detection scheme is not very high (1 ... 1.5 dB). This proves that effect of RCS fluctuations is already reduced by the effect of target element range resolution.

5. APPLICATION OF SIMULATION TO RADAR TRACKING

Theoretical investigations by Delano, Ostrovityanov, and others on range, angular, and Doppler glint of targets illuminated by narrowband signals are widely known [2]. Now on the basis of backscattering simulation we can have more detailed information

Especially helpful backscattering simulation proved to be for the case of wideband signals.

Particularly, it was shown that information about the target angular coordinates and range can be much more accurate when the train of "slow fluctuating" (see Section 3) wideband echo signals is received. This effect is achieved due to resolution of the target elements and formation of the RP.

The simulation results show that if the signal spectrum is widened from 1 MHz to 100 MHz and the SNR is large then the azimuth measurement accuracy of surveillance radar can be increased by 1.5 to 6 times depending on the target type. Measurement accuracy is increased in this case due to possibility of averaging the angular estimates for various range cells. Similar increase in azimuth measurement accuracy can be achieved for short-range radar with monopulse type angle measurements. In such a radar angle measurements are most affected by the target angular glint.

Accuracy of range measurements for the point target, according to works by Woodward, increases proportionally to the signal's bandwidth. But real radar targets are not point ones for the case of wideband illumination. Nevertheless, simulation shows that expansion of the signal bandwidth from 1 MHz to 80 MHz can increase the range measurement accuracy by 2 to 4 times depending on the SNR.

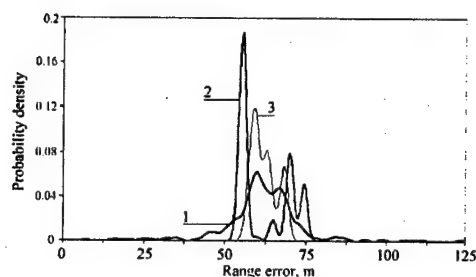


Fig. 8.

When the target elements are resolved then the measurement errors become significantly non Gaussian. This very complicates their theoretical analysis and increases the role of simulation. In Fig. 8 the probability density functions of the range measurement error [2] are shown for Tu-16 aircraft for its:

- narrowband (1 MHz) illumination (curve 1);
- wideband (80 MHz) illumination and range estimation by the maximum of output signal (curve 2);
- wideband (80 MHz) illumination and range estimation by the median of output signal (curve 3).

It is seen from Fig. 8 that selection of the measurement method influences the accuracy of measurement.

Furthermore, unlike to the case of Gaussian error distributions, range measurement accuracy in this case is influenced by selection of the cost function [11]. For example, if the squared cost function is used then measurement accuracy is 2 to 3 times higher (depending on the signal-to-noise ratio) than in the case of quasisimple one. Increase in the target range measurement accuracy can in its turn significantly improve target tracking in range.

Backscattering simulation helped us to reveal one more advantage of the wideband illumination signals. Such illumination signals can provide surveillance radar with the possibility of accurate measuring target's radial velocity at a single antenna pattern sweep on target. Measurement is based on estimation of shift between the envelopes of successive RPs in train. The measurement accuracy in this case is higher than that in the case of narrowband radar with tracking.

Unlike to the narrowband measurement, accuracy of wideband measurement is not affected significantly by the target maneuvering. Use of wideband illumination signals (together with appropriate measurement algorithms) for the target tracking allows early maneuver detection, simplifies identification of radar echoes and adaptation to maneuvers.

6. CONCLUSIONS

The authors of paper are of the opinion that computer simulation of target radar backscattering is an essential part of the perspective radar design. This statement is

confirmed by the experience accumulated in the monograph [2] and by the experience of further studies.

REFERENCES

1. Shirman Y. D., Gorshkov S. A., Leshchenko S. P., Bratchenko G. D., Orlenko V. M. *Methods of Radar Recognition and Their Simulation* // Scientific and Technical Series. Radar and Radiometry. – Moscow: IPRZHR. – 2000. – issue III, p. 5-64 (in Russian).
2. Computer Simulation of Aerial Target Radar Scattering, Recognition, Detection, and Tracking/ Y. D. Shirman, S. A. Gorshkov, S. P. Leshchenko, V. M. Orlenko, S. Y. Sedyshev, O. I. Sukharevskiy /Y. D. Shirman editor. – Boston – London: Artech house, 2002.
3. Radar Target Backscattering Simulation Software and User's Manual/ Gorshkov S. A., Leshchenko S. P., Orlenko V. M., Sedyshev S. Yu, Shirman Y. D. – Boston-London: Artech House, 2002.
4. Kravtsov S. V., Leshchenko S. P. Simulation of Electromagnetic Field Scattering on the Aerial Target Propeller // *Electromagnetic Waves and Electronic Systems*, No. 4, vol. 4, 1999, pp. 39-44 (in Russian).
5. Orlenko V. M., Leshchenko S. P., Bratchenko G. D., Shirman Y. D. "Signal-Trajectory Casing" of the Target Backscattering Model // *Electromagnetic Waves and Electronic Systems*, No. 3, vol. 4, 1999, pp. 38-43.
6. Shirman Y. D., Leshchenko S. P., Orlenko V. M. About the Simulation of Aerial Target Backscattering and Its Use in Radar Recognition Technique // *Bulletin of Bauman State Technical University*, Moscow, No. 4, 1998, pp. 14 – 25 (in Russian).
7. Leshchenko S. P. Information Measure and Reliability of Aerial Target Recognition Using Their Range Profiles // *Collection of papers of KMU*, Kharkov: KMU, 2001, issue 7(37), p. 69 – 72 (in Russian).
8. Orlenko V. M., Bityutskiy A. S. Single-Stage Neural Recognition of Types of Aerial Targets Using their Single Range Profiles // *Collection of scientific papers of KMU*, Kharkov: KMU, 2003 (in Russian).
9. Orlenko V. M., Bityutskiy A. S. Two-Stage Neural Recognition of Types of Aerial Targets Using their Single Range Profiles // *Collection of scientific papers of KMU*, Kharkov: KMU, 2003 (in Russian).
10. Leshchenko S. P., Orlenko V. M., Shirman Y. D. Peculiarities of Radar Detection in Case of Wideband Illumination // *Journal of Communication Technology and Electronics*, Moscow (in Russian).
11. Leshchenko S. P. Possibilities of Wideband Radar to Measure the Coordinates and Track Aerial Targets // *Collection of papers of KMU*, Kharkov: KMU, 2002, Issue 1(39), pp. 90-92 (in Russian).

COMBINED DIRECTION FINDERS OF NOISE RADIATION SOURCES BASED ON ADAPTIVE LATTICE FILTERS

D. I. Lekhovitsky, D. V. Atamansky, V. V. Djus, N. A. Staheev

Kharkov, Ukraine <David@rls.kharkiv.com>

Abstract

It is proposed and investigated the combined direction finder of independent noise radiation sources, which is realized on the unified base of adaptive lattice filters. Its important practical advantages are substantiated in comparison with the well-known combined direction finders on the base of eigenstructured spectral analysis methods of MUSIC type.

1. INTRODUCTION

In different countries, already for several decades the intensive investigations of spectral analysis methods of random processes of different physical nature have been carried out, whose resolution capability is beyond the Raleigh bound determined by the dimensions of spatial-temporal observation interval. One of the most important practical applications of these methods is the estimation of angular coordinates (direction finding) of noise radiation sources (NRS) in spatial multi-channel receiving systems with phased antenna arrays (PAA) (DOA estimation).

In spite of a great number of proposed "superresolution" methods of the space-time spectral analysis (STSA) the search of new approaches to direction finding of NRS lasts [1-11]. A. B. Gershman's approach based on the use of combined direction finders is considered to be the most perspective, in which the information from the whole complex ("bank") of well-known methods of STSA is combined [3-5]. In such a "bank" under the corresponding unification strategy it is possible to use effectively the advantages of the methods included in "bank" and simultaneously to reduce their own disadvantages.

The specific peculiarity of the "banks" suggested in [3-5] is their so-called "eigenstructured (ES)" STSA methods, potentially more effective than "non eigenstructured (NES)" methods. The latter does not take into consideration the *a priori* information about the coincidence of a signal component rank of covariance matrix (CM) of Gaussian output signals $M > 1$ of spatial receiving channels with number $n < M$ of external independent NRS, essentially used in ES-methods. Such a coincidence, however, takes place only in an idealized situation of completely identical reception channels not typical for practice. So the real capabilities of "ES-banks" can be essentially lower than po-

tential ones, in connection with this their practical advantages are not so obvious.

In development of the combined direction finding idea in [8] it is suggested to of a "bank" from the well-known NES methods, and a number of their modifications as well. In these methods, the NRS information is taken from the parameters of their spectral functions (SF) depending upon the matrix inverse to CM of the analyzed process. The important advantage of these methods consists in the possibility of their simple realization on the unified structural algorithmic base of adaptive lattice filters (ALF) [7-9].

In the given paper, the resolutions of "ES-bank" and "ALF-bank" are quantitatively compared, and the important practical advantages of "ALF-bank" are shown in real conditions of non-identical reception channels.

2. "ALF-BANK" STRUCTURE

Spectral functions $\hat{S}(\alpha) = S(\alpha, \hat{\Psi})$ of a number of well-known NES of STSA methods are of the following form [6,8,10,11]

$$\hat{S}_1(\alpha) = (\mathbf{x}^*(\alpha) \hat{\Psi} \mathbf{x}(\alpha))^{-1}, \quad (1a)$$

$$\hat{S}_2(\alpha) = \hat{\omega}_{mm} |\mathbf{e}_m^* \hat{\Psi} \mathbf{x}(\alpha)|^{-2}, \quad m \in 1, M, \quad (1b)$$

$$\hat{S}_3(\alpha) = \hat{\omega}_{mm} \mathbf{x}^*(\alpha) \hat{\Psi} \mathbf{x}(\alpha) |\mathbf{e}_m^* \hat{\Psi} \mathbf{x}(\alpha)|^{-2}, \quad (1c)$$

$$\hat{S}_4(\alpha) = \mathbf{x}^*(\alpha) \hat{\Psi} \mathbf{x}(\alpha) (\mathbf{x}^*(\alpha) \hat{\Psi}^2 \mathbf{x}(\alpha))^{-1}, \quad m \in 1, M, \quad (1d)$$

$$\hat{S}_5(\alpha) = (\mathbf{x}^*(\alpha) \hat{\Psi}^2 \mathbf{x}(\alpha))^{-1}. \quad (1e)$$

SF $\hat{S}_1(\alpha)$ characterizes the Capon method of "minimum dispersion (MD)", $\hat{S}_2(\alpha)$ is the Burg method of "linear predication (LP)", $\hat{S}_3(\alpha)$ is the variety of "modified Capon algorithm (MCA)", $\hat{S}_4(\alpha)$ is the Borgotti-

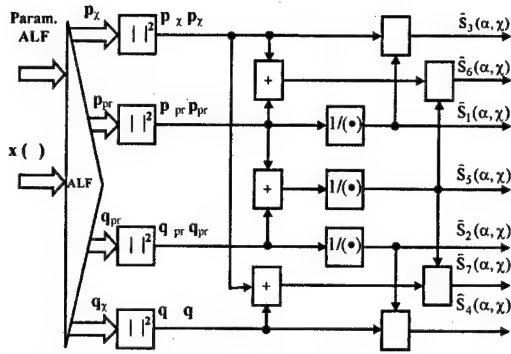


Fig. 1. SF formation on ALF scheme.

Lagunas (BL) method, $\hat{S}_5(\alpha)$ is the "heat noise (HN)" method.

In all SF $\mathbf{x}(\alpha) = \{x_l(\alpha)\}_{l=1}^M$ is the non-random M -dimensional steering vector (of search) "in the direction" α , which depends on spatial arrangement and characteristics M of receiving elements (modules) of PAA, \mathbf{e}_m is the m -th ($m \in 1, M$) column of an identity $M \times M$ matrix \mathbf{I}_M , $(*)$ is the sign of hermitian conjugate, $\hat{\Psi} = \hat{\Phi}^{-1}$ is the matrix inverse to the used estimation $\hat{\Phi}$ of the *a priori* unknown true CM Φ of PAA output signals.

The common feature of all SFs (1) is their dependence on the same $M \times M$ matrix $\hat{\Psi}$. In connection with this they can be formed on the base of common filter with matrix pulse characteristic (PC), proportional to the matrix $\hat{\Psi}$ or to its multipliers of different kinds.

Of a great number of the well-known filters having the necessary PC, the most practically interesting ALF [7-9] are those with $2M \times M$ matrix PC of a view

$$\hat{\mathbf{W}} = \begin{bmatrix} \hat{\mathbf{H}} \\ \hat{\mathbf{N}}^* \end{bmatrix}, \quad (2a)$$

which is composed of the estimates of the lower ($\hat{\mathbf{H}}$) and upper ($\hat{\mathbf{N}}^*$) triangular $M \times M$ matrix-multipliers of matrix $\hat{\Psi}$ in the representations

$$\hat{\Psi} = \hat{\mathbf{H}}^* \hat{\mathbf{H}} = \hat{\mathbf{N}} \hat{\mathbf{N}}^*, \quad \hat{\Psi} = \hat{\Phi}^{-1}. \quad (2b)$$

The algorithms of forming the maximum likelihood (ML) matrix estimations $\hat{\mathbf{W}}$ (ALF tuning) by K -dimensional training sample $\mathbf{Y} = \{\mathbf{y}_k\}_{k=1}^K$ of M -dimensional vectors $\mathbf{y}_k = \{y_i^{(k)}\}_{i=1}^M$, $k \in 1, K$ of complex amplitude indications of the analyzed process are considered in details in [9].

The values of SF $\hat{S}(\alpha)$ of (1a, b, c) methods at analysis arbitrary point α from the chosen sector $\alpha_a \in (\alpha_{\min}, \alpha_{\max})$ can be obviously formed by means of combining the modulus squares of vector elements

$$\hat{\mathbf{p}} = \{\hat{p}_m\}_{m=1}^M = \hat{\mathbf{H}}\mathbf{x}, \quad (3a)$$

$$\hat{\mathbf{q}} = \{\hat{q}_m\}_{m=1}^M = \hat{\mathbf{N}}^*\mathbf{x}, \quad (3b)$$

at ALF outputs with PC (2a) obtained by transformation in it of the M -dimensional steering vector $\mathbf{x} = \mathbf{x}(\alpha)$. In particular, SF (1a) of Capon's method

$$\hat{S}_1(\alpha) = (\hat{\mathbf{p}}^* \hat{\mathbf{p}})^{-1}, \quad \text{SF (1b) of the LP method at } m=1 \quad \hat{S}_2(\alpha) = |\hat{q}_1|^{-2} \quad \text{and at } m=M \quad \hat{S}_2(\alpha) = |\hat{p}_M|^{-2} \quad (\text{Fig. 1}).$$

Along with (1), one can form on ALF base a number of other SF with practically useful properties, in particular, SF [8]

$$\hat{S}_1(\alpha, \chi) = (\hat{\mathbf{p}}_{\text{pr}}^* \hat{\mathbf{p}}_{\text{pr}})^{-1}, \quad \hat{S}_2(\alpha, \chi) = (\hat{\mathbf{q}}_{\text{pr}}^* \hat{\mathbf{q}}_{\text{pr}})^{-1}, \quad (4a)$$

$$\hat{S}_3(\alpha, \chi) = \frac{\hat{\mathbf{p}}_{\text{pr}}^* \hat{\mathbf{p}}_{\text{pr}}}{\hat{\mathbf{p}}_{\text{pr}}^* \hat{\mathbf{p}}_{\text{pr}}}, \quad \hat{S}_4(\alpha, \chi) = \frac{\hat{\mathbf{q}}_{\text{pr}}^* \hat{\mathbf{q}}_{\text{pr}}}{\hat{\mathbf{q}}_{\text{pr}}^* \hat{\mathbf{q}}_{\text{pr}}}, \quad (4b)$$

$$\hat{S}_5(\alpha, \chi) = (\hat{\mathbf{p}}_{\text{pr}}^* \hat{\mathbf{p}}_{\text{pr}} + \hat{\mathbf{q}}_{\text{pr}}^* \hat{\mathbf{q}}_{\text{pr}})^{-1}, \quad (4c)$$

$$\hat{S}_6(\alpha, \chi) = \hat{\mathbf{p}}^* \hat{\mathbf{p}} (\hat{\mathbf{p}}_{\text{pr}}^* \hat{\mathbf{p}}_{\text{pr}} + \hat{\mathbf{q}}_{\text{pr}}^* \hat{\mathbf{q}}_{\text{pr}})^{-1}, \quad (4d)$$

$$\hat{S}_7(\alpha, \chi) = \frac{\hat{\mathbf{p}}_{\text{pr}}^* \hat{\mathbf{p}}_{\text{pr}} + \hat{\mathbf{q}}_{\text{pr}}^* \hat{\mathbf{q}}_{\text{pr}}}{\hat{\mathbf{p}}_{\text{pr}}^* \hat{\mathbf{p}}_{\text{pr}} + \hat{\mathbf{q}}_{\text{pr}}^* \hat{\mathbf{q}}_{\text{pr}}}. \quad (4e)$$

As $\hat{\mathbf{p}}_{\chi} = \{\hat{p}_m\}_{m=1}^{\chi}$ and $\hat{\mathbf{q}}_{\chi} = \{\hat{q}_m\}_{m=M-\chi+1}^M$, here are designated χ -dimensional subvectors formed by the first $\chi = 1, M-1$ vector components $\hat{\mathbf{p}}$ (3a) and the last χ vector components $\hat{\mathbf{q}}$ (3b) respectively, and as $\hat{\mathbf{p}}_{\text{pr}} = \{\hat{p}_m\}_{m=1+\chi}^M$ and $\hat{\mathbf{q}}_{\text{pr}} = \{\hat{q}_m\}_{m=1}^{M-\chi}$ - $(M-\chi)$ -dimensional subvectors composed of the rest elements of these vectors. SF formation scheme (4) on ALF base is shown in Fig. 1.

SF (1), (4) with partial or full parameters set $\chi \in 0, (M-1)/M$ in typical cases $M \gg 1$ form rather capacious "ALF-banks" essentially simpler for realization than the well-known "ES-banks" [3-5]. In connection with this it is important to compare the effectiveness (the resolution, the accuracy, the size of a training sample) of combined direction finders on the base of considered "banks" of STSA methods.

The comparison results of their resolution, which were obtained with mathematical simulation method are analyzed below.

3. MATHEMATICAL SIMULATION RESULTS AND THEIR ANALYSIS

The NRS direction finding procedure by "ALF-bank" consists in formation of its SF $\hat{S}(\alpha)$ at points α located in the chosen sector α_a and consequent finding of their general maxima.

The general ones mean such SF maxima, for which the following conditions are met

$$\hat{S}(\alpha_n)/\hat{S}(\eta_{n-1}) \geq \gamma_0, \quad \hat{S}(\alpha_n)/\hat{S}(\eta_n) \geq \gamma_0, \quad (5)$$

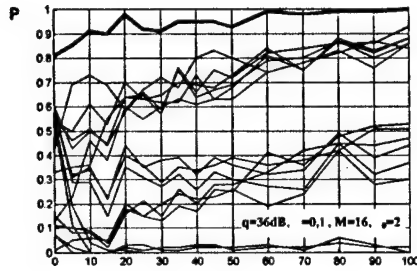


Fig. 2. The correct resolution probability versus the size of training sample for methods (1), (4) and ALF bank.

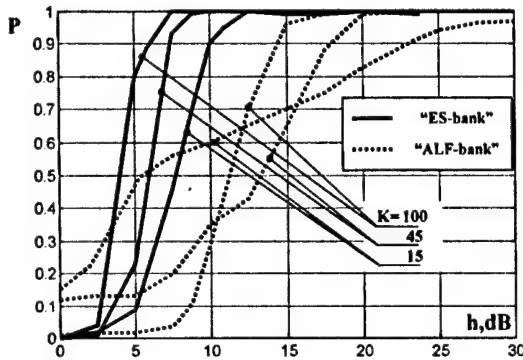


Fig. 3. NRS resolution with ALF and ES banks.

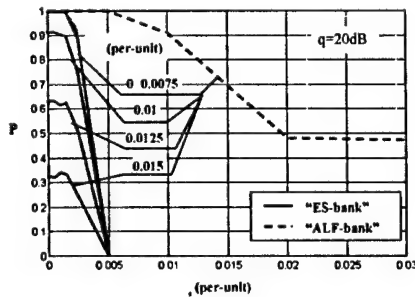


Fig. 4. The correct resolution probability versus the parameters of non-identical PC reception channels of PAA.

where $\alpha_n \in \alpha_a$, ($n \in 1, \hat{N}$) are arranged in increasing order (ordinate) SF maxima coordinates, $\eta_n \in \alpha_a$, ($n \in 0, \hat{N}$) are the coordinates of $\hat{N} + 1$ SF ranged minimum values in analysis sector α_a , γ_0 is the a priori chosen threshold (usually $\gamma_0 = (2..3)$ dB).

For the j -th ($j \in 1, G$) direction finder, the maxima number satisfying conditions (6), is taken as the number \hat{N}_j of NRS resolved with this direction finder, and their coordinates $\alpha_n^{(j)}$, $n \in 1, \hat{N}$ are considered to be the directions to the n -th ($n \in 1, \hat{N}$) NRS. It is supposed that "ALF-bank" resolves them every time when at least one of G direction finders (methods) of the "bank" resolves them (strategy 1 of G). The

number of sources N_B resolved with the bank is determined by the maximum number of NRS resolved with all direction finders ($N_B = \max \hat{N}_j$, $j \in 1, G$).

Fig. 2 shows, as an example, the results of resolving two equal power NRS with relative (with respect to the width of matched radiation pattern (RP) of the antenna) angular distance $\Delta = 0,1$ and generalized signal-to-noise ratio (SNR) for each NRS $q = Mh = 36$ dB, where h is the NRS intensity with respect to the intensity of internal noise of a PAA element. Here for the $M = 17$ -element uniform linear array (ULA), the dependencies of the correct resolution probability P on the effective size $\delta = K - M$ of the K -dimensional training sample used at forming ML of estimation $\hat{\Phi}$ of the *a priori* unknown CM Φ are shown.

The probability of correct resolution P is calculated as a ratio of the number of tests, at which the value $\hat{N}_B = n = 2$, to their general number $NN = 500$. A family of thin solid lines in Fig. 2 corresponds to SF (1), (Fig. 1).

One can see that the correct resolution probability of "ALF-bank" is considerably higher than of any other method included in it. In this respect, it is fully analogous to "ES-bank" [3-5].

The results of comparison of these "banks" resolution are shown in Fig. 3. Here for the $M = 10$ -element ULA under conditions [3], the dependencies of the correct resolution probability of "ES-bank" (solid curves) and "ALF-bank" (dotted curve) on the relative intensity $h_1 = h_2 = h$ of two equal power NRS with angular coordinates $\theta_1 = 20^\circ$, $\theta_2 = 22^\circ$ are presented. Number \hat{N} of NRS for "ES-bank" is determined by "MDL-criteria", which is the strategy component of the use of these methods and, on their base, "banks" [1-6, 11]. The plots are given for different sizes of training sample $K = 15, 45, 100$, the reception channels are assumed to be identical.

As it follows from the curves analysis, Fig. 2, under these idealized conditions, "ES-bank" can be more effective than "ALF-bank". This conclusion, however, can be unfair under real conditions of non-identity of the spatial reception channels characteristics.

As an illustration, in Fig. 4, there are shown plots, which characterize the resolution of ALF and ES "banks" under typical for practice conditions of non-identity of bell PC reception channels. The argument of a family of plotted curves is the root-mean-square error (RMSE) of central frequencies (σ_μ) and their parameter is RMSE of duration (σ_η) of PC reception channels. The correct resolution probability P , as well as in Fig. 3, corresponds to the plot ordinate.

One can see that "ALF-bank" possesses the considerably less sensitivity to the effects of considered mismatching – already at $\sigma_\mu \geq 0,005$ it appears to be more effective.

It is connected with the fact that in real conditions of non-identical characteristics of reception channels, one of the main assumptions is violated (about the coinci-

dence of effective rank r_E of CM Φ with the number n of point independent NRS) considerably used at ES-methods synthesis of STSA. This violation takes place both at finite and infinite ($K \rightarrow \infty$) size of training sample. As it is shown in [7], in the latter case, this matrix represents the "Shur-Hadamard product"

$$\Phi = \{\varphi_{ij}\}_{i,j=1}^M = \Phi_{id} \otimes A, \varphi_{ij} = \varphi_{ij}^{(id)} \cdot a_{ij}, (6)$$

of idealized CM $\Phi_{id} = \{\varphi_{ij}^{(id)}\}_{i,j=1}^M$ with effective rank $r_{id} = n$ and CM $A = \{a_{pq}\}_{i,j=1}^M$ of reception channels PC of $r_A = 1$ rank at the identity and $r_A > 1$ rank at non-identity of their characteristics. The effective matrix rank (6) in the general case is equal to [7]

$$r_E = \min \{ M, n \cdot r_A \} (7)$$

and already at minor differences of reception channels characteristics can noticeably differ from the true number n of NRS. Under these conditions, the ways of NRS number determination (resolution) by effective CM rank determined by MDL, AIC and other criteria [1-6,10,11], which are used in ES-methods and "banks" on their base, appear to be considerably less effective for this problem solution than NES-methods and "ALF-banks" on their base, in which it is solved without the information about CM rank.

As detailed check have shown, this conclusion appears to be true not only with respect to the resolution, but to the accuracy of angular coordinates estimation. Besides, "ALF-bank" is more simple in technical realization as it doesn't require solving of the complicated problem of search of eigendecomposition CM numbers and vectors, whose size can be rather large.

By these reasons, it is "ALF-bank" that can be recommended for practical realization of the fruitful idea [3-5] of combined direction finding of noise radiation sources.

REFERENCES

1. Abramovich Yu. I., Kachur V. G., Mikhailyukov V. N. Efficiency of Cancellation of Jammer in Systems with Nonidentical Channels. Radiotechn. and Electron, vol.34, № 6, June 1989, pp.1196-1205.
2. Abramovich Yu. I., Spenser N. K. and Gorokhov A. Yu. Separation of Independent Radiation Sources in Nonequally-Spaced Antenna Arrays. Telecommunications and Radio Engineering, № 12, December 2001, pp.3-18.
3. Gershman A. B. and Bohme I. F. Pseudorandomly Generated Estimator Banks: a New Resampling Scheme for Improving the Threshold Performance of Second and Higher-Order Direction Finding Methods. // Proc. of the Second Int. Conf. on Antenna Theory and Techniques, 20-22 May 1997, Kiev.
4. Gershman A. B. Direction Finding Using High-Resolution Bearing Estimators of Various Type. Radiotechn. and Electron., vol.40, № 6, June 1995, pp.918-924.
5. Gershman A. B. Pseudo-Randomly Generated Estimator Banks: a New Tool for Improving the Threshold Performance of Direction Finding. IEEE Trans. Signal Processing, SP-46, May 1998, pp.1351-1364.
6. Krim H. and Viberg M. Two Decades of Array Signal Processing Research. IEEE Signal Processing Magazine, July 1996, pp.67-95.
7. Lekhovitsky D. I., Atamansky D. V., Djus V. V., Misic F. F. A Comparison of Resolution Capability of Combined DOA Estimators of Various Types in Receiving Systems with Non-Identical Channels. To be published Telecommunications and Radio Engineering.
8. Lekhovitsky D. I., Atamansky D. V., Kirillov I. G. The Variety of «Super-Resolution» Analyzers of the Space-Time Spectra of Random Signals on the Basis of Whitening Adaptive Lattice. Telecommunications and Radio Engineering, vol. 45, № 2, 2000, pp.40-55.
9. Lekhovitsky D. I., Milovanov S. B., Rakov I. D., Sverdlov B. G. Universal Adaptive Lattice Filters. Adaptation with the Given Root from the Estimate Correlation Matrix. Radiophysics, vol.35, № 11-12, September-December 1992, pp.969-992.
10. Marple S. Lawrence Digital Spectral Analysis with Applications. Prentice-Hall, Englewood Cliffs, New Jersey, 1987.
11. Stoica P. and Moses R. Introduction to Spectral Analysis, Prentice Hall, Upper Saddle River, New Jersey, 1997.

PERFECTION OF THE ALGORITHM FOR UNCORRELATED SIGNALS ANGULAR DISCRIMINATION BY MEANS OF WAVELET TRANSFORMATION

L. A. Titarenko, B. Yu. Bordjugov

Kharkov National University of Radio Electronics, Kharkov, Ukraine
<tkc@kture.kharkov.ua>

Abstract

Methods of signals' wavelet denoising on the antenna array transducers' output are given. The comparative analysis of the algorithms efficiency based on the example of the algorithm for uncorrelated signals discrimination with the methods adaptation with formation of "zeros" of the radiation pattern in the directions of signals' sources outside the main maximum.

Keywords: Antenna array, wavelet transformation, denoising, uncorrelated signal, radiation pattern.

1. INTRODUCTION

Wavelet-analysis is widely used in the modern signal procession methods in spite of rather high calculation complexity. Modern DSP processors used in the antenna technique are capable to perform signals procession with values of the algorithms computational complexity of 70-80 MIPS (million of instructions per second). Taking into account that fast wavelet-transformation are developed and for the resent time there are no more convenient apparatus for signal procession in the frequency and temporal regions simultaneously then it becomes clear the importance of wavelets in the antenna technique and particularly in the antenna array technique.

Methods of wavelet-denoising used in the antenna technique are applied, primarily, to suppress the antenna array transducers heat noise. In this case a dyad wavelet-transform is used where redundancy is eliminated in the course of wavelet-transform. Comparison of different methods efficiency in wavelet-denoising application by the example of operation of the algorithm based on the adaptive formation of the radiation pattern (RP) "zeros" in the signals' sources direction excluding the RP main lobe direction is given. This algorithm is free from "indistinguishability" by the angular position of the signal weaker in power.

2. WAVELET-TRANSFORM AND WAVELET-DENOISING

Let us consider the signal

$$s(t) = a(t) \sin[\omega_0 t + \theta(t)], \quad (1)$$

where $a(t)$ is the signal envelope; ω_0 is the carrier; $\theta(t)$ is the modulating function.

Let the signal $s(t)$ be distorted by the white noise $\sigma e(t)$ with a power equal to σ^2 . We will get a data sequence $x(t_0), x(t_1), \dots, x(t_{n-1})$ on the time interval $[0, 1]$, which will be presented as follows:

$$x(t_k) = s(t_k) + \sigma e(t_k), \quad t = k/n, \quad n = 2^{J+1}, \quad (2)$$

where $J+1$ are positive numbers responsible for computing capacity of equipment. For convenience sake let us write $x(k), s(k)$ and $e(k)$ instead of $x(t_k), s(t_k)$ and $e(t_k)$. Now we turn to the matrix notation, then

$$\begin{aligned} x &= (x(0), x(1), \dots, x(n-1))^T, \\ s &= (s(0), s(1), \dots, s(n-1))^T, \\ e &= (e(0), e(1), \dots, e(n-1))^T. \end{aligned} \quad (3)$$

As it is known wavelet analysis represents the linear orthonormal transformation, i.e. we get $n \times n$ orthonormal matrix W containing some coefficients $c_0, c_1, \dots, c_{2N-1}$. This matrix transform transfers vector x to $w = Wx$, where vector x can be reconstructed as $x = W^T w = W^T w_s + \sigma W^T w_e$. The components of w are indexed with the dyad method, i.e.

$$w = (w(j, k), j = -1, 0, 1, \dots, J; k = 0, 1, \dots, 2^J - 1)^T, \quad (4)$$

where w_s and w_e are vectors of wavelet-coefficients of the signal source $s(t)$ and $e(t)$.

In this case it is possible to use the following three denoising methods to remove noise from signals [1]:

$$\begin{aligned}\bar{w}_s(j, k) &= \\ &= \begin{cases} w(j, k) \exp\left(-\frac{\lambda}{|w(j, k)| - \lambda}\right), & \text{if } |w(j, k)| \geq \lambda \\ 0, & \text{otherwise.} \end{cases} \\ \bar{w}_s(j, k) &= \begin{cases} w(j, k), & \text{if } |w(j, k)| \geq \lambda \\ 0, & \text{otherwise.} \end{cases} \quad (5) \\ \bar{w}_s(j, k) &= \begin{cases} \text{sgn}(w(j, k))(|w(j, k)| - \lambda) & \text{if } |w(j, k)| \geq \lambda \\ 0, & \text{otherwise.} \end{cases}\end{aligned}$$

where \bar{w}_s is an estimated value of the wavelet-coefficients; $\alpha \in (0, 1)$ is a fiducial probability level; $\lambda = \sqrt{2}\sigma \text{erfinv}(\alpha)$ is a confidence interval value $[-\lambda, \lambda]$; $\text{erfinv}(\alpha)$ - is an inverse function of errors $\text{erf}(\alpha) = \frac{2}{\sqrt{\pi}} \int_{-\infty}^{\alpha} \exp(-t^2) dt$.

3. DESCRIPTION OF SIGNALS MODELS AND ALGORITHM FOR WEIGHT COEFFICIENTS CHOICE

Let us consider M -elemental antenna array (AA) affected simultaneously by K signal sources. The output signal $U(t)$ of AA performing a weighted summation of the transducers' (AA radiators) voltage can be written as

$$U(t) = Y(t)W^T, \quad (6)$$

where $Y(t) = N(t) + \sum_{k=1}^K S_k u_k(t)$ is a vector of signals on the AA radiators output; S_k is a row vector with a dimensionality of $1 \times M$ whose elements are defined by the following relation, $S_{mk} = \exp[-i\kappa(x_m \cos(\varphi_k) + y_m \sin(\varphi_k))]$; $u_k(t)$ is a function describing temporal dependence of the k -th signal; $W = [w_1, \dots, w_M]$ is a row vector of weight coefficients; x_m, y_m are the coordinates of the m -th radiator ($m = \overline{1, M}$); $\kappa = 2\pi/\lambda$ is a wave number of free space; λ is an operating wavelength; φ_k is an angular position of the k -th signal source ($k = \overline{1, K}$); $N(t) = [n_1(t), \dots, n_M(t)]$ is a signals' row vector of thermal noise in the radiators. Expression for signal power on the AA input is as follows [2]:

$$\begin{aligned}P_a &= |Y(t)W^T|^2 = \\ &= \frac{1}{N} \sum_{i=1}^N \left| N(\Delta t \cdot i) + \sum_{k=1}^K S_k u_k(\Delta t \cdot i) \right| \cdot W^T, \quad (7)\end{aligned}$$

where P_a is an averaged power in the interval; N is a number of references in the interval $[t_1, t_2]$; Δt is a digitization interval.

As all the parameters of the received signals can be a priori unknown then it is expedient to use Frost adaptive algorithm with protection of the main maxi-

mum to form the RP "zeros". In this case the weight coefficients' vector is defined by the relation [3]

$$W = (A^* R^{-1} A^T)^{-1} R^{-1} A^T, \quad (8)$$

where $T, *$ are the signs of transportation and complex conjugation, respectively; A is a row vector with dimensionality of $1 \times M$, whose elements are numbers $a_m = \exp[i\kappa(x_m \cos(\varphi_0) + y_m \sin(\varphi_0))]$; φ_0 is an angular position of the RP main maximum at some time; R is a signals' covariance matrix with dimensionality of $M \times M$ defined by the accumulation for the temporal sampling of the duration equal to the oscillation period with the following formula:

$$R = \overline{Y^T(t)Y^*(t)}. \quad (9)$$

The comparative analysis of wavelet-denoising algorithms will be demonstrated by the example of the circular AA consisting of $M = 25$ radiators with a simultaneous reception of $K = 2$ signal sources. The AA radiators are placed on the circle whose radius is 2λ with a step of 0.5λ . The temporal dependence $u_k(t)$ will be assumed to be equal to $u_2(t) = \sqrt{P_2} \cos(\omega t)$, respectively; P_1, P_2 is power of the first and the second signal sources, respectively; duration of the temporal sampling when forming the elements of the matrix R is equal to the signals' oscillation period. Thermal noise is modulated with a sequence of random numbers distributed by the normal law with a zero mathematical expectation and mean square deviation σ .

Relation of the first signal power to thermal noise power is as follows:

$$Q = \lg(P_2 / \sigma^2). \quad (10)$$

When realizing the algorithm it is convenient to use the relation

$$\sigma = \sqrt{\frac{P_1}{10^{Q/10}}}. \quad (11)$$

The signal power on the AA output depending on the angular position of the RP side lobe φ_0 in the angles' sector $\varphi_0 \in [0^\circ, 90^\circ]$ is investigated. Let the signals arrive from the directions $\varphi_1 = 20^\circ$ and $\varphi_2 = 80^\circ$.

4. SIMULATION RESULTS

To estimate the efficiency of the wavelet denoising methods the dependence of the difference $|s(t) - \hat{s}(t)|$ mean square error value on the signal/noise relation Q was used, where $s(t)$ is the signal without noise; $\hat{s}(t)$ is the estimate after reconstruction with the above mentioned methods (Fig. 1). The following parameters' values were used: fiducial probability $\alpha = 0.95$, wavelet Daubechies h2 with the values of the filter coefficients equal to 0.3415 0.5915 0.1585 -0.0915 when realizing algorithms. The dependence given in Fig. 1 is the result of averaging of 200 independent experiments.

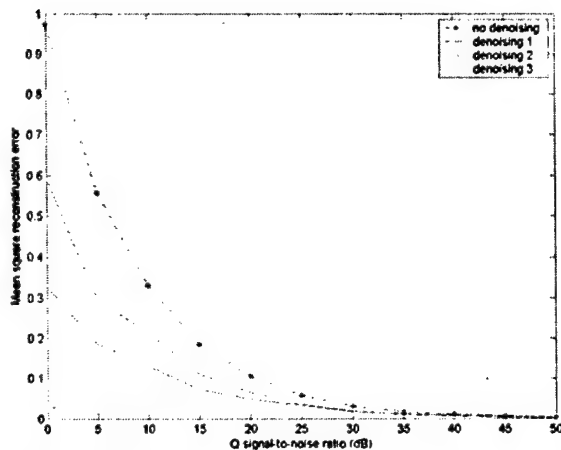


Fig. 1. Dependence of signal reconstruction mean square error on signal / noise ratio

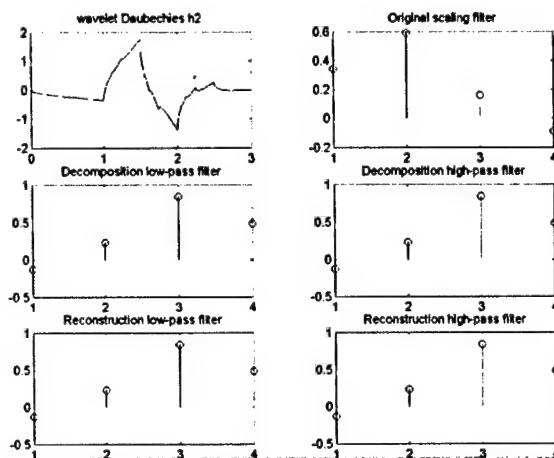


Fig. 2. The plots of wavelet Daubechies dB2 and derived filters' coefficients

5. CONCLUSIONS

Efficiency of the signal arrival angles definition was investigated through the utilization of the adaptive antenna array using different algorithms of denoising with wavelet transformations. Analyzing the obtained results it may be concluded that using different methods of denoising it is possible to obtain different degrees of signals' procession depending on different requirements.

The comparative analysis of the algorithms' efficiency was performed using as an example the algorithms for discriminating non-correlated signals

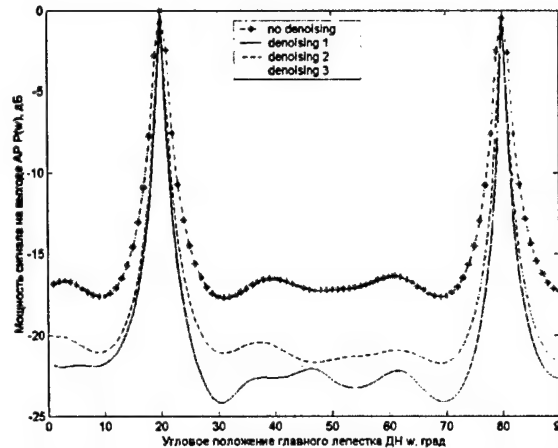


Fig. 3. Dependence of signal power in the AA output on the RP main lobe angular position with $P_1 = P_2$

applying the adaptation methods with formation of the radiation pattern "zeros" in the directions of sources of signals falling outside the main minimum. The simulation results given in Fig. 3 demonstrate an increase of 5–10 dB in the signals' sources angular position definition efficiency through the use of the developed algorithm depending on the fiducial probability level and the used type of wavelet.

The immediate more precise quantitative results in increasing efficiency of the signals' sources angular position definition are the object of further investigations with different wavelets and fiducial probability equations.

REFERENCES

1. Ching P. C., So H. C., Wu S. Q. On Wavelet Denoising and its Applications to Time Delay Estimation // IEEE Transactions on signal processing., 1999. Vol. 47, No 10, p. 2879.
2. Robert A. Monzingo, Tomas W. Miller. Introduction to Adaptive Arrays. A Wiley.-interscience publication. John Wiley & Sons. New York. Chichester. Brisbane. Toronto. 1980. 446 p.
3. Vertogradov V. V., Gabrielian D. D., Zvezdina M. Yu., Shevchenko V. N. Perfection of the algorithm of non-correlated signals differing on the based of the adaptive formation of radiation pattern "nulls" // Radio Electronics Journal, № 10, 2001. [in Russian]

EFFECTIVE PARAMETER ESTIMATION OF EXPONENTIAL SIGNALS IN ADAPTIVE ARRAYS

M. V. Andreev, O. O. Drobakhin

Dnipropetrovsk National University,
Dnipropetrovsk, Ukraine <microwave@mail.dsu.dp.ua>

Abstract

Application of the method of least squares for parameter estimation of exponential signals for processing data received by antenna array on several samples of observations has been considered. Effective algorithms of this method have been proposed; the explicit analytical expressions of the first and second derivatives of objective function of the least squares method have been obtained. Accuracy properties of the method and results of the method application for determination of parameters of moving sources are presented.

Keywords: the adaptive arrays, exponential signals, method of least squares, quasisolution searching.

1. INTRODUCTION

Target location by means of antenna arrays data processing is one of basic problems in modern radiophysics. It is a key problem to estimate parameters of exponential signals using the several samples of observations at presence of various noise perturbations (Stoica and Sharman, 1990). Its solution allows one to determine natural frequencies and directions on sources of radiation and reradiations in many applications of radar, radio astronomy and radiophysical measuring, mobile (SDMA) and satellite communication.

The traditional approach for parameter estimation of exponential signals on observation sample is use of methods of parametric spectral analysis. The ability of Fourier transform to fulfill angular or frequency separation of signals from sources is restricted by size of sampling in accordance with Rayleigh criterion. High resolution is ensured with use of maximum likelihood method, which is reduced to the method of least squares under realization of some requirements.

However use of the method of least squares for parameter estimation of the additive exponential model guesses the solution of complex problem of finding of global maximum of non-unimodal function of many variables that demands the considerable computing resources.

In this paper an opportunity of the realization of effective procedure of parameter estimation of exponential signals on several samples of observations has been considered and accuracy properties of the suggested algorithms are analyzed. The suggested method is tested on readily available experimental data with the purpose of comparison with other methods.

2. PROBLEM STATEMENT

Let plane waves from several sources fall on the linear equidistant array with N sensors and with step d .

Let's assume, that the source can differ as a frequency f_q ($q = 1, 2, \dots, Q$) and an angle β_p ($p = 1, 2, \dots, P$) between a direction on source and an axis of array. Let's inject a combined parameter of m -th source taking into account two specified factor:

$$\omega_m = \omega_{qp} = 2\pi f_q \cos \beta_p, \quad (1)$$

where $m = q + Q(p-1)$; $M = QP$. Then the phase delay of wave from m -th source for two next sensors is

$$\Delta\varphi_m = \omega_m d/c = \omega_m \Delta t, \quad (2)$$

where c is velocity of wave, $\Delta t = d/c$.

Let's guess that for determination of parameters of sources a matrix \mathbf{X} from K sequential snapshots of output signals from array with N sensor is formed as

$$\mathbf{X} = [\bar{\mathbf{x}}_1 \ \bar{\mathbf{x}}_2 \ \dots \ \bar{\mathbf{x}}_K] = \begin{bmatrix} x_{11} & x_{12} & \dots & x_{1K} \\ x_{21} & x_{22} & \dots & x_{2K} \\ \vdots & \vdots & \ddots & \vdots \\ x_{N1} & x_{N2} & \dots & x_{NK} \end{bmatrix}. \quad (3)$$

In case of propagation of plane waves from the sources a received signal can be presented by the following model:

$$\mathbf{X}_M(\bar{\omega}, \mathbf{R}) = \mathbf{E}(\bar{\omega})\mathbf{R}, \quad (4)$$

where $\mathbf{E}(\bar{\omega}) = [\bar{\mathbf{e}}_1 \ \bar{\mathbf{e}}_2 \ \dots \ \bar{\mathbf{e}}_M]$ is a matrix of exponential with columns

$$\bar{\mathbf{e}}_m = [1 \ \exp(-j\Delta\varphi_m) \ \dots \ \exp(-j(N-1)\Delta\varphi_m)]^T,$$

$\mathbf{R} = [\bar{\mathbf{r}}_1 \ \bar{\mathbf{r}}_2 \ \dots \ \bar{\mathbf{r}}_K]$ is matrix of amplitudes with columns $\bar{\mathbf{r}}_k = [r_{1k} \ r_{2k} \ \dots \ r_{Mk}]^T$. Thus, k -th signal of the array of sensors can be noted as

$$\bar{\mathbf{x}}_k = \sum_{m=1}^M r_{mk} \bar{\mathbf{e}}_m + \bar{\mathbf{v}}_k = \mathbf{E}(\bar{\omega})\bar{\mathbf{r}}_k + \bar{\mathbf{v}}_k, \quad (5)$$

where $\bar{\mathbf{v}}_k$ is a column vector with Gaussian white noise.

The vector $\vec{\omega} = [\omega_1 \ \omega_2 \ \dots \ \omega_M]$ determines a form of the matrix $\mathbf{E} = \mathbf{E}(\vec{\omega})$. For estimation of directions of arrival of waves and its frequencies the determination of vector $\vec{\omega} = [\omega_1 \ \omega_2 \ \dots \ \omega_M]$ with source parameters is required using the received signal \mathbf{X} .

3. EFFECTIVE METHODS OF THE SOLUTION OF THE PROBLEM

3.1. SOLUTION OF THE PROBLEM BY METHOD OF LEAST SQUARES

Because the level of the noise and non-informative deterministic components in signal \mathbf{X} may be considerable, in many cases the classical solution of inverse problem can not exist and have not sense. Therefore for determination of values $\vec{\omega}$ it is necessary to use generalization of concept of the solution of an inverse problem – quasisolution. For this case the quasisolution searching is reduced to finding values $\vec{\omega}$ and \mathbf{R} , which minimizing a functional of a discrepancy $\rho(\mathbf{X}_M(\vec{\omega}, \mathbf{R}), \mathbf{X})$. This discrepancy is defined as the Euclidean distance between $\mathbf{X}_M(\vec{\omega}, \mathbf{R})$ and \mathbf{X} .

From the point of view of statistical performances the high resolving ability is ensured with use of maximum likelihood method, which at realization of some requirements is reduced to method of least squares. Therefore the method of least squares used in this paper. It consists of finding of such values of matrix \mathbf{R} and vector $\vec{\omega}$, which minimize discrepancies between model and all K snapshots of signals from array of sensors. Thus, objective function of next form was subject for minimization:

$$\rho(\vec{\omega}, \mathbf{R}) = \frac{1}{K} \sum_{k=1}^K \|\vec{x}_k - \mathbf{E}(\vec{\omega}) \vec{r}_k\|^2 = \frac{\|\mathbf{X} - \mathbf{E}(\vec{\omega}) \mathbf{R}\|_E^2}{K}. \quad (6)$$

The parameters \vec{r}_k are included in model (5) linearly and the method of least squares determines their best values as

$$\vec{r}_k(\vec{\omega}) = (\mathbf{E}^H \mathbf{E})^{-1} \mathbf{E}^H \vec{x}_k = \mathbf{H}^{-1} \vec{g}_k, \quad (7)$$

where $\mathbf{H} = \mathbf{E}^H \mathbf{E}$ is Gramme matrix for the exponential curves determined by values of vector $\vec{\omega}$, and the vector $\vec{g}_k = \mathbf{E}^H \vec{x}_k = [\vec{e}_1^H \vec{x}_k \ \vec{e}_2^H \vec{x}_k \ \dots \ \vec{e}_M^H \vec{x}_k]^T$ defines values of the spectral conjugate signal for values $\vec{\omega} = [\omega_1 \ \omega_2 \ \dots \ \omega_M]$. Elements of matrix \mathbf{H} are determined by the following expressions ($k, l = 1, 2, \dots, M$):

$$H_{lm} = \sin N \left[N, (\omega_l - \omega_m) \frac{d}{2c} \right] \exp \left[j(\omega_l - \omega_m) \frac{D}{2c} \right],$$

where $D = (N-1)d$ is length of array, and $\sin N(N, x)$ is next function: $\sin(N \cdot x) / N \cdot \sin(x)$. Let's view H_{lm} as functions $S(\omega_l - \omega_m)$. Elements of the vector $\vec{g}_k = [g_{1k} \ g_{2k} \ \dots \ g_{Mk}]^T$ are determined according to expression ($m = 1, 2, \dots, M$; $k = 1, 2, \dots, K$):

$$g_{mk} = g_k(\omega_m) = \frac{1}{N} \sum_{n=1}^N x_{nk} \exp(j(n-1)\Delta t \omega_m). \quad (8)$$

The matrix of optimum amplitudes for K snapshots of the signal from the array looks like

$$\mathbf{R}(\vec{\omega}) = (\mathbf{E}^H \mathbf{E})^{-1} \mathbf{E}^H \mathbf{X} = \mathbf{E}^+ \mathbf{X} = \mathbf{H}^{-1} \mathbf{G}, \quad (9)$$

where $\mathbf{E}^+ = (\mathbf{E}^H \mathbf{E})^{-1} \mathbf{E}^H$ is pseudoinverse matrix for matrix \mathbf{E} and matrix \mathbf{G} contains values of the spectral conjugate signal

$$\mathbf{G} = \mathbf{E}^H \mathbf{X} = [\vec{g}_1 \ \vec{g}_2 \ \dots \ \vec{g}_K]. \quad (10)$$

Substituting values of optimum amplitudes (9) in the objective function (6) we obtain the objective function with smaller dimensionality. It depends only from vector $\vec{\omega}$:

$$\rho(\vec{\omega}) = \frac{1}{K} \sum_{k=1}^K \|(\mathbf{I} - \mathbf{P}) \vec{x}_k\|^2 = \frac{1}{K} \|(\mathbf{I} - \mathbf{P}) \mathbf{X}\|_E^2, \quad (11)$$

where matrix $\mathbf{P} = \mathbf{E}(\mathbf{E}^H \mathbf{E})^{-1} \mathbf{E}^H = \mathbf{E} \mathbf{E}^+$ is a projector on the linear subspace defined by vectors $[\vec{e}_1 \ \vec{e}_2 \ \dots \ \vec{e}_M]$. This objective function can be transformed to

$$\rho(\vec{\omega}) = \|\mathbf{X}\|_E^2 - \frac{1}{K} \sum_{k=1}^K \vec{x}_k^H \mathbf{P} \vec{x}_k. \quad (12)$$

Transferring in the spectral conjugate area it is possible to obtain more effective view of the objective function for calculation

$$\rho(\vec{\omega}) = \|\mathbf{X}\|_E^2 - \frac{1}{K} \sum_{k=1}^K \vec{g}_k^H \mathbf{H}^{-1} \vec{g}_k = \|\mathbf{X}\|_E^2 - \frac{1}{K} \sum_{k=1}^K \vec{g}_k^H \vec{r}_k. \quad (13)$$

For the fixed matrix \mathbf{X} its norm is a constant. Therefore minimization of the objective function (12) is completely equivalent to a maximization of the objective function in form

$$\delta(\vec{\omega}) = \frac{1}{K} \sum_{k=1}^K \vec{x}_k^H \mathbf{P} \vec{x}_k = \text{tr} \mathbf{P} \mathbf{C}, \quad (14)$$

and minimization of the objective function (13) is completely equivalent to a maximization of the objective function of next form

$$\delta(\vec{\omega}) = \frac{1}{K} \sum_{k=1}^K \vec{g}_k^H \vec{r}_k = \frac{1}{K} \text{tr} \mathbf{G}^H \mathbf{R}. \quad (15)$$

In (14) the correlation matrix of size $N \times N$ $\mathbf{C} = \sum_{k=1}^K \vec{x}_k \vec{x}_k^H / K$ is used.

3.2. METHODS OF ACCELERATION OF THE SOLUTION SEARCHING

Minimization of the objective function (15) demands the considerable computing operational resources. Searching of a minimum can be accelerated using the methods of minimization based on application of the information about the first and second derivatives of the objective function. This information is desirable to obtain in explicit form using analytical expressions.

For this purpose it is necessary to obtain an explicit expression of the derivative of the objective function (15) with respect to parameter ω . The derivative of the objective function (15) on ω_m is determined as

$$\frac{\partial \delta}{\partial \omega_m} = \frac{1}{K} \sum_{k=1}^K \left[2 \operatorname{Re} \left\{ \bar{\mathbf{g}}_k^H \mathbf{H}^{-1} \frac{\partial \bar{\mathbf{g}}_k}{\partial \omega_m} \right\} - \bar{\mathbf{g}}_k^H \mathbf{H}^{-1} \frac{\partial \mathbf{H}}{\partial \omega_m} \mathbf{H}^{-1} \bar{\mathbf{g}}_k \right].$$

Taking into account that at evaluation of the objective function (15) is supposed implicit determinations of a vector of amplitudes in the form (7) obtained expression can be simplified to

$$\begin{aligned} \frac{\partial \delta}{\partial \omega_m} &= \frac{1}{K} \operatorname{Re} \left\{ \sum_{k=1}^K \bar{\mathbf{r}}_k^H \left(2 \frac{\partial \bar{\mathbf{g}}_k}{\partial \omega_m} - \frac{\partial \mathbf{H}}{\partial \omega_m} \bar{\mathbf{r}}_k \right) \right\} = \\ &= \frac{1}{K} \operatorname{Re} \left\{ \sum_{k=1}^K \bar{\mathbf{r}}_k^H \left(\frac{\partial \bar{\mathbf{g}}_k}{\partial \omega_m} + \bar{\mathbf{v}}_{mk} \right) \right\}. \end{aligned} \quad (16)$$

In expression (16) the next vector is used

$$\begin{aligned} \bar{\mathbf{v}}_{mk} &= \frac{\partial \bar{\mathbf{g}}_k}{\partial \omega_m} - \frac{\partial \mathbf{H}}{\partial \omega_m} \bar{\mathbf{r}}_k = \\ &= \begin{pmatrix} r_{mk} \frac{\partial S(\omega_1 - \omega_m)}{\partial \omega_m} \\ \vdots \\ \frac{\partial g_{mk}}{\partial \omega_m} - \sum_{l=1, l \neq m}^M r_{lk} \frac{\partial S(\omega_m - \omega_l)}{\partial \omega_m} \\ \vdots \\ r_{mk} \frac{\partial S(\omega_M - \omega_m)}{\partial \omega_m} \end{pmatrix}. \end{aligned} \quad (17)$$

In expression (17) components of the vector of derivatives $\partial \bar{\mathbf{g}}_k / \partial \omega_m$ are presented in the following form

$$\begin{aligned} \frac{\partial g_{mk}}{\partial \omega_m} &= \frac{\partial g_k(\omega_m)}{\partial \omega_m} = \\ &= \frac{j \Delta t}{N} \sum_{n=1}^N x_{nk} (n-1) \exp(j(n-1) \Delta t \omega_m) \end{aligned}$$

Components of the matrix of derivatives $\partial \mathbf{H} / \partial \omega_m$ are defined by the next derivative

$$\frac{\partial S(\omega)}{\partial \omega} = S(\omega) W(\omega),$$

$$\text{where } W(\omega) = j \frac{D}{2c} + \frac{d}{2c} \left[N \operatorname{ctg} \left(N \frac{d}{2c} \omega \right) - \operatorname{ctg} \left(\frac{d}{2c} \omega \right) \right].$$

Using the given expressions it is possible to present a derivative from the objective function (15) as follows:

$$\begin{aligned} \frac{\partial \delta}{\partial \omega_m} &= \frac{2}{K} \operatorname{Re} \left\{ \sum_{k=1}^K r_{mk}^* \left[\frac{\partial g_{mk}}{\partial \omega_m} - \right. \right. \\ &\quad \left. \left. \sum_{l=1, l \neq m}^M r_{lk} S(\omega_m - \omega_l) W(\omega_m - \omega_l) \right] \right\} \end{aligned}$$

Making differentiation (16) with respect to ω_l the second derivative of the objective function can be noted as

$$\begin{aligned} \frac{\partial^2 \delta}{\partial \omega_l \partial \omega_m} &= \frac{1}{K} \operatorname{Re} \left\{ \sum_{k=1}^K \left[2 \frac{\partial \bar{\mathbf{r}}_k^H}{\partial \omega_l} \left(\frac{\partial \bar{\mathbf{g}}_k}{\partial \omega_m} - \frac{\partial \mathbf{H}}{\partial \omega_m} \bar{\mathbf{r}}_k \right) + \right. \right. \\ &\quad \left. \left. + \bar{\mathbf{r}}_k^H \left(2 \frac{\partial^2 \bar{\mathbf{g}}_k}{\partial \omega_l \partial \omega_m} - \frac{\partial^2 \mathbf{H}}{\partial \omega_l \partial \omega_m} \bar{\mathbf{r}}_k \right) \right] \right\}. \end{aligned}$$

$$\text{As } \frac{\partial \bar{\mathbf{r}}_k^H}{\partial \omega_l} = \frac{\partial}{\partial \omega_l} (\bar{\mathbf{g}}_k^H \mathbf{H}^{-1}) = \left(\frac{\partial \bar{\mathbf{g}}_k^H}{\partial \omega_l} - \bar{\mathbf{r}}_k^H \frac{\partial \mathbf{H}}{\partial \omega_l} \right) \mathbf{H}^{-1}$$

finally we obtain a second derivative of the objective function (15) in form:

$$\begin{aligned} \frac{\partial^2 \delta}{\partial \omega_l \partial \omega_m} &= \frac{1}{K} \operatorname{Re} \left\{ \sum_{k=1}^K \left[\bar{\mathbf{r}}_k^H \left(2 \frac{\partial^2 \bar{\mathbf{g}}_k}{\partial \omega_l \partial \omega_m} - \frac{\partial^2 \mathbf{H}}{\partial \omega_l \partial \omega_m} \bar{\mathbf{r}}_k \right) + \right. \right. \\ &\quad \left. \left. + 2 \left(\frac{\partial \bar{\mathbf{g}}_k^H}{\partial \omega_l} - \bar{\mathbf{r}}_k^H \frac{\partial \mathbf{H}}{\partial \omega_l} \right) \mathbf{H}^{-1} \left(\frac{\partial \bar{\mathbf{g}}_k}{\partial \omega_m} - \frac{\partial \mathbf{H}}{\partial \omega_m} \bar{\mathbf{r}}_k \right) \right] \right\}. \end{aligned}$$

The matrix of second derivatives of the objective function (15) can be defined as:

$$\mathbf{Q} = \frac{1}{K} \operatorname{Re} \left\{ \sum_{k=1}^K [\mathbf{U}_k + 2 \mathbf{V}_k^H \mathbf{H}^{-1} \mathbf{V}_k] \right\}, \quad (18)$$

where $\mathbf{V}_k = [\bar{\mathbf{v}}_{1k}, \bar{\mathbf{v}}_{2k}, \dots, \bar{\mathbf{v}}_{Mk}]$ is a matrix of size $M \times M$ formed by a vector-column $\bar{\mathbf{v}}_{mk}$ which is defined in (17); \mathbf{U}_k is a matrix of size $M \times M$ with elements of next view ($l, m = 1, 2, \dots, M$)

$$\begin{aligned} U_{lm}^k &= \bar{\mathbf{r}}_k^H \left(2 \frac{\partial^2 \bar{\mathbf{g}}_k}{\partial \omega_l \partial \omega_m} - \frac{\partial^2 \mathbf{H}}{\partial \omega_l \partial \omega_m} \bar{\mathbf{r}}_k \right) = \\ &= \begin{cases} 2 r_{mk}^* r_{lk} \frac{\partial^2 S(\omega_m - \omega_l)}{\partial \omega_l \partial \omega_m}, & l \neq m; \\ 2 r_{mk}^* \left[\frac{\partial^2 g_{mk}}{\partial \omega_m^2} - \sum_{i=1, i \neq m}^M r_{ik} \frac{\partial^2 S(\omega_m - \omega_i)}{\partial \omega_m^2} \right], & l = m; \end{cases} \\ \frac{\partial^2 g_{mk}}{\partial \omega_m^2} &= -\frac{(\Delta t)^2}{N} \sum_{n=1}^N x_{nk} (n-1)^2 \exp(j(n-1) \Delta t \omega_m). \end{aligned}$$

For determination of second derivatives from elements of matrix \mathbf{H} it is possible to use that

$$\frac{\partial^2 S(\omega)}{\partial \omega^2} = S(\omega) \left\{ W^2(\omega) + \frac{\partial W(\omega)}{\partial \omega} \right\},$$

where

$$\frac{\partial W(\omega)}{\partial \omega} = -\left(\frac{d}{2c} \right)^2 \left[\frac{N^2}{\sin^2 \left(N \frac{d}{2c} \omega \right)} - \frac{1}{\sin^2 \left(\frac{d}{2c} \omega \right)} \right].$$

3.3. EFFECTIVE REALIZATION OF ALGORITHM OF THE SOLUTION SEARCHING

Direct minimization of the objective function (15) without successful information about initial values can provide only infinitesimal probability of determination of true values of parameters of model (4). This situation

is a result of the considerable non-unimodal character of the indicated objective function and high dimensionality of a problem of nonlinear minimization.

It is possible to overcome the problem of initial approach on the basis of the concept of the quasiresolution within the framework of various classes of inserted complicated models of the investigated object:

$$M_1 \subset M_2 \subset \dots \subset M_l \subset \dots$$

The operator of the direct problem $\mathbf{X}_{M_l}(\tilde{\omega}, \mathbf{R})$ exists for every model M_l and for every model (even for not quite adequate) it is possible to find the quasiresolution $(\tilde{\omega}_l, \mathbf{R}_l)$, so that will be valid

$$\rho(\mathbf{X}_{M_l}(\tilde{\omega}_l, \mathbf{R}_l), \mathbf{X}) \geq \dots \geq \rho(\mathbf{X}_{M_1}(\tilde{\omega}_1, \mathbf{R}_1), \mathbf{X}) \geq \dots$$

Complication of the model can be realized, for example, by increasing of the order of the model. It is supposed that for simpler model its natural quasiresolution may be found easier than for more complicated one.

Thus, the use of a chain of inserted complicating models allows us to solve of a problem of a choice of initial values: the quasiresolution of $(l-1)$ -th stage can be used as initial values at quasiresolution searching of l -th stage.

The algorithm of sequential overgrowth of the order of the model has been implemented that allows us to use standard methods of local optimization for the search of quasiresolution. Three alternatives of the algorithm which are differed by the selected method of minimization of the objective function and, accordingly, by the type of the necessary information were considered: the algorithm 0 is based on simplex method of Nelder-Mead (it uses only values of the objective function); the algorithm 1 is based on quasi-Newton method BFGS with cubic linear searching (it uses values of the objective function and its first derivative); the algorithm 2 is based on interior-reflective Newton method (it uses values of the objective function, its first and second derivative).

4. RESULTS

Accuracy properties of surveyed algorithms have been calculated for classical test example of Tufts and Kumaresan (1982) to provide an opportunity of comparison with other methods. The model with two uncorrelated Gaussian sources ($M = 2$) with equal power ($\eta_k = 1$; $r_{2k} = \exp(j\pi/4)$) with $\omega_1 = 2\pi \cdot 0.5$; $\omega_2 = 2\pi \cdot 0.52$; $N = 25$ and with number statistically independent snapshots $K = 10$ was used. Means $\{\tilde{\omega}_1, \tilde{\omega}_2\}$ and variances $\{\sigma_{\omega_1}^2, \sigma_{\omega_2}^2\}$ of estimations of the component of the vector $\tilde{\omega}$ were computed using results of the estimation for 1000 various noise realizations of the matrix \mathbf{X} . The mean square error of estimations

$$e_{\omega}^2 = \frac{1}{2} \sum_{m=1}^2 (\sigma_{\omega_m}^2 + |\omega_m - \tilde{\omega}_m|^2)$$

was computed for the comparative analysis of algorithms. The obtained dependences $10 \log(e_{\omega}^2 / N \Delta t)$

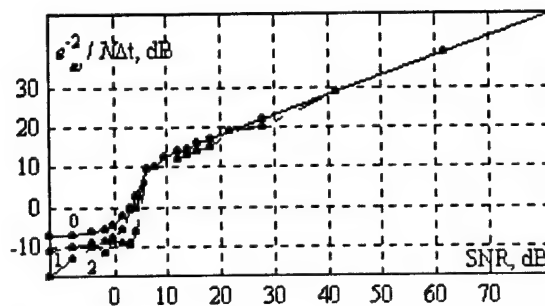


Fig. 1. Dependence mean square error of estimations on signal/noise ratio.

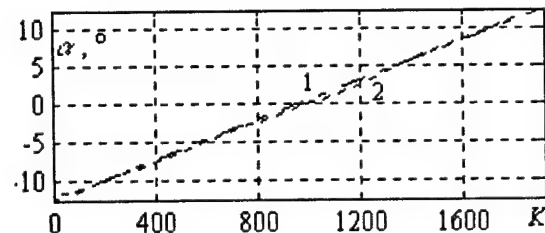


Fig. 2. The estimation of trajectory of the moving source.

on a signal/noise ratio for various realizations of the algorithm (0 – algorithm 0; 1 – algorithm 1; 2 – algorithm 2) are presented on Fig. 1.

Practical opportunities of the surveyed approach were explored in the test problem of determination of an angular trajectory $\alpha = \pi/2 - \beta_1$ of moving source using the experimentally obtained snapshots of the signal from the 6-element array (UW STAT), which has offered Pierre, Scott and Hays (1997). It enables to compare the suggested method with other methods, which were tested on these data. The data set no. 1 with one moving source with constant velocity has been used. A sliding window with $K = 60$ snapshots was used to estimate the source trajectory.

The true source trajectory (1) of the moving source and restored (2) using the measurement data by means of surveyed method are presented on Fig. 2.

The obtained results have confirmed an opportunity of an effective use of surveyed method, and not only for determination of parameters of stationary sources, but also a trajectory of the moving source.

REFERENCES

1. Stoica P., Sharman K. C. Maximum likelihood methods for direction-of-arrival estimation // IEEE Trans. on Acoustics, Speech and Signal Processing. 1990. Vol. 38. No 7, p. 1132-1143.
2. Tufts D. W., Kumaresan R. Frequency estimation of multiple sinusoids: making linear prediction perform like maximum likelihood // Proc. IEEE. 1982. Vol. 70. No 9, p. 975-989.
3. Pierre W., Scott E. D., Hays M. P. A sensor array testbed for source tracking algorithms // Proc. of ICASSP '97, Munich, Germany, April 1997.

MULTI-BASE INSAR WITH ENHANCED SIGNAL PROCESSING

Alexander V. Ksendzuk, Valery K. Volosyuk

Kharkov National Aerospace University (KhAI), Kharkov, Ukraine,
<kav@ai.kharkov.com>, <ks_alex@ukr.net>

Abstract

Synthetic aperture radar interferometer provides three-dimensional information by using the phase as an information source. An interferogram contains the amplitude as well as the phase information of a SAR image pair. The resultant phase of the interferogram is only measured modulo 2π . To calculate the elevation of each point it is necessary to add the correct integer number of phase cycles to each phase measurement. The problem of solving this 2π -ambiguity is called phase unwrapping. On the one hand decrease of the interferometer's carrier frequency causes larger altitude variation which can be resolved without ambiguity. However, on the other hand decrease of carrier frequency causes decrease of accuracy of the relief altitude estimation. This contradiction may be resolved for example in the multi-frequency interferometric system, but it is expensive. This paper presents a method for the phase-ambiguity resolution in the two-frequency interferometer. By multiplying signals with different carrier frequency, it is possible to resolve phase-ambiguity as well as provide high-precision of relief altitude estimation. This work presents an analytic equation for the errors in the InSAR, for the carrier frequency calculation. The modeled results show accurate relief estimation as well as phase ambiguity resolution.

Keywords: SAR, Interferometer, Phase unwrapping, Multibase SAR.

Radar interferometry is a technique for extracting three dimensional information of the Earth's surface by using the phase content of the radar signal as an additional information source derived from the complex radar data.

The general geometry of SAR interferometry is illustrated in Fig. 1.

The phase difference, $\Delta\varphi$ between the signals received from the same surface element at the two antennas positions is

$$\Delta\varphi[\vec{r}, h(\vec{r})] = kD \frac{H - h(\vec{r})}{R_0}, \quad (1)$$

where $k = \frac{2\pi}{\lambda} = \frac{\omega}{c}$ – wave number; λ – the wavelength; ω_0 – carrier frequency; H – SAR altitude; D – interferometer base; R_0 – slant range; \vec{r} – surface coordinates.

Signal in the interferometers of antennas 1 and 2 may be written

$$\begin{aligned} u_1(t) &= \text{Re} \int_D F[\vec{r}, \vec{\lambda}(\vec{r})] G(t, \vec{r}) S_0[t - \tau(t, \vec{r})] \times \\ &\quad \times \exp\{j\omega_0[t - \tau(t, \vec{r})]\} d\vec{r} + n_1(t) \\ u_2(t) &= \text{Re} \int_D F[\vec{r}, \vec{\lambda}(\vec{r})] G(t, \vec{r}) S_0[t - \tau(t, \vec{r}) - \tau'] \times \\ &\quad \times \exp\{j\omega_0[t - \tau(t, \vec{r}) - \tau']\} d\vec{r} + n_2(t) \end{aligned} \quad (2)$$

where u_1, u_2 – received signals; $F[\vec{r}, \vec{\lambda}(\vec{r})]$ – complex scattering coefficient; $\vec{\lambda}(\vec{r})$ – electro physical parameters; $G(t, \vec{r})$ – directional pattern; S_0 – complex envelope of the signal; $\tau(t, \vec{r})$ – time delay for the 1st antenna; $\tau(t, \vec{r}) + \tau'$ – time delay for the 2nd antenna; $n(t)$ – additive noise.

Optimal processing algorithm may be derived from

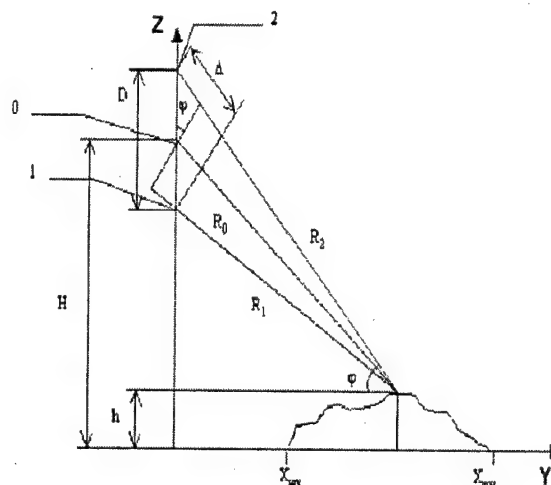


Fig. 1. Interferometer geometry

the equation $\frac{\delta}{\delta \lambda(\vec{r})} \{ \ln p[\vec{u}(t)/h(\vec{r})] \} = 0$ where $\frac{\delta}{\delta \lambda(\vec{r})}$ – variational derivative.

With a Gaussian approximation probability density may be written as

$$p[\vec{u}(t)/\vec{\lambda}(\vec{r})] = K \times \exp \left\{ -\frac{1}{2} \int_0^T \int_0^T \vec{u}(t_1) \underline{W}[t_1, t_2; \vec{\lambda}(\vec{r})] \vec{u}^T(t_2) dt_1 dt_2 \right\},$$

where K – constant; $\underline{W}[t_1, t_2; \vec{\lambda}(\vec{r})]$ – reverse-correlation matrix; $\underline{W}[t_1, t_2; \vec{\lambda}(\vec{r})]$ may be found from the inverse integral equation

$$\int_0^T \underline{R}[t_1, t_2; \vec{\lambda}(\vec{r})] \cdot \underline{W}[t_2, t_3; \vec{\lambda}(\vec{r})] dt_2 = \underline{\delta}(t_1 - t_3).$$

Optimal processing algorithm is given by the equation

$$\begin{aligned} \int_0^T \int_0^T \frac{\delta \{ u_1(t_1) u_2(t_2) \}}{\delta h(\vec{r})} \underline{W}_{12}[t_1, t_2; \vec{\lambda}(\vec{r})] dt_1 dt_2 = \\ = \frac{1}{2} \operatorname{Re} \int_D \int_D \dot{F}^*[\vec{r}_1, \vec{\lambda}(\vec{r}_1)] \dot{F}[\vec{r}_2, \vec{\lambda}(\vec{r}_2)] \times \\ \times \frac{\delta \exp(j\Omega [H, h(\vec{r}_2), D])}{\delta h(\vec{r}_2)} \frac{1}{2} \operatorname{Re} \int_D \sigma^0(\vec{r}) \times \\ \times \exp(j\Omega [H, h(\vec{r}), D]) \int_0^T \int_0^T \int_0^T \int_0^T \dot{S}_{P1}^*(t_1, \vec{r}_1) \cdot \\ \cdot \underline{W}_{12}[t_1, t_3; \vec{\lambda}(\vec{r})] \dot{S}_{P2}(t_3, \vec{r}) \dot{S}_{P1}(t_1, \vec{r}_2) \\ \cdot \underline{W}_{12}[t_2, t_4; \vec{\lambda}(\vec{r})] \dot{S}_{P2}^*(t_4, \vec{r}) dt_1 dt_2 dt_3 dt_4 d\vec{r} d\vec{r}_1 d\vec{r}_2 \end{aligned} \quad (3)$$

The solution, which gives optimal processing algorithm in the interferometer, will be

$$\begin{aligned} Y_{IW}(\vec{r}) = \int_0^T \int_0^T u_1(t_1) \underline{W}_{12}[t_1, t_3; \vec{\lambda}(\vec{r})] \dot{S}_{P2}(t_3, \vec{r}) dt_1 dt_3 \times \\ \times \int_0^T \int_0^T u_1(t_1) \underline{W}_{12}[t_1, t_3; \vec{\lambda}(\vec{r})] \dot{S}_{P1}^*(t_3, \vec{r}) dt_1 dt_3 \end{aligned} \quad (4)$$

where $\dot{S}_{P1}(t_3, \vec{r})$ – point signal.

As we can see from the last equation proposed algorithms differ from the classic SAR interferometer algorithm. The most important operation is the decorrelation of the input signal by the function $\underline{W}_{12}[t_1, t_3; \vec{\lambda}(\vec{r})]$ and further matched filtering with the point signal $\dot{S}_{P1}(t, \vec{r})$.

An interferogram (left part of the equation (4)) for the proposed algorithm (as well as for classic processing algorithm) contains the amplitude and the phase information of a SAR image pair. The phase difference is used to determine altitude of the surface point. The resultant phase of the interferogram, which is directly related to the topography, is only measured

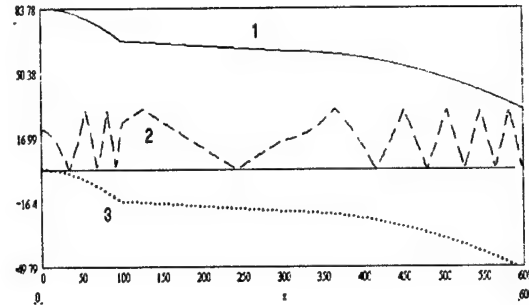


Fig. 2. Modelling results

modulo 2π . To calculate the elevation of each point it is necessary to add the correct integer number of phase cycles to each phase measurement. The problem of solving this 2π -ambiguity is called phase unwrapping.

This problem appears independently of the interferometric processing method. Altitude ambiguity interval mainly depends on base and wavelength. Moreover, it is obvious that for classic interferometer altitude ambiguity interval and its measurements precision is in a contradiction. The more phase measurement precision (smaller base or smaller wavelength) the more uncertainly, and vice versa.

There are many different methods for the two-dimensional phase unwrapping. However, most of them require additional (a-priori) information or some empiric assumption. Therefore, in the classic interferometer it is impossible to provide high precision of the altitude measurements without uncertainty.

If we already estimate complex image and its modulo (radar cross-section) and absolute phase $\exp\{j\hat{\Omega}[\vec{r}, h(r)]\}$ altitude estimation may be found from

$$\hat{\Omega}[\vec{r}, h(r)] = \arccos \left[\cos[kD \frac{H - h(r)}{R_0(r)}] \right]. \quad (5)$$

As we can see, it is necessary to estimate altitude $h(r)$ from the ambiguous function with the period 2π .

Function $\hat{\Omega}[\vec{r}, h(r)]$ may be estimated directly from the (5) as follows

$$\hat{\Omega}[\vec{r}, h(\vec{r})] = C_0 \pm \int_{\vec{r}_{\text{anch}}}^{\vec{r}} \left| \frac{d\hat{\Omega}[\vec{r}, h(\vec{r})]}{d\vec{r}} \right| d\vec{r}, \quad (6)$$

where C_0 – constant denotes phase of the mean altitude H .

Sign \pm depends on the altitude behavior; if altitude is the monotone increasing function sign must be positive, otherwise it must be negative.

When altitude has a constant first derivative (due to a-priori information) it is easy to obtain altitude estimation by using (6). Cross-section of modeling results are shown in Fig. 2.

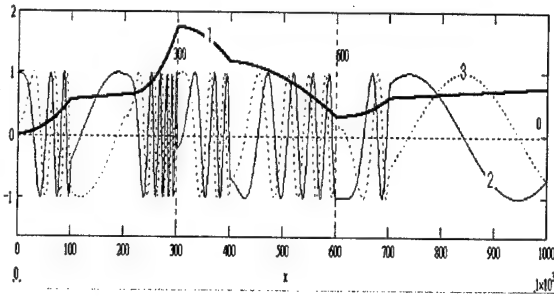


Fig. 3. Phase behavior

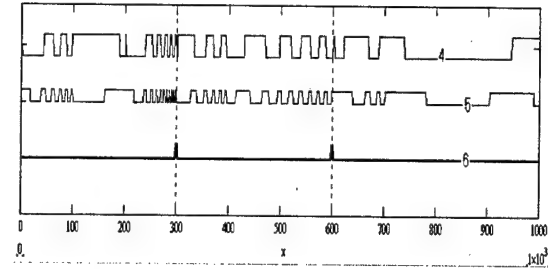


Fig. 4. Estimation results

In Fig. 2: 1 – behavior of the $D \frac{H - h(\vec{r})}{R_0(\vec{r})}$, 2 – function $\arccos\left\{\cos\left\{kD \frac{H - h(\vec{r})}{R_0(\vec{r})}\right\}\right\}$, 3 – result of the usage equation (6), without constant C_0 estimation.

However, if altitude changes arbitrary it is necessary to find what kind of the sign must be used in the equation (6). Therefore, we need to determine where altitude changes from monotone increasing to monotone decreasing. To do this it is necessary to find points where second derivative of the $\hat{\Omega}(\vec{r}, h(r))$

$$(d^2 \hat{\Omega}(\vec{r}) / d\vec{r}^2 = \frac{d^2}{d\vec{r}^2} \arccos\left\{\cos\left\{kD \frac{H - h(\vec{r})}{R_0(\vec{r})}\right\}\right\})$$

changes its sign. Moreover, we have to eliminate all points where $\cos(kD \frac{H - h(\vec{r})}{R_0(\vec{r})})$ has a local maximum or minimum. One of the possible methods is based on the next equation:

$$H_{\vec{r}} = \text{not} \left\{ \frac{d^2 \arccos\left\{\cos\left\{kD \frac{H - h(\vec{r})}{R_0(\vec{r})}\right\}\right\}}{d\vec{r}^2} \right\} \text{ and } \left\{ \text{not max} \left[\arccos\left\{\cos\left(kD \frac{H - h(\vec{r})}{R_0(\vec{r})}\right)\right\} \right] \right\} \text{ and } \left\{ \text{not min} \left[\arccos\left\{\cos\left(kD \frac{H - h(\vec{r})}{R_0(\vec{r})}\right)\right\} \right] \right\} \quad (7)$$

Algorithm (7) leaves out points where altitude changes from monotone increasing to monotone decreasing if this space point is the local mini-

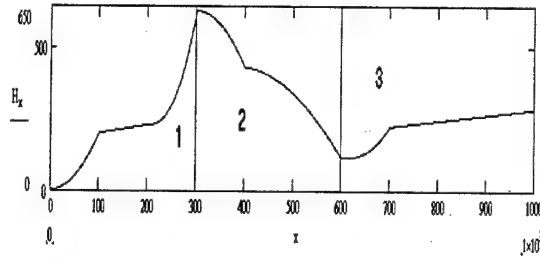


Fig. 5. Altitude behavior

mum/maximum of the ambiguous function

$$\arccos\left\{\cos\left(kD \frac{H - h(\vec{r})}{R_0(\vec{r})}\right)\right\}.$$

In Fig. 3: 1, 3 – altitude monotone increasing zone, 2 – monotone decreasing zone. In this figure: 1 – function $kD \frac{H - h(\vec{r})}{R_0(\vec{r})}$, 2, 3 – functions $\cos(kD \frac{H - h(\vec{r})}{R_0(\vec{r})})$ and $\sin(kD \frac{H - h(\vec{r})}{R_0(\vec{r})})$, correspondingly.

Functions in the equation (7) are shown below in the Fig. 4. In this figure:

$$4 – \text{function } \max\left\{\arccos\left\{\cos\left(kD \frac{H - h(\vec{r})}{R_0(\vec{r})}\right)\right\}\right\},$$

$$5 – \min\left\{\arccos\left\{\cos\left(kD \frac{H - h(\vec{r})}{R_0(\vec{r})}\right)\right\}\right\},$$

6 – result of the space point estimation (8) where altitude changes from monotone increasing to monotone decreasing.

With two-base interferometer algorithm (7) must be modified to

$$J_{\vec{r}} = \left\{ \frac{d^2 \arccos\left\{\cos\left\{kD_1 \frac{H - h(\vec{r})}{R_0(\vec{r})}\right\}\right\}}{d\vec{r}^2} \right\} \text{ and } \left\{ \frac{d^2 \arccos\left\{\cos\left\{kD_2 \frac{H - h(\vec{r})}{R_0(\vec{r})}\right\}\right\}}{d\vec{r}^2} \right\} \text{ and } \left\{ \text{not max}_i \left[\arccos_i \left\{ \cos\left(kD_i \frac{H - h(\vec{r})}{R_0(\vec{r})}\right)\right\} \right] \right\} \text{ and } \left\{ \text{not min} \left[\arccos \left\{ \cos\left(kD_1 \frac{H - h(\vec{r})}{R_0(\vec{r})}\right)\right\} \right] \right\} \left\{ \text{not max} \left[\arccos \left\{ \cos\left(kD_2 \frac{H - h(\vec{r})}{R_0(\vec{r})}\right)\right\} \right] \right\} \text{ and } \left\{ \text{not min} \left[\arccos \left\{ \cos\left(kD_2 \frac{H - h(\vec{r})}{R_0(\vec{r})}\right)\right\} \right] \right\} \quad (8)$$

Usually it is not necessary to use all equation (9), quite enough to find points with first two members.

For the modelling was used the same altitude as shown in Fig. 4 and simplified algorithm (7) which finds space points where altitude changes from mono-

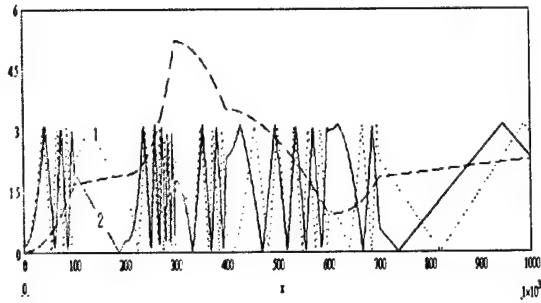


Fig. 6. Altitude and phase

tone increasing to monotone decreasing with first two members of the (8).

Modelling results are shown in Figs. 6, 7.

In Fig. 6 bold dotted line denotes behaviour of the altitude and 1,2 denotes space functions

$$\arccos\left\{\cos\left(k D_1 \frac{H - h(\vec{r})}{R_0(\vec{r})}\right)\right\} \quad \text{and}$$

$$\arccos\left\{\cos\left(k D_2 \frac{H - h(\vec{r})}{R_0(\vec{r})}\right)\right\} \quad \text{respectively.}$$

Results of the application algorithm (8) are shown below in the Fig. 6.

In Fig. 7: 1 – function $\frac{d^2}{d\vec{r}^2} \arccos\left[\cos\left\{k_1 D \frac{H - h(\vec{r})}{R_0(\vec{r})}\right\}\right]$, 2- function $\frac{d^2}{d\vec{r}^2} \arccos\left[\cos\left\{k_2 D \frac{H - h(\vec{r})}{R_0(\vec{r})}\right\}\right]$, 3- result of the 1,2 logical multiplication.

Two-base interferometer has a lower probability of living out points where altitude changes from monotone increasing to monotone decreasing. When altitude changes entail absolute phase changes on $C \cdot 2\pi$ it is impossible to find exact altitude without a-priori information. It is necessary to choose λ (wavelength) and D (interferometer base) to avoid ambiguity.

When maximum altitude jump is known $\Delta h(\vec{r})$ it is possible to provide non-ambiguous altitude measurements for selected ranges $R_0(\vec{r}) \in [R_{0MIN}(\vec{r}) \dots R_{0MAX}(\vec{r})]$ by choosing frequency and base.

Potential exactness of the altitude estimation for the great signal-to-noise ratios may be founded from the equation $\sigma_{\Delta}^2 = \frac{1}{\mu(2\pi \frac{D}{\lambda})^2}$, where μ denotes sig-

nal-to-noise ratio.

It is obvious that for classic interferometer altitude ambiguity interval and altitude measurements precision are in contradiction. The more measurement pre-

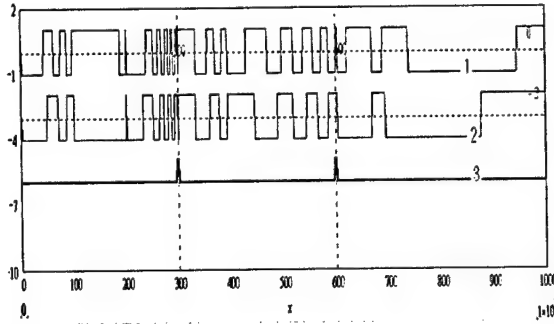


Fig. 7. Results

cision (smaller base or smaller wavelength) the more uncertainly, and vice versa.

Multi-base (in a simplest case 2-base interferometer) allow to avoid uncertainly in altitude measurements as well as provide high accuracy in the one-base interferometer.

When maximum altitude jump is given for the smaller base (D_1) must satisfy an equation:

$$f_{MIN} = f_1 = \frac{c \cdot R_{0MAX}}{2D\Delta h_{MAX}}, \quad (9)$$

where R_{0MAX} – maximal slant range for the scene; Δh_{MAX} – maximum supposed altitude jump.

The second base frequency (D_2) must be chosen to provide altitude ambiguity interval less than altitude estimating errors on the first (D_1) frequency

$$\frac{c \cdot R_{0MAX}}{2fD_2} < \frac{1}{\mu(2\pi \frac{D_1}{\lambda})^2}. \quad (10)$$

In this case (for given maximum altitude jump) in the two-base interferometer potential exactness may be found with the equation when D_2 chosen from the exact equality.

When potential exactness (variation of the altitude estimation errors) is given in reverse order to above computation we can estimate ambiguity altitude interval.

REFERENCES

1. Ksendzук A. V., 2001. Estimating input signal covariance function in SAR. CIC-PRODIS.- Mexico city, Mexico.- pp. 65-70.
2. Ksendzук A. V. Space ambiguity function for the optimal processing algorithms for the stochastic surface models.
<http://jre.cplire.ru/jre/nov00/6/text.html>

PHASED ANTENNA ARRAY WITH EXCITATION ADAPTIVE TO CONSTRUCTION DISTORTIONS

U. R. Liepin, D. V. Karlov, G. A. Golovin, N. N. Petrushenko

Kharkiv Military University, Kharkiv, Ukraine

Abstract

The dependencies of errors of phasing of antenna arrays (PAA) with spatial excitation from parameters of distortion of a hull structure surveyed is reviewed. The opportunity of build-up of algorithms of adaptation to such distortions is rotined, utilizing results of built-in system of UHF of the check of PAA, the expected results from their application rated.

Keywords: Adaptation, distortion of a construction of PAA.

1. INTRODUCTION

The solution of problems of adaptation of the phased antenna array (PAA) in mobile radio systems (MRS) to technical condition is possible when PAA incorporates a control system of a beam (beam control system – BCS) of the built-in microwave array construction control system. Antenna construction distortions resulting in change of co-ordinates of radiator phase centres with respect to the designed ones lead to in deterioration of operation of PAA and MRS as a whole [1].

In mobile MRS, there are usually applied transceiving PAAs with spatial excitation. For power collimation in such arrays there are used the same phase shifters (PS), as for the beam control. For this reason, it is expedient to solve the problem of definition of the antenna construction condition simultaneously with that of PAA PS diagnostics. The PAA diagnostics methods developed recently [2, 3] allow solving a complex of problems, which includes the following:

- determine real values of implemented phase distribution (PD) of PAA PS when acting on them with nominal steering signals [2, 3];
- determine errors in realization of PD in the antenna aperture taking into account the design collimation correction and PS electrical lengths codes stored in the BCS processor [4, 5];
- using the results of the PD control, restore distortions of the antenna array construction;
- make corrections to BCS algorithms taking into account detected changes in the antenna construction and error in PS functioning.

The given above list of procedures of control and PAA adjusting is urgent at the finite probability of extreme case occurrence in the process of exploitation, maintenance and transportation of MRS with PAA.

2. STATEMENT OF THE PROBLEM

Assume that the array aperture coincides with a plane xOy of the rectangular co-ordinate system, whereas the normal to the aperture is directed along a Oz -axis. In this case, errors of phasing of the array with spatial excitation at the expense of antenna construction distortion, in accordance with [4], can be presented as:

$$\Delta\psi_{i,k} = \frac{2\pi}{\lambda} \left\{ \cos\theta_x i d_x \left(1 - h_i + \frac{\Delta x_i}{i d_x} \right) + \right. \\ \left. + \cos\theta_y i d_y \left(1 - h_k + \frac{\Delta y_k}{k d_y} \right) + z_i \cos\theta_c \right\}, \quad (1)$$

where $i \in 0, N_x - 1$; $k \in N_y - 1$ is the number of

rows and columns of PAA radiators;

$\cos\theta_x = \sin\theta_c \cos\varphi_c$;

$\cos\theta_y = \sin\theta_c \cos\varphi_c$ are directing cosines;

θ_c, φ_c are elevation angle and of an azimuth of direction of phasing, respectively;

d_x, d_y are distances between lines and columns of radiators;

$x_i = i d_x + \Delta x_i$; $y_k = k d_y + \Delta y_k$ are

Cartesian coordinates of an i, k radiator;

$\Delta x_i, \Delta y_k$ are biases of the i -th row and of the k -th column relative to their design positions;

$h_{i,k}$ are transfer coefficients of devices converting digital codes to phase shifts (for example, transformers of 'code-current', power amplifiers and ferrite PSs [4, 5]);

$z_{i,k} = z_i = z_k$ of- bias of the i, k -th radiator along the Oz axis.

It follows from (1), that the PAA adjustment can be realized with the following methods:

- measure $\Delta x_i, \Delta y_k, z_{i,k}$ and remove a reason of $\Delta\psi_{i,k}$ emergence by restoration of a design condition of the array construction;

- change transfer coefficients $h_{i,k}$ BCS so that to compensate the influence of $\Delta x_i, \Delta y_k$ and minimize $\Delta \psi_{i,k}$.

In PAA with spatial excitation, distortions of an array construction influence also on the concordance of conformity with their design values.

When there is no PS in an antenna aperture, there is established the initial PD due to sphericity of a wave radiated by the feed [4]

$$\varphi_{i,k} = -\frac{2\pi}{\lambda} \left[\sqrt{x_i^2 + y_k^2 + f_0^2} - f_p \right], \quad (2)$$

where f_p is the distance from a feed phase centre up to aperture phase centre.

The codes of phase shifts assigned for compensation of both the phase front sphericity and the dispersion of PS electrical lengths $\varphi_{0,i}$, should meet conditions

$$\psi_{i,k}^k = \varphi_{i,k} + \varphi_{0,i}. \quad (3)$$

It is expedient to include in quantity $\varphi_{0,i}$ also addition necessary for compensation of a $z_{i,k}$ divergence along Oz -axis.

At the row-column control of FS, $\varphi_{i,k}$ are calculated by the approximate relation

$$\varphi_{i,k} = -\frac{2\pi}{\lambda} \left[\frac{(id_x)^2 + (kd_y)^2}{2f_p^2} \right] = \varphi_i + \varphi_k. \quad (4)$$

It is not difficult to show, that the errors in estimation of the collimation correction $\Delta \varphi_{i,k}$, when the array construction changes, are equal to:

$$\Delta \varphi_{i,k} = \frac{2\pi}{\lambda} \left[\frac{id_x \Delta x_i + kd_y \Delta y_k}{f_p} \right]. \quad (5)$$

From (5) it follows that, having obtained numerical estimates of $\Delta \varphi_{i,k}$, it is possible to solve two important problems: to correct tables of the collimation corrections and determine distortions of antenna construction. The numerical values of $\Delta x_i, \Delta y_k$, one can use, in turn, for correction of $h_{i,k}$ with the purpose of minimization of $\Delta \psi_{i,k}$ corresponding to (1).

3. METHODS OF MEASUREMENTS

In PAA with spatial feeding, it is possible to measure $\varphi_{i,k}$ and $\Delta \varphi_{i,k}$ only with indirect methods. Most rationally is to make this with the methods described in [2, 3].

A method based on application of the Walsh transform (a DWT method in [2, 3]) consists in representation of the antenna array amplitude-phase distribution (APD) by a Walsh series and in the time successive measurements of a series coefficients. Coordinates of a sounding signal (SS) source are considered known. Further, applying the procedure of the inverse DWT, it is possibility to reconstruct the APD actually realized in the antenna. Having compared The measured values

$\varphi_{i,k}$ (taking into account the information about $\varphi_{0,i}$) with their calculated values one can estimate PAA construction distortions. However, in this case, unknown is an ability of antenna array PS to compensate the sphericity of the phase front with the needed accuracy.

In [2, 3], there is proposed the adaptive method of measurements of a series coefficients, with which the phase distribution (PD) is represented, - the Newton method. Its essence is in organization of an iterative procedure of search of those coefficients of a Walsh series, which satisfy a condition of obtaining SS maximum power in the array adder. The obtained estimates of coefficients are recalculated in PDS and realized with array PS with a reversed sign. Thus, two problems are solved simultaneously: $\varphi_{i,k}$ are measured (at known $\varphi_{0,i}$) and the array PS capabilities are assessed to minimize $\Delta \varphi_{i,k}$ down to given values.

It is known that the measurement method basing on the Newton procedures form asymptotically optimum estimates of the measured values at an attainable minimum number of iterations. The versions of realizing the Newton method at PAA diagnostics are specified in [2, 3].

4. RECOMMENDATION ON APPLICATION; EXPECTED RESULTS

The procedures described above can be used as basis when creating the microwave control and PAA adjustment system built-in in MRS. The presence of the computer and the analog-to-digit converter of receiving signals, being incorporated in MRS are the sufficient condition for the method realization without additional apparatus expenses. As SS sources, there can be used the sources of information signals; specially organized SS or re-reflectors of signals radiated with PAA in the transmission mode [2, 3].

The MRS built-in microwave system of the antenna control allows the following:

- lowering an antenna structure weight at the expense of lowering the requirements to its rigidity;
- bringing together the implemented and potential characteristics of PAA at the replacement of BCS element basis with more modern and precise;
- increasing serviceability of the antenna metal construction at the replacement of PAA element basis.

REFERENCES

1. Ya. S. Shifrin, L. G. Komienko. Field statistics of antenna arrays.- Antenny, 2000. № 1(44). P. 3-27.(in Rus.)
2. Ya. S. Shifrin, U. R. Liepin, Phaseless methods of PAA diagnostics.- Антенны, 2000, № 1(44), P. 84-99.(in Rus.)
3. Shifrin Y. S., Liepin U. R. Methods of PPA Diagnostics. Telecommunications and Radio Engineering, 2002, v.58, N8, pp. 99-119.
4. V. I. Samoilenko, Yu. A. Shishov. Control of phased antenna arrays.- M.: Radio I Svyaz, 1983.-P. 240.

AN ADAPTIVE PARAMETER ESTIMATION OF GAUSSIAN SIGNAL IN THE PRESENCE OF AN UNKNOWN GAUSSIAN NOISE

V. I. Turchin

Institute of Applied Physics of RAS, Nizhny Novgorod, Russia
<turchin@hydro.appl.sci-nnov.ru>

Abstract

The parametric estimation technique for a source emitting white Gaussian noise in the presence of white Gaussian noise background with an unknown covariance matrix is considered. Simultaneous estimation of both the source parameters and the unknown covariance matrix of noise background can be conducted when the source moves, i.e. its steering vector varies in time. For this scenario, the maximum-likelihood statistic was derived for estimation of the source power and the noise covariance matrix. Simplification of maximum-likelihood equations was performed assuming a great number of snapshot vectors and low signal-to-noise ratio. The results of stochastic numerical simulation are given in case of a point source moving across the uniform sensor array (it was assumed that the source track lies in near-field zone of sensor array) in the presence of uniform noise background and strong interference. The effectiveness of the adaptive beamformer using the inverse estimate of the covariance matrix of non-uniform noise background was demonstrated.

Keywords: Maximum-likelihood parametric estimation, Gaussian signal, adaptive beamformer.

1. INTRODUCTION

Parameter estimation of spatially distributed noise sources in the presence of some noise background is an important requirement in passive remote sensing, e.g., in radioastronomy, hydroacoustics, etc. In most scenarios the vector snapshots of array output in the case of narrow bandwidth assumed to be white zero-mean Gaussian noise with some $N \times N$ covariance matrix Φ where N is the number of array sensors. Estimation of the parameters characterizing the sources: source powers, directions-of-arrival (DOA), etc. assumes some *a priori* known structure of the covariance matrix. Numerous issues were addressed at the parameter estimation for various models of covariance matrix structure. Well-known MUSIC, ESPRIT, and other high-resolution methods involve the spatial harmonic model of statistically independent sources with a uniform noise background. A lot of papers were addressed at the model involving several point sources and the unknown structured covariance matrix of noise background. For instance, DOA estimation was studied in the presence of unknown diagonal matrix [1,2]. However, in some scenarios we cannot exploit any *a priori* structure of the covariance matrix, except its part concerning the spatial structure of estimated source (or sources). In this case, for instance, the full covariance matrix can be written as

$$\Phi = \theta_0 \mathbf{a} \mathbf{a}^H + \mathbf{K}, \quad (1)$$

where θ_0 is the unknown source power, \mathbf{a} is the steering

vector depending on unknown parameters (e.g., DOA), and \mathbf{K} is any unknown matrix. Evidently, the parameter θ_0 cannot be found from known full covariance matrix (1) even if the steering vector is known.

The correct solution of the above mentioned problem can be found when the steering vector of estimated source varies during observation time, i.e., the full covariance matrix is non-stationary. This approach was proposed in [3] where the unknown covariance matrix of an extended moving source was estimated in the presence of an unknown noise background.

This work is focused on the simplified problem: the maximum-likelihood power estimation for one moving point-source in the presence of unknown noise background.

2. SIGNAL MODEL

Let $N \times 1$ complex-valued vectors \mathbf{x}_j stand for sensor array outputs, where j is the discrete time, $j = 1, \dots, J$. These vectors assumed to be zero-mean Gaussian distributed with the covariance matrix Φ_j

$$E\{\mathbf{x}_j \mathbf{x}_j^H\} = \Phi_j \delta_{jj}, \quad (2)$$

where δ_{jj} is the Kronecker symbol, $(\cdot)^H$ denotes Hermitian conjugation, and

$$\Phi_j = \theta_0 \mathbf{a}_j \mathbf{a}_j^H + \mathbf{K}, \quad (3)$$

the vectors \mathbf{a}_j represent time series of steering vectors varying due to source motion. The log-likelihood function for model (2) is

$$\Lambda(\theta_0, \mathbf{K}) = -\sum_{j=1}^J [\ln \det \Phi_j + \mathbf{x}_j^H \Phi_j^{-1} \mathbf{x}_j] - J \ln 2\pi \quad (4)$$

and inserting (3) into (4) results in

$$\Lambda = -J \ln \det K - \sum_{j=1}^J [\ln(1 + \theta_0 \omega_j) - \theta_0 \frac{|X_j|^2}{1 + \theta_0 \omega_j} + x_j^H K^{-1} x_j] - J \ln 2\pi, \quad (5)$$

where

$$\omega_i = \mathbf{a}_i^H \mathbf{K}^{-1} \mathbf{a}_i, \chi_i = \mathbf{a}_i^H \mathbf{K}^{-1} \mathbf{x}_i. \quad (6)$$

Therefore, a correct estimation of source power θ_0 requires simultaneous estimation of \mathbf{K} .

3. THE ADAPTIVE ESTIMATOR OF A SOURCE POWER

The maximum-likelihood equations for estimates of θ_0 and \mathbf{K} ,

$$\frac{\partial \Lambda}{\partial \theta_i} = 0, \left(\frac{\partial \Lambda}{\partial \mathbf{K}^{-1}} \right)^T = 0, \quad (7)$$

can be written as the system of two non-linear equations

$$\sum_{j=1}^J \left[\frac{\omega_j}{1 + \theta_0 \omega_j} - \frac{|\chi_j|^2}{(1 + \theta_0 \omega_j)^2} \right] = 0,$$

$$\mathbf{K} = \mathbf{X} - \theta_0 \frac{1}{J} \sum_{j=1}^J \frac{1}{1 + \theta_0 \omega_j} [\chi_j^* \mathbf{x}_j \mathbf{a}_j^H + \chi_j \mathbf{a}_j \mathbf{x}_j^H - (1 + \frac{\theta_0 |\chi_j|^2}{1 + \theta_0 \omega_j}) \mathbf{a}_j \mathbf{a}_j^H], \quad (8)$$

where

$$\mathbf{X} = \frac{1}{J} \sum_{j=1}^J \mathbf{x}_j \mathbf{x}_j^H$$

Direct solution of (4) is difficult. Thus, some simplification of (8) is required. Two assumptions can be taken into account for this simplification. The first one is that the sums in (8) are close to the sums of expectations.

$$\frac{1}{J} \sum_{j=1}^J [\cdot] \approx \frac{1}{J} \sum_{j=1}^J \mathbb{E}\{[\cdot]\},$$

when $J \gg 1$. The second assumption is that $\theta_0 \omega_j \ll 1$. Note that this dimensionless parameter characterizes signal-to-noise ratio (SNR), and the case of low SNR is of a greatest importance.

Using

$$\begin{aligned} \mathbf{E}\{\chi_j^* \mathbf{x}_j \mathbf{a}_j^H\} &= \mathbf{E}\{\chi_j \mathbf{a}_j \mathbf{x}_j^H\} = (1 + \theta_0 \omega_j) \mathbf{a}_j \mathbf{a}_j^H, \\ \mathbf{E}\{|\chi_j|^2\} &= \omega_j(1 + \theta_0 \omega_j), \end{aligned}$$

and the above mentioned assumptions, the following simplification of the second equation in (8) can be found

$$\mathbf{K} = \mathbf{X} - \theta_0 \mathbf{A}, \quad (9)$$

where

$$\mathbf{A} = \frac{1}{J} \sum_{j=1}^J \mathbf{a}_j \mathbf{a}_j^H$$

The same simplification of the first equation in (8) gives

$$\theta_0 = \sum_{j=1}^J (|\chi_j|^2 - \omega_j) / \sum_{j=1}^J \omega_j^2. \quad (10)$$

Inserting (9) into (10) results in the simple nonlinear equation for the estimate of θ_0 :

$$\theta_0 = \frac{\sum_{j=1}^J \{ |a_j^H (X - \theta_0 A)^{-1} x_j|^2 - a_j^H (X - \theta_0 A)^{-1} a_j \}}{\sum_{j=1}^J [a_j^H (X - \theta_0 A)^{-1} a_j]^2} \quad (11)$$

Substituting the solution (11) into (9) gives the estimate of unknown matrix \mathbf{K} .

4. NUMERICAL SIMULATION

The scenario for numerical simulation is illustrated by Fig. 1. The point source of Gaussian signal moves over a uniform linear sensor array; the source track is perpendicular to the array. The track parameters and the source velocity V are assumed to be known.

It was assumed that the current distances $r_{n,j}$ between the source and n th array sensors at j th time instance t_j are

$$r_{n,i} = \sqrt{r_0^2 + (Vt_i)^2 + (l_n - l_0)^2}$$

where $l_n = (n - (N + 1)/2)d$, $n = 1, \dots, N$, d is array spacing, r_0 , l_0 are track parameters. The current steering vectors for this scheme are

$$\mathbf{a}_j = \left(\frac{r_0}{r_{1,j}} e^{ikr_{1,j}}, \dots, \frac{r_0}{r_{N,j}} e^{ikr_{N,j}} \right)^T,$$

where $\kappa = 2\pi f_0 / c$, f_0 is the central frequency, and c is the propagation speed.

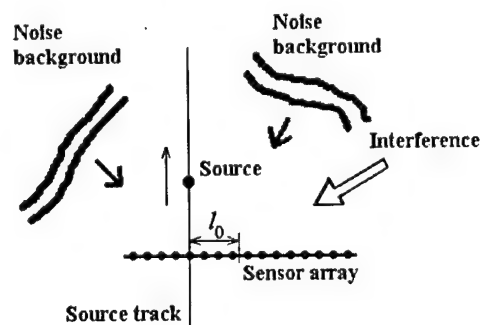


Fig. 1. Scheme for numerical simulation

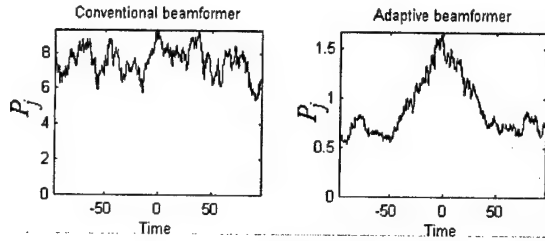


Fig. 2. Examples of conventional and adaptive estimator outputs

The estimates P_j of current power of array output in the presence of a uniform noise background can be written as

$$P_j = \left(\frac{1}{J_1} \sum_{j'=j-J_0}^{j+J_0} |a_0^H x_{j'}|^2 \right) / (a_0^H a_0)^2 \quad (12)$$

where $J_1 = 2J_0 + 1$ is an average interval, and the constant steering vector a_0 corresponds to a_j for the time instance $t_j = 0$, i.e. for the minimal distance r_0 between the source and the array. The estimate (12) involves a conventional beamformer with the steering vector a_0 . Maximum of P_j corresponds approximately to the source power θ_0 :

$$\max_j \{P_j\} \simeq \theta_0 + \sigma^2 / a_0^H a_0 \quad (13)$$

Some bias in this estimate can be easily eliminated. In the case of arbitrary noise covariance matrix, the estimate (12) should be rewritten using the adaptive beamforming

$$P_j = \left(\frac{1}{J_1} \sum_{j'=j-J_0}^{j+J_0} |a_0^H K^{-1} x_{j'}|^2 \right) / (a_0^H K^{-1} a_0)^2. \quad (14)$$

The numerical simulation of the above scheme was carried out for the examination of the proposed technique, which permits us to estimate simultaneously the source power θ_0 as well as the covariance matrix K . The estimate of this matrix is determined by (9) after inserting the solution of Eq. (11) into (9). Note that the estimation of K plays more important role as compared with the estimation of θ_0 , since (11) is more sensitive to the mismatch between the shape of source field covariance matrix at the sensor array and its model $\theta_0 a_j a_j^H$ in comparison with (13). The simulation was performed for the covariance matrix involving a uniform noise background and the strong interference:

$$K = \sigma^2 I + \sigma_{in}^2 a_{in} a_{in}^H$$

where I is identity matrix, and

$$a_{in} = (e^{-ikl_1 \sin \alpha_{in}}, \dots, e^{-ikl_N \sin \alpha_{in}})^T,$$

α_{in} is the interference DOA. It was assumed for simulation $\theta_0 = 1$, $\sigma^2 = 10$, $\sigma_{in}^2 = 10^2$, $\sin \alpha_{in} = 0.7$ and $N = 16$.

The results of the numerical simulation are illustrated by Fig.2 for the conventional beamformer (12) and adaptive beamformer (14) with inserting the estimate of covariance matrix (9).

As follows from Fig. 2, the adaptive estimator reproduces the increase and decrease of the array output power corresponding to source motion in contrast to the estimator using the conventional beamformer.

5. CONCLUSION

The maximum-likelihood parameter estimation technique was developed for snapshot vectors of sensor array output in the case of a moving source emitting white Gaussian noise and a non-uniform stationary unknown noise background. The simplified maximum-likelihood equations were derived for a great number of snapshots and low SNR. The effectiveness of this approach was confirmed by the numerical simulation.

ACKNOWLEDGEMENT

This work was supported by Russian Foundation of Basic Research, Grant 03-02-17035, and by the Grant of Russian Ministry of Industry and Science HIII-1641.2003.2.

REFERENCES

1. A. L. Matveyev, A. B. Gershman, and J. F. Boehme "On the direction estimation Cramer-Rao bounds in the presence of uncorrelated unknown noise", *Circuits, Syst., Signal Process.*, vol.18, pp.479-487, 1999.
2. M. Pesavento and A. B. Gershman, "Maximum-likelihood direction-of-arrival estimation in the presence of unknown nonuniform noise", *IEEE Trans. Signal Processing*, vol.49, pp.1310-1324, Jul.2001.
3. N. K. Vdovicheva, V. I. Turchin, and I. Sh. Fiks, "Remote sensing of moving wide-band sources", *Radiophysics and Quantum Electronics*, vol.41, No.9, pp.783-792, 1998.

AN ADAPTIVE PARAMETRIC ESTIMATION OF SPACE-TIME DETERMINISTIC SIGNAL AGAINST UNKNOWN GAUSSIAN NOISE BACKGROUND

A. A. Rodionov and V. I. Turchin

Institute of Applied Physics of RAS, Nizhny Novgorod, Russia
<turchin@hydro.appl.sci-nnov.ru>

Abstract

Parametric estimation technique for deterministic space-time signals on the output of linear sensor array in the presence of white Gaussian noise with unknown covariance matrix is considered. For this scenario, the derived maximum-likelihood statistics become invariant with respect to the structure of noise covariance matrix, i.e., using of derived statistics corresponds exactly to adaptive array processing. It was found that in the simplest case of one source and factorized spatial and time components of deterministic signal, the statistic can be represented exactly as the combination of two trivial statistics: the first one corresponds to conventional time matched filtering and adaptive beamforming with the weight vector obtained from empirical covariance matrix of snapshots (i.e., from observed mixture of noise and deterministic component), and the second one is the same statistic derived for unknown shape of steering vector. A stochastic numerical simulation showed that the statistic proposed eliminates some estimate bias appearing for the adaptive beamformer with inverse covariance matrix of snapshots.

Keywords: Maximum likelihood parametric estimation, adaptive space-time processing, adaptive beamformer.

1. INTRODUCTION

The widely used space-time signal model characterizing snapshots of array output, e.g., in radar or sonar applications, can be represented as an additive mixture of deterministic component of known space-time shape with some unknown parameters (complex-valued amplitude, direction of arrival, time delay, Doppler frequency shift, etc.) and zero mean random Gaussian component (ambient noise, interference, etc.). As a rule, the estimator of unknown parameters is derived from likelihood function providing asymptotic minimum of estimate covariance. Computational effectiveness of this approach often depends on the number of unknown parameters maximizing the likelihood function (LF). In some cases, on the first stage, particular LF maximum can be found analytically with respect to a subset of unknown parameters. Substituting these analytic estimates into LF gives the estimator for the rest of unknown parameters. This estimator does not depend on the parameters excluded on the first stage, i.e., it is invariant with respect to the values of excluded parameters. For instance, unknown parameters appearing linearly in the deterministic component and characterizing unknown complex-valued amplitudes are excluded in a well-known simple manner. A more complex problem is to exclude noise covariance matrix when it is unknown. Note that the estimator after excluding the covariance ma-

trix becomes invariant with respect to the structure of this matrix, i.e., exploiting of this estimator can be considered as the exact form of space-time adaptive processing [1].

Parametric estimation in the presence of unknown noise covariance has been recently studied for some models of snapshot vectors [2,3] under assumption that time waveforms corresponding to each source are unknown. Therefore, the problem was formulated as simultaneous estimation of these waveforms and directions of arrival. This work is focused on another problem: simultaneous estimation of several scalar parameters under assumption that both the spatial and time shapes of deterministic component are known. As will be shown, this model permits us to derive the estimators in a simple closed form.

2. GENERAL FORM OF ADAPTIVE ESTIMATOR

Consider the case when j th $N \times 1$ complex-valued snapshot vector of sensor array outputs \mathbf{x}_j can be modeled as

$$\mathbf{x}_j = \mathbf{m}(t_j, \theta) + \xi_j, \quad j = 1, \dots, J, \quad (1)$$

where $N \times 1$ vectors ξ_j are zero-mean white Gaussian noise with the unknown covariance ma-

trix $\mathbf{K} = E\{\xi_j \xi_j^H\}$, and $N \times 1$ vector $\mathbf{m}(t, \theta)$ represents the deterministic component with known space-time shape and unknown parameter vector θ . Log-likelihood function for the model (1) is

$$\Lambda(\theta, \mathbf{K}) = -[J \ln \det \mathbf{K} + \sum_{j=1}^J \delta_j^H \mathbf{K}^{-1} \delta_j + C], \quad (2)$$

$$\delta_j = \mathbf{x}_j - \mathbf{m}_j, \quad (3)$$

where $\mathbf{m}_j = \mathbf{m}(t_j, \theta)$, $C = J \ln 2\pi$, $(\cdot)^H$ stands for Hermitian conjugation. The estimate $\hat{\mathbf{K}}$ providing particular global maximum of (2) is found in a trivial manner (see, e.g., [4])

$$\hat{\mathbf{K}} = \frac{1}{J} \sum_{j=1}^J \delta_j \delta_j^H \quad (4)$$

Inserting (4) into (2) gives the statistic which is invariant with respect to the structure of noise covariance matrix:

$$\hat{\theta} = \arg \max_{\theta} T_i(\theta);$$

$$T_i(\theta) = \Lambda(\theta, \hat{\mathbf{K}}) = -J \ln \det \hat{\mathbf{K}} - J - C \quad (5)$$

where $\hat{\theta}$ is the maximum-likelihood estimate of parameter vector. Equations (3)–(5) represent general form of adaptive estimator. Note that (5) has a similar form to the statistics proposed in [2, 3], however (5) represents the exact form of maximum-likelihood statistic when the space-time shape of deterministic signal is known.

Evidently, Eq. (5) cannot be interpreted in terms of beamforming and matched time filtering. This interpretation can be given for simplified model of deterministic component with factorized spatial and time signals.

3. FACTORIZED MODEL OF SPACE-TIME SIGNAL

The simplest model of deterministic component in the case of one source and narrowband received signal can be formulated as follows:

$$\mathbf{m}_j = \theta_0 \mathbf{a} s_j, \quad (6)$$

where \mathbf{a} is a steering vector, s_j is time series, and θ_0 is the unknown complex-valued amplitude. It is assumed that both the spatial and time multipliers in (6) depend on unknown parameter vector θ_1 , i.e., $\theta^T = (\theta_0, \theta_1^T)$, where T denotes transpose. It is assumed that $J^{-1} \sum_{j=1}^J |s_j|^2 = 1$.

Implementation of the model (6) results in the following transformation of (4)

$$\hat{\mathbf{K}} = \mathbf{X} + (\theta_0 \mathbf{a} - \mathbf{y})(\theta_0 \mathbf{a} - \mathbf{y})^H - \mathbf{y} \mathbf{y}^H, \quad (7)$$

where

$$\mathbf{y} = \frac{1}{J} \sum_{j=1}^J s_j^* \mathbf{x}_j, \quad \mathbf{X} = \frac{1}{J} \sum_{j=1}^J \mathbf{x}_j \mathbf{x}_j^H. \quad (8)$$

Note that \mathbf{y} represents array output after conventional matched time filtering, and \mathbf{X} is the empirical covariance matrix of snapshots that are mixture of noise and deterministic component. Substituting (7) into (5) gives

$$T_i(\theta_1, \theta_0) = J \ln[\det \mathbf{X} \cdot T_{i,0}(\theta_1, \theta_0)] - J - C, \quad (9)$$

where

$$T_{i,0} = (\mu_{yy} - 1) \mu_{aa} - |1 - \mu_{ay}|^2, \quad (10)$$

$$\mu_{aa} = |\theta_0|^2 \mathbf{a}^H \mathbf{X}^{-1} \mathbf{a}, \quad \mu_{yy} = \mathbf{y}^H \mathbf{X}^{-1} \mathbf{y},$$

$$\mu_{ay} = \theta_0 \mathbf{y}^H \mathbf{X}^{-1} \mathbf{a}.$$

Further maximizing of (10) with respect to θ_0 results in the estimator of θ_1 :

$$\hat{\theta}_1 = \arg \max_{\theta_1} T_{i,1}(\theta_1),$$

$$T_{i,1}(\theta_1) = T_{i,0}(\theta_1, \hat{\theta}_0) - 1 = \frac{T_{a,s}}{T_{a,s} - T_s + 1} \quad (11)$$

where

$$T_{a,s} = \frac{|\mathbf{a}^H \mathbf{X}^{-1} \mathbf{y}|^2}{\mathbf{a}^H \mathbf{X}^{-1} \mathbf{a}}, \quad (12)$$

$$T_s = \mathbf{y}^H \mathbf{X}^{-1} \mathbf{y}. \quad (13)$$

We have found that the maximum-likelihood estimator (11) of parameter vector θ_1 is the simple combination of two well known statistics (12), (13) used in radar applications for evaluation of probabilities of false alarm and detection [1]. The first one is the adaptive beamformer combined with conventionally matched time filtering. The second one corresponds to incoherent spatial processing which can be employed when the shape of the steering vector is unknown, i.e., if each element of \mathbf{a} is an unknown parameter. Note that maximization of (11) with respect to \mathbf{a} yields the estimate $\hat{\mathbf{a}} = \mathbf{y}$ and the exact equality

$$T_{i,1} \equiv T_s \quad (14)$$

When only spatial signal parameters appearing in the vector \mathbf{a} are unknown, their estimation can be performed using (12) since (11) is the monotonous function of $T_{a,s}$. Another case of unknown time parameters appearing in the time series s_j (or when both the spatial and time parameters are unknown) requires simultaneous exploiting of both the Eqs. (12), (13) combined according to (11). Although (12) can be also used in this case, estimation performance becomes worse as compared with (11) as follows from numerical simulation.

Numerical stochastic simulation was performed for evaluating of estimation performance of the statistics (11), (12), (13) for uniform linear array. This simulation was conducted under assumption that $\mathbf{K} = \sigma^2 \mathbf{I}$, where \mathbf{I} is identity matrix. The estimation of frequency f was modeled, and source bearing was assumed to be known: $s_j = \exp 2\pi i f t_j$, $a_n = \exp(i 1.4 n)$, $N = 32$,

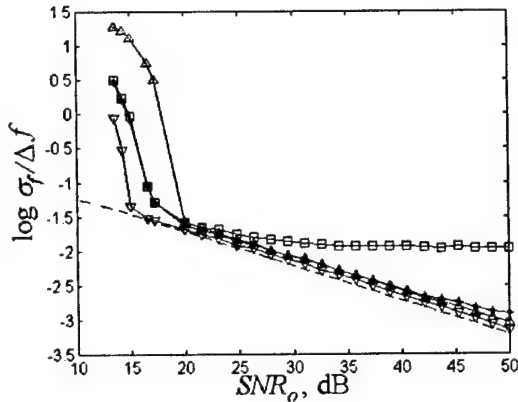


Fig. 1. The ratios $\sigma_f / \Delta f$ (log-scale) versus output SNR for the statistics (11) -*, (12) -□, (13) -▽, (15) -Δ and CRLB (dashed line)

$J = 128$ (the parameter vector θ_1 is represented by one scalar parameter f). The RMS of frequency estimate σ_f was computed for the statistics (11)–(13) and for the statistic $T_{a,s}^{(0)}$,

$$T_{a,s}^{(0)} = \frac{|\mathbf{a}^H \mathbf{y}|^2}{\mathbf{a}^H \mathbf{a}} \quad (15)$$

assuming the uniform noise covariance matrix is \mathbf{a} priori known. The simulation was performed with $\sim 10^5$ samples. The ratios $\sigma_f / \Delta f$ versus output signal-to-noise ratio SNR_o

$$SNR_o = 20 \log |\theta_0| / \sigma + 10 \log NJ \text{ [dB]},$$

are given in Fig. 1 with the Cramer-Rao lower bound (CRLB). Here, Δf is the resolution in the frequency domain: $\Delta f^{-1} = T \sim J$, T is observation time, and CRLB corresponds to the scenario with the known uniform covariance matrix.

As follows from Fig. 1, the statistics (11), (13) provide RMS of estimates close to CRLB when $SNR_o > 20$ dB. On the contrary, usage of the statistic (12) leads to some bias in the estimate; the difference

between RMS and CRLB increases with increasing of the output SNR. This fact can be explained by presence of deterministic component in snapshots used for computation of empirical covariance matrix \mathbf{X} . However, the difference between (11) and (12) is negligible in some range ($\sim 18 \dots 25$ dB) in the neighborhood of the output SNR corresponding to sharp increase of RMS.

4. CONCLUSION

Maximum-likelihood estimator for the mixture of deterministic space-time signal with known shape and white Gaussian noise with unknown covariance matrix is proposed; this estimator does not depend on the structure of arbitrary noise covariance matrix. For the simplest case of one source and factorized space-time signal the estimator can be represented exactly as the combination of well-known statistics: adaptive beamforming combined with conventional matched time filtering and spatially incoherent processing. Numerical simulation has confirmed that the estimator proposed has improved performance as compared to the well-known adaptive beamformer.

ACKNOWLEDGMENT

This work was supported by the Office of Naval Research

REFERENCES

1. K. F. McDonald and R. S. Blum, "Exact performance of STAP algorithms with mismatched steering and clutter statistics", *IEEE Trans. Signal Processing*, vol.48, pp.2750-2763, Oct.2000.
2. M. Pesavento and A. B. Gershman, "Maximum-likelihood direction-of-arrival estimation in the presence of unknown nonuniform noise", *IEEE Trans. Signal Processing*, vol.49, pp.1310-1324, Jul.2001.
3. M. Agrawal and S. Prasad, "A modified likelihood function approach to DOA estimation in the presence of unknown spatially correlated Gaussian noise", *IEEE Trans. Signal Processing*, vol.48, pp.2743-2749, Oct.2000.
4. Y. Bard. *Nonlinear Parameter Estimation*, Academic Press, N.Y., 1974.

ADAPTIVE ALGORITHM OF FILTRATION OF TARGET TRAJECTORY PARAMETERS

Karlov V. D., Rafalskiy U. I., Yarovoy S. V., Petrushenko N. N., Chelpanov A. V.

Abstract

The algorithm of filtration of the targets trajectory parameters which provides detection and recognition of abnormal situations and target manoeuvre and selection of abnormal observations, measurement and the registration of acceleration at target manoeuvre and increases an accuracy of the target trajectory parameters estimation is considered.

The use of a deterministic trajectory model during tracking targets leads to the non-optimum filtration of its parameters, what, in its turn, reduces a noise stability of the tracking regime.

Under real conditions the difference between the parameters of a target trajectory and the deterministic model is stipulated by the presence of abnormal situations (due to failures of the measuring equipment) and by the target manoeuvre.

The account of a possibility of abnormal situations (AS) and manoeuvre of the tracked target leads to the necessity of widening an effective filter pass band and, hence, to worsening the accuracy performances when estimating trajectory parameter of non-maneuvring targets.

The algorithms of filtration of parameters of a target trajectory which are most similar to the proposed one, are described in [1, 2]. Their key feature is a too cumbersome scheme and therefore, a considerable scope of evaluations to be carried out.

The authors have tried to avoid shortages of similar algorithms in the offered algorithm [1, 2]. The detection and recognition of AS and the target manoeuvre, the AS selection, measurement and account of acceleration at the target manoeuvre is implemented in the algorithm. Thus, the accuracy of estimation of target trajectory parameters has been increased.

The sequence of the information processing can be divided into two stages.

At the first stage, the recurrent filtration of measurements over basic points ($i = 1, 2, \dots, n$) with an estimation of current values of target trajectory parameters (coordinates and derivatives) \hat{x}_{1i} , \hat{x}_{2i} and errors correlation matrix (ECM) y_{1i} is carried out in a Kalman filter. Besides, the sequence of tracking dynamic errors – mismatches between the measured and extrapolated values of parameters (values of discrepancy) Z_{1i} is formed.

At the second stage of processing in a Kalman filter, the accumulated sequence of measurements beginning from the last basic point

$y_i = y_{n-i+1}$ ($j = n - i + 1$) with an estimation of trajectory parameters (\hat{x}_{2j} , \hat{x}_{2j} , y_{2j} , Z_{2j}) is filtrated.

Then, the aggregate sequence of absolute values of discrepancies relevant to basic points is formed:

$$Z_{ci} = |Z_{1i}| + |Z_{2n-j+1}|. \quad (1)$$

It is necessary to recognize abnormal discrepancies in the obtained sequence of discrepancies Z_{ci} , and by their values the solution about the presence of AS or target manoeuvre has to be made. The analysis is carried out over samples S_k in a "sliding" m -size window:

$$S_k = \sum_{i=k-m+1}^k Z_{ci}, \quad (2)$$

where $k = m, m+1, \dots, n$.

The size of the window is defined by an amount of abnormal discrepancies caused by AS (or target manoeuvre). As a rule, one AS causes occurrence of two-three abnormal discrepancies [3]. Taking into account that the analysis is conducted over a sequence of aggregate values Z_{ci} , the number of abnormal discrepancies is doubled and the size of the window m has to be chosen five, i.e. $m = 5$ (in primary sequences, the abnormal discrepancies are located on different sides from AS).

The solution about the presence of AS is made when values S_k exceed some threshold S_0 :

$$S_k \geq S_0. \quad (3)$$

If there are several such values (in succession), the maximum one is taken:

$$S_r = \max_k \{S_k\}. \quad (4)$$

Taking into account shifting by $m/2$ of a serial number of maximum sample S_r with respect to the number of AS, there is taken the AS number equal to

$$\xi = r - 2. \quad (5)$$

The AS selection is carried out by assigning a weight of $P_\xi = 0$ to AS with the number ξ .

The abnormal discrepancies take place even in the case of target manoeuvre at the discordance of a real

target trajectory with the chosen model (degree of an approximating polynomial).

Therefore, in the case of exceeding a threshold of a detection $S_k \geq S_0$, the additional analysis on the presence of target manoeuvre is necessary.

The basic feature of parameters of maneuvering target trajectory is that the values of estimations of their modification rate \hat{x}_ξ differ on intervals under observation, which are located before the manoeuvre area (at $i = 1, 2, \dots, \xi - 1$) and after it ($i = \xi + 1, \xi + 2, \dots, n$), i.e. the component of acceleration $g = \ddot{x}_\xi$ takes place.

Therefore, the manoeuvre detection is carried out by comparison of the threshold g_0 with a value of acceleration:

$$g_\xi \geq g_0, \quad (6)$$

where $g_\xi = \hat{x}_{\xi+1} - \hat{x}_{\xi-1}$, $\hat{x}_{\xi-1}, \hat{x}_{\xi+1}$ are current estimates of the rate obtained at a filtration of direct and inverse sequences of basic points of the target trajectory.

In order to define the quality performances of AS detection or target manoeuvre, it is necessary to know the distribution law of discrepancy values in the presence and absence of the perturbing factors.

In the absence of AS "the updating process" Z_i is white Gauss noise with a mean value and variance equal to [3]:

$$M\{z\} = 0; \quad D\{z\} = 1.5\sigma_x^2, \quad (7)$$

where σ_x^2 is the variance of separate measurements.

For sample of m aggregate discrepancies S_k we obtain

$$D_S = 3m\sigma_x^2. \quad (8)$$

In the presence of perturbations (AS, manoeuvre) there is a bias of discrepancy values $\Delta_n = M\{S_k\}$, according to the magnitude of a measuring error or manoeuvre intensity.

For a measurement error δ the mean value of an abnormal discrepancy makes the magnitude [3]:

$$\Delta_n = \frac{1}{2}\delta. \quad (9)$$

The mean value of the discrepancy due to the target manoeuvre with intensity g varies according to a square component law [3]:

$$\Delta_{ni} = \varphi(i) \frac{T^2(i - \xi)^2 g}{12}, \quad (10)$$

where T is the rate of the information updating; ξ is the number of a basic point relevant to the beginning of manoeuvre; $\varphi(i)$ is the smoothing function.

The AS probability of false detection (or manoeuvre) can be presented through an integrated cumula-

tive distribution function of the normal random variable:

$$P_{fd} = 1 - F\left(\frac{S_0}{\sqrt{D_S}}\right). \quad (11)$$

Correspondingly, the AS detection probability is:

$$P_0 = F\left(\frac{S_0 - \Delta_n}{\sqrt{D_S}}\right), \quad (12)$$

where

$$F(x) = \frac{1}{\sqrt{2\pi}} \int_{-\infty}^x \exp\left(-\frac{t^2}{2}\right) dt. \quad (13)$$

The threshold magnitude S_0 is chosen basing on the specified probability of false alarm.

It is possible to estimate the positive effect achieved with the proposed algorithm in the following way.

First of all, the estimation accuracy increases at the expense of removing AS from a sequence of filtrated basic points.

Second, at manoeuvre detection, estimation and taking into account acceleration, the trajectory parameters are determined with the higher accuracy, since the square-law component is taken into account (10).

Third, at the two-sided filtration, as compared with the recurrent algorithm, the size of measuring sample used during processing increases. Because of this, the accuracy of trajectory parameter estimations and reliability of AS and manoeuvre detection increases.

Quantitatively the gain B in the potential accuracy of the smoothed estimation at two-sided filtration as compared with usual recurrent processing can be estimated with the help of a variances ratio [4]:

$$B = \frac{D_{x1}}{D_{x2}} = 2 - \frac{2}{1 + \sqrt{1 + q}}, \quad (14)$$

where D_{x1} , D_{x2} are estimation variances at one-sided and two-sided filtration of measurements, respectively; q is the signal/noise ratio at carrying out the measurements, which defines the variance of separate samplings. At $q \gg 1$, value B tends to two.

REFERENCES

1. Kuz'min S. Z. Digital radiolocation. - K.: KVIC, 2000. - 255 p. (in Rus.)
2. Grishin U. P., Kazarinov U. M. False-safe dynamic system. - M.: Radio i svyaz, 1985. - 185p. (in Rus.)
3. Savrasov U. S. Algorithms and programs in a radiolocation. - M.: Radio i svyaz, 1985. - 216 p. (in Rus.)
4. Tikhonov V. I., Kharisov V. N. A statistical analysis and synthesis of radio engineering devices and systems. - M.: Radio i svyaz, 1991. - 608 p. (in Rus.)

SIGNAL PROCESSING USING METHODS OF DIMENSIONALITY REDUCTION OF REPRESENTATION SPACE

Popovskiy V. V.

Kharkiv National University of Radio Electronics, Department of
Telecommunication Kharkiv, Ukraine

Abstract

The universal method of processing of signals with the help of downturn of their dimension is considered

1. INTRODUCTION

It is known [1, 2] that transfer from one-dimensional signal presentations $S(t)$ to 2 or more dimensional enables to involve additional physical parameters and properties, extending possibilities on their modulation, processing, increasing interference-free-feature, etc. Thus, [1, 3] for n -dimensional signals such important properties as polarization and level of this polarization, coherence and level of coherence, can be indicated. For the signals, extending presentation in the time and frequency domain, it is possible to get the time-bandwidth product $B = \Delta F \cdot \tau \gg 1$, where ΔF is the occupied frequency content, τ is the duration of information pulse.

2. THE ESSENCE OF THE METHOD

Random signal processing in a common case is reduced to getting presentation of this signal $\vec{S}(t)$ from the set of its presentation $\{S\}$ to the set of its solutions $\{R\}$, as a rule, consisting of the determinate values:

$$S \xrightarrow{f} R. \quad (1)$$

Dimensionalities (dim) of sets $\{S\}$ and $\{R\}$ can coincide or can be different. It is known from the theory of sets that presentation (1) in

$$\dim \{S\} > \dim \{R\} \quad (2)$$

is confluent and in a common case is connected with information loss. However, in practice the presentation of (2) type is often used in reception and processing of communication signals. So, in usual meeting of the conditions in reception $\dim \{R\} = 1$ (single-fold reception) use of space or other method of diversification onto N - branches, when $\vec{S}(t) = (S_1(t), S_2(t), \dots,$

$\dots, S_N(t))^T$, is a confluent presentation of space values of random N -dimensionality signals into one-dimensional space of solutions $\{S\}$ in the output of the count detector or demodulator. The positive properties, obtained by this, are as follows: fading depths on the count detector output in comparison with fading in independent reception branches enable to improve the equivalent signal-interference situation by dozens decibels.

Presentation (2) of such a type takes place in the space-time processing of signals using adaptive antenna arrays (AAP), aimed at space-concentrated interference elimination $\xi(t)$. If on the input of each of the antenna elements AAP the distribution density is $w(\vec{S}(t)/\vec{\xi}(t), t)$, then we obtain conversion of the density to the presentation

$$w(\vec{S}(t)/\vec{\xi}(t), t) = w(\vec{S}(t), t), \quad (3)$$

on the total count detector output, that enables further using of standard methods of optimal decision-making (integral reception, reception using the matched filter, etc.) Fig. 1 shows common structural diagram of N - element AAP with the amplification weight factors $W(t)$, forming vector $\vec{w}(t) = (w_1(t), w_2(t), \dots, w_N(t))^T$, included into each of N reception branches.

Figure 2 shows general structural diagram of reception of N -position broad-band signal (BBS) $\vec{S}(t)$. When using N - position pseudorandom sequence (PRS) and when this PRS coincides with the reference one, the equivalent signal-noise ratio on the output of the total count detector in the known PRS increases by the base times. By this increasing of interference-free-feature of reception is achieved by the base times.

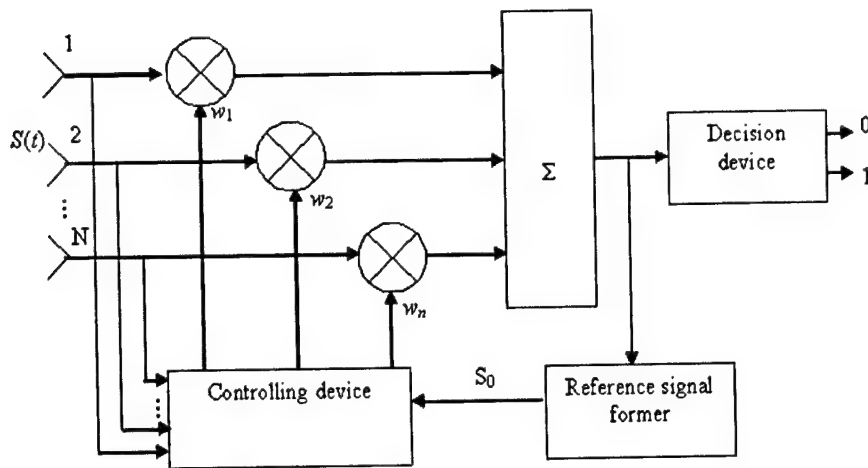


Fig. 1. General Structural Diagram

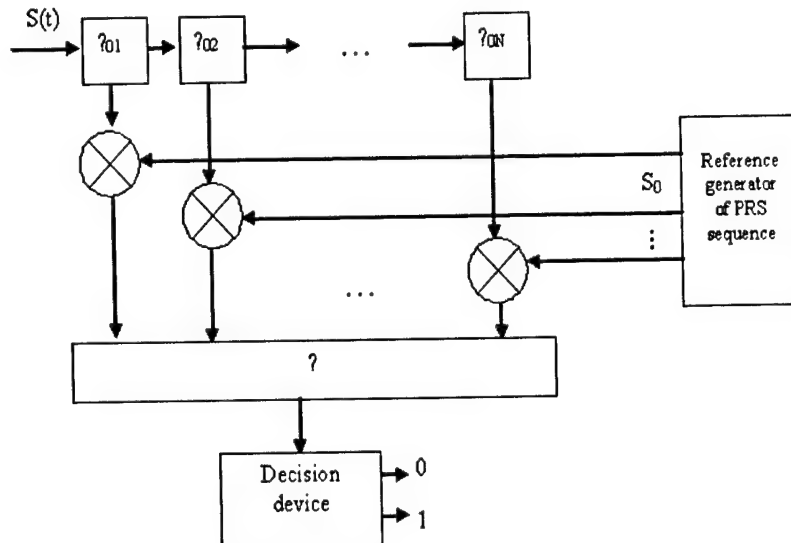


Fig. 2. General Structural Diagram of N Position Signal Reception

Comparison of algorithms on Figures 1 and 2 shows closeness of their structural diagrams. The algorithm of signal reception with the transversal filter is reduced to the similar type of diagrams. We can indicate a number of other algorithms where presentation from N -dimensional to one-dimensional space is made with acquiring useful properties.

From the mathematical point of view [4], selecting such presentation (2) and obtaining statistics (3), we achieve fulfillment of sufficiency of this statistics. Thus [4], if the interference parameter θ of the condition of getting the sufficient statistics t , not dependent on θ , is calculated as follows:

$$M\{c(v)\} = \int c(v)h(x/t)g(t/\theta)dx = \quad (4)$$

$$= M\{M(c(v)/t)\},$$

where mathematical expectation $M\{\cdot\}$ beyond the braces is taken by distribution of t statistics. So,

function from t $M(c(v)/t)$ does not depend on θ , because t - sufficient statistics.

This work has methodical, generalizing nature, and is aimed at drawing the attention of specialists and scientists to the unity of the definitions and solutions of the problems, connected with N -dimensional presentation and confluent presentations.

REFERENCES

1. Andropov I. S., Fink L. M. Transfer of discrete messages by parallel channels. - M.: Sov. Radio, 1971, - 408 p.
2. Podimov A. P., Popovskiy V. V. Statistic theory of polarization-time signal processing in communication lines. - M.: Radio i Sviaz, 1984 - 272 p.
3. Monzingo Miller. Adaptive antenna arrays.
4. Kendall M., Stuart A. Statistic conclusions and links. - M.: Nauka, 1973 - 900 p.

ADAPTIVE ANTENNA ARRAYS IN THE AUXILIARY RECEIVING CHANNEL OF THE INTERFERENCE COMPENSATOR FOR USER RADIOACCESS SYSTEMS

Kolyadenko Yu. Yu.

Department of Telecommunicationa, Kharkiv National University of Radio Electronics, Kharkiv, Ukraine

Abstract

The principles of construction of adaptive interference compensators for user radioaccess systems are considered. It is proposed to use the adaptive antenna array in the basic receiving channel, which will allow adjusting zero of the radiation pattern in a direction of arrival of a useful signal. The analysis of the efficiency of the adaptive interference compensator with the adaptive basic receiving channel is carried out. It is shown, that the efficiency of such an adaptive compensator is constant at any direction of a signal arrival except when angles of arrival of the signal and interference concur.

1. INTRODUCTION

User Radioaccess Systems (URAS) have come into growing popularity. They received the most application in organization of local networks, where owing to small distances one can manage with signal levels of less than 1 W. These powers are so small that they practically do not create interferences for other systems. This circumstance enabled authorities regulating a radio-frequency spectrum to allow the work of these systems without license and registration at range domains allotted for the work of industrial, medical, domestic devices and plants. Namely from these devices and plants, there is possible the interference exposure, which can appear significant and capable to prevent the normal work of URASs.

Besides, there are enough sources of other interferences: various contact groups, car ignition systems, arcing, welding and much another things of natural and artificial origin, which may be interpreted as external interferences.

Thus, it turns out to be problematic to organize radio-communication at non-licensed domains of the radiofrequency range. Many URASs developed for the use at non-licensed domains of a radio-frequency spectrum, have no any protective functions, methods or algorithms, whereas some URASs, for example, those using IEEE 802.11 protocols are provided with several such functions (frequency DFS and power control TPC).

For the impulse and other spatially lumped interferences control, rather effective is a method of space-

time signal processing with the help of adaptive antenna arrays (AAA) and adaptive interference compensators (AIC) [1,2,3]

2. THE ESSENCE OF THE METHOD

As a reference signal for AAA, there can be used the information about the direction of arrival (DOA) of the useful signal. However, in the presence of a powerful interference, it is difficult to define DOA in URAS.

In AIC, a reference signal is being formed in an auxiliary receiving channel (ARC), wherein the useful signal is absent.

The problem of removal of the useful signal $s(t)$ in the auxiliary channel is an original problem. For its solution, there can be used, for example, the information about $s(t)$ DOA or polarization. Then directing the ARC antenna by a RP null or by null of the polarization pattern to a signal $s(t)$, we shall obtain the value to be found as

$$y_o(t) = n_o(t) + v_o(t), \quad (1)$$

where $n_o(t)$ is an interference in ARC, $v_o(t)$ is noise in ARC.

Under real conditions – inside or outside, a direction to an interference source hardly will become known, and besides, a maintenance staff poorly familiar with the electromagnetics and antenna theory hardly will manage with proper mounting of an antenna of the auxiliary channel. In addition, DOA of the useful signal can permanently changing, what re-

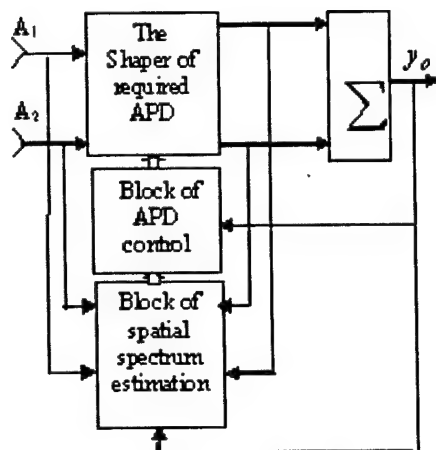


Fig. 1.

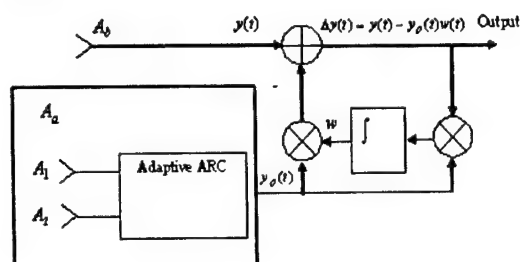


Fig. 2.

quires readjustment in real time of the ARC antenna RP zero in its DOA. For solution of the problem of adaptive compensation of interferences, it is necessary to find such technical solutions, that all specified actions of organization of the auxiliary channel were as much as possible simplified, automatized or formalized.

In this paper, the possibility of application in ARC of a two-element AAA is considered. For formation of the required amplitude-phase distribution (APD) of the field on the AAA aperture, there is used a device of a signal spatial spectrum estimation.

The algorithm of formation of the field optimum APD on the aperture of the ARC antenna array analytically is as follows

$$\hat{\tilde{w}}(t)_{out\ b} = R_{yy}^{-1} R_h, \quad (2)$$

where R_{yy} is the correlation matrix of the mixture of signals, interferences and noise received by the antenna array; R_h is the controlling interference vector (CIV).

The block diagram of ARC formation is given in Fig. 1.

In the block of the spatial spectrum estimation, the DOA of the sufficiently powerful interference is being defined. Further this information is used for formation of R_{sp} and R_{p} in the block of the APD control.

An estimate of the weighing coefficient vector $\tilde{w}(t)$ for ARC is found as a result of some gradient

procedure, for example, a recursive procedure with a constant step factor μ :

$$\frac{d\hat{w}(t)}{dt} = \mu y_o(t) \Delta y(t). \quad (3)$$

Fig. 2 shows a block diagram of AIC synthesized in accordance with equation (3). Obviously, the procedure of CIV estimation by (3) may be modernized and reduced, for example, to the Robins-Monro, Newton-Raphson or Kalman-Biusi expression [3,4].

The comparative analysis of the efficiencies obtained by (3) for AIC with ARC and without it is carried out. In this case, dipoles with one wavelength quarter arm were used as antennas. The ARC antenna is focused by the RP zero to 0° .

As a criterion of the AIC efficiency, there is taken the parameter traditional for problems of space-time signal processing – signal-interference-noise-ratio (SINR) being here a ratio of a level of useful signal P_s to the sum of levels of a narrow-band interference P_i and such an interference as white noise P_n received at the waveband of the useful signal. In order to obtain numerical values, the following ratios between levels of realizations received in the main channel are taken as initial ones: $P_s/P_n = 20$ dB,

$P_i/P_n = 30$ dB. The interference DOA is $Q_i = 90^\circ$.

The experiment computer simulation consisted in that when changing an angle of arrival of the useful signal, its power in ARC also changed at the expense of the antenna transfer factor. The leakage of the useful signal into the auxiliary channel destructively influences on the AIE efficiency. We have obtained SINRs also at the compensator output.

There are shown in Fig. 3 the dependencies of SHNR for AIC with the adaptive ARC (a) and with the usual ARC without tuning (b), respectively.

From the obtained plots, it is seen that the efficiency of AIC with the adaptive ARC decreases insignificantly (by 3.3.5 dB), when angles of arrival of signal and interference coincide. In this case, in ARC, the effect of AAA blinding displays itself. At the same time, the more an interference level, the less this effect shows itself. For comparison, in Fig. 3a (a top curve) the dependence SINR at $P_i/P_n = 50$ dB is given.

Fig. 3b shows the dependence of SINR versus an angle of arrival of a signal without adaptive ARC. From the obtained plot it is visible, that in process of moving of a useful signal source, the efficiency in the beginning reduces smoothly. Herewith the effect of leakage of the useful signal into ARC reveals itself. When a level of signal reaches values of over $0.7P$, what corresponds to $Q \sim 60^\circ \dots 120^\circ$, the efficiency decreases sharply, for together with the interference, the useful signal is being compensated too.

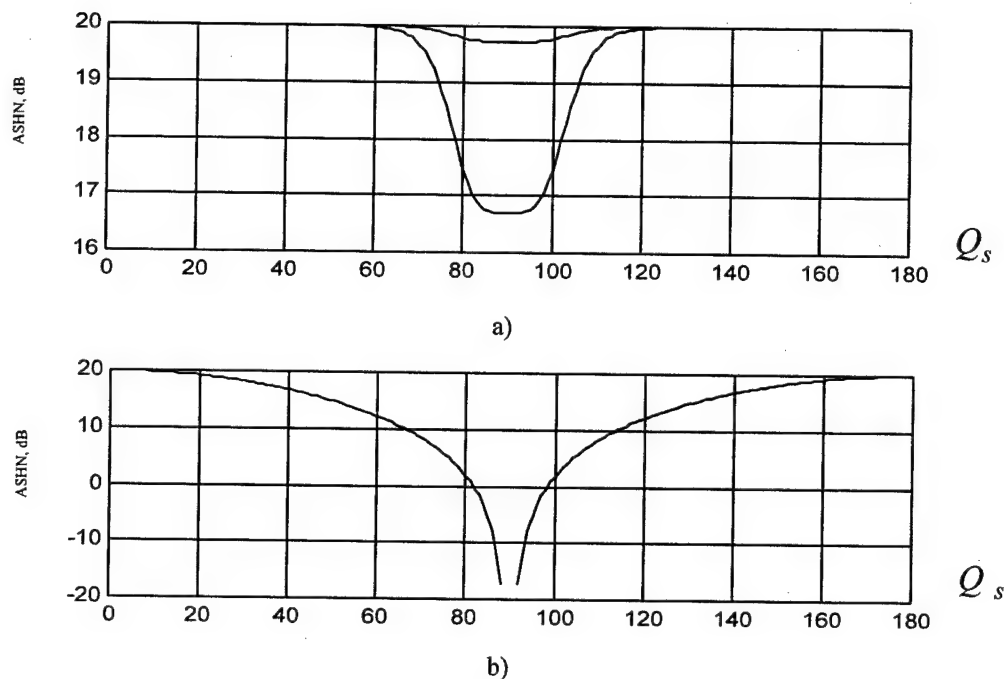


Fig. 3.

REFERENCES

1. B. Widdrow *et al.* Adaptive unterference equalizers. Principles of construction and applications. // translated Proceedings of IEEE 1975. V.63. №12. P. 69-99.
2. R. A. Monzigo, T. U. Miller Adaptive antenna arrays: Introduction in theory. Trnsl..from Eng.. M.: Radio I svyaz', 1986. - P.486. (in Russian)
3. Rodimov A. P., Popovskiy V. V. Statistical theory of polarization-time processing of signals and interferences M.: Radio I svyaz'. 1984. P. 272. (in Russian)
4. Popovskiy V. V. Equalizer of interferences for multi-channel measurer // Izvestiya vuzov. Radioelektronika. 1985. V. 28, № 3. pp. 84 - 86. (in Russian)
5. Popovskiy V. V. Adaptive antenna array with the equalizer of interferences at the input // Antenny № 35, M.: Radio I svyaz'. 1987. pp.50-55. (in Russian)
6. Shifrin Ya. S. Questions of the statistical antenna theory - M. Sovetskoe Radio, 1970 (in Russian) Published in English as "Statistical Antenna Theory", Golem Press, Co, USA, 1971.
7. Greene C. A., Moller R. T. The effect of normally distributed random phase errors on synthetic array gain patterns // IRE Trans. 1962. Vol. MIL-6. No 2, p. 130.

INTELLECTUAL ANTENNAS AND ELECTROMAGNETIC COMPATIBILITY IN THE FUTURE SYSTEMS OF MOBILE COMMUNICATION

Blinov V. S.

Kharkov National University of Radioelectronics, Kharkov, Ukraine
<blinov@kture.kharkov.ua>

Abstract

The tendencies of increase of knowledge of a society, the growth of mobility of population, the increase of loading on systems of a radio communication, including mobile and systems of a user radio access, aggravate the problem of electromagnetic compatibility and rational use of a radiospectrum [1]. Avalanche growth of number of subscribers of such systems, volume and kinds of the transmitted information stimulate the alternation of generations of systems to more perfect. The important role in reconciliation of inconsistent requirements of high throughput and EMC of radiomeans should be played by antennas of radio stations. They, probably, should be adaptive, intellectual, advanced aeriels. It is the subject of the given research.

Key words: intellectual antennas, mobile communication, user's radioaccess, electromagnetic compatibility

1. INTRODUCTION

Mobile communication and user's radio access develop in the world rough rates [2]. The spectrum and quality of given services continuously extends, they become mass, popular and adapted to individual needs of users. According to the forecasts of analysts significant growth of the share of incomes of operators from granting services of data transmission is expected in the nearest years. The companies that have the licenses for granting of services of mobile communication of 3-rd generation is expected become the largest Internet providers.

Systems of mobile communication are created on the basis of three base technologies of a radio access:

FDMA-Frequency Division Multiple Access;
TDMA-Time Division Multiple Access;
CDMA-Code Division Multiple Access.

2. POSSIBILITY OF GENERATIONS OF MOBILE COMMUNICATION AND RADIO ACCESS

The first-generation (1G) in 1970s and second-generation (2G) of cellular systems in 1980s were used mainly for voice transmission and to support circuit-switched services [3]. 1G systems were implemented based on analogous technologies. However, 2G systems were digital systems such as the Global system for Mobile Communication (GSM), IS-54 Digital Cellular, Personal Digital Cellular System (PDS) and IS-95. The systems operate nationwide or

internationally, and are mainstream systems nowadays. The data rates for users in air links of the systems are limited to less than several tens kilobit per second.

At the end of 1999 the ITU-R Sector approved the specifications of the International Mobile Telecommunication in 2000 (IMT-2000) of 3G relatively radio-interfaces (RF front-end), which involve terrestrial components (Mohr 2000):

- IMT-2000 direct spread CDMA based on 3GPP concept;
- IMT-2000 multicarrier CDMA based on 3GPP2;
- IMT-2000 TDD CDMA based on 3GPP concept;
- IMT-2000 single-carrier TDMA based on the evolution of ANSI-136 with EDGE and a high speed mode;
- IMT-2000 multicarrier TDMA based on the DECT concept.

IMT-2000 is an important step to enable such services. Therefore, direct services applied via different access systems will be moving forces for future developments.

It is expected that due to the dominating role of mobile radio access the number of portable handsets will exceed the number of PCs connected to the Internet in 2004 approximately. Therefore, mobile terminals will be major human-machine interface in the future instead of PCs.

Key possibilities of next generation of mobile communications are multimedia communications, wireless access to broadband fixed networks, and free roaming

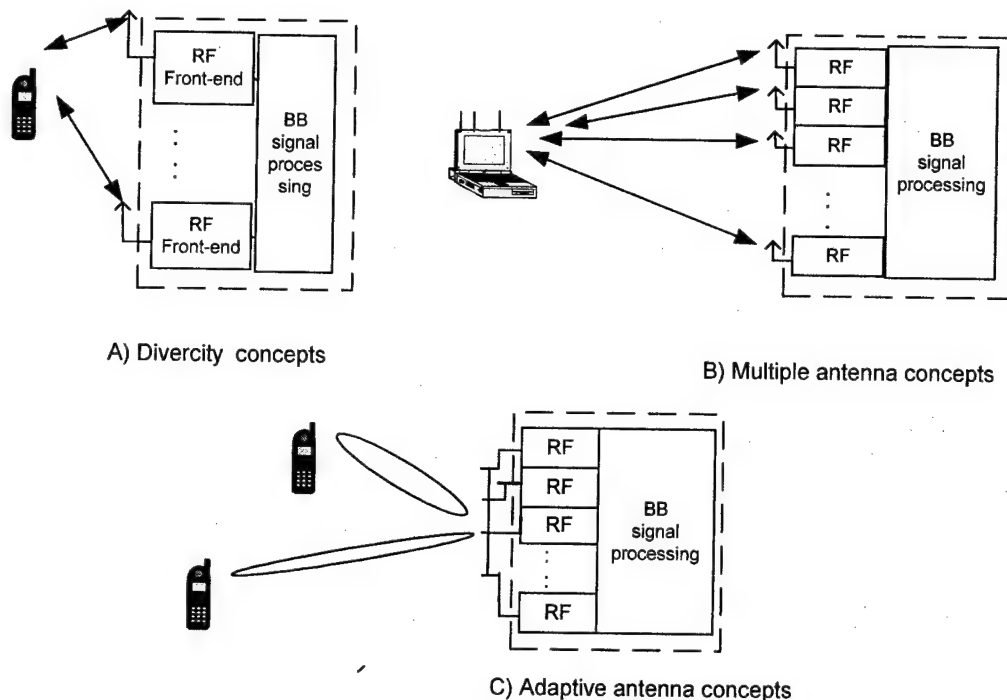


Fig. 1. Intellectual antenna concepts

roaming among different systems [3]. The next generations include the fourth (4G) and fifth generations (5G), and 4G is used in a broad sense to include several systems. Also many new types of communication systems such as broadband wireless access systems, millimeter-wave LANs, intelligent transport systems (ITSs), and high altitude stratospheric platform station (HASP) systems are appeared. When 4G systems are used in a narrow sense as cellular systems, they will be specified as 4G-cellular. Generations of mobile communications, and their key words and typical systems are shown in Table [3].

3. ELECTROMAGNETIC COMPATIBILITY AND ADVANCED ANTENNA CONCEPTS

Future mobile and access systems have to use the frequency resources as efficiently as possible [4]. Therefore, several physical-level-related techniques have to be investigated:

- Optimization of development and upgrade of access systems by channel modulation and coding schemes for further enhancement of spectrum efficiency and system performance;
- Advanced detection schemes such a multiuser detection and interference cancellation that can gain from a priori knowledge about intra- and intercell interference signal;
- Signal processing algorithms to trade off between performance gain and computing complexity;
- Compression techniques for source signal coding to reduce the needed user data rate.

The improvement of algorithms of supporting this mainly physical level must be expressed in the following:

- Link adaptation according to the channel conditions, traffic load and services for better usage of the frequency resources and improvement of system performance;
- Spectrum is shared between different systems during the investigation of coexistence conditions between different radio access systems;
- Advanced antenna improves link quality and channel capacity (Fig. 1).

These concepts are used to increase the channel capacity of the radio link. Diversity concepts (Fig. 1A) basically reduce the impact of fading due to multipath transmission. Multiple antenna concepts (Fig. 1B) are a further extension of diversity concepts gaining from uncorrelated multipath transmission channels between the different antenna elements on base station and terminal sides. The basic idea is to reuse the same frequency band simultaneously for parallel transmission channels by space-time coding to increase the channel capacity

Adaptive antenna concepts (Fig. 1C) improve link quality by reducing the co-channel interference from different direction and, in the more advanced space-division multiple access (SDMA) concept, by reusing the same frequency channels simultaneously for different users in distinct directions. System aspects are similar to common control channels and the signal transmission concept. They are an essential part of advanced antenna concepts in order to achieve the

	1980s	1990s	2000s	2010s	2020s
Generation	First	Second	Third	Fourth	Fifth
Keywords	Analog	Digital personal	Global word standards	High data rate High mobility IP-based	High data rate High mobility IP-based
Systems	Analog cellular Analog cordless	Digital cellular (GSM, IS-54, PDC) Digital cordless (DECT, PHS)	IMT-2000 (3G-cellular)	4G-cellular Broadband access ITS, HASP	5G-cellular Broadband access ITS, HASP
Data rate Mb/c			2	2-20	20-100

same range extension for common control channels as for traffic channels.

These are key concepts using the frequency spectrum as efficiently as possible without major impact on evolving access systems. Concepts like Universal Mobile Telecommunication System (UMTS) have already taken into account necessary prerequisites for adaptive antenna concepts. However, economic implementation of the different RF front-ends and baseband signal processing are technical problems. Table. Classification of Generation of Mobile Communications

Design and evaluation of the system requires a realistic wideband channel characterization for new frequency bands up to about 60 GHz. Channel models based on wideband propagation measurements are needed for international standardization process, taking into account the models for direction of wave arrival [4].

Smart antennas have intelligent functions such as suppressions of interference signals, and digital beamforming with adaptive space-time processing algorithms [3]. Owing to these characteristics smart antennas have been considered as key technologies for future mobile communications. One type of smart antennas, adaptive array antennas (AAAs), are expected to reduce interference and lower transmission power.

Interference canceling with an AAA and an interference canceling equalizer (ICE) promise to increase capacity of the systems [3].

REFERENCES

1. Blinov V. S., Moskalets N. V. System aspects of creation of information system of radio-frequency monitoring // Materials of 1-st International Radio-electronic Forum « Applied radioelectronics. A condition and prospects of development »-Kharkov-2002.
2. Shvidenko G. L. The condition, level and tendencies of development of mobile communication in the world and Ukraine // Materials of scientifically-practical conferences „ Radio technologies in development and modernizations of rural and suburban communication ”-Kyiv, Ukrtelecom-2001.
3. Ohmori S., Yamao Y. The Future Generations of Mobile Communications Based on Broadband Access Technologies // IEEE Communication Magazine-Vol.38, No 12, p.p. 134-142.
4. Mohr W., Konhauser W. Access Network Evolution Beyond Third Generation Mobile Communications // IEEE Communication Magazine-Vol.38, No 12, p.p.122-133.

Authors List

A

<i>Acosta-Salas J.</i>	97
<i>Ahn D.-S.</i>	87
<i>Akhoondzadeh L.</i>	509
<i>Alpatova A. V.</i>	248
<i>Andreev M. V.</i>	401
<i>Andrenko S. D.</i>	300
<i>Andriychuk M. I.</i>	199
<i>Anohina O. D.</i>	748
<i>Antipov I. E.</i>	518
<i>Antonov A. V.</i>	485
<i>Antonyuk V. P.</i>	512
<i>Antyufeyev V. I.</i>	671
<i>Ardenne A.</i>	633
<i>Artishev A. I.</i>	667
<i>Artuynov S. V.</i>	345
<i>Atamansky D. V.</i>	394
<i>Averin I. M.</i>	333
<i>Avgust I. V.</i>	726

B

<i>Bagatskaya O. V.</i>	785, 830
<i>Bagdasaryan S. T.</i>	381
<i>Bagno D. V.</i>	362
<i>Bakhrakh L. D.</i>	535
<i>Bakhvalov V. N.</i>	318, 320
<i>Basarab M. A.</i>	190, 196
<i>Bastián, J. A.</i>	341
<i>Belous O. I.</i>	823
<i>Belyaev A. S.</i>	87
<i>Berdnik S. L.</i>	273
<i>Bibikov S. B.</i>	679
<i>Bilanovskij M. M.</i>	255
<i>Blinov V. S.</i>	424
<i>Bobkov Yu. Y.</i>	203
<i>Bondarchuk G. M.</i>	644
<i>Bondarenko B. F.</i>	644
<i>Bondarenko I. N.</i>	168
<i>Bondarik A. V.</i>	761
<i>Bordjugov B. Yu.</i>	398
<i>Boromekova M. A.</i>	474
<i>Borovkov A. I.</i>	651

<i>Borulko V. F.</i>	493, 496
<i>Bozzi M.</i>	453
<i>Bratchikov A. N.</i>	617
<i>Breinbjerg O.</i>	113
<i>Bregman J.D.</i>	633
<i>Bukharov S. V.</i>	499
<i>Bulikov Ye.</i>	310
<i>Burkovsky S. I.</i>	378
<i>Burmasov V. A.</i>	320, 323, 789
<i>Bustamente Bello R.</i>	337
<i>Butakova S. V.</i>	241, 564
<i>Butrym A. Yu.</i>	598, 601, 605
<i>Bykov V. N.</i>	671, 701

C

<i>Chabanenko I. P.</i>	818
<i>Chebakov I. A.</i>	523
<i>Chelpanov A. V.</i>	417
<i>Chepiga V. N.</i>	168
<i>Cheshko T. M.,</i>	823
<i>Chukanova G. A.</i>	807
<i>Chumachenko S. V.</i>	304
<i>Chumachenko V. A.</i>	312
<i>Cordero G.</i>	539
<i>Covarruvias M.</i>	539
<i>Cremonini A.</i>	628
<i>Cruz C.</i>	539

D

<i>Danilytchev M. V.</i>	637
<i>Deguchi H.</i>	52
<i>Demidchik V. I.</i>	723
<i>Djus V. V.</i>	394
<i>Dmitriyeva N. V.</i>	644
<i>Dokhov A. I.</i>	834
<i>Don N.</i>	779
<i>Doroshenko V. A.</i>	158, 178
<i>Drobakhin O. O.</i>	401, 684
<i>Dubrov M. N.</i>	294
<i>Dubrovka F. F.</i>	91, 229, 233, 590
<i>Dubrovka R. F.</i>	233

Authors List

Dudnik B. S. 518
Dumin A. N. 583
Dumina O. A. 583

E

Eder J. 611
Egorov Ye. N. 87
Emel'chenkov F. I. 296
Ena G. O. 255
Ermolayev V. T. 333
Essiben D. J.-F. 117
Evdokimov V. V. 677
Evseeva M. V., 823
Evstropov G. A., 47

F

Falkovich I. S. 539, 631
Fetsun A. V. 739
Filinsky L. A. 684
Fisun A. I. 821, 823
Flaksman A. G. 333
Flekser P. M. 36

G

Gabriel'yan D. D. 141
Gaev A. V. 651
Galimov M. R. 101
Ganin S. A. 87
Gavva D. S. 852
Gazian L. 682
Gerasimov Yu. M. 485
Gershman A. B. 30
Gigolo A. I. 523
Girchenko A. G. 664
Glamazdin V. V. 251
Glebov V. V. 677, 701
Glushenko V. M. 255
Gnilenko A. B. 716
Goblyk V. 825
Godin S.M. 171, 173
Golovin G. A. 409
Golovin V. V. 474
Golubin M. V. 224
Gorin A. M. 248
Gorobets N. N. 459, 465, 468
Gorobets Yu. N. 821
Gorodetskaya E. Yu. 348
Grabina V. A. 821, 823

Grechko L. G. 674
Gretskih D. V. 842, 846
Grichaninyuk A. M. 671
Gridin A. A. 631
Grinev A. Yu. 523, 362
Grusha G. V. 574
Gusevsky V. I. 206, 209
Gutman A. A. 580

H

Himmelman V. G. 68, 651
Homenko S. I. 570, 572
Hubar V. A. 745

I

Illyashenko L. N. 696
Il'nitskiy L. Y. 739, 742
Ilyasov Yu. P. 648
Islamov I. J. 729
Ivanchenko D. D. 598, 677, 701
Ivanchenko I. 481
Ivanov A. I. 719
Ivashina M. V. 633
Ivkin P. V. 782

J

Jørgensen E. 113

K

Kad'kalo I. N. 248
Kalinichenko N. N. 631
Kamishhev T. V. 171, 173
Kang B.-S. 87
Karelin S. 481
Karlova D. V. 409
Karlova V.D., 417
Kasyanov A. 640
Katrich V. A. 273, 276, 280, 583
Kazanskiy O. V. 598, 601
Kazanskiy V.B. 772, 775
Keyghobad K. 509
Khachaturov V. R. 345
Khaikin V. 640
Khandogina E. 682
Khardikov V. V. 598, 601
Kharlamova D. M. 348
Khlusov V. A. 587

Authors List

Kholod P. V.	542, 546, 549	Kukobko S. V.	657
Khoroshun V. V	726	Kulik D. Yu.	570
Khymych H. P.	233	Kulikovskij Ed. I.	679
Kim O. S.	233, 113	Kulishenko S. F.	767
Kim Y.-S.	87	Kulishenko V. F.	318
Kirana A. Y.	21	Kurov N. K.	701
Kirilenko A. A.	767, 779	Kushnirenko A. G.	818
Kirillov I. G.	378	Kutuza B. G.	130, 637
Klepher E.I.	512		
Klimov K.N.	171, 173	L	
Kliuchnikau V. A.	712	Labunko O. S.	141
Klonova Yu. V.	320	Lamarre J.-M.	237
Klooster C.G.M. van't	57	Larin V.	682
Klooster Kees van't	611, 617, 624	Lavrentiev M. V.	209
Knyazeva L. V.	667	Laz'ko E.	481
Kobrin K. V.	769	Lecacheux A.	631
Kobzev A. V.	345	Lee E. G.	341
Kolchigin N. N.	598, 601, 677, 701	Lekhovitsky D. I.	36, 378, 394
Kolosova Y. V.	315, 320, 323	Lerman L. B.	664, 674
Kolyadenko Yu Yu.	421	Leshchenko S. P.	389
Komarov P. A.	491	Levagin G. A.	168
Komyachko A. A.	125	Leyva-Montiel J. L.	97, 527, 531
Kondrat'yev Ye. V.	684	Liepin U. R.	409
Konovalenko A. A.	57, 631	Ligthart L. P.	21
Kontar' A. A.	515, 517	Liske O. M.	512
Kopeikyn V. V.	561	Litvin M. M.	255
Kornienko L. G.	285	Litvin S. M.	255
Korolev A.	481	Litvin Y. P.	818
Korshunov I. P.	809	Litvinov D. D.	701
Korshunova E. N.	809	Lobkova L. M	472, 474
Kosharniy V. V.	818	Los V. F.	535
Kostyr A. V.	828	Luchaninov A. I.	81
Kotov Yu. V.	296	Luk'yanov A. S.	296
Koval Ya. A.	518	Lukashuk E. V.	315, 318
Kovalchuk V. A.	285	Lukin K. A.	288, 290
Kovalyov I. P.	333	Lukyanchikov A. V.	491
Kozakoff D. J.	25	Lukyanchuk G. A.	577
Kozar A. I.	145	Lukyanova (Bliznyuk)	481
Kozlov V. A.	818	N.	
Kravchenko V. F.	183, 190	Lupan Y. O.	644
Kravtchenko V. M.,	828	Lyaschenko V. A.	273
Krayushkin V. A.	671	Lytvyненко L. N.	57
Krupnov O. O.	229		
Kryachko V. A.	376	M	
Kryzhanovskiy V. V.	307	Machuev Yu. I.	651
Ksendzuk A. V	405, 757	Magro V. I	245
Ku B.-J.	87	Maksimova N. G.	594
Kuchinsky G. S.	68	Malashenkov S. P.	661, 664

Authors List

Malekhanov A. I. 348
 Malyuskin O. V. 830
 Manoylov V. P. 816
 Manuilov M. B. 769
 Mariotti S. 628
 Martynenko S. A. 276
 Martynyuk S. E. 91, 799
 Masyuk V. M. 216, 220
 Matveev R. F. 294
 Meincke P. 113
 Mickhayluck Yu. P. 751
 Mikryukov A. S. 507
 Mirkamali A. 509
 Misajlov V. L. 594
 Mishchenko S. E. 488
 Mishustin B. A. 501, 504
 Mitrofanova T. V. 734
 Modelski J. 687
 Mokeev Yu. G. 677
 Morales-Mendoza L. J. 531
 Morozov G. A. 101
 Morozov O. G. 101
 Morozov V. M. 245
 Murphy J. A. 237
 Myakinkov A. V. 355
 Myasnikova S. E. 624
 Mytsenko I. M. 572

N

Naidenko V. I. 731
 Nakano Miyatake M. 337, 341
 Natarov M. P. 251, 290
 Nazarchuk L. U. 816
 Nazarenko T. G. 125
 Nesterenko G. V. 518
 Nesterenko M. V. 280
 Nicolaev A. G. 637
 Nikitin N. M. 370
 Novikov V. E. 692

O

Obelchenko V. V. 518
 Ogurtsova T. N. 546, 549
 Oleynikov V. 856
 Olshevskiy A. L. 18
 Omarov M. A. 842
 Onipko A. F. 677
 Onufriyenko V. M. 107

Orfei A. 628
 Orlenko V. M. 389
 Orlov V. V. 679
 Orlov S. V. 671
 Otchenashko S. N. 789
 Ovchinnikova E. V. 77
 Ovsyanikov V. V. 468

P

Paliy O. V. 716
 Parshin V. V. 624
 Pazynin V. L., 110, 705
 Perekaty V. N. 327
 Peretyatko T. V. 165
 Pérez Meana H. 337, 341
 Perregrini L. 453
 Petrov V. V. 734
 Petrushenko N. N. 409, 417
 Pilenkova V. I. 818
 Pivnenko S. N. 465, 601
 Platonov S. Y. 644
 Pluzhnikov A. D. 352
 Pochanin G. P. 542, 546, 549
 Pochanina I. Ye. 542
 Podlevskiy B. M. 213
 Pogarsky S. A. 312
 Pokataev V. N. 818
 Polishko S. V. 36
 Polyarus A. V. 594
 Ponce-Davalos J. L. 527
 Popenko N. 481
 Popov A. I. 823
 Popov A. V. 561
 Popovskiy V. V. 419
 Potapova O. V. 258
 Potapova V. M. 818
 Poyedinchuk A. 779
 Pribludova E. N. 352
 Protsenko M. B. 491
 Prudyus I. N. 512
 Pshenichnaya S. V. 276
 Puzanov A. O. 692

R

Rafalskii U. I. 417
 Redkina E. A. 504
 Reutov A. S. 264
 Reutov A. C. 87

<i>Rodenko S. N.</i>	42	<i>Shubny A. I.</i>	251
<i>Rodionov A. A.</i>	414	<i>Shubov A. G.</i>	87
<i>Roenko A. N.</i>	572	<i>Shugurov A. S.</i>	818
<i>Rogulyev V. A.</i>	47	<i>Shulga S. N.</i>	785, 830
<i>Roshchin V. V.</i>	171, 173	<i>Shurda G. G.</i>	807
<i>Rospopa V. O.</i>	229	<i>Sibruk L. V.</i>	742
<i>Rozdobudko V. V.</i>	362	<i>Sidorenko Y. B.</i>	300
<i>Ruban V. P.</i>	553	<i>Sin'kov V. V.</i>	692
<i>Ruchentov V. A.</i>	171, 173	<i>Sinyavsky G. P.</i>	769
<i>Rucker H.</i>	631	<i>Sirenko K. Yu.</i>	110
<i>Rudakov V. I.</i>	813, 828	<i>Sirenko Yu. K.</i>	110, 705
<i>Rudenko V. N.</i>	323	<i>Sitsko N. U.</i>	723
<i>Rudnik A. G.</i>	261	<i>Skobelev S. P.</i>	477
<i>Rybalko A. M.</i>	846	<i>Skresanov V. N.</i>	251, 290
<i>Ryndyk A. G.</i>	355	<i>Slyozkin V. G.</i>	501, 504
S		<i>Slyusar V. I.</i>	374
<i>Salamatin V. V.</i>	577	<i>Soleimani M.</i>	509
<i>Saprykin S. D.,</i>	47	<i>Solonskaya S. V.</i>	834
<i>Savenko P. A.</i>	708	<i>Solyanik O.</i>	856
<i>Savochkin A. A.</i>	751	<i>Soroka A. S.</i>	261
<i>Sazonov A. Z.</i>	657	<i>Soshenko V. A.</i>	692
<i>Sedyshev P. Yu.</i>	42	<i>Sosulnikov V. P.,</i>	47
<i>Sedyshev Yu. N.</i>	42	<i>Staheev N. A.</i>	394
<i>Semchuk A. Yu.</i>	674	<i>Starostenkov E. A.</i>	47
<i>Semenikhina D. V.</i>	837	<i>Stepanenko P. Y.</i>	590, 796, 799
<i>Semenova E. K.</i>	178	<i>Storozh V. G.</i>	512
<i>Sestoretiskii B. V.</i>	171, 173	<i>Strelchenko V. I.</i>	834
<i>Shakhbazov V. G.</i>	821, 823	<i>Sugonyak Z. V.</i>	742
<i>Shamanov A. N.</i>	535	<i>Sukharevsky O. I.</i>	657
<i>Shaposhnikov S. S.</i>	809	<i>Sukhomlinov D. V.</i>	842
<i>Sharygin G. S.</i>	587	<i>Sultanov O. Z.</i>	384
<i>Sharygina L. I.</i>	587	<i>Suserov Yu. A.</i>	87
<i>Shatrov A. D.</i>	809	<i>Syrotyuk V. H.</i>	233
<i>Shatsman L. G.</i>	370	<i>Sytnik O. V.</i>	359
<i>Shckorbatov Yu. G.</i>	821, 823	<i>Syvozalizov M. A.</i>	726
<i>Shevchenko D. V.</i>	651	<i>Szafran M.</i>	687
<i>Shigesawa H.</i>	52	T	
<i>Shilo S. A.</i>	671, 701	<i>Takano T.</i>	63
<i>Shifrin Ya. S.</i>	81	<i>Tapia-Sanchez D.</i>	337
<i>Shirman Y. D.</i>	389	<i>Tarshin V. A.</i>	381
<i>Shirokov I. B.</i>	387	<i>Temchenko V. S.</i>	362
<i>Shishkova A. V.</i>	465	<i>Tereschenko V. M.</i>	590, 796, 799
<i>Shishlov A. V.</i>	87, 264	<i>Tereshchenko A. I.</i>	805
<i>Shitikov A. M.</i>	87, 761	<i>Titarenko L. A.</i>	398
<i>Shkvarko Yu. V.</i>	97, 527, 531	<i>Titov A. A.</i>	556
<i>Shokalo V. M.</i>	846	<i>Titov A. N.</i>	556
<i>Shrenk O. E.</i>	255		

432 International Conference on Antenna Theory and Techniques, 9-12 September, 2003, Sevastopol, Ukraine